

Marthe Bacal *Editor*

Physics and Applications of Hydrogen Negative Ion Sources

Springer Series on Atomic, Optical, and Plasma Physics

Volume 124

Editor-in-Chief

Gordon W. F. Drake, Department of Physics, University of Windsor, Windsor, ON, Canada

Series Editors

James Babb, Harvard-Smithsonian Center for Astrophysics, Cambridge, MA, USA

Andre D. Bandrauk, Faculté des Sciences, Université de Sherbrooke, Sherbrooke, QC, Canada

Klaus Bartschat, Department of Physics and Astronomy, Drake University, Des Moines, IA, USA

Charles J. Joachain, Faculty of Science, Université Libre Bruxelles, Bruxelles, Belgium

Michael Keidar, School of Engineering and Applied Science, George Washington University, Washington, DC, USA

Peter Lambropoulos, FORTH, University of Crete, Iraklion, Crete, Greece

Gerd Leuchs, Institut für Theoretische Physik I, Universität Erlangen-Nürnberg, Erlangen, Germany

Alexander Velikovich, Plasma Physics Division, United States Naval Research Laboratory, Washington, DC, USA


The Springer Series on Atomic, Optical, and Plasma Physics covers in a comprehensive manner theory and experiment in the entire field of atoms and molecules and their interaction with electromagnetic radiation. Books in the series provide a rich source of new ideas and techniques with wide applications in fields such as chemistry, materials science, astrophysics, surface science, plasma technology, advanced optics, aeronomy, and engineering. Laser physics is a particular connecting theme that has provided much of the continuing impetus for new developments in the field, such as quantum computation and Bose-Einstein condensation. The purpose of the series is to cover the gap between standard undergraduate textbooks and the research literature with emphasis on the fundamental ideas, methods, techniques, and results in the field.

Marthe Bacal
Editor

Physics and Applications of Hydrogen Negative Ion Sources

 Springer

Editor

Marthe Bacal 
University Pierre and Marie Curie
Laboratory of Plasma Physics
Ecole Polytechnique
Paris, France

ISSN 1615-5653 ISSN 2197-6791 (electronic)
Springer Series on Atomic, Optical, and Plasma Physics
ISBN 978-3-031-21475-2 ISBN 978-3-031-21476-9 (eBook)
<https://doi.org/10.1007/978-3-031-21476-9>

© The Editor(s) (if applicable) and The Author(s), under exclusive license to Springer Nature Switzerland AG 2023

This work is subject to copyright. All rights are solely and exclusively licensed by the Publisher, whether the whole or part of the material is concerned, specifically the rights of translation, reprinting, reuse of illustrations, recitation, broadcasting, reproduction on microfilms or in any other physical way, and transmission or information storage and retrieval, electronic adaptation, computer software, or by similar or dissimilar methodology now known or hereafter developed.

The use of general descriptive names, registered names, trademarks, service marks, etc. in this publication does not imply, even in the absence of a specific statement, that such names are exempt from the relevant protective laws and regulations and therefore free for general use.

The publisher, the authors, and the editors are safe to assume that the advice and information in this book are believed to be true and accurate at the date of publication. Neither the publisher nor the authors or the editors give a warranty, expressed or implied, with respect to the material contained herein or for any errors or omissions that may have been made. The publisher remains neutral with regard to jurisdictional claims in published maps and institutional affiliations.

This Springer imprint is published by the registered company Springer Nature Switzerland AG
The registered company address is: Gewerbestrasse 11, 6330 Cham, Switzerland

Preface

This book discusses the physics and applications of negative hydrogen/deuterium (H^-/D^-) ion sources in the context of magnetic confinement fusion research and high-energy proton accelerator applications.

On the route of sustainable power from magnetic confinement fusion reactions, ITER (“the way” in Latin) is an international nuclear fusion research and engineering megaproject aimed at creating a device in which fusion processes create energy on Earth in a way that is similar to the way energy is produced in the Sun. It is currently under construction at Saint Paul-lez-Durance, in southern France.

The ITER machine is the stage before a demonstration fusion reactor, the goal being to explore and to study the physics and technology at a scale close to that of the reactor. The fusion power will however be moderate: 500 MW of D–T fusion reactions in the plasma core are expected to last <3600 s, without electricity production. Its goal is to establish the technological feasibility of fusion energy for peaceful use. The cross section of the D-T fusion reaction varies with the interaction energy, having a maximum at about 100 keV. Therefore, to have the required high rate of fusion reactions means that not only must the density of the reactants, D^+ and T^+ , be high enough, and that they are confined long enough in the plasma that they will “find” each other and react, but also that that they are hot enough that the rate of fusion reactions is high enough to produce the required energy from a fusion reactor. Neutral beam systems are one of the possible ways to heat the plasma in ITER, and future fusion devices, to the temperatures at which sufficient fusion reactions occur. Achievement of an economic fusion reactor imposes a high level of unprecedented requirements for neutral beam systems; the first one is the nuclear safety which requires access to all injector components to allow preventive (and curative) maintenance by remote handling.

The heating neutral beam injectors of ITER are designed to deliver 16.7 MW of 1 MeV D^0 (deuterium atoms) or 0.87 MeV H^0 (hydrogen atoms) to the ITER plasma for up to 3600 s. They will be the most powerful neutral beam injectors ever built, delivering higher energy neutral beams to the plasma in a tokamak for longer than any previous systems have done. The design of the heating neutral beams is based on the acceleration and neutralisation of negative ions as the efficiency of conversion of

accelerated positive ions is very low at the required energy (Hemsworth et al. 2005) so that a realistic design based on the neutralisation of accelerated positive ions is not possible, whereas the neutralisation efficiency of hydrogen and deuterium negative ions remains acceptable ($\approx 56\%$) (Hemsworth et al. 2017).

ITER is still an experimental device and will not produce any electricity. DEMO is a proposed class of nuclear fusion experimental reactors that are intended to demonstrate the net production of electric power from nuclear fusion. The EU DEMO design of 2 to 4 gigawatts of thermal output will be on the scale of a modern electric power station.

DEMO will link the energy production by nuclear fusion with electricity generation and should be the last machine before a commercial fusion reactor.

The interest for H^-/D^- ion beams is due to the need for energetic beams of neutral hydrogen/deuterium atoms for heating the plasma in tokamaks up to the burning temperature, and for driving current in the fusing plasma. The latter arises because the tokamak type of fusion device (of which ITER is one) requires a substantial current (10s of MA) circulating in the plasma in order to produce the confining magnetic field configuration. That current is initially produced inductively, but other means are necessary to produce the current for long pulses, or continuously, as required for a reactor. A natural “bootstrap” current is driven by the plasma pressure occurs in the outer parts of the plasma, but external means are needed to produce the current near the main axis of the tokamak machine. Injecting neutral beams can do just that. That is known as current drive.

Since high-energy atomic beams are required in fusion research, the need for producing their precursors, the negative ion beams, became urgent. This imposed the development of negative hydrogen ion sources, which are based on two types of processes:

- In the *plasma volume*, H^-/D^- ions are formed by dissociative attachment of electrons to ro-vibrationally excited hydrogen/deuterium molecules.
- On *surfaces*, H^-/D^- ions are formed by the interaction between hydrogen/deuterium particles and low work function surface facing the plasma.

The use of negative ion sources in high-energy accelerators began in the 1950s, *e.g.* in Tandem Van-de-Graaf accelerators (Alvarez 1951). In the 1960s, negative ion sources were used in cyclotrons (Ehlers 1965) and the use of charge-exchange injection of H^- ions (Martin 1971) (see the review by Dimov (1996)). The implementation of charge-exchange injection in numerous circular high-energy accelerators led to the development of hydrogen negative ion source research and development worldwide. The first generation of negative hydrogen ion sources were charge exchange sources, using a single aperture proton source. To increase the intensity, multi-aperture sources were used in the early 1970s (Dimov et al. 1974; Fasolo 1977). Further increase of the intensity was obtained by using double charge exchange in alkali metal vapor (Hooper et al. 1977; Semashko et al. 1977).

However, in the 1970s a new step in the development of negative ion sources with parameters sufficient for modern accelerators was the development of the plasma-surface sources. In these sources, the addition of caesium vapor to the

hydrogen discharge generates low work function surfaces capable of emitting H^- ions under bombardment by plasma atoms or ions. At the Institute of Nuclear Physics in Novosibirsk (USSR) (Belchenko et al. 1973), small discharge devices in planatron (magnetron) and Penning geometry were studied, while at Lawrence Berkeley National Laboratory (Ehlers et al. 1980), a surface-plasma source was based on a negatively biased caesiated electrode called a converter, collecting the positive ions extracted from the plasma confined in a magnetic multipole. The H^- ion production process in these sources is designated as the surface-plasma production mechanism.

In 1977, at Ecole Polytechnique (Palaiseau, France), the presence of an unexpectedly high fraction of H^- ions in low pressure hydrogen discharges was identified (Nicolopoulou et al. 1977). This result was confirmed in 1979 using the photodetachment technique (Bacal et al. 1979) and demonstrated the existence of the volume production mechanism.

The H^-/D^- ion source research in the following decades was dedicated to understanding the physics underlying these two mechanisms. In the meantime, the embodiment of these mechanisms in the design of new sources was actively developed.

The development of negative ion sources was discussed at the International Symposia on the Production and Neutralization of Negative Hydrogen Ions and Beams between 1977 and 2006, and their proceedings were published in special issues of *Rev. Sci. Instrum.* Since 2008, this research was presented at the symposia called NIBS (Negative Ion Beams and Sources), which published their own proceedings.

This book presents the fundamental aspects of hydrogen negative ion production in the negative ion sources (Chaps. 1, 2, and 3), their modelling and neutralisation of the accelerated beams (Chaps. 4, 5, and 6), particular aspects of volume negative ion source physics (Chaps. 7, 8, 9, 10, 11, 12, and 13), particular aspects of surface-plasma production physics (Chaps. 14 and 16), particular aspects of negative ion source technique and technology (Chaps. 17, 18, 19, and 20), and also the diagnostic of negative ions in plasma (Chap. 15). Bibliography

Paris, France
Barcelona, Spain

Marthe Bacal
Ronald Stephen Hemsworth

References

- L.V. Alvarez, *Rev. Sci. Instrum.* **22**, 705 (1951)
 M. Bacal, G.W. Hamilton, *Phys. Rev. Lett.* **42**(23), 1538 (1979)
 Y.I. Belchenko, G.I. Dimov, V.G. Dudnikov, *Izv. Akad. Nauk SSSR, Ser. Fiz.* **37**, 2573 (1973)
 G.I. Dimov, *Rev. Sci. Instrum.* **67**(10), 3393 (1996)
 G.I. Dimov, G.V. Roslyakov, *Priboory Tekh. Eksper. (Instrum. Exp. Tech., in russian)* **29** (1974)
 K.W. Ehlers, K.N. Leung, *Rev. Sci. Instrum.* **51**, 721 (1980)
 J.A. Fasolo, *IEEE Trans. Nucl. Sci.* **NS-24**, 1597 (1977)

- R.S. Hemsworth, D. Boilson, H.P.L. De Esch, A. Krylov, P.I. Massmann, L. Svensson, *Nucl. Fusion* **46**, S239–S249 (2006)
- R.S. Hemsworth et al., *N. J. Phys.* **19**, 025005 (2017)
- E.B. Hooper, Jr., O.A. Anderson, T.J. Orzechowski, P. Poulsen, *Proc. Symp. on the Production and Neutralization of Negative Hydrogen Ions and Beams*, Sept. 26–30 (1977), BNL Report 50727, K. Prelec, Editor, 163 (1977)
- E. Nicolopoulou, M. Bacal, H.J. Doucet, *J. Phys. (Paris)* **38**, 1399–1404 (1977), also in *Proc. Symp. on the Production and Neutralization of Negative Hydrogen Ions and Beams*, BNL Report 50727, K. Prelec, Editor, 26 (1977)
- N.N. Semashko, V.V. Kusnetsov, A.I. Krylov, *Proc. Symp. on the Production and Neutralization of Negative Hydrogen Ions and Beams*, Sept. 26–30 (1977), BNL Report 50727, K. Prelec, Editor, 170 (1977)
- Simonin, C. Blondel, W. Chaibi, C. Dechelle, C. Drag, E. Villedieu, *Nucl. Fusion* **61**, 046003 (2021)

Contents

1	Fundamental Processes of Hydrogen Negative Ion Production in Ion Source Plasma Volume	1
	Marthe Bacal and Motoi Wada	
2	Fundamental Aspects of Surface Production of Hydrogen Negative Ions	29
	Motoi Wada	
3	Modeling of Reaction Dynamics in Volume-Production Negative Hydrogen Ion Sources	51
	Wei Yang	
4	Particle-In-Cell Modeling of Negative Ion Sources for Fusion Applications	71
	Francesco Taccogna, Gwenael Fubiani, and Pierpaolo Minelli	
5	Electrostatic and Electromagnetic Particle-In-Cell Modelling with Monte-Carlo Collision for Negative Ion Source Plasmas	101
	Kenji Miyamoto and Takanori Shibata	
6	Plasma and Gas Neutralisation of High-Energy H^- and D^-	139
	Ronald Stephen Hemsworth and Alexander Panasenkov	
7	Advanced Models for Negative Ion Production in Hydrogen Ion Sources	167
	Roberto Celiberto, Mario Capitelli, Annarita Laricchiuta, Lucia Daniela Pietanza, and Gianpiero Colonna	
8	The Plasma Sheath in Negative Ion Sources	189
	R. McAdams, A. J. T. Holmes, and D. B. King	

9 Helicon Volume Production of H^- and D^- Using a Resonant Birdcage Antenna on RAID	217
Ivo Furno, Riccardo Agnello, Alan Howling, Philippe Guittienne, Remy Jacquier, Christine Stollberg, Marcelo Baquero, Lyes Kadi, Claudio Marini, Jia Han, Stéphane Béchu, Gwenael Fubiani, Alain Simonin, and Francesco Taccogna	
10 Plasma Electrode for Cesium-Free Negative Hydrogen Ion Sources .	251
Mamiko Sasao and Gilles Cartry	
11 Low-Temperature High-Density Negative Ion Source Plasma	277
Hiroshi Horiike and Yoshikazu Okumura	
12 ECR-Driven Negative Ion Sources Operating with Hydrogen and Deuterium	303
P. Svarnas, M. Mitrou, J. L. Lemaire, L. Gavilan, N. de Oliveira, and S. Béchu	
13 Vibrational Spectroscopy of Hydrogen Molecules by Detecting H^- (D^-) and Its Use in Studies Relevant to Negative Ion Sources	349
Iztok Čadež and Sabina Markelj	
14 Physics of Surface-Plasma H^- Ion Sources	379
Yuri I. Belchenko and Motoi Wada	
15 Hydrogen Negative Ion Density Diagnostic in Plasma	417
Marthe Bacal and Motoi Wada	
16 RF-Driven Ion Sources for Neutral Beam Injectors for Fusion Devices	427
Ursel Fantz	
17 Ion Source Engineering and Technology	465
Dan Faircloth	
18 Radio Frequency-Driven, Pulsed High-Current H^- Ion Sources on Advanced Accelerators	513
Martin P. Stockli	
19 Development of High-Current Negative-Ion-Based Beam Source at the National Institutes for Quantum Science and Technology (QST) in Japan for JT-60 U and ITER Neutral Beam Injectors	577
Takashi Inoue	
Postface	609

Contributors

Riccardo Agnello Swiss Plasma Center (SPC), Ecole Polytechnique Fédérale Lausanne (EPFL), Lausanne, Switzerland

Marthe Bacal University Pierre and Marie Curie, Laboratory of Plasma Physics, Ecole Polytechnique, Paris, France

Marcelo Baquero Swiss Plasma Center (SPC), Ecole Polytechnique Fédérale Lausanne (EPFL), Lausanne, Switzerland

Stéphane Béchu Université Grenoble-Alpes, CNRS, Grenoble INP, LPSC-INP23, Grenoble, France

Yuri I. Belchenko Budker Institute of Nuclear Physics, Novosibirsk, Russia

Iztok Čadež Jožef Stefan Institute, Ljubljana, Slovenia

Mario Capitelli CNR ISTP (Istituto per la Scienza e Tecnologia dei Plasmi) Bari Section, Bari, Italy

Gilles Cartry Aix-Marseille University, Marseille, France

Roberto Celiberto Dipartimento di Ingegneria Civile, Ambientale, del Territorio, Edile e di Chimica (DICATECh), Politecnico di Bari, Bari, Italy
CNR ISTP (Istituto per la Scienza e Tecnologia dei Plasmi) Bari Section, Bari, Italy

Gianpiero Colonna CNR ISTP (Istituto per la Scienza e Tecnologia dei Plasmi) Bari Section, Bari, Italy

N. de Oliveira DESIRS beamline, Synchrotron SOLEIL, Gif sur Yvette, France

Dan Faircloth STFC UKRI, Oxfordshire, UK

Ursel Fantz Max Planck Institut für Plasmaphysik, Garching, Germany

Gwenael Fubiani CNRS-Laboratoire PLASMA et Conversion d'Énergie, Université de Toulouse, Toulouse Cedex, France

Ivo Furno Swiss Plasma Center (SPC), Ecole Polytechnique Fédérale Lausanne (EPFL), Lausanne, Switzerland

L. Gavilan Space Science and Astrobiology Division, NASA Ames Research Center, Moffett Field, CA, USA

Philippe Guittienne Swiss Plasma Center (SPC), Ecole Polytechnique Fédérale Lausanne (EPFL), Lausanne, Switzerland

Jia Han Swiss Plasma Center (SPC), Ecole Polytechnique Fédérale Lausanne (EPFL), Lausanne, Switzerland

Ronald Stephen Hemsworth Neutral Beam Expert with Fusion for Energy, Barcelona, Spain

A. J. T. Holmes Marcham Scientific, Hungerford, Berkshire, UK

Hiroshi Horiike Nuclear Engineering, Osaka University, Osaka, Japan

Alan Howling Swiss Plasma Center (SPC), Ecole Polytechnique Fédérale Lausanne (EPFL), Lausanne, Switzerland

Takashi Inoue National Institutes for Quantum Science and Technology, Naka, Ibaraki, Japan

Remy Jacquier Swiss Plasma Center (SPC), Ecole Polytechnique Fédérale Lausanne (EPFL), Lausanne, Switzerland

Lyes Kadi Swiss Plasma Center (SPC), Ecole Polytechnique Fédérale Lausanne (EPFL), Lausanne, Switzerland

D. B. King United Kingdom Atomic Energy Authority, Culham Centre for Fusion Energy, Culham Science Centre, Abingdon, Oxon, UK

Annarita Laricchiuta CNR ISTP (Istituto per la Scienza e Tecnologia dei Plasmi) Bari Section, Bari, Italy

J. L. Lemaire Institut des Sciences Moléculaires d'Orsay (ISMO), CNRS-Université Paris-Sud (UMR8214), Orsay, France

Claudio Marini Swiss Plasma Center (SPC), Ecole Polytechnique Fédérale Lausanne (EPFL), Lausanne, Switzerland

Sabina Markelj Jožef Stefan Institute, Ljubljana, Slovenia

R. McAdams United Kingdom Atomic Energy Authority, Culham Centre for Fusion Energy, Culham Science Centre, Abingdon, Oxon, UK

Pierpaolo Minelli CNR-Institute for Plasma Science and Technology, Bari, Italy

M. Mitrou University of Patras, Electrical and Computer Engineering Department, Patras, Greece

Université Grenoble Alpes, CNRS, Grenoble INP (Institute of Engineering), Grenoble, France

Kenji Miyamoto Naruto University of Education, Naruto, Japan

Yoshikazu Okumura National Institute for Quantum Science and Technology, Chiba, Japan

Alexander Panasenkov National Research Center Kurchatov Institute, Moscow, Russia

Lucia Daniela Pietanza CNR ISTP (Istituto per la Scienza e Tecnologia dei Plasmi) Bari Section, Bari, Italy

Mamiko Sasao Office for R&D promotion, Doshisha University, Kyoto, Japan

Takanori Shibata Accelerator Laboratory, KEK, Tsukuba, Japan

Alain Simonin CEA, IRFM, St-Paul-lez-Durance, France

Martin P. Stockli Spallation Neutron Source, Oak Ridge National Laboratory, Oak Ridge, TN, USA

Christine Stollberg Swiss Plasma Center (SPC), Ecole Polytechnique Fédérale Lausanne (EPFL), Lausanne, Switzerland

P. Svarnas University of Patras, Electrical and Computer Engineering Department, Patras, Greece

Francesco Taccogna CNR-Institute for Plasma Science and Technology, Bari, Italy

Motoi Wada Graduate School of Science and Engineering, Doshisha University, Kyotanabe, Kyoto, Japan

Wei Yang College of Science, Donghua University, Shanghai, China

Chapter 1

Fundamental Processes of Hydrogen Negative Ion Production in Ion Source Plasma Volume



Marthe Bacal  and Motoi Wada

Abstract Negative hydrogen/deuterium ions can be formed by processes occurring in the plasma volume and on surface facing the plasma. The principal mechanism leading to the formation of these negative ions in the plasma volume is dissociative electron attachment to ro-vibrationally excited hydrogen/deuterium molecules. The existing theoretical models and reported experimental results on this mechanism are summarized. The performance of the negative hydrogen ion sources that emerged from these studies is reviewed.

Keywords Hydrogen · Deuterium · Negative ion source · Dissociative electron attachment · Neutralization efficiency · Neutral beam · Vibrational excitation · Plasma electrode

1.1 Need of Negative Ion Beams for Magnetic Confinement Fusion Research and for High Energy Accelerators

This chapter discusses the negative hydrogen/deuterium (H^-/D^-) ion production mechanisms in the context of negative hydrogen ion sources for magnetic confinement fusion research and high-energy proton accelerator applications. Toward the route of sustainable power from magnetic confinement fusion reactions, the International Tokamak Experimental Reactor (ITER) is currently under construction at Cadarache in France. ITER will operate to produce a net output of fusion power that exceeds the heating power by a factor of $Q = 10$ and should produce a self-sustaining fusion burning plasma for several hundred seconds. Demonstrating the

M. Bacal (✉)

University Pierre and Marie Curie, Laboratory of Plasma Physics, Ecole Polytechnique, Paris, France

M. Wada

Doshisha University, Kyoto, Japan
e-mail: mwada@mail.doshisha.ac.jp

production of net electricity and operating with a closed fuel cycle are crucial steps toward the exploitation of fusion power. These are the aims of the demonstration fusion reactor (DEMO) proposed to be built after ITER (Federici et al. 2012). Neutral beam heating power as high as 33 MW is planned for ITER, while 135 MW will be necessary for the steady-state operation of the next-generation fusion reactor, DEMO. McAdams (2014) discusses the physics and technological challenges for the neutral beam systems to meet the requirements for DEMO and beyond.

In ITER, a D^- negative ion current of 40 A is accelerated up to 1 MV before negative ions are neutralized to pass through the confinement magnetic field. The pulse length is 3600 s. The development of negative ion sources and extractors for long-pulse and high-power ion beams are pursued in fusion research institutes worldwide, e.g. IPP Garching (Fantz et al. 2014a, b) (Germany), Consorzio RFX (Padova, Italy) (Agostinetti et al. 2016), JAEA (Kashiwagi et al. 2014; Umeda et al. 2014) and NIFS (Takeiri et al. 2013) (Japan).

A beam of energetic hydrogen atoms, also called neutral beam, can be generated from positive hydrogen ion beams by letting them pass through a gas neutralizer. However, the neutralization efficiency of positive hydrogen ions declines rapidly as the ion kinetic energy exceeds 60 keV/amu. The neutralization efficiency becomes prohibitively low above this energy (Hemsworth and Inoue 2005) (see Fig. 1.1). The neutralization efficiency of negative hydrogen ions in a neutralizer cell of optimum thickness remains acceptable at higher ion kinetic energy and is nearly independent on beam energy above 100 keV/nucleon. Since high-energy atomic beams are required in fusion research, the need for producing their precursors, the negative ion beams, became urgent. This imposed the development of negative hydrogen ion sources, which are based on two types of processes:

- In the *plasma volume*, H^-/D^- ions are formed by dissociative attachment of electrons to ro-vibrationally excited hydrogen/deuterium molecules.

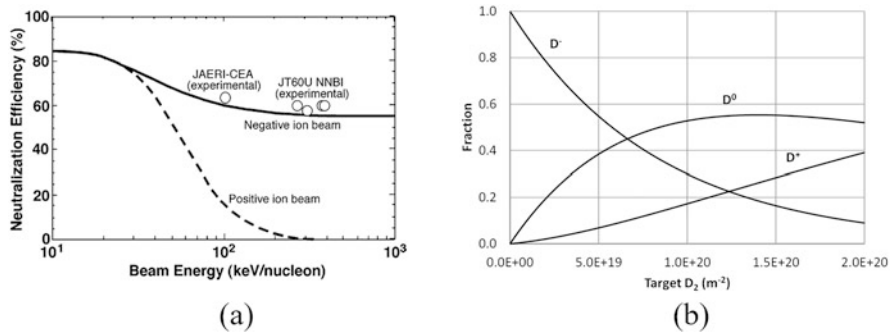


Fig. 1.1 (a) Neutralization efficiency versus beam energy. (Reproduced from Bacal and Wada (2015) Fig. 1). The beam energy is in keV/nucleon; therefore, this figure applies to all the isotopes of hydrogen. (b) Dependence of the fractions of D^- , D^0 , and D^+ on the deuterium molecule line density for the incident D^- ion energy of 1 MeV. (Reproduced from Hemsworth and Inoue (2005) with permission of IEEE)

- On *surfaces*, H^-/D^- ions are formed by the interaction between hydrogen/deuterium plasma and low work function surface facing the plasma.

The use of negative ion sources began in the 1950s, e.g. in Tandem Van-de-Graaf accelerators (Alvarez 1951). In the 1960s, negative ion sources were used in cyclotrons (Ehlers 1965) and the use of charge-exchange injection of H^- ions (Martin 1971) (see a review by Dimov (1996)). The implementation of charge-exchange injection in numerous circular high-energy accelerators led to the development of hydrogen-negative ion source research and development worldwide. The first generation of negative hydrogen ion sources were charge exchange sources, using a single aperture proton source. To increase the intensity, multiaperture sources were used in the early 1970s (Dimov et al. 1974; Fasolo 1977). Further increase of the intensity was obtained by using double charge exchange in alkali metal vapor (Hooper Jr. et al. 1977; Semashko et al. 1977).

However, in the 1970s, a new step in the development of negative ion sources with parameters sufficient for modern accelerators was the development of plasma-surface sources. In these sources, the addition of caesium vapor to the hydrogen discharge generates low-work function surfaces capable of emitting H^- ions under bombardment by plasma atoms or ions. At the Institute of Nuclear Physics in Novosibirsk (USSR) (Belchenko et al. 1973), small discharge devices in planatron (magnetron) and Penning geometry were studied, while at Lawrence Berkeley National Laboratory (Ehlers and Leung 1980), a surface-plasma source was based on a negatively biased caesiated electrode called converter, collecting the positive ions extracted from the plasma confined in a magnetic multipole. The H^- ion production processes in these sources are designated as the surface production mechanism.

In 1977 at Ecole Polytechnique (Palaiseau, France), the presence of an unexpectedly high fraction of H^- ions in low-pressure hydrogen discharges was identified (Nicolopoulou et al. 1977). This result was confirmed in 1979 using the photodetachment technique (Bacal and Hamilton 1979). This was the demonstration of the existence of the volume production mechanism. The H^-/D^- ion source research in the following decades was dedicated to understanding the physics underlying these two mechanisms. In the meantime, the embodiment of these mechanisms in the design of new sources was actively developed.

This chapter is dedicated to discussing volume H^-/D^- ion production mechanisms. In Sect. 1.2, dedicated to the volume production mechanism, we will present: (A) the early experiments (before 1978) with direct extraction negative ion sources, which indicated that H^- production in plasmas was not due to mechanisms known earlier; (B) H^- ion formation mechanisms in the plasma volume: the dissociative electron attachment to rovibrationally excited hydrogen molecules appeared to be the principal mechanism leading to negative ion production in plasmas in pure hydrogen/deuterium; (C) experimental verification of the volume production mechanism: a comparison of predictions of this physical model to the measured characteristics in a typical plasma source, the magnetic multipole, operating in pure hydrogen.

In Sect. 1.3, two important volume ion sources are described, namely the Penning sources and the magnetically filtered multicusp negative ion source. In Sect. 1.4, the characteristics of the main H^- ion reactions will be discussed.

1.2 The Volume Production Mechanism

1.2.1 *Early Direct Extraction Negative Ion Sources (Before 1980)*

A review of the early direct extraction negative ion sources in pure hydrogen by Prelec and Sluyters (1973) describes four types of such sources: duoplasmatrons, hollow discharge duoplasmatrons, Penning sources, and magnetron sources. Moak et al. (1959) from Oak Ridge first reported the possibility of extracting an H^- beam directly from a duoplasmatron. In 1965, Lawrence et al. (1965) found that the intensities of H^- ion currents could be increased and the co-extracted electron currents reduced by off-axis extraction. However, the negative ion currents were in the tens of microamps range. In the same year (1965) Ehlers and Leung in Berkeley reported the extraction of a continuous H^- current of 5.3 mA (with a current density of 40 mA/cm^2) from a hot-cathode Penning-type source (Ehlers and Leung 1980). In 1973, a magnetron-type source, the planotron, was developed by Belchenko et al. (1974), (Belchenko et al. 1988) in the Budker Institute for Nuclear Physics in Novosibirsk. In this source, the discharge chamber has the shape of a race track, and the plasma is kept circulating in the narrow space by the ExB drift motion. A short pulsed beam (1 μs , 3 Hz) of H^- ions with a current of 20 mA was obtained through an emission slit of $1 \times 10 \text{ mm}^2$.

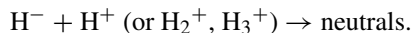
1.2.2 *Observation of a New H^- Ion Formation Mechanism in the Plasma Volume*

In 1977, Nicolopoulou et al. (1977) calculated the equilibrium density of hydrogen negative ions in a low-pressure hydrogen plasma taking into account the known production and destruction processes. At that time, the known production processes due to low energy electrons were dissociative electron attachment to hydrogen molecules in their ground state and dissociative recombination of molecular positive ions H_2^+ . Measurement of the negative ion density in a plasma produced in a magnetic multipole using a probe diagnostic technique indicated that the measured H^- ion density was higher by a factor of 100 than the equilibrium density calculated by considering the known formation and destruction processes.

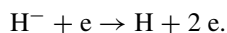
This result was confirmed in 1979 by Bacal and Hamilton (1979) using a photodetachment diagnostic technique for the measurement of the H^- ion density.

Due to the low binding energy of the electron in H^- ion, the electron detachment in collisions with other particles is fairly efficient. The H^- ions can be destroyed in the plasma volume by the following processes (Janev et al. 2003; Barnett et al. 1977):

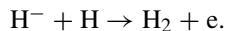
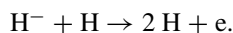
By two-body recombination or mutual neutralization:



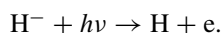
By collision with an electron:



By collision with an atom (associative detachment):



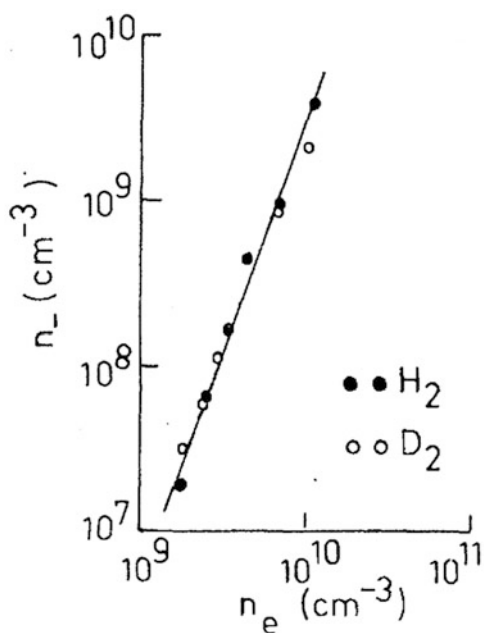
Or by photodetachment:



A detailed description of the photodetachment reaction and the corresponding negative ion density diagnostic technique is presented in Chap. 15.

The first confirmation of high negative ion density in hydrogen isotope plasmas using laser light included the measurement with a deuterium plasma. Figure 1.2 shows the dependence of the negative ion density n_- upon the electron density n_e in H_2 and D_2 plasmas confined only by their ambipolar potential. The neutral gas

Fig. 1.2 Dependence of n_- upon n_e in H_2 and D_2 Bacal and Hamilton (1979), © 1979. (Reproduced from Bacal and Wada (2015), Fig. 2)

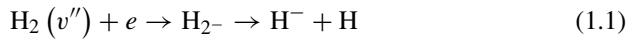


density was $2 \times 10^{14} \text{ cm}^{-3}$. Figure 1.2 indicates that the negative-ion density is not isotope dependent but increases approximately in proportion to n_e^3 in the studied range of electron density. In H_2 , the electron temperature varied in the range from 0.10 to 0.40 eV, while at maximum density, the ratio of n_-/n_e was 0.35.

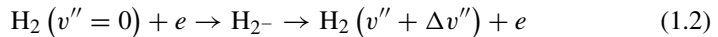
Two mechanisms, unknown at that time, involving intermediate states to form H^- were proposed (Nicolopoulou et al. 1977; Bacal et al. 1979) in order to explain the observed nonlinear dependence of the H^- density upon the plasma density and the high H^- density: (1) dissociative attachment (DA) of electrons to vibrationally excited hydrogen molecules (Wadehra and Bardsley 1978; Allan and Wong 1978; Wadehra 1984), (2) DA to electronically excited long-lived states of hydrogen molecules $\text{H}_2(\text{C}^3\Pi_u)$, with assumed higher DA cross sections (Bottcher and Buckley 1979).

1.2.3 H^- Formation by DA to Excited H_2 Molecules

The theoretical work on DA started in the sixties. The resonance theory of DA, involving the concept of an intermediate resonance negative ion state, was formulated in the fundamental papers of Bardsley (1968) and O'Malley (1966). The theory of dissociative electron attachment to hydrogen molecules relies on the model of *resonance* or *temporary negative ions* (Schulz 1973a, b). These terms designate a compound state formed by the interaction of an incident electron with a target molecule in which the incident electron is temporarily captured in the neighborhood of the molecule. The decay of this compound state can lead to DA with the formation of a negative ion H^- and a neutral atom H:



Or to the vibrational excitation of the molecule (denoted e-V excitation):



In 1979, the theoretical work of Wadehra and Bardsley (1978) and the experimental work of Allan and Wong (1978) showed that the cross sections for DA to vibrationally excited H_2 molecules increase by four orders of magnitude from $v'' = 0$ to $v'' = 4$. The cross sections calculated by Wadehra and Bardsley (1978) are shown in Fig. 1.3 for the vibrational excitation. Similar increases in cross sections for higher rotational levels are also reported. Figure 1.4 shows the direct comparison of the internal-state dependence of threshold energy for dissociative attachment cross sections in H_2 and D_2 determined in the experiment of Allan and Wong (1978) with the results of the theoretical calculation of Wadehra and Bardsley (1978). This

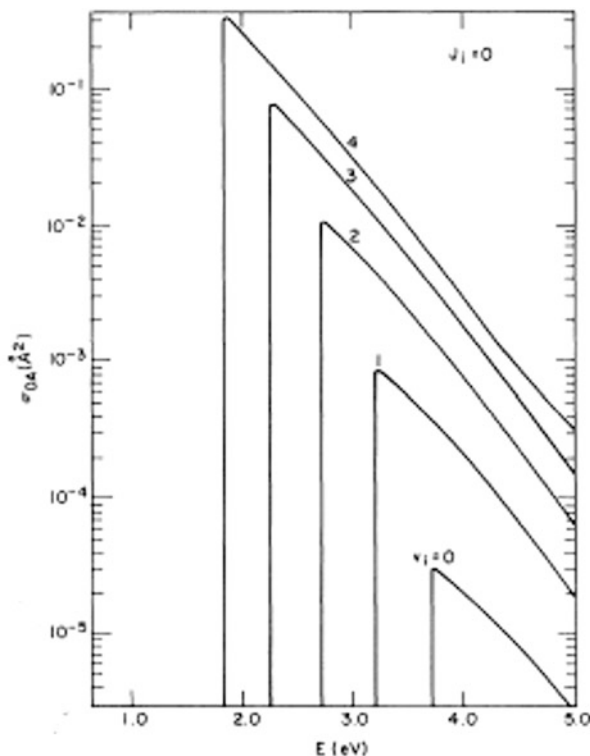


Fig. 1.3 Dissociative attachment cross section for various vibrational states of H_2 , each in the rotational state $J = 0$ Wadehra and Bardsley (1978), © 1978. (Reproduced from Bacal and Wada (2015), Fig. 3)

figure shows that the increase is even stronger for deuterium. Note in Fig. 1.4 that the cross-section enhancement due to vibrational excitation is much larger than that due to rotational excitation at the same internal energy.

In 1984, Wadehra (1984) found that the ground electronic state of H_2 can support at least 294 rovibrational levels and calculated the rates of dissociative electron attachment to them. He found that the maximum possible rate is about 10^{-8} cm^3/sec , as can be seen in Fig. 1.5, which shows these rates for all possible J levels for $v'' = 0, 2$, and 4 at the electron temperature of 1 eV. An important conclusion of Wadehra (1984) is that the crucial factor that determines the attachment rates and average energy of the extracted negative ions is the total internal energy of the gas molecule.

According to Bardsley et al. (1978), the vibrational and rotational enhancement of the DA cross sections arises from an increase in the survival factor, which is the probability that the resonant state dissociates without autoionization. This factor is increased because electron capture can occur at a larger distance due to the

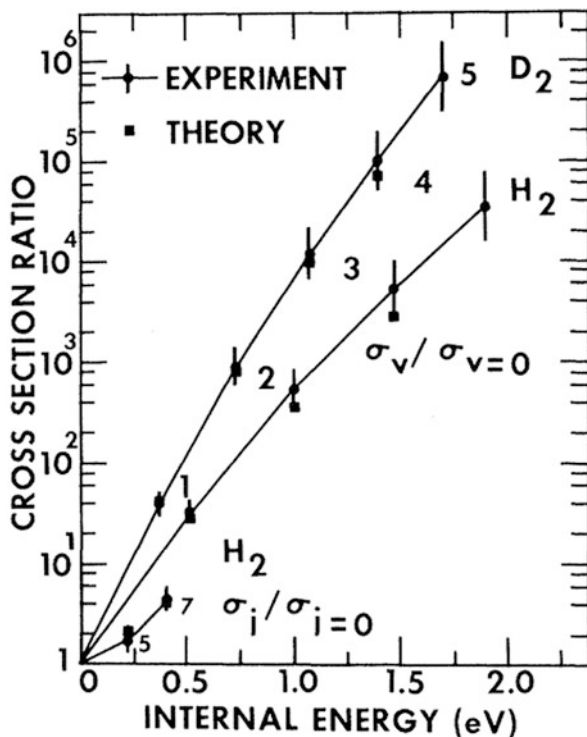


Fig. 1.4 Internal state dependence of threshold dissociative attachment cross sections in H₂ and D₂, Allan and Wong (1978) © 1978. (Reproduced from Bacal and Wada (2015), Fig. 5)

larger amplitude of the vibrational motion in excited vibrational states and to the centrifugal stretching in excited rotational states.

The dependence of the DA rates on the electron temperature is reported by Wadehra (1984) for all the vibrational and rotational states of H₂ and D₂. These rates can be as high as $10^{-8} \text{ cm}^3 \text{ s}^{-1}$ when the molecules have the highest vibrational states. The DA cross sections to rovibrational levels of the hydrogen and deuterium molecules were calculated independently by Gauyacq (1985) close to the energetic threshold. The results account well for the increase of the threshold attachment with the internal energy of the molecule, observed by Allan and Wong (1978). The vibrational and rotational enhancement of the DA process is similar to that found by Bardsley and Wadhwa (1979).

The theory of DA was developed further more recently by Fabrikant et al. (2002) and Domcke (1991). Domcke's review (Domcke 1991) describes the application of the resonance model to the theory of inelastic electron-molecule collisions. An improved nonlocal resonance model proposed by Čizek et al. (1998) was used

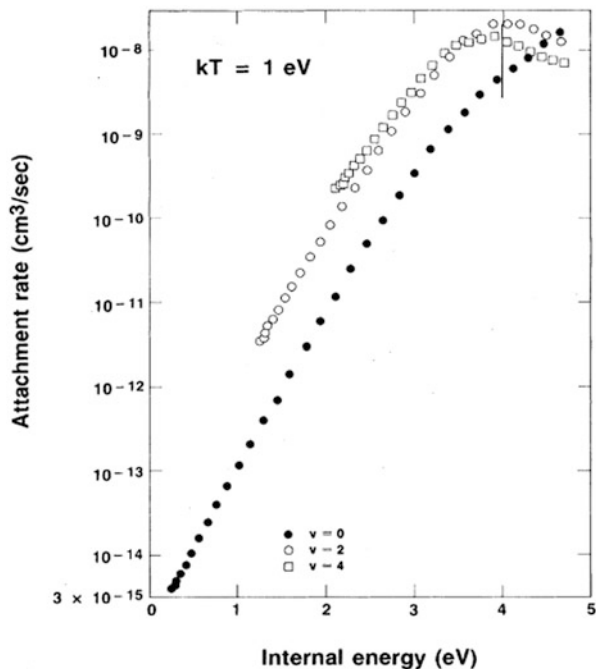


Fig. 1.5 Rates of dissociative electron attachment to all possible J levels of hydrogen for $v = 0, 2$ and 4 at electron temperature of 1 eV . The vertical line at 3.994 eV defines the internal energy above which the attachment process becomes exoergic Wadehra (1984) © 1984 The American Physical Society. (Reproduced from Bacal and Wada (2015), Fig. 6)

by Horacek et al. (2004) for the calculation of cross sections of electron DA of molecular hydrogen by the impact of low-energy electrons. This model also shows that the magnitude of the DA cross-section in the low-energy range increases rapidly with the increasing vibrational quantum number of the target molecule: the DA cross-section increases by nearly five orders of magnitude from $v'' = 0$ to $v'' = 8-9$. This feature is illustrated in Fig. 1.6a, where DA cross sections calculated by this theory are plotted for a series of initial vibrational states, from $v'' = 0$ to $v'' = 11$.

However, the theory of Horacek et al. (2004) leads to a new view on the effect of rotational excitation on the DA cross-section. Figure 1.6b shows the effect of rotational excitation of the target for $v'' = 0$ as obtained from this theory. It shows that with increasing J , the rotational heating becomes more efficient than the vibrational heating, opposite to what is well known at low J . The highest cross-section for an endothermic DA process is obtained for $v'' = 2, J = 23$. This reaction opens at 113 meV , and the cross-section reaches the value of 20.1 \AA^2 at 249 meV .

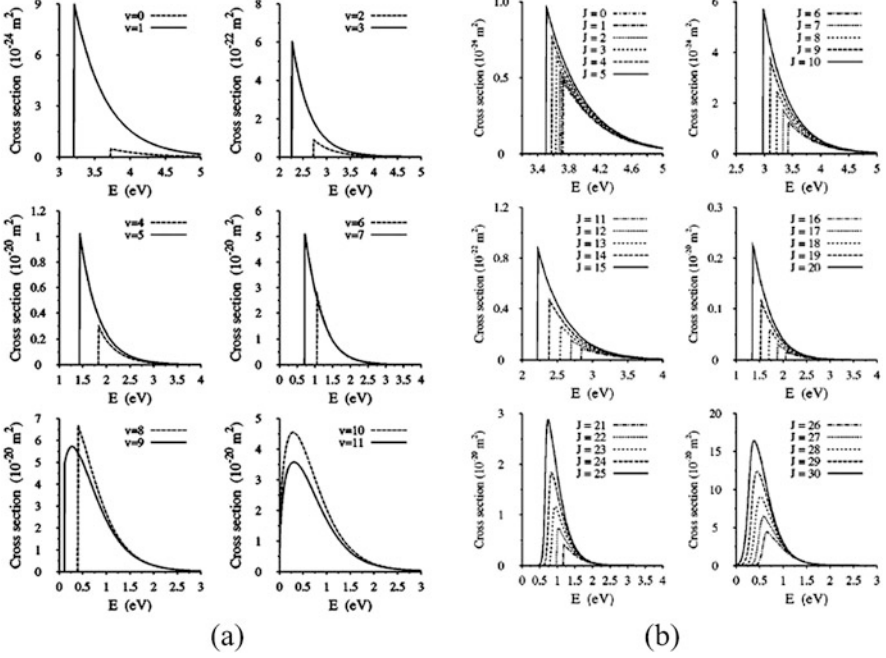
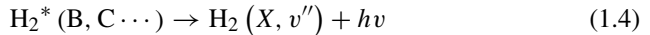
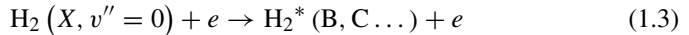


Fig. 1.6 (a) DA cross sections calculated by Horacek et al. for a set of initial target states $v//$. The rotational quantum number is $J = 0$. (b) DA cross sections for $v = 0$ and $J = 1, 2, \dots, 30$. (Reprinted from Horacek et al. (2004), Fig. 2. Reproduced from Bacal and Wada (2015), Fig. 7)

1.2.4 Excited H_2 Populations in Low-Temperature Plasmas

Following these pioneering works, it was questioned what processes are generating sufficient density of highly rovibrationally excited hydrogen molecules. A review on the physics aspects of negative ion sources (Bacal 2006) indicated that both electron-molecule collisions in the plasma volume and recombinative desorption of atomic hydrogen on wall surfaces contribute to the generation of rovibrationally excited molecules. An effective source of highly vibrationally excited molecules, generated in electron-molecule collisions, was identified in 1980 by Kunkel (1980, private communication): the radiative decays from higher electronic states excited by collisions of ground state molecules with energetic primary electrons:



This process is denoted by E-V singlet excitation.

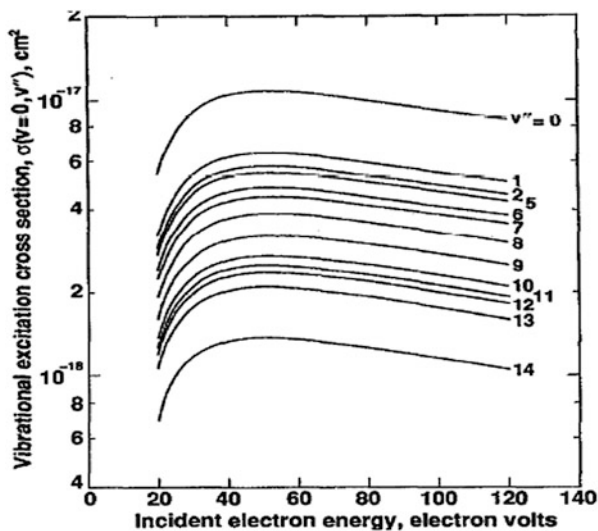


Fig. 1.7 Cross section for the excitation of the vibrational levels of hydrogen molecules by electron collisional excitation through the B and C states. (Reproduced from Bacal and Wada (2015), Fig. 9, with permission of AIP Publishing)

Electrons impacting on H_2 molecules in their ground electronic state will generate excitations to all members of both the singlet and the triplet electronic spectrum. A major portion of the singlet excitations will return to the ground state by direct or successive radiative decays. These decays generate a final vibrational population distribution that differs from the original v distribution. The triplet decays will not result in final molecular products but instead will generate atomic fragments via the dissociation process. The electron excitation cross sections leading from $v'' = 0$ of the ground state through the B and C singlet states to v'' levels of the ground state (Eqs. 1.3 and 1.4) were calculated by Hiskes (Hiskes 1980, 1991) These and other earlier calculations (Marx et al. 1985; Cacciatore et al. 1990) extended them to include excitations from $v'' > 0$ initial levels. The principal excitations in this excitation-radiative sequence (the $E-V$ process) proceed through the *B and C* singlet states. Their cross-sections are shown in Fig. 1.7. The maxima of all cross sections vary monotonically with v'' . The $v'' = 3, 4$ results are not shown. The populations of $H_2 X (v'')$ in the upper 10 vibrational levels will provide the major portion of the total dissociative attachment leading to negative ions in the hydrogen discharge. The effective cross section for excitation of this group of vibrational levels is approximately $3 \times 10^{-17} \text{ cm}^2$ at 100 eV (Hiskes 1980), large enough so that the excitation process considered here may contribute significantly to the total negative ion formation.

Concerning the cross sections for $E-V$ excitation for higher initial levels, Table V (Hiskes 1991) shows that the largest excitations occur along the diagonal, $v'' = v$,

with cross sections diminishing from these maximum values as one moves away from the diagonal. They show similar trends, notably the maxima at $v'' = v$.

The analysis of the collisional attenuation of the $E-V$ process, summarized in Table VI of Hiskes (1991), shows that for electron densities above 10^{15} electrons/cm³ and the electron temperature $kT = 3-5$ eV, the $E-V$ process is effectively quenched, due to secondary excitation and ionization.

The vacuum ultraviolet emission from a low-pressure hydrogen plasma, associated with the process described by Eq. 1.4, has been used by Graham (1988) to study the production mechanism for vibrationally excited ground state molecules. His most interesting observation is that there is a substantial contribution to the high vibrational levels of the ground state from both B and C states.

Several experimental techniques were dedicated to in situ observation of ro-vibrationally excited molecules in low-pressure hydrogen plasma. Péalat et al. (1985) used Coherent Antistokes Raman Scattering to observe a ro-vibrationally excited molecular population in a multicusp discharge. In this experiment, molecules with $v'' \leq 3$ only were detected. Hall et al. (1988) observed vibrational excitation up to $v'' = 9$ in a gas cell without a discharge when a tungsten or tantalum filament was heated. Crossing an electron beam of variable energy with the molecular beam of hydrogen flowing out from the cell and observing the H^- ion yield allowed relative vibrational populations to be determined from the observed peak intensities by use of the dissociative attachment cross sections of Gauyacq (1985). Figure 1.8 presents the vibrational populations from Hall et al. (1988) as a function of vibrational energy for hot tungsten and tantalum filaments. The proposed mechanism is the recombinative desorption of atomic hydrogen on the cell surfaces following atomization of H_2 on the filament.

This detection technique was used by Schermann et al. (1991) to observe the effect of the discharge on the vibrational populations of H_2 detected up to $v'' = 6$. It was observed that the excitation to $v'' \geq 4$ tends to weaken during the discharge. When the tungsten (W) filaments were replaced by tantalum (Ta) filaments, higher populations for $v'' \geq 4$ were obtained. The tantalum-covered surfaces were irreversibly modified by the discharge and were losing much of their ability to populate high vibrational levels. The initial populations are recovered only after a long bake-out of the walls. With higher discharge currents, the vibrational distributions are approaching a Boltzmann distribution.

Recently the comparison of extracted H^- current and negative ion density of sources with tantalum and tungsten (W) filaments with those of sources with sheet Ta or W plasma electrodes (Bacal et al. 2021) confirmed the observation that the Ta films deposited by evaporation from filaments produced the highest negative ion density and extracted current.

Vacuum ultraviolet laser absorption spectroscopy has been employed by Young et al. (1991) to measure the populations and temperatures of ground state H atoms and vibrationally excited H_2 molecules in a volume H^- source. The experimental apparatus has been described in detail by Stutzin et al. (1988, 1989). The vibrational

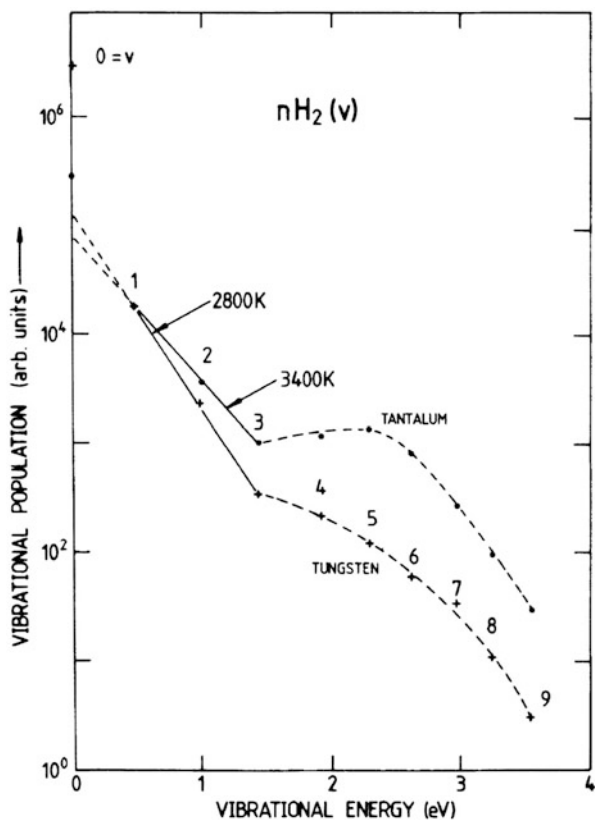


Fig. 1.8 Vibrational populations as a function of vibrational energy for tungsten and tantalum filaments (Hall et al. 1988). (Reproduced from Bacal and Wada 2015, Fig. 10)

population distribution was found to exhibit a Boltzmann distribution for $v'' = 1$ through $v'' = 8$, with $T_{\text{vib}} = 4150$ K (see Fig. 1.9). This is in contrast with the model of the source chemistry for the same source conditions by Hiskes and Karo (1989) predicting a high vibrational temperature in this v'' range.

For determining the densities of ro-vibrationally excited molecules in a low-temperature plasma produced in a magnetic multipole plasma source with dc filament excitation, Mosbach (2005) applied laser-induced fluorescence spectroscopy in the VUV (for molecules with high v'') and optical emission spectroscopy (for molecules with $v'' < 4$). Mosbach reported that the population distribution is non-Boltzmann. At high vibrational states, a plateau is formed, and for low discharge current, a hump appears (see Fig. 1.10).

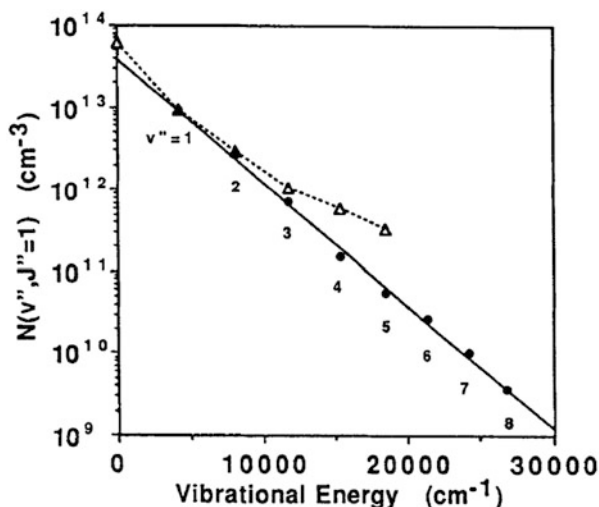
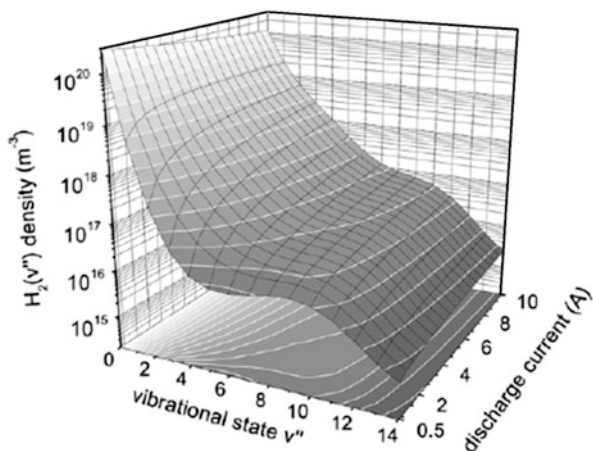


Fig. 1.9 Vibrational population distribution for a volume source. The experimental points (the closed circles) were obtained at 25 A, 120 V and 8 mTorr H_2 . The solid line corresponds to a vibrational temperature of 4150 K. The triangles represent the calculated values of Hiskes and Karo (1989), normalized to the experimental data at $v'' = 1$ (Young et al. 1991). (Reproduced from Bacal and Wada (2015), Fig. 11)

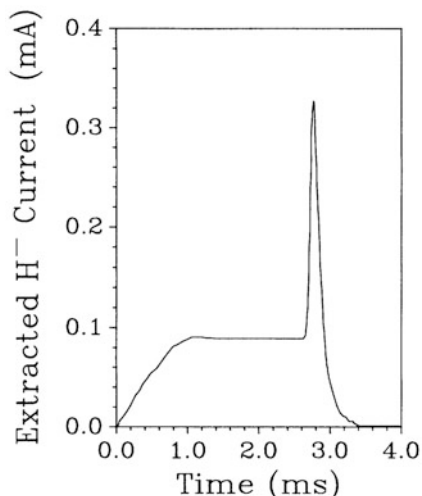
Fig. 1.10 The total density of vibrational states as a function of discharge current (Mosbach 2005) @ 2005 Institute of Physics. (Reproduced from Bacal and Wada (2015), Fig. 12)



1.2.5 Experimental Validation of the Volume Production Mechanism

An experimental validation of the volume production mechanism is the existence of an afterglow peak in the extracted negative ion current from a pulsed hydrogen discharge in a multicusp ion source (Hopkins and Mellon 1991). In this experiment,

Fig. 1.11 The extracted negative ion current from a pulsed hydrogen discharge. The gas pressure is 2.4 mTorr, the discharge pulse length is 2.7 ms, the repetition rate is 87 Hz, and the discharge current is 15 A (Hopkins and Mellon 1991). (Reproduced from Bacal and Wada (2015), Fig. 1.13)



the vibrationally excited molecules are produced by energetic electrons, and they live some time after the end of the discharge pulse. Low-energy electrons attach to these molecules in the afterglow, while electron detachment by fast electrons is reduced. As a result, an increase in the negative ion density and extracted current occurs, as shown in Fig. 1.11.

An important diagnostic effort by Mosbach allowed the comparison of the \ddagger the H^- ion density measured by laser-induced photodetachment to that calculated from the measured spectrum of rovibrationally excited ground state hydrogen molecules, shown in Fig. 1.10 as a function of the discharge current. The calculated density of the negative ions as a function of the discharge current is in good agreement with the measured H^- density, as shown in Fig. 1.12. This agreement proves the validity of the volume production mechanism on which the model used in the calculation is based.

The effect of wall material on the H^- ion production has been studied by two approaches. In the first approach, Leung et al. (1985) and Fukumasa and Saeki (1987) installed thin metal liners on the chamber wall and compared the extracted negative ion current measured with liners made of different materials. They found that the extracted H^- current was the highest with Al and Cu liners compared to other metals. Stainless steel produced the lowest one. The positive effect of Al but not of Cu was observed by the University of Paris group (Čadez et al. 1993). Čadez (2021, private communication) suggested that contamination by hydrocarbon and oxide surfaces plays an important role in the lack of reproducibility from different results.

In the second approach, Inoue et al. (1992) modified the way of changing the wall material by evaporating filament material and found that the extracted H^- current can be 50% larger and the extracted electron current 20% lower when tantalum filaments were used, compared to the use of tungsten filaments (see also (Bacal et al.

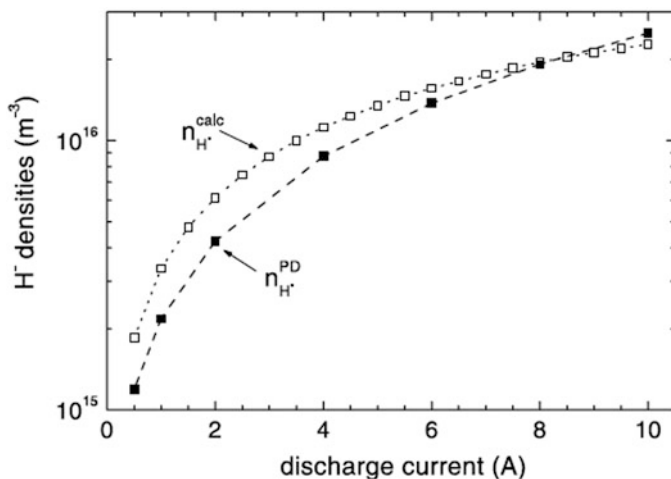


Fig. 1.12 Comparison of H^- ion densities measured by laser-induced photodetachment (full squares) and calculated from vibrational population distributions of ground state hydrogen molecules (open squares) (Mosbach 2005). (Reproduced from Bacal and Wada (2015))

2021)). They also reported that a freshly deposited metal film performed better than an old one. The observations of Inoue et al. (1992) relative to the better performance of sources with tantalum-covered walls compared to sources with tungsten-covered walls were confirmed by the work of Hall et al. (1988), Čadež et al. (1988) and Schermann et al. (1991), as well as by the work with H^- ion sources at TRIUMF (Kuo et al. 1996) and Culham. At DESY, Peters (2000) showed that a tantalum cylinder inserted in the collar of the extraction opening increased by 15% the extracted current with respect to that found with a steel collar. Spence and Lykke (1988) sputtered a thin layer of tantalum on the inner surface of a microwave-driven ion source to enhance H^- production and avoid the difficulties with a bulk liner used in their earlier experiments. Bacal et al. (2004) studied plasma chambers in which the walls were covered by tungsten or tantalum films, resulting from evaporation and/or sputtering of corresponding filaments, and also covered by caesium, as a result of Cs seeding. They showed that tantalum and caesium films deposited on the walls lead to an enhancement of extracted H^- current (by a factor 2) and to a large reduction of the extracted electron current compared to a deposited tungsten film (see Fig. 1.13). It was also shown that a fresh tantalum film leads to the enhancement of the negative ion density by 60–90%. The addition of argon leads to a slight decrease in hydrogen negative ion density while the electron density stays constant. The final minimum negative ion density is approximately 40% lower than the initial one in pure hydrogen plasma.

The effect of surface reactions in volume hydrogen negative ion sources has been extensively discussed. Thus, Leung et al. (1985) attributed the effect of the wall material to different secondary electron emission coefficients. Inoue et

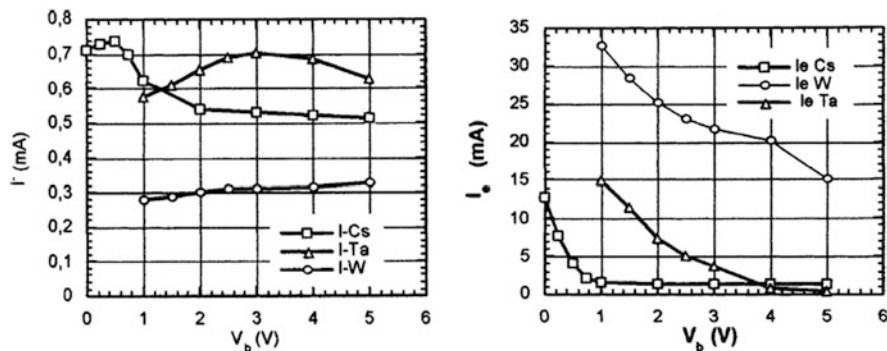


Fig. 1.13 Variation of extracted negative ion and electron currents with plasma electrode bias. The effect of films of tantalum, tungsten, and cesium deposited on the walls is shown (Bacal et al. 2004). (Reproduced from Bacal and Wada (2015), with permission of AIP Publishing)

al. (1992) considered that two surface reactions were important in this context: the collisional wall de-excitation of vibrationally excited molecules and the wall recombination of atoms (followed by the recombinative desorption of hydrogen molecules) see (Béchu et al. 2013). In low-power operation, the de-excitation of vibrationally excited molecules through wall collisions may be the dominant destruction mechanism for these precursors of the H^- ions.

Negative atomic hydrogen ion (H^-) densities were measured in a pulsed low-pressure E-mode inductively-coupled radio-frequency (rf) driven plasma in hydrogen by means of laser photodetachment and a Langmuir probe by Ellis et al. (2020). This investigation was focused on the influence of different metallic surface materials on the volume production of H^- ions. The H^- density was measured above a thin disc of either tungsten, stainless steel, copper, aluminum, or molybdenum placed onto the lower grounded electrode of the plasma device as a function of gas pressure and applied rf power. For copper, aluminium, and molybdenum, the H^- density was found to be quite insensitive to pressure and rf power, with values ranging between 3.6×10^{14} and $5.8 \times 10^{14} \text{ m}^{-3}$. For stainless steel and tungsten, the H^- dependency was found to be complex, apart from the case of a similar linear increase from 2.9×10^{14} to $1.1 \times 10^{15} \text{ m}^{-3}$ with rf power at a pressure of 25 Pa.

1.3 Volume Production of H^- Ion Sources

1.3.1 Penning Source

A review presenting the H^- ion sources based on volume production by dissociative attachment (denoted Volume Production Sources, VPS) was published in 2005

(Bacal et al. 2005). This chapter covers only a brief introduction to the development of VPS. We refer the readers to the mentioned review for a detailed presentation of this development. Shortly after the early attempts (1959) to extract directly negative ions from a duoplasmatron, three main types of VPS became available (Bacal et al. 2005): the Penning discharge ion source (1965), the tandem multicusp bucket (Leung et al. 1983; Bacal et al. 1980) and several versions of RF sources (Peters 2000; Spence and Lykke 1988). Multicusp bucket VPS for fusion applications have been developed in the US (e.g. (Leung et al. 1983)), France (Bacal et al. 1980), UK (Green 1985), and Japan (Horiike et al. 1986; Okumura et al. 1986).

In 1963–1965 at Berkeley, the hot-cathode reflex-type (or Penning) plasma source of D^- and H^- ions with a continuous current of 2 and 5.3 mA (current density 40 mA/cm^2), respectively, was developed by Ehlers (1965). The scheme of a reflex-type ion source is shown in Fig. 1.14. The Ehlers source can easily be built into the center of cyclotrons and is used in many cyclotrons for accelerating negative ions.

In Dimov's review (Dimov 1996), it is reported that the Ehlers H^- ion source was used until 1987 in the TRIUMF cyclotron (meson factory). However, the Ehlers source was installed outside. The beam of H^- ions was injected along the cyclotron axis with an energy of 300 keV. The Ehlers-type source was also used in a Van de Graaf accelerator which accelerated H^- ions up to 1.5 MeV, with a current of 1 mA in pulses of 1.5 ms. Later a current of 11 mA was obtained by J.E. Osher with a Calutron source (see the book (Zhang 1999)) with an extraction slit of $3.2 \text{ mm} \times 57 \text{ mm}$.

Twenty years later, some basic understanding of the operation of the Penning type H^- ion source was obtained by Jimbo (1984), Jimbo et al. (1986), and Goretsky et al. (1996) based on the volume production mechanism. The plasma of a Penning-type discharge is formed of two regions: the central hot plasma region, containing fast electrons oscillating between the hot cathode and the anticathode, and the

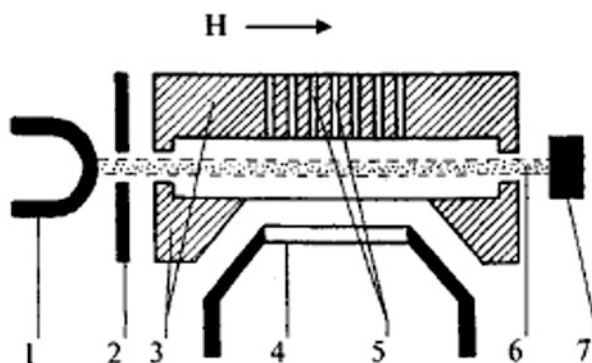


Fig. 1.14 Scheme of reflex-type ion source: (1) heated cathode, (2) cathode aperture, (3) anode chamber, (4) extraction electrode, (5) holes for gas supply, (6) discharge column, (7) anticathode (Goretsky et al. 1996) © 1996. (Reproduced from Bacal and Wada (2015), Fig. 20)

cold plasma region, limited by the cylindrical wall (Fig. 1.14). The ionization and the vibrational excitation of molecules occur in the central region. Outside this central hot plasma column, the electron temperature decreases along the radius. H^- ions are formed by dissociative attachment to vibrationally excited molecules in the relatively cold surrounding region, close to the emission slit. Goretsky et al. (1996) report the extraction of an ion current of 40 mA, with a current density of 80 mA/cm^2 . It should be noted that in both the initial source of Ehlers (1965), as in the source of Jimbo et al. (1986), the hot cathode and the anticathode were made of tantalum, which, as shown later by Inoue et al. (1992) improves the volume production when deposited as a thin film on the wall. This may explain in part the good performance of these sources.

An intense volume H^- ion source based on a Penning-type discharge was developed at Oak Ridge National Laboratory: the Volume Ionization with Transverse Extraction (VITEX) (Tsai et al. 1987). The extracted current was 25 mA, with a current density of 125 mA/cm^2 .

The Penning discharge H^- ion source has been operated with caesium in Novosibirsk, leading to the discovery of the plasma-surface production of these ions by Belchenko et al. (1974) and the development of the surface-plasma sources (SPS). The operation of these sources without caesium, in pure hydrogen, i.e. in the volume production regime, in a version of SPS called planatron, was described by Belchenko et al. (1988). In an attempt to replace caesium with a low work function and low vapor pressure material, Leung et al. (1987) operated a Penning source with LaB_6 cathodes in a caesium-free discharge. They found that the extracted H^- current density was comparable to that in the cesium-mode operation (350 mA/cm^2 was obtained with an arc current of 55 A).

1.3.2 The Magnetically Filtered Multicusp Volume Negative Ion Source

An important step in the development of the negative ion sources was the understanding that the volume production was due to the following two-step process:

1. Excitation of molecules in collisions with electrons to a ro-vibrationally excited state, by the e-V process (Eq. 1.2) or the E-V process (Eqs. 1.3 + 1.4).
2. Dissociative electron attachment to form the negative ion (DA), Eq. (1.1).

Since the negative ion destruction rate in collision with electrons increases rapidly with the increasing electron temperature, it follows that low electron temperature plasmas are needed to produce high negative ion densities. A direct consequence of this is the concept of tandem or magnetically filtered negative ion source. The magnetic filter provides a limited region with the field lines of force traversing perpendicularly to the axis of the beam extraction, which divides the ion

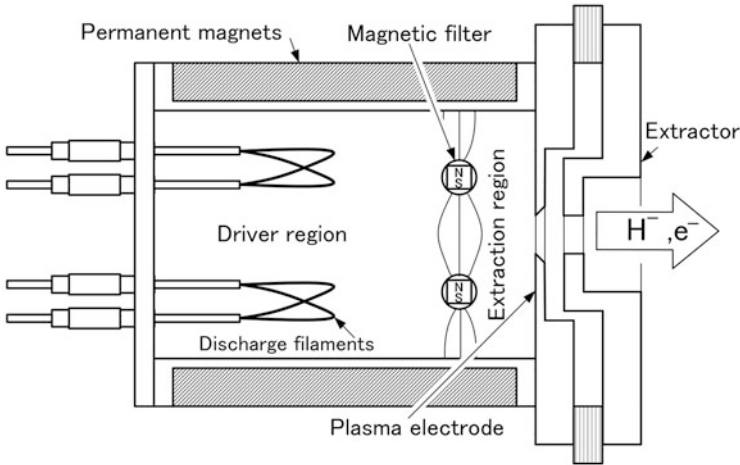


Fig. 1.15 A schematic illustration of a tandem negative ion source

source volume into two regions (this is the reason for this source to be denoted as a tandem source):

- (a) The “driver” or “source” region containing either the filaments in arc discharge sources or the rf antenna in rf sources.
- (b) The “target” or “extraction” region, limited by an electrode containing the extraction openings, which is denoted as plasma electrode (PE) or plasma grid.

The typical ion source geometry is schematically illustrated in Fig. 1.15.

1.3.2.1 Role of the Magnetic Filter

The magnetic filter field should be strong enough to prevent the energetic primary electrons in the driver region from entering the extraction region. However, positive and negative ions and cold electrons can move across the magnetic filter. Due to the confinement by the magnetic filter, a relatively large concentration of fast electrons builds up in the driver chamber while a low-temperature plasma fills the extraction chamber. Vibrationally excited molecules can be formed in the driver region, essentially by the E-V process (Eqs. 1.3 + 1.4). They can be converted to negative ions by DA in collision with slow electrons in both chambers, but the chance of the negative ions surviving is larger in the extraction region.

The first experiments with the negative ion tandem source were performed in the early eighties at the Lawrence Berkeley National Laboratory (US) (Leung et al. 1983) and at Ecole Polytechnique (France) (Leung and Bacal 1984). The magnetic filter was of internal rod-type, i.e., it was constructed by inserting square permanent magnet rods into copper tubes through which a square broach had been

passed. At Ecole Polytechnique, a large source (44 cm in diam by 45 cm high) named CAMEMBERT III was used as a plasma generator for investigating the low-pressure hydrogen plasma by laser photodetachment, Langmuir probes, and ion extraction (Courteille et al. 1993). The primary electrons were provided by electron emission from tungsten filaments or small ECR modules inserted in the plasma. The multicusp ion source geometry is also evaluated from the tandem configuration (Leung and Bacal 1984) toward the “hybrid” configuration, in which the primary electrons are confined in the multicusp magnetic field (Courteille et al. 1995). Ivanov (2004) demonstrated experimentally in this source using two laser beam photodetachment the existence of two negative ion populations. This diagnostic technique is described in Chap. 22.

1.3.2.2 Role of the Plasma Electrode

Leung and Bacal (1984) showed that the presence of the magnetic filter corroborated with a positive bias of the plasma electrode (denoted V_b) enhanced in a limited range of this bias the extracted negative ion current and reduced the co-extracted electron current, as well as the electron density in the target chamber. The measurement of the negative ion density by photodetachment (Bacal 2000) showed that the plasma electrode bias could maximize the relative negative ion density (i.e. the ratio N^-/N_e) in the target chamber, with a maximum value $N^-/N_e = 0.13$ measured with a discharge of $50 \text{ V}^{-1} \text{ A}$ (see Fig. 1.16). This is in contrast with the relative negative ion density in the driver chamber that exhibited only a modest variation around the value of $N^-/N_e = 1.15 \times 10^{-2}$. The observed reduction of the axial potential gradient across the two chambers when the plasma electrode is positively biased allows the flow of the negative ions from the driver into the target chamber, which causes the increase of the negative ion density in this chamber. An important consequence of the increase of the plasma potential in the target chamber with V_b is the fact that the negative ions can reach the plasma electrode and the extractor. This feature was observed in other volume sources, e.g., in the microwave-driven source described by Svarnas et al. (2007). Figure 1.17 shows a typical evolution with V_b of the plasma electrode current and the extracted negative ion and electron currents.

However, an earlier example of tandem source concept (designated as a hybrid source) was described in 1980 (Bacal et al. 1980). This source contained a virtual magnetic filter located next to the plasma electrode which became widely used in the following years. The multicusp structure of this ion source was formed by 10 external magnet columns parallel to the source axis. Ten filaments were located inside the source, in the multicusp magnetic field of the external magnets. The multicusp magnetic field acted as a virtual magnetic filter for the electrons emitted by the filaments. In this case, the driver plasma region is located near the wall, while the extraction plasma region is the central plasma.

Replacing one of the end walls by the PE equipped with an extraction system provided the opportunity to observe the effect of a weak magnetic field at the PE surface upon the extracted currents (Bacal et al. 1988). This magnetic field is the

Fig. 1.16 H^- ion relative density (N^-/N_e) in the target (extraction) chamber of a tandem source versus the plasma electrode bias voltage (Leung and Bacal 1984) © 1984. (Reproduced from Bacal and Wada (2015), Fig. 22)

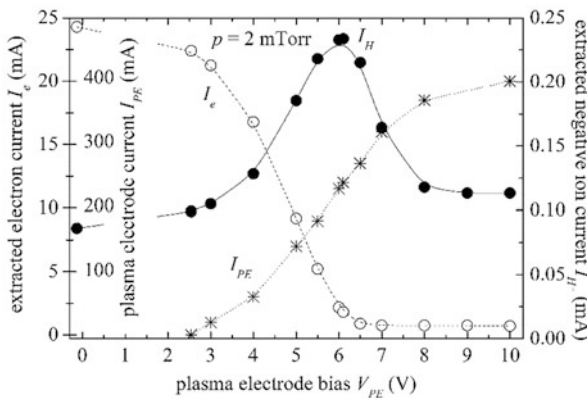
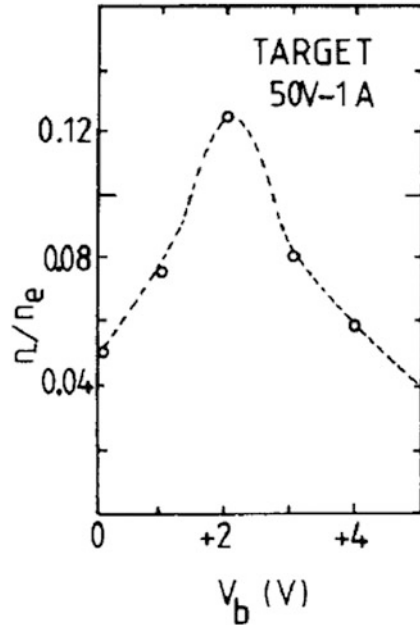


Fig. 1.17 Typical evolution of the extracted electron and negative-ion currents as a function of the plasma electrode bias. The plasma electrode current is also shown (Svarnas et al. 2007). (Reproduced from Bacal and Wada (2015), Fig. 23)

stray magnetic field produced by the magnets enclosed in the extractor and can be idealized as parallel to the PE. The field is denoted as the PE magnetic field hereafter in this section. The PE magnetic field magnetically insulates the PE from the plasma. In Fig. 1.18, the dependence of the extracted negative ion and electron currents on the PE bias V_b is shown for three values of the intensity of the PE magnetic field. The negative ion current I^- exhibits the most pronounced maximum and attains the

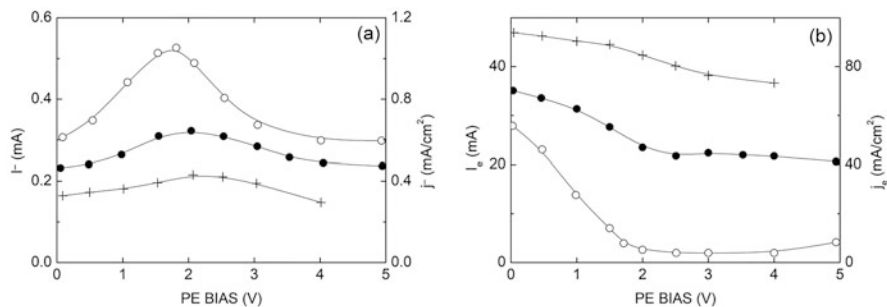


Fig. 1.18 Dependence of the extracted negative ion (a) and electron (b) currents upon the PE bias, with different stray magnetic fields in front of the PE: open circle – high B, full circle medium B, cross – low B. 50 V, 10 A, 2.5 mTorr discharge. Extraction voltage: 1 kV (Bacal et al. 1988). (Reproduced from Bacal and Wada (2015), Fig. 24)

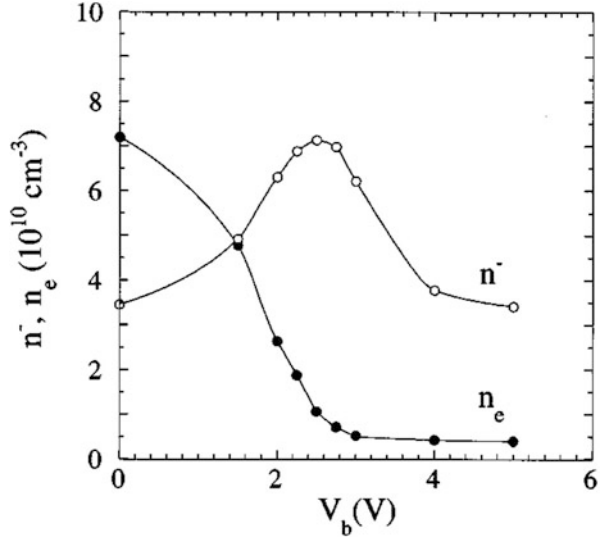
highest value, while the electron current I_e exhibits the most considerable drop when the PE magnetic field is the strongest. In this case, the maximum magnetic field, at 1 cm from the PE, is 21 Gauss. In the “low B” case, the maximum magnetic field at 1 cm from the PE is 6 Gauss (Bacal et al. 1988). The fraction of the electrons in negatively charged particles present in the plasma is reduced by the PE magnetic field as they are hindered from reaching the PE. This fraction increases with the value of the PE magnetic field. Therefore, the extracted electron current is reduced when the PE magnetic field is enlarged.

When biased positively with respect to the walls, the PE collects a large electron current, as can be seen in Fig. 1.14. Since the region close to the PE cannot be easily reached by electrons from the main plasma, the electron population in this region is strongly depleted when the applied PE bias potential allows the electrons to flow up to the PE. It was shown by Svarnas et al. (2007) that the negative ion density increases in the region where the electron density is reduced. This suggests that the negative ions penetrate from the main plasma into the magnetized region close to the PE, where the plasma neutrality requires negatively charged species capable of passing across the filter field. The negative ions are unaffected by the weak magnetic field. This explains the enhancement of the extracted negative ion current when the extracted electron current is reduced. Figure 1.19 shows the measured variation with V_b of the electron density n_e and negative ion density n^- at 8 mm from the PE in a 50 V, 50 A discharge at 3 mTorr (El Balghiti-Sube et al. 1996; Bacal et al. 1998) in the larger source Camembert III. A very high ratio of $n^-/n_e = 12$ occurs in these conditions at $V_b = 2.5$ V.

A plasma with such a high n^-/n_e ratio contains a very low electron fraction, and the negative ion density is only slightly lower than the positive ion density, namely $n_e = (12/13)n^+$. Therefore such a plasma is designated as “ion-ion plasma.”

Simulation results for the negative ion and vibrationally excited molecule production in the source Camembert III, obtained using two multidimensional Monte Carlo simulation codes, were reported by Hatayama et al. (2002). Sakurabayashi

Fig. 1.19 Variation with plasma electrode bias V_b of the negative ion density n^- and electron density n_e at 8 mm from the PE, in a weak, transverse magnetic field 50 V, 50 A, 3 mTorr discharge (El Balghiti-Sube et al. 1996). (Reproduced from Bacal and Wada (2015), Fig. 26)



et al. (2002) studied the H^- ion trajectories of both volume and surface-produced H^- ions, showing that the wall loss is significant at low pressure (1 mTorr). The goal of the study of Kuppel et al. (2011) is to highlight the combined effects of the weak magnetic field and the PE bias voltage upon the extraction process of H^- ions and electrons. They showed that applying the magnetic field (without the PE bias) enhances H^- ion extraction, while it drastically reduces the extracted electron current. Secondly, the extracted H^- ion current has a maximum when the PE bias is equal to the plasma potential, while the extracted electron current is significantly reduced by applying the PE bias. This is in agreement with the experimental results.

The various consequences of biasing the plasma electrode in multicusp H^- ion sources were summarized in Bacal et al. (2014a, b). The PE bias controls the current collected by the PE, the extracted negative ion and electron currents, and the potential drop across the magnetic filter. Moreover, the positive bias of the PE depletes the electron population and concentrates the H^- ions near its surface, generating an ion-ion plasma. As shown by Hall et al. (1988), Schermann et al. (1991), and Young et al. (1991), the PE surface recycles hydrogen atoms to vibrationally excited hydrogen molecules. This strongly depends on the surface temperature.

1.4 Conclusion

The H^-/D^- ion formation and destruction mechanisms in the H_2 low-pressure discharge plasma volume are presented. The important role of the magnetic filter, separating the plasma chamber of the tandem source in a driver, or source, chamber,

and an extraction chamber, is pointed out. The role of the plasma grid is also discussed, and relevant experimental results are presented.

References

- P. Agostinetti, D. Aprile, V. Antoni, et al., Nucl. Fusion **56**(1), 016015 (2016)
- M. Allan, S.F. Wong, Phys. Rev. Lett. **41**, 1791 (1978)
- L.V. Alvarez, Rev. Sci. Instrum. **22**, 705 (1951)
- M. Bacal, Rev. Sci. Instrum. **71**, 3981 (2000)
- M. Bacal, Nucl. Fusion **46**(6), S250 (2006)
- M. Bacal, G.W. Hamilton, Phys. Rev. Lett. **42**(23), 1538 (1979)
- M. Bacal, M. Wada, Appl. Phys. Rev. **2**, 021305 (2015)
- M. Bacal, A. M. Bruneteau, H. J. Doucet, W. G. Graham, G. W. Hamilton, BNL Report 51304, T. Sluyters Editor (1980)
- M. Bacal, J. Bruneteau, P. Devynck, Rev. Sci. Instrum. **59**(10), 2152 (1988)
- M. Bacal, F. El Balghiti-Sube, L.I. Elizarov, A.Y. Tontegode, Rev. Sci. Instrum. **69**, 932–934 (1998)
- M. Bacal, A.A. Ivanov Jr., M. Glass-Maujean, Y. Matsumoto, M. Nishiura, M. Sasao, M. Wada, Rev. Sci. Instrum. **75**, 1699 (2004)
- M. Bacal, A. Hatayama, J. Peters, IEEE Trans. Plasma Sci. **33**, 1845 (2005)
- M. Bacal M. Sasao, M. Wada, R. McAdams, Fourth Intern. Symp. on Negative Ions, Beams and Sources (NIBS 2014), Garching, Germany (2014a)
- M. Bacal, R. McAdams, E. Surrey, Rev. Sci. Instrum. **86**, 02B103 (2014b)
- M. Bacal, K. Maeshiro, S. Masaki, M. Wada, Plasma Sources Sci. Technol. **30**, 075014 (2021)
- J.N. Bardsley, J. Phys. B **1**, 349 (1968)
- J.N. Bardsley, J.M. Wadhera, Phys. Rev. **A20**(4), 1398 (1979)
- C.F. Barnett, J.A. Ray, E. Ricci, et al., *Atomic Data for Controlled Fusion Research* (Oak Ridge National Laboratory, Oak Ridge, Tennessee 37830, 1977)
- S. Béchu, A. Soum-Glaude, A. Bès, P. Svarnas, S. Aleiferis, A.A. Ivanov Jr., M. Bacal, Phys. Plasmas **20**, 101601 (2013)
- Y.I. Belchenko, G.I. Dimov, V.G. Dudnikov, Izv. Akad. Nauk SSSR, Ser. Fiz. **37**, 2573 (1973)
- Y.I. Belchenko, G.I. Dimov, V.G. Dudnikov, Sov. Phys. Tech. Phys. **18**, 1083 (1974)
- Y.I. Belchenko, G.I. Dimov, V.G. Dudnikov, A.S. Kuprianov, Rev. Phys. Appliquée **23**, 1847 (1988)
- C. Botcher, B.D. Buckley, J. Phys. **B12**, L497 (1979)
- M. Cacciatore, M. Capitelli, R. Celiberto, P. Cevet, C. Gorse, AIP Conf. Proc. **210**, 74 (1990)
- I. Čadež, R.I. Hall, M. Landau, F. Pichou, C. Schermann, J. Phys. B **21**, 3271 (1988)
- I. Čadež, C. Scherman, M. Landau, F. Pichou, D. Popovic, R.I. Hall, Z. Phys. **D26**, 238 (1993)
- M. Čizek, J. Horacek, W. Domke, J. Phys. **B31**, 1271 (1998)
- C. Courteille, J. Bruneteau, F.P.G. Valckx, Z. Sledziewski, M. Bacal, **64**(11), 3205 (1993)
- C. Courteille, A.M. Bruneteau, M. Bacal, Rev. Sci. Instrum. **66**(3), 2533 (1995)
- Dimov, Rev. Sci. Instrum. **67**(10), 3393 (1996)
- G.I. Dimov, G.V. Roslyakov, P. Tekh, Eksper. (Instrum. Exp. Tech., in russian) **29** (1974)
- W. Domcke, Phys. Rep. **208**, 97 (1991)
- K.W. Ehlers, Nucl. Instrum. Methods **32**(2), 309–316 (1965)
- K.W. Ehlers, K.N. Leung, Rev. Sci. Instrum. **51**, 721 (1980)
- F. El Balghiti-Sube, F.G. Baksht, M. Bacal, Rev. Sci. Instrum. **67**(6), 221 (1996)
- J. Ellis, J. Branson, K. Niemi, E. Wagenaars, T. Gans, J. Phys. D. Appl. Phys. **53**, 485202 (2020)
- I.I. Fabrikant, J.M. Wadekra, Y. Xu, Phys. Scr. **T96**, 45 (2002)
- U. Fantz, L. Schiesko, D. Wunderlich, Plasma Sources Sci. Technol. **23**, 044002 (2014a)
- U. Fantz, P. Franzen, B. Heinemann, D. Wunderlich, Rev. Sci. Instrum. **85**, 02B305 (2014b)
- J.A. Fasolo, IEEE Trans. Nucl. Sci. **NS-24**, 1597 (1977)

- G. Federici, W. Biel, M.R. Gilbert, R. Kemp, N. Taylor, R. Wenninger, *Nucl. Fusion* **57**, 092002 (2012)
- O. Fukumasa, S. Saeki, *J. Phys. D* **26**, 237 (1987)
- J.P. Gauyacq, *J. Phys. B : Atom. Mol. Phys.* **18**, 1859 (1985)
- V.P. Goretsky, A.V. Riabtsev, I.A. Soloshenko, A.F. Tarasenko, A.I. Schedrin, *Rev. Sci. Instrum.* **67**(4), 1622 (1996). © 1996 The American Institute of Physics
- W.G. Graham, *J. Phys. D. Appl. Phys.* **17**, 2225 (1988)
- Green, Proc. 11th Symp. Fusion Eng., Austin, TX, Nov 1985, pp. 103 (1985)
- Hall et al., *Phys. Rev. Lett.* **60**(4), 337 (1988)
- A. Hatayama, T. Sukarabayashi, K. Miyamoto, M. Ogasawara, M. Bacal, *Rev. Sci. Instrum.* **73**(2), 910 (2002)
- R.S. Hemsworth, T. Inoue, *IEEE TPS* **33**(6), 1799 (2005)
- J.R. Hiskes, *J. Appl. Phys.* **51**, 4592 (1980)
- J.R. Hiskes, A.M. Karo, *Appl. Phys. Lett.* **54**, 508 (1989)
- J.R. Hiskes, *J. Appl. Phys.* **70**, 3409 (1991)
- E.B. Hooper, Jr., O. A. Anderson, T.J. Orzechowski, P. Poulsen, Proc. Symp. On the Production and Neutralization of Negative Hydrogen Ions and Beams, Sept. 26–30 (1977), BNL Report 50727, K. Prelec, Editor, 163 (1977)
- M.B. Hopkins, K.N. Mellon, *Phys. Rev. Lett.* **67**(4), 449–452 (1991)
- J. Horacek, M. Cizek, K. Houfek, P. Kolorenc, W. Domcke, *Phys. Rev. A* **70**, 052712 (2004)
- H. Horiike, Y. Ohara, Y. Okumura, T. Shibata, S. Tanaka, “Conceptual Design of Negative-Ion-Based 500 keV 20 MW Neutral Beam Injector”, Japan Atomic Energy Research Institute, Rep. JAERI-M86–064, Apr. 1986
- T. Inoue, Y. Masuda, Y. Ohara, Y. Okumura, M. Bacal, P. Berlemont, *Plasma Sources Sci. Technol.* **1**, 75 (1992)
- A.A. Ivanov, *Rev. Sci. Instrum.* **75**, 1754 (2004)
- R.K. Janev, D. Reiter, U. Samm, *Collision Processes in Low Temperature Plasma* (2003)
- K. Jimbo, *Phys. Fluids* **27**, 2752 (1984)
- K. Jimbo, K.N. Leung, K.W. Ehlers, R.V. Pyle, *Nucl. Instrum. Methods Phys. Res.* **248**(Sect. A), 282 (1986)
- M. Kashiwagi et al., *Rev. Sci. Instrum.* **85**, 02B320 (2014)
- T. Kuo, D. Yuan, K. Jayamma, M. McDONALS, R. Baartman, P. Schmor, G. Duto, *Rev. Sci. Instrum.* **67**, 1314 (1996)
- S. Kuppel, D. Matsushita, A. Hatayama, M. Bacal, *J. Appl. Phys.* **109**, 013305 (2011)
- P. Lawrencen, K.E. Beauchamp, J.L. McKibben, *Nucl. Instrum. Methods* **32**, 357 (1965)
- K.N. Leung, M. Bacal, *Rev. Sci. Instrum.* **55**(3), 338 (1984)
- K.N. Leung, K.W. Ehlers, M. Bacal, *Rev. Sci. Instrum.* **54**, 56 (1983)
- K.N. Leung, K.W. Ehlers, R.V. Pyle, *Appl. Phys. Lett.* **47**, 227 (1985)
- K.N. Leung, G.J. De Vries, K.W. Ehlers, L.T. Jackson, J.W. Stearns, M.D. Williams, M.G. McHaeg, D.P. Ball, W.T. Lewis, P.W. Allison, *Rev. Sci. Instrum.* **58**(2), 235 (1987) also *AIP CP* **158**, 356 (1987)
- R.L. Martin, *IEEE Trans. Nucl. Sci.* **NS-18**, 953 (1971)
- J. Marx, A. Lebehoh, R. Campargue, *J. Phys. (Paris)* **46**, 1667 (1985)
- McAdams, *Rev. Sci. Instrum.* **85**, 02B319 (2014)
- C.D. Moak, H.E. Banta, J.T. Thurston, J.W. Johnson, R.F. King, **30**, 694 (1959)
- T. Mosbach, *Plasma Sources Sci. Technol.* **14**, 610 (2005)
- E. Nicolopoulou, M. Bacal, H.J. Doucet, *J. Phys. (Paris)* **38**, 1399–1404 (1977),. also in Proc. Symp. on the Production and Neutralization of Negative Hydrogen Ions and Beams, BNL Report 50727, K. Prelec, Editor, 26 (1977)
- T.F. O’Malley, *Phys. Rev.* **150**, 14 (1966)
- Y. Okumura, H. Horiike, T. Inoue, T. Kurashima, S. Matsuda, Y. Ohara, S. Tanaka, *AIP Conf. Proc.* **158**, 309–318 (1986)
- M. Péalat, J.-P.E. Taran, M. Bacal, A.M. Bruneteau, *J. Chem. Phys.* **82**, 4943 (1985)
- Peters, *Rev. Sci. Instrum.* **71**, 1069 (2000)

- K. Prelec, T. Sluyters, *Rev. Sci. Instrum.* **44**, 1451 (1973)
- T. Sakurabayashi, A. Hatayama, K. Miyamoto, M. Ogasawara, M. Bacal, *Rev. Sci. Instrum.* **73**(2), 1048 (2002)
- C. Schermann, R.I. Hall, M. Landau, F. Pichou, I. Cadez, *AIP Conf. Proc.* **210**, 159–168 (1991)
- G.J. Schulz, *Rev. Mod. Phys.* **45**(3), 425 (1973a)
- G.J. Schulz, *Rev. Mod. Phys.* **45**, 423–486 (1973b)
- N. N. Semashko, V. V. Kusnetsov, A. I. Krylov, *Proc. Symp. on the Production and Neutralization of Negative Hydrogen Ions and Beams*, Sept. 26–30 (1977), BNL Report **50727**, K. Prelec, Editor, 170 (1977)
- D. Spence, K.R. Lykke, *Proc. XIX Intern. Linear Accelerator Conference*, Argonne National Lab., 1998, Report ANL-98/28; 1998, 508–510 (1988)
- G.C. Stutzin, A.T. Young, A.S. Schlachter, K.N. Leung, W.B. Kunkel, G.T. Worth, R.R. Stevens, *Rev. Sci. Instrum.* **59**(8), 1479 (1988)
- G.C. Stutzin, A.T. Young, A.S. Schlachter, K.N. Leung, W.B. Kunkel, *Chem. Phys. Lett.* **155**, 475 (1989)
- P. Svarnas, J. Breton, M. Bacal, R. Faulkner, *IEEE Trans. Plasma Sci.* **35**, 1156–1162 (2007)
- Y. Takeiri et al., *AIP Conf. Proc.* **1515**, 139 (2013)
- C.C. Tsai, W.K. Dagenhart, W.L. Stirling, G.C. Barber, et al., *AIP Conf. Proc.* **158**, 194 (1987)
- N. Umeda et al., *Rev. Sci. Instrum.* **85**, 02B304 (2014)
- J.M. Wadehra, *Phys. Rev. A* **29**, 106 (1984)
- J.M. Wadehra, J.N. Bardsley, *Phys. Rev. Lett.* **41**(26), 1795–1798 (1978)., also in *Phys. Rev. A*, **20**, 1398 (1979)
- A.T. Young, G.C. Stutzin, K.N. Leung, W.B. Kunkel, *AIP Conf. Proc.* **210**, 450–461 (1991)
- H. Zhang, *Ion Sources* (Science Press, Springer, 1999) © Science Press Beijing and Springer-Verlag Berlin Heidelberg New York 1999

Chapter 2

Fundamental Aspects of Surface Production of Hydrogen Negative Ions



Motoi Wada

Abstract A low-energy proton leaves solid metal surface as a negative hydrogen (H^-) ion when it picks up two electrons from the metal conduction band. Charge exchange foils served as the source of H^- ions for a tandem acceleration, and the H^- production efficiency was found improved as the work function of the foil surface was lower. Simple structure discharge sources produced H^- ions with high efficiency when they maintained hydrogen discharges with the addition of cesium (Cs) into the plasma. The principal mechanism of these high efficiency source for producing H^- ions was found to be negative ionization of hydrogen positive ions and neutrals leaving the surface of an electrode immersed in a plasma. The surface of the beam extraction aperture of a contemporary H^- ion source is covered with Cs to enhance the ratio of extracted H^- ion current to co-extracted electron current. The H^- ion current extracted through an aperture covered with Cs shows a clear correlation to the photoelectric signal indicating the H^- ion production at a low work function surface. This chapter describes the fundamental processes related to surface production of H^- ions.

Keywords Work function · Adsorption · Secondary Emission · Negative ion

2.1 Introduction

2.1.1 Early Observations

Emission of negative hydrogen (H^-) ions from a solid surface was observed for a metal sample under exposure to positive lithium ion beams as early as 1931 by Woodcock (1931). Alvarez (1951) proposed to utilize H^- ions produced by passage

M. Wada (✉)
Doshisha University, Kyotanabe, Kyoto, Japan
e-mail: mwada@mail.doshisha.ac.jp

of positive hydrogen ion beam through a thin foil for tandem acceleration with a Van de Graaff apparatus. Baragiola et al. (1973) found that the charge state fractions of the hydrogen ion beam produced through a foil of $10 \mu\text{g}/\text{cm}^2$ thickness were different from those for thick gas target; the foil showed characteristic electron transfer to hydrogen as a solid material forming a H^- ion leaving the surface. Philips (1955) showed the negative ionization fraction was affected by the material covering the surface of the beam exit side of the foil. Thus, the condition of the surface from where H^- ions were produced was known to affect the negative ion fraction of the beam.

Some of these early observations also indicated that fractions of H^- ions against protons increased with decreasing incident proton energy. Verbeek et al. (1976) have shown that the energy distribution of H^- ions produced from 15.3 keV protons injected onto a solid Au surface contained a larger amount of lower-energy component in addition to a group of H^- ions converted from protons reflected at the surface. They also found that the ratio of H^- ions produced by reflection to incident protons decreased by changing the surface to Ta and increased by changing it to ThO_2 . Difference in work function, ϕ_w , of the surfaces of Ta ($\phi_w = 5.6 \text{ eV}$), Au ($\phi_w = 4.8 \text{ eV}$), and ThO_2 ($\phi_w = 2.0 \text{ eV}$) was considered to cause the difference in the measured fraction of H^- ions to protons. These results suggest that two factors, the particle energy and the work function, determine the fraction of H^- ions against the incident protons.

2.1.2 High-Current Surface Plasma Source

Demonstration of high-intensity H^- ion beam extraction by Belchenko et al. (1974) exceeding $1 \text{ A}/\text{cm}^2$ current density triggered the intensive research on surface production of H^- ions in many research institutes. Belchenko (1993) defined the SPS as a source in which the negative ion production occurs on electrodes in contact with the gas discharge plasma. Two versions of SPS were developed, namely, the “planotron” with the magnetron discharge geometry and the Penning type SPS (Belchenko and Kupriyanov 1994a). In the magnetron geometry, H^- ions produced at the cathode surface are self-extracted across the sheath to reach the extraction electrode. On the other hand, the cathode faces against the extraction electrode perpendicularly in the Penning geometry. The details of these sources are introduced in the later chapter of this book and the book compiled by Dudnikov (2019).

These sources had small dimensions and were operated at high power densities. Belchenko and Kupriyanov (1994a, b) and Dudnikov (2017) showed the energy spectrum of the extracted H^- ions containing two groups with the majority of 80–85% having the kinetic energy corresponding to the cathode potential. These H^- ions were considered formed on the cathode surface. The remaining 15–20% exhibited their origin was in the space where the electric potential was close to the anode. This component can be considered formed as the result of charge exchange near the extractor, electron volume process, and/or the surface production at the

anode surface. The “physical principles of the surface plasma method for producing beams of negative ions” were first discussed by Belchenko et al. (1977) in the First Symposium on the Production and Neutralization of Negative Ions and Beams in September 1977 at Brookhaven National Laboratory.

2.1.3 Cs Operation of Volume Production Source

In the 1977 Brookhaven meeting, Bacal et al. (1977) reported that high H^- ion density can be realized in a hydrogen plasma volume. Since then, volume sources and surface sources were studied as two different types of H^- ion sources, while Leung and Ehlers (1981) showed their multicusp ion source produced both surface-produced and volume-produced H^- ions. About one decade later, Walther et al. (1988) injected Cs into their volume production type ion source: a 2.5 cm diameter small ion source with a magnetic filter and a plasma electrode (See Chap. 1 of this book by Bacal). They investigated volume H^- ion source operation with Cs and compared the result to the operation with Xe. Injection of Cs into a pure hydrogen discharge increased the H^- ion current to 16 times, while Xe injection increased to 3.7 times. They showed Ba also enhanced H^- ion current as Cs (Walther et al. 1989). Surface production of H^- ions at the plasma electrode, the electrode with the H^- ion beam extraction hole opened at the center, was speculated as the possible mechanism enhancing the negative ion current. Leung et al. identified that the H^- ions having the energy of the electrical potential of the anode were extracted from the ion source (Leung et al. 1989). After Okumura et al. (1990) demonstrated the extraction of an ampere-class H^- ion current beam from their Cs-seeded large ion source for neutral beam heating, contemporary negative hydrogen ion sources are operated with Cs.

There exists a difference in source geometry between a volume production type source and a surface production type source; the plasma grid (PG) serves as the H^- ion production surface in a Cs operation of volume type ion source. The energy spectra of plasma particles striking the surface are also different between these two types. A surface source often shows a large beam divergence corresponding to a large energy spread in the beam transverse direction. The H^- ion beam extracted from a volume source operated with Cs exhibits a smaller beam divergence indicating the average of random velocity of H^- ions is small; the source produces H^- ions with low kinetic energies. This chapter discusses the fundamental processes related to surface production of H^-/D^- ions.

2.2 Mechanism of Negative Ion Surface Production

2.2.1 Theoretical Background

A simple model of H^- surface production can be described as a schematic shown in Fig. 2.1. The H^- ion production surface faces against the plasma and releases

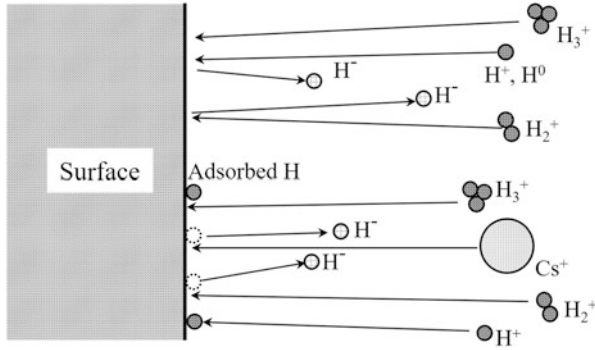


Fig. 2.1 A schematic illustration of H^- surface production. Hydrogen ions and neutrals bombard the H^- ion production surface, and part of these fluxes are converted to H^- ions. In a H^- ion source, atomic and molecular hydrogen ions as well as Cs^+ bombard the surface to produce H^- ions by backscattering and ion-stimulated desorption processes

H^- ions toward the plasma. Two fundamental processes are responsible for the production of H^- ion flux from the surface: particle reflection and ion-induced desorption of hydrogen atoms adsorbed on the surface. In both processes, the kinetic energy of the incoming ions affects the resulting flux from the H^- ion production surface. Electrons and photons can also cause negative ion emission from the surface, but they are excluded in the figure as these processes contribute little to H^- ion production in a H^- ion source. The simplest form to compute the surface produced H^- ion current density from the surface can be written for the particle reflection process.

$$j_R = j_0 R_{N0} \eta_{0^-} + \sum_{n=1}^3 n j_{n^+} R_{Nn} \eta_{n^-} \quad (2.1)$$

Here, $j_0, j_{1^+}, j_{2^+}, j_{3^+}$ are the current densities of atomic hydrogen, H^+ ions, H_2^+ ions, and H_3^+ ions, respectively. The particle reflection coefficients, R_{Nn} , and the negative ionization efficiencies η_{n^-} for corresponding species are the functions of particle incident energy and dependent upon energy reflection coefficients. Data on these reflection coefficients are summarized for plasma-surface interaction studies in nuclear fusion research (Eckstein 2009).

Similarly, the H^- ion current produced from the ion-induced desorption process can be summarized in the following form with the surface adsorbed hydrogen density ρ_s .

$$j_D = \sum_n Y_{sn} j_n + \beta_n^- \rho_s \quad (2.2)$$

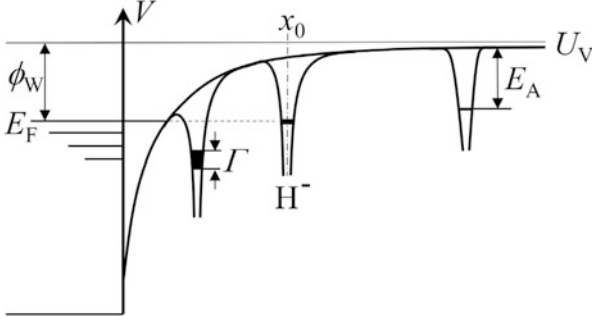


Fig. 2.2 Potential diagram near the H^- ion production surface. U_V vacuum level, E_A electron affinity, ϕ_w work function, E_F Fermi level, Γ : level broadening. At the distance x_0 , the sum of electron affinity and the image potential becomes equal to the work function; see Eq. (2.3)

Here, Y_{sn} is the ion-induced desorption yield, or the sputtering yield against adsorbed hydrogen due to an incident ion of species n . The incident positive ion fluxes, j_{n+} , include Cs^+ ion flux as well as fluxes of hydrogen ions and neutrals. Coefficients β_n^- are the probabilities for H^- ions to escape the surface vicinity without losing the electrons in the affinity level. Provided one assumes a hydrogen atom is leaving from surface as a H^- ion in the initial condition, η_n^- can be replaced with β_n^- .

In their report of the ion source study in the first Brookhaven meeting, Belchenko et al. (1977) introduced the work by Kishinevskii (1975) to explain the role of Cs injection in enhancing the H^- ion current production. A simplified potential diagram for a H^- ion travelling in the vicinity of metal surface is schematically illustrated in Fig. 2.2. The H^- affinity level shifts due to image potential. Until a H^- ion reaches the distance x_0 where the sum of the affinity level, E_A , and the image potential becomes equal to the metal work function, ϕ_w , the electron in the filled conduction band level in the metal can tunnel to the H^- ion affinity level. This distance can be written with the elementary charge e and the permittivity of vacuum ϵ_0 .

$$x_0 = \frac{e}{16\pi\epsilon_0(\phi_w - E_A)} \quad (2.3)$$

As x_0 increases with decreasing work function, the probability for a H^- ion to escape from the surface increases. Kishinevskii (1975) computed the probability by calculating the electron loss rate (or neutralization rate) $w(x)$ at the distance x through the following equation.

$$\beta^- = \exp \left[- \int_{x_0}^{\infty} \frac{w(x)}{v_{\perp}(x)} dx \right] \quad (2.4)$$

The equation shows the H^- ion velocity component normal to the surface, v_\perp , should be large for the H^- ion to escape the surface region before the electron tunnels back to a metal band level. Note that Kishinevskii evaluated β^- as the function of $v_\perp(x_0)$: v_\perp at the distance x_0 , which is larger than the surface normal velocity component of H^- ions far from the surface corresponding to the increase in kinetic energy by $e(\phi_w - E_A)$.

Hiskes and Karo (1977) included the effect of the surface dipole formed by Cs adsorption on the surface and determined the energy shift as well as the broadening, Γ (see Fig. 2.2), as a complex eigen value problem. They predicted the H^- escape probability or “survival probability,” higher than that calculated by Kishinevskii. Rasser et al. described the negative ionization from clean tungsten, cesiated tungsten, and thick cesium surfaces at low energies with two models: a probability model and an amplitude model (Rasser et al. 1982). In both models the electron motion is described quantum mechanically and the nuclear motion classically. The electron affinity level of an atom close to the metal shifts negative by image forces and broadens due to the resonant transition of an electron between the conduction band of the metal and the valence shell of the atom. Results by Rasser et al. predicted negative ion fractions lower than Kishinevskii’s model, as they have included the effect due to density of states near the surface. The maximum negative ionization efficiencies calculated by Rasser et al. are 4% on W(110), 40% on cesiated tungsten, and 15% on thick cesium.

Rasser et al. (1982) showed that their equation derived from a quantum mechanical model can be reduced to the following simple formula to compute β^- , which was derived by Blandin et al. (1976) for the case of small β^- .

$$\beta^- = \frac{2}{\pi} \exp\left(-\frac{\pi(\phi_w - E_A)}{2av_\perp}\right) \quad (2.5)$$

Here, a is the exponential decay constant of the transition rate at a large distance. The equation can only give a rough estimation of escape probability for the case that v_\perp can be regarded constant, but useful in estimating the dependence upon the work function and upon the exit velocity. Hiskes et al. (1976) discussed the kinetic energy necessary for negative ions to leave the surface to be 0.77 eV for Cs and 1.25 eV for sodium. These energies should be provided through a particle reflection process or the ejection energy at an ion-induced desorption (sputtering) process of adsorbed atoms. This is why the energy reflection coefficient, R_E , is also considered important in determining the negative hydrogen ion yield as well as particle reflection coefficient R_N (Bacal et al. 2014).

Yields of H^- ions for conditions similar to Rasser et al. with a simple surface geometry were calculated by Cui (1991). In early theoretical models, results were tabulated as functions of the normal velocity component of hydrogen leaving the surface. Effects due to oblique trajectory were investigated by Koppers et al. (1998), and the probability of negative ion formation was shown to be the function of angle of H^- ions leaving the surface. Gainullin and Dudnikov (2020) introduced

the electron wave packet for the theoretical analysis of electron transfer in a one-dimensional potential geometry. Wimmer et al. and Chubb et al. computed the local density of states for Cs adsorbed W (Wimmer et al. 1983) and Cs adsorbed Mo (Chubb et al. 1987), respectively. Low-energy hydrogen scattering at a cesium adsorbed Mo surface was computed by Rutigliano et al. (2017) by molecular dynamics (MD) simulation. Their MD calculation predicted the H^- angular distribution more forwardly peaked than the D^- angular distribution (Rutigliano et al. 2020).

2.2.2 Experiments on Fundamental Processes

Atomic and molecular positive hydrogen ion beams can serve as the particle sources to study H^- ion formation through particle reflections. When they studied the energy distribution of H^- ions produced by hydrogen ion bombardment on a tungsten surface, Levine and Berry (1960) found low and high energy peaks corresponding to ion-induced desorption and reflection of incident positive ions. Echstein et al. (1980) measured the charge states of hydrogen reflected at the surface of Cs covered Ni to find the negative ion fraction decreased with increasing incident beam energy above 500 eV/H. Hiskes and Karo discussed the probability of incoming positive ions to be negatively ionized during the process of hydrogen ion reflections (Hiskes and Karo 1977). In their report on NISEC (negative ion secondary emission coefficient), Hiskes and Schneider (1980) formulated the equations of formation and survival probabilities. The experimentally measured dependence of negative ionization efficiency upon incident H/D energy was compared with the theory for the reflection processes at thick alkali metal surfaces (Hiskes and Schneider 1981). They prepared clean alkali metal surfaces by depositing alkali metals on a cooled metal target contained in an UHV system. The surface was bombarded by hydrogen and deuterium molecular ion beams, and the amount of produced negative ion current was measured to obtain the negative ion yield. They have observed clear shifts of the maximum negative ion yields to higher incident energies by switching the isotope ions from hydrogen to deuterium; the exit velocity dependence of β^- appeared corresponding to the difference in isotope mass. Schneider et al. (1981) showed the dependence of D^- ion yield upon the change in work function using the same experimental device. Their result shown in Fig. 2.3 clearly indicates the maximum D^- ion yield at the minimum work function condition. Meanwhile, higher energy D^- exhibited larger negative ionization efficiency when the Cs thickness was smaller than the coverage of the minimum work function.

The H^- ion production by reflection of hydrogen positive ions striking a Cs covered tungsten surface at an oblique angle was studied experimentally by van Wunnik and Los (1983), who showed a clear correlation between the conversion efficiency from positive hydrogen ions to H^- ions and the work function. The measured conversion efficiency increased with the angle with respect to the surface normal to show the maximum at around 85° . They also measured the angle resolved energy spectrum showing the energy loss due to the adsorbed layer; the incident

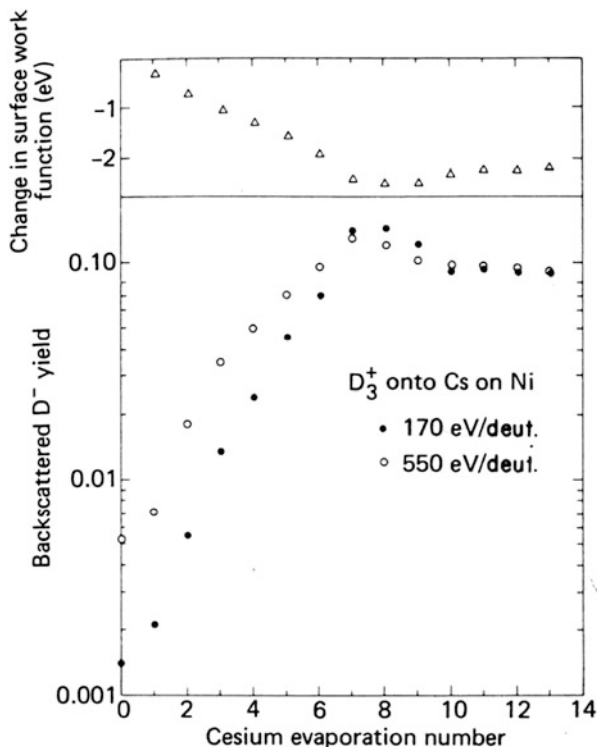


Fig. 2.3 Correlation between surface work function and backscattered D^- ion yield. The thickness of Cs layer on nickel increases as more Cs is evaporated to the nickel target. (Reproduced from Schneider et al. (1981) with the permission from the American Physical Society. Copyright 1981 The American Physical Society)

positive ions undergo collisions with atoms in solid situated within a few layers at the top surface losing a small energy. The measured energy spectrum changed as their detector was positioned to collect H^- ions reflected into different exit angles (van Wunnik et al. 1983) corresponding to the development of surface collision cascade. These results were compared with the theoretical model developed by Rasser et al. (1982).

Extraction and transport of ion beams become more difficult for lower beam energy as the beams diverge due to space charge. Ion-induced desorption of surface adsorbed H/D should emit small kinetic energy H^-/D^- ions, which show the effect of outgoing velocity dependence upon the isotope mass difference. Yu bombarded his Mo (100) sample contained in his UHV system with Ne^+ ions from 150 eV to 3.5 keV energy to measure H and D negative ion yields (Yu 1978); surface adsorbed H and D were sputtered by Ne^+ ions, and part of them were negatively ionized. The pure Mo sample was coated with hydrogen or deuterium by introducing the gases into the vacuum system, and the Cs was deposited on the hydrogen isotope

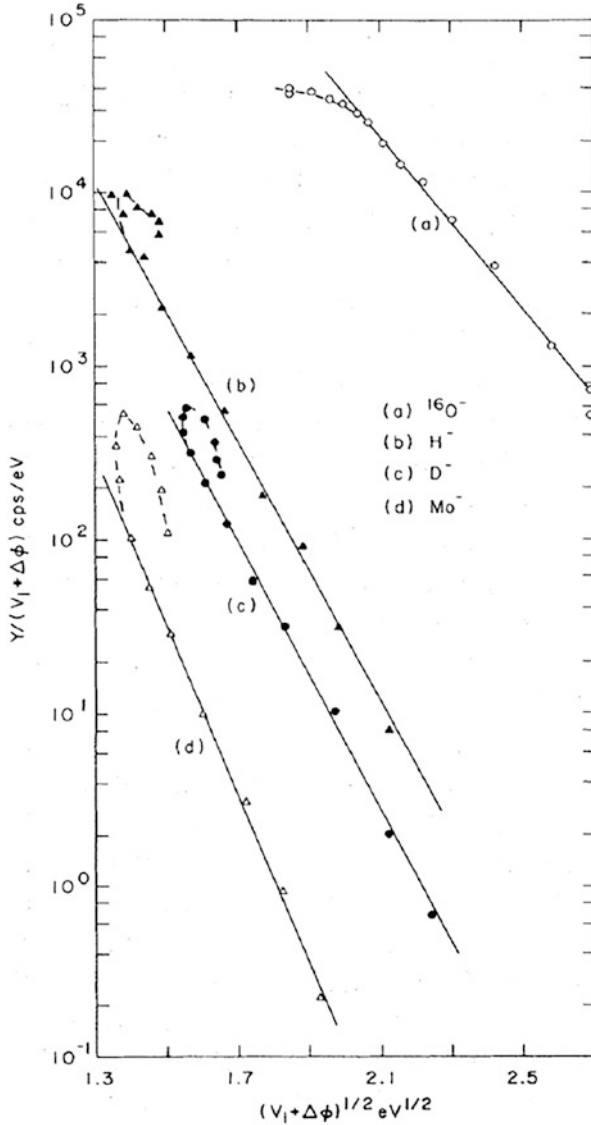


Fig. 2.4 Normalized negative ion yield by Ne^+ sputtering after Yu (1978). (Reproduced with permission from The American Physical Society. Copyright 1978 The American Physical Society)

adsorbed sample. Yu found the efficiency to produce D^- ions was about one order of magnitude lower than the efficiency to produce H^- ions for the same work function condition, as shown in Fig. 2.4. This isotope effect can be attributed to the smaller D^- ion velocity component normal with respect to the low work function surface than the H^- ion normal velocity component. Meanwhile, Yu fit the dependence of

negative ion current to a tunneling probability based on the measured change of the target work function.

Ernst-Vidalis et al. (1992) studied the H^- ion emission due to ion-stimulated desorption by Ar^+ ion bombardment onto a Cs covered Mo (1 1 0) surface. The measured H^- ion yield showed an exponential increase against the work function reduction. Seidl and Pargellis investigated the H^- ion yield from hydrogen adsorbed Mo under Cs^+ ion bombardment (Seidl and Pargellis 1982). At enough H_2 pressure higher than 10^{-4} Torr (or 0.013 Pa) and proper Cs coverage about 0.65 monolayer, the H^- ion yield was more than 35% for 750 eV incident Cs^+ .

In the sputtering process, sputtered atoms escape the surface with kinetic energy less than sublimation energy, and the bright beam can be formed through the process. Another way to produce H^-/D^- ions with smaller velocities is to convert thermal atoms of hydrogen isotopes to their negative ions. Surface production of H^-/D^- ions by directing H/D atoms produced by a tungsten furnace to a low work function surface was attempted by Graham (1979). Keeping the tungsten tube furnace temperature at 2500 K, he found that the rapid increase in negative ion signal counts was correlated to the reduction of work function of the Cs covered polycrystalline Mo surface. However, the yield was too small to make a quantitative comparison in the efficiency between hydrogen and deuterium atoms. Surface negative ionization efficiency for thermal hydrogen atoms was estimated to be as low as 1.5×10^{-4} H^- ions per incident atom according to the measurement made by Pargellis and Seidl (1982) with their tungsten oven maintained at 2400 K.

Large beam divergence due to space charge of a hydrogen/deuterium ion beam makes the H^- ion yield measurement at low energy difficult. Seidl et al. had assembled their system to measure H^- ion yield from cesiated Mo surface under bombardment of hydrogen positive ions with the energy down to less than 5 eV per proton (Seidl et al. 1996). Their results shown in Fig. 2.5 indicate a nearly constant H^- ion yield above 15 eV. This observation suggests the possibility of large current H^- ion production with low incident hydrogen ion energies as the H^- ion collection efficiency could have been reduced due to space charge. Seidl's research group also reported that work function and ion yield became different as the conditions for Cs and hydrogen supply onto the Mo target were changed. The target temperature was an important factor determining the amount of hydrogen co-adsorbed on a Mo surface at different coverage of Cs (Ernst-Vidalis et al. 1987). In the "dynamically cesiated condition," Cs was supplied to the surface from the backside while heated to temperature above 240 °C during the hydrogen ion bombardment. This Cs supply procedure realized a higher H^- ion yield compared with Cs deposition onto the target surface prior to the ion bombardment. (See Fig. 2.5.) The dependence of H^- ion yield upon the work function changes by the amount of co-adsorbed hydrogen on a Cs adsorbed surface, as van Amersfoort et al. reported (van Amersfoort et al. 1986). Before their ion reflection experiment, Seidl and his co-workers measured the H^- formation efficiencies for processes involving hydrogen Cs co-adsorbed conditions under lower energy particle incidence: backscattering of thermal hydrogen atoms (Pargellis and Seidl 1982) and desorption induced by Cs ion sputtering (Seidl and Pargellis 1982). Production of H^- ions by injecting

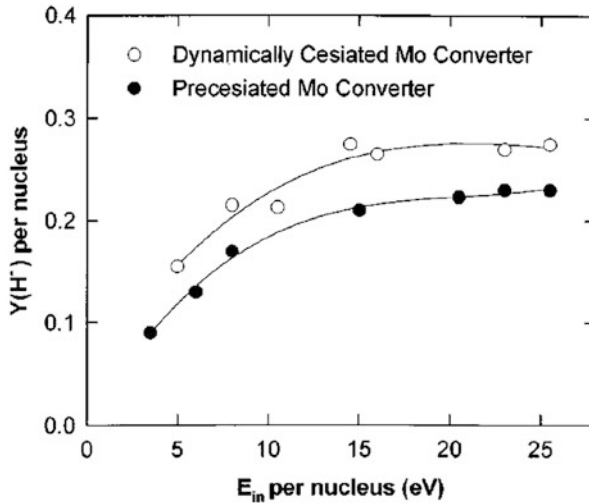


Fig. 2.5 The H^- ion yield per hydrogen as a function of incident energy per hydrogen for different methods to supply Cs onto the Mo converter (H^- ion production surface.) Dynamical cesiation produces more H^- ions than the Cs covered surface prepared before hydrogen ion bombardment. (Reproduced from Seidl et al. (1996) with the permission from AIP publishing. Copyright 1996 AIP Publishing LLC)

thermal H atoms to low work function surface was later confirmed by Lee and Seidl (1992) using an electron cyclotron resonance (ECR) plasma. Meanwhile, H^- ion production from a low work function surface under an exposure to atomic hydrogen produced by an RF discharge was confirmed by Okuyama and Mori (1992).

Figure 2.1 does not include H^- ion yields due to electron and photon irradiations as efficiencies for these processes are considered low in the H^- ion source operation conditions. Not many electrons in plasma can reach negatively biased H^- ion production surface. Electron temperature near the plasma grid must be kept low enough to reduce coextracted electron current, and few energetic electrons strike the PG surface. Thus, the electron fluxes to the surface are not expected very high for these two cases. The H^- ion emission due to electron bombardment was studied by Hoffman et al. for an *a*-Si-H sample (Hoffman and Petravic 1996), and H adsorbed diamond sample (Hoffman et al. 2001). They extended their study using D adsorbed diamond to report that the H^- ion yield was two orders of magnitude smaller compared with H^+ ion yield, while more than about 10 eV electron energy was necessary to detect sizable signal of negative ions (Hoffman et al. 2002). Ernst-Vidalis et al. (1992) investigated the electron stimulated desorption of Cs-H₂ covered Mo, but reported the data on H^+ ion emission current only. Electron stimulated desorption from SiO₂ was found to include H^- , O^- , and Si^- by Lanzillotto et al. (1991), who demonstrated that the O^- ion yield resembled the Auger electron yield.

Hurych et al. (1988) measured the H^- ion yield by irradiating a Cs covered W surface with photons of the energy from 40 to 50 eV. They found the H^- ion signal decreased rapidly in accordance with the time of the UV exposure which could have caused the increase of work function or depletion of hydrogen adsorbed on the surface. Baker et al. (1994) measured the photon-stimulated desorption yield from a BaO surface, and the threshold for the H^- ion emission was about 3 eV, while the yield was below 10^{-7} H^- /photon for photon energy less than 5 eV. Small amount of H^- ion current can be produced from thermal desorption process. Palmer (1984) reported that H^- ion signal was detected not only in the temperature increasing process but also in the temperature decreasing process from his hydrogen adsorbed Cs covered W surface.

2.2.3 *Experimental Results Using Ion Sources*

The original SPS were operated with high power densities, and the discharge noise made precise measurement on fundamental processes using SPS impossible. Ehlers and Leung (1980) put in a negative ion production surface called converter in a field-free region of a plasma confined quietly in a multicusp device (Limpacher and Mackenzie 1973). The converter surface was biased negatively with respect to the plasma, while the discharge power supply system was controlled independently from the converter bias. This ion source configuration made it possible to study the interaction between a low discharge power hydrogen plasma and a H^- ion production surface. Introduction of small amount of Cs into a hydrogen discharge caused enhancement of surface produced H^- ions by orders of magnitude (Ehlers and Leung 1980). The effect of converter material upon the produced H^- ion current extracted from the ion source was investigated by Leung and Ehlers (1984).

Wada et al. (1983) measured photoelectric current from the copper converter to measure the work function by directing monochromatic light produced by coupling narrow bandwidth optical interference filters and a high-power (1 kW) Xe short arc lamp. A small (15 cm diameter 18 cm long) multicusp ion source with the converter was operated at a discharge power as low as 5 W (100 V 50 mA) to reduce plasma noise. The measured correlation between the work function and the surface produced H^- ion current looked consistent with Eq. (2.5); the H^- ion current from the converter normalized to the ion saturation current showed an exponential dependence against the change in measured work function. However, the converter current became unstable during a plasma operation, and the copper converter was found sputtered after the operation. The material of the converter was changed to Mo with the sputtering yield smaller than Cu against Cs. The correlation between the photoelectric work function and the H^- ion yield from the converter was investigated by changing the converter bias voltage. The results are summarized in Fig. 2.6 (Wada et al. 1990). The measured H^- ion yields increased exponentially against the reduction of work function. For the same work function, the H^- ion

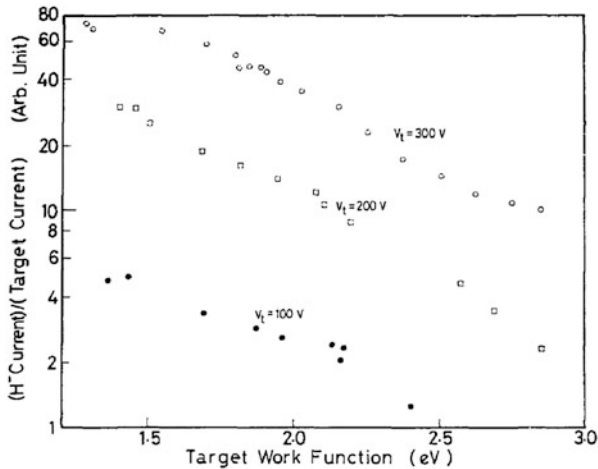


Fig. 2.6 Correlation between work function and H^- ion yield (detected H^- ion current normalized to converter current.) for a Mo converter immersed in a dilute ($\sim 10^9 \text{ cm}^{-3}$ density) plasma. (Reproduced from Wada et al. (1990) with the permission from AIP. Copyright 1990 AIP Publishing LLC)

yields were higher for larger converter bias voltage corresponding to larger exit velocity of H^- ions.

These experimental results seem to show the expected dependence of H^- ion yield upon the converter work function and that upon the H^- ion exit velocity. As the converter bias was raised, more H^- ions are produced. The escape velocity should increase to increase the survival probability, while sputtering yields of surface adsorbed hydrogen also increase with increasing positive ion incident energies. One should note the ion species in the plasma may change due to injection of Cs, and the adsorption of hydrogen on the surface should be affected by Cs co-adsorption on the Mo surface (Ernst-Vidalis et al. 1987). The difference in surface structure changes the collision cascade which alters the velocity and angular distributions of hydrogen leaving the surface and thus the H^- ion yield (Wada et al. 2014).

The energy spectra of H^- ions produced from the surface of different measured values of converter work function were compared. In Fig. 2.7 (Wada et al. 1990), the H^- ion energy spectrum near the work function minimum condition showed a peak at an energy slightly above the converter potential. This group of H^- ions having the small energy spread can be formed by ion-induced desorption. Meanwhile, more Cs introduced into the discharge formed the converter surface accumulating the Cs layer thicker than the work function minimum condition. As the work function increased from the minimum, the sharp peak reduced the height, and the energy group reaching up to 150% of the converter bias predominated the spectrum. The H^- ions of this energy group were probably produced from reflection process of H_2^+ ions in the plasma. The height of the low-energy peak component should be affected not only by work function but also due to the surface structure: hydrogen

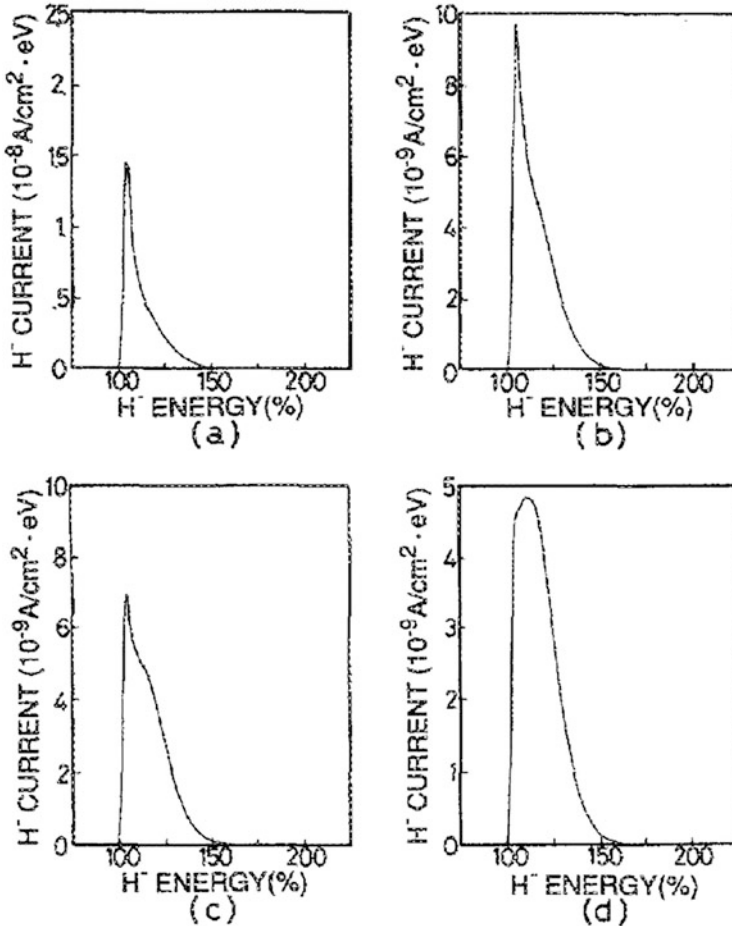


Fig. 2.7 H⁻ energy spectra for different converter work functions for Cs coverage thicker than for the work-function minimum. The measured work functions of the H⁻ production surface were (a) 1.44 eV, (b) 1.68 eV, (c) 1.90 eV, and (d) 1.95 eV. (Reproduced from Wada et al. (1990) with the permission of AIP. Copyright 1990 AIP Publishing LLC)

surface density on a Cs-Mo surface that should change with the amount of Cs adsorbed on the surface.

Through introducing the result measured by Wada et al. (1984), Hiskes et al. (1984) showed that the amount of H⁻ ions produced at the surface is predominated by the particle reflection components. The angular distribution of H⁻ ions produced by particle reflection is broader than that produced by desorption process making the contribution to the extracted beam apparently small. The reduction of converter voltage should decrease the beam divergence of surface produced H⁻ ions as well as their energy spread. The energy spectrum of H⁻ ions produced from a low voltage

(-12 V) converter surface showed a full width at half maximum as large as 4.5 eV indicating the presence of reflection component, while the surface production of H^- ions from a Mo surface in a cesiated discharge was confirmed down to 6 V converter bias potential (Wada and Tsuda 1994).

2.3 Surface H^- Ion Production at Low Energy

2.3.1 Negative Ion Production at Cs Covered PG Surface

When Okumura et al. (1990) injected Cs into their large-scale ion source developed at Japan Atomic Energy Research Institute (JAERI) to confirm the results reported by Walther et al. (1988), they put a liner structure (see Fig. 2.8) in their source to maintain high wall temperature. This large ion source with the size indicated in Fig. 2.8 was designed as a volume production-type H^- ion source and was equipped with the magnetic filter and the plasma grid. An ampere-level H^- ion current was extracted with the reduced arc power and the coextracted electron current by adding Cs into the ion source keeping the PG bias from -5 to $+10$ V with respect to the anode. The temperature of the PG was found to be an important parameter enlarging the H^- ion current intensity and reducing the co-extracted electron current. The observed substantial decrease of co-extracted electron current due to Cs injection

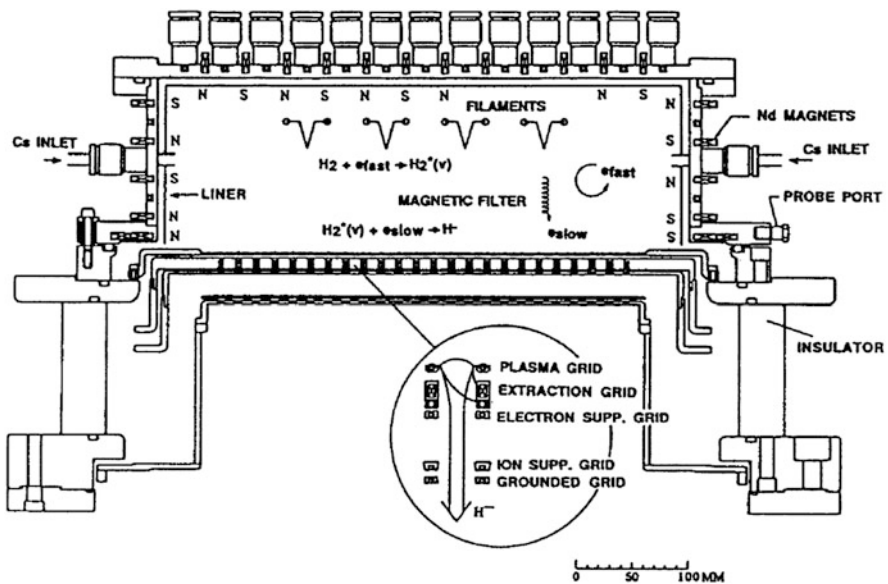


Fig. 2.8 The first large H^- ion source operated with Cs. (Reproduced from Okumura et al. (1990) with the permission from AIP. Copyright 1990 AIP Publishing LLC)

made the stable source operation with extraction of large H^- ion current possible. Since then, the H^- ion source designs include Cs injectors, magnetic filters, and plasma grids.

The clear correlation between the H^- ion current and the PG temperature observed by Okumura et al. indicated the importance of H^- surface production in the vicinity of the extraction hole. Local supply of Cs to a collar structure surrounding the extraction hole of a source developed for the Superconducting Super Collider enhanced the H^- ion beam current by a factor of three (Leung et al. 1993). This structure made a several weeks' long operation of a high-intensity H^- ion source for an accelerator possible with initial Cs supply about 10 mg to the collar (Stockli et al. 2010). The small surface area of the collar should reduce the amount of Cs for realizing low work function. The amount of Cs injection into a H^- ion source with a large area PG can be also reduced by improving the way to supply Cs to PG. In an advanced design H^- ion source, Cs is delivered to a temperature-controlled PG from the periphery (Belchenko et al. 2016); performance of the ion source is determined by the work function of the PG.

Shinto et al. (1996) estimated the work function of their ion source PG by directing Ar laser light to measure the photoelectric current. Their 20-cm-diameter 27-cm-long multicusp ion source was operated with 175 W (70 V 2.5 A) arc discharge power and the work function measurement was done after turning off the plasma. Directing the light from an Ar^+ laser with the wavelength tuning function at 457.9, 488, and 514.5 nm through an optical fiber, the photoelectric current was detected phase sensitively with a lock-in amplifier. As the photon wavelength range covered by the laser was narrow, and far from the threshold wavelength for the minimum work function condition, the measurement may become inaccurate by fitting the photoelectric quantum efficiency to the near threshold curve. To avoid inaccurate work function determination with limited sample wavelengths, they measured the photoelectron yield of a Cs covered Mo surface in a separate experimental system with a Xe arc lamp light source coupled to a monochromator. Through comparing the photoelectron emission curve obtained from a continuous wavelength scanning, the work function of the PG was estimated from the measured photoelectron yields at the Ar^+ ion laser wavelengths for the work function minimum condition. While the photoelectric current was measured during the turn-off time of the discharge, the duration of the turn off time was adjusted to control the temperature of the PG and the work function. The extracted H^- ion current increased up to 300% of the original value at the minimum work function condition by the Cs injection as shown in Fig. 2.9. The reference H^- ion current at 4.5 eV work function in the figure was assumed produced with the PG surface of pure Mo work function, or the condition that no Cs was injected to the ion source.

Morishita et al. (2001) measured the correlation between the photoelectric current and the extracted H^- ion current using a set up similar to the one employed by Shinto et al. but with much higher discharge power for the source operation. The diameter and the length of the ion source were 27 cm and 27 cm, respectively. The source operation H_2 pressure was kept at 0.17 Pa, while the maximum arc discharge

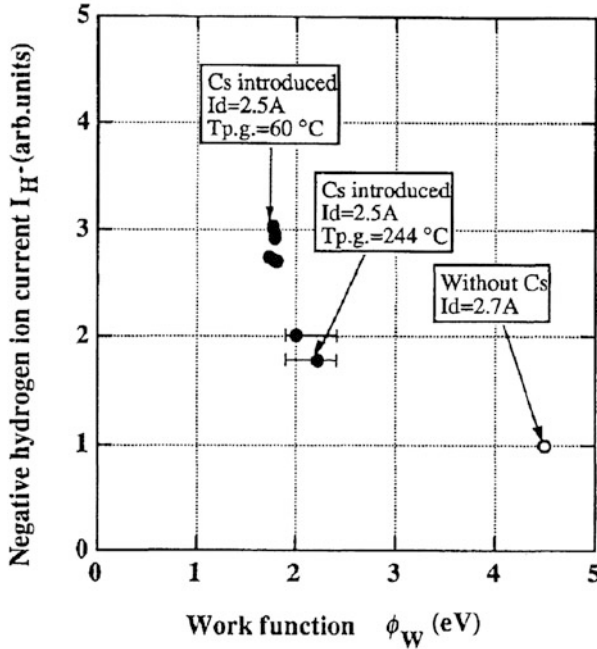


Fig. 2.9 The correlation between the H^- ion current extracted from a Cs seeded H^- ion source and the measured work function of the PG. (Reproduced from Shinto et al. (1996) with the permission from The Physical Society of Japan and the Japan Society of Applied Physics)

power was 10 kW. A four-grid extraction system composed of the plasma grid, extraction grid, electron suppressor grid, and ground grid formed the H^- ion beam accelerated up to 15 kV. Optical fibers are used to guide the light beam to the high voltage terminal from Ar^+ laser oscillated at 488 nm. The light emission intensity of Cs was also monitored with the laser-induced photoelectric current. A Langmuir probe inserted to the ion source characterized the plasma parameters, which were about 4.5 eV electron temperature and 500 mA/cm² ion saturation current density. The increase in wall temperature from 30° C to 110° C made the Cs emission intensity twelve times larger, while the probe ion saturation current stayed constant with the slight decrease of electron temperature.

Accurate determination of work function is only possible by comparing the dependence of photoelectric current intensity upon the photon energy when the photon energy is set far above the photoelectric threshold. Thus, Morishita et al. plotted the photoelectron yield as the indication of work function reduction with the extracted H^- ion current for different plasma grid temperature. Their result clearly indicated a strong correlation between photoelectron yield at 488 nm and the H^- ion current indicating H^- ion production at the PG surface. Meanwhile, the Cs emission intensity stayed almost constant corresponding to nearly constant density of Cs in the plasma; Cs^+ sputtering was not considered as the principal mechanism of H^-

ion current enhancement. The work function reduction causing the extracted H^- ion current increase suggests the H^- ion production by low-energy hydrogen particle incidence.

Tungsten filament cathodes excited arc discharges in the experiment by Shinto et al. and Morishita et al., while the inner wall surface including PG should have been coated with W by evaporation from the cathodes. This means that the surface structure of PG was not the hydrogen co-adsorbed Cs/Mo but the hydrogen co-adsorbed Cs/W. Alton (1986) proposed an empirical formula for the maximum work function change $\Delta\phi_m$ for the adsorbate ionization potential, electron affinity, and the substrate work function to be I_A , E_A , and ϕ_0 , respectively.

$$\Delta\phi = -1.24 \left[\phi_0 - \frac{1}{2} (I_A + E_A) \right] \quad (2.6)$$

Thus, the PG material can be optimized so as to realize the lowest work function. Kashiwagi et al. (2002) put different kinds of sample materials into a larger (34 cm diameter, 34 cm long) ion source with the Cs- H_2 plasma excited by 5 kW 2.45 GHz microwave power. Photoelectric current from Cs covered samples were compared, and they found both Ni and Au produced the largest current. The measured higher yield of the photoelectric current can be attributed to the combination of work function and the photon absorption at the material surface. Other parameters like particle and energy reflection coefficients should change the overall H^- ion production at a PG.

2.3.2 Contamination of PG Surface by Impurities

Research and development projects of H^-/D^- ion sources for NBI are being propelled with radio frequency (RF) plasma drivers after Krylov et al. (2006) clarified the long-term Cs operation problem of an arc discharge source, and Fantz et al. (2006) demonstrated the effectiveness of RF power for exciting an impurity-free H^- ion source plasma. Tungsten evaporation from cathode filaments covers the Cs deposited on the source wall requiring additional Cs injection to keep low work function on the PG. Takeiri et al. (2009) showed the Cs consumption increased in proportion to the cathode filament weight loss, while Oka et al. (2000) reported earlier that a larger amount of Cs was required when the number of filament cathodes of an arc discharge source was increased. The source developed for ITER NBI (Serianni et al. 2019) drives the plasma at 0.9 to 1.1 MHz frequency with up to 200 kW power to reduce Cs consumption rate. A compact source (Rizzolo et al. 2013) supplies Cs to this high-power system by controlling the flow rate.

As shown in Fig. 2.8, Cs is often sprayed into a H^- ion source to cover the inner side wall of a real size NB-injector source. Source discharges heat up the inner wall to vaporize Cs and Cs atoms move in the source to reach PG. When one

calculates the necessary amount of Cs to cover 1 m^2 area of PG at a half-monolayer thickness, the amount does not exceed even a mg. However, a H^-/D^- ion source requires additional Cs injection after the initial conditioning even when the plasma is excited by an RF power, and deuterium operation needs higher rate of Cs injection than hydrogen operation (Wunderlich et al. 2018). Erosion of Cs on PG by plasma impurities may become larger in deuterium plasma environment (Wada 2018) and the Cs accumulation in a future ion source for a fusion reactor can be intolerably large (Hemsworth and Boilson 2017). Thus, a series of searches for alternative materials suitable for PG surface of a high-performance H^- ion source has started. Friedl et al. (2018) investigated lanthanated and bariated materials finding their work functions did not decrease low enough as the ones at thermionic electron emission temperatures. Highly reactive nature of materials with intrinsic low work function often causes chemical reaction that makes the usage of the materials difficult to prepare PG, as reported by Cristofaro et al. (2020) on Eu. However, a proper preconditioning of the material like $12\text{CaO}\cdot 7\text{Al}_2\text{O}_3$ may realize enhanced surface production in accordance with the intrinsic low work function (Sasao et al. 2018).

2.4 Conclusion

The fundamental process related to H^- ion surface production was summarized. The efficiency of H^-/D^- ion production at a converter surface or a planatron cathode surface can be estimated from the experimentally obtained data. The amount of extractable H^- ion current from the ion source with the PG covered with Cs may not be computed straight forwardly, as the surface produced H^- ions once penetrate the plasma in front of the PG, change direction in the plasma, and must be extracted through holes opened on the PG. The maximum current density extractable from an ion source may be obtained using a simple model like virtual cathode (McAdams et al. 2012), while the precise energy and angular distributions together with local transport processes are required to be examined for an accurate analysis. For example, as we have seen in Chap. 1, adsorption of Cs on PG may reduce local concentration of atomic hydrogen near the extraction hole to decrease H^- ion destruction rate by associative detachment. Tsumori et al. (2017) clarified the PG bias voltage changed dynamically the flow pattern of H^- ions originating from the PG. Thus, some more data compilation on both surface and volume processes are necessary to fully describe the angular and velocity distributions of H^- ions crossing across the sheath formed at the extraction aperture. The final beam quality extracted from the source is determined by the plasma-wall interaction at the PG surface.

References

- G.D. Alton, Surf. Sci. **175**, 226 (1986)
- L. Alvarez, Rev. Sci. Instrum. **22**, 705 (1951)
- M. Bacal, E. Nicolopoulou, H.J. Doucet, Proceedings of the symposium on the production and neutralization of negative ions and beams. K. Prelec ed. **BNL-50727**, 26 (1977)
- M. Bacal, A. McAdams, E. Surrey, Rev. Sci. Instrum. **85**, 02B103 (2014)
- D.H. Baker, R.L. Champion, L.D. Doverspike, Y. Wang, Appl. Phys. Lett. **64**, 1880 (1994)
- R.A. Baragiola, E.R. Salvatelli, E. Alonso, Nucl. Instrum. Methods **110**, 507 (1973)
- Y.I. Belchenko, Rev. Sci. Instrum. **64**, 1387 (1993)
- Y.I. Belchenko, A.S. Kupriyanov, Rev. Sci. Instrum. **65**, 417 (1994a)
- Y.I. Belchenko, A.S. Kupriyanov, Rev. Sci. Instrum. **65**, 1170 (1994b)
- Y.I. Belchenko, G.I. Dimov, V.G. Dudnikov, Nucl. Fusion **14**, 113 (1974)
- Y.I. Belchenko, G.I. Dimov, V.G. Dudnikov, Proceedings of the symposium on the production and neutralization of negative ions and beams. K. Prelec ed. **BNL-50727**, 79 (1977)
- Y. Belchenko, G. Abdrashitov, P. Deichuli, A. Ivanov, A. Gorbovsky, A. Kondakov, A. Sanin, O. Sotnikov, I. Shikhovtsev, Rev. Sci. Instrum. **87**, 02B316 (2016)
- A. Blandin, A. Nourtier, D. Hone, J. Physique **37**, 369 (1976)
- S.R. Chubb, E. Wimmer, A.J. Freeman, J.R. Hiskes, A.M. Kao, Phys. Rev. B **36**, 4112 (1987)
- S. Cristofaro, R. Friedl, U. Fantz, J. Vac. Sci. Technol. A **38**, 063003 (2020)
- H.L. Cui, J. Vac. Sci. Technol. **A9**, 1823 (1991)
- V.G. Dudnikov, AIP Conf. Proc. **1869**, 030044 (2017)
- V. Dudnikov, *Development and Applications of Negative Ion Sources* (Springer Nature Switzerland, 2019)
- W. Echststein, H. Verbeek, R.S. Bhattacharya, Surf. Sci. **99**, 356 (1980)
- W. Eckstein, *IPP-Report IPP 17/12* (Max-Planck-Institut, Plasmaphysik, 2009)
- K.W. Ehlers, K.N. Leung, Rev. Sci. Instrum. **51**, 721 (1980)
- M.-L. Ernst-Vidalis, M. Kamaratos, C. Papageorgopoulos, Surf. Sci. **189/190**, 276 (1987)
- M.-L. Ernst-Vidalis, C. Papageorgopoulos, U. Stawinski, E. Bauer, Phys. Rev. B **45**, 1793 (1992)
- U. Fantz, H.D. Franzen, E. Speth, R. Hemsworth, D. Boilson, A. Krylov, Rev. Sci. Instrum. **77**, 03A516 (2006)
- R. Friedl, S. Cristofaro, U. Fantz, AIP Conf. Proc. **2011**, 050009 (2018)
- I.K. Gainullin, V.G. Dudnikov, Plasma Res. Exp. **2**, 045007 (2020)
- W.G. Graham, Phys. Lett. **73A**, 186 (1979)
- R.S. Hemsworth, D. Boilson, AIP Conf. Proc. **1869**, 060001 (2017)
- J.R. Hiskes, A. Karo, Proceedings of the symposium on the production and neutralization of negative ions and beams. K. Prelec ed. **BNL-50727**, 42 (1977)
- J.R. Hiskes, P.J. Schneider, J. Nucl. Mater. **93&94**, 536 (1980)
- J.R. Hiskes, P.J. Schneider, Phys. Rev. B **23**, 949 (1981)
- J.R. Hiskes, A.M. Karo, E. Wimmer, A.J. Freeman, S.R. Chubb, J. Vac. Sci. Technol. **A2**, 670 (1984)
- J.R. Hiskes, A. Karo, M. Gardner, J. Appl. Phys. **47**, 3888 (1976)
- A. Hoffman, M. Petravic, Phys. Rev. B **53**, 6996 (1996)
- A. Hoffman, A. Laikhtman, S. Usatze, M. Hadj Hamou, M.N. Hedhili, J.-P. Guillotin, Y. Le Coat, D. Teiller Billy, R. Azria, M. Tronc, Phys. Rev. B **63**, 045401 (2001)
- A. Hoffman, A. Laikhtman, R. Azria, Y. Le Coat, M. Hdj Hamou, M. Tronc, Diamond Related Mater. **11**, 867 (2002)
- Z.D. Hurych, P. Soukiassian, M.H. Baskishi, A.S. Bommannavar, C.E. Young, E.L. Schweitzer, M.J. Pellin, D.M. Gruen, Phys. Rev. B **38**, 8002 (1988)
- M. Kashiwagi, T. Morishita, Y. Okumura, M. Taniguchi, M. Hanada, K. Watanabe, A. Krylov, Rev. Sci. Instrum. **73**, 964 (2002)
- M.E. Kishinevskii, Zh. Tekh. Fiz. **45**, 1281 (1975); translated in Sov. Phys. Tech. Phys. **20**, 799 (1975)

- W.R. Koppers, B. Berenbak, D. Vlachos, U. van Slooten, A.W. Kleyn, *Phys. Rev.* **57**, 13246 (1998)
- A. Krylov, D. Boilson, U. Fantz, R.S. Hemsworth, O. Provitina, S. Pontremoli, B. Zaniol, *Nucl. Fusion* **46**, S324 (2006)
- A.-M. Lanzilotto, T.E. Madey, R.A. Baragiola, *Phys. Rev. Lett.* **67**, 232 (1991)
- B.S. Lee, M. Seidl, *Appl. Phys. Lett.* **61**, 2857 (1992)
- K.N. Leung, K.W. Ehlers, *J. Appl. Phys.* **52**, 3905 (1981)
- K.N. Leung, K.W. Ehlers, *J. Nucl. Mater.* **128-129**, 694 (1984)
- K.N. Leung, S.R. Walther, W.B. Kunkel, *Phys. Rev. Lett.* **62**, 764 (1989)
- K.N. Leung, D.A. Backman, D.S. MacDonald, *Rev. Sci. Instrum.* **64**, 970 (1993)
- L.P. Levine, H.W. Berry, *Phys. Rev.* **118**, 158 (1960)
- R. Limpaecher, K.R. Mackenzie, *Rev. Sci. Instrum.* **44**, 726 (1973)
- R. McAdams, D.B. King, A.J.T. Holmes, E. Surrey, *Rev. Sci. Instrum.* **83**, 02B109 (2012)
- T. Morishita, M. Kashiwagi, M. Hanada, Y. Okumura, K. Watanabe, A. Hatayama, M. Ogasawara, *Jpn. J. Appl. Phys.* **40**, 4709 (2001)
- Y. Oka, Y. Takeiri, Y.I. Belchenko, M. Hamabe, O. Kaneko, K. Tsumori, M. Osakabe, E. Asano, T. Kawamoto, R. Akiyama, *Rev. Sci. Instrum.* **71**, 1379 (2000)
- Y. Okumura, M. Hanada, T. Inoue, H. Kojima, Y. Matsuda, Y. Ohara, M. Seki, K. Watanabe, *AIP Conf. Proc.* **210**, 169 (1990)
- T. Okuyama, Y. Mori, *Rev. Sci. Instrum.* **63**, 2711 (1992)
- R.L. Palmer, *AIP Conf. Proc.* **111**, 281 (1984)
- A. Pargellis, M. Seidl, *Phys. Rev. B* **25**, 4356 (1982)
- J.A. Philips, *Phys. Rev.* **97**, 404 (1955)
- B. Rasser, J.N.M. van Wunnik, J. Los, *Surf. Sci.* **118**, 697 (1982)
- A. Rizzolo, M. Pavei, N. Pomaro, *Fusion Eng. Design* **88**, 1007 (2013)
- M. Rutigliano, A. Palma, N. Sann, *Surf. Sci.* **664**, 194 (2017)
- M. Rutigliano, A. Palma, N. Sann, *Surf. Sci.* **693**, 121545 (2020)
- M. Sasao, R. Moussaoui, D. Kogut, J. Ellis, G. Cartry, M. Wada, K. Tsumori, H. Hosono, *App. Phys. Express* **11**, 066201 (2018)
- P.J. Schneider, K.H. Berkner, W.G. Graham, R.V. Pyle, J.W. Sterns, *Phys. Rev. B* **23**, 941 (1981)
- M. Seidl, A. Pargelis, *Phys. Rev.* **26**, 1 (1982)
- M. Seidl, H.L. Cui, J.D. Isenberg, H.J. Kwon, B.S. Lee, S.T. Melnychuk, *J. Appl. Phys.* **79**, 2896 (1996)
- G. Serianni et al., *Fusion Eng. Design* **146, Part B**, 2539 (2019)
- K. Shinto, Y. Okumura, T. Ando, M. Wada, H. Tsuda, T. Inoue, K. Miyamoto, A. Nagase, *Jpn. J. Appl. Phys.* **35**, 1894 (1996)
- M.P. Stockli, B. Han, S.N. Murray, T.R. Pennisi, M. Santana, R.F. Welton, *Rev. Sci. Instrum.* **81**, 02A729 (2010)
- Y. Takeiri, K. Tsumori, K. Ikeda, M. Osakabe, K. Nagaoka, Y. Oka, E. Asano, T. Kondo, M. Sato, M. Shibuya, S. Komada, O. Kaneko, *AIP Conf. Proc.* **1097**, 470 (2009)
- K. Tsumori, Y. Takeiri, K. Ikeda, H. Nakano, S. Geng, M. Kasaki, K. Nagaoka, T. Tokuzawa, M. Wada, K. Sasaki, S. Nishiyama, M. Goto, M. Osakabe, *AIP Conference Proceedings* **1869**, 030001 (2017).; *J. Appl. Phys.* **59**, 241 (1986)
- P. W. van Amersfoort, J. J. C. Geerlings, R. Rodink, E. H. A. Granneman, J. Los, *J. Appl. Phys.* **59**, 241 (1986)
- J.N.M. van Wunnik, J. Los, *Phys. Scr.* **T6**, 27 (1983)
- J.N.M. van Wunnik, J.J.C. Geerlings, E.H.A. Granneman, J. Los, *Surf. Sci.* **131**, 17 (1983)
- H. Verbeek, W. Eckstein, S. Datz, *J. Appl. Phys.* **47**, 1785 (1976)
- M. Wada, *Rev. Sci. Instrum.* **89**, 052103 (2018)
- M. Wada, H. Tsuda, *AIP Conf. Proc.* **287**, 746 (1994)
- M. Wada, K.H. Berkner, R.V. Pyle, J.W. Sterns, *J. Vac. Sci. Technol.* **A1**, 981 (1983)
- M. Wada, R.V. Pyle, J.W. Stearns, *AIP Conf. Proc.* **111**, 247 (1984)
- M. Wada, R.V. Pyle, J.W. Sterns, *J. Appl. Phys.* **67**, 6334 (1990)
- M. Wada, T. Kasuya, T. Kenmotsu, M. Sasao, *Rev. Sci. Instrum.* **85**, 02B114 (2014)
- S.R. Walther, K.N. Leung, W.B. Kunkel, *J. Appl. Phys.* **64**, 3424 (1988)

- S.R. Walther, K.N. Leung, W.B. Kunkel, Appl. Phys. Lett. **54**, 210 (1989)
E. Wimmer, A.J. Freeman, J.R. Hiskes, A.M. Karo, Phys. Rev. B **28**, 3074 (1983)
K.S. Woodcock, Phys. Rev. **38**, 1696 (1931)
D. Wunderlich, R. Riedl, U. Fantz, B. Heinemann, W. Kraus, Plasma Phys. Control. Fusion **60**,
085007 (2018)
M.L. Yu, Phys. Rev. Lett. **40**, 574 (1978)

Chapter 3

Modeling of Reaction Dynamics in Volume-Production Negative Hydrogen Ion Sources



Wei Yang

Abstract In this chapter, the Global Model for Negative Hydrogen Ion Source (GMNHIS) used for the description of the volume production of negative hydrogen ions is presented. The GMNHIS (Yang et al., *Phys Plasmas* 25:113509, 2018) has performed a quite comprehensive benchmarking test against another independently developed code, Global Enhanced Vibrational Kinetic Model (GEVKM) (Averkin et al., *IEEE Trans Plasma Sci* 43:1926, 2015), and it has been validated against experimental measurements operated at an Electron Cyclotron Resonance (ECR) source (Aleiferis et al., *Plasma Sources Sci Technol* 27:075015, 2018) used for the production of negative hydrogen ions. A convenient analytical model (Yang et al., *Plasma Sources Sci Technol* 28:10LT01, 2019) used for the determination of the Vibrational Distribution Function (VDF) of hydrogen molecules that plays an important role in the volume production of negative hydrogen ions is introduced. The VDF is determined by the excitation of vibrational levels by an external source and deactivation in collisions with the wall. The analytical model for VDF of hydrogen molecules has been verified by comparing it with the GMNHIS. These models are intended to provide some insight into the formation of VDF of hydrogen molecules and into the improvement of volume-production Negative Hydrogen Ion Source (NHIS) performance.

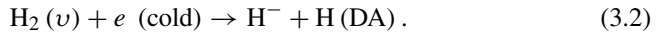
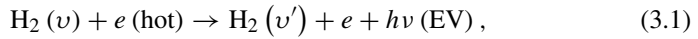
Keywords Volume-production mechanism · Reaction dynamics · Global model · Benchmarking and validation · Analytical model · Vibrational kinetics

3.1 Introduction

Two kinds of production mechanisms of negative hydrogen ions are respectively surface creation and volume creation. In a surface-production source, when energetic

W. Yang (✉)
College of Science, Donghua University, Shanghai, China

positive ions and H atoms collide with the surface electrodes of the plasma source coated with a low-work function material, they are converted into negative hydrogen ions on surfaces (Belchenko 1993). The enhancement in the production of negative hydrogen ions requires a material with low work function (e.g. cesium) deposited on the electrode (Hemsworth et al. 2009). The use of cesium may cause problems in unstable operation and maintenance (Speth et al. 2006), even if it is capable of making negative ion sources to meet the specific requirements for ITER (Franzen et al. 2014). A cesium-free ion source based on the volume-production mechanism of negative hydrogen ions can help to avoid the above difficulties. Specifically, the negative hydrogen ions are produced in the plasma bulk via the following two-step process (Allan et al. 1978):



The vibrationally excited states of hydrogen molecules are firstly created in collisions with hot electrons via electron impact excitation (EV), which refers to excitation to singlet states followed by radiative decay. Then, electrons attach to vibrationally excited states of hydrogen molecules in the process of dissociative attachment (DA) to produce negative hydrogen ions. The cross sections of vibrationally excited states of hydrogen molecules have been theoretically (Wadehra et al. 1978) and experimentally (Allan et al. 1978) proven to be remarkably larger used for the DA reactions. It has been widely reported in the past (Celiberto et al. 2001; Janev et al. 2003; Celiberto et al. 2012) that the DA reactions make a major contribution to the volume production of negative hydrogen ions. The initial vibrational state and the electron energy significantly affect the cross-sections of the DA processes. The excitation and deactivation of vibrational states govern the vibrational kinetics characterized by the VDF.

Numerical simulations play key roles in improving the understanding of discharge physics and providing theoretical predictions. The global model is usually used to study complicated plasma chemistries because it does not solve numerically for the spatial variation of plasma properties but rather depends upon an analytical solution for the respective profiles (Lieberman et al. 2005). The significant numerical efficiency makes it an ideal tool for obtaining the dependence of plasma parameters on a wide range of external ones and investigating plasma chemical dynamics, especially in the identification and analysis of main reaction channels (Thorsteinsson et al. 2010). Global models have been developed by many researchers to study hydrogen discharges (Zorat et al. 2000; Gaboriau et al. 2014; Huh et al. 2015; Averkin et al. 2015; Samuelli et al. 2016). A benchmarked and validated model is required to facilitate insight into the volume-production mechanism of negative hydrogen ions and to further improve the performance of Negative Hydrogen Ion Source (NHIS). Benchmarking means a comparison of different codes with each other (Surendra 1995; Turner et al. 2013; Carlsson et al. 2017), while validation is a comparison of simulation results with experimental

data (Oberkampff et al. 1998). Both of them are essential for making simulation codes as predictive tools. Nevertheless, the global-model approach makes it difficult to decouple the combined effects of different kinetic processes responsible for forming the VDF. Hence, a convenient analytical solution is required to allow for a straightforward VDF calculation and to analyze which factors predominantly affect the VDF formation.

This chapter is organized as follows. A global model named Global Model for Negative Hydrogen Ion Source (GMNHIS) (Yang et al. 2018) with comprehensive chemically reacting dynamics is briefly described in Sect. 3.2. Benchmarking test of GMNHIS against another independently developed code, Global Enhanced Vibrational Kinetic Model (GEVKM) (Averkin et al. 2015) for a Radio Frequency (RF) discharge (Gao et al. 2018) is presented in Sect. 3.3. Section 3.4 shows the validation of GMNHIS against experimental measurements in an ECR discharge (Aleiferis et al. 2018). Section 3.5 describes an analytical model used for the determination of VDF at low pressures where NHIS are generally operated (Yang et al. 2019). Finally, the conclusion is given in Section 3.6. The results presented in this chapter mainly refer to the previous studies of the author (Yang et al. 2018, 2019).

3.2 Brief Description of GMNHIS

The GMNHIS includes four fundamental conservation laws: mass conservation described through a particle balance for each species except for the ground-state hydrogen molecules; the density of ground-state hydrogen molecules determined by the equation of state; quasi-neutrality condition due to the charge conservation; and energy conservation law expressed via power balance. In the GMNHIS, the power has been assumed to be deposited uniformly into the plasma bulk, and a Maxwellian electron energy distribution function (EEDF) has been assumed. Temperatures of ions and neutral gas have been fixed in the simulation at 600 K. The basic equations are shown as follows, while the detailed description of the GMNHIS can refer to the study (Yang et al. 2018).

3.2.1 Particle Balance Equation

The particle balance equation for neutral particle species, except for molecular hydrogen, is expressed as

$$n_i u_{B,i} \frac{A_{\text{eff}1,i}}{V} - \Gamma_j \frac{A_n}{V} + \sum R_j = 0. \quad (3.3)$$

The positive ions reaching the walls are recycled as neutral particles in the plasma bulk (the first term). V , n_i , $u_{B,i}$, and $A_{\text{eff},i}$ are respectively the volume of the discharge chamber, the volume-averaged density, the Bohm speed, and the effective loss area of a positive ion i . If a perfect open boundary is considered at the bottom of the source chamber, e.g., the driver chamber of an RF ion source, the ions flowing out of the bottom of the source chamber do not recycle as particles (Chabert et al. 2012). In that case, $A_{\text{eff},i}$ is required to exclude the area at the bottom of the chamber. The neutral particles flowing out of the bottom of the chamber are lost (the second term). The quantity R_j in the third term is the volume reaction rate for the creation or loss process of neutral particle species j .

Particle balance for the ion species is expressed as

$$-n_i u_{B,i} \frac{A_{\text{eff},i}}{V} + \sum R_i = 0. \quad (3.4)$$

The first term shows that positive ions reaching the walls are lost. R_i is the volume reaction rate for the creation or loss for positive ion species i . $A_{\text{eff},i}$ that is different from $A_{\text{eff},i}$ in Eq. (3.3) considers all the inner surface area of the chamber.

The total particle density is constrained by the given operating pressure P . Meanwhile, the quasi-neutrality condition has been adopted in the discharge. These two criteria can be given respectively as

$$P = \sum_j n_j k_B T_{\text{gas}}, \quad (3.5)$$

$$n_e = n_+ - n_-. \quad (3.6)$$

T_{gas} is the gas temperature, and k_B is the Boltzmann constant. n_j , n_e , n_+ , and n_- are respectively the densities of neutral particles, electrons, positive ions, and negative ions.

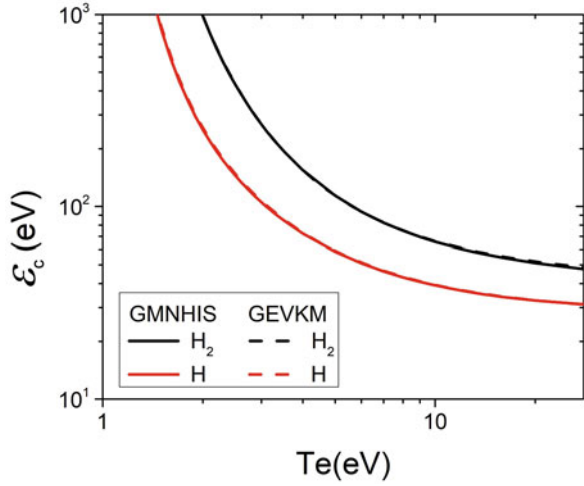
3.2.2 Power Balance Equation

The power balance equation refers to the balance between the absorption power and the bulk power losses caused by elastic and inelastic collisions, as also power losses due to charged particles flowing to the walls:

$$P_{\text{abs}} = P_V + P_W. \quad (3.7)$$

P_{abs} is the absorption power per unit volume. P_V is the power loss per unit volume through volume reactions:

Fig. 3.1 Collisional energy loss versus electron temperature for H and H₂. (Reproduced from (Yang et al. 2018), with the permission of AIP Publishing)



$$P_V = n_e \sum_j \left(\sum_i n_j \varepsilon_{\text{inel},j}^{(i)} k_{\text{inel},j}^{(i)} + n_j \frac{3m_e}{m_j} T_e k_{\text{el},j} \right), \quad (3.8)$$

where $\varepsilon_{\text{inel},j}^{(i)}$ is the threshold energy of an inelastic process i involving species j , and $k_{\text{inel},j}^{(i)}$ is the corresponding rate coefficient. $k_{\text{el},j}$ is the rate coefficient for electron-species j elastic collision. m_e is the electron mass, m_j is the mass of species j , and T_e is the electron temperature. The collisional energy loss per electron-ion pair created is given by $\varepsilon_c = \sum_i \varepsilon_{\text{inel},j}^{(i)} k_{\text{inel},j}^{(i)} / k_{\text{iz},j}$, and it is shown in Fig. 3.1 versus electron temperature for H and H₂. $k_{\text{iz},j}$ is the rate coefficients of ionizations for H and H₂. Note that both models (GMNHIS and GEVKM) achieve very good agreement with each other. The power balance equation is usually used to determine the electron density, so the electron densities predicted by the two models will be expected to be in agreement with each other.

P_W is the power loss at the chamber wall per unit volume:

$$P_W = \sum_i n_i (\varepsilon_i + \varepsilon_e) u_{B,i} \frac{A_{\text{eff}}}{V}, \quad (3.9)$$

where ε_i is the mean kinetic energy per each ion lost, and ε_e is the mean kinetic energy per each electron lost (Lieberman et al. 2005).

Table 3.1 Reaction set involving vibrational states considered in the GMNHIS

Reaction	Description
$e + \text{H}_2(\nu) \rightarrow e + \text{H}_2(\nu')$	Resonant electron-vibration excitation: eV
$e + \text{H}_2(\nu) \rightarrow e + \text{H}_2(\nu') + h\nu$	Radiative decay and excitation: EV
$e + \text{H}_2(\nu) \rightarrow e + \text{H} + \text{H}$	Dissociation via $b^3\Sigma_u^+$: Dis
$e + \text{H}_2(\nu) \rightarrow \text{H} + \text{H}^-$	Dissociative electron attachment: DA
$\text{H} + \text{H}_2(\nu) \rightarrow \text{H} + \text{H}_2(\nu')$	Vibrational-translational relaxation: Vt
$\text{H}_2(\omega) + \text{H}_2(\nu) \rightarrow \text{H}_2(\omega) + \text{H}_2(\nu \pm 1)$	Vibrational-translational relaxation: VT
$\text{H}^- + \text{H}_2(\nu) \rightarrow \text{H}_2(\nu - 2) + \text{H} + e$	Electron detachment: EDV
$e + \text{H}_2 \rightarrow e + \text{H}_2(X)$	Electronic excitation
$\text{H}_2(\nu) + \text{wall} \rightarrow \text{H}_2(\nu'), (\nu' < \nu)$	Vibrational relaxation: WR

3.2.3 Chemistry Mechanism in the Volume-Production NHIS

The kinetic reactions taken into account in the GMNHIS involves ground-state hydrogen molecules $\text{H}_2(\nu = 0)$, 14 vibrationally-excited hydrogen molecules $\text{H}_2(\nu = 1 - 14)$, hydrogen atoms $\text{H}(n = 1)$, electronically excited hydrogen atoms $\text{H}(n = 2, 3)$, molecular hydrogen ions H_3^+ and H_2^+ , atomic hydrogen ions H^+ , negative hydrogen ions H^- , and electrons. In this chapter, special attention is paid to the vibrational kinetics of hydrogen molecules since it affects the production of H^- ions. The reaction set involving vibrational states is shown in Table 3.1. The excitation/de-excitation mechanisms of vibrationally excited H_2 include electron impact through the resonant state H_2^- (eV) and the singlet excited electronic states ($\text{B}^1\Sigma_u^+, \text{C}^1\Pi_u$) (EV). The latter, followed by a radiative transition to a vibrational state, is the main process that creates a non-Boltzmann vibrational distribution in the NHIS. The EV process involving the $\text{H}_2(\nu = 0)$ molecules can remarkably increase the densities of highly vibrational states that are the most efficient in the volume-production of H^- ions because of the higher density of the $\text{H}_2(\nu = 0)$ than that of other vibrational states $\text{H}_2(\nu = 1 - 14)$. The vibrational-translational relaxation in collisions with ground-state hydrogen molecules (VT) can depopulate highly vibrational states $\text{H}_2(\nu = 10 - 14)$, especially at relatively high pressures. The importance of $\text{H}_2(\nu)$ wall relaxation (WR) has been stressed in previous work (Hiskes et al. 1989). The vibrational-translational relaxation in collisions with H atoms (Vt) and the electron detachment in collisions with vibrational states of hydrogen molecules (EDV) have also been included in the GMNHIS because of their roles played at high pressures. The dissociation of $\text{H}_2(\nu)$ molecules (Dis) can affect the electron parameters. Dissociative electron attachment to $\text{H}_2(\nu)$ molecules (DA) mainly contributes to the production of H^- ions. In addition, various electronic excitations of hydrogen molecules ($X = b^3\Sigma_u^+, a^3\Sigma_g^+, c^3\Pi_u, B^1\Sigma_u^+, C^1\Pi_u, E, F^1\Sigma_g^+, e^3\Sigma_u^+$) have been included in the GMNHIS. Because of the low densities of electronically excited states, they are usually not explicitly tracked in the particle balance equations but added to account for energy losses in the power balance equation. Other reaction processes related to the basic H_2 reactions can refer to the study (Yang et al. 2018).

3.3 Benchmarking of GMNHIS for RF Discharge

In this part, the benchmarking of GMNHIS against GEVKM for a cylindrical RF discharge is shown (Yang et al. 2018). The source chamber is a quartz tube, and its height is 14 cm and inner diameter is 12 cm. The absorption power is fixed at 1000 W, and the gas pressure range is from 1 to 30 Pa. There are three differences between these two codes. Firstly, the particle balance equation with the consideration of pumping of feedstock gas in and out is implemented to calculate the density of H_2 molecules in the GEVKM, while in the GMNHIS, the density of H_2 molecules is calculated using the equation of state according to specified gas temperature and discharge pressure. The influence of this difference on plasma parameters can be ignorable in the parameter range investigated. Secondly, the GEVKM includes some additional heavy-particle collisions that are important at high pressures, while the GMNHIS excludes these reactions due to the relatively low pressures considered. Finally, the different approximation methods for calculating rate coefficients have been used in two codes. The GMNHIS adopted the lookup table, while the GEVKM adopted the fitting.

3.3.1 *Negative Hydrogen Ion Density and Electronegativity Versus Pressure*

Figures 3.2a, b respectively shows H^- density and n_{H^-}/n_e (electronegativity) versus pressure computed with two codes. The H^- densities predicted by the two codes agree well with each other in the pressure range investigated, except for the small discrepancy at relatively high pressures where GEVKM predicts a slightly lower value than GMNHIS. As for the electronegativity versus pressure, the two models are in good agreement. The slight difference in the H^- density and the electronegativity at higher pressures can be understood by studying the electron properties and other parameters responsible for the creation and loss of H^- ions.

3.3.2 *Electron Temperature and Electron Density Versus Pressure*

Electron temperature and electron density versus pressure are respectively presented in Figs. 3.3a, b. The two codes achieve excellent agreement in electron temperature and electron density in the pressure range investigated except for 1 Pa. Therefore, the differences of H^- density and electronegativity predicted by the two codes at relatively high pressures are not caused by electron properties.

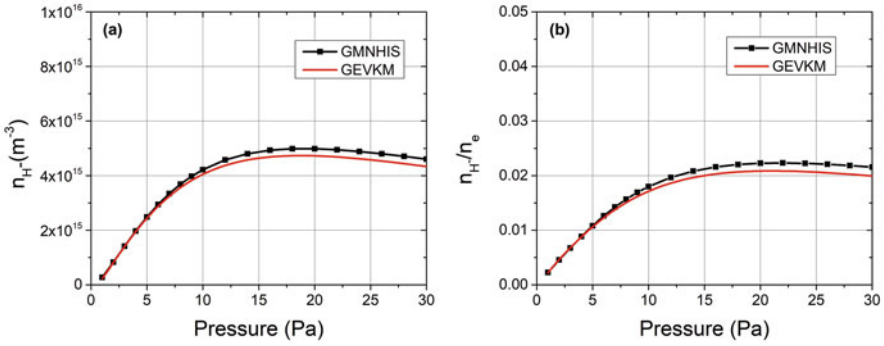


Fig. 3.2 H⁻ density (a) and n_{H^-}/n_e (b) versus pressure. (Reproduced from (Yang et al. 2018), with the permission of AIP Publishing)

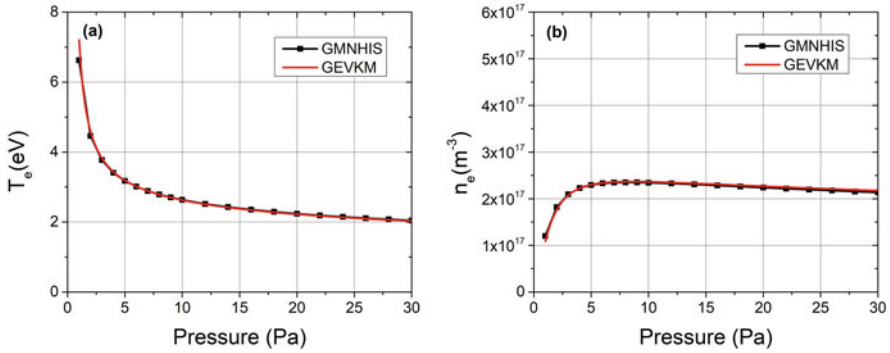
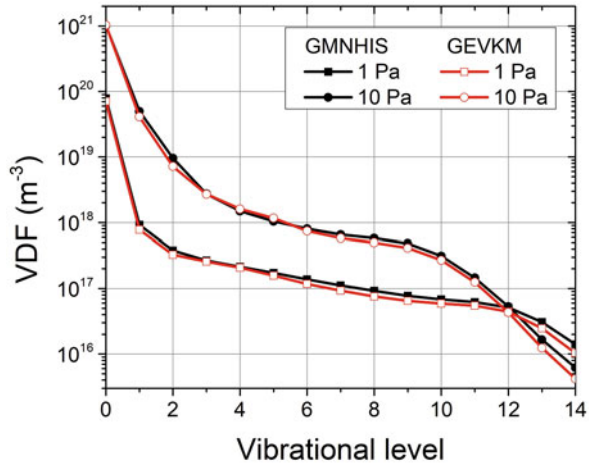


Fig. 3.3 Electron temperature (a) and electron density (b) versus pressure. (Reproduced from (Yang et al. 2018), with the permission of AIP Publishing)

3.3.3 VDFs at Two Different Pressures

The DA processes of H₂(ν) molecules are responsible for H⁻ production. The VDF at two pressures of 1 and 10 Pa is shown in Fig. 3.4. Both codes show the VDF is non-Boltzmann, characterized by a plateau at the intermediate vibrational levels. This is because the eV processes through cold electrons mainly contribute to relatively low vibrational levels ($\nu \leq 3$), while the EV processes through hot electrons mainly contribute to relatively high vibrational levels ($\nu > 3$). The higher pressure leads to a significant decrease in the density of very high vibrational states due to the VT processes. The higher H⁻ density predicted by the GMNHIS than that in the GEVKM is possibly due to the slightly higher density values of VDF, given that electron densities and electron temperatures predicted by the two codes are almost the same.

Fig. 3.4 VDF of $H_2(v)$ molecules at 1 Pa and at 10 Pa. (Reproduced from (Yang et al. 2018), with the permission of AIP Publishing)



3.3.4 Densities of Positive Ions and H ($N = 1-3$) Atoms Versus Pressure

The two codes achieve very good qualitative and even quantitative agreement for the densities of H_3^+ and H_2^+ versus pressure (see Fig. 3.5). As increasing pressure, the variation of H_3^+ density versus pressure is analogous to that of electron density, as H_3^+ is the main ion species. The GMNHIS predicts a slightly higher density of H^+ ions at higher pressures. It is possible because the charge-exchange reaction between H^+ and $H_2(v)$ has been ignored in the GMNHIS. The collision reaction between H ($n = 2$) and H_2 is the most important reaction that produces the H_3^+ in the GMNHIS (Yang et al. 2018). The densities of H ($n = 2, 3$) predicted by the two codes agree very well with each other (see Fig. 3.6a), so the H_3^+ densities predicted by both codes are in good agreement. The electronic excitation of H atoms is the main source for H ($n = 2$) atoms at pressures above 2 Pa. Therefore, good agreement for H ($n = 2$) density predicted by both codes is due to almost the same H atom density (see Fig. 3.6b).

3.4 Validation of GMNHIS for ECR Discharge

Validation of the model plays a key role in making code valuable as a predictive tool. Validation of GMNHIS for an ECR discharge is shown in this part (Yang et al. 2018). The experimental ECR source consists of a cube-shaped stainless-steel chamber with necessary viewports for plasma diagnostics (Aleiferis et al. 2018).

Fig. 3.5 Positive ion density versus pressure. (Reproduced from (Yang et al. 2018), with the permission of AIP Publishing)

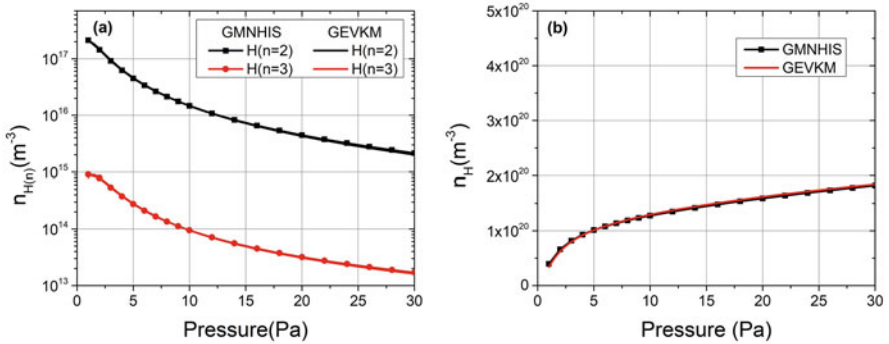
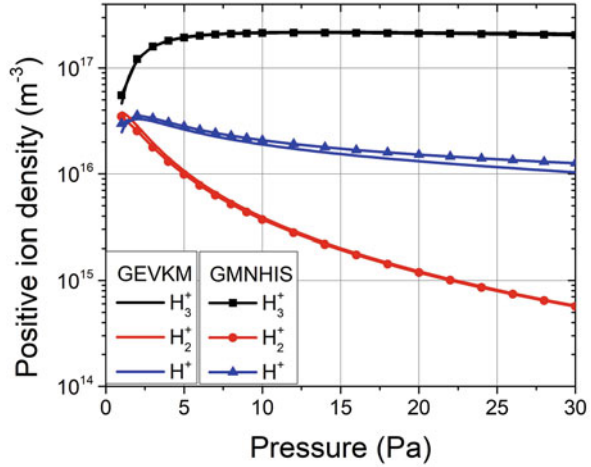


Fig. 3.6 Densities of electronically excited H atoms (a) and of ground-state H atoms (b) versus pressure. (Reproduced from (Yang et al. 2018), with the permission of AIP Publishing)

The side lengths X , Y , and Z of the chamber are 24 cm. The plasma is sustained by a matrix arrangement of five dipolar ECR plasma sources, represented by five circles in the top view of the experimental setup. The power supply of each individual source can provide up to 180 W. Such multipolar sources can produce uniform large-size low-pressure plasmas. The experimental measurements were taken at the center axis 6.5 cm below the magnets. The plasma is considered to only exist in the volume below the magnets due to the presence of grounded guides above the magnets. The input power is assumed to be uniformly absorbed by the plasma that extends vertically down to 6.5 cm below the magnets (upper region) where the discharge is concentrated. The plasma is considered to freely diffuse between the edge of the upper region and the bottom of the chamber (lower region) where no ionization is assumed. A perfect open-boundary condition is imposed in GMNHIS for predicting the plasma parameters in the upper part of the chamber. The densities of different species at the location where the experimental measurements were taken

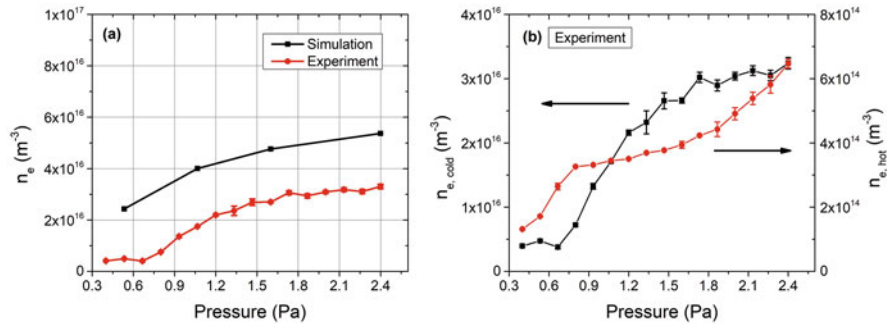


Fig. 3.7 (a) Electron density versus pressure and (b) cold and hot electron densities versus pressure. The experimental data is obtained using the same experimental setup as the study (Aleiferis et al. 2018). (Reproduced from (Yang et al. 2018), with the permission of AIP Publishing)

(axially 6.5 cm below the magnets) are assumed to correspond to volume-averaged densities obtained with GMNHIS. The absorption power is fixed at 900 W in the simulations. Four cases with different operating pressures are considered, namely 4, 8, 12, and 18 mTorr.

3.4.1 Electron Density Versus Pressure

Figure 3.7a shows that the electron density first rapidly increases, and then the increasing rate is declined as increasing pressure. Experiments and simulations achieve qualitative agreement. Quantitatively, the electron density predicted by GMNHIS is higher than the experimental values. This is possible because the GMNHIS considers volume-averaged values while the local values have been adopted in the experimental measurements. In addition, the power of 900 W has been assumed to be deposited into the limited volume in the GMNHIS, which can lead to an overestimation of ionization rate and, therefore, electron density in the simulations. In Fig. 3.7b, the experimental cold and hot electron densities versus pressure display different variation trends. As pressure increases, the hot electron density increases, whereas the cold electron density first increases and then saturates. The experimental data above is obtained using the same experimental setup as the study (Aleiferis et al. 2018).

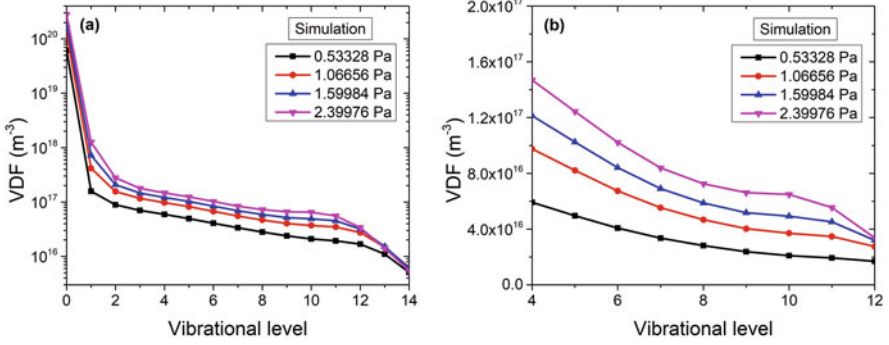


Fig. 3.8 VDF at different pressures is shown as (a) the logarithmic plot for all the vibrational states ($0 \leq \nu \leq 14$) and (b) the linear plot for higher vibrational states ($4 \leq \nu \leq 12$). (Reproduced from (Yang et al. 2018), with the permission of AIP Publishing)

3.4.2 Pressure Dependence of VDF

In addition to electron properties, the production of H^- ions is very sensitive to the VDF. The VDF is usually shown as the logarithmic plot (see Fig. 3.8a). To clearly present the dependence of VDF on pressure, it is shown as the linear plot for higher vibrational states ($4 \leq \nu \leq 12$) (see Fig. 3.8b). As the pressure is increased, the densities of vibrational states ($4 \leq \nu \leq 11$) monotonically increase. The pronounced decrease of $\text{H}_2(\nu = 12)$ density at high pressure is because of the VT processes.

3.4.3 Determination of Negative Hydrogen Ion Density

The density of H^- ions is estimated based on the balance of creation and loss (Yang et al. 2018):

$$n_{\text{H}^-} = \frac{\sum_{\nu=0}^{14} n_{\text{H}_2(\nu)} n_e \langle \sigma_{\text{DA}}(\varepsilon), \varepsilon \rangle}{k_{\text{MN}} n_+ + k_{\text{AD}} n_{\text{H}} + n_e \langle \sigma_{\text{ED}}(\varepsilon), \varepsilon \rangle + k_{\text{EDV}} n_{\text{H}_2(\nu)}}, \quad (3.10)$$

where the production rate of H^- ions through the DA process is shown in the numerator, while the H^- losses, i.e., mutual neutralization with positive ions (MN), associative detachment via H atoms (AD), electron detachment (ED), and electron detachment in collisions with $\text{H}_2(\nu)$ molecules (EDV) are included in the denominator. The densities on the RHS of Eq. (3.10) are obtained with the GMNHIS. The rate coefficients for reactions involving electrons (DA and ED) are obtained based on the cross section $\sigma(\varepsilon)$ and the EEDF. The reaction rate coefficients involving ions and neutrals are denoted by k . The experimental EEDFs obtained using the same experimental setup as the study (Aleiferis et al. 2018)

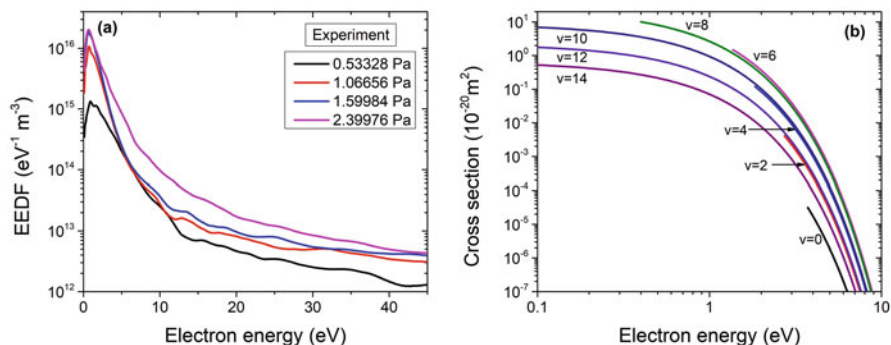


Fig. 3.9 (a) Experimental EEDF versus electron energy at different pressures and (b) cross section of DA processes for selected vibrational states. The experimental EEDFs are obtained using the same experimental setup as the study (Aleiferis et al. 2018). (Reproduced from (Yang et al. 2018), with the permission of AIP Publishing)

almost present bi-Maxwellian distributions, as shown in Fig. 3.9a. The cross section increases by orders of magnitude with the vibrational level of H_2 molecules increasing from 0 to 4 (Janev et al. 2003). However, the threshold energy decreases with increasing vibrational level and has a maximum value of 3.72 eV for $\nu = 0$. Consequently, high vibrational levels of H_2 molecules and low energy electrons dominantly contribute to the production of H^- ions at low pressures here.

As the pressure increases, the H^- density first increases and then saturates (see Fig. 3.10a). This dependence is qualitatively reproduced by the calculation based on Eq. (3.10). The increase of H^- density at relatively high pressure can possibly be limited by the saturation of cold electron density shown in Fig. 3.7b, although the monotonous increase of the $\text{H}_2(4 \leq \nu \leq 11)$ densities shown in Fig. 3.8b should have promoted the production of H^- ions via the DA processes. The experimental electronegativity is qualitatively reproduced by the simulation (see Fig. 3.10b). The consideration of the experimental EEDF with more cold electrons contributing to the H^- production achieves the high electronegativity in the simulation. The H^- density directly calculated from GMNHIS assuming a Maxwellian EEDF is lower by around an order of magnitude than that obtained using Eq. (3.10).

3.4.4 Production and Loss Mechanisms of Negative Hydrogen Ions

The evaluation of pressure dependence of the production and loss rates of H^- ions can gain insight into the pressure dependence of H^- density (see Fig. 3.11). The DA processes of the cold electrons to high vibrational states $\text{H}_2(\nu = 6 - 11)$ dominate the production of H^- ions. As the pressure increases, the production rate of H^- ions via the DA processes increases, and the increase is more sluggish at higher

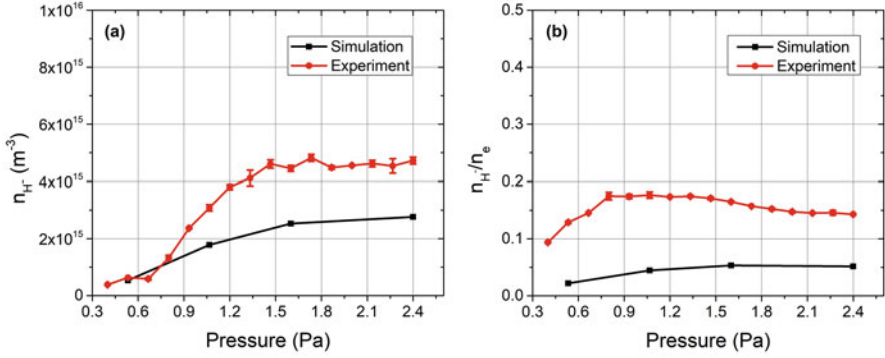


Fig. 3.10 H^- density (a) and n_{H^-}/n_e ratio (b) versus pressure. The experimental data is obtained using the same experimental setup as the study (Aleiferis et al. 2018). (Reproduced from (Yang et al. 2018), with the permission of AIP Publishing)

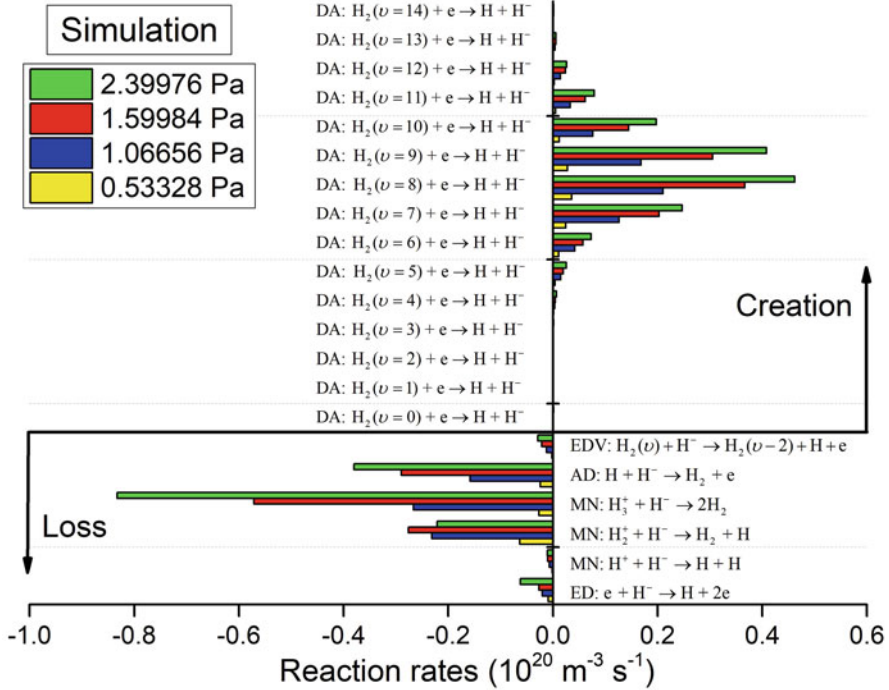
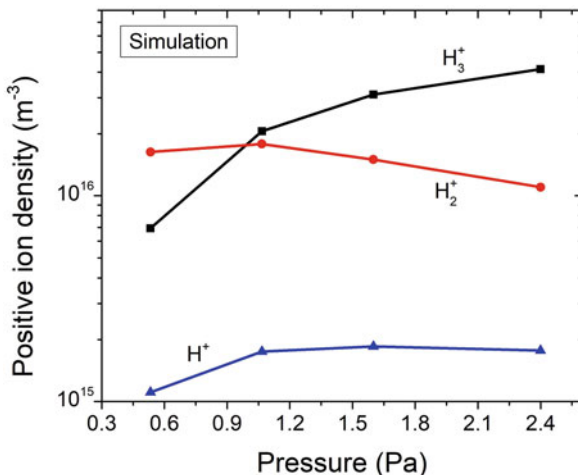


Fig. 3.11 Reaction rates of the production and loss reactions of H^- ions at different pressures. (Reproduced from (Yang et al. 2018), with the permission of AIP Publishing)

pressure because of the saturation of cold electrons. The AD process and the MN processes of H_3^+ and H_2^+ with H^- dominates the loss mechanisms of H^- ions. The enhancement in densities of H atoms and H_3^+ ions (see Fig. 3.12) promotes the AD

Fig. 3.12 Positive ion density versus pressure. (Reproduced from (Yang et al. 2018), with the permission of AIP Publishing)



process and MN process of H_3^+ with H^- as increasing pressure. The variation in the reaction rate of the MN process of H_2^+ with H^- pressure is similar to that of the density of H_2^+ ions versus pressure (Fig. 3.12). The contributions of other processes can be ignorable in the pressure range investigated.

3.5 Analytical Model for VDF

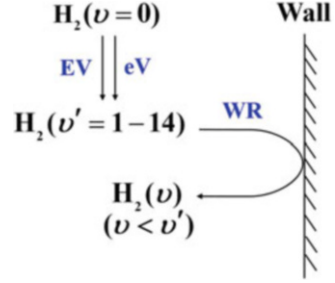
3.5.1 Reduced Set of Processes for Vibrational Kinetics

The GMNHIS includes quite comprehensive reactions involving vibrational states of H_2 molecules. By evaluating all reaction (see Table 3.1) rates associated with the production and loss of vibrational states $H_2(\nu = 1 - 14)$ according to GMNHIS, the main reactions can be identified. The simplified reactions involving vibrational states of H_2 molecules includes the eV and EV processes of ground-state molecules $H_2(\nu = 0)$ to levels $H_2(\nu = 1 - 14)$ as well as the WR process of level ν' to lower level $\nu (< \nu')$ (see Fig. 3.13).

3.5.2 Particle Balance for Vibrational States

Based on the particle balance for vibrational states, the densities of $H_2(\nu = 1 - 14)$ satisfy the following equation

Fig. 3.13 Schematics of the reduced set of processes for the formation of VDF. (Reproduced from (Yang et al. 2019), with the permission of IOP Publishing)



$$S_v = k_{\text{WR},v} n_{\text{H}_2(v)} + k_{\text{out}} n_{\text{H}_2(v)} - \sum_{v'=v+1}^N k_{\text{WR},v'} \gamma_{v' \rightarrow v} n_{\text{H}_2(v')}, \quad (3.11)$$

where the source rate via electron impact excitations $S_v = (k_{\text{eV},0 \rightarrow v} + k_{\text{EV},0 \rightarrow v}) n_{\text{H}_2(0)} n_e$. The rate coefficients $k_{\text{eV},0 \rightarrow v}$ and $k_{\text{EV},0 \rightarrow v}$ are obtained under assuming a Maxwellian EEDF. The first term on the RHS of Eq. (3.11) represents the loss rate of vibrational states on the wall. The rate coefficient for $k_{\text{WR},v}$ is given according to work (Chantry 1987) and can refer to the study (Yang et al. 2019). The second term on the RHS of Eq. (3.11) represents the loss rate of the vibrational states out of the chamber accounted for by the GMNHIS, and k_{out} is the corresponding rate coefficient. The last term on the RHS of Eq. (3.11) is the source rate via the de-excitation of higher vibrational states on the wall. $\gamma_{v' \rightarrow v}$ is the de-excitation probability for a vibrational level v' to relax to lower states v .

3.5.3 Repopulation Probabilities of Vibrational States on the Wall

A convenient analytical solution would help to facilitate physical insight and verify complex numerical models. It could be achieved if $\gamma_{v' \rightarrow v}$ had a simplified form. Fig. 3.14a shows the experimental values of $\gamma_{v' \rightarrow v}$ (Stutzin et al. 1988; Hiskes et al. 1989). The $\gamma_{v' \rightarrow v}$ distribution depends on the initial vibrational state v' and keeps the normalization. $\gamma_{v' \rightarrow v}$ is simplified by averaging values $\gamma_{v' \rightarrow v} = (1/v') \theta(v' - v)$ for each initial vibrational state as shown in Fig. 3.14b.

Figure 3.15 shows VDFs predicted by the GMNHIS with the reduced set of reactions (see Fig. 3.13) under experimental $\gamma_{v' \rightarrow v}$ (Stutzin et al. 1988; Hiskes et al. 1989) and also substituted $\gamma_{v' \rightarrow v} = (1/v') \theta(v' - v)$ at gas pressures of 4 and 18 mTorr. It was found the proposed $\gamma_{v' \rightarrow v}$ yield rather accurate VDF.

Figure 3.16 shows the VDFs predicted by the GMNHIS with the full set of reactions (Yang et al. 2018) under experimental $\gamma_{v' \rightarrow v}$ (Stutzin et al. 1988; Hiskes et al. 1989) and substituted $\gamma_{v' \rightarrow v} = (1/v') \theta(v' - v)$ at pressures of 4 and 18 mTorr. Similarly, the proposed $\gamma_{v' \rightarrow v}$ produces almost the same VDF. The VDFs with full simulation (see Fig. 3.16) and with reduced set (see Fig. 3.15) are in good

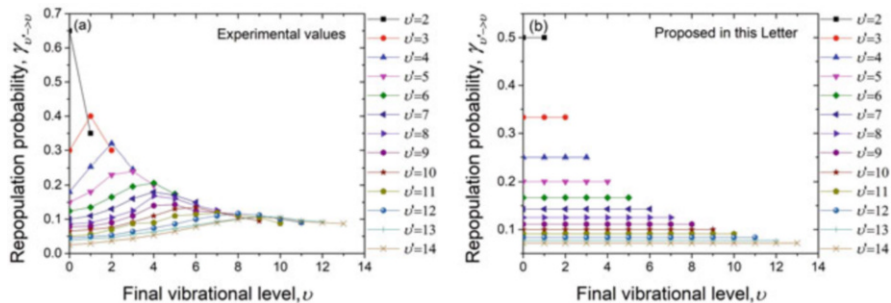
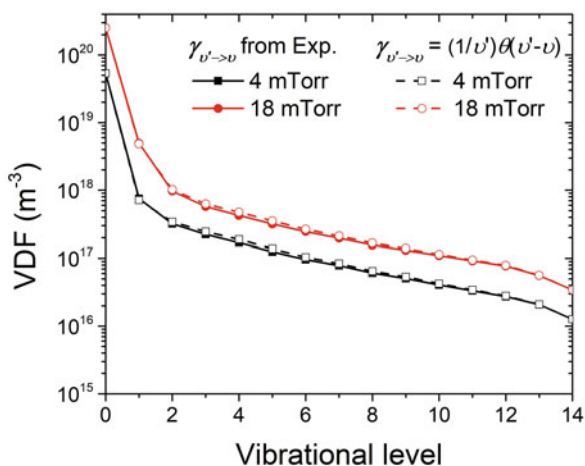


Fig. 3.14 Repopulation probability $\gamma_{v' \rightarrow v}$ in wall collisions: (a) experimental data (Stutzin et al. 1988; Hiskes et al. 1989); (b) approximate $\gamma_{v' \rightarrow v} = (1/v') \theta(v' - v)$. (Reproduced from (Yang et al. 2019), with the permission of IOP Publishing)

Fig. 3.15 VDFs predicted by the GMNHIS with the reduced set of reactions under experimental $\gamma_{v' \rightarrow v}$ (Stutzin et al. 1988; Hiskes et al. 1989) and approximate $\gamma_{v' \rightarrow v} = (1/v') \theta(v' - v)$ at pressures of 4 and 18 mTorr. (Reproduced from (Yang et al. 2019), with the permission of IOP Publishing)



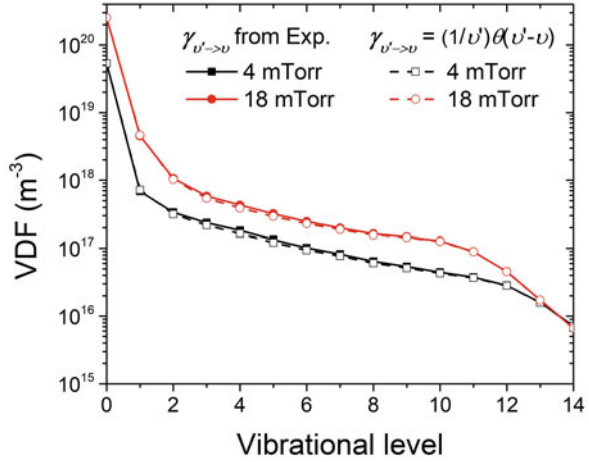
agreement with each other except for the highest vibrational states due to the VT process being neglected in the reduced set of reactions. The densities of very high vibrational levels can be depleted by the VT process, but its effect is weakened as pressure is decreased.

3.5.4 Reduced Linear Model for VDF

Using the simplified $\gamma_{v' \rightarrow v}$ form, Eq. (3.11) is given as

$$S_v = k_{\text{WR},v} n_{\text{H}_2(v)} + k_{\text{out}} n_{\text{H}_2(v)} - \sum_{v'=v+1}^N \frac{1}{v'} k_{\text{WR},v'} n_{\text{H}_2(v')}. \quad (3.12)$$

Fig. 3.16 VDFs obtained using full GMNHIS under experimental $\gamma_{v' \rightarrow v}$ (Stutzin et al. 1988; Hiskes et al. 1989) and approximate $\gamma_{v' \rightarrow v} = (1/v') \theta(v' - v)$ at pressures of 4 and 18 mTorr. (Reproduced from (Yang et al. 2019), with the permission of IOP Publishing)



It is analytically solved in Appendix A of the study (Yang et al. 2019), and the solution is given as

$$k_{\text{WR},v} n_{\text{H}_2(v)} = \beta_v S_v + \frac{\beta_v}{v+1} \left\{ \beta_{v+1} S_{v+1} + \sum_{k=v+2}^N \beta_k S_k \prod_{n=v+1}^{k-1} \alpha_n \right\}, \quad (3.13)$$

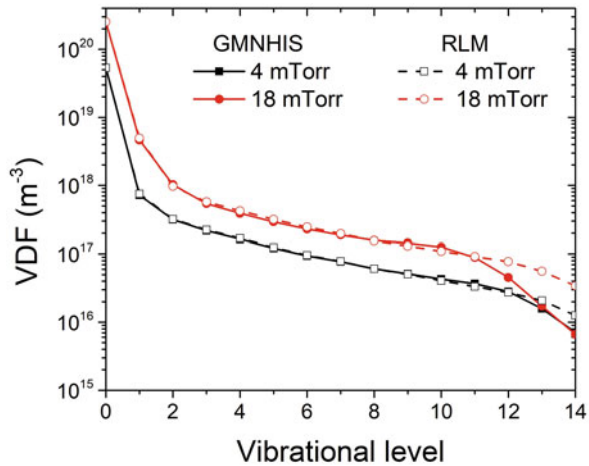
where $\beta_v = \frac{k_{\text{WR},v}}{k_{\text{WR},v} + k_{\text{out}}}$ and $\alpha_n = (\beta_n + n)/(n + 1)$. If the closed boundary at the bottom of the chamber is considered $\alpha_v = \beta_v = 1$, the solution is given as

$$k_{\text{WR},v} n_{\text{H}_2(v)} = S_v + \frac{1}{v+1} \sum_{k=v+1}^N S_k. \quad (3.14)$$

The analytical solution for $n_{\text{H}_2(v)}$ is called Reduced Linear Model (RLM). The LHS and RHS of Eq. (3.14) respectively represent the volumetric loss via interaction with the wall and the volumetric source via electron impact excitation.

The RLM is verified by comparing its predictions with the results obtained using full GMNHIS. The VDFs obtained using these two models are nearly indistinguishable except for the highest vibrational levels due to VT process being excluded in the RLM. The highest vibrational states contribute very little to the production of H^- ions (Gaboriau et al. 2014; Yang et al. 2018), so it is not necessary to accurately predict VDF for those states (Fig. 3.17).

Fig. 3.17 VDFs predicted by full GMNHIS and the RLM at pressures of 4 and 18 mTorr. (Reproduced from (Yang et al. 2019), with the permission of IOP Publishing)



3.6 Conclusion

In this chapter, the Global Model for Negative Hydrogen Ion Source (GMNHIS) with comprehensive reaction dynamics is described. Benchmarking of GMNHIS numerical code against another independently developed code can help fix a number of mistakes in both codes and ascertain the chemical reaction data used. Separately collected chemistry reaction data for both codes allows to find some inconsistencies in the published literature. The qualitative agreement for the plasma parameters between GMNHIS simulation and experimental data in an ECR validates the simulations based on the adopted H_2 reaction set and various assumptions used in the GMNHIS. Subsequently, a Reduced Linear Model (RLM) of the vibrational distribution function (VDF) of H_2 molecules at low pressures is presented for low-pressure NHIS. The RLM is derived by (a) reducing the reaction set of vibrational kinetics of H_2 molecules according to the GMNHIS and (b) using approximate function for the wall-repopulation probability from higher state to lower state. The RLM can be used as a simple verification test for complex full numerical models. It allows for a fast and straightforward VDF calculation and also enables analysis of the contribution of different kinetic processes to the VDF formation. The presented models can be used for predicting the production of negative hydrogen ions, improving the performance of NHIS, and ultimately aiding in developing optimized negative ion beams for ITER and prospective fusion reactors.

References

- S. Aleiferis, P. Svarnas, S. Bechu, O. Tarvainen, M. Bacal, *Plasma Sources Sci. Technol.* **27**, 075015 (2018)
M. Allan, S. Wong, *Phys. Rev. Lett.* **41**, 1791 (1978)
S.N. Averkin, N.A. Gatsonis, L. Olson, *IEEE Trans. Plasma Sci.* **43**, 1926 (2015)

- Y. Belchenko, Rev. Sci. Instrum. **64**, 1385 (1993)
- J. Carlsson, A. Khrabrov, I. Kaganovich, T. Sommerer, D. Keating, Plasma Sources Sci. Technol. **26**, 014003 (2017)
- R. Celiberto, R.K. Janev, A. Laricchiuta, M. Capitelli, J.M. Wadehra, D.E. Atems, At. Data Nucl. Data Tables **77**, 161 (2001)
- R. Celiberto, R.K. Janev, J.M. Wadehra, J. Tennyson, Chem. Phys. **398**, 206 (2012)
- P. Chabert, M.J. Arancibia, J. Bredin, L. Popelier, A. Aanesland, Phys. Plasmas **19**, 073512 (2012)
- P.J. Chantry, J. Appl. Phys. **62**, 1141 (1987)
- P. Franzen, U. Fantz, Fusion Eng. Des. **89**, 2594 (2014)
- F. Gaboriau, J.P. Boeuf, Plasma Sources Sci. Technol. **23**, 065032 (2014)
- F. Gao, H. Li, W. Yang, J. Liu, Y.R. Zhang, Y.N. Wang, Phys. Plasmas **25**, 013515 (2018)
- R. Hemsworth, H. Decamps, J. Graceffa, B. Schunke, M. Tanaka, M. Dremel, A. Tanga, H.P.L. De Esch, F. Geli, J. Milnes, T. Inoue, D. Marcuzzi, P. Sonato, P. Zaccaria, Nucl. Fusion **49**, 045006 (2009)
- J.R. Hiskes, A.M. Karo, Appl. Phys. Lett. **54**, 6 (1989)
- S.R. Huh, N.K. Kim, B.K. Jung, K.J. Chung, Y.S. Hwang, G.H. Kim, Phys. Plasmas **22**, 033506 (2015)
- R.K. Janev, D. Reiter, U. Samm, *Collision Processes in Low-Temperature Hydrogen Plasma* (Forschungszentrum, Zentralbibliothek, 2003)
- M.A. Lieberman, A.J. Lichtenberg, *Principles of Plasma Discharges and Materials Processing*, 2nd edn. (Wiley-Interscience, New York, 2005)
- W. L. Oberkampf, M. Sindir, A. T. Conlisk, AIAA Paper No. G-077-1998 (1998)
- C.M. Samuelli, C.S. Corr, Plasma Sources Sci. Technol. **25**, 015014 (2016)
- E. Speth, H.D. Falter, P. Franzen, U. Fantz, M. Bandyopadhyay, S. Christ, A. Encheva, M. Froschle, D. Holtum, B. Heinemann, W. Kraus, A. Lorenz, C. Martens, P. McNeely, S. Obermayer, R. Riedl, R. Suss, A. Tanga, R. Wilhelm, D. Wunderlich, Nucl. Fusion **46**, S220 (2006)
- G.C. Stutzin, A.T. Young, A.S. Schlachter, W.B. Kunkel, Bull. Am. Phys. Soc. II **33**, 2091 (1988)
- M. Surendra, Plasma Sources Sci. Technol. **4**, 56 (1995)
- E.G. Thorsteinsson, J.T. Gudmundsson, Plasma Sources Sci. Technol. **19**, 015001 (2010)
- M. Turner, A. Derzsi, Z. Donko, D. Eremin, S. Kelly, T. Lafleur, T. Mussenbrock, Phys. Plasmas **20**, 013507 (2013)
- J.M. Wadehra, J.N. Bardsley, Phys. Rev. Lett. **41**, 1795 (1978)
- W. Yang, S.N. Averkin, A.V. Khrabrov, I.D. Kaganovich, Y.N. Wang, Phys. Plasmas **25**, 113509 (2018)
- W. Yang, A.V. Khrabrov, I.D. Kaganovich, Y.N. Wang, Plasma Sources Sci. Technol. **28**, 10LT01 (2019)
- R. Zorat, J. Goss, D. Boilson, D. Vender, Plasma Sources Sci. Technol. **9**, 161 (2000)

Chapter 4

Particle-In-Cell Modeling of Negative Ion Sources for Fusion Applications



Francesco Taccogna, Gwenael Fubiani, and Pierpaolo Minelli

Abstract A two- and three-dimensional (2D and 3D) Cartesian, three-velocities (3 V), Particle-in-Cell Monte Carlo collisions (PIC-MCC) model of a tandem-type Inductively Coupled Plasma (ICP) discharge is presented. The conditions are similar to those of negative ion sources for fusion applications, i.e., a high absorbed power (on the order of 100 kW), a high-density plasma (typically $5 \times 10^{17} \text{ m}^{-3}$), and a low neutral gas pressure (0.3 Pa) in a large volume vessel with a magnetic field barrier. We show that the plasma transport properties may be calculated with sufficient accuracy by implementing a larger than the real value of the vacuum permittivity in Poisson's equation. This approach is appropriate for nonturbulent plasmas, provided that the sheath length is small with respect to the quasi-neutral plasma dimensions. Furthermore, the calculation of the radio-frequency (RF) power coupling with the plasma (which is provided by an external antenna) is simplified by assuming that the electrons in the discharge interact with a uniform RF power profile and that their energy distribution function is Maxwellian in that region. Such approximation is relevant when the electron collision mean-free path is larger than the discharge dimensions and electrons are nonmagnetized. The simulation results are used to describe the plasma transport across the magnetic filter including the role of the Hall current ($\mathbf{E} \times \mathbf{B}$ and diamagnetic drifts), the dynamics of neutrals (notably the question of neutral depletion and physical chemistry), and lastly, the physical mechanisms involved with the extraction of negatively charged particles from the ion source, namely negative ions and electrons.

Keywords Negative ion source · Particle-in-Cell kinetic model · Direct Simulation Monte Carlo Collision · Extraction meniscus physics · ExB and diamagnetic drifts

F. Taccogna (✉) · P. Minelli
CNR-Institute for Plasma Science and Technology, Bari, Italy
e-mail: francesco.taccogna@cnr.it

G. Fubiani
CNRS-Laboratoire PLASMA et Conversion d'Energie, Toulouse Cedex, France

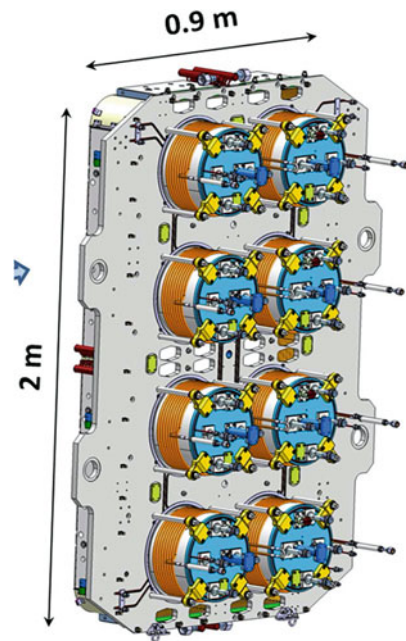
4.1 Introduction

This chapter describes the modeling of hydrogen Negative Ion Sources (NIS) using a particle-based algorithm known as the Particle-In-Cell with Monte-Carlo collision (PIC-MCC) technique (Birdsall and Langdon 1991; Hockney and Eastwood 1981; Tskhakaya et al. 2007; Taccogna 2015) with an emphasis on magnetized plasma sources relevant to the ITER Neutral Beam Injector (NBI) (Takeiri 2010; Hemsworth et al. 2017).

We will focus specifically on RF-driven tandem-type ion sources. These devices typically have a large volume with a height of 2 m, a width of 0.9 m, and a length of 0.4 m for the ITER ion source prototype represented in Fig. 4.1. The latter is powered by eight Inductively Coupled Plasma (ICP) RF discharges, each with a power of up to 100 kW. The plasma density is typically on the order of $5 \times 10^{17} \text{ m}^{-3}$ averaged over the ion source volume.

The tandem concept relies on using a magnetic filter (inside a so-called “expansion chamber” attached to the eight discharges in Fig. 4.1) transverse to the particle flow exiting the RF discharges in order to reduce the electron current density and temperature in the region where negative ions are extracted. A low electron temperature near the apertures is beneficial for the extraction of negative ions as it increases their mean-free path before being destroyed by electron-induced detachment collisions. Electrons are typically strongly magnetized by the magnetic filter field while ions are only slightly magnetized at best (because the plasma

Fig. 4.1 SPIDER ITER negative ion source prototype developed at Consorzio RFX in Padova, Italy. (Reproduced from (Heinemann et al. 2017) with permission from IOP)



potential drop between the discharge and the extraction region, which accelerates the positively charged ions, is a tenth of volts). In addition, the magnetic field induces a drift motion ($\mathbf{E} \times \mathbf{B}$ and diamagnetic ones) for the electrons which are directed toward one of the lateral walls of the ion source; this results in a polarization of the plasma to limit the particle losses on the surface (because of the restoring force between charged particles). This mechanism is analogous to the Hall effect in semiconductors, and it renders the plasma parameters asymmetric in the transverse direction.

Negative ions are either produced inside the plasma volume by the dissociative attachment of the vibrationally excited hydrogen isotope molecules (Bacal and Wada 2015) or by the surface conversion of a positive ion or a neutral atom impacting a surface. The latter corresponds to the transfer from the material of one or more electrons by a tunneling process which implies that the negative ion production yield is highly dependent on the potential barrier (also called “work function”) between the impacting particles and the surface. In practice, the work function of metals (copper or molybdenum) is reduced by the adjunction of cesium gas inside the source which will result in the deposition of a thin layer covering the surfaces (Seidl et al. 1995). Alternatively, the production of negative ions inside the plasma volume relies on a two-step process, where first, the hydrogen isotope molecules are vibrationally excited to high quantum numbers ($\nu > 4$) inside the discharge (where the electron temperature T_e is large, typically on the order of 10 eV) and second, the negative ions are generated as the by-product of a collision between an electron and these molecules in a region of the ion source with $T_e \sim 1$ eV. The cross section for the process is very sensitive to both, the vibrational level of the molecules and the electron energy (see Fig. 4.5).

The working condition of fusion-type ion sources is a low background gas pressure $P_g \sim 0.3$ Pa. The total collision mean-free path for the hydrogen molecules is about 10 cm (Fubiani et al. 2017) while it is ~ 1 m for the hydrogen atoms. Hence, the former typically undergoes many collisions before reaching the ion source walls, while the latter interact mainly with surfaces. In addition, a large fraction of the atoms originates from the recombination of fast protons at the surface. As a result, the atomic hydrogen isotope species (fundamental for the negative ion production by atomic conversion on low work function surfaces) typically has a non-Maxwellian distribution function.

Lastly, negative ions are extracted from the plasma by applying a positive voltage (5–10 kV) between the plasma grid (PG) and the extraction grid (EG), which is the first grid of an electrostatic accelerator (Fubiani et al. 2008; Fubiani et al. 2009; de Esch et al. 2015; Hemsworth et al. 2017). The latter, in the case of the ITER MAMuG concept, consists of five acceleration grids (each with a 200 kV potential difference) in addition to the EG. There are 1280 independent negative ion beamlets that are extracted from the PG while the acceptance of the accelerator is within a margin of 10%, implying that the beamlet current density extracted from the plasma must be highly symmetric. Electrons are also co-extracted from the plasma source alongside negative ions, but due to their significantly lower mass, they are deflected by the magnetic field of permanent magnets embedded in the EG. As a result, only

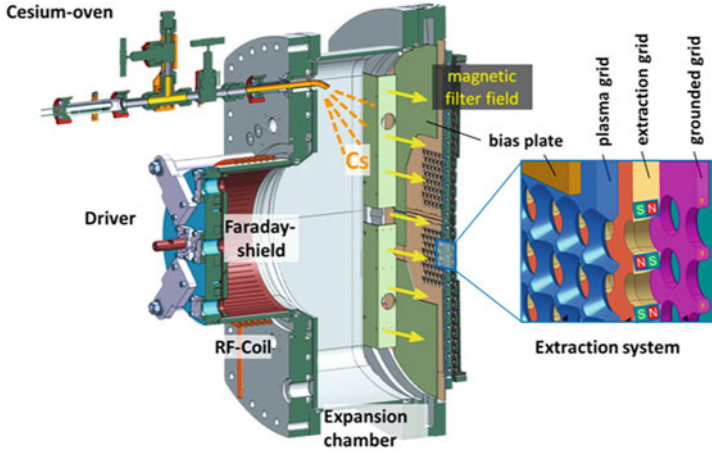


Fig. 4.2 Schematic representation of the BATMAN prototype ion source, Marx Planck Institute, Garching, Germany. (Reproduced with permission from Heinemann et al. 2017) with permission from IOP)

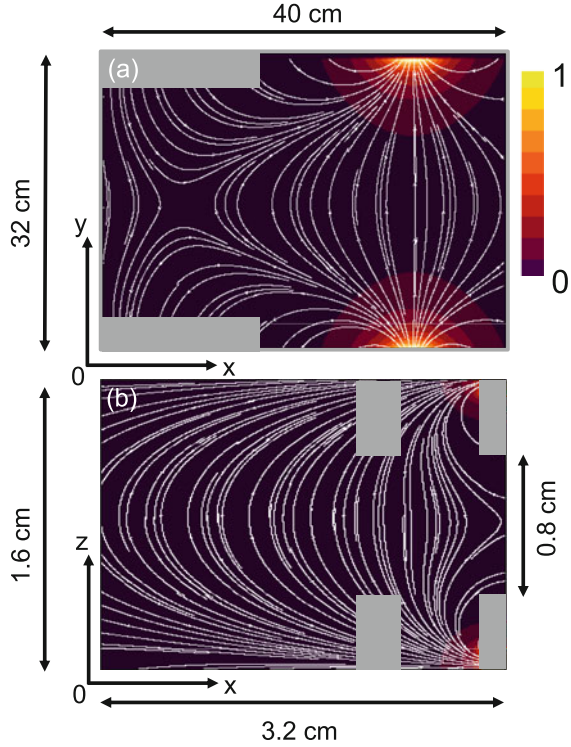
a small fraction of co-extracted electrons is transmitted across the EG ($\sim 2\%$ in the ITER accelerator) (Fubiani et al. 2008).

Figure 4.2 displays the BAVarian Test MACHine for Negative ions (BATMAN) developed at the Max-Planck Institut für Plasmaphysik in Garching, Germany. BATMAN is a one-driver ITER prototype magnetized plasma source that is well suited for modeling due to its small dimensions. Figure 4.3 plots the magnetic filter field profile (75 G maximum) generated by permanent magnets placed on the lateral walls of the ion source (see also Fig. 4.2) together with the cusp-field profile acting as a magnetic field barrier in front of each of the extraction apertures (the field strength is about 140 G on the PG surface facing the plasma).

The development, comprehension, and optimization of negative hydrogen ion sources are greatly improved by the numerical modeling of the plasma generation, transport, and extraction properties. The PIC-MCC technique does not have any restrictions on the shape of the particle distribution function and is hence particularly well suited to model the plasma working conditions described hereafter:

- Gas kinetics at pressures of about 0.3 Pa (2.2 mTorr) have an associated Knudsen number typically greater than one (especially for the atoms as mentioned earlier) and hence a Lagrangian model using macroparticles to describe the gas phase-space characteristics (so-called Direct-Simulation-Monte-Carlo—DSMC—models) is required in place of solving the Navier-Stokes equation. The calculation of the vibrational distribution function (VDF) of hydrogen molecules requires the same approach; the VDF is also non-Maxwellian and its shape has a significant impact on the negative ion production rate through the electron dissociative attachment of molecules.

Fig. 4.3 (a) 2D normalized magnetic field profile from (a) permanent magnets embedded on the lateral walls of the BATMAN ion source model (so-called filter field) and (b) cusp field profile in front of an extraction aperture (so-called electron suppression field). The RF discharge volume lies between the grey rectangles in (a). The two apertures in (b) corresponds to the PG (left) and EG (right)



- The electron energy distribution function is not Maxwellian in filament-driven discharges and typically also in the region of the antenna in RF plasmas working at low frequencies (~ 1 MHz) due to a non-local heating of the electrons (anomalous skin effect) (Tyshetskiy et al. 2002) and the ponderomotive force (Godyak et al. 2001).
- Lastly, the distribution function of negative ions produced on the PG surface by neutral atoms (which is the main production mechanism) and positively charged ions is also not Maxwellian as it is related to one of the incoming particle species. In addition, they are accelerated by the plasma sheath toward the ion source volume (which is not well modeled by fluid algorithms) and space charge limited due to the large (negative) ion density in front of the surface. The negative ion current density produced by the neutral flux in the BATMAN ion source prototype is estimated to be ~ 600 A/m² (Fubiani et al. 2017; McAdams et al. 2011). This leads to the formation of a potential well, resulting in a large fraction of negative ions being backscattered toward the electrode.

4.2 The Particle-In-Cell Technique

The Particle-In-Cell (PIC) procedure (Birdsall and Langdon 1991; Hockney and Eastwood 1981; Tskhakaya et al. 2007; Lapenta 2012) is a characteristic solution of the Vlasov equation (Nicholson 1983). An ensemble of real particles of the same species is grouped in a so-called macroparticle, which is a numerical artifact allowing the model of the phase space transport properties of the plasma with a lower than the real number of numerical particles. A macroparticle is equivalent to a Dirac delta function in velocity space (Eulerian representation of a point particle). Their trajectories are identical to one of the real particles because of the same charge-to-mass ratio in the Lorentz force. The latter is the force acting on charged particles in a plasma. In a PIC algorithm, the point-like properties of a macroparticle, such as its charge and current that it carries, are smoothed over the cell size, typically by interpolating these quantities over the neighboring cell nodes. A bilinear interpolation, for instance, in 2D is the typical scheme used in PIC algorithms (so-called Cloud-In-Cell—CIC—approach). Charge and current densities are the source terms for Maxwell’s equations that provide the self-electromagnetic forces due to the charge separation and the particle motion. In low-temperature plasmas such as ion sources, the magnetic field induced by the particle current is negligible compared to the one imposed externally; hence, the electrostatic approximation is sufficient.

We performed the simulations discussed hereafter with an explicit PIC model. In explicit PIC algorithm the electric field is derived from the charge density calculated at the previous time step (which is a source term for Poisson’s equation). The cell size must be lower than the electron Debye length and the time step a fraction of the electron plasma frequency; otherwise, a numerical instability will be seeded from the background noise. The number of particles per cell must be typically >40 to reduce the artificial numerical heating due to the discrete particle representation.

The electrostatic PIC-MCC cycle is displayed in Fig. 4.4: first, the particle charge is interpolated on a mesh (step 3, “charge deposition”), and after solving Poisson’s equation (step 4), the electric field is interpolated back to the particle location (“field interpolation,” step 5), to update the particle trajectory during the time lag Δt . Lastly, the coarse-grained representation of particle–particle interactions, i.e., the collision operator in the Boltzmann equation, is implemented via a probabilistic method (step 2) (Nanbu 2000; Taccogna 2015; Fubiani et al. 2017). In the model, neutrals are either considered as nonmoving background species with a given density profile or are actually implemented as macroparticles and their trajectories integrated. In the case of the former, collisions between charged particles and neutrals are performed by the so-called Monte-Carlo (MC) method, while for the latter, actual particle-particle collisions are evaluated using a Direct-Simulation-Monte-Carlo (DSMC) algorithm (Nanbu 2000). Both are similar except that in the MC method, one artificially extracts a neutral particle velocity v_{neu} from a Maxwellian distribution function at a temperature T_{neu} . The probability for the occurrence of a reaction is calculated from the tabulated cross-sections and particles are scattered in their centre-of-mass after the collision.

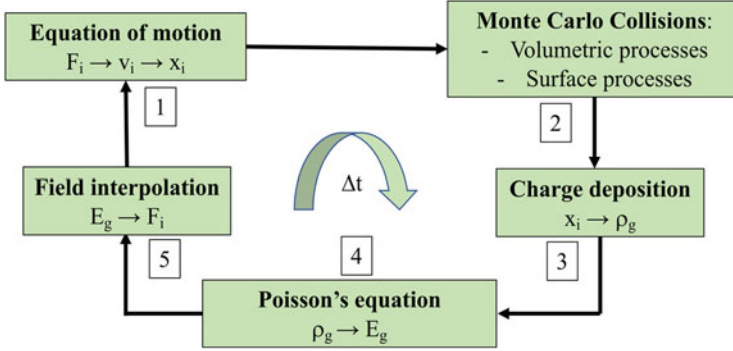


Fig. 4.4 Diagram showing one integration time steps in a PIC-MCC simulation

The PIC-MCC numerical constraints are absent when solving for the gas dynamics. For atoms and molecules, the computational complexity is associated with the necessity to include their internal quantum (electronic and vibrational) structure. In the case of hydrogen gas, for instance:

- The excitation of the hydrogen atom from the ground state to the electronic level $n = 2-5$.
- The vibrational excitation of the hydrogen molecule ground electronic state $H_2(X^1\Sigma^+_g; \nu = 0-14)$.
- The excitation of H_2 molecules from the ground state $X^1\Sigma^+_g$ to excited singlet and triplet electronic states: $B^1\Sigma_u, B'^1\Sigma_u, B''^1\Sigma_u, C^1\Pi_u, D^1\Pi_u, D'^1\Pi_u, a^3\Sigma^+_g, c^3\Pi_u, d^3\Pi_u$, and Rydberg states (Taccogna et al. 2007; Fubiani et al. 2017). This level of detail is important to properly quantify the electron energy collision losses but also to characterize the negative ion production by the electron dissociative attachment (DA) process of the molecules because it is highly dependent on their vibrational levels. The two systems, plasma and gas, are typically solved separately by considering distinct time steps. This is due to the fact that the spatial and time scales for the plasma and gas are very different: the plasma reaches a steady state condition in about tens of microseconds, which is approximately the time lag for the ions to reach the walls of the ion source (i.e., after millions of PIC cycles with timesteps of picoseconds in order to solve for the electron plasma frequency $\omega_{pe} [s^{-1}] \simeq 2\pi \times 9000 n_e^{1/2} [cm^{-3}]$), while neutrals needs milliseconds (the time step for the gas is usually $\Delta t_{DSMC} \sim 10$ ns). The typical mesh size for the plasma is tens of micrometers (corresponding to a plasma density of $\sim 5 \times 10^{17} m^{-3}$ and an electron temperature of ~ 5 eV; $\lambda_{De} [cm] \simeq 740 \sqrt{T_e [eV] / n_e [cm^{-3}]}$), while the gas cell size (related to the gas mean free path and gradient length) is on the millimeter scale and hence the simulations are performed on separate meshes. The plasma and gas are coupled via the elastic and inelastic processes (including ionization) in the device volume and also through the recombination on surfaces where a flux of energetic, positive ions is neutralized during the impact.

Cross sections for collisions between neutrals inside the ion source volume, as well as backscattering, dissociation, or recombination probabilities against the ion source walls, are required for the modeling of the neutral particle dynamics (and the associated neutral depletion). For a detailed description of the physical-chemistry processes, see (Fubiani et al. 2017). In a low-pressure plasma device, such as the one used for fusion applications, the plasma-wall processes have a strong impact on the source characteristics. Low-temperature backscattered molecular hydrogen is assumed to be in thermal equilibrium with the wall. An average reflection energy coefficient $R_E = E_b/E_{in} \leq 1$, where E_{in} (E_b) is the incident (backscattered) particle kinetic energy, is considered for fast atoms and recombined ions ($R_E = 0$ corresponds by definition to an accommodation at the wall temperature in the model). These estimates are based on Monte Carlo calculations in ideal conditions (i.e., a clean surface) from the TRIM code (Eirene). Average particle reflection probability R_N is also taken from the same database. Furthermore, we assume that atoms that are not backscattered will recombine. The interaction of H_2^+ and H_3^+ ions with the walls and the corresponding coefficients are not well known. For H_2^+ , we use coefficients that are consistent with the measurements of (Krischok et al. 1999). For H_3^+ , we assume that 2/3 will produce H atoms with $R_E = 0.5$ and 1/3 H_2 molecules (the H_3^+ flux to the walls is relatively small with respect to the H_2^+ and H^+ , and the results are not very sensitive to these coefficients).

PIC-MCC models have been optimized to run on supercomputers via a parallelization of the algorithms using MPI and OpenMP libraries. An additional method to accelerate the convergence time of the ion source plasma simulation is obtained by replacing the vacuum permittivity ϵ_0 in Poisson's equation With a given value ϵ ,

$$\nabla^2\varphi = -\rho/\epsilon, \quad (4.1)$$

ρ is the total charged density. This assumption is equivalent to modeling a plasma density smaller by a scaling factor $\alpha = \epsilon/\epsilon_0$ while allowing to artificially consider the real plasma densities for the calculation of the collisions between charged particles. The plasma sheath is hence larger by a factor $\sqrt{\alpha}$ that does not have any consequences on the plasma behavior as long as (1) the plasma is quiescent or without any enhanced transport due to instabilities with frequencies and growth rates related to the vacuum permittivity and (2) the particle kinetics inside the plasma sheath are preserved. In such situations and for a fixed neutral background density, the plasma potential, temperature, and density (which must be normalized to its maximum) profiles are independent of the amplitude of the discharge external power (Fubiani and Boeuf 2014; Fubiani et al. 2017).

The tandem prototype ion sources have an ICP discharge that couples a high RF power (typically 100 kW at 1 MHz frequency) to a hydrogen or deuterium plasma. We do not simulate in this chapter directly the interaction of the RF field with the plasma (Ippolito et al. 2017) but assume instead that some power is absorbed. Every time step, macroparticles which are found inside the region of RF power deposition (the so-called driver in Fig. 4.6) are heated according to some artificial heating collision frequency. Electrons, being the lightest particles, are assumed to

absorb all of the external power. Redistribution of energy to the heavier ions and neutrals is done through collisions (both elastic and inelastic) and the ambipolar potential. Electrons undergoing a heating collision have their velocities replaced by a new set sampled from a Maxwellian distribution with a temperature calculated from the average specie kinetic energy inside the power deposition region added to the absorbed energy per colliding particles, i.e.,

$$\frac{3}{2}T_H = \langle E_k \rangle_H + \frac{P_{\text{abs}}}{eN_{\text{eh}}\nu_h} \quad (4.2)$$

where T_h (eV) is the heating temperature in electron-Volts (eV), $\langle E_k \rangle_h$ is the average electron kinetic energy, P_{abs} (W) is the absorbed power, ν_h is the heating frequency, and N_{eh} is the number of electrons, respectively. For a given time step, $N_{\text{em}}\nu_h\Delta t$ colliding macroelectrons are chosen randomly, where N_{em} is the total number of macroparticles inside the heating region. Note that electrons are not magnetized inside the BATMAN ICP discharge, and we further neglect the anomalous skin or ponderomotive effects induced by the antenna at low RF frequencies.

4.3 Plasma Transport Across the Magnetic Barrier

Next, we describe the plasma properties in a typical ITER prototype ion source (Boeuf et al. 2012; Fubiani and Boeuf 2014; Taccogna and Minelli 2017; Fubiani et al. 2017). We focus on the one-driver BATMAN device as it is more suitable for modeling in 3D because of its relatively small dimensions: 40 cm in total length, 32 cm width, and 58 cm height with a driver discharge diameter of 24.5 cm for a 16 cm length. Figure 4.5 shows a schematic representation of the simulation domain. The magnetic filter field B_F (see Fig. 4.3) is transverse to the charged particle flux exiting the driver discharge. The field profile is well fitted by a Gaussian on axis with a maximum strength of 75 G. The hydrogen isotope ions may be considered nonmagnetized (except for the lightest species, which might be slightly affected by the field) while the electrons are strongly magnetized in the expansion chamber resulting in a drift directed toward one of its lateral walls. The electron flux may be expressed as follows (Boeuf et al. 2012):

$$\Gamma_e = \frac{1}{1 + h^2} [\mathbf{G} + \mathbf{h} \times \mathbf{G} + (\mathbf{h} \cdot \mathbf{G}) \mathbf{h}], \quad (4.3)$$

With

$$\mathbf{G} = -\mu [n_e \mathbf{E} + \nabla (n_e T_e)], \quad (4.4)$$

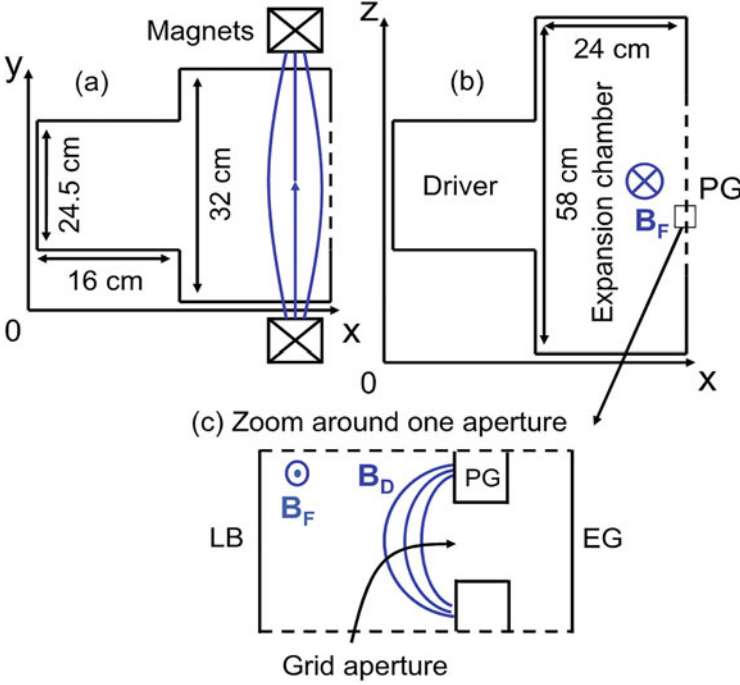


Fig. 4.5 Schematic view of the BATMAN geometry. On the left side, the driver where the power from RF coils (not simulated) is coupled to the plasma. The box on the right-hand-side (rhs) is the expansion chamber which is magnetized. The magnetic filter field \mathbf{B}_F is generated by a set of permanent magnets located on the lateral walls of the chamber near the PG (Fig. 4.3). Field lines are outlined in blue. The dashed line on the rhs of (a) and (b) correspond to the PG. The simulation domain for the modeling of negative ion extraction from the PG surface with a higher numerical resolution is displayed in (c). \mathbf{B} is the magnetic field generated by permanent magnet bars embedded inside the extraction grid (cusp magnetic field)

where $\mathbf{h} = \Omega_e/\nu_e = \mu\mathbf{B}$ is the Hall parameter, $\mu = |e|/(m_e\nu_e)$ is the electron mobility without magnetic field, e is the elementary charge, m_e is the electron mass, ν_e is the electron elastic collision frequency, and $T_e(n_e)$ is the electron temperature (density), respectively. For $h \gg 1$ and in the plane perpendicular to the magnetic field lines, $\mathbf{h} \cdot \mathbf{G} = 0$, which gives

$$\Gamma_e = -\frac{\mathbf{G} \times \mathbf{B}}{\mu B^2}. \quad (4.5)$$

The electron motion is consequently dominated by the magnetic drift, which is composed of diamagnetic and $\mathbf{E} \times \mathbf{B}$ terms. For the magnetic field configuration displayed in Fig. 4.5a, b, the electron flux diffusing from the driver toward the extraction region experiences globally, in addition to the ambipolar field, a force $\mathbf{F}_H = -en_e\mathbf{E}_H$ in the $-\mathbf{J}_{ex} \times \mathbf{B}$ direction (force per unit volume, with

$\mathbf{J}_{\text{ex}} = -e\Gamma_e \mathbf{e}_x$ the electron current density axial component) which is perpendicular to the direction of the unit vector \mathbf{e}_x and the magnetic field. The force is directed toward the top wall of the expansion chamber in our case ($e\Gamma_{\text{ex}}B_y$ with $\Gamma_{\text{ex}} > 0$). The presence of walls intercepting the Hall current hence leads to charge separation and to the creation of an average electric field that opposes the effect of the Lorentz force, as in the Hall effect (Kunkel 1981). This Hall electric field, \mathbf{E}_H (downward directed in our case), induces in turn an $\mathbf{E}_H \times \mathbf{B}$ drift which increases the electron transport across the magnetic field barrier with respect to an ideal 1D filter along (OX) without transverse walls. As a consequence, the electron cross-field mobility scales as $1/B$ rather than the classical $1/B^2$ (Hagelaar and Oudini 2011; Fubiani et al. 2012). We, therefore, expect that the Hall effect will create a plasma asymmetry with electric potential and a plasma density higher at the top of the chamber (large Z) than at the bottom (small Z). The polarization induces a transverse asymmetry in the plasma parameters that has been observed both in the models (Fubiani et al. 2017; Taccogna and Minelli 2017) and in the experiments (Schiesko et al. 2012; Fantz et al. 2014; Wimmer et al. 2016). Note that the drift is also found in fluid models (Hagelaar and Oudini 2011; Lishev et al. 2018). The combined $\mathbf{E} \times \mathbf{B}$ and diamagnetic drifts, which are *usually* in opposite directions, result in a skewed transport of the electron current across the magnetic filter toward the PG, as shown in Fig. 4.6c. For instance, the flux from $x \approx 25$ cm up to the grid ($x \approx 40$ cm) is driven by the diamagnetic drift; $G_x > 0$ in Eq. (4.5) with $|\partial_x p_e/n_e| > |E_x|$ and $\Gamma_{ez} < 0$. Figure 4.6 shows the 2D profiles for the electron density (a), temperature (b), and current density (c) together with the plasma potential (f) in the plane perpendicular to the magnetic filter field lines (where the electron drift occurs), while the plasma properties in the plane of the magnetic field are displayed in (d) for the electron temperature and (e) for the plasma potential, respectively. The magnetic field maximum is 30 G in (a)–(d) and 75 G in (e) and (f). The plasma asymmetry is clearly visible in the electron drift plane. In (d), the electron temperature profile closely follows the magnetic field lines.

Positive ions are only slightly magnetized at best (this is the case for the lightest species, such as protons) and flow down the plasma potential toward the ion source walls. In the expansion chamber, the electron and ion current density distribution are strongly non-ambipolar, i.e., $\mathbf{j}_e \neq \mathbf{j}_i$, locally; and only the total electron and ion currents collected on the ion source walls are equal. The transverse asymmetry of the potential due to the Hall effect affects the plasma density, which has a maximum off (the OX) axis inside the expansion chamber. The asymmetry is modified by the shape of the magnetic filter field profile and the PG bias voltage (Fubiani and Boeuf 2014; Lishev et al. 2018). Shifting either the maximum of the magnetic field towards the driver or similarly increasing the bias voltage (a larger electron current is then drawn from the driver across the filter in that case) leads to a larger transverse plasma asymmetry. Similar plasma behaviors have been described in ion sources with greater aspect ratios (Heinemann et al. 2019; Toigo et al. 2017) such as the half-size ITER ELISE ion source prototype for instance (Fubiani and Boeuf 2015).

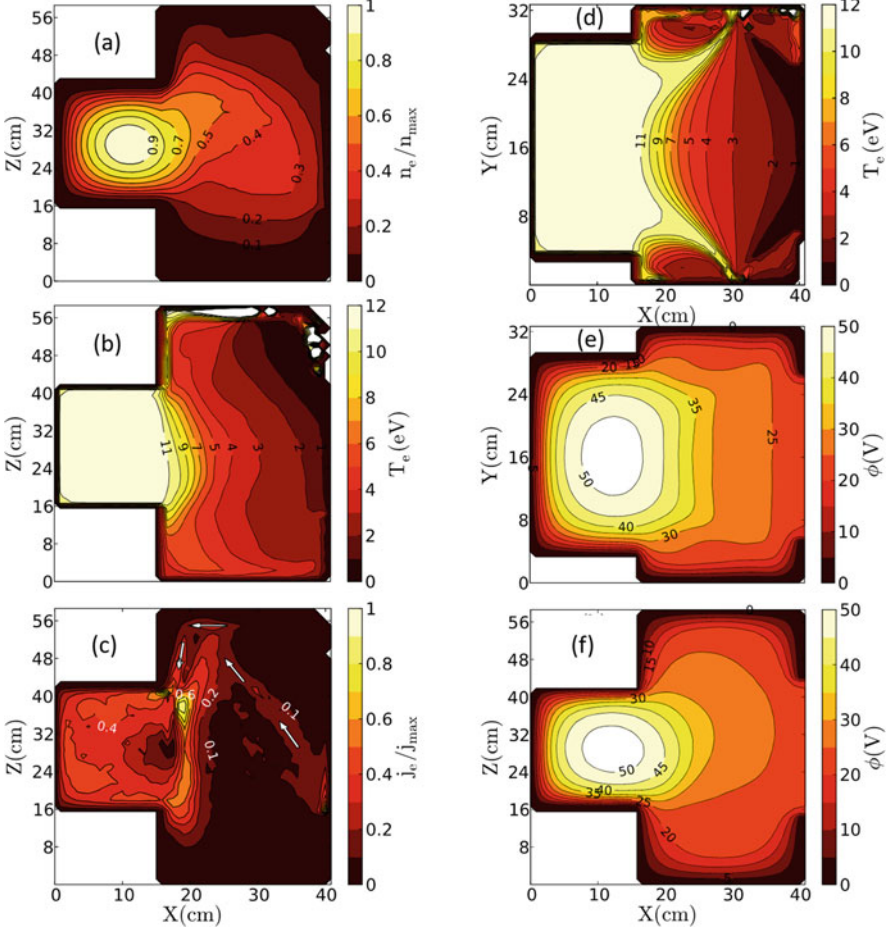


Fig. 4.6 3D plasma properties of the BATMAN negative ion source for a hydrogen background gas filling pressure of 0.3 Pa (without plasma discharge), a magnetic filter field generated by permanent magnets and an absorbed power $P_{\text{abs}} = 60$ kW. The dimensions of the PG are 20.5×27.8 cm². In (a), normalized plasma density in the $Y = 0$ plane, perpendicular to the magnetic field lines. $n_{\text{max}} = 2.3 \times 10^{18}$ m⁻³. The 2D electron temperature profile is displayed in (b), in (c), the normalized electron current density, with $j_{\text{max}} = 1.6 \times 10^4$ A/m², in (d) the electron temperature profile in the $Z = 0$ plane, which includes the magnetic field lines, in (e) and (f) the plasma potential profiles in both the $Y = 0$ and $Z = 0$ planes, respectively. In (a)–(d), the magnetic filter field peaks at 9 cm from the PG with a strength of 30 G and a PG bias voltage of 30 V while in (e) and (f) the magnetic field is maximum on the PG (75 G) and $V_{\text{PG}} = 20$ V. Note that a reduced set of cross sections was implemented in (a)–(d) without loss of generality. The numerical resolution is $128 \times 96 \times 192$ grid nodes and the scaling factor $\alpha = 36 \times 10^3$. The white arrows in (c) correspond to the direction of the electron current

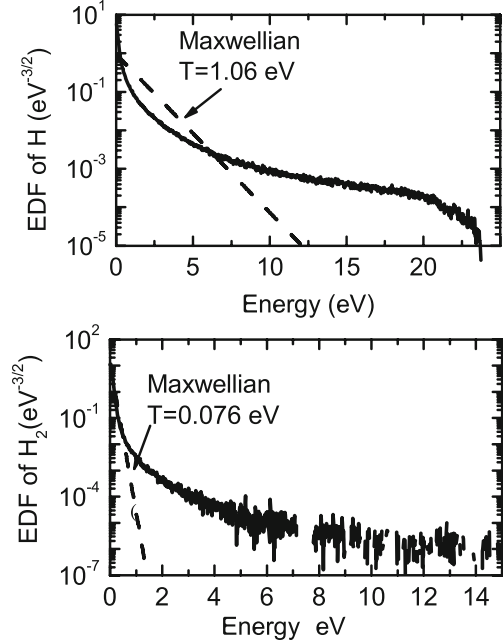
4.4 Gas Dynamics and Vibrational Kinetics

Gas dynamics is studied in this chapter by self-consistently coupling a 2D fluid plasma model (Hagelaar and Oudini 2011; Fubiani et al. 2017) with a kinetic description of neutral transport based on the DSMC (Direct Simulation Monte Carlo) technique. The objective is to estimate the spatial and velocity distribution of hydrogen atoms and molecules in low-pressure and high-power conditions where the neutral Knudsen number is not small with respect to unity. Figure 4.7 shows the atomic hydrogen energy distribution function (top) calculated by the DSMC in the center of the BATMAN prototype negative ion source for a 60 kW absorbed power and 0.3 Pa background gas pressure. The distribution function is highly non-Maxwellian, and its properties are mostly controlled by the production and collisions of H atoms against the walls of the ion source (the total mean-free path is of the order of 1 m, i.e., significantly larger than the dimensions of the device). H atoms are mostly created and heated by the neutralization of fast ions (and dissociation in the case of molecular ones) on the ion source walls ($\sim 45\%$ of the atom production and $\sim 77\%$ of the energy gain) and by the volume dissociation of H_2 . H_x^+ ions (where $x = 1-3$) are mainly generated inside the discharge where the amplitude of the plasma potential is typically ~ 50 V in the experiments (McNeely et al. 2009), and hence these positive ions impact the walls with high energy. This explains the origin of the large energy tail in the distribution function of atomic hydrogen, as shown in Fig. 4.7. H atoms lose most of their energy through collisions with surfaces ($\sim 95\%$).

H_2 molecules are created uniquely through the recombination of H_x^+ ions and H atoms on the walls. Molecular hydrogen is assumed to be emitted from the surfaces as a Maxwellian flux at $T_w = 300$ K (where T_w is the temperature of the surface), i.e., at thermal equilibrium with respect to the wall (Fubiani et al. 2017). The energy distribution function is well fitted by a Maxwellian (up to about $6 T_{\text{H}_2}$), as shown in Fig. 4.7. The mean-free path is ~ 10 cm, i.e., smaller than the dimension of the ion source. The energy tail is induced by the collisions with the warm H atoms; a molecular hydrogen is mainly heated through elastic collisions with atoms ($\sim 65\%$ of power gain) and by electrons. $T_{\text{H}} \sim 1$ eV and $T_{\text{H}_2} \simeq 0.08$ eV is estimated for 60 kW and 0.3 Pa in the center of the discharge, which is consistent with the experimental observations (McNeely et al. 2011).

The simulations have been performed either with or without a magnetic filter field in the expansion chamber. The magnetized case corresponds to a maximum field amplitude of $B_{\text{max}} = 15$ G close to the PG, which is lower than the field in the actual experiment (~ 75 G on the axis), but nevertheless the Hall parameter $h = \mu \mathbf{B}$ greatly exceed unity, and the electrons are strongly magnetized. The indirect effect of the magnetic field on the neutral dynamics is that the depletion of H_2 occurs in the area where the electron density is highest (i.e., in the driver when the expansion chamber is magnetized) because molecular hydrogen is dissociated or ionized mainly by electrons. The density profile of hydrogen atoms is, on the contrary, quite insensitive to the magnetic field due to the fact that the volume losses

Fig. 4.7 Energy distribution function for molecular (top) and atomic (bottom) hydrogen in the center of the negative ion source. We implemented a 60 kW absorbed power, 0.3 Pa background gas pressure and no magnetic filter field. 2D fluid calculation for the plasma and DSMC for the neutrals



(ionization) are significantly smaller than for H_2 ($\sim 14\%$ of the total losses) and that the mean free path greatly exceeds the ion source dimensions. The 2D density and temperature profiles for the neutrals are shown in Fig. 4.8.

Note that due to the significant effect of particle–surface interactions on the neutral properties, model results are strongly dependent on the particle R_N , energy R_E reflection, and recombination $\gamma_{\text{rec}} = 1 - R_N$ coefficients of molecules, atoms, and ions on the walls, which are not well known experimentally (Fubiani et al. 2017). Assuming, for instance, that the neutral hydrogen atoms are backscattered off the walls with the same temperature as the surface, we find that (1) the amplitudes of the molecular hydrogen temperature and density in Fig. 4.8 are only slightly modified while (2) the H atom temperature is on average divided by 5 and the density as a consequence is larger by a factor of 2.

The vibrational distribution function (VDF) of the hydrogen molecules is also non-Maxwellian (Capitelli et al. 2006; Gaboriau and Boeuf 2014; Taccogna et al. 2007). The supra-thermal VDF characterized by the typical long plateau for $\nu = 3\text{--}12$ is clearly visible in Fig. 4.9. The vibrational population can actually be well represented by a two-temperature distribution with $T_{03} = 0.2$ eV and $T_{07} = 0.7$ eV, mainly generated by electron-induced resonant (eV) $\text{H}_2(X^1\Sigma_g^+, \nu_i) + e \rightarrow \text{H}_2(X^1\Sigma_g^+, \nu_f) + e$ and excitation-radiative decay (EV) $\text{H}_2(X^1\Sigma_g^+, \nu_i) + e \rightarrow \text{H}_2^* + e \rightarrow \text{H}_2(X^1\Sigma_g^+, \nu_f) + e + h\nu$ vibrational excitations.

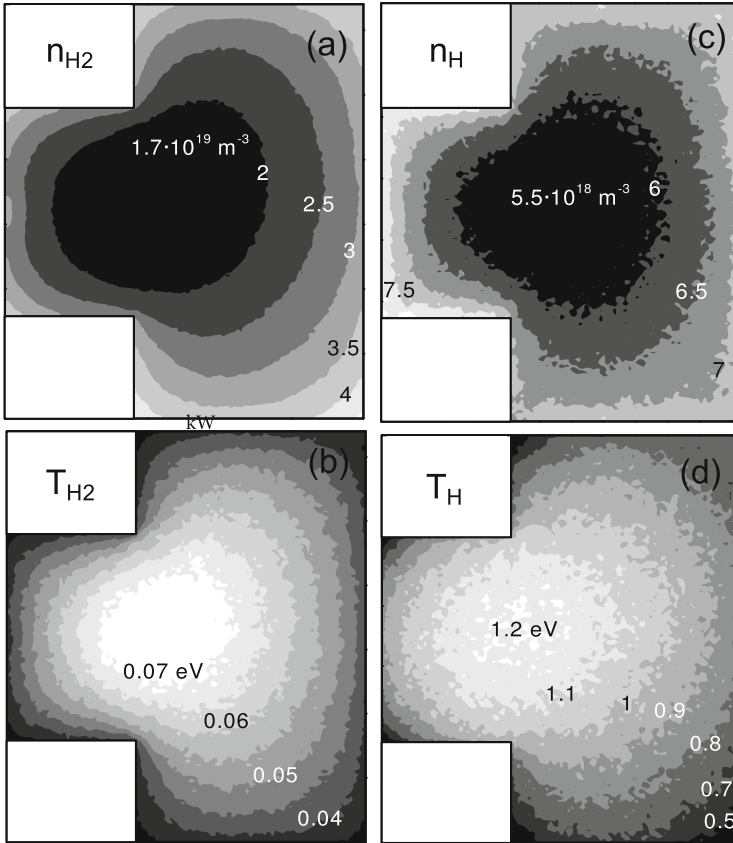
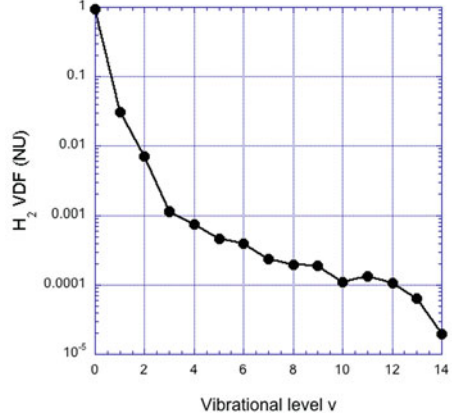


Fig. 4.8 Molecular hydrogen density (a), temperature (b), H atom density (c), and temperature (d) profiles, respectively. 2D fluid and DSMC calculation with $P = 60$ kW, a background gas pressure of 0.3 Pa, $B_{\max} = 15$ G, and a PG bias voltage of 10 V

4.5 Negative Ion Production on Surfaces

The hydrogen atoms flux impacting the PG estimated from the simulation of Fig. 4.7 is $\Gamma_{\text{H}} \approx 2.4 \times 10^{22} \text{ m}^{-2} \text{ s}^{-1}$ for a 60-kW absorbed power, 0.3 Pa background hydrogen gas pressure, a magnetic filter field with a maximum of 15 G near the PG, and a PG bias voltage of 10 V. Seidl et al. (1995) have derived the averaged conversion yield $\langle Y \rangle(T_{\text{H}})$ from experimental data for a Mo/Cs surface with dynamic cessation assuming that the distribution function of the atomic specie was Maxwellian. Note that the experiments were not performed in plasma. In our case, the distribution function is highly non-Maxwellian, and hence a range for the yield may be estimated either by (4.1) fitting the energy distribution function of the atoms with a Maxwellian distribution,

Fig. 4.9 Vibrational distribution function of the electronic ground state of molecular hydrogen in an ITER prototype ion source



$$\langle Y \rangle = R_N \eta_0 \exp\left(-\frac{E_{th}/R_E}{T_H}\right), \quad (4.6)$$

where $T_H \approx 0.8$ eV in the vicinity of the PG in the model or (4.2) considering the atoms as a “beam,”

$$Y E_{in} = R_N \eta_0 (E_{in} - E_{th}/R_E), \quad (4.7)$$

In both cases, $R_N \eta_0 = 0.42$ and $E_{th}/R_E = 1.05$ eV is assumed (Seidl et al. 1995). E_{in} is the incident energy of the atom. Using Eq. (4.6), we find $\langle Y \rangle \approx 11.5\%$ and hence $j_G \approx 440$ A/m² while Eq. (4.7) gives $j_G \approx 690$ A/m² ($\langle Y \rangle \approx 18\%$). j_G is the negative ion current density generated on the PG surface.

Such a large current density typically generates a virtual cathode in front of the grid surface (Taccogna et al. 2008; Wunderlich et al. 2009; McAdams et al. 2011) (a sharp and localized drop of the potential plasma profile that is schematically shown in Fig. 4.10) because the plasma cannot cancel out the space charge resulting from the negative ion charge density. A large fraction of the negative ions is hence reflected back on the PG grid surface. The depth of the potential well, φ_c is modulated by the positive ion density coming from the plasma discharge. Negative ions with a kinetic energy $E_0 \geq \sqrt{2e|\varphi_c|/m_n}$ can escape the potential well (e is the elementary charge and m_n the negative ion mass). The ion (saturation) current density is consequently,

$$j_{sat} = -e \int_{E_0}^{+\infty} v_x f(v_x) dv_x \quad (4.8)$$

Assuming that the negative ion distribution function along (Ox) is Maxwellian,

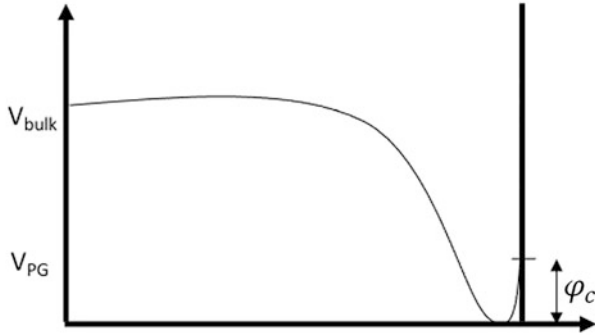


Fig. 4.10 Schematic view of the virtual cathode profile in front of the PG. The potential well appears when the negative ion density emitted from the right-hand-side surface is not fully compensated by the incoming positive ions from the bulk region

$$f(v_x) = n_G \sqrt{\frac{m_n}{2\pi T_n}} \exp\left(-\frac{m_n v_x^2}{2T_n}\right), \quad (4.9)$$

and that no collisions occur between the PG and the minimum of the virtual cathode (φ_c), we have,

$$j_{\text{sat}} = j_G \exp\left(-\frac{e|\varphi_c|}{T_n}\right), \quad (4.10)$$

where T_n is the negative ion temperature. The transport properties of the ions are hence strongly dependent on the plasma sheath in front of the surface where they are produced. The extent of the virtual cathode is typical of tens of micrometers for plasma densities of $\sim 10^{17} \text{ m}^{-3}$ at the sheath entrance. This is far smaller than the distance where experimental measurements are operated, and hence models are an important addition to study in detail the mechanisms leading to the extraction of the ions. These simulations require a fine grid resolution to include the multi-apertures embedded into the plasma grid (PG). Two types of algorithms were recently described in the literature:

- Simulation domains include the entire ion source volume but (for now) on a 2D mesh. These calculations are generally performed at a lower plasma density (i.e., implementing a scaling factor α) but allow to model with a higher degree of precision of the particle flux distribution functions impacting the PG. The simulation plane corresponds to the one perpendicular to the magnetic field lines, Fig. 4.5b, to include the particle drifts and hence to simulate the Hall effect. These types of models may also estimate the impact of the plasma asymmetry on the extracted beam characteristics.
- Another approach is to model one single aperture. The simulation domain is then restricted to zoom near the PG with periodic conditions on boundaries

perpendicular to the grid surface. The model hence simulates a configuration with an infinite number of apertures. The plasma is generated by injecting a Maxwellian flux of electron-ion pairs in a given region on the left-hand side of the simulation domain, as shown in Fig. 4.5c. The real plasma density may be simulated but typically in 2D as a large number of mesh nodes is required to properly resolve the virtual cathode profile. This approach is hence simplified and may be used to model in detail the negative ion beam phase-space properties (including the onset of aberrations) and the beam perveance versus the extraction voltage (Fubiani et al. 2017, 2018). These types of models can be coupled to a ray-tracing algorithm to simulate the beam transport inside the accelerator.

4.5.1 2.5D of the Whole Ion Source Volume Including the Apertures

3D PIC-MCC calculations are restricted to low plasma densities, typically $\sim 5 \times 10^{13} \text{ m}^{-3}$ on 40 CPU cores with $128 \times 96 \times 192$ grid nodes (40 ppc) for the prototype source at BATMAN discussed in the previous sections (Fig. 4.6). The scaling factor is hence $\sim 10^4$ (i.e., the density is about 10^4 times lower than the real density). A solution to increase the numerical resolution is to approximate the particle losses in the direction parallel to the magnetic field lines (which we call a 2.5D PIC-MCC model) (Fubiani et al. 2017). The particle transport is hence simulated in the plane perpendicular to the magnetic field lines (i.e., where the magnetized drift motion takes place). We assume that the plasma is uniform along the unsimulated direction (Oy) and that the field lines are straight, and we use the following considerations to estimate the charged particle losses:

- The ion dynamics in the direction perpendicular to the 2D simulation plane are not calculated and we estimate instead the ion losses from the Bohm fluxes to the walls. The loss frequency at a given location in the simulation plane is obtained from (Lieberman and Lichtenberg 2005, chap. 6, p. 169 and 172) $\nu_L = 2\alpha u_B/L_y$, where $u_B = \sqrt{eT_e(x, y)/m_i}$ is the local Bohm velocity, L_y is the length of the ion source in the third dimension, $\alpha = n_s/\langle n \rangle \sim 0.5$, n_s is the local plasma density at the sheath edge, $\langle n \rangle$ the average density, T_e (m_i), the local electron temperature (ion mass), respectively.
- The electron and negative ion trajectories are followed along (Oy), assuming that the plasma potential is flat (i.e., no electric field). When a negatively charged particle reaches a wall, it is removed if its kinetic energy in the y-direction is greater than the difference between the plasma $\varphi(x, z)$ and the wall φ_w potentials, i.e., $m_p v_y^2 \geq (\varphi - \varphi_w)$. m_p is the particle mass.

Macroparticles are created anywhere between $0 \leq y \leq L_y$ in the third dimension (via ionization processes). The 2.5D model estimates plasma characteristics that are averaged over L_y .

Figure 4.11 shows the proton and negative ion current density profiles in the extraction region of the BATMAN ion source prototype (up to 4 cm in front of the PG). The size of the simulation domain is $40 \times 58 \text{ cm}^2$ and the grid resolution 1024×1532 with a scaling factor $\alpha = 400$, 40 particles per cell and seven apertures of 1.5 cm diameter, respectively (Fig. 4.11 plots a zoom near three apertures). The background gas is hydrogen, with 0.3 Pa pressure, an absorbed power of 60 kW in the driver, and a PG positively biased at +20 V with respect to the ion source walls (which are at ground potential). Negative ions were only produced on the PG surface as a by-product of neutral hydrogen atom impacts in this calculation as it was shown that for large bias voltages (such that the PG is approximately floating), the fraction of negative ions produced by neutrals significantly exceeds the one induced by positive ions (Fubiani and Boeuf 2013; Wunderlich et al. 2014). The Hall effect (the fact that the magnetized electron drift is bounded) generates an asymmetric plasma potential profile in the expansion chamber (as in Fig. 4.7) which, added to the slight magnetization of the positively and negatively charged ions, results in an oblique ion flux profile near the PG (Fig. 4.11). The Larmor radius for the protons, for instance, is about 2 cm in that region (corresponding to an average kinetic energy of $\sim 1 \text{ eV}$) while the collision mfp is $\sim 40 \text{ cm}$. In addition, the positive ion flux distribution function is non-Maxwellian on the PG (Fubiani and Boeuf 2013). As a result of the magnetization, the X-points visible on the right-hand side (RHS) plot of Fig. 4.12 (streamlines are highlighted in white), which corresponds to the transition region where the negative ions are no longer extracted, is shifted off the aperture axis. This observation has been confirmed by experimental measurements (Geng et al. 2017; Denizeau et al. 2020). A large fraction of the negative ions that are extracted hence come preferably from one side of the aperture (Fubiani et al. 2017; Taccogna and Minelli 2017). The plasma meniscus (boundary that separates the quasi-neutral plasma from the void of the accelerator vessel in front of the aperture) is also slightly uneven. Lastly, Fig. 4.12 shows the positive ion density (summed over all the ion species) on the PG surface. The latter is highly asymmetric, and this translates into a virtual cathode depth (and hence a negative ion saturation current j_{sat} (Eq. (4.10))), which is also non-monotonic between apertures. The consequences of the extracted negative ion beamlet current density profile are still an open question.

The co-extraction of electrons alongside the negative ions is another critical issue, as a maximum of one electron per ion is required to avoid damage to the accelerator grids (Fubiani et al. 2008, 2009). It has been observed in the experiments (Wimmer et al. 2016) and confirmed by PIC-MCC modeling that a positive PG bias may greatly reduce the extracted electron current. Figure 4.13 plots the axial plasma potential profile for a bias voltage of 10–30 V (corresponding to the 3D PIC-MCC calculation of Fig. 4.5). The magnetic filter field screens efficiently the effect of the bias, and as a consequence, the potential in the driver region remains unaffected. The potential in the expansion region increases together with the bias while the sheath amplitude decreases. The electron current drawn from the driver is hence increasingly more collected by the PG surface due to the lower sheath barrier, resulting in a co-extracted electron current that drops significantly. The plasma

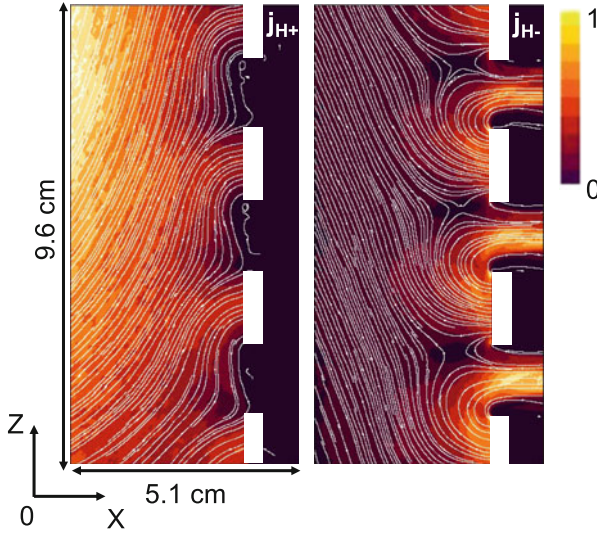


Fig. 4.11 2D normalized proton and negative ion current density profiles in the plane perpendicular to the magnetic filter field lines. The negative ions are uniquely produced on the PG surface. The magnetic filter field vector is perpendicular to the simulation domain and pointing toward the sheet

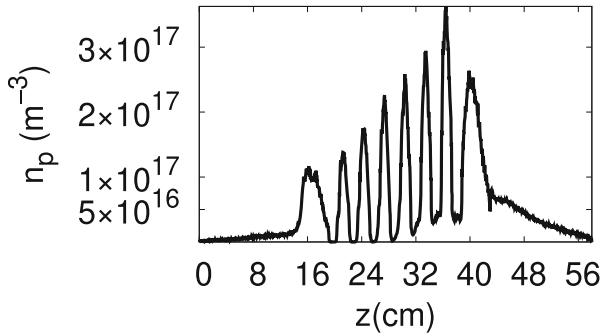


Fig. 4.12 Positive ion density profile on the PG surface. 2.5D PIC-MCC calculation of the ITER prototype BATMAN negative ion source

potential profile becomes somewhat flat when the PG is floating. This configuration is beneficial to the extraction of the negative ions as the residence time of the latter near the apertures is considerably increased in that case (Fubiani et al. 2017).

A detailed description of the transport of *electrons* across an aperture must be studied in 3D because the magnetic filter field lines (B_F in Fig. 4.5) are typically perpendicular to the cusp profile (B_D) generated by a set of permanent magnets inserted inside the extraction grid (EG).

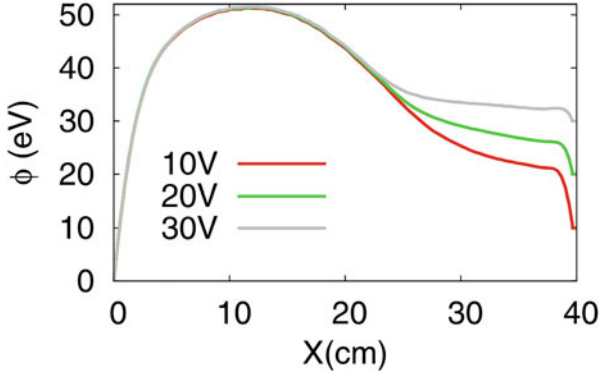


Fig. 4.13 Axial plasma potential profile vs. the PG bias voltage (the remaining ion source walls are grounded). 3D PIC-MCC calculation corresponding to the simulation parameters of Fig. 4.7e, f

4.5.2 Charged Particle Extraction Dynamics Across Apertures

Figure 4.5c shows the simulation domain for either a 2D or 3D PIC-MCC calculation of the negative ion and electron extraction from the plasma across slit (in 2D) or circular (in 3D) apertures. The main role of the cusp magnetic field is to deflect the electrons co-extracted from the ion source such that they are collected on the EG (Fubiani et al. 2008, 2009). The magnetic field penetrates a couple of centimeters inside the extraction region of the plasma source surrounding each aperture. It hence acts as a magnetic barrier for the electrons, which are strongly magnetized. The cusp field amplitude (B_D) on the front side of the PG is about 140 G. The magnetic filter (B_F) and cusp fields are perpendicular to each other's with $B_F = 75$ G. The simulation domain consists of a region around a single aperture with periodic boundary conditions at the top and bottom which is hence equivalent to modeling an infinite number of apertures (Fubiani et al. 2017, 2018; Boeuf et al. 2016; Garrigues et al. 2016; Wunderlich et al. 2018; Hatayama et al. 2018; Taccogna et al. 2010; Taccogna et al. 2011, 2013). The plasma is not generated self-consistently as in the previous sections from the power absorbed in the discharge. Figure 4.16 shows schematically that the charged particle flows in the vicinity of a given aperture. One defines an artificial volume on the left-hand-side of the domain (so-called “plasma bulk” in Fig. 4.14) where pairs of positive ions and electrons (or also negative ions to model the fraction of these ion population produced by the dissociative attachment of the hydrogen isotope molecules in the plasma volume) are injected each time a positive ion is lost on a physical boundary (i.e., of Dirichlet type). This technique mimics plasma generation while preserving the structure of the plasma sheath. In addition, the electron temperature is artificially maintained, with a value given as an external parameter, to fix the plasma properties in that region. In principle, the particle distribution function and the stoichiometric ratio

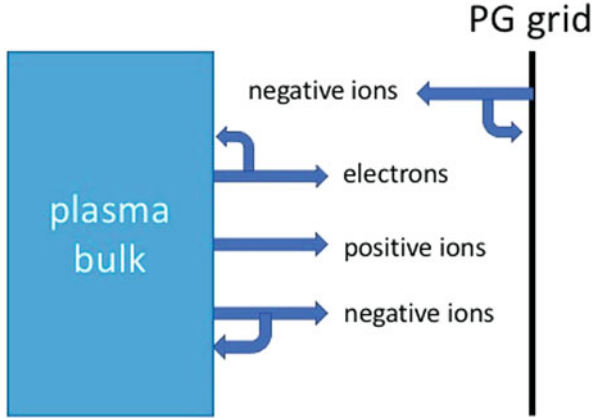


Fig. 4.14 Schematic representation of the charged particle flows in the extraction region of the plasma source. Some negative charges coming from the bulk region will be reflected by the plasma sheath near the PG

between species may be chosen such as to reproduce incoming fluxes of charged particles inside the extraction region as observed in the experiments or the models of the whole ion source volume (see the preceding sections). The advantage of this approach is its capability to provide a detailed description of the negative ion dynamics from the PG across the aperture without the use of a scaling factor $\alpha = \varepsilon/\varepsilon_0$ which will affect the aperture-to-plasma sheath size ratio in front of the caesiated surface where the ions are generated and accelerated.

Figure 4.15 shows the 2D normalized negative ion current density profiles j_{H-}/j_{\max} for a bevel (top) and chamfered (bottom) slit aperture geometries, respectively, with $j_{\max} = 200 \text{ A/m}^2$. The negative ion current streamlines are also shown (in green) together with the plasma meniscus (in white). The size of the simulation domain for the simulation is $32 \times 16 \text{ mm}^2$ in 2D (Fig. 4.15 shows a portion of the domain) and a numerical mesh of 4096×2048 nodes is necessary to properly resolve the plasma, beam, and virtual cathode properties for an average plasma density of $3 \times 10^{17} \text{ m}^{-3}$. The electron temperature is 2 eV, the negative ion current on the PG surface is $j_G = 600 \text{ A/m}^2$ (a half-Maxwellian with a 1 eV temperature), and the potential on the EG, 1.5 kV, respectively. The cusp magnetic field surrounding the aperture is in the xy plane, while B_F is pointing in the direction of the (Oz) axis. There are no negative ions produced inside the plasma volume in this calculation. As stated above (see Fig. 4.11), the negative ion current density profile is asymmetric due to the slight magnetization of the ions. In Fig. 4.15, the X-point visible on the current streamlines is shifted off-axis (Geng et al. 2017), with the negative ions originating preferably from one side of the aperture (Gutser et al. 2010). This renders the ion beamlet current density profile asymmetric, with some noticeable effects on the beam transport properties inside the accelerator vessel, as observed in the experiments (Denizeau et al. 2020). The ratio of the extracted

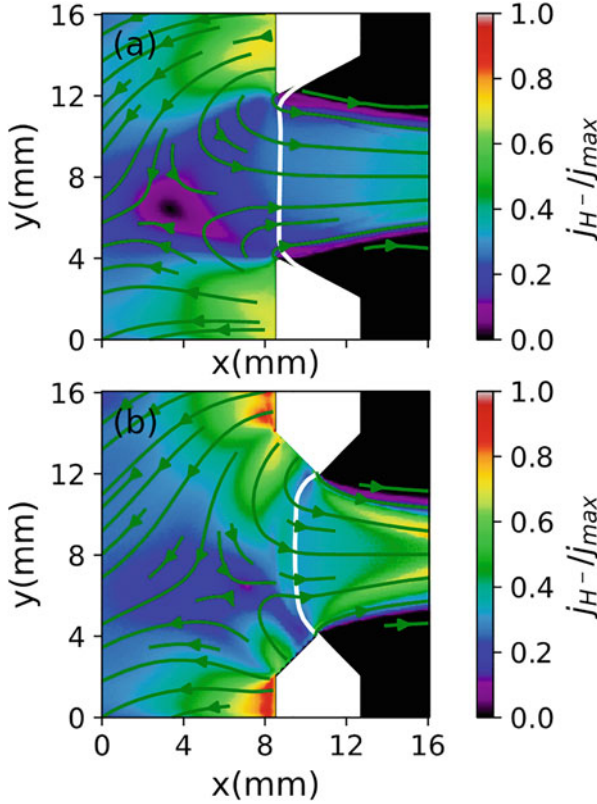


Fig. 4.15 2D normalized negative ion current density profiles in front of a slit aperture for a bevel (top) and chamfered (bottom) geometry. 2D PIC-MCC calculation. $j_{\max} = 200 \text{ A/m}^2$, the negative ion current on the PG surface is $j_G = 600 \text{ A/m}^2$ and the EG potential, 1.5 kV. The current streamlines are shown in green and the plasma meniscus in white (corresponding to an isopotential). There isn't any scaling in this calculation ($\alpha = 1$)

ion current originating from the chamfered surface compared to the front side, Fig. 4.15a, is ~ 1.7 while the surface area ratio is $\sqrt{2}$, indicating that the proximity of the accelerator vessel raises the extraction probability on the chamfered side (58% probability vs. 33%). Furthermore, the plasma density extends up to the tip of the chamfered surface. The positive ion density reduces the depth of the potential well and, as a result, increases the negative ion saturation current j_{sat} (Eq. (4.10)). The negative ions are hence moving from the plasma across the meniscus for working conditions such that the beamlets are in a so-called perveance match (laminar). The minimum virtual cathode depth is about -1.3 V near the front side and -2.1 V close to the tip (the higher extraction probability is hence impeded by the larger potential drop). As a general result, the model shows that the extracted negative ion beamlet current is *somewhat* proportional to the surface area of the aperture facing the plasma with $(I_c/I_b)(S_b/S_c) \approx 1.2$ where I (S) is the extracted ion current

(grid surface area) and “c” (“b”) stands for “chamfered” (“bevel”), respectively. Similar conclusions were drawn from the experiments (Kashiwagi et al. 2014). One of the main differences between the bevel and chamfered grid configurations is that some aberrations on the beamlet profile are observed for the latter. The extraction probability for a negative ion produced on the PG surface is $\sim 35\%$ for the bevel configuration and $\sim 45\%$ globally for the chamfered one, which is similar to estimates derived from test particle models (Gutser et al. 2010). Lastly, note that the negative ion beam and meniscus profiles derived from Fig. 4.15 may be implemented in a ray-tracing model to simulate the beam transport inside the accelerator (Veltri et al. 2017; Hurlbatt et al. 2019).

The co-extracted electron current remains substantial in the experiments (with a ratio of about one electron per extracted negative ion) besides the use of a bias voltage on the PG to lower the sheath potential and hence collect electrons at the location where the cusp magnetic field profile of the extraction magnets (B_D) is short-circuited by the grid surface. The cusp field should, in principle, act as a barrier. 3D PIC-MCC calculations of the electron dynamics in the vicinity of an aperture have demonstrated that the curved plasma potential iso-contours at the location of the meniscus induce an $\mathbf{E} \times \mathbf{B}_D$ drift for the magnetized electrons which is directed toward the EG on one side of the aperture (depending on the direction of B_D) (Fubiani et al. 2020). Figure 4.16a shows a schematic representation of the electron drift motion (which is tangential to the iso-potential line) driving electrons across the aperture. The electron density profile on the front side of the PG (facing the plasma) is displayed in Fig. 4.16b. The cusp magnetic field is uniform along (Oy), and the mirror point is located in the z -direction between apertures. The electrons escape toward the lateral side of the aperture in this configuration, and the location alternates following the direction of the magnetic field vector. Note that replacing the circular apertures with a hypothetical slit that would be infinite along (Oy) would induce a significant drop in the co-extracted electron current as the drift would be uniquely parallel to the PG surface. Electron transport across the aperture would be driven by collisions in that case.

4.6 Conclusions

The numerical modeling of a fusion-type negative ion source brought some physical insight which, when combined with experimental measurements, did improve significantly the understanding of these devices. Models provided trends similar to the ones observed in the experiments but also some detailed analysis of the ion source plasma properties, which would otherwise be accessible experimentally with difficulty. As a summary, a brief comparison between the model predictions and experimental observations is discussed below:

- The Hall effect has not been precisely measured in the experiments, but its indirect consequences have been clearly observed. The Hall electric field (plasma

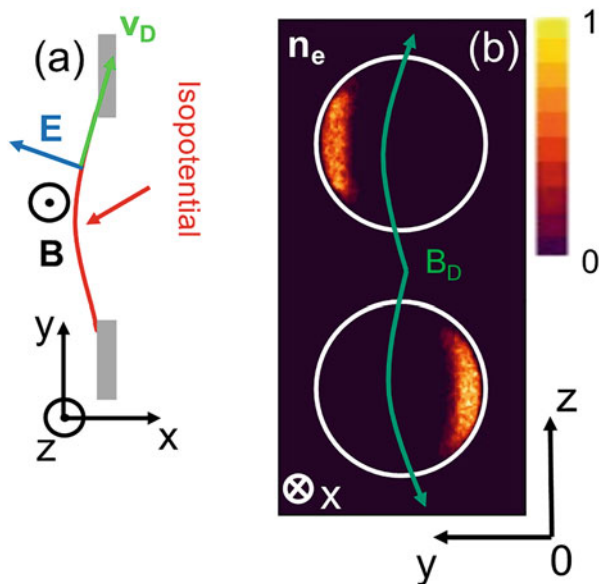


Fig. 4.16 (a) Schematic representation of the $E \times B_D$ drift induced by the plasma meniscus (in red). (b) electron density profile as seen from the front side of the PG (facing the plasma)

polarization) resulting from the electron drift (Hall current) inside the magnetic filter field of the expansion chamber in tandem-type negative ion sources induces an asymmetry in the plasma parameters. Two Langmuir probes positioned transversely near the top and bottom parts of the discharge and moving along the longitudinal axis of the BATMAN prototype source have measured this asymmetry (Schiesko et al. 2012; Fantz et al. 2014; Wimmer et al. 2016) which we reproduced qualitatively in Fig. 4.6.

- The neutral depletion was evaluated with a baratron in the experiments both inside the driver and the expansion chamber (McNeely et al. 2011). Temperatures and densities of the same order of magnitude were calculated in the model for hydrogen at 0.3 Pa (Figs. 4.7 and 4.8). Fluid/DSMC calculations confirmed that the neutral atom temperature is significantly larger than the temperature of H_2 at low pressure with a ratio of densities $n_H/n_{H_2} \sim 30\%$.
- The flattening of the plasma potential in the extraction region when biasing the PG positively with respect to the other surfaces was reported by K. Leung et al. (1987) in an ion source with a magnetic filter and driven by hot cathodes (tungsten filaments). A similar behavior was observed in the model (Fig. 4.13). One direct consequence is that the co-extracted electron current continuously decreases with a larger PG bias, and the extracted negative ion current peaks when the grid is floating (Wimmer et al. 2016; Leung et al. 1987).
- Lastly, the experiment of Kashiwagi et al. (2014) and the PIC-MCC calculations (Fig. 4.15) both concluded that the extracted negative ion current from the ion

source is approximately proportional to the electrode surface surrounding the aperture and facing the plasma when comparing a flat versus a chamfered geometry. The slight magnetization of the negative ions resulting in an asymmetric beamlet current density profile was measured in Geng et al. (2017) on the Kamaboko device.

There are still many open problems related to the physics of magnetized plasma sources. However, one of the main directions to improve the numerical model predictions presented in this chapter (besides technical improvements like parallelization to run efficiently on a large number of computer nodes, for instance) will be to couple PIC-MCC and DSMC algorithms to self-consistently include the transport of neutrals. This will allow us to describe the hydrogen isotope effect observed in the experiments. Another important effort should be devoted to designing plasma sources without asymmetries in the plasma parameters which will require a rethinking of the magnetic filter field configuration (such that the electron Hall current profile follows a closed loop).

Bibliography

- M. Bacal, M. Wada, Negative hydrogen ion production mechanisms. *Appl. Phys. Rev.* **2**, 021305 (2015)
- C.K. Birdsall, A.B. Langdon, *Plasma Physics Via Computer Simulation* (IOP Publishing, Boca Raton, 1991)
- J.P. Boeuf, J. Claustre, B. Chaudhury, G. Fubiani, Physics of a magnetic filter for negative ion sources. II. $E \times B$ drift through the filter in a real geometry. *Phys. Plasmas* **19**, 113510 (2012)
- J.P. Boeuf, G. Fubiani, L. Garrigues, Issues in the understanding of negative ion extraction for fusion. *Plasma Sources Sci. Technol.* **25**, 045010 (2016)
- M. Capitelli, M. Cacciatore, R. Celiberto, O. De Pascale, P. Diomede, F. Esposito, A. Gicquel, C. Gorse, K. Hassouni, A. Laricchiuta, S. Longo, D. Pagano, M. Rutigliano, Vibrational kinetics, electron dynamics and elementary processes in H₂ and D₂ plasmas for negative ion production: Modelling aspects. *Nucl. Fusion* **46**, S260 (2006)
- R. Celiberto, K. Janev, A. Laricchiuta, M. Capitelli, J.M. Wadehra, D.E. Atems, Cross section data for electron-impact inelastic processes of vibrationally excited molecules of hydrogen and its isotopes. *At. Data Nucl. Data Tables* **77**(2), 161 (2001)
- H.P.L. de Esch, M. Kashiwagi, M. Taniguchi, T. Inoue, G. Serianni, P. Agostinetti, G. Chitarin, N. Marconato, E. Sartori, P. Sonato, P. Veltri, N. Pilan, D. Aprile, N. Fomesu, V. Antoni, M.J. Singh, R.S. Hemsworth, M. Cavenago, Physics design of the HNB accelerator for ITER. *Nucl. Fusion* **55**, 096001 (2015)
- S. Denizeau, A. Aprile, G. Fubiani, F. Taccogna, P. Minelli, M. Ichikawa, J. Hiratsuka, M. Kashiwagi, A. Kojima, G. Chitarin, Experimental and numerical investigation on the asymmetry of the current density extracted through a plasma meniscus in negative ion accelerator. *Plasma Sources Sci. Technol.* **29**, 075012 (2020)
- Eirene. database (<http://eirene.de/html/surfacedata.html>)
- U. Fantz, L. Schiesko, D. Wunderlich, Plasma expansion across a transverse magnetic field in a negative hydrogen ion source for fusion. *Plasma Sources Sci. Technol.* **23**, 044002 (2014)
- G. Fubiani, J.P. Boeuf, Role of positive ions on the surface production of negative ions in a fusion plasma reactor type negative ion source—Insights from a three dimensional particle-in-cell Monte Carlo collisions model. *Phys. Plasmas* **20**, 113511 (2013)

- G. Fubiani, J.P. Boeuf, Plasma asymmetry due to the magnetic filter in fusion-type negative ion sources: Comparisons between two and three-dimensional particle-in-cell simulations. *Phys. Plasmas* **21**, 073512 (2014)
- G. Fubiani, J.P. Boeuf, Three-dimensional modeling of a negative ion source with a magnetic filter: Impact of biasing the plasma electrode on the plasma asymmetry. *Plasma Sources Sci. Technol.* **24**, 055001 (2015)
- G. Fubiani, H.P.L. de Esch, S. Simonin, R.S. Hemsworth, Modeling of secondary emission processes in the negative ion based electrostatic accelerator of the international thermonuclear experimental reactor. *Phys. Rev. Spec. Top. Accel Beams* **11**, 014202 (2008)
- G. Fubiani, R.S. Hemsworth, H.P.L. de Esch, L. Svensson, Analysis of the two accelerator concepts foreseen for the neutral beam injector of the international thermonuclear experimental reactor. *Phys. Rev. Spec. Top. Accel Beams* **12**, 050102 (2009)
- G. Fubiani, G.J.M. Hagelaar, J.P. Boeuf, S. Kolev, Modeling a high power fusion plasma reactor-type ion source: Applicability of particle methods. *Phys. Plasmas* **19**, 043506 (2012)
- G. Fubiani, L. Garrigues, G. Hagelaar, N. Kohen, J.P. Boeuf, Modeling of plasma transport and negative ion extraction in a magnetized radio-frequency plasma source. *New J. Phys.* **19**, 015002 (2017)
- G. Fubiani, L. Garrigues, J.P. Boeuf, Modeling of negative ion extraction from a magnetized plasma source: Derivation of scaling laws and description of the origins of aberrations in the ion beam. *Phys. Plasmas* **25**, 023510 (2018)
- G. Fubiani, Y. Jiang, J.P. Boeuf, $E \times B$ electron drift current across the aperture of an ion source surrounded by a cusped magnetic field profile. *Phys. Plasmas* **27**, 093506 (2020)
- F. Gaboriau, J.P. Boeuf, Chemical kinetics of low pressure high density hydrogen plasmas: Application to negative ion sources for ITER. *Plasma Sources Sci. Technol.* **23**, 065032 (2014)
- L. Garrigues, G. Fubiani, J.P. Boeuf, Appropriate use of the particle-in-cell method in low temperature plasmas: Application to the simulation of negative ion extraction. *J. Appl. Phys.* **120**, 213303 (2016)
- S. Geng, K. Tsumori, H. Nakano, M. Kasaki, K. Ikeda, M. Osakabe, K. Nagaoka, Y. Takeiri, M. Shibuya, Response of H^- ions to extraction field in a negative hydrogen ion source. *Fusion Eng. Des.* **123**, 481–484 (2017)
- V.A. Godyak, B.M. Alexandrovich, V.I. Kolobov, Lorentz force effects on the electron energy distribution in inductively coupled plasmas. *Phys. Rev. E* **64**, 026406 (2001)
- R. Gutser, D. Wunderlich, U. Fantz, the NNBI-Team, Transport of negative hydrogen and deuterium ions in RF-driven ion sources. *Plasma Phys. Control. Fusion* **52**, 045017 (2010)
- G.J.M. Hagelaar, N. Oudini, Plasma transport across magnetic field lines in low-temperature plasma sources. *Plasma Phys. Control. Fusion* **53**, 124032 (2011)
- A. Hatayama, S. Nishioka, K. Nishida, S. Mattei, J. Lettry, K. Miyamoto, T. Shibata, M. Onai, S. Abe, S. Fujita, S. Yamada, A. Fukano, Present status of numerical modeling of hydrogen negative ion source plasmas and its comparison with experiments: Japanese activities and their collaboration with experimental groups. *New J. Phys.* **20**, 065001 (2018)
- B. Heinemann, U. Fantz, W. Kraus, L. Schiesko, C. Wimmer, D. Wunderlich, F. Bonomo, M. Frösche, R. Nocentini, R. Riedl, Towards large and powerful radio frequency driven negative ion sources for fusion. *New J. Phys.* **19**, 015001 (2017)
- B. Heinemann, Wunderlich, W. Kraus, F. Bonomo, U. Fantz, M. Frösche, I. Mario, R. Riedl, C. Wimmer, Achievements of the ELISE test facility in view of the ITER NBI. *Fusion Eng. Des.* **146A**, 455 (2019)
- R.S. Hemsworth, D. Boilson, P. Blatchford, M. Dalla Palma, G. Chitarin, H.P.L. de Esch, F. Geli, M. Dremel, J. Graceffa, D. Marcuzzi, G. Serianni, D. Shah, M. Singh, M. Urbani, P. Zaccaria, Overview of the design of the ITER heating neutral beam injectors. *New J. Phys.* **19**, 025005 (2017)
- R.W. Hockney, J.W. Eastwood, *Computer Simulation Using Particles* (McGraw-Hill, Boca Raton, 1981)

- A. Hurlbatt, N. den Harder, D. Wunderlich, U. Fantz, the NNBI Team, The particle tracking code BBCNI for large negative ion beams and their diagnostics. *Plasma Phys. Control. Fusion* **61**, 105012 (2019)
- N.D. Ippolito, F. Taccogna, P. Minelli, M. Cavenago, P. Veltri, Particle model of a cylindrical inductively coupled ion source. *AIP Conf. Proc.* **1869**, 030040 (2017)
- R.K. Janev, W.D. Langer, K. Evans, Jr., and D.E. Post, Jr., *Elementary Processes in Hydrogen-Helium Plasmas, Cross sections and reaction rate coefficients* (Springer, Berlin, 1987)
- M. Kashiwagi, N. Umeda, H. Tobar, A. Kojima, M. Yoshida, M. Taniguchi, M. Dairaku, T. Maejima, H. Yamanaka, K. Watanabe, T. Inoue, M. Hanada, Development of negative ion extractor in the high-power and long-pulse negative ion source for fusion application. *Rev. Sci. Instrum.* **85**, 02B320 (2014)
- S. Krischok, H. Müller, V. Kempter, Surface induced dissociation in slow collisions of H_2^+ and O_2^+ : Information from the ion impact electron spectra. *Nucl. Instrum. Methods Phys. Res. B* **157**, 198 (1999)
- W.B. Kunkel, Hall effect in a plasma. *Am. J. Phys.* **49**, 733 (1981)
- G. Lapenta, Particle simulations of space weather. *J. Comp. Phys.* **231**, 795–821 (2012)
- K.N. Leung, M. Bacal, H^- ion density measurement in a tandem multicusp discharge. *Rev. Sci. Instrum.* **55**(3), 338–341 (1984)
- M.A. Lieberman, A.J. Lichtenberg, *Principles of Plasma Discharges and Materials Processing* (Wiley Interscience, Hoboken, NJ, 2005)
- S. Lishev, L. Schiesko, D. Wunderlich, C. Wimmer, U. Fantz, Fluid-model analysis on discharge structuring in the RF-driven prototype ion- source for ITER NBI. *Plasma Sources Sci. Technol.* **27**, 125008 (2018)
- R. McAdams et al., Transport of negative ions across a double sheath with a virtual cathode. *Plasma Sources Sci. Technol.* **20**, 035023 (2011)
- P. McNeely, S.V. Dudin, S. Christ-Koch, U. Fantz, the NNBI Team, A Langmuir probe system for high power RF-driven negative ion sources on high potential. *Plasma Sources Sci. Technol.* **18**, 014011 (2009)
- P. McNeely, D. Wunderlich, the NNBI Team, Neutral depletion in an H^- source operated at high rf power and low input gas flow. *Plasma Sources Sci. Technol.* **20**(4), 045005 (2011)
- K. Nanbu, Probability theory of electron–molecule, ion–molecule, molecule–molecule, and coulomb collisions for particle modeling of materials processing plasmas and gases. *IEEE Trans. Plasma Sci.* **28**, 971 (2000)
- D. Nicholson, *Introduction to Plasma Theory* (Wiley, New York, 1983)
- L. Schiesko, P. McNeely, P. Franzen, U. Fantz, the NNBI Team, Magnetic field dependence of the plasma properties in a negative hydrogen ion source for fusion. *Plasma Phys. Control. Fusion* **54**, 105002 (2012)
- M. Seidl, H.L. Cui, J.D. Isenberg, H.J. Kwon, B.S. Lee, S.T. Melnychuk, Negative surface ionization of hydrogen atoms and molecules. *J. Appl. Phys.* **79**(6), 2896 (1995)
- F. Taccogna, Monte Carlo collision method for low temperature plasma simulation. *J. Plasma Phys.* **81**(1), 305810102 (2015)
- F. Taccogna, P. Minelli, PIC modeling of negative ion sources for fusion. *New J. Phys.* **19**, 015012 (2017)
- F. Taccogna, R. Schneider, S. Longo, M. Capitelli, Modeling of a negative ion source. I. Gas kinetics and dynamics in the expansion region. *Phys. Plasmas* **14**, 073503 (2007)
- F. Taccogna, R. Schneider, S. Longo, M. Capitelli, Modeling of a negative ion source. II. Plasma-gas coupling in the extraction region. *Phys. Plasmas* **15**, 103502 (2008)
- F. Taccogna, P. Minelli, S. Longo, M. Capitelli, R. Schneider, Modeling of a negative ion source. III. Two-dimensional structure of the extraction region. *Phys. Plasmas* **17**, 063502 (2010)
- F. Taccogna, P. Minelli, P. Diomede, S. Longo, M. Capitelli, R. Schneider, Particle modelling of the hybrid negative ion source. *Plasma Sources Sci. Technol.* **20**, 024009 (2011)
- F. Taccogna, P. Minelli, S. Longo, Three-dimensional structure of the extraction region of a hybrid negative ion source. *Plasma Sources Sci. Technol.* **22**, 045019 (2013)

- Y. Takeiri, Negative ion source development for fusion application. *Rev. Sci. Instrum.* **81**, 02B114 (2010)
- V. Toigo et al., The ITER neutral beam test facility towards SPIDER operation. *Nucl. Fusion* **57**, 086027 (2017)
- D. Tskhakaya, K. Matyash, R. Schneider, F. Taccogna, The particle-in-cell method. *Contrib. Plasma Physics* **47**(8–9), 563 (2007)
- Y.O. Tyshetskiy, A.I. Smolyakov, V.A. Godyak, On nonlocal heating in inductively coupled plasmas. *Plasma Sources Sci. Technol.* **11**, 203–207 (2002)
- P. Veltri, E. Sartori, P. Agostinetti, D. Aprile, M. Brombin, G. Chitarin, N. Fonnesu, K. Ikeda, M. Kisaki, H. Nakano, A. Pimazzoni, K. Tsumori, G. Serianni, Ion beam transport: Modelling and experimental measurements on a large negative ion source in view of the ITER heating neutral beam. *Nucl. Fusion* **57**, 016025 (2017)
- C. Wimmer, U. Fantz, the NNBI-Team, Extraction of negative charges from an ion source: Transition from an electron repelling to an electron attracting plasma close to the extraction surface. *J. Appl. Phys.* **120**, 073301 (2016)
- D. Wunderlich, R. Gutser, U. Fantz, PIC code for the plasma sheath in large caesiated RF sources for negative hydrogen ions. *Plasma Sources Sci. Technol.* **18**, 045031 (2009)
- D. Wunderlich, S. Mochalskyy, U. Fantz, P. Frenzen, the NNBI-Team, Modelling the ion source for ITER NBI: From the generation of negative hydrogen ions to their extraction. *Plasma Sources Sci. Technol.* **23**, 015008 (2014)
- D. Wunderlich, S. Mochalskyy, I.M. Montellano, A. Revel, Review of particle-in-cell modeling for the extraction region of large negative hydrogen ion sources for fusion. *Rev. Sci. Instrum.* **89**, 052001 (2018)

Chapter 5

Electrostatic and Electromagnetic Particle-In-Cell Modelling with Monte-Carlo Collision for Negative Ion Source Plasmas



Kenji Miyamoto and Takanori Shibata

Abstract Particle-In-Cell with Monte-Carlo collisions (PIC-MCC) simulation is a powerful tool for analysis of the underlying physics in a negative ion source and a useful guideline to a new source design and the alternative operating conditions. In this chapter, the fundamentals of the PIC-MCC modelling and the important simulation results are reviewed. The negative ion sources for fusion devices and accelerators are modelled, and the physical issues such as the RF plasma discharge, negative ion extraction mechanism, and negative ion beam optics are summarized.

Keywords Numerical modelling · Particle-In-Cell with Monte-Carlo Collisions · Beam extraction · RF-ICP ion sources · Beam optics · Plasma meniscus

5.1 Fundamentals of Negative Ion Source Plasma Modelling by Particle-In-Cell

5.1.1 Numerical Modelling for Negative Ion Source Development

In the field of fusion applications or particle accelerators, the following improvements have been always required for the negative hydrogen ion sources;

- Increase in the negative hydrogen ion (H^-) beam current.
- Reduction of the beam emittance.
- Extension of the ion source lifetime.

K. Miyamoto (✉)
Naruto University of Education, Naruto, Japan
e-mail: kmiyamot@naruto-u.ac.jp

T. Shibata
Accelerator Laboratory, KEK, Tsukuba, Japan

Recently, numerical modellings and simulations are playing more important roles to design ion sources and to improve their performances. These approaches make it possible to understand detailed physics of the ion source plasmas, for example, (1) physical processes to lead the plasma non-uniformity due to the magnetic drifts (Shibata et al. 2013), (2) the cause of the beam-halo from the surface negative ion sources (Miyamoto et al. 2012), or (3) plasma ignition mechanism in radio frequency (RF) inductively-coupled plasma (ICP) type ion sources (Shibata et al. 2017). Based on this physics understanding, it is possible to predict the performances of new ion sources.

Also, a large number of the sample particles or the numerical cells have been available in the simulation due to the development of the calculation resources. Especially, Particle-In-Cell (PIC) modelling (Birdsall and Langdon 1985) has become a powerful method to calculate plasma behavior in the given ion source design by solving charged particle transport and electromagnetic field simultaneously. These PIC modellings are effective to obtain plasma behavior which is difficult to be measured. In this chapter, two main physics are focused on the calculation. The first calculation is the H^- beam extraction physics from the negative ion source. The H^- beam is extracted from the plasma by voltage application at the beam extraction aperture up to a few 10 kV. The divergence angle of the beam is mainly decided by the equipotential surface formed by the applied voltage and by space charge distributions due to charged particles (electrons, positive ions and H^-) especially in the region close to the extraction aperture. The second calculation is the plasma generation process in the RF driven H^- ion sources which are becoming widely applied to the fusion plasma heating and to the high-intensity proton accelerators. The RF-driven ion sources are mainly classified into three types from the viewpoint of the RF power-coupling/absorption with the plasma (Chabert and Braithwaite 2011; Lieberman and Lichtenberg 1994) RF capacitive coupling plasma (RF-CCP), RF inductive coupling plasma (RF-ICP) and resonant-type wave coupling (ex. ECR: Electron Cyclotron Resonance). In this chapter, we briefly summarize the main physics processes of the negative ion source in the first section (Sect. 5.1.1.1). Also, a summary of the fundamentals of electrostatic and electromagnetic PIC methods is given in Sects. 5.1.2 and 5.1.3. If readers are familiar with these methods, it is recommended to skip the remaining part of this section and proceed directly to subsequent Sects. 5.2, 5.3, and 5.4. In these sections, various examples of the PIC applications and the present understandings of main phenomena in negative ion source plasmas are explained. In Sects. 5.2 and 5.3, the physics of beam extraction, plasma-meniscus formation and its effects on beam emittance will be mainly discussed. In Sect. 5.4, the plasma generation process is modeled for the radio-frequency type ion sources for accelerators.

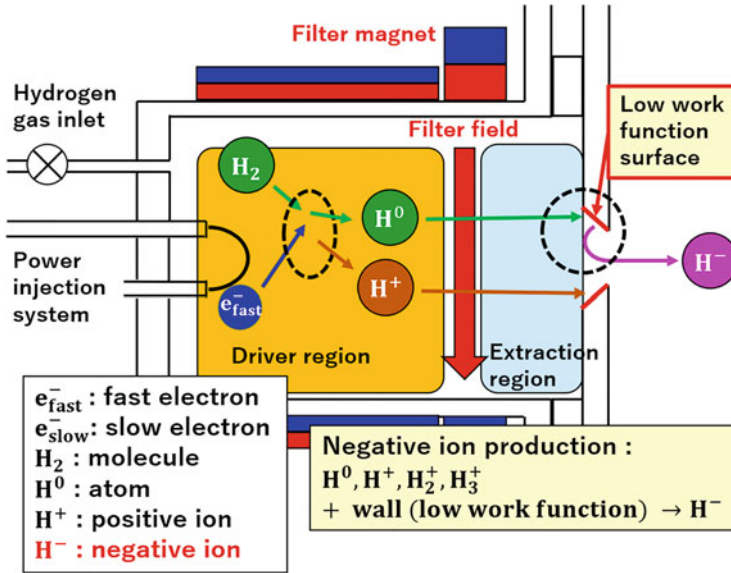


Fig. 5.1 Drawing of the surface production process

5.1.1.1 Main Physical Processes in Negative Ion Sources

The main physical processes to be included in the numerical modelling are listed-up as follows: (1) plasma particle, momentum and energy transport processes (especially transport in the magnetic field), (2) space charge layer between the quasi-neutral bulk plasma and the wall (plasma sheath layer), (3) atomic and molecular processes (ionization, dissociation, negative ion production, . . . etc.) and (4) power absorption and heating process of plasma (Fantz et al. 2020; Tsumori et al. 2010; Stockli et al. 2020; Oguri et al. 2021). Figure 5.1 shows a schematic drawing of the physical processes in an arc-discharge hydrogen negative ion source as an example. High-energy electrons are created and accelerated by the arc-voltage applied between the hot cathode (filament) and the chamber wall. Neutral H_2 molecules fed through the gas inlet into the chamber are dissociated and/or ionized via collisions with these high-energy electrons. Hydrogen (H) atoms and ions (H^+ , H_2^+ and H_3^+) are produced in the plasma chamber. High energy electrons (over 20 eV) also produce vibrational excited molecules $H_2(v)$ through the so-called EV-process, which in turn plays a key role for the H^- volume production by the dissociative attachment [$H_2(v) + e \rightarrow H + H^-$] with slow electrons (0.5–1 eV) (Bacal et al. 2005; Bacal and Wada 2015). In order to reduce the electron energy and enhance the H^- volume production, a strong transverse magnetic field across the source chamber (so-called magnetic filter: MF) (Holmes 1982) is produced by filter magnet as shown in Fig. 5.1. Due to the MF, a low temperature around 1 eV and low density plasma is generated in the vicinity of the extraction aperture. This

region is called the extraction region. In addition to the volume H^- production, surface production process of H^- ions is significant in H^- ion sources for fusion and accelerator applications. Usually, a large amount of H^- ions is produced by the incident of hydrogen particles (H , H^+ , H_2^+ and H_3^+) on the low work-function solid surface (for example, Cs-coated tungsten surface) as shown in Fig. 5.1. To understand transport process both of the volume and the surface produced H^- ions toward the extraction aperture is important to extract a large amount of H^- current with good beam optics.

Another issue for the understanding of H^- ion extraction is the “sheath” structure near the wall as listed above. Especially, the sheath structure in front of the plasma grid (PG) [or plasma electrode (PE)] and extraction aperture is one of the dominant processes for beam extraction. In a usual electropositive plasma which consists of only positive ions and electrons, it is well known (Lieberman and Lichtenberg 1994) that a thin non-neutral layer (ion-sheath layer) is produced in front of the wall, because electrons are far mobile and lost to the wall faster than positive ions and the plasma potential becomes positive with respect to the grounded wall. This positive plasma potential prevents further loss of electrons and accelerates the ions towards the wall. Finally, the positive ion and the electron fluxes to the wall are balanced, which leads the system to a quasi-steady state.

The sheath structure in electronegative plasmas with negative ions, however, is more complex and one of the most interesting and key physics issues (Lieberman and Lichtenberg 1994). In addition to the electronegativity, the external positive voltage (typically several 10 kV) is applied to the extraction grid (EG) [or extraction electrode (EE)] in H^- ion sources with respect to the PG to extract H^- ions. This applied voltage penetrates into the plasma through the extraction aperture and makes the potential structure near the aperture more complex. As will be discussed in Sect. 5.3, the understanding and controlling of the potential structure close to the extraction aperture play a key role to obtain good beam convergence. Electronegativity and resulting sheath characteristics also play an important role in the coupling of the RF power with plasma (Lieberman and Lichtenberg 1994; Lieberman et al. 1999). In Sect. 5.4, the major transport process of the electronegative plasma in the capacitively-coupled (CC) and the inductively-coupled (IC) electromagnetic fields is modelled. The numerical results are compared with the experimental results for the source design upgrade of the RF ion sources for accelerator application.

5.1.2 Basic Equations of the PIC Modelling

The potential field of each charged particle decays rapidly with the Debye length. The typical electron temperature and density in the negative ion sources are $T_e = 4 - 5$ eV and $n_e = 10^{17} - 10^{18} \text{ m}^{-3}$ for the arc-driven type and T_e up to a few 10 eV and $n_e = 10^{18} - 10^{19} \text{ m}^{-3}$ for the RF-driven type, respectively. In these negative ion sources, the Debye length is around 10^{-5} m, which is generally much smaller than the source size. Under such conditions, potential distribution or electromagnetic

field is decided from the macroscopic charge density distribution or the plasma current distribution. The PIC modelling is applicable to solve these macroscopic plasma behaviors. On the other hand, Coulomb potential rises rapidly when the charged particles approach a distance smaller than the Debye length. In this case, strong Coulomb scattering takes place in a short moment, which can be treated as a collision-like process. This rapid interaction is so-called Coulomb collision. The Coulomb collision is dominant for the diffusion of the charged particles across the magnetic field in the ion sources operated in low gas pressures. The other dominant effect is inelastic collisions between charged and neutral particles. The inelastic processes are important not only to obtain negative ion production rate, but also to obtain production and loss rate of the charged particles via ionization or recombination processes. In the modellings of negative ion sources in this chapter, the Coulomb collision and the inelastic collision processes are solved by Monte-Carlo methods together with the PIC methods. These modellings are so-called PIC-MCC modelling.

5.1.2.1 Electrostatic PIC

The PIC modelling is divided into two main types, whether the model takes into account the displacement current terms in the Maxwell equations or not. The PIC model which ignores the displacement current is so-called “electrostatic PIC model” (Birdsall and Langdon 1985). The beam extraction mechanisms of volume- or surface-produced negative ions and co-extracted electrons are investigated for the negative ion source development. Generally, a direct current extraction voltage is applied between the extraction electrodes. In these cases, electrostatic approximation ($\mathbf{E} = -\nabla\phi$) is applied to the Maxwell equation. The electrostatic potential ϕ in the plasma can be solved by Poisson’s equation (see Eq. 5.1);

$$\nabla^2\phi = -\rho/\varepsilon_0, \quad (5.1)$$

where ρ and ε_0 are charge density and permittivity, respectively. Most of the Poisson solvers for the plasma calculation adopt the iterative method, such as Jacobi, Gauss-Seidel, Successive-Over-Relaxation (SOR), or advanced Conjugate-Gradient (CG) methods for the memory saving and the reduction of the calculation time. In the PIC simulation, a spatial distribution of the charge density ρ is obtained from the particle transport calculation for the charged particles. For the transport calculation, the equations of motion;

$$m_s (d\mathbf{v}_s)/dt = q_s (\mathbf{E} + \mathbf{v}_s \times \mathbf{B}) + \mathbf{F}_{\text{coll}}, \quad (5.2)$$

$$(d\mathbf{r}_s)/dt = \mathbf{v}_s \quad (5.3)$$

are solved for positive and negative ions or electrons. Mass, charge, velocity, and position of these charged particles are denoted as m_s , q_s , \mathbf{v}_s , and \mathbf{r}_s , respectively. The

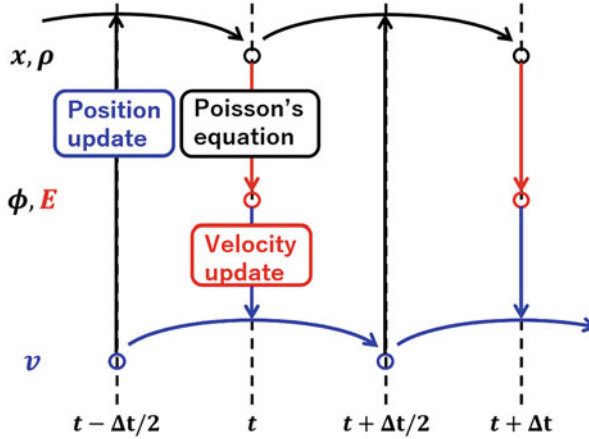


Fig. 5.2 Update flow of position, velocity and electrical potential in the electrostatic PIC model

subscript “s” represents particle species. The electric field \mathbf{E} is obtained by using the scalar potential ϕ in Eq. (5.1). The collision term \mathbf{F}_{coll} are contributions from the Coulomb collision among charged particles or the elastic and inelastic collision processes. The treatments of these effects with Monte-Carlo method are explained in Sect. 5.1.3. For the position and the velocity update of each charged particle in Eqs. (5.2) and (5.3), Boris-Bunemann version of Leap-Frog method (Birdsall and Langdon 1985) is one of the most powerful solvers. Figure 5.2 shows the schematic drawing of the updating of particle parameters in the Leap-Frog method. The velocity update timing is shifted by $\Delta t/2$ from position update, where Δt is the time-step width in the program. From the position update information, charge density ρ , potential ϕ and electric field \mathbf{E} are updated simultaneously by the Poisson solver. Resultantly, velocity change from $t - \Delta t/2$ to $t + \Delta t/2$ is calculated by substituting the electric field at the centre time t . On the other hand, position update from t to $t + \Delta t$ is performed by using centre velocity at $t + \Delta t/2$.

5.1.2.2 Electromagnetic PIC

The plasma generation in radio-frequency (RF) driven negative ion sources is attracting strong interest in fusion and accelerator device upgrades. For understandings of the RF-ICP plasmas, electromagnetic (EM)-PIC modelling is applied. In the electromagnetic EM-PIC model, electrostatic (scalar) potential is not used. Instead, the following Maxwell equations are directly solved to obtain the electromagnetic field;

$$\nabla \times \mathbf{B} = \mu_0 \varepsilon_0 \left(\mathbf{j}_{\text{pl}} + \mathbf{j}_{\text{coil}} + \frac{\partial \mathbf{E}}{\partial t} \right), \quad (5.4)$$

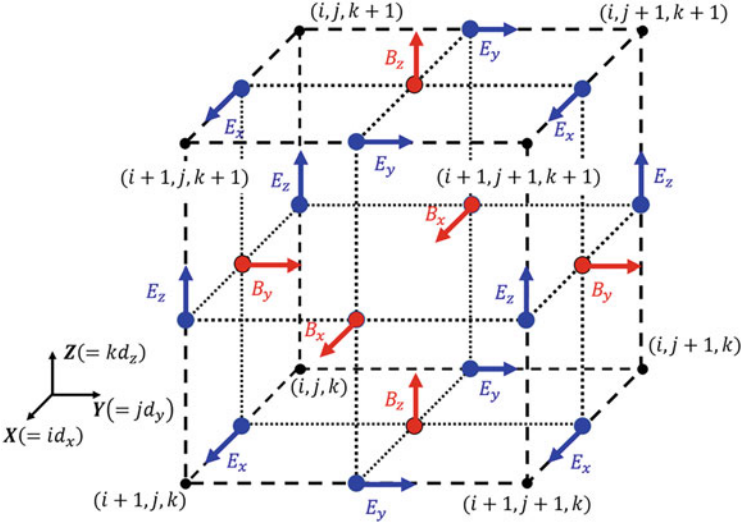


Fig. 5.3 Concept of Yee lattice in the EM-PIC model

$$\nabla \times \mathbf{E} = -\frac{\partial \mathbf{B}}{\partial t}, \quad (5.5)$$

where \mathbf{j}_{pl} and \mathbf{j}_{coil} correspond to the plasma current and the external current induced to the RF antenna coils, respectively. The constant μ_0 is permeability in vacuum. In Sect. 5.4, Maxwell equations are solved by Finite-Differential Time-Domain (FDTD) method. One of the most popular techniques is the Yee algorithm (Yee 1966). As shown in Fig. 5.3, spatial mesh points of the discretized electromagnetic field are shifted by half of the PIC cell size as

$$E_x^t \left(i + \frac{1}{2}, j, k \right), E_y^t \left(i, j + \frac{1}{2}, k \right), E_z^t \left(i, j, k + \frac{1}{2} \right) \quad (5.6)$$

and

$$B_x^{t+\Delta/2} \left(i, j + \frac{1}{2}, k + \frac{1}{2} \right), B_y^{t+\Delta/2} \left(i + \frac{1}{2}, j, k + \frac{1}{2} \right), B_z^{t+\Delta/2} \left(i + \frac{1}{2}, j + \frac{1}{2}, k \right), \quad (5.7)$$

where (i, j, k) are labels corresponding to X, Y, Z positions $X = id_x, Y = jd_y,$ and $Z = kd_z$ with cell sizes $d_x, d_y, d_z,$ respectively. The cell sizes should satisfy the Courant-Friedrich-Levy (CFL) condition (Lewy et al. 1928);

$$\Delta t \leq c \times \left\{ \frac{1}{d_x^2} + \frac{1}{d_y^2} + \frac{1}{d_z^2} \right\}^{-\frac{1}{2}}. \quad (5.8)$$

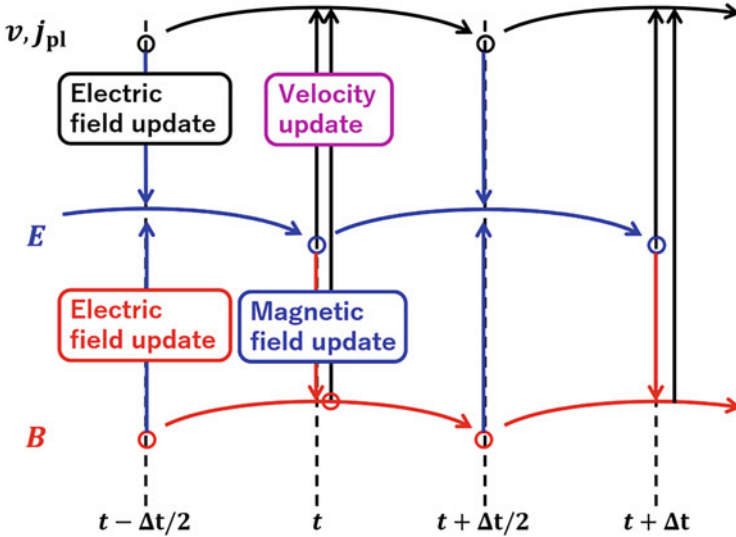


Fig. 5.4 Update flow of plasma current, electric field and magnetic field in the EM-PIC model

Contribution from the plasma current density $j_{pl} = \sum_s q_s n_s v_s$ from each particle species in Maxwell's equation is calculated from the particle transport process in the same manner as the electrostatic PIC modelling (Sect. 5.1.2.1). The update flow of the electromagnetic field and the plasma current update timings are shown in Fig. 5.4. The update time of the j_{pl} , E and B is shifted by half-time-step $\Delta t/2$. Only in the update procedure of the velocity, the average magnetic field from $t - \Delta t/2$ to $t + \Delta t/2$ is calculated as the centre value.

5.1.3 Collision Processes

As for the modelling of collision processes, (a) binary collision model (BCM) and (b) null collision model (NCM) are very useful numerical techniques for the Coulomb collision process and for the inelastic collision (ionization, dissociation, ... etc.) process, respectively. Both the BCM and the NCM are based on the Monte-Carlo method. Detailed principles and numerical procedures are given for the BCM and in Ref. (Vahedi and Surendra 1995) for the NCM.

Also, it should be noted that it is generally impossible for the PIC modelling to simulate negative ion sources with the same size and/or dimensions as the real system. In PIC simulations, the numerical grid size Δx , Δy , Δz should satisfy the following constraint, Δx , Δy , $\Delta z \leq \lambda_D$ (λ_D : Debye length) to avoid the artificial numerical heating/cooling of the superparticles (Birdsall and Langdon 1985). For

typical plasma density and temperature of negative ion source plasmas, usually, the system size L (or characteristic scale-length of the bulk quasi-neutral plasma region) is much larger than λ_D ($L \gg \lambda_D$). Therefore, an unrealistically huge number of spatial grids and also particles is needed to simulate whole the target system.

5.2 Negative Ion Extraction Mechanism from the Surface Production Ion Source

In general, a Cs vapor is introduced to a negative ion source in order to enhance a negative ion current density via the surface production process (Leung et al. 1989; Okumura et al. 1990). Simultaneously, preferable effects for the negative ion operation such as the decrease of the co-extracted electrons are obtained. The negative ion sources for the fusion and accelerator applications are required to produce the negative ion beam with *good beam optics* as well as with *high current density*. For example, the beam divergence angle of 3 - 7 mrad is required in the design of ITER-NBI (Hemsworth et al. 2017; Singh et al. 2017). In order to satisfy this requirement, it is indispensable to clarify the transport mechanism of the surface-produced H^- ions close to the extraction aperture. As will be shown in Sect. 5.3.3, the negative ion beam optics depends on the transport process of the H^- ions.

5.2.1 Surface Produced H^- Extraction Under the Low Source Filling Gas Pressure

The experiments in the arc discharge source for the fusion application have shown that the H^- ions emitted from the PG surface are extracted from the bulk plasma which is deeply inside (1 - 2 cm from the PG surface) rather than directly from the tip of the PG without passing through the bulk plasma (Ikeda et al. 2013; Tsumori and Wada 2017). It is very interesting and important to make clear the extraction mechanism and/or process of surface-produced H^- ions. The three-dimensional (3D) Monte-Carlo transport simulation for the surface produced H^- ions have first discussed the extraction mechanism from the bulk plasma (Matsushita et al. 2008; Kameyama et al. 2011). Since the surface-produced H^- ions move toward the bulk plasma, it is necessary to change the direction of H^- ion velocity toward the extraction aperture. This velocity reversal is observed in the experiment (Geng et al. 2017). It has also been suggested by Kameyama et al. that the velocity reversal is due to the collisional momentum exchange (Kameyama et al. 2011). Under the relatively low-pressure conditions in the negative ion source for fusion application, for example, 0.3 Pa at ITER-NBI (Hemsworth et al. 2009), it is pointed out that the dominant collision process for the H^- ions might be the Coulomb collision with the H^+ ions (Bacal et al. 1991). Thus, the effect of the Coulomb

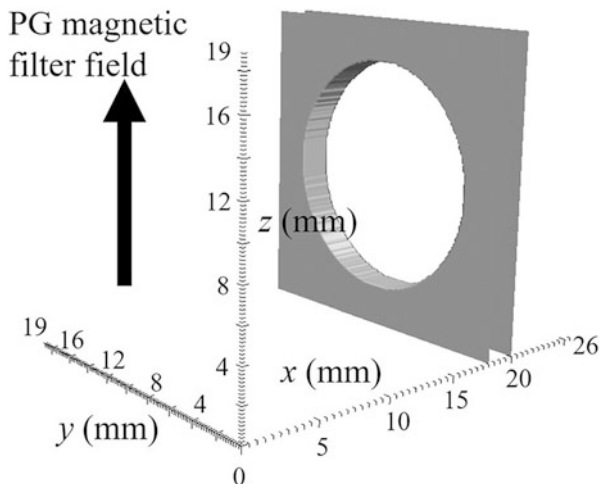


Fig. 5.5 3D geometry of the simulation domain. (Reproduced from (Nishioka et al. 2018) with permission of the American Institute of Physics)

collision seems to be very important for the velocity reversal. However, the results have shown that the total extracted H^- ion current by the simulation is much smaller than that for experiments (Hanada et al. 2006) mainly because the self-consistent electric field has been neglected. Therefore, the extraction mechanism of the surface-produced H^- ions is investigated with the 3D PIC-MCC simulation in which the self-consistent electric field can be obtained (Nishioka et al. 2018).

The extraction region of the negative ion source for JT-60U is modelled. The model geometry is shown in Fig. 5.5. The PG with a single aperture is included in the simulation domain. The x -axis is taken to be the direction of H^- extraction, whereas the z -axis is parallel to the direction of the magnetic filter. The electron suppression magnetic field is perpendicular to the magnetic filter.

In order to reduce the computational cost, the reduced size scaling is employed. A characteristic length of the simulation domain L_{sim} can be given as $L_{\text{sim}} = sL_{\text{real}}$, where s and L_{real} are the scaling factor ($s = 3.7 \times 10^{-2}$) and a characteristic length in a real system. The detailed description will be found in Sect. 5.3.2. The main physical parameters are summarized in Table 5.1. A binary collision model (BCM) by the Monte-Carlo method is applied to the Coulomb collision.

Figure 5.6 shows the trajectories of the surface-produced H^- ions (a) with and (b) without the Coulomb collision. In the case of the Coulomb collision, The H^- ions are extracted not only directly from the PG surface but also via the bulk plasma, which agrees well with the experimental results (Ikeda et al. 2013; Tsumori and Wada 2017). On the other hand, almost all the H^- ions are extracted directly from the PG surface for the case without the Coulomb collision. It is shown that a part of the surface produced H^- ions is extracted from the bulk plasma due to the Coulomb collision under such a low neutral pressure condition in fusion application.

Table 5.1 Main physical parameters for the 3D PIC-MCC simulation

Physical quantity	Value
Electron density	$1.0 \times 10^{18} \text{ m}^{-3}$
H^+ density	$1.11 \times 10^{18} \text{ m}^{-3}$
Volume-produced H^- density	$0.1 \times 10^{18} \text{ m}^{-3}$
H_2 molecular density	$1.9 \times 10^{18} \text{ m}^{-3}$
Electron temperature	1.0 eV
H^+ temperature	0.25 eV
Volume-produced H^- temperature	0.25 eV
H_2 molecular temperature	0.1 eV
Surface-produced H^- temperature	1.0 eV
H- emission rate from the Cs covered PG	100 mA/cm ²

Reproduced from (Nishioka et al. 2018) with permission of the American Institute of Physics

Figure 5.7 shows the ion velocity distribution function of the x -component (v_x) in the bulk plasma ($5 \text{ mm} < x < 10 \text{ mm}$) for the (a) surface-produced H^- ions and (b) H^+ ions, respectively. In Fig. 5.7a, the case without the Coulomb collision shows that most of the H^- ions have the velocities toward the inside of the ion source: $v_x < 0$. Moreover, there is the peak around $v_x = -2 \times 10^4 \text{ m/s}$, which corresponds to the kinetic energy of 1.9 eV in the x -component. This kinetic energy is almost the same as the potential difference between the bulk plasma and the virtual cathode, that is, around 1.7 eV. The surface produced H^- ions which have enough initial kinetic energy to overcome the virtual cathode (Hatayama 2008) can only reach the bulk plasma through acceleration by the sheath. This is the reason for the peak around $v_x = -2 \times 10^4 \text{ m/s}$. For the case with the Coulomb collision in Fig. 5.7a, the surface produced H^- ions with the velocities toward the extraction aperture ($v_x > 0$) increase. In other words, a part of the H^- ions reverse the direction of their velocities toward the extraction aperture due to the Coulomb collision. On the other hand, the particle flux of the H^+ ions toward the extraction aperture decreases in the case of the Coulomb collision. This also shows that the velocity reversal of the surface-produced H^- ions is due to the momentum exchange with the H^+ ions.

5.2.2 Surface-Produced H^- Extraction Under the High Source Filling Gas Pressure

The dominant collision process related to the H^- ion extraction for the negative ion source with a high source filling gas pressure is different from that for low gas pressure. A typical source filling gas pressure is relatively high (3 Pa) at the Linac4 negative ion source for particle accelerator in CERN (Lettry et al. 2016), and the H^- ion extraction mechanism of this negative ion source is studied to improve

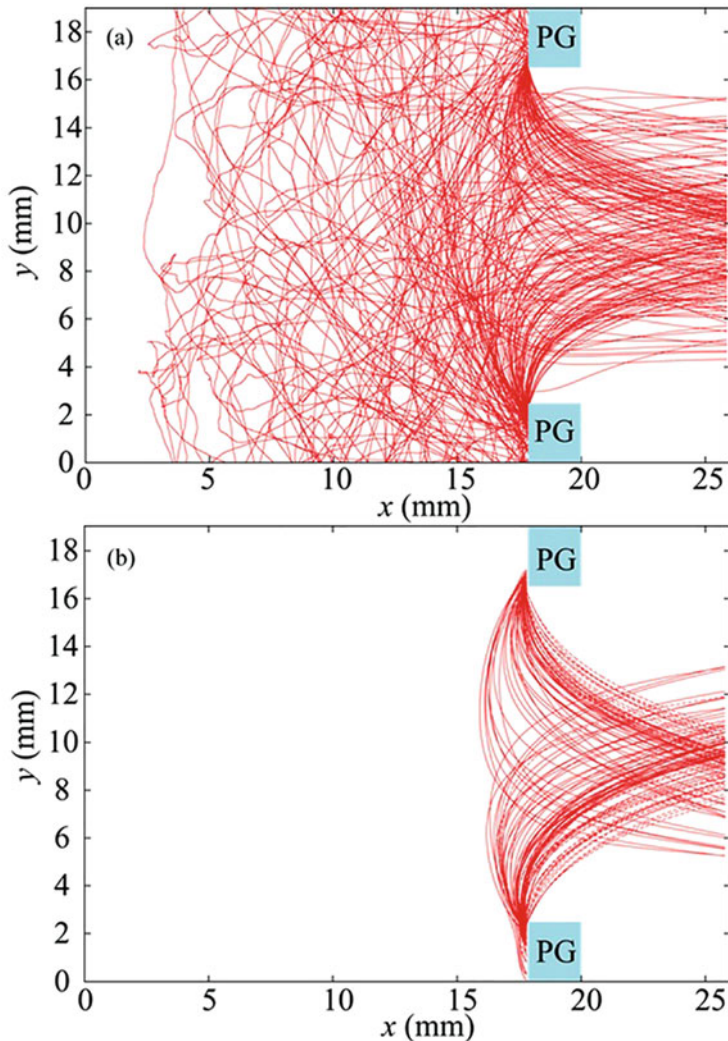


Fig. 5.6 Trajectories of the surface produced H^- ions which are only extracted in the x - y mid plane for the case (a) with and (b) without Coulomb collision with H^+ ions. (Reproduced from (Nishioka et al. 2018) with permission of the American Institute of Physics)

the beam optics (Abe et al. 2016, 2018). Figure 5.8a shows a schematic drawing of the extraction region in the Linac4 negative ion source. In the 2D model, the region surrounded by the broken line in Fig. 5.8a is modelled. Figure 5.8b shows a simulation domain. In this study, two cases are compared as shown in Table 5.2.

The mean free paths of the elastic collision with the H_2 molecules and the charge exchange collision with the H atoms are estimated to be 5 mm and 13 mm, respectively.

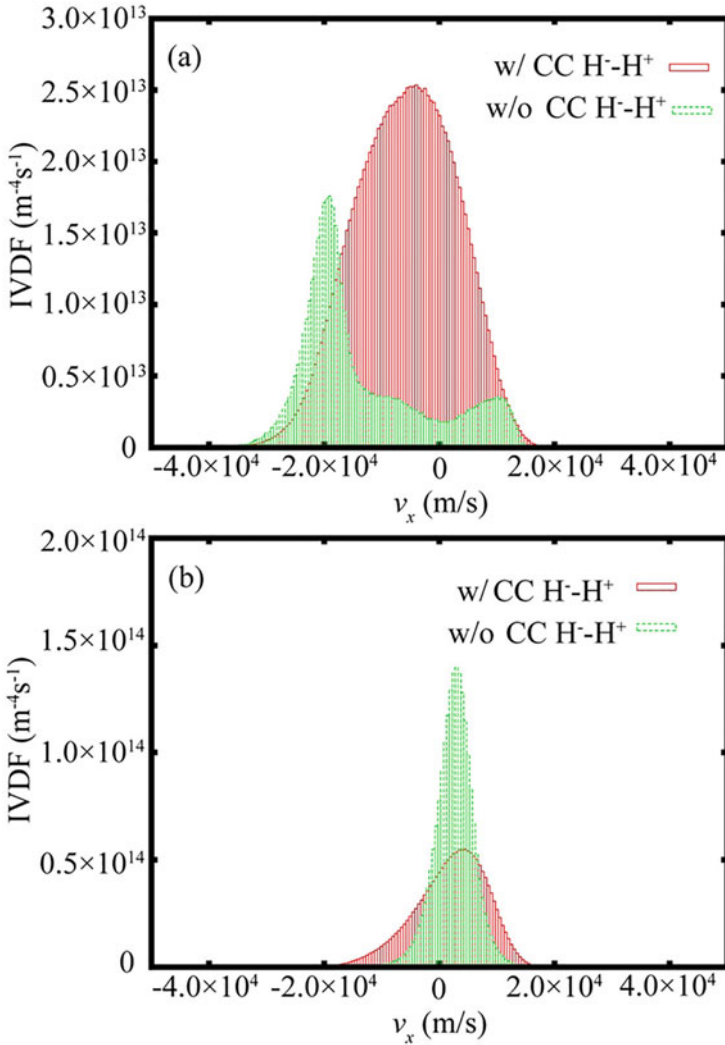


Fig. 5.7 Ion Velocity Distribution Function (IVDF) of the x component in the bulk plasma for the case (a) the surface produced negative ions and (b) H^+ ions. (Reproduced from (Nishioka et al. 2018) with permission of the American Institute of Physics)

Thus, the velocity of the H^- ion will be changed through these collisions with the neutral particles. The collisions listed in Table 5.2 are introduced by the null collision method (Vahedi and Surendra 1995) under the assumption that there is a uniform neutral gas background with constant densities and temperatures. The flow of the surface-produced H^- ions is shown in Fig. 5.9 for (a) case 1 and (b) case 2. In Fig. 5.9, N_x and N_y are the mesh numbers in the x -direction and y -direction, respectively. The flow reversal of the surface-produced H^- ions occurs at a deeper

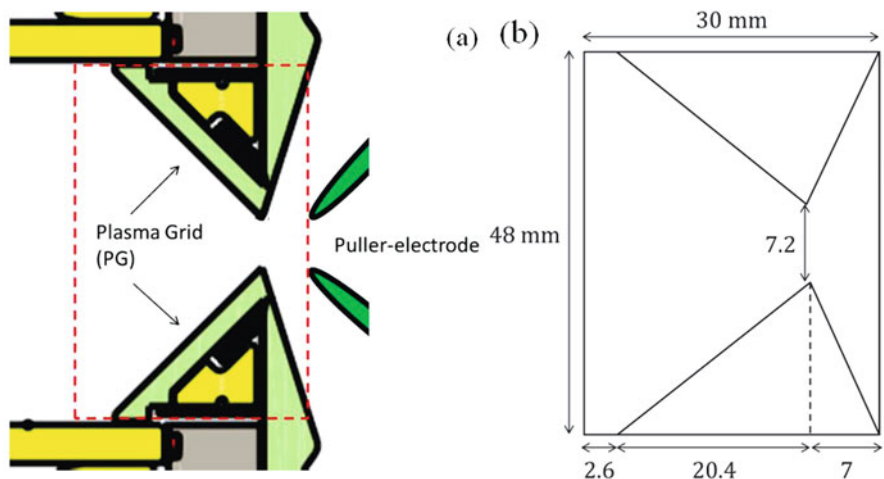


Fig. 5.8 (a) Schematic drawing of the extraction region in the Linac4 negative ion source. (b) Schematic view of the simulation domain. (Reproduced from (Abe et al. 2016) with permission of the American Institute of Physics)

Table 5.2 Particle collision processes in the simulation

Particle	Reaction	Formula	Case 1	Case 2
Electron	Elastic	$e + H_2 \rightarrow e + H_2$	Yes	Yes
Electron	Elastic	$e + H \rightarrow e + H$	Yes	Yes
Surface produced H^-	Associative detachment	$H^- + H \rightarrow H_2 + e$	Yes	Yes
Surface produced H^-	Elastic	$H^- + H_2 \rightarrow H^- + H_2$	No	Yes
Surface produced H^-	Charge exchange	$H^- + H \rightarrow H + H^-$	No	Yes

Reproduced from (Abe et al. 2018) with permission of the American Institute of Physics

position inside the plasma for case 2 than for the case 1. The potential profiles are shown in Fig. 5.10. For case 1, the flow reversal of the surface-produced H^- ions occurs under the electric field for extraction. In contrast, the flow reversal of the surface-produced H^- ions occurs in the area where the penetration of the electric field for extraction is negligible for case 2. It is shown that the flow reversal of the surface-produced H^- ions is caused by the collisions with the neutral particles under the high source filling gas pressure. These modelling results suggest that the collision processes such as the Coulomb collision (at low source filling gas pressure) and the collisions with neutral particles (at high source filling gas pressure) are significant for the extraction of the surface-produced negative ions.

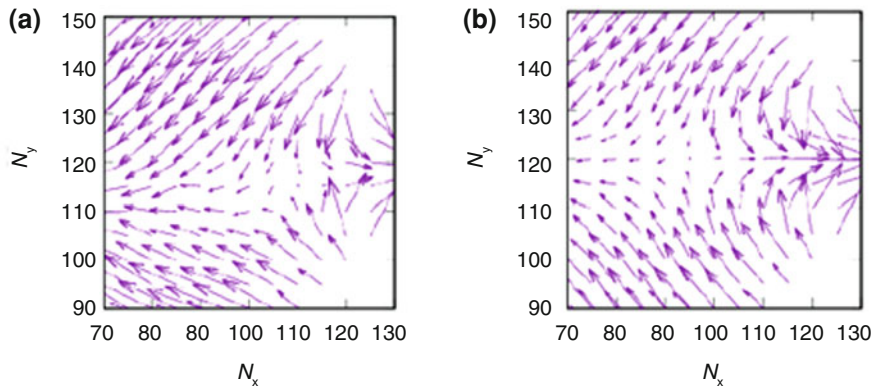


Fig. 5.9 Flow reversal of the surface produced H^- ions for (a) case 1 and (b) case 2. (Reproduced from (Abe et al. 2018) with permission of the American Institute of Physics)

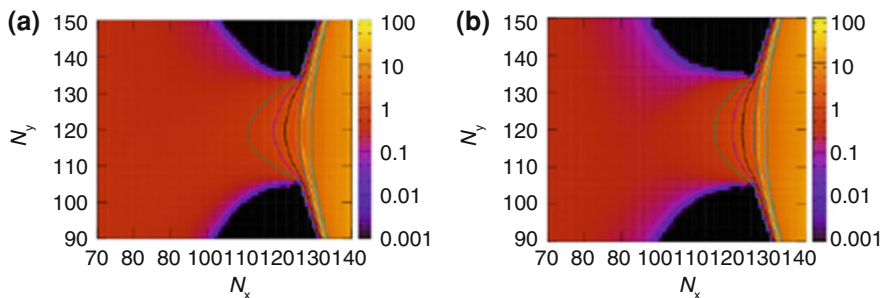


Fig. 5.10 Potential profiles for (a) case 1 and (b) case 2

5.3 Plasma Meniscus and Negative Ion Beam Optics

A plasma meniscus is an emission surface of the ions at the plasma boundary (Brown 2004). The shape of the plasma meniscus depends on the plasma density, the electric field for ion extraction, and so on. If the plasma density is too high, the plasma meniscus shape is convex (Fig. 5.11b). If the plasma density is too low, the plasma meniscus shape is concave (Fig. 5.11c). In general, an ion beam trajectory is determined by the shape of the plasma meniscus. In this section, the relation between the plasma meniscus and negative ion beam optics will be described.

5.3.1 Asymmetry of the Plasma Meniscus

For a positive ion source, the plasma meniscus is defined as the surface where an ion saturation current density is equal to a space charge current density (Humphries

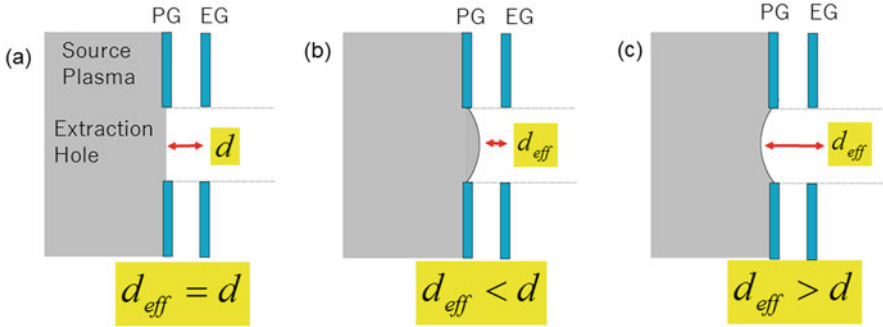


Fig. 5.11 Schematic drawings of the three types of plasma meniscus for (a) $d_{\text{eff}} = d$, (b) $d_{\text{eff}} < d$, (c) $d_{\text{eff}} > d$ where d and d_{eff} are the geometrical and ion sheath distances between the PG and EG, respectively

1990). Similarly, for a negative ion source, the plasma meniscus can be defined as the surface where the electron and negative ion saturation current densities are equal to their space charge current densities. Thus, the plasma meniscus strongly depends on electron loss along/across the magnetic field line and the resultant plasma density profile near the extraction hole.

It is pointed out in other PIC simulations that the asymmetry of the plasma density profile is caused by the $E \times B$ drift and/or diamagnetic drift under the magnetic fields (Mochalskyy et al. 2010; Boeuf et al. 2012; Fubiani and Boeuf 2013). However, the effects of the magnetic field on the plasma meniscus are hardly discussed in these Refs. Not only the effects of the magnetic field on the source plasma characteristics but also its effects on the plasma meniscus and beam optics have been first analyzed in detail with PIC modelling (Miyamoto et al. 2012).

In the model, the physical quantities such as the particle density, the electrostatic potential, and so on are normalized in PIC simulations. The normalization of these quantities is listed in Table 5.2. The extraction region of the negative ion source is modelled with a 3D geometry.

The simulation domain includes the plasma grid (PG) with a single aperture. The overall view of the 3D PIC model is shown in Fig. 5.5 of Sect. 5.2. The x -axis is taken to be the direction of the H^- extraction. The magnetic filter and the electron suppression magnetic field (Kisaki et al. 2009) are taken into account. The y -axis is parallel to the direction of the electron suppression magnetic field, while the z -axis is parallel to the direction of the magnetic filter. The magnetic field distributions along the line of $\tilde{y} = \tilde{z} = 0$ are shown in Fig. 5.12. The typical strengths of the magnetic filter and electron suppression magnetic field near the exit of the PG are 40 Gauss and 300 Gauss, respectively.

The main physical parameters in the source region are summarized in Table 5.1. In the present simulation, the electron density and the electron temperature are $1.0 \times 10^{18} \text{ m}^{-3}$ and 1 eV, respectively. Thus, the electron Debye length is evaluated to be $7.4 \times 10^{-6} \text{ m}$, while the overall length from the source plasma

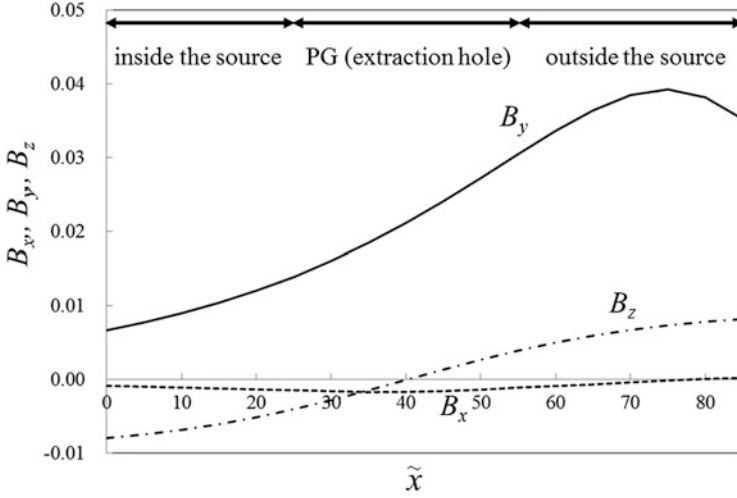


Fig. 5.12 The magnetic field distribution along the line of $\tilde{y} = \tilde{z} = 0$

region to the accelerator is of the order of several centimeters. This difference makes it impossible to model the overall region of the ion source even under the current performance of supercomputers. One useful and powerful solution is to use the size-scaling (Miyamoto et al. 2013; Fubiani et al. 2017). The scale factor s is defined as $L_{\text{sim}} = sL_{\text{real}}$, where L_{sim} is the size in the simulation, and L_{real} is the real size. The scale factor s is taken to be 3.7×10^{-2} . The validity of the reduced size-scaling model has been already discussed by comparing the results with those of the full-size model and shown that no essential difference in basic results has been observed between these two models (Okuda et al. 2013; Kameyama et al. 2012). A lot of comparisons with experimental results obtained in various ion sources have been also done so far to validate and improve the size-scaling model. These comparisons with experiments also show effectiveness of the model.

The strengths of the applied voltage and the magnetic fields are determined with the size-scaling in the following manner: The extraction voltage is adjusted between the PG and the $\tilde{x} = \tilde{x}_{\text{max}}$ boundary in order to obtain the perveance matching as mentioned above (i.e. ion saturation current = space-charge limited extraction current) for the real negative ion source. Thus, one can obtain the perveance relation between the simulation and the real negative ion source

$$\frac{\pi (r_{\text{PG}})_{\text{sim}}^2 J_{\text{H}^-}}{(V_{\text{ext}})_{\text{sim}}^{1.5}} = \frac{\pi (r_{\text{PG}})_{\text{real}}^2 J_{\text{H}^-}}{(V_{\text{ext}})_{\text{real}}^{1.5}}, \quad (5.9)$$

where the subscript *sim* corresponds to the size or applied voltage in the simulation, while the subscript *real* corresponds to the real one. The real applied voltage for extraction $(V_{\text{ext}})_{\text{real}}$ is taken to be 8 kV. In Eq. (5.9), J_{H^-} is the negative ion current density, and the r_{PG} is the radius of the PG aperture.

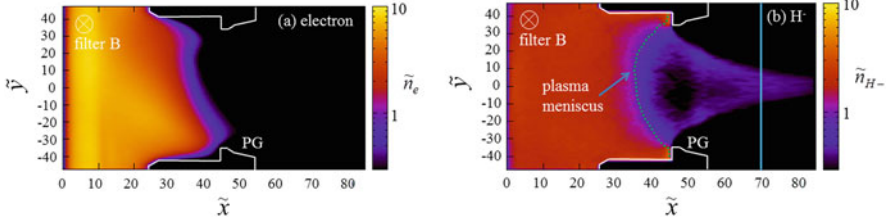


Fig. 5.13 The spatial profiles of (a) electron and (b) H^- ion density in the x - y plane, which is perpendicular to the magnetic filter. (Reproduced from (Miyamoto et al. 2015) with permission of the American Institute of Physics)

Larmor radii of electrons are also scaled down as $(r_L)_{\text{sim}} = s(r_L)_{\text{real}}$, where $(r_L)_{\text{sim}}$ and $(r_L)_{\text{real}}$ are the Larmor radii in simulation and real system, respectively. Thus, the magnetic field in the simulation B_{sim} is given by Eq. 5.10:

$$B_{\text{sim}} = \frac{v_{\text{sim}}}{sv_{\text{real}}} B_{\text{real}}, \quad (5.10)$$

where B_{real} is a real strength of the magnetic field, and v_{sim} is the negative ion velocity in the simulation while v_{real} is the real negative ion velocity.

The normalized density profiles at $\tilde{z} = 0$ in the x - y plane, which is perpendicular to the magnetic filter, are shown in Fig. 5.13 for (a) electron and (b) H^- ion around the PG. It is shown that the density profile of the electron is asymmetric near the PG although it is symmetric in the source plasma region, for example, $\tilde{x} = 10$. This asymmetric density profile near the PG is caused by the $E \times B$ drift, where E is the electric field for the extraction of negative ions, and B is the magnetic filter. The contour map of the electric potential near the PG is shown in Fig. 5.14. Notice that the asymmetry of the electron density is prominent in the location where the electric field is strong, for example, around $\tilde{x} = 40$. Thus, the asymmetry of the electron density profile results in the asymmetry of the shape of the plasma meniscus.

The negative ion beam profile along the line of $\tilde{x} = 70$ in Fig. 5.13b is shown in Fig. 5.15. The negative ion beam profile is asymmetric, which is also reported in the experimental result (Guster et al. 2010). For example, as shown in red ellipses, the extracted negative ion current density on the upper side of this profile ($\tilde{y} > 0$) is larger than that on the lower side ($\tilde{y} < 0$). Moreover, as shown in the blue ellipses, the tail on the lower side of this profile is broadened slightly compared with that on the upper side. This asymmetry of the negative ion beam profile is caused by the *curvature of the plasma meniscus*: the curvature of the lower side of the plasma meniscus ($\tilde{y} < 0$) is smaller than that of the upper side ($\tilde{y} > 0$), and thus the trajectories of negative ions from the lower side of the plasma meniscus become broader than those from the upper side.

Not being shown here as a figure because of page limitation, the asymmetry of the electron density profile caused by the $E \times B$ drift can be observed also in the x - z plane, which is perpendicular to the electron suppression magnetic field.

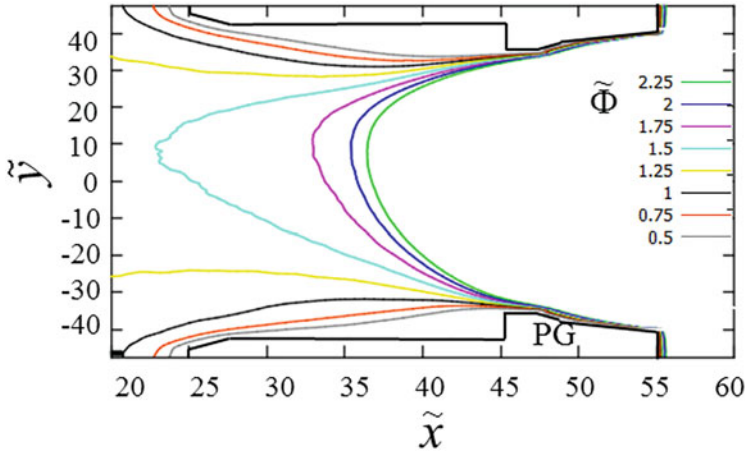


Fig. 5.14 A contour map of the electric potential near the PG at $\tilde{z} = 0$ in the x - y plane. (Reproduced from (Miyamoto et al. 2015) with permission of the American Institute of Physics)

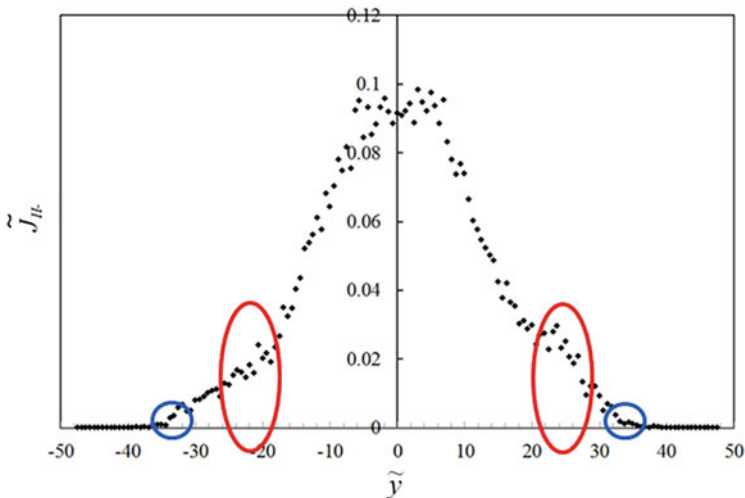


Fig. 5.15 The negative ion beam profile along the line of at $\tilde{x} = 70$ in Fig. 5.13b. (Reproduced from (Miyamoto et al. 2015) with permission of the American Institute of Physics)

In this case, however, *not* the filter magnetic field, *but* the electron suppression magnetic field plays a significant role to produce the $E \times B$ drift and the resultant asymmetry of the electron density profile in the x - z plane. This asymmetry is more prominent compared with the result in Fig. 5.13a since the strength of the electron suppression magnetic field is larger than that of the magnetic filter (see Fig. 5.12). The asymmetry of the electron density profile consequently results in the asymmetries of the shape of the plasma meniscus and the negative ion density

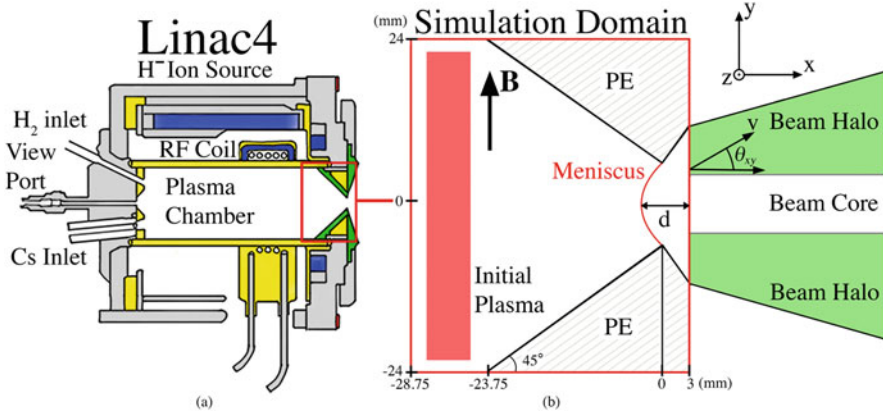


Fig. 5.16 (a) 2D cross-sectional view of the Linac4 negative ion source. In the numerical simulation, the H^- extraction region close to the plasma electrode (PE) and extraction aperture is taken as the simulation domain. (b) A zoomed-in-view of the simulation domain. The divergence angle θ_{xy} of the extracted particles are evaluated at the end of the simulation. (Reproduced from (Lindqvist et al. 2019) with permission of the American Institute of Physics)

profile. The asymmetry of the negative ion beam profile is also more prominent compared with that in Fig. 5.15.

5.3.2 Effects of Extraction Voltage on the Plasma Meniscus and Beam Optics

The shape of the plasma meniscus is determined from the electric field for negative ion extraction as well as the spatial profiles of the charged particles such as electrons, positive and negative ions in the extraction region. Here, effects of the extraction voltage on the plasma meniscus and beam optics are studied with Keio BFX 3D PIC extraction code for the Linac4 negative ion source (Lindqvist et al. 2019). The geometry used in this study is shown in Fig. 5.16. In this study, the surface-produced H^- ions are neglected and only the volume production case is included.

Figure 5.17 shows the divergence angle of extracted H^- ions as a function of the extraction voltage. The divergence angle is evaluated at the right-hand side boundary of the simulation domain. The divergence angle is defined as an average of the absolute values of the angle ($|\theta_{xy}|$) between the velocity vector and the x -axis (see Fig. 5.16) for all the H^- ions. As clearly seen in Fig. 5.17, there is the minimum divergence angle in the range 9.2–11.5 kV, and the lowest divergence angle is achieved at 10.7 kV. In this simulation, the average H^+ ion density in the bulk plasma, where plasma quasi-neutrality is held, is $\sim 4 \times 10^{17} \text{ m}^{-3}$. Here, we define the plasma meniscus as the contour lines where the H^+ plasma density corresponds to the density of the sheath edge, i.e. the meniscus boundary. The plasma meniscus

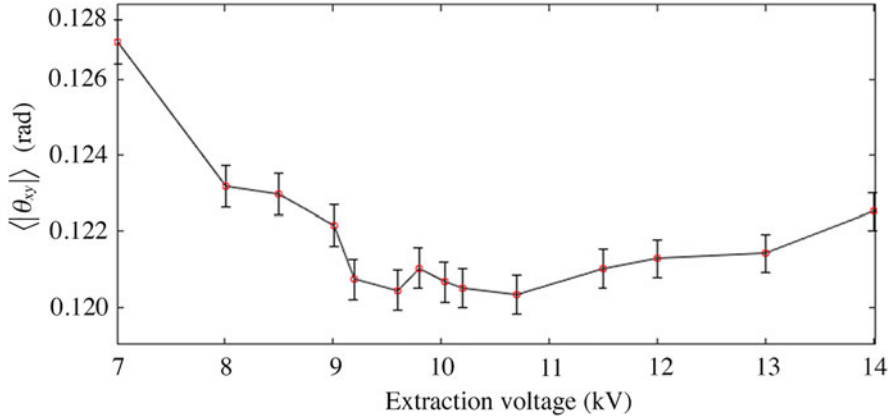


Fig. 5.17 Beam divergence angle as a function of the extraction voltage. Absolute values of the divergence angle ($|\theta_{xy}|$ see Fig. 5.16) are averaged over all the H^- ions passing through the PE apertures. (Reproduced from (Lindqvist et al. 2019) with permission of the American Institute of Physics)

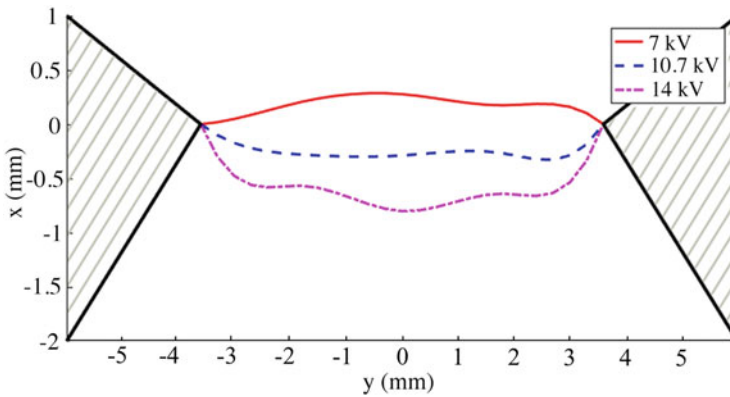


Fig. 5.18 Comparison of the plasma meniscus for extraction voltages 7 kV, 10.7 kV, 14 kV plotted as the contour line where the H^+ density is $\sim 2.4 \times 10^{17} \text{ m}^{-3}$. (Reproduced from (Lindqvist et al. 2019) with permission of the American Institute of Physics)

is plotted for 7 kV, 10.7 kV, and 14 kV in Fig. 5.18. The meniscus is convex for 7 kV, almost flat for 10.7 kV, and concave for 14 kV. It is shown that the correlation between extraction voltage and beam divergence angle is explained by the change in the shape of the plasma meniscus. The magnetic field results in an asymmetry of the curvature of the plasma meniscus periphery in all three cases.

Figure 5.19 shows the divergence angle and beam profile as a function of the y -position. In all cases, the H^- ions extracted from the periphery of the plasma meniscus have a higher divergence angle than the ones extracted from the centre of the plasma meniscus. The negative ion beam is completely divergent for 7 kV.

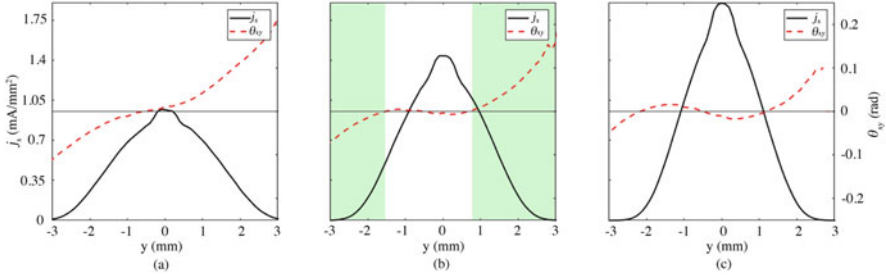


Fig. 5.19 Beam current density and divergence angle as a function of the y -position for H^- ions. Extraction voltages: (a) 7 kV, (b) 0.7 kV and (c) 14 kV. The green regions in Fig. (b) represent the beam halo component. (Reproduced from (Lindqvist et al. 2019) with permission of the American Institute of Physics)

The negative ion beam is over-focused for 14 kV. For 10.7 kV; however, the H^- ions at the centre of the beam have a low divergence angle. We can here observe a tendency of a focused beam core and a diverging beam halo, which is defined by $\theta_{xy} < 0$ for $y < 0$, and $\theta_{xy} > 0$ for $y > 0$ (Miyamoto et al. 2012). The detail of the physical mechanism of the beam halo formation will be shown in the next section.

5.3.3 Negative Ion Beam Acceleration and Beam Optics

It is essential for the negative ion source to produce a negative ion beam with good optics. For example, the beam divergence angle of 3 - 7 mrad is required in the design of ITER-NBI (Hemsworth et al. 2017; Singh et al. 2017). Especially, it is crucial to suppress a beam halo since the beam halo can contribute to the reduction of the beam transmission and increase of the heat loads even at the optimum perveance for minimizing the divergence of the beam core. The beam halo appears directly as the beam profile (Holmes and Nightingale 1986; de Esch and Svensson 2011), or indirectly as a component of the heat loads in the accelerator grids (Hanada et al. 1998). The physics of the negative ion beam optics, especially the relation between the meniscus and beam halo is investigated using the 2D PIC simulation (Miyamoto et al. 2013). A schematic view of the simulation model is shown in Fig. 5.20. The extractor consists of the extraction grid (EXG) and the electron suppression grid (ESG). The accelerator consists of the first acceleration grid (A1G), the second acceleration grid (A2G), and the grounded grid (GRG). In this model, it is possible to simulate not only the source plasma with surface H^- production, but also the H^- acceleration self-consistently without any assumption of plasma meniscus, while most of the conventional beam acceleration codes/models need the assumptions for the plasma meniscus.

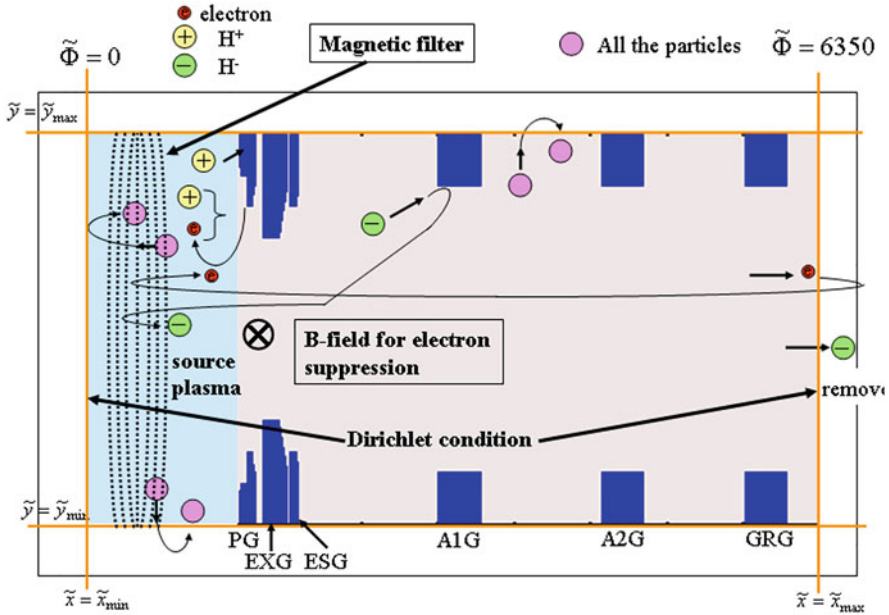


Fig. 5.20 A schematic view of the 2D PIC simulation model from the source plasma to the accelerator. (Reproduced from (Miyamoto et al. 2013) with permission of the American Institute of Physics)

A snapshot of the negative ion beam profile is shown in Fig. 5.21. One can find that some of the negative ions are intercepted on the grids in the accelerator although most of the negative ions pass through the GRG aperture without an interception.

The typical trajectories of the negative ions extracted from the central region of the meniscus are shown in Fig. 5.22 while the typical trajectories of the negative ions extracted from the edge of the meniscus are shown in Fig. 5.23. In Figs. 5.22 and 5.23, the trajectories in the extractor are also enlarged. It is shown that the beam halo consists of the negative ions extracted from the periphery of the meniscus, while the beam core consists of the negative ions extracted from the central region of the meniscus. Some of the surface-produced negative ions, which are launched from the side wall or the edge of the PG aperture, pass the periphery of the meniscus. Due to the curvature of the meniscus, these negative ions are over-focused in the extractor. The electrostatic lens near the beam axis hardly focuses the negative ion beams. Therefore, these negative ions are not focused by the electrostatic lens formed around the ESG and become the beam halo. On the other hand, some of the surface-produced negative ions move into the source plasma region, and are extracted from the central region of the meniscus. Since the central region of the meniscus is almost flat, these negative ions are not over-focused in the extractor. These negative ions are focused by the electrostatic lens formed around the ESG.

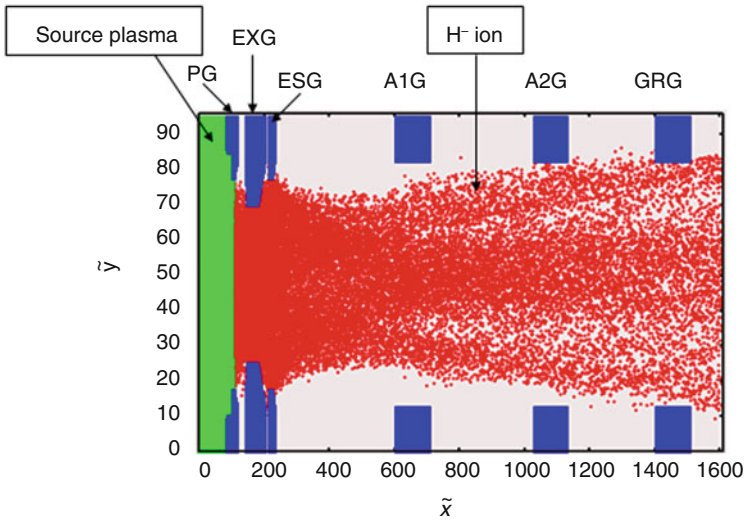


Fig. 5.21 A snap shot of the negative ion beam profile in the extractor/accelerator. (Reproduced from (Miyamoto et al. 2013) with permission of the American Institute of Physics)

The above physical mechanism of the beam halo formation has also been confirmed using the 3D PIC-MCC simulation (Miyamoto et al. 2018).

The intercepted negative ions cause the heat loads of the grids in the accelerator. The fractions of heat loads due to the intercepted negative ions to the total beam power are estimated to be 3.9% at A1G, 3.4% at A2G and 4.2% at GRG, respectively in the 3D PIC-MCC simulation. The heat loads due to the intercepted negative ions become larger in the downstream grid. This tendency agrees well with the experimental result (2.4% at A1G, 3.0% at A2G and 5.0% at GRG) (Kamada et al. 2009). Moreover, the simulation result of the heat loads of the acceleration grids quantitatively agrees with the experimental result.

As described in Sect. 5.2.1, the surface-produced H^- ions emitted from the PG surface are extracted from the bulk plasma which is deeply inside rather than directly from the tip of the PG without passing through the bulk plasma. The extraction and transport process of the surface produced H^- affects the characteristics of the H^- ion beam optics: the H^- ions extracted directly from the tip of the PG pass the edge of the meniscus and become the beam halo with bad beam optics, while the H^- ions from the bulk plasma are mainly extracted from the central region of the meniscus and becomes the beam core with good beam optics.

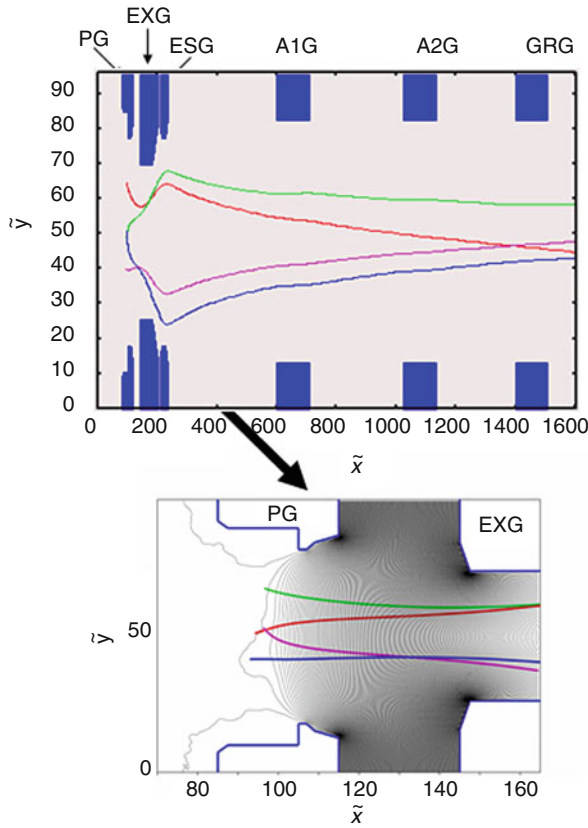


Fig. 5.22 Typical trajectories of the negative ions which are extracted from the central region of the meniscus. (Reproduced from (Miyamoto et al. 2013) with permission of the American Institute of Physics)

5.4 EM-PIC-MCC Modelling in the RF Driven Negative Ion Source for Accelerators

5.4.1 Introduction

In these 10 years, the radio-frequency (RF) type negative hydrogen ion (H^-) sources have been applied to the high-power proton accelerators (Stockli et al. 2020; Oguri et al. 2021; Lettry et al. 2018). For the improvement of the ion source performance, such as beam intensity, emittance or lifetime of ion sources, understanding of the RF plasma is necessary. By controlling of the plasma transport toward the cesiated plasma electrode (PE) surface, amount of the surface-produced H^- can be increased which results in the increase of beam brightness. The effective H^- production

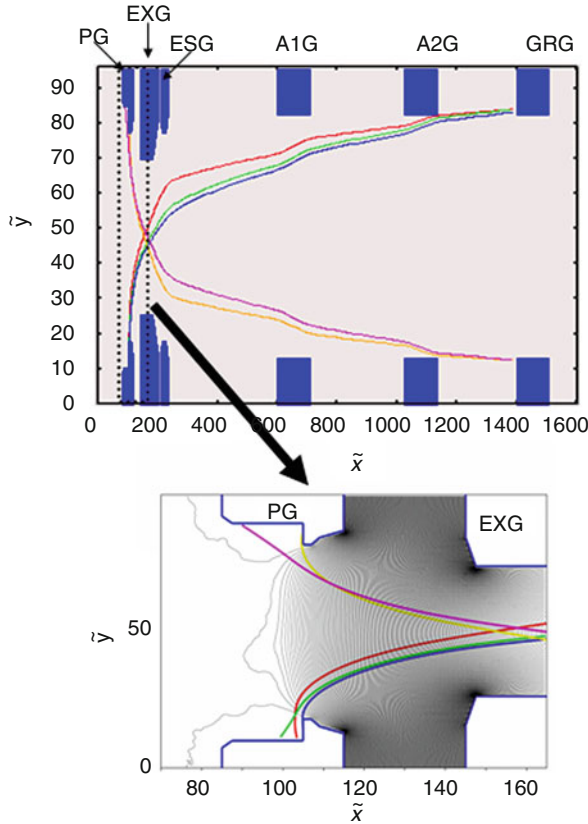


Fig. 5.23 Typical trajectories of the negative ions which are extracted from the edge of the meniscus. (Reproduced from (Miyamoto et al. 2013) with permission of the American Institute of Physics)

results in the reduction of the required input RF power to the plasma. This leads to an extension of the RF antenna lifetime for the internal antenna-type RF ion sources (Oguri et al. 2021). However, the RF plasma diagnosis is limited compared to that of arc-driven plasma due to its high-density plasma and time variation of plasma parameters. In these plasmas, photometry and spectroscopy measurements are powerful tools to obtain plasma signals. For example, Balmer lines of hydrogen atoms are strong signals in ion sources which also include information on the time structure of plasma parameters. However, diagnoses of detailed plasma transport or spatial distributions are difficult because the measured line intensity is an integration of produced protons inside the line of sight of the viewing port. To understand more detailed plasma behavior, numerical results by EM-PIC modelling are applied and compared with the line intensity measurements to validate the physical model. From the validated modelling, relation between the plasma transport and the source design

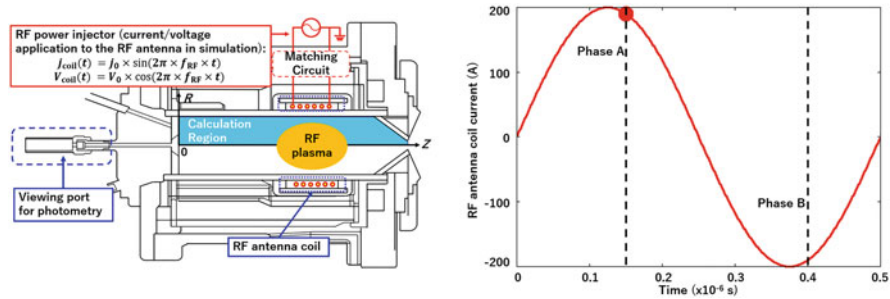


Fig. 5.24 (a) Geometry of CERN LINAC4 RF ion source and (b) RF antenna coil current in the calculation

can be clarified. In Sects. 5.4.2 and 5.4.3, examples of the EM-PIC-MCC modelling applications to the E- and the H- mode RF plasmas for the accelerators are shown. A hint to the source design upgrade for the effective H⁻ surface production supported by the PIC modelling is discussed in Sect. 5.4.3.

5.4.2 PIC Simulation of the E-Mode RF Plasma

Figure 5.24a shows a schematic drawing of the RF H⁻ ion sources in CERN Linac4. The RF plasma is generated by applying alternate current with RF frequency with $f_{RF} = 2$ MHz to the antenna coil (Lettry et al. 2018). The time variation of the antenna coil current j_{coil} in one RF-cycle and the specific phases, which are denoted as A and B for later discussion, are shown in Fig. 5.24b. The RF plasma ignition starts from the E-mode state which relatively low-density plasma takes place. The capacitively coupled (CC) electric field E_{CC} is formed by the voltage difference between the RF antenna coil terminals connected to the alternate power supply and to the ground. The ionization process between hydrogen neutrals and electrons is enhanced by the electric field, which increases plasma density for ignition. Photometry measurement of Balmer alpha (H_{α}) line is adopted for the RF plasma diagnosis (Lettry et al. 2015). The viewing port for the photometry is located at the backplate on axis as in Fig. 5.24 and is connected to the photo-multiplier tube through the band-path filter for H_{α} . The H_{α} line intensity and the RF current j_{coil} in two RF-cycles of the E-mode state are shown in Fig. 5.25 (Shibata et al. 2015). A pair of high and low peaks are observed in one RF-cycle at the different phases A and B. To understand this asymmetric line intensity time structure, the EM-PIC modelling (Mattei et al. 2014) is coupled with neutral models. Balance of the input and the output power with the plasma density ramp-up is also confirmed. In the EM-PIC modelling, equations of the motions are solved for electrons and positive ions (H^+ , H_2^+ and H_3^+) including the Coulomb and inelastic collision processes. The CC electric field due to the alternate voltage application at the RF antenna coil terminals is also solved. Figure 5.26

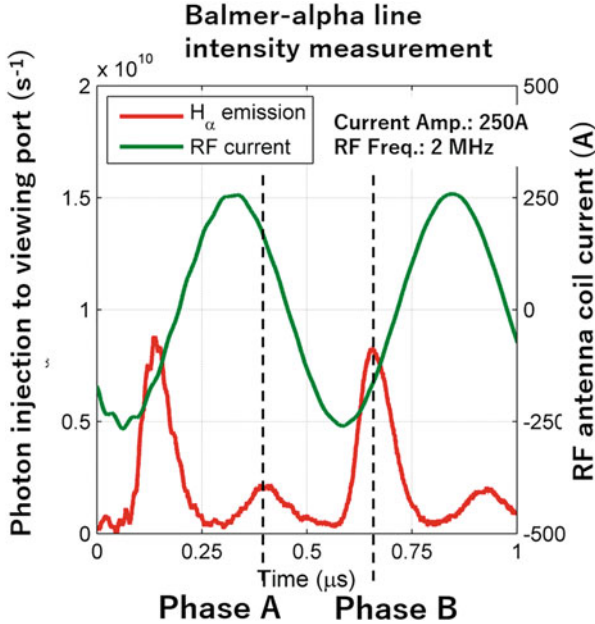


Fig. 5.25 Time structure of H_{α} line intensity observed in the photometry measurement of Linac4 ion source. (Reproduced from (Shibata et al. 2015) with permission of the American Institute of Physics)

shows the spatial distribution of E_{CC} field due to the RF voltage application. From the electron energy distribution function obtained at each mesh point from the EM-PIC modelling, the photon production rate for H_{α} is estimated by a Collisional Radiative (CR) model and neutral transport model (Sawada and Fujimoto 1995). Contributions of injecting photons to the optical viewing port from each position in the chamber are the product of the Gaussian function for angle and decay function for distance. From this relation, number of the injecting photons to the optical viewing port was obtained.

Figure 5.27 shows spatial distributions of the electron average energy in the phase A and the opposite phase B in one RF-cycle. Ratio of the high energy electrons increases near the RF antenna terminal (around $z = 80$ mm) in the phase A, while the electron energy is enhanced near the backplate and the plasma electrode ($z = 0$ and $z = 120 - 130$ mm) in the opposite phase B, which is due the CC electric field oscillation in 2 MHz. Spatial distributions of the H_{α} photon production rate corresponding to the phases A and B in Fig. 5.25 are shown in Fig. 5.28. The higher H_{α} intensity peak takes place at the phase B, in which the fast electrons are produced near the backplate (the viewing port). On the other hand, the lower peak is seen at the phase A, in which the electrons are accelerated towards the RF antenna terminal. The atomic and molecular densities are stable between these phases. Therefore, the asymmetric peaks of the Balmer lines are due to the increase in the average electron

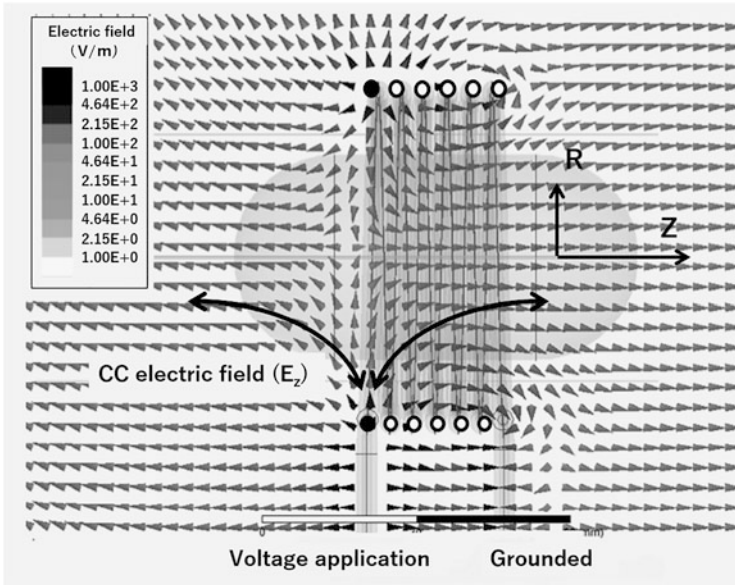


Fig. 5.26 Spatial distribution of the E_{CC} field in the present PIC modelling

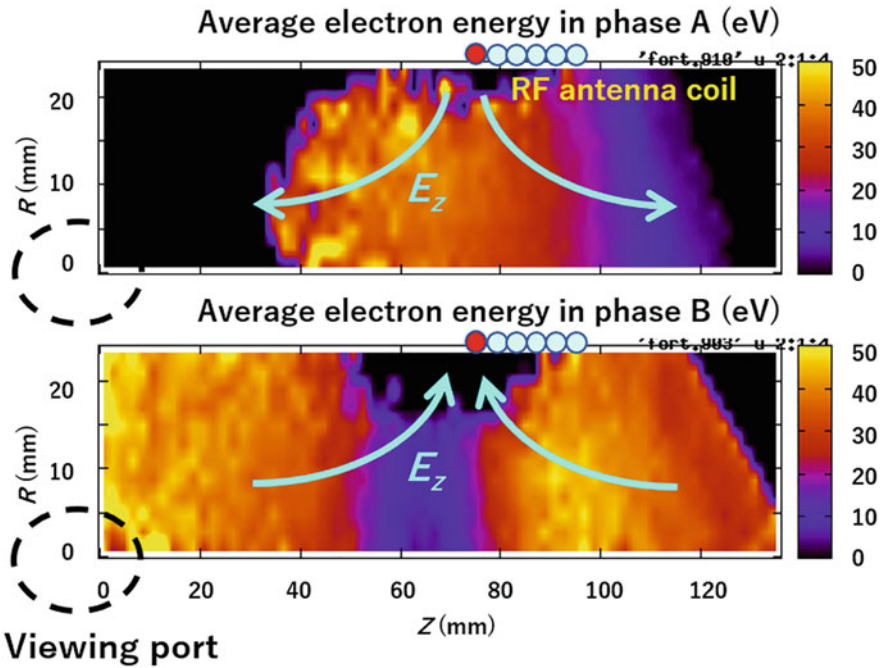


Fig. 5.27 Average electron energy calculated by EM-PIC-MCC simulation for the phases A and B in Fig. 5.24

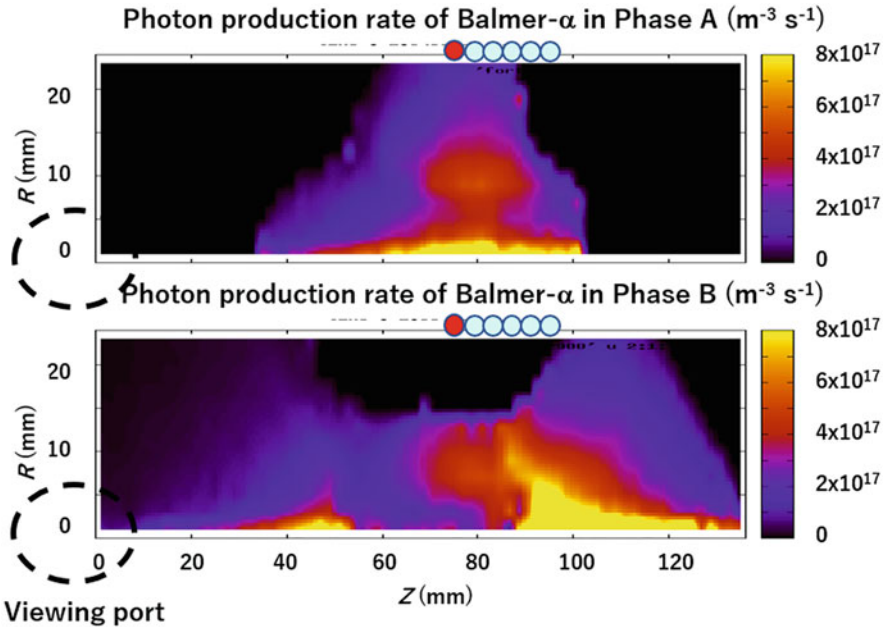


Fig. 5.28 Spatial distribution of photon production rate for H_{α} line in phases A and B. (Reproduced from (Shibata et al. 2015) with permission of the American Institute of Physics)

energy and the resultant electron density ramp-up via ionization process. Figure 5.29 is the numerical result of the H_{α} proton number injected to the viewing port in two RF cycles. As the asymmetric peak structure in phases A and B is consistent between the experiment and the calculation, this result supports the first result of the electron acceleration due to the axial CC electric field. Moreover, the physical model in the simulation is qualitatively validated through the comparison. These numerical techniques are also applied to model the H-mode plasma, the main operation mode with high plasma density, in the Linac4 ion source (Mattei et al. 2014).

5.4.3 PIC Simulation of H-Mode RF Plasma

Figure 5.30 shows J-PARC RF ion source and the calculation geometry. The ion source is equipped with an internal RF antenna coil and a pair of rod filter magnets. In the operation of the ion source, the H-mode RF plasma is generated. The 2 MHz RF power is applied to the antenna coil with repetition 25 Hz and pulse width 800 μ s to produce 60–72 mA of H^{-} beam to the J-PARC Linac. Typical forward power injected to the plasma is to the 25–30 kW. In the photometry measurements, the Balmer line intensity shows characteristic oscillation. Figure 5.31 is the time variation of the H_{α} line intensity and the current in the RF antenna. While the

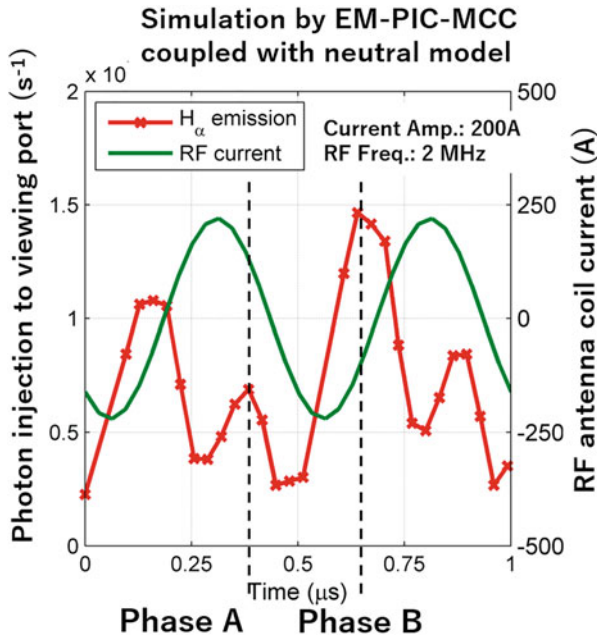


Fig. 5.29 Time structure of calculated H_{α} line intensity in the photometry measurement. (Reproduced from (Shibata et al. 2015) with permission of the American Institute of Physics)

RF current oscillates in the RF frequency of 2 MHz, the Balmer line intensity oscillates in the doubled frequency, namely 4 MHz. These characteristic features are explained by the EM-PIC modelling of the H-mode plasma (Shibata et al. 2018). Figure 5.32 shows the time variation of spatially averaged densities of electrons and positive ions in the simulation. In the H-mode state, in which the electron density becomes around 10^{19} m^{-3} , the plasma density begins to oscillate at 4 MHz. As mentioned in Sect. 5.4.2, the Balmer photon production rate is enhanced by the electron density, the H_{α} line intensity also oscillates with 4 MHz. Figures 5.33 and 5.34 are spatial distributions of the electron density and the inductively-coupled (IC) magnetic field B_{IC} in the axial (z) direction formed by plasma current in the azimuthal direction. The B_{IC} field has a maximum twice in one RF cycle. Figures 5.33(a1), 5.33(b1), 5.34(a1) and 5.34(b1) correspond to the time when the electron density peaks take place (phase A and B in Fig. 5.32, respectively). In these phases, the charged particles are confined by the B_{IC} field and the high plasma density takes place, which results in the high Balmer line emission from the plasma. On the other hand, Figs. 5.33(a2), 5.33(b2), 5.34(a2) and 5.34(b2) are the electron density and the IC magnetic flux density at few 10 ns after the electron density peaks around phase A and B in Fig. 5.32. Due to reduction of the B_{IC} field, electron loss to the wall in the radial direction is increased. As the B_{IC} field has maximum intensity twice in one RF cycle, the plasma density also has double peaks. These basic characteristics

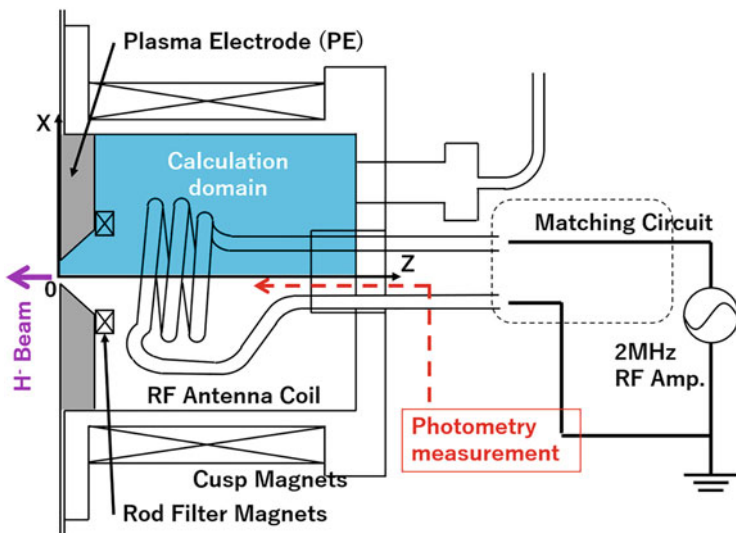


Fig. 5.30 Schematic drawings of J-PARC RF ion source and the PIC calculation domain

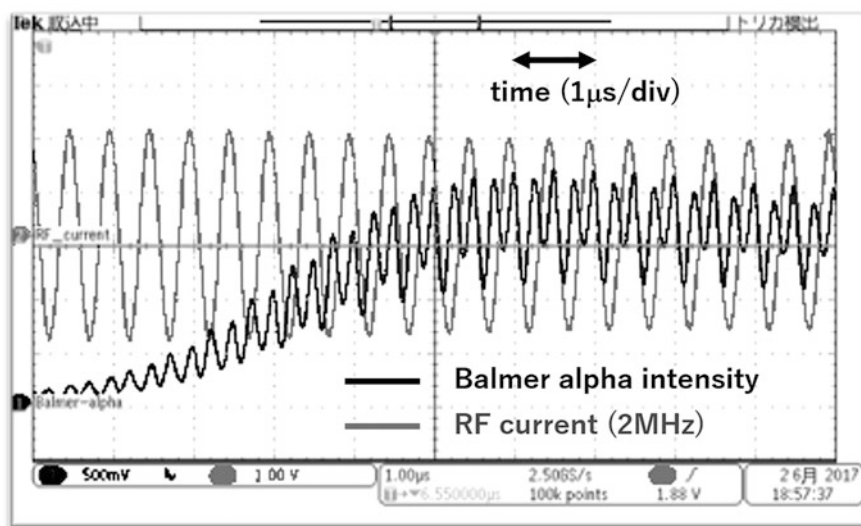


Fig. 5.31 Time variation of H_{α} line intensity and the RF coil current in J-PARC RF ion source. (Reproduced from (Shibata et al. 2018) with permission of the American Institute of Physics)

of the H-mode plasma observed in the photometry measurement are confirmed by the EM-PIC modellings.

The calculations are applied to the source design. Figure 5.35 is the spatial distribution of the proton density which has similar distribution with H_2^+ density

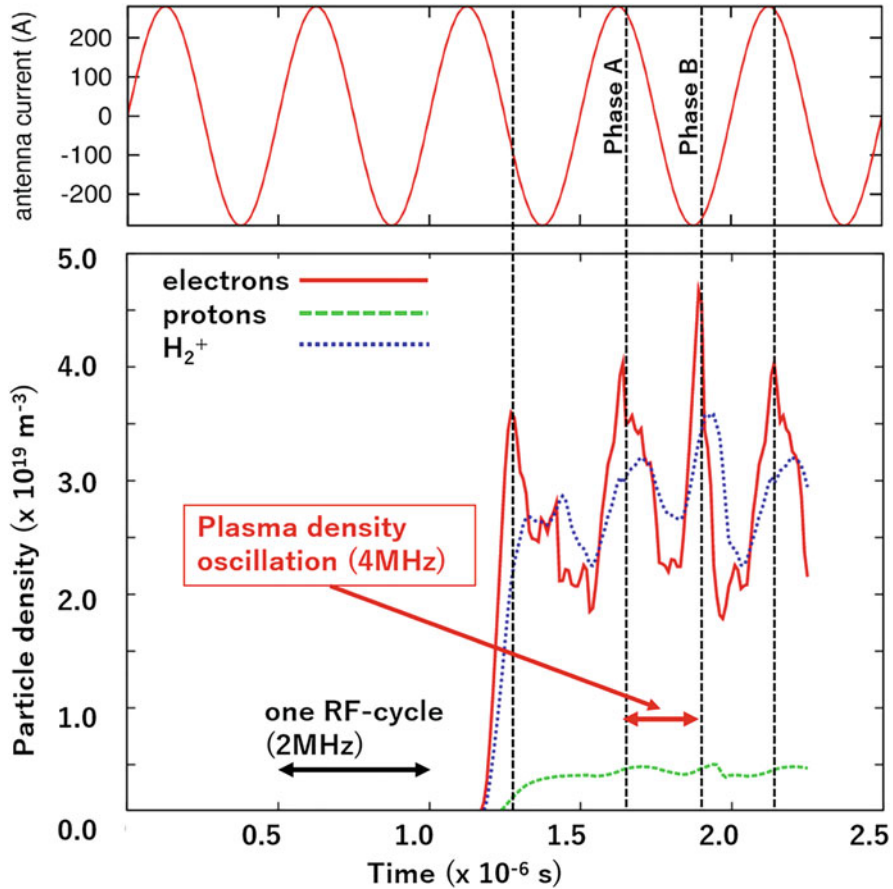


Fig. 5.32 Time variation of the RF antenna current and the calculated plasma density in H-mode. The plasma density is spatially averaged. Vertical scale modified from the original figure. (Reproduced from (Shibata et al. 2017) with permission of the American Institute of Physics)

(Shibata 2016). The ions have relatively high density inside the RF antenna coil ($z > 30$ mm and $R < 10$ mm in Fig. 5.35) and near the PE surface (around $z = 10$ mm and $R = 20$ mm), where the H^- ions are produced. In the region close to the RF antenna (driver region), the ions are produced via ionization processes and trapped along the IC magnetic field. At the extraction region, this B_{IC} field line intersects with the transverse magnetic field by the rod filter magnets. Resultantly, the positive ions are directed towards the filter magnets. On the other hand, elastic and charge exchange collisions among the heavy particles (including neutrals) play a role to diffusion perpendicular to the field line. The collision frequency is estimated to be few 10^5 s^{-1} for thermal velocity of the ions while cyclotron frequency near the filter magnet is around 10^6 s^{-1} . The estimated characteristic length from the original field line is around 10^{-2} m, which is similar value to the distance between the filter

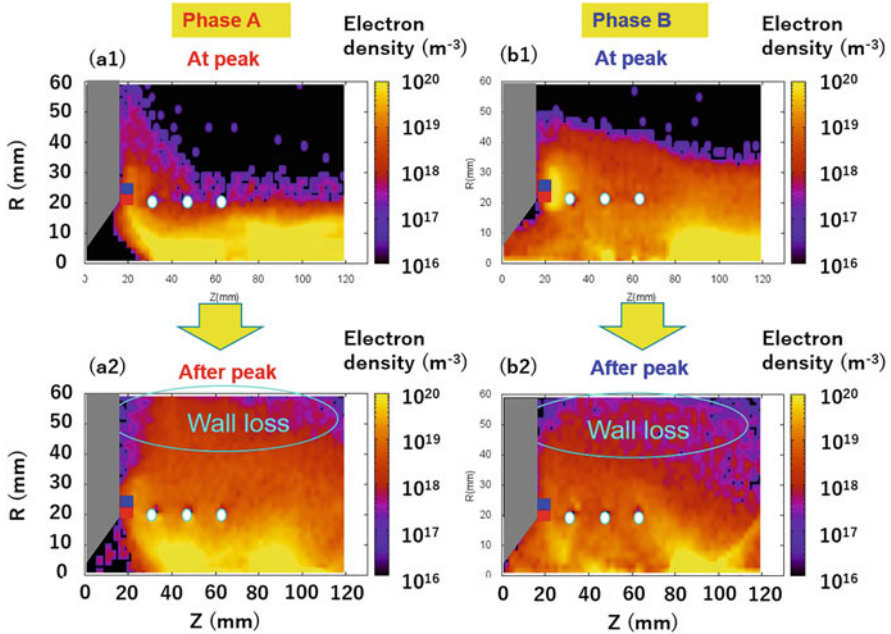


Fig. 5.33 Spatial distributions of electron density. The figures (a1) and (a2) correspond to the electron density at the peak and few 10 ns after the peak in phase A of Fig. 5.32, respectively. The figures (b1) and (b2) correspond to those in phase B of Fig. 5.32. (Reproduced from (Shibata et al. 2017) with permission of the American Institute of Physics)

magnet and centre of the taper part on the PE. This results are consistent with the strong dependence of the H^- current extracted from the ion source to the rod filter magnet configuration (Ueno et al. 2014, 2015).

5.5 Conclusion

In the present chapter, several dominant plasma physics are solved by the application of the PIC modellings with Monte-Carlo collisions (PIC-MCC). The H^- beam extraction mechanisms from the surface production type negative ion sources in several different operating conditions are shown in Sect. 5.2. Related to this section, the formation mechanism of the plasma meniscus, which determines the beam emittance and the deflection due to the drifts, is clarified in Sect. 5.3. These calculations are performed by the electrostatic PIC-MCC modellings. On the other hand, in Sect. 5.4, the plasma ramp-up processes in the RF driven type ion sources are clarified by the electromagnetic (EM) PIC-MCC modelling. Several hints for the stable RF plasma ramp-up process are suggested from the simulation by visualizing the electromagnetic field and the flux of charged particles individually. The PIC

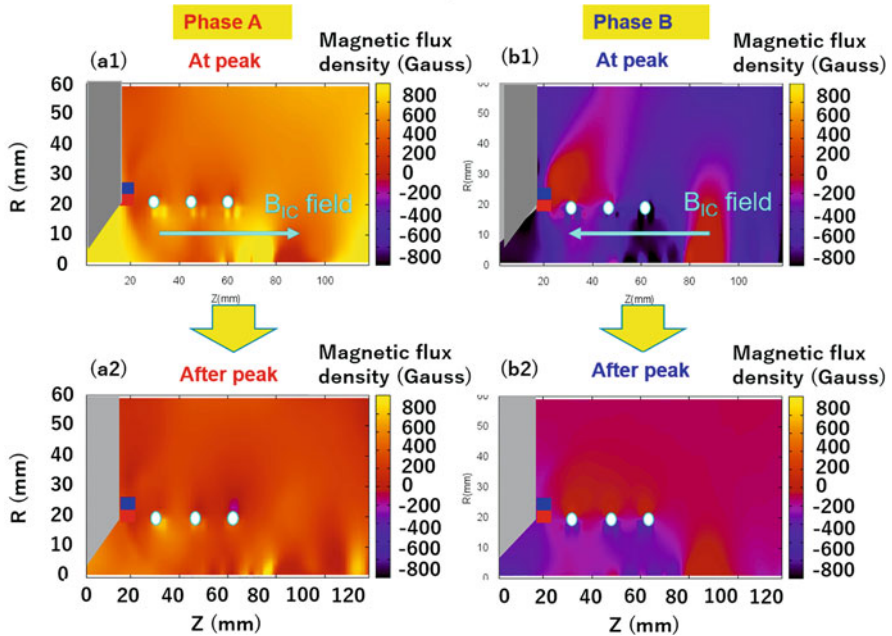


Fig. 5.34 Spatial distributions of axial IC magnetic flux density. The figures (a1) and (a2) correspond to the time at the peak in phase A of Fig. 5.32 and few 10 ns after the peak, respectively. The figures (b1) and (b2) correspond to those in phase B of Fig. 5.32. (Reproduced from (Shibata et al. 2017) with permission of the American Institute of Physics)

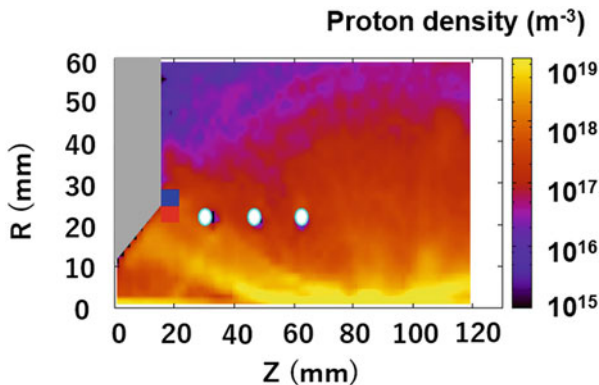


Fig. 5.35 Spatial distribution of proton density in the H-mode simulation. The distribution has weak time dependence

modelling is a powerful tool to obtain information on the plasma parameters which are hardly measured. In the matured negative ion source development, it is becoming difficult to obtain solutions of the source designs to improve the H⁻ beam

performance. Understandings of the plasma behavior and its relation to the source equipment by these PIC modellings are becoming more important from now on.

References

- S. Abe, S. Nishioka, S. Mattei, et al., AIP Conf. Proc. **1869**, 030051 (2016)
 S. Abe, S. Nishioka, S. Mattei, et al., AIP Conf. Proc. **2011**, 080020 (2018)
 M. Bacal, M. Wada, Appl. Phys. Rev. **2**, 021305 (2015)
 M. Bacal, P. Berlemont, A.M. Bruneteau, et al., J. Appl. Phys. **70**, 1212–1219 (1991)
 M. Bacal, A. Hatayama, J. Peters, IEEE Trans. Plasma Sci. **33**, 1845–1871 (2005)
 C.K. Birdsall, A.B. Langdon, *Plasma Physics Via Computer Simulation* (Mc-Graw Hill, New York, 1985)
 J.P. Boeuf, J. Claustre, B. Chaudhury, et al., Phys. Plasmas **19**, 113510 (2012)
 I.G. Brown, *The Physics and Technology of Ion Sources* (Wiley-VCH Verlag GmbH & Co, US KGaA, Weinheim, 2004), pp. 62–64
 P. Chabert, N. Braithwaite, *Physics of Radio Frequency Plasmas* (Cambridge University Press, New York, 2011)
 H.P.L. de Esch, L. Svensson, Fusion Eng. Des. **86**, 363–368 (2011)
 U. Fantz, D. Wunderlich, R. Riedl, et al., Fusion Eng. Des. **156**, 111609 (2020)
 G. Fubiani, J.P. Boeuf, Phys. Plasmas **20**, 113511 (2013)
 G. Fubiani, L. Garrigues, G. Hagelaar, et al., New J. Phys. **19**, 015002 (2017)
 S. Geng, K. Tsumori, H. Nakano, et al., Fusion Eng. Des. **123**, 481–484 (2017)
 R. Guster, D. Wunderlich, U. Fantz, et al., Plasma Phys. Control. Fusion **52**, 045017 (2010)
 M. Hanada, Y. Fujiwara, K. Miyamoto, et al., Rev. Sci. Instrum. **69**, 947–949 (1998)
 M. Hanada, T. Seki, N. Takado, et al., Rev. Sci. Instrum. **77**, 03A515 (2006)
 A. Hatayama, Rev. Sci. Instrum. **79**, 02B901 (2008)
 R. Hemsworth, H. Decamps, J. Graceffa, et al., Nucl. Fusion **49**, 045006 (2009)
 R.S. Hemsworth, D. Boilson, P. Blatchford, et al., New J. Phys. **19**, 025005 (2017)
 A.J.T. Holmes, Rev. Sci. Instrum. **53**, 1523–1526 (1982)
 A.J.T. Holmes, et al., Rev. Sci. Instrum., **57**, 2402 (1986)
 S. Humphries, *Charged Particle Beams* (Wiley, New York, 1990), pp. 289–300
 K. Ikeda, H. Nakano, K. Tsumori, et al., New J. Phys. **15**, 103026 (2013)
 M. Kamada, M. Hanada, Y. Ikeda, et al., AIP Conf. Proc. **1097**, 412–420 (2009)
 N. Kameyama, D. Matsushita, S. Koga, et al., AIP Conf. Proc. **1390**, 39–47 (2011)
 N. Kameyama, T. Fukuyama, S. Wada, et al., Rev. Sci. Instrum. **83**, 02A721 (2012)
 M. Kasaki, M. Hanada, M. Kamada, et al., AIP Conf. Proc. **1097**, 344–352 (2009)
 J. Lettry, D. Aguglia, J. Alessi, et al., AIP Conf. Proc. **1655**, 030005 (2015)
 J. Lettry, D. Aguglia, J. Alessi, et al., Rev. Sci. Instrum. **87**, 02B139 (2016)
 J. Lettry, S. Bertolo, U. Fantz, et al., AIP Conf. Proc. **2052**, 050008 (2018)
 K.N. Leung, C.A. Hauck, W.B. Kunkel, et al., Rev. Sci. Instrum. **60**, 531–538 (1989)
 H. Lewy, K. Friedrichs, R. Courant, Math. Ann. **100**, 32–74 (1928)
 M.A. Lieberman, A.J. Lichtenberg, *Principals of Plasma Discharges and Materials Processing* (Wiley, New York, 1994)
 M.A. Lieberman, A.J. Lichtenberg, A.M. Marakhtanov, Appl. Phys. Lett. **75**, 3617–3619 (1999)
 M. Lindqvist, S. Nishioka, K. Miyamoto, et al., J. Appl. Phys. **126**, 12303 (2019)
 D. Matsushita, N. Takado, A. Hatayama, Rev. Sci. Instrum. **79**, 02A527 (2008)
 S. Mattei, M. Ohta, M. Yasumoto, et al., Rev. Sci. Instrum. **85**, 02B115 (2014)
 K. Miyamoto, S. Okuda, A. Hatayama, Appl. Phys. Lett. **100**, 233507 (2012)
 K. Miyamoto, S. Okuda, A. Hatayama, et al., Appl. Phys. Lett. **102**, 023512 (2013).; K. Miyamoto, S. Okuda, A. Hatayama et al., AIP Conf. Proc., **1515**, 22–30 (2013)

- K. Miyamoto, S. Nishioka, I. Goto, et al., AIP Conf. Proc. **1655**, 05004 (2015)
- K. Miyamoto, S. Nishioka, A. Hatayama, et al., AIP Conf. Proc. **2011**, 050012 (2018)
- S. Mochalsky, A.F. Lifschitz, T. Minea, Nucl. Fusion **50**, 105011 (2010)
- S. Nishioka, S. Abe, K. Miyamoto, et al., J. Appl. Phys. **123**, 063302 (2018)
- H. Oguri, K. Ohkoshi, K. Shinto, et al., JPS Conf. Proc. **33**, 011008 (2021)
- S. Okuda, K. Miyamoto, T. Fukuyama, et al., AIP Conf. Proc. **1515**, 107–113 (2013)
- Y. Okumura, M. Hanada, T. Inoue, et al., AIP Conf. Proc. **210**, 169–183 (1990)
- K. Sawada, T. Fujimoto, J. Appl. Phys. **78**, 2913 (1995)
- T. Shibata, High density plasma calculation of J-PARC RF negative ion source, the 5th International Symposium on Negative Ions, Beams and Sources (Tue_O11), 12th – 16th September 2016 St. Anne's College, Oxford, UK
- T. Shibata, M. Kashiwagi, T. Inoue, et al., J. Appl. Phys. **114**, 143301 (2013)
- T. Shibata, S. Mattei, K. Nishida, et al., AIP Conf. Proc. **1655**, 020008 (2015)
- T. Shibata, H. Asano, K. Ikegami, et al., AIP Conf. Proc. **1869**, 030017 (2017)
- T. Shibata, K. Shinto, A. Takagi, et al., AIP Conf. Proc. **2011**, 020008 (2018)
- M.J. Singh, D. Boilson, A.R. Polevoi, et al., New J. Phys. **19**, 055004 (2017)
- M.P. Stockli, B. Han, M. Clemmer, et al., Rev. Sci. Instrum. **91**, 013321 (2020)
- K. Tsumori, M. Wada, New J. Phys. **19**, 045002 (2017)
- K. Tsumori, Y. Takeiri, O. Kaneko, et al., Fusion Eng. Technol. **58**, 489–496 (2010)
- A. Ueno, I. Koizumi, K. Ohkoshi, et al., Rev. Sci. Instrum. **85**, 02B133 (2014)
- A. Ueno, K. Ohkoshi, K. Ikegami, et al., AIP Conf. Proc. **1655**, 030010 (2015)
- V. Vahedi, M. Surendra, Comput. Phys. Commun. **87**, 179–198 (1995)
- K. Yee, IEEE Trans. Antennas Propag. **14**, 302–307 (1966)

Chapter 6

Plasma and Gas Neutralisation of High-Energy H^- and D^-



Ronald Stephen Hemsworth and Alexander Panasenkov

Abstract In this chapter, the various reactions occurring when a beam initially composed of only D^- or H^- passes through a hydrogen or deuterium gas or plasma neutraliser are identified and the differential equations governing the evolution of the species mix in the beam are derived, taking account of the likely significant level of dissociation of the neutral gas in the plasma neutraliser. Those equations are solved with the simplifying assumption that the dominant positive ion in the plasma neutraliser is H^+ or D^+ , which is likely to be the case for the degree of ionisation of the plasma required to have a substantial enhancement of the beam neutralisation over that of a simple gas neutraliser.

Additionally, as the cross-section for the various reactions is essential for the calculation of the beam neutralisation, the relevant cross-sections are presented as a function of the projectile energy (in the laboratory frame), the energy range being that which is relevant to future neutral beam systems for a fusion reactor based on magnetic confinement of a reacting plasma.

Results are presented for a 500 keV H^- beam passing through a hydrogen gas neutraliser and a plasma neutraliser with various degrees of ionisation, and different degrees of dissociation of the neutral gas in the plasma neutraliser.

Keywords Plasma · Neutralisation · Negative ion · Neutral beam · Gas neutralisation · Plasma neutralisation · Ionisation fraction · Dissociation · Cross-section · Plasma species · Beam species

R. S. Hemsworth (✉)
Neutral Beam Expert with Fusion for Energy, Barcelona, Spain

A. Panasenkov
National Research Center Kurchatov Institute, Moscow, Russia
e-mail: Panasenkov_AA@nrcki.ru

6.1 Background

Plasma neutralisers have often been suggested as a way to significantly increase the neutralisation of accelerated D^- above that achievable with gas neutralisers, which are used in the present generation of negative ion based neutral beam injectors, and thus to increase the global efficiency of the injectors (Berkner et al. 1980). The plasma neutraliser that is most likely to be used in an injector on a fusion reactor is a deuterium plasma as that avoids contaminating the ion source, the injector pumping system, and the reactor with unwanted gas species. The neutralisation efficiency with a deuterium plasma neutraliser has often been quoted as being greater than or equal to 70% for a sufficiently ionised plasma; it is $\approx 56\%$ for a gas neutraliser. Berkner et al. (1980) give calculations for the neutralisation of 300 keV D^- beam and McAdams (2014) give the neutralisation of a 1 MeV D^- beam; neither take account of the plasma composition, i.e. the mix of positive ion species, the dissociation of the neutral gas, nor the latest measurements, or calculations, of cross-sections.

The design and realisation of a plasma neutraliser are beyond the scope of this chapter. However, it is worth noting that the possible development of a beam-driven plasma neutraliser with the plasma confined by an array of permanent magnets, see Surrey and Holmes (2013) and McAdams (2014), would lead to a significant simplification of the design and operation of such a neutraliser. Also, using a deuterium plasma would reduce the possible pollution of a reacting $D^+ - T^+$ plasma by gas from the neutraliser as well as avoiding the complication of the fuelling and gas recycling system of a fusion reactor that would occur should another gas be used.

It is argued below that the consequence of the presence of molecular ion species in a hydrogen plasma neutraliser with a relevant degree of ionisation is unlikely to be significant. However, whilst the dissociation of the neutral gas will be unimportant for high degrees of ionisation in the plasma neutraliser (since there will be relatively few neutral particles present), high levels of ionisation of the plasma in the neutraliser are very difficult to achieve, and dissociation could be significant at lower, perhaps achievable, ionisation levels (e.g. $\leq 20\%$), which, as shown by Berkner et al. (1980), McAdams (2014), and the calculations presented below, can still lead to a significant enhancement of the beam neutralisation compared to that achievable with a simple gas neutraliser.

In this chapter the relevant reactions between a D^- or H^- beam and the neutral and charged particles in a plasma, or gas, neutraliser are identified, and the differential equations that need to be solved in order to calculate the neutralisation of a D^- or H^- beam passing through a gas or a plasma neutraliser are derived. Those equations can be solved both numerically and analytically, which allows the species mix in the beam as a function of the line density in the neutraliser (defined in Sect. 6.4 below) to be calculated, from which the gas or plasma target needed to obtain the maximum neutralisation efficiency for a D^- or H^- beam can be obtained.

As the cross-section for the various reactions is key to such calculations, a literature survey has been carried out to identify the best available measurements and/or calculated values of the relevant cross-sections. Those cross-sections are presented as a function of the energy of the projectile particles over a range of energies that are relevant to future neutral beam systems for a fusion reactor based on the magnetic confinement of a reacting plasma.

Results are presented for a 500 keV H^- beam passing through a neutraliser with various degrees of ionisation in the neutraliser and different degrees of dissociation of the neutral gas in the neutraliser.

6.2 Reactions

In this section, and throughout the following text, the fast particles in a reaction are underlined, e.g. $\underline{H^-}$ is the fast H^- fraction in the beam.

With few exceptions, the cross-sections of $\underline{D^-}$, $\underline{D^0}$, and $\underline{D^+}$ reacting with D , D_2 and positive deuterium ions have not been measured, but some of the equivalent reactions with $\underline{H^-}$, $\underline{H^0}$, and $\underline{H^+}$ have been. However, the cross-sections with fast deuterium particles are the same as those with fast hydrogen particles at the same interaction velocity, i.e. with twice the fast hydrogen particle energy, hence the change of species when $\underline{D^-}$ passes through a deuterium gas or plasma neutraliser will be equivalent to the species change when $\underline{H^-}$ with half the $\underline{D^-}$ energy passes through a hydrogen gas or plasma neutraliser if that plasma has the same species mix as the deuterium gas or plasma neutraliser. In the rest of this section, only reactions with fast hydrogen particles are discussed.

A hydrogen plasma will contain the following species: H^+ , H_2^+ , H_3^+ , *electrons*, H and H_2 ; a gas neutraliser will contain only H and H_2 . A plasma neutraliser will also contain some H^- , but the density of H^- will be very low and will be assumed to be negligible. A beam initially consisting of only $\underline{H^-}$ will, during its passage through a gas or plasma neutraliser, create $\underline{H^0}$ and $\underline{H^+}$. As the momentum transfer cross-sections are very small at the energies of interest (≈ 500 keV/nucleon), those particles will have essentially the same energy as the initial $\underline{H^-}$. Possible charge-changing reactions between the three types of fast particles ($\underline{H^-}$, $\underline{H^0}$ and $\underline{H^+}$) and the particles in the gas or plasma neutraliser and the possible reaction channels are given in Table 6.1.

Several energetically possible reaction channels would lead to changing the mass of the fast particle that results from the reaction. As momentum must be conserved in the reaction, only a very limited number of the reactant and product trajectories can meet that criterion. Therefore, it is assumed that those reaction channels will have very small cross-sections, and those reactions are not included in Table 6.1. The excluded reaction channels are given in Table 6.2.

It is possible that slow H^- is formed by electron capture from the projectile $\underline{H^-}$ or $\underline{H^0}$ in some of the reactions listed in Table 6.1, but there is no mention of slow H^- formation in the literature. It seems probable that those reaction channels have

very small cross-sections. That is likely since an electron detached from \underline{H}^- or \underline{H}^0 will have an energy that is high compared to the binding energy with H^0 (0.75 eV) and, in order for the detached electron to be captured by an H atom, the energy of the detached electron would need to be reduced to below 0.75 eV. In the case of detachment from 500 keV, \underline{H}^- or \underline{H}^0 projectile, the velocity of the detached electron would be the same as, or very similar to, that of the precursor \underline{H}^- or \underline{H}^0 , so its energy would be ≈ 272 eV. Therefore, it is very unlikely that the detached electron would be captured by an H atom, and the cross sections for such reaction channels are assumed to be very small. They are not included in Table 6.1.

Table 6.1 Charge-changing reactions between the three types of fast particles in the beam (\underline{H}^- , \underline{H}^0 , and \underline{H}^+) and the particles in the gas or plasma neutraliser and the possible reaction channels

Reaction	Channel	Symbol	Reaction number	Figure
$\underline{H}^- + \underline{H}^+ \Rightarrow$	$\underline{H}^0 + H$	$P1_{-1,0,a}$	1a	Fig. 6.1
	$\underline{H}^0 + H^+ + e$	$P1_{-1,0,b}$		
	$\underline{H}^+ + H^+ + 2e$	$P1_{-1,1}$	1b	Fig. 6.2
$\underline{H}^- + H_2^+ \Rightarrow$	$\underline{H}^0 + H_2^+ + e$	$P2_{-1,0}$	2a	
	$\underline{H}^0 + H_2$			
	$\underline{H}^0 + H^+ + H + e$			
	$\underline{H}^0 + 2H^+ + 2e$			
	$\underline{H}^+ + H_2^+ + 2e$	$P2_{-1,1}$	2b	
	$\underline{H}^+ + H_2 + e$			
	$\underline{H}^+ + H^+ + H + 2e$			
	$\underline{H}^+ + 2H + e$			
$\underline{H}^- + H_3^+ \Rightarrow$	$\underline{H}^0 + H_3^+ + e$	$P3_{-1,0}$	3a	
	$\underline{H}^0 + H_2 + H$			
	$\underline{H}^0 + H_2 + H^+ + e$			
	$\underline{H}^0 + 3H$			
	$\underline{H}^0 + 2H + H^+ + e$			
	$\underline{H}^0 + 2H^+ + H + 2e$			
	$\underline{H}^0 + 3H^+ + 3e$			
	$\underline{H}^0 + H_2^+ + H + e$			
	$\underline{H}^0 + H_2^+ + H^+ + 2e$	$P3_{-1,1}$	3b	
	$\underline{H}^+ + H_3^+ + 2e$			
	$\underline{H}^+ + H_2^+ + H + 2e$			
	$\underline{H}^+ + H_2^+ + H^+ + 3e$			
	$\underline{H}^+ + H_2 + e$			
	$\underline{H}^+ + H^+ + H + 2e$			
	$\underline{H}^+ + 2H^+ + 3e$			
	$\underline{H}^+ + 3H^+ + 4e$			

(continued)

Table 6.1 (continued)

Reaction	Channel	Symbol	Reaction number	Figure
$\underline{H}^- + H_2 \Rightarrow$	$\underline{H}^0 + H_2 + e$	$S2_{-1,0}$	4a	Fig. 6.3
	$\underline{H}^0 + H_2^+ + 2e$			
	$\underline{H}^0 + 2H$			
	$\underline{H}^0 + H^+ + H + 2e$			
	$\underline{H}^0 + 2H^+ + 3e$			
$\underline{H}^- + H_2 \Rightarrow$	$\underline{H}^+ + H_2 + e$	$S2_{-1,1}$	4b	Fig. 6.4
	$\underline{H}^+ + H_2^+ + 2e$			
	$\underline{H}^+ + H^+ + H + 2e$			
	$\underline{H}^+ + 2H^+ + 3e$			
	$\underline{H}^+ + 2H + 2e$			
$\underline{H}^- + H \Rightarrow$	$\underline{H}^0 + H + e$	$S1_{-1,0}$	5a	Fig. 6.3
	$\underline{H}^0 + H^+ + 2e$			
	$\underline{H}^+ + H + 2e$	$S1_{-1,1}$	5b	Fig. 6.4
$\underline{H}^- + e \Rightarrow$	$\underline{H}^0 + 2e$	$SE_{-1,0}$	6a	Fig. 6.1
	$\underline{H}^+ + 3e$	$SE_{-1,1}$	6b	Fig. 6.2
$\underline{H}^+ + H_2 \Rightarrow$	$\underline{H}^0 + H_2^+$	$S2_{1,0}$	7a	Fig. 6.5
	$\underline{H}^0 + H^+ + H$			
	$\underline{H}^0 + 2H^+ + e$			
	$\underline{H}^- + 2H^+$	$S2_{1,-1}$	7b	Fig. 6.9
$\underline{H}^+ + H \Rightarrow$	$\underline{H}^0 + H^+$	$S1_{10}$	8	Fig. 6.5
$\underline{H}^0 + H \Rightarrow$	$\underline{H}^+ + H + e$	$S1_{0,1}$	9	Fig. 6.7
$\underline{H}^0 + H_2 \Rightarrow$	$\underline{H}^+ + H_2 + e$	$S2_{0,1}$	10	Fig. 6.6
	$\underline{H}^+ + 2H + e$			
	$\underline{H}^+ + H + H^+ + 2e$			
	$\underline{H}^- + H_2^+$	$S2_{0,-1}$	10b	Fig. 6.7
	$\underline{H}^- + 2H^+ + e$			
$\underline{H}^- + 2H^+$				
$\underline{H}^0 + e \Rightarrow$	$\underline{H}^+ + 2e$	$SE_{0,1}$	11	Fig. 6.8
$\underline{H}^0 + H^+ \Rightarrow$	$\underline{H}^+ + H^+ + e$	$P1_{0,1}$	12	Fig. 6.10
$\underline{H}^0 + H_2^+ \Rightarrow$	$\underline{H}^+ + H_2^+ + e$	$P2_{0,1}$	13a	
	$\underline{H}^+ + H^+ + H + e$			
	$\underline{H}^+ + 2H^+ + 2e$			
	$\underline{H}^- + 2H^+$	$P2_{0,-1}$	13b	
$\underline{H}^0 + H_3^+ \Rightarrow$	$\underline{H}^+ + H_2 + H$	$P3_{0,1}$	14a	
	$\underline{H}^+ + 3H$			
	$\underline{H}^+ + H^+ + 2H + e$			
	$\underline{H}^+ + 2H^+ + H + 2e$			
	$\underline{H}^+ + 3H^+ + 3e$			
	$\underline{H}^- + H_2^+ + H^+$	$P3_{0,-1}$	14b	
$\underline{H}^- + 3H^+ + e$				

Table 6.2 Reaction channels not listed in Table 6.1

$\underline{H}^- + H^+ \Rightarrow H^+ + H + e$	$\underline{H}^- + H_3^+ \Rightarrow \underline{H}_2^+ + H^+ + 2e$
$\underline{H}^- + H^+ \Rightarrow \underline{H}_2$	$\underline{H}^- + H_3^+ \Rightarrow \underline{H}_3^+ + H + e$
$\underline{H}^- + H^+ \Rightarrow \underline{H}_2^+ + e$	$\underline{H}^- + H_3^+ \Rightarrow \underline{H}_3^+ + H^+ + 2e$
$\underline{H}^- + H_2^+ \Rightarrow \underline{H}_2^0 + H$	$\underline{H}^- + H_2 \Rightarrow \underline{H}_2^+ + H + 2e$
$\underline{H}^- + H_2^+ \Rightarrow \underline{H}_2^0 + H^+ + e$	$\underline{H}^- + H_2 \Rightarrow \underline{H}_2^+ + H^+ + 3e$
$\underline{H}^- + H_2^+ \Rightarrow \underline{H}_2^+ + H$	$\underline{H}^- + H_2 \Rightarrow \underline{H}_3^+ + 2e$
$\underline{H}^- + H_2^+ \Rightarrow \underline{H}_3^+ + e$	$\underline{H}^- + H \Rightarrow \underline{H}_2^+ + 2e$
$\underline{H}^- + H_3^+ \Rightarrow \underline{H}_2^0 + 2H$	$\underline{H}^+ + H_2 \Rightarrow \underline{H}_2^+ + H$
$\underline{H}^- + H_3^+ \Rightarrow \underline{H}_2^0 + H^+ + H + e$	$\underline{H}^0 + H \Rightarrow \underline{H}^- + H^+$
$\underline{H}^- + H_3^+ \Rightarrow \underline{H}_2^0 + 2H^+ + 2e$	$\underline{H}^0 + H \Rightarrow \underline{H}_2^+ + e$
$\underline{H}^- + H_3^+ \Rightarrow \underline{H}_2^+ + H + e$	

The symbols given in the third column of Table 6.1 are used in the equations below for calculating the species change as an \underline{H}^- beam traverses a hydrogen plasma neutraliser. Their interpretation is:

- $S1_{x,y}$ for reactions with H ;
- $S2_{x,y}$ for reactions with H_2 ;
- $P1_{x,y}$ for reactions with H^+ ;
- $P2_{x,y}$ for reactions with H_2^+ ;
- $P3_{x,y}$ for reactions with H_3^+ ;
- $SE_{x,y}$ for reactions with electrons;

where the subscripts x and y indicate the charge of the fast initial and product fast species with 1 corresponding to a positive charge, 0 to no charge and -1 to a negative charge. Note that reaction $P1_{-1,0}$ has two channels, which have been designated $P1_{-1,0,a}$ and $P1_{-1,0,b}$ to clarify some explanation of this reaction in Table 6.3 and in the caption to Fig. 6.1 below.

6.3 Basic Equations

The equations governing the change in \underline{H}^- , \underline{H}^0 and \underline{H}^+ as they pass through the neutraliser in the x direction are:

$$\begin{aligned}
 \frac{d\underline{H}^-}{dx} = & \{-P1_{-1,0} * H^+ - P1_{-1,1} * H^+ - P2_{-1,0} * H_2^+ - P2_{-1,1} * H_2^+ \\
 & - P3_{-1,0} * H_3^+ - P3_{-1,1} * H_3^+ - S2_{-1,0} * H_2 - S2_{-1,1} * H_2 \\
 & - S1_{-1,0} * H - S1_{-1,1} * H - SE_{-1,0} * n_e - SE_{-1,1} * n_e\} * \underline{H}^- \\
 & + S21_{-1} * H_2 * \underline{H}^+ + S10_{-1} * H * \underline{H}^0 + S20_{-1} * H_2 * \underline{H}^0 \\
 & + P20_{-1} * \underline{H}^0 * H_2^+ + P30_{-1} * \underline{H}^0 * H_3^+
 \end{aligned} \tag{6.1}$$

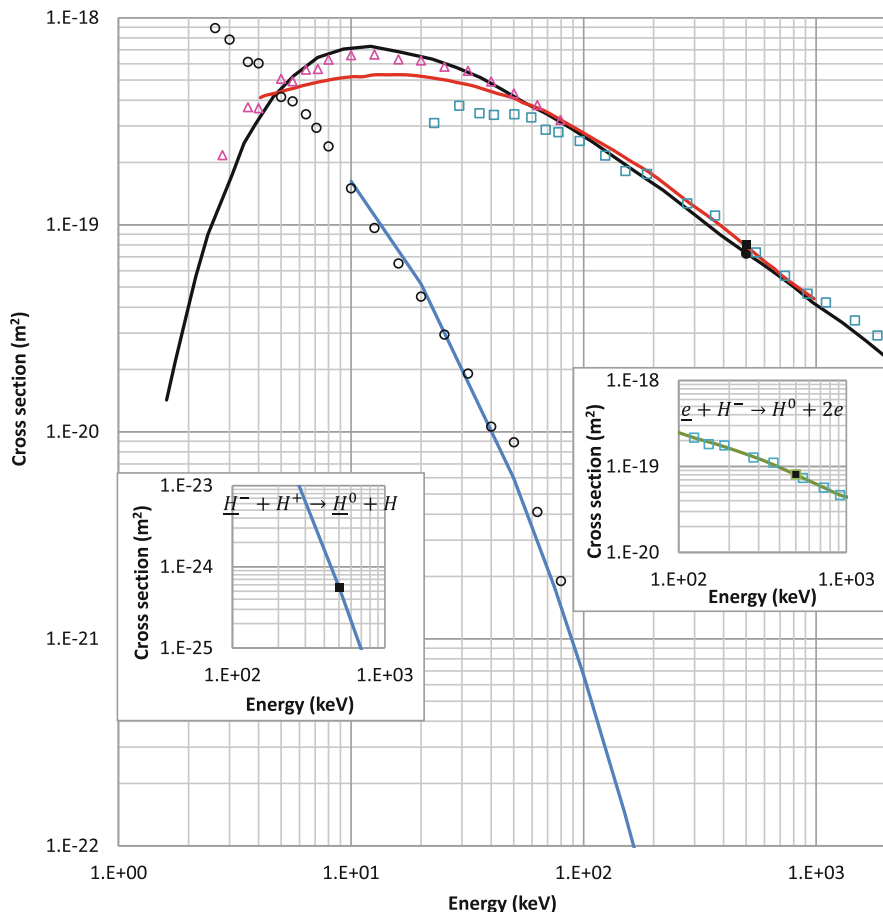


Fig. 6.1 The black and the red curves are the calculated cross sections for $P1_{-1,0,b}$, i.e. $H^- + H^+ \rightarrow H^0 + H + e$ from Belčić (1997), Ling et al. (2007) and L. Ling, 2019, private communication respectively as a function of the projectile energy. The open, magenta, triangles are the measurements of Melchert et al. (1999), the open light blue squares are the measurements of Peart et al. (1976) of $e + H^- \rightarrow H^0 + 2e$, plotted as though H^- were the projectile, i.e. with the same interaction velocity. The black, filled, circle and square show the fits to the black and red curves for an interaction energy of 500 keV of $7.25 \times 10^{-20} \text{ m}^2$, $8 \times 10^{-20} \text{ m}^2$, respectively. The “by eye” fit to the Peart et al. (1976) data for $SE_{-1,0}$ is $8.1 \times 10^{-20} \text{ m}^2$, see the insert on the right side of the figure.

The open, black, circles are the measured cross sections for $P1_{-1,0,a}$ from Schön et al. (1987), Szücs et al. (1984), and Melchert et al. (1999) and the light blue curve shows the calculated cross sections for $P1_{-1,0,a}$ from Mančev et al. (2013). The cross section for $P1_{-1,0,a}$, i.e. $H^- + H^+ \rightarrow H^0 + H$ calculated by Mančev et al. (2013) at an interaction energy of 500 keV is $5.63 \times 10^{-25} \text{ m}^2$, see the insert on the left side of the figure

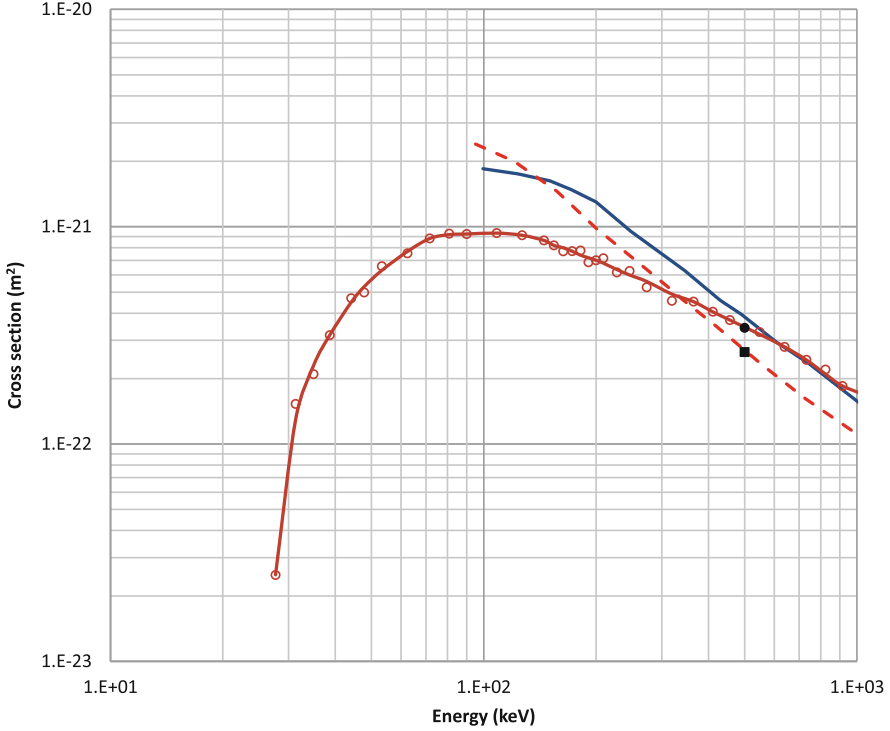


Fig. 6.2 Cross sections for SE_{-1,1}, i.e. $\underline{H}^- + e \rightarrow \underline{H}^+ + 3e$ (blue curve) and P1_{-1,1}, i.e. $\underline{H}^- + H^+ \rightarrow \underline{H}^+ + H^+ + 2e$ (red curve, red dash curve and open red circles) as a function of the projectile energy. The red, open, circles are the measurements of Yu et al. (1992) and the red curve is a by-eye fit to those data. The blue and the red dash curves are the calculated values for the cross sections for SE_{-1,1} and P1_{-1,1}, i.e. $\underline{H}^- + H^+ \rightarrow \underline{H}^+ + H^+ + 2e$, from Belkić (1999) as a function of the projectile energy. The black filled circle is a fit to the red curve and the black, filled, square is a fit to the red dash curve at 500 keV, $3.43 \times 10^{-22} \text{ m}^2$ and $2.65 \times 10^{-22} \text{ m}^2$ respectively

$$\begin{aligned} \frac{d\underline{H}^0}{dx} = & \left\{ -S1_{0,1} * \underline{H} - S1_{0,-1} * \underline{H} - S2_{0,1} * \underline{H}_2 \right. \\ & - S2_{0,-1} * \underline{H}_2 - SE_{0,1} * n_e - P1_{0,1} * \underline{H}^+ - P2_{0,1} * \underline{H}_2^+ \\ & \left. - P2_{0,-1} * \underline{H}_2^+ - P3_{0,1} * \underline{H}_3^+ - P3_{0,-1} * \underline{H}_3^+ \right\} * \underline{H}^0 \\ & + P1_{-1,0} * \underline{H}^+ * \underline{H}^- + P2_{-1,0} * \underline{H}_2^+ * \underline{H}^- \\ & + P3_{-1,0} * \underline{H}_3^+ * \underline{H}^- + S2_{-1,0} * \underline{H}_2 * \underline{H}^- + S1_{-1,0} * \underline{H} * \underline{H}^- \\ & + SE_{-1,0} * n_e * \underline{H}^- + S2_{1,0} * \underline{H}_2 * \underline{H}^+ + S1_{1,0} * \underline{H} * \underline{H}^+ \end{aligned} \quad (6.2)$$

$$\underline{H}^+ = 1 - \underline{H}^- - \underline{H}^0 \quad (6.3)$$

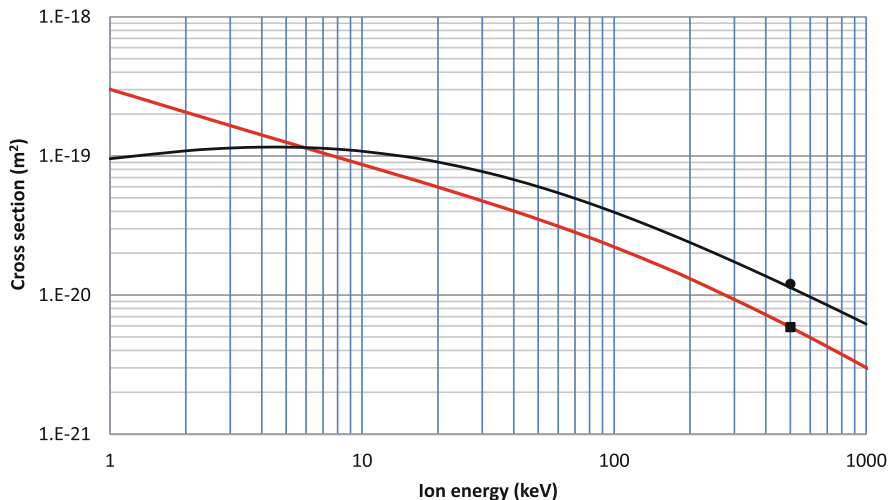


Fig. 6.3 Cross sections for $S2_{-1,0}$, i.e. $\underline{H}^- + H_2 \rightarrow \underline{H}^0 + \dots$, black curve, and $S1_{-1,0}$, i.e. $\underline{H}^- + H \rightarrow \underline{H}^0 + \dots$, red curve, as a function of the projectile energy from the compilation edited by Barnett (1990). The black, filled, circle and square show the fits to the black and red curves for an interaction energy of 500 keV of $1.13 \times 10^{-20} \text{ m}^2$ and $5.89 \times 10^{-21} \text{ m}^2$ respectively

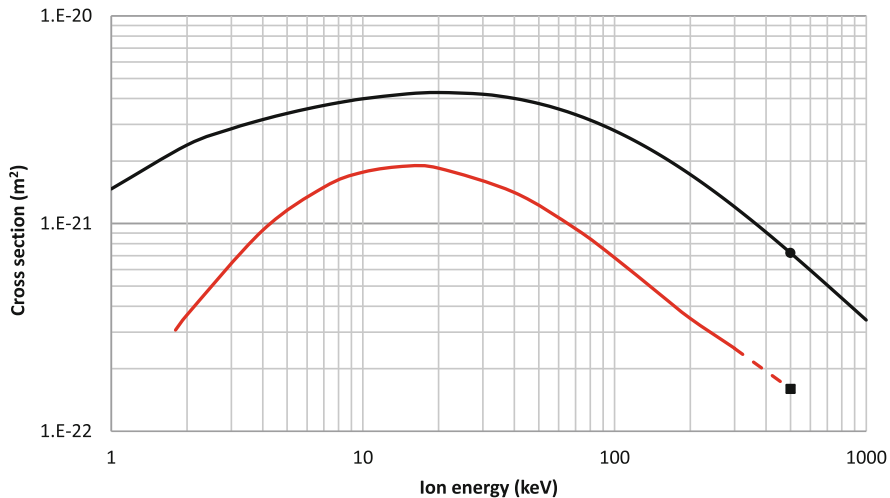


Fig. 6.4 Cross-sections for $S2_{-1,1}$, i.e. $\underline{H}^- + H_2 \rightarrow \underline{H}^+ + \dots$, black curve, and $S1_{-1,1}$, i.e. $\underline{H}^- + H \rightarrow \underline{H}^+ + \dots$, red curve, as a function of the projectile energy from the compilation edited by Barnett (1990). The black filled square is a simple by-eye extrapolation of the red curve to 500 keV ($1.6 \times 10^{-22} \text{ m}^2$). The black filled circle is a fit to the black curve at 500 keV ($7.22 \times 10^{-22} \text{ m}^2$)

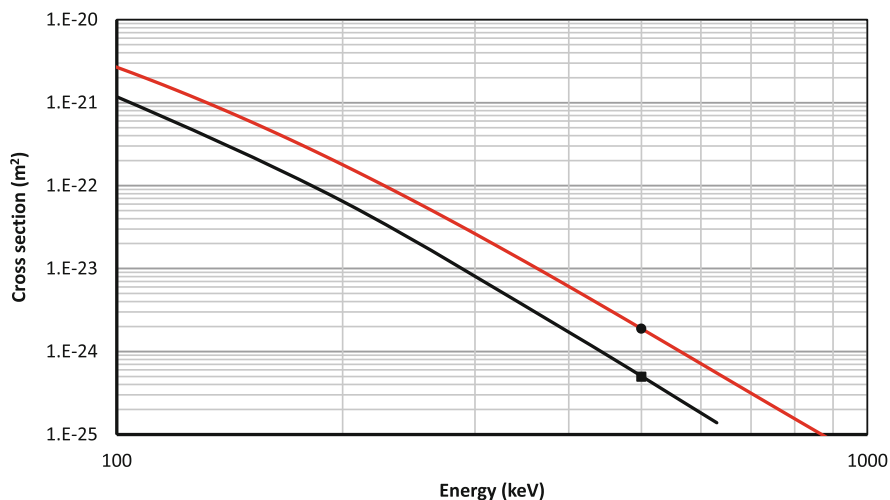


Fig. 6.5 Cross-sections for $S2_{1,0}$, i.e. $H^+ + H_2 \rightarrow H^0 + \dots$, red curve, and $S1_{1,0}$, i.e. $H^+ + H \rightarrow H^0 + H^+$, black curve, as a function of the projectile energy from the compilation edited by Barnett (1990). The black filled circle and square points are the fits to the red and black curves at 500 keV, $1.88 \times 10^{-24} \text{ m}^2$ and $4.95 \times 10^{-25} \text{ m}^2$ respectively

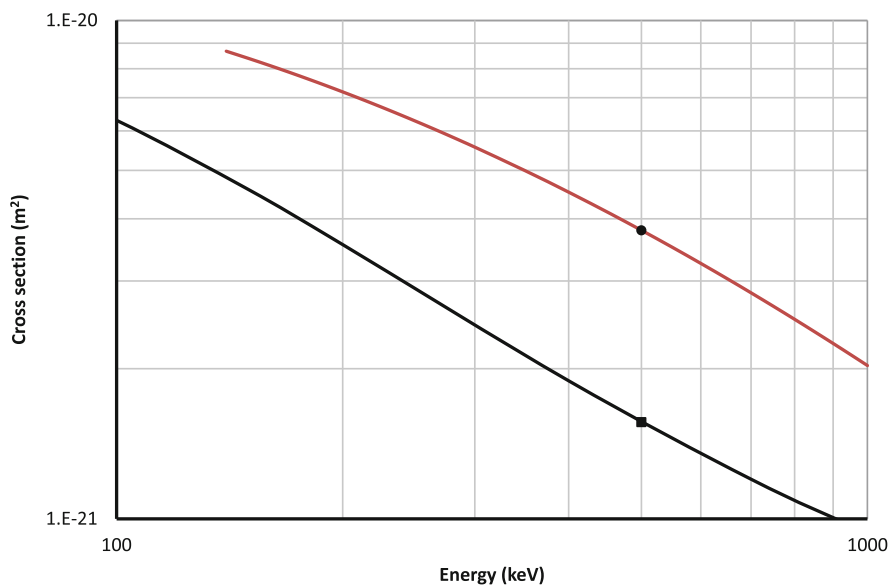


Fig. 6.6 Cross-sections for $S2_{0,1}$, i.e. $H^0 + H_2 \rightarrow H^+ + \dots$, red curve, and $S1_{0,1}$, i.e. $H^0 + H \rightarrow H^+ + H + e$, black curve, as a function of the projectile energy from the compilation edited by Barnett (1990). The black filled circle and square points are the fits to the red and black curves at 500 keV, $3.79 \times 10^{-21} \text{ m}^2$ and $1.56 \times 10^{-21} \text{ m}^2$ respectively

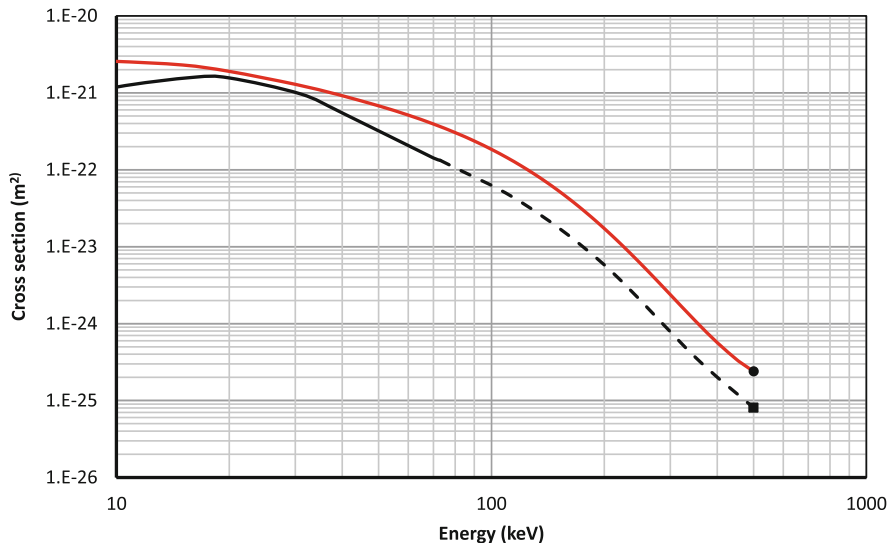


Fig. 6.7 Cross-sections for $S_{20,-1}$, i.e. $H^0 + H_2 \rightarrow H^- + \dots$, red curve, and $S_{10,-1}$, i.e. $H^0 + H \rightarrow H^- + H^+$, black curve, as a function of the projectile energy from the compilation edited by Barnett (1990). The black dash curve is an extrapolation of the black curve assuming that the ratio $S_{20,-1}/S_{10,-1}$ remains constant from 73 keV to 500 keV. The black filled circle and square are fits to the red and black dash curve at 500 keV, $2.39 \times 10^{-25} \text{ m}^2$ and $8.1 \times 10^{-26} \text{ m}^2$ respectively

In the above equations, H , H_2 , H^+ , H_2^+ and H_3^+ are the densities of those (slow) particles and n_e is the electron density in the neutraliser.

The above equations can be solved numerically for a given species composition in the neutraliser, if all the relevant cross-sections were known. *Unfortunately, no measurement or calculation of any of the cross-sections for the reactions between the H^- beam and the molecular ion species have been found in the literature.* A similar situation exists for measurements of a number of the other reactions, especially at the interaction velocities of interest for neutral beam injectors on a fusion reactor, i.e. when the fast, heavy (hydrogenic) particle has an energy of the order of 500 keV/nucleon. Therefore:

Some assumptions about the unknown cross-sections are necessary to solve the equations.

Experience with positive ion sources used for neutral beam injection has shown that with ionisation rates of $<2\%$, the dominant positive ion is H^+ and that the proton fraction increases as the degree of ionisation increases. As will be seen below, a plasma neutraliser needs to have an ionisation fraction $\gg 2\%$, hence the first assumption is that the H_2^+ and H_3^+ densities in the plasma neutraliser will be

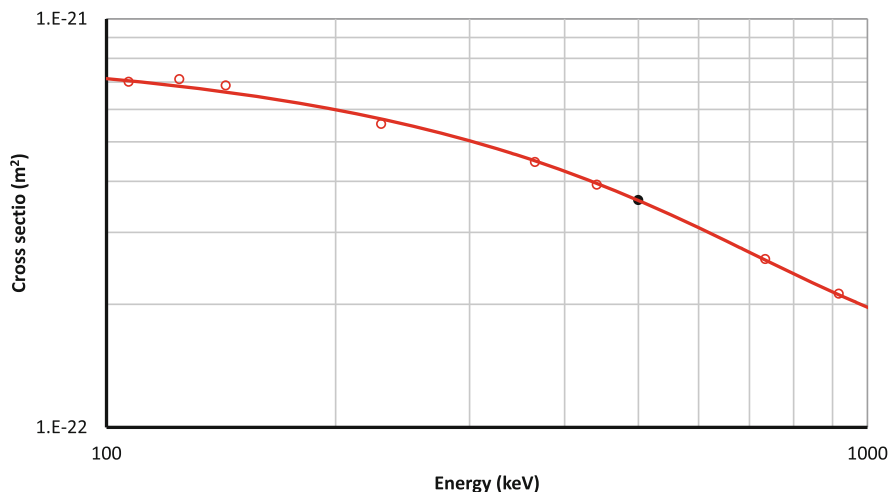


Fig. 6.8 Cross-sections for $SE_{0,1}$, i.e. $\underline{H}^0 + e \rightarrow \underline{H}^+ + 2e$ as a function of the projectile energy from Fite and Brackmann (1958), plotted with \underline{H}^0 as the projectile, i.e. with the same interaction velocity as in the measurements, which used the electron as the projectile. The open red circles are the measured values and the red line is a polynomial fit to the data. The black filled circle is a fit to the red curve at 500 keV, $3.55 \times 10^{-21} \text{ m}^2$

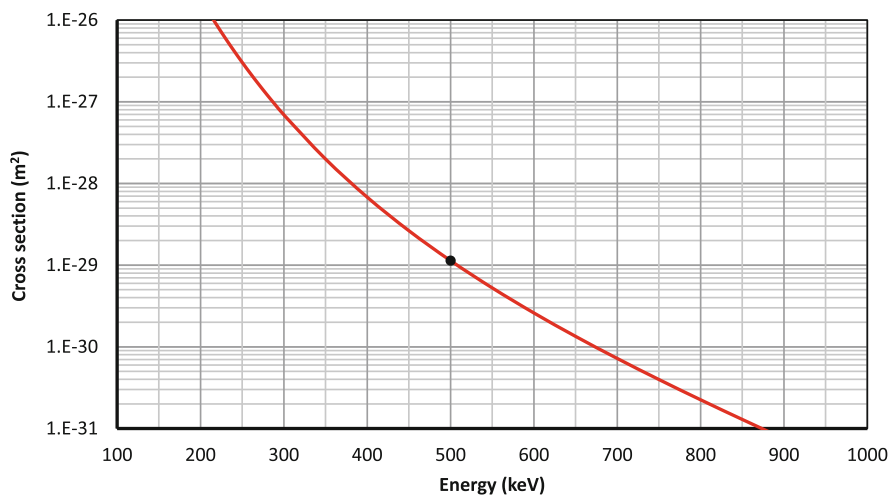


Fig. 6.9 Cross-sections for $S2_{1,-1}$, i.e. $\underline{H}^+ + H_2 \rightarrow \underline{H}^- + \dots$, red curve as a function of the projectile energy from the compilation edited by Barnett (1990). The black filled circle is a fit to the red curve at 500 keV, $1.13 \times 10^{-29} \text{ m}^2$

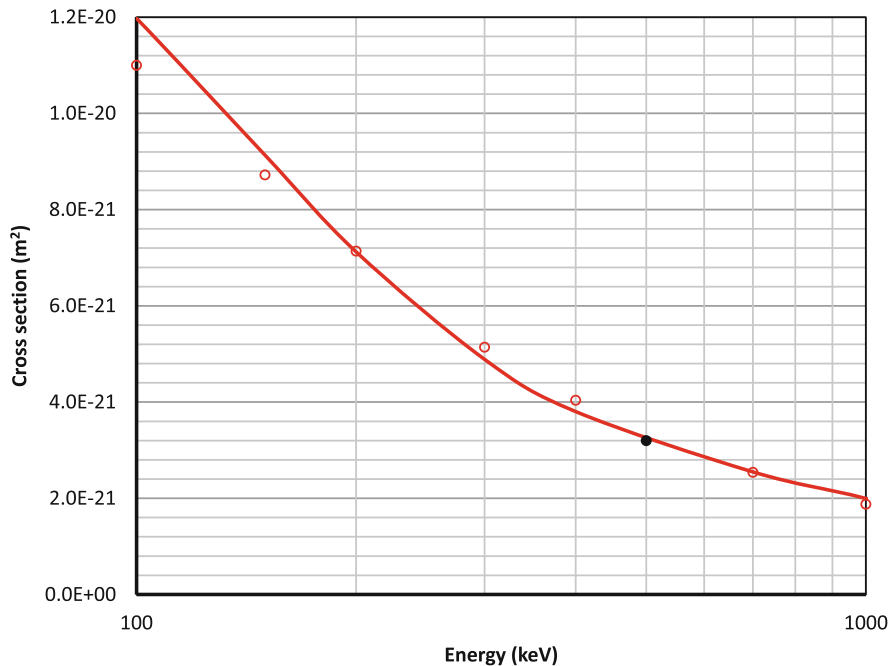


Fig. 6.10 Cross-sections for $P_{10,1}$, i.e. $H^0 + H^+ \rightarrow \underline{H}^+ + H^+ + e$, red curve as a function of the projectile energy from the compilation edited by Barnett (1990). The black filled circle is a fit to the red curve at 500 keV, $3.2 \times 10^{-21} \text{ m}^2$

very low and thus that reactions with those ions can be neglected, i.e. it is assumed that:

$$H_2^+ = H_3^+ = 0 \quad (6.4)$$

$$H^+ = n_e \quad (6.5)$$

It is worth noting that assuming that the cross-sections with H_2^+ and H_3^+ are the same as with H^+ gives the same result.

Secondly, the cross-sections for the channels of the reactions 6.7b, 6.9b, 6.10b, 6.13b and 6.14b, would lead to \underline{H}^- formation in collisions of \underline{H}^+ with H_2 , and of \underline{H}^0 with H , H_2 , H_2^+ and H_3^+ respectively are assumed to be small, and they are set to zero. This assumption seems reasonable at high projectile energies as, in each case, the electron(s) detached from the target particle need to be accelerated in the collision from the speed of the target particle, which will be very low compared to the projectile particle, up to the speed of the projectile particle, and the detached electrons must be travelling in the same direction as the projectile particle. As momentum must be conserved in the reaction, such events are likely to be very rare.

With the above-mentioned assumptions, Eqs. 6.1 and 6.2 above reduce to:

$$\begin{aligned} \frac{d\underline{H}^-}{dx} = & \left\{ -P_{1,-1,0} * H^+ - P_{1,-1,1} * H^+ - S_{2,-1,0} * H_2 - S_{2,-1,1} * H_2 \right. \\ & \left. - S_{1,-1,0} * H - S_{1,-1,1} * H - SE_{-1,0} * n_e - SE_{-1,1} * n_e \right\} * \underline{H}^- \\ & + S_{2,1,-1} * H_2 * \underline{H}^+ + S_{1,0,-1} * H * \underline{H}^0 + S_{2,0,-1} * H_2 * \underline{H}^0 \end{aligned} \quad (6.6)$$

$$\begin{aligned} \frac{d\underline{H}^-}{dx} = & \left\{ - (P_{1,-1,0} + P_{1,-1,1} + SE_{-1,0} + SE_{-1,1}) * n_e - S_{2,-1,0} * H_2 \right. \\ & \left. - S_{2,-1,1} * H_2 - S_{1,-1,0} * H - S_{1,-1,1} * H \right\} * \underline{H}^- + S_{2,1,-1} * H_2 * \underline{H}^+ \\ & + (S_{1,0,-1} * H + S_{2,0,-1} * H_2) * \underline{H}^0 \end{aligned} \quad (6.7)$$

$$\begin{aligned} \frac{d\underline{H}^0}{dx} = & \left\{ -S_{1,0,1} * H - S_{1,0,-1} * H - S_{2,0,1} * H_2 - S_{2,0,-1} * H_2 \right. \\ & \left. - SE_{0,1} * n_e - P_{1,0,1} * H^+ \right\} * \underline{H}^0 + P_{1,-1,0} * H^+ * \underline{H}^- \\ & + S_{2,-1,0} * H_2 * \underline{H}^- + S_{1,-1,0} * H * \underline{H}^- + SE_{-1,0} * n_e * \underline{H}^- \\ & + S_{2,1,0} * H_2 * \underline{H}^+ + S_{1,1,0} * H * \underline{H}^+ \end{aligned} \quad (6.8)$$

$$\begin{aligned} \frac{d\underline{H}^0}{dx} = & \left\{ -S_{1,0,1} * H - (S_{2,0,1} + S_{2,0,-1}) * H_2 - (SE_{0,1} + P_{1,0,1}) * n_e \right\} * \underline{H}^0 \\ & + (P_{1,-1,0} + SE_{-1,0}) * n_e * \underline{H}^- + S_{2,-1,0} * H_2 * \underline{H}^- + S_{2,1,0} * H_2 * \underline{H}^+ \\ & + S_{1,-1,0} * H * \underline{H}^- + S_{1,1,0} * H * \underline{H}^+ \end{aligned} \quad (6.9)$$

6.4 Cross-Sections

It is evident that using the correct values of the cross-sections is necessary if the calculation of the change in the beam species as the beam passes through the neutraliser is to be accurate. Therefore, a careful evaluation of the cross-sections available in the literature has been carried out, as discussed below. However, as neither the measurements nor the calculations of the required cross-sections are perfect, the effect of changing the values of the cross-sections is discussed further in Sect. 6.7.

Typically, the cross-sections for 500 keV \underline{H}^- are not directly given in the literature, so these were deduced either by using the Chebyshev fits to the experimental data given in the compilation of Barnett (1990) (the fits are excellent in all the relevant cases) or by a by-eye fit to the experimental data in the references. Figures 6.1, 6.2, 6.3, 6.4, 6.5, 6.6, 6.7, 6.8, 6.9, and 6.10 show the cross-section data as a function of the interaction energy over relevant energy ranges as well as the value at

500 keV (for the heavy particles). Only the latest measurements or calculations that are known to the authors are shown in Figs. 6.1, 6.2, 6.3, 6.4, 6.5, 6.6, 6.7, 6.8, 6.9, and 6.10.

The cross-section of the two channels for electron detachment from H^- by protons ($P1_{-1,0,a}$ and $P1_{-1,0,b}$) have not been measured for H^- energies above ≈ 100 keV. However, recent calculations of those cross-sections (Belkić 1997; Ling et al. 2007; L. Ling, 2019, private communication) that overlap with the measured values and extend to projectile energies of 500 keV, have a good agreement where the measured and calculated cross-sections overlap, which gives confidence in deducing the value for a,500 keV H^- projectiles from a fit to the calculated values around 500 keV, see Fig. 6.1. However, as the cross-sections for $P1_{-1,0,b}$ calculated by Belkić (Belkić 1997) agree somewhat better with the measured cross-sections where they overlap than those calculated by Ling et al (2007) and L. Ling, 2019, private communication, the cross-section calculated at 500 keV by Belkić ($7.25 \times 10^{-20} \text{ m}^2$) is preferred over that calculated by L. Ling, 2019, private communication ($8.0 \times 10^{-20} \text{ m}^2$) for the calculations presented below. Using the value calculated by L. Ling, 2019, private communication has only a small effect on the results presented below.

Note that in Figs. 6.1, 6.2, 6.3, 6.4, 6.5, 6.6, 6.7, 6.8, 6.9, and 6.10 the energy of the projectile is given in the laboratory frame of reference, with the target considered to be at rest.

In Table 6.3 below the letter and digits after (Barnett 1990), are the page designation in that reference.

Table 6.3 Selected cross-sections for an initial 500 keV H^- beam passing through a hydrogen plasma

Reaction symbol	Cross-section (m^2)	References	Figure
$P1_{-1,0,b}$	5.63×10^{-25}	(Mančev et al. 2013)	Fig. 6.1
$P1_{-1,0,b}$	7.25×10^{-20}	(Belkić 1997)	Fig. 6.1
$P1_{-1,1}$	2.65×10^{-22}	(Belkić 1999)	Fig. 6.2
$S2_{-1,0}$	1.13×10^{-20}	(Barnett 1990) F8	Fig. 6.3
$S1_{-1,0}$	5.89×10^{-21}	(Barnett 1990) F2	Fig. 6.3
$S2_{-1,1}$	7.22×10^{-22}	(Barnett 1990) F10	Fig. 6.4
$S1_{-1,1}$	1.6×10^{-22}	(Barnett 1990) F4	Fig. 6.4
$SE_{-1,0}$	8.1×10^{-20}	(Peart et al. 1970)	Fig. 6.1
$SE_{-1,1}$	3.43×10^{-22}	(Yu et al. 1992)	Fig. 6.2
$S1_{1,0}$	4.95×10^{-25}	(Barnett 1990) A22	Fig. 6.5
$S2_{1,0}$	1.88×10^{-24}	(Barnett 1990) A28	Fig. 6.5
$P1_{0,1}$	3.2×10^{-21}	(Barnett 1990) D6	Fig. 6.10
$S2_{0,1}$	3.79×10^{-21}	(Barnett 1990) E6	Fig. 6.6
$S2_{0,-1}$	2.39×10^{-25}	(Barnett 1990) A8	Fig. 6.7
$S2_{1,-1}$	1.13×10^{-29}	(Barnett 1990) A30	Fig. 6.9
$S1_{0,1}$	1.56×10^{-21}	(Barnett 1990) E2	Fig. 6.6
$S1_{0,-1}$	8.1×10^{-26}	(Barnett 1990) A2	Fig. 6.7
$SE_{0,1}$	3.55×10^{-21}	(Fite and Brackmann 1958)	Fig. 6.8

6.5 Calculation Method

For small changes in x , Eqs. 6.6 and 6.7 become:

$$d\underline{H}^- = \left[\begin{aligned} & - (P1_{-1,0} + P1_{-1,1} + SE_{-1,0} - SE_{-1,1}) * n_e - S2_{-1,0} * H_2 \\ & - S2_{-1,1} * H_2 - S1_{-1,0} * H - S1_{-1,1} * H \} * \underline{H}^- + S2_{1,-1} * H_2 * \underline{H}^+ \\ & + (S1_{0,-1} * H + S2_{0,-1} * H_2) * \underline{H}^0 \end{aligned} \right] * dx \quad (6.10)$$

$$d\underline{H}^0 = \left[\begin{aligned} & - (S1_{0,1} + S1_{0,1}) * H - (S2_{0,1} + S2_{0,-1}) * H_2 \\ & - (SE_{0,1} + P1_{0,1}) * n_e \} * \underline{H}^0 + (P1_{-1,0} + SE_{-1,0}) * n_e * \underline{H}^- \\ & + S2_{-1,0} * H_2 * \underline{H}^- + S2_{1,0} * H_2 * \underline{H}^+ + S1_{-1,0} * H * \underline{H}^- \\ & + S1_{1,0} * H * \underline{H}^+ \end{aligned} \right] * dx \quad (6.11)$$

Now:

The plasma ionisation fraction, f_{ion} is defined as:

$$f_{\text{ion}} = \frac{H^+ + H_2^+ + H_3^+}{H + H_2 + H^+ + H_2^+ + H_3^+} \quad (6.12)$$

Substituting for H^+ , H_2^+ and H_3^+ from Eqs. 6.4 and 6.5 in Eq. 6.10:

$$f_{\text{ion}} = \frac{n_e}{H + H_2 + n_e} \quad (6.13)$$

Re-arranging Eq. 6.13:

$$H + H_2 = n_e * \left\{ \frac{1 - f_{\text{ion}}}{f_{\text{ion}}} \right\} \quad (6.14)$$

The dissociation degree of the neutral gas, f_{diss} is defined as:

$$f_{\text{diss}} = \frac{H/2}{H_2 + H/2} \quad (6.15)$$

Rearranging Eq. 6.15:

$$H = \frac{2 * f_{\text{diss}}}{(1 - f_{\text{diss}})} * H_2 \quad (6.16)$$

Substituting for H from Eq. 6.16 into Eq. 6.14 and rearranging:

$$H_2 = n_e * \left\{ \frac{(1 - f_{\text{ion}}) * (1 - f_{\text{diss}})}{f_{\text{ion}} * (1 + f_{\text{diss}})} \right\} \quad (6.17)$$

Substituting for H_2 from Eq. 6.17 into Eq. 6.16 and rearranging:

$$H = \left\{ \frac{2 * f_{\text{diss}} * (1 - f_{\text{ion}})}{f_{\text{ion}} * (1 + f_{\text{diss}})} \right\} * n_e \quad (6.18)$$

Now it is convenient to calculate the change in the beam species as a function of the line density in the plasma neutraliser rather than calculating it as a function of x . The line density, Π , is defined as:

$$\Pi = (H_2 + H + H^+ + H_2^+ + H_3^+ + n_e) * x \quad (6.19)$$

i.e. it is the sum of all the target particles times the distance through the plasma in the neutraliser.

Substituting for $H^+ + H_2^+ + H_3^+$ from Eqs. 6.4 and 6.5 in Eq. 6.19:

$$\Pi = (H_2 + H + 2 * n_e) * x \quad (6.20)$$

Note that this definition of the line density is the same as that used by Berkner et al. (1980) when there is no dissociation.

It is assumed that the ionisation fraction and the dissociation fraction are constant along the neutraliser, then:

$$d\Pi = (H_2 + H + 2 * n_e) * dx \quad (6.21)$$

Rearranging Eq. 6.21:

$$dx = \frac{d\Pi}{(H_2 + H + 2 * n_e)} \quad (6.22)$$

For simplicity in writing the equations below, let:

$$H = n_e * M \quad (6.23)$$

$$H_2 = n_e * N \quad (6.24)$$

where M and N are constants for a given projectile energy that can be derived from Eqs. 6.15 and 6.16.

Equation 6.22 then becomes:

$$dx = \frac{d\Pi}{n_e * (2 + M + N)} \quad (6.25)$$

Substituting for dx from Eq. 6.25 into Eqs. 6.10 and 6.11:

$$\begin{aligned} d\underline{H}^- = & \left[\left\{ - (P_{1,-1,0} + P_{1,-1,1} + SE_{-1,0} + SE_{-1,1}) * n_e - (S_{2,-1,0} + S_{2,-1,1}) * H_2 \right. \right. \\ & \left. \left. - S_{1,-1,0} * H - S_{1,-1,1} * H \right\} * \underline{H}^- + (S_{1,0,-1} * H + S_{2,0,-1} * H_2) * \underline{H}^0 \right. \\ & \left. + S_{2,1,-1} * H_2 * \underline{H}^+ \right] * \frac{d\Pi}{n_e * (2 + M + N)} \end{aligned} \quad (6.26)$$

$$\begin{aligned} d\underline{H}^0 = & \left[\left\{ - (S_{1,0,1} + S_{1,0,-1}) * H - (S_{2,0,1} + S_{2,0,-1}) * H_2 - (SE_{0,1} + P_{1,0,1}) \right. \right. \\ & \left. \left. * n_e \right\} * \underline{H}^0 + (P_{1,-1,0} + SE_{-1,0}) * n_e * \underline{H}^- + S_{2,-1,0} * H_2 * \underline{H}^- + S_{2,1,0} \right. \\ & \left. * H_2 * \underline{H}^+ + S_{1,-1,0} * H * \underline{H}^- + S_{1,1,0} * H * \underline{H}^+ \right] * \frac{d\Pi}{n_e * (2 + M + N)} \end{aligned} \quad (6.27)$$

Substituting for H and H_2 from Eqs. 6.23 and 6.24 in Eqs. 6.26 and 6.27 and rearranging:

$$\begin{aligned} d\underline{H}^- = & \left[\left\{ - (P_{1,-1,0} + P_{1,-1,1} + SE_{-1,0} + SE_{-1,1}) - (S_{2,-1,0} + S_{2,-1,1}) * N \right. \right. \\ & \left. \left. + S_{2,1,-1} * N * \underline{H}^+ + (S_{1,0,-1} * M + S_{2,0,-1} * N) * \underline{H}^0 \right. \right. \\ & \left. \left. - (S_{1,-1,0} + S_{1,-1,1}) * A \right\} * \underline{H}^- \right] * \frac{d\Pi}{(2 + M + N)} \end{aligned} \quad (6.28)$$

$$\begin{aligned} d\underline{H}^0 = & \left[\left\{ - (S_{1,0,1} + S_{1,0,-1}) * M - (S_{2,0,1} + S_{2,0,-1}) * N - (SE_{0,1} + P_{1,0,1}) \right\} * \underline{H}^0 \right. \\ & \left. + (P_{1,-1,0} + SE_{-1,0} + S_{2,-1,0} * B + S_{1,-1,0} * M) * \underline{H}^- \right. \\ & \left. + (S_{2,1,0} * N + S_{1,1,0} * M) * \underline{H}^+ \right] * \frac{d\Pi}{(2 + M + N)} \end{aligned} \quad (6.29)$$

Equations 6.28, 6.29 and 6.3 can be easily solved numerically. This is done by setting \underline{H}^- to 1, and all the other fast species (\underline{H}^0 and \underline{H}^+) to 0. Then, Eqs. 6.28 and 6.29 are used to calculate the reduction in \underline{H}^- and change in \underline{H}^0 as the beam passes through an incremental line density, $d\Pi$. The change in \underline{H}^+ is given by Eq. 6.3. The new values of \underline{H}^- , \underline{H}^0 and \underline{H}^+ are then used in Eqs. 6.28, 6.29 and 6.3 to get the changes in those species over the next $d\Pi$ increment and so on.

Now, for simplicity in writing the equations in the following text, let:

$$\theta 1 = \left\{ (P_{1,-1,0} + P_{1,-1,1} + SE_{-1,0} + SE_{-1,1}) + (S_{2,-1,0} + S_{2,-1,1}) * N \right. \\ \left. + (S_{1,-1,0} + S_{1,-1,1}) * M \right\} / (2 + M + N) \quad (6.30)$$

$$\theta 2 = S_{2,1,-1} * N / (2 + M + N) \quad (6.31)$$

$$\theta 3 = \left\{ S_{10,-1} * M + S_{20,-1} * N \right\} / (2 + M + N) \quad (6.32)$$

$$\varnothing 1 = \left\{ (S_{10,1} + S_{10,-1}) * M + (S_{20,1} + S_{20,-1}) * N \right. \\ \left. + (SE_{0,1} + P_{10,1}) \right\} / (2 + M + N) \quad (6.33)$$

$$\varnothing 2 = \left\{ P_{1,-1,0} + SE_{-1,0} + S_{2,-1,0} * N + S_{1,-1,0} * M \right\} / (2 + M + N) \quad (6.34)$$

$$\varnothing 3 = \left\{ S_{2,1,0} * N + S_{1,1,0} * M \right\} / (2 + M + N) \quad (6.35)$$

Then:

$$d\underline{H}^- = \left[-\theta 1 * \underline{H}^- + \theta 2 * \underline{H}^0 + \theta 3 * \underline{H}^+ \right] * d\Pi \quad (6.36)$$

$$d\underline{H}^0 = \left[-\varnothing 1 * \underline{H}^0 + \varnothing 2 * \underline{H}^- + \varnothing 3 * \underline{H}^+ \right] * d\Pi \quad (6.37)$$

Equations 6.36, 6.37 and 6.3 are essentially the same as the equations solved by Kim and Haselton (1979) for the species variation with an \underline{H}^+ beam passing through an H_2 gas neutraliser, but with different reactions in the equations, hence cross-sections and combinations thereof, and with the initial beam species being \underline{H}^- . The solution to eqs. 6.36, and 6.37 are:

$$H^- = A_1 * \exp(-\alpha_1 * \Pi) + A_2 * \exp(-\alpha_2 * \Pi) + A_3 \quad (6.38)$$

$$H^0 = B_1 * \exp(-\alpha_1 * \Pi) + B_2 * \exp(-\alpha_2 * \Pi) + B_3 \quad (6.39)$$

And H^- can be derived from Eq. 6.3.

In Eqs. 6.38 and 6.39:

$$A_1 = \frac{\alpha_2 * A_3 - \alpha_2 + \varnothing 2 + \theta 1 - \varnothing 2}{(\alpha_1 - \alpha_2)} = \frac{\alpha_2 * A_3 - \alpha_2 + \theta 1}{(\alpha_1 - \alpha_2)} \quad (6.40)$$

$$A_2 = \frac{-\alpha_1 * A_3 + \alpha_1 - \varnothing 2 - (\theta 1 - \varnothing 2)}{(\alpha_1 - \alpha_2)} = \frac{-\alpha_1 * A_3 + \alpha_1 - \theta 1}{(\alpha_1 - \alpha_2)} \quad (6.41)$$

$$A_3 = \frac{p * \theta 3 + \varnothing 3 * (\theta 2 - \theta 3)}{\alpha_1 * \alpha_2} \quad (6.42)$$

$$B_1 = \frac{\alpha_2 * B_3 - \varnothing 2}{\alpha_1 - \alpha_2} \quad (6.43)$$

$$B_2 = \frac{-\alpha_1 * B_3 + \varnothing 2}{\alpha_1 - \alpha_2} \quad (6.44)$$

$$B_3 = \frac{q * \varnothing 3 + \theta 3 * (\varnothing 2 - \varnothing 3)}{\alpha_1 * \alpha_2} \quad (6.45)$$

$$\alpha_1 = \frac{1}{2} * \left\{ p + q + \left[(p - q)^2 + 4 * (\varnothing 2 - \varnothing 3) * (\theta 2 - \theta 3) \right]^{1/2} \right\} \quad (6.46)$$

$$\alpha_2 = \frac{1}{2} * \left\{ p + q - \left[(p - q)^2 + 4 * (\varnothing 2 - \varnothing 3) * (\theta 2 - \theta 3) \right]^{1/2} \right\} \quad (6.47)$$

$$p = \varnothing 1 + \varnothing 3 \quad (6.48)$$

$$q = \theta 1 + \theta 3 \quad (6.49)$$

It is to be noted that there are two errors in the equations given in (Kim and Haselton 1979):

- The 2nd term of Eq. 6.38 (Equation 4 in Kim and Haselton 1979) is written as $A_2 * \exp(\alpha_2 * \Pi)$. That is incorrect as it should be $A_2 * \exp(-\alpha_2 * \Pi)$.
- The numerator of the equation for B_2 is given as $(-\alpha_2 * B_3 + \varnothing 2)$, it should be $(-\alpha_1 * B_3 + \varnothing 2)$, as it is in Eq. 6.44.

Differentiating Eq. 6.39:

$$\frac{dH^0}{d\Pi} = -\alpha_1 * B_1 * \exp(-\alpha_1 * \Pi) - \alpha_2 B_2 * \exp(-\alpha_2 * \Pi) \quad (6.50)$$

The maximum neutral fraction occurs when $\frac{dH^0}{d\Pi} = 0$, ie. when:

$$\{\alpha_1 * B_1 * \exp(-\alpha_1 * \Pi_m) + \alpha_2 B_2 * \exp(-\alpha_2 * \Pi_m)\} = 0 \quad (6.51)$$

where Π_m is the neutralisation target when \underline{H}^0 is at its maximum. Rearranging Eq. 6.51:

$$\frac{\exp(-\alpha_1 * \Pi_m)}{\exp(-\alpha_2 * \Pi_m)} = \exp((\alpha_2 - \alpha_1) * \Pi_m) = \frac{\alpha_2 * B_2}{\alpha_1 * B_1} \quad (6.52)$$

Then we have:

$$\Pi_m = \frac{1}{(\alpha_2 - \alpha_1)} * \ln \left[\frac{\alpha_2 * B_2}{\alpha_1 * B_1} \right] \quad (6.53)$$

The maximum neutral fraction can be found from Eq. 6.39 by setting the neutralisation target to Π_m .

6.6 Results

Equations 6.28, 6.29, and 6.3 have been solved numerically and Eqs. 6.38, 6.39 and 6.3 give the analytical solutions for \underline{H}^- , \underline{H}^0 and \underline{H}^+ . The exact agreement was found between the numerical and analytical solutions; which gives confidence that the analytical solution presented above is both correct and correctly used. Also, the species fractions at the exit of the neutraliser were calculated with no ionised fraction in the neutraliser and no dissociation of the gas, i.e. when the neutraliser is a simple gas neutraliser, for various \underline{H}^- energies and compared to previous calculations, e.g. Hemsworth (2014). Perfect agreement was found when the same cross-sections are used in the two sets of calculations. It is to be noted here that the definition of f_{ion} in Eqs. 6.12 and 6.13 leads to division by zero in those and some subsequent equations when f_{ion} is zero. Therefore, when calculating the species with a gas neutraliser, and using either a numerical solution to Eqs. 6.28, 6.29 and 6.3, or the analytical solutions given above, f_{ion} should be set to a negligible, but non-zero value, such as 10^{-5} .

For all the results reported in this chapter, the \underline{H}^- energy was 500 keV and the calculated cross-section from Belkić (1997) was used for $P1_{-1,0,b}$, i.e. for $\underline{H}^- + H^+ = \underline{H}^0 + H^+ + e$.

Figure 6.11 shows the species fractions at the exit of the neutraliser as a function of the line density in the neutraliser using the cross-sections given in Table 6.3, column 2, for 10% ionisation with no dissociation and 30% dissociation of the neutral gas.

Figure 6.12 shows the calculated \underline{H}^0 fractions as a function of the line density in the plasma neutraliser for various ionisation fractions, with 0%, and 30%

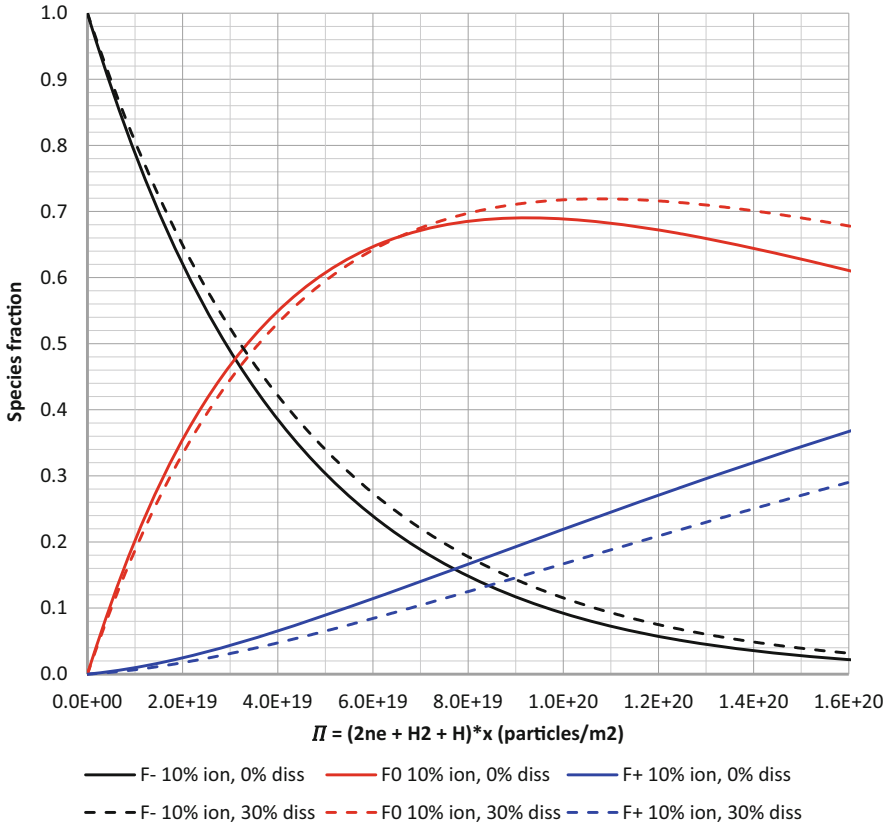


Fig. 6.11 Calculated species fractions as a function of the line density in the plasma neutraliser with 10% ionisation fraction for an H^- energy of 500 keV: the black curves are the H^- fractions, the red curves are the H^0 fractions, and the blue curves are the H^+ fractions. The solid curves are calculated with no dissociation and the dashed curves are the same as the solid curves but with 30% dissociation

dissociation respectively. The legend of each of those figures gives the ionisation fractions associated with each curve.

Figure 6.13 shows the maximum H^0 fraction as a function of the line density in the plasma neutraliser with the ionisation fractions in the plasma neutraliser as indicated in the legend, with no dissociation, 30% dissociation 60% dissociation, which allows the effect of dissociation on the attainable H^0 fraction to be appreciated.

Figure 6.14 shows the maximum H^0 fraction beam as a function of the ionisation fraction in the plasma neutraliser with 0%, 30% and 60% dissociation, and, for comparison, the maximum H^0 fraction calculated by McAdams (2014) with no dissociation of the neutral gas (R. McAdams, 2021, private communication). It has been verified that the difference between the calculations given in (McAdams 2014) and those presented here for no dissociations is the use in (McAdams 2014) of different cross-sections from those given in Table 6.3.

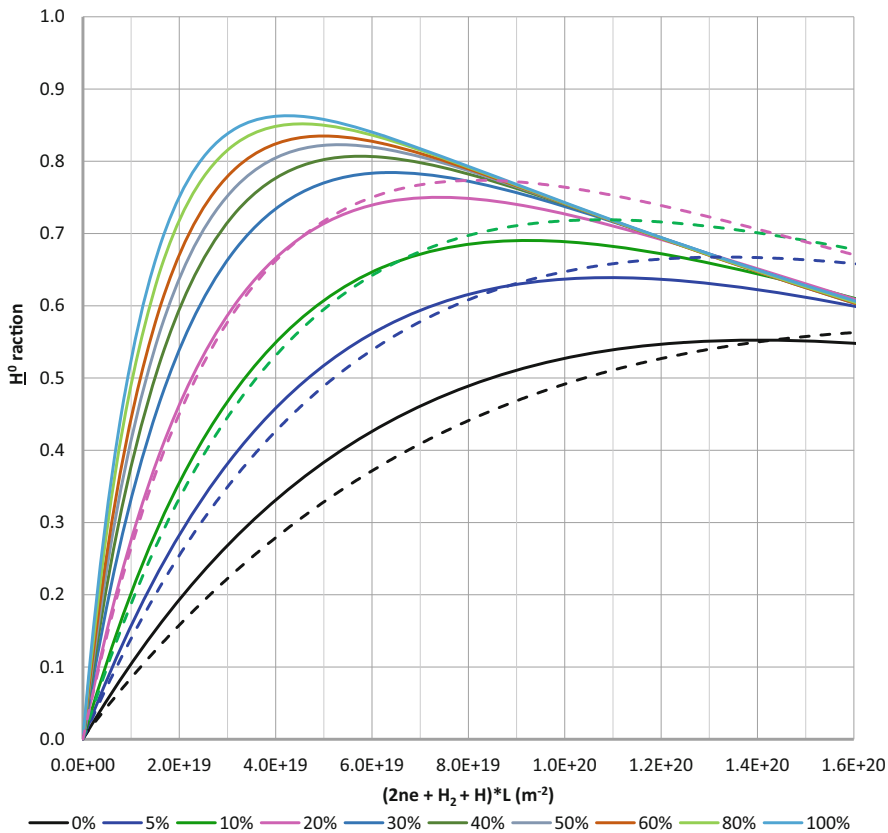


Fig. 6.12 The solid curves show the calculated H^0 fractions as a function of the line density in the plasma neutraliser with no dissociation and the ionisation fractions indicated in the figure legend for an H^- energy of 500 keV. The dashed curves show the calculated H^0 fractions with 30% dissociation for ionisation fractions of 0%, 5%, 10% and 20% using the same colours as for the curves with no dissociation

Figure 6.15 shows the line density required to achieve the maximum H^0 fraction as a function of the degree of ionisation in the plasma neutraliser for the ionisation fractions indicated in the figure legend.

6.7 Discussion and Conclusions

This chapter presents the equations to calculate the expected neutralisation and species mix at the neutraliser exit when using either hydrogen gas, or a hydrogen plasma, to neutralise a high energy beam of H^- , and the analytical solution to those equations is given. In addition, a careful evaluation of the reactions and their

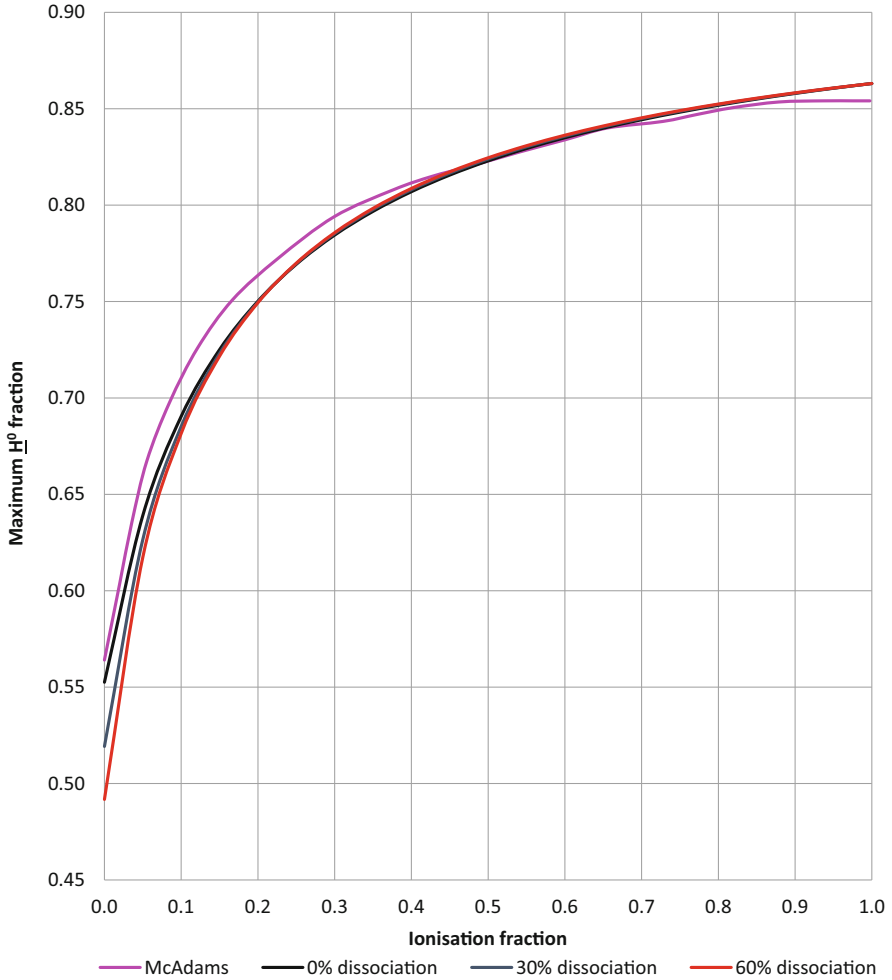


Fig. 6.13 Maximum H^0 fraction from a 500 keV H^- beam as a function of the ionisation fraction in the plasma neutraliser. The black curve is with no dissociation, the blue curve is with 30% dissociation, and the red curve is with 60% dissociation. Shown for comparison is the magenta curve, which is taken from McAdams (2014), which is with no dissociation of the neutral gas (McAdams (2014) and McAdams, 2021, private communication). The difference between the magenta and black curves is due to differences in the cross sections used

associated cross-sections has been carried out and the necessary cross-sections are listed in Table 6.3 along with the values of the cross sections for a beam energy of 500 keV. An exact calculation is not possible as many of the cross sections have been neither measured nor calculated. In particular, no cross-sections are measured or calculated for H^- reacting with any of the molecular ions in the plasma. However, experience with positive ion sources used for neutral beam injection has shown

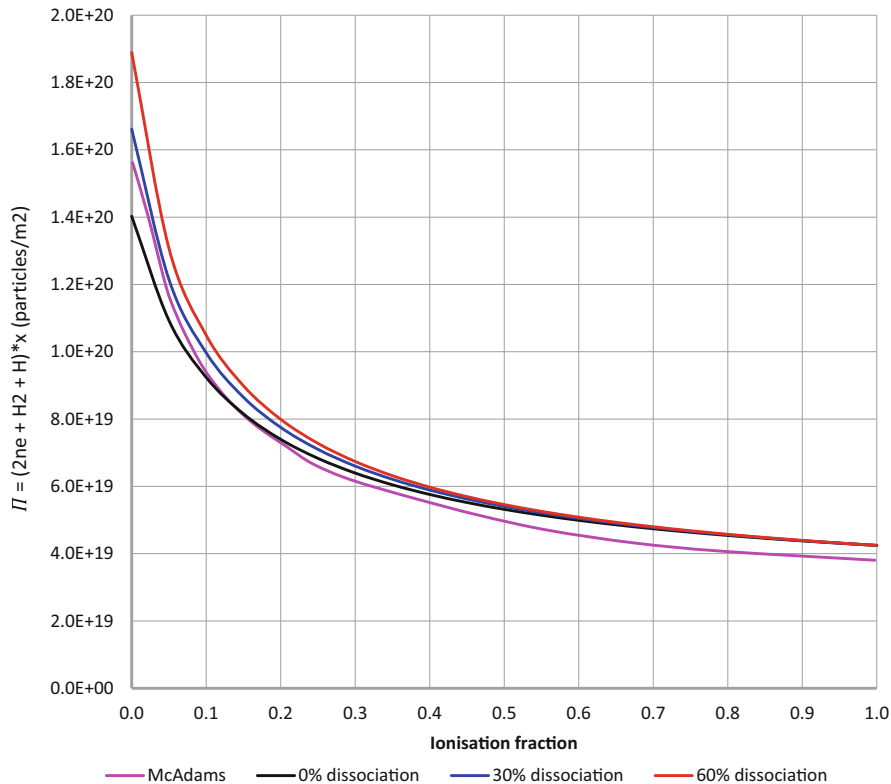


Fig. 6.14 Line density required to achieve the maximum H^0 fraction from a 500 keV H^- beam as a function of the degree of ionisation in the plasma. The black curve is with no dissociation, the blue curve is with 30% dissociation, and the red curve is with 60% dissociation. Shown for comparison is the magenta curve, which is taken from McAdams (2014), which is with no dissociation of the neutral gas (R. McAdams, 2021, private communication). The difference between the magenta and black curves is due to differences in the cross sections used

that with ionisation rates of $<2\%$, the dominant positive ion is H^+ and that the proton fraction increases as the degree of ionisation increases. Therefore, it has been assumed that the density of molecular ions is negligible and therefore that reactions with the molecular ions can be neglected. Also, no measurements are available for the stripping of H^- by protons at any energy close to 500 keV. Fortunately, in the latter case, there are calculated cross-sections, in particular from Belkić (1997) and Ling et al. (2007) that give good agreement with measurements up to H^- energies of 100 keV, which gives confidence in using the calculated cross-sections at higher energies.

The conclusions from the calculations can be summarised as follows:

- 6.1 Figure 6.13 shows that achieving a neutralisation fraction of $\approx 75\%$ requires an ionisation fraction of just above 20% with or without dissociation of up to 60%.

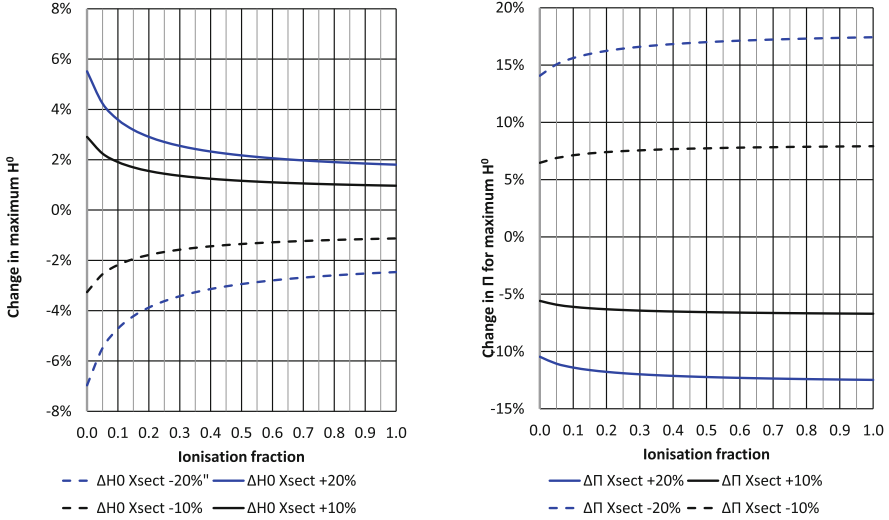


Fig. 6.15 Changes in the calculated maximum neutral fraction and the line density needed to achieve that as a function of the ionisation fraction of the plasma in the neutraliser with the charge changing cross sections of H^- changed by $\pm 10\%$, black curves, or $\pm 20\%$, blue curves, as indicated in the figure legend. The dissociation fraction of the neutral gas is 30% in all cases

- 6.2 Figure 6.11 shows the species fractions obtained from an initial 500 keV H^- beam passing through a hydrogen plasma target with 10% ionisation and with dissociation levels of the neutral gas of 0% and 30%.
- 6.3 Figure 6.12 shows the neutral fraction obtained with various degrees of ionisation as a function of the line density with no dissociation and with 30% dissociation of the neutral gas. It can be seen that the neutral fraction becomes less when there is some dissociation of the neutral gas, but that decrease becomes less as the degree of ionisation increases, becoming negligible for ionisation fractions $\geq 30\%$.
- 6.4 As can be seen from Fig. 6.13, the updated cross-sections given in Table 6.3, column 2 lead to a small decrease in the achievable peak neutralisation fractions with no dissociation for ionisation levels $< 50\%$ compared to the values given by R. McAdams, 2021, private communication. With dissociation the achievable neutralisation increases with dissociation, but for ionisation levels above $\approx 80\%$ the increase is negligible.
- 6.5 Figure 6.14 shows that the necessary line density needed to have the peak neutralisation fraction increases with dissociation, but that is negligible for ionisation fractions above $\approx 60\%$. As plasma neutralisers with ionisation fractions above 60% seem highly unlikely, it can be concluded that dissociation means that higher line densities will be needed to achieve the maximum neutralisation fraction for a realistic plasma neutraliser.

As noted in Sect. 6.2 above, some of the important cross-sections for H^- impacting the ions in a hydrogen plasma neutraliser have not been measured at the energies of interest, but there are calculated values of the cross-section at those energies for some of the cross sections. Unfortunately, there are no measured or calculated cross-sections known to the authors of any of the cross-sections for reactions between H^- and H_2^+ or H_3^+ . Therefore, it has been necessary to assume that the H_2^+ and H_3^+ fractions in the plasma neutraliser will be negligible, which it expected to be the case, or to assume that the cross-sections for the reactions with and H_2^+ and H_3^+ are the same as the reactions with H^+ . Therefore, the authors encourage experimental confirmation of either of those assumptions.

Also, as noted in Sect. 6.4, neither the measurements nor the calculations of the required cross-sections are perfect. Therefore, the consequence of errors in the used cross-sections has been assessed by calculating the effect on the maximum neutral fraction and the required plasma target to reach the maximum neutral fraction of changing the cross-sections leading to a change in charge of the H^- (the first seven cross-sections of Table 6.3) by $\pm 10\%$ and $\pm 20\%$.

The fractional, changes in the maximum achievable H^0 and the line density needed to achieve the maximum H^0 are shown in Fig. 6.15. It can be seen that the changes in the achievable H^0 are small, typically $< 5\%$ even with a 20% change in the cross-sections. The changes in the required line density are small for a change of $\pm 10\%$ in the cross-sections, but they are not negligible for a 20% change in the cross sections, reaching 15–17%.

Overall, it can be concluded that errors in the cross-sections of up to $\pm 20\%$ do not significantly affect the maximum achievable H^0 results presented in this chapter and the change in the required line density is acceptable.

Acknowledgments The authors would like to acknowledge the useful discussions with, and comments and corrections suggested by, Prof. A J T Holmes, Scientific Director Marcham Scientific Ltd., and Dr. R McAdams of the UKAEA.

References

- C. F. Barnett (ed.), ORNL-6086, 1990. Available to download at: https://inis.iaea.org/collection/NCLCollectionStore/_Public/22/011/22011031.pdf
- D. Belkić, J. Phys. B Atomic Mol. Phys. **30**, 1731–1745 (1997)
- D. Belkić, Nucl. Inst. Methods Phys. Res. B **154**, 62–72 (1999)
- K.H. Berkner, R.V. Pyle, S.E. Savas, K.R. Stalder, *Second International Symposium on the Production and Neutralization of Negative Ions and Beams* (Brookhaven National Laboratory, Upton, NY, 1980), pp. 293–297. Available to download at: https://inis.iaea.org/collection/NCLCollectionStore/_Public/12/614/12614518.pdf
- W.L. Fite, R.T. Brackmann, Phys. Rev. **112**, 1141–1151 (1958)
- R. S. Hemsworth, ITER IDM, reference: Neutralisation (76NBCJ v1.5) (2014)
- J. Kim, H.H. Haselton, J. Appl. Phys. **50**(6), 3802–3807 (1979)
- L. Ling, W. Jian-Guo, Chin. Phys. Lett. **24**(11), 3115–3118 (2007)
- I. Mančev, N. Milojević, D. Belkić, EPL **103**, 23001 (2013)

- R. McAdams, *Rev. Sci. Inst.* **85**, 02B319 (2014)
- F. Melchert, S. Krüdner, K. Huber, E. Salzborn, *J. Phys. B Atomic Mol. Opt. Phys.* **32**, L139–L144 (1999)
- B. Peart, D.S. Walton, K.T. Dolder, *J. Phys. B: Atom. Molec. Phys.* **3**, 1346–1356 (1970)
- B. Peart, R. Grey, K.T. Dolder, *J. Phys. B: Atom. Molec. Phys.* **9**(17), 3047–3053 (1976)
- W. Schön, S. Krüdner, F. Melchert, K. Rinn, M. Wagner, E. Salzborn, *J. Phys. B: At. Mol. Phys.* **20**, L759 (1987)
- E. Surrey, A. Holmes, *AIP Conf. Proc.* **1515**, 532–540 (2013)
- S. Szücs, M. Karemera, M. Terao, F. Brouillard, *J. Phys. B: At. Mol. Phys.* **17**, 1613–1622 (1984)
- D.J. Yu, S. Rachat, J. Jureta, P. Defrance, *J. Phys. B Atomic Mol. Opt. Phys.* **25**, 4593–4460 (1992)

Chapter 7

Advanced Models for Negative Ion Production in Hydrogen Ion Sources



Roberto Celiberto, Mario Capitelli, Annarita Laricchiuta,
Lucia Daniela Pietanza, and Gianpiero Colonna

Abstract An advanced chemical model, based on the state-to-state approach, is applied to the modeling of a multicusp negative ion source. Simulations are performed with the *GPKin* kinetic code that solves the Boltzmann equation for free electrons self-consistently coupled with the Master Equations, following the evolution of the non-equilibrium electron energy distribution function (EEDF) and the vibrational kinetics of the ground and excited singlet electronic states of the H₂ molecule. The virtual experiments reproduce the conditions of an experiment in the literature, showing the predictive character of the present approach and validating the model. The sensitivity of the results to the selected database of cross-sections for the electron impact-induced processes is investigated, clarifying the impact of more accurate datasets for specific processes in the mechanisms of negative ion production.

Keywords H₂ cross-section database · Self-consistent kinetics · Vibrational kinetics · Non-equilibrium EEDF · Metastable state

7.1 Introduction

Neutral beam injection is the efficient heating mechanism powering TOKAMAK devices. The beam is produced by accelerating and neutralizing negative ions from different plasma sources, helicon, ECR, RF, intensively investigated experimentally

R. Celiberto

Dipartimento di Ingegneria Civile, Ambientale, del Territorio, Edile e di Chimica (DICATECh),
Politecnico di Bari, Bari, Italy

CNR ISTP (Istituto per la Scienza e Tecnologia dei Plasmi) Bari Section, Bari, Italy

M. Capitelli · A. Laricchiuta · L. D. Pietanza · G. Colonna (✉)

CNR ISTP (Istituto per la Scienza e Tecnologia dei Plasmi) Bari Section, Bari, Italy

e-mail: gianpiero.colonna@cnr.it

© The Author(s), under exclusive license to Springer Nature Switzerland AG 2023

M. Bacal (ed.), *Physics and Applications of Hydrogen Negative Ion Sources*,

Springer Series on Atomic, Optical, and Plasma Physics 124,

https://doi.org/10.1007/978-3-031-21476-9_7

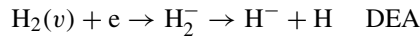
(Taccogna et al. 2021; Zamengo et al. 2021; Agnello et al. 2019; Aleiferis et al. 2018; Bentounes et al. 2018). The predictive modeling of negative ion sources is considered a priority goal in the fusion community and large efforts have been put in the last decade to detail the plasma properties with real-geometry multi-dimensional simulations (Taccogna et al. 2021; Fubiani et al. 2017), able to aid the solution of engineering in the different regions of source, from the negative ion production to the extraction to form the beam. Global, zero-dimensional kinetic models, despite their inability to account for those aspects, are still relevant to the full understanding of the mechanisms of negative ion formation, implementing advanced chemical schemes and identifying the processes whose accuracy critically impacts the model reliability. In fact, the assessment of data accuracy and uncertainty quantification are the main issues the community of theoretical chemistry is facing (Chung et al. 2016), not to mention the need for consistency in level-specific datasets. Ab initio models require, in principle, the knowledge of the cross-section data for all the collision and radiative processes occurring at the level of the microscopic particles. For plasma systems containing molecules, two aspects should be stressed in the formulation of theoretical modeling. The first point is represented by the fact that the rovibronic internal degrees of freedom of molecular species characterize the behaviour of the molecules in the plasma so that each quantum state plays an independent role in collision physics. As a consequence, the number of active species is not limited to the chemical compounds present in the system but is extended to all the possible molecular quantum states (Capitelli et al. 2009). This gives rise to a plethora of collision processes, to be included in a simulation, that demands the determination of scattering cross-sections for the appropriate range of collision energies and for each accessible quantum state. This entails, as a second aspect, the knowledge of very large sets of cross-section data to be used as primary information of an ab initio modeling, which can be achieved by resorting to theoretical calculations based on fast and as accurate as possible computational methods.

The present contribution focuses on hydrogen negative ion multicusp source, where a role of utmost importance is played by electron impacts with internally excited H_2 molecules (Taccogna et al. 2021; Capitelli et al. 2006; Bacal and Hamilton 1979). Cross-sections data for these processes, involving in particular the H_2 vibrational levels have been produced in the past decades by resorting to a wide spectrum of classical, semiclassical and quantum mechanical methods, and a brief review is provided in Ref. (Celiberto et al. 2022). For instance, one of the most popular approaches, among the others, to the electron-molecule cross-section calculations, is represented by the Gryzinski method (Gryziński 1965) as formulated for molecules by Bauer and Bartky (1965), which, being characterized by simplicity and computational rapidity, has found particular favour in the fusion community. The method, in fact, has been largely applied to electron-impact collisions (Celiberto et al. 2001a; Wunderlich 2021; Li et al. 2022) despite its limitations, coming from the classical and semi-empirical description of the electron motion, the uncertainty in setting some computational parameters (Bauer and Bartky 1965) and the complete suppression of quantum phenomena in electron-scattering.

Recently, new sets of cross-section data, obtained by the molecular convergent close-coupling (MCCC) quantum mechanical approach, have been made available in the literature for electron- H_2 collisions (Scarlett et al. 2017, 2018, 2019, Tapley et al. 2018a, b; Zammit et al. 2016, 2017), so that a reformulation of a plasma modeling for negative ion production, based on input cross-section data of a better accuracy, is in order. In Sect. 7.2 we review the old and new cross-sections, while in Sect. 7.3 the details of the numerical model for the multicusp negative ion source are illustrated. In Sect. 7.4 the kinetic model and the simulation conditions are detailed. The results for the kinetic simulation of the H_2 plasma in the multicusp source, the sensitivity analysis and the comparison with the experiments are discussed in Sect. 7.5. Conclusions are drawn in Sect. 7.6.

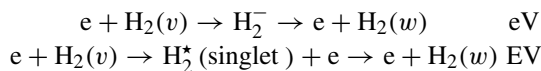
7.2 H_2 Cross-Sections

It is well assessed that the process leading to the production of H^- in volume sources is the dissociative electron attachment (DEA), via the resonant electron capture in a bound state of the temporary molecular negative ion



DEA is highly efficient when initiated from vibrationally excited molecules, being the cross-section lowered in the threshold energy and enhanced of orders of magnitudes in the peak absolute value (Bardsley and Wadehra 1979). The DEA spectrum is characterized by three main peaks associated with the relevant resonances at 3.6 eV ($X^2\Sigma_u^+$), 10 eV ($B^2\Sigma_g^+$) and 14 eV (the Rydberg $2\Sigma_g^+$ state), and the dynamics has been deeply investigated in the past (Celiberto et al. 2001a, 2012, 2013; Horáček et al. 2004, 2006; Wadehra 1986; Bardsley and Wadehra 1979), despite the role of dissociative attachment from Rydberg states of H_2 molecule, lying close to the H_2^+ ground state, which is still an open problem in the literature (Hassouni et al. 1998; Pinnaduwege et al. 1999).

The large dependence of DEA cross-sections makes the onset of the vibrational non-equilibrium in the H_2 distribution (VDF) in volume negative ion sources key in the accurate description of the mechanism of formation of negative ions. The vibrational pumping results from the interplay of two processes



the low-energy electrons, promoting the resonant vibrational excitations (eV processes) that is a competing channel to DEA, and the electrons of higher energy able to excite the high-threshold singlets of the spectrum, radiatively coupled to the ground state and involved in an indirect two-step EV mechanism of vibrational

excitation, mainly populating the tail of the H₂ VDF. The $B^1\Sigma_u^+$ and $C^1\Pi_u$ states have been identified as the main contributors (Hiskes 1980, 1991; Hiskes and Karo 1984, 1989) to the radiative cascade and the low-lying Rydberg singlets, belonging to the same symmetries, account for the remaining fraction.

A complete database of vibrational-specific cross-sections also considering the role of the dissociative radiative decay processes, relevant for the vibrational levels lying close to the dissociation limit, was obtained by Celiberto et al. (1994, 2001a) and Laricchiuta et al. (2006), exploiting the semi-classical impact parameter method (IPM) and allowed also the investigation on the existence of an isotopic effect (Celiberto et al. 2001b). Recently, a complete revision of the database of electron-impact induced processes has been carried out by the theoretical group in Perth, deriving complete state-resolved cross-sections in the framework of the MCCC formalism and setting the reference for dynamical results (Scarlett et al. 2017, 2018, 2019; Tapley et al. 2018a, b; Zammit et al. 2016, 2017).

A systematic comparison of MCCC cross-sections with the semiclassical IPM shows that the larger deviations are localized in the near-threshold region, where, as expected and in line with other first-order approaches, the IPM overestimates the cross-section, while a substantial agreement is observed above 100 eV. In Fig. 7.1, the distribution versus the final vibrational levels at 50 eV of the collision energy (a value close to the maximum of cross-sections) for excitations starting from $v_i = 0$ and 10 are shown, the CCC results including all the relevant radiative singlets in the spectrum, while the IPM only the four principal contributors, i.e. B , B' , C and D singlet states. The MCCC results are in striking agreement with those obtained by Hiskes (1991) for the $v_i = 0 \rightarrow v_f$ excitations, while the IPM approach overestimates the cross-sections. It is worth noting that the discrepancy remains within a factor of two and is even compressed when initial vibrational excited levels

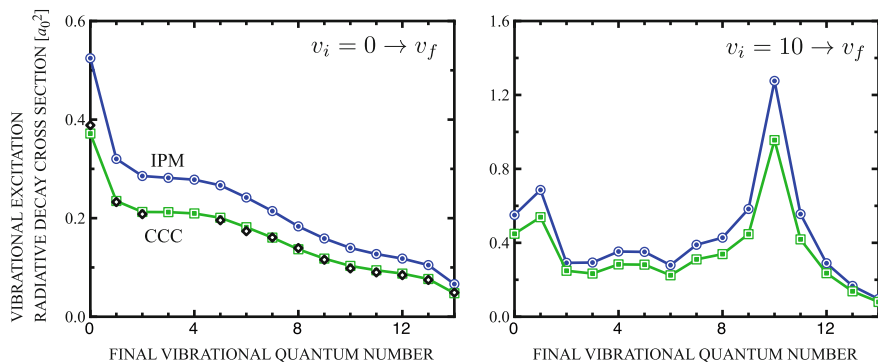


Fig. 7.1 Distribution of vibrational excitation radiative decay EV cross-sections versus final vibrational quantum number for excitations from the $v_i = 0$ and 10 at the collision energy $E = 50$ eV. (Circles) IPM approach (Celiberto et al. 2001a; Laricchiuta et al. 2006), (squares) CCC method (Scarlett et al. 2019), (diamonds) Hiskes results (Hiskes 1991). (Reproduced from Taccogna et al. (2021). Reproduced with permission of Springer Nature)

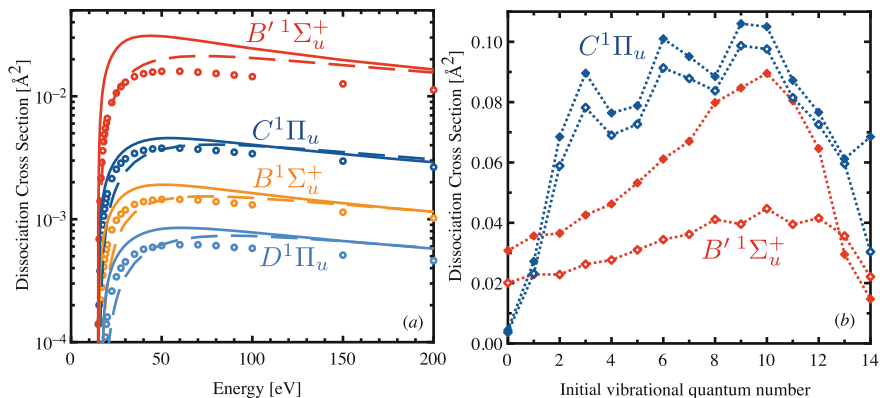


Fig. 7.2 (a) Direct dissociative excitation cross-sections through singlet states from the $v_i = 0$: solid lines (Celiberto et al. 2001a), long-dashed lines (MCCC database; Tapley et al. 2018b), open circles (Liu et al. 2011); (b) Direct dissociative excitation cross-sections as a function of the initial vibrational quantum number at the collision energy $E = 50$ eV for the $B'^1\Sigma_u^+$ and $C^1\Pi_u$ states. Close diamonds (Celiberto et al. 2001a), open diamonds (MCCC database; Tapley et al. 2018b)

are considered, as shown for $v_i = 10$. The satisfactory comparison confirms that the semi-classical approach could be a reasonable choice for non-resonant excitations in dipole-allowed transitions.

The same general considerations can be extended to the direct dissociative excitation processes induced by electron impact in singlet states, as appreciable in Fig. 7.2a, where the energy profile for the dissociative transitions through the first four singlets and initiated from the $v_i = 0$ level obtained within the IPM (Celiberto et al. 2001a) and MCCC (Tapley et al. 2018b) methods are displayed and also compared with the cross-sections estimated in Ref. (Liu et al. 2011) within a modified Born approximation with an excitation shape function experimentally measured.¹ In Fig. 7.2b, the vibrational profiles for the dissociative excitations through the B' , C states at a selected value of the collision energy, demonstrate the agreement for transitions initiated from vibrationally excited molecules and the capability of IPM to correctly reproduce the vibrational dependence and to give a quantitative estimation within a factor 2 in the worst case.

The H_2 dissociation channels by electron impact are also of great relevance in the vibrational kinetic scheme, being the process responsible for destroying the vibrational content of molecules on one hand and possibly leading to the production of excited atomic species on the other.

Actually, the H_2 dissociation proceeds mainly through the triplet states, i.e. the purely repulsive $b^3\Sigma_u^+$ state and the $a^3\Sigma_g^+$ and $c^3\Pi_u$ states with direct and indirect mechanisms that will be discussed in Sect. 7.4.

¹ Reported results from Ref. (Liu et al. 2011) correspond to $T = 300$ K, assuming negligible contribution from vibrationally excited state.

The state-specific dissociation cross-sections for the excitation to the $b^3\Sigma_u^+$ state have been obtained in the past in the framework of different theories, namely the classical Gryzinski (Celiberto et al. 2001a), quantum R-matrix (Stibbe and Tennyson 1998; Trevisan and Tennyson 2002) and complex Kohn variational (Rescigno and Schneider 1988) approaches, showing a general agreement. The results for the first vibrational levels are displayed in Fig. 7.3a, b for the threshold and the maximum energy regions, respectively. In the same figures the old available experimental measurements for the level $v_i = 0$, obtained with accurate electron energy-loss spectroscopy (EELS) (Khakoo and Segura 1994; Nishimura and Danjo 1986), are reported. The newly calculated MCCC results (Scarlett et al. 2018; MCCC database), however, have changed the scene, predicting for $v_i = 0$ a different position of the maximum with an absolute value a factor two smaller and reconciling for the vibrational dependence to the R-Matrix results in Ref. (Stibbe and Tennyson 1998). This triggered new experiments with a transmission-free time-of-flight electron spectrometer eventually finding an excellent agreement (Zawadzki et al. 2018) between experiment and theory. In Fig. 7.3c the comparison of the MCCC cross-sections for higher vibrational levels (MCCC database) with the only complete dataset previously available (Celiberto et al. 2001a) is displayed, exhibiting a markedly different behavior in both the energy and vibrational dependence and thus expecting to have a significant impact in the H_2 plasma kinetics.

The same is observed for the excitation to $a^3\Sigma_g^+$ and $c^3\Pi_u$ states, whose MCCC cross-sections are compared in Fig. 7.4 with the Gryzinski datasets (Cacciatore and Capitelli 1981) obtained many years ago. The regularly increasing maxima predicted by the classical approach are opposed to the more irregular, but generally decreasing trend in the MCCC cross-sections with the initial vibrational quantum number. MCCC maxima are shifted closer to the threshold, with a consequent

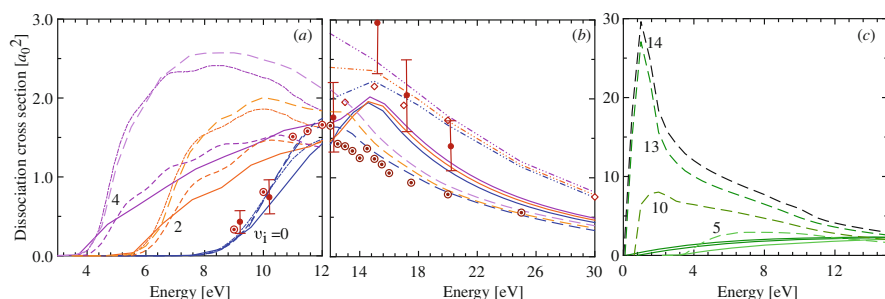


Fig. 7.3 Dissociative excitation cross-section of $b^3\Sigma_u^+$ state in $e-H_2$ collisions as a function of collision energy for different initial vibrational levels: the threshold and (b) peak regions: solid lines (Celiberto et al. 2001a), dashed-dotted lines (Rescigno and Schneider 1988), long-dashed-short-dashed lines (Stibbe and Tennyson 1998), short-dashed lines (Trevisan and Tennyson 2002), long-dashed lines (MCCC database). Experimental results for $v_i = 0$: circles (Khakoo and Segura 1994), open diamonds (Nishimura and Danjo 1986), centered-circles (Zawadzki et al. 2018). (c) Comparison of MCCC (MCCC database) and Gryzinsky (Celiberto et al. 2001a) cross-sections for initial vibrational levels $v_i \geq 5$

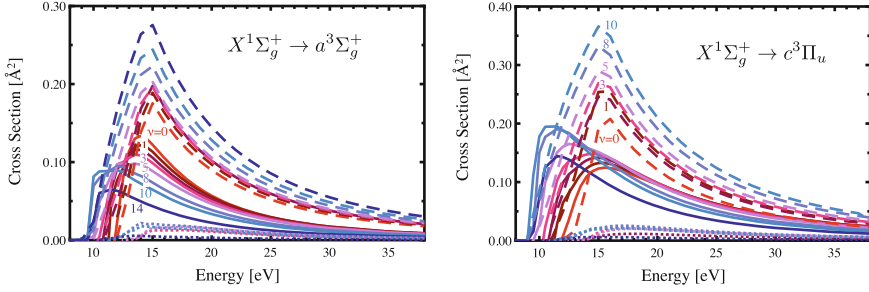


Fig. 7.4 Excitation cross-sections to the $a^3\Sigma_g^+$ and $c^3\Pi_u$ states in e- H_2 collision as a function of collision energy for selected initial vibrational levels. (solid lines) MCCC total excitation, (dotted lines) MCCC direct dissociative excitation (MCCC database), (dashed lines) Gryzinski excitation (Cacciatore and Capitelli 1981)

steeper increase of the cross-section in the threshold region. For the sake of clarity, the Gryzinski results accounted for the excitations to the bound levels of the excited triplet states only, while the plotted MCCC data correspond to total excitation, thus include the direct dissociation channel, however representing a small contribution as also shown in Fig. 7.4.

7.3 Numerical Model

The numerical calculations have been performed with the *GPKin* code (Colonna 2020), which solves the master equations, self-consistently coupled with the Boltzmann equation, in 0D time-dependent mode (Colonna et al. 2016b) or 1D stationary mode, for supersonic nozzle expansion (Colonna et al. 2001) and shock tubes (Colonna et al. 2020). The code can also include an external applied electric field (E), given as a time profile of E/N (N is the heavy particle density), also considering an RC polarization circuit, or calculated from a power supply. The magnetic field can also be considered in the Boltzmann equation (Colonna et al. 2016a). Equilibrium constants are calculated using a statistical mechanics approach (Capitelli et al. 2012). The schematics of the *GPKin* code, illustrating the connections among the different modules, is reported in Fig. 7.5.

The evolution of the chemical species and level kinetics is calculated through a set of nonlinear equations that in general can be written as (Formaggia and Scotti 2011)

$$\frac{d\vec{N}}{dt} = \hat{M}(\vec{N}, \vec{n}) \cdot \vec{N} \quad (7.1)$$

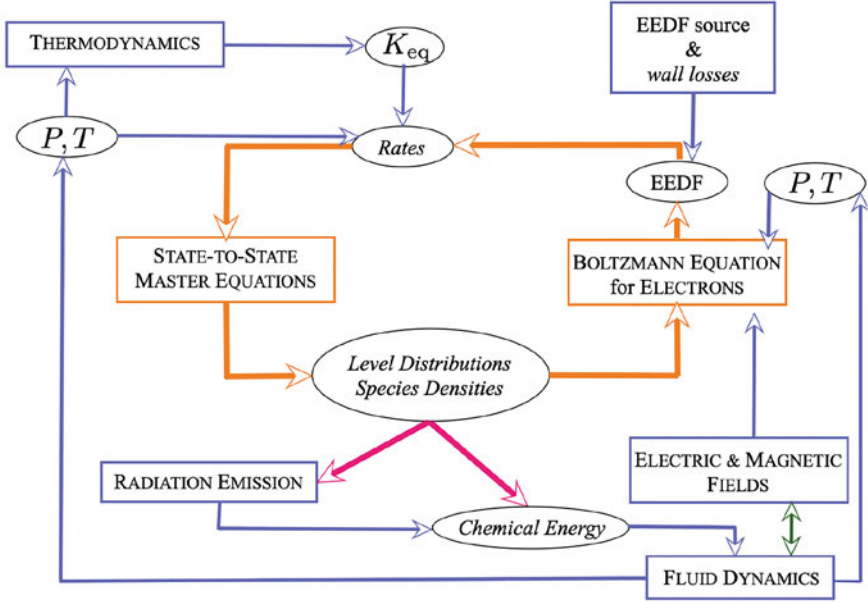


Fig. 7.5 Schematics of the GPKin code

where \vec{N} is the vector of species concentration, \vec{n} is the discretized electron energy distribution function (EEDF) and $\hat{M}(\vec{N}, \vec{n})$ is the non-linear kinetic matrix. The Eq. (7.1) is solved by using the second-order algorithm proposed by Verwer (1994).

The electron energy distribution is calculated by solving, in each time step the Boltzmann equation (Colonna et al. 2016a), becoming on the discrete energy grid

$$\frac{d\vec{n}}{dt} = \hat{C}(\vec{N}) \cdot \vec{n} + \hat{R}(\vec{N}, \vec{n}) \cdot \vec{n} + \hat{T}(\vec{n}) \cdot \vec{n} + \vec{G} - \hat{L} \cdot \vec{n} \quad (7.2)$$

where \vec{n} is the discrete electron energy distribution normalized to 1 (in eV^{-1}) \hat{C} represents the matrix operator containing the linear terms, i.e. elastic, inelastic and superelastic collisions, ionization, dissociation/recombination (Capitelli et al. 2016), dissociative attachment etc., \hat{R} represents the non-linear terms due to electron-ion three-body recombination, \hat{T} the non-linear terms due to electron-electron collisions, \vec{G} is the electron source and \hat{L} is a diagonal matrix accounting for the wall losses. To reduce the number of energy grid points and keep high accuracy also at low energy a variable mesh size Δ_i has been considered, starting from values slowly growing with the energy.

For a null electric field, the elastic collision terms calculated according to the formula in Rockwood (1973) can lead to the instabilities, therefore we have used the approach described in Elliot and Greene (1976). While the contribution of inelastic

and superelastic collisions are obtained in the standard approach (Rockwood 1973; Elliot and Greene 1976), the reverse of chemical processes has been calculated generalizing the detailed balance principle as described in Capitelli et al. (2016) and Colonna et al. (2016a).

The elements of the source terms are given by Pagano et al. (2007)

$$G_i = \frac{I_i}{V_s q_e \Delta_i} \quad (7.3)$$

and those of \hat{L} can be calculated as (Gorse et al. 1987).

$$L_{ii} = \frac{A_{\text{eff}}}{4V_s} \sqrt{\frac{2q_e \varepsilon_i}{m_e}} \left(1 - \frac{V_p}{\varepsilon_i}\right) \quad (7.4)$$

for $\varepsilon_i > V_p$ and zero elsewhere, where V_s is the source volume, q_e and m_e the charge and mass of electrons, ε_i and Δ_i are the center and amplitude of the i th interval in eV, I_i the current of electrons with energy in the i th interval, A_{eff} is the effective surface for electron loss and V_p is the plasma potential. The electron current is assumed to be a monoenergetic beam with energy V_d and therefore the source term act only in the single energy interval containing V_d . The loss term calculated with Eq. (7.4) contains an effective surface that is treated as an external parameter. An alternative equation was proposed by Pagano et al. (2007), Arslanbekov et al. (2001), writing the loss term as $L_{ii} = 1/\tau_w(\varepsilon_i)$ where the lifetime is calculated as

$$\tau_w(\varepsilon) = \frac{\Lambda}{D(\varepsilon)} \frac{1}{2} \left(\frac{2\Lambda + \lambda(\varepsilon)}{\lambda(\varepsilon)} \right) \frac{4\pi}{v(\varepsilon) \delta\Omega} \quad (7.5)$$

where $v(\varepsilon)$ is the total collision frequency

$$v(\varepsilon) = \sqrt{\frac{2q_e \varepsilon}{m_e}} \sum_s N_s \sigma_s^e(\varepsilon) = \sqrt{\frac{2q_e \varepsilon}{m_e}} \frac{1}{\lambda(\varepsilon)} \quad (7.6)$$

$D(\varepsilon)$ is the electron diffusion coefficient

$$D(\varepsilon) = \frac{\lambda^2(\varepsilon) v(\varepsilon)}{3} \quad (7.7)$$

$\delta\Omega$ the wall loss cone

$$\delta\Omega = 2\pi \left(1 - \sqrt{\frac{V_p}{\varepsilon}}\right) \quad (7.8)$$

different from zero when $\varepsilon_i > V_p$ and Λ is the characteristic diffusion length that, for a cylindrical source with height L and radius R , can be calculated as

$$\frac{1}{\Lambda^2} = \left(\frac{2.405}{R}\right)^2 + \left(\frac{\pi}{L}\right)^2 \quad (7.9)$$

Electron induced processes are included in Eq. (7.1) calculating the rate coefficients from the electron distribution as

$$k_\pi = \sum_i n_i \sqrt{\frac{2q_e \varepsilon_i}{m_e}} \sigma_\pi(\varepsilon_i) \Delta_i \quad (7.10)$$

where k_π is the rate of the π th process and $\sigma_\pi(\varepsilon_i)$ the cross-section. The equation for electron density should include also source G and loss L terms calculated as

$$G = \sum_i G_i \quad L = \sum_i L_{ii} n_i \Delta_i \quad (7.11)$$

The diffusion terms of ions and neutrals, including excited state deactivation, have been included following the procedure described in Pagano et al. (2007).

7.4 Global Kinetic Model of Multicusp Negative Ion Source

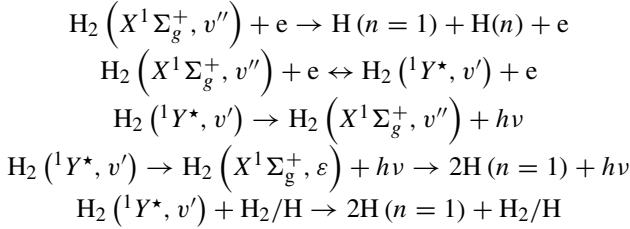
7.4.1 Kinetic Scheme

The kinetic scheme for the hydrogen plasma includes a complete CR model for atomic hydrogen H ($n \leq 10$) and for the H₂ molecule, with excited singlet ($B, B', B'', {}^1\Sigma_u^+, C, D, D', {}^1\Pi_u$) and triplet ($b^3\Sigma_u^+, a^3\Sigma_g^+, c^3\Pi_u$) electronic states, accounting for those collisional processes responsible for the redistribution of energy among the translational and the internal degrees of freedom (VTa, VTm and VV processes) relevant to the vibrational kinetics of the ground state and for the dissociation and ionization/recombination kinetics (Colonna et al. 2017).

The original model, based on the state-resolved database built at the plasma-chemistry group in Bari for electron-H₂ system, exploiting the IPM method for dipole-allowed excitations, the Gryzinski classical method for forbidden excitation transitions and ionization and the complex potential theory for resonant vibrational excitations and dissociative attachment (Celiberto et al. 2001a; Wadehra 1986), was further improved (Colonna et al. 2017) to follow the vibrational kinetics of H₂ singlet excited states. The IPM cross-sections for the $B, B', {}^1\Sigma_u^+, C, D, {}^1\Pi_u$ states,²

² The $B'' {}^1\Sigma_u^+$ and $D' {}^1\Pi_u$ states were not resolved, representing a small contribution to excitation and emission.

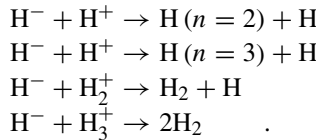
smoothed to delete the unphysical threshold peaks (Colonna et al. 2017), were resolved on the final vibrational level, and the VDF of these excited singlet states $^1Y^*$ results on the interplay of level-dependent radiative decay probability, including dissociation channels and represented by the Einstein coefficients for spontaneous emission, of superelastic collisions and of collisional quenching, following the network of inelastic processes



The triplet states mainly determine the dissociation dynamics through different mechanisms, i.e. the direct dissociation through the purely repulsive $b^3 \Sigma_u^+$ state, the spontaneous radiative decay of the $a^3 \Sigma_g^+$ to the $b^3 \Sigma_u^+$ state competing with its conversion to the $c^3 \Pi_u$ state, this last undergoing dissociation through collisional quenching and predissociation (Wedding and Phelps 1988). The $c^3 \Pi_u$ is the metastable of H_2 and therefore could play a significant role in the kinetics, acting as an energy reservoir and releasing back energy to electrons through secondary collisions.

Accurate data for the collisional quenching of singlet states are not available in the literature and also the products are not well identified, though it is suggested that the mechanisms entail the formation of H_3 molecule, eventually leading to dissociation (Hassouni et al. 1999). The measured averaged cross-section for the quenching of the $B^1 \Sigma_u^+$ state is 80 \AA^2 , a value close to the experimental cross-section for the quenching of the $c^3 \Pi_u$ state (Wedding and Phelps 1988), therefore the rates for singlets are assumed equal to that for the triplet state (Colonna et al. 2017).

Finally, complete ion chemistry, including H^- and H_3^+ (Janev et al. 2003; Matveyev and Silakov 1995), is accounted for, i.e. charge exchange processes, also involving vibrationally excited molecules, the ion conversion reactions of H_2^+ to H^+ and H_3^+ and the mutual neutralization of positive ions in collision with H^-



The chemical model above represents here the reference, model (A), for the analysis of the sensitivity of the results with respect to a different choice of the datasets for triplet and singlet excitations in $e - \text{H}_2$ collisional system, for the kinetic

simulation of a multicusp ion source reproducing the operational conditions in Refs. (Mosbach 2005; Pagano et al. 2007). In particular:

- Model (B) – inclusion of MCCC cross-sections for $b^3\Sigma_u^+$, $a^3\Sigma_g^+$, $c^3\Pi_u$ states
- Model (C) – inclusion of MCCC cross-sections for $b^3\Sigma_u^+$, $a^3\Sigma_g^+$, $c^3\Pi_u$ states and of MCCC fully-resolved vibrational-specific cross-sections for B , $B^1\Sigma_u^+$, C , $D^1\Pi_u$ states
- Model (D) – model (C) neglecting the metastable $c^3\Pi_u$ and the quasi-metastable $a^3\Sigma_g^+$ states.

7.4.2 Multicusp Source

The multicusp source (schematics in Fig. 7.6) is a magnetically confined plasma of cylindrical geometry, with eight rows of permanent magnets with alternating polarity mounted on the outer surface of a discharge vessel and parallel to the

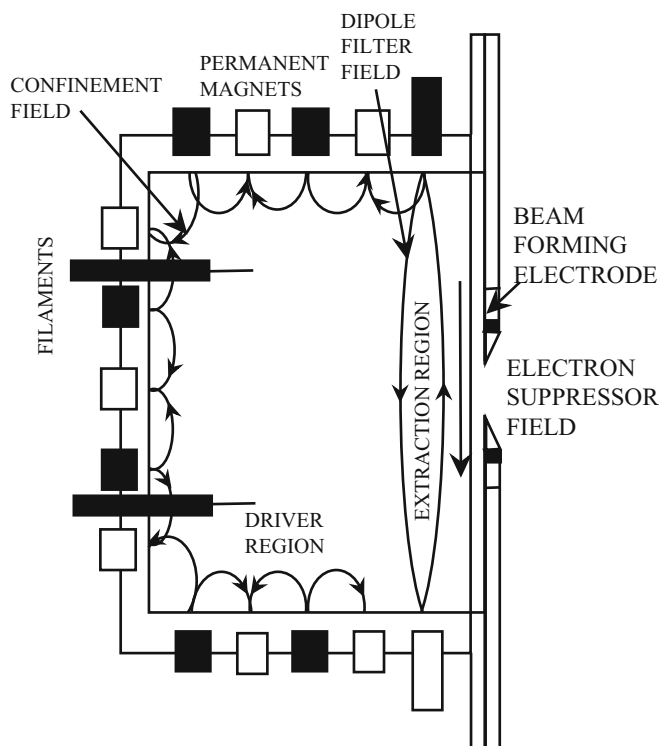


Fig. 7.6 Schematics of a magnetic multicusp negative ion source. (Reproduced from Capitelli et al. (2016). Reproduced with permission of Springer Nature)

Table 7.1 Geometrical and plasma parameters of the source (Mosbach 2005; Pagano et al. 2007)

Source radius	9.75 cm		
Source height	36 cm		
Λ	by Eq. (7.9)		
P	1.5 Pa		
V_d	100 V		
I_d [A]	0.5	5	10
T_s [K]	350	500	800
V_p [V]	1.5	2.8	3.5
γ_H	0.15		

cylinder axis, plus four additional rows of magnets located on the top and bottom flanges. Electrons are thermo-emitted from hot tungsten filaments (cathodes) and accelerated by the voltage (V_d) applied between the filaments and the reactor walls (anode). The geometrical and plasma parameters of the source are given in Table 7.1.

The pressure and the discharge voltage are invariant parameters in the simulations, while the source temperature, T_s , and the plasma potential, V_p , are increased as the discharge current, I_d , increases in order to reproduce the experimentally observed variation of the translational temperature of H_2 molecules (Mosbach 2005) on the increase of filament heating current and to tune the rate of electron wall loss for the control of the charge density in the plasma volume, as detailed in Sect. 7.3. The low-pressure condition affects the kinetics, making inefficient the collisional quenching and enhancing the surface processes, responsible for the vibrational deactivation and the atom recombination at the wall. In the model, the heterogeneous processes are described by a constant recombination coefficient, γ_H , accounting for a global average effect due to the vessel surface, whose value is given in Table 7.1 (Pagano et al. 2007).

7.5 Results

Before starting the analysis, as a general consideration it can be stated that models (B) and (C) give very close results for all the considered conditions, thus allowing us to conclude that, in this regime, the improved accuracy in the cross-sections for singlet state excitations has no appreciable impact on the global kinetics.

In Fig. 7.7 the temporal evolution of chemical species mole fractions, except H_2 , up to a stationary condition at $t = 0.001$ s, are displayed for the discharge current $I_d = 0.5$ A. Electron collisions induce in molecular hydrogen dissociation and ionization with the formation, at the first stage, of H_2^+ , rapidly converted to H^+ and, subsequently, to H_3^+ , which becomes the dominant cationic species. The H^- negative ion, remaining a minority species in the plasma, is formed later when the vibrational pumping mechanism leads to the formation of a plateau in the VDF of the ground state of H_2 on a timescale of 10^{-4} s, as shown in Fig. 7.8,

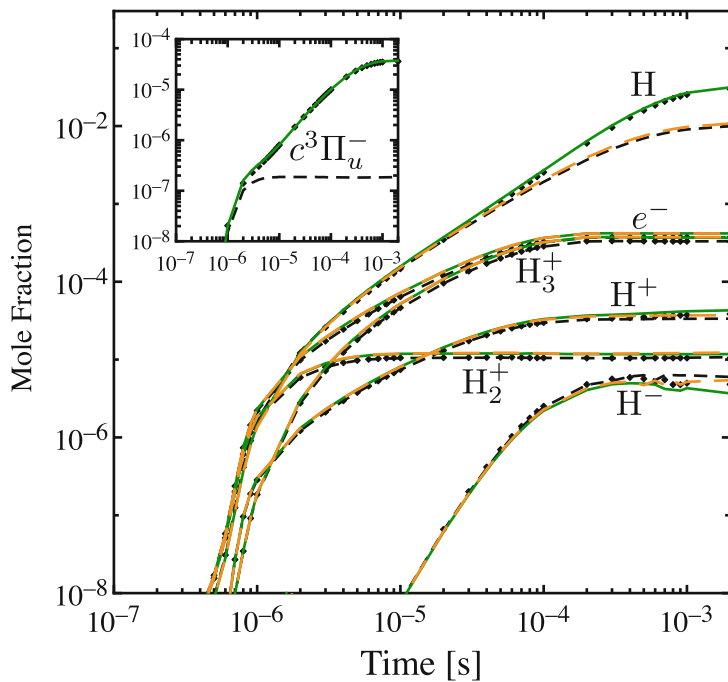


Fig. 7.7 Temporal evolution of plasma composition at $I_d = 0.5$ A. dashed lines – model (A), close diamonds – model (B), solid line – model (C), long-dashed lines – model (D)

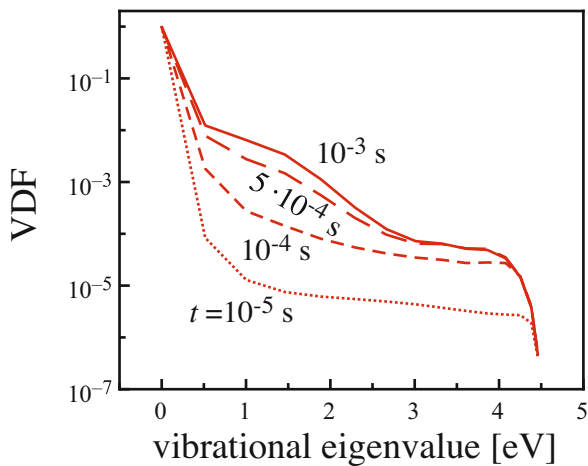


Fig. 7.8 VDF of the ground state of H_2 at different times in the plasma evolution for model (A)

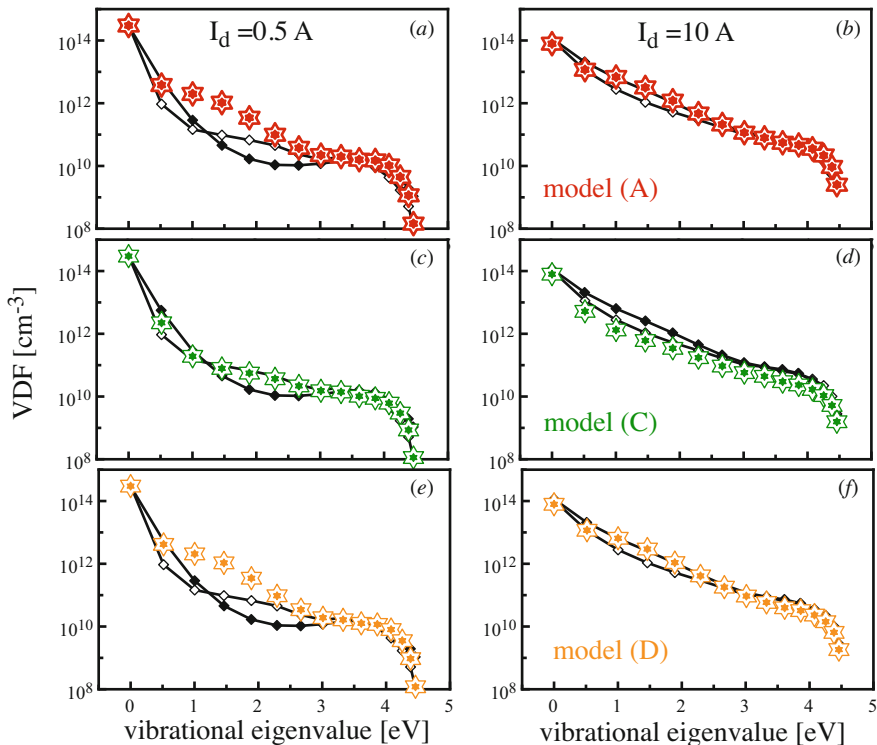


Fig. 7.9 Stationary VDF obtained by different models, at two different values of the discharge current, compared with the experimental distributions in Ref. (Mosbach 2005) (close diamonds) and with the previous kinetic model (Pagano et al. 2007) (open diamonds). (a) model (A), $I_d = 0.5$ A; (b) model (A), $I_d = 10$ A; (c) model (C), $I_d = 0.5$ A; (d) model (C), $I_d = 10$ A; (e) model (D), $I_d = 0.5$ A; (f) model (D), $I_d = 10$ A

activating the DEA process. Regardless the choice of the model, the general features of the evolution are the same but the positive deviation of the atomic hydrogen mole fraction and the small flexion of the H^- for $t \geq 10^{-4}$ s. The more effective dissociation in models (B) and (C) is expected by the faster growth in the threshold region of the cross-sections for triplet excitations in MCCC database, as discussed in Sect. 7.2. In fact, as appreciable in the inset of Fig. 7.7, the mole fraction of the metastable state for models (B) and (C) significantly increases in time reflecting on the dissociation profile. However, neglecting $a^3\Sigma_g^+$ and $c^3\Pi_u$ states (model (D)), the differences disappear, enlightening their role in the dissociation kinetics.

In Fig. 7.9, the stationary VDFs of the ground state, at two different values of I_d and obtained with different models, are presented. The distribution is pumped by the collisional dynamics (the low-threshold eV and the high-threshold EV processes) exhibiting a markedly non-Boltzmann character with the well-known plateau and the overpopulated tail observed experimentally (Mosbach 2005) and predicted also with the previous self-consistent kinetic approach in Ref. (Pagano et al. 2007).

Considering the case $I_d = 0.5$ A, model (A) (Fig. 7.9a) and model (D) (Fig. 7.9e) predict close values for the VDF, indicating that the $a^3\Sigma_g^+$ and $c^3\Pi_u$ triplets in the old database do not significantly contribute to the dissociation dynamics in this regime. Differently, model (C) (Fig. 7.9c) gives a slightly lower VDF with respect to models (A) and (D), these differences are attributed to an indirect effect of triplet excitations. In fact, the enhanced dissociation due to the MCCC cross-sections affects the collision frequency of VTa processes, that act de-activating the intermediate vibrational levels ($1 \leq v_i \leq 6$), in turn compressing the mechanism of vibrational excitation in the ground state and the DEA production of H^- negative ions.

Unexpectedly, results in Ref. (Pagano et al. 2007) are different from model (A), while showing a very good agreement with model (C), despite the fact that the database implemented in Ref. (Pagano et al. 2007) was also based on the IPM/Gryzinski electron- H_2 cross-sections. However, in the old kinetics, the effect of VTa processes was artificially enhanced considering the rates calculated at an effective temperature higher than the temperature of the source, thus leading to a colder distribution. The agreement between model (C) and Ref. (Pagano et al. 2007) is therefore accidental and attributable in both models to the higher efficiency of the VTa de-activation, but determined by different factors: in the model (C) by a higher atomic density while in Ref. (Pagano et al. 2007) by higher rate coefficients.

It is worth noting that other differences exist in the old kinetics (Pagano et al. 2007): the EV processes were included directly, thus assuming the radiative decay as the only possible final channel and not accounting for the competing quenching and the superelastic collisions considered instead in the present kinetics. Furthermore, the excitations of triplets $a^3\Sigma_g^+$, $c^3\Pi_u$ states were treated as pure dissociation channels.

At higher discharge currents, $I_d = 10$ A, the increase in the electron density and the higher tails of the EEDF (Fig. 7.10b) determines the formation of distributions characterized by a higher degree of vibrational excitation, compressing the differences among the models.

The comparison with the experimental distributions (Mosbach 2005) is quite satisfactory, the tails are well predicted indicating the reliability of the kinetic model for the EV mechanism, which is relevant to the population of vibrational levels close to the dissociation. The enhanced dissociation introduced by the MCCC database in the model (C) affects the H_2 density scaling down the whole distribution (Fig. 7.9d) and introducing deviations with respect to the experimental VDF.

Extending the analysis, the electron energy distribution function (Fig. 7.10) is characterized by a markedly non-Maxwell behavior. The features of the EEDF energy profile, with the high-energy peak representing the monochromatic beam of electrons thermo-emitted by the filament in the source and the regular oscillations due to the interplay of degradation of electron energy in inelastic collisions and the electron-electron collisions smoothing out the secondary peaks at lower energies, were already observed in the past (Bretagne et al. 1985, 1991; Gorse et al. 1985, 1987) and are in a quantitative agreement with the EEDFs in Ref. (Pagano et al. 2007). In Ref. (Mosbach 2005) there were evidences of bi-Maxwellian EEDFs

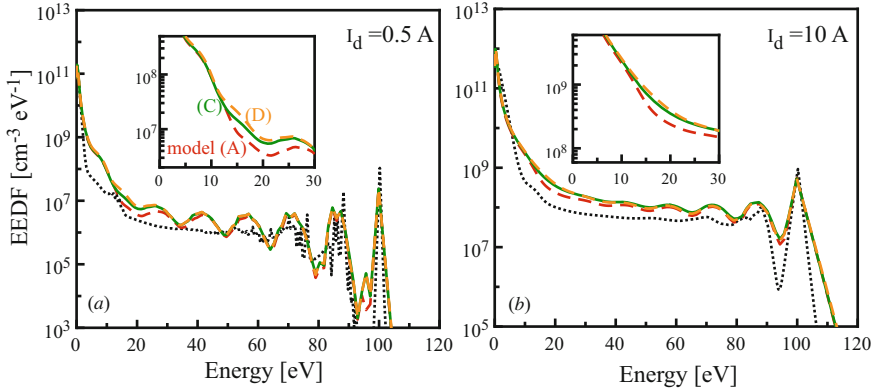


Fig. 7.10 Stationary EEDF obtained by different models, at two different values of the discharge current, compared with the previous kinetic model (Pagano et al. 2007) (dotted lines). The insets report the magnification of the energy region where differences are localized

associated with two distinct groups of electrons, *slow* electrons characterized by a low temperature and a tail of *fast* electrons at a higher temperature. At $I_d = 0.5$ A, Fig. 7.10a, the inclusion of MCCC triplets and singlets (model (C)), with respect to model (A), produces an increase of the distribution at the energies corresponding to the excitation of triplets ($10 \leq E \leq 25$ eV). This is due to the different energy profile of the corresponding cross-sections, characterized by higher maxima at higher energies and depleting the EEDF due to the electrons-impact induced inelastic process through triplets. The slight increase observed with the model (D) at the same energies has to be ascribed, instead, to the lack of these energy-loss channels. However, the small deviation of the model (C) with respect to model (D) seems to indicate the onset of an almost-stationary condition for the metastable, resulting from the quasi-equilibration of inelastic and superelastic collisional processes, that makes the transitions semi-transparent to electrons (Colonna 2020). At $I_d = 10$ A the EEDF is considerably enhanced, especially in the high-energy tail, and the energy profile is smoother due to the increased electron density that makes more effective the electron-electron collisions.

The theoretical electron temperatures, calculated from the mean electron energy, are poorly affected by the choice of the model, and the values of $T_e = 0.5, 0.7$ and 1.1 eV, corresponding to $I_d = 0.5, 5$ and 10 A respectively, are in good agreement with the experimental temperatures of *slow* electron in Ref. (Mosbach 2005).

Finally, Fig. 7.11a shows the comparison of the stationary density of H^- with the experimental values (Mosbach 2005). As in Ref. (Pagano et al. 2007), despite the quantitative agreement at lower values of I_d , the kinetic models do not reproduce the growth of the negative ion density with the discharge current. The improved database of $e - H_2$ inelastic scattering, including the MCCC cross-sections, systematically lowers the H^- predictions to be attributed to the enhanced dissociation through triplet states. The differences in the negative ion yield between

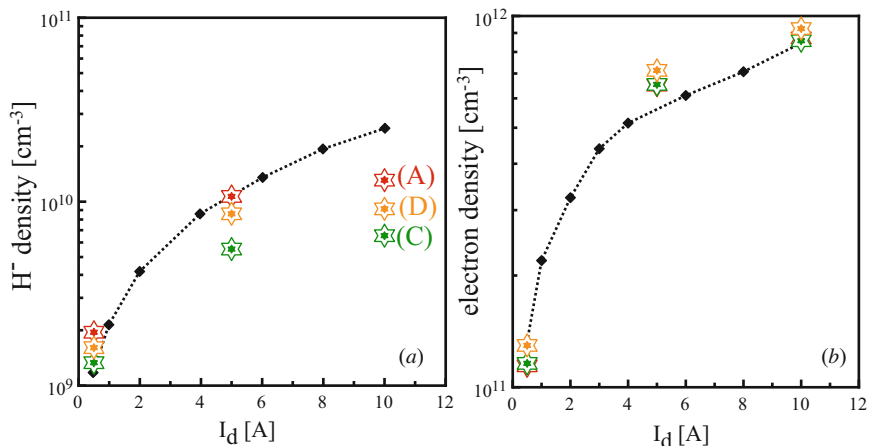


Fig. 7.11 Stationary density of H^- (a) and of electrons (b) obtained by different models as a function of the discharge current, compared with the experimental values (Mosbach 2005) (close diamonds)

model (A) and model (D) have to be attributed to the slightly higher IPM cross-sections for singlet excitation reflecting on the tail of the VDF and thus promoting more effectively DEA from the highest vibrational levels of the ground state. Less model-dependence is found in the theoretical values of the electron density, in Fig. 7.11b, which shows also a better agreement with the experiment (Mosbach 2005).

7.6 Conclusions

The construction of an accurate and detailed state-to-state dynamical database is key in the reliable kinetic modeling of many low-temperature non-equilibrium technological plasmas. Negative ion sources for neutral beam injection in tokamaks are intensively investigated, with the development of multi-dimensionality codes for the real-geometry simulations of the source, including modules for the kinetic description of the processes governing the negative ion formation in the plasma volume and at the surface.

Despite the level of complexity in these simulations, intended to support the engineering design, the investigations using global zero-D kinetic codes could still significantly contribute to the research in the field, shedding light on the collisional mechanisms and assessing the sensitivity of the chemistry to the accuracy of datasets for specific processes.

In this chapter, the state-to-state, self-consistent kinetic approach in the *GPKin* code is applied to the modeling of a traditional caesium-free multicusp negative ion source, thus focusing on the volume production of H^- , through DEA processes

activated by the vibrational non-equilibrium in the ground state of H_2 molecule. The advanced and detailed chemical model, developed in the plasma-chemistry group in Bari, including state-specific cross-sections for the electron-impact induced processes, rates of collisional energy transfer and complete ion kinetics for conversion and neutralization, has been exploited for the kinetic simulation of the source in the experimental conditions of Ref. (Mosbach 2005).

The study confirms the predictive character of the chemical model demonstrated in Ref. (Pagano et al. 2007), with a quantitative agreement with the experiment in the estimation of chemical species densities and plasma parameters at the stationary state, is mainly intended for the analysis of the sensitivity of the results to a different choice of the cross-section database for the $e - H_2$ system. In fact, the MCCC database (MCCC database) of cross-sections, nowadays available to the modeling community, sets the new standard of accuracy for data and imposes an estimation of the impact on global kinetics.

The results clearly show the relevance of the state-specific cross-sections for the forbidden excitations of the triplet states of H_2 , as also shown in Ref. (Wunderlich et al. 2021), that affects the plasma composition, with the enhancement of the global dissociation, and in turn the efficiency of processes shaping the VDF, resulting in a less pumped distribution. On the other hand, in the conditions explored in the kinetic simulations the impact of MCCC cross-sections for excitation and dissociative excitation of singlet states is small, not appreciably modifying any of the plasma characteristics.

Bibliography

- R. Agnello, S. Béchu, I. Furno, P. Guittienne, A.A. Howling, R. Jacquier, et al., Negative ion characterization in a helicon plasma source for fusion neutral beams by cavity ring-down spectroscopy and Langmuir probe laser photodetachment. *Nucl Fusion* **60**(2), 026007 (2019)
- S. Aleiferis, P. Svarnas, S. Béchu, O. Tarvainen, M. Bacal, Production of hydrogen negative ions in an ECR volume source: Balance between vibrational excitation and ionization. *Plasma Sources Sci. Technol.* **27**(7), 075015 (2018)
- R.R. Arslanbekov, A.A. Kudryavtsev, L.D. Tsendin, Electron-distribution-function cutoff mechanism in a low-pressure afterglow plasma. *Phys. Rev. E* **64**(1), 016401 (2001)
- M. Bacal, G.W. Hamilton, H^- and D^- production in plasmas. *Phys. Rev. Lett.* **42**(23), 1538 (1979)
- J.N. Bardsley, J.M. Wadehra, Dissociative attachment and vibrational excitation in low-energy collisions of electrons with H_2 and D_2 . *Phys. Rev. A* **20**(4), 1398 (1979)
- E. Bauer, C.D. Bartky, Calculation of inelastic electron—Molecule collision cross sections by classical methods. *J. Chem. Phys.* **43**(7), 2466–2476 (1965)
- J. Bentounes, S. Béchu, F. Biggins, A. Michau, L. Gavilan, J. Menu, L. Bonny, D. Fombaron, A. Bès, Y.A. Lebedev, V.A. Shakhatov, P. Svarnas, T. Hassaine, J.L. Lemaire, A. Lacoste, Effects of the plasma-facing materials on the negative ion H^- density in an ECR (2.45 GHz) plasma. *Plasma Sources Sci. Technol.* **27**(5), 055015 (2018)
- J. Bretagne, G. Delouya, C. Gorse, M. Capitelli, M. Bacal, Electron energy distribution functions in electron-beam-sustained discharges: Application to magnetic multicusp hydrogen discharges. *J. Phys. D. Appl. Phys.* **18**(5), 811 (1985)

- J. Bretagne, W.G. Graham, M.B. Hopkins, A comparison of experimental and theoretical electron energy distribution functions in a multicusp ion source. *J. Phys. D. Appl. Phys.* **24**(5), 668 (1991)
- M. Cacciatore, M. Capitelli, Cross sections and rate coefficients for electronic excitation of the triplet states of the hydrogen molecule in different vibrational levels. *Chem. Phys.* **55**(1), 67–72 (1981)
- M. Capitelli, M. Cacciatore, R. Celiberto, O. De Pascale, P. Diomede, F. Esposito, A. Giquel, C. Gorse, K. Hassouni, A. Laricchiuta, S. Longo, D. Pagano, M. Rutigliano, Vibrational kinetics, electron dynamics and elementary processes in H_2 and D_2 plasmas for negative ion production: Modelling aspects. *Nucl. Fusion* **46**(6), S260 (2006)
- M. Capitelli, R. Celiberto, F. Esposito, A. Laricchiuta, Molecular dynamics for state-to-state kinetics of non-equilibrium molecular plasmas: State of art and perspectives. *Plasma Process. Polym.* **6**(5), 279–294 (2009)
- M. Capitelli, G. Colonna, A. D'Angola, *Fundamental Aspects of Plasma Chemical Physics: Thermodynamics in Springer Series on Atomic, Optical, and Plasma Physics*, vol. 66, (Springer, New York, 2012)
- M. Capitelli, G. Colonna, F. Esposito, K. Hassouni, A. Laricchiuta, S. Longo, *Fundamental Aspects of Plasma Chemical Physics: Kinetics in Springer Series on Atomic, Optical, and Plasma Physics*, vol. 85, (Springer, New York, 2016)
- R. Celiberto, M. Capitelli, U.T. Lamanna, Vibrational excitation of $H_2(X^1\Sigma_g^+, v)/D_2(X^1\Sigma_g^+, v)$ through excitation of electronically excited singlet states and radiative cascade. *Chem. Phys.* **183**(1), 101–106 (1994)
- R. Celiberto, R.K. Janev, A. Laricchiuta, M. Capitelli, J.M. Wadehra, D.E. Atems, Cross section data for electron-impact inelastic processes of vibrationally excited molecules of hydrogen and its isotopes. *At. Data Nucl. Data Tables* **77**(2), 161–213 (2001a)
- R. Celiberto, R.K. Janev, A. Laricchiuta, Total and dissociative electron-impact cross sections for $X^1\Sigma_g^+ \rightarrow B^1\Sigma_u^+$ and $X^1\Sigma_g^+ \rightarrow C^1\Pi_u$ transitions of vibrationally excited tritium and deuterium-tritium molecules. *Phys. Scripta* **64**(1), 26 (2001b)
- R. Celiberto, R.K. Janev, J.M. Wadehra, J. Tennyson, Dissociative electron attachment to vibrationally excited H_2 molecules involving the $^2\Sigma_g^+$ resonant Rydberg electronic state. *Chem. Phys.* **398**, 206–213 (2012)
- R. Celiberto, R.K. Janev, V. Laporta, J. Tennyson, J.M. Wadehra, Electron-impact vibrational excitation of vibrationally excited H_2 molecules involving the resonant $^2\Sigma_g^+$ Rydberg-excited electronic state. *Phys. Rev. A* **88**(6), 062701 (2013)
- R. Celiberto, J.D. Gorfinkiel, A. Laricchiuta, J. Tennyson, *Methods for electron-molecule scattering*, in *Plasma Modeling: Methods and Applications*, ed. by G. Colonna, A. D'Angola, (IOP Publishing, Bristol, 2022)
- H.K. Chung, B.J. Braams, K. Bartschat, A.G. Császár, G.W.F. Drake, T. Kirchner, V. Kokoouline, J. Tennyson, Uncertainty estimates for theoretical atomic and molecular data. *J. Phys. D. Appl. Phys.* **49**(36), 363002 (2016)
- G. Colonna, M. Tuttafesta, D. Giordano, Numerical methods to solve Euler equations in one-dimensional steady nozzle flow. *Comput. Phys. Commun.* **138**(3), 213–221 (2001)
- G. Colonna, A. D'Angola, Chapter 2: The Two-Term Boltzmann Equation, in *Plasma Modeling: Methods and Applications*, ed. by G. Colonna, A. D'Angola, (IOP Publishing, Bristol, 2016a)
- G. Colonna, L.D. Pietanza, G. D'Ammando, Selfconsistent Kinetics, in *Plasma Modeling: Methods and Applications*, ed. by G. Colonna, A. D'Angola, (IOP Publishing, Bristol, 2016b)
- G. Colonna, L.D. Pietanza, G. D'Ammando, R. Celiberto, M. Capitelli, A. Laricchiuta, Vibrational kinetics of electronically excited states in H_2 discharges. *Eur. Phys. J. D* **71**(11), 1–8 (2017)
- G. Colonna, On the relevance of superelastic collisions in argon and nitrogen discharges. *Plasma Sources Sci. Technol.* **29**(6), 065008 (2020)
- G. Colonna, L.D. Pietanza, A. Laricchiuta, Ionization kinetic model for hydrogen-helium atmospheres in hypersonic shock tubes. *Int. J. Heat Mass Transf.* **156**, 119916 (2020)
- C.J. Elliot, A.E. Greene, Electron energy distribution in e-beam generated Xe and Ar plasmas. *J. Appl. Phys.* **47**, 2946–2953 (1976)

- L. Formaggia, A. Scotti, Positivity and conservation properties of some integration schemes for mass action kinetics. *SIAM J. Numer. Anal.* **49**, 1267–1288 (2011)
- G. Fubiani, L. Garrigues, G. Hagelaar, N. Kohen, J.P. Boeuf, Modeling of plasma transport and negative ion extraction in a magnetized radio-frequency plasma source. *New J. Phys.* **19**(1), 015002 (2017)
- C. Gorse, M. Capitelli, J. Bretagne, M. Bacal, Vibrational excitation and negative-ion production in magnetic multicusp hydrogen discharges. *Chem. Phys.* **93**(1), 1–12 (1985)
- C. Gorse, M. Capitelli, M. Bacal, J. Bretagne, A. Lagana, Progress in the non-equilibrium vibrational kinetics of hydrogen in magnetic multicusp H^- ion sources. *Chem. Phys.* **117**(2), 177–195 (1987)
- M. Gryziński, Classical theory of atomic collisions. I. Theory of inelastic collisions. *Phys. Rev.* **138**(2A), A336 (1965)
- K. Hassouni, A. Gicquel, M. Capitelli, The role of dissociative attachment from Rydberg states in enhancing H^- concentration in moderate-and low-pressure H_2 plasma sources. *Chem. Phys. Lett.* **290**(4–6), 502–508 (1998)
- K. Hassouni, A. Gicquel, M. Capitelli, J. Loureiro, Chemical kinetics and energy transfer in moderate pressure H_2 plasmas used in diamond MPACVD processes. *Plasma Sources Sci. Technol.* **8**(3), 494 (1999)
- J.R. Hiskes, Cross sections for the vibrational excitation of the H_2 ($X1_g^+$) state via electron collisional excitation of the higher singlet states. *J. Appl. Phys.* **51**(9), 4592–4594 (1980)
- J.R. Hiskes, Cross sections for the vibrational excitation of the H_2 $X1_g^+$ $X1_g^+(v)$ levels generated by electron collisional excitation of the higher singlet states. *J. Appl. Phys.* **70**(7), 3409–3417 (1991)
- J.R. Hiskes, A.M. Karo, Generation of negative ions in tandem high-density hydrogen discharges. *J. Appl. Phys.* **56**(7), 1927–1938 (1984)
- J.R. Hiskes, A.M. Karo, Analysis of the H_2 vibrational distribution in a hydrogen discharge. *Appl. Phys. Lett.* **54**(6), 508–510 (1989)
- J. Horáček, M. Čížek, K. Houfek, P. Kolorenč, W. Domcke, Dissociative electron attachment and vibrational excitation of H_2 by low-energy electrons: Calculations based on an improved nonlocal resonance model. *Phys. Rev. A* **70**(5), 052712 (2004)
- J. Horáček, M. Čížek, K. Houfek, P. Kolorenč, W. Domcke, Dissociative electron attachment and vibrational excitation of H_2 by low-energy electrons: Calculations based on an improved nonlocal resonance model. II. Vibrational excitation. *Phys. Rev. A* **73**, 022701 (2006)
- R.K. Janev, D. Reiter, U. Samm, *Collision Processes in Low-Temperature Hydrogen Plasmas* (Forschungszentrum Jülich, Zentralbibliothek, 2003)
- M.A. Khakoo, J. Segura, Differential cross sections for the electron impact excitation of the $b^3\Sigma_u^+$ continuum of molecular hydrogen. *J. Phys. B* **27**(11), 2355 (1994)
- A. Laricchiuta, R. Celiberto, F. Esposito, M. Capitelli, State-to-state cross sections for H_2 and its isotopic variants. *Plasma Sources Sci. Technol.* **15**(2), S62 (2006)
- Z. Li, D. Li, J. Yang, X. Jiang, W. Jiang, D. Chen, Non-dissociative ionization cross section of the electronically excited H_2 and D_2 with atomic-limit principal quantum number $n = 3$ and 4. *Atom. Data Nucl. Data Tables* **143**, 101476 (2022)
- X. Liu, D.E. Shemansky, P.V. Johnson, C.P. Malone, M.A. Khakoo, I. Kanik, Electron and photon dissociation cross sections of the H_2 singlet ungerade continua. *J. Phys. B* **45**(1), 015201 (2011)
- A.A. Matveyev, V.P. Silakov, Kinetic processes in a highly-ionized non-equilibrium hydrogen plasma. *Plasma Sources Sci. Technol.* **4**(4), 606 (1995)
- MCCC. Molecular Convergent Close-Coupling Database, URL: <https://www.mccc-db.org/>. Department of Physics Curtin University, (Perth, Australia). Accessed 1 Jan 2022
- T. Mosbach, Population dynamics of molecular hydrogen and formation of negative hydrogen ions in a magnetically confined low temperature plasma. *Plasma Sources Sci. Technol.* **14**(3), 610 (2005)
- H. Nishimura, A. Danjo, Differential cross section of electron scattering from molecular Hydrogen. II. $b^3\Sigma_u^+$ excitation. *J. Phys. Soc. Jpn.* **55**(9), 3031–3036 (1986)

- D. Pagano, C. Gorse, M. Capitelli, Modeling multicusp negative-ion sources. *IEEE Trans. Plasma Sci.* **35**(5), 1247–1259 (2007)
- L.A. Pinnaduwa, W.X. Ding, D.L. McCorkle, S.H. Lin, A.M. Mebel, A. Garscadden, Enhanced electron attachment to Rydberg states in molecular hydrogen volume discharges. *J. Appl. Phys.* **85**(10), 7064–7069 (1999)
- S.D. Rockwood, Elastic and inelastic cross sections for electron-Hg scattering from Hg transport data. *Phys. Rev. A* **8**, 2348 (1973)
- T.N. Rescigno, B.I. Schneider, Electron-impact excitation of the $b^3\Sigma_u^+$ state of H_2 using the complex Kohn method: R dependence of the cross section. *J. Phys. B* **21**(22), L691 (1988)
- L.H. Scarlett, J.K. Tapley, D.V. Fursa, M.C. Zammit, J.S. Savage, I. Bray, Low-energy electron-impact dissociative excitation of molecular hydrogen and its isotopologues. *Phys. Rev. A* **96**(6), 062708 (2017)
- L.H. Scarlett, J.K. Tapley, D.V. Fursa, M.C. Zammit, J.S. Savage, I. Bray, Electron-impact dissociation of molecular hydrogen into neutral fragments. *Eur. Phys. J. D* **72**, 34 (2018)
- L.H. Scarlett, J.K. Tapley, J.S. Savage, D.V. Fursa, M.C. Zammit, I. Bray, Vibrational excitation of the state via electron-impact excitation and radiative cascade. *Plasma Sources Sci. Technol.* **28**(2), 025004 (2019)
- D.T. Stibbe, J. Tennyson, Near-threshold electron impact dissociation of H_2 within the adiabatic nuclei approximation. *N. J. Phys.* **1**(1), 2 (1998)
- F. Taccogna, S. Bechu, A. Aanesland, P. Agostinetti, R. Agnello, S. Aleiferis, et al., Latest experimental and theoretical advances in the production of negative ions in caesium-free plasmas. *Eur. Phys. J. D* **75**(8), 227 (2021)
- J.K. Tapley, L.H. Scarlett, J.S. Savage, M.C. Zammit, D.V. Fursa, I. Bray, Vibrationally resolved electron-impact excitation cross sections for singlet states of molecular hydrogen. *J. Phys. B* **51**(14), 144007 (2018a)
- J.K. Tapley, L.H. Scarlett, J.S. Savage, D.V. Fursa, M.C. Zammit, I. Bray, Electron-impact dissociative excitation cross sections for singlet states of molecular hydrogen. *Phys. Rev. A* **98**(3), 032701 (2018b)
- C.S. Trevisan, J. Tennyson, Calculated rates for the electron impact dissociation of molecular hydrogen, deuterium and tritium. *Plasma Phys. Control. Fusion* **44**(7), 1263 (2002)
- J.G. Verwer, Gauss-Seidel iteration for stiff ODEs from chemical kinetics. *SIAM J. Sci. Comput.* **15**, 1243–1250 (1994)
- A.B. Wedding, A.V. Phelps, Quenching and excitation transfer for the $c^3\Pi_u^-$ and $a^3\Sigma_g^+$ states of H_2 in collisions with H_2 . *J. Chem. Phys.* **89**(5), 2965–2974 (1988)
- J.M. Wadehra, Vibrational excitation and dissociative attachment, in *Nonequilibrium vibrational kinetics - Topics in Current Physics* vol 39, ed. M. Capitelli (Springer-Verlag, Berlin), pp. 191–232 (1986)
- D. Wunderlich, Vibrationally resolved ionization cross sections for the ground state and electronically excited states of the hydrogen molecule and its isotopomers. *At. Data Nucl. Data Tables* **140**, 101424 (2021)
- D. Wunderlich, L.H. Scarlett, S. Briefi, U. Fantz, M.C. Zammit, D.V. Fursa, I. Bray, Application of molecular convergent close-coupling cross sections in a collisional radiative model for the triplet system of molecular hydrogen. *J. Phys. D. Appl. Phys.* **54**(11), 115201 (2021)
- M. Zawadzki, R. Wright, G. Dolmat, M.F. Martin, B. Diaz, L. Hargreaves, et al., Low-energy electron scattering from molecular hydrogen: Excitation of the $X^1\Sigma_g^+$ to $b^3\Sigma_u^+$ transition. *Phys. Rev. A* **98**(6), 062704 (2018)
- A. Zamengo, M. Bigi, A. Maistrello, M. Recchia, Power supply system for large negative ion sources: Early operation experience on the SPIDER experiment. *Fusion Eng. Des.* **173**, 112790 (2021)
- M.C. Zammit, J.S. Savage, D.V. Fursa, I. Bray, Complete solution of electronic excitation and ionization in electron-hydrogen molecule scattering. *Phys. Rev. Lett.* **116**(23), 233201 (2016)
- M.C. Zammit, J.S. Savage, D.V. Fursa, I. Bray, Electron-impact excitation of molecular hydrogen. *Phys. Rev. A* **95**(2), 022708 (2017)

Chapter 8

The Plasma Sheath in Negative Ion Sources



R. McAdams, A. J. T. Holmes, and D. B. King

Abstract Negative ion sources for applications such as Neutral Beam Injection (NBI) have to rely on the production of the negative ions on a low work function surface such as caesium to attain the required extracted current densities. It is shown through an analytical model how the injection of these surface-produced negative ions affects the sheath structure through the production of a virtual cathode. This virtual cathode also affects the transport of negative ions from the wall to the plasma and hence the current density available for extraction.

Keywords Negative ion source · Neutral beam injection · Plasma sheath · Surface production · Virtual cathode

8.1 Introduction

Negative ion sources (Bacal et al. 2021) are used in a number of applications. Those sources used for applications such as neutral beam injection (NBI) in the development of present and future magnetic fusion energy devices such as LHD (Takeiri et al. 2007), JT-60SA (Kashiwagi et al. 2022) and ITER (Fantz et al. 2017; Hemsworth et al. 2017) consist of large volume plasmas (of the order of 1–2 m in length). The negative ion production is predominantly by atoms and ions from the plasma striking a low work function material such as a caesium layer on a metal surface such as the source walls or plasma grid. This is necessary as the extracted current densities from volume production alone are not high enough for these applications. In these sources, the region between the bulk plasma and the

R. McAdams (✉) · D. B. King
United Kingdom Atomic Energy Authority, Culham Centre for Fusion Energy, Culham Science Centre, Abingdon, Oxon, UK
e-mail: roy.mcadams@ukaea.uk

A. J. T. Holmes
Marcham Scientific, Hungerford, Berkshire, UK

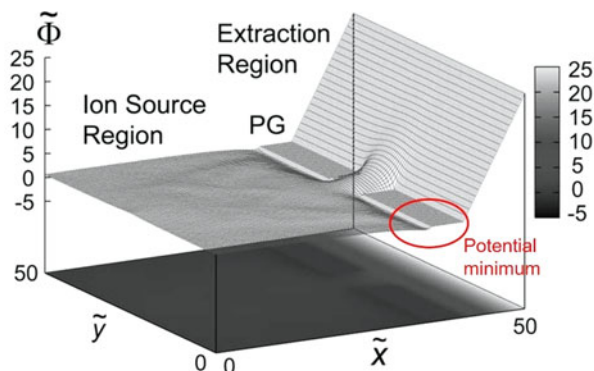


Fig. 8.1 A 2D3V PIC code simulation of the potential in an ion source showing a potential minimum in the sheath. (Note the distances are in Debye lengths. Reproduced from Hatayama (2008) with the permission of AIP Publishing)

wall is known as the sheath. It is usually only 10 s of microns wide. This chapter will show how the properties of this very narrow sheath compared to the size of the source can have a major influence on the production of negative ions at the low work function surface and their movement back into the plasma from where they can be extracted and formed into a usable beam.

In a plasma consisting of positive ions and electrons (and negative ions not produced at the wall with a density low compared to the electrons), a potential difference exists between the plasma and the wall over the sheath region. The potential through the sheath shows no structure as will be shown. Modelling of these sources to include the plasma and the surface production of negative ions and the beam extraction tended to use Particle in Cell (PIC) codes. It was noticed quite early on that there was a structure in the sheath that was formed. By structure, it is meant that instead of a smooth monotonic potential variation between the wall and the plasma, a potential minimum is formed near the wall from where the negative ions are being produced. As examples of this Figs. 8.1 and 8.2 shows the results of (Hatayama 2008; Taccogna et al. 2010) using 2D PIC codes which clearly show a potential minimum.

Finally, as an example of this structure in the sheath from simulations, Fig. 8.3 shows a 1D PIC result by (Wunderlich et al. 2009). Figure 8.3a shows how this sheath structure is formed as the atomic hydrogen density increases and hence the production of negative ions is increased. Figure 8.3b also shows that as the atomic hydrogen density increases the negative ion current reaching the plasma saturates.

This chapter aims to apply an analytical model of the sheath which includes negative ion formation at the wall to give physical insight into the processes taking place. This will show how the sheath plays an important role in the physics of the ion source. Initially, a brief recapitulation is given in Sect. 8.2 of the sheath properties for a simple plasma containing only electrons and positive ions. In Sect. 8.3 surface production of negative ions is described and the simple sheath concept is

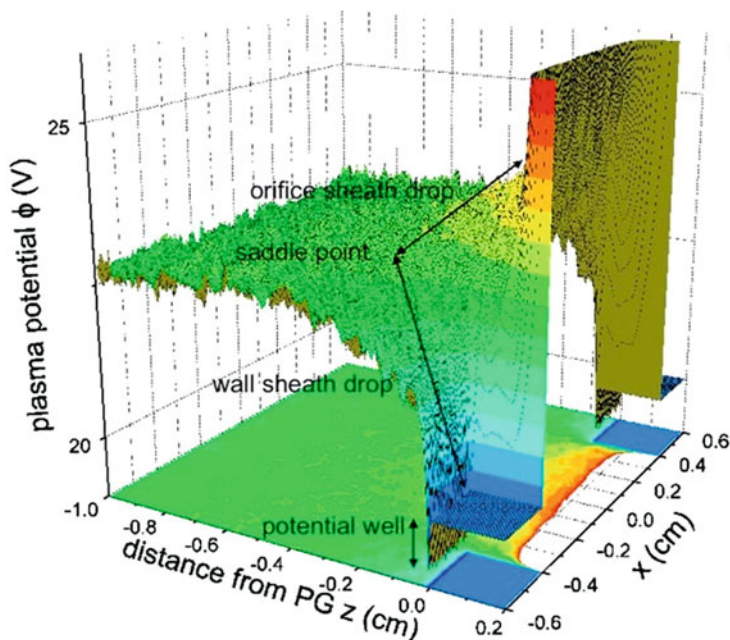


Fig. 8.2 A 2D PIC/Monte Carlo code simulation of the potential in an ion source showing a potential minimum in the sheath. (Reproduced from Taccogna et al. (2010) with the permission of AIP Publishing)

expanded to take into account how the sheath properties are changed by the emission of negative ions from the wall. The expanded model is applied to a plasma example in Sect. 8.4 including the effect of the surface work function, and some comments are made on the possible effects of electrons being injected into the sheath from the wall.

8.2 The Plasma Sheath

The plasma sheath is formed in a relatively narrow region formed between the bulk plasma and the walls of the vessel containing it. The walls are usually metallic. In a negative ion source that depends on surface production for most of the negative ions to be used in any application, these negative ions affect the sheath properties and the movement of negative ions across it. Before going on to discuss the plasma sheath in a negative ion source where there is a relatively large amount of negative ion production at the walls of the ion source, it is worthwhile recapping the properties of the plasma sheath and its connection to the bulk plasma for a simple plasma containing singly charged positive ions and electrons with no negative ions. The

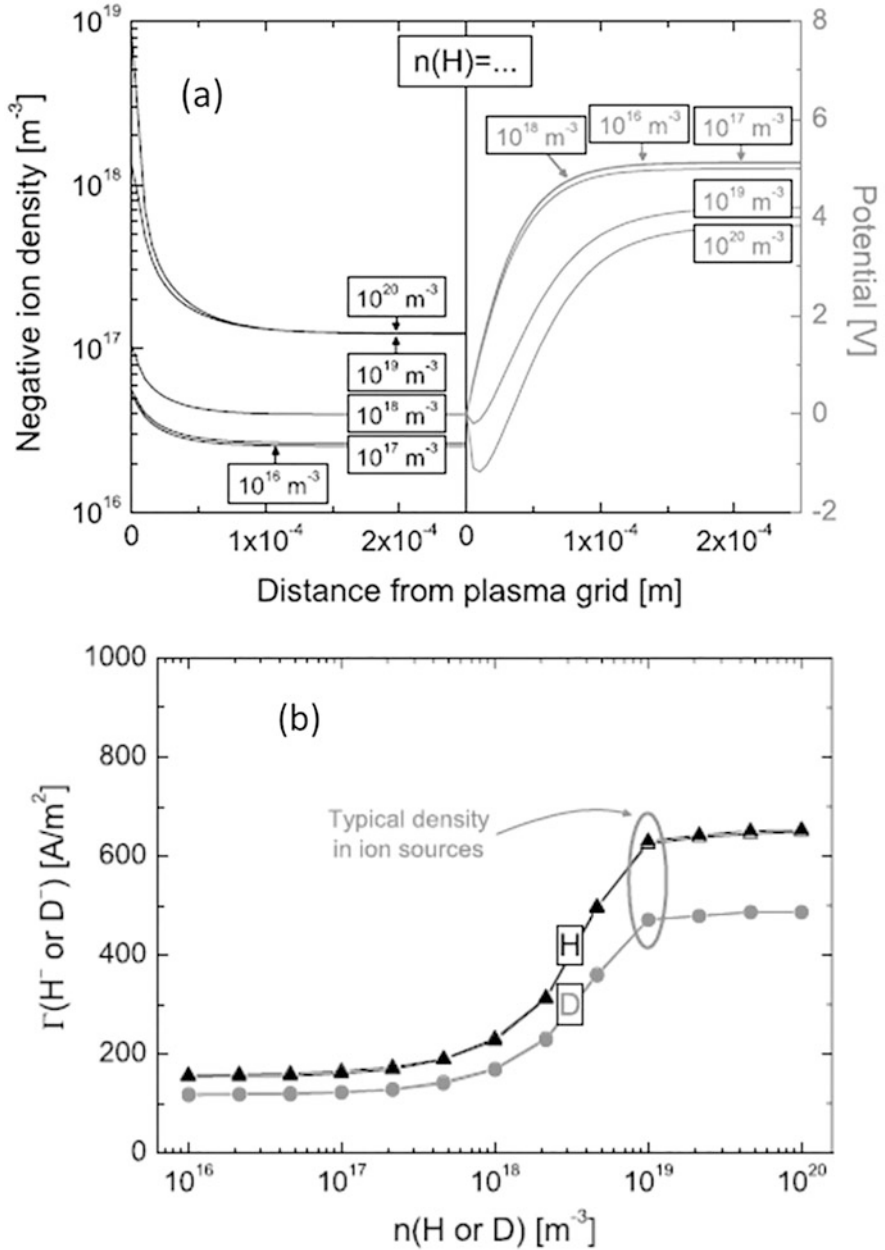


Fig. 8.3 (a) Formation of a virtual cathode in the plasma sheath and (b) the saturation of the transported negative ion current density across the sheath as the atomic hydrogen density is increased in a 1D-PIC simulation. (Figures from Wunderlich et al. (2009) © IOP Publishing. Reproduced with permission. All rights reserved)

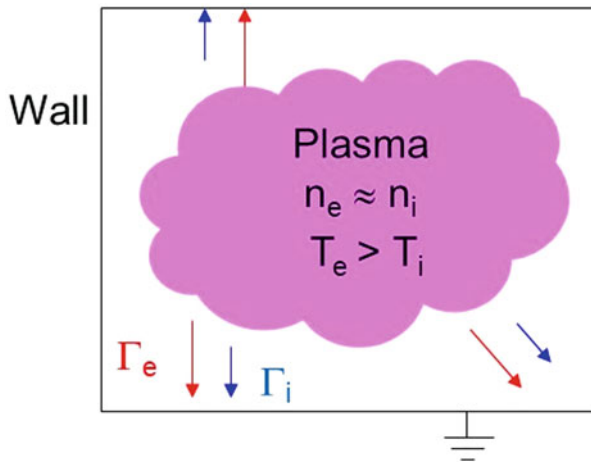


Fig. 8.4 A simple plasma in a grounded box

approach used follows work such as (Lieberman and Lichtenberg 2005; Chen 1984; Forrester 1988).

The plasmas formed in negative ion sources such as multicusp sources are weakly ionized. The energy that is used to generate the plasma such as inductively with radio frequency waves or via an arc discharge ends up heating the electrons to a very large extent. The electrons generally have a Maxwellian or quasi-Maxwellian distribution with a temperature of a few eV. The positive ions remain relatively cool and in general, are close to the gas temperature. Thus, for electron and ion temperatures T_e and T_i respectively $T_e > T_i$. There is quasi-neutrality in the plasma and for the respective electron and ion densities n_e and n_i , $n_e \approx n_i$. The situation is shown schematically in Fig. 8.4.

As $T_e > T_i$ and $m \ll M$ (m and M being the electron and ion masses respectively), the electron velocity is much greater than that of the ions. In the absence of magnetic fields, the flux of electrons, Γ_e , moving from the plasma to the wall, and being lost at the wall, is much greater than that of the ions Γ_i . That cannot occur as the plasma would gain an increasingly positive net charge thus violating plasma quasi-neutrality. Instead, the plasma is maintained at a positive potential relative to the wall potential, ϕ_w , which ensures that the fluxes of electrons and positive ions leaving the plasma are equal, $\Gamma_e = \Gamma_i$, and plasma neutrality is maintained. The region between the plasma and the wall where the potential difference exists is the plasma sheath. The electron and ion densities in the sheath are not equal and quasi-neutrality is violated. The positive ions are accelerated across the sheath to reach the wall. Not all the electrons are prevented from reaching the wall as they have a temperature of a few eV and a Maxwellian or quasi-Maxwellian velocity distribution. The width of the sheath is only a times the Debye screening length $\lambda_D \sim$ a few tens of microns.

Taking a 1-dimensional sheath, the potential ϕ is taken to be zero at the sheath edge and $-\phi_w$ ($x = 0$) at the wall. This sheath edge represents the point at which

quasi-neutrality is no longer valid. The electrons are assumed to have a Maxwellian energy distribution and for simplicity the ions have $T_i \approx 0$. The assumption is made that the ions have a velocity u_{i0} at the sheath edge and a density n_{i0} . The continuity of the ion flux gives

$$n_i(x)u_i(x) = n_{i0}u_{i0} \quad (8.1)$$

where n_i and u_i denote the density and velocity of the ions. Strictly this continuity only holds when there is no ionization within the sheath but that is a reasonable assumption since the sheath is so thin. Similarly, conservation of energy gives

$$\frac{1}{2}Mu_i^2(x) = \frac{1}{2}Mu_{i0}^2(x) - e\phi(x) \quad (8.2)$$

leading to

$$n_i = n_{i0} \left(1 - \frac{\phi}{\phi_0}\right)^{\frac{1}{2}} \quad (8.3)$$

where ϕ_0 is the equivalent energy of the ions at the sheath edge. (In reality the ions have distribution of energies centered around ϕ_0 , but for simplicity that is neglected here.)

Assuming the electron density in the sheath has a Boltzmann distribution

$$n_e = n_{e0} \exp\left(\frac{e\phi}{kT_e}\right) = n_{i0} \exp\left(\frac{e\phi}{kT_e}\right) = n_0 \exp\left(\frac{e\phi}{kT_e}\right) \quad (8.4)$$

where k is Boltzmann's constant, and since at the sheath edge plasma neutrality is valid, the electron density at the sheath edge, $n_{e0} = n_{i0} = n_0$.

Now, Poisson's equation can be used to describe the potential in the sheath. This is

$$\frac{d^2\phi}{dx^2} = \frac{e(n_e - n_i)}{\epsilon_0} \quad (8.5)$$

and using Eq. (8.3) for the ion density the Boltzmann distribution for the electrons gives

$$\frac{d^2\phi}{dx^2} = \frac{n_0 e}{\epsilon_0} \left[\exp\left(\frac{e\phi}{kT_e}\right) - \left(1 - \frac{\phi}{\phi_0}\right)^{\frac{1}{2}} \right] \quad (8.6)$$

To arrive at the potential in the sheath this equation must be integrated numerically with values for the various parameters. Some insight to the nature of the solution and the value of ϕ_0 in particular can be found by examining this equation

under the conditions $\phi \ll kT_e$ and $\phi \ll \phi_0$ i.e. close to the sheath edge. In that case the equation can be simplified by expanding the terms giving

$$\frac{d^2\phi}{dx^2} = \frac{n_0 e^2}{\epsilon_0 k T_e} \phi \left[1 - \frac{kT_e}{2e\phi_0} \right] = \frac{\phi}{\lambda_D^2} \left[1 - \frac{kT_e}{2e\phi_0} \right] \quad (8.7)$$

where λ_D is the Debye screening length.

The bracketed factor $[1 - kT_e/2e\phi_0]$ is critical in determining the nature of the solution. If $kT_e/2e\phi_0 > 1$ then the solution to Eq. (8.7) is oscillatory which is not physically realistic as it would lead to trapped particles. This factor represents $(n_e - n_i)$ and in the sheath this must be negative from the previous discussion as the electrons are attenuated by the Boltzmann factor. Thus, it must be the case that $[1 - kT_e/2e\phi_0] > 0$ and so the positive ion energy when they arrive at the sheath edge $\phi_0 > kT_e/2e$. This is known as the Bohm sheath criterion and $kT_e/2e$ is the Bohm energy. The corresponding ion velocity is known at the ion sound speed. The electron temperature determines the ion energy at the sheath edge. The region between the sheath edge and the bulk plasma in which the positive ions gain the Bohm energy is known as the presheath.

Since the ions have gained an energy ϕ_0 between the bulk plasma and the sheath edge there must also be a corresponding ion density change. If n_p is the electron (and ion density in the bulk plasma) then

$$n_{e0} = n_p \exp\left(\frac{\phi_s}{kT_e}\right) = n_p \exp(-0.5) = 0.606n_p \quad (8.8)$$

Thus the plasma density at the sheath edge is $\approx 0.61n_p$.

The question naturally arises as to where the ion energy ϕ_0 comes from. Because of collisions between the positive ions and the atoms and molecules, which have masses similar to the mass of the ions, the positive ions have a temperature, similar to that of the gas, which is very low compared to that of the electrons. This energy can only be gained by the existence of an electric field between the bulk plasma and the sheath edge. In this presheath the particles are collisional and the fluid equations must be used. The velocity, v , of the particles is given from the fluid equation

$$v = \frac{eE - \frac{kT}{n} \frac{dn}{dx}}{m\nu} \quad (8.9)$$

with E as the electric field, e is the charge of the particle (the sign of which depends on whether it is positively or negatively charged), m is the electron or ion mass, n is the density and ν is the collision frequency. Again, the fluxes must be equal, and solving for the electric field gives

$$E = -\frac{kT_e M \nu_i - kT_i m \nu_e}{M \nu_i + m \nu_e} \frac{dn/dx}{en} \quad (8.10)$$

and since $T_i \ll T_e$ and $M \gg m$ this becomes

$$E \approx -\frac{kT_e}{en} \frac{dn}{dx} \quad (8.11)$$

The equal fluxes moving to the sheath edge is ambipolar diffusion. Take as an example a plasma with $n_p = 10^{18} \text{ m}^{-3}$ and $T_e = 5 \text{ eV}$. There is a density change of $\Delta n \approx 0.4n_p$ between the bulk plasma and the sheath edge and taking Δx as 0.1 m as a typical dimension, a value of the electric field of $E = 221220 \text{ V/m}$ is obtained. From Poisson's equation

$$\frac{dE}{dx} \sim \frac{E}{L} = \frac{e}{\epsilon_0} (n_e - n_i) \quad (8.12)$$

This gives, for an electric field of 20 V/m and a length of 0.1 m from above, a value of $n_e - n_i$ of 10^{10} m^{-3} . For the plasma with $n_p = 10^{18} \text{ m}^{-3}$ this is one part in 10^8 i.e. quasi-neutrality is a very good approximation but small changes in the charge balance can lead to appreciable electric fields.

In the simple plasma in a box concept, the positive ion and electron fluxes are equal between the sheath edge and the wall (Note that in reality that may not be the case for all of the source wall. For example, part of the walls could be the anode of an arc discharge. In the case, the sheath potential must adjust to make the flux to that part of the source equal to the net charge flux, electrons minus ions, to the cathode). In the plasma in a box case, the electron flux is thermal and its value at the wall can be equated with that of the ions at the sheath edge to give (with T_e in eV)

$$0.61n_p \sqrt{\frac{eT_e}{M}} = 0.61 \frac{n_p}{4} \sqrt{\frac{8eT_e}{\pi m}} \exp\left(\frac{\phi_w}{T_e}\right) \quad (8.13)$$

where m is the electron mass. Rearranging gives the potential between the wall and the sheath edge

$$\phi_w = \frac{1}{2} T_e \ln\left(2\pi \frac{m}{M}\right) \quad (8.14)$$

As an example, with deuterium ions (D^+) and an electron temperature of $T_e = 2 \text{ eV}$ the potential between the wall and the sheath edge is -6.4 V or $-3.2T_e$ although this will change if the surface is biased to draw a net current.

In summary, the situation of this simple description of the plasma and sheath is shown in Fig. 8.5.

Or in more pictorial form (Fig. 8.6).

A relatively simple picture of a plasma sheath has been developed above. Much more detailed descriptions including the problem of connecting the plasma to the sheath can be found in (Lieberman and Lichtenberg 2005; Chen 1984; Forrester 1988) amongst many others. Sheath physics remains a very active research topic

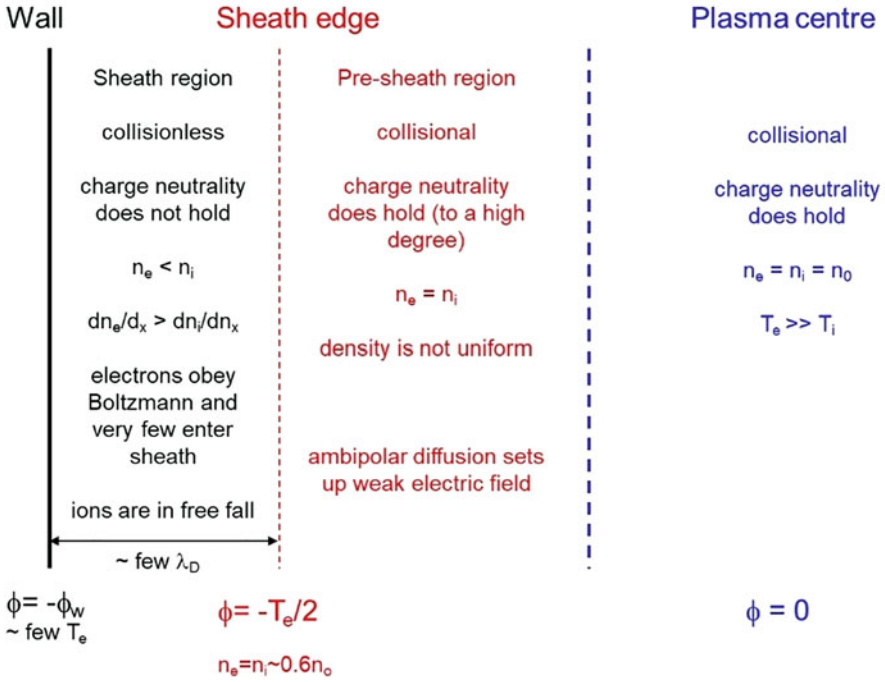


Fig. 8.5 The simple description of the plasma and the sheath

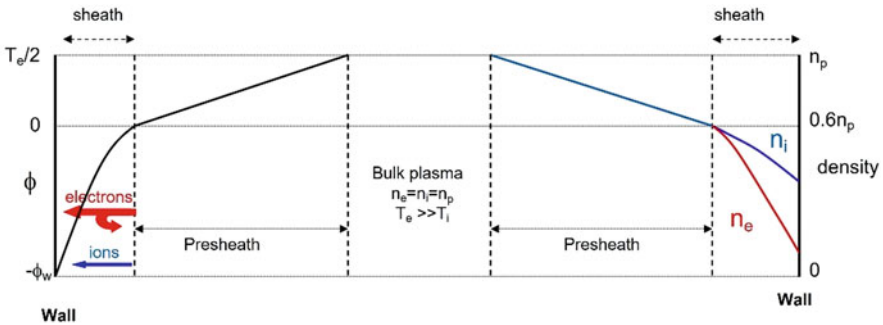


Fig. 8.6 Pictorial depiction of the simple plasma and sheath. (Note that the sheath widths are greatly exaggerated)

today. However, the above description is an adequate foundation for the problem of how the sheath is altered by the production of negative ions at the walls. These negative ions disturb the space charge in the sheath and the potential across it and this in turn affects how they are transported across that potential. This has implications for the production of high-current negative ion sources for applications such as heating and diagnostics of fusion plasmas.

8.3 Production and Transport of Negative Ions Across the Sheath

8.3.1 Surface Production of Negative Ions

Before going on to describe the sheath in a negative ion source where the negative ions are formed on a surface the production of negative ions on such a surface will be discussed. Negative ion sources for applications such as fusion research are based on the use of caesium applied to the plasma grid which forms the source wall in front of the extractor/accelerator. Negative ions are formed through negative surface ionisation when hydrogen atoms or ions approach and impinge on and are reflected from a low work function metal surface such as caesium (van Amersfoort et al. 1985). Figure 8.7a shows the process.

A proton approaching the surface will be neutralised by resonant neutralisation into an excited state followed by Auger decay to the ground state. As the neutralised proton or atom from the plasma approaches the surface the affinity level associated with the negative ion, E_A , is shifted and its width increases. Very close to the surface this affinity level falls below the Fermi energy, ϵ_F . An electron can then transfer from the metal into the affinity level of the neutral particle forming a negative ion. It is also established that some of the negative ions can be formed by sputtered atoms due to impinging atomic or molecular ions which “capture” an electron from the surface in the same way as described for an incoming atom. This is shown schematically in Fig. 8.7b. The benefit of a low work function surface such as cesium is clear. The overlap between the affinity level and the electrons in the conduction band is maximized allowing negative ion formation. The work function, W , for caesium on a metal surface can be as low as 1.45 eV for a coverage of about 0.6 monolayers (van Amersfoort et al. 1985).

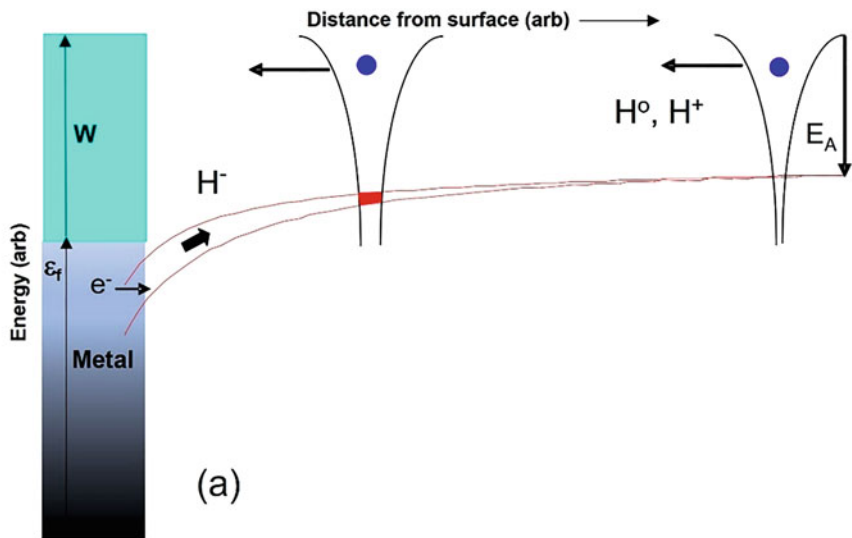
Negative ions formed at the surface will be transported across the sheath and into the plasma due to the positive potential between the wall and the plasma and can then be extracted to form a negative ion beam.

Figure 8.8 shows the conversion efficiency of protons as a function of proton energy on various caesiated surfaces (Seidl et al. 1996) together with the theoretical calculation by (Rasser et al. 1982).

In Fig. 8.8 the curve from (Rasser et al. 1982) is a straightforward equation for the conversion probability in terms of the work function W and electron affinity E_A

$$P = \frac{2}{\pi} \left[\exp \left(-\frac{\pi (W - E_A)}{2av} \right) \right] \quad (8.15)$$

where v is the proton velocity and $a = 3.1 \times 10^{-5}$ eV s/m is a screening constant. Equation (8.15) shows clearly the dependence of the efficiency on the factor $W - E_A$. (Seidl et al. 1996) showed data where the efficiency for H^+ and H_2^+ ions is only dependent on the energy per nucleon. The efficiency for H^- production from



Incident plasma particles

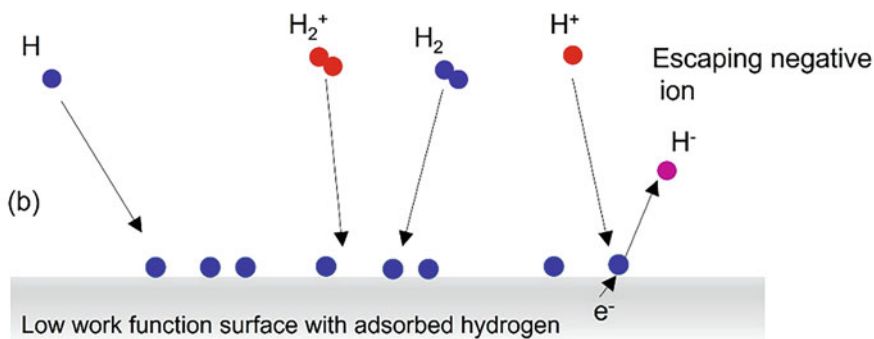


Fig. 8.7 (a) Formation of negative ions on a low work function, W , surface by hydrogen atoms and ions by negative surface ionisation. Reproduced (and redrawn) from van Amersfoort et al. (1985) with the permission of AIP Publishing and (b) by sputtering of adsorbed hydrogen atoms

atoms is shown in Fig. 8.9. The efficiency increases as the atomic energy increases and reaches a maximum at an atomic temperature of ~ 2.5 eV.

From these graphs the yield of negative ions from the surface can be estimated. The current density (Am^{-2}) of negative ions produced by a thermal flux of atoms Γ_H with temperature T_H impinging on the caesiated surface is given by

$$[j_{H^-}]_H = eY(T_H)\Gamma_H = eY(T_H)\frac{1}{4}n_H\sqrt{\frac{8eT_H}{\pi M_H}} \quad (8.16)$$

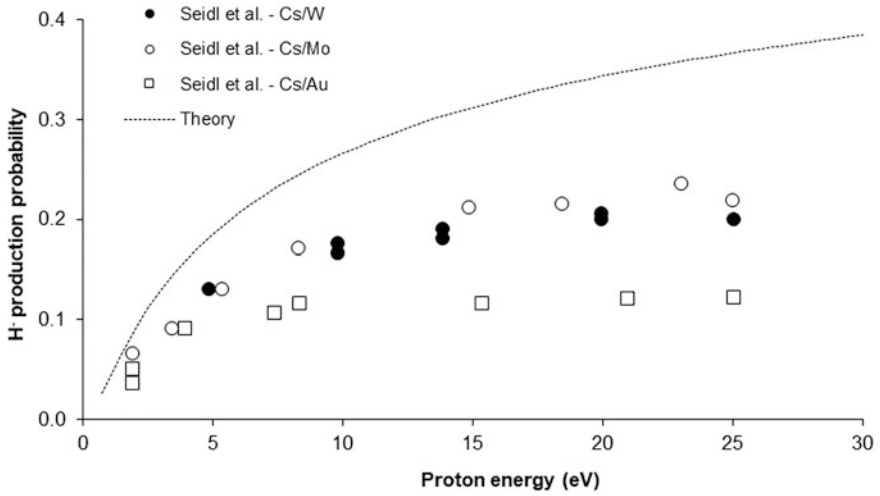


Fig. 8.8 H^- production efficiency as a function of proton energy on various metals with a caesium covering measurements (Seidl et al. 1996) and a calculation using Eq. (8.15) with a work function of 1.5 eV

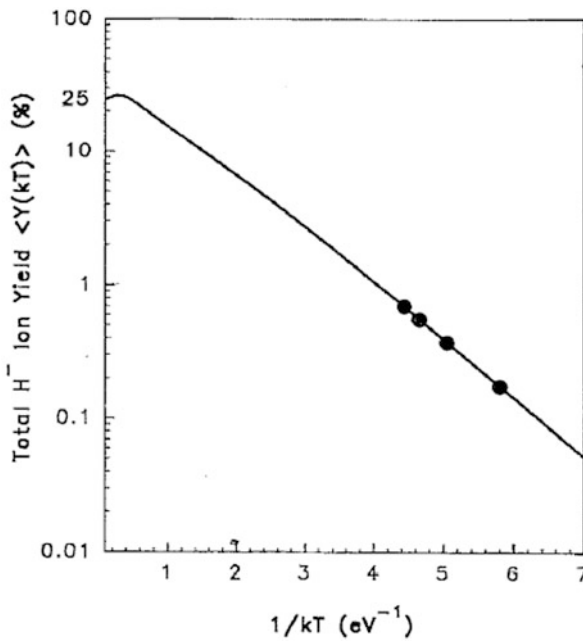


Fig. 8.9 H^- production efficiency as a function of atomic temperature for H^0 atoms on a caesium surface. (Reproduced from Lee and Seidl (1992) with permission from AIP)

where $Y(T_H)$ is the yield, n_H is the density of hydrogen atoms and M_H is the ion mass. Using values from the simulation of (Wünderlich et al. 2009) where n_H is 10^{19} m^{-3} , T_H is 0.9 eV and $Y(T_H) = 0.12$ the current density of negative ions produced at the surface is $\approx 670 \text{ Am}^{-2}$. Similarly, the yield for positive ions of energy E on reaching the surface can be written

$$[j_{H^-}]_{H^+} = eY(E)0.6n_p\sqrt{\frac{eT_e}{M}} \quad (8.17)$$

with n_p as the positive ion plasma density and $Y(E)$ is the yield at ion energy E . The flux at the sheath edge has been used since it is conserved and is thus the flux at the wall. The energy E can be found from Eq. (8.14) as $E \sim \phi_W + T_e/2$ (allowing for the energy of the ions at the sheath edge). Again from (Wünderlich et al. 2009) $n_p \approx 4 \times 10^{17} \text{ m}^{-3}$ and $T_e = 2 \text{ eV}$. This gives $\phi_W = 5.7 \text{ V}$ and $E = 6.7 \text{ V}$ and $Y(E) \approx 0.15$ and so the current density of negative ions produced by positive ions under these circumstances is $\approx 80 \text{ Am}^{-2}$.

The flux of negative ions produced by the atoms is approximately 8–9 times that produced by the positive ions. Moreover, the ratio of the total negative ion flux from the wall produced by both atoms and positive ions to that of positive ions reaching the wall is, in this case, approximately 1.4. The negative ion space charge is significantly higher than that of the positive ions in this sheath and this has implications for the structure of the sheath itself.

8.3.2 The Formation of a Virtual Cathode

Consider the flow of current between two infinite planes with each plane being at a different potential. The current flows from a plane at $-V_c$ volts (the cathode) towards a plane at zero volts (the anode) as shown in Fig. 8.10.

When there is no emission from the cathode the potential between the planes is linear and the field is constant throughout. As the amount of emitted current increases a build-up of space charge at the cathode results in the field near the cathode being reduced. As the emission increases, a point is reached where the field at the cathode is zero. This is the space charge limited condition. The maximum amount of current that can reach the anode is the space charge limited current density is determined by a solution to the Poisson equation with $E = 0$ at the cathode. This maximum current density is given by the Child-Langmuir equation

$$j = \frac{4\epsilon_0}{9} \sqrt{\frac{2e}{M}} \frac{V_c^{\frac{3}{2}}}{d^2} \quad (8.18)$$

As the emission increases further, the space charge continues to build up and the field at the cathode becomes negative and since the potential must reach zero at

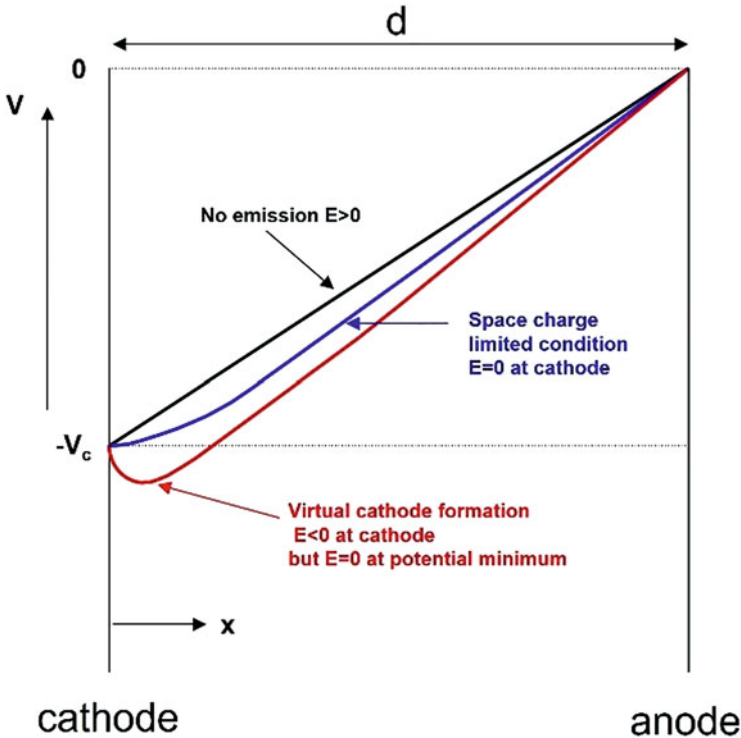


Fig. 8.10 The potential between two planes as the amount of emission is varied

distance d a minimum in the potential is formed. The region where the potential is below $-V_c$ is known as the virtual cathode. The point at which the field is zero becomes the effective point of emission. Particles emitted at the cathode must overcome the potential barrier between the cathode and the virtual cathode if they are to reach the anode. There are three requirements for a virtual cathode to be formed:

1. The emitted current density must exceed the space charge limited current density as outlined above.
2. The particles must be emitted with a finite energy so that the potential between the emission surface and the minimum of the virtual cathode can be overcome.
3. The emitted particles must have a distribution of energies otherwise they may be reflected at some point in the sheath and this would create a point where their velocity would be zero leading to an infinite density requirement.

These concepts can now be applied to the emission of negative ions into the plasma sheath.

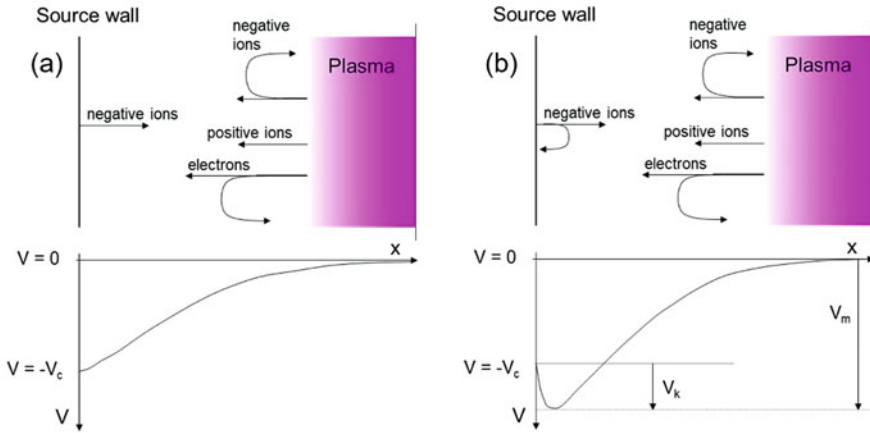


Fig. 8.11 The schematic of the sheath (a) without and with (b) the virtual cathode

8.3.3 The Virtual Cathode in a Plasma-Based Ion Source

The situation that will be analysed is shown in Fig. 8.11. The plasma is taken to consist of positive ions, electrons and negative ions with a density that is low compared to that of the electrons. The source wall or cathode is at a potential V_c with respect to the plasma. In practice the plasma grid through which the negative ions are extracted is biased positively, as that is found, experimentally, to reduce the co-extracted electron flux. The negative ions will be those emitted from the wall which have been transported across the sheath and the plasma may also contain negative ions produced by dissociative attachment of low energy electrons to vibrationally excited molecules; see for example (Bacal et al. 2021). The positive ions move down the potential gradient whereas most of the electrons and negative ions do not penetrate far into the sheath. At low emission current densities, the negative ion space charge is not sufficient to form a virtual cathode as in Fig. 8.11a. As the negative ion emission rate from the wall increases the point is reached where a virtual cathode is formed. The depth of the virtual cathode is V_k with respect to the wall voltage and so the potential minimum is $V_m = V_c + V_k$. Due to the virtual cathode, negative ions emitted at the wall must overcome the potential barrier due to the virtual cathode. Similarly positive ions which reach the minimum of the virtual cathode must overcome the potential barrier due to the virtual cathode in order to reach the wall.

The approach to analysing and solving the appropriate equations for the two situations shown in Fig. 8.11 follows that of (McAdams et al. 2011), although much of the mathematical details are omitted here.

As pointed out above the negative ions must have a distribution of energies if a virtual cathode is to be formed. The negative ions are formed from incident atoms (and ions) which do indeed have a distribution of energies. The energy of the

negative ion is related to that of the incident atom by an energy reflection coefficient, R_E (Seidl et al. 1996). The minimum work function for a caesiated surface is $W \approx 1.5$ eV and only those atoms (or ions) with energy greater than a threshold energy $E_{\text{thr}} = W - E_A \approx 0.75$ eV can form negative ions. For a Maxwellian distribution of energies of the incident atoms with associated temperature T_H an average energy of the emitted negative ions, $\langle E_{H^-} \rangle$ can be calculated as

$$\langle E_{H^-} \rangle = \frac{R_E \int_{E_{\text{thr}}}^{\infty} E^{\frac{1}{2}} (E - E_{\text{thr}}) \exp\left(-\left(\frac{E}{T_H}\right)\right) dE}{\int_{E_{\text{thr}}}^{\infty} E^{\frac{1}{2}} \exp\left(-\left(\frac{E}{T_H}\right)\right) dE} \quad (8.19)$$

Taking a value of R_E of 0.7 (Seidl et al. 1996) this gives a value of $\langle E_{H^-} \rangle = 0.7$ eV for an atomic temperature of $T_H = 0.8$ eV. Measurements by (Melnychuk et al. 1989) show results that the negative ions are formed with a Maxwellian energy distribution with a temperature equal to that of the incident atoms in which case the average energy would be higher than that given above i.e. $\approx 3R_E T_H/2 = 0.84$ eV.

The sheath physics can now be analysed according to the two situations shown in Fig. 8.11 i.e. up to the point of the formation of a virtual cathode and after the formation of a virtual cathode.

8.3.3.1 The Sheath before the Formation of a Virtual Cathode

As the current of emitted negative ions increases, the electric field at the emitting surface decreases until it becomes zero and as discussed above this is the space charge limited condition. This situation was analysed initially by (Amemiya et al. 1998) for the case of electrons emitted from the wall into the sheath. The approach by (McAdams et al. 2011) up to the point of formation of the virtual cathode follows that of (Amemiya et al. 1998) but allows for the initial energy of the particles emitted from the wall into the sheath. The approach is to solve Poisson's equation in the sheath.

The densities of the positive ions, electrons and negative ions at the sheath edge are n_{i0} , n_{e0} and n_{n0} with temperatures T_i , T_e and T_n respectively. As in Sect. 8.2, the potential at the sheath edge is taken as $V = 0$ and the wall is at a potential (Fig. 8.11a) $V = V_c$ which allows for the case where the wall is biased. The positive ions arrive at the sheath edge with an energy eV_0 . This is not the Bohm energy since there are negative ions emitted from the wall and in the plasma. The positive ion density in the sheath is then from Eq. (8.3)

$$n_i = n_{i0} \left(\frac{V_0}{V_0 - V} \right)^{\frac{1}{2}} \quad (8.20)$$

with V measured from the sheath edge and is a negative quantity. The positive ion initial energy comprises of the energy due to the potential difference between the plasma and the sheath edge, U_0 , and their thermal energy $T_i/2$ i.e.

$$V_0 = U_0 + \frac{T_i}{2} \quad (8.21)$$

The negative ions emitted from the wall have a current density j_b and have a density in the sheath of n_b and their initial energy is eU_b . Notationally the subscript b is used to denote the “beam” of negative ions emitted from the wall. It is not a true beam and is quite distinct from the negative ion beam extracted from the source. The density of these emitted negative ions in the sheath is

$$n_b = \frac{j_b}{ev_b} = \frac{j_b}{e(2e[V_c + U_b + V]/M_b)^{\frac{1}{2}}} \quad (8.22)$$

where v_b and M_b are the velocity and mass respectively of the negative ions emitted from the wall. As discussed earlier the negative ions emitted from the wall have a Maxwellian energy distribution where the low energy particles ($E < R_E E_{\text{thr}}$) are missing. To simplify the mathematics, it will simply be assumed that the negative ions are emitted with a Maxwellian energy distribution and associated temperature T_b giving

$$U_b = \langle E_{H^-} \rangle = \frac{T_b}{2} \quad (8.23)$$

The electrons and negative ions in the sheath from the plasma are taken to have Maxwellian distributions also

$$n_e = n_{e0} \exp\left(\frac{V}{T_e}\right) \quad \text{and} \quad n_n = n_{n0} \exp\left(\frac{V}{T_n}\right) \quad (8.24)$$

Now Poisson’s equation for the potential in the sheath can be written down

$$-\frac{d^2V}{dx^2} = \frac{e}{\epsilon_0} \left[n_{i0} \left(1 - \frac{V}{V_0}\right)^{-\frac{1}{2}} - \frac{j_b}{e} \left(\frac{M_b}{2e}\right)^{\frac{1}{2}} (V_c + U_b + V)^{-\frac{1}{2}} - n_{e0} \exp\left(\frac{V}{T_e}\right) - n_{n0} \exp\left(\frac{V}{T_n}\right) \right] \quad (8.25)$$

To make the solution start at the fixed potential of the cathode (wall) set $\phi = V_c + V$ and the first integral of this equation can be carried out analytically (McAdams et al. 2011) to give an expression for $(d\phi/dx)^2$ subject to the boundary condition that electric field is zero at the sheath edge ($\phi = V_c$) although the details are omitted here. The boundary conditions used by (Amemiya et al. 1998) are that the plasma is quasi-neutral at the sheath edge i.e., $n_{i0} = n_b + n_{e0} + n_{n0}$ and that the derivative of the total net charge density with respect to the potential is zero at the

sheath edge. These lead to an expression for the kinetic energy of the positive ions at the sheath edge

$$V_0 = \frac{n_{i0}}{2 \left(\frac{n_{e0}}{T_e} + \frac{n_{n0}}{T_n} - \frac{j_b}{e} \left(\frac{M_b}{e} \right)^{1/2} (2V_c + 2U_b)^{-\frac{3}{2}} \right)} \quad (8.26)$$

It can be seen that the negative ions in the plasma decrease the initial energy of the positive ions, whereas the negative ions from the cathode act to increase it. If there is no emission from the wall but the plasma contains negative ions Eq. (8.26) reproduces the results of (Boyd and Thompson 1959; Braithwaite and Allen 1988). Notice that if there were no emitted negative ions nor negative ions in the plasma V_0 would reduce to $T_e/2$ i.e., the usual Bohm energy.

The maximum negative ion current density emitted from the cathode before the virtual cathode is formed, $j_{b \max}$, can then be calculated. This occurs when the electric field at the cathode is zero. This criterion gives the result

$$j_{b \max} = \frac{2n_{i0}V_0 \left(\left(1 + \frac{V_c}{V_0}\right)^{1/2} - 1 \right) + n_{e0}T_e \left(\exp\left(\frac{-V_c}{T_e}\right) - 1 \right) + n_{n0}T_n \left(\exp\left(\frac{-V_c}{T_n}\right) - 1 \right)}{\frac{2}{e} \left(\frac{M_b}{2e} \right)^{1/2} \left[(V_c + U_b)^{1/2} - U_b^{1/2} \right]} \quad (8.27)$$

These equations can be solved for all unknown parameters given the electron and negative ion densities and temperatures and the negative ion current and initial energy. Once obtained, the potential in the sheath can be found by integrating numerically the equation for $(d\phi/dx)^2$.

8.3.3.2 The Plasma Sheath with a Virtual Cathode

When the emission current of negative ions from the cathode is higher than $j_{b \max}$ as given in Eq. (8.27) the electric field at the cathode is negative and a virtual cathode must be formed as shown in Fig. 8.11b. The depth of the virtual cathode is V_k relative to the cathode. The potential relative to the sheath edge is then $V_m = V_c + V_k$. The analysis is more complicated than in the case where a virtual cathode is not formed. It does become a little simpler when it is realized that from the point in the sheath where the potential is minimum (at the bottom of the virtual cathode) to the sheath edge the solution to the sheath equations must be the same as the space charge limited condition where the electric field is zero at the cathode. The space charge limited current density at the virtual cathode is the fraction of the emitted current density which overcomes the potential barrier between the cathode and the virtual cathode i.e.

$$j_{b \max} = j_b \exp\left(-\frac{V_k}{T_b}\right) \quad (8.28)$$

It remains then to solve Poisson's equation in the region between the cathode and the minimum of the virtual cathode. The two solutions must be continuous at the potential minimum i.e., $d\phi/dx = 0$ at $\phi = 0$. In this region, the potential is designated θ and is zero at the potential minimum. For the positive ions there are two cases. When $\theta < V_m + U_0$ all the positive ions reach the cathode and conservation of flux can be used to determine the positive ion density in this region.

$$\theta < V_m + U_0 \quad n_i = \frac{n_{i0} V_0^{\frac{1}{2}}}{(V_m + V_0 - \theta)^{\frac{1}{2}}} \quad (8.29)$$

When $\theta > V_m + U_0$ the positive ions are retarded similarly to the negative ions and electrons from the plasma and a Boltzmann factor is used to account for this. This leads to

$$\theta > V_m + U_0 \quad n_i = \frac{n_{i0} V_0^{1/2}}{(T_i/2)^{1/2}} \exp\left(-\frac{(\theta - V_m - U_0)}{T_i}\right) \quad (8.30)$$

The densities in the two cases are continuous when $\theta = V_m + U_0$ but the density at the critical potential is slightly higher than that at the sheath edge since the potential energy U_0 is considered for the transition to a Boltzmann distribution and not the total energy V_0 .

For the electrons and negative ions from the plasma, the fluxes that reach the virtual cathode, j_{ev} and j_{nv} respectively are conserved as they are accelerated towards the cathode i.e.

$$j_{ev} = en_{e0} \left(\frac{eT_e}{m}\right)^{\frac{1}{2}} \exp\left(-\frac{V_m}{T_e}\right)$$

where m is the electron mass. Then

$$n_e = \frac{j_{ev}}{e\left(\frac{2e}{m}\left(\theta + \frac{T_e}{2}\right)\right)^{\frac{1}{2}}} = n_{e0} \exp\left(-\frac{V_m}{T_e}\right) \times \left(1 + \frac{2\theta}{T_e}\right)^{\frac{1}{2}} \quad (8.31)$$

There is a similar equation for the plasma negative ions

$$n_n = \frac{j_{nv}}{e\left(\frac{2e}{M_b}\left(\theta + \frac{T_n}{2}\right)\right)^{\frac{1}{2}}} = n_{e0} \exp\left(-\frac{V_m}{T_n}\right) \times \left(1 + \frac{2\theta}{T_n}\right)^{\frac{1}{2}} \quad (8.32)$$

The densities can now be used in Poisson's equation to give the potential in the region between the minimum of the virtual cathode and the wall. The potential θ is zero at the minimum and $d\theta/dx = 0$.

The negative ions from the cathode have a flux in the virtual cathode sheath

$$j_b(\theta) = j_b \exp\left(\frac{(\theta - V_k)}{T_b}\right) \quad (8.33)$$

and the negative ion density is

$$n_b = \frac{j_b \exp\left(\frac{(\theta - V_k)}{T_b}\right)}{e\left(\frac{2e}{M_b} \frac{T_b}{2}\right)^{\frac{1}{2}}} \quad (8.34)$$

At $\theta = 0$ i.e. the potential minimum $j_b = j_{b \max}$ and at $\theta = V_k$ (the cathode) j_b is simply the emitted current density. Equations (8.33) and (8.34) are consistent with Eq. (8.28).

The densities can now be used in Poisson's equation to give the potential in the region between the minimum of the virtual cathode and the wall. The potential θ is zero at the minimum and $d\theta/dx = 0$. The solution for the case $j_b = j_{b \max}$ in the no virtual cathode case can be used in the region between the virtual cathode and the sheath edge. These solutions are appropriately matched and give the potential between the cathode and the sheath edge. Descriptions of how to solve these equations are given in (McAdams et al. 2011).

8.4 The Plasma Sheath with Negative Ions Emitted at the Wall

8.4.1 The Sheath Structure and Its Implications

To illustrate the formation of the virtual cathode as calculated by this analytical model the plasma conditions of $n_{i0} \sim 3.9 \times 10^{17} \text{ m}^{-3}$, $T_i = 0.8 \text{ eV}$, $n_{e0} \sim 3.5 \times 10^{17} \text{ m}^{-3}$, $T_e = 2 \text{ eV}$, $n_H = 10^{18} \text{ m}^{-3}$, $T_H = 0.8 \text{ eV}$ and a cathode potential of $V_c = -5 \text{ V}$. These conditions are very similar to those used by (Wunderlich et al. 2009). Figure 8.12 shows the potential in the sheath at three different values of the emitted current density.

At the lowest current density, the potential rises monotonically from the cathode to the plasma. At a current density of $\sim 600 \text{ Am}^{-2}$, the field at the cathode is approximately zero and this is the space charge limited condition. At higher emitted current densities the virtual cathode is formed. For the case of 800 Am^{-2} , the virtual cathode depth is approximately 0.4 V. The effect of the virtual cathode on the transported negative ion current density from the wall to the plasma is shown in Fig. 8.13. As the emitted current density is increased initially all the emitted current density is transported across the sheath to the plasma. The virtual cathode is formed at an emitted current density of just below 600 Am^{-2} and its depth increases at the

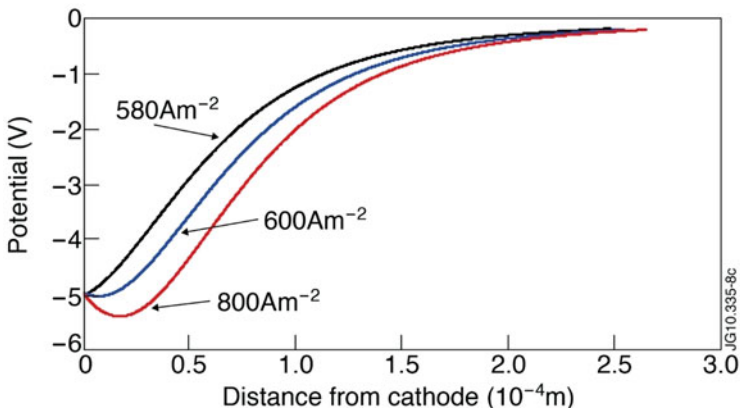


Fig. 8.12 The sheath potential for three values of the emitted current density of 580, 600 and 800 A m^{-2}

emitted current density is increased. Once formed, increasing the emitted current density has very little effect on increasing the transported negative ion current to the plasma. This has important implications for negative ion sources as it effectively places a limit on the extractable current density.

These results are in good agreement with the 1D-PIC calculations of (Wunderlich et al. 2009) which are shown in Fig. 8.3. Using these plasma conditions in (Wunderlich et al. 2009) and an emitted current density of 600 A m^{-2} as the point at which the virtual cathode is formed gives, via Eq. (8.16), an atomic hydrogen density of $\sim 10^{19} \text{ m}^{-3}$. This corresponds very well with the results in Fig. 8.3.

It was mentioned earlier that it is common practice to bias the plasma grid, on which the negative ions are formed, more positive than the rest of the ion source as that has been shown experimentally to reduce the flux of the co-extracted electrons. The effect of changing the cathode potential on the virtual cathode formation and the current density transported across the sheath is shown in Fig. 8.14 for two values of the emitted current density with the plasma conditions used in Figs. 8.12 and 8.13. For the case of an emitted current density of 600 A m^{-2} the virtual cathode is not formed and the transmitted current density is not attenuated unless the cathode voltage is greater than approximately -5 V in accordance with Figs. 8.12 and 8.13. At 800 A m^{-2} of emitted current density the virtual cathode persists at potential differences as high as 10 V and the negative ion current density is attenuated out to this voltage. It might have been thought that at high enough values of potential difference all the emitted current density would have been transported across the sheath and no virtual cathode would be formed.

At high values of V_c the maximum negative ion current that can be transported is independent of V_c and only depends on the positive ion density n_{i0} and the energy of the positive ions at the sheath edge, V_0 , as given in eq. (8.26) i.e.

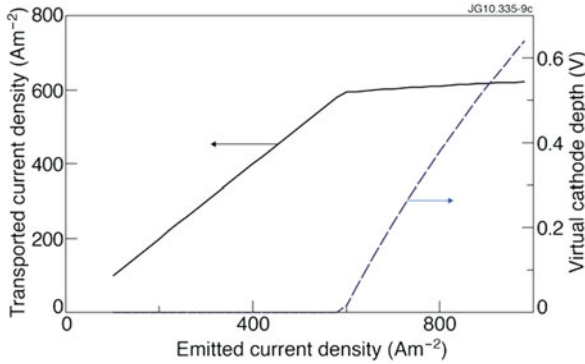


Fig. 8.13 The effect of the virtual cathode on the transported current density of negative ions

$$j_{b \max} \approx en_{i0} \sqrt{\frac{2eV_0}{M_b}} \quad (8.35)$$

which is effectively the flux of positive ions at the sheath edge. If the surface production rate exceeds this positive ion flux, then a virtual cathode will always be formed and the transported flux of negative ions will be limited. This has implications for the production of higher current densities. Increasing the surface production will not increase the negative ion flux available for extraction. This can only be achieved by increasing the positive ion flux in the sheath to compensate for the negative ion space charge.

The examples given above have been used to illustrate the processes occurring in the sheath. The negative ions in the plasma have not been explicitly accounted for because their density is low and flux to the wall was small. These negative ions arise from those transported across the sheath plus those produced by dissociative attachment of low energy electrons to vibrationally excited molecules. Taking a value of electron density $n_{e0} = 3.7 \times 10^{17} \text{ m}^{-3}$ the negative ion to electron density in the plasma can be varied. The other plasma parameters in this example are $T_e = 2 \text{ eV}$, the positive and negative ion temperatures are $T_i = T_n = 0.8 \text{ eV}$, the emitted negative ion energy $T_b/2 = 0.7 \text{ eV}$ and the cathode potential is $V_c = -4 \text{ V}$. The emitted negative ion current density is set to 600 Am^{-2} . The effect of changing the negative ion density is shown in Fig. 8.15.

As the negative ion density increases the depth of the virtual cathode falls until it is zero at a value of n_{n0}/n_{e0} just above 0.2. From this point the negative ion density continues to increase until all the emitted current density reaches the plasma. This is understood in terms of plasma neutrality. As the negative ion density increases the positive ion density in the plasma must also increase to maintain plasma neutrality for a fixed electron density. The flux of positive ions across the sheath will also increase and this will act to compensate for the space charge of the emitted negative ions thus reducing the depth of the virtual cathode.

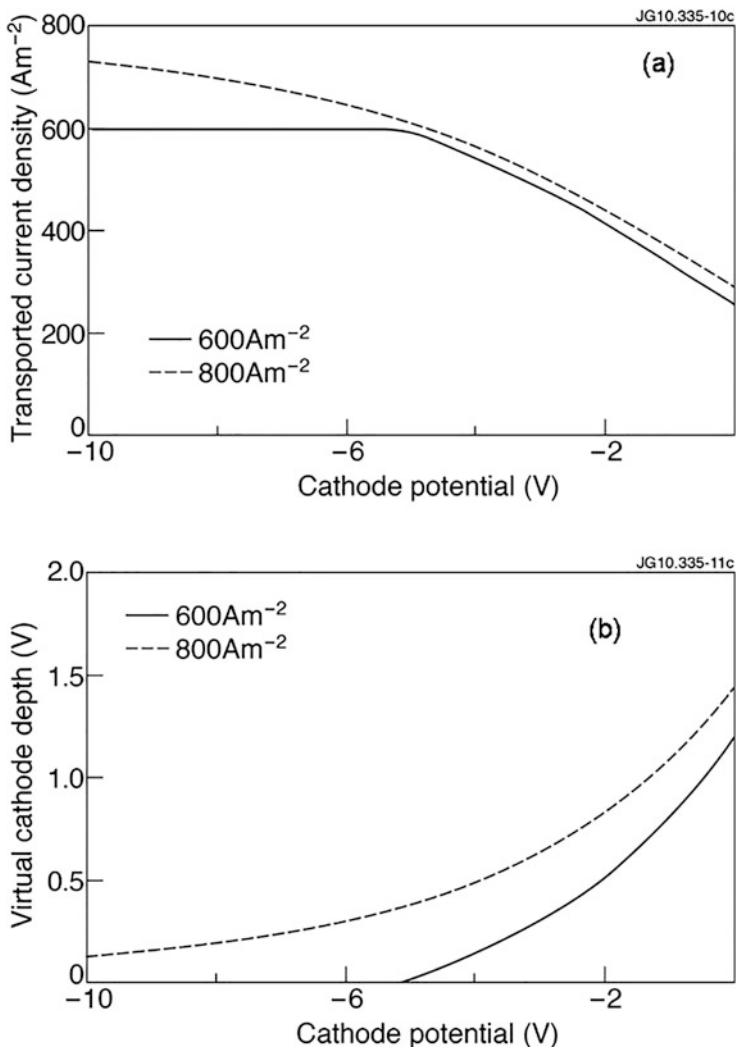


Fig. 8.14 The effect of changing the cathode potential on (a) the transported negative ion current density across the sheath and (b) depth of the virtual cathode for two values of emitted current density

8.4.2 The Effect of Surface Work Function

The minimum work function of 1.45 eV of a caesiated surface is achieved at a caesium coverage of approximately 0.6 monolayers (van Amersfoort et al. 1985). This leads to the maximum probability of negative ion formation by atoms or ions in caesiated negative ion sources, such as those for fusion applications. Maintaining

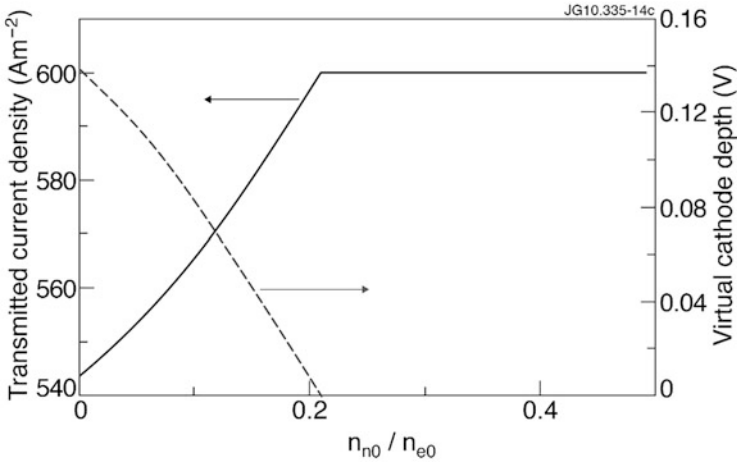


Fig. 8.15 The effect of changing the negative ion density in the plasma. The plasma conditions are given in the text

such a precise coverage is very difficult and steps are taken to control surface temperatures and the caesium delivery (Fantz et al. 2017). Under realistic plasma and vacuum conditions, the measured work function is somewhat higher than this minimum. It was shown by (Gutser et al. 2011) that the measured work function could be ≈ 2.2 eV but was variable depending on the conditions. This will affect the production of negative ions from the surface. The effect of surface work function has been investigated by (King et al. 2013) where using a model of surface production, the sheath model has been applied to investigate how the work function affects the sheath.

Figure 8.16 shows an example of the work of (King et al. 2013) where for different work functions, the transported current density and the depth of the virtual cathode is plotted as the cathode voltage is changed. At the minimum work function of ~ 1.5 eV where the production of negative ions on the surface is highest increasing the magnitude of the cathode voltage increases the transmitted negative ion current density and decreases the depth of the virtual cathode. At a higher work function of 2 eV, the production of negative ions is reduced and all the emitted negative ions' current density reaches the plasma across the sheath. The virtual cathode is only formed at very low (negative) potentials. At a work function of 2.5 eV, the virtual cathode is now not formed due to the even further reduced negative ion production. These examples show how this relatively straightforward model can provide powerful physical insights into the process of negative ion production and transport across the sheath.

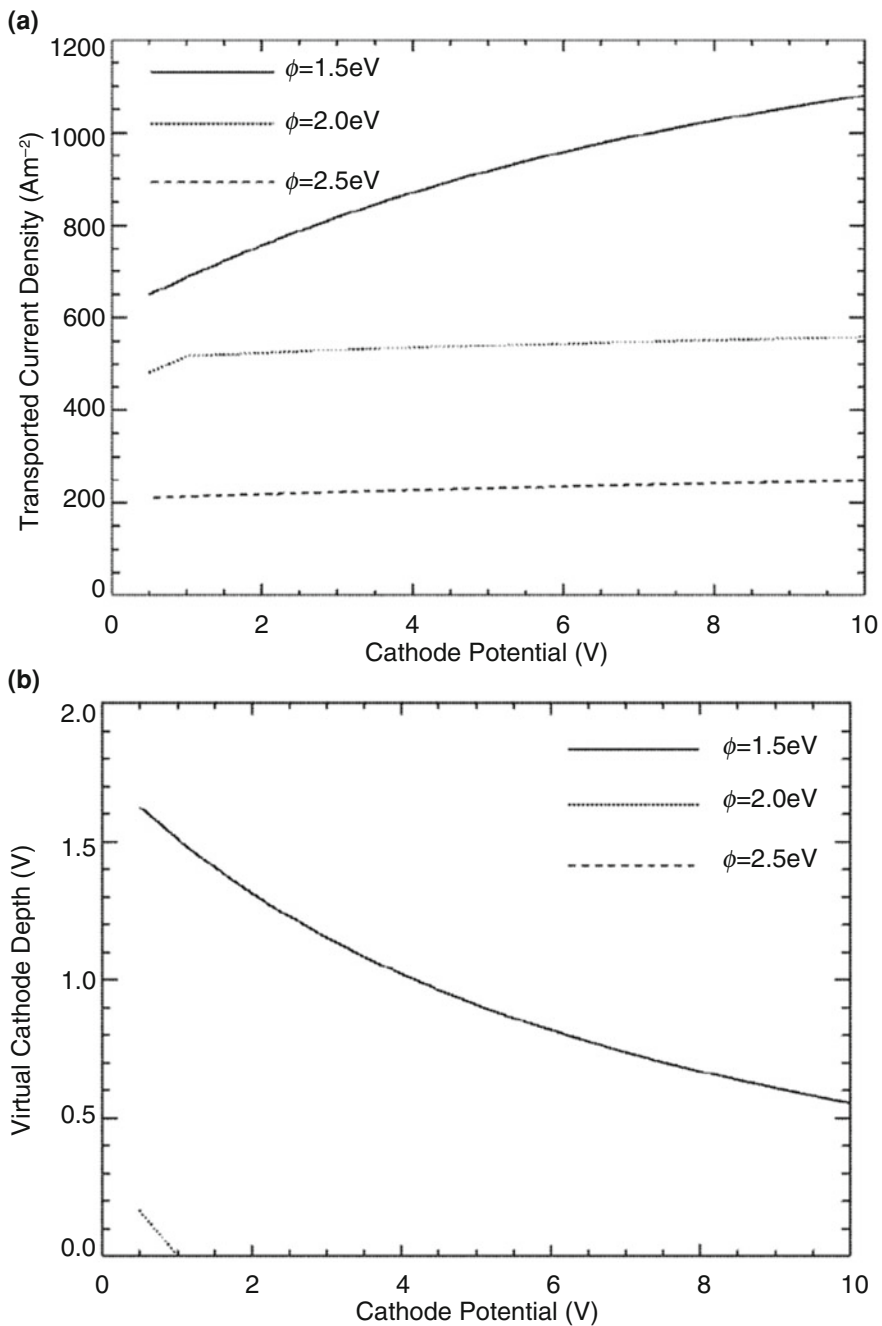


Fig. 8.16 The effect of work function, ϕ , on (a) the transported current density and (b) the virtual cathode depth as the cathode potential is varied. (Taken from King et al. (2013))

8.4.3 The Emission of Electrons into the Sheath

The description of the sheath and the formation of the virtual cathode has only included the emission of negative ions from the low work function surface. In the plasma, light is produced. Photons striking the ion source walls will produce photo-electrons which are emitted into the sheath. Their flux will be increased if the work function is lowered by a caesium coating on the wall. If sufficient photo-electrons are produced these will alter the sheath structure by adding to the negative space charge. The production of photo-electrons on low-work function surfaces has been investigated by (Laulainen et al. 2017). They suggested that for a filament-driven discharge the photo-electron current from the source wall was of the order 1 A per kW of discharge and it was enhanced by 2–3.5 times for a low work function surface. Taking the ITER source (Hemsworth et al. 2017) and assuming that the production rate is the same for an RF discharge of 800 kW then approximately 2800 A of photo-electrons might be expected. If all these were emitted from the plasma grid, which has an area of $\sim 1.2 \text{ m}^2$ (Hemsworth et al. 2017), the emitted current density of photo-electrons, j_{e-pe} , would be $\sim 2300 \text{ Am}^{-2}$ which is slightly higher than the emitted negative ion current density, j_{H^-} .

In the sheath the ratio of the photo-electron density, n_{e-pe} , to the negative ion density, n_{H^-} is

$$\frac{n_{e-pe}}{n_{H^-}} = \frac{j_{e-pe}}{j_{H^-}} \frac{v_{H^-}}{v_{e-pe}} = \frac{j_{e-pe}}{j_{H^-}} \sqrt{\frac{m}{M_{H^-}}} \quad (8.36)$$

where v_{H^-} and v_{e-pe} are the velocities of the negative ions and photo-electrons and M_{H^-} and m are the mass of the negative ion and electron respectively. Thus using the numbers above the density of photo-electrons to hydrogen negative ions is $\sim (2300/600)/43 = 0.09$. In deuterium, which will be used for fusion applications such as ITER, this ratio becomes ~ 0.06 . Hence it appears that photo-electrons may perturb the sheath slightly, particularly in hydrogen operation. This type of consideration can readily be accommodated by the sheath model.

8.5 Beam Extraction

Although the intention of this chapter has been to describe the physics of the sheath in negative ion sources, it is worthwhile making a few comments concerning the extraction of the negative ions.

The negative ions are extracted into an accelerator through one wall of the ion source. This wall, known as the plasma grid (PG), has a number of extraction apertures and it forms the first grid of an accelerator. Negative ions arriving from the plasma at an extraction aperture are accelerated away by a positive potential applied to a downstream electrode. As has been described, across the thin sheath

in front of the plasma grid is a potential difference, with the plasma grid being at a negative potential relative to the plasma. These sheath and presheath potentials inhibit negative ions from reaching the extraction apertures in the plasma grid. Also, negative ions created on the plasma grid surface, which form the majority of negative ions in front of the plasma grid, are moving away from the plasma grid and the extraction apertures.

In order for negative ions to be extracted through the plasma grid apertures they must be moving towards the plasma grid and have sufficient energy to overcome the potential barrier. One mechanism for achieving that is charge exchange between the H^- (or D^-) moving away from the plasma grid and a hydrogen (or deuterium) atom with sufficient energy moving towards the plasma grid. Another possibility is 180-degree scattering via coulomb or other collisions to reverse the negative ion trajectory.

In negative ion sources, for applications such as fusion, the ion trajectories are also influenced by local magnetic and electric fields. This overall complex situation is beyond the scope of this chapter but is subject to ongoing studies.

8.6 Conclusions

It has been demonstrated that the narrow sheath region can play a large role in determining and indeed limiting the transport of negative ions across it. This is particularly so when there is a high amount of negative ion production at the surface. The limitation is due to the excess of negative ion charge density in the sheath compared to the positive ion density arising from the bulk plasma. The mitigation of this limitation then lies in increasing the positive ion flux across the sheath. This suggests a future direction of research if negative ion current densities are to be increased to higher values than those achieved at present.

Acknowledgments This work was funded by the RCUK Energy Programme [Grant number EP/I501045]. The authors would like to thank Dr. R Hemsworth for comments and useful suggestions.

References

- H. Amemiya, B.M. Annaratone, J.E. Allen, *Aust. J. Plant Physiol.* **60**, 81 (1998). <https://doi.org/10.1017/S0022377898006837>
- M. Bacal, M. Sasao, M. Wada, *J. Appl. Phys.* **129**, 221101 (2021). <https://doi.org/10.1063/5.0049289>
- R.L.F. Boyd, J.B. Thompson, *Proc. R. Soc. Lond.* **252**, 102 (1959). <https://doi.org/10.1098/rspa.1959.0140>
- N.S.J. Braithwaite, J.E. Allen, *J. Phys. D. Appl. Phys.* **21**, 1733 (1988). <https://doi.org/10.1088/0022-3727/21/12/011>

- F.F. Chen, *Introduction to Plasma Physics and Controlled Fusion* (Plenum Press, New York, 1984). <https://doi.org/10.1007/978-3-319-22309-4>
- U. Fantz, C. Hopf, D. Wunderlich, et al., *Nucl. Fusion* **57**, 116007 (2017). <https://doi.org/10.1088/1741-4326/aa778b>
- A.T. Forrester, *Large Ion Beams: Fundamentals of Generation and Propagation* (Wiley, New York, 1988) ISBN 13: 9780471625575
- R. Gutser, C. Wimmer, U. Fantz, *Rev. Sci. Instrum.* **82**, 023506 (2011). <https://doi.org/10.1063/1.3541790>
- A. Hatayama, Proceedings of the 12th International Conference on Ion Sources. *Rev. Sci. Instr.* **79**, 02B901 (2008). <https://doi.org/10.1063/1.2819320>
- R.S. Hemsworth, D. Boilson, P. Blatchford, et al., *New J. Phys.* **19**, 025005 (2017). <https://doi.org/10.1088/1367-2630/19/2/025005>
- M. Kashiwagi, J. Hiratsuka, M. Ichikawa, et al., *Nucl. Fusion* **62**, 026025 (2022). <https://doi.org/10.1088/1741-4326/ac388a>
- D.B. King, A.J.T. Holmes, R. McAdams, et al., Third International Symposium on Negative Ions, Beams and Sources (NIBS 2012). *AIP Conf. Proc.* **1515**, 49–58 (2013). <https://doi.org/10.1063/1.4792769>
- J. Laulainen, S. Aleiferis, T. Kavlas, et al., *Phys. Plasmas* **24**, 103502 (2017). <https://doi.org/10.1063/1.4998005>
- B.S. Lee, M. Seidl, *Appl. Phys. Lett.* **61**, 2857 (1992). <https://doi.org/10.1063/1.108056>
- M.A. Lieberman, A.J. Lichtenberg, *Principles of Plasma Discharges and Materials Processing* (Wiley, New York, 2005) ISBN 0-471-72001-1
- R. McAdams, A.J.T. Holmes, D.B. King, et al., *Plasma Sources Sci. Technol.* **20**, 035023 (2011). <https://doi.org/10.1088/0963-0252/20/3/035023>
- S.T. Melnychuk, M. Seidl, W. Carr, et al., *J. Vac. Sci. Technol.* **A7**, 2127 (1989). <https://doi.org/10.1116/1.575986>
- B. Rasser, J.N.M. Van Wunnik, J. Los, *Surf. Sci.* **118**, 697 (1982). [https://doi.org/10.1016/0039-6028\(82\)90216-3](https://doi.org/10.1016/0039-6028(82)90216-3)
- M. Seidl, H.L. Cui, J.D. Isenberg, et al., *J. Appl. Phys.* **79**, 2896 (1996). <https://doi.org/10.1063/1.361285>
- F. Taccogna, P. Minelli, S. Longo, et al., *Phys. Plasmas* **17**, 063502 (2010). <https://doi.org/10.1063/1.3431635>
- Y. Takeiri, O. Kaneko, K. Tsumori, et al., 11th International Symposium on the Production and Neutralization of Negative Ions and Beams. *AIP Conf. Proc.* **925**, 211 (2007). <https://doi.org/10.1063/1.2773661>
- P.W. van Amersfoort, J.J.C. Geerlings, L.T. Kwakman, et al., *J. Appl. Phys.* **58**, 3566 (1985). <https://doi.org/10.1063/1.335732>
- D. Wunderlich, R. Gutser, U. Fantz, *Plasma Sources Sci. Technol.* **18**, 045031 (2009). <https://doi.org/10.1088/0963-0252/18/4/045031>

Chapter 9

Helicon Volume Production of H^- and D^- Using a Resonant Birdcage Antenna on RAID



Ivo Furno, Riccardo Agnello, Alan Howling, Philippe Guittienne, Remy Jacquier, Christine Stollberg, Marcelo Baquero, Lyes Kadi, Claudio Marini, Jia Han, Stéphane Béchu, Gwenael Fubiani, Alain Simonin, and Francesco Taccogna

Abstract Negative ion production by volumetric processes is investigated in the RAID linear device using experiments and modeling. Measurements by optical emission spectroscopy, cavity ring-down spectroscopy, and Langmuir probe assisted laser photodetachment are combined and reveal that H^- and D^- ions are distributed in a halo around the plasma column with densities of $2 \times 10^{16} \text{ m}^{-3}$ for only a few kilowatts of RF power in a Cs-free plasma. A hydrogen transport fluid code shows that RAID plasmas have a hot electron core favorable to ro-vibrational excitation and dissociation of H_2 molecules. Dissociative attachment to ro-vibrationally excited H_2 molecules is the only significant source of H^- anywhere in the RAID volume.

Keywords Helicon plasmas · RAID · Resonant antennas · Negative ion diagnostics · Volume production · Fluid simulations

I. Furno · R. Agnello · A. Howling · P. Guittienne · R. Jacquier · C. Stollberg · M. Baquero · L. Kadi · C. Marini · J. Han
Swiss Plasma Center (SPC), Ecole Polytechnique Fédérale Lausanne (EPFL), Lausanne, Switzerland
e-mail: ivo.furno@epfl.ch

S. Béchu
Université Grenoble-Alpes, CNRS, Grenoble INP, LPSC-INP23, Grenoble, France

G. Fubiani
LAPLACE, CNRS, Université de Toulouse, Toulouse, France

A. Simonin
CEA, IRFM, St-Paul-lez-Durance, France

F. Taccogna (✉)
Institute for Plasma Science and Technology, CNR, Bari, Italy
e-mail: francesco.taccogna@cnr.it

9.1 Introduction

Since the first experiments performed by Boswell (1970), helicon sources have been extensively studied and they are proven to be very efficient for high-density plasma production, electron density = $10^{18} - 10^{19} \text{ m}^{-3}$ (in noble gases, typically argon) with moderate injection power at low pressure. Historically, they have found applications in semiconductor manufacturing and ion thruster systems.

From its beginnings in 2017, the Resonant Antenna Ion Device (RAID) at the Swiss Plasma Center of EPFL (École Polytechnique Fédérale de Lausanne), Switzerland, has been operated to explore the main technology and physics issues related to high-power, steady-state helicons. In this chapter, we describe the experimental activities on RAID to investigate the formation of negative ions by volumetric processes in H/D helicon plasmas. With a continuously improving set of state-of-the-art diagnostics and of theoretical and modeling tools, research on RAID has today reached a level at which quantitative comparisons between theory and experiment can be performed. This has resulted in a better understanding of the complex plasma chemistry involved in H/D discharges as well as of helicon wave generation by resonant antennas.

This chapter is organized as follows. In Sect. 9.2, a description of RAID and its main ancillaries is provided. Section 9.3 details the principal diagnostics used to study negative ion physics. Section 9.4 summarizes the most salient measurements of negative ions using a combination of these diagnostics. The development and first results of a hydrogen transport fluid model are presented in Sect. 9.5 to interpret the experimental results. Finally, summary and outlook are given in Sect. 9.6.

9.2 The Resonant Antenna Ion Device (RAID)

RAID generates a cylindrical plasma column along a linear magnetic field, producing steady-state helicon plasma discharges in various gases including H_2 and D_2 (Furno et al. 2017; Agnello et al. 2018, 2020; Marini et al. 2017) as well as He, Ar, N_2 , and Ne for a wide range of plasma physics investigations (Thompson et al. 2017). A photograph of RAID is shown in Fig. 9.1a. The red glow from the cylinder on the left is the plasma emission seen through the water-cooled ceramic tube (it is not red hot) surrounded by the resonant antenna generating the plasma. Figure 9.1b shows the visible light emission from a typical hydrogen plasma discharge. This picture is taken from the end of the plasma column near the target through an off-axis viewport. The plasma column impinges on a target, also partially visible in the picture. In this section, the RAID experimental apparatus is described together with its main ancillaries and diagnostics.

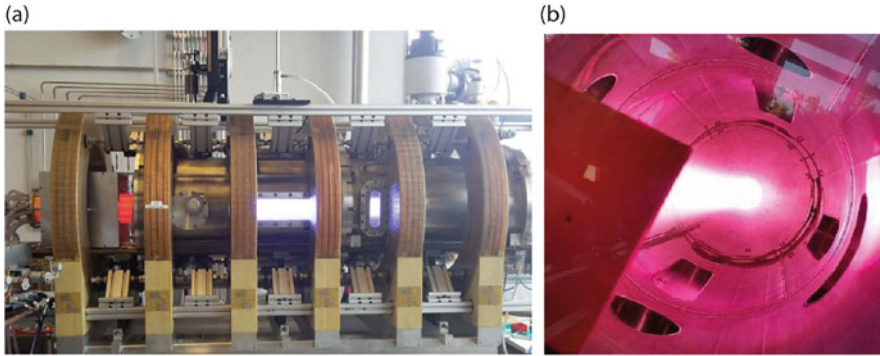


Fig. 9.1 Pictures of the RAID experiment at the Swiss Plasma Center of École Polytechnique Fédérale de Lausanne. **(a)** The RAID vacuum vessel is surrounded by six water cooled coils. **(b)** Downstream view of a visible light emission from a typical plasma column in hydrogen. The target is partially visible in the foreground

9.2.1 RAID Vacuum Vessel, Pumping System, and Magnetic Field

Figure 9.2 shows a schematic drawing of RAID with its main elements. The stainless vacuum vessel is linear (1.9 m total length and 0.4 m internal diameter) and is made of two movable sectors with multiple diagnostic access and it is surrounded by six water-cooled magnetic field coils. The vacuum vessel is also water-cooled and allows for long-time (up to days) continuous operation with stable and reproducible plasma conditions. The pumping system consists of a primary rotary pump and a turbopump located on the top-right of the vessel. The gas pressure is regulated by mass flow controllers at a constant turbo pumping speed of 170 l/s corresponding to a baseline gas pressure of better than 7×10^{-6} mbar. The six magnetic field coils generate an axial magnetic field (up to 800 G on axis), which is needed to propagate helicon waves (Guittienne et al. 2021) and to radially confine the plasma. RAID operates with two separate groups of identical coils, a source coil, the first coil on the left in Fig. 9.2, and five vessel coils. The distance between each coil is $21(\pm 0.5)$ cm to optimize the axial homogeneity of the magnetic field. Two DC power supplies feed the two sets of coils with a current ripple lower than 1%. The coils are actively cooled by forced water convection in the copper pipes allowing for continuous operation. Each coil is made of $9(\text{radial}) \times 4(\text{axial})$ turns with a central channel for water cooling. The coil internal and external diameters are 52 cm and 82.6 cm, respectively. Each turn is electrically isolated with resin. The coil ohmic resistance is $\sim 5 \text{ m}\Omega$ and its inductance is $\sim 6.4 \text{ mH}$. More details on the coils can be found in Müller et al. (2007). The polarity of the source coil can be reversed with respect to the other five coils, to create a divergent magnetic field at the antenna position. This promotes plasma ignition and stabilizes the helicon regime, resulting in a stable plasma over a wider operational space. The reason for this improvement is not well

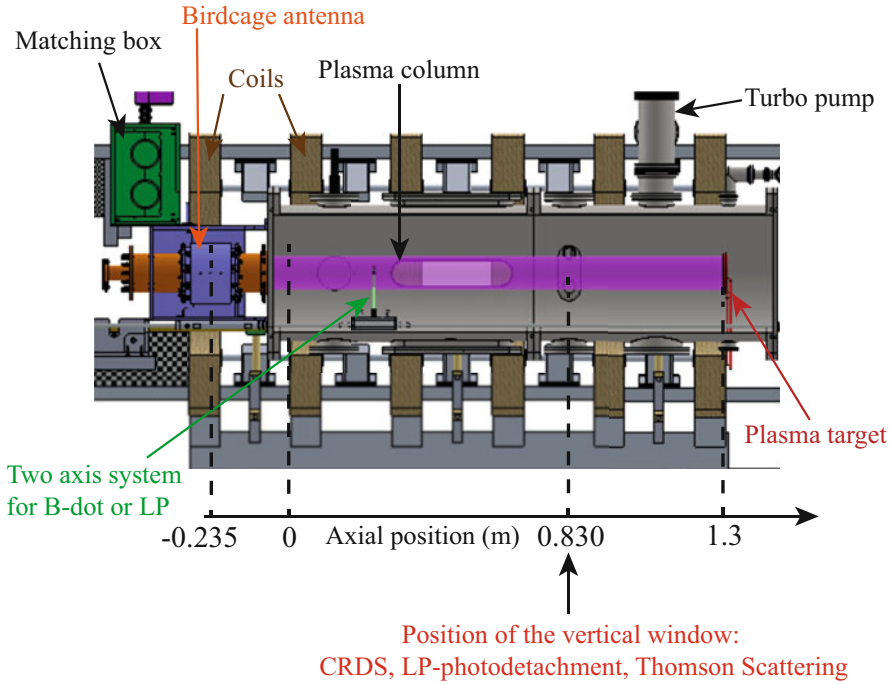


Fig. 9.2 Schematic of the Resonant Antenna Device including the location of the main diagnostics

understood but might be due to the effect of a magnetic field gradient helping to confine slower electrons in the antenna region thus enhancing the ionization.

Figure 9.3 shows the spatial and on-axis magnetic field produced in standard conditions (see below for the definition of standard conditions), namely with -40 A in the source coil (producing a counter-field) and 150 A in the vessel coils. The on-axis magnetic field intensity shows a strong gradient in the antenna region, a peak at 20 mT in the center of the vessel, and a decay to 10 mT at the target position. Most helicon sources operate with uniform magnetic fields, even though the propagation of helicon waves in divergent magnetic field geometries was also investigated (Takahashi et al. 2016). When only the source coil is turned on, the plasma is partially transported in the main chamber; when all coils are turned off, the plasma coupling is purely inductive and the plasma is confined in the region of the ceramic tube corresponding to the antenna length.

9.2.2 RAID Plasma Source: The Birdcage Antenna

RAID plasmas are ignited and sustained by an innovative helicon source consisting of a resonant network antenna. This antenna has a birdcage geometry (Guittienne

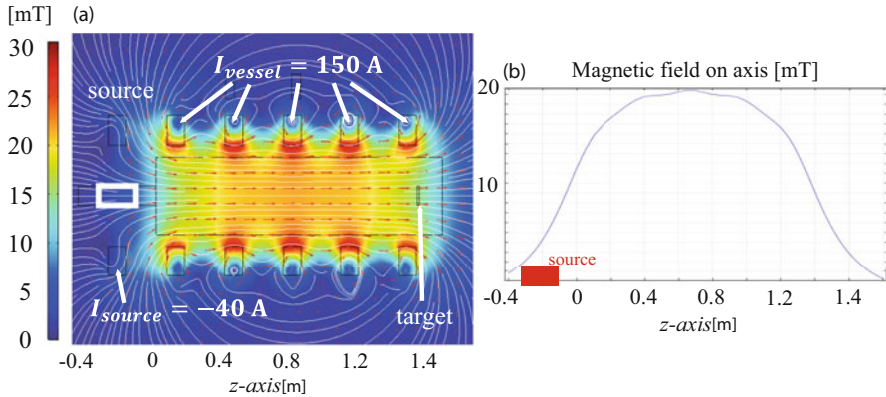


Fig. 9.3 (a) Magnetic field mapping in standard conditions: -40 A in the source coil (counter field) and 150 A in the vessel coils and (b) intensity of the magnetic field on axis for same parameters and axial position of the antenna in red. At the maximum axial field strength near $z = 0.7$ m, the magnetic field is almost uniform over the vessel cross-section, falling by 1% at $r = 0.1$ m and by 10% at the wall, $r = 0.2$ m

et al. 2005, 2021), shown in Fig. 9.4, and is installed on the left end-flange of the device (Fig. 9.2). Its length is 15 cm, its center is at the axial position $z = -0.235$ m, and it surrounds the ceramic tube. The ceramic tube is made of an assembly of two coaxial tubes (internal diameter 9.5 cm and external diameter 11.5 cm) made of alumina, Al_2O_3 . Between the two tubes, there are 8 equally spaced channels for water cooling, necessary to avoid vacuum joint melting. After many hours of continuous operation, the internal surface of the ceramic shows no sign of sputter damage, with no more than a thin dark coating which could be of metallic origin. Faraday screens are therefore not necessary because the low-amplitude RF plasma potential induced by the birdcage does not form a high voltage sheath with high-energy ion bombardment. Alternatively, the ceramic tube can be mounted with a half-helix antenna whose dimensions are very similar to the birdcage antenna. The birdcage antenna is commonly used in nuclear magnetic resonance for excitation and detection. In helicon wave physics, different antenna configurations were developed with the main idea to match the RF field generated to the helicon wave field in plasma, such as Nagoya, half-helix, Boswell type, and paddle shaped (Chabert and Braithwaite 2011). Since the helicon field has a rotating pattern, these antennas are usually in a twisted geometry to enhance the matching. The birdcage antenna is designed to generate a rotating azimuthal distribution of RF currents. It features 9 parallel copper bars, of inductance L and resistance R , in cylindrical geometry. The end of each leg is connected to its closest neighbors via mica capacitors of $C = 3840$ pF. The birdcage antenna has a resonant frequency which is specific to the geometric arrangement and the impedance of its components. When it is excited by a radiofrequency source, an azimuthal sinusoidal distribution of oscillating currents is generated in the antenna legs. The R , L , C values are chosen

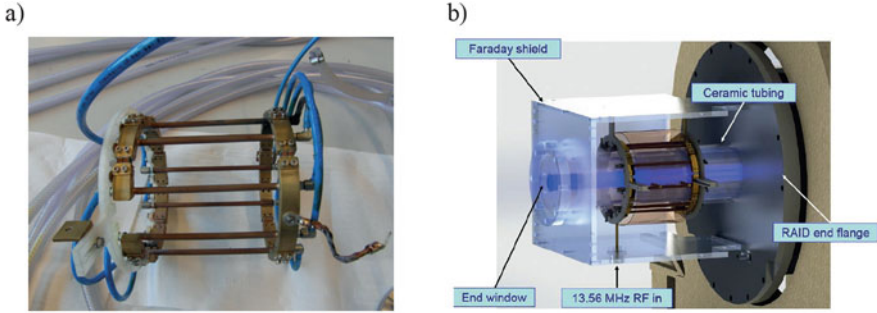


Fig. 9.4 (a) Picture of the birdcage antenna showing the copper legs, the position of the capacitors, and the tubes for water cooling. (b) Location of the birdcage antenna mounted on the ceramic tubing at the RAID and flange. The antenna is enclosed in a Faraday screen to limit RF emissions

Table 9.1 RAID general machine and plasma parameters

Device parameters		Plasma parameters	
Antenna type	Birdcage/Half-helix	Electron density n_e	$10^{16}\text{--}10^{19}\text{ m}^{-3}$
Antenna length	15 cm	Plasma width (FWHM of n_e)	6 cm
RF power (nominal)	0.3–10 kW cw	Electron Temperature	1–10 eV
Magnetic field on axis	50–800 G	Ion Temperature	~ 0.1 eV
Gas species	H ₂ , D ₂ , Ar, He, N ₂ , Ne	Ion Flux (on target)	$\sim 10^{21}\text{ m}^{-2}\text{ s}^{-1}$
Pressure	0.15–1 Pa	Power Flux (on target)	$\sim 100\text{ kW/m}^2$

so that it resonates close to 13.56 MHz, a standard industrial frequency. Extensive treatment of birdcage theory can be found in Refs. Guittienne et al. (2005, 2021).

9.2.3 Plasma Parameters in RAID and Standard Conditions

Table 9.1 summarizes the ranges of device and plasma parameters. Plasma columns have peaked radial profiles in n_e and T_e , with typical FWHM of 6 cm along the radial direction. The source is usually operated with the parameters listed in Table 9.2; we define “standard conditions” as follows: 0.3 Pa pressure measured during the plasma by a capacitive gauge mounted on the vacuum vessel; a current in the vessel coils of 150 A and -40 A in the coil surrounding the antenna, also called counter-field coil. Plasmas in standard conditions have fewer density fluctuations, and the RF power for ignition is minimized. In standard conditions and 3 kW RF power, the peak electron density is about $\sim 2 \times 10^{18}\text{ m}^{-3}$ for H₂ or D₂ and $\sim 1 \times 10^{19}\text{ m}^{-3}$ for argon. Furthermore, a stable helicon plasma is obtained with only 300 W in argon and 1000 W in hydrogen and deuterium. The operation with light molecule plasmas is more difficult compared to heavy atom plasmas because: (1) the Bohm velocity, $u_B = \sqrt{k_b T_e / m_i}$, is larger for light ion plasmas, leading to larger axial losses and

Table 9.2 RAID “standard conditions” for H₂ or D₂ plasma discharge

Gas pressure	0.3 Pa	RF power	1–8 kW
Vessel peak field	200 G	Vessel coils current	150 A
Field in antenna center	30 G	First coil current	–40 A
Birdcage boundary	Dielectric	Downstream boundary	Floating

(2) when molecular gases are used, a large fraction of the antenna power is used to excite the ro-vibrational channels or to dissociate the molecule (Hjartarson et al. 2010). In RAID, H₂ plasma ignition cannot be achieved with H₂ alone. Instead, the plasma is first ignited using a mixture of H₂ and Ar, and then the Ar gas flow is stopped resulting in a pure H₂ plasma.

9.3 Overview of RAID Diagnostics

RAID is equipped with basic plasma diagnostics as well as sophisticated state-of-the-art systems, enabling a full characterization of the various plasma components (electrons, ions, molecules, etc.).

9.3.1 Diagnostics of Electron Parameters

The relatively low temperatures and densities of RAID plasmas, in some regimes, allow the use of Langmuir probes (LPs) to measure the electron density and temperature profiles across the entire device. However, LPs suffer strong heating for an electron density larger than a few 10^{18} m^{-3} , which is achieved in argon for a relatively low RF power ($\sim 600 \text{ W}$) and in hydrogen or deuterium for about 3000 W RF power. This limits the use of LPs to the edge of the plasma column and to low RF powers. To overcome this limitation, microwave interferometry and incoherent Thomson scattering are used in parallel with LPs, allowing to probe all RAID plasma regimes as well as to extract absolutely calibrated electron density profiles. These techniques and the experimental setup on RAID are described in this section.

Langmuir Probes (LP) Electron density and temperature along the vessel are measured by means of LPs mounted on a two-axis system (Fig. 9.2), which can scan axially and radially inside the plasma column holding either a LP or a B-dot magnetic coil probe (Jacquier et al. 2019). Single tip LPs, RF compensated LPs, as well as double tip LPs are used depending on the plasma conditions.

Microwave Interferometry Measurements of electron density can also be performed using a heterodyne microwave interferometer. 100 GHz mm-waves are

injected into the plasma, and the phase change is directly related to the line-integrated value of n_e along the mm-wave beam. By vertically displacing the system, one can then obtain absolute line-integrated measurements of n_e at different positions. In combination with LP data, these measurements are used to obtain absolute electron density radial profiles, which can be compared with TS data.

Thomson Scattering (TS) This non-intrusive technique is used to measure the electron velocity distribution function (EVDF), thereby providing the electron temperature and possible drift velocity, as well as the absolute calibrated electron density. The setup operates in the incoherent scattering regime, where the photon energy is altered solely due to the Doppler shift by the free electron velocity in the plasma along the probe vector. A preliminary system used polychromators and a 1064 nm laser (Agnello et al. 2020). The improved TS system uses a spectrometer and a 532 nm laser focused to 1 mm beam diameter. The scattered radiation is collected with a spatial resolution of 4 mm along the laser beam at a 90° scattering angle and is guided to a high-throughput spectrometer (FL = 200 mm, 2400 l/mm) by an optical fiber. A photo multiplier tube (PMT) with a rise time of 0.57 ns detects the scattered light. The spectrum is scanned by varying the spectrometer grating angle. The setup has a spectral resolution of 0.8 nm and can therefore measure electron temperatures >0.4 eV. A satisfactory signal-to-noise ratio is achieved by collecting up to 20,000 laser shots per wavelength. The uncertainties of the measured electron parameters are obtained from a Bayesian analysis approach, which also evaluates cross correlations between different parameters.

9.3.2 *Diagnostics for Negative Ions: Optical Emission Spectroscopy, Cavity Ring-Down, and Photodetachment*

Negative ions in plasmas could be theoretically detected by LPs by measuring the shape of the second derivative of the current–voltage probe characteristic. This technique is used when the plasma electronegativity $\alpha = n_-/n_e$ is about 1 or more (Popov et al. 2013). However, in the case of low-temperature hydrogenic plasmas, the electronegativity is of the order of 0.1, and the negative ion density is too small, resulting in too noisy I–V curves. Therefore, the measurements of negative ions in such plasmas require other dedicated techniques.

The measurements of negative ions in RAID are performed by direct techniques such as Cavity-Ring Down Spectroscopy (CRDS) and LP Laser Photodetachment (LPLP). These techniques are routinely employed in negative ion sources for fusion (Berger et al. 2009; Christ-Koch et al. 2009; Fantz et al. 2006) but have rarely been employed in helicon plasma devices. Indirect techniques, such as optical emission spectroscopy (OES) supported by collisional radiative codes, are also used on RAID. These techniques as well as the experimental setup on RAID including the technical challenges are reviewed below.

9.3.2.1 Optical Emission Spectroscopy (OES)

Passive spectroscopic measurements of Balmer and Lyman lines and of the Fulcher- α bands are performed with an $f/2$ spectrometer, for both hydrogen and deuterium (Marini et al. 2017). The setup consists of a field lens coupled via an optical fiber bundle to a high-throughput spectrometer and a detector. The input optics is a Navitar $f/1.4$ 35 mm lens, and the image focal plane is optimized to image the RAID axis at 25 cm from the lens. The input lens is mounted on a RAID lateral port to sample the plasma column at different axial positions along the device. The fiber bundle is composed of 19 fibers of numerical aperture 0.22, with a fused silica core of diameter 365 μm . The diameter of their adjacent images on the focal plane is 2.9 mm, resulting in a 55.1 mm wide sampling region. Collected light is analyzed by a high-throughput spectrometer, which is composed of two Nikon $f/2$ 200 mm lenses and a Horiba holographic grating of 2400 lines per mm groove density blazed at 400 nm. This is sufficient to resolve most of the Fulcher- α molecular lines. The spectrometer uses an Andor iXon Ultra 897 camera, which features a back-illuminated 512×512 pixel frame transfer sensor and an optional electron multiplying (EM) readout register. The multiple viewing lines and an absolute intensity calibration are tomographically inverted to determine the absolute plasma radiance profile with a spatial resolution <3 mm.

9.3.2.2 Cavity Ring-Down Spectroscopy (CRDS)

In CRDS, first introduced by O'Keefe to measure absorption spectra (O'Keefe and Deacon 1988), a light pulse bounces multiple times between two high reflectivity (HR) mirrors to measure the medium absorbance. The main features of CRDS are that it is very sensitive, directly measures the number density of the species of interest, and is independent of the intensity of the light source. The main element of a CRDS system is the optical cavity made of two HR mirrors between which the light undergoes multiple reflections, thus multiplying the interaction length of the light with the absorbing medium. CRDS can be applied as a plasma diagnostic to measure the number density of different plasma species. In fusion, it is particularly interesting for the detection of H^- and D^- in negative ion sources (Berger et al. 2009; Nakano et al. 2016).

In RAID, to measure H^- and D^- densities, the employed light source is a pulsed Nd:YAG laser whose photon energy ($E = 1.2$ eV, corresponding to a wavelength of $\lambda = 1064$ nm) is large enough to strip the weakly bound electron of H^- ($E_{\text{binding}} = 0.75$ eV) by photodetachment, $h\nu + H^- \rightarrow H + e$. The light reflected back and forth inside the cavity is lost both because of the transmission of the mirrors and the presence of an absorbing medium along the line of sight (LOS) of the laser. The signal leaking through the cavity consists of a train of pulses whose intensity shows an exponential decay $I(t) = I_0 e^{-t/\tau}$, where I_0 is the initial intensity and τ can be expressed as $\tau = \frac{L}{c(1-R+\alpha d)}$, where L is the cavity length, c the speed of light, and R the reflectivity of the mirrors. The absorption coefficient is given by $\alpha = \bar{n}_{H^-} \sigma_{H^-}$,

where σ_{H^-} is the interaction cross-section ($\sigma_{\text{H}^-} = 3.5 \times 10^{-21} \text{ m}^2$ at a wavelength of 1064 nm) and \bar{n}_{H^-} is the H^- line-integrated density. d is the path length of the laser beam in the absorbing medium and is usually the parameter known with the least accuracy. The line-averaged density \bar{n}_{H^-} is

$$\bar{n}_{\text{H}^-} = \frac{1}{\sigma_{\text{H}^-}} \frac{L}{cd} \left(\frac{1}{\tau} - \frac{1}{\tau_0} \right), \quad (9.1)$$

where τ_0 and τ are the values of the decay time in the absence and presence of absorbing medium (H^-/D^-), respectively.

9.3.2.3 CRDS Experimental Setup in RAID

OES measurements first suggested that negative ions are distributed on a radial shell ~ 1 cm thickness with the radial center of the layer at ≈ 4 cm for a H_2 plasma. At this radial location, we expect a higher density of negative ions than on-axis because the electron temperature drops to 1–2 eV, which reduces dissociative attachment. We then decided to explore this radial shell by CRDS.

Figure 9.5 shows a picture of the experimental setup of the CRDS in RAID, from the laser injection side (Agnello et al. 2018). In Fig. 9.5a, the laser beam (in red) passes through the optical insulator, it is reflected by three mirrors, and it is finally injected into the cavity. Approximately 4% of the impinging laser energy enters the cavity. From the detection side, in Fig. 9.5b, the detector measures the light leaking from the cavity. The detector objective is connected to the mirror mounting with a conical adapter. Figure 9.6a and b shows a schematic of the CRDS experimental setup installed on RAID. The optical cavity is 91 cm long, enough to avoid overlapping of the laser pulses inside the cavity, which may result in multiple cavity modes and then in a non-exponential decay of the measured ring down signal.

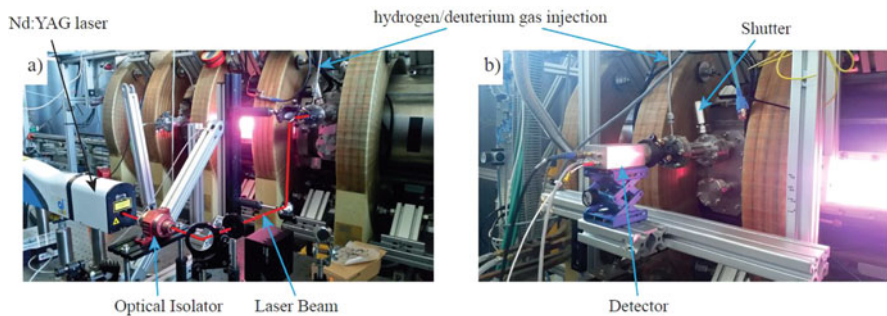


Fig. 9.5 Photo of the CRDS experimental setup in RAID: (a) injection side of the laser: the laser beam passes through the optical isolator, is reflected by three mirrors, and is injected inside the optical cavity. (b) Detection side: the detector collects the light leaking the optical cavity

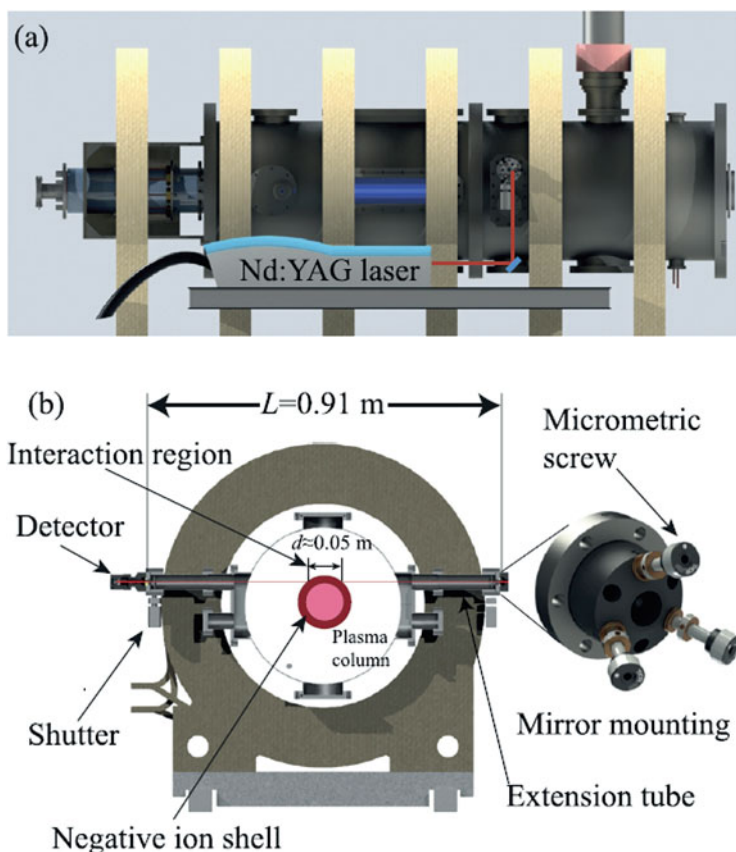


Fig. 9.6 (a) Side view of RAID: the laser beam is steered and enters the optical cavity perpendicular to the RAID axis. (b) Transverse section of RAID in the CRDS plane: the line of sight of the laser beam (schematically shown in red) is 4 cm displaced from the plasma column center so that it traverses the negative ion shell (as expected from OES measurements (Marini et al. 2017)). Reproduced from *Review of Scientific Instruments* **89**, 103504 (2018); doi: 10.1063/1.5044504, with the permission of AIP Publishing (Agnello et al. 2018)

The HR mirrors are positioned on vacuum tight mirror mountings on two tube extensions. This is also to minimize the solid angle of exposure of the mirrors to the plasma. To limit the exposure time of the mirrors to the plasma, a mechanical shutter in each extension is closed when the CRDS is not operational. Moreover, to reduce the effect of energetic particles impacting the mirror HR coating, the feeding hydrogen gas is flushed in front of the HR mirrors. Argon, which is needed to facilitate the plasma ignition, is injected from the back flange of the helicon antenna.

First measurements were performed with D_2 plasmas in standard conditions to compare with past OES measurements (Marini et al. 2017). The technique consists in measuring τ before, during, and after a plasma discharge. A typical

τ measurement in a D_2 plasma at 5 kW RF power and with an argon plasma at 700 W RF power is shown in Fig. 9.7a, b, respectively. The entire time range for the deuterium is divided into four intervals marked by the letters A, B, C, and D.

In Fig. 9.7a, during the first 300 s (interval A), only D_2 gas is present and the RF power is off. Argon gas is injected to facilitate plasma ignition a few seconds before it. At $t = 300$ s, the plasma discharge is initiated and the argon gas flow is progressively decreased. During this period of 50 s, τ_D decreases due to the combination of D^- absorption and a thermal effect on the cavity. After $t = 350$ s, only D_2 is injected and maintained stable for about 150 s (interval C). Then, the plasma is turned off at $t = 500$ s when τ_D exhibits a jump from $34.8 \mu\text{s}$ to $37.1 \mu\text{s}$ between two consecutive acquisitions (see zoom box at $t = 500$ s in Fig. 9.7a) due to the sudden disappearance of D^- . Finally, τ_D tends to its value before the plasma discharge (interval D).

As one can clearly see in Fig. 9.7a, together with the rapid jump due to the plasma extinction, a slower variation can be observed, lasting some minutes after the plasma is turned off. τ_D takes more than 10 min to recover to its initial value before the plasma discharge. Even during the plasma D_2 discharge, τ_D is observed to drift. These long period drifts are most likely due to thermal effects causing a distortion of the optical cavity.

To verify that the sudden jump observed at $t = 500$ s in Fig. 9.7a is due to the disappearance of negative ions, a test with an argon plasma of similar electron density, not contributing to laser absorption, was performed. No jump occurred when the argon plasma was turned off (see zoom box in Fig. 9.7b), confirming that the jump seen in D_2 plasma is due to the disappearance of negative ions produced in this plasma. A gradual drop $\delta\tau_{Ar}$ of about $0.5 \mu\text{s}$, at the limit of the sensitivity, is observed when the argon plasma is turned on. This is probably due to a loss of alignment caused by the thermal expansion of the cavity. When the argon plasma is turned off, τ_{Ar} recovers slowly to its pre-discharge value after some minutes. Thus, the fast dynamics of τ that characterizes the plasma extinction (of the order of $100 \mu\text{s}$), with respect to the slow drift of optical cavity thermal expansion, can be taken as a signature of the negative ion disappearance in H_2 and D_2 plasmas. By making a linear fit of τ_D a few seconds before and after the τ_D jump (see Fig. 9.7a), the D^- density can be calculated. In this way, any fast transient effects ($10^1 \mu\text{s}$) on negative ion density (Hopkins and Mellon 1991) at plasma extinction are avoided. The error on the calculation of \bar{n}_{D^-} is estimated using the errors on the coefficients of the linear fit. An average density \bar{n}_{D^-} of $(3.05 \pm 0.09) \times 10^{16} \text{ m}^{-3}$, on a 5 cm path length, is deduced; this value is comparable to the results of OES in hydrogen. To summarize, the CRDS diagnostic measured D^- density in agreement with previous OES measurements. Further results are shown in Sect. 9.4.2.

9.3.2.4 Langmuir Probe Laser Photodetachment (LPLP)

CRDS at a fixed measurement position is not sufficient to determine the local negative ion density since its signal results from the interaction of the laser beam

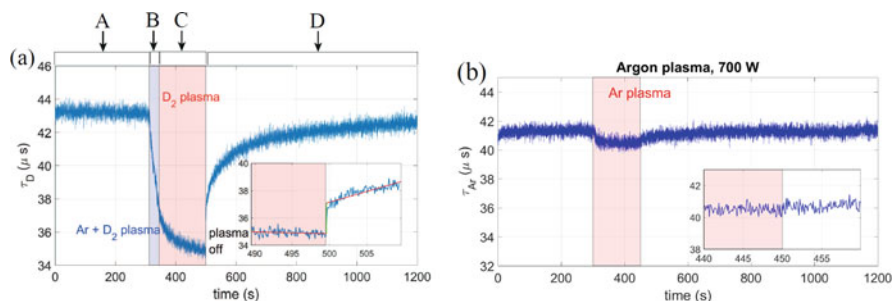


Fig. 9.7 The time evolution of τ before, during, and after the plasma discharge for (a) D_2 5 kW plasma and (b) Ar 700 W plasma, at 0.3 Pa. Red areas show when the plasma is on. The box inset is a zoom around the instant when the plasma is turned off ($t = 500$ s for D_2 and $t = 450$ s for Ar). The D_2 exhibits a jump due to D^- disappearance (zoom box in (a)), while no jump is observed for the Ar plasma (zoom box in (b)). Reproduced from *Review of Scientific Instruments* **89**, 103504 (2018); doi: 10.1063/1.5044504, with the permission of AIP Publishing (Agnello et al. 2018)

along the whole path intersecting the plasma. Moving the laser beam across the plasma column could be used to Abel invert the data to reconstruct the n_- radial profile by assuming cylindrical symmetry. However, this method is impractical due to the lengthy alignment procedure. LPLP can alternatively be used to obtain relative negative ion profiles with a spatial precision comparable to the laser beam diameter. A full review of LPLP can be found in Bacal (2001); Baghiti-Sube et al. (1996); here, we briefly review the basic purposes of LPLP and its implementation on RAID (Agnello et al. 2020).

In H^- or D^- ions, the extra electron is weakly bound to the atom. A laser pulse with sufficient energy can photodetach a large number of electrons from the negative ions along the laser path in the plasma. A laser requires a relatively low energy flux (~ 10 mJ/cm²) to photoneutralize all H^- or D^- ions along its path (Bacal 2001). Moreover, since the laser pulses are very short (~ 5 ns in RAID), the photodetachment process happens on a time scale much shorter than that of the plasma evolution, allowing to temporally resolve the negative ion density. LPs can be employed to measure both the photodetached electrons and the local plasma density (Bacal 2001). The LP probe is coaxial with the axis of the laser beam and biased at a potential V_{LP} higher than the local plasma potential V_p . When $V_{LP} > V_p$, the LP draws a current I_{dc} , proportional to the local electron density n_e . The laser pulse causes a very fast increase of the detected current over a few ns, I_{pd} , proportional to the number of photodetached electrons. The negative ion density n_- can then be estimated by $n_-/n_e = I_{pd}/I_{dc}$.

Figure 9.8a shows a picture of the experimental setup of the LPLP system on RAID. Unlike the CRDS setup, the laser beam measurement position is not constrained by the position of the HR mirrors but can be vertically displaced along the window. The laser pulses are produced by the same Nd:YAG laser described in Sect. 9.3.2.3 and injected into the vacuum vessel by an optical beam path similar to that used for CRDS but with varying injection position. To detect the photodetached

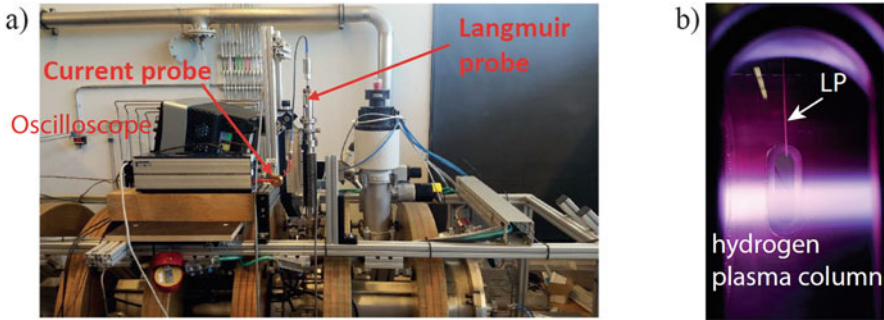


Fig. 9.8 (a) Experimental setup for LPLP measurements in RAID showing the positioning of the LP, of the current probe and of the oscilloscope. (b) Picture of the interior of the vessel showing a hydrogen plasma column and the location of the Langmuir Probe for photodetachment measurements

electrons, a LP moving in the vertical direction is employed. The probe is displaced by a stepper motor, and the vacuum is maintained by a bellows. The probe tip is L-shaped co-axially aligned with the direction of the laser beam. The probe is biased at $V_{\text{bias}} = 26 \text{ V}$ above the plasma potential, which is $V_{\text{plasma}} = 12 (\pm 1) \text{ V}$ for $r < 0.06 \text{ m}$, for both H_2 and D_2 plasmas, and independent of gas pressure. Figure 9.8b shows a picture of the ceramic stick of the LP probe inside the vessel, at its most external radial position ($r_{\text{max}} = 10 \text{ cm}$).

To measure at different radial locations in the plasma column, the LP and the laser measurement position have to be simultaneously displaced. The laser beam and LP tip are aligned at each measurement position by vertically displacing the reflecting laser beam injection mirror and the LP by the same distance. Alignment is obtained by detecting the laser beam spot after the exit window by flash paper and the shadow of the LP tip on the beam spot can be seen. The length of the vertical windows allows measurement of the cross-section plasma column up to $r_{\text{max}} = 7 \text{ cm}$. To filter out the DC component of the signal collected when the probe bias is at V_{bias} from the fast transient due to the photodetachment, we employ an AC toroidal current transformer with 2.5 V/A sensitivity and upper cut-off frequency at 1.17 GHz. Signals are acquired by an oscilloscope mounted on the top of RAID (see Fig. 9.8a) to minimize the length of the cable to avoid parasitic capacitance effects. Photodetachment signals are usually acquired in a few microseconds temporal window with a sampling rate of 10 GS/s. Signals are triggered by a photodiode sensitive to the laser wavelength detecting the passage of the laser pulse before entering the vessel. The noise level on the single LPLP signal is such that averaging over several hundred acquisitions is usually required.

Typical photodetachment signals are shown in Fig. 9.9 for different powers. The laser pulse strikes the LP tip at $t = 0 \text{ s}$ causing the overshoot (increase of the collected electron current) whose amplitude is indicated by the vertical arrow for the 5 kW case. The subsequent undershoot and the lack of “plateau” have been reported by other authors such as by P. Devynck et al. (1989), M. Bacal (2001),

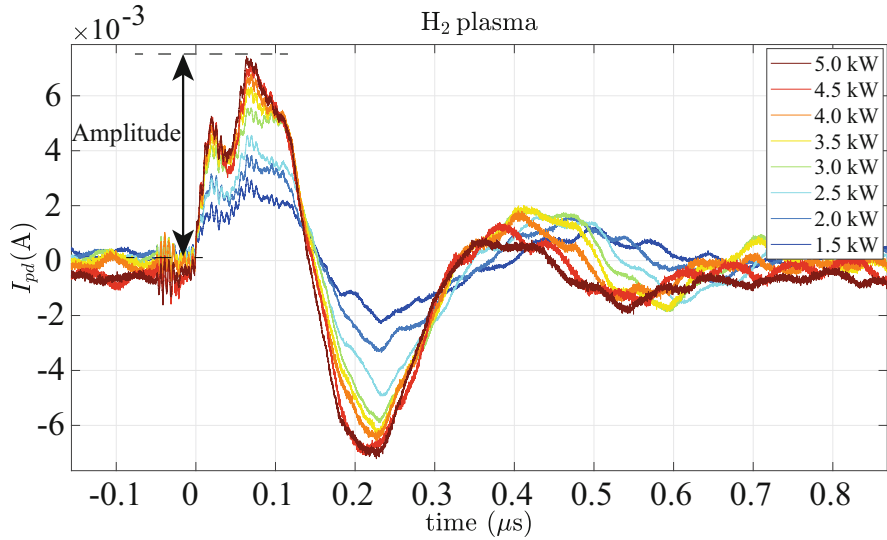


Fig. 9.9 Typical photodetachment signals for a H_2 plasma. The laser strikes the LP tip at $t = 0$ s causing the overshoot whose amplitude is indicated by the arrow. Reproduced from Agnello et al. (2020) with IAEA permission

and S. Aleiferis (2016). This effect is partly due to the motion of ions caused by the thermal motion of the electrons (Friedland et al. 1994). The large undershoot and the double peak might also be an effect of the different dynamics of the electrons, and the ions at the LP. Electrons are magnetized, having a Larmor radius which is comparable to, or smaller than, the LP radius of 0.2 mm. Ion trajectories, however, are not magnetically confined to the probe area because, in a magnetic field of 200 G, they have an ion Larmor radius of ~ 1.6 mm, much bigger than the LP tip radius (Agnello et al. 2020). Numerical simulations using a particle-in-cell code have been performed to model the temporal dynamics of the observed photodetachment signal (Oudini et al. 2021). If the laser pulse strikes the probe when there is no plasma, no variation of the signal is detected. The amplitude increases with RF power confirming the trend observed during CRDS tests.

9.4 Measurements of Negative Ions

Experimental activities on RAID investigate the formation of negative ions by volumetric processes in H/D plasmas. By continuously improving the diagnostics, theory, and simulation tools, research on RAID has reached a level at which quantitative comparisons between theory and experiments can now be performed. Negative ions measured by OES, CRDS, and LPLP are reviewed here.

9.4.1 First Evidence of Negative Ions in RAID Using OES

An optical emission spectroscopy campaign performed in RAID in 2017 gave the first hints of the presence of negative hydrogen ions in RAID plasma (Marini et al. 2017). The first Balmer lines α , β , and γ and the Fulcher- α band were measured for both H_2 and D_2 plasmas. The radiance profiles were Abel inverted to obtain the absolute emissivity radial profiles. The absolute line emissivities were then interpreted with the collisional radiative code YACORA (Wünderlich et al. 2006) to estimate the degree of dissociation, the density profiles of atomic and molecular species and of the ions, including H^- and D^- . YACORA solves the rate equations for 40 states of H, taking into account the excitation and de-excitation by electron collision, the spontaneous emission, the recombination of H^+ , the dissociation of H_2 , and the mutual neutralization of H^- with the positive ions. Three-body reactions are also taken into account. However, the opacity is neglected because of the low pressure (0.3 Pa). Figure 9.10 shows in (a) the degree of dissociation, in (b) the degree of ionization, in (c) the density of H^+ , and in (d) the density of H^- . The degrees of dissociation and ionization are defined, respectively, as

$$D_d = \frac{\frac{n_{\text{H}}}{n_{\text{H}_2}}}{\frac{n_{\text{H}}}{n_{\text{H}_2}} + 2}; \quad D_i = \frac{n_e}{n_{\text{H}} + n_{\text{H}_2}}. \quad (9.2)$$

As defined, D_i takes no account of the presence of negative ions in the plasma, and D_i would vary from zero, with no ionization, to infinity, when there are no neutral particles in the plasma. Therefore, this definition is only valid for low ionization rates with negligible negative ion densities. The dissociation is quite flat in the center of the plasma column around 20%, and the ionization is peaked at the center reaching about 0.7%. Also, n_{H^+} is narrow peaked at the center reaching $2 \times 10^{17} \text{ m}^{-3}$. The most interesting plot is that of the density of the negative ions H^- , showing an off-axis peak at $\sim 4 \text{ cm}$, where the density reaches $2 \times 10^{16} \text{ m}^{-3}$. These measurements were the first evidence of volume produced negative ions in RAID and motivated the design of the laser-based diagnostics discussed in Sects. 9.3.2.2 and 9.3.2.4, namely CRDS and LPLP.

9.4.2 Measurements of Negative Ions Using CRDS

In this section, we describe the results obtained using CRDS published in Ref. Agnello et al. (2020). The purpose of the experiments was to perform parametric scans in RF power, magnetic field, and gas pressure, to investigate the behavior of the source at higher powers (up to 8 kW) as well as to optimize the CRDS technique. Figure 9.11 shows measurements of the negative ion density in H_2 and D_2 plasmas for different RF powers and gas pressures. CRDS data were analyzed employing the technique described in Sect. 9.3.2.3. H^- and D^-

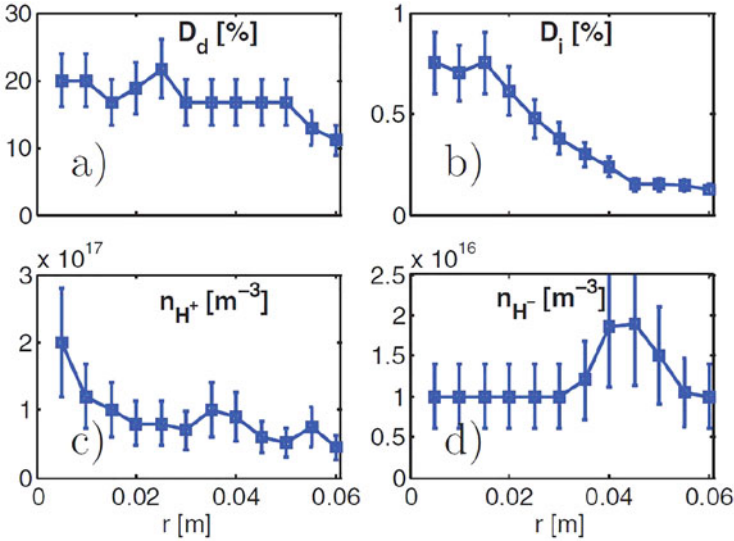


Fig. 9.10 (a) Degree of dissociation, (b) degree of ionization, (c) density of H^+ , and (d) density of H^- , estimated by YACORA for an input power of 3 kW in hydrogen in RAID. Reproduced from Marini et al. (2017) with IAEA permission

line-integrated density increases with RF power for both plasmas. For power larger than 4 kW, however, the growth rate is reduced for H^- . Note that these values are obtained in cw operation on RAID, so the production of negative ions is in steady state. RAID operation at 0.2 Pa is possible, but this results in less negative ion production, and therefore the following experimental investigations were performed at 0.3 Pa.

9.4.3 Measurements of Negative Ions with LPLP

LPLP was also used to perform negative ion measurements in the plasmas of Sect. 9.4.2. Figure 9.12 summarizes the results obtained with laser photodetachment while varying the RF power. Measurements were performed for $0.04 < r < 0.065$ m because I_{dc} was too high and risked damaging the probe for small radii, and the window height limited the LOS of the laser at large radius. The left and the right columns show the results for H_2 and D_2 plasmas, respectively. In Fig. 9.12a, the amplitudes of the photodetachment signals are shown. On average, a weaker signal is measured in the case of D_2 . Figure 9.12b shows the electron current I_{dc} when the probe is biased at $V_{bias} = 26$ V above the plasma potential. On average, more electrons are collected in the case of D_2 suggesting that the electron density is higher in these plasmas. Figure 9.12c shows the ratios n_{H^-}/n_e and n_{D^-}/n_e . Although the

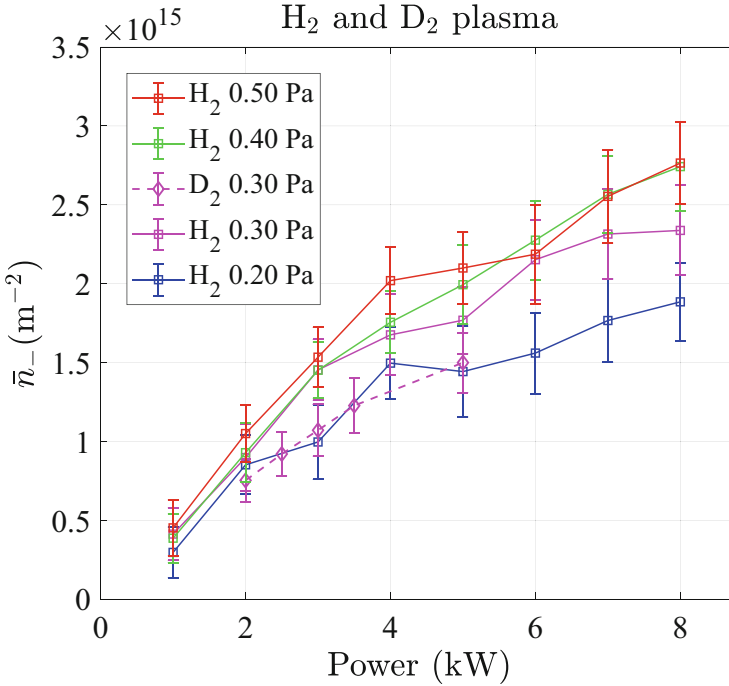
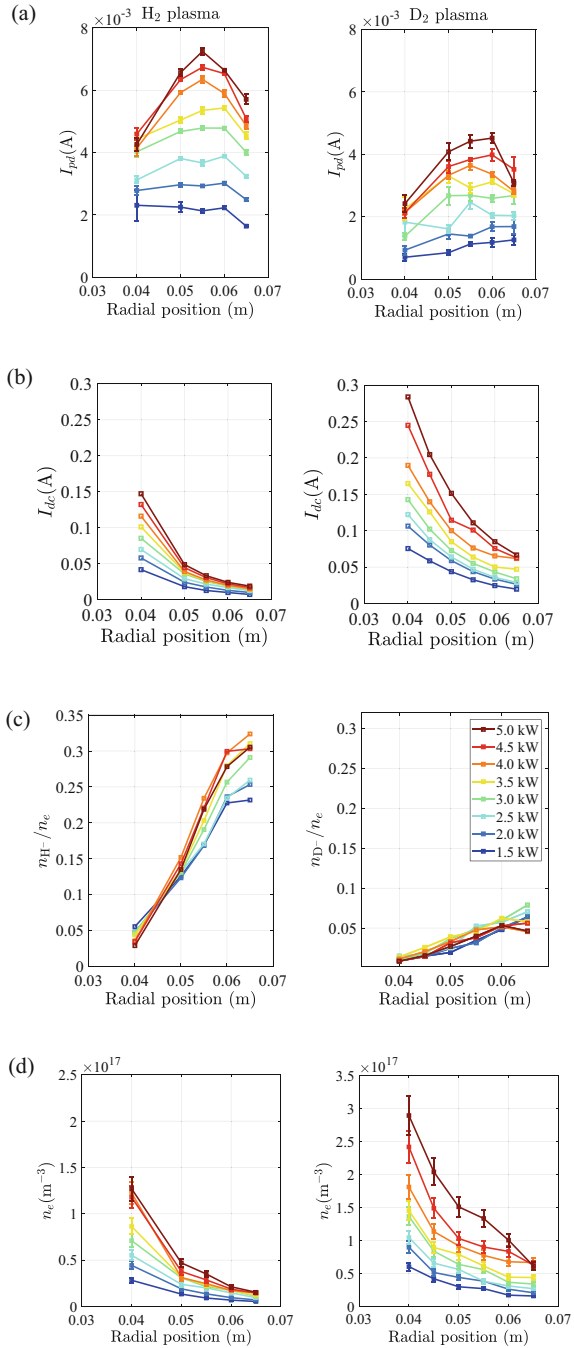


Fig. 9.11 Line-integrated negative ion density as a function of RF power at different pressures for H₂ and D₂ plasmas, demonstrating the steady-state production of negative ions up to 8 kW of RF power. Reproduced from Agnello et al. (2020) with IAEA permission

electrons are magnetized, the electron transport coefficient is the same both for the photodetached electrons and for the electrons collected by the probe when biased above V_{plasma} . This is justified as follows: the background electrons have an energy of about 1.5 eV in this region of the plasma column, and the photodetached electrons are released into the plasma with an energy of ~ 0.45 eV. Thus, the ratio of the Larmor radii of the two types of electrons in the local magnetic field will be ~ 1.7 , and the transport of the electrons in that field should be similar. At $r = 0.06$ m, n_{H^-}/n_e reaches 0.3, while n_{D^-}/n_e reaches about 0.05. Also, the profile ratios are only weakly dependent on power, as shown in Fig. 9.12c. The independence of the ratio n_-/n_e from the RF power might be an advantage for negative ion extraction because it makes the negative ion yield in the source easier to tune. The difference between n_{H^-}/n_e and n_{D^-}/n_e arises mainly because the electron densities in D₂ plasmas are approximately a factor 3 higher than in H₂ plasmas for the same RF power, as shown in Fig. 9.12d, which means that the D⁻ and H⁻ densities are similar, for the same RF power, in the D₂ and H₂ plasmas in RAID. At 5 kW power and $r = 0.04$ m (where the fixed LOS of CRDS is located), n_e reaches $\sim 1.3 \times 10^{17} \text{ m}^{-3}$ in H₂ and $\sim 2.9 \times 10^{17} \text{ m}^{-3}$ in D₂. Although the absolute value of n_e might be unreliable because of electron magnetization, this data completes the

Fig. 9.12 Results of the laser photodetachment measurements for H_2 (left column) and D_2 (right column) plasmas at 0.3 Pa. **(a)** Photodetachment amplitudes I_{pd} , **(b)** electron current I_{dc} collected when the probe is biased at $V_{bias} = 26$ V above the plasma potential, **(c)** ratio n_{H^-}/n_e , and **(d)** electron density n_e . On the edge of the plasma column, hydrogen plasmas have lower electron density and a higher ratio n_{H^-}/n_e . Reproduced from Agnello et al. (2020) with IAEA permission



set of quantities that can be obtained only relying on the LP laser photodetachment technique. The higher density in D₂ is also measured by microwave interferometry at the edge, at the measurement position $r = 0.04$ m, revealing a line-integrated density a factor 2 higher in the case of deuterium.

The n_e profiles are obtained from the analysis of IV curves measured with the same LP used for laser photodetachment. The electron energy distribution function (EEDF) is calculated using the Druyvesteyn formula (Druyvesteyn 1930), and the second derivative of the measured electron current is calculated with a Savitzky–Golay filter to obtain the floating and plasma potential. An effective electron temperature T_e and the total electron density are then obtained by numerically integrating the EEDF. More details of the analysis can be found in Béchu et al. (2013). The data shown in Fig. 9.12a, b, and d can be used to calculate the negative ion density. The negative ion density peaks at $r \sim 0.055$ m and H⁻ and D⁻ are distributed in a shell-like shape, as also measured by OES. The peak density of H⁻ is $7.7 \times 10^{15} \text{ m}^{-3}$, which is a factor of ~ 2.5 lower compared to $2.0 \times 10^{16} \text{ m}^{-3}$ measured via OES (Marini et al. 2017). The disagreement between OES and laser photodetachment might be due to an incorrect estimate of n_e via LPs.

9.4.4 Combining CRDS and LPLP to Extract Absolute Negative Ion Density Profiles

In this section, we focus only on the data at 0.3 Pa since this is the pressure relevant to present NBI systems, such as the system designed for ITER, although lower pressure may be more relevant for future systems (Hemsworth et al. 2017). The measurement of n_e via LPs in a plasma with magnetized electrons might lead to error on the final estimate of negative ion density. To overcome this problem, we can use the line-integrated negative ion density measured using CRDS for absolute calibration. Using a form factor approach (Agnello et al. 2020), one can deduce n_-^{peak} , which provides the absolute negative ion density profile. The results are summarized by Fig. 9.13 showing n_{H^-} and n_{D^-} profiles. Only 2, 3, and 5 kW RF powers are shown for clarity. The peak value obtained at 5 kW for H₂ is $1.9 (\pm 0.3) \times 10^{16} \text{ m}^{-3}$, close to the value measured by OES (Marini et al. 2017), which was $3.0 (\pm 0.8) \times 10^{16} \text{ m}^{-3}$. For D⁻, the peak value for 5 kW results in $1.8 (\pm 0.3) \times 10^{16} \text{ m}^{-3}$, smaller than $4.5 (\pm 2.0) \times 10^{16} \text{ m}^{-3}$ measured with OES. The discrepancy is probably due to errors in the deuterium cross-sections used in the OES analysis. More accurate deuterium cross-sections are now available in the recent analysis of Laporta et al. (2021). In Fig. 9.14, we plot the peak value of n_- for increasing powers, showing a linear trend, and the negative ion density with electron density measured by the LP at $r = 0.055$ m, close to n_- peak values. n_- increases almost linearly with n_e , and higher values may be attained by increasing the RF power. The lower ratio n_-/n_e in the case of deuterium is clearly visible. This suggests that the co-extracted electrons might be a more important issue for

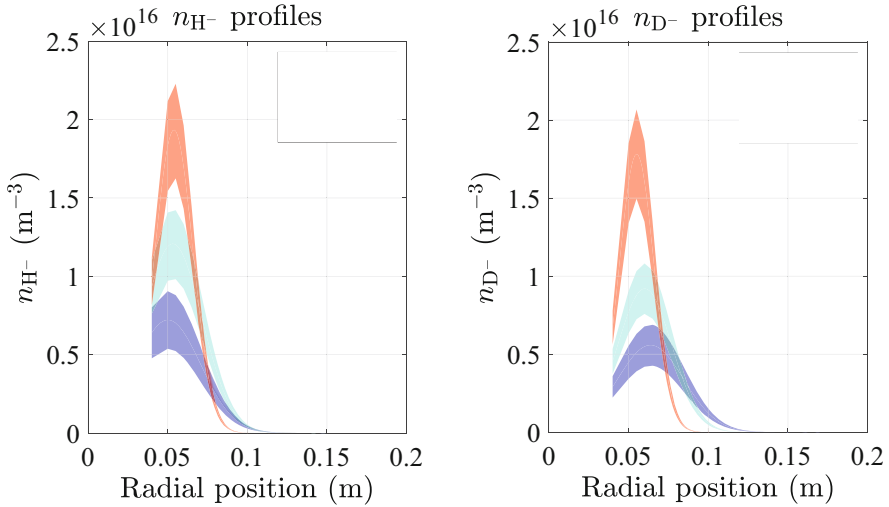


Fig. 9.13 n_{H^-} and n_{D^-} radial profiles for different powers obtained using the relative negative ion profiles measured with laser photodetachment and calibrated with CRDS line-integrated measurements. Reproduced from Agnello et al. (2020) with IAEA permission

D^- extraction. The isotopic effect in negative ion and electron density has been investigated by some authors (Skinner et al. 1993; Bruneteau et al. 1996; Fukumasa and Yoshino 1998), and it is due to a combination of different phenomena which we briefly explain as follows: calculations and experiments show that n_e is higher in deuterium than in hydrogen plasmas, which is mostly due to ion transport. Positive ions are indeed mostly lost by transport to the walls where they are neutralized. For deuterium, the transport of positive ions is a factor $1/\sqrt{2}$ smaller than for hydrogen because of the mass difference. This might explain in part the higher n_e in deuterium (Skinner et al. 1993). Concerning the isotope effect on the negative ion density, the lower value in deuterium might be due to the higher degree of dissociation in deuterium leading to increased cooling of $D_2(v)$ in collision with D and then less efficient D^- production (Skinner et al. 1993). For a better understanding of the processes, modeling is envisaged, which is the subject of the next section.

9.5 A 1.5D Fluid: Monte Carlo Model of a Hydrogen Helicon Plasma

To advance the understanding of the physics underlying the generation and transport of H^- and D^- in RAID, we use numerical simulations coupled to experimental data in this section. While a full description of the helicon wave propagation and power absorption coupled to a transport/chemistry model would be the ultimate

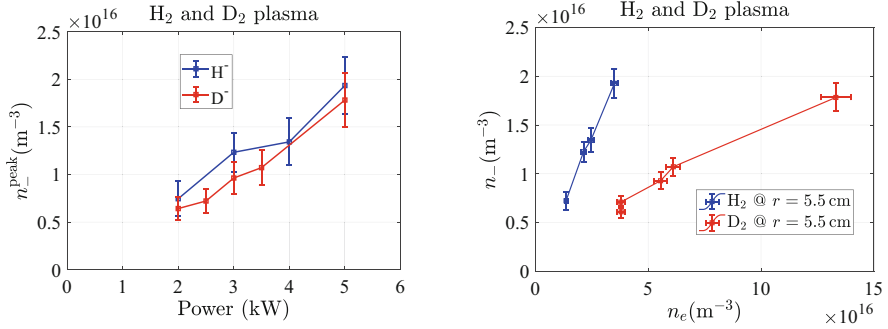


Fig. 9.14 Left: peak negative ion density as a function of RF power at 0.3 Pa. Right: negative ion density vs. electron density in hydrogen and deuterium plasmas. n_- increases with power, and higher density is observed in the case of H^- . Reproduced from Agnello et al. (2020) with IAEA permission

goal, this is clearly beyond the scope of the present work. Instead, we develop a model that combines two separately self-consistent approaches: a plasma fluid model calculating ion transport and a Monte Carlo (MC) model to determine neutral and ro-vibrational density profiles of H_2 . Using the electron density and temperature profiles measured by Langmuir probes as input data, the densities of H^+ , H_2^+ , H_3^+ , and H^- are computed in a 1.5D (dimensional) geometry.

The fluid approach can be applied in RAID since the ion-neutral collision mean free path (mfp) is smaller than the typical size of the device. The magnetic field can play an important role in plasma transport in low-pressure plasma sources (Hagelaar and Oudini 2011). Typical values of RAID magnetic field are such that the ion and electron Larmor radii are much smaller than the vessel radius of 20 cm (see Sect. 9.3.2.4), and therefore the plasma in RAID is strongly magnetized. It is assumed that the plasma species are diluted in a H_2 background. Ion transport is then described by classical drift–diffusion equations in the presence of a uniform magnetic field.

9.5.1 Description of the Fluid Model

Conservation of mass and momentum and Poisson’s equations are used in the fluid description. Each ion species is denoted by the subscript s for H^+ , H_2^+ , H_3^+ , or H^- . The equations are:

$$\begin{aligned} \nabla \cdot \mathbf{\Gamma}_s &= S_s - L_s, \\ 0 &= q_s n_s (\mathbf{E} + \mathbf{u}_s \times \mathbf{B}) - k_b T_s \nabla n_s - m_s n_s \nu_s \mathbf{u}_s, \end{aligned}$$

$$\nabla^2 V = -\frac{e}{\epsilon_0}(n_{\text{H}^+} + n_{\text{H}_2^+} + n_{\text{H}_3^+} - n_{\text{H}^-} - n_e), \quad (9.3)$$

where n_s is the number density, m_s the mass, \mathbf{u}_s the fluid velocity of the species, $\mathbf{E} = -\nabla V$ the electric field, \mathbf{B} the magnetic field, q_s the electron charge magnitude, $\mathbf{\Gamma}_s = n_s \mathbf{u}_s$ the species flux, ν_s the momentum collisional transfer frequency, and S_s and L_s the source and the loss terms. The magnetic field \mathbf{B} is the DC field generated by the coils (200 G) since the magnetic field of the helicon wave is only a few Gauss (Guittienne et al. 2021). A steady-state plasma is considered, and the electron inertia is neglected compared to the combined effect of \mathbf{E} and \mathbf{B} . The ion distribution function is considered isotropic, and the ion temperature gradient is neglected in the pressure term. Plasma quasi-neutrality is guaranteed by the electric field generated by the charge separation. Equation (9.3) is then solved using COMSOL Multiphysics (COMSOL 2018).

In RAID, the vessel walls are far from the edge of the plasma column and electrically conducting, suggesting that boundary conditions are mainly dominated by the end plates, where plasma losses and recombination processes occur (Shinohara et al. 1998; Fubiani et al. 2021). A rigorous description of wall losses would require a self-consistent treatment of the plasma sheath (a few millimeters in front of the wall) where quasi-neutrality is lost and strong electric fields appear. Instead, the ion boundary losses are computed using the Bohm criterion, which, for positive ions, is $\Gamma_{\text{wall}} = -n_s \sqrt{qT_e/(m_s e)}$. Negative ions are confined to the plasma bulk in electropositive plasmas (Chabert and Braithwaite 2011) owing to the typical low ion temperature (~ 0.1 eV), which prevents them from escaping from the plasma potential well. H⁻ ions are therefore entirely produced and destroyed in the plasma volume. In RAID, it is therefore crucial to understand their production and destruction channels, discussed in Sect. 9.5.4, and how they can be controlled to optimize negative ion yield.

9.5.2 Reaction Rates

In this model, binary reactions between electrons, neutrals, and ion species are considered. Three-body reactions are neglected in this low pressure regime. The reaction rate $R_{12} = k(T_1, T_2)n_1n_2 \text{ m}^{-3}\text{s}^{-1}$ is regulated by a rate coefficient $k(T_1, T_2)$ dependent on the reactant temperatures T_1 and T_2 shown in Table 9.3. The channels for the volume production of H⁻ are given by reactions 3, 7, and 22, but dissociative attachment, 3, is by far the most effective channel for H⁻ production in the RAID plasma. The net source term for each ion species is reported in the following equations (Agnello et al. 2022):

Table 9.3 Plasma reactions and rates used for this fluid transport model. Reaction 3 is for vibrational states $\nu = 0 - 14$. For Reaction 3, the dissociative attachment reaction rate provided in Ref. Janev et al. (2003) was used; for the others, the reaction rates are provided in Ref. Santoso (2018). We note that for deuterium, the vibrational excitation and dissociation by electron impact were recently given in Laporta et al. (2021). From Agnello et al. (2022), copyright IOP Publishing. Reproduced with permission. All rights reserved

	Reaction	Reaction rate (k_n) [m^3s^{-1}]
1	$e + \text{H}_2 \rightarrow \text{H}_2^+ + 2e$	$7.27 \cdot 10^{-15} T_e^{0.549} e^{-15.5/(T_e-0.001)} + 1.37 \cdot 10^{-14} T_e^{-0.557} e^{-20.3/T_e}$
2	$e + \text{H}_2 \rightarrow 2\text{H} + e$	$1.54 \cdot 10^{-14} T_e^{0.06} e^{8.63/T_e} + 1.11 \cdot 10^{-13} T_e^{-0.813} e^{-13.4/T_e}$
3	$e + \text{H}_2 \rightarrow \text{H} + \text{H}^-$	$1.972 \sigma_\nu^{(0)} \frac{T_e^{1/2}}{1+T_e/E_0} e^{-\frac{\Delta E_{th,\nu}}{T_e}} \left[\frac{[E_{th,\nu}]}{T_e} + \frac{1}{1+T_e/E_0} \right] \times (10^{-14})$
4	$e + \text{H} \rightarrow \text{H}^+ + 2e$	$9.74 \cdot 10^{-15} T_e^{-0.174} e^{-14.3/(T_e-0.001)} + 6.35 \cdot 10^{-15} T_e^{0.433} e^{-16.4/T_e}$
5	$\text{H} + \text{H}_2^+ \rightarrow \text{H}_2 + \text{H}^+$	$1.54 \cdot 10^{-14} T_e^{-0.859} e^{-4.61/(T_i-0.786)} + 1.64 \cdot 10^{-15} T_i^{-0.353} e^{-0.258/T_i}$
6	$e + \text{H}_2^+ \rightarrow \text{H} + \text{H}^+ + e$	$3.50 \cdot 10^{-13} T_e^{-1.25} e^{-3.19/(T_e-0.008)} + 1.77 \cdot 10^{-13} T_e^{-0.0924} e^{-3.04/T_e}$
7	$e + \text{H}_3^+ \rightarrow \text{H}_2^+ + \text{H}^-$	$1.93 \cdot 10^{-15} T_e^{-1.07} e^{-6.26/(T_e+0.131)} + 5.35 \cdot 10^{-17} T_e^{-0.371} e^{-2.07/T_e}$
8	$\text{H}_2 + \text{H}_2^+ \rightarrow \text{H} + \text{H}_3^+$	$6.29 \cdot 10^{-15} T_i^{-1.46} e^{-2.22/(T_i+0.356)} + 2.71 \cdot 10^{-16} T_e^{-1.30} e^{-0.317/T_i}$
9	$\text{H}^+ + \text{H}^- \rightarrow 2\text{H}$	$4.46 \cdot 10^{-14} T_i^{-0.281} + 1.26 \cdot 10^{-14} e^{-1.96/T_i}$
10	$\text{H}_2^+ + \text{H}^- \rightarrow \text{H}_2 + \text{H}$	$2.23 \cdot 10^{-14} T_i^{0.425} + 8.93 \cdot 10^{-14} T_i^{-0.261}$
11	$\text{H}_3^+ + \text{H}^- \rightarrow \frac{\text{H}_2}{2} + 3\text{H}$	$1.70 \cdot 10^{-14} T_i^{0.313} + 5.75 \cdot 10^{-14} T_i^{-0.288}$
12	$e + \text{H}^- \rightarrow \text{H} + 2e$	$4.58 \cdot 10^{-13} T_e^{0.287} e^{-4.41/(T_e+0.117)} + 2.71 \cdot 10^{-14} T_e^{0.62} e^{-1.82/T_e}$
13	$e + \text{H}_3^+ \rightarrow 2\text{H} + \text{H}^+ + e$	$2.69 \cdot 10^{-13} T_e^{-0.245} e^{-15.6/(T_e+0.003)} + 1.01 \cdot 10^{-12} T_e^{-0.464} e^{-26.8/T_e}$
14	$\text{H}_2 + \text{H}^+ \rightarrow \text{H}_3^+ + h\nu$	$1.63 \cdot 10^{21}$
15	$e + \text{H}_2^+ \rightarrow 2\text{H}$	$2.29 \cdot 10^{-14} T_e^{-0.571} + 3.31 \cdot 10^{-15} T_e^{-0.152} T_e$
16	$e + \text{H}_3^+ \rightarrow 3\text{H}$	$3.36 \cdot 10^{-15} T_e^{-0.716} + 3.73 \cdot 10^{-14} T_e^{-0.67} e^{6.40/T_e}$
17	$e + \text{H}_3^+ \rightarrow \text{H} + \text{H}_2$	$2.03 \cdot 10^{-15} (T_e^{-0.189} + 0.04 T_e^{-1.49}) + 5.57 \cdot 10^{-14} T_e^{1.23} e^{-6.21/T_e}$
18	$\text{H} + \text{H}^- \rightarrow \text{H}_2 + e$	$2.16 \cdot 10^{-13} T_i^{-1.89} e^{-12.7/(T_i+1.17)} + 1.30 \cdot 10^{-15} T_i^{-0.418} e^{-0.192/T_i}$
19	$\text{H}_2 + \text{H}^- \rightarrow \text{H} + \text{H}_2 + e$	$1.62 \cdot 10^{-16} T_i^{0.417} e^{-6.47/(T_i+0.132)} + 5.70 \cdot 10^{-16} T_i^{0.550} e^{-2.19/T_i}$
20	$\text{H} + \text{H}^- \rightarrow 2\text{H} + e$	$3.81 \cdot 10^{-15} T_i^{0.280} e^{-3.76/(T_i+0.626)} + 4.55 \cdot 10^{-16} T_i^{0.603} e^{-0.375/T_i}$
21	$\text{H}_2 + \text{H}^+ \rightarrow \text{H} + \text{H}_2^+$	$5.54 \cdot 10^{-16} T_i^{-0.453} e^{-3.26/(T_i-0.001)} + 5.98 \cdot 10^{-18} T_i^{-2.88} e^{-0.310/T_i}$
22	$e + \text{H} \rightarrow \text{H}^- + h\nu$	$5.75 \cdot 10^{-20} (T_e^{-0.0285} - 0.94 T_e^{-0.05}) + 6.54 \cdot 10^{-19} T_e^{-5.18} e^{-72.4/T_e}$

$$\begin{aligned}
\nabla \cdot \Gamma_{H^+} &= k_4 n_e n_H + k_5 n_H n_{H^+} + k_6 n_e n_{H_2^+} - k_9 n_{H^+} n_{H^-} + k_{13} n_e n_{H_3^+} \\
&\quad - k_{14} n_{H_2} n_H - k_{21} n_{H_2} n_{H^+}, \\
\nabla \cdot \Gamma_{H_2^+} &= k_{11} n_e n_{H_2} - k_5 n_H n_{H_2^+} - k_6 n_e n_{H_2^+} + k_7 n_e n_{H_3^+} - k_8 n_{H_2} n_{H_2^+} \\
&\quad - k_{10} n_{H_2^+} n_{H^-} - k_{15} n_e n_{H_2^+} + k_{21} n_{H_2} n_{H^+}, \\
\nabla \cdot \Gamma_{H_3^+} &= -k_7 n_e n_{H_3^+} + k_8 n_{H_2} n_{H_2^+} - k_{11} n_{H_3^+} n_{H^-} - k_{13} n_e n_{H_3^+} + k_{14} n_{H_2} n_{H^+} \\
&\quad - k_{16} n_e n_{H_3^+} - k_{17} n_e n_{H_3^+}, \\
\nabla \cdot \Gamma_{H^-} &= n_e \sum_{v=0}^{14} k_3(v) n_{H_2(v)} + k_7 n_e n_{H_3^+} - k_9 n_{H^+} n_{H^-} - k_{10} n_{H_2^+} n_{H^-} - k_{11} n_{H_3^+} n_{H^-} \\
&\quad - k_{12} n_e n_{H^-} - k_{18} n_H n_{H^-} - k_{19} n_{H_2} n_{H^-} - k_{20} n_H n_{H^-} + k_{22} n_e n_H.
\end{aligned}$$

The term $\sum_{v=0}^{14} k_3(v) n_{H_2(v)}$ describes the generation rate of H^- by dissociative attachment from ro-vibrationally excited H_2 and is calculated by taking into account the density of H_2 molecules in each vibrational state v , computed by the MC model (see Sect. 9.5.3). The most important H^- destruction processes are the mutual neutralization (MN) with positive ions (R9–11), the electron detachment (ED) (R12), and the associative detachment (AD) with neutrals (R18–20). Measured electron temperature and density from LPs and microwave interferometry are used as input to compute transport and chemistry. Figure 9.15 shows typical profiles 1 m from the antenna, for 3 kW RF power and 0.3 Pa.

Molecular hydrogen can be ro-vibrationally excited by electron impact or by decay from the excited molecule, sustaining 15 vibrational states in the electronic ground state. Experimental and theoretical studies have revealed that dissociative attachment to these vibrationally excited states is the main mechanism responsible for volume production of negative ions (Bacal 2006; Bacal et al. 2021). A full description of the hydrogen plasma would include collisions between H_2 in its various ro-vibrational states and other plasma species. This would complicate the model without significantly changing the ion transport. Since for RAID plasma, only about 1% of H_2 is excited compared to background H_2 (Fubiani et al. 2017), the overall ion transport and chemistry will be only weakly influenced by the excited H_2 . To approximate the contribution of the dissociative attachment to H^- production, the MAR (molecular activated recombination) rate coefficient could be used as a reasonable approximation for the dissociative attachment reaction rate (Pigarov and Krasheninnikov 1996). In this study, however, we use a Monte Carlo model to estimate the radial density profiles of each ro-vibrational state of H_2 which are then inserted as input into the fluid model.

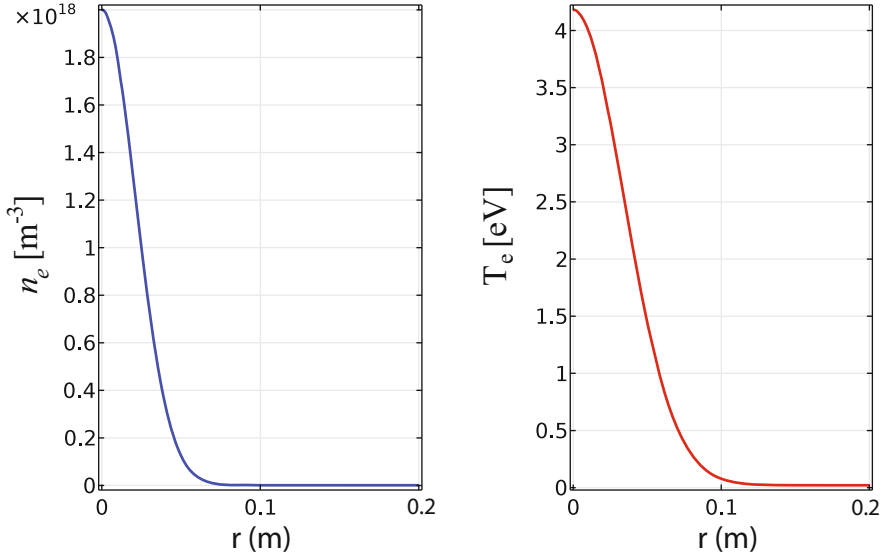


Fig. 9.15 Electron density and temperature radial profiles used as input in the model, obtained by fitting experimental data (Agnello 2020). These profiles are representative for a hydrogen plasma discharge with 3 kW RF power and 0.3 Pa gas pressure at 1 m from the center of the antenna. From Agnello et al. (2022), copyright IOP Publishing. Reproduced with permission. All rights reserved

9.5.3 A Monte Carlo (MC) Model to Determine Neutral Density Profiles

To improve the self-consistency of the model, the plasma dynamics is coupled with the H_2 vibrational kinetics because the H^- production depends strongly on the molecular vibrational distribution function (VDF). A Monte Carlo (MC) approach is used considering the charged particles as a fixed background with non-uniform density and temperature distributions obtained from the plasma fluid model. This gas–plasma decoupling is a necessary hypothesis due to the very different plasma and gas kinetic time scales, μs and ms , respectively.

The MC model (Taccogna et al. 2007) is 1D in the radial direction keeping the same geometrical reduction arguments used for the plasma fluid model. The simulation starts with a uniform radial distribution of molecules; at each time step, a certain number of molecules are injected uniformly along the radial domain to keep the number of molecules fixed. This mimics the continuous axial flow of molecules keeping the gas pressure constant. Each particle contains information about its electronic (for atoms) and ro-vibrational (for molecules) state. Only the fundamental electronic state of H_2 is taken into account. Rotational states are not considered since the high ionization coefficient and the electron temperature guarantee a rotational equilibrium. The most relevant collisions with electrons and H^+ ions (the dominant ion species, see Sect. 9.5.4) are considered through the use

of state selective cross-sections (Celiberto et al. 2001; Krstic and Schultz 2003; Hunter and Kuriyant 1977), while neutral–neutral collisions are negligible due to the low pressure regime. The equations of motion of particles are solved, and surface processes are modeled by using appropriate coefficients (Kim et al. 1999; Rutigliano et al. 2014). For molecules, relaxation and dissociation coefficients are taken from Billing and Cacciatore (1995); Hiskes and Karo (1989). The gas subsystem reaches a steady-state condition after 4 ms. The radial averaged VDF shows the typical parabolic Treanor behavior for the first 4 vibrational levels and hyperbolic plateau for ≥ 4 , corresponding to a two-temperature distribution $T_{01} = 2000$ K and $T_{07} = 7000$ K. Once the n_H and n_{H_2} radial density profiles have been determined, the degrees of ionization and dissociation (9.2) can be computed; the degree of ionization is peaked at the center where it reaches about 2%. This is qualitatively similar to the OES result in Fig. 9.10b, although about 3 times larger. Given the very different methods, experimental errors, and rate constant uncertainties, this discrepancy is not unexpected. The degree of dissociation is slightly hollow at the center and $\approx 10\%$ across the vessel, and thus the H_2 molecular density is dominant, satisfying the fluid model assumption of plasma species diluted in a H_2 background.

9.5.4 Transport of the Ion Species

Solution of the coupled equations Eq. (9.3) yields the density of each ion species, Fig. 9.16, together with the net source rate profiles (production–destruction) for H^+ , H_2^+ , H_3^+ , and H^- . H^+ and H_2^+ show centrally peaked density profiles, while H_3^+ peaks at the column edge at $r \approx 5$ cm. The H^- density profile also shows a shell-like structure, whose density and ≈ 1 cm width are comparable to measurements by laser-based diagnostics (Agnello et al. 2020). At the position of the H^- density peak, H_2^+ and H_3^+ densities are also comparable to that of H^+ . This shows that the plasma column is characterized by a hot and dense core of ionizing plasma dominated by H^+ and H_2^+ , surrounded by a ring of H_3^+ and H^- . The peak density is sensitive to axial losses which are not self-consistently calculated here. To have an insight on plasma species radial transport, Fig. 9.17 shows the absolute values and direction of the radial flux for each plasma species. H^+ and H_2^+ fluxes peak at about 2 cm from the center and are lost in a few centimeters due to volume destruction processes with background gas. The net generation rate of H_3^+ occurs at a ring of radius 1 cm in Fig. 9.16a, and the outward drift in the radial electric field shown in Fig. 9.17 combines to give a ring profile of maximum H_3^+ density at 4.5 cm, as shown in Fig. 9.16b. H^- are transported inward across the radius.

In conventional negative ion sources for fusion, negative ion production is achieved in two steps in separate volumes: a *driver* region where molecular hydrogen (or deuterium) is dissociated and an *expansion* region with a cesiated surface where H/D atoms attach electrons. In the case of a Cs-free negative ion source such as RAID, where negative ions are produced only in the plasma volume, it is interesting to study the contribution of production and destruction processes

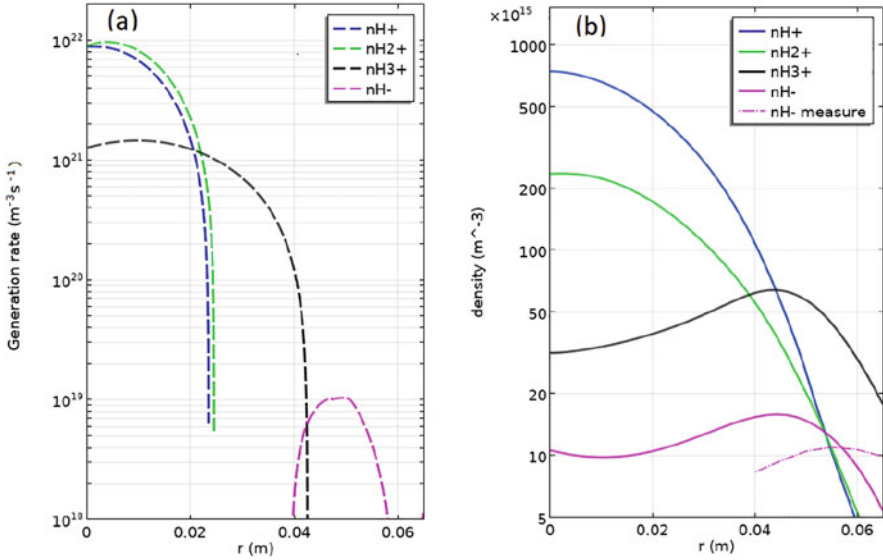


Fig. 9.16 (a) Net generation rate and (b) density profiles of ion species computed by the fluid model, including experimental n_{H^-} data. From Agnello et al. (2022), copyright IOP Publishing. Reproduced with permission. All rights reserved

along the radial direction. Figure 9.18 shows the reaction rates for H^- production (dashed lines) and destruction processes (solid lines) for electron collision reactions on the left and for reactions involving only heavy species on the right. The dissociative attachment reaction from H_2 ro-vibrational excited states is the main contributor to negative ion production (Bacal et al. 2021). The main destruction processes in the plasma center are electron detachment and mutual neutralization with H^+ . However, at the edge of the plasma column, where H^- peaks ($r \approx 5$ cm), the most important destruction channels are associative detachment and mutual neutralization with H_3^+ and H_2^+ . Thus, negative ions are mostly produced on axis but are efficiently destroyed by electron detachment. They mostly survive on the edge of the column because T_e is lower so that a net creation of H^- occurs as shown in Fig. 9.16, which gives the sum of all the production and destruction rates for H^- .

9.6 Conclusions

The present work broadens the knowledge of the plasma in a high-power helicon plasma source and provides new insights into the generation and transport of negative ions in linear helicon devices supported by numerical simulations. By developing dedicated state-of-the-art diagnostics on RAID, we can now perform detailed measurements of electron temperature and density profiles together with

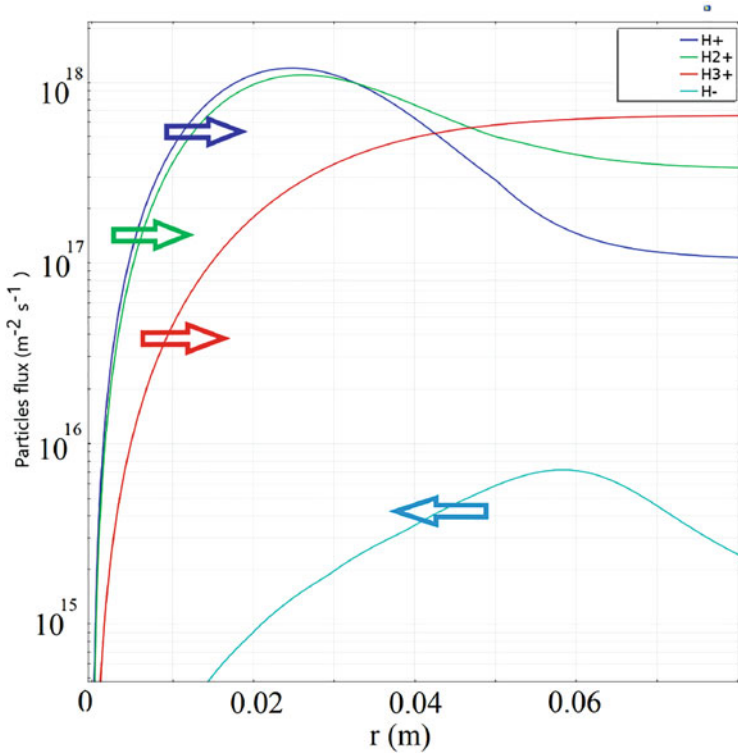


Fig. 9.17 Fluxes of ions across the radius are dominated by drift in the outward radial electric field. Positive ions are therefore transported outwards, whereas H^- are transported inward and destroyed by electron detachment and mutual neutralization with positive ions. From Agnello et al. (2022), copyright IOP Publishing. Reproduced with permission. All rights reserved

absolute measurements of negative ion density profiles in hydrogen and deuterium helicon plasmas. These experimental results are compared with numerical simulations using a 1.5D fluid model describing ion transport and chemistry of the hydrogenic species. We discovered that in RAID negative ions have a net production rate in a shell at the edge of the plasma column from where they diffuse toward the axis. H^- are mainly destroyed in the plasma center by electron detachment and are mainly neutralized by associative detachment at the edge. Future developments on H^- volume production in helicon sources should investigate the optimal balance between the various competing mechanisms to maximize the volume density of H^- close to the extraction region. In parallel, we will continue improving the set of diagnostics, in particular with the development of a two-photon laser-induced fluorescence (TALIF) system, which will allow precise experimental measurements of atomic hydrogen and deuterium to reach a better understanding of the physics of volumetric H-/D- production in helicon plasmas.

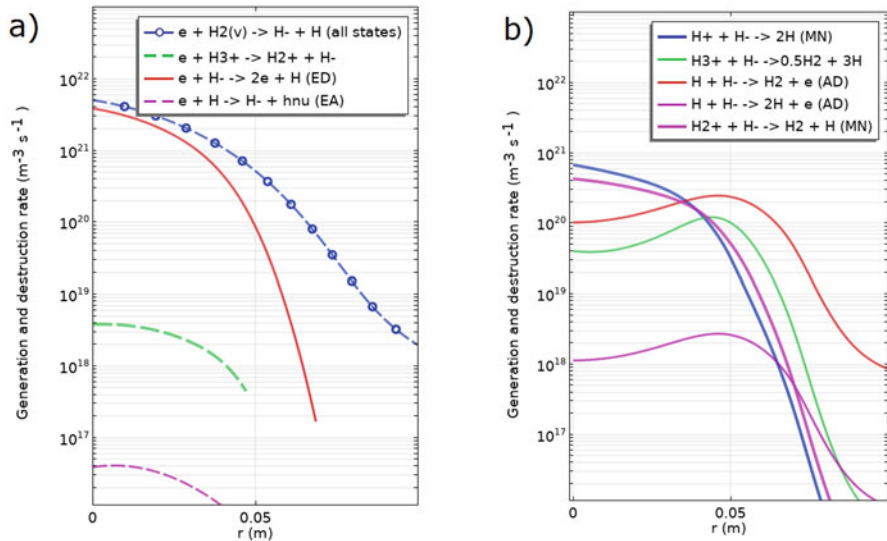


Fig. 9.18 Individual production (dotted lines) and destruction (continuous lines) processes of H^- along the radius (a) caused by electrons and (b) caused by ions and neutrals. The dissociative attachment from ro-vibrationally excited H_2 is the dominant production process. In the plasma center, H^- is mainly detached by electron impact, while at the edge, mutual neutralization processes with positive ions and associative detachment are the main loss reactions. From Agnello et al. (2022), copyright IOP Publishing. Reproduced with permission. All rights reserved

Acknowledgments This work has been carried out within the framework of the EUROfusion Consortium and has received funding from the Euratom research and training program 2014–2018 and 2019–2020 under grant agreement No 633053. The views and opinions expressed herein do not necessarily reflect those of the European Commission. This work was supported in part by the Swiss National Science Foundation.

References

- R. Agnello, *Negative Hydrogen Ions In a Helicon Plasma Source*. PhD thesis (EPFL, Switzerland, 2020)
- R. Agnello, Y. Andrebe, H. Arnichand, P. Blanchard, T.D. Kerchove, I. Furno, A.A. Howling, R. Jacquier, A. Sublet, Application of Thomson scattering to helicon plasma sources. *J. Plasma Phys.* **86**, 905860306 (2020)
- R. Agnello, M. Barbisan, I. Furno, P. Guittienne, A.A. Howling, R. Jacquier, R. Pasqualotto, G. Plyushchev, Y. Andrebe, S. Béchu, I. Morgal, A. Simonin, Cavity ring-down spectroscopy to measure negative ion density in a helicon plasma source for fusion neutral beams. *Rev. Sci. Instrum.* **89**, 103504 (2018)
- R. Agnello, S. Béchu, I. Furno, P. Guittienne, A.A. Howling, R. Jacquier, G. Plyushchev, M. Barbisan, R. Pasqualotto, I. Morgal, A. Simonin, Negative ion characterization in a helicon plasma source for fusion neutral beams by cavity ring-down spectroscopy and Langmuir probe laser photodetachment. *Nucl. Fusion* **60**, 026007 (2020)

- R. Agnello, G. Fubiani, I. Furno, P. Guittienne, A. Howling, R. Jacquier, F. Taccogna, A 1.5D fluid—Monte Carlo model of a hydrogen helicon plasma *Plasma Phys. Control. Fusion* **64**, 055012 (2022)
- S. Aleiferis, *Experimental Study of H^- Negative ion Production by Electron Cyclotron Resonance Plasmas*, PhD thesis (Université Grenoble-Aples, Grenoble, 2016)
- M. Bacal, Photodetachment diagnostic techniques for measuring negative ion densities and temperatures in plasmas. *Rev. Sci. Instrum.* **71**, 3981 (2001)
- M. Bacal, Physics aspects of negative ion sources. *Nucl. Fusion* **46**, S250–S259 (2006)
- M. Bacal, M. Sasao, M. Wada, Negative ion sources. *J. Appl. Phys.* **129**, 221101 (2021)
- F.E. Baghiti-Sube, F. Basht, M. Bacal, Photodetachment diagnostics of plasma with a high n_-/n_e ratio. *Rev. Sci. Instrum.* **67**, 2221 (1996)
- S. Béchu, A. Soum-Glaude, A. Bès, A. Lacoste, P. Svarnas, S. Aleiferis, A.A. Ivanov, M. Bacal, Multi-dipolar microwave plasmas and their application to negative ion production. *Phys. Plasmas* **20**, 101601 (2013)
- M. Berger, U. Fantz, S. Christ-Koch, NNBI Team, Cavity ring-down spectroscopy on a high power RF driven source for negative hydrogen ions. *Plasma Sources Sci. Technol.* **18**(2), 025004 (2009)
- G.D. Billing, M. Cacciatore, Recombination coefficient and final state vibrational distribution for the reaction: $H+Had+Cu(111)=H2(v)+Cu(111)$, in *7th International Symposium on Production and Neutralization of Negative Ions and Beams, AIP Conference Proceedings*, vol. 380(118) (1995)
- R.W. Boswell, Plasma production using a standing helicon wave. *Phys. Lett.* **33A**(7), 457–458 (1970)
- A.M. Bruneteau, C. Courteille, R. Leroy, M. Bacal, Investigation of two negative hydrogen and deuterium ion sources: Effect of the volume. *Rev. Sci. Instrum.* **67**, 3827 (1996)
- R. Celiberto, R.K. Janev, A. Laricchiuta, M. Capitelli, J.M. Wadehra, D.E. Atems, Cross section data for electron-impact in elastic processes of vibrationally excited molecules of hydrogen and its isotopes. *At. Data Nucl. Data Tables* **77**, 161 (2001)
- P. Chabert, N. Braithwaite, *Physics of Radio-Frequency Plasmas* (Cambridge University Press, Cambridge, 2011)
- S. Christ-Koch, U. Fantz, M. Berger, NNBI Team, Laser photodetachment on a high power, low pressure rf-driven negative hydrogen ion source. *Plasma Sources Sci. Technol.* **18**(2), 025003 (2009)
- COMSOL, Multiphysics® v. 5.6. (2018)
- P. Devynck, J. Auvray, M. Bacal, P. Berlemont, J. Bruneteau, R. Leroy, R.A. Stern, photodetachment technique for measuring H- velocities in a hydrogen plasma. *Rev. Sci. Instrum.* **50**, 2944 (1989)
- M.J. Druyvesteyn, Der Niedervoltbogen. *ZS. f. Phys.* **69**, 781 (1930)
- U. Fantz, H. Falter, P. Franzen, D. Wunderlich, M. Berger, A. Lorenz, W. Kraus, P. McNeely, R. Riedl, E. Speth, Spectroscopy—a powerful diagnostic tool in source development. *Nucl. Fusion* **46**(6), S297–S306 (2006)
- L. Friedland, C.I. Ciubotariu, M. Bacal, Dynamic plasma response in laser-photodetachment experiments in hydrogen plasmas. *Phys. Rev. E* **49**, 4353 (1994)
- G. Fubiani, R. Agnello, I. Furno, L. Garrigues, P. Guittienne, G. Hagelaar, A. Howling, R. Jacquier, B. Reman, A. Simonin, F. Taccogna, Negative hydrogen ion dynamics inside the plasma volume of a linear device: Estimates from particle-in-cell calculations. *Phys. Plasmas* **28**, 063503 (2021)
- G. Fubiani, L. Garrigues, G. Hagelaar, N. Kohen, J.P. Boeuf, Modeling of plasma transport and negative ion extraction in a magnetized radio-frequency plasma source. *New J. Phys.* **19**(1), 015002 (2017)
- O. Fukumasa, K. Yoshino, Isotope effect and cesium dependence of negative ion production in volume and ion sources. *Rev. Sci. Instrum.* **69**, 941 (1998)

- I. Furno, R. Agnello, U. Fantz, A. Howling, R. Jacquier, C. Marini, G. Plyushchev, P. Guittienne, A. Simonin, Helicon wave-generated plasmas for negative ion beams for fusion. *EPJ Web of Conferences* **157**, 03014 (2017)
- P. Guittienne, E. Chevalier, C. Hollenstein, Towards an optimal antenna for helicon wave excitation. *J. Appl. Phys.* **98**, 083304 (2005)
- P. Guittienne, R. Jacquier, B.P. Duteil, A.A. Howling, R. Agnello, I. Furno, Helicon wave plasma generated by a resonant birdcage antenna: magnetic field measurements and analysis in the RAID linear device. *Plasma Sources Sci. Technol.* **30**, 075023 (2021)
- G.J.M. Hagelaar, N. Oudini, Plasma transport across magnetic field lines in low-temperature plasma sources. *Plasma Phys. Control. Fusion* **53**, 124032 (2011)
- R.S. Hemsworth, D. Boilson, P. Blatchford, M.D. Palma, G. Chitarin, H.P.L. de Esch, F. Geli, M. Dremel, J. Graceffa, D. Marcuzzi, G. Serianni, D. Shah, M. Singh, M. Urbani, P. Zaccaria, Overview of the design of the ITER heating neutral beam injectors. *New J. Phys.* **19**(2), 025005 (2017)
- J.R. Hiskes, A.M. Karo, Analysis of the H_2 vibrational distribution in a hydrogen discharge. *Appl. Phys. Lett.* **54**, 508 (1989)
- A.T. Hjartarson, E.G. Thorsteinsson, J.T. Gudmundsson, Low pressure hydrogen discharges diluted with argon explored using a global model. *Plasma Sources Sci. Technol.* **19**(6), 065008 (2010)
- M.B. Hopkins, K.N. Mellon, Enhanced production of negative ions in low-pressure hydrogen and deuterium discharges. *Phys. Rev. Lett.* **67**, 449 (1991)
- G. Hunter, M. Kuriyant, Proton collisions with hydrogen atoms at low energies: Quantum theory and integrated cross-sections proton collisions with hydrogen atoms at low energies: Quantum theory and integrated cross-sections, in *Proceedings of the Royal Society of London. Series A, Mathematical and Physical Sciences*, vol. 353 (1977), pp. 575–588
- R. Jacquier, R. Agnello, B.P. Duteil, P. Guittienne, A. Howling, G. Plyushchev, C. Marini, A. Simonin, I. Morgal, S. Bechu, I. Furno, First B-dot measurements in the RAID device, an alternative negative ion source for DEMO neutral beams. *Fusion Eng. Des.* **146**, 1140–1144 (2019)
- R.K. Janev, D. Reiter, U. Samm, Collision Processes in Low-Temperature Hydrogen Plasmas. FZ-Jülich Report No. 4105 (2003)
- Y. Kim, J. Ree, H. Shin, Formation of vibrationally excited hydrogen molecules on a graphite surface. *Chem. Phys. Lett.* **314**, 1 (1999)
- P.S. Krstic, D.R. Schultz, Elastic processes involving vibrationally excited molecules in cold hydrogen plasmas. *J. Phys. B: At. Mol. Opt. Phys.* **36**, 385 (2003)
- V. Laporta, R. Agnello, G. Fubiani, I. Furno, C. Hill, D. Reiter, F. Taccogna, Vibrational excitation and dissociation of deuterium molecule by electron impact. *Plasma Phys. Control. Fusion* **63**, 085006 (2021)
- C. Marini, R. Agnello, B.P. Duval, I. Furno, A.A. Howling, R. Jacquier, A.N. Karpushov, G. Plyushchev, K. Verhaegh, P. Guittienne, Spectroscopic characterization of H_2 and D_2 helicon plasmas generated by a resonant antenna for neutral beam applications in fusion. *Nucl. Fusion* **57**, 036024 (2017)
- S.H. Müller, A. Diallo, A. Fasoli, I. Furno, B. Labit, M. Podestà, Plasma blobs in a basic toroidal experiment: Origin, dynamics, and induced transport. *Phys. Plasmas* **14**, 110704 (2007)
- H. Nakano, K. Tsumori, M. Shibuya, S. Geng, M. Kasaki, K. Ikeda, K. Nagaoka, M. Osakabe, Y. Takeiri, O. Kaneko, Cavity ringdown technique for negative-hydrogen-ion measurement in ion source for neutral beam injector. *J. Instrum.* **11**(03), C03018–C03018 (2016)
- A. O’Keefe, D.G. Deacon, Cavity ring-down optical spectrometer for absorption measurements using pulsed laser sources. *Rev. Sci. Instrum.* **59**, 2544 (1988)
- N. Oudini, A. Bendib, R. Agnello, I. Furno, F. Taccogna, Laser photo-detachment combined with Langmuir probe in magnetized electronegative plasma: how the probe size affects the plasma dynamic? *Plasma Sources Sci. Technol.* **30**, 115005 (2021)
- A. Pigarov, S. Krashennikov, Application of the collisional-radiative, atomic-molecular model to the recombining divertor plasma. *Phys. Lett. A* **222**, 251–257 (1996)

- T.K. Popov, M. Mitov, A. Bankova, P. Ivanova, M. Dimitrova, S. Rupnik, J. Kovačič, T. Gyergyek, M. Cerček, F.M. Dias, Langmuir probe method for precise evaluation of negative-ion density in electronegative gas discharge magnetized plasma. *Contrib. Plasma Phys.* **53**, 51–56 (2013)
- M. Rutigliano, P. Gamallo, R. Sayos, S. Orlandini, M. Cacciatore, A molecular dynamics simulation of hydrogen atoms collisions on an H-preadsorbed silica surface. *Plasma Sources Sci. Technol.* **23**, 045016 (2014)
- J.S. Santoso, *Production of Negative Hydrogen Ions in a High-Powered Helicon Plasma Source*. PhD thesis (Australian National University, Canberra, 2018)
- S. Shinohara, N. Kaneda, Y. Kawai, Effects of antenna wavenumber spectrum and metal end plate on plasma characteristics excited by helicon wave. *Thin Solid Films* **316**, 139–147 (1998)
- D.A. Skinner, A.M. Bruneteau, P. Berlemont, C. Courteille, R. Leroy, M. Bacal, Isotope effect and electron-temperature dependence in volume h and d ion sources. *Phys. Rev. E* **48**, 2122 (1993)
- F. Taccogna, R. Schneider, S. Longo, M. Capitelli, Modeling of a negative ion source. I. Gas kinetics and dynamics in the expansion region. *Phys. Plasmas* **14**, 073503 (2007)
- K. Takahashi, S. Takayama, A. Komuro, A. Ando, Standing helicon wave induced by a rapidly bent magnetic field in plasmas. *Phys. Rev. Lett.* **116**, 135001 (2016)
- D. Thompson, R. Agnello, I. Furno, A. Howling, R. Jacquier, G. Plyushchev, E. Scime, Ion heating and flows in a high power helicon source. *Phys. Plasmas* **24**, 063517 (2017)
- D. Wunderlich, D. Dietrich, U. Fantz, Application of a collisional radiative mode to atomic hydrogen for diagnostic purposes. *J. Quant. Spectrosc. Radiat. Transf.* **110**(1), 62–71 (2006)

Chapter 10

Plasma Electrode for Cesium-Free Negative Hydrogen Ion Sources



Mamiko Sasao and Gilles Cartry

Abstract Aiming at future cesium-free negative hydrogen ion sources, various materials for a plasma electrode are investigated from viewpoints of production mechanism (dissociative attachment, desorption by sputtering, electron pick-up backscattering, etc.), and practical application. Carbon materials, such as highly oriented pyrolytic graphite (HOPG), microcrystalline diamond, and C12A7 electride, were experimentally examined and compared with a low-work-function metal, gadolinium (Gd). Roles of surface work function and band gap were discussed.

Keywords Cesium-free · Plasma electrode · Desorption · Backscattering · Work function · Band gap · HOPG · Diamond · C12A7 electride

10.1 Introduction

In Neutral Beam Injection (NBI) systems of nuclear fusion reactors, negative hydrogen isotope ion beams are widely utilized, because of high neutralization efficiency (Hemsworth et al. 2009), such as those in LHD (Takeiri et al. 2000), JT-60SA (Hanada et al. 2016) and ITER (Hemsworth et al. 2009, 2017). In addition, negative hydrogen-ion-based injectors are implanted in particle accelerators (Faircloth and Lawrie 2018), for example, at J-PARC (Ueno et al. 2013; Shinto et al. 2018), Linac4 at CERN (Lettry et al. 2014), SNS-Oak Ridge (Stockli et al. 2013), China Spallation Neutron Source (CSNS) (Wei et al. 2009), Los Alamos Neutron Science Center (LANSCE)/PFR (Keller et al. 2009), ISIS Spallation Neutron and Muon Facility (Faircloth et al. 2011), and so on.

M. Sasao (✉)

Office for R&D promotion, Doshisha University, Kyoto, Japan
e-mail: msasao@mail.doshisha.ac.jp

G. Cartry

Aix-Marseille University, Marseille, France
e-mail: gilles.cartry@univ-amu.fr

In ion sources of these injectors, cesium (Cs) vapor is introduced to lower the work function of the plasma electrode (PE), hence, enhancing the H^- current and suppressing the co-extracted electron current, and be operated at lower ion source pressure. However, there are some disadvantages. The lifetime of the optimum Cs coverage is limited, and Cs leakage and adhesion to the accelerator section cause problems. Frequent maintenance stops of the beam due to cesium replenishment and cleaning of ion sources should be avoided. In future nuclear fusion reactors (Zohm et al. 2017; Okano 2019), such as DEMO reactors, more attention should be paid to the issues related to reliability (Sonato et al. 2016) in addition to the capability of a maintenance period of the order of months and years.

Negative-ion sources have recently received attention due to their application in microelectronics areas, such as proton implantation for surface modification (Woo et al. 2004) or smart-ion-beam cut of wafers (Ahmed et al. 2002) because the charge-up problem of positive-ion injection can be avoided. Cs contamination on the surroundings of the apparatus is a fatal drawback for application in microelectronics.

In this chapter, we discuss on plasma electrode materials for Cesium-free negative hydrogen ion sources. From the engineering viewpoint, the materials should be chemically stable, robust mechanically, and robust against thermal stress. High heat conductivity and workability are required. Also, availability with reasonable cost should be considered as well. Here, two production approaches are considered: one is to create a population of highly excited ro-vibrational hydrogen molecules, $H_2(v)$ on the PE surface. Then, H^- is produced through dissociative attachment of slow (~ 1 eV) electrons with the $H_2(v)$. The other one is to create H^- on the PE surface, and/or to remove H^- ions efficiently from it. As candidates of PE materials of the latter approach, nonmetallic materials, that is, various carbon surfaces, nanoporous electride, and a low-work-function metal (Gd), as a reference, are investigated.

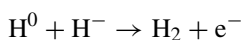
10.2 Materials for Production of Highly Excited Ro-vibrational Hydrogen Molecules

One of the key issues in H^- volume production is the separation of low-temperature plasma for Dissociative Electron Attachment (DEA) from the region which contains high-energy electrons for the production of highly excited ro-vibrational hydrogen molecules. In order to minimize the H^- destruction before being extracted, an idea to produce ro-vibrational hydrogen molecules on the PE surface is attractive. The population of hydrogen vibrational levels from metal walls was studied, and new observations were reported in 1988 by Hall et al. (1988) and Eenshuistra et al. (1988). Hall et al. observed hydrogen Re-combinative Desorption (RD) from the tungsten (W) and tantalum (Ta) covered walls of a hot cell where the atomic hydrogens are generated by dissociation of H_2 by a hot W or Ta filament. They found that the recombined hydrogen molecules followed a Boltzmann distribution

near 3000 K up to $\nu = 3$ and for higher levels, the populations were well in excess of this temperature. Further information can be seen in Chap. 1 in this book.

Since then, the vibrational excitation of desorbing molecules on a surface had been paid attention to, experimentally and theoretically. For example, the formulation based on the concept of a reaction path on a 2D or 3D potential energy surface allowed prediction of the vibrational excitation of desorbing molecules (Brenig et al. 1990), and the role of rotational motion in the associative desorption dynamics was studied (Diño et al. 1997).

In actual ion source experiments, it had been known that the evaporation of Ta from operating filaments in hydrogen arc discharges showed effects similar to those of Cs (Inoue et al. 1992; Bacal et al. 2004; Masaki et al. 2019), and W, as well with fewer effects. These effects are not only the increase of the negative-ion density and extracted H^- current, but also the reduction of the co-extracted electron current. However, the mechanisms of these effects are still not clear. The work functions of W (~ 4.45 eV) and Ta (~ 4.22 eV) are too high to produce H^- on their surfaces. One of the interpretations is due to the reduction of the negative hydrogen ion destruction rate by associative electron detachment with atomic hydrogen,



resulting from the reduction of the atomic hydrogen density by absorption on evaporated Ta films. Another explanation is the production of ro-vibrational $H_2(\nu)$ molecules of high ν on the Ta (or W) surface through re-combinative desorption as mentioned above, or through a three-step-process, in which the first step is the emission by the wall of a vibrationally excited molecule, formed by RD followed by the E-V excitation of this molecule by Franck-Condon transitions (Bacal et al. 2004).

Recently, an investigation on the effect of tantalum (Ta) plasma electrode (PE) and the effect due to tungsten (W) and tantalum (Ta) adsorption on a stainless-steel plasma electrode was carried out in order to design an efficient Cs-free H^- ion source (Masaki et al. 2019; Bacal et al. 2021). They compared the PE bias dependence of negative hydrogen ion extracted current, co-extracted electron, and the H^- ion density of the PE covered by Ta and W films and the PE made from Ta foil. Figure 10.1 shows the H^- ion density, n_{H^-} , measured at approximately 10 cm from the PE by the photo-detachment method (Bacal 2000). The results showed that freshly deposited Ta enhanced the H^- ion density. In addition, increased negative hydrogen ion extracted current, and reduced the co-extracted electron current were observed with a Ta-adsorbed PE in the same way as a cesium-adsorbed film.

Although the advantage of Ta was experimentally indicated, simulation research including the production of ro-vibrational $H_2(\nu)$ molecules of high ν , on a Ta PE surface, and the adsorption of atomic hydrogen on it are needed to clarify the mechanism of the PE material effect, in addition to further experimental studies of various combination of filament and PE materials, under various plasma conditions.

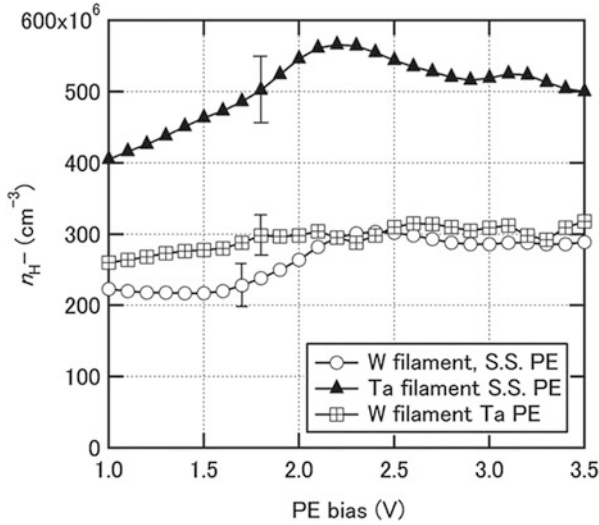


Fig. 10.1 Negative hydrogen ion density versus PE bias voltage, for two different filament materials, W and Ta, for PE deposition, and two different PE materials: stainless steel and tantalum. (Reproduced with permission from Bacal et al. (2021), Fig. 5. Copyright 2021, IOP Science)

A theoretical investigation on the vibrational excitation of desorbing molecules, based on the first principle to design the most suitable surface for high ν molecules is awaited.

10.3 Materials for Negative-Ion Surface Production

10.3.1 Basic Mechanisms of Negative-Ion Formation on Plasma Electrode Surfaces

In ion sources, in general, material surfaces of plasma containers are constantly bombarded by plasma particles, that is, electrons, ions, and neutral particles. Among them, positive ions are assumed to undergo rapid neutralization on the surface. Therefore negative-ion formation can be thought of as the capture of an electron by a neutral projectile irrespective of whether the incoming particle is originally an atom or an ion. Negative ions can be formed through the following:

1. The electron-pick-up during the *backscattering* process of incoming particles.
2. The desorption process of pre-implanted particles by *sputtering*.

Electron transfer from or to a metal surface (see Fig. 10.2) is mainly governed by two basic parameters (Cartry et al. 2017). One is the difference in energy (mismatch) between the affinity level of the negative ion and the Fermi level or the valence band

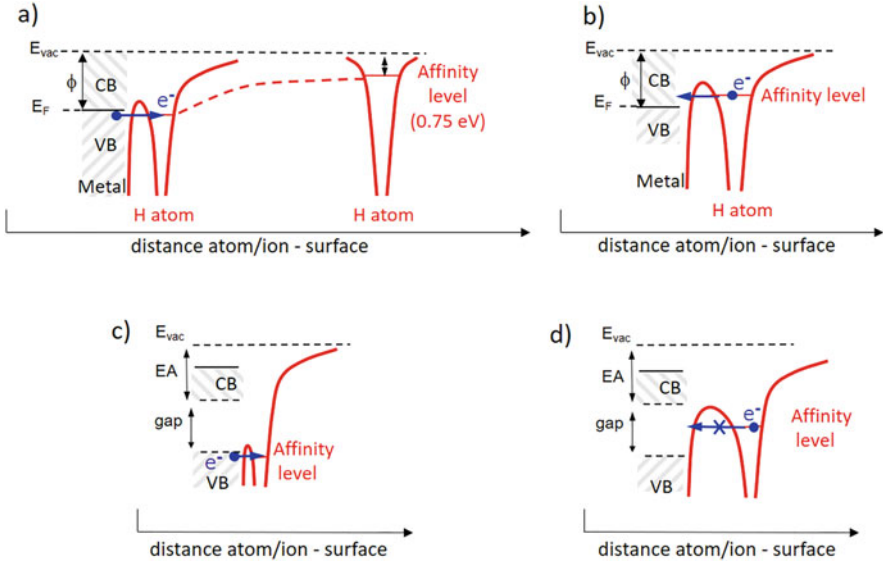


Fig. 10.2 Sketch of the mechanism of electron capture by an incoming hydrogen atom on a metal surface (**a, b**) and on an insulator (**c, d**). (**a**) The H atom at large distance is not interacting with the surface; on the approach the affinity level is downshifted; at a short distance, population of the affinity level from occupied states of the material by tunneling is possible. (**b**) As the H^- ion is moving away from the surface, the electron can transfer back to empty states of the conduction band. (**c**) Electron transfer from the insulator valence band to the affinity level takes place at even shorter distance than on metal. (**d**) When the H^- ion is moving away from the surface, the electron cannot transfer back to the surface because of the band gap. E_{vac} = vacuum level, E_F = Fermi level, VB = valence band, CB = conduction band, ϕ = work function, EA = electro-affinity. (Reproduced from Cartry et al. (2017), Fig. 1 with minor editing)

where electrons are to be captured. The second parameter is the coupling between these levels, given by the wave function overlap, which governs the exchange rate. Both ingredients depend on the distance to the surface and the projectile's parallel velocity. On approaching the surface, the affinity level is smoothly downshifted by the image potential, while electron tunneling transfer rates in both directions between the surface and the projectile affinity-level increase quasi-exponentially. At some distance, rates are so large that memory of the initial charge state is lost (the memory loss effect). Close to the surface the projectile equilibrium charge state is a negative ion (Fig. 10.2a). However, when leaving the surface, the affinity level rises back and overlaps with empty states in the conduction band (Fig. 10.2b), so that the electron will eventually return to the surface unless the rates have sufficiently decreased or the available time is too short, that is, the velocity too large. This leads to the concept of freezing distance (Rasser et al. 1982; Los and Geerlings 1990), describing the velocity-dependent critical distance where electron transfer rates become negligible; the outgoing negative-ion fraction reflects only the local capture and loss rates.

When depositing cesium on the surface, the material work-function is lowered reducing the energy barrier so that the freezing distance is now placed in the region where negative ions dominate. If the work-function is low enough, the freezing distance will remain in the favorable region even for low-velocity projectiles allowing atoms with \sim eV energies to contribute to the negative-ion production. This explains the success of the giant negative-ion source for ITER where the atomic flux, which largely exceeds the ionic flux, is able to contribute to negative-ion surface production.

For insulators or semiconductors, electrons are localized and more deeply bound, resulting in much lower electron capture rates, so that even full neutralization of positive ions is not granted. Still, a general mechanism explaining significant negative-ion formation has been identified (Borisov and Sidis 1996). In addition to the image potential effect, the downshift of the affinity level is further amplified by the Coulomb interaction between the negative ion and the localized hole (Fig. 10.2c). Furthermore, on the outgoing part of the trajectory, the electron loss back to the surface can be reduced or suppressed because no empty states are present in the band gap to recapture the electrons (Fig. 10.2d). Such models have explained that on LiF (100) surfaces, known to have one of the deepest valence bands, yields of 10% H^- have been observed at grazing incidence (Blauth and Winter 2011).

Numerous low-work function elements can be found in the periodic table. However, most of them are not practically usable, being chemically unstable, and having low melting points, such as alkali metals, alkaline earth metals, Li (2.90 eV), Na (2.54 eV), K (2.29 eV), Rb (2.17 eV), Cs (2.05 eV), Ca (2.91 eV), Sr (2.71 eV), and Ba (2.50 eV) (Kawano 2022). Work functions of some rare-earth element metals are less than 3.1 eV, such as Ce (2.89 eV), Pr (2.83), Sm (2.81 eV), Eu (2.74 eV), Gd (3.09 eV), Ho (3.05), and Yb (2.91 eV) (Kawano 2022), but they are of high-scarcity-value-metals, and some of them are reactive. It might be difficult to use them as PE material.

The next candidates are alloys and inorganic chemicals. Given the applicability in future negative-ion sources, Friedl and Cristofaro studied lanthanated tungsten and molybdenum alloys, lanthanum hexaboride, LaB_6 , and porous tungsten with oxidized barium, calcium, and aluminum, as well as molybdenum implanted with Cs (Friedl et al. 2018; Cristofaro 2019). They investigated achievable work function at ion source relevant conditions, in particular for temperatures below 500 °C. In contrast to their usual application as electron emitters at temperatures above 1000 °C, the work functions of the investigated materials under these conditions do not decrease below 3.6 eV (measured global minimum, achieved with LaB_6). For the lanthanated materials, the obtained work function values are stable under plasma exposure times of several hours. However, for all the materials the work function is subject to degradation in absence of heating or plasma exposure. Compared to Cs evaporation, with work function values measured down to 2.1 eV, they concluded that none of the materials tested so far can be regarded as an actual alternative (Friedl et al. 2018).

Observations of H^- production from some high-work-function materials, had been reported. For instance, Maazouz et al. (1996) and Wurz et al. (1997) pub-

lished an observation of negative ions induced by positive hydrogen ion beams on aluminium (Al) and diamond surfaces, respectively. Actually, as explained before, insulating materials or semiconductor materials, in particular large band gap materials, could be interesting for enhancing negative-ion surface production in plasmas. Here, we consider nonmetallic materials, that is, various carbon surfaces, and nanoporous electride, and a low-work-function metal (Gd), as a reference.

10.3.2 Carbon Materials

Carbon is one of the most abundant elements on the earth's crust, with various allotropes, such as graphite, diamond, amorphous carbon and fullerenes, as well as carbon nanotubes and graphenes. They show the highest thermal conductivity among all known materials under normal conditions. Carbon fiber composites (CFCs) were used in many tokamaks as divertor material because of their high heat resistivity and excellent mechanical property properties. In addition, the surface processing technologies of carbon materials have advanced recently. By deposition of intrinsic, lightly or highly doped layers using boron (p-doped), nitrogen, or phosphorous (n-doped) dopants, the electronic properties of diamond can be controlled. In addition, diamond surface properties depend on the crystallographic orientation of the exposed surface as well as on the termination of the dangling bonds which can be oxygen or hydrogen terminated. It is known that hydrogenated diamond layers may exhibit negative electron affinity (i.e., the minimum of the conduction band can be above the vacuum level) (Diederich et al. 1998, 1999).

In the context of tokamak divertor physics, the H^- production on carbon material surfaces attracted attention since the 1990s (Tsumori et al. 1996). Angle- and energy-resolved intensity distributions of H^+ and H^- ions scattered from solid surfaces of carbon nanowalls, HOPG, Mo, W, etc., have been studied by injecting proton and hydrogen molecular ion beams of low energy (0.1–3 keV) by Yamaoka et al. (2006; Tanaka et al. 2020). At shallow incident and reflection angles, the H^-/H^+ ratio increases as the incident beam energy per nucleon decreased when molecular ion beams are injected. In the study of ion beam-surface scattering experiments of hydrogen with energy from several hundred eV to few keV under grazing incidence, a negative-ion yield of 10% on graphite (HOPG) has been obtained (Xiang 2012), and slightly lower yields have been reported on diamond-like carbon (DLC) (Lienemann et al. 2011) (here, the yield is defined as the ratio between the negative-ion flux leaving the surface and the positive-ion flux impinging on the surface).

Aiming to investigate the negative-ion surface production mechanism in detail and the possibility of application to cesium-free H^- sources as a PE material, Cartry and his group at PIIM Aix-Marseille University have carried out a series of experimental study studies on the negative-ion surface production on carbon materials, such as highly oriented pyrolytic graphite (HOPG), variety of diamond and diamond-like carbon processing materials, immersed in a hydrogen plasma, by

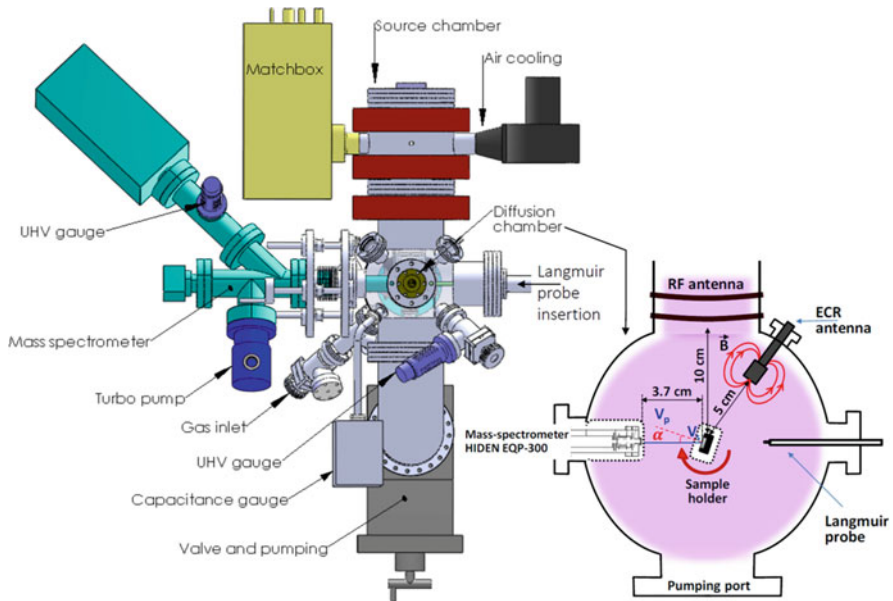


Fig. 10.3 Schematic of the experimental set-up. On left, a global view of the equipment is given. On right details concerning the diffusion chamber and the measurement zone are given. White areas around the sample holder represent the sheath. V_p is the plasma potential, V_s is the sample bias. Negative ions are emitted from the sample surface (shown in grey) and a part of them is collected by the mass-spectrometer placed in front. Angle α stands for the tilt of the sample with respect to the mass-spectrometer axis. The sketch shows the two available plasma excitation sources, the RF coupling by the top external antenna, or the microwave coupling by an internal ECR antenna

measuring angle-resolved energy spectra of H^- . Most of their early works can be found in the Reference (Cartry et al. 2017).

Figure 10.3 shows the schematic view of experimental set-up of surface negative-ion production measurement device at PIIM Aix-Marseille University (Kogut et al. 2017; Cartry et al. 2017). The plasma was generated at 1 or 2 Pa, either by capacitive coupling from an external antenna using a 20 W, 13.56-MHz generator (RF), or at 1 Pa by an Electron Cyclotron Resonance (ECR) antenna driven by a 60 W, 2.45-GHz generator. The typical plasma density in the diffusion chamber, as measured by a Langmuir probe, was $n_e = 2 \times 10^{13} \text{ m}^{-3}$ and the electron temperature was $T_e = 3.5 \text{ eV}$, giving an ion flux to the sample of the order of $10^{17} \text{ m}^{-2} \text{ s}^{-1}$ in RF mode. In the case of an ECR plasma, $n_e = 2.5 \times 10^{15} \text{ m}^{-3}$, $T_e = 1.0 \text{ eV}$, and the ion flux to the sample was $\sim 7 \times 10^{18} \text{ m}^{-2} \text{ s}^{-1}$. The sample holder lay in the center of the diffusion chamber, facing a Hidren-EQP300 mass spectrometer equipped with an energy filter. The sample could be biased negatively by an external DC power supply and could be heated by a resistive heater embedded inside the sample holder. The sample temperature was monitored by a thermocouple placed at the backside of the sample but it was calibrated versus the target surface temperature. The uncertainty

on the temperature measurement was estimated to still be quite high (on the order of ± 50 K) due to uncertainty in the thermal contact between the sample and the sample holder. During RF plasma, without external heating, the sample temperature was maintained at room temperature because the impinging ion flux is low enough. During ECR plasmas the sample temperature rose by about 70 K due to the higher ion flux. Pristine materials were used for each series of experiments: nonexposed new diamond layers or freshly cleaved HOPG samples (Cartry et al. 2017).

The sample was negatively biased with respect to the plasma potential so that negative ions (NI) emitted from the surface were accelerated towards the plasma and self-extracted from the plasma to the mass spectrometer, where they were detected according to their energy. However, the negative-ion energy distribution function thus measured is different from the energy distribution function of emitted ions principally because of the limited acceptance angle of the mass spectrometer that does not allow for collecting the full negative-ion flux. Simulations were needed to take into account this effect. In order to determine the energy and angle distribution function of the emitted negative ions they calculated ion trajectories, that is, those inside the sheaths in front of the mass spectrometer, and in front of the sample, using Child Langmuir law, as a function of ion emission angle and energy. They used the SRIM (Ziegler et al. 2008) software to generate initial angular and energy distributions of hydrogen particles (1) *backscattered* or (2) *sputtered* from the surface upon hydrogen positive-ion bombardment. Assuming that these distributions were those of negative ions. This was justified in their earlier works showing that negative ions were formed by backscattering of impinging positive ions and by the sputtering of adsorbed hydrogen atoms under these experimental conditions (Schiesko et al. 2008; Schiesko et al. 2009). A comparison between computed and experimental negative-ion energy distribution functions is presented in Fig. 10.4 for zero tilt angle, considering different hydrogenation, ζ_{H} , of carbon material. It shows that the hydrogen surface coverage participating in the sputtering process is about 30%. Analysis of the results also demonstrated that the sputtered negative ions were emitted at a lower angle and lower energy than backscattered ions. While about 40% of ions being detected have been created by the sputtering process when the tilt angle $\alpha = 0^\circ$, 95% of ions were emitted by the backscattering process for the surface bias $V_s = -130$ V. An important outcome of the analysis was that comparing different materials at tilt angle $\alpha = 0^\circ$ is not sufficient to conclude on their respective efficiency towards negative-ion surface production since only about 2% of the emitted negative-ion are detected by the mass spectrometer. For instance, HOPG gave a much higher negative-ion signal than gadolinium material at tilt angle $\alpha = 0^\circ$. However, when considering the overall negative-ion emission by measuring NIEDF at several tilt angles it has been shown that HOPG and Gd demonstrate about the same yield. A comparison between different materials at tilt angle $\alpha = 0^\circ$ makes sense only if materials exhibit similar angular emission of negative ions, which is the case for carbon layers. The good agreement between calculations and experiments for $\zeta_{\text{H}} = 30\%$ validated the initial choice of the distribution function of the emitted negative ions from the surface by SRIM computations for hydrogenated carbon layers. But this could not, a priori, be generalized to any material.

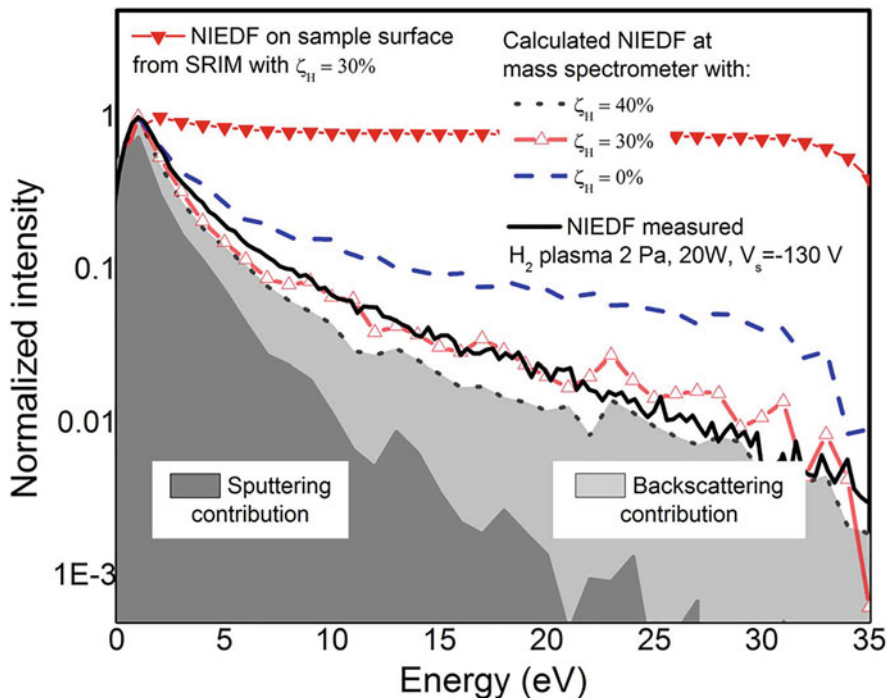


Fig. 10.4 Negative ion energy distribution function (NIEDF) measured at PIIM Aix-Marseille University with a HOPG sample in a H_2 , 2 Pa, 20 W RF plasma, for a surface bias $V_s = -130$ V. (the plasma was H_3^+ dominated). Solid triangles represent the distribution function of the emitted negative-ions on sample surface from SRIM calculations assuming impacts of 50 eV H^+ ions (corresponding to 150 eV H_3^+ ions dissociated at impact) on hydrogenated carbon material with 30% of hydrogen ($\zeta_{\text{H}} = 30\%$). Dash line, full line with open triangle, and dot line are NIEDF at the mass spectrometer for different hydrogenation of carbon material (ζ_{H} from 0% to 40%), calculated using the distribution on sample surface (shown in the case of 30% by solid triangles). The contributions of sputtering and backscattering are shown for $\zeta_{\text{H}} = 40\%$. (Reproduced from Cartry et al. (2017), Fig. 3)

They introduced the second method to derive the emitted negative-ions energy distribution functions from the sample surface. In this method, distribution functions at the mass spectrometer were measured for several tilt angles (see Fig. 10.5a), by rotating the sample holder (see Fig. 10.3b), an inverse calculation was performed to determine the emitted negative-ions energy distribution functions without any a priori assumption (Kogut et al. 2017), by using a complex inverse computation. The details are given in the reference (Kogut et al. 2017). The emitted negative-ion energy distribution functions on the surface obtained with the second method are presented in Fig. 10.5b.

There is an overall good agreement between both methods. The second method could be generalized to any kind of material and any negative-ion type. The results in Fig. 10.5 were obtained with HOPG material but identical results were obtained with diamond layers. However, the emitted negative-ion energy distribution functions

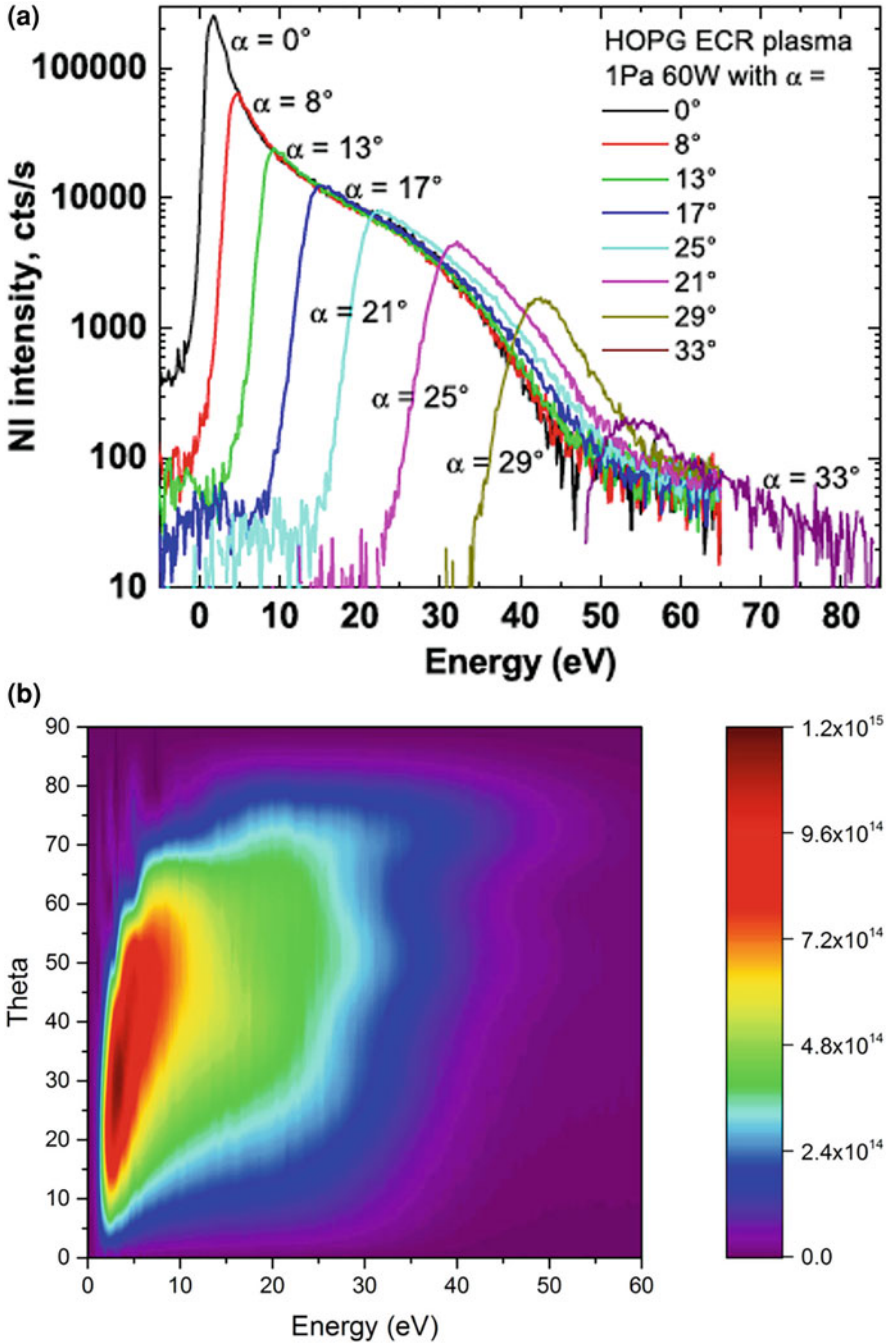


Fig. 10.5 (a) Experimentally measured NIEDF for different tilt angles of the HOPG sample: from $\alpha = 0^\circ$ to 35° . Measurements were made in an ECR 1 Pa, 60 W plasma. (b) distribution function of the emitted negative-ions on the sample surface computed using the NIEDFs (shown in (a)) measured at mass spectrometer as input. The color coded intensity map indicates the number of NI emitted from the surface at an angle θ and with an energy E . (Reproduced from Cartry et al. (2017), Fig. 4)

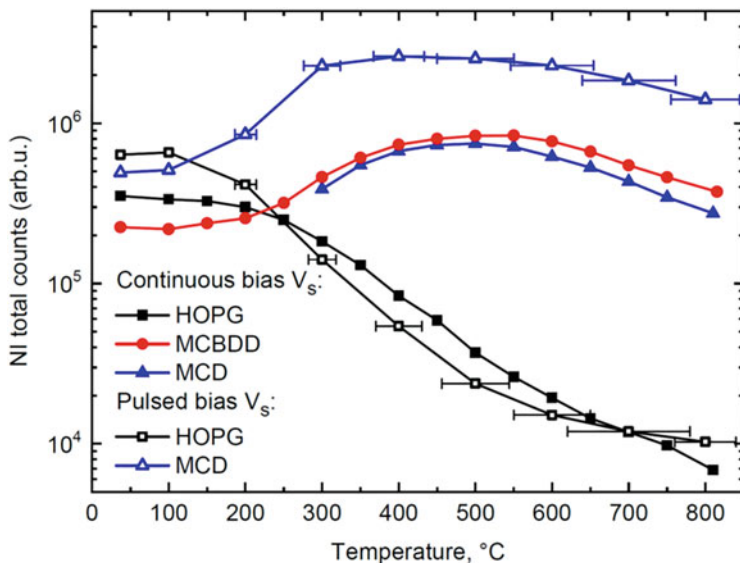


Fig. 10.6 Negative ion yield dependence on the surface temperature for HOPG, MCBDD, and MCD for constant bias (solid symbols) and pulsed bias (empty symbols). Here the negative ion total counts of the Y-axis is the integration of NI counts/s over all the NI distribution (area below NIEDF curves such as those of Fig. 10.5). Plasma parameters: 2.0 Pa of D_2 -RF plasma, 20 W. Pulsed bias parameters: $T_{\text{pulse}} = 15 \mu\text{s}$, $T_{\text{acq}} = 10 \mu\text{s}$, $f = 10 \text{ kHz}$, $V_s = -130 \text{ V}$. (Reproduced from Cartry et al. (2017), Fig. 5)

measured from the Gd show different behavior. The tail of the distribution is significantly higher than in the case of HOPG. This is due to an increased contribution of backscattered particles with high energies. As Gd atoms are much heavier than carbon ones, the hydrogen momentum transfer to the bulk of the Gd material is less efficient and light hydrogen ions are more efficiently scattered by the gadolinium surface (Kogut et al. 2017).

Figure 10.6 shows the comparison of the surface temperature dependence of relative negative-ion yields measured at $\alpha = 0^\circ$ in a D_2 RF plasma (2 Pa, 20 W, surface bias $V_s = -130 \text{ V}$), for graphite (HOPG) and diamond materials of two kinds of layers: (i) microcrystalline boron-doped diamond (MCBDD), whose boron doping is estimated to be $1.5 \times 10^{21} \text{ cm}^{-3}$, (ii) microcrystalline diamond (MCD), which is very similar to MCBDD but without boron doping. The negative-ion yield was defined as the ratio between the negative-ion flux leaving the surface and the positive-ion flux impinging on the surface (it was checked that the angular emission behavior of all the layers studied was identical). By comparing doped and non-doped microcrystalline diamond layers, it can be observed that boron doping does not seem to influence either the negative-ion yield or the global behavior of the yield with temperature. The negative-ion yield on diamond exhibits a maximum of around 400–500 °C, while the yield on graphite is continuously decreasing.

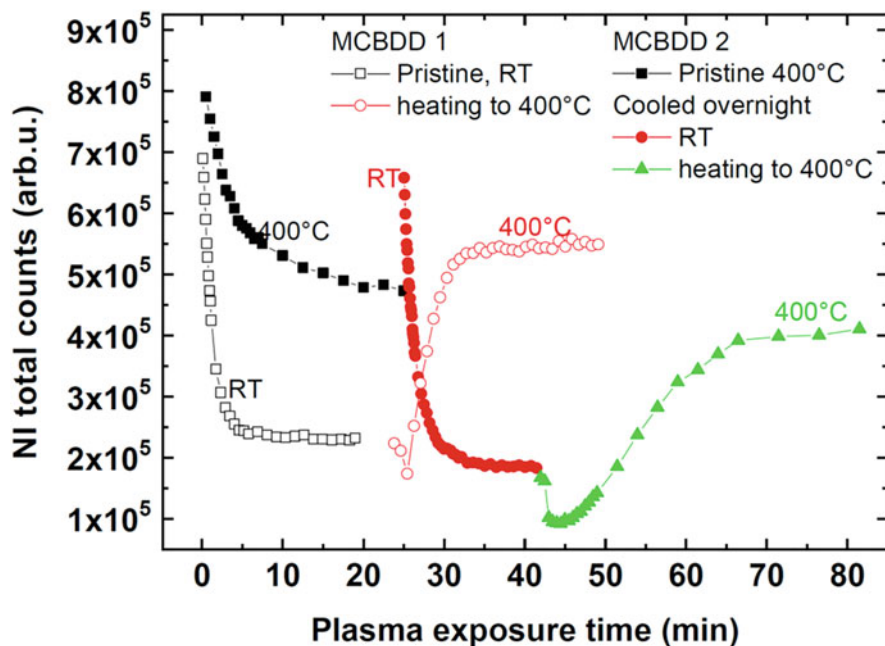


Fig. 10.7 Time evolution of the negative-ion counts, as being explained in the caption of Fig. 10.6, from MCBDD under plasma exposure at different surface temperatures. Each sample was heated under vacuum to 500 °C for 5 min to release impurities before being returned to room temperature for the start of experiments. Empty symbols correspond to the MCBDD1 sample and solid symbols to MCBDD2. The colour and shape of symbols indicate the chronological order of the experiments: black squares, red circles and green triangles. The sample surface temperature during plasma exposure is indicated next to the curves with a corresponding colour. The samples were biased at $V_s = -130$ V in a D_2 , 2 Pa, 20 W plasma. (Reproduced from Cartry et al. (2017), Fig. 6b)

Regarding the increase of the negative-ion yield for two diamond layers with surface temperature, surface analyses, in particular Raman spectroscopy, have provided insight into the understanding (Kumar et al. 2011; Ahmad et al. 2014). At room temperature, the ion bombardment created some defects in the material and lead to its hydrogenation. The impacts of positive ions with energy (~ 45 eV, H_3^+ dominating) probably led to the creation of a hydrogenated carbon layer having a certain hybridization ratio sp^2/sp^3 at room temperature. The authors reported that Raman spectra reveal that sp^2 phases on the MCBDD surface disappeared with the temperature increase indicating that defects, non-diamond phases produced by plasma exposure were annealed and etched away by the plasma at high temperature. This was confirmed by the time evolution of the negative-ion yield under D_2 plasma exposure as shown in Fig. 10.7. The empty symbols represent the negative-ion (NI) yield from the first series of measurements on a virgin MCBDD sample. The NI yield decreased during the first 5 min (probably connected to the degradation), but the NI yield increased significantly during the first 5 min after the heating to 400 °C,

as can be seen by the red empty circle symbols. Similar results were obtained with the second sample (solid symbols).

In negative-ion sources for nuclear fusion neutral beams, the plasma grid is biased only a few volts below the plasma potential, and defects in diamond layers would be much mitigated. Actually, the authors conducted NI yield time evolution measurements at $V_s = -20$ V, and -10 V (corresponding to 12 eV, and 9 eV nucleon⁻¹ including the plasma potential) and still observed a yield decrease of the same magnitude as the one displayed on Fig. 10.7. Only when reaching 5 eV nucleon⁻¹, the authors were able to observe a constant yield that they attributed to the absence of surface degradation. Such a low energy, 5 eV nucleon⁻¹, is typical of positive-ion impact energy on the plasma grid in negative-ion sources for fusion. However, under these conditions, the authors were not able to infer if diamond layers were still efficient for negative-ion surface production since the signal was low due to a very low negative-ion extraction efficiency from the sample to the mass spectrometer. As a consequence, the authors used a bias of -20 V (12 eV nucleon⁻¹) as a test condition for negative-ion surface production under low-energy ion bombardment. The authors tested variety of nanocrystalline diamond layers fabricated with the different percentages of CO₂ gas mixture during the deposition process, and a (100) single crystal boron doped diamond, in addition to the HOPG and MCBDD samples at low bias voltage ($V_s = -20$ V). The same global behaviors of negative-ion yield were observed. The yield is decreasing for HOPG while it is increasing for all diamond layers up to a maximum around 400–500 °C after which it decreases, indicating that the temperature increase favored surface reconstruction and the recovery of pristine diamond electronic properties.

Recently, Smith et al. (2020) investigated NI yield from the nitrogen-doped diamond films during exposure to a low-pressure deuterium plasma (2 Pa, helicon source at 26 W). Under conditions where positive ions from the plasma bulk bombard nitrogen-doped diamond film with energies of 11 eV (low energy) and 48 eV (high energy), mass spectrometry measurements were carried out using the device in Fig. 10.3, to determine the negative-ion yield when the film temperature was scanned between 30 °C and 750 °C (see Fig. 10.8). Here, the nitrogen-doped diamond film (MCNDD) was fabricated by introducing 50-ppm nitrogen in the gas phase during diamond growth using the PECVD technique. In low-energy ion bombardment at $V_s = -20$ V to MCNDD, the negative-ion yield increased by a factor of 2 compared to an un-doped diamond at 550 °C, and a factor of 1.5 compared to boron-doped diamond was observed as shown in Fig. 10.8b. Measurements with MCNDD sample temperature below 400–500 °C were not possible because the diamond layer was behaving as an insulator. As a consequence, the DC biased was not applied to the diamond surface, suppressing the possibility of negative-ion extraction. MCNDD donor levels are typically 1.6 eV below the conduction band and are not ionized at room temperature. The appearance of electrical conductivity at 400–500 °C is most probably related to the ionization of a non-negligible proportion of donor levels. In order to be able to study insulator samples, they developed a pulsed bias technic (Achkasov et al. 2019). The sample insulating thin layer act as a capacitance. When applying the pulsed DC bias to the

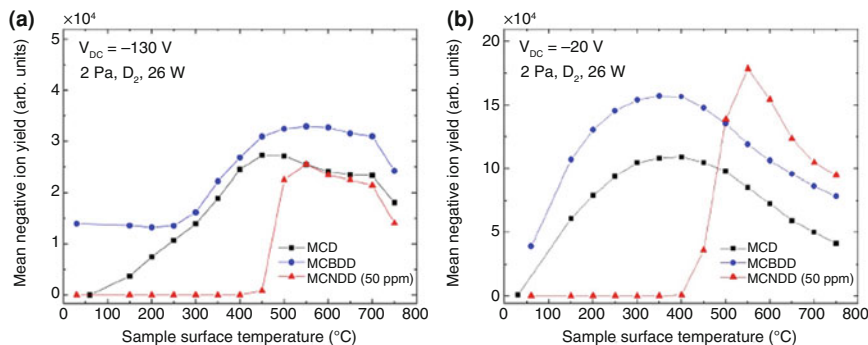


Fig. 10.8 Negative ion yield with respect to film surface temperature for micro-crystalline diamond (MCD), micro-crystalline boron doped diamond (MCBDD) and micro-crystalline nitrogen doped diamond (MCNDD) for (a) $V_s = -130 \text{ V}$ and (b) $V_s = -20 \text{ V}$. Low pressure deuterium plasma operated at 2 Pa and 26 W. Here, the negative ion yield is defined as the ratio between the negative-ion total counts and the positive ion flux impinging on the surface, in arbitrary units. (Reproduced with permission of IOP Publishing from Smith et al. (2020), Fig. 6)

back side of the sample, the voltage drop across this capacitance is initially zero and the DC bias appears on the sample's top surface. Positive ions are attracted, charge the capacitance and decrease the top surface voltage. If the pulse is long enough to allow for negative-ion measurement by the mass spectrometer (typically $10 \mu\text{s}$ is enough) and short enough to ensure a negligible voltage drop during the measurement (typically $0.1 \text{ V}/\mu\text{s}$ in their experimental conditions), negative-ions can be measured even for insulating thin layers using short DC pulse bias with low duty cycle. The apparent higher negative-ion yield that was observed with pulse bias (see Fig. 10.6 and (Cartry et al. 2017), and (Achkasov et al. 2019)) has been later explained by an increased positive-ion flux for short DC pulse bias compared to cw DC bias (Smith et al. 2021). With the help of the pulsed bias technique they have been able to study MCNDD layers from room temperature to $800 \text{ }^{\circ}\text{C}$ and concluded that (i) nitrogen doping is indeed enhancing negative-ion surface production, and (ii) a certain (low) level of sp² defects might be required to optimize negative-ion surface production on the diamond.

Comparing the efficiency of different samples towards negative-ion surface production in a given experimental device is quite straightforward. For instance, as discussed earlier, Cartry et al. have compared negative-ion counts detected by a mass spectrometer, with different tilt angles between the sample and the mass spectrometer, for different samples. Kurutz et al., have compared the negative-ion photo-detachment signal in the plasma volume for a reference case where negative-ion volume production dominates to situations where various large sample materials were introduced in the plasma reactor (Kurutz et al. 2017). However, comparing negative-ion surface production between two samples studied in different plasma reactors is not straightforward as relative measurements are no more sufficient. For that reason, Cartry et al. have replaced the mass spectrometer detection with

a Magnetized Retarding Field Energy Analyzer (MRFEA) detector (Taccogna et al. 2021). This diagnostic has been first developed for heavy ions in the context of plasma space propulsion and has been studied and re-employed for light H^- or D^- negative ions in the context of negative-ion sources for magnetically confined fusion applications. It consists of a single grid Retarding Field Energy Analyzer (RFEA) equipped with a magnetic barrier (500 Gauss) that magnetizes and traps electrons and lets positive and negative ions go through. The large MRFEA opening compared to the small mass spectrometer entrance orifice allows for the measurement of negative-ion currents as opposed to negative-ion counts with the mass spectrometer. Knowing the measured negative-ion current (from MRFEA measurements) and the negative-ion emission angles and energies (from mass spectrometer analyses), they have been able to quantify the total negative-ion sample current. They have estimated that the negative-ion yield (sample emitted negative-ion flux divided by the sample incoming positive-ion flux) is on the order of 3% for a boron-doped diamond layer at 400 °C, $V_s = -130$ V, pressure between 0.7 and 2 Pa and power between 200 and 800 W. For comparison, the negative-ion yield obtained with a Cs-covered molybdenum converter can reach up to 30% as measured in the past in a dedicated experiment (Seidl et al. 1996) where the Cs coverage could be optimized. The Cs coverage in a real negative-ion source cannot be controlled and optimized as efficiently as in a dedicated experiment and it is highly probable that the negative-ion yield is lower. Still, it shows the high efficiency of Cs and the challenge that represents the discovery of an alternative solution.

Using a carbon PE would lead to hydrocarbon deposition on the negative-ion source walls. Undesirable consequences could be managed using approaches developed in the microelectronic industry for wall conditioning or wall cleanings, such as a pre-coating or regular oxygen plasma cleaning. Although further optimization of the surface electronic properties and investigation on its applicability to negative-ion sources as a PE are needed, the experimental observation shown above indicates that diamond-like carbon layers are attractive as H^- production surfaces at relatively high temperature (400–500 °C), where defects produced by particle bombardment are annealed and at least partially etched away. It should be mentioned that the high H^- production rate of diamond-like carbon layers may owe to the wide gap between the valence band and the conduction band, which contributes to the relatively high escaping probability of H^- .

10.3.3 Nanoporous C12A7 Electride

In 2003, Hosono and his coworkers found that a refractory oxide $12CaO \cdot 7Al_2O_3$ (C12A7) can be transformed into an electride of low work function (Sushko et al. 2003; Matsuishi et al. 2003; Hosono 2013), by exchanging clathrated oxygen ions to form high-density electrons in the cages. When 100% of clathrated oxygens were removed, it showed conductivity approximately 1000 siemens per centimeter at 300 K, demonstrating that the encaged electron behaves as an anion (Miyakawa et

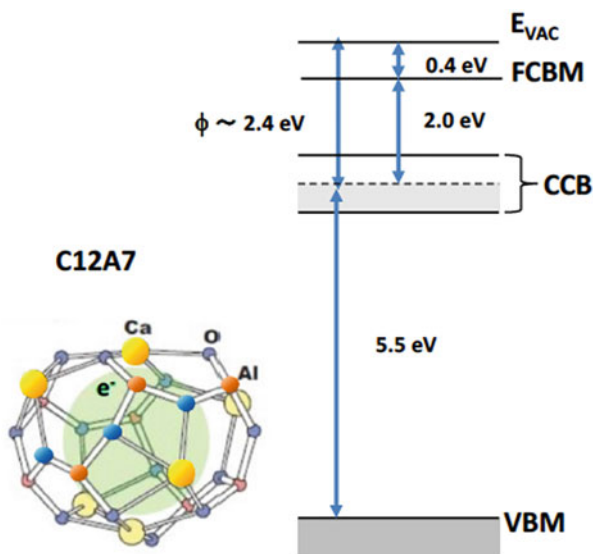


Fig. 10.9 The cage structure of C12A7 electride. Electrons are accommodated in the sub-nanometer-sized cages which are connected with each other. As is shown in the energy diagram of the left, the connected cages form a new conduction band called “cage conduction band” (CCB), below the cage flame conduction band minimum (FCBM). The work function (ϕ) is 2.4 eV, comparable to metal potassium, but chemically and thermally stable owing to that electrons are sitting within the cages composed of a rigid Ca-AL-O network. Evac: vacuum level, VBM: valence band maximum. The band gap is 7.5 eV

al. 2003). They reported that the resulting $[\text{Ca}_{24}\text{Al}_{128}\text{O}_{64}]^{4+}(4e^-)$ may be regarded as an “electride,” and clarified the unique properties, that is, they have a very low work function of 2.4 eV (Toda et al. 2007), which is comparable to that of metal potassium, but chemically and thermally stable. Figure 10.9 shows the schematic energy diagram of C12A7 electride (Sasao et al. 2018).

Indirect evidence of H^- formation from C12A7 electride was shown by exposing a sample to atomic hydrogen (H^0) flux and detecting the negative current generated on it (Sasao et al. 2017). The current observed was almost similar level with that obtained from a low-work-function bi-alkali-covered molybdenum surface (~ 2.3 eV) in the same condition.

A high production rate of negative hydrogen ion (H^-) was directly observed from a C12A7 electride surface immersed in hydrogen/deuterium low-pressure plasmas (Sasao et al. 2018), using the device shown in Fig. 10.3 in Sect. 10.3.2. The production rate was compared with that from a clean molybdenum surface (See Fig. 10.10). Here, the bombarding energy on the target was about 35 eV, and 15 eV, respectively for the target bias of -80 V and -20 V, because the major plasma ion component was H_3^+ , and the plasma potential was about +8 V. In the sputtering-dominated region (0–10 eV in H^- energy) of the negative-ion energy distribution,

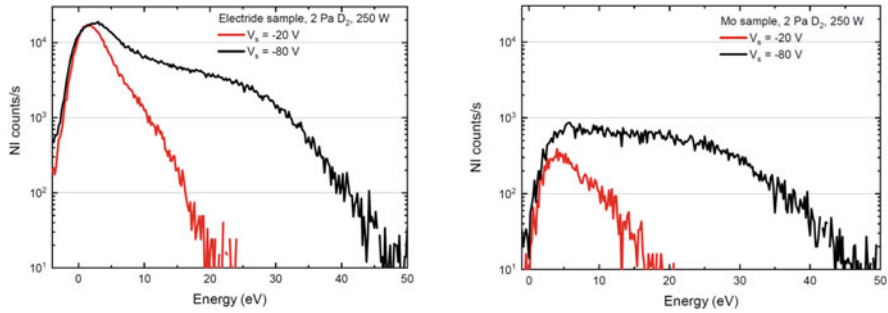


Fig. 10.10 Negative ion spectrum from a C12A7 electride (a) and molybdenum (b) in RF plasma. The red and black lines show those obtained when $V_s = -20$ V and -80 V, respectively. The vertical axis is H^- counts per second detected by the mass spectrometer, and horizontal axis is the negative ion energy after subtraction of energy gain by the target bias voltage, so that it corresponds to the initial energy of negative ions leaving the target

the C12A7 electride showed ~ 50 times larger counts than Molybdenum, and ~ 7 times larger in the backscattering-dominated region.

Temperature dependence of H^- counts (integrated over the whole H^- energy range) and H^- peak counts that is dominated by those from desorption by sputtering of the C12A7 electride sample are compared with those of HOPG in Fig. 10.11. Here the samples were biased at -130 V, immersed in a 60 W ECR, 1 Pa H_2 plasma. The C12A7 electride produces 30% less compared with HOPG below 300°C , but 30% higher at the higher temperature, showing its temperature stability (Moussaoui 2018).

Extraction of H^- beam from a compact ECR source with a C12A7 electride PE was examined, and compared with PEs of Molybdenum and Aluminum (Kobayashi et al. 2018; Eguchi et al. 2020). Figure 10.12 shows the negative-ion beam current extracted from PE made of C12A7 electride (red), aluminum (green), and molybdenum (purple) as a function of the acceleration voltage, when the ion source pressure was $2.0\text{--}2.2 \times 10^{-1}$ Pa and ECR input power was 28–30 W (Eguchi et al. 2020). The PE of the C12A7 electride showed the largest H^- current. The ratio of the negative-ion beam current extracted from PE made of C12A7 electride to that of clean Mo is about factor 14. It is nearly the same value of the C12A7 electride/Mo ratio of the backscattering component measured using an energy-resolved mass spectrometer as shown in Fig. 10.10, but the ratio is smaller than the one corresponding to the desorption component.

The plasma parameters of the ECR source mentioned above were measured with a Langmuir probe. The PE was installed to investigate how an electride PE changes the plasma parameters from those with a Mo PE. The effect upon the plasma parameters in front of the PE due to the material was elucidated by changing the probe position axially along the beam extraction direction. Analyses of the measured probe characteristics revealed that electride PE has a higher electron density (n_e) and lower electron temperature (T_e) than the Mo PE. When the PE was biased

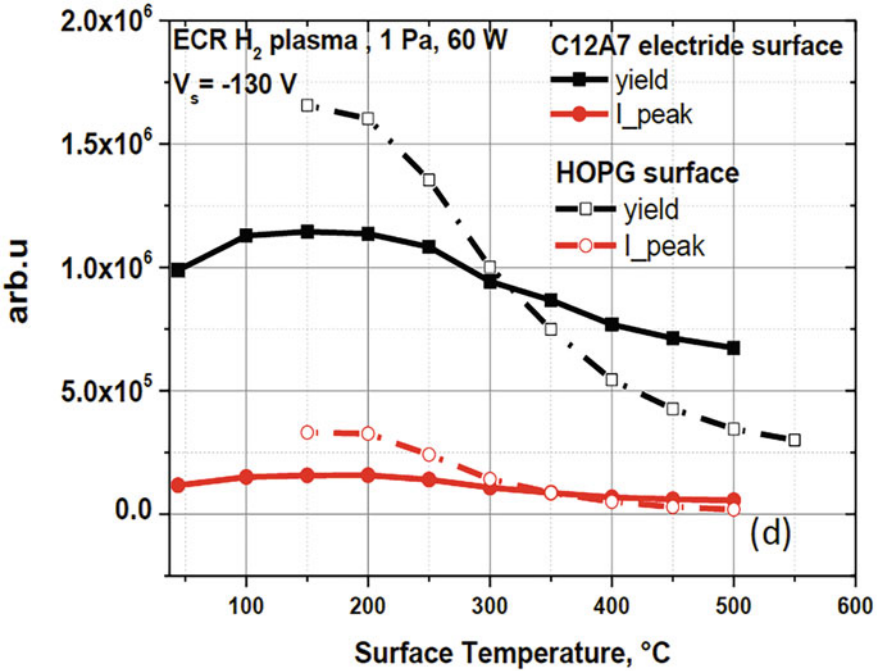


Fig. 10.11 The H⁻ yields and peak counts from C12A7 Electride and HOPG samples measured at -130 V bias in a 1 Pa, 60 W ECR H₂ plasma, using the device shown in Fig. 10.3 in Sect. 10.3.2. (Reproduced with permission from Moussaoui (2018), Fig. 5.13(d))

negatively, the ratio of the positive saturation current (I_i) to the negative saturation current ($I_e + I_{H^-}$) for the electride PE was about 1.6 times the ratio for the Mo PE, indicating the presence of negative-ion density component in the plasma in front of the electride PE (Bito et al. 2022). A similar observation was reported from a NIFS-middle size RF source with an electride PE (Shimizu et al. 2021).

One of important key issues for materials to be used as a PE is durability in an ITER-class ion source. A C12A7 electride material was studied regarding the work function behavior in a hydrogen and deuterium plasma environment at ITER-class ion source relevant conditions (Heiler et al. 2021). While the minimum measured work function obtained during the campaign was 2.9 ± 0.1 eV with an optimization potential to lower values at better vacuum conditions and higher annealing temperatures, it demonstrated promising properties in terms of plasma resilience. In addition, an interesting behavior was observed on the work-function dependence on the polarity and the applied bias potential, that is the application of a positive bias potential lowers the work function, and an extended long-term plasma exposure has a beneficial impact on the work function performance of the electride. Similar behavior has been observed in the plasma reactor shown in Fig. 10.3, where exposure of the electride at floating potential to a hydrogen plasma has decreased

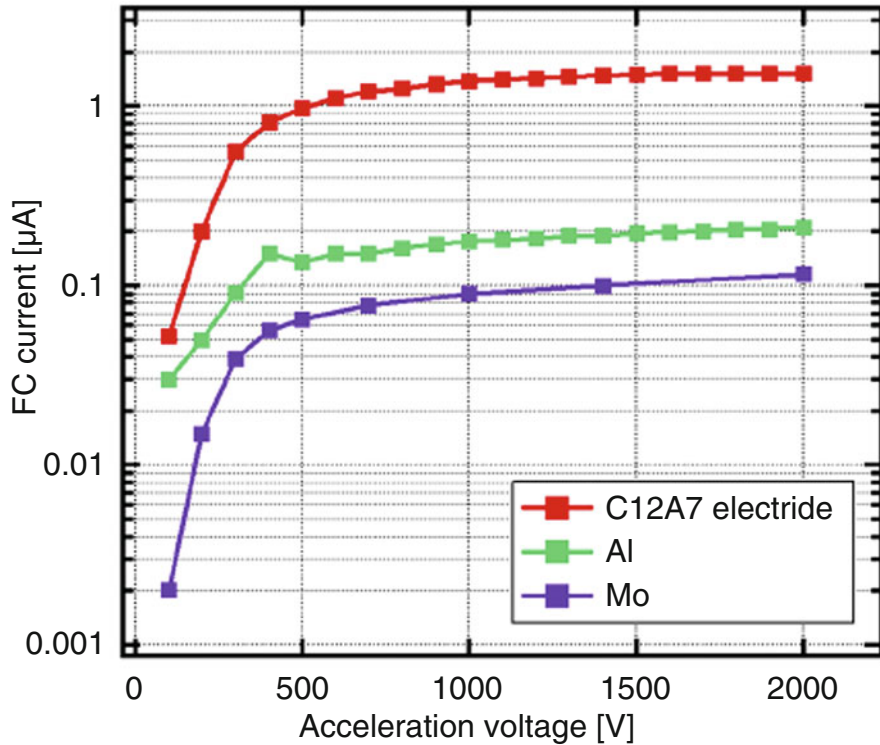


Fig. 10.12 Negative ion beam current extracted from the PE made of C12A7 electride (red), aluminum (green), and molybdenum (purple), measured by a Faraday Cup (FC), as a function of the acceleration voltage. The H_2 pressure was 1.5×10^{-1} Pa, and ECR input power was 28–30 W. (Reproduced from Eguchi et al. (2020), Fig. 3 with the permission of AIP Publishing)

its work function from 3.65 eV to 3.05 eV (Taccogna et al. 2021). No systematic study has been undertaken to evaluate the influence of the plasma duration or plasma density, but there is a high chance that the work function could be reduced further under hydrogen plasma with low-energy ion bombardment. On the contrary high-energy bombardments (surface bias of -60 V, about 20 eV nucleon $^{-1}$) tend to increase the work function, as observed also in (Heiler et al. 2021).

10.4 Discussions and Summary

Cesium-free H^- ion sources will be strongly demanded in future nuclear fusion technology, beam application to surface modification, tandem accelerators, and reliable H^- injectors of high-energy accelerators.

Intense R&D activities on volume-production-type H^-/D^- sources, such as sheet plasma sources (Tonegawa et al. 2021), Helicon volume source (Chap. 9), ECR-driven negative-ion sources (Chap. 12), et al., are now moving forward. By using a suitable PE material that produces highly excited vibrational molecules effectively on it, the H^- production rate in those sources might be enhanced.

In surface-production-type H^-/D^- sources, the key challenge is to find an alternative material to Cs-covered metal low-work function layers giving highly efficient negative-ion surface production. In this chapter, high-resistive or semi-conductive materials, such as HOPG, microcrystalline diamond (MCD), and C12A7 electrified are investigated as possible candidates for a plasma electrode surface and compared with a low-work-function metal, Gd (work function 3.09 eV).

An interesting observation was reported in negative-ion energy distribution functions from these materials immersed in an H_2 (or D_2) plasma, and biased negatively. Contributions from the electron pick-up-back-scattering process and the desorption by sputtering in H^- production, were observed under positive-ion bombardment energy of about 50 eV nucleon⁻¹, and materials tested showed characteristic negative-ion energy distribution functions. Here, samples were bombarded by positive ions, but the measured distribution functions can be considered similar to those bombarded by hydrogen atoms. That of Gd was mostly from backscattering, but that of HOPG was dominated by desorption, and the one from C12A7 electrified was from both processes. While every sample showed different temperature dependence, negative-ion yields integrated over the emitting energy were about the same level within factor 2 at room temperature. At higher temperature, 400–500 °C, MCD has demonstrated higher negative-ion production efficiency by about a factor 3–5. It should be noted that HOPG surface produced negative ions efficiently as much as the surface of a low-work-function metal Gd (3.09 eV), despite being a semi-metal with high work function (4.5 eV) (Hansen and Hansen 2001). The high H^- production rate of MCD may owe to the wide gap between the valence band and the conduction band, which contributes to the relatively high escaping probability of H^- .

In negative-ion sources for fusion, the best results have been obtained so far with a slightly positive bias on the plasma electrode (grid), close to the plasma potential. Studies at lower positive-ion energy (~10–15 eV nucleon⁻¹, lower bias) have revealed that MCD and electrified materials can maintain a high efficiency towards negative-ion surface production while the one of HOPG drops with the suppression of the sputtering process.

Among materials introduced in this chapter, C12A7 electrified has beneficial properties, a low work function (2.4 eV), a band gap, and a reduced reactivity to hydrogen compared to MCD. The C12A7 electrified, which is chemically stable, robust mechanically and robust against thermal stress, was tested and used as a PE in a compact ECR-source of less than 50 W. Although H^- current more than 10 times larger than that from a clean Mo PE was reported (Eguchi et al. 2020), the current density is still much less than the requirement level. An experiment using a high-power source with optimized extraction system is awaited. The durability of

C12A7 electride in a high-power ion source was studied regarding the work function behavior in a hydrogen and deuterium plasma environment at ITER-class ion source relevant conditions (Heiler et al. 2021). An interesting behavior was observed on the work-function dependence on the polarity and the applied bias potential, that is the application of a positive bias potential lowers the work function, and an extended long-term plasma exposure has a beneficial impact on the work function performance of the electride. Similar behavior has been observed where exposure of the electride at floating potential to a hydrogen plasma has decreased its work function from 3.65 eV to 3.05 eV (Taccogna et al. 2021).

Maintenance ability is an issue of importance. Negative-ion sources sometime suffer from sputtering of ion source chamber walls, particularly from sputtering of back-plates by back-streaming positive ions. It is reported that impurities on the C12A7 electride PE contaminated or covered by sputtered material were removed by hand-polishing and the original low-work function surface was recovered by repetitive heating (Bito 2022). Studies on in-situ cleaning of the surface are now going on using various methods like plasma sputtering, or reactive plasma treatment.

HOPG or MCD has not yet been used as a PE. Fabrication or machining to a certain shape/size PE might not be easy at a reasonable cost. Furthermore, carbon reactivity against hydrogen is an issue. However, studies have shown that the electronic properties of diamond favor negative-ion surface production. Therefore, it can be assumed that dielectric materials with a band gap, and/or negative-ion electron affinity, might have the potential to be a PE candidate of Cs-free ion sources at relatively high-temperature operation with pulsed- or tailored RF voltages-biasing (Achkasov et al. 2019).

Acknowledgments The authors would like to thank Roba Moussaoui and Dmitri Kogut for use of their original figures. The authors would like to acknowledge the deep discussions with Motoi Wada, and the support and advice by Hideo Hosono, Naomichi Miyakawa, Satoru Watanabe for the use of C12A7 electride. The C12A7 electride was supplied by Asahi Glass Co. LTD.

References

- K. Achkasov, R. Moussaoui, D. Kogut, E. Garabedian, J.-M. Layet, A. Simonin, A. Gicquel, J. Achard, A. Boussadi, G. Cartry, *J. Appl. Phys.* **125**, 033303 (2019)
- A. Ahmad, C. Pardanaud, M. Carrère, J.-M. Layet, A. Gicquel, P. Kumar, D. Eon, C. Jaoul, R. Engeln, G. Cartry, *J. Phys. D. Appl. Phys.* **47**, 85201 (2014)
- S. Ahmed, K. Amirov, U. Larsson, P. Too, B.J. Sealy, R. Gwilliam, *Proceedings of 14th Indium Phosphide and Related Materials Conference* (IEEE, Stockholm, 2002), p. 225
- M. Bacal, *Rev. Sci. Instrum.* **71**, 3981 (2000)
- M. Bacal, A.A. Ivanov, M. Glass-Maujean, Y. Matumoto, M. Sasao, M. Wada, *Rev. Sci. Instrum.* **75**, 1699 (2004)
- M. Bacal, K. Maeshiro, S. Masaki, M. Wada, *Plasma Sources Sci. Technol.* **30**, 075014 (2021)
- K. Bito, M. Sasao, M. Wada, Presented at ICIS 2021, September 20–24, 2021 Online, *J. Phys. Conf. Ser.*, to be published (2022)
- K. Bito, Master thesis, Doshisha University (2022)
- D. Blauth, H. Winter, *Nucl. Instrum. Methods Phys. Res. B* **269**, 1175 (2011)

- A.G. Borisov, V. Sidis, *Phys. Rev. Lett.* **77**, 1893 (1996)
- W. Brenig, S. Kiichenhoff, H. Kasai, *Appl. Phys. A Mater. Sci. Process.* **51**, 115 (1990)
- G. Cartry, D. Kogut, K. Achkasov, J.-M. Layet, T. Farley, A. Gicquel, J. Achard, O. Brinza, T. Bieber, H. Khemliche, P. Roncin, A. Simonin, *New J. Phys.* **19**, 025010 (2017)
- S. Cristofaro, Ph.D. Thesis, IPP 2019-05 (2019)
- L. Diederich, O.M. Küttel, P. Aebi, L. Schlapbach, *Surf. Sci.* **418**, 219 (1998)
- L. Diederich, O.M. Küttel, P. Aebi, L. Schlapbach, *Relat. Mater.* **8**, 743 (1999)
- W.A. Diño, H. Kasai, A. Okiji, *Phys. Rev. Lett.* **78**, 286 (1997)
- P.J. Eenshuistra, J.H.M. Bonnie, J. Los, H.J. Hopman, *Phys. Rev. Lett.* **60**, 341 (1988)
- T. Eguchi, M. Sasao, Y. Shimabukuro, F. Ikemoto, M. Kasaki, H. Nakano, K. Tsumori, M. Wada, *Rev. Sci. Instrum.* **91**, 013508 (2020)
- D.C. Faircloth, S.R. Lawrie, A.P. Letchford, C. Gabor, M. Whitehead, T. Wood, M. Perkins, *AIP Conf. Proc.* **1390**, 205 (2011)
- D. Faircloth, S. Lawrie, *New J. Phys.* **20**, 025007 (2018)
- R. Friedl, S. Cristofaro, U. Fantz, *AIP Conference Proceedings* **2011**, 050009 (2018)
- R. Hall, I. Čadež, M. Landau, F. Pichou, C. Schermann, *Phys. Rev. Lett.* **60**, 337 (1988)
- M. Hanada, A. Kojima, H. Tobari, R. Nishikiori, J. Hiratsuka, M. Kashiwagi, N. Umeda, M. Yoshida, M. Ichikawa, K. Watanabe, Y. Yamano, L.R. Grisham, *Rev. Sci. Instrum.* **87**, 02B322 (2016)
- W.N. Hansen, G.J. Hansen, *Surf. Sci.* **481**, 172 (2001)
- A. Heiler, R. Friedl, U. Fantz, R. Nocentini, M. Sasao, *AIP Conf. Proc.* **2373**, 020004 (2021)
- R. Hemsforth, H. Decamps, J. Graceffa, B. Schunke, M. Tanaka, M. Dremel, A. Tanga, H.P.L. De Esch, F. Geli, J. Milnes, T. Inoue, D. Marcuzzi, P. Sonato, P. Zaccaria, *Nucl. Fusion* **49**, 045006 (2009)
- R.S. Hemsforth, D. Boilson, P. Blatchford, M.D. Palma, G. Chitarin, H.P.L. De Esch, F. Geli, M. Dreime, J. Graceffa, D. Marcuzzi, G. Serianni, D. Shah, M. Singh, M. Urbani, P. Zaccaria, *New J. Phys.* **19**, 025005 (2017)
- H. Hosono, *Jpn. J. Appl. Phys.* **52**, 090001 (2013)
- T. Inoue, Y. Matsuda, Y. Ohara, Y. Okumurat, M. Bacal, P. Berlemont, *Plasma Sources Sci. Technol.* **1**, 75 (1992)
- H. Kawano, *Prog. Surf. Sci.* **97**, 100583 (2022)
- R. Keller, O. Tarvainen, E. Chacon-Golcher, E.G. Geros, K.F. Johnson, G. Rouleau, J.E. Stelzer, T.J. Zaugg, *AIP Conf. Proc.* **1097**, 161 (2009)
- M. Kobayashi, M. Sasao, M. Kasaki, T. Eguchi, M. Wada, *AIP Conf. Proc.* **2052**, 020003 (2018)
- D. Kogut, K. Achkasov, J.P.J. Dubois, R. Moussaoui, J.B. Faure, J.M. Layet, A. Simonin, G. Cartry, *Plasma Sources Sci. Technol.* **26**, 045006 (2017)
- P. Kumar, A. Ahmad, C. Pardanaud, M. Carrère, J.-M. Layet, G. Cartry, F. Silva, A. Gicquel, R. Engeln, *J. Phys. D. Appl. Phys.* **44**, 372002 (2011)
- U. Kurutz, R. Friedl, U. Fantz, *Plasma Phys. Control. Fusion* **59**, 075008 (2017)
- J. Lettry, D. Aguglia, P. Andersson, S. Bertolo, A. Butterworth, Y. Coutron, A. Dallochio, E. Chaudet, J. Gil-Flores, R. Guida, R. Hansen, A. Hatayama, I. Koszar, E. Mahner, C. Mastrostefano, S. Mathot, S. Mattei, Ø. Midttun, P. Moyret, D. Nisbet, K. Nishida, M. O'Neil, M. Ohta, M. Paoluzzi, C. Pasquino, H. Pereira, J. Rochez, J. Sanchez Alvarez, J. Sanchez Arias, R. Scrivens, T. Shibata, D. Steyaert, N. Thaus, T. Yamamoto, *Rev. Sci. Instrum.* **85**, 02B122 (2014)
- J. Lienemann, D. Blauth, M. Busch, S. Wethekam, H. Winter, P. Wurz, S.A. Fuselier, E. Hertzberg, *Nucl. Instrum. Methods Phys. Res. B* **269**, 915 (2011)
- J. Los, J.J.C. Geerlings, *Phys. Rep.* **190**, 133 (1990)
- M. Maazouz, R. Baragiola, A. Borisov, V.A. Esaulov, J.P. Gauyacq, L. Guillemot, S. Lacombe, D. Teillet-Billy, *Surf. Sci. Lett.* **364**, L568 (1996)
- S. Masaki, K. Maeshiro, K. Tsumori, M. Wada, *Plasma Fusion Res.* **14**, 3401136 (2019)
- S. Matsuishi, Y. Toda, M. Miyakawa, K. Hayashi, T. Kamiya, M. Hirano, I. Tanaka, H. Hosono, *Science* **301**(5633), 626 (2003)
- R. Moussaoui, Ph.D. Thesis 2018, Aix-Marseille Université, Faculté des Sciences, (2018)

- M. Miyakawa, K. Hayashi, M. Hirano, Y. Toda, T. Kamiya, H. Hosono, *Adv. Mater.* **15**, 1100 (2003)
- K. Okano, *J. Fusion Energy*. **38**, 138 (2019)
- B. Rasser, J.N.M. van Wunnik, J. Los, *Surf. Sci.* **118**, 697 (1982)
- M. Sasao, K. Tanemura, M. Wada, K. Tsumori, *AIP Conf. Proc.* **1869**, 020005 (2017)
- M. Sasao, R. Moussaoui, D. Kogut, J. Ellis, G. Cartry, M. Wada, K. Tsumori, H. Hosono, *Appl. Phys. Express* **11**, 066201 (2018)
- L. Schiesko, M. Carrère, G. Cartry, J.M. Layet, *Plasma Sources Sci. Technol.* **17**, 035023 (2008)
- L. Schiesko, M. Carrère, J.M. Layet, G. Cartry, *Appl. Phys. Lett.* **95**, 191502 (2009)
- M. Seidl, H.L. Cui, J.D. Isenberg, H.J. Know, B.S. Lee, S.T. Melnychuk, *J. Appl. Phys.* **79**, 2896–2901 (1996)
- S. Shimizu, H. Nakano, K. Saito, M. Sasao, M. Wada, K. Bito, A. Ando, Presented at The 30th International Toki Conference, 18Ea7, 16–19 November, 2021 (2021)
- K. Shinto, K. Ohkoshi, T. Shibata, K. Nanmo, K. Ikegami, A. Takagi, Y. Namekawa, A. Ueno, H. Oguri, *AIP Conf. Proc.* **2052**, 050002 (2018)
- G.J. Smith, J. Ellis, R. Moussaoui, C. Pardanaud, C. Martin, J. Achard, R. Issaoui, T. Gans, P. Dedrick, G. Cartry, *J. Phys. D: Appl. Phys.* **53**, 465204 (2020)
- G.J. Smith, L. Tahri, J. Achard, R. Issaoui, T. Gans, J.P. Dedrick, G. Cartry, *J. Phys. D: Appl. Phys.* **54**, 435201 (2021)
- P. Sonato, P. Agostinetti, U. Fantz, T. Franke, I. Furno, A. Simonin, M.Q. Tran, *New J. Phys.* **18**, 125002 (2016)
- M.P. Stockli, B.X. Han, S.N. Murray, T.R. Pennisi, M. Santana, R.F. Welton, *AIP Conf. Proc.* **1515**, 292 (2013)
- P.V. Sushko, A.L. Shluger, K. Hayashi, M. Hirano, H. Hosono, *Phys. Rev. Lett.* **91**, 126401 (2003)
- F. Taccogna, S. Bechu, A. Aanesland, P. Agostinetti, R. Agnello, S. Aleiferis, T. Angot, V. Antoni, M. Bacal, M. Barbisan, J. Bentounes, A. Bès, M. Capitelli, G. Cartry, M. Cavenago, R. Celiberto, G. Chitarin, R. Delogu, A. De Lorenzi, F. Esposito, M. Fadone, N. Ferron, G. Fubiani, I. Furno, L. Gavilan, P. Guittienne, A. Howling, A. Jacquier, A. Laricchiuta, J.M. Layet, J.L. Lemaire, S. Longo, B. Maurice, P. Minelli, M. Minissale, M. Mitrou, R. Moussaoui, A. Pimazzoni, C. Poggi, D. Rafalskyi, E. Salomon, E. Sartori, M. Sasao, G. Serianni, E. Spada, S. Suweis, P. Svarnas, L. Tahri, M. Ugoletti, V. Variale, P. Veltri, *Eur. Phys. J. D* **75**, 227 (2021)
- Y. Takeiri, O. Kaneko, K. Tsumori, Y. Oka, M. Osakabe, K. Ikeda, E. Asano, T. Kawamoto, R. Akiyama, *Rev. Sci. Instrum.* **71**, 1225 (2000)
- N. Tanaka, F. Ikemoto, I. Yamada, Y. Shimabukuro, M. Kasaki, W.A. Diño, M. Sasao, M. Wada, *Rev. Sci. Instrum.* **91**, 013313 (2020)
- Y. Toda, H. Yanagi, E. Ikenaga, J.J. Kim, M. Kobata, S. Ueda, T. Kamiya, M. Hirano, K. Kobayashi, H. Hosono, *Adv. Mater.* **19**, 3564 (2007)
- A. Tonegawa, H. Kaminaga, K. Hanai, T. Takimoto, K.N. Sato, K. Kawamura, *Nucl. Fusion* **61**, 106030 (2021)
- K. Tsumori, W.R. Koppers, R.M.A. Heeren, M.F. Kadodwala, A.W. Kleyn, J.H.M. Beijersbergen, *AIP Conf. Proc.* **380**, 36 (1996)
- A. Ueno, Y. Namekawa, S. Yamazaki, K. Ohkoshi, I. Koizumi, K. Ikegami, A. Takagi, H. Oguri, *AIP Conf. Proc.* **1515**, 331 (2013)
- J. Wei, H. Chen, C.Y. Chen, Y. Chi, C. Deng, H. Dong, L. Dong, S. Fang, J. Feng, S. Fu, L. He, W. He, Y. Heng, K. Huang, X. Jia, W. Kang, X. Kong, J. Li, T. Liang, G. Lin, Z. Liu, H. Ouyang, Q. Qin, H. Qu, C. Shi, H. Sun, J. Tang, J. Tao, C. Wang, F. Wang, D. Wang, Q. Wang, S. Wang, T. Wei, J. Xi, T. Xu, Z. Xu, W. Yin, X. Yin, J. Zhang, Z. Zhang, Z. Zhang, M. Zhou, T. Zhu, *Nucl. Instrum. Methods Phys. Res. A* **600**, 10 (2009)
- H.J. Woo, H.W. Choi, G.D. Kim, J.K. Kim, W. Hong, Y.Y.J. Kigam, W.B. Choi, Y.H. Bae, *Proceedings of APAC 2004*, Gyeongju, Korea, 435 (2004)
- P. Wurz, R. Schletti, M.R. Aellig, *Surf. Sci.* **373**, 56 (1997)
- Y. Xiang, PhD Thesis Université Paris-Sud (2012)
- H. Yamaoka, Y. Matsumoto, M. Nishiura, K. Tsumori, H. Sugawara, S. Takeuchi, K. Shinto, M. Sasao, M. Wada, *Rev. Sci. Instrum.* **77**, 03C301 (2006)

- J.F. Ziegler, J.P. Biersack, M.D. Ziegler, *2008 SRIM—The Stopping and Range of Ions in Matter* (Lulu Press, Morrisville, NCE, 2008)
- H. Zohm, F. Träuble, W. Biel, E. Fable, R. Kemp, H. Lux, M. Siccino, R. Wenninger, *Nucl. Fusion* **57**, 086002 (2017)

Chapter 11

Low-Temperature High-Density Negative Ion Source Plasma



Hiroshi Horiike and Yoshikazu Okumura

Abstract Ion source design for high-power neutral beams for present large fusion plasmas are described. Positive or negative hydrogen ion beams are extracted from an ion source by electro-static acceleration systems. The key aspect of the present negative ion sources is based on that of high current positive ion sources with high proton content. This means that the confinement of low-temperature plasma with a strong cusp magnetic field minimizes the plasma loss on components such as filament, electrode, flange, and anode, allowing the coexistence of dense plasma and very low-electron temperature plasma in a box without a partition. The key features of the design are similar for sources of positive and negative ions. A rod-type magnetic filter is not employed anymore to avoid excessive losses. Instead, electrons are trapped by a magnetic field in a region far from the ion extraction region in order to reduce electron temperature and the destruction of molecular ions or negative ions. The ion source consists of one box but the discharge is designed to form a tandem structure.

Keywords Ion species ratio · Chamber · Filament and anode area · Negative ion · Mode flap · Electron temperature

Nomenclature

n, n_0	Plasma density
e	Electron charge
v_e	Electron velocity
T_e	Electron temperature

H. Horiike (✉)

Professor Emeritus, Faculty of Engineering, Osaka University, Osaka, Japan
e-mail: horiike@nucl.eng.osaka-u.ac.jp

Y. Okumura

National Institute for Quantum Science and Technology, Chiba, Japan

m_e	Electron mass
m_i	Ion mass
N_1	The density of H_1^0
N_2	The density of H_2 ,
n_1	The density of H_1^+ ,
n_2	The density of H_2^+ ,
T_1	Containment time of H_1^0 ,
τ_1	Containment time of H_1^+ .
τ_2	Containment time of H_2^+
γ	Recombination factor for atoms on the wall surface
S_F	Area of the filament
S_A	Area of the anode
V	Volume of a cube or a chamber

11.1 Introduction

Important applications of ion beams are the additional heating and current drive of the nuclear fusion plasma. For this application H or D ion beams have to be neutralized to (a) penetrate through the strong magnetic field applied for confinement and (b) prevent charge up of the plasma. Here, beam energy and power are important for the attainment of a good heating profile.

Hydrogen ion beams are extracted from a source plasma where ions have an isotropic Maxwellian distribution of thermal velocities, and form a so-called drift Maxwellian distribution with acceleration. Thus, the beam shows a Gaussian profile in current, whose variance is governed by the plasma temperature. Therefore, low temperature is required to minimize beam losses in the beam transport duct.

11.2 Magnetic Multipole Plasma Source and Its Filaments

The invention of the magnetic multipole confinement by Limpaecher and MacKenzie was a revolution in source design, characterized by a weak or no magnetic field but a peripheral anode of limited area in a rectangular box (Limpaecher and MacKenzie 1973; Ehlers 1978). This configuration was based on the so-called field-free source, in which wires of tungsten or tantalum serve as filament cathodes and thus plasma losses on the cathode surface are minimized. The advantage of this design is due to the uniform illumination over a wide ion-extraction area, but it is not very efficient requiring very high arc current due to the absence of a magnetic shield.

The new design was based on the use of the multipole magnetic field to shield the source chamber walls which serve as an anode, providing far better plasma confinement and efficient ionization (Ehlers and Leung 1979; Leung and Ehlers

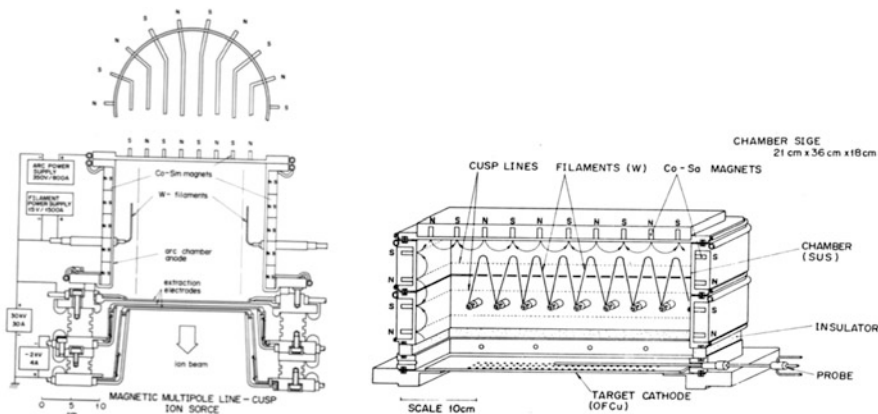


Fig. 11.1 Circular and rectangular magnetic multipole ion sources. (Reproduced from Sakuraba et al. (1980) with permission of JAEA)

1984). In Fig. 11.1, two types of this design built at JAERI (Japan Atomic Energy Research Institute) are presented (Sakuraba et al. 1980). The multipole provides a very uniform plasma in a large volume of low magnetic field surrounded by a magnetic barrier. Its plasma confinement property fairly depends on attached strong permanent magnets. This magnetic field prevents plasma particles to leak out to the wall, greatly reducing loss area, in comparison with the field-free source.

The boundary of the uniform plasma region in which the density is constant is close to the 20–30 Gauss contour where plasma pressure is equal to the magnetic field pressure, i.e.

$$\beta = \Sigma nkT / \left(B^2 / 2\mu_0 \right) = \text{Particle pressure/Magnetic field pressure} = 1 \tag{11.1}$$

where β denotes the plasma pressure normalized by magnetic field pressure, B is the magnetic flux density and μ_0 is the magnetic permeability in vacuum. The five surfaces other than the ion-extraction area are covered with cusp magnets and the filaments are attached to the side walls.

Among several configurations of cusp geometries, line cusp configuration is preferable due to stronger magnetic field on the inner surface of the chamber, leading to stronger magnetic barrier over the surface (Arakawa et al. 1980). The point cusp configuration which consists of a single magnet is weaker in confinement field strength (Ehlers and Leung 1979; Tanaka et al. 1981). The cusp line aligned perpendicular to the beam axis gives better results. This is because the cusp magnetic field nearest to the ion-extraction area expands toward the edge region of that area and the support flange so as to reduce plasma losses there. These configurations are compared in Fig. 11.2.

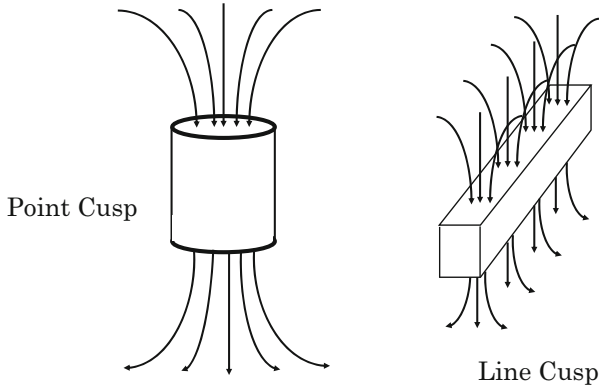


Fig. 11.2 Point cusp (left) and line cusp (right)

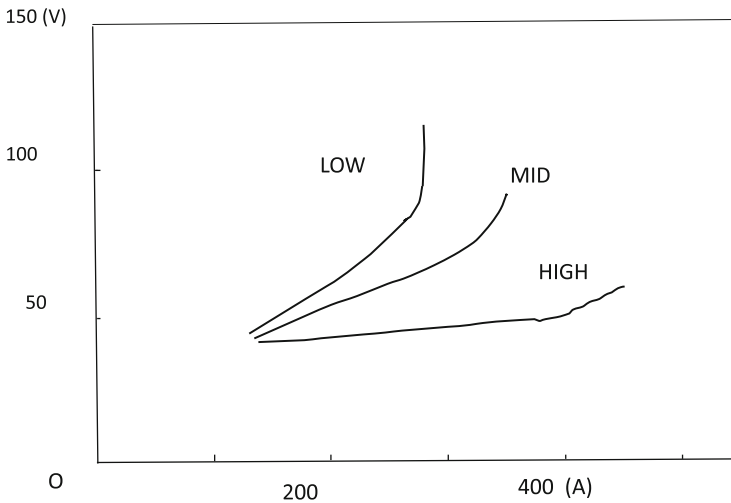


Fig. 11.3 Arc discharge characteristics of magnetic multipole source

The arc discharge operates as follows. Electrons released from the filament are accelerated in the cathode sheath and go into the plasma. These energetic electrons are capable of multiple ionization of molecules or atoms to produce plasma. Some plasma ions reach the cathode surface, but their contribution as the current carrier is small, because a proton is 1837 times heavier than an electron. The plasma contains primary electrons, thermal electrons, and thermal ions. These electrons are attracted to the anode through the anode sheath on its surface. Typical discharge characteristics are shown in Fig. 11.3, where notations indicate the heating power of the filament. The curve LOW indicates discharge characteristic in the temperature limited condition, High that in space-charge limited condition and MID in between. A schematical potential profile of the discharge is shown in Fig. 11.4.

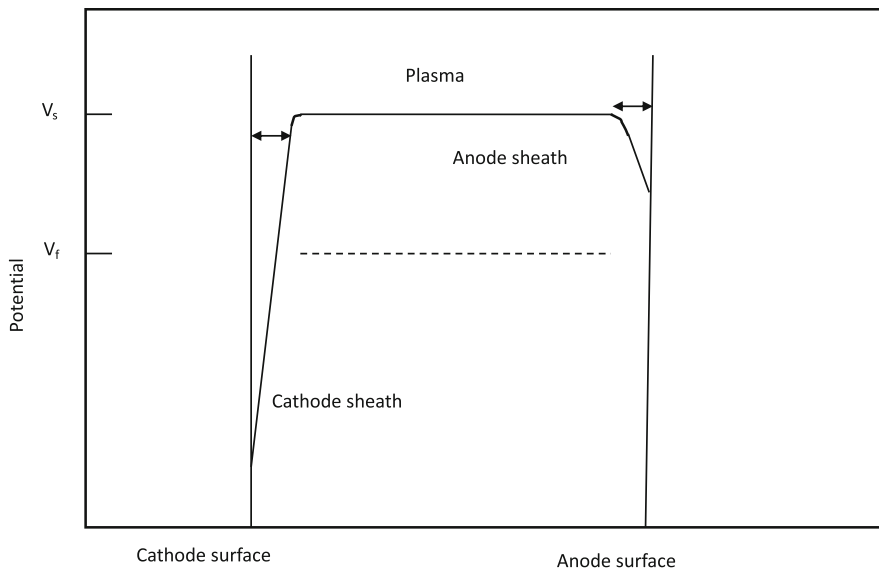


Fig. 11.4 Potential distribution in arc discharge. The solid line shows the space potential and dotted line the floating potential

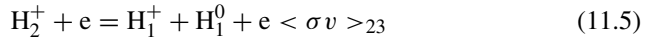
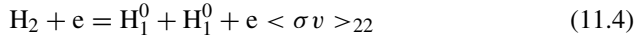
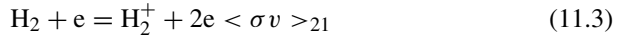
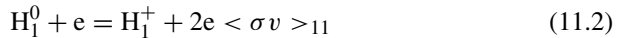
11.3 The Discharge Mechanism and the Ion Species Ratio

The magnetic multipole source consists of a large box with cusp magnets as an anode and filaments as a cathode. In case of hydrogen plasma molecular ions of H_2^+ and H_3^+ are produced, and dissociate into H_1^+ of a half and a third of the acceleration energy during neutralization. In a core fusion plasma, these low-energy atoms do not reach the central region but heat the edge region, which is an inefficient heating accompanied by enhanced edge recycling. (The edge recycling occurs when energetic plasma particles impinge on the first wall, from which secondary emitted wall atoms jump back to the plasma as highly charged impurity ions). Therefore, the reduction of molecular ion density is an essential parameter for efficient beam heating.

Primary electrons emitted from a cathode are accelerated by the cathode sheath, ionize gas molecules, and are lost to surrounding walls. A gas molecule hit by this electron is excited or ionized to a molecular ion, and further dissociates into an atom and an atomic ion. In case of no confinement field, ions and electrons are so promptly lost to the walls that a lot of primary electrons are necessary to attain a certain level of plasma density. Accordingly, this raises the electron temperature and molecular ion density and reduces the proton ratio. Therefore, better confinement of plasma and primary electrons is important to attain a higher proton ratio as was verified experimentally (Horiike et al. 1981).

The ratio of proton to molecular ions is discussed here (Surrey and Holmes 2014).

Related reactions are as follows:



From these reactions H_1^+ , H_2^+ , H_3^+ are produced. Among them the density of H_3^+ originating from H_2^+ and H_2 can be reduced by reducing H_2^+ and the gas pressure. The key is in the reduction of H_2^+ . We consider here the ratio of $\text{H}_1^+/\text{H}_2^+$ and ignore reactions (11.7) and (11.8) since the rate of reaction Eq. (11.7) is very small in low-density region. Then dominant reactions are narrowed down to reactions (11.2) to (11.5) as (11.6) can be included in (11.5). The particle balance equations can be written as:

$$2N_2n_e < \sigma v >_{22} + n_2n_e < \sigma v >_{23} = N_1n_e < \sigma v >_{11} + N_1 \frac{\gamma}{T_1} \quad \text{for } \text{H}_1^0 \quad (11.9)$$

$$n_2n_e < \sigma v >_{23} + N_1n_e < \sigma v >_{11} = n_1/\tau_1 \quad \text{for } \text{H}_1^+ \quad (11.10)$$

$$N_2n_e < \sigma v >_{21} = n_2n_e < \sigma v >_{23} + n_2/\tau_2 \quad \text{for } \text{H}_2^+ \quad (11.11)$$

here N_1 is the density of H_1^0 ,

- N_2 —the density of H_2 ,
- n_1 —the density of H_1^+ ,
- n_2 —the density of H_2^+ ,
- T_1 —containment time of H_1^0 ,
- τ_1 —containment time of H_1^+
- τ_2 —containmentconfinement time of H_2^+
- γ —recombination factor for atoms on the wall surface.

From these follows the density ratio:

$$\frac{n_1}{n_2} = n_e \tau_1 \langle \sigma v \rangle_{23} \left[1 + \frac{\left(1 + 2 \frac{\langle \sigma v \rangle_{22} \left(1 + \frac{1}{n_e \tau_2 \langle \sigma v \rangle_{23}} \right)}{\langle \sigma v \rangle_{21}} \right)}{1 + \frac{\gamma}{n_e T_1 \langle \sigma v \rangle_{11}}} \right] \quad (11.12)$$

Note that n_1 increases with n_2 when τ_1 and T_1 are longer and τ_2 is shorter, i.e. the proton ratio increases with longer containment time of H_1^0 as well as H_1^+ , and with shorter containment time of H_2^+ .

Next, the containment time is estimated. For the Maxwellian distribution, the particle flux incident on an area is expressed as $\frac{1}{4}n\bar{v}S$, where S is the area of one side of a cube. The loss rate of the particles in the cube in unit time is written as nV/τ , equating these $\frac{1}{4}n\bar{v}S = nV/\tau$ or $\tau = 4V/\bar{v}S$.

Thus, $T_1 = 4V_c/v_0S_0$, $\tau_1 = 2V_p/C_{s1}S_L$ and $\tau_2 = 2V_p/C_{s2}S_L$, where v_0 is the thermal velocity of H_1^+ , V_c the volume of the source chamber, S_0 the inner surface area of the chamber, V_p the volume of the plasma, S_L the effective ion loss area, and C_{s1} , C_{s2} are ion sound velocity of H_1^+ and H_2^+ respectively by the Bohm criterion. For a magnetic multipole source, particles are lost on the plasma grid (the uppermost electrode of the extraction electrode system), anode, and cathode.

According to the above analysis, a high-magnetic field ion source was designed and tested (Okumura et al. 1984). Its shape and cusp field profile are shown in Figs. 11.5 and 11.6. The chamber is 25 cm wide, 40 cm long, and 34 cm deep for an extraction area of 12 cm \times 27 cm. These dimensions are larger than in the other sources and stronger samarium-cobalt magnets were employed in order to attain better plasma containment. The magnetic field profiles with samarium-cobalt magnets and AlNiCo ones are compared in Fig. 11.6. As a result of changing the magnet strength, the proton percentage of 92% and 80% was obtained as shown in Figs. 11.7 and 11.8. The proton ratio variation by 12% is due mainly to that of H_2^+ fraction. Various source designs are compared in Table 11.1 and the scaling equation for the proton ratio is obtained,

$$\Gamma = 0.23 \frac{V_p}{S_L} / \left(1 + 0.23 \frac{V_p}{S_L} \right) \quad (11.13)$$

This is the so-called ‘‘Okumura scaling’’. This ion source has been used in JT-60 beam heating.

An opposite application of the above theory is a low proton ratio ion source. In the fusion plasma experiment, it is required to vary the heating profile by the neutral beams while keeping the injection power constant. Since the beamline was fixed to the torus axis in most cases, a simple way to obtain this is to vary the proton ratio in order to vary the effective beam energy while keeping injection power constant (Ehlers and Leung 1983a, b). A modified ion source in JT-60 is shown in Fig. 11.9 (Watanabe et al. 1988). The back plate provided with magnets was modified so that it could be moved up and down. This allows to vary the height of the source

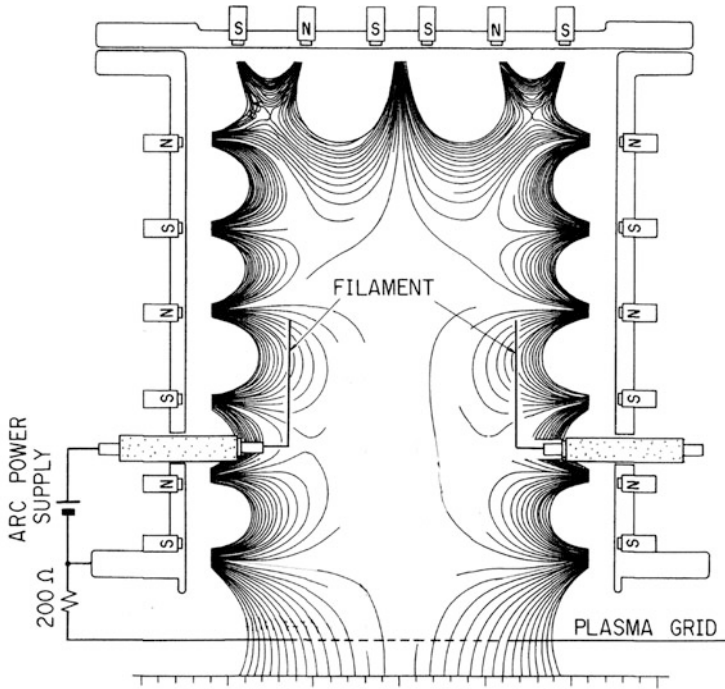


Fig. 11.5 High magnetic Field Ion Source (JT-60 ion source) cross-sectional view. Thin curves denote magnetic field lines

plasma and to change the ion species ratio. The experimental results indicated that by decreasing the height to 16 cm from the original 34 cm, the proton ratio decreased to 62% while the arc power efficiency decreased by 25%.

The newest entry to the design is cylindrical shaping. The chamber design described above requires a very thin wall in front of the magnets. Oxygen-free copper as the wall material is too weak to ensure mechanical integrity and reliability of the chamber for long time of operation. This point and consideration for V_p/S_L resulted in the adoption of cylindrical shape (Horiike et al. 1987a). The original design is shown in Fig. 11.10 which was designed to extract 12 cm \times 90 cm cross-section beam with a high proton ratio. The chamber is 34 cm in diam. and 103 cm long, and is equipped with the same SmCo magnets described above. Sixteen tungsten filaments of 1.8 mm in diam were installed and produced very uniform plasmas over 13 cm \times 90 cm area with a proton ratio of up to 90%. The value of V_p/S_L in Eq. (11.13) is 52.8 for this dimension which leads to a proton ratio of 92.4% of the proton ratio due to the Okumura scaling.

Another way for attaining higher proton ratio is the introduction of a magnetic fence inside the chamber, which is called the magnetic filter. This is typically a combination of parallel thin copper tubes forming a thin magnetic fence in the

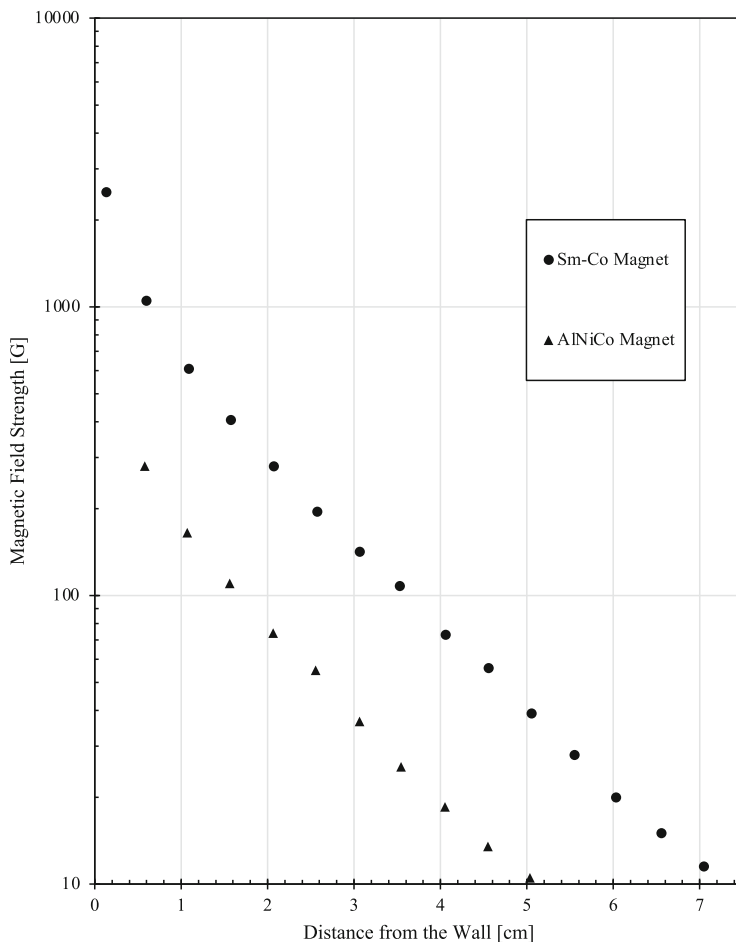


Fig. 11.6 Magnetic field intensity distributions in JT-60 ion source with magnets of SmCo and ALNICO

plasma region, as indicated in Fig. 11.11. This magnetic fence repels primary electrons coming from the cathode region while thermal ions and electrons are allowed to go through it. The plasma region is divided into two regions: the source region containing the filaments and a high density of primary electrons, and the extraction region where the density of primary electrons is low.

Analysis of the complicated configurations such as explained above cannot be performed by zero-dimensional analysis as previously studied, but estimated by two or three-dimensional orbit analysis. For this purpose, a very simple and convenient software was developed by Ohara et al. (1987). This software employs the magnetic charge model for the purpose of quick calculation since no plasma is in the vicinity of a magnet where the model is not valid. Once many magnets are considered in

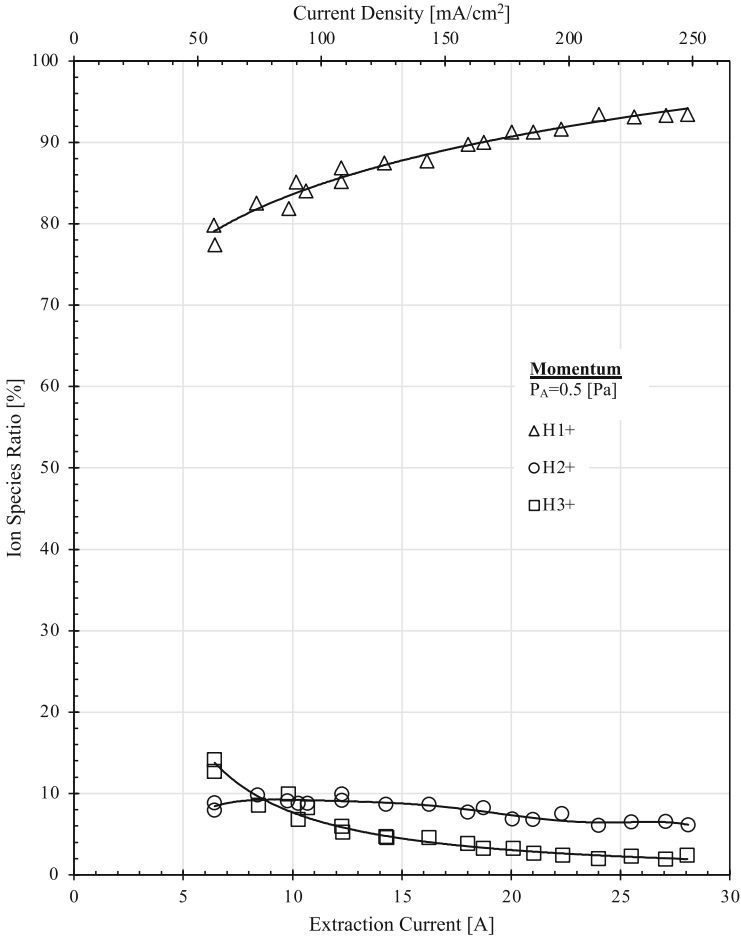


Fig. 11.7 Ion species ratio in JT-60 ion source with Sm-Co magnets

this model, the field strength is obtained by simply summing the contributions from all magnets, and 2D or 3D orbit tracing is easily performed. Orbit simulations of primary electrons in magnetic field are promptly repeated for various cusp magnets or filament configurations. This code allowed us to perform 2D or 3D iterative arrangement of magnets, filaments, and different configurations with a personal computer. Analytical results for JT-60 ion source and cylindrical one in the cross sections are shown in Fig. 11.12. Using this code, very subtle arrangements of magnets and filaments were at first performed and 95% proton-ratio ion beam was attained by adapting a magnetic filter arrangement in cusp configuration (Watanabe et al. 1990, 1991). One is an external filter configuration that is formed by reversing the opposite side of magnet polarity so as to increase transverse field intensity near the plasma grid. The other is the super cusp configuration in which the field

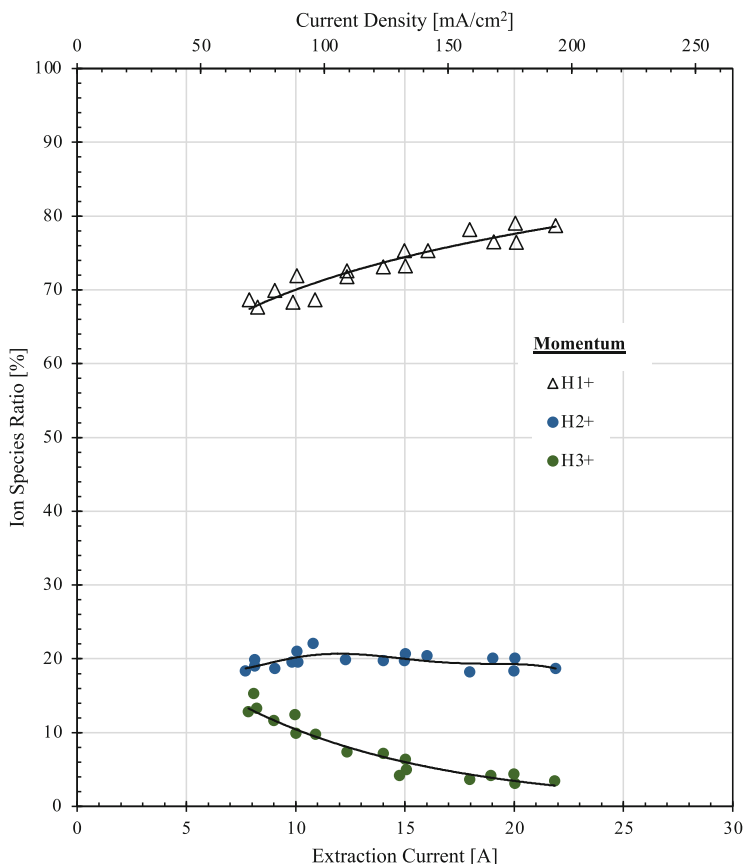


Fig. 11.8 Ion species ratio in JT-60 ion source with AlNiCo magnets

line connects the top magnet of the chamber to both sides of the magnets nearest to the plasma grid. Both filter configurations confine the primary electrons near the filaments to reduce the electron temperature in the extraction region. In these sources, the floating potential of the extraction electrode or the plasma grid was as low as 5 V negative with respect to the anode potential. The floating potential of the plasma grid depends on the energy spectrum of electrons. In case of a high density of primaries, the floating potential is low (close to the cathode potential) and many H₂ molecules are ionized to generate H₂⁺. Inversely in the case of high floating potential, the primary electron density near the electrode is low, and fewer molecular ions are produced. In the experiment, the proton ratio is found to be inversely proportional to the floating potential of the plasma grid, and the usefulness of the Ohara code was also proven. The observed traces on the anode wall or estimated discharge profiles are well explained or reconstructed using the Ohara code analysis.

Dense plasma is produced with discharge far from the extraction region, which then diffuses there while dissociating molecular ions or generating negative ions.

11.4 Mode Flap in Arc Discharge

Stable discharge is established due to reasonable balance of electron flux from the cathode to the anode. Various combinations of chamber, filament area, and anode area were tested, and it was found that the discharge exhibits a phenomenon called mode flap or mode switch (Goede and Green 1982; Goebel 1982; Holmes 1981). High confinement cusp field reduces so much the anode area that the discharge exhibits the mode flap phenomenon (Tanaka et al. 1986).

According to analyses and experiments so far, plasma source properties were classified into three cases (i) cathode limitation dominates discharge voltages in case of large anode area and small cathode, designated as low impedance mode or efficient mode, (ii) anode limitation dominates discharge voltages in case of small anode area and large cathode, designated as high impedance mode or inefficient mode (iii) mode flap region appears in-between high impedance discharge and low impedance one, while the plasma containment properties are completely constant for both modes like those in Figs. 11.13, and 11.14a, b.

In case (i), the discharge is limited by lower gas pressure, corresponding to break-up in the cathode sheath criterion by deficit neutral density to produce sufficiently dense plasma to sustain sufficient cathode sheath voltage. In this mode, plasma has a potential higher than or similar to the anode potential as is depicted in Fig. 11.4. On the contrary in case (ii), the discharge is characterized by the plasma potential much lower than the anode potential. Primary electrons accelerated by the cathode sheath have lower energy and are inefficient in producing plasma. Because the discharge is forced to follow a terminal voltage applied by the power supply, deficient part of voltage is generated in the anode sheath. Thus, high voltage but low current discharge occurs. In-between these two cases (iii), jumps occur in plasma potential and discharge is submitted to mode flap. The plasma potential with respect to the anode is considered to play governing role.

11.5 Cusp Leak Width

The cusp magnetic field and plasma flow in it is a key to understanding the source plasma. The research was motivated by mechanical tolerance at high current discharge. The anode wall tends to break in high current discharge along thin traces of discharge. This was studied using a Langmuir probe made of a thin thermocouple. It was found that the profiles of heat flux and electron temperature were narrower in width than those of ion current density, and varied with the ion mass. The peak

Table 11.1 Ion source parameters and proton ratio predicted by Eq. 11.13

Name	(A) Small rectangular	(B) Cylindrical	(C) Prototype A	(D) Prototype B	(E) JT60 product	(F) JT60 weak magnet
Length	19.2	26 diam	36	36	40	40
Width	12		21	21	25	25
Depth	15.5	22	21.5	23.5	34	34
Chamber volume	3571	11,700	16,300	17,800	34,000	34,000
Chamber surface	1428	2859	3963	4191	6420	6420
V_c/S_0	2.5	4.1	4.1	4.24	5.3	5.3
Filament diam.	1.5	1.5	1.8	1.8	2.7	2.7
Length	18	18	19	19	19	19
Number	4	8	8	8	6	6
Magnetic field strength on wall	0.125	0.125	0.125	0.14	0.27	0.06
Cusp length	258	510	764	832	950	950
Uniform density area on plasma grid	172	380	500	500	544	756
Anode area	93 + 31	184 + 41	275	272	160	726
Filament Area	50	100	110	110	110	110
Plasma volume	1642	7080	10,000	11,000	20,000	24,000
Ion loss characteristic length	6.3	13.7	15.7	17.5	37	19.8
Proton ratio by scaling law	58	76	78	80	90	83
Proton ratio measured	57	72	75–80	80	91	80

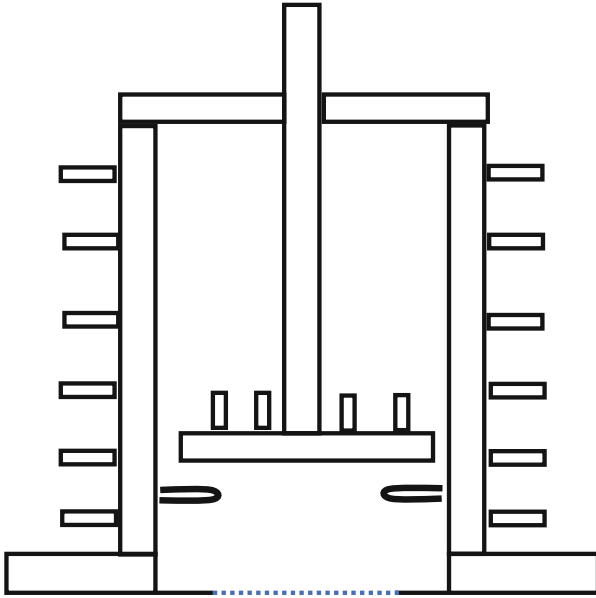


Fig. 11.9 JT-60 ion source in which the ion species ratio could be varied

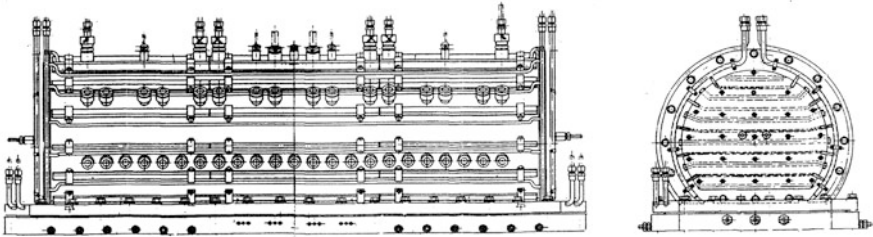


Fig. 11.10 Cylindrical ion source designed to extract $12\text{ cm} \times 90\text{ cm}$ cross-section beam with high proton ratio. (Reproduced from Horiike's design data)

width was found to decrease with the energy of primary electrons (Horiike et al. 1987a, 1999; Murata 1999).

Two narrow lines of discharge traces were often observed in a configuration when the filament crosses the cusp line, as shown in Fig. 11.15. The bent part of a filament crosses one cusp line at the center. In this cusp field B_x components have inversed polarities against the cusp line and generate Grad.B drift of inverse direction along the cusp line as indicated by blank arrows. In this configuration two peaks are observed on the cusp line which a filament hangs over, but a single peak appears on the cusp line which it does not hang over. Turning on and off of a filament correlated with a peak, we concluded that the primary electrons emitted from a filament are trapped by the cusp magnetic field nearby and impinge on anode

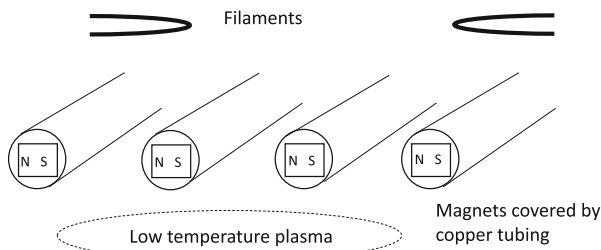


Fig. 11.11 Conceptual design of the magnetic filter

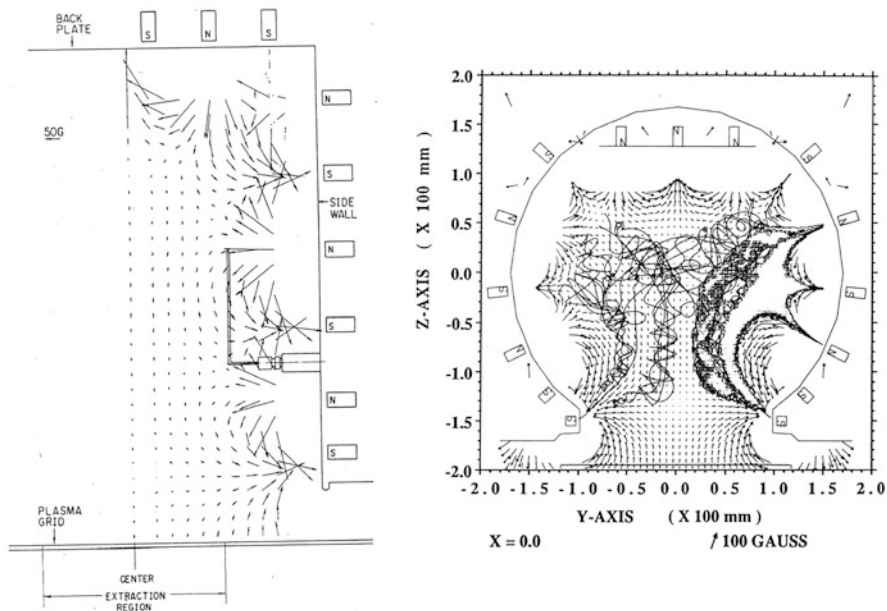


Fig. 11.12 Magnetic field vectors and electron orbits calculated by Ohara code. Left—JT-60 ion source, right—the cylindrical ion source for 95% proton ratio. (Reproduced from Tanaka et al. (1986) and from Watanabe et al. (1991) with permission of AIP)

wall guided by the field line while drifting in Grad.B direction along the cusp line. This drift is reversed symmetrically with respect to the cusp line. The peak power nearer to a filament is higher but it decreases considerably on the opposite side of the chamber wall. In Fig. 11.16 two peak profiles are shown at three distances from the chamber wall (anode). These were measured on the central cusp line in Fig. 11.15 between two identical filaments and the other two on the opposite side of the chamber. It was verified that one peak comes from one filament direction and the other peak from the other direction (Yamashita 2001; Kosaka et al. 2002). It is seen that the probe scan line measured farther from the wall shows higher and broader

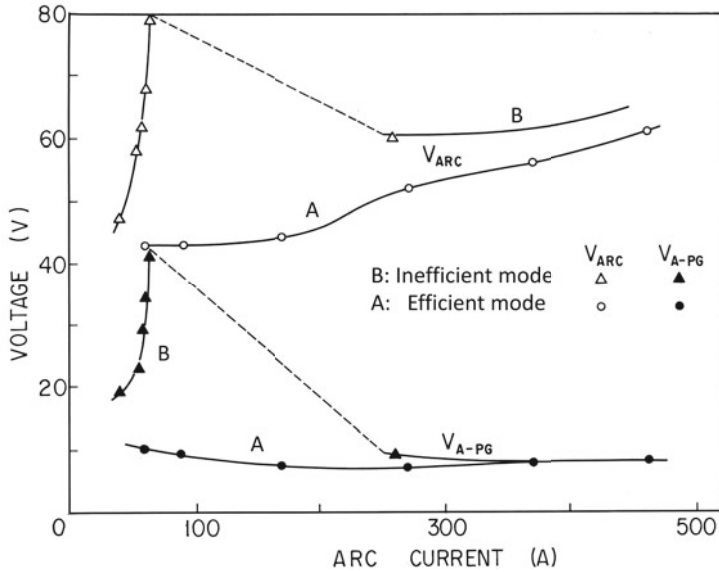


Fig. 11.13 Discharge characteristics of: A-inefficient mode and B-efficient mode, with mode transition shown by dotted lines. (Drawn from Horiike's original data)

peaks. This may indicate that primary electrons are reflected by the cusp field and that density is decreasing towards the wall direction.

11.6 Need of Negative Ion Beams

Need of the hydrogen negative ion beam comes from the beam energy requirement for effective heating of the fusion plasma. With the increase of the plasma scale from those of DIII-D and PLT through to the three large tokamaks TFTR, JET, JT-60, and ITER (International Thermonuclear Fusion Experimental Reactor), the requirement on beam energy increased and 1 MeV beam is planned for ITER. In order to attain neutral (i.e. atom) beams of such high energy, it is very inefficient to neutralize positive ion beams. This is because neutralizing efficiency of hydrogen depends on the ratio of charge exchanges cross sections of (H^+ to H^0) and (H^0 to H^+) or σ_{10}/σ_{01} . These cross sections decrease with the increase of energy above 100 keV, but σ_{10} decreases much faster than σ_{01} , resulting in a very small neutralization efficiency above 100–200 keV. For negative hydrogen ions, high neutralization efficiency of up to 58% by gas cell, up to 85% by plasma cell, and nearly 100% by laser cell can be attained.

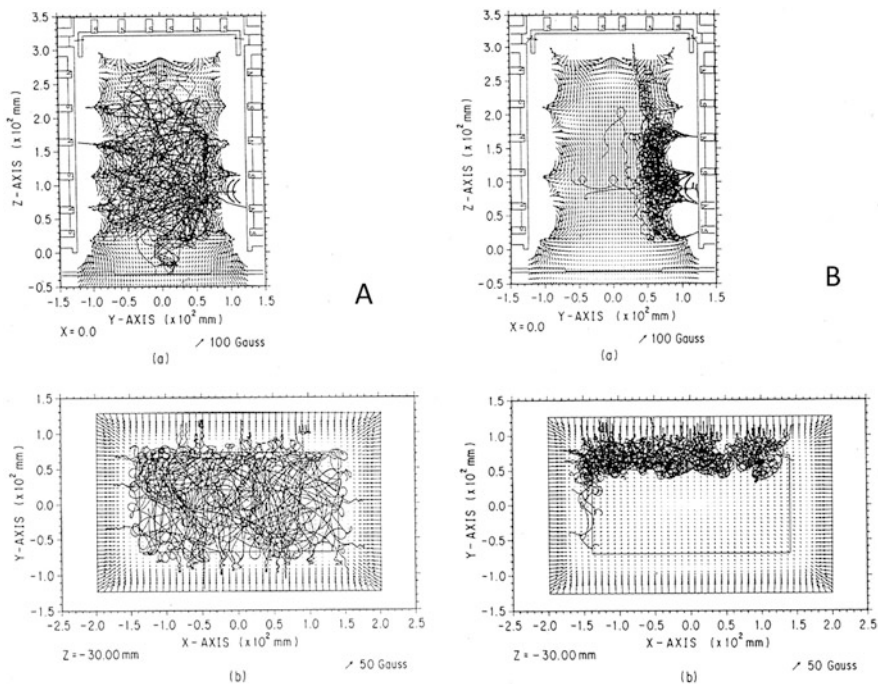


Fig. 11.14 Three dimensional primary electron orbits in A efficient mode of discharge and B inefficient mode. (Reproduced from Ohara et al. (1987) with permission of AIP)

Positive ions are formed when an outermost electron is stripped from atoms by a collision with electrons with energy higher than the ionization potential. Negative ions are formed when an additional electron is attached to a neutral atom. A hydrogen atom consists of a proton surrounded by an electron cloud of spherically symmetric distribution. Therefore, coulomb force to an outer electron is the sum of attractive force with proton and repulsive force with orbit electron. But the latter is weaker because of the distribution of electron cloud. As a result, an electron affinity force of 0.754 eV or 72.8 kJ/mol works in hydrogen and 0.616 eV or 59.6 kJ/mol in Lithium.

A heating power of more than 10 MW net power for plasma is necessary for recent large devices. ITER neutral beams of 16 A(net) at 1 MeV are planned. To inject this neutral beam current into core plasma requires extracting approximately 40 A ion beam from an ion source because several loss processes are inevitable during acceleration and transport. Considering the realistic dimension of the plasma source and electrostatic acceleration system the ion extraction current density of 200 A/m² is planned in ITER

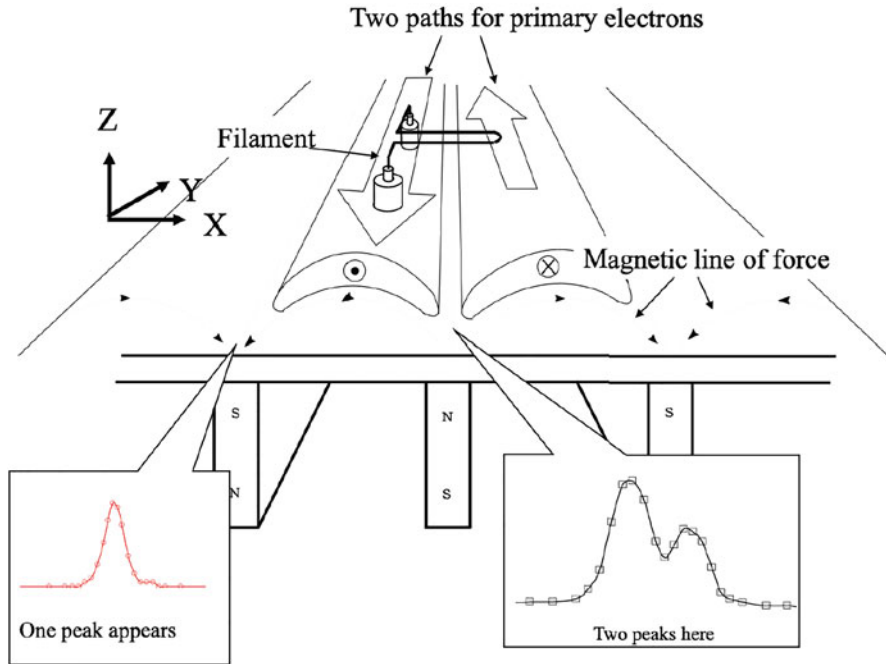


Fig. 11.15 Configuration of line cusp magnetic field and filament position. On the central cusp line two peaks are observed but only one on the left or right lines

11.7 Negative Ion Production

Negative ions can be produced by three methods. The first one is charge exchange illustrated in Fig. 11.17. Here negative ions are produced by the attachment of two electrons to a positive ion while these are passing through a charge exchange gas of alkali metal vapor. This method is physically simple and hydrogen-negative ion beams of 2.2 A at 10 keV (Kuznetsov et al. 1985) or 5.5 A at 80 kV (Kwan et al. 1986) were produced.

The second method is negative ion surface production illustrated in Fig. 11.18 and also discussed in detail in Chap. 2 of this book.

11.8 Volume Production

The third method, volume production, was discovered following the observation by Nicolopoulou et al. (1977), which revealed that the actual negative ion density in a low-pressure hydrogen discharge is more than 100 times larger than that assumed previously. An explanation of this observation, namely the dissociative electron

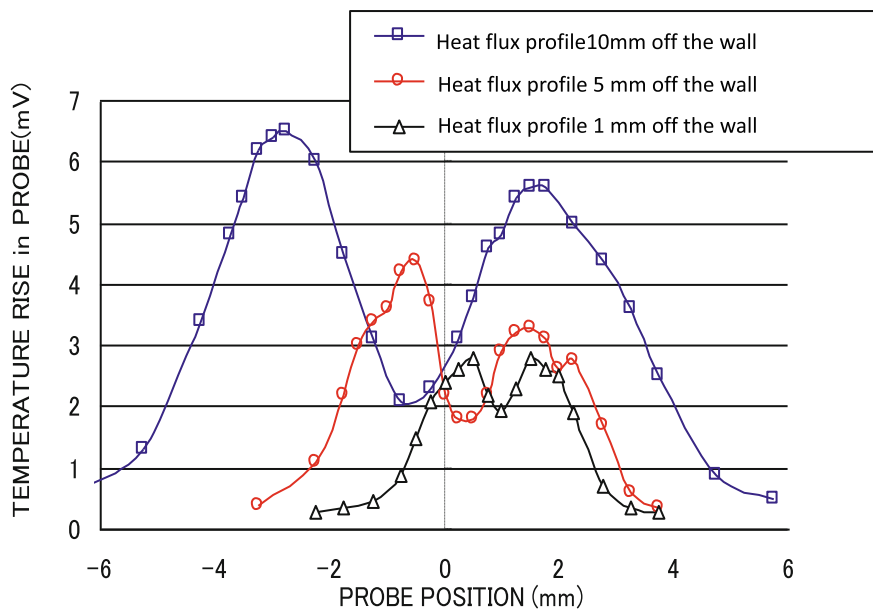


Fig. 11.16 Two peaks of heat flux on the cusp line at the center in Fig. 11.15. Four filament discharge of 173 A at 84 V, 3 mTorr of hydrogen

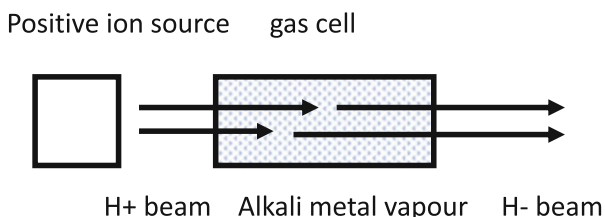
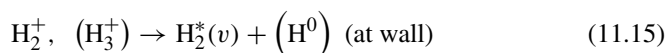


Fig. 11.17 Charge exchange method of negative beam production

attachment to vibrationally excited molecules. The physics of volume production is discussed in detail in Chap. 1 of this book.

Among the volume production reactions, the dominant ones are compared in Fig. 11.19, where <ED> denotes electron detachment and <DA> dissociative electron attachment.

Some important vibrational excitation reactions are listed below:



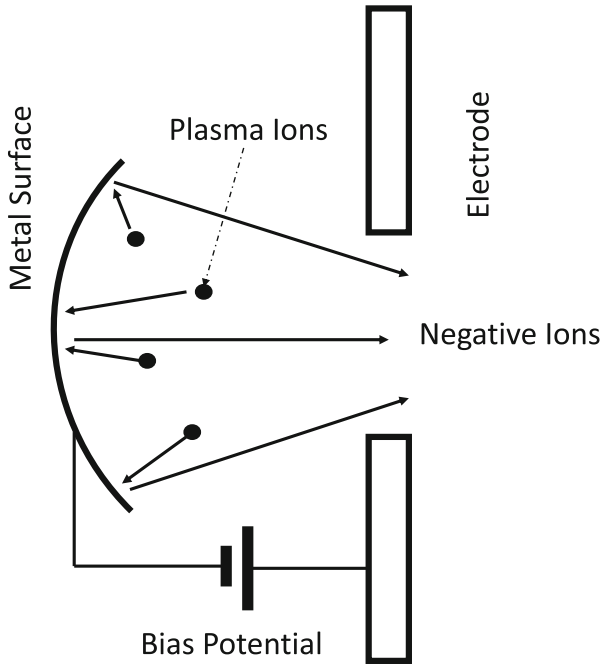
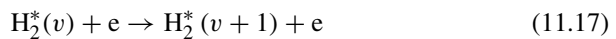
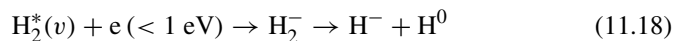


Fig. 11.18 Negative ion surface production method



where v denotes the molecule's vibrational excitation level and the subscript "fast" denotes the electrons with energy higher than 20 eV. Very slow electrons of less than 1 eV cause dissociative attachment of the vibrationally excited molecules and thus an electron and a negative ion are born:

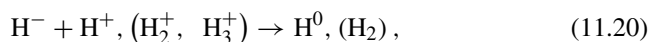


It was found that out of 13 levels of vibrationally excited levels those with $v > 6$ contribute mainly to negative ion formation (Leung and Kunkel 1987).

Thus, reaction (11.14) followed by reaction (11.18) are the dominant processes of negative hydrogen ion production. On the other hand, there are destruction processes related to the low electron affinity such as electron detachment,



mutual neutralization



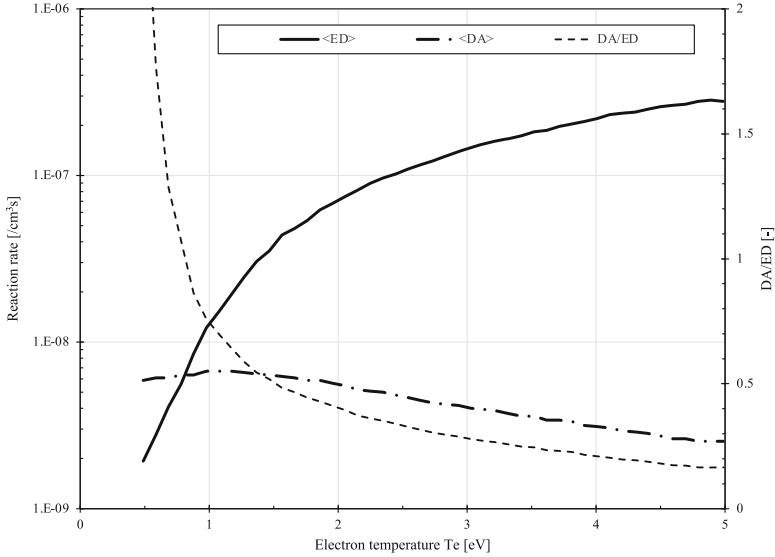
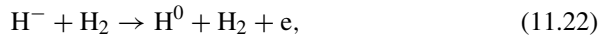


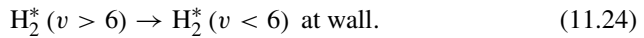
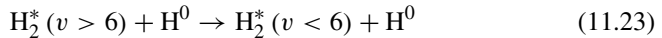
Fig. 11.19 Comparison of reaction rates of dissociative electron attachment <DA>, and destruction in electron collision <ED> as a function of electron temperature. Their ratio is shown by the dotted line. (Reproduced from Hemsworth and Inoue (2005), with permission of IEEE with permission of IEEE)

associative detachment



The reaction (11.19) is the dominant process.

The loss processes of $H_2^*(v)$ are:



The dotted line in Fig. 11.19 shows the ratio of these reactions in arbitrary units (Inoue et al. 1989). While the dissociative attachment shows a modest electron energy dependence, the electron detachment increases steeply in the 3 eV to 1 eV region by more than one order. As a result, the ratio of these two processes increases rapidly with the decrease of T_e from 3 eV to less than 1 eV, and the negative ion density can be maximized at approximately 1 eV or less. However, high-energy electrons are necessary for the efficient production of $H_2^*(v)$. These are contradictory requirements to be satisfied in the same chamber. This is done by separating the

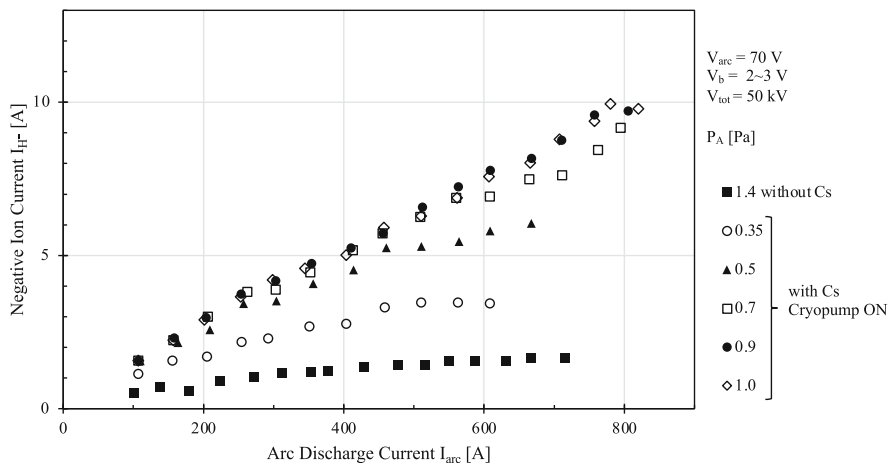


Fig. 11.20 Negative ion current dependence on discharge current for various gas pressure. (Reproduced from Kojima et al. 1990)

chamber volume into two regions, of high and low electron temperature. Such a separation is achieved using a magnetic filter as described above. A rod filter has a large loss area for plasma. Instead, as described, a strong coupling of filaments with cusp magnetic field is utilized to confine primary electrons near filament region and prevent them from reaching the ion-extraction region by applying magnetic field across it. Excited atoms diffuse towards the extraction region, where the temperature is kept low due to the strong magnetic field separating these two regions. Two-to-three-dimensional magnetic configuration analysis is performed to design a suitable configuration for efficient negative ion production. Such a magnetic field configuration is sometimes called the external filter configuration (Okumura et al. 1987).

Since the density of $H_2^*(v)$ is proportional to gas density, a negative ion beam with an ion density of 200 A/m^2 was obtained at a gas pressure of more than 1 Pa. At this pressure, the stripping loss of negative ions during their acceleration is very large and it is important to reduce the operating gas pressure.

From Eq. (11.14) it follows that the negative ion density depends on e_{fast} or the discharge current. Figure 11.20 shows that the H^- current increases with the discharge current but gradually saturates (Kojima et al. 1990; Leung et al. 1990). The saturation may be attributed to the dissociation of H_2 into atoms, shown in Figs. 11.7 and 11.8, and to the increase of the electron temperature. The increase in H_2 pressure leads to the increase of the formation of vibrationally excited molecules, reaction (11.14), but also the increase of the destruction of H^- ions by associative detachment, reaction (11.22).

Negative ion current dependence on the gas pressure at different values of the discharge current is shown in Fig. 11.21. The H^- current increases with the pressure due to the increase of $H_2^*(v)$ density and to the reduction of electron temperature, but

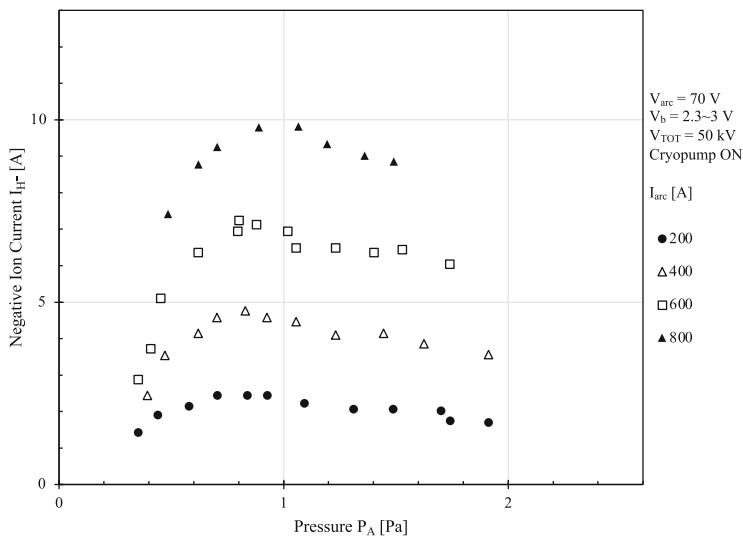


Fig. 11.21 Dependence negative ion current on gas pressure. (Reproduced from Kojima et al. 1990)

saturates probably because of associative detachment, reaction (11.22). The pressure at which the H^- current attains a maximum increase with the discharge current.

Since negative ions are produced efficiently with Cs coverage on the convertor of a surface production source, it was assumed that in the case of volume production Cs atom feeding into the chamber should also work. It was tested and verified to be very effective for negative ion production in low-pressure regions (Kwan et al. 1991; Suzuki et al. 1992). The significant effect of Cs feed is in a reduction of the work function on the surfaces especially that of the plasma grid. The work function of the grid in a magnetic multipole ion source was measured and it was revealed that the production efficiency increases rapidly with reduction of work function of the plasma grid surface (Hemsworth and Inoue 2005; Suzuki et al. 1992; Shimizu et al. 2003). In the experiment Au, Ag, Cu, Mo and Ni were tested for candidate materials for plasma electrode. While without Cs seeding Au was superior to the others owing to its lowest work function, it was found that once covered by Cs these materials showed no difference.

It was also revealed that W atoms deposited by the filament sublimation reduce the production efficiency, which can be recovered with new Cs coverage on it. It was shown that this property depends on the electrode temperature showing an optimum at 200–300 °C.

Finally, the negative ion acceleration procedure is analyzed. The electrons have to be swept out before they are accelerated to high energy. Therefore, ions and electrons are extracted by a low voltage applied between the plasma grid and the extraction grid. Applying a weak magnetic field electrons are bent out and impinge on the side wall next to the second electrode. The heavier particles, the

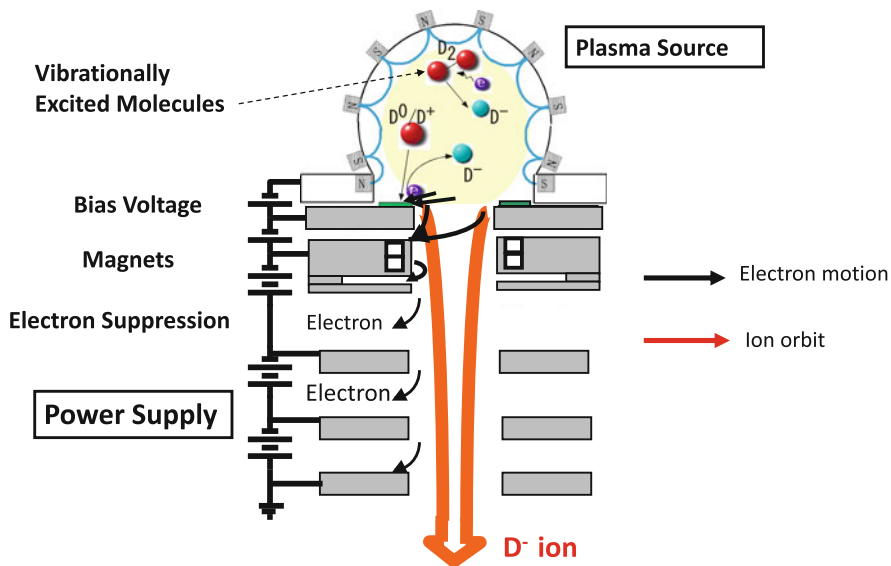


Fig. 11.22 Cross-sectional view of negative ion acceleration system. The plasma source is located on the upper side of the plasma grid wherefrom the charged particles are accelerated downwards

ions, penetrate through the magnetic field almost straight. This configuration is presented in Fig. 11.22. Usually an extraction voltage of a few kV is applied between the plasma grid and the extraction grid (Hemsworth and Inoue 2005). Follows the electron suppression grid which serves for the suppression of back-streaming electrons, consisting of secondary electrons or beam plasma electrons which are generated on the downstream side of the accelerator. Finally follows the full energy extraction electrode which consists of multiple acceleration stages.

Negative ion beams have very small divergence, and geometrical losses with negative ion beams are much smaller than those with positive ion beams. This is attributed to the beam plasma component. The beam plasma is generated by the ionization of background gas by beams. In case of negative ion beam, the space charge of the beam ions is negative and the positive ions of beam plasma are attracted to neutralize the beam space charge. In case of positive ion beams, the polarity is reversed and the electrons from beam plasma are attracted to neutralize the beam space charge. Though the temperature of the beam plasma is very low (approximately 1 eV) the electrons escape quickly from the beam region, but ions have a much lower temperature and move very slowly. This difference is accountable for the beam divergence behavior in negative ions beam and positive ions beam.

References

- Y. Arakawa, M. Akiba, H. Horiike, et al., Japan Atomic Energy Research Institute JAERI-M 8869 (1980)
- K.W. Ehlers, Contributed Paper IAEA, Workshop on Neutral Injection, Culham (1978)
- K.W. Ehlers, K.N. Leung, *Rev. Sci. Instrum.* **50**, 1353 (1979)
- K.W. Ehlers, K.N. Leung, *Rev. Sci. Instrum.* **54**, 677 (1983a)
- K.W. Ehlers, K.N. Leung, US Patent File 26 July (1983b)
- D.M. Goebel, *Phys. Fluids* **25**(6), 1093 (1982)
- A.P.H. Goede, T.S. Green, *Physics Fluids* **25**(10), 1797 (1982)
- R.S. Hemsworth, T. Inoue, *IEEE Trans. Plasma Sci.*, Special Issue on Ion Sources, **33**(6), 1799 (2005)
- A.J.T. Holmes, *Rev. Sci. Instrum.* **52**(12), 1814 (1981)
- H. Horiike, M. Akiba, Y. Arakawa, et al., *Rev. Sci. Instrum.* **52**, 567 (1981)
- H. Horiike, M. Akiba, T. Inoue, et al., 11th Symposium on Ion Sources and Ion Assisted Technol., Tokyo, (1987a)
- H. Horiike, A. Masato, Y. Ohara, et al., *Phys. Fluids* **30**(10), 3268 (1987b)
- H. Horiike, S. Kazama, T. Murata, et al., E-P-99-31 Tech. Meet. Plasma Sci. Technol., IEE Japan, (1999)
- T. Inoue, M. Araki, M. Hanada, et al., *Nucl. Instrum. Methods Phys. Res.* **B37/38**, 111 (1989)
- H. Kojima, M. Hanada, T. Inoue, et al., Proc. 13th Sympo. on Ion Sources and Ion Assisted Technol. 90, Tokyo, Japan, 1990
- T. Kosaka, H. Yamashita, S. Miyamoto, et al., *Rev. Sci. Instrum.* **73**(2), 961 (2002)
- V.V. Kuznetsov, et al., Proc. IAEA Tech. Commit. Meet. Negative Ion Beam Heating, Grenoble (1985)
- J.W. Kwan et al., *Rev. Sci. Instrum.* **57**, 831 (1986)
- J.W. Kwan, G.D. Ackermann, O.A. Anderson, et al., *Rev. Sci. Instrum.* **62**(6), 1521 (1991)
- K.N. Leung, K.W. Ehlers, *Rev. Sci. Instrum.* **55**, 342 (1984)
- K.N. Leung, W.B. Kunkel, LBL-Report 23157 (1987)
- K.N. Leung, O.A. Anderson, C.F. Chan, et al., *Rev. Sci. Instrum.* **61**(9), 2378–2382 (1990)
- R. Limpaecher, K.R. MacKenzie, *Rev. Sci. Instrum.* **44**, 726 (1973)
- T. Murata, Master's thesis Department of Electronic Information and Energy Engineering Graduate School of Engineering, Osaka University 1999)
- E. Nicolopoulou, M. Bacal, H.J. Doucet, *J. Phys. (Paris)* **38**, 1399 (1977)
- Y. Ohara, M. Akiba, H. Horiike, et al., *J. Appl. Phys.* **61**(4), 1327–1328 (1987)
- Y. Okumura, H. Horiike, K. Mizuhashi, *Rev. Sci. Instrum.* **55**, 1 (1984)
- Y. Okumura, M. Akiba, M. Hanada, et al., IAEA Tech. Commit. Meet. Negative Ion Beam Heating, Culham Lab. 1987
- J. Sakuraba, M. Akiba, Y. Arakawa, et al., JAERI-M 8740 (1980)
- T. Shimizu, M. Morishita, M. Kashiwagi, et al., JAERI-Tech2003-006, (2003)
- E. Surrey, A.J.T. Holmes, *PSS&T* **24**, 1 (2014)
- Y. Suzuki, M. Hanada, Y. Okumura, et al., JAERI-M 92–168 (1992)
- S. Tanaka, M. Akiba, H. Horiike, et al., 9th Symposium on Engineering Problems of Fusion Research, Chicago, p. 1342, 1981
- S. Tanaka, M. Akiba, H. Horiike, et al., *Rev. Sci. Instrum.* **57**(2), 147 (1986)
- K. Watanabe, M. Dairaku, N. Ebisawa, et al, JAERI-M 88–022, (1988)
- K. Watanabe, M. Araki, M. Dairaku, et al., *Rev. Sci. Instrum.* **61**(6), 1964 (1990)
- K. Watanabe, M. Araki, M. Dairaku, et al., *Rev. Sci. Instrum.* **62**(9), 2143 (1991)
- H. Yamashita, Master Thesis Department of Electronic Information and Energy Engineering Graduate School of Engineering, Osaka University, (2001)

Chapter 12

ECR–Driven Negative Ion Sources Operating with Hydrogen and Deuterium



P. Svarnas, M. Mitrou, J. L. Lemaire, L. Gavilan, N. de Oliveira, and S. Béchu

Abstract This chapter is devoted to the fundamental principles of electron cyclotron resonance (ECR) sources yielding H^- and D^- negative ions. Initially, it provides a brief but meaningful overview of the theoretical framework for ECR plasmas along with commonly employed experimental configurations, unveiling thus the distinct features of this special category of high-frequency electrical discharges. It is highlighted that it is not aimed to cover the vast field of microwave discharges (e.g., microwave discharges in waveguides and resonators), nor the vast field of wave-heated discharges (e.g., helicon discharges and surface wave discharges). Such an attempt would be a utopia within the frame of one book chapter. Therefore, Sect. 12.1 of this chapter presents elementary physical quantities of plasmas, related to the ECR idea, and an idealized, simplified concept of the complex wave propagation in ECR plasmas where the wave energy absorption is achieved through collision-less heating mechanism (Firdman and Kennedy, *Plasma physics and engineering*. New York: Taylors & Francis Books Inc., 2004;

P. Svarnas (✉)

University of Patras, Electrical and Computer Engineering Department, Patras, Greece
e-mail: svarnas@ece.upatras.gr

M. Mitrou

University of Patras, Electrical and Computer Engineering Department, Patras, Greece

Université Grenoble Alpes, CNRS, Grenoble INP (Institute of Engineering), Grenoble, France

J. L. Lemaire

Institut des Sciences Moléculaires d'Orsay (ISMO), CNRS-Université Paris-Sud (UMR8214),
Orsay, France

L. Gavilan

Space Science and Astrobiology Division, NASA Ames Research Center, Moffett Field, CA,
USA

N. de Oliveira

DESIRS beamline, Synchrotron SOLEIL, Gif sur Yvette, France

S. Béchu

Université Grenoble Alpes, CNRS, Grenoble INP (Institute of Engineering), Grenoble, France

© The Author(s), under exclusive license to Springer Nature Switzerland AG 2023

303

M. Bacal (ed.), *Physics and Applications of Hydrogen Negative Ion Sources*,

Springer Series on Atomic, Optical, and Plasma Physics 124,

https://doi.org/10.1007/978-3-031-21476-9_12

Williamson et al., *J. Appl. Phys.* 72:3924, 1992). The presentation concerns low-pressure, nonthermal, and nonequilibrium plasmas. Then, the core of this review is devoted to the targeted application of ECR heating to negative ion sources operating with molecular hydrogen (H_2) and deuterium (D_2). Once again, the relatively vast field is impossible to be treated in the context of this chapter, but the authors hope that the cited sources are worthy representatives. Fundamental processes governing the H^- and D^- ion production (destruction) are summarized in Sect. 12.2, while the extended Sect. 12.3 provides recent experimental results from ECR-driven sources and comments on them in detail. Diagnostic techniques applicable to these sources are also mentioned at the beginning of Sect. 12.3. This chapter closes with Sect. 12.4, where additional ECR sources are touched upon and negative ion-extracted currents from different sources are compared. The review is throughout supported by future-proof classic or up-to-date bibliography for further reading.

Keywords ECR plasmas · Hydrogen · Deuterium · Negative ions · Ion sources · Ion beams

12.1 Fundamental Principles of Electron Cyclotron Resonance (ECR) Heating¹

Microwave generation of plasmas has been employed since the invention of high power, microwave sources in World War II. However, traditional microwave generation of plasmas has inherent limitations such as low critical plasma densities and requirement for high resonant microwave cavity quality factor (Lieberman and Lichtenberg 2005). Analytically, the electron plasma frequency, i.e., the frequency with which electrons oscillate among the heavier, immobile ions when the electron population is disturbed, equals (Roth 1995)

$$\omega_{ep} = 2\pi \nu_{ep} = \sqrt{\frac{n_e e^2}{m_e \epsilon_0}} \quad (12.1)$$

If a plasma is irradiated with externally applied electromagnetic radiation of frequency $\omega_0 = 2\pi \nu_0$, there is a critical electron number density $(n_e)_c$ below which the radiation will be transmitted through the plasma, otherwise if n_e exceeds $(n_e)_c$, the radiation will be reflected (Roth 1995). This critical number density is the threshold for which $\omega_0 = \omega_{ep}$. As a reminder, if $\omega > \omega_{ep}$ the electrons have too much

¹ It is evident that this section comprises an introductory text on the ECR (propagating wave) heating to facilitate the presentation of the ECR sources below. Rigorous consideration of the ECR heating mechanisms (e.g., collisional versus collisionless), magnetic field optimization, impedance matching issues etc. can be found in dedicated reports, e.g., (Williamson et al. 1992; Gammino et al. 2010; Asmussen and Mak 1994).

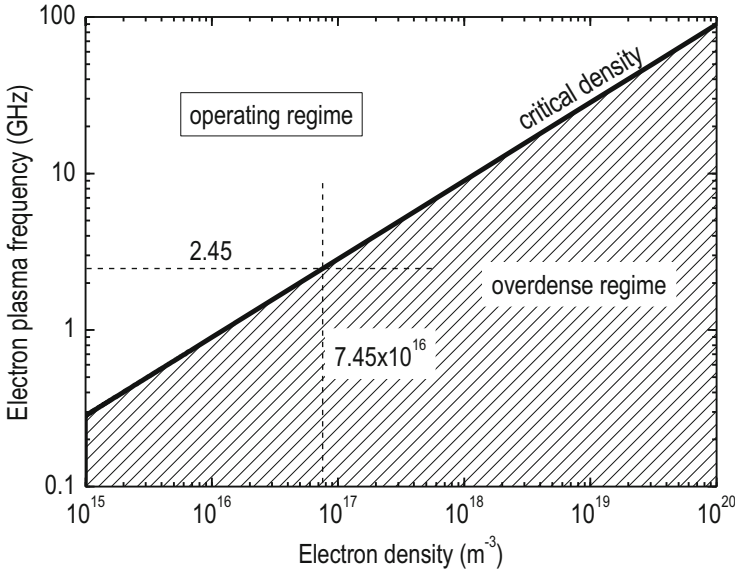


Fig. 12.1 The solid line indicates the critical electron number density for different electron plasma frequencies. The widely used industrial frequency of 2.45 GHz is marked and corresponds to a density of $7.45 \times 10^{16} \text{ m}^{-3}$. Over-dense plasmas are those below and to the right of the critical density. (Reproduced from Roth (1995) with the permission of Taylor & Francis Publishing)

inertia to respond to the electric field of the wave, and the radiation can propagate through the plasma without significant reflection or attenuation, whereas, if $\omega < \omega_{ep}$ the radiation will be reflected. Thus, substitution in Eq. (12.1) gives the following formula:

$$(n_e)_c = \frac{\omega_0^2 m_e \epsilon_0}{e^2} = \frac{4 \pi^2 m_e \epsilon_0}{e^2} \nu_0^2 \quad (12.2)$$

Equations (12.1) and (12.2) are graphically correlated in Fig. 12.1.

The introduction of a steady state magnetic field \mathbf{B} , in which there is a resonance between the externally applied frequency and the electron cyclotron frequency somewhere within the discharge, allows operation at high density and without a cavity resonance (Lieberman and Lichtenberg 2005). The gyrating electrons rotate in phase with the right-hand circularly polarized wave, seeing a steady-state electric field over many gyro-orbits. Thus, the high field of the cavity resonance, acting over a short time, is replaced by a much lower field, but acting over a much longer time. This leads to sufficient energy gain of the electrons to allow ionization of the background gas. Furthermore, the injection of the microwaves along the magnetic field, with electron gyrofrequency $\omega_{ec} > \omega_0$ at the entry into the discharge region, allows wave propagation to the absorption zone $\omega_{ec} \approx \omega_0$, even in a dense plasma with $\omega_{ep} > \omega_0$ (Lieberman and Lichtenberg 2005).

Strictly speaking (Roth 1995), the resonance in question is much closer to the upper hybrid frequency

$$\omega_{\text{uh}} = \sqrt{\omega_{\text{ec}}^2 + \omega_{\text{ep}}^2} \quad (12.3)$$

than to the electron gyrofrequency

$$\omega_{\text{ec}} = \frac{eB}{m_e} \quad (12.4)$$

In order to heat a magnetized plasma with the extraordinary mode of electromagnetic radiation (Roth 1995), i.e., the electric field vector to be perpendicular to the confining magnetic field, incident radiation $\omega_0 = 2\pi \nu_0$ at the electron gyrofrequency $\omega_{\text{ec}} = 2\pi \nu_{\text{ec}}$ (i.e., consider the case where $\nu_0 \approx \nu_{\text{ec}} < \nu_{\text{uh}}$) should be above the electron plasma frequency in order to penetrate the plasma and heat it throughout its volume without significant reflection or attenuation. Hence, this condition states that

$$\omega_{\text{ec}} \geq \omega_{\text{ep}} \implies \frac{eB}{m_e} \geq \sqrt{\frac{n_e e^2}{m_e \epsilon_0}} \quad (12.5)$$

and, solving for B , a lower limit for the magnetic induction required to apply ECR heating to a plasma with a given electron density n_e is obtained, i.e.,

$$B \geq \sqrt{\frac{n_e m_e}{\epsilon_0}} \quad (12.6)$$

On the other hand, the power input to a magnetized plasma in the individual particle regime has a sharp maximum near the ECR frequency $\omega_{\text{ec}} = 2\pi \nu_{\text{ec}}$, given by Eq. 12.4 as a function of the magnetic induction of the externally applied magnetic field (Roth 1995). This dependence is presented in Fig. 12.2. For the widely used industrial frequency of 2.45 GHz, a magnetic induction of 87.5 mT is required, which is easily within reach of low-power direct current electromagnets or permanent magnets.

The basic principle of ECR heating is better explained in Fig. 12.3 (Lieberman and Lichtenberg 2005). A linearly polarized microwave field launched into the source chamber can be decomposed into the sum of two counter-rotating circularly polarized waves. Assuming a sinusoidal steady state with the incident wave polarized along \mathbf{x}_0 (\mathbf{x}_0 stands for the unit vector along the x-axis; similarly, \mathbf{y}_0 is the unit vector along the y-axis), i.e.,

$$\mathbf{E}(\mathbf{r}, t) = \mathbf{x}_0 E_x(\mathbf{r}) \cos(\omega_0 t) \quad (12.7)$$

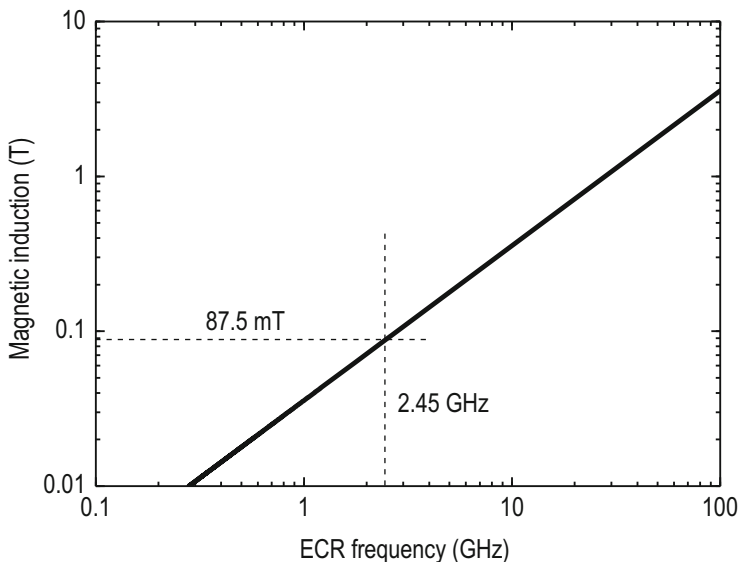


Fig. 12.2 Magnetic induction requirement for fulfilling the ECR condition (Eq. 12.4) at different frequencies. The conventionally pair (2.45 GHz, 87.5 mT) is marked on the plot. (Reproduced from Roth (1995) with the permission of Taylor & Francis Publishing)

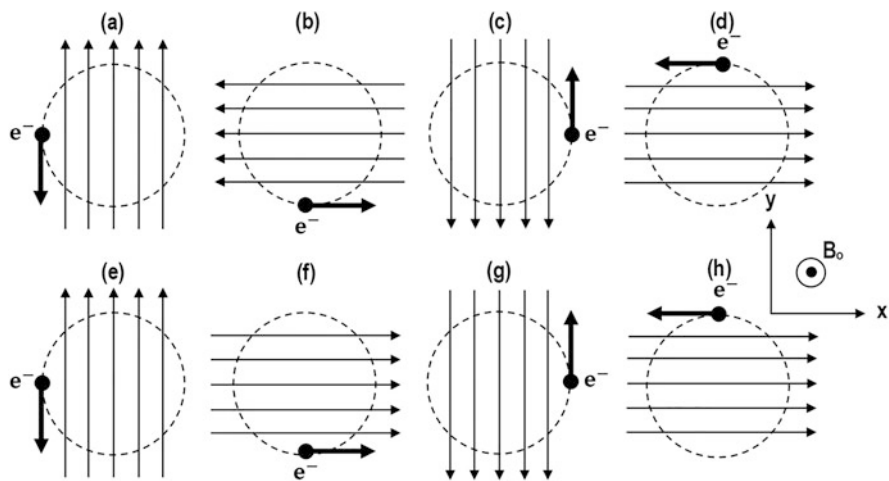


Fig. 12.3 Basic principle of ECR heating. (a–d) Continuous energy gain for the RHP. (e–h) Oscillating energy for LHP: (e) gain; (f) loss; (g) gain; (h) loss. (Reproduced from Lieberman and Lichtenberg (2005) with the permission of John Wiley & Sons Publishing)

where the complex amplitude E_x is here taken to be pure real, the resulting expression is

$$\mathbf{x}_0 E_x = (\mathbf{x}_0 - j \mathbf{y}_0) E_r + (\mathbf{x}_0 + j \mathbf{y}_0) E_l \quad (12.8)$$

where E_r and E_l are the amplitudes of the RHP and LHP waves, respectively, with $E_r = E_l = E_x/2$. Then electric field vector of the RHP wave rotates in the right-hand sense around the magnetic field at a frequency ω_0 while an electron in a uniform magnetic field B_0 also gyrates in a right-hand sense at a frequency ω_{ec} . Thus, as shown in Fig. 12.3a–d, for $\omega_{ec} = \omega_0$, the force $\mathbf{F}_E = -e\mathbf{E}$ accelerates the electron along its circular orbit, resulting in a continuous transverse energy gain. On the other hand, as shown in Fig. 12.3e–h, the LHP wave field produces an oscillating force whose time average is zero, resulting in no energy gain.

From a practical point of view, a typical setup for generating power microwaves for ECR heating is presented in Fig. 12.4. In this figure, the microwave power delivery is based on a conventional 2.45 GHz magnetron system. More details on the individual components can be found in previous references (Roth 1995). Nowadays, solid-state, fully controllable microwave power supplies are available (e.g., Sairem Ltd.).

Apart from the microwave power supply and control, determinant factors for the properties of the generated ECR plasmas are the magnetic field configuration adopted and the vacuum chamber dimensions which in the case of the microwave radiation are comparable with the corresponding wavelength (i.e., ≈ 12.23 cm at 2.45 GHz) and in turn, may raise impedance matching issues (Asmussen and Mak 1994). In Sect. 12.3, where existing negative ion sources are presented, different designs are demonstrated. Particularly, as regard the magnetic field configuration, Fig. 12.5 illustrates typical multipolar magnetic field cusp configurations, which can reduce wall losses and increase plasma density.

In Fig. 12.5a a picket fence multipolar cusp is generated by a series of current-carrying wires on the outside of a vacuum vessel wall (Roth 1995). Adjacent conductors have equal currents flowing in opposite directions. The same configuration can also be generated (and usually is) by a row of permanent magnets. The confined plasma will be kept away from the vessel wall by the increasing magnetic field, with some particles lost along the line cusp which contacts the wall halfway between the conductors (Roth 1995). In the case of volume production negative ion sources, the negative ion yield is benefited by the trapping of high energy electrons in the magnetic field lines, as is discussed later. It is usual practice to put water cooling lines outside the vacuum vessel halfway between the conductors, where the cusp deposits the plasma constituents with their accompanying heat load.

Multipolar cusp confinement can be designed by small permanent magnets too, and Fig. 12.5b–d shows four different ways (Roth 1995). Figure 12.5b shows the checkerboard array which produces cusps both axially and azimuthally, with the plasma axis pointing upward. Figure 12.5c is an axisymmetric cusp array that gives a series of axisymmetric cusps along the axial length of the vacuum vessel wall. In Fig. 12.5d there is the longitudinal cusp array, which gives a series of longitudinal cusps which vary in azimuth as one moves around the circumference of the vessel,

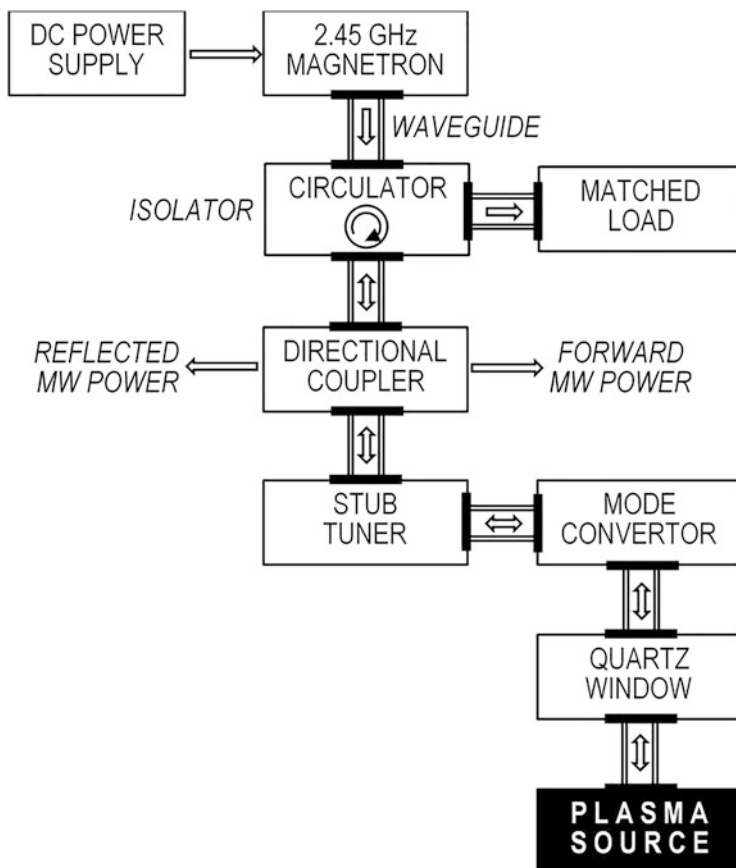


Fig. 12.4 Conventional concept of the major components of an ECR-driven plasma source. The role of the individual components is discussed in (Roth 1995). (Reproduced from Roth (1995) with the permission of Taylor & Francis Publishing)

but with little or no axial variation. Finally, Fig. 12.5e refers to a longitudinal cusp array, where the multipolar cusp confinement is achieved by parallel rows of permanent magnets located on the exterior periphery of the cylindrical portion of the vacuum chamber.

A special design of ECR configuration is shown in Fig. 12.6. In this case the magnetic fields are not adjacent to the vessel walls as in Fig. 12.5. The design for each elementary plasma source is based on multi-dipolar plasma principles (Lacoste et al. 2002). The plasma source is made up of two main parts, i.e., a permanent magnet with an azimuthal symmetry around its magnetization axis and a microwave applicator constituted by a coaxial line, parallel to the magnetization vector and open on the rear pole of the magnet. In the design proposed in Fig. 12.6, the inner conductor of the coaxial line penetrates inside the cylindrical magnet through a hole drilled on its axis. The magnets are completely encapsulated in a

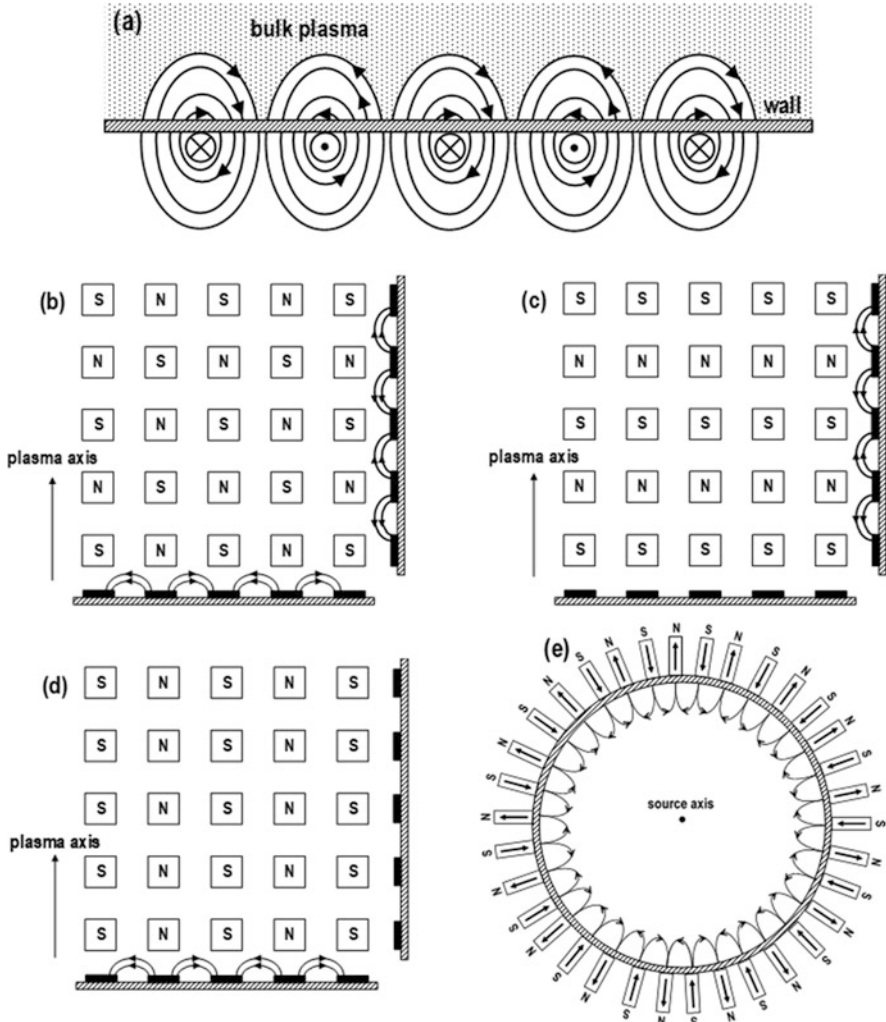


Fig. 12.5 Different magnetic field configurations: (a) picket fence multipolar magnetic field; (b) checkerboard array; (c) axisymmetric cusp array; (d) longitudinal cusp array; (e) longitudinal cusp array multipolar magnets for confinement of cylindrical microwave plasmas. (Reproduced from Roth (1995) with the permission of Taylor & Francis Publishing)

metallic (stainless steel) envelope and water-cooled by using the inner tube inside the magnet. The microwave power can thus be transmitted without loss to the region of the ECR coupling in front of the rear pole of the magnet with the help of a coaxial line: there is no possibility for microwaves to be absorbed by the plasma before reaching the ECR coupling region or to radiate toward an adjacent elementary source. Therefore, there is no possibility of interference between the elementary

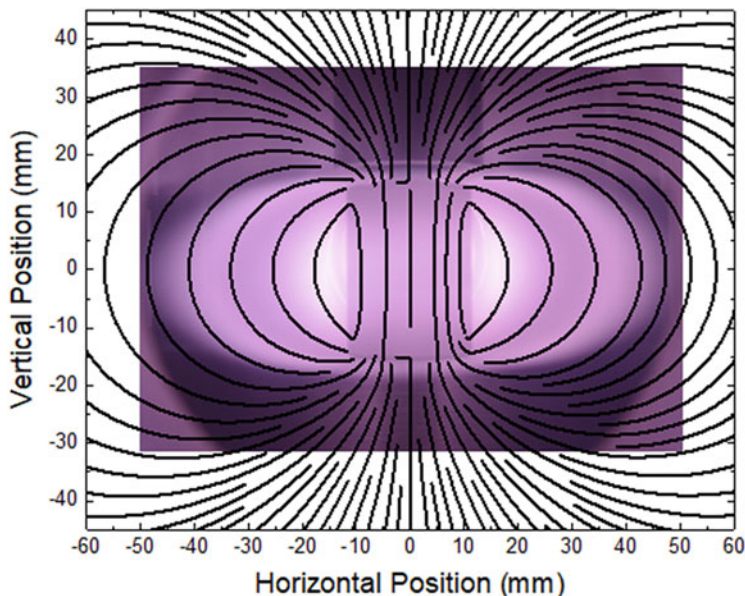


Fig. 12.6 ECR elementary module driving low-pressure H_2 plasma. The encapsulated permanent magnet is surrounded by the ECR zone and the opening of the microwave applicator on its rear pole is distinguished. The streamlines of the simulated magnetic field are superimposed. (Reproduced from Aleiferis et al. (2018) with the permission of IOP Publishing)

sources. In addition, as these elementary sources are at the ground potential, arcing does not appear between them and the reactor walls. Therefore, large-size uniform plasmas can be obtained by assembling as many elementary plasma sources as necessary in a two-dimensional network. These elementary plasma sources can be assembled in different ways, e.g., networks of elementary plasma sources with alternate or identical magnetic polarities, rectangular or hexagonal networks, or other combinations.

12.2 H^- and D^- Negative Ion Production and Destruction Processes in ECR-Driven Plasmas

The development of modern negative ion sources started in the 70s with the discovery of two important negative ion formation processes, namely (Bacal 2006; Bacal et al. 2021): (i) surface production and (ii) volume production. The first process refers to the so-called resonant tunneling ionization and this is based on anion formation on low-work function surfaces, which are typically metals covered by a (sub-micro)layer of an alkali element (e.g., cesium). The second process is mainly due to dissociative electron attachment (DA) of low energy electrons to

Table 12.1 Tabulation of main reactions for the volume production and destruction of H^- negative ions. Principal ones are highlighted in gray. Equivalent reactions are valid in the case of D^- negative ions

Production		
$e + H_2(X^1\Sigma_g^+;v) \rightarrow H_2 \rightarrow H + H^-$	Dissociative electron attachment: DEA	Bardsley et al. (1979); Celiberto et al. (2001)
$e + H_2^+ \rightarrow H^+ + H^-$	Dissociative recombination: DR	Bacal and Wada (2020); Peart et al. (1975)
$e + H_3^+ \rightarrow H_2^+ + H^-$	Dissociative recombination: DR	Bardsley and Wadehra (1979)
$e + H_2(v,J) \rightarrow H^- + H^+ + e$	Polar dissociation	Bardsley and Wadehra (1979)
$H_2 + H_2^+ \rightarrow H^- + H + 2H^+$	Ion-molecule collisions	Bardsley and Wadehra (1979) (by analogy
$H_2 + H_2^+ \rightarrow H^- + H^+ + H_2^+$		with reactions in D_2)
Destruction		
$H^- + H \rightarrow H_2 + e$	Associative detachment: AD	Miller (2012)
$H^- + H \rightarrow H_2(v) + e$	Associative detachment (AD) with creation of vibrationally excited molecules	Graham (1995)
$H^- + H \rightarrow 2H + e$	Non-associative detachment: non-AD	Javen et al. (2003)
$H^- + e \rightarrow H + 2e$	Electron detachment: ED	Javen et al. (2003)
$H^- + H_2(v) \rightarrow H_2(v-2) + H + e, 2 \leq v \leq 6$	Electron detachment in collisions with vibrationally excited molecules: EDV	Yang et al. (2018); Dem'yanov et al.(1985)
$H^- + H_2 \rightarrow H_2 + H + e$	Collisional detachment: CD	Huq et al. (1983)
$H^- + H^+ \rightarrow 2H$	Mutual neutralization: MN	Yang et al. (2018); Eerden et al. (1995)
$H^- + H^+ \rightarrow H + H(n=2, 3)$		Yang et al. (2018); Matveyen & Silakov (1995)
$H^- + H_2^+ \rightarrow H_2 + H$		Yang et al. (2018); Matveyen & Silakov (1995)
$H^- + H_2^+ \rightarrow 3H$		Yang et al. (2018); Eerden et al. (1995)
$H^- + H_2^+ \rightarrow H + H_2(v)$		Graham et al. (1995)
$H^- + H_3^+ \rightarrow 2H_2$		Yang et al. (2018); Matveyen & Silakov (1995)
$H^- + H_3^+ \rightarrow 4H$		Yang et al. (2018); Eerden et al. (1995)
$H^- + H_3^+ \rightarrow 2H + H_2(v)$		Graham et al. (1995)

(ro)vibrationally excited molecules. Although the two processes may coexist in a negative ion source, the first dominates in cesiated sources and the second in cesium-free, volume production sources. The design of the negative ion sources operating with molecular hydrogen (H_2) or deuterium (D_2) to yield the corresponding ions (H^- or D^-) has been extensively based on both concepts (surface and volume production). Reviews of this task can be found in the literature (Bacal and Wada 2015, 2020). That said, regarding the available ECR-driven sources, they are mostly based on the volume production mechanisms. Various H^- or D^- ion production and destruction paths are possible in volume production sources. Table 12.1 summarizes some of them and the principal ones are highlighted in gray.

Regarding the main production path, i.e., DEA, Fig. 12.7 shows the associated cross section. In both H_2 and D_2 gases, the cross sections peak at relative low energy electrons, whereas it increases for diminishing energy. Such low energy electrons are readily produced in the ECR sources as part of bi-Maxwellian electron energy distribution functions (EEDFs), as it will be discussed below in case studies.

On the other hand, DEA reaction necessitates the existence of (ro)vibrationally excited molecules. Table 12.2 presents the (de)excitation paths of these molecules and the dominant ones are highlighted in gray. Vibrational excitation of molecules

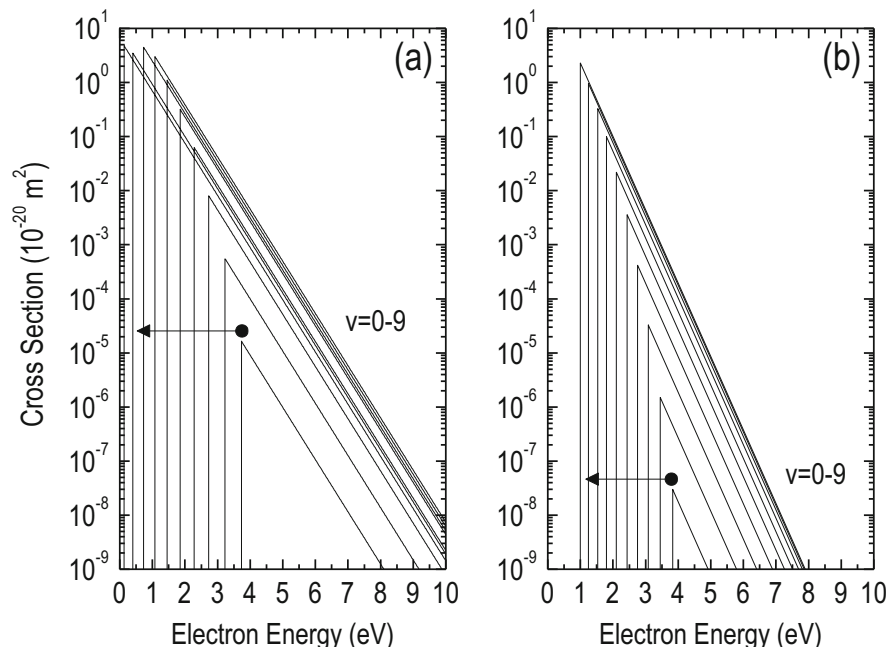


Fig. 12.7 Cross sections of the DEA reaction in the case of (a) H_2 and (b) D_2 . The curves are plotted according to the available data Tables in Ref. (Celiberto et al. 2001)

in collisions with low energy electrons (eV excitation) is effective in changing the vibrational state (Capitelli et al. 2006), but the most probable change in v is $\Delta v = \pm 1$ (Bacal 2006). A high collision rate or low vibrational de-excitation rate would thus be required to significantly populate the spectrum. In addition, apart from this change of vibrational level by one, eV excitation results in an equilibrium of lower vibrational levels (Capitelli et al. 2006; Mosbach 2005).

Conversely, the predominant channel for the formation of highly vibrationally excited molecules is related to excitation to singlet electronic states followed by spontaneous emission (EV excitation) (Hiskes 1980). The cross sections involved in the EV excitation, both in H_2 and D_2 , are given in Fig. 12.8, while Franck-Condon factors are presented elsewhere (Fantz and Wunderlich 2006). High-energy electrons are a prerequisite for excitation. Thus, while DEA entails low energy electrons, at the same time it implies the need for high energy electrons since (ro)vibrationally excited molecules are precursors of the reaction itself. As will be discussed below (see also Béchu et al. 2013), ECR plasmas are capable of providing such dual populations (i.e., cold and hot) in a spatially resolved manner.

A challenging effect relative to volume production is the formation of the H_2 and D_2 excited molecules through wall processes (Harris and Kasemo 1981; Rutigliano et al. 2001; Rutigliano and Cacciatore 2011), instead of reactions in the bulk plasma. Two vibrational excitation processes have been identified: (i) production

Table 12.2 Tabulation of main reactions for the population and de-excitation of vibrational states in H_2 . Principal ones, discussed in this chapter, are highlighted in gray. Equivalent reactions are valid in the case of D_2 ions

Excitation		
$H_2(X^1\Sigma_g^+, v_i) + e \rightarrow H_2(X^1\Sigma_g^+, v_f) + e, v_f > v_i$	Resonant electron-vibration excitation: eV	Capitelli et al. (2006)
$H_2(X^1\Sigma_g^+, v_i) + e \rightarrow H_2(B^1\Sigma_u^+, C^1\Pi_u) + e \rightarrow H_2(X^1\Sigma_g^+, v_f) + e + h\nu, v_f > v_i$	Radiative decay and excitation: EV	Celiberto et al. (2001)
4 steps reactions	Recombination and dissociation of ions H_2^+ and H_3^+ on surfaces	Hiskes and Karo (1990)
$H + H(\text{wall}) \rightarrow H_2(v)$	Recombinative desorption: RD	Hall et al. (1988); Jackson and Lemoine (2001)
De-excitation		
$H_2(v_i) + H \rightarrow H_2(v_f) + H, v_f < v_i$	Vibrational-translational relaxation in collisions with atoms: V-t	Yang et al. (2018); Gordiets et al. (1998)
$H_2(v_i) + H_2(v_j) \rightarrow H_2(v_i) + H_2(v_j-1)$	Vibrational-translational relaxation in collisions with molecules: V-T	Matveyev and Silakov (1995)
$H_2(v_i) + \text{wall} \rightarrow H_2(v_f), v_f < v_i$	Wall relaxation: WD	Yang et al. (2018); Hiskes and Karo (1989)

of vibrationally excited molecules due to the recombination of molecular hydrogen ions on the walls (Hiskes and Karo 1990), and (ii) production of a wide spectrum of rovibrationally excited molecules in the recombinative desorption process of atomic hydrogen on some metal surfaces (Hall et al. 1988). The surface recombination mechanisms can be of three generic types (Kolasinski 2019; Cacciatore and Rutigliano 2008, 2009): (i) Langmuir-Hinshelwood (thermal diffusion of two adsorbates) (Baxter and Hu 2002; Morisset et al. 2004) and, more importantly in terms of energy deposition into the formed molecules, (ii) Eley-Rideal (direct impact of an atom from the plasma with an adsorbate) (Eley and Rideal 1940), and (iii) hot-atom reactions (indirect collision consisting of several encounters with the surface and adsorbates) (Kammler et al. 2000). The hot-atom reactions replace in some cases the Eley-Rideal mechanism when a gas-phase atom incident on a surface combines with a particle adsorbed onto that surface. ECR-based experiments designed for exploiting these mechanisms are illustrated in the next section.

Instead, Fig. 12.9 presents the cross section of one of the main destruction reactions (Table 12.1), i.e., electron detachment (ED). Considering the above discussion on the necessity of high energy electrons to produce excited molecules, which in turn lead to negative ion production in volume sources, and the fact that ED becomes more probable when electrons of similar energies (i.e., around 20 eV) are present, it is evident that a complicated balance between various species should be considered to unfold the physics of volume sources. In the next sections, case studies of operating ECR sources are given, supporting all the statements and concepts analyzed now. Finally, it is underlined that the volumetric rates of both the production and destruction processes depend strongly on the electron energy distribution functions.

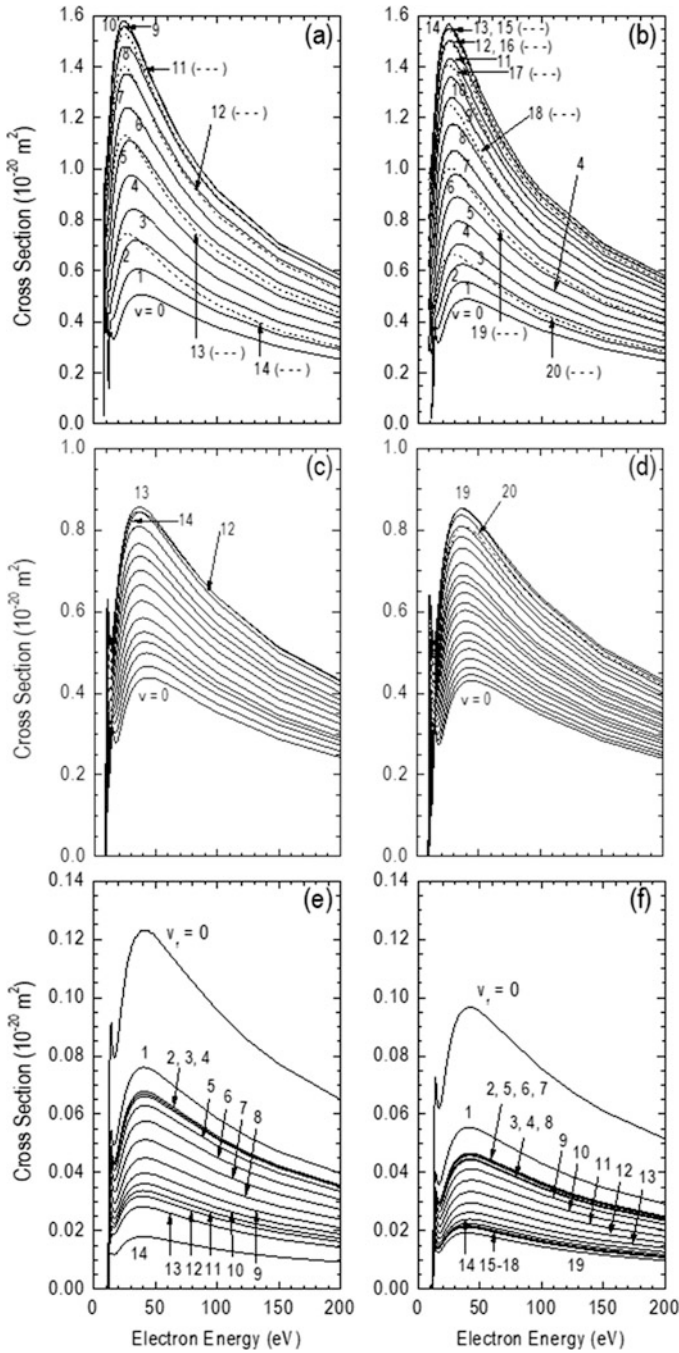


Fig. 12.8 Cross sections related to the EV process: (a) $\text{H}_2(X^1\Sigma_g^+; v_i) + e \rightarrow \text{H}_2(B^1\Sigma_u^+) + e$; (b) $\text{D}_2(X^1\Sigma_g^+; v_i) + e \rightarrow \text{D}_2(B^1\Sigma_u^+) + e$; (c) $\text{H}_2(X^1\Sigma_g^+; v_i) + e \rightarrow \text{H}_2(C^1\Pi_u) + e$; (d) $\text{D}_2(X^1\Sigma_g^+; v_i) + e \rightarrow \text{D}_2(C^1\Pi_u) + e$; (e) $\text{H}_2(X^1\Sigma_g^+; v_i) + e \rightarrow \text{H}_2(B^1\Sigma_u^+, C^1\Pi_u) + e \rightarrow \text{H}_2(X^1\Sigma_g^+; v_f) + e + h\nu, v_f > v_i = 0$; (f) $\text{D}_2(X^1\Sigma_g^+; v_i) + e \rightarrow \text{D}_2(B^1\Sigma_u^+, C^1\Pi_u) + e \rightarrow \text{D}_2(X^1\Sigma_g^+; v_f) + e + h\nu, v_f > v_i = 0$. The curves are plotted according to the available data Tables in Ref. (Celiberto et al. 2001)

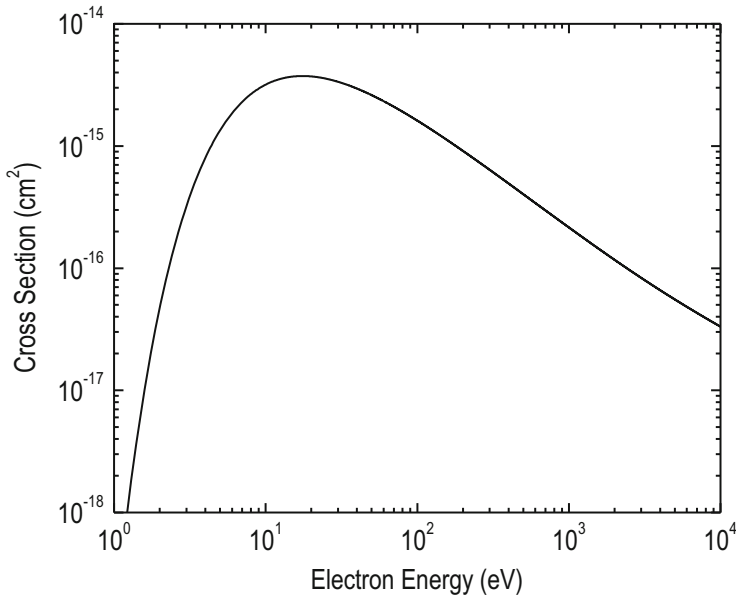


Fig. 12.9 Cross section of the electron detachment (ED) reaction in hydrogen, according to analytic fit equation. (Janev et al. 2003)

12.3 Representative H^- and D^- Negative Ion Sources

In this section, following the aforementioned presentation on the ECR heating concept and the reactions that rule the negative ion volume production, representative ECR-driven sources that have provided numerous experimental results are considered. Different designs and a wide variety of operational windows are discussed. Selected results are reviewed and analyzed, unveiling the main features and the capacity of the ECR volume sources.

Such results have been obtained by means of various tailored diagnostics. In general, the diagnostics employed for the plasma interrogation with respect to the ECR source principles, refer both to the charged species and excited neutral probing. Thus, principal techniques include the following: (i) Electrostatic probes for measurements of the plasma potential, plasma density, electron temperature, and EEDFs (Godyak and Demidov 2011); (ii) Laser-induced photo-detachment for measurements of the negative ion H^- and D^- density (Bacal 2000); (iii) Optical emission spectroscopy for recording atomic and molecular transitions, and thus relative densities of neutral species (e.g., degree of dissociation) (Fantz 2006); (iv) VUV spectroscopy for accessing molecular plasma processes, including volumetric rates of ionization, dissociation and excitation to high vibrational levels and metastable states (Komppula et al. 2015); (v) Laser-induced fluorescence spectroscopy to measure the densities of rovibronically excited molecules (Mosbach

2005); (vi) VUV Fourier transformer absorption spectroscopy based on synchrotron radiation for direct measurements of electronic ground state ro-vibrationally excited molecules in ECR plasmas (Béchu et al. 2020).

12.3.1 *Camembert III*

The source Camembert III is a large volume negative ion source, driven at 2.45 GHz microwave power. It is composed of three main elements: (i) A magnetic multipole chamber (Courteille et al. 1995), having a configuration like that shown in Fig. 12.5e. Briefly, the sidewall of the cylindrical stainless-steel chamber is 44.0 cm in diameter and 45.0 cm in height. Sixteen columns of samarium-cobalt magnets (3.5 kg on their surface) are installed with the “N” and the “S” poles alternatively facing the plasma. These magnets are contained in water-cooled stainless-steel tubes ($\varnothing 2.6$ cm) welded to the internal surface of the source to allow steady-state, high-power discharge operation. The plasma diameter is therefore 38.8 cm (approximately). The end plates are not magnetized. One end of the chamber is bounded, in part, by the stainless-steel plasma electrode (PE; $\varnothing 10$ cm) of the extractor, which contains an extraction hole of $\varnothing 0.8$ cm, and in part by a water-cooled annular copper plate. This plate is connected to the plasma chamber sidewall, which is grounded. The neighboring plasma is magnetized and due to this and to a small positive bias of the plasma electrode, large densities of volume produced negative ions concentrate in this region. This fact is illustrated by the experimental results below. (ii) A two-dimensional network of seven elementary independent plasma sources like those of Fig. 12.6. The network is installed on the top flange of the source. Six of the seven modules form an imaginary circle and are mounted on its circumference (per 60 degrees) in such a way that “N” poles face the plasma, whereas the seventh module is mounted in the center of the circle with its “S” pole facing the plasma. (iii) An ion- and electron-extraction system of four electrodes (Bacal et al. 1985), including the plasma electrode which is in contact with the plasma, as mentioned above.

Due to this configuration, three regions may be distinguished. (i) A driven region, which is located near the network of the seven elementary ECR sources and, possibly, on the periphery of the chamber within the strong multi-cusp magnetic field. In this region, the plasma is produced by the electrons accelerated in the ECR coupling area due to the microwave electric field applied via the coaxial lines (Fig. 12.6). These fast-hot electrons oscillate within two field lines and two mirror points in front of the opposite poles of the magnet, and drift azimuthally around the magnet acting as a tri-dimensional magnetron structure. The EEDFs can be assumed to be the sum of this hot electron population and another cold electron population, with Maxwellian distribution functions (see Sect. 12.3.2). The plasma produced by the inelastic collisions of the hot electrons along their itinerary then diffuses away from each magnet. The hot electrons remain trapped in the magnetic field, whereas the excited molecules and the cold population of electrons diffuses

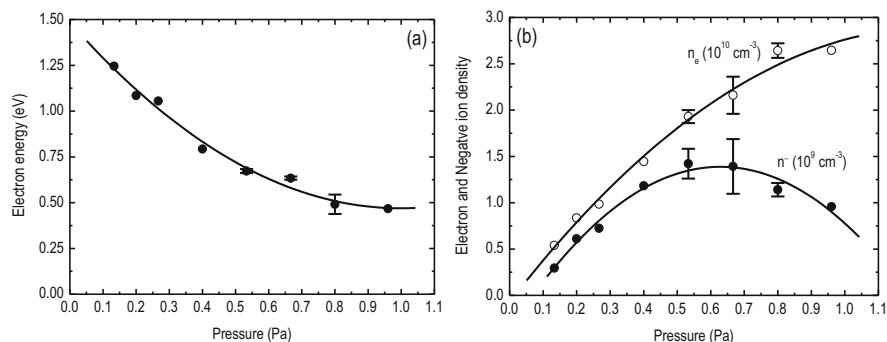


Fig. 12.10 Basic plasma parameters, as a function of the operating hydrogen pressure, in the source Camembert III. **(a)** Cold electron energy. **(b)** Cold electron density (\circ); Negative ion H^- density (\bullet). (Reproduced from Svarnas et al. (2006) with the permission of AIP Publishing)

away from the magnetic field under the influence of density gradients and the resulting space charge electric field (Lagarde et al. 2001). (ii) A production region, which extends over the central magnetic field free region. Here, the diffused excited molecules and the cold electrons lead to enhanced DEA process. Finally, (iii) a near-extractor region, where a weakly magnetized region is bounded by the plasma electrode. This magnetic field is the stray magnetic field originating in the rear of the magnets located within the extractor. Its maximum value is 20 G at 10 mm above the plasma electrode surface.

Figure 12.10 provides values of the main plasma parameters as a function of the working pressure during the source operation with hydrogen (0.9 kW). The main part of the plasma density refers to cold electrons. Densities up to about $3 \times 10^{10} \text{ cm}^{-3}$ are achieved in the production region (ii). At the same time, the electron temperature lies within the range demanded for efficient DEA (compare Figs. 12.7a and 12.10a). H^- ion densities up to about $1.5 \times 10^9 \text{ cm}^{-3}$ are yielded. The latter passes through a maximum at around 0.6 Pa and this has been correlated with the loss of vibrationally excited species due to VT process (Svarnas et al. 2006).

In this source, the weakly magnetized region (iii) has been studied extensively by varying the plasma electrode bias and observing the resultant effects on the local plasma parameters and the extracted currents (Svarnas et al. 2007). It is seen (Fig. 12.11a) that, the plasma electrode current increases monotonously versus the plasma electrode potential. Optimization of the source appears possible for bias values slightly higher (typically 1 V) than the local plasma potential (typically 4 V to 6 V). At that point, the extracted electron current decreases sharply, and the extracted H^- ion current peaks. The correlation of this peak with the plasma parameters measured in the region (iii) is illustrated in Fig. 12.11b. In this figure, the electron-to-negative ion density ratio matches the electron-to-negative ion extracted current ratio for variable plasma electrode bias.

In more detail (Svarnas et al. 2007), the decrease in the extracted electron current is the result of the depletion of the electron population by the positively biased

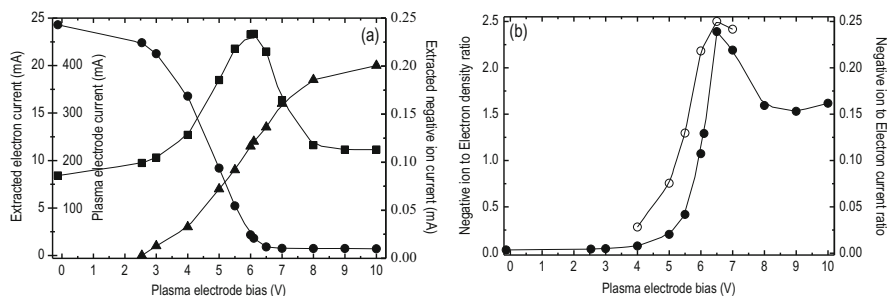


Fig. 12.11 Dependence on the plasma electrode bias of the: (a) plasma electrode current (▲), extracted electron current (●), and extracted negative ion current (■) at 0.27 Pa; (b) ratios of the negative ion to electron densities (○) and the negative ion to electron extracted currents (●) at 0.27 Pa and 0.75 cm above PE. (Reproduced from Svarnas et al. (2007) with the permission of IEEE Publishing)

plasma electrode. The weak magnetic field in front of this electrode prevents the replacement of these depleted electrons by new electrons arriving from the bulk plasma. This disturbs the local plasma neutrality and thus other negatively charged species should replace the depleted electrons. Therefore, the volume produced H^- negative ions, originating in the production region (ii), arrive within the magnetized region over the positively biased plasma electrode. As far as the bias level breaks the local plasma potential, the H^- ions are no longer electrostatically trapped and can thus be extracted. The maximum extraction is obtained at about 1 V above the plasma potential. When the bias increases further, the volume produced H^- ions are accelerated towards the plasma electrode and the H^- ion velocity increases over the plasma electrode. The H^- ion residence time decreases due to the larger velocity and the H^- ion density goes down. Eventually, H^- ions can be collected by the plasma electrode.

Figure 12.12 compares directly the H^- ion densities between the regions (ii) (15 cm above the plasma electrode) and (iii) (0.75 cm above the plasma electrode) and the corresponding extracted current, over the entire range of the operating pressure. Two points are stressed. Firstly, the H^- ion extracted current can only be correlated with the related H^- ion density close to the extraction aperture and not with the one yielded far away from this. Secondly (not shown here), the mentioned role of the stray magnetic field over the extraction aperture is critical, since it leads to an enhanced negative ion-to-electron density ratio, as compared to the values obtained at longer distances where this magnetic field is negligible.

12.3.2 *Prometheus I*

The source Prometheus I (Aleiferis et al. 2016, 2018) consists of a cubic (240 mm inner edge) stainless steel chamber with the necessary viewports for plasma diag-

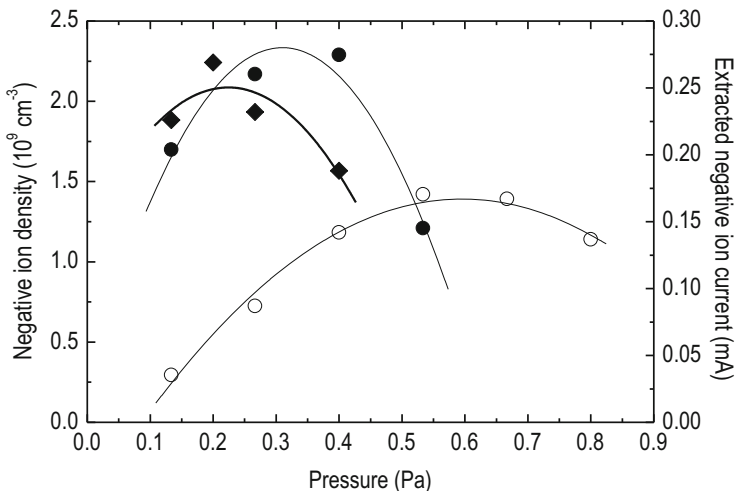


Fig. 12.12 Correlation between the negative ion density and the corresponding extracted current, for variable operating pressure in hydrogen. H^- negative ion density at 15 cm (\circ) and 0.75 cm (\bullet) above the plasma electrode surface, and extracted negative ion current (\blacklozenge). (Reproduced from Svarnas et al. (2007) with the permission of IEEE Publishing)

nostics. The plasma is sustained by a 2D network of five ECR plasma elementary sources like those shown in Fig. 12.6. Four sources are installed at the vertices and the fifth at the center of an imaginary square (160 mm side length) on the top flange of the high vacuum chamber. The four permanent magnets face the plasma with their “S” poles and the fifth with its “N” pole. Each elementary source is driven by an independent microwave solid-state power supply (2.45 GHz) able to provide up to 180 W. A tuner embedded on the main body of each source is used for impedance matching which maximizes the microwave power absorbed by the plasma. The elementary sources and their power supplies are cooled by water which is circulated by a closed system. The source operates either with hydrogen (H_2) or deuterium (D_2), within a pressure range between 0.13 and 2.67 Pa.

Figure 12.13 shows that two electronic populations are produced due to ECR heating, a “cold” and a “hot” one, having about one order of magnitude difference in their temperatures. At the same time, Fig. 12.14 gives the absolute density values of these populations, unveiling a difference of about two orders of magnitude in favor of the cold population. These measurements are carried out 65 mm downstream of the ECR zone middle planes (Mitrou et al. 2022). The hot population downstream of the ECR zones is a fingerprint of the energetic electrons generated in these zones, whereas the cold population refers to the electrons escaping these zones (Lagarde et al. 2001). The former promotes ro-vibrational excitation of molecules (EV reaction) which eventually diffuse away from the heating zones. The latter promotes H^- and D^- ion production through the dissociative attachment (DA) reaction, between them

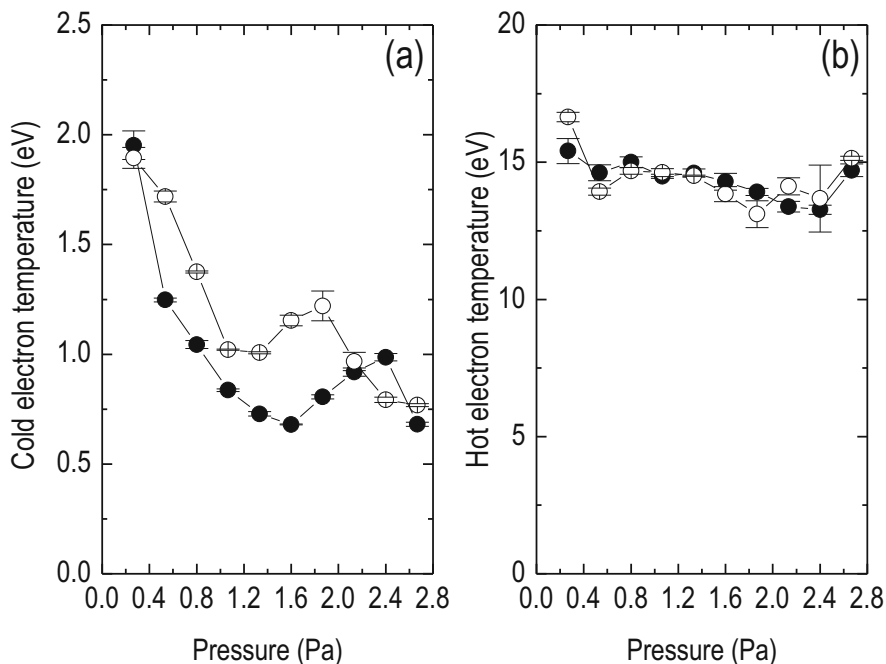


Fig. 12.13 (a) Cold and (b) hot electron temperature versus the operating gas pressure. • H₂; ○ D₂; 0.9 kW. (Reproduced from Mitrou et al. (2022) with the permission of IOP Publishing)

and the diffused excited molecules, in the source volume. The densities of both populations tend progressively to a quasi-saturation as the gas pressure increases.

On the other hand, Fig. 12.15a makes a direct comparison between the negative ion yields achieved in the two gases (Mitrou et al. 2022). At a first glance, H⁻ and D⁻ densities have a qualitatively and quantitatively similar evolution as a function of the operating pressure, i.e., a sharp increase is followed by a quasi-saturated phase. Despite that, an obvious isotope effect is exhibited by a different presentation of the data. In Fig. 12.15b the relative negative ion density is given, unveiling a strong isotope effect in support of the H⁻ ions and a sharp optimum of around 1.33 Pa in both gases (Mitrou et al. 2022). On the top of that, Fig. 12.16a compares the H⁻ and D⁻ densities under equal plasma density (cold electrons), following pressure elimination (Mitrou et al. 2022). Higher values for the H⁻ ion density, are observed. The corresponding curves versus the hot electrons (Fig. 12.16b) are associated with closer experimental points in the two gases.

Further insight into this source operation has been achieved by varying the microwave power injected by the five ECR modules, up to 0.9 kW, for three different pressures (0.53, 1.07, and 1.60 Pa). Regarding the plasma potential, higher values are measured, in both H₂ and D₂ gases, as the power increases and the pressure decreases. However, it appears higher (up to about 2 V) in the case of D₂ gas,

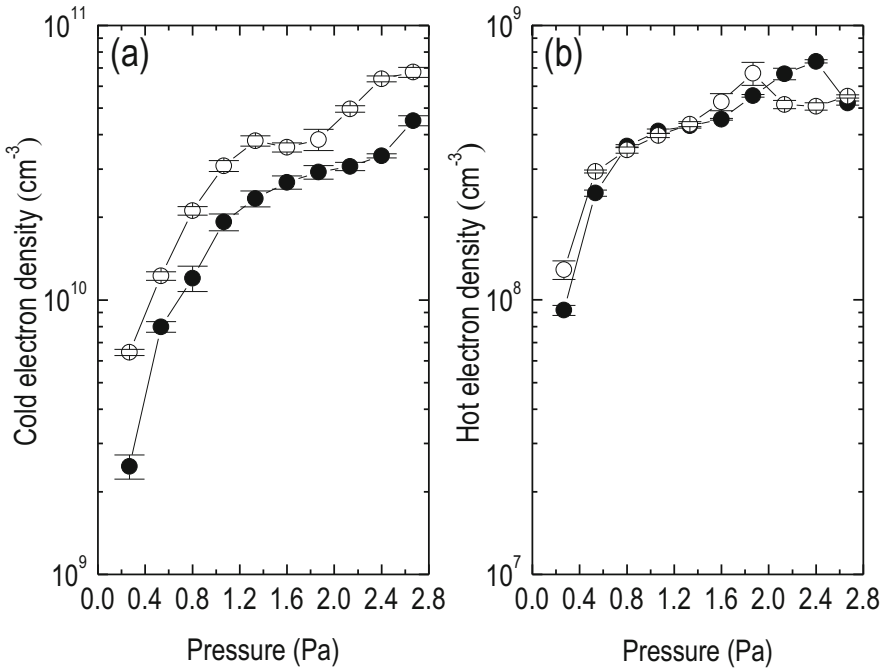


Fig. 12.14 (a) Cold and (b) hot electron density versus the operating gas pressure. • H₂; ◊ D₂; 0.9 kW. (Reproduced from Mitrou et al. (2022) with the permission of IOP Publishing)

independently of the pressure and the power. Then, similar to the results of Fig. 12.13a, deuterium is associated with higher cold electron energies than hydrogen does, and this energy increases in a non-monotonic way versus the power. Regarding the hot electron population, values between 14 and 16 eV are constantly recorded, as in Fig. 12.13b. On the other hand, both cold and hot electron densities increase as a function of microwave power, whereas D₂ yields higher densities of cold electrons. The difference in the hot electron density between the two gases is less pronounced. Representative data on these plasma parameters are tabulated below for facilitating the comparison (Table 12.3).

Regarding the H⁻ and D⁻ ion yields, Fig. 12.17 illustrates the density values as a function of the power at different working pressures. In general, the production efficiency in both gases seems comparable, but Fig. 12.18 demonstrates an isotope effect similar to that of Fig. 12.15b. Thus, H₂ promotes higher relative negative ion density under all conditions, and, additionally, an optimal operational window is revealed in both H₂ and D₂. The latter corresponds to an intermediate pressure and power levels. Finally, by eliminating the power and plotting the negative ion density versus the cold or hot electron density, the trends of Fig. 12.16 are reproduced.

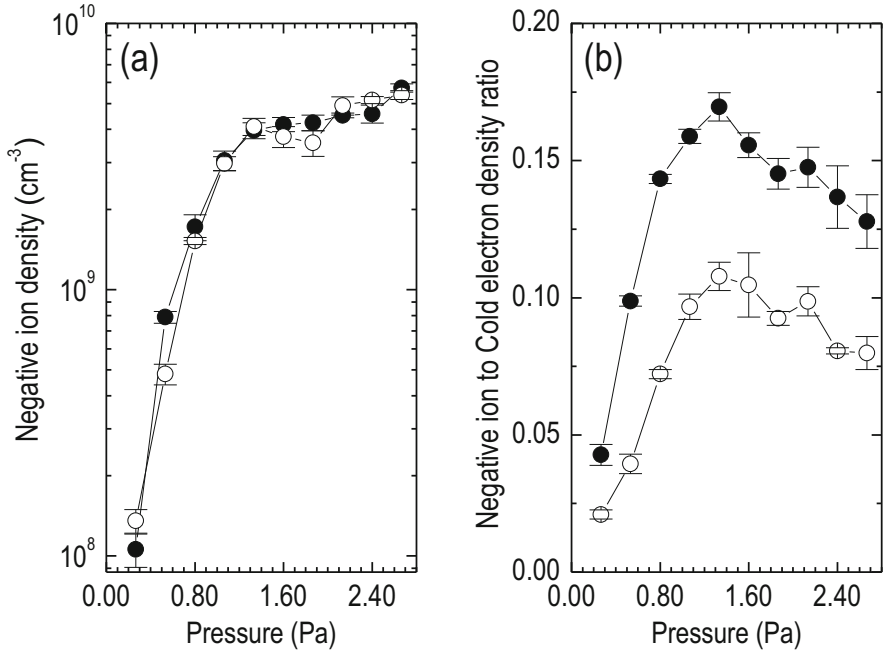


Fig. 12.15 (a) H^- and D^- ion density and (b) H^- and D^- ion to cold electron density ratio, versus the operating gas pressure. • H_2 ; ○ D_2 ; 0.9 kW. (Reproduced from Mitrou et al. (2022) with the permission of IOP Publishing)

12.3.3 ECR with Driven Plasma Rings

An alternative type of ECR source with stratified plasma has been proposed by (Dougra-Jabon et al. 1992) as a good alternative for hydrogen-negative ion production. In this source, a mechanism of electron heating in the resonance zones takes place and leads to ring structure creation. A radial ambipolar electric field emerging between the heating rings and the cold plasma results in the azimuth drift rotation of these rings. It has been found (Dougar-Jabon et al. 1998) that the ring-driven structure is a controlling factor for negative ion production.

The concept of the source is given in Fig. 12.19 and details have been reported previously (Dougar-Jabon et al. 1992, 1998; Dougar-Jabon 2001; Velasco et al. 2015). Briefly, the discharge chamber comprises a 13 cm in diameter and 8 cm long aluminum cylinder, placed axisymmetrically between two identical Sm-Co magnetic poles with a surface magnetization of 1100 G. The magnets create a mirror trap. The magnetic field in the plasma volume is modified by the variation of the distance between the magnets, but its configuration remains of the mirror type. An oscillator of 2.45 GHz excites a microwave field of TE_{111} mode in the chamber volume, whose electrical component is perpendicular to the static magnetic force lines. The fundamental resonance surface and the surfaces corresponding to

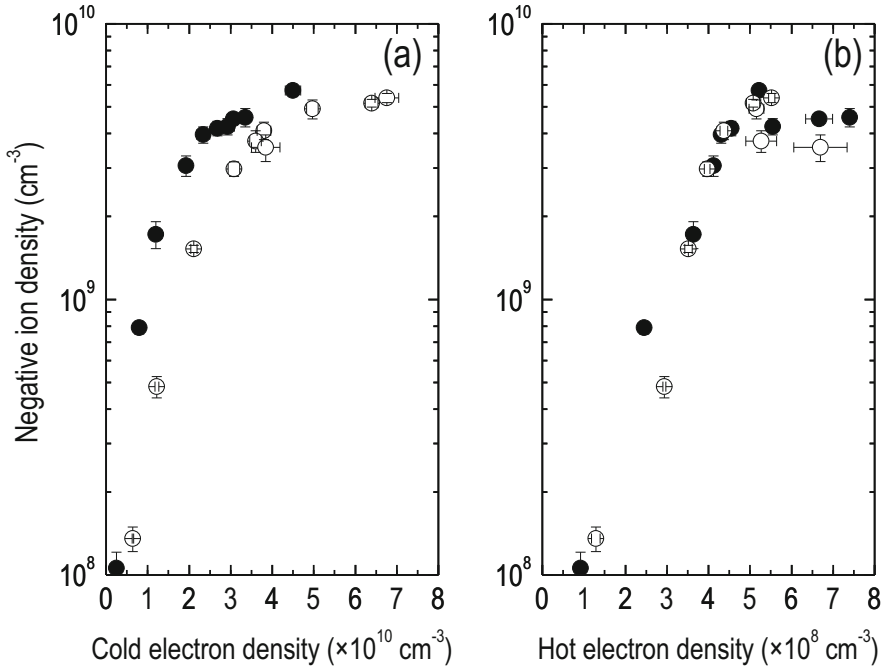


Fig. 12.16 H^- and D^- ion density versus (a) cold and (b) hot electron density. Data pairs are created with pressure elimination. • H_2 ; ○ D_2 ; 0.9 kW. (Reproduced from Mitrou et al. (2022) with the permission of IOP Publishing)

the first three harmonics of the fundamental electron cyclotron frequency shape hyperboloids of one sheet, i.e.,

$$B_{\text{cl},k}(r, z) = \frac{m c \omega}{e k} \quad (12.9)$$

where ω stands for the microwave frequency and $k = 1, 2, 3, 4$. The fundamental resonance ($k = 1$) is observed at the surface $B_{\text{cl},1}(r, z) = 845$ G which has a radius in the midplane of the magnetic trap equal to 1.6 cm (when the space between the poles is 8.9 cm), whereas the radii corresponding to the harmonics $k = 2, 3$, and 4 are 4.3, 5.1, and 6.1 cm, respectively.

Though ECR interaction takes place on the whole surface of the resonance hyperboloids, the energetic electrons are in a stable position only in the midplane of the mirror trap where they form a multiring structure. The cross section of these hyperboloids and the electron rings within the discharge are illustrated in Fig. 12.19. A radial ambipolar electric field emerging between the heated rings and the cold plasma results in azimuth drift rotation of these rings. Rotation speeds are ranged from about 3×10^7 m s $^{-1}$ for the $k = 4$ ring to 2×10^8 m s $^{-1}$ for the $k = 1$ ring. To form an ion beam, a carefully designed extraction system is installed on the source

Table 12.3 Key parameters of the ECR plasma in the source Prometheus I, when it works within different operational windows

	0.53 Pa		1.07 Pa		1.60 Pa	
	H ₂	D ₂	H ₂	D ₂	H ₂	D ₂
0.15 kW						
$V_{\text{pl.}}$ (V)	5.47	6.64	5.37	6.62	5.05	6.54
$T_{\text{e}}^{\text{cold}}$ (eV)	0.63	0.91	0.58	0.74	0.55	0.67
$T_{\text{e}}^{\text{hot}}$ (eV)	10.72	14.12	13.92	15.19	14.39	15.16
$n_{\text{e}}^{\text{cold}}$ (m ⁻³)	1.62×10^{15}	2.65×10^{15}	2.96×10^{15}	4.56×10^{15}	3.29×10^{15}	5.98×10^{15}
$n_{\text{e}}^{\text{hot}}$ (m ⁻³)	5.29×10^{13}	5.66×10^{13}	9.73×10^{13}	1.05×10^{14}	1.12×10^{14}	1.19×10^{14}
0.5 kW						
$V_{\text{pl.}}$ (V)	7.52	8.33	7.01	8.11	6.59	7.91
$T_{\text{e}}^{\text{cold}}$ (eV)	0.91	1.53	0.72	0.96	0.57	0.82
$T_{\text{e}}^{\text{hot}}$ (eV)	15.34	14.12	15.38	15.06	15.72	15.19
$n_{\text{e}}^{\text{cold}}$ (m ⁻³)	4.95×10^{15}	6.70×10^{15}	1.28×10^{16}	1.86×10^{16}	2.09×10^{16}	3.04×10^{16}
$n_{\text{e}}^{\text{hot}}$ (m ⁻³)	1.34×10^{14}	1.77×10^{14}	2.67×10^{14}	2.84×10^{14}	3.27×10^{14}	3.16×10^{14}
0.9 kW						
$V_{\text{pl.}}$ (V)	8.11	10.13	7.72	9.06	7.03	8.49
$T_{\text{e}}^{\text{cold}}$ (eV)	1.28	1.69	0.83	1.02	0.69	1.16
$T_{\text{e}}^{\text{hot}}$ (eV)	15.11	14.31	15.13	14.71	15.01	13.54
$n_{\text{e}}^{\text{cold}}$ (m ⁻³)	7.06×10^{15}	1.39×10^{16}	1.91×10^{16}	3.29×10^{16}	2.82×10^{16}	3.51×10^{16}
$n_{\text{e}}^{\text{hot}}$ (m ⁻³)	2.29×10^{14}	2.79×10^{14}	3.82×10^{14}	3.92×10^{14}	4.36×10^{14}	5.33×10^{14}

(Dougar-Jabon et al. 1998). This is presented in detail elsewhere (Dougar-Jabon et al. 2001). In addition, to create better conditions for negative ion production, the discharge plasma can be enriched with electrons of low energy, due to two systems of heated tungsten filaments 0.3 mm in diameter (Velasco et al. 2015).

The source has been operated with hydrogen and deuterium. The main part of the discharge is occupied by plasma with a volume averaged density of around $5 \times 10^{16} \text{ m}^{-3}$ and an electron temperature of 50–60 eV ($2.66 \times 10^{-2} \text{ Pa}$ of H₂; 200 W) (Dougar-Jabon et al. 1998). Figure 12.20a shows the dependence of the H⁻ and D⁻ currents at a microwave power of 200 W on the gas pressure, when the ring corresponding to the second harmonic of the fundamental electron cyclotron frequency touches the plasma electrode (upper electrode of the extraction system in Fig. 12.19). For both types of negative ions, a maximum is observed within the narrow pressure range of $(2.66\text{--}3.99) \times 10^{-4} \text{ Torr}$. The H⁻ ion current is higher all over the pressure range. In this figure, the experimental conditions regarding the positive ion current are identical with those for the negative ions, with the exception of the extraction voltage polarity. Then, Fig. 12.20b unveils that the intensity of the D⁻ ion beam falls faster than the H⁻ one as the microwave power is diminished. This keeps true for the entire pressure range of Fig. 12.20a. Finally, Fig. 12.20c gives the H⁻ and D⁻ ion extracted current as a function of the plasma electrode immersion depth into the discharge chamber (up to 1.3 cm). These curves show clearly that the generation of both H⁻ and D⁻ ions with a high efficiency does not take place until one of the rotating rings enters into direct contact with the plasma electrode. The

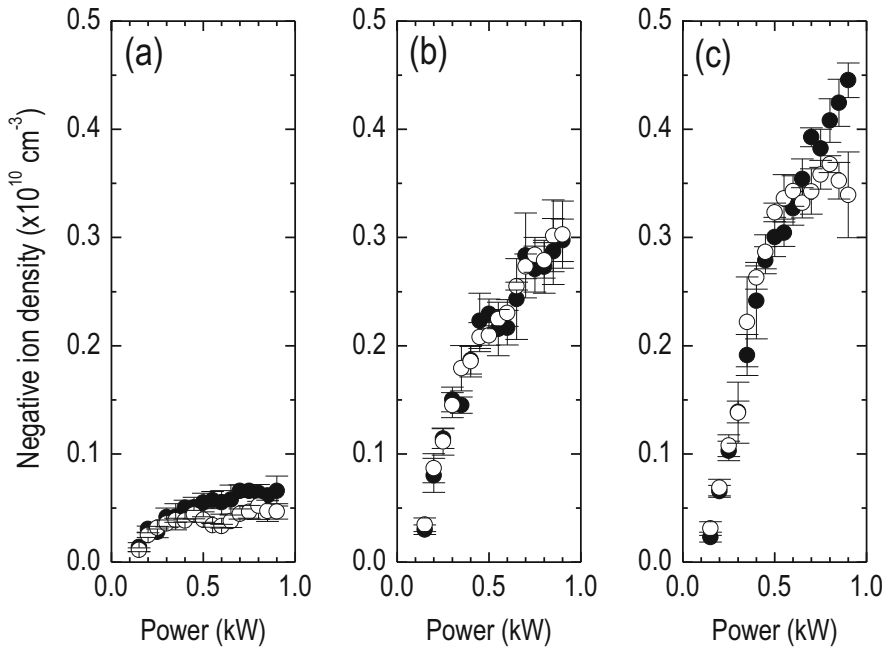


Fig. 12.17 Negative ion density as a function of the microwave power at (a) 0.53 Pa, (b) 1.07 Pa, and (c) 1.60 Pa. Solid circles: H_2 plasma. Open circles: D_2 plasma

peaks for $k = 3$ and $k = 4$ illustrate cases when the plasma electrode comes into contact with the respective cyclotron harmonic rings.

These results testify that the vast majority of the negative ions are not formed through the capture of the plasma electrons, since they have too high energy to promote dissociative attachment directly, and that the plasma electrode surface plays a critical role since its immersion into the plasma affects the negative ion extracted currents. Thus, it has been demonstrated (Dougar-Jabon et al. 1998) that the negative ion generation mechanism is the volume vibrational excitation of hydrogen molecules, due to the energetic electrons, followed by the dissociative attachment of the electrons emitted by the plasma electrode under ion flux bombardment. In a more recent study (Dougar-Jabon 2001), the importance of the molecules excited to high-lying Rydberg states was considered to be higher than that of the vibrationally excited ones, while the role of the secondary electrons was once more underlined.

12.3.4 HOMER

A schematic representation of the ECR configuration called HOMER (HOMogeneous Electron cyclotron Resonance plasma) is given in Fig. 12.21, while details

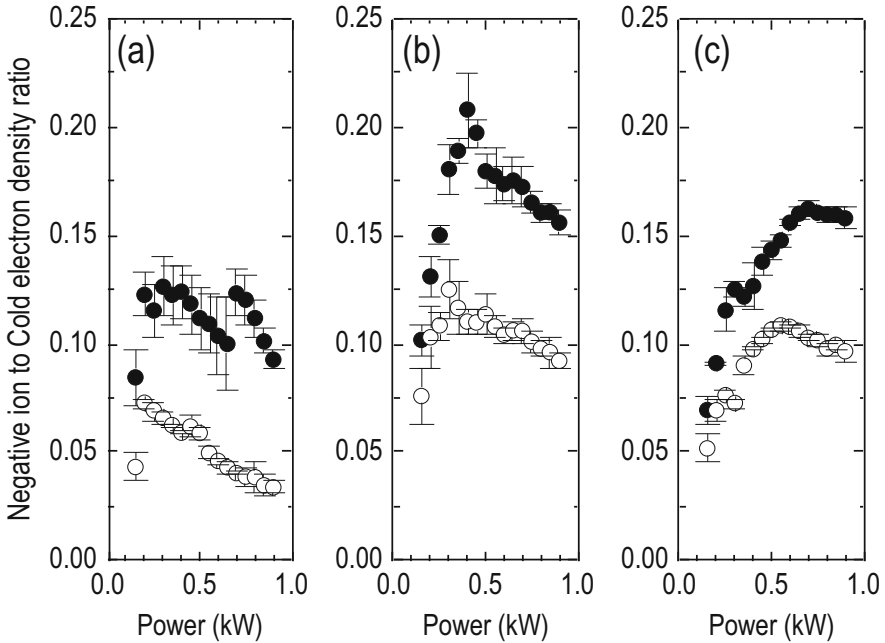


Fig. 12.18 Negative ion to Cold electron density as a function of the microwave power at (a) 0.53 Pa, (b) 1.07 Pa, and (c) 1.60 Pa. Solid circles: H₂ plasma. Open circles: D₂ plasma

are given in (Rauner et al. 2015; Kurutz and Fantz 2015). It consists of a cylindrical vacuum chamber having a height of 31 cm and a 7.5 cm radius, manufactured using stainless steel. The microwave (2.45 GHz) power, generated by a magnetron having a maximum power output of 1 kW, is transmitted through a borosilicate window from the top side of the vessel. An axial magnetic field of 87.5 mT, needed for electron cyclotron resonant heating, is generated homogeneously over the whole volume by two water-cooled solenoids located at the top and the bottom of the vacuum vessel.

HOMER is equipped with a meshed grid located just below the first field coil. This mesh prevents the microwave from expanding into the lower part of the chamber, thereby applying the tandem principle, i.e., by dividing the source into two regions: the heated, driver region at the top (height 12 cm), and the non-heated, diffusive region extending over the lower part (height 19 cm). This method has the advantage that no additional magnetic fields are required which interfere with the already present magnetic field of the ECR setup (Kurutz et al. 2017). Furthermore, the destruction of negative ions due to electron detachment in the downstream section below the grid is reduced. The grid potential can be biased relative to the grounded walls or set to be floating for influencing the diffusion of charged particles through the grid. Dedicated investigations regarding the influence of the meshed grid on the plasma parameters at HOMER are given by (Kurutz and Fantz

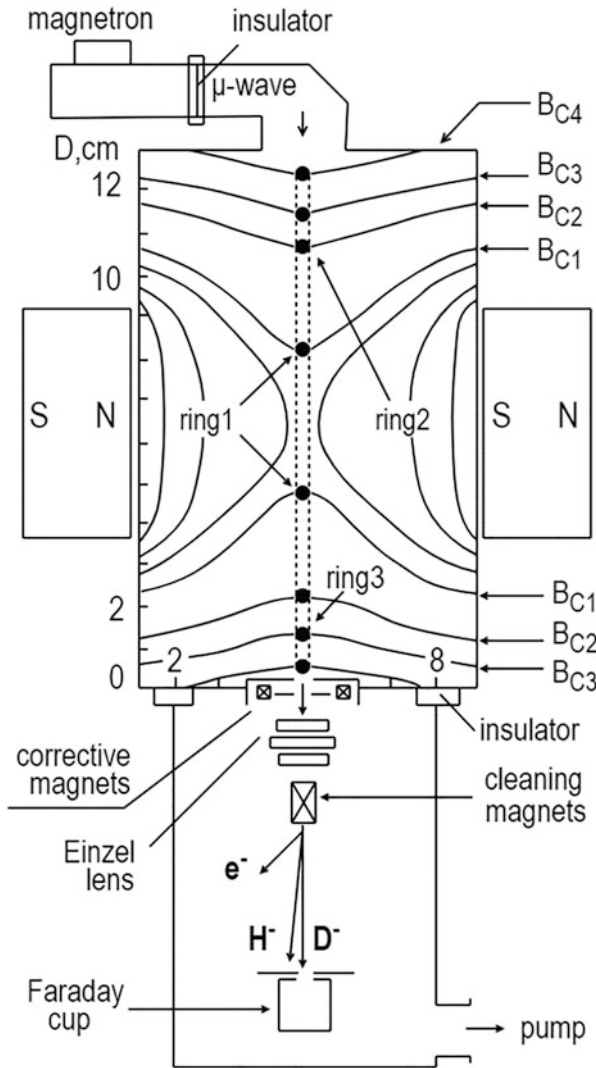


Fig. 12.19 Assembly of the discharge chamber with the extraction system, concerning the ECR source with stratified plasma. (Reproduced from Dougar-Jabon (2001) with the permission of IOP Publishing)

2015). In the downstream region, the source is also equipped with the necessary viewports for the simultaneous installation of different diagnostics. In the diffusive downstream region beneath the meshed grid a horizontal oriented sample holder of $8.5 \times 6 \text{ cm}^2$ made of stainless steel is located. The sample holder is thermally and electrically insulated and its axial position is variable. Samples can be heated up to $800 \text{ }^\circ\text{C}$ via heating elements inside the sample holder, while the sample holder

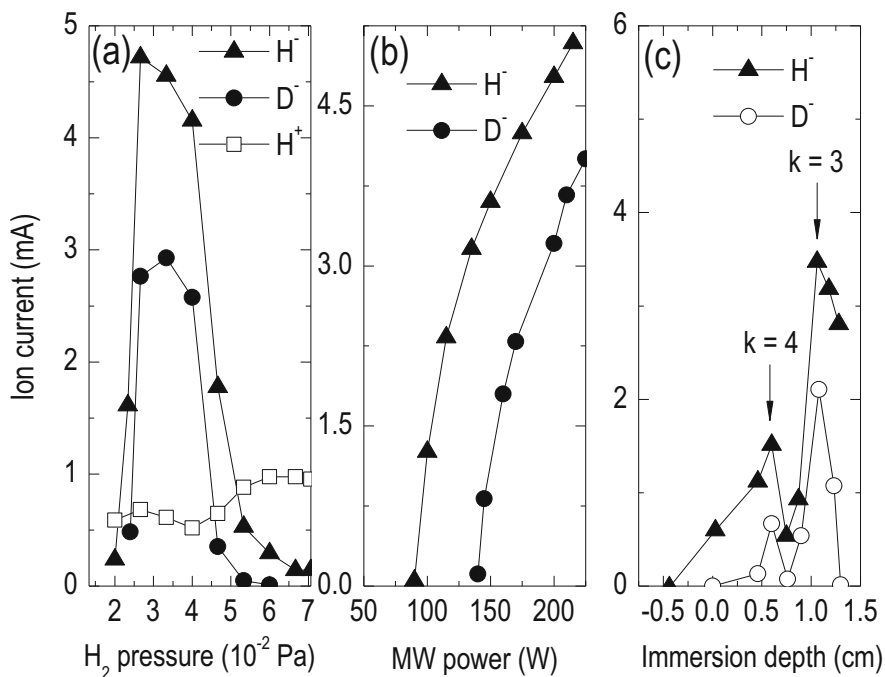


Fig. 12.20 Variation of the extracted negative ion currents as a function of the (a) gas pressure (200 W), (b) microwave power (3.33×10^{-2} Pa), and (c) immersion depth of the plasma electrode (2.66×10^{-2} Pa; 175 W). (Reproduced from Dougar-Jabon (2001) with the permission of IOP Publishing)

bias can be modified relative to the grounded walls or the meshed grid affecting the energy of charged particles impinging on the investigated samples (Kurutz and Fantz 2015). Later on (Friedl et al. 2020) introduced a prolonged vessel for line of sight optical emission spectroscopy measurements in both the heated and expanding parts of the plasma. Although more extensive studies have undergone for a hydrogen plasma, deuterium discharges have also been regularly studied in HOMER. The diagnostics used to determine the plasma parameters in each case include Langmuir probes, laser induced photodetachment, cavity ring-down spectroscopy, and optical emission spectroscopy. A detailed description of these setups and the application of each diagnostic technique may be found in the works cited in this section.

The produced hydrogen and deuterium plasmas in HOMER, in the investigated pressure range of 0.3–3 Pa, are in general characterized by an electron density between 10^{16} and 10^{17} m^{-3} , an electron temperature (in the diffusive region) of about 1–2 eV, and a neutral atomic density, n_H , in the range 10^{18} – 10^{19} m^{-3} (Kurutz and Fantz 2015). Furthermore, in the same pressure range and at varying microwave power between 200 W and 500 W, the maximum negative ion hydrogen density equals $3.9 \times 10^{15} \text{ m}^{-3}$ (Rauner et al. 2015).

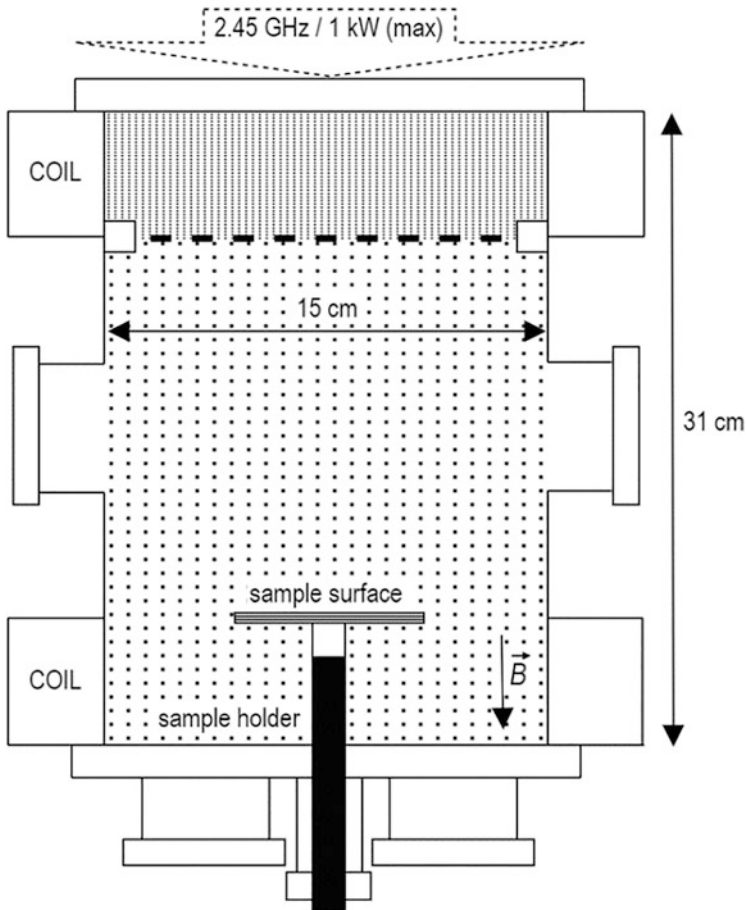


Fig. 12.21 Concept of the basic version of the small scale, test bed HOMER. (Reproduced from Kurutz and Fantz (2015) with the permission of AIP Publishing)

Changing from H_2 to D_2 , both the ion density and the atomic density are increased in D_2 . The increased positive ion density is directly linked to a higher electron density and it can be explained by a better coupling of the microwave to the deuterium plasma. The increased atomic density is attributed to the higher dissociative cross section for D_2 . Other plasma parameters like gas temperature, the EEDF, or the vibrational distribution of the molecular ground state show only very slight differences between the isotopes. Regarding negative ion formation, the higher electron density in D_2 indicates an enhanced negative ion volume production compared to H_2 . On the other hand, the higher atomic density in deuterium results in a comparably enhanced negative ion destruction within the volume due to the associative detachment process but also to an increased atomic flux onto the surface. Due to the only limited contribution of surface production, in this case, the different

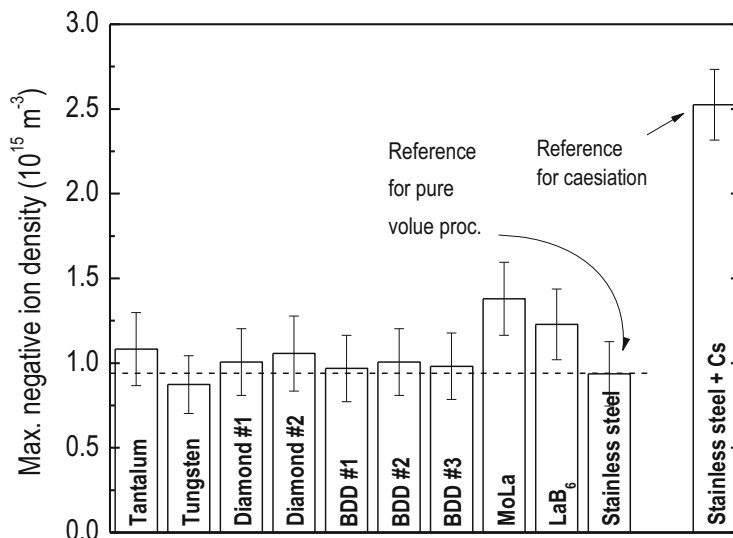


Fig. 12.22 Maximal measured negative ion density for different materials at the same external experimental conditions: measured in a distance of 2.5 cm to unbiased samples, at 0.3 Pa H₂ pressure and 300 W discharge power. (Reproduced from Kurutz et al. (2017) with the permission of IOP Publishing)

effects seem to compensate for each other leading to virtually identical negative ion densities in D₂ and H₂ (Friedl et al. 2017).

A large portion of the experimentation carried out at HOMER has been devoted to the investigation of the influence of various sample materials facing the plasma on negative ion production, either it is indirectly by enhanced volume production, or direct by enhanced surface production (Friedl et al. 2017; Kurutz and Fantz 2015; Kurutz et al. 2017). The main motivation behind these studies is the desire to find an alternative material to cesium (Cs) that can be efficient enough to be utilized in future negative ion sources. The main results are summarized in Fig. 12.22. Among the investigated Cs-free materials neither any of the investigated diamond materials nor bulk samples made of tantalum nor tungsten resulted in an enhanced negative ion density relative to the pure volume reference case. Moreover, all diamond materials significantly influenced the bulk plasma and showed clear signs of plasma-induced erosion. Hence, these materials cannot be seen as alternatives to the application of Cs (Kurutz et al. 2017). In contrast, both low work function materials MoLa and LaB₆ lead to systematically increased negative ion density compared to the pure volume reference case (Kurutz et al. 2017). Measured negative ion densities furthermore exceeded those expected from modelling of the volume processes, which indicates a direct negative ion surface production.

In another report (Friedl et al. 2020), an extensive spectroscopic study of a hydrogen discharge (HOMER) coupled with collisional radiative modelling highlights

the possibility of identifying individual contributions of the different excitation channels for the Balmer series. In low-pressure, low-temperature hydrogen plasmas electron impact excitation, dissociative excitation, and dissociative recombination are prominent excitation channels for the Balmer series. These processes can have a specific influence on the translational energy of excited atoms which is correlated with the width of the respective line profiles. On this basis, an elaborate analysis of the Balmer emission lines' profiles from the diffusive region of the hydrogen plasma revealed that the dissociative recombination channel has a significant contribution to the excitation of the Balmer series and gives rise to a broad component in the line profiles of all the Balmer lines. Moreover, it is demonstrated and emphasized that the use of the simple line-ratio method (H_γ /Fulcher) for the determination of the hydrogen atomic density can lose its validity if processes like the latter are neglected.

12.3.5 ROSAE (I, II, and III)

ROSAE (ecR HydrOgen plaSma for neutrAl bEam) reactors (versions I, II, and III) have been designed to study interaction processes between H_2 and D_2 plasmas and plasma-facing materials, with a special focus on the recombinative desorption mechanisms (see Table 12.2). In ROSAE I, seven elementary, dipolar, plasma sources, like those of Fig. 12.6, are installed above a PyrexTM cylinder (200 mm in diameter and 200 mm in height). The PyrexTM cylinder is housed in the Camembert III vacuum chamber, as shown in Fig. 12.23a (Bacal et al. 2004). The plasma is produced in the electronic cyclotronic resonance (2.45 GHz) regions of the elementary sources and diffuses in the PyrexTM cylinder, preventing however its diffusion toward the vacuum chamber walls. A PyrexTM disk is also placed at the bottom of the cylinder, leaving thus as plasma entrance only the upper, open side of the cylinder. This arrangement is presented in Fig. 12.23b, c. The aim of the PyrexTM cylinder is the creation of a smaller volume of plasma than the one produced in the Camembert III chamber, to promote surface reactions with samples of limited size (48 mm in diameter); see sample holder in Fig. 12.23d. In the Camembert III chamber the surface-to-volume ratio is close to 0.005, while in ROSAE I it equals 0.025. As is seen in the photos of Fig. 12.23b, d, the sample forms a detachable part of the PyrexTM cylinder wall, while a load lock chamber is used for the sample interchange under vacuum conditions. In addition, the sample temperature is controllable by means of a closed-loop system and the sample electrical potential may be biased.

The reference material is a disk of PyrexTM. Three different materials have been investigated: PyrexTM, graphite (HOPG), and tantalum (Ta), at the same total microwave power (1 kW) and hydrogen pressure 0.8 Pa. Conventional electrostatic probes and laser-induced photodetachment are employed for the plasma interrogation.

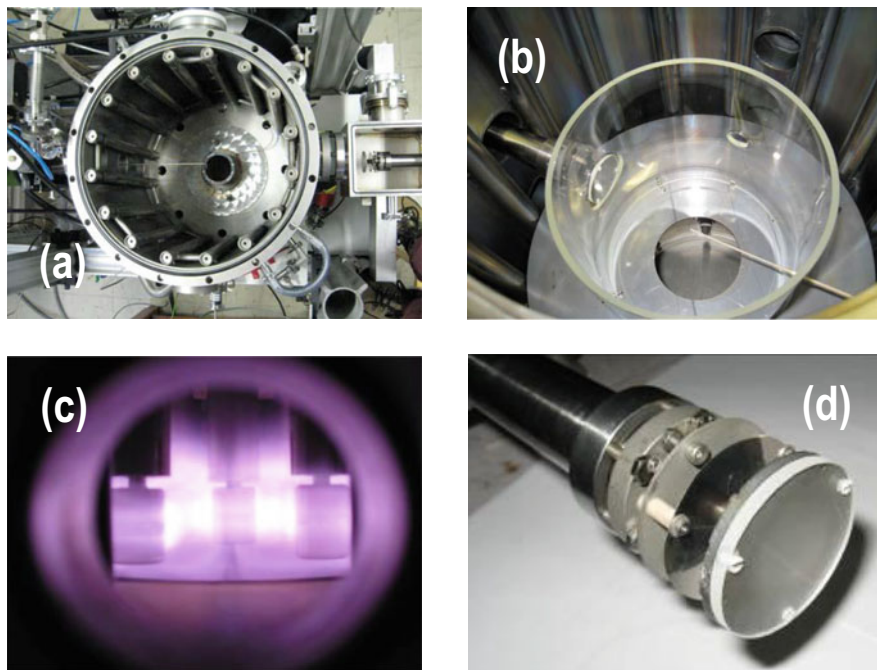


Fig. 12.23 (a) The interior of the Cabembert III multi cusp chamber. (b) The Pyrex™ cylinder installed at the center of the Camembert III chamber. (c) Photo of three (out of seven) elementary plasma sources in operation. (d) Sample holder, where a Pyrex™ specimen (48 mm in diameter) is mounted

Despite the small surface (0.007 m^2) of the samples, compared to the whole Pyrex™ cylinder surface facing the plasma (0.16 m^2), measurements of the peak of the photodetached electron signals versus the sample temperature show observable differences (each signal peak is reduced to the background electron density current and this ratio provides an analogy to the negative ion density (Bacal 2000)). A significant increase of 26% has been obtained for the HOPG samples between 263 and 293 K. For the Ta samples, a less significant variation has been mentioned within the same temperature range. The Pyrex™ samples have induced the largest increase, i.e. 45%, when the temperature increases from 263 to 393 K. These results can be interpreted as the variation of the recombination coefficient of H atoms (γ_H), which varies with the temperature differently in the case of Pyrex™ and metals. For Pyrex™ and Quartz, previous results (Wood and Wise 1958, 1961) indicate an important variation of the γ_H coefficient as a function of the surface temperature. As a matter of fact, it decreases from about 10^{-3} down to 2×10^{-5} for a temperature increase between about 75 and 115 K, whereas it rises monotonously up to 3×10^{-2} when the temperature approaches 500 K. On the contrary, in the case of metals, recombination coefficient γ_H is not affected by the temperature variation between 300 and 1000 K (Taccogna et al. 2007) and stays close to 0.5.

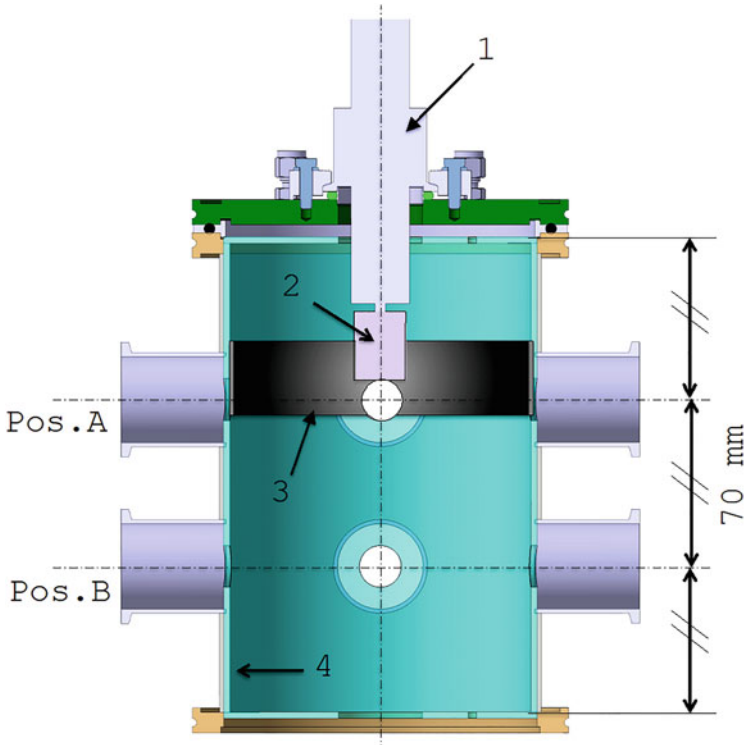


Fig. 12.24 ROSAE III conceptual design (vertical section). (1): dipolar plasma source; (2): permanent magnet; (3): mounted specimen in the form of sheet; (4): Pyrex™ shell

In response to the preliminary, encouraging results obtained in ROSAE I, a second prototype was developed (ROSAE II), which led finally to the experimental setup ROSAE III (Fig. 12.24). The ROSAE III structure consists of a stainless steel cylindrical chamber of 150 mm in diameter. It houses a Pyrex™ cylindrical shell being 140 mm in diameter and 200 mm in height, defining thus a surface-to-volume ratio equal to 0.038. Either one or four dipolar sources, like those of Fig. 12.6, can be adapted to the upper flange of the chamber. These sources pass through a Pyrex™ disc facing the plasma, i.e., covering the inner surface of the top stainless steel flange. As Fig. 12.24 depicts, the specimens are in the form of sheets (0.1 mm in thickness), made of bulk material. Stainless steel (SS), tantalum (Ta), and tungsten (W) have been tested. Plasma has been probed by means of electrostatic probes, laser-induced photodetachment, and optical emission spectroscopy. Representative results are given in Fig. 12.25.

Comparative measurements before and after mounting the SS sheet opposite to the plasma source (Fig. 12.25a), do not show any particular effect on the plasma density n_e in position B (Fig. 12.24) where negative ions are formed by DA of cold electrons. Additionally, at the same position, the electron energy kT_e ranges from

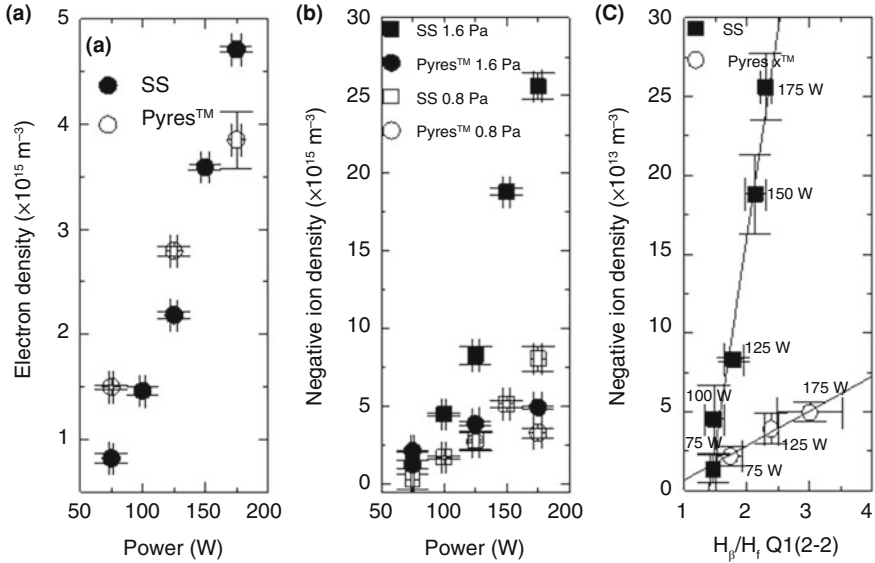


Fig. 12.25 Basic plasma parameters in ROSAE III, in the cases of PyrexTM and stainless steel (Pos. B—Fig. 12.24; single dipolar plasma source). (a) Electron density vs. power (1.6 Pa). (b) Negative ion density vs. power, at 0.8 and 1.6 Pa. (c) Negative ion density vs. the H_{β} to $H_{\text{fulcher}}Q_1(2-2)$ intensity ratio, at different power levels (1.6 Pa)

0.9 to 1.3 eV (Bentounes et al. 2018) when the delivered microwave power increases between 75 and 175 W. This holds true independently of the plasma-facing material (PyrexTM or SS). Although n_e and kT_e are not affected by the plasma facing-material, the H^- negative ion density n_{H^-} highly does.

Figure 12.25b presents the variation of this quantity versus the microwave power at two different pressures, i.e., 0.8 and 1.6 Pa. In the PyrexTM case, n_{H^-} is not significantly affected either by the microwave power or by the hydrogen pressure, remaining close to a value of about $5 \times 10^{13} \text{ m}^{-3}$. Though, the stainless steel specimen leads to an almost fivefold value of n_{H^-} , i.e., negative ion density up to about $2.5 \times 10^{14} \text{ cm}^{-3}$ is achieved at 1.6 Pa.

The observed increase in the negative ion density in the case of the stainless steel sheet, may be considered with respect to the data given in Fig. 12.25c. It is proposed that either the SS sheet increases the ro-vibrational molecular density (at the same plasma density and electron energy) or it decreases the atomic density. Following the first assumption, the sheet increases the production of negative ions through DA, whereas, following the second assumption, it decreases the destruction of negative ions due to collisions with H atoms. The H_{β} to $H_{\text{fulcher}}Q_1(2-2)$ intensity ratio, i.e., the ratio of the intensity of the radiative transitions Balmer ($n = 4 \rightarrow 2$) and $d^3\Pi_u \rightarrow \alpha^3 \Sigma_g^+$ respectively, may provide the relative density of H atoms (Fantz et al. 2006). In Fig. 12.25c, for a mutual atom-to-molecule ratio, e.g., 2.5, the negative ion density is lower than $5 \times 10^{13} \text{ cm}^{-3}$ with PyrexTM, whereas it

becomes higher than $2.5 \times 10^{14} \text{ cm}^{-3}$ with the SS sheet. This demonstrates the efficient increase of negative ion via DA. In order to investigate the production of ro-vibrational excited molecules, the following (SCHEME) reactors were designed.

12.3.6 Scheme (I, II, and II+)

The SCHEME (Source of exCited HydrogEn MolEcules) reactors (versions I and II) have been designed for dedicated studies on plasma-surface interactions, using synchrotron radiation. The ratio of the plasma-facing surface to the plasma volume equals 0.04, which is practically the same as in ROSAE III reactor (i.e., 0.038). However, to improve the temperature control of the plasma-facing surfaces, a coolable copper cylinder interfaces both a stainless steel chamber and a glass cylindrical shell, with the latter to be made of Quartz (aluminosilicate glass, Schott™ 8250, 3 mm thick).

The concept design of the Scheme I reactor is shown in Fig. 12.26. The above mentioned Quartz cylinder is 124 mm in diameter and 150 mm in height, while it is ended by a Quartz disk on both sides. This amorphous glass surface serves as a reference surface of low atom recombination coefficient ($\gamma_{\text{H}} = 0.004$ at 290 K). Hence, ro-vibrationally excited molecules are created essentially in the ECR coupling zone close to the permanent magnet of the dipolar plasma source (see details “c” and “d” in Fig. 12.26). In order to study other materials, tantalum (Ta), tungsten (W) or stainless steel (SS) foil (0.1 mm thick) is flattened on the inner surface of this Quartz tube. The temperature of the Quartz and the specimen temperature are controllable and maintained at 288 K. This keeps the atom recombination coefficient of the Quartz cylinder as close as possible to 0.004 and thus prevents recombinative desorption on its surface. At the same time, over the temperature range between 240 and 300 K, metallic surfaces have a higher recombination coefficient ($\gamma_{\text{H}} \approx 0.5$) and thus promote surface recombination of atoms originating in the plasma volume. As the investigated material (Ta, W or SS) is placed on the Quartz surface, its potential is floating, which does not induce a potential modification between the Quartz and the metallic surfaces.

For the last 8 years, the Scheme I setup was transported and temporarily installed at the SOLEIL synchrotron (France), as part of experimental campaigns with the objective of using VUV radiation to study the molecular hydrogen excitations in plasmas. Scheme I setup was installed on the branch B end station (delivering a monochromatized beam) of the DESIRS (Dichroïsme Et Spectroscopie par Interaction avec le Rayonnement Synchrotron) beam line of the synchrotron for conducting absorption spectroscopy experiments. DESIRS is an undulator based beamline covering the VUV range (5–40 eV) with a unique combination of ultra high resolution spectral purity, flux, and fully variable polarization (de Oliveira et al. 2009, 2011). During these first experiments, a solar blind photoelectron multiplier tube, with a MgF₂ window, was set on the radiation beam axis. The radiation beam

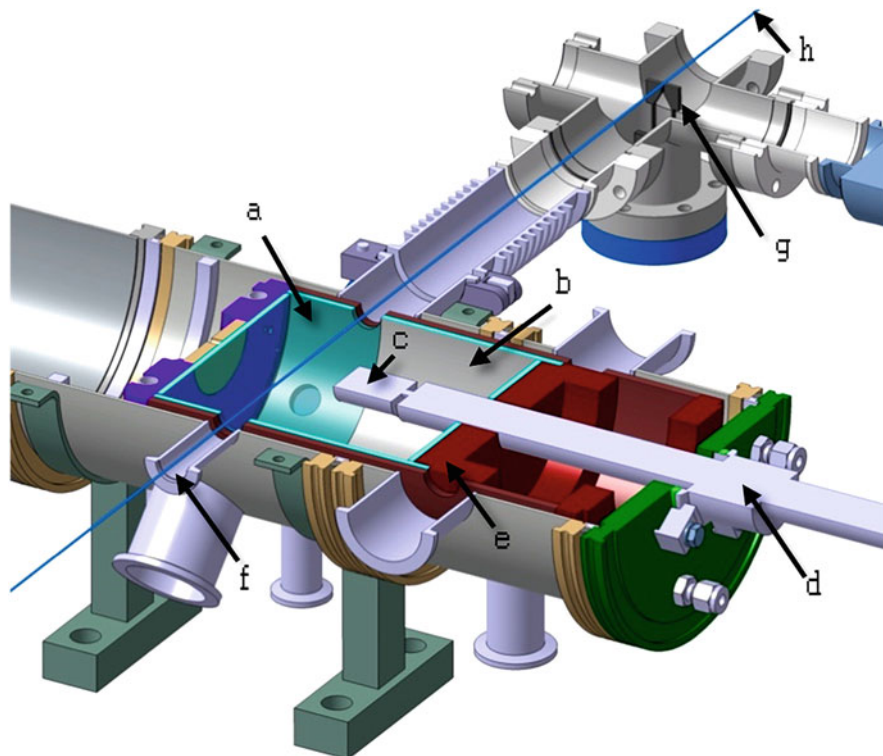


Fig. 12.26 Scheme I conceptual design (horizontal section). (a): Quartz cylinder; (b): mounted specimen; (c): permanent magnet; (d): dipolar plasma source; (e): coolable copper; (f): solar blind photoelectron multiplier tube position; (g): tuning fork—optical chopper; (h): radiation beam

was chopped by a tuning fork (oscillating at 130 Hz) for phase-sensitive signal detection. This phase-sensitive, lock-in detection, rejected the continuous stray light emitted by the plasma. These preliminary experiments (Béchu et al. 2017) were carried out by using three hot tungsten filaments in the glass chamber, instead of a plasma source. H_2 molecules were partially dissociated into atoms following thermal and catalytic effects sustained by the hot filaments. Then, the dissociation was less efficient, the light coming from the filament was essentially in the infrared range and, due to the absence of electronic collisions, less exciting species had to be considered. In order to isolate the synchrotron beam line (very low pressure) from the glass chamber (H_2 pressure), a MgF_2 window was inserted in the position “h” (Fig. 12.26). Following this initial campaign, information obtained by laser-induced fluorescence and synchrotron radiation absorption, gave the first stepping stones for further experimental adjustments to increase spectral resolution. Such an improvement was obtained when the 2400 grooves mm^{-1} grating of the 6.56 m normal incidence monochromator of the branch B was employed. Thus, with both entrance and exit slits set at 50 μm , a resolution of 30 mÅ was achieved.

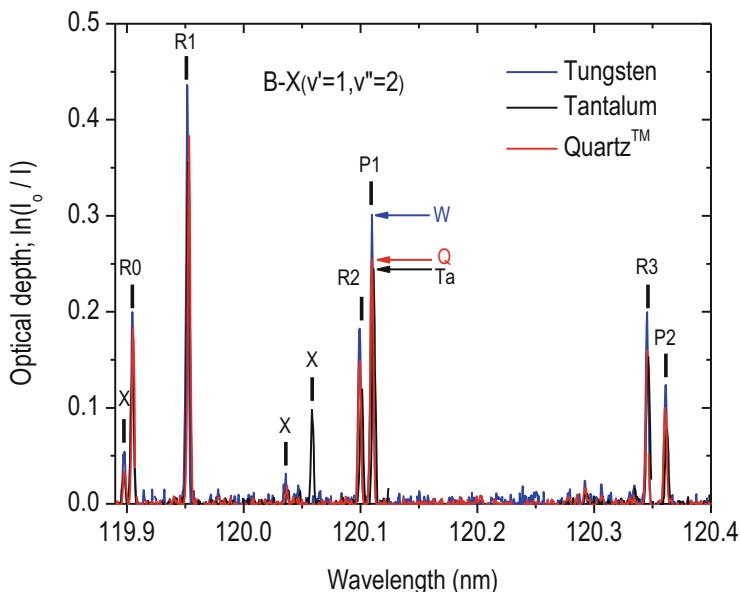


Fig. 12.27 Synchrotron beam absorption spectra (optical depth) of hydrogen ECR plasma faced by three different materials: Quartz Tungsten (blue); Tantalum (black). 1.6 Pa; 150 W

Figure 12.27 summarizes the main results obtained with this high-resolution setting on the branch B. It shows a few rotational transitions of the vibrational $BX(v' = 1 \leftarrow v'' = 2)$ transition, proving thus that the $v'' = 2$ vibrational level of the electronic ground state (at about 10.419 eV) was populated. Rovibrational transitions were recorded in the ECR plasma for three different specimens (detail “b” in Fig. 12.26): quartz, tungsten and tantalum. Significant differences were observed, particularly in the tungsten case. In addition to the transition $BX(v' = 1 \leftarrow v'' = 2)$, which characterizes the population $v'' = 2$ level of the electronic ground state, similar spectra have been recorded for the three materials up to the transitions $BX(v' = 1 \leftarrow v'' = 3, 4, 5, 6)$. All these transitions were selected on the basis of favorable Franck-Condon factors (Fantz and Wunderlich 2006).

It was clearly understood with these first experiments that increased spectral resolution was needed (from 3.0 to 0.7 pm, FWHM), in order to separate most of the H_2 observable lines, and also to reduce the long acquisition time imposed by the wavelength scanning of the monochromator. It thus required the use of the high-resolution VUV Fourier transform spectrometer (FTS) permanently installed on the same DESIRS beam line (Béchu et al. 2020). Another advantage lied in the relatively fast recording time to get a complete spectrum. Additional advantage was the access to the full VUV range without any window, at the expense nevertheless of two additional differential pumping sets. They were placed, in combination with thin diaphragms (0.1 mm thick and 3×5 mm aperture), as close as possible to both sides of the reactor in addition to the pumping sets already provided for safety on

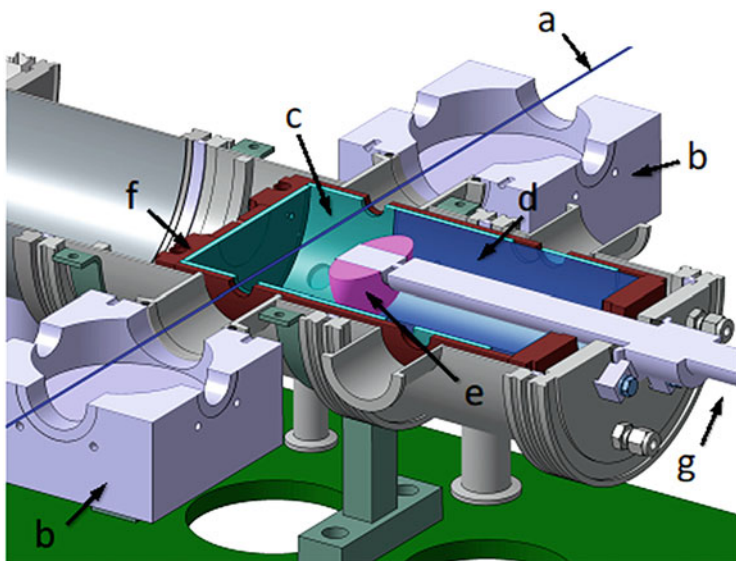


Fig. 12.28 Scheme II+ conceptual design (horizontal section). (a): radiation beam; (b): differential pumping system; (c): Quartz shell; (d): mounted specimens; (e): ECR coupling zone; (f): cooling copper; (g): dipolar plasma source

the SR beam exit and the FTS entrance. With 50 l s^{-1} turbo pumps it was possible to work up to 0.8 Pa with H_2 . For that purpose, an updated reactor (Scheme II; Fig. 12.28) was developed, based on the initial concept of Scheme I.

Thanks to these modifications, spectra measurements down to wavelengths as short as 90 nm were used to scan both the H Lyman alpha lines and the $\text{BX}(v' = 0)$ molecular lines up to high v' . Hence, dissociation ratio of the molecular gas was measured as well as the densities of rotational states of the gas ($v'' = 0$) in plasma OFF and ON conditions. These measurements, corresponding to a calibration procedure, were mandatory to get absolute distribution of ro-vibrational states ($v' = 0, v''$) in the plasma. An even higher pumping capacity (upgraded to 300 l s^{-1}) was achieved with slight modifications in the original design of Scheme II (hence named Scheme II+ in Fig. 12.28). The improved setup, in a subsequent run, allowed measurements in windowless mode up to 3.2 Pa while keeping the pressure as low as below 10^{-5} Pa outside the reactor.

In order to cover the $\text{BX}(v' = 0, v'' = 0 - 8)$ transitions in the $65,000$ to $97,500 \text{ cm}^{-1}$ energy range (Fig. 12.29), as the energy coverage of an undulator setting was close to 3500 cm^{-1} (FWHM), nine overlapping settings were used for scanning the ro-vibrational components at the quantum levels v' with a spectral resolution of 0.95 pm . The sampling rate was 512 kSamples , allowing a recording of this spectral range within about 120 min . Different materials (Quartz as a reference surface; Ta; W; and SS) were studied at three pressures ($0.8, 1.6, \text{ and } 3.2 \text{ Pa}$), two power levels (150 and 250 W), and two gases (H_2 and D_2). Before each series of

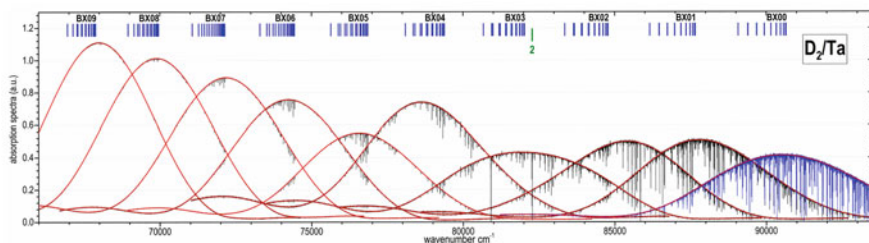


Fig. 12.29 Absorption spectra (black) and fitted continua (red), in the different Gaussian-like spectral windows corresponding to different undulator settings, that were used to record the $D_2^*(v' = 0, v'' = 0 - 8)$ transitions of the $D_2^*(v'', J'')$ molecule. (Data obtained with Scheme II+ reactor)

measurements with a specific material, a cleaning of the investigated surface with plasma (gas mixture of Ar and H_2 or D_2), sustained for 10 min, was performed, followed by 15 min of warming up in pure H_2 or D_2 . As the plasma source was movable along its axis, different positions inside the reactor could be used to probe the plasma in the plasma source vicinity while the synchrotron beam location was constant. The most significant results are given below, whereas complete results could be found in already published papers (Bentoune et al. 2018; Béchu et al. 2017, 2020) or they will be published soon.

Under these improved experimental conditions, all Lyman transitions below Lyman- α (also called Ly-1) that are not partially or fully blended by molecular lines became observable. Figure 12.30 presents absorption lines of Ly-3 up to Ly-8, i.e., from 97.2517 down to 92.3148 nm. The oscillator strengths of these lines are much more lower than Ly-1 which avoids line saturation. Indicatively, at 0.8 Pa and 150 W, the absolute density of H atoms was found to be $3 \times 10^{19} \text{ m}^{-3}$ with full Quartz versus $1.3 \times 10^{18} \text{ m}^{-3}$ with a Ta specimen.

Figure 12.31 shows, after data processing, the VUV excited deuterium optical depth, $\ln(I_0/I)$, with respect to the wavenumber, obtained in the spectral window centered at $74,200 \text{ cm}^{-1}$. In addition to the BX06 band, the BX27 band is observed in its wing. In fact, all band data obtained inside the FWHM of a given undulator setting were useful with a good signal-to-noise ratio depending also on the oscillator strength of the transition.

Hence, by carefully observing the spectra, additional vibrational transitions were unveiled, i.e., $BX(v' = 1 - m, v'' = 0 - n)$, on the top of $BX(v' = 0, v'' = 0 - n)$. They were used to improve the accuracy of the results, allowing a better identification of the role of the different materials in populating the vibrational distribution functions (VDFs) of hydrogen (or deuterium) in the plasma. Among the 121 $BX(v' = 0 - 10, v'' = 0 - 10)$ potentially observable transitions, about 58 were useful to accurately determine, in conjunction with the FC factors, the vibrational populations in each v'' level of the ground state, then giving access to the VDF of the plasma. The calibration was made by using the $BXv'0$ data obtained without plasma (see details in (Béchu et al. 2020)).

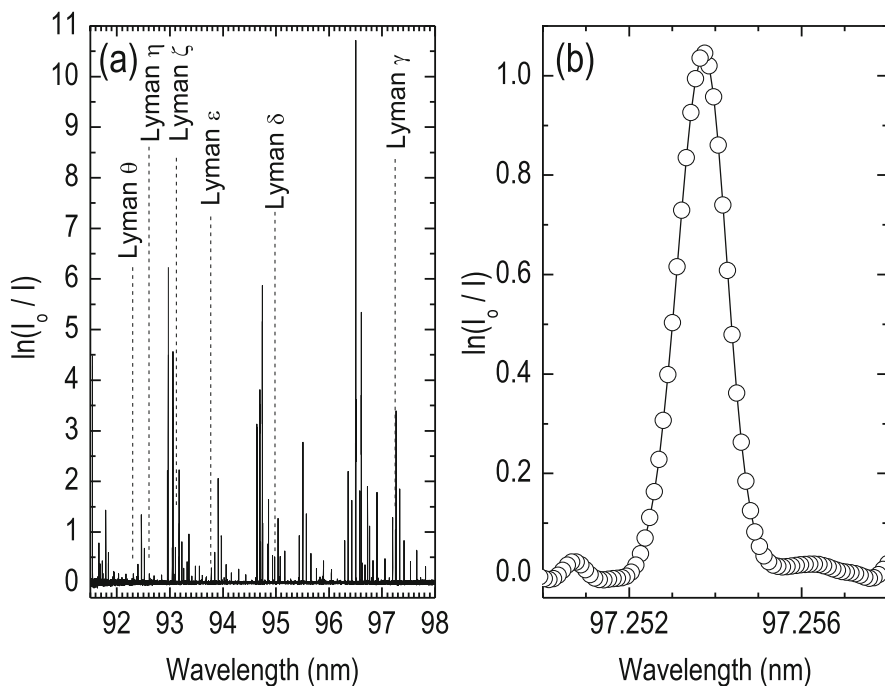


Fig. 12.30 (a) Optical depth of $H(n = 1)$ obtained at 150 W and 0.8 Pa, using Quartz in the Scheme II+ reactor. (b) Focus on the Lyman- γ transition

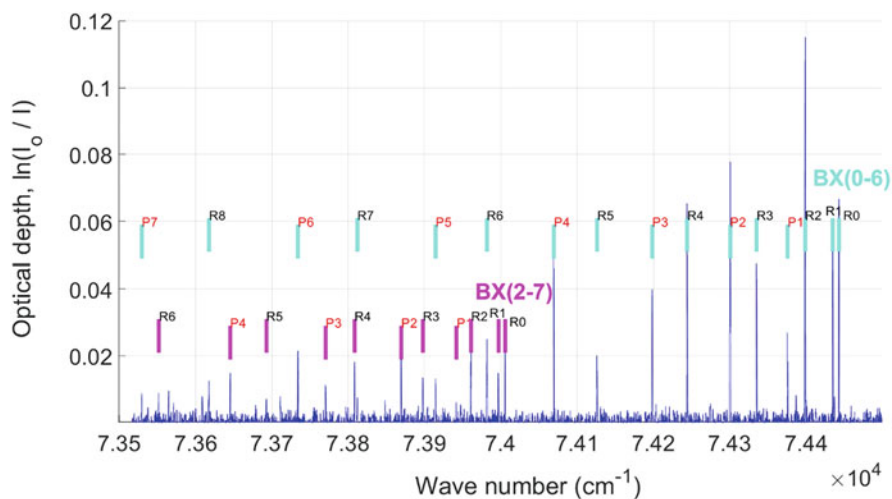


Fig. 12.31 Optical depth of the $D_2(v' = 0, v'' = 0 - 6)$ transition of the $D_2^*(v'', J'')$ molecule in the plasma. (Data obtained with Ta, at 150 W and 0.8 Pa, in the reactor Scheme II+)

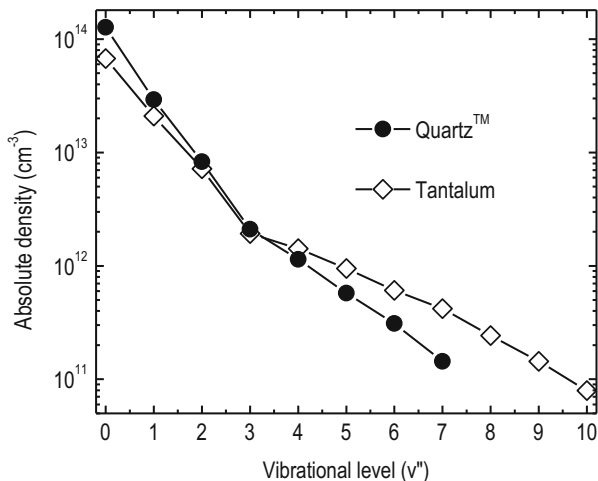


Fig. 12.32 Absolute vibrational distribution function in ECR D_2 plasma, in the case of two different materials-specimens (0.8 Pa; 150 W). Reactor Scheme II+

Thus, the spectra were processed in such a way to obtain absolute vibrational distribution functions which allowed for an overall comparison for the different vibrational quantum levels, when different materials were tested. An example is given in Fig. 12.32, showing that Ta promotes a higher production of quantum levels above $v'' = 3$. An increase by 2.6 is seen for $v'' = 7$, as compared to Quartz. This experimental result shows a similar trend with that reported by quantum dynamic calculations for graphite (Jackson and Lemoine 2001), where the average quantum number for molecules produced by recombinative desorption was found to be close to 8. On the other hand, for lower vibrational levels, Quartz yielded higher populations (e.g., by a factor of 1.7 at $v'' = 0$). Complementary studies, including laser photodetachment and electrostatic probe measurements, at similar conditions, have provided an analogous increase of negative ions whilst electron density remained nearly constant. In light of the results provided by this particular diagnostic technique (absorption of synchrotron radiation), the interpretation of previously published results (Bacal et al. 2004) can be further enhanced.

12.4 Other Sources and Extracted Currents in ECR Sources

In this final paragraph of this chapter, additional ECR sources are touched upon and H^- negative ion-extracted currents from different sources are compared.

At Argonne National Laboratory (Spence and Lykke 1998), the H^- and D^- ion source refers to a magnetically confined microwave-driven (ECR) source, purchased from Atomic Energy of Canada, Ltd., which is powered by a 2.45 GHz microwave

generator (2 kW). The microwave generator is coupled to the source via a circulator and a four-stub autotuner. The ion source is attached to a large, high vacuum, oil-free diagnostic chamber with a base pressure of about 1.33×10^{-6} Pa. The mechanism for H^- ion production is via DA, while the initial production of $H_2(v)$, i.e., the precursor of H^- , is assumed to be by excitation of ground state molecules. However, in order to take advantage of the recombination desorption of hydrogen atoms on the tantalum surface and, thus, enhanced $H_2(v)$ population, a thin layer of Ta is sputtered on the inner surface of the source. Results confirm the importance of the recombination desorption mechanism to $H_2(v)$ production. Finally, the total H^- (D^-) ion current being extracted from the 5 mm diameter source aperture was estimated to be 4–5 mA (at 700 W cw), indicating little or no isotope effect.

At Peking University (Zhang et al. 2018), an improved with respect to a previous version, 2.45 GHz microwave-driven (ECR) source, has been installed. The microwave is fed into the source chamber through a dielectric window made of three pieces of Al_2O_3 and one piece of boron nitride to prevent electron bombardment. The ECR magnetic field is generated by a set of ring-shaped Nd-Fe-B permanent magnets, surrounding the source chamber. Furthermore, a pair of filter magnets form a transversal filter magnetic field, separating thus physically the source into the ECR driving zone and the H^- ion formation zone. This Cs-free source yielded a maximum 8.5 mA pure H^- beam. The beam was extracted at 50 kV with a time structure of 100 Hz/0.3 ms. The emittance (rms) of the beam was 0.25π mm mrad. The improved H^- ion source and extraction system were maintenance-free for more than 200 h in operation. Once again, negative ions was assumed to be produced via DA, while a tantalum lining with a thickness of 0.1 mm was installed inside the whole source chamber to enhance the $H_2(v)$ production.

At Saclay (Gobin et al. 2006), two coils have been used to provide an axial magnetic field of 875 G for the 2.45 GHz driven source. The magnetic coils are located around the source chamber. A protected quartz window separates the standard WR284 rectangular waveguide, toward the plasma side, from the 1.2 kW magnetron microwave generator. A potential biased metallic grid has replaced the initial magnetic filter and allows for the separation of the H^- ion production zone from the ECR zone. The grid is connected to the plasma electrode, and both are negatively biased with respect to the plasma chamber which is connected to negative high potential. The source has been designed to produce low energy beam in pulsed mode. The source typically operates at 1–2 ms at a frequency between 5 and 10 Hz. At typical working pressure (i.e., nearly 2.66×10^{-6} Pa in the extraction chamber, which corresponds to around 0.26 Pa in the plasma chamber) about 2 mA of H^- ion current has be extracted at 6 kV. These ions were collected on a Faraday cup through an aperture of 50 mm in diameter. The source reliability has been checked in pulsed mode (2 ms pulse width at a period of 100 ms) during 5 days and a continuous operation without any human intervention has been achieved. At much lower pressure in the extractor (i.e., 6.66×10^{-4} Pa), 2.8 mA of H^- ion current has been claimed (see (Gobin et al. 2006) for discussion).

Finally, the source with driven plasma rings (Sect. 12.3.3) has yielded negative ion extracted current around 5 mA (Fig. 12.20) and the source Camembert III (Sect. 12.3.1) around 0.25 mA (Fig. 12.12).

References

- S. Aleiferis, O. Tarvainen, P. Svarnas, M. Bacala, S. Béchu, Experimental investigation of the relation between H^- negative ion density and Lyman- α emission intensity in a microwave discharge. *J. Phys. D. Appl. Phys.* **49**, 095203 (2016)
- S. Aleiferis, P. Svarnas, S. Béchu, O. Tarvainen, M. Bacal, Production of hydrogen negative ions in an ECR volume source: Balance between vibrational excitation and ionization. *Plasma Sources Sci. Technol.* **27**, 075015 (2018)
- J. Asmussen, P. Mak, Control of multipolar electron cyclotron resonance discharges using internal cavity impedance matching. *Rev. Sci. Instrum.* **67**, 1753 (1994)
- M. Bacal, F. Hillion, M. Nachman, Extraction of volume-produced H^- ions. *Rev. Sci. Instrum.* **56**, 649 (1985)
- M. Bacal, Photodetachment diagnostic techniques for measuring negative ion densities and temperatures in plasmas. *Rev. Sci. Instrum.* **71**, 3981 (2000)
- M. Bacal, A.A. Ivanov Jr., M. Glass-Maujean, Y. Matsumoto, M. Nishiura, M. Sasao, M. Wada, Contribution of wall material to the vibrational excitation and negative ion formation in hydrogen negative ion sources. *Rev. Sci. Instrum.* **75**, 1699 (2004)
- M. Bacal, Physics aspects of negative ion sources. *Nucl. Fusion* **46**, S250 (2006)
- M. Bacal, M. Wada, Negative hydrogen ion production mechanisms. *Appl. Phys. Rev.* **2**, 021305 (2015)
- M. Bacal, M. Wada, Negative ion source operation with deuterium. *Plasma Sources Sci. Technol.* **29**, 033001 (2020)
- M. Bacal, M. Sasao, M. Wada, Negative ion sources. *J. Appl. Phys.* **129**, 221109 (2021)
- J.N. Bardsley, J.M. Wadehra, Dissociative attachment and vibrational excitation in low-energy collisions of electrons with H_2 and D_2 . *Phys. Rev. A* **20**, 1398 (1979)
- R.J. Baxter, P. Hu, Insight into why the Langmuir-Hinshelwood mechanism is generally preferred. *J. Chem. Phys.* **116**, 4379 (2002)
- S. Béchu, A. Soum-Glaude, A. Bes, A. Lacoste, P. Svarnas, S. Aleiferis, A.A. Jr Ivanov, M. Bacal, Multi-dipolar microwave plasmas and their application to negative ion production. *Phys. Plasmas* **20**, 101601 (2013)
- S. Béchu, S. Aleiferis, J. Bentounes, L. Gavilan, V.A. Shakhmatov, A. Bès, P. Svarnas, S. Mazouffre, N. de Oliveira, R. Engeln, J.L. Lemaire, Detection of rovibrationally excited molecular hydrogen in the electronic ground state via synchrotron radiation. *Appl. Phys. Lett.* **111**, 074103 (2017)
- S. Béchu, J.L. Lemaire, L. Gavilan, S. Aleiferis, V. Shakhmatov, Y.A. Lebedev, D. Fombaron, L. Bonny, J. Menu, A. Bès, P. Svarnas, N. de Oliveira, Direct measurements of electronic ground state ro-vibrationally excited D_2 molecules produced on ECR plasma-facing materials by means of VUV-FT absorption spectroscopy. *J. Quant. Spectrosc. Radiat. Transf.* **257**, 107325 (2020)
- J. Bentounes, S. Béchu, F. Biggins, A. Michau, L. Gavilan, J. Menu, L. Bonny, D. Fombaron, A. Bès, A. Lebedev Yu, V.A. Shakhmatov, P. Svarnas, T. Hassaine, J.L. Lemaire, A. Lacoste, Effects of the plasma-facing materials on the negative ion H^- density in an ECR (2.45 GHz) plasma. *Plasma Sources Sci. Technol.* **27**, 055015 (2018)
- M. Cacciatore, M. Rutigliano, The semiclassical and quantum-classical approaches to elementary surface processes: Dissociative chemisorption and atom recombination on surfaces. *Phys. Scr.* **78**, 058115 (2008)

- M. Cacciatore, M. Rutigliano, Dynamics of plasma-surface processes: E-R and L-H atom recombination reactions. *Plasma Sources Sci. Technol.* **18**, 023002 (2009)
- M. Capitelli, M. Cacciatore, R. Celiberto, O. De Pascale, P. Diomede, F. Esposito, A. Gicquel, C. Gorse, K. Hassouni, A. Laricchiuta, S. Longo, D. Pagano, M. Rutigliano, Vibrational kinetics, electron dynamics and elementary processes in H₂ and D₂ plasmas for negative ion production: modelling aspects. *Nucl. Fusion* **46**, S260 (2006)
- M. Capitelli, R. Celiberto, G. Colonna, F. Esposito, C. Gorse, K. Hassouni, A. Laricchiuta, S. Longo, Formation of Vibrationally and Rotationally Excited Molecules during Atom Recombination at Surfaces, in *Fundamental Aspects of Plasma Chemical Physics*, (Springer, New York, 2016)
- R. Celiberto, R.K. Janev, A. Laricchiuta, M. Capitelli, J.M. Wadehra, D.E. Atems, Cross section data for electron-impact inelastic processes of vibrationally excited molecules of hydrogen and its isotopes. *At. Data Nucl. Data Tables* **77**, 161 (2001)
- C. Courteille, A.M. Bruneteau, M. Bacal, Investigation of a large volume negative hydrogen ion source. *Rev. Sci. Instrum.* **66**, 2533 (1995)
- A.V. Dem'yanov, N.A. Dyatko, I.V. Kochetkov, A.P. Napartovich, A.F. Pal', V.V. Pichugin, A.N. Starostin, Properties of a beam-driven discharge in an H₂-Ar mixture. *Sov. J. Plasma Phys.* **11**, 210 (1985)
- N. de Oliveira, M. Roudjane, D. Joyeux, D. Phalippou, J.-C. Rodier, L. Nahon, High-resolution broad-bandwidth Fourier-transform absorption spectroscopy in the VUV range down to 40 nm. *Nat. Photo-Dermatology* **5**, 149 (2011)
- N. de Oliveira, D. Joyeux, D. Phalippou, J.C. Rodier, F. Polack, M. Vervloet, L. Nahon, A Fourier transform spectrometer without a beam splitter for the vacuum ultraviolet range: From the optical design to the first UV spectrum. *Rev. Sci. Instr.* **80**, 043101 (2009)
- V.D. Dougra-Jabon, A.J. Velasco, F.A. Vivas, Hydrogen negative ion production in an electron cyclotron resonance driven plasma. *Rev. Sci. Instrum.* **69**, 950 (1998)
- V.D. Dougra-Jabon, D.V. Reznikov, R. Santos Mayorga, Negative hydrogen ion ECR source. *Rev. Sci. Instrum.* **63**, 2529 (1992)
- V.D. Dougra-Jabon, Production of hydrogen and deuterium negative ions in an electron cyclotron resonance driven plasma. *Phys. Scri.* **63**, 322 (2001)
- M.J.J. Eerden, M.C.M. van de Sanden, D.K. Otorbaev, D.C. Schram, Cross section for the mutual neutralization reaction H₂⁺ + H⁻, calculated in a multiple-crossing Landau-Zener approximation. *Phys. Rev. A* **51**, 3362 (1995)
- D.D. Eley, E.K. Rideal, Parahydrogen conversion on Tungsten. *Nature* **146**, 401 (1940)
- U. Fantz, Basics of plasma spectroscopy. *Plasma Sources Sci. Technol.* **15**, S137 (2006)
- U. Fantz, H. Falter, P. Franzen, D. Wunderlich, M. Berger, A. Lorenz, W. Kraus, P. McNeely, R. Riedl, E. Speth, Spectroscopy – A powerful diagnostic tool in source development. *Nucl. Fusion* **46**, S297 (2006)
- U. Fantz, D. Wunderlich, Franck-Condon factors, transition probabilities, and radiative lifetimes for hydrogen molecules and their isotopomers. *At. Data Nucl. Data Tables* **92**, 853 (2006)
- A. Firdman, L.A. Kennedy, *Plasma Physics and Engineering* (Taylors & Francis Books Inc., New York, 2004)
- R. Friedl, U. Kurutz, U. Fantz, Efficiency of Cs-free materials for negative ion production in and plasmas. *AIP Conf. Proc.* **1869**(030022) (2017)
- R. Friedl, D. Rauner, A. Heiler, U. Fantz, Dissociative recombination and its impact on the line profile of the hydrogen Balmer series. *Plasma Sources Sci. Technol.* **29**, 015014 (2020)
- S. Gammino, L. Celona, G. Ciavola, F. Maimone, D. Mascali, Review of high current 2.45 GHz electron cyclotron resonance sources (invited). *Rev. Sci. Instrum.* **81**, 02B313 (2010)
- R. Gobin, P. Auvray, M. Bacal, J. Breton, O. Delferrière, F. Harrault, A.A. Ivanov Jr., P. Svarnas, O. Tuske, Two approaches for H⁻ ion production with 2.45 GHz ion sources. *Nucl. Fusion* **46**, S281 (2006)
- V.A. Godyak, V.I. Demidov, Probe measurements of electron-energy distributions in plasmas: What can we measure and how can we achieve reliable results? *J. Phys. D. Appl. Phys.* **44**, 233001 (2011)

- B. Gordiets, C.M. Ferreira, M.J. Pinheiro, A. Ricard, Self-consistent kinetic model of low-pressure N₂-H₂ flowing discharges: I. Volume processes. *Plasma Sources Sci. Technol.* **7**, 363 (1998)
- W.G. Graham, The kinetics of negative hydrogen ions in discharges. *Plasma Sources Sci. Technol.* **4**, 281 (1995)
- P.I. Hall, I. Čadež, M. Landau, F. Pichou, C. Schermann, Vibrational excitation of hydrogen via recombinative desorption of atomic hydrogen gas on a metal surface. *Phys. Rev. Lett.* **60**, 337 (1988)
- J. Harris, B. Kasemo, On precursor mechanisms for surface reactions. *Surf. Sci.* **105**, L281 (1981)
- J.R. Hiskes, Cross sections for the vibrational excitation of the H₂ ($X^1\Sigma_g^+$) state via electron collisional excitation of the higher singlet states. *J. Appl. Phys.* **51**, 4592 (1980)
- J.R. Hiskes, A.M. Karo, Analysis of the vibrational distribution in a hydrogen discharge. *Appl. Phys. Lett.* **54**(6), 508 (1989)
- J.R. Hiskes, A.M. Karo, Recombination and dissociation of H₂⁺ and H₃⁺ ions on surfaces to form H₂ (ν'): Negative-ion formation on low-work-function surfaces. *J. Appl. Phys.* **67**, 6621 (1990)
- M.S. Huq, L.D. Doverspike, R.L. Champion, Electron detachment for collisions of H⁻ and D⁻ with hydrogen molecules. *Phys. Rev. A* **27**(6), 2831 (1983)
- B. Jackson, D. Lemoine, Eley-Rideal reactions between H atoms on metal and graphite surfaces: The variation of reactivity with substrate. *J. Chem. Phys.* **114**, 474 (2001)
- R.K. Janev, D. Reiter, U. Samm, *Collision Processes in Low-Temperature Hydrogen Plasma* (Forschungszentrum, Zentralbibliothek, 2003)
- T. Kammler, D. Kolovos-Vellianitis, J. Küppers, A hot-atom reaction kinetic model for H abstraction from solid surfaces. *Surf. Sci.* **460**, 91 (2000)
- K.W. Kolasinski, *Surface Science: Foundations of Catalysis and Nanoscience*, 4th edn. (Wiley, 2019)
- J. Komppula, O. Tarvainen, T. Kalvas, H. Koivisto, R. Kronholm, J. Laulainen, P. Myllyperkiö, VUV irradiance measurement of a 2.45 GHz microwave-driven hydrogen discharge. *J. Phys. D: Appl. Phys.* **48**(365201), 365201 (2015)
- U. Kurutz, U. Fantz, Investigations on caesium-free alternatives for H⁻ formation at ion source relevant parameters. *AIP Conf. Proc.* **1655**, 020005 (2015)
- U. Kurutz, R. Friedl, U. Fantz, Investigations on Cs-free alternatives for negative ion formation in a low pressure hydrogen discharge at ion source relevant parameters. *Plasma Phys. Control. Fusion* **59**, 075008 (2017)
- A. Lacoste, T. Lagarde, S. Béchu, Y. Arnal, J. Pelletier, Multi-dipolar plasmas for uniform processing: Physics, design and performance. *Plasma Sources Sci. Technol.* **11**, 407 (2002)
- T. Lagarde, Y. Arnal, A. Lacoste, J. Pelletier, Determination of the EEDF by Langmuir probe diagnostics in a plasma excited at ECR above a multipolar magnetic field. *Plasma Sources Sci. Technol.* **10**, 181 (2001)
- M.A. Lieberman, A.J. Lichtenberg, *Principles of Plasma Diagnostics and Material Processing*, 2nd edn. (Wiley, Hoboken, NJ, 2005)
- A.A. Matveyev, V.P. Silakov, Kinetic processes in a highly-ionized non-equilibrium hydrogen plasma. *Plasma Sources Sci. Technol.* **4**, 606 (1995)
- K.A. Müller, H. Bruhns, M. Čížek, J. Eliášek, R. Cabrera-Trujillo, H. Kreckel, A.P. O'Connor, X. Urbain, D.W. Savin, Isotope effect for associative detachment: H(D)⁻ + H(D) → H₂(D₂) + e⁻. *Phys. Rev. A* **86**, 032714 (2012)
- M. Mitrou, P. Svarnas, S. Béchu, H⁻ and D⁻ production efficiency in a multi-dipole ECR-plasma source as a function of gas pressure. *J. Phys. Conf. Ser.* **2244**, 012007 (2022)
- S. Morisset, F. Aguilon, M. Sizun, V. Sidis, Quantum dynamics of H₂ formation on a graphite surface through the Langmuir Hinshelwood mechanism. *J. Chem. Phys.* **121**, 6493 (2004)
- T. Mosbach, Population dynamics of molecular hydrogen and formation of negative hydrogen ions in a magnetically confined low temperature plasma. *Plasma Sources Sci. Technol.* **14**, 610 (2005)

- B. Peart, K.T. Dolder, Collision between electrons and H_2^+ ions VI. Measurements of cross sections for the simultaneous production of H^+ and H^- . *J. Phys. B: Atom. Molec. Phys.* **8**, 1570 (1975)
- D. Rauner, U. Kurutz, U. Fantz, Comparison of measured and modelled negative hydrogen ion densities at the ECR-discharge HOMER. *AIP Conf. Proc.* **1655**(020017) (2015)
- J.R. Roth, *Industrial Plasma Engineering* (Institute of Physics Publishing Ltd., London, 1995)
- M. Rutigliano, M. Cacciatore, G. Billing, Hydrogen atom recombination on graphite at 10 K via the Eley-Rideal mechanism. *Chem. Phys. Lett.* **340**, 13 (2001)
- M. Rutigliano, M. Cacciatore, Eley-Rideal recombination of hydrogen atoms on a tungsten surface *Phys. Chem. Chem. Phys.* **13**, 7475 (2011)
- D. Spence, K.R. Lykke, Production of negative hydrogen and deuterium ions in microwave-driven ion sources, Proc. 19th Linear Accelerator Conference (LINAC), Chicago, IL, USA, TU4048, 508 (1998)
- P. Svarnas, J. Breton, M. Bacal, T. Mosbach, Pressure optimization for H^- ion production in an electron cyclotron resonance-driven and a filamented source. *Rev. Sci. Instrum.* **77**, 03A532 (2006)
- P. Svarnas, J. Breton, M. Bacal, R. Faulkner, Plasma electrode bias effect on the H^- negative-ion density in an electron cyclotron resonance volume source. *IEEE Trans. Plasma Sci.* **35**, 1156 (2007)
- F. Taccogna, R. Schneider, S. Longo, M. Capitelli, Modeling of a negative ion source. I. Gas kinetics and dynamics in the expansion region. *Phys. Plasmas* **14**(73503), 073503 (2007)
- A.J.C. Velasco, A.L.C. Parra, W.A.P. Serrano, Negative ion generation and isotopic effect in electron cyclotron resonance plasma. *IEEE Trans. Plasma Sci.* **43**, 1729 (2015)
- M.C. Williamson, A.J. Lichtenberg, M.A. Lieberman, Self-consistent electron cyclotron resonance absorption in a plasma with varying parameters. *J. Appl. Phys.* **72**, 3924 (1992)
- B.J. Wood, H. Wise, Diffusion and heterogeneous reaction. II. Catalytic activity of solids for hydrogen atom recombination. *J. Chem. Phys.* **29**, 1416 (1958)
- B.J. Wood, H. Wise, Kinetics of hydrogen atom recombination on surfaces. *J. Phys. Chem.* **65**, 1976 (1961)
- W. Yang, S.N. Averkin, A.V. Khrabrov, I.D. Kaganovich, Y.N. Wang, S. Aleiferis, P. Svarnas, Benchmarking and validation of global model code for negative hydrogen ion sources. *Phys. Plasmas* **25**, 113509 (2018)
- T. Zhang, S.-X. Peng, W.-B. Wu, H.-T. Ren, J.-F. Zhang, J.-M. Wen, T.-H. Ma, Y.-X. Jiang, J. Sun, Z.-Y. Guo, J.-E. Chen, Practical 2.45-GHz microwave-driven Cs-free H^- ion source developed at Peking University. *Chin. Phys. B* **27**(105208), 105208 (2018)

Chapter 13

Vibrational Spectroscopy of Hydrogen Molecules by Detecting H^- (D^-) and Its Use in Studies Relevant to Negative Ion Sources



Iztok Čadež and Sabina Markelj

Abstract In this chapter, we present a method for vibrational spectroscopy of hydrogen molecules based on the properties of the dissociative electron attachment. This method is most sensitive to highly excited molecules that are of primary importance for volume negative ion sources. Its sensitivity to highly excited molecules is the same for all hydrogen isotopologues. This makes the method suitable not only for studies relevant to the hydrogen ion volume sources but also for plasma-wall interaction studies in tokamaks. The basics of the method and two corresponding instruments are discussed. Results obtained using these instruments as well as the potential use of this technique for further studies are presented.

Keywords Hydrogen molecule · Vibrational spectroscopy · Dissociative attachment · Atom surface recombination · Negative ion source · Edge plasma

13.1 Introduction

Studies of processes involving hydrogen molecules have recently been strongly boosted by the development of controlled fusion for energy production. Here, data are needed not only for ions and molecules containing light hydrogen (H) but also for ions and molecules containing D and T isotopes which are the fuel for the energy release fusion D-T reaction in the hot core plasma in tokamaks. The development of high-intensity neutral beams of hydrogen atoms is a field of high technological importance as these beams are one of the crucial tools for fusion plasma heating in the tokamak reactor (Hemsworth et al. 2017). The initial stage of a neutral beam system is an effective source of negative hydrogen ions. Ro-vibrationally excited

I. Čadež (✉) · S. Markelj
Jožef Stefan Institute, Ljubljana, Slovenia
e-mail: iztok.cadez@ijs.si

hydrogen molecules in the ground electronic state are of fundamental importance for negative ion volume sources (Bacal and Wada 2015, 2020; Taccogna et al. 2021) as the electron attachment to such molecules leads effectively to the formation of the needed hydrogen negative ions, H^- or D^- . Cross sections and reaction rates for the whole manifold of processes involving ro-vibrationally excited hydrogen molecules are therefore required for the development of an effective negative ion source. The relevant database, as well as modelling methods for negative ion sources, are continuously updated and developed (e.g. (Capitelli et al. 2006) and Chaps. 3, 4, and 7 in this book).

Hydrogen reactions on surfaces are among the most studied surface reactions of fundamental scientific importance. It was observed that vibrationally excited hydrogen molecules are created by atom recombination on metal surfaces (Hall et al. 1988; Eenshuistra et al. 1988; Rettner and Auerbach 1995). The knowledge of this reaction is therefore important for choosing materials to be used in the volume sources of negative hydrogen ions (e.g. Bacal et al. 2021). Beam-like setups are typically used when studying the kinetics of hydrogen atoms on a surface and the production of hydrogen molecules via atom recombination processes (e.g. Kammler et al. 1997; Winkler 1998). Molecules produced via recombination in such experiments are detected and analyzed by a quadrupole mass spectrometer, translational spectroscopy, and various laser techniques. The adsorbed species on the surface are studied by thermal desorption spectroscopy (e.g. Tamm and Schmidt 1969; Rettner and Ashfold 1991) and more recently also by ion beam methods (e.g. Markelj et al. 2013; Založnik et al. 2016). The internal energy of hydrogen molecules released from the surface depends on surface exposure conditions to hydrogen, surface composition and properties, and surface temperature. For a particular case, the relative contribution of the three main recombination mechanisms, Langmuir–Hinshelwood (LH), Eley–Rideal (ER), and hot-atom ER, depends on these surface properties (e.g. Rettner and Ashfold 1991; Jackson et al. 2002). Important progress has recently been achieved in the theoretical description of hydrogen recombination on a surface by Rutigliano and Cacciatore from the Bari group (Cacciatore and Rutigliano 2009; Rutigliano and Cacciatore 2011) and by Pétuya and co-workers (e.g. Pétuya et al. 2015; Galparsoro et al. 2015).

Studies of vibrationally excited hydrogen molecules in plasma are much more complex and difficult than in the relatively mild environment of neutral atoms and molecules mentioned above. Laser-based methods were used for studies of vibrationally excited hydrogen in the volume source (Mosbach et al. 2000) and a plasma jet produced by the cascading arc source (Gabriel et al. 2010). The presence of vibrationally excited hydrogen molecules in the ground electronic state was identified in the divertor plasma of a tokamak by analysis of the Fulcher band emission spectrum (Fantz et al. 2001). Their role in the scenario of plasma detachment from the target plates of the divertor is well recognized (Kukushkin et al. 2005; Okamoto et al. 2007) and included in detailed edge plasma modelling (Guillemaut et al. 2014). Active research on the role of hot hydrogen molecules is in progress (Verhaegha et al. 2020) to predict conditions in the edge plasma of ITER. A detailed up-to-date review of the role of atomic and molecular processes in fusion

edge plasma is presented by Krashennikov et al. (2020). Studies of processes with vibrationally excited molecules relevant to edge plasma are performed also at linear plasma devices (Hollmann et al. 2006; Akkermans et al. 2020) which provide an easier variation of experimental parameters than in tokamaks. Fantz and Wunderlich collected available data on atomic and molecular properties, Franck–Condon factors, transition probabilities, and radiative lifetimes for isotopologues of hydrogen molecules (Fantz and Wunderlich 2004). Various reaction rates and cross sections for vibrationally excited hydrogen molecules are included in the database of the Eirene modelling code and are continuously being updated (Reiter et al. 2005).

In this chapter, we present a method for performing vibrational spectroscopy of hydrogen molecules based on the detection of negative ions produced by the process of dissociative electron attachment (DEA). A short overview of DEA to hydrogen is given in Sect. 13.2. The physical basics of the developed method for hydrogen vibrational spectroscopy (HVS) and two experimental setups based on this method are described in Sect. 13.3, and some characteristic results are given in Sect. 13.4. Finally, in Sect. 13.5, a general comment is provided together with perspectives for the future use of the described method.

13.2 Dissociative Electron Attachment to Hydrogen

Dissociative electron attachment is a resonant electron–molecule collisional process. It proceeds in two steps: first, the incoming electron is attached to the target molecule, and an intermediary quasi-bound state of the negative molecular ion is formed. This compound state is characterized by a finite lifetime and it can dissociate into a neutral fragment and a negative ion (second step) if energy conditions are fulfilled. Alternatively, the compound state decays by autodetachment of the extra electron, and a neutral molecule is left in its initial or some excited state—resonant elastic or inelastic scattering. These processes are said to be resonant because they occur only in certain electron energy ranges, where electronic states of the compound system exist. DEA is quantitatively characterized by its cross section (CS) which is experimentally determined by measuring the negative ion current collected along a certain length of a well-defined electron beam passing through the target gas of known density.

DEA to the hydrogen molecule, mainly to its lightest isotopologue H₂,



is one of the benchmark cases of electron-molecule resonant collisions. It was extensively studied in the past, both experimentally and, even more so, theoretically. A detailed overview of DEA to hydrogen isotopologues, H₂, HD, and D₂, can be found in the review by Yoon and collaborators (2010) and a shorter update in the review by Fabrikant and collaborators (2017).

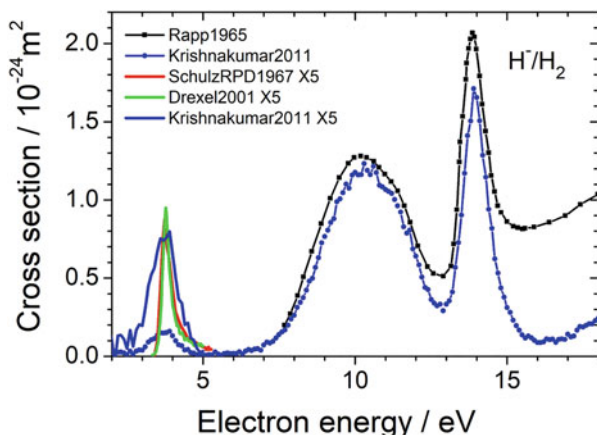


Fig. 13.1 The most recent measured absolute cross section for DEA to H_2 (Krishnakumar et al. 2011) together with earlier measurements (Rapp et al. 1965; Schultz and Asundi 1967; Drexel et al. 2001). Cross sections below 5 eV are multiplied by 5 for better display

The experimentally determined absolute DEA cross-section for H_2 is shown in Fig. 13.1. Three DEA regions are distinguished, two narrow ones at around 4 eV and 14 eV, and a broad one between 7 and 13 eV. In early work by Schulz (1959) it was shown that H^- ions from 7–13 eV process have appreciable kinetic energy while those from 14 eV have low, down to near-zero energy. This was explained by the purely repulsive character of the potential function for the compound state for the 7–13 eV DEA channel and a potential curve with attractive character for the 14 eV (later also for the DEA at 4 eV). The DEA cross-section to H_2 is rather small, two orders of magnitude smaller than DEA cross-sections to some heavier common molecules such as H_2O , NH_3 , CO , or O_2 .

Three DEA channels in H_2 are explained by three resonant states (H_2^-) through which the process proceeds. Electronic compound resonant states cannot be represented by potential curves dependent on the bond length, R , in the same way as for neutral molecules as these states are unstable. In the first approximation, the so-called local complex potential (LCP) theory (e.g. Wadehra and Bardsley 1978), they are represented by a complex, R -dependent, potential. The real part of such potential is then used for discussion of the DEA dynamics. Although the LCP model is not the most rigorous it is a useful tool for the explanation of DEA details. The real parts of resonant potentials leading to DEA in H_2 as a function of the bond length are shown in Fig. 13.2 together with the potential of the ground state of the neutral molecule. Red vertical arrows indicate the lowest electron energy needed for DEA to occur through attractive potential.

Symmetries of resonant states are determined by molecular structure theory (see the calculations for H_2^- by Stibbe and Tennyson (1998)) and experimentally by measurements of H^- angular distributions (Tronc et al. 1977, 1979; Prabhudesai et al. 2020).

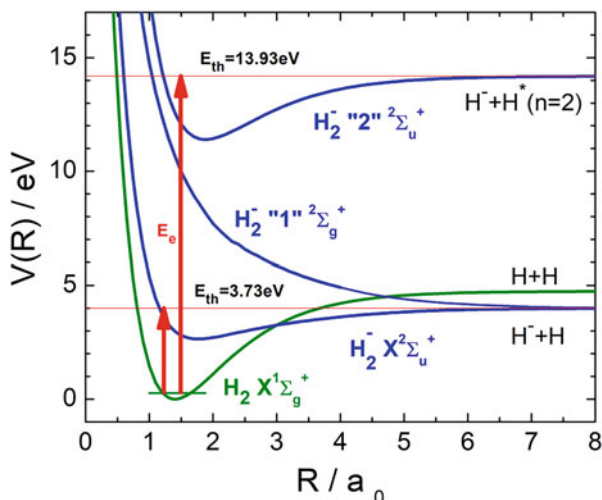


Fig. 13.2 Real parts of the three lowest resonant state potentials in hydrogen, $X^2\Sigma_u^+$, $'1''^2\Sigma_g^+$ and $'2''^2\Sigma_u^+$ which lead to DEA for electron energy below 15.5 eV. The ground state potential $X^1\Sigma_g^+$ of the neutral molecule (Wolniewicz 1993) is also shown

The energy balance for DEA, without contributions due to the electron momentum transfer and target thermal motion, is:

$$E_e + E_{v,J} = E_{ex} + E_{kf} + D_e - EA \quad (13.2)$$

where E_e stands for the incident electron energy, $E_{v,J}$ is the initial ro-vibrational energy of the neutral target molecule, E_{ex} and E_{kf} are the electronic excitation energy and total kinetic energy of fragments, respectively, D_e is the depth of the hydrogen molecule ground electronic potential ($D_e = 4.7485$ eV (Wolniewicz 1993)), and EA is the electron affinity of the negative ion ($EA(H) = 0.7542$ eV, $EA(D) = 0.7546$ eV (Bacal and Wada 2020)). The dissociation energy, $D_0 = D_e - E_{0,0}$ is precisely determined by spectroscopic methods ($D_0(H_2) = 4.4781$ eV, $D_0(HD) = 4.5137$ eV, $D_0(D_2) = 4.5562$ eV (Wolniewicz 1993)). From D_e and D_0 one gets the energies of the ground ro-vibrational states, $E_{0,0}(H_2) = 0.2705$ eV, $E_{0,0}(HD) = 0.2348$ eV, $E_{0,0}(D_2) = 0.1923$ eV.

The shape of the DEA cross section as a function of electron energy depends on the position of the resonant state potential in the Franck-Condon region of the target state. If the resonant state is characterized by the potential with a potential well, then there exists the threshold energy at which DEA becomes energetically possible. Below this energy, the resonant state if already formed can decay only by autodetachment and the CS for DEA exhibits a sudden vertical rise at the threshold. Such a situation occurs for the 4 eV and 14 eV peaks in H_2 . There is no DEA threshold if the V^- potential is entirely repulsive because the total energy is sufficient for dissociation whenever the compound state is formed. Therefore, for

the 7–13 eV process in hydrogen, dissociating fragments, both in the ground state as in the 4 eV process, are formed with higher kinetic energy.

The threshold energy of the incident electron, E_{th} , is determined by the condition $E_{\text{kf}} = 0$:

$$E_{\text{th}} = E_{\text{ex}} + D_0 - EA - (E_{v,J} - E_{0,0}) \quad (13.3)$$

The 4 eV DEA in H_2 has therefore a threshold at $E_{\text{th}}(\text{H}_2;0,0) = 3.724$ eV ($E_{\text{ex}} = 0$ eV, ground state H) while the threshold for the 14 eV process is $E_{\text{th}}(\text{H}_2;0,0) = 13.923$ eV as the H atom fragment is created in the $n = 2$ excited state, ($E_{\text{ex}}(\text{H};n = 2) = 10.199$ eV and $E_{\text{ex}}(\text{D};n = 2) = 10.202$ eV, from <https://webbook.nist.gov>). Respective thresholds in D_2 are 3.802 eV and 14.004 eV. These both DEA channels exhibit a rather narrow peak in the H^- ion yield curve as a function of electron energy. Above the electron energy of 14 eV there is a series of weak DEA channels dissociating to the excited atoms in $n = 3, n = 4, \dots$ state up to the threshold for ion-pair production ($\text{H}^+ + \text{H}^-$) at 17.322 eV (Čadež et al. 2004) (17.405 eV for $\text{D}^+ + \text{D}^-$) ($IE(\text{H}) = 13.598$ eV; $IE(\text{D}) = 13.603$ eV, from <https://webbook.nist.gov>).

The peak cross section in H_2 for the 4 eV process is about ten times smaller than that for the 14 eV. It is important to note that for both vertical onsets DEA channels, the experimental values depend strongly on the energy resolution of the electron beam (e.g. Drexel et al. 2001; Krishnakumar et al. 2011) as a sharp, step-like cross section must be convoluted with a broader energy distribution of the electron beam.

The pronounced relative mass increase, 1:2:3 for hydrogen isotopes H, D, and T, leads to a strong isotope effect in DEA, especially for the 4 eV process, and represents an additional charm of the DEA studies. The low mass of hydrogen has also the consequence that additional attention has to be devoted to the interpretation of the experimental results as the incident electron momentum transferred to the molecule is not negligible as it is in the case with heavier molecules.

The cross-section for DEA to D_2 is smaller than that for H_2 due to a slower dissociation of the more massive nuclei leading to a decreased survival probability of negative ion compound state to dissociating. Namely, a slower nuclear motion increases the probability of electron autodetachment. The most recently measured DEA cross sections for H_2 and D_2 by Krishnakumar and co-workers (2011) are shown in Fig. 13.3. The cross section for D^-/D_2 is multiplied by 3 showing that the cross sections for H_2 are about 3 times bigger than for D_2 for the 14 eV process, and about 18–20 times for the 7–13 eV process. The isotope effect is the most pronounced for the 4 eV process, more than 200 times smaller CS in D_2 than in H_2 (Yoon et al. 2010), making the signal of D^- from D_2 barely detectable under standard experimental conditions.

The most fascinating property of DEA to hydrogen, H_2 and D_2 , is a spectacular increase of the 4 eV cross section with the target gas temperature discovered by Allan and Wong (1978). This observation was interpreted by the strong dependence

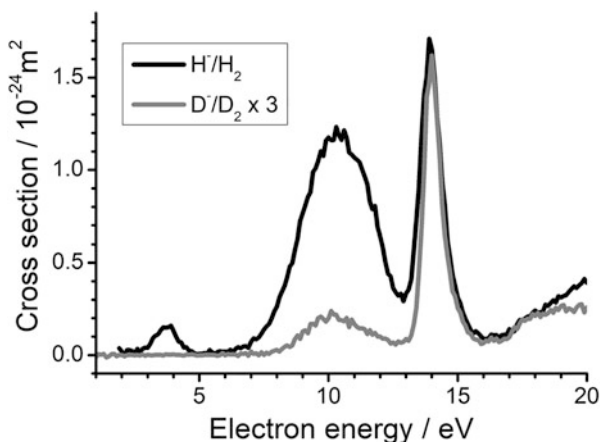


Fig. 13.3 Absolute cross section for the formation of H^- from H_2 (black line) and for D^- from D_2 (grey line) measured by Krishnakumar and co-workers (2011). The Cross section for D_2 is multiplied by 3

of the DEA cross section on the ro-vibrational excitation of the hydrogen molecule. The theoretical explanation and quantitative evaluation were published by Wadehra and Bardsley (1978) simultaneously with this experimental finding. A satisfactory quantitative agreement between theory and experiment was achieved using the LCP model developed earlier (Bardsley et al. 1966). This discovery was induced by the need to explain previously observed unexpected high concentrations of H^- ions in ion source plasma (Nicolopoulou et al. 1977; Bacal and Hamilton 1979). More details on the historic details of this discovery can be found in Bacal and Wada (2015).

13.3 Hydrogen Vibrational Spectroscopy (HVS) by Negative Ion Detection

The first experimental demonstration of HVS by detecting negative ions from DEA was conceived, constructed, and performed at Université Pierre et Marie Curie (Paris 6), France during 1986–1987. This work was initiated by the need for data on $\text{H}_2(\nu)$ formation in the plasma of volume-negative ion sources, promoted by Marthe Bacal of the Ecole Polytechnique, Palaiseau, and it followed the proposal of Jean-Pierre Ziesel from Université Paris-Sud, Orsay who speculated that DEA could be used for diagnostics of vibrationally excited hydrogen molecules.

13.3.1 Basics of the Use of DEA Properties for Hydrogen Vibrational Spectroscopy (HVS)

In the following we are mostly interested in the 4 eV DEA process, and, to a lesser extent, that at 14 eV. Both of these processes exhibit a vertical threshold of the DEA cross-section as they proceed through resonant states with attractive potentials (Fig. 13.2). The real and imaginary parts of the complex negative ion potential, $W(R) = V^-(R) - i/2 \Gamma(R)$ for the $X^2\Sigma_u^+$ compound state for the 4 eV process in H_2 are shown in Fig. 13.4 (from the classical LCP model of Bardsley and Wadehra). The ground electronic state of H_2 is also shown. Vibrational levels of H_2 are marked, illustrating that only states from $\nu = 0$ to $\nu = 9$ have thresholds for DEA for $E_e > 0$ eV while states above $\nu = 9$ can attach even the zero-energy electrons, leading to slightly energetic fragments.

There are three main properties of the 4 eV DEA to hydrogen which are favorable for using this process for HVS. The first property is the displacement of the DEA threshold to a lower energy with internal excitation of the target molecule (according to Eq. (13.3)). This means that the vibrational level of the target molecule can be identified by its threshold energy. The DEA threshold $E_{th}(0,0)$ for all isotopologues are given in Table 13.1 together with vibrational spacing of the first excited vibrational level, $(E_{1,0} - E_{0,0})$ (Fantz and Wunderlich 2004). The highest pure vibrational level (i.e. for $J = 0$) still having a threshold for $E_e > 0$ eV for each isotopologue, ν_{max} is also given.

The second important property of DEA to hydrogen is that the CS exhibits a sharp, vertical rise at the threshold, and then decreases exponentially. If one uses an ion detection system selectively highly sensitive to very low energy, the “zero

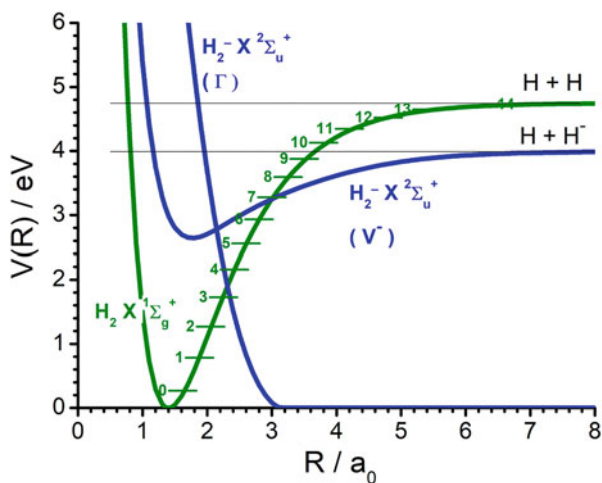
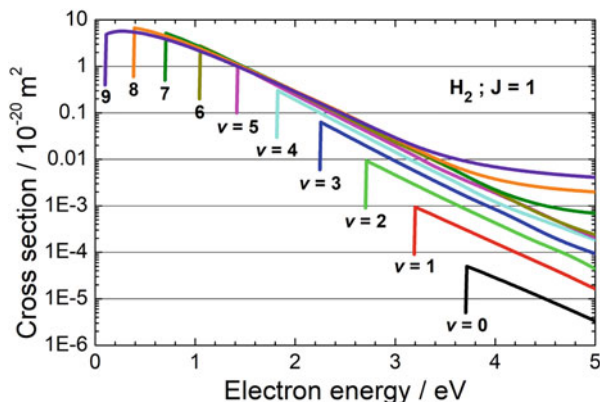


Fig. 13.4 Ground-state, $X^1\Sigma_g^+$ for H_2 and the real and imaginary parts of the complex potential (Bardsley and Wadehra 1979) for the lowest, $X^2\Sigma_u^+$ state of H_2^-

Table 13.1 Threshold energy for DEA to $\nu = 0, J = 0$, the first vibrational energy level (Fantz and Wunderlich 2004), and limiting ν_{max} for all hydrogen isotopologues

	H_2	HD	D_2	HT	DT	T_2
$E_{\text{th}}(0,0)/\text{eV}$	3.725	3.761	3.803	3.774	3.820	3.838
$(E_{1,0} - E_{0,0})/\text{eV}$	0.516	0.450	0.371	0.426	0.340	0.306
$\nu_{\text{max}} (J = 0)$	9	10	13	11	14	16

**Fig. 13.5** Cross sections for DEA to $\text{H}_2(\nu, J = 1)$ as calculated by Horáček et al. (2004)

energy”, ions then peaks in the ion yield occur at the thresholds for the ground state and ro-vibrationally excited states when the electron energy is scanned.

Finally, the third important property of the 4 eV DEA to hydrogen is that the CS rises extremely fast with vibrational and rotational excitation of the target (Allan and Wong 1978). While the CS for the ground state molecules is very small, almost negligible for heavier isotopologues, it becomes very large, in the 10^{-16} cm^2 range, for highly excited molecules for all isotopologues (at and above $\nu = 5$ in H_2 , $\nu = 6$ in HD, and $\nu = 8$ in D_2). This phenomenon was fully elaborated by the rigorous non-local theory of resonant electron scattering by Horáček and co-workers (2004). The theoretical DEA cross sections are available for all ro-vibrationally excited hydrogen isotopologues containing H, D, and T and those for $\text{H}_2(\nu, J = 1)$ are shown in Fig. 13.5.

The present method for diagnostics of hydrogen molecules based on DEA applies not only to vibrationally but also to ro-vibrationally excited molecules as CS is strongly dependent also on rotational excitation. The main limitation of the present experimental technique is the relatively low electron beam energy resolution for separating closely spaced ro-vibrationally excited states. However, vibrational spacing between lower vibrational levels in hydrogen is rather large (see Table 13.1), due to the low hydrogen mass, and also the energy of rotational levels increases with J by the square law so the method is applicable for some specific studies.

The experimental setup needed for HVS by DEA consists of an electron gun that provides an electron beam of variable energy from as close as possible to 0 eV up to

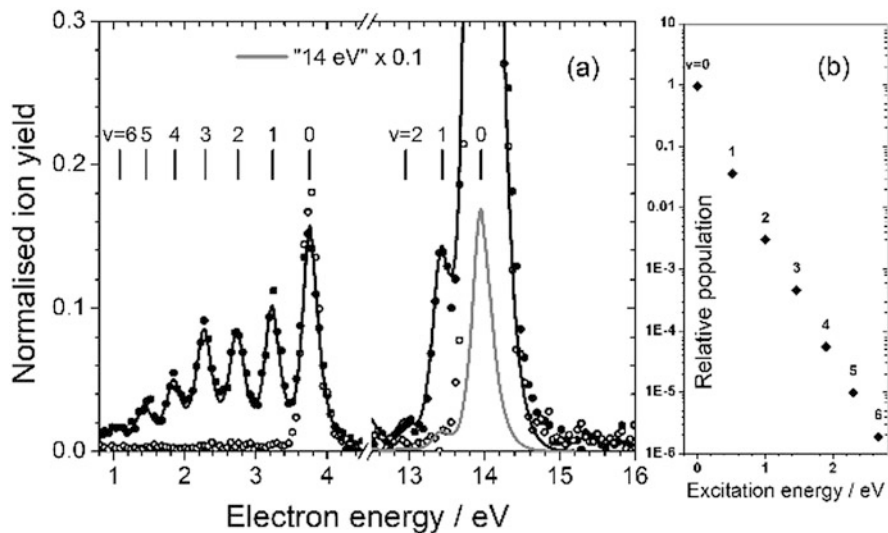


Fig. 13.6 (a) Experimental H^- yield in the region of the 4 eV and 14 eV processes in H_2 . Open circles – ion yield for room temperature target gas; full circles – ion yield for vibrationally hot target gas. The convoluted spectrum used for the determination of relative vibrational state populations is shown by the full line. (b) Relative populations of vibrational states. (Adapted from Čadež et al. (2015), with the permission of NSS)

5 eV or up to 16 eV if the 14 eV process is to be used for diagnostics. This beam goes through the target hydrogen gas and then it is dumped into a Faraday cup collector. The negative ion yield spectrum is recorded by scanning the electron energy and simultaneously detecting the zero-energy ions. Such an ion yield spectrum allows the detection and quantification of vibrationally excited molecules present in the interaction region. This is illustrated by two spectra recorded with cold hydrogen gas (open circles) and gas where vibrational excitation is present (full circles) as shown in Fig. 13.6. The vertical lines in the figure denote the threshold energies for each vibrational level.

When the target hydrogen is at the room temperature, then only a single peak positioned at 3.7 eV is present in the ion yield spectrum corresponding to the 4 eV process. However, if the excited molecules are present in the target region then the ion yield exhibits separate peaks at the respective threshold for each individual vibrational state. Each peak corresponds to a specific vibrational state of the target molecule and its height is proportional to their concentration. In the figure, we see that states up to $v = 6$ are identified.

In order to determine the relative populations of the excited states, it is necessary to perform deconvolution of the experimental ion yield spectrum. A straightforward procedure is to assume that the contribution of each vibrational state to the spectrum is proportional to the relative DEA cross section multiplied by the apparatus response function (Popović et al. 1990). This function was assumed to have the

shape of the ion peak corresponding to $\nu = 0$ in the spectrum recorded with the room-temperature hydrogen. A more detailed deconvolution procedure was developed later by Markelj and co-workers (2008), Markelj and Čadež (2011) taking into account the cross sections of Horáček and co-workers (2004), electron beam energy resolution, and model ion extraction function.

When interpreting the experimental ion yield spectra where the ion yield from excited states is similar to the ground state signal, as in the case shown in Fig. 13.6, one has to bear in mind that the observed comparable heights are purely fortuitous. This simply indicates that as ν increases the increasing cross sections just compensate for the weakening populations.

For the sake of completeness, the simultaneously recorded part of the ion yield spectrum including the 14 eV process is also shown in Fig. 13.6. One can see that for the hot target $\nu = 1$ and $\nu = 2$ peaks also appear at their corresponding energy below $\nu = 0$ of the 14 eV process but their intensity relative to the $\nu = 0$ is much smaller. Although the 14 eV process is much less convenient for vibrational spectroscopy in H_2 , it is still important in the D_2 case. Namely, the vibrational states, $\nu = 0$ and 1 of the 4 eV process in D_2 are barely detectable and the 14 eV process is needed for ion yield deconvolution due to its much weaker isotope effect (Markelj and Čadež 2011).

13.3.2 Experimental Setups

The original experimental implementation of vibrational spectroscopy of hydrogen molecules by detecting negative ions from DEA was achieved at the Laboratoire de Dynamique Moléculaire et Atomique (LDMA), CNRS and Université Pierre et Marie Curie (Paris VI), Paris, France in the late 1980s. Later, in the early 2000s, a new instrument for HVS, based on the same principles, was developed at the Jožef Stefan Institute (JSI) in Ljubljana, Slovenia.

13.3.2.1 Electrostatic Setup at LDMA Paris

The experimental setup for the first studies of vibrational distributions in hydrogen by DEA (Electrostatic setup I) was a modified high-resolution electron spectrometer previously used for studies of electron scattering by atoms and molecules. This spectrometer, described in detail by Hall and co-workers (1973), was modified so that a rotatable electron analyser was replaced by an ion detection line. Besides this, a gas needle for target beam formation used in previous experiments was replaced by a gas cell where vibrationally hot hydrogen could be prepared. A schematic representation of this setup is shown in Fig. 13.7. The electron beam source was composed of an electron gun with a hairpin cathode followed by an electrostatic 127° electron energy filter, and exit-focusing optics. The electron beam energy could be continuously varied between close to 0 eV up to about 20 eV and the energy

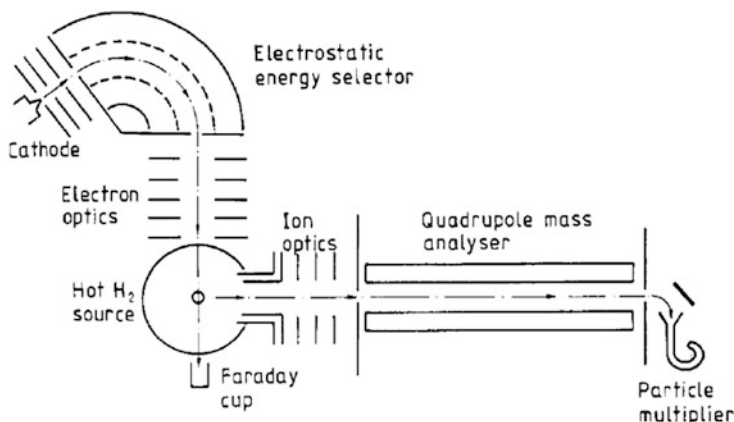


Fig. 13.7 Schematic diagram of the experimental apparatus at LDMA (Popović et al. 1990). © IOP Publishing. (Reproduced with permission. All rights reserved)

spread in the beam was typically between 60 and 100 meV, depending on the beam intensity, typically about 20 nA. The electron beam is directed in front of the exit orifice of a source of excited molecules and it is then collected by a Faraday cup.

The key element of the spectrometer is the ion detection line mounted at 90° with respect to the e-beam. It has to provide high efficiency for the collection of zero-energy ions and, at the same time, the separation of ions by their mass. The entrance optics for ions was inspired by the field penetration technique developed earlier for electron threshold spectroscopy (Cvejanović and Read 1974). A very weak electric field penetrates into the interaction region where the electron beam crosses the gas beam from the source. It ensures the collection of almost all zero-energy ions created by DEA but only a fraction of those with higher energy. After being extracted from the interaction region, ions are focused by a three-electrode lens to form an ion beam which is let through a quadrupole mass filter. The mass filter separates negative hydrogen ions from omnipresent electrons and heavier negative ions from impurities. It also ensures the separation of H^- and D^- if both are produced by DEA to HD or from a mixture of H_2 and D_2 . Finally, ions are detected by an off-axis channel electron multiplier and the signal is recorded by a standard particle counting technique.

For the first measurements, the source of the target hydrogen beam was a cylindrical gas cell with a tungsten filament. This filament, when resistively heated to temperatures between 1300 K and 2000 K is used to dissociate hydrogen molecules in the cell. The cell was made from stainless steel and its walls were cooled by water flow. The internal diameter of the source was 22 mm and its length 55 mm. The source was surrounded by a μ -metal shield to prevent stray magnetic fields to penetrate into the interaction region. This is especially important and critical as very low-energy electrons are used for diagnostics.

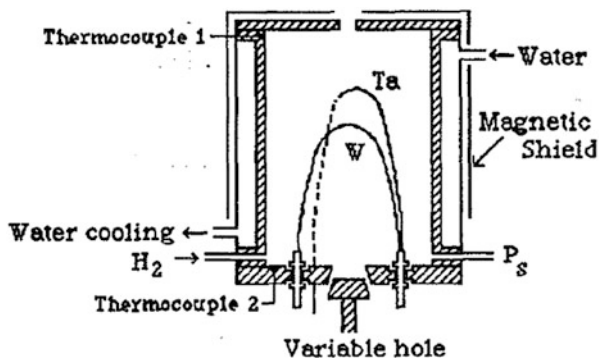


Fig. 13.8 Schematic diagrams of the source of excited hydrogen molecules used for measurements in experiments at LDMA. (Reproduced from Schermann et al. (1994), with the permission of AIP Publishing)

Hydrogen gas is introduced at the bottom of the cell and flows out of it into the vacuum chamber through the circular orifice at the top. Hydrogen atoms, created by molecule dissociation at the hot filament, recombine on the cell wall and vibrationally excited molecules are created. Therefore, hydrogen gas in the cell contains molecules in the ground and vibrationally excited states as well as atoms. The effusive gas beam from the exit orifice at the top of the cell is intercepted by the electron beam in the high vacuum region outside the source.

The electrode system, together with the source of hydrogen atoms and vibrationally hot molecules, was housed within a high vacuum chamber. Earth and stray magnetic fields were shielded by a double μ -metal shield. The first results of the application of DEA for HVS (Hall et al. 1988; Čadež et al. 1988; Popović et al. 1990; Schermann et al. 1991) were obtained on the described spectrometer.

The spectrometer was later upgraded for a more systematic study of the influence of surface material on the production of vibrationally excited H_2 and a new setup was constructed, Electrostatic setup II. The same electrode system which was developed and used in the first arrangement was transferred into a new larger UHV chamber. The gas inlet system was equipped with computer-controlled valves and flowmeters. The new source of vibrationally hot hydrogen was constructed, shown in Fig. 13.8, and described in detail by Schermann and co-workers (1994). It housed two filaments, one to dissociate hydrogen when recording vibrational spectra and the other used for in situ evaporating the desired material to the inner wall of the cell. This second filament was made of the material to be deposited in the case of high-melting point metals and evaporation was performed by its gradual resistive heating until it burns. For the low-melting point metals, this filament was made of tungsten with wrapped pieces of wires of studied metal. Evaporation was performed by heating support tungsten filament until pieces of metal are completely evaporated. The temperatures of filaments were determined and monitored by measuring their resistance. The wall of the cell was cooled by a water flow or, alternatively, by

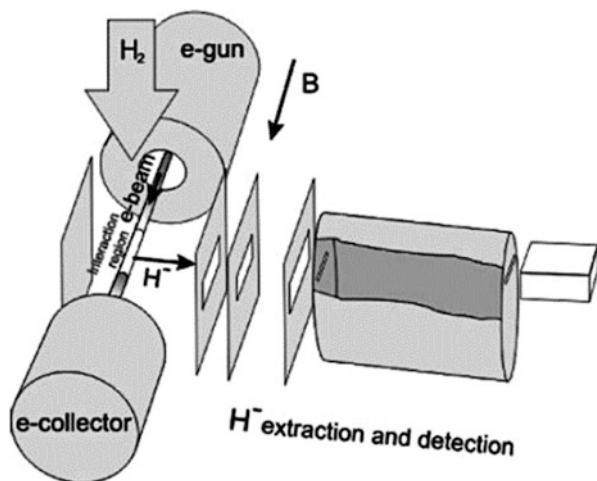


Fig. 13.9 Schematic representation of the setup using a homogeneous magnetic field. (Reproduced from Markelj and Čadež (2011), with the permission of AIP Publishing)

air or liquid nitrogen. The cell had two apertures, one of 4 mm in diameter, at the top of the cell, directed to the interaction region, and another of variable size at the bottom. This second aperture allowed variation of the residence time of molecules in the cell by a factor of 10 while keeping the effusive beam conditions the same. Thermocouples were installed to measure the wall temperature while the cell pressure was measured by the capacitance manometer. A small stainless steel disc was mounted to the bottom of the cell to allow the ex-situ check of the evaporated film by scanning electron microscopy and energy dispersive X-ray analysis (SEM-EDS). The published results (Čadež et al. 1993, 1997, 2004; Schermann et al. 1994; Gough et al. 1996) were obtained with the new apparatus.

13.3.2.2 Magnetic Setup in JSI Ljubljana

Another vibrational spectrometer was later developed at the Jožef Stefan Institute (JSI) in Ljubljana, Slovenia, following the interest in vibrationally excited hydrogen molecules observed in the edge plasma of tokamaks divertor.

The new spectrometer utilized an arrangement of magnetic and electrostatic fields in contrast to the first one which was using electrostatic elements coupled to an RF quadrupole mass filter. This magnetic spectrometer is shown in Fig. 13.9.

A homogeneous magnetic field B generated by external Helmholtz coils is used to collimate a low-energy electron beam. A tantalum disk cathode is the source of electrons and a set of cylindrical electrodes is used to form an electron beam of variable energy. After passing the interaction region, the electron beam is damped into a Faraday cup collector where the electron current is measured.

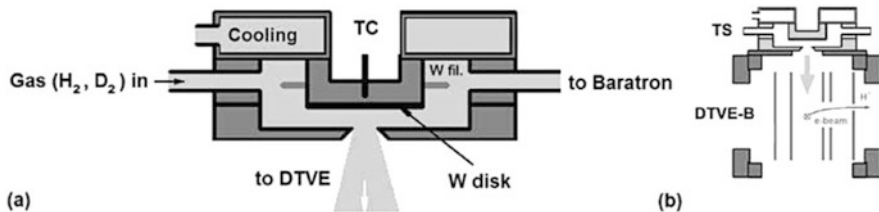


Fig. 13.10 A scheme of the test source (TS) used for measurements of the vibrational distribution of molecules produced by atom recombination on a sample surface, marked as the W disk (a). The detection setup with TS mounted on the vibrational spectrometer marked as DTVE-B (b). (Reproduced from Markelj and Čadež (2011), with the permission of AIP Publishing)

This simple electron gun produces a beam with a rather broad energy distribution which is however reliably represented by the unperturbed distribution of thermionic emission. Ions produced by DEA in the interaction region are extracted by specific ion optics composed of rectangular aperture electrodes and two defining slits. A field penetration concept is again used to efficiently collect the zero-energy ions. This ion optics also serves as a simple mass filter and can distinguish H^- from D^- . Ion optics was designed using the charged particle simulation software CPO3D (Read and Bowring 2011) and described in detail by Markelj and co-workers (2008).

The use of a rectangular aperture lens provides an efficient collection of ions along about 1 cm of the e-beam in the interaction region. The combined action of the electrostatic extraction field and homogeneous magnetic field provides the preferential detection of low-energy ions and their separation by mass. After being extracted, selected, and transmitted, the ions are detected by a channel electron multiplier having a rectangular entrance aperture. The operation of the spectrometer is computer-controlled and all relevant experimental data are recorded together with the ion yield spectrum, $Y_{\text{ion}} = f(E_e)$.

The source of hot hydrogen molecules used in the first measurements with the magnetic spectrometer, shown in Fig. 13.10 also contained a hot tungsten filament. It was mounted at the top of the vibrational spectrometer and details are given in Markelj and Čadež (2011). It was constructed at LDMA in Paris and the main body was made from copper and had a cylindrical shape. A tungsten dissociation filament was positioned around the central cold finger where a disc sample was mounted. In this way, the sample surface is not directly exposed to the dissociation filament. This allows a better definition of the surface temperature and also does not lead to contamination of the sample by evaporation of filament material. The idea behind this source was to allow more direct observation of molecules produced at the sample surface which is closely positioned in front of a large, 6 mm diameter orifice facing the interaction region. Although the exit of the cell was quite far, 4 cm, from the e-beam i.e. from the interaction region, the sensitivity was satisfactory due to the open structure of the electrode system which was mounted just above the vacuum pump.

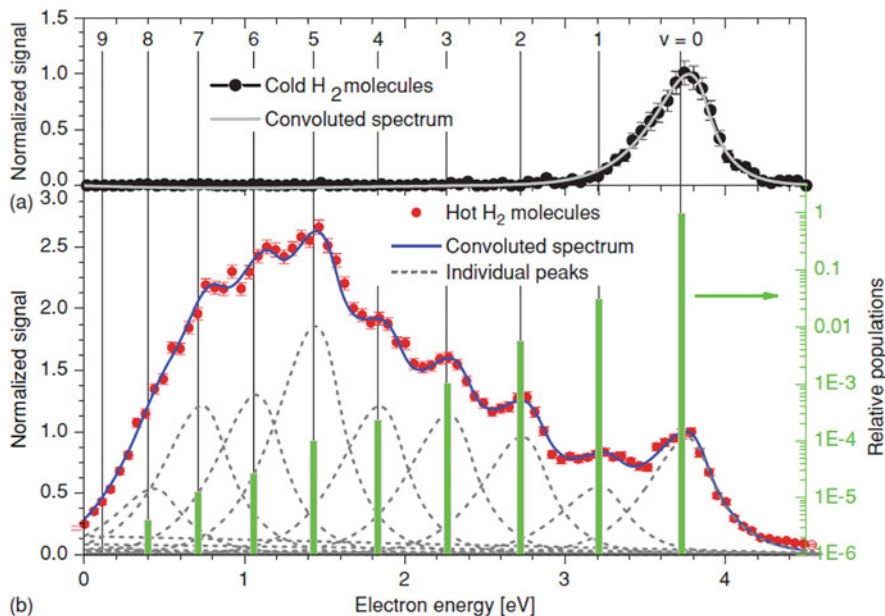


Fig. 13.11 Experimental H^- yield spectra and calculated model spectra for cold (a) and for hot (b) H_2 molecules. Individual peak position, relative contribution, and deduced population for each vibrational state for the hot hydrogen spectrum are shown. (Reproduced from Markelj and Čadež (2011), with the permission of AIP Publishing)

A detailed deconvolution procedure was developed for the magnetic vibrational spectrometer (Markelj et al. 2008; Markelj and Čadež 2011) by using theoretical DEA cross sections of Horáček and co-workers (2004) for ro-vibrational states of H_2 (up to $v = 9$ and up to $J = 14$) and D_2 (up to $v = 13$ and up to $J = 14$). The energy distribution of the electron beam was well characterized by thermionic emission from a Ta-disc cathode and the ion extraction efficiency function was obtained from ion trajectory simulations by the CPO3D software (Read and Bowring 2011). As all components needed for the deconvolution were well defined, it was possible to get reliable vibrational distributions even though the energy resolution of the electron beam was poor. One example of experimental spectra for the cold and hot H_2 is shown in Fig. 13.11.

The simple low-resolution electron gun was at a later stage (Založnik 2016), replaced by a trochoidal electron monochromator (Allan 1989) and the spectra with better resolution were obtained as the one shown in Fig. 13.6. However, most of the published data from the magnetic setup were obtained with a low-resolution gun.

Metal cells with a hot dissociation filament were a very practical source of excited molecules for acquiring information on the dependence of excitation efficiency on the choice of metallic surface, atom flux, and gas pressure. Some information on isotope exchange and surface hydrogen concentration in such a

cell was obtained by an in situ ion beam technique ERDA (Markelj et al. 2007). In addition, such a cell is interesting for modeling (e.g. Založnik et al. 2013) as only neutral particles are present: atoms and ro-vibrationally excited molecules in the ground electronic state. However, data from experiments with a gas cell do not provide a deeper insight into the basic, elementary process of atom recombination on the surface. Interest in such information stimulated the experiment upgrading at JSI.

13.3.2.3 Beam-Like Experimental Setup in JSI Ljubljana

The initial configuration with a gas cell and hot filament was first upgraded by replacing the hot filament as a source of atoms by a commercial hydrogen atom beam source, HABS (from MBE, <http://www.mbe-components.com/products/gas/habs.html>, see also (Tschersich et al. 2008)) placed in the same vacuum chamber as the vibrational spectrometer (Markelj 2010). Finally, a differentially pumped beam-like geometry (Fig. 13.12) was set in order to provide well-defined conditions for the study of hydrogen atom recombination in a more direct way (Založnik et al. 2014; Založnik 2016).

In the differentially pumped arrangement, the setup was divided into two regions, the detection region with vibrational spectrometer and the reaction region where the studied sample is exposed to the hydrogen atom beam. Each of the two regions

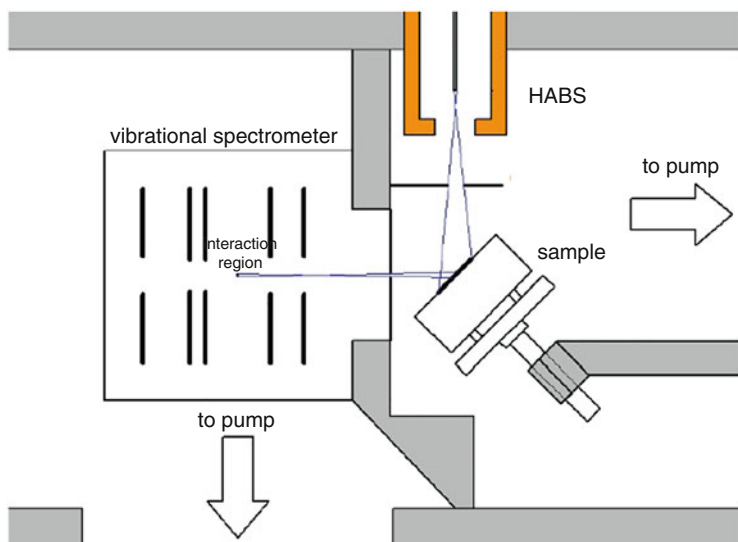


Fig. 13.12 The scheme of the differentially pumped experimental setup. The barrier with only a narrow slit separates the detection region from the region housing a sample and HABS. (Adapted from Založnik (2016))

was pumped by a separate turbomolecular pump. The two regions were connected by a narrow slit parallel to the spectrometer's electron beam. This slit allows molecules from the sample surface to enter straight into the vibrational spectrometer while stray molecules from the reaction region are preferentially pumped out by a turbomolecular pump.

The studied sample is mounted on a temperature-controlled holder and exposed to the hydrogen atom beam from HABS. Absolute quantification of hydrogen atom flux to the sample surface was done using the method based on chemical erosion of amorphous hydrogenated carbon (a-C:H) film developed at the IPP, Garching, Germany (Schwarz-Selinger et al. 2000; Schluter et al. 2008). The hydrogen beam from HABS is only partially dissociated and a fraction of hot molecules is present together with atoms. The vibrational spectrometer is positioned so that molecules from the irradiated area of the sample can go directly to the interaction region. There are two components of molecules from the sample which get analyzed: molecules produced by atom recombination (which are of main interest) and reflected undissociated molecules from the beam. Although some modeling is still needed for the final evaluation of measured data such a design of experimental setup ensures conditions for the fully quantitative treatment of studied processes (Založnik 2016).

13.4 Applications and Results

13.4.1 Metal Cell with the Hot Tungsten Filament

The electrostatic setup I at LDMA The first achievement of HVS using DEA was performed by reconstruction of the high-resolution electrostatic spectrometer as described above. The source of excited molecules was a gas cell intended to be used as a small hot cathode discharge source. However, the first measurements already showed the appearance of unexpected vibrational excitation when hydrogen was introduced into the cell and the filament heated to an incandescent temperature but in the absence of any discharge. This discovery, described by Hall and co-workers (1988), determined further experimental activities with the spectrometer. Vibrational state distributions of hydrogen effusing from the cell were deduced from the ion yield spectra by dividing the height of each peak corresponding to the particular ν , by the respective theoretical DEA cross section calculated by Gauyacq (1985). A high vibrational temperature of 2800 K was obtained for $\nu = 1$ to $\nu = 3$ vibrational states with a hot W filament. It was shown that this high temperature could only be produced by wall recombination of the H atoms created by H_2 atomization at the filament and not by direct molecule heating on the filament. A different vibrational distribution was obtained when the tungsten was replaced by tantalum as filament material. The vibrational temperature of the $\nu = 1$ to $\nu = 3$ vibrational levels was higher, 3400 K. The populations of the states from $\nu = 4$ to $\nu = 9$ were observed to be higher than those characterized by the above vibrational

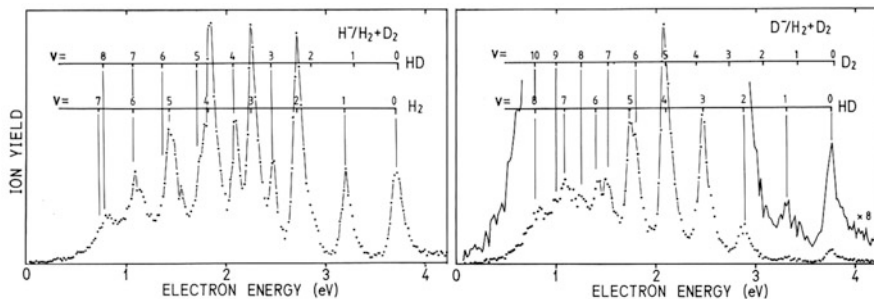


Fig. 13.13 H^- and D^- yield spectra for the case when a 1:1 mixture of H_2 and D_2 was admitted into the source (Hall et al. 1988, unpublished)

temperatures. Populations for the Ta filament for these higher states were about one order of magnitude higher than those for W when both distributions were normalised to $v = 1$. The observed difference in distributions was explained by filament material being deposited on the stainless steel inner wall of the gas cell after the filament started to be operated at high temperature.

A proof that atom recombination is the source of high vibrational excitation was also the observed appearance of the H^- and D^- ions from DEA to HD when a 1:1 mixture of H_2 and D_2 was introduced into the cell as shown in Fig. 13.13. The respective threshold energies for individual vibrational states of H_2 , HD and D_2 are marked. Peaks due to vibrationally excited HD molecules created by the H-D surface recombination are clearly identified. The discovery of important excitation of high vibrational states of hydrogen molecules by atom recombination on a metal surface and its dependence on surface material instigated further research activity. The existence of hydrogen excitation by surface recombination of atoms was observed, almost at the same time, by a group at the FOM Institute for Atomic and Molecular Physics, Amsterdam, The Netherlands (Eenshuistra et al. 1988).

Most studies with a gas cell as a source of ro-vibrationally excited molecules were performed under low-pressure conditions where the particle mean free path exceeds the cell dimensions. Under such conditions clear vibrational H^- yield spectra were observed accompanied by weak, mainly unresolved, contributions from excited rotational states. This rotational excitation manifests itself mainly in a broadening of vibrational peaks and the deconvolution procedure allows determining both, the vibrational and rotational temperatures. On the contrary, if the gas pressure in the cell is higher, one also observes stronger contribution from rotational states originating from vibration-rotation excitation transfer by volume collisions and well resolved peaks corresponding to (v, J) states can be identified. Such a case, where the gas pressure in the cell is $P_s = 0.9$ mbar is shown in Fig. 13.14. Deconvolution of this spectrum showed that vibrational temperature is about $T_v = 1800$ K while the rotational temperature is also high, $T_R = 1500$ K (Popović et al. 1990). At the lower pressures mostly used for measurements, the

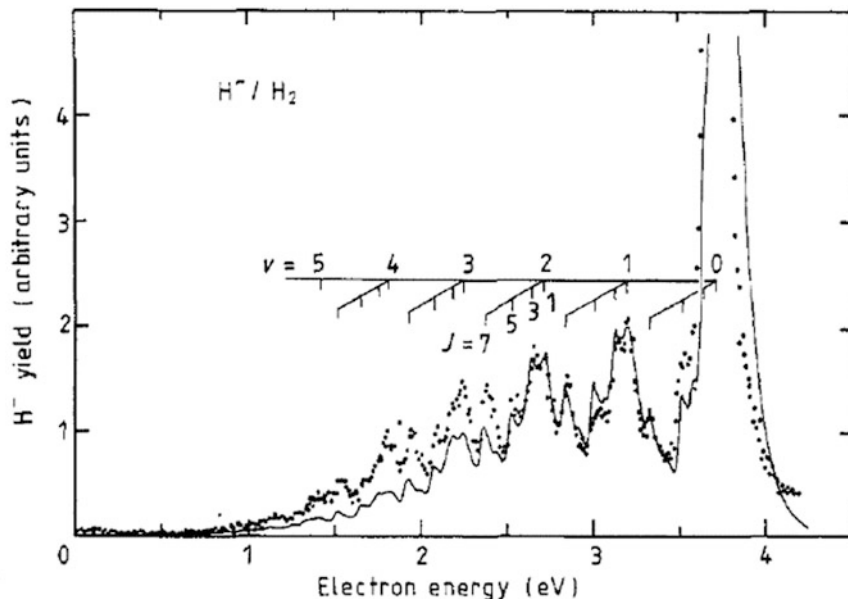


Fig. 13.14 H^- yield spectrum in the region of the 4 eV process in H_2 at estimated source pressure $P_s = 0.9$ mbar (Popović et al. 1990). © IOP Publishing. (Reproduced with permission. All rights reserved)

rotational temperature was always much lower than that for vibration, mainly around $T_R = 500$ K.

By simultaneously recording the ion yield spectrum for the 4 eV and 14 eV process and assuming a known theoretical DEA cross section for the 4 eV process, it was possible to deduce the ν -dependence of the CS for the 14 eV process in H_2 and D_2 (Čadež et al. 1988).

In one set of experiments, following the initial intention to study molecular excitation from a hydrogen discharge, biased buffer plates, and isolation grids were mounted at the exit side of the gas cell. A hot filament discharge could be maintained in the cell by biasing the filament with respect to the grounded wall and a stable discharge current of $I_d = 3$ A was obtained at about 50 V. Measurements were performed for discharge currents between 1 A and 3 A at the cell pressure between 27 and 87 μbar . Strong enhancement of $\nu = 1$ to $\nu = 4$ vibrational states was observed with vibrational temperatures 2200–2350 K as well as low rotational temperatures (Schermann et al. 1991).

Electrostatic setup II at LDMA Extensive measurements of the influence of the material evaporated to the cell wall on vibrational excitation of H_2 molecules were performed at the new setup built for this study and described in Sect. 13.3.2.1 (Schermann et al. 1994). It ensured conditions for clean and reproducible measurements under well-characterized conditions. The influence of twelve different metals

(Al, Ag, Au, Cu, Fe, Nb, Mo, Pt, Re, Ta, Ti, and W) evaporated to the internal wall of the cell on the vibrational distribution was studied. These metals could roughly be divided into two groups with respect to the characteristics of H^- ion yield spectra. In the first group, Al, Fe, Mo, Nb, Ta, Ti, and W, one observes peaks for the states up to $\nu = 7, 8$, and even 9 with comparable intensity to $\nu = 0$. In the second group, Ag, Au, Cu, Re, and Pt, only the states with $\nu \leq 4$ were observed. The common property of most of the studied cases was that the shape of the ν -excited part of the ion yield spectra was not dependent on dissociation filament temperature and would increase relative to the $\nu = 0$ peak with filament temperature. Further, the shape of the spectra was not dependent on the cell pressure in the range of 5–50 μbar but only the intensity would scale linearly with it. Also, no important influence of the molecule residence time in the cell on the ion yield spectra was observed. All this indicated that the measured vibrational distributions reflect the nascent distribution of excited molecules formed by atom recombination on the wall. A further common characteristic of the recorded spectra was that a clear vibrational series was observed and rotational excitation was always much weaker than that of vibration. For most cases, the rotational temperature was between 500 and 700 K. The highest was for Al and Nb, around 2000 K, and the lowest was for Ta, around 300 K.

The ion yield spectra for tungsten and niobium are shown in Fig. 13.15 and the corresponding vibrational population distributions in Fig. 13.16. Both distributions are normalized to the population of $\nu = 1$ as the peak at $\nu = 0$ is mainly due to the background gas and molecules which transit the gas cell without undergoing dissociation at the filament.

The ion yield spectra for different metals from the same group were different as seen in the two cases shown in Fig. 13.15. The vibrational distributions determined by deconvolution of experimental spectra were usually not found to be strictly Boltzmannian (see Fig. 13.16). In the case of tungsten, the vibrational temperature for the first three vibrational states is 3900 K and for niobium 2700 K but for

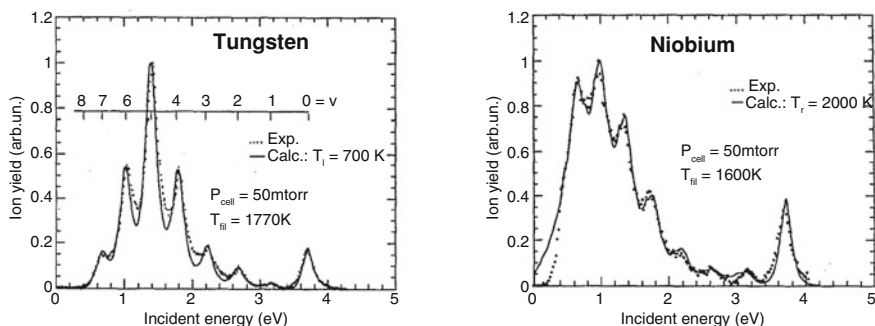


Fig. 13.15 H^- yield spectra for tungsten and niobium evaporated to the source wall. The source pressure for both cases is 67 μbar . (Reproduced from Schermann et al. (1994), with the permission of AIP Publishing)

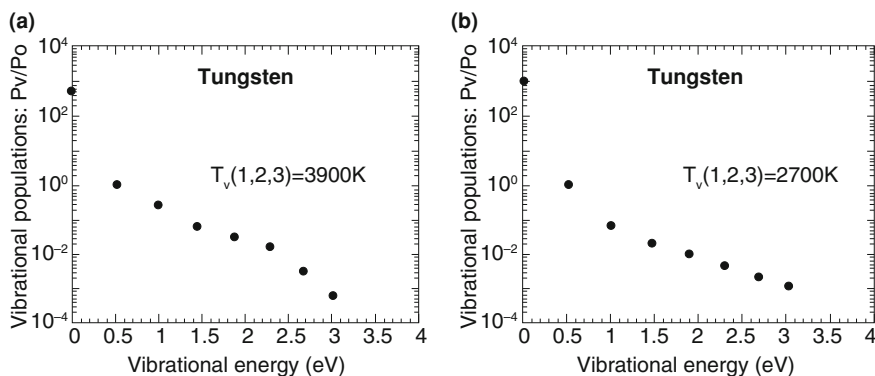


Fig. 13.16 Vibrational state populations for spectra from Fig. 13.15. Broader vibrational peaks for Nb as compared to W are a consequence of the higher rotational temperature. (Reproduced from Schermann et al. (1994), with the permission of AIP Publishing)

niobium the higher vibrational states ($v > 3$) exhibit much higher vibrational temperature.

The observed strong vibrational excitation of recombined molecules was tentatively correlated to the chemisorption binding energy. Mainly those metals which strongly chemisorb hydrogen lead to vibrational excitation to high, $v > 4$, vibrational states. Two possible mechanisms for the formation of high vibrational states were proposed. The first proposed mechanism was Langmuir–Hinshelwood (LH) type recombination of two loosely bound atoms trapped in assumed physisorption sites on the surface saturated by chemisorbed atoms. Another proposed mechanism leading to a highly excited molecule was the Eley–Rideal (ER) recombination of the incoming atom with non-thermalized hydrogen atom in the chemisorption potential, commonly known as the hot-atom ER mechanism. Yet another, less probable, possibility was mentioned: ER recombination with an atom in the subsurface.

Measurements were also performed with a discharge deposited C film (Gough et al. 1996) motivated by the problems in astrochemistry. Further on, a detailed study was done with an evaporated gold surface (Čadež et al. 1997) and some initial measurements with a Si film were also performed.

Magnetic setup at JSI The main motivation for the construction of a new vibrational spectrometer at JSI was the interest in getting relevant information on excited hydrogen for studies of plasma-wall interaction in tokamaks. For this reason, a new version of a vibrational spectrometer using a magnetic field for e-beam collimation was constructed and measurements were performed with both H_2 and D_2 from the beginning. Detailed studies were done with W and Cu (Markelj 2010; Markelj and Čadež 2011). Samples used for the study were 25 mm diameter discs made of oxygen-free high conductivity (OFHC) copper, 1 mm thick, and 0.3 mm thick 99.95% pure tungsten foil. Both samples were polished and cleaned by standard high vacuum procedures.

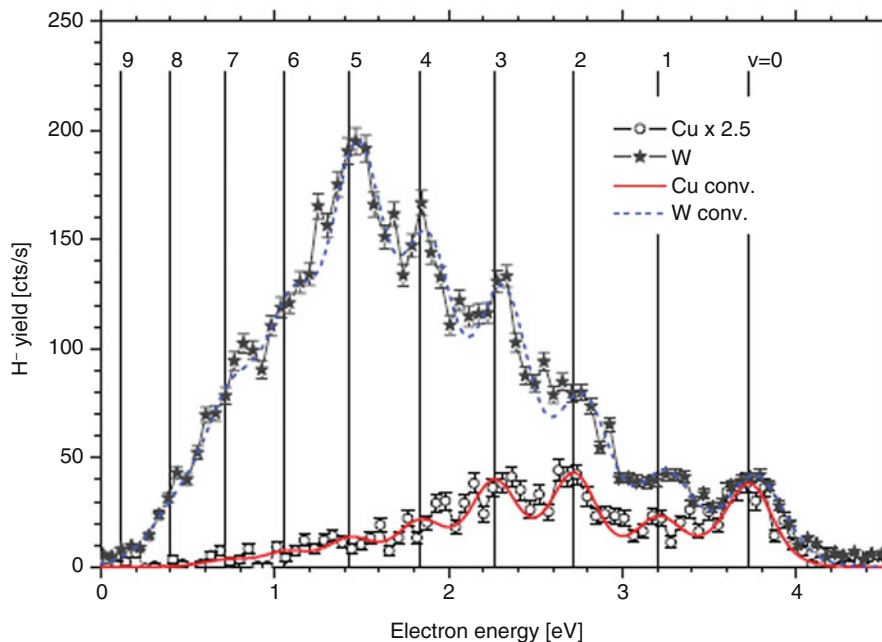


Fig. 13.17 The representative spectra for copper (circles) and tungsten (stars) as obtained for H_2 at dissociation filament temperature $T_f = 1960$ K. The corresponding modeled spectra are also shown by the lines. (Reproduced from Markelj and Čadež (2011), with the permission of AIP Publishing)

Measurements using the magnetic setup with W and Cu in H_2 were mainly in agreement with the results from the electrostatic setup. Respective H^- yield spectra are shown in Fig. 13.17 together with the calculated spectra from the deconvolution. A weaker excitation is observed for Cu compared to W, as expected but one does not see the cut-off in the excitation spectrum from Cu for $\nu > 4$ but rather a steady decrease of signal for high ν . This could be explained by the presence of impurities on the sample which is not present when film evaporation is done in situ in a high vacuum. This weak signal could also originate from the region in TS behind the sample. Another difference between the old measurements on electrostatic setup and measurements with TS is the character of the vibrational distribution deduced from experimental ion yield spectra. Almost Boltzmannian distributions are obtained from the deconvolution of H^- spectra for both W and Cu as shown in Fig. 13.20. This difference in the ν -distributions can be a consequence of more numerous wall collisions on the path from formation to detection of excited molecules in the gas cell used in the electrostatic setup. It can also be due to the experimental problem of focussing a very low-energy electron beam which is more critical for an electrostatic than for the magnetically collimated e-gun.

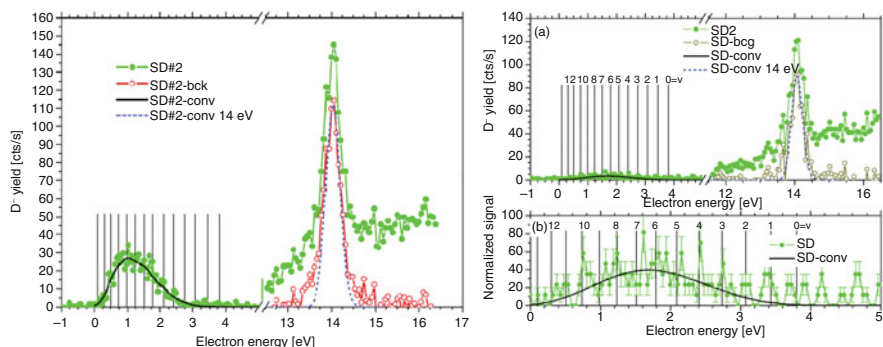


Fig. 13.18 Left: The D⁻/D₂ yield spectrum for $T_f = 1960$ K obtained with W sample and the same spectrum with subtracted linear background in the range of the 14-eV peak. Right: The D⁻/D₂ yield spectrum for $T_f = 2075$ K with the Cu sample (a). Enlarged part of spectrum in the 0–5 eV range shows weak vibrational excitation (b). Deconvoluted spectra are shown as full curves. (Reproduced from Markelj and Čadež (2011), with the permission of AIP Publishing)

Ion yields recorded with D₂, together with deconvoluted spectra (full lines), are shown in Fig. 13.18. These measurements revealed a similar intensity of the D⁻/D₂ ion yield as for H⁻/H₂ in the region of high ν for the case of the W sample but a significant difference for the lower ones due to the strong isotope effect in DEA. It was imperative to include 14 eV peak recordings in order to analyze D⁻ spectra by the deconvolution procedure. A scaled and translated to the lower energy (by 10.2 eV) fit of the 14-eV peak with cold D₂ was used as an apparatus function for the deconvolution of the 4-eV spectra. In each case, a linear background has to be subtracted from the 14 eV yield (Markelj and Čadež 2011). A very weak signal was also observed for high ν for the Cu sample.

Vibrational distributions obtained by deconvolution of H⁻ and D⁻ spectra for both, W and Cu are shown in Fig. 13.19. Similar to the case of H₂, close to Boltzmann distributions are also obtained for D₂. The vibrational temperature determined for H₂ is 3750 ± 100 K for tungsten and 2700 ± 200 K for copper. These temperatures for D₂ are 3300 ± 100 K and 2500 ± 500 K for W and Cu, respectively.

A Monte Carlo simulation was developed (Markelj 2010; Markelj and Čadež 2011) in order to get some physical insight into the recombination process and understand experimental results. The time variation of hydrogen surface concentration and the molecule formation rate after the start of exposure to hydrogen atoms was simulated by observing an initially bare surface exposed to $N_p = 50,000$ particles impacting on the surface each second that corresponds to atom flux density of 0.05 atomic monolayer per second. It was assumed in the simulation that the main production of molecules for W proceeds through the hot-atom recombination with an adsorbed atom. The results show that the recombination proceeds mainly through the weak binding sites, once they are occupied.

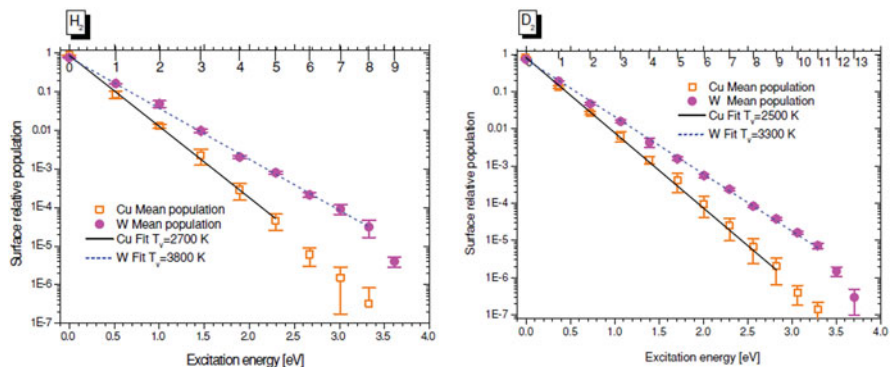


Fig. 13.19 Left: $\text{H}_2(v)$ relative populations for Cu and W samples. Full (Cu) and dotted (W) lines represent a data fit with the Boltzmann distribution, with vibrational temperature $T_v = 2700$ K for Cu and 3800 K for W. Right: The same for $\text{D}_2(v)$ with vibrational temperature $T_v = 2500$ K for Cu and 3300 K for W. (Reproduced from Markelj and Čadež (2011), with the permission of AIP Publishing)

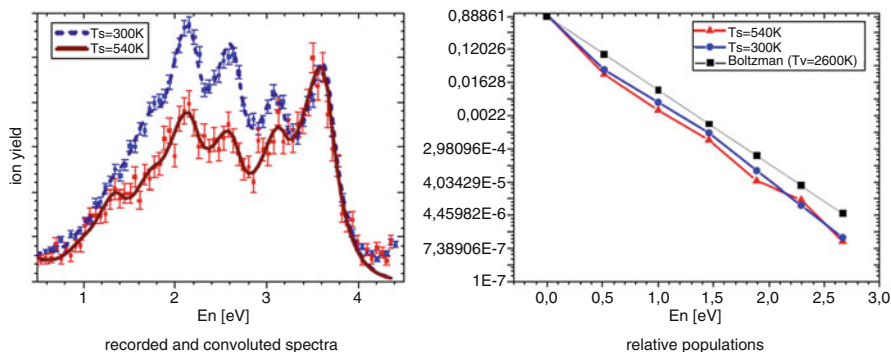


Fig. 13.20 (a) Recorded and calculated spectra and (b) relative populations for PCW for $T_s = 300$ K (blue points and lines) and $T_s = 540$ K (red points and lines). For comparison a Boltzmann distribution corresponding to vibrational temperature $T_v = 2600$ K is also shown. (Reproduced from Založnik et al. (2014), with the permission of NSS)

13.4.2 Atom Recombination on Metal Exposed to Atom Beam

An example from measurements using the differentially pumped spectrometer described above is shown in Fig. 13.20 (Založnik et al. 2014). Two H^- spectra measured with polycrystalline tungsten (PCW) samples at temperatures, $T_s = 300$ K and $T_s = 540$ K are shown. Also shown are calculated synthetic spectra as a full line through experimental points and vibrational distributions extracted by the ion yield deconvolution (Markelj and Čadež 2011).

Lower vibrational excitation was observed in the case of higher sample temperature which is explained by a different surface concentration and population

of different adsorption sites on the surface (Markelj et al. 2013). At higher temperatures, the surface states with low binding energy are poorly populated and the recombination of atoms proceeds mainly through atoms adsorbed in states with higher binding energy resulting in less available energy for the leaving molecule. Moreover, the Langmuir–Hinshelwood mechanism becomes dominant, reducing the probability of Eley–Rideal and hot-atom recombination. One can see that the vibrational distribution of detected molecules corresponds to about 2600 K if one compares the measured distribution to a Boltzmann distribution. This yields the excitation which is lower than that obtained by metal cell measurements with W (Markelj and Čadež 2011; Schermann et al. 1994). This could be due to the fact that the wall surface was cooled directly in the case of the metal cell yielding a lower sample temperature (below 300 K) thus resulting in a higher excitation and yield of negative ions. Further studies have shown (Založnik 2016) a decrease of overall vibrational excitation and also yield of hydrogen negative ions with increasing sample temperature up to 770 K on polycrystalline W and W single crystals. This is due to different recombination mechanisms, which dominate at different sample temperatures. At low temperatures, the sample surface is saturated with adsorbed hydrogen atoms, which results in a high probability for the ER recombination but a small probability for the LH recombination. For higher sample temperatures the population of adsorbed atoms is lower due to the increased probability for the LH recombination. The probability for the ER recombination is thus reduced and the LH recombination becomes dominant which results in a low excitation since the thermal energy is used for desorption.

13.4.3 Results of Some Other Applications of HVS Based on DEA

Vibrational relaxation by volume collisions Noticeable influence of the vibration-vibration and vibration-rotation transition collisions was observed in two experiments although these processes were not the subject of our research. The first was the observation of important rotational excitation of H_2 from the hydrogen cell with hot filament under relatively high pressure as shown in Fig. 13.14. The second case was from the study of the influence of small hydrocarbon molecules on the H_2 vibrational excitation (Čadež et al. 2011). It was observed that introduction of CH_4 together with H_2 into the cell with a hot filament leads to the reduction of vibrational excitation of the H_2 molecules by almost one half. This is attributed to the vibration-vibration/rotation transfer from H_2 to CH_4 as no similar reduction was observed when CH_4 was replaced by Ne.

Decomposition of polyatomic molecules Two short studies of thermal decomposition of polyatomic molecules on hot tungsten were performed illustrating the applicability of HVS for relevant studies. In the first (Čadež et al. 2011), light hydrocarbons, CH_4 , C_2H_4 and C_2H_6 were let into the reaction cell with a hot

tungsten filament. Vibrationally excited H_2 was observed for C_2H_4 and C_2H_6 . In the second (Markelj et al. 2017), NH_3 was let through the tungsten capillary of HABS at different temperatures, and the H^- yield spectrum was recorded. Appreciable vibrational excitation of resulting H_2 was detected for the states $v = 1-3$ at the highest capillary temperature $T_{\text{HABS}} = 2040$ K. The hot tungsten capillary is a complex reactor and the gas composition evolves from the entrance to the exit as does the pressure. In the beginning, NH_3 decomposes according to the reaction $2\text{NH}_3 \rightarrow \text{N}_2 + 3\text{H}_2$ and later H_2 gets thermally dissociated so that the emerging beam is composed of NH_3 , N_2 , H_2 , and H with temperature-dependent relative contributions. The observed vibrational excitation of H_2 was attributed to the H atom recombination on the vacuum chamber surfaces because it was not present at lower capillary temperature.

13.5 Perspectives

Vibrational spectroscopy of hydrogen isotopologues based on DEA described in this Chapter is a relatively simple particle diagnostics similar to the common mass spectroscopy. Its main advantage is its high sensitivity to excited hydrogen molecules which makes it well suited to hydrogen negative ion source studies. Besides the experiments described in this chapter, the method has not been used elsewhere. Contrary to this, various powerful laser-based optical spectroscopic methods have been widely used for studies of the ro-vibrational hydrogen molecules in plasmas (see e.g. Béchu et al. 2020). The coherent anti-Stokes Raman scattering (CARS), vacuum-ultraviolet laser-induced fluorescence (VUV LIF) (e.g. Mosbach et al. 2000), and resonant enhanced multiphoton ionization (REMPI) (e.g. Gabriel et al. 2010; Umemoto 2010) were successfully used. These methods enable in situ time-resolved determination of the population of individual ro-vibrational states. However, optical methods besides being rather complicated have also restrictions regarding the range of accessible states, spatial resolution and sensitivity.

The application potential of hydrogen vibrational spectroscopy based on DEA is not yet fully recognized. Results from experiments performed using the described setups call for further, more systematic, application of the method. The main initial motivation for the development of the method was to use it as diagnostics for vibrationally hot hydrogen from plasma. This application of the method was not developed because the discovery of vibrational excitation by atom recombination on metals absorbed most of our attention once the method was operational. However, its use for plasma diagnostics still remains a very tempting goal for the time to come. For such an application it is necessary to eliminate sources of noise due to plasma. This includes shielding electromagnetic fields, eliminating charged particles, and, in particular, the noise due to metastable neutrals from plasma. Application to the afterglow plasma diagnostics is the most promising.

Further work on modeling the hydrogen cell with a hot filament would be promising for acquiring quantitative data on processes involving vibrationally excited

molecules. This would include vibrational relaxation by wall collision, vibration-vibration and vibration-rotation excitation transfer, and thermal dissociation at the filament.

Simultaneous application of some of the mentioned sensitive optical methods with the present method based on DEA to the same hot hydrogen gas would allow new detailed experimental determination of the CS dependence of DEA on hydrogen ro-vibrational excitation.

Acknowledgments The authors gratefully acknowledge collaboration with colleagues from Paris, Belgrade, and Ljubljana as well as financial support for this work by various institutions. Experimental activity on the project in Ljubljana was greatly facilitated thanks to the loan of experimental equipment for hydrogen vibrational spectroscopy from Université Pierre et Marie Curie, Paris, France by an agreement between CNRS, France and JSI, Slovenia, which is gratefully acknowledged. Special thanks are due to R. I. Hall for initiating the work on the described spectroscopy method, long-time collaboration, and support.

References

- G.R.A. Akkermans, I.G.J. Classen, R. Perillo, H.J. van der Meiden, F. Federici, S. Brezinšek, *Phys. Plasmas* **27**, 102509 (2020). <https://doi.org/10.1063/5.0017714>
- M. Allan, *J. Electron Spectrosc. Relat. Phenom.* **48**, 219 (1989)
- M. Allan, S.F. Wong, *Phys. Rev. Lett.* **41**, 1791 (1978)
- M. Bacal, G. Hamilton, *Phys. Rev. Lett.* **42**, 1538 (1979)
- M. Bacal, M. Wada, *Appl. Phys. Rev.* **2**, 021305 (2015)
- M. Bacal, M. Wada, *Plasma Sources Sci. Technol.* **29**, 033001 (2020)
- M. Bacal, K. Maeshiro, S. Masaki, M. Wada, *Plasma Sources Sci. Technol.* **30**, 075014 (2021)
- J.N. Bardsley, J.M. Wadehra, *Phys. Rev. A* **20**, 1398 (1979)
- J.N. Bardsley, A. Herzenberg, F. Mandl, *Proc. Phys. Soc.* **89**, 321 (1966)
- S. Béchu, J.L. Lemaire, L. Gavilan, S. Aleiferis, V. Shakhmatov, Y.A. Lebedev, D. Fombaron, L. Bonny, J. Menu, A. Bès, P. Svarnas, N. de Oliveira, *J. Quant. Spectrosc. Radiat. Transf.* **257**, 107325 (2020)
- M. Cacciatore, M. Rutigliano, *Plasma Sources Sci. Technol.* **18**, 023002 (2009)
- I. Čadež, R.I. Hall, M. Landau, F. Pichou, C. Schermann, *J. Phys. B Atomic Mol. Phys.* **21**, 3271 (1988)
- I. Čadež, C. Schermann, M. Landau, F. Pichou, D. Popović, R.I. Hall, *Z. Phys. D* **26**, 328 (1993)
- I. Čadež, R.I. Hall, M. Landau, F. Pichou, C. Schermann, *J. Chem. Phys.* **106**, 4745 (1997)
- I. Čadež, R.I. Hall, M. Landau, F. Pichou, M. Winter, C. Schermann, *Acta Chim. Slov.* **51**, 11 (2004)
- I. Čadež, S. Markelj, A.R. Milosavljević, *Nucl. Eng. Des.* **241**, 1267 (2011)
- I. Čadež, S. Markelj, A. Založnik, *Proc. 24th Int. Conf. Nuclear Energy for New Europe 2015*, Portorož, Slovenia, September 14-17, Nuclear Society of Slovenia (NSS), (2015) p. 706
- M. Capitelli, M. Cacciatore, R. Celiberto, O. De Pascale, P. Diomede, F. Esposito, A. Gicquel, C. Gorse, K. Hassouni, A. Laricchiuta, S. Longo, D. Pagano, M. Rutigliano, *Nucl. Fusion* **46**, S260 (2006)
- S. Cvejanović, F.H. Read, *J. Phys. B* **7**, 1180 (1974)
- H. Drexel, G. Senn, T. Fiegele, P. Scheier, A. Stamatović, N.J. Mason, T.D. Mark, *J. Phys. B Atomic Mol. Phys.* **34**, 1415 (2001)
- P.J. Eenshuistra, J.H.M. Bonnie, J. Loss, H.J. Hopman, *Phys. Rev. Lett.* **60**, 341 (1988)

- I.I. Fabrikant, S. Eden, N.J. Mason, J. Fedor, in *Advances in Atomic, Molecular, and Optical Physics*, ed. by E. Arimondo, C. C. Lin, S. F. Yelin, vol. 66, (Academic Press, Burlington, 2017), p. 545
- U. Fantz, D. Wunderlich, Franck-Condon Factors, in *Transition Probabilities and Radiative Lifetimes for Hydrogen Molecules and Their Isotopomers*, INDC(NDS)-457, IAEA, Vienna, Austria (2004). <http://www-amdis.iaea.org/data/INDC-457>
- U. Fantz, D. Reiter, B. Heger, D. Coster, J. Nucl. Mater. **290-293**, 367 (2001)
- O. Gabriel, J.J.A. van den Dungen, D.C. Schram, R. Engeln, J. Chem. Phys. **132**, 104305 (2010)
- O. Galparsoro, R. Pétuya, J.I. Juaristi, C. Crespos, M. Alducin, P. Larrégaray, J. Phys. Chem. C **119**, 15434 (2015)
- J.P. Gauyacq, J. Phys. B **18**, 1859 (1985)
- S. Gough, C. Schermann, F. Pichou, M. Landau, I. Čadež, R.I. Hall, Astron. Astrophys. **305**, 687 (1996)
- C. Guillemaut, R.A. Pitts, A.S. Kukushkin, J.P. Gunn, J. Bucalossi, G. Arnoux, P. Belo, S. Brezinsek, M. Brix, G. Corrigan, S. Devaux, J. Flanagan, M. Groth, D. Harting, A. Huber, S. Jachmich, U. Kruezi, M. Lehnen, C. Marchetto, S. Marsen, A.G. Meigs, O. Meyer, M. Stamp, J.D. Strachan, S. Wiesen, M. Wischmeier, JET EFDA Contributors, Nucl. Fusion **54**, 093012 (2014)
- R.I. Hall, G. Joyez, J. Mazeau, J. Reinhardt, C. Schermann, J. Phys. France **34**, 827 (1973)
- R.I. Hall, I. Čadež, M. Landau, F. Pichou, C. Schermann, Phys. Rev. Lett. **60**, 337 (1988)
- R.S. Hemsworth, D. Boilson, P. Blatchford, P.M. Dalla, G. Chitarin, H.P.L. de Esch, F. Geli, M. Dremel, J. Graceffa, D. Marcuzzi, G. Seriani, D. Shah, M. Singh, M. Urbani, P. Zaccaria, New J. Phys. **19**, 025005 (2017)
- E.M. Hollmann, A.Y. Pigarov, Z. Yan, Phys. Plasmas **13**, 052510 (2006)
- J. Horáček, M. Čížek, K. Houfek, P. Kolorenč, W. Domcke, Phys. Rev. A **70**, 052712 (2004)
- B. Jackson, X. Sha, Z.B. Guvenc, J. Chem. Phys. **116**, 2599 (2002)
- T. Kammeler, J. Lee, J. Kuppers, J. Chem. Phys. **106**, 7362 (1997)
- S. Krashennnikov, A. Smolyakov, A. Kukushkin, *On the Edge of Magnetic Fusion Devices*, Springer Series in Plasma Science and Technology (Springer Nature Switzerland AG, Cham, 2020)
- E. Krishnakumar, S. Denifl, I. Čadež, S. Markelj, N.J. Mason, Phys. Rev. Lett. **106**, 243201 (2011)
- A.S. Kukushkin, H.D. Pacher, V. Kotov, D. Reiter, D. Coster, G.W. Pacher, Nucl. Fusion **45**, 608 (2005)
- S. Markelj, *Interaction and Production of vibrationally excited hydrogen molecules on surfaces*, PhD Thesis. University of Ljubljana, Slovenia (2010)
- S. Markelj, I. Čadež, J. Chem. Phys. **134**, pp124707 (2011)
- S. Markelj, I. Čadež, P. Pelicon, Z. Rupnik, Nucl. Instr. Methods B **259**, 989 (2007)
- S. Markelj, Z. Rupnik, I. Čadež, Int. J. Mass Spectrom. **275**, 64 (2008)
- S. Markelj, O.V. Ogorodnikova, P. Pelicon, T. Schwarz-Selinger, I. Čadež, Appl. Surf. Sci. **282**, 478 (2013)
- S. Markelj, A. Založnik, I. Čadež, J. Vac. Sci. Technol. A **35**, 061602 (2017)
- T. Mosbach, H.-M. Katsch, H.F. Döbele, Phys. Rev. Lett. **85**, 3420 (2000)
- E. Nicolopoulou, M. Bacal, H.J. Doucet, J. Phys. (Paris) **38**, 1399 (1977)
- A. Okamoto, S. Kado, K. Sawada, Y. Kuwahara, Y. Iida, S. Tanaka, J. Nucl. Mater. **363-365**, 395 (2007)
- R. Pétuya, P. Larrégaray, C. Crespos, P. Aurel, H.F. Busnengo, A.E. Martínez, J. Phys. Chem. C **119**, 3171 (2015)
- D. Popović, I. Čadež, M. Landau, F. Pichou, C. Schermann, R.I. Hall, Meas. Sci. Technol. **1**, 1041 (1990)
- V.S. Prabhudesai, N.J. Mason, E. Krishnakumar, J. Phys. Conf. Ser. **1412**, 052006 (2020)
- D. Rapp, T.E. Sharp, D.D. Briglia, Phys. Rev. Lett. **14**, 533 (1965)
- F.H. Read, N.J. Bowring, Nucl. Inst. Methods Phys. Res. A **645**, 273-277 (2011). <http://www.electronoptics.com/>
- D. Reiter, M. Baelmans, P. Börner, Fusion Sci. Technol. **47**, 172 (2005). <http://www.eirene.de/>

- C. T. Rettner, M. N. R. Ashfold (eds.), *Dynamics of Gas-Surface Interaction* (The Royal Society of Chemistry, Cambridge, 1991)
- C.T. Rettner, D.J. Auerbach, Phys. Rev. Lett. **74**, 4551 (1995)
- M. Rutigliano, M. Cacciatore, Phys. Chem. Chem. Phys. **13**, 7475 (2011)
- C. Schermann, R.I. Hall, M. Landau, F. Pichou, I. Čadež, AIP Conf. Proc. **210**, 159 (1991)
- C. Schermann, F. Pichou, M. Landau, I. Čadež, R.I. Hall, J. Chem. Phys. **101**, 8152 (1994)
- M. Schluter, C. Hopf, T. Schwarz-Selinger, W. Jacob, J. Nucl. Mater. **376**, 33 (2008)
- G.J. Schultz, R.K. Asundi, Phys. Rev. **158**, 25 (1967)
- G.J. Schulz, Phys. Rev. **113**, 816 (1959)
- T. Schwarz-Selinger, A. von Keudell, W. Jacob, J. Vac. Sci. Technol. A **18**, 995 (2000)
- D.T. Stibbe, J. Tennyson, J. Phys. B Atomic Mol. Phys. **31**, 815 (1998)
- F. Taccogna, S. Bechu, et al., Eur. Phys. J. D **75**, 227 (2021)
- P.W. Tamm, L.D. Schmidt, J. Chem. Phys. **51**, 5352 (1969)
- M. Tronc, F. Fiquet-Fayard, C. Schermann, R.I. Hall, J. Phys. B **10**, 305 (1977)
- M. Tronc, R.I. Hall, C. Schermann, H.S. Taylor, J. Phys. B **12**, L279 (1979)
- K.G. Tschersich, J.P. Fleischhauer, H. Schuler, J. Appl. Phys. **104**, 034908 (2008)
- H. Umemoto, Chem. Vap. Depos. **16**, 275 (2010)
- K. Verhaegha, B. Lipschultz, J. Harrison, B. Duval, C. Bowman, A. Fil, D.S. Gahle, D. Moulton, O. Myatra, A. Perek, C. Theiler, M. Wensing, MST1 team, TCV team, preprint, to be published (2020). <https://doi.org/10.13140/RG.2.2.28699.49441>
- J.M. Wadehra, J.N. Bardsley, Phys. Rev. Lett. **41**, 1795 (1978)
- A. Winkler, Appl. Phys. A Mater. Sci. Process. **67**, 637 (1998)
- L. Wolniewicz, J. Chem. Phys. **99**, 1851 (1993)
- J.-S. Yoon, Y.-W. Kim, D.-C. Kwon, M.-Y. Song, W.-S. Chang, C.-G. Kim, V. Kumar, B.J. Lee, Rep. Prog. Phys. **73**, 116401 (2010)
- A. Založnik, *Interaction of Atomic Hydrogen with Materials Used for Plasma-Facing Wall in Fusion Devices*, PhD Thesis, University of Ljubljana, Slovenia (2016)
- A. Založnik, I. Čadež, S. Markelj, V. Žigman, Proc. 22nd Int. Conf. Nuclear Energy for New Europe 2013, Bled, Slovenia, September 9-12, Nuclear Society of Slovenia (NSS) (2013), p. 1406
- A. Založnik, S. Markelj, I. Čadež, Proc. 23rd Int. Conf. Nuclear Energy for New Europe 2014, Portorož, Slovenia, September 8-11, Nuclear Society of Slovenia (NSS) (2014), p. 1104
- A. Založnik, P. Pelicon, Z. Rupnik, I. Čadež, S. Markelj, Nucl. Instr. Methods B **371**, 167–173 (2016)

Chapter 14

Physics of Surface-Plasma H^- Ion Sources



Yuri I. Belchenko and Motoi Wada

Abstract Surface-plasma sources (SPS) deliver intense and bright negative ion (NI) beams for accelerators and fusion plasma neutral beam heating systems. High efficiency of SPS is achieved by the proper combination of plasma and electrode surfaces in gas discharge devices optimized for NI production, transport, and extraction. Plasma provides an intense bombardment of discharge electrodes by “primary” energetic particles: hyperthermal atoms and positive ions. The near-electrode potential sheath of gas discharge pre-accelerates the primary positive ions to the NI production electrode and extracts the produced NI flux back to the plasma—where NIs are transported to the extraction apertures. The self-adjusting thickness of the gas discharge near-electrode potential sheath permits pre-acceleration of the primary positive ion flux and the secondary NI flux without a space-charge limit. The decrease of electrode work function by the deposition of alkali metal additives increases the NI surface production on the gas discharge electrodes. The persistent alkali metal coverage of gas discharge electrodes leads to the long-term highly efficient NI production of SPS. The principal mechanisms of intense surface-plasma NI production in the SPS are interrelated. The dynamic plasma particle bombardment modifies the electrode surface synergistically and the resulting surface condition determines the NI emission from the electrode in an SPS. The efficiency of negative ion production on the gas-discharge cathode and anode surfaces, as well as on the surfaces of NI emitters in plasma separated from the discharge circuit, is discussed.

Keywords Negative ion · Ion source · Surface production · Gas discharge · Extraction · Work function

Y. I. Belchenko (✉)
Budker Institute of Nuclear Physics, Novosibirsk, Russia
e-mail: belchenko@inp.nsk.su

M. Wada
Graduate School of Science and Engineering, Doshisha University, Kyoto, Japan

© The Author(s), under exclusive license to Springer Nature Switzerland AG 2023
M. Bacal (ed.), *Physics and Applications of Hydrogen Negative Ion Sources*,
Springer Series on Atomic, Optical, and Plasma Physics 124,
https://doi.org/10.1007/978-3-031-21476-9_14

379

14.1 Introduction

Surface-plasma sources (SPS) deliver intense and bright negative ion (NI) beams for accelerators and for fusion neutral beam injectors. The electrodes or NI emitters with a low work function are used in SPS for the enhancement of negative ion production. The addition of a small amount of cesium into the discharge enhances the brightness and intensity of the SPS-produced negative ion beams (Belchenko et al. 1973a, b, 1974a, b). High efficiencies in confinement and extraction of NI are achieved in an SPS by the strong coupling between the plasma and the electrode surface conditions. Gas discharge plasma provides an intense bombardment of electrodes by energetic plasma particles. The self-extraction of the secondary NI flux across the sheath without a space-charge limit is accomplished by high-density positive ions and neutrals crossing the thin sheath region in front of the NI production surface.

The detailed study of surface-plasma sources and negative ion production on gas-discharge surfaces using cesium catalysis has been carried out during the last five decades. Major results have been discussed and published in the proceedings of eleven regular symposiums on Production and Neutralization of Negative Ions and Beams (1977–2006) and of seven symposiums on Negative Ion Beam and Sources (2008–2020). Detailed reviews on surface-plasma sources and fundamental processes of negative ion formation in SPS have been given in many papers such as Belchenko (1993), Belchenko et al. (1977a, 2018a, b), Hiskes (1976, 1979), Schmidt (1990), Holmes (1992), Wada (1998), Peters (2000), Moehs (2002), Stockli (2012), Bacal and Wada (2015), and Faircloth and Lawrie (2018).

This chapter describes the physics of a surface-plasma H^- ion source and the mechanisms of intense surface-plasma NI production in an SPS. The efficiencies of negative ion production on the electrodes of various SPS are discussed.

14.2 Mechanism of Surface-Plasma Negative Ion Production

14.2.1 Main Physical Processes in SPS

There are four main physical processes leading to efficient NI production in an SPS.

- Intense fluxes of energetic hydrogen ions and hydrogen atoms from plasma bombard the electrode surface, and a high-density flux of secondary hydrogen particles leaving the discharge electrodes is formed due to backscattering and desorption.
- The enhanced energy of primary and secondary hydrogen particles enhances the non-equilibrium kinetic emission of negative ions from the electrodes.

- The deposition of catalyst (alkali metal) on the discharge electrodes enhances the surface negative ion (NI) production.
- The discharge maintains the conditions in the plasma and at the electrode surfaces suitable for enhanced NI production and extraction.

The principal schemes of the SPS NI production at the “cathode” and “anode” electrodes are shown in Fig. 14.1.

In an SPS with the NI production at the electrode biased negatively with respect to plasma (at the cathode or the special converter located in plasma volume—Fig. 14.1a), an intense flux of incident positive ions H^+ , H_2^+ , H_3^+ , and Cs^+ is accelerated from the dense plasma to the electrode by the applied electric potential across sheath formed between the plasma and the surface. Thus, an increased energy of incident positive ions of about 70–300 eV suitable for the surface conversion to NI is provided. The same electric field across the sheath accelerates back the cathode-produced NI flux through backscattering and desorption processes. The “cathode-produced” or converter-produced NIs back-accelerated by the near-electrode potential sheath can cross the dense plasma volume without losing electrons in the affinity level to reach the source extraction aperture.

At the anode surface or the plasma electrode surface which are positively biased with respect to the near-anode/extractor hole plasma (Fig. 14.1b), the incident flux of energetic particles consists mainly of superthermal atoms, H^0 . The positive ions H^+ , H_2^+ , H_3^+ , and Cs^+ reach the positively biased anode or plasma electrode if they have high enough kinetic energy to overcome the potential barrier of the near-anode sheath. The anode-produced NIs are guided by the electric field induced by the extraction electrode (not shown in Fig. 14.1) toward the extraction aperture being reflected at the edge of the anode plasma.

In principle, there is no need to form a thick plasma layer or to increase the filling gas pressure for surface-plasma NI production. A high-level H^- yield is maintained at low pressure in the SPS discharge, and the total extracted H^- ion current is directly proportional to the emission hole area. In SPS the saturation of

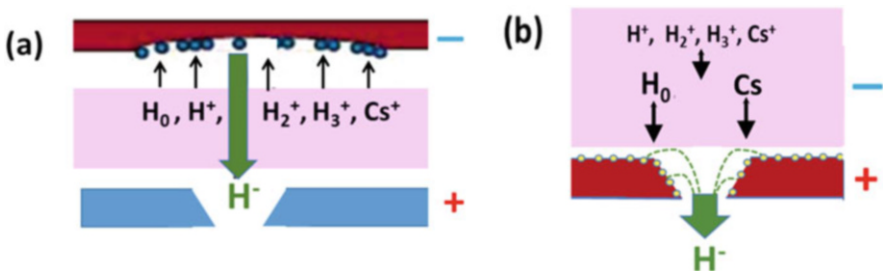


Fig. 14.1 Principal schemes of negative ion production and extraction in the SPS: (a) at the cathode or the converter biased negatively with respect to plasma; (b) at the anode or at the plasma electrode biased positively with respect to the near-anode plasma. (Reproduced from Belchenko et al. (2018b) with permission from AIP Publishing)

the negative ion yield with the increase of the discharge current is recorded at a very high level of discharge current density (see Fig. 14.11 below).

The intense NI production leads to an essential change of the plasma composition in the extraction region of SPS: the electron component of the plasma is partially replaced by the negative ion component and an ion-ion plasma with a reduced number of electrons is formed (Belchenko et al. 1975). The flux of accompanying electrons, co-extracted with the negative ions from the cesiated SPS, is remarkably reduced by electron pumping from the ion-ion plasma with applying a positive bias to the plasma electrode of SPS (Leung et al. 1983).

The indicated properties are vital for the giant long-pulsed SPS of neutral beam injectors for fusion.

14.2.2 First Surface-Plasma Sources

The first generation of experimental surface-plasma sources of hydrogen negative ions was developed in 1971–1973. A several-fold increase of H^- ion beam current was achieved with the compact planotron SPS (Belchenko et al. 1973a, 1974a, b, c). The first planotron SPS scheme is shown in Fig. 14.2. It consists of gas-discharge assembly 1,2, installed between the dipole magnetic field poles 6. The planotron assembly includes a spool-like cathode consisting of central plane 1 attached to side shields 1a, and an anode chamber 2. A high-current hydrogen-cesium discharge is ignited in the cathode-anode gap around the central cathode plane. Negative ions are extracted through the emission slit 3 by the electric field, applied between the anode and extraction electrode 4.

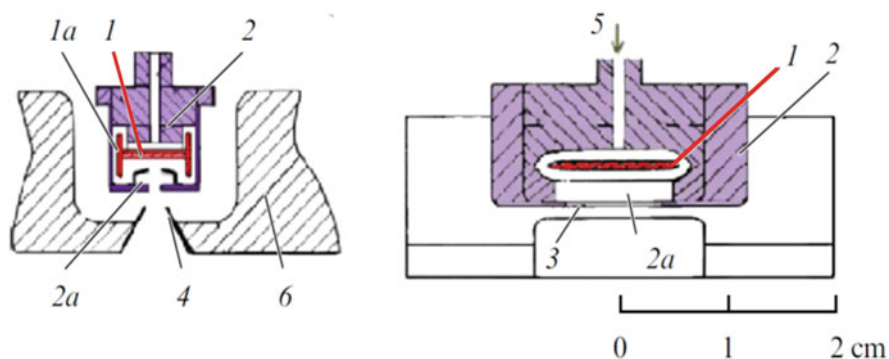


Fig. 14.2 Layout of the first surface-plasma source with the planotron geometry of electrodes (Belchenko et al. 1973a). At left—cross section along the magnetic field, at right—cross section across the magnetic field: 1—cathode central plane, 1a—cathode side shields, 2—anode chamber, 2a—near-anode cavity, 3—emission slit, 4—extraction electrode, 5—gas input, 6—magnet poles. (Reproduced from Belchenko et al. (2018a) with permission from Physics-Uspekhi)

The structure of planotron discharge with the thin cathode sheath and a thin layer of dense plasma is optimized for the negative ion surface production, transport of the formed ions through the plasma and their extraction from the source. Electron oscillations between the cathode shields $1a$ and the enhanced ionization in the crossed $E \times B$ fields around the cathode plane made the high current discharge (~ 100 A, 100 V) possible at low pressure (< 0.1 Tor) in the narrow inter-electrode gap. Electron filtering by the transverse magnetic field provides a lower electron temperature in the near-anode cavity plasma ($2a$ in Fig. 14.2) compared to that in the main discharge column. H^- beams with the current up to 0.88 A and the emission current density up to 3.7 A/cm² was achieved from the first planotron sources (Belchenko et al. 1974a, b, c).

14.2.3 Studies of Intense Negative Ion Production in the First SPS

The intense surface-plasma negative ion production in the hydrogen-cesium planotron discharge was confirmed by a series of experimental studies of the negative ions extracted from a planotron source. One of the key observations was the energy spectrum of the extracted H^- ion beams and its change with the varying cesium and hydrogen feed to the discharge. The energy spectrum of the H^- ion beam consisted of two characteristic groups corresponding to the different regions of the production of negative ions in the discharge, as shown in Fig. 14.3 (Belchenko et al. 1973b).

The position of the left-side peak of the spectrum or the low-energy H^- group in Fig. 14.3 was independent of the changes in discharge voltage and hydrogen feed (distributions 1–8 in Fig. 14.3). The intensity of this low-energy group became higher with the increasing hydrogen feed to the discharge (distributions 5–8 in Fig. 14.3b). The energy of this low-energy group of H^- ions corresponded to the extraction potential, i.e., these ions were formed at the anode surface or in the near-anode region of the discharge.

The position of the second group with the higher ion energy (right-side peak in Fig. 14.3) corresponds to the SPS cathode potential and shifts in accordance with the change of discharge voltage (distributions 1–4 in Fig. 14.3a). The intensity of this high-energy group negative ions was observed to be higher for lower discharge voltages of about 120–150 V (distributions 1, 2 in Fig. 14.3a) and at lower hydrogen feed (distribution 5 in Fig. 14.3b). The energy width of the cathode potential group was several times larger than that of the anode potential group, which suggests a strong energy scattering of negative ions formed at the cathode. Thus, the high-energy group of the extracted negative ions was attributed to the surface production at the cathode, while the low-energy group could consist of H^- ions produced at the anode surface and slow “charge-exchanged” H^- ions formed by charge-exchange of fast cathode-produced H^- ions in collisions with slow H^0 atoms according to the reaction.

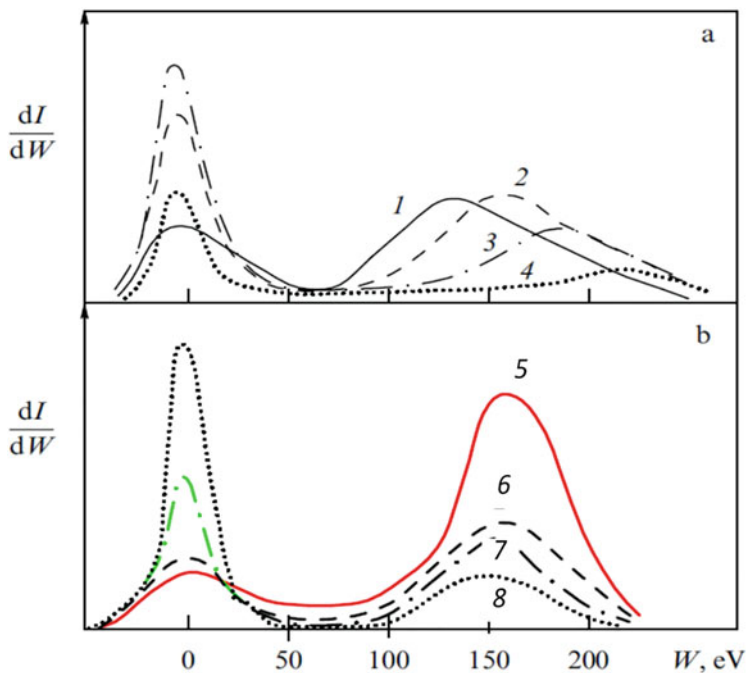
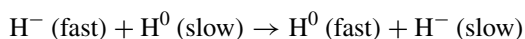


Fig. 14.3 Energy spectra of negative ions, extracted from the different modes of the planotron source (Belchenko et al. 1973b). (a)—at different discharge voltages U_d , controlled by Cs seed: 1—at $U_d = 120$ V, 2— $U_d = 150$ V, 3— $U_d = 160$ V, 4— $U_d = 210$ V; (b)—at different hydrogen feed Q (molecules per pulse): 5—at $Q = 10^{16}$, 6— $Q = 1,2 \cdot 10^{16}$, 7— $Q = 1,7 \cdot 10^{16}$, 8—at $Q = 2,2 \cdot 10^{16}$ mol/pulse. Ion energy $W = 0$ on the abscissa corresponds to the anode potential of planotron. (Reproduced from Belchenko et al. (2018a) with permission from Physics-Uspekhi)



The intensity of the extracted hydrogen negative ion beam decreased to half by modifying the discharge source geometry to a Penning configuration by removing the planotron central cathode plate. The energy spectrum of the beam, extracted from this Penning discharge contains only the low-energy “anode” group, and its energy spread was narrower as compared with that of the planotron source. It was suggested that the low-energy H^- ion group was produced in the near-anode cavity $2a$ of the Penning source. The sources with Penning discharge configuration producing bright negative ion beams were successfully used in accelerators as well (see below). Thus, a new method to produce intense negative ion beams by making use of surface-plasma interactions was established. Many types of pulsed SPS with hydrogen NI production at the discharge electrodes and at the converter biased independently from the cathode were developed in the 1970s.

14.3 Surface Processes of Negative Ion Formation in SPS

An introduction to elementary processes for negative ion surface production is given in Chap. 2 of this book. In a cesiated SPS, H^- ions are formed at a low work function electrode under an intense plasma bombardment due to the synergy of various fundamental processes. This chapter highlights the processes specifically related to high-efficiency SPS H^- surface production.

14.3.1 Negative Ion Secondary Emission

Negative hydrogen ions are produced in the SPS by processes of negative ion secondary emission (NISE) due to hydrogen particle backscattering and/or impact desorption from the adsorbed layers at the discharge electrode surfaces. The processes of NISE on the cesiated electrode are schematically illustrated in Fig. 14.4. The molybdenum SPS electrode covered by cesium-hydrogen layer with cesium atoms at the top and hydrogen atoms in between is schematically shown in the left side of Fig. 14.4a. It is bombarded by plasma particles from the right: by hydrogen ions and atoms as well as by neutral and ionized cesium. The secondary surface produced H^- ions (backscattered or desorbed) leave the electrode to the right and pass the critical distance x_0 with the velocity v_{\perp} .

The potential diagram of a negative ion interacting with the metal surface during the passage of near-surface region is shown in Fig. 14.4b. The electron affinity of hydrogen atom S is 0.754 eV and is smaller than the work function φ of typical metals or alkali-coated electrodes which is in the range $\varphi = 1.5\sim 4.5$ eV. In the near-surface region the affinity level is lowered with respect to the vacuum potential due to the image force, and at the “critical distance” x_0 the affinity level of ion and the Fermi-level E_F of electrons in the metal are at the same depth from the vacuum potential. The rate of electron exchange $\omega_e(x)$ between the atom and the metal conduction band is high and at the distance $x < x_0$ the affinity level of outgoing hydrogen ion is dominantly occupied. After passing the critical distance x_0 , where the affinity level becomes higher than E_F and where the electron tunneling back to the metal starts to dominate, an outgoing H^- ion can lose the affinity level electron while traveling in the region $x > x_0$.

The probability for the outgoing hydrogen particle to survive as a H^- ion is larger for the higher escape velocity v_{\perp} , and for the larger critical distance x_0 , which depends upon the metal-atom properties derived from the equality $U(x_0) = \varphi - S$ of the image potential drop $U(x_0)$ with the difference of electron affinity S and surface work function φ (see Fig. 14.4b). The image potential drop is given by $U(x) = -(e/4x_0)$ with the unit charge e and the Coulomb constant k .

The calculated dependencies of the negative ion fraction $\beta^-(v_{\perp}, \varphi) = H^-/(H^- + H_0)$ on the outgoing velocity v_{\perp} and work function φ of the H^- ion production surface, based on this so-called probability model are shown in Fig. 14.5 (Kishinevskii

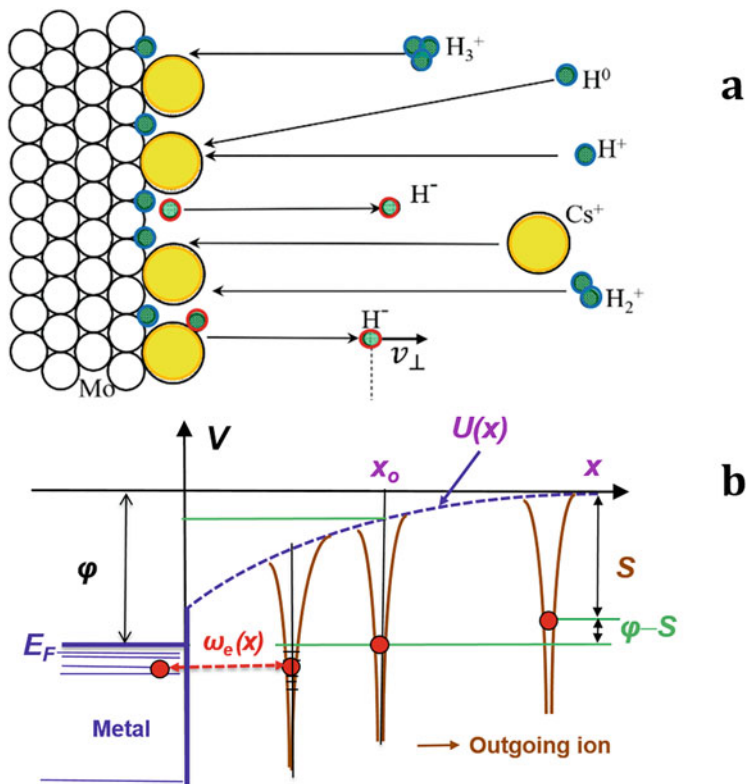


Fig. 14.4 The processes involved in negative ion secondary emission in SPS. (a) Mo electrode with Cs atoms on the top and hydrogen atoms in between Cs and Mo bombarded by hydrogen and cesium ions and atoms. The surface produced H^- ion passes the critical distance x_0 with velocity v_{\perp} . (b) Potential diagram of hydrogen negative ion interacting with metal surface. E_F —Fermi level, ϕ —surface work function, ω_e —rate of electronic exchange between ion and metal, $U(x) = -k(e/4x)$ —image force potential, S —electron affinity. (Reproduced from Belchenko et al. (2018a) with permission from Physics-Uspexhi)

1975). An increased value of negative ion fraction $\beta^- > 0.2$ was predicted for the electrode work function $\phi \sim 1.7$ eV and H^- ions exit energy >5 eV. For a higher probability of negative ion survival, the velocity of outgoing secondary H^- ion should be higher. This can be easily obtained in the processes of particle reflection from the surface and adsorbate or substrate sputtering (desorption) by ions and atoms.

The detailed theory of NISE was further developed (Rasser et al. 1982), and it was confirmed by a series of experiments performed in high-vacuum environment with well-controlled surface conditions (Geerlings et al. 1985; Hiskes and Schneider 1981).

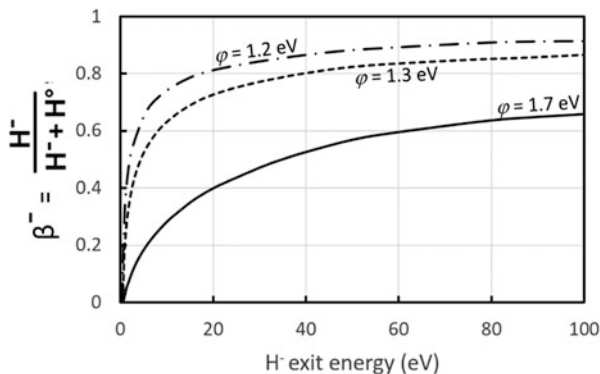


Fig. 14.5 Calculated dependencies of negative ion fraction $\beta^- = H^-/(H^- + H_0)$ of emitted hydrogen particles versus energy of outgoing particle for surfaces with work function 1.2, 1.3, and 1.7 eV. (Reproduced from the data reported by Kishinevskii (1975) with permission from Physics-Uspekhii)

14.3.2 H⁻ Production by Hydrogen Particles Backscattering (Reflection)

14.3.2.1 H⁻ Production by Backscattering of Energetic Hydrogen Ions and Atoms

In an SPS with the NI production at the cathode or biased converter, an intense flux of molecular hydrogen ions, H⁺, H₂⁺ and H₃⁺ are accelerated to 100–300 eV energy across the sheath to reach the surface of a H⁻ ion production electrode. The final energies per proton for H⁺, H₂⁺, and H₃⁺ are 100%, 50%, and 33.3% of the sheath potential. They are reflected at the electrode with the particle reflection coefficients R_N corresponding to the energy. The NI energy and angular distributions are determined by the electrode conditions, including surface layer composition, roughness, adsorbate structure and thickness. The reflection of energetic hydrogen particles from the Mo surface is larger at lower energy and, according to Fig. 14.5, a higher value of β^- and thus a higher efficiency of forming H⁻ ions is expected for incoming H₃⁺ ions. The formed H⁻ ions are accelerated back to the plasma with the maximum kinetic energy 2, 1.5, and 1.33 times the sheath potential for reflection with incident H⁺, H₂⁺, and H₃⁺ ions, respectively.

The first fundamental data on NI production by particle reflection from the cesiated surface (with various cesium coverage on Ni) were reported by Schneider et al. (1981). More than 10% conversion efficiency was reported for the work function minimum condition in the wide range of positive ion energy 150–600 eV/deuteron. In these experiments the incident particles struck the surface perpendicularly, while (van Wunnik et al. 1983) investigated the effect due to the incident angle on the H⁻ ion production by particle reflection for Cs covered W surface. Both the particle reflection coefficient and the energy reflection coefficient increase as the angle of

incidence with respect to the surface normal becomes larger. Thus, about 30–35% conversion efficiency to H^- ion was found at an oblique incident angle $80\text{--}85^\circ$ of incoming protons with energy 100–200 eV.

14.3.2.2 H^- Production by Backscattering of Thermal Hydrogen Atoms

A high-power density discharge in a hydrogen gas can produce a high-intensity flux of thermal hydrogen atoms onto a SPS electrode. However, the backscattering of thermal hydrogen atoms at the surface produces the outgoing thermal atoms with low exit velocity and the backscattered H^- ion yield is strongly dependent upon the temperature of the hydrogen atoms as reported by Pargellis and Seidl (1982). The measured efficiencies were too small in the early experiments with H^- and D^- formation by backscattering on the Cs-covered Mo of thermal atom fluxes emitted from a tungsten furnace (Graham 1979).

Negative hydrogen ion production by scattering of thermal hydrogen atoms from a low work function surface was studied by Seidl et al. (1990) and Melnychuk and Seidl (1991). The highest negative ion yield $R^- \sim 0.01$ was measured at the temperature 0.21 eV for a thick coating of cesium oxides with a work function as low as 1.1 eV. They also showed that the H^- yield depended exponentially on the inverse of the gas temperature and that the backscattered H^- ions have a Maxwellian energy distribution with a temperature equal to the atomic gas temperature. Note that the temperature of hydrogen atoms in hydrogen discharges of SPS is substantially higher than that of furnace-produced hydrogen atoms.

14.3.2.3 H^- Production by Backscattering of Suprathermal Hydrogen Atoms

The increased values of backscattered H^- ion yield $R^- \sim 0.1$ was observed for suprathermal (>1 eV) hydrogen atoms from low work function (<1.5 eV) surfaces (Seidl et al. 1990). It was confirmed in experiments with backscattering of suprathermal hydrogen atoms using an ECR source (Lee and Seidl 1992) and a 27.2-MHz RF discharge source (Okuyama and Mori 1992).

An intense flux of suprathermal hydrogen atoms bombarding the electrodes is produced in the SPS discharges due to hydrogen dissociation by hot electrons (Franck-Condon principle) and to ion backscattering and ion impact desorption from the adsorbates on the walls. The temperature of hydrogen atoms measured by emission spectroscopy has the value of 1.5–2 eV in the Penning and planotron SPS (Smith et al. 1987, 1990; Antsiferov et al. 1990).

Low-energy incidence of suprathermal hydrogen atoms onto an electrode guarantees low-energy spread of produced H^- ions and low damage of converter electrode in the SPS.

14.3.3 Negative Ion Production by Desorption (Sputtering)

Ion-induced (knock-on) desorption takes place when the kinetic energy transferred from the incident particle to an adsorbate atom is higher, than the energy of desorption. Chemical desorption releases an adsorbed atom through a chemical reaction induced by the incident particle; an unstable or volatile condition is formed on the surface leading to particle emission. Chemical desorption can occur down to the thermal energy of the incident particles and the rate increases under irradiation of electrons and photons. In gas discharge the desorption of hydrogen particles takes place mainly due to ions and atoms, while the efficiency for desorption due to electrons or photons is several orders of magnitude lower (Hurych et al. 1988; Ernst-Vidalis et al. 1992; Baker et al. 1994).

14.3.3.1 Negative Ion Production Due to Impact Desorption by Light Ions and Atoms

Hydrogen ions and atoms can efficiently transfer their momentum to surface adsorbed hydrogen atoms (van Amersfoort et al. 1986). The impact desorption of hydrogen by light ions or atoms is more efficient than that by heavy particles.

The calculated cross section of deuterium desorption from nickel is in the range $1.5\text{--}1.2 \cdot 10^{-16}$ cm² for an incident nucleon energy range of 50–500 eV per nucleon (Taglauer 1984). The desorption yield, Y , of deuterium from stainless steel with the coverage 2×10^{15} atom/cm² was about 0.12 atoms/ion, and Y increased to 0.24 atom/ion when the beam of hydrogen ions with the energy 330 eV/nucleon was directed to the surface. Increased energy of the particles desorbed by light ions is favorable for negative ion emission.

Impact desorption or sputtering of surface adsorbed hydrogen due to plasma ions was proposed as the mechanism to produce H⁻ from the early stage of SPS research and development (Belchenko et al. 1977a). A sharp peak of negative ions, produced by desorption by positive ions was recorded in the energy spectrum of the H⁻ beam, extracted from the converter SPS (Ehlers and Leung 1980). Meanwhile, atomic and molecular hydrogen ions may not have enough momentum to cause collision cascade with substrate Mo and adsorbed Cs.

14.3.3.2 Negative Ion Production Due to Impact Desorption by Heavy Ions

The direct momentum transfer of heavy ions to a surface-adsorbed H atom could be small, but the substrate Mo can receive momentum from incoming heavy ions and transfer the momentum to adsorbed H atom through a surface collision cascade. The heavy ions sputter the impurities and cesium from the shallow surface. Also, they knock out defects formed on the surface layer whose dangling bonds can be

terminated by the absorbed hydrogen. As a result, the processes of negative ion production by desorption due to heavy ions depend on a number of factors, including the way hydrogen and cesium supply onto the surface and the rate at which the surface structures are reorganized.

Yu studied the evolution of H^- ion desorption yield, $Y^- = I^-_{out} / I^+_{in}$, due to the irradiation by Ne^+ ions of a Mo-H-Cs surface created by consecutive adsorption of hydrogen and cesium on a molybdenum surface (Yu 1977, 1978). Primary Ne^+ ions with energies of 150 and 500 eV were incident on the surface at an angle of 45° . An exponential growth of negative ion yield Y^- was recorded with the decreasing surface work function, while characteristic loops were observed for Y^- at different cesium coverages: the negative ion yield was 1.5–3 times higher for a thicker cesium coverage as compared with the thinner Cs coverage of the same work function. It shows that the H^- desorption ion yield is not a single-valued function of the work function. The larger Y^- at a thicker Cs coverage can be caused by a decrease in the binding energy of hydrogen atoms on the surface. The D^- yield was an order of magnitude lower than the H^- yield under similar experimental conditions.

The absolute value of H^- ion desorption yield was measured in experiments with Mo-H-Cs surface bombardment by Cs^+ ions as well. It was reported, that H^- ion desorption yield can reach a value of $Y^- > 0.02$ during a continuous supply of hydrogen and cesium onto a molybdenum surface for Cs^+ ion energy ~ 200 eV, but it decreased to 3×10^{-3} when the Cs^+ ion energy was reduced to 150 eV (Lopes et al. 1986). The lower Cs^+ ion energy leads to the reduction of the momentum transfer from incoming Cs^+ to adsorbed hydrogen, decreasing the emitted H^- ion exit energy. Also, the rate of adsorbed hydrogen removal decreases with decreasing Cs^+ ion energy, so the hydrogen coverage may be thicker at a lower Cs^+ ion energy condition (Seidl and Pargellis 1982).

About a two times higher H^- desorption yield of $Y^- \sim 0.05$ was measured at optimal current density of cesium ions with energy ~ 200 eV in the case of simultaneous hydrogen gas and cesium vapor feed from the sources placed near the surface (Greer and Seidl 1984). It was shown that the yield is not a single valued function of the work function, but it is maximized through maintaining the optimum flux ratio of $Cs^+/H_2/Cs$. A stable coverage with minimum work function is produced at the surface and remains almost unchanged for a wide range of Cs^+ ion bombardment current density if a sufficient flux of neutral cesium and hydrogen is provided to fill the vacant sites caused by sputtering (Fig. 4 in Greer and Seidl (1984)).

The desorption yield values $Y^- = 1.2 \div 1.45$ were observed at the optimal current density of the cesium ions with energy $1 \div 1.7$ keV in the case of the preliminary irradiation of the surface by hydrogen plasma (Bender et al. 1977). This Y^- value was 2–3 times larger than Y^- observed by the authors under similar conditions for hydrogen and cesium co-adsorption from the gas phase.

14.3.3.3 Total H⁻ Ion Production by Backscattering and Desorption by Hydrogen Ions

An absolute value of the total H⁻ ion yield due to low-energy H⁺ and H₂⁺ ion bombardment of cesiated surfaces prepared by hydrogen gas exposure was measured by Isenberg et al. (1992), by Tompa et al. (1986) and by Seidl et al. (1996). All the secondary negatively charged ions were collected, and the total yield of H⁻ ions produced by backscattering and desorption, $K^- = Y^- + R^-$, was measured. It was found that the total H⁻ yield depended upon incident ion energy, the surface work function, the way to cover the surface with Cs, and the amount of hydrogen adsorbed on the cesiated surface.

The dependencies of total H⁻ ion yield K^- versus energy of H⁺ and H₂⁺ ions, incident normally to the cesiated Mo surface, exposed to about 11 L of hydrogen are shown for two cases of surface cesiation in Fig. 14.6 (Seidl et al. 1996). The maximum total yield of $K^- = 0.27$ per nucleon was obtained for a dynamically cesiated Mo converter (Cs supplied from the backside of the Mo converter reached the front surface due to heating) with 1.5 eV work function obtained at incident ion energy >15 eV per nucleon. The same negative ion yield per nucleon was measured for both H⁺ and H₂⁺ incident ions of the same energy per nucleon. This indicates that all the molecular ions are dissociated during the negative ionization through collision process at the converter surface.

The total H⁻ yield, produced by bombardment of a Cs-H-Mo surface with low-energy hydrogen ions depended on the dose of hydrogen pre-exposure, as shown in Fig. 14.7 (Isenberg et al. 1992). The surface with a work function value as low as

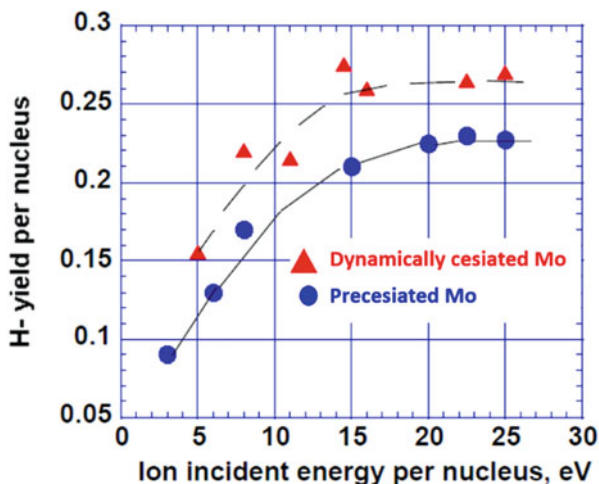


Fig. 14.6 Total H⁻ yield from the cesiated Mo surfaces versus energy of incident H⁺ and H₂⁺ ions. Circles—precesiated Mo converter exposed to 11 L of hydrogen; triangles—dynamically cesiated Mo converter. (Reproduced from Seidl et al. (1996) with permission from AIP Publishing)

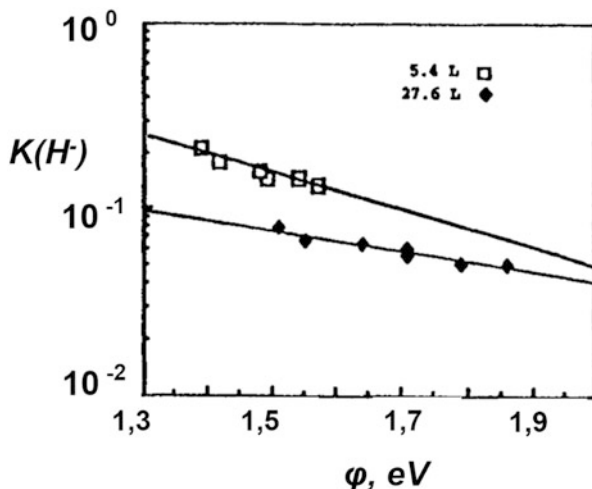


Fig. 14.7 Total H^- yield $K(H^-)$, produced by bombardment of Cs–H–Mo surface with 20 eV hydrogen ions versus surface work function for two different H_2 exposures of 5.4 L and 27.6 L (Reproduced from Isenberg et al. (1992) with permission from AIP Publishing)

1.3 eV was obtained after a higher exposure to 7.6 L exposure to hydrogen, but the total H^- yield was two times higher in case of lower (5.4 L) hydrogen exposure. This shows that negative ion production by impact desorption and backscattering depends on the Cs–H–Mo surface structure even in the same co-adsorption species conditions and could be largely different due to the hydrogen coverage even at the same surface work function values.

The total negative ion yield of $K^- \sim 0.2\text{--}0.25$ per nucleon (Fig. 14.6) may be obtained in the SPS with negative ion production on the cesiated electrodes, biased negatively relative to hydrogen-cesium plasma, like in planotron (magnetron) or converter sources (see Sect. 14.4.1). A relatively high H^- ion yield $K^- > 0.03$ at low incident hydrogen ion energy >3 eV may be produced in the large negative ion sources for fusion by bombardment of the cesiated plasma electrodes with superthermal Franck–Condon hydrogen atoms produced by dissociation of molecular hydrogen excited by plasma hot electrons.

14.3.4 Negative Ion Yield Due to Mixed Ion Bombardment

The synergy of elementary surface processes for the total negative ion yield was recorded when the simultaneous bombardment of cesiated electrodes with hydrogen and cesium ions was studied. This is shown in Table 14.1 which summarizes the data on the total negative ion yield $K^- = Y^- + R^-$ obtained during the simultaneous bombardment of cesiated electrodes with hydrogen and cesium ions (Seidl et al.

Table 14.1 Total negative ion yield K^- during simultaneous bombardment of cesiated electrodes with hydrogen and cesium ions by Seidl et al. (1987)

	Ion energy 200 eV			Ion energy 125 eV
	j_{Cs^+}	j_H	K^-	K^-
j_{Cs^+} , mA/cm ²	0.03	0.04	0.13	0.35
j_H , mA/cm ²	0.00	0.76	0.63	2.34
H ⁻ yield	0.02	0.03	0.31	0.18

1987). The total negative ion yield had the value of $K^- = 0.03$ per ion in the case of electrode bombardment by positive ions with energy 200 eV and an incident flux composition $j_{Cs^+}:j_H = 0.04:0.76$ (the third column of Table 14.1), and it increased ten times to the value of $K^- = 0.31$ when the proportion of cesium ion flux is increased to $j_{Cs^+}:j_H = 0.13:0.63$ (the fourth column of Table 14.1). The synergistic effect associated with the increased cesium flux probably caused the activation of a Cs-covered NI emission surface by removing excess Cs and the poisoning impurities (oxides, carbides) from the surface.

14.3.5 Surface Negative Ion Production in Plasma Environment

The negative ion production efficiency can be higher under gas-discharge conditions than in systems designed for investigating fundamental processes under well-defined but separately controlled Cs and hydrogen deposition conditions. The following studies on the surface negative ion production in plasma environment revealed that the plasma condition affects the surface properties and can enhance negative ion production.

14.3.5.1 Hydrogen-Cesium Plasma

The surface conditions are quite dynamic in the hydrogen-cesium plasma environment. Energetic hydrogen ions and atoms as well as cesium ions and atoms strike the surface to form a dynamically stable cesium-hydrogen-covered electrode. Surface adsorbed Cs can be sputtered out by Cs⁺ and heavy impurity ions (Wada 2018), and the surface can be partially covered by electrode material (W or Mo) that is released by ion bombardment. High-energy H⁺ ions can be implanted in the shallow region of the electrode surface to be an acceptor of electrons from Cs on the top layer (see Fig. 14.4a) to reduce work function by forming an adsorbate structure similar to the work function minimum condition for Cs-H-W (Papageorgopoulos and Chen 1973). A hydrogen atom below the Cs top layer can be negatively ionized to be sputtered out as a H⁻ ion.

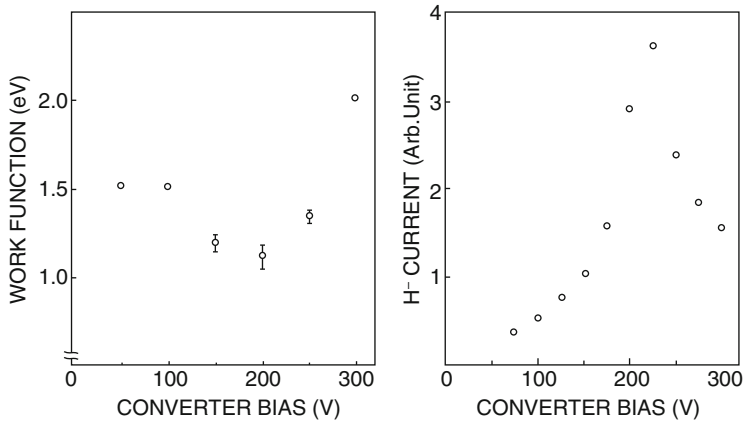


Fig. 14.8 Work function of cesiated molybdenum converter (left) and H^- current from converter (right) versus converter bias with respect to anode. The cesiated molybdenum converter is immersed into dilute hydrogen-cesium plasma. (Reproduced from Wada et al. (1990) with permission from AIP Publishing)

A larger reduction in the electrode work function was produced through the electrode activation in hydrogen-cesium plasma. A Cu electrode, activated by a hydrogen-cesium discharge, had a minimum work function $\phi \sim 1.38$ eV (Wada et al. 1983). This value was lower than that reported for optimum coverage of Cs on Cu in high vacuum conditions. The effects of plasma on the Mo converter work function and on negative ion production were studied by Wada et al. (1990). The irradiation of electrically biased cesiated molybdenum converter by positive ions from dilute hydrogen-cesium plasma with density of 10^9 cm^{-3} was studied. The dependencies of the converter work function and of H^- yield versus converter bias with respect to the multicusp chamber wall serving as the discharge anode are shown in Fig. 14.8. An additional activation of cesiated converter by positive ions, extracted from the hydrogen-cesium plasma was recorded by changing the converter bias voltage. While the work function showed the minimum for 150–250 V bias, the H^- ion current took the maximum from 200 to 250 V.

Figure 14.9 shows the exponential dependencies of H^- ion yields upon the surface work function at a different bias of the cesiated Mo converter with respect to the anode (Wada et al. 1990). As it is shown in Figs. 14.8 and 14.9, the minimum work function of cesiated Mo electrode, activated by a hydrogen-cesium discharge, had a low value of $\phi < 1.3$ eV. The possible reason for the observed reduction of the converter work function in plasma could be a shallow implantation of hydrogen ions and atoms into the surface layer. This larger surface hydrogen density can enhance H^- surface production by impact desorption as well. This model explains an enhanced value of total H^- ion yield $K^- \sim 0.38$ observed during the bombardment of the cesiated molybdenum converter, biased to a potential of about 150 V with respect to cesium-hydrogen plasma (Katsch and Wiesemann 1984). Similar values

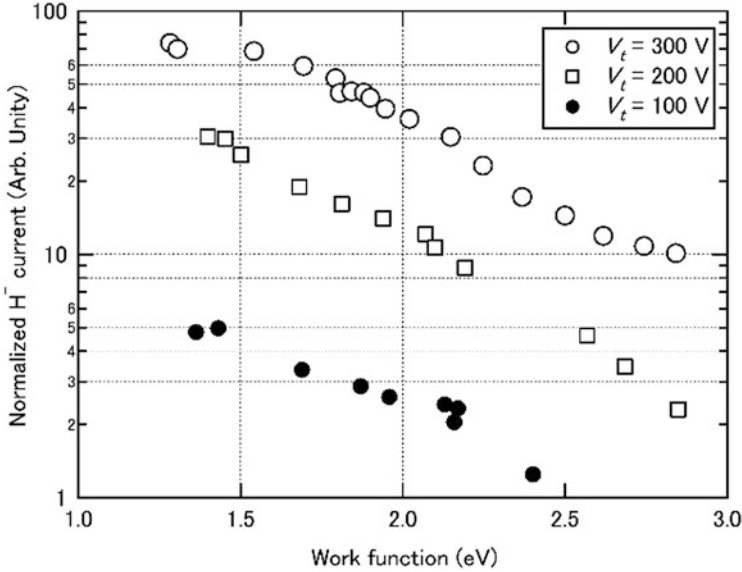


Fig. 14.9 Work function dependence of H⁻ ion yield for a Cs covered Mo converter in a Cs-H₂ discharge at a different bias of converter with respect to the discharge anode. (Reproduced from Wada et al. (1990) with permission from AIP Publishing)

of total negative ion yield can be expected for SPSs with negative ion production on the cathodes and converters as these electrodes are constantly bombarded by energetic ions from cesium-hydrogen plasmas (see Sects. 14.4.1 and 14.4.3).

14.3.6 Hydrogen Plasma with Addition of Inert Gases

Up to tenfold enhancement of negative ion production from the cesiated converter, made of porous tungsten button through which liquid cesium diffuses to the surface, was obtained by adding inert gases (Ar and Xe) to the hydrogen plasma (van Os and van Amersfoort 1987). The cesium coverage of converter and its work function were kept constant during the experiment, so the recorded tenfold enhancement was explained as the enhanced NI yield due to the impact desorption of hydrogen negative ions by heavy ions. It was also confirmed by the energy spectra of extracted negative ions, shown in Fig. 14.10. A sharp peak corresponding to the converter electric potential appeared in the H⁻ energy distribution curve for H₂ + Ar discharge. This peak corresponds to the H⁻ ions produced at the converter surface by impact desorption of Ar⁺ ions.

On the other hand, the impact desorption by heavy ions from a surface with lower hydrogen ion exposure is smaller (see, e.g., the data of columns 2 and 3 in Table 14.1). The recorded increase of the desorbed H⁻ fraction obtained during

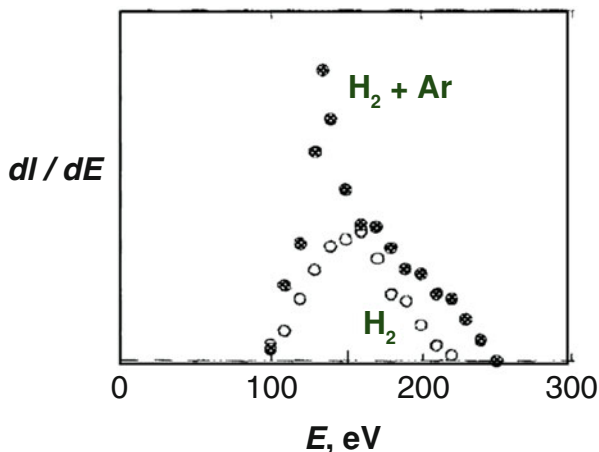


Fig. 14.10 Energy distribution of the H^- beam, produced at the converter, immersed into plasma of pure hydrogen discharge (open circles, 0.4 Pa) and of discharge with the addition of partial argon pressure of 4×10^{-2} Pa (filled circles). Porous cesiated tungsten converter, through which liquid cesium diffuses to the surface, is biased at -138 V with respect to the grounded anode. (Reproduced from van Os and van Amersfoort (1987) with permission from AIP Publishing)

simultaneous bombardment by hydrogen and heavy ions (Fig. 14.10) shows that the NI yield due to the synergistic ion bombardment can be higher than that for the bombardment with hydrogen ions only. These effects: the work function reduction and the enhanced desorption yield due to interaction with heavy ion containing hydrogen discharge plasma can cause the high-efficiency negative ion production in SPSs.

14.4 Channels and Efficiency of Negative Ion Production in SPS

The efficiency of negative ion formation in a single surface collision event may be high, but it could be difficult to achieve an intense H^- production in the ion sources, where the “fragile” surface for high-efficiency H^- emission has to be preserved from intense plasma bombardment and contamination by impurities. Fortunately, the efficiency of H^- production in an intense surface-plasma was proved in the first modification of the pulsed SPS under “dirty” gas-discharge conditions and high-power density plasma bombardment of the electrodes (Belchenko et al. 1973a, 1974a).

14.4.1 SPSs with High-Current $E \times B$ Discharges

14.4.1.1 Planotron (Magnetron) SPSs

Two modifications of SPSs using high-current pulsed discharges in crossed $E \times B$ fields, using the planotron (magnetron) and Penning electrode configuration were developed at BINP (Budker Institute for Nuclear Physics) for accelerator use. The cross sections of the first experimental planotron with the flat cathode surface are shown in Fig. 14.2. This planotron SPS delivered H^- beams with a current up to 0.3 A, emission current density up to 3.7 A/cm^2 and pulse duration of 1 ms at the discharge power 12 kW (with discharge current 100 A and voltage 120 V) (Belchenko et al. 1973a). The corresponding power efficiency of H^- ion beam production reached the value of 25 mA/kW.

A typical dependence of negative ion current density (normalized to emission slit area) versus discharge current density at the cathode (normalized to cathode area) for this planotron without Cs and that with Cs are shown in Fig. 14.11 (Belchenko et al. 1973a, 1974a). As it is shown in Fig. 14.11, an average conversion efficiency $\chi = j_{H^-} / j_d \sim 0.1$ for the discharge current density j_d to the H^- beam emission current density j_{H^-} was obtained in the planotron SPS cesiated mode.

In standard operation conditions of the planotron SPS more than 90% of the extracted H^- ions were produced at the cathode central plane due to backscattering and desorption from positive hydrogen ion impacts, as it was confirmed by the energy distribution of extracted negative ions (curve 5 in Fig. 14.3). The charge-exchange “anode” group of extracted H^- beam increased in accordance with the hydrogen feed to discharge (curve 8 in Fig. 14.3).

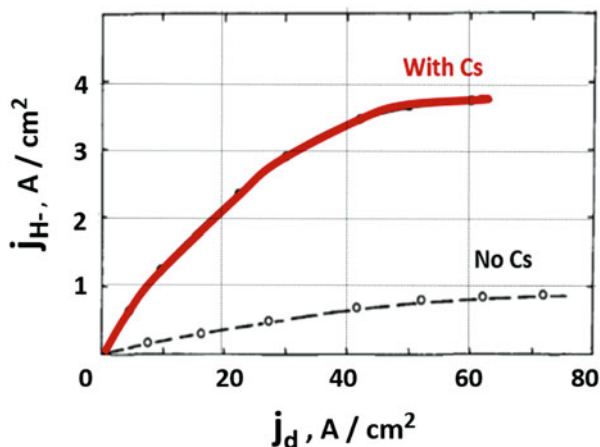


Fig. 14.11 Negative ion current densities, extracted from a planotron versus discharge current density at the planotron cathode for the conditions with Cs and without Cs (Belchenko et al. 1974a). (Reproduced from Belchenko et al. (2018b) with permission from Physics-USpekhi)

The positive ion current j^+ to the cesiated cathodes of $E \times B$ glow discharges (like planotron and Penning SPS) forms only a small part of discharge current j_d in the well-cesiated cathode condition with the typical value $j^+ / j_d \sim 1/7$ (Belchenko and Dudnikov 1976, Belchenko et al. 1977a). Therefore, the efficient H^- ion yield due to backscattering and desorption from the cathode has a high value of $F^- = j_{H^-} / j^+ \sim 0.6$ per an incident positive ion. This high value of F^- in the planotron SPS is about 2 times higher than the total yield per nucleon, $K^- \sim 0.25$, measured for the bombardment of Cs-H-Mo surface by positive hydrogen ions with energy 15–25 eV/nucleon as shown in Fig. 14.6 (Seidl et al. 1996). The observed difference in K^- and F^- can be explained by an increased fraction of molecular hydrogen ions H_2^+ and H_3^+ in the positive ion flux to the planotron cathode.

An important feature of the high-current planotron (magnetron) SPS is the self-activation of the cathode surface due to cesium recirculation in the near-cathode plasma (see below), which supports the stable cathode coverage of cesium under the reduced amount of cesium feeding to the discharge (Belchenko et al. 1977a, b, c; Antsiferov et al. 1990), and the reduced hydrogen gas flow due to a blocking effect by a dense plasma discharge. The reduced gas flow was confirmed by measuring the local pressure with a specially made differential ionization gauge. The hydrogen flow from the emission apertures of high-current planotron SPS is reduced by a factor of 5–10 during discharge pulse (Apolonskii et al. 1980). This multiple-stage control of hydrogen density in the beam extraction and formation areas of the pulsed SPS effectively decreased the H^- ion stripping losses during the beam transport from the source. A pulsed planotron (magnetron) SPS producing pulsed 50 mA H^- beam was developed and routinely used for a long time at the Fermilab (Schmidt and Curtis 1979), BNL (Alessi et al. 1987) and DESY (Peters 1994).

A further improvement of pulsed SPS for accelerators was achieved by introducing the geometrical focusing (GF) of the cathode-produced H^- ions (Prelec and Sluyters 1975; Belchenko and Dudnikov 1978, 1979, 1981; Ehlers and Leung 1980; Alessi and Sluyters 1980). A semi-cylindrical groove or semi-spherical indent was made on the planotron (magnetron) cathode surface as schematically shown in the left part of Fig. 14.12. In the case of a concave surface, most of the cathode-produced H^- ions are accelerated by the electric field of the near-cathode sheath and are geometrically focused on the emission aperture. The efficiency of GF cathode-produced H^- ions in a high-current SPS discharge is determined by the shape and thickness of the near-electrode potential drop, the molecular composition of positive ion current, plasma density spatial distribution, roughness of concave emitter surface *etc.* (Belchenko et al. 1994a).

On the right part of Fig. 14.12 the dependencies of H^- yield (I^-) and those of the anode-produced (A) and cathode-produced H^- groups (C), extracted through the emission hole positioned at various distances with respect to the focal point at the anode of the semiplanotron SPS are plotted. The diameter of the emission hole was 0.8 mm and the radius of the cathode indent was 3.0 mm. The H^- yield and the signal of cathode-produced H^- ion group took maxima when the emission hole was situated at the focal point of the cathode indent (0 shift in Fig. 14.12). The cathode-produced ions were focused to a spot with diameter of ~ 1 mm at the anode plane

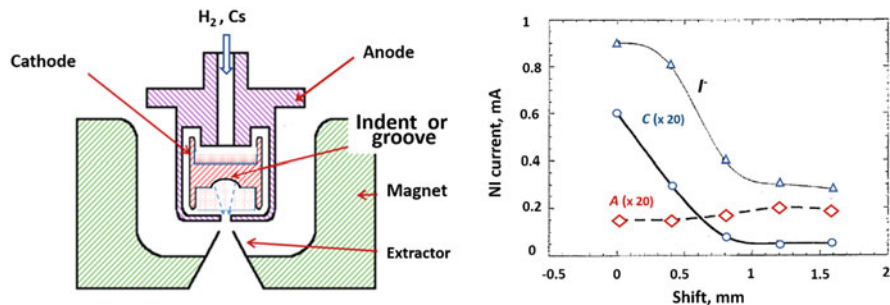


Fig. 14.12 At left—planotron (magnetron) SPS with geometrical focusing of anode-produced negative ions to the emission aperture. A semi-cylindrical groove or semi-spherical indent is made on the cathode surface. At right—the intensity of negative ion current I^- (triangles), the intensity of the cathode-produced group indicated by C (circles), and the intensity of the anode-produced group indicated by A (diamonds) are plotted for various shifts of extraction aperture with respect to the geometrical focal point at the anode; emission aperture positioned at the focal point corresponds to the zero shift. The radius of the focusing indent at the cathode surface is 3 mm. (Reproduced from Belchenko et al. (2018b) with permission from Physics-Uspekhi)

(FWHM), and there were no cathode-produced ions extracted through the emission hole when the emission aperture was situated more than 1 mm away from the focal point. The total H^- yield was about three times higher in the case of the extraction through the emission hole situated at the geometrical focal point (at zero shift in Fig. 14.12) as compared with that through the hole with 1.5 mm shift. In contrast, the signal of anode-produced H^- current was larger for the emission hole shifted from the focal points, where the plasma density should be lower. The hydrogen flux to the emission hole responsible for the H^- anode production could change slightly.

Geometrical focusing of the cathode-produced negative ions (see Fig. 14.12 right) permits to reduce the size of the emission aperture and allows the source operation at a substantially lower discharge power. As a result, a long-term service of planotron (magnetron) source with the maintenance duration up to 9 months was achieved. The planotron (magnetron) SPS with the concave cathode delivered H^- beams with current up to 0.1 A, emission current density up to 1.5 A/cm^2 at the discharge power 15 kW (10 A /150 V) with high power efficiency of H^- ion beam production of 67 mA/kW. This value is ~ 3 times higher than that obtained from the planotron with flat cathode (Alessi 2002). Thus, planotron (magnetron) SPSs with geometrical focusing were used as “working horses” at the BNL (Alessi 2002), Fermi-Lab (Moehs et al. 2002), and DESY proton accelerators (Peters 1994, 1998, 2009). Several honeycomb semiplanotron SPS’s with an extended cathode surface and with the spherical GF of the cathode-produced H^- ions to multiple emission holes were developed. They have provided the pulsed multi-ampere H^- beams beam with current up to 11 A (Belchenko 1983, Belchenko and Dimov 1984a, b) and the long-pulsed beams with current of about 1 A (Belchenko and Kupriyanov 1988, 1990, 1994b)

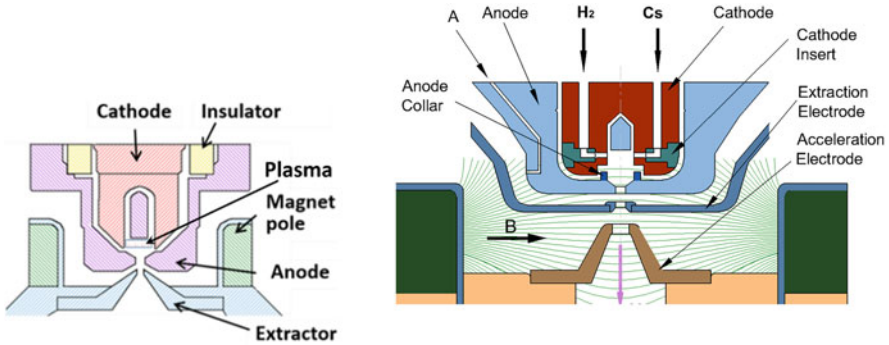


Fig. 14.13 Schematic cross section of the Penning source (view along magnetic field). At left—high-current pulsed source with thick electrodes, at right—direct current Penning SPS with plasma injection from hollow cathodes. (Reproduced from Belchenko et al. (2013a) and Belchenko et al. (2018a) with permission from AIP Publishing)

14.4.1.2 Penning SPSs

As it was clarified in the studies of the first generation SPSs, the H^- ion beam extracted from a Penning SPS reached only half of the intensity of that extracted from a planotron SPS but with a remarkably lower energy spread of H^- (Belchenko et al. 1973b; Belchenko and Kupriyanov 1992). A pulsed Penning SPS was designed and built to produce a bright H^- beam (Dudnikov 1974; Dimov et al. 1977; Allison 1977). The schematic cross section of the BINP Penning source with the reinforced electrode structure is schematically shown at left in Fig. 14.13. These Penning SPSs could deliver pulsed H^- beams with a current of up to 150 mA, pulse duration of 0.2 ms with small emittance and high brightness at the 15 kW discharge power (10 A / 150 V) (Derevyankin and Dudnikov 1984; Sherman et al. 1991). The ISIS operational Penning SPS routinely produces 35 mA of H^- ion current during a 200 μ s pulse at 50 Hz for uninterrupted periods of up to 50 days (Faircloth et al. 2007). The power efficiency of H^- ion beam production at ISIS source is ~ 9 mA/kW (at 50 A / 80 V discharge).

The structure of the high current Penning discharge is ideal for H^- ion surface-plasma production. The cathode of Penning discharge is bombarded by an intense flux of molecular positive ions, accelerated in the near-cathode potential drop to the energy of about $\sim 0.7 eU_d$ (where U_d is discharge voltage). About 30–70% of the incoming ion flux is reflected from the cathode as atoms (and partially as negative ions) with an energy of ~ 0.1 – $0.5 eU_d$. This intense flux of reflected atoms with energy 5–30 eV bombards the cesiated anode and produces an effective conversion to anode-produced H^- ions. The temperature of hydrogen atoms in Penning discharge is high (>1 eV) (Antsiferov et al. 1990; Sherman et al. 1991), so the anode surface is bombarded by an intense flux of superthermal hydrogen atoms, producing an effective surface conversion to H^- ions as well. The anode-produced H^- ions are extracted easily through the direct pass to the emission

aperture. They also come to the emission hole following the negative potential of near-anode plasma and/or being bent by the transverse magnetic field. An additional amount of extracted H^- ion flux is provided due to charge-exchange of fast cathode-produced H^- ions through collisions with slow hydrogen atoms.

All groups of H^- ions: the surface-produced group and the charge-exchange-produced H^- group have low-energy spread, so the beam extracted from the Penning SPS has a very small emittance (Derevyankin and Dudnikov 1984). It is worth noting that the enhanced thickness of the anode plate near the emission aperture of this source enhances the anode-surface H^- production and increases the energy spread of the produced H^- beam as compared with that in the sources with a thin anode plate (Belchenko and Kupriyanov 1994a; Faircloth and Thomason 2006). The pulsed Penning SPS was successfully tested in spaceflight for firing the neutral beam of Strategic Defense Initiative experiment BEAR (Schrage et al. 1989), and is used at the meson factories in Oxford (Sidlow and West 1992) and in Moscow (Belov et al. 1992). The details of Penning SPS construction and operation are presented in Chap. 17 of this book.

14.4.2 Direct Current SPSs

Several successive modifications were made to produce an intense H^- emission from the cesiated SPS in a continuous wave (CW) mode. An experimental LBL multicusp SPS with internal converter (Leung and Ehlers 1982) has produced a steady-state H^- ion beam current higher than 1 A with an impurity level of less than 1%. An experimental direct current H^- ion beam of 50 mA has been extracted from a continuously operated SPS source with a cesiated converter electrode (Piosczyk and Dammertz 1986). About 2.5 mA dc H^- beam was obtained from a compact experimental semiplanotron SPS at 70 W discharge power (Bashkeev and Dudnikov 1990) and a ~ 20 mA H^- dc beam was extracted from the experimental multicusp ion source with arc discharge filaments at TRIUMF (Kuo et al. 1998).

A compact direct current SPS, delivering 8 mA CW H^- beam to a tandem accelerator was developed and has been in use for a long time in the accelerator source of neutrons at BINP (Belchenko and Savkin 2004). The schematic view of this direct current Penning SPS is shown on the right side of Fig. 14.13. It uses a Penning discharge with hydrogen and cesium feed through holes in the cathodes. The special hollow cathode units are inserted in the cathode protrusions. Each hollow cathode unit has a tip with a small aperture as shown in Fig. 14.14. The hydrogen and cesium are fed to the hollow cathode cavities through channels in the cathode body. Penning discharge is driven by the plasma injection from these hollow cathode units. The dc hydrogen pressure in the hollow cathode units is about 10 times higher, than that in the main discharge chamber. Gas escaping through the hollow cathode apertures provides gas for the Penning discharge operation as well. The source was preliminarily heated by the embedded ohmic heater to provide the electrodes outgassing and heating before the cesium seed. A triode system extracts

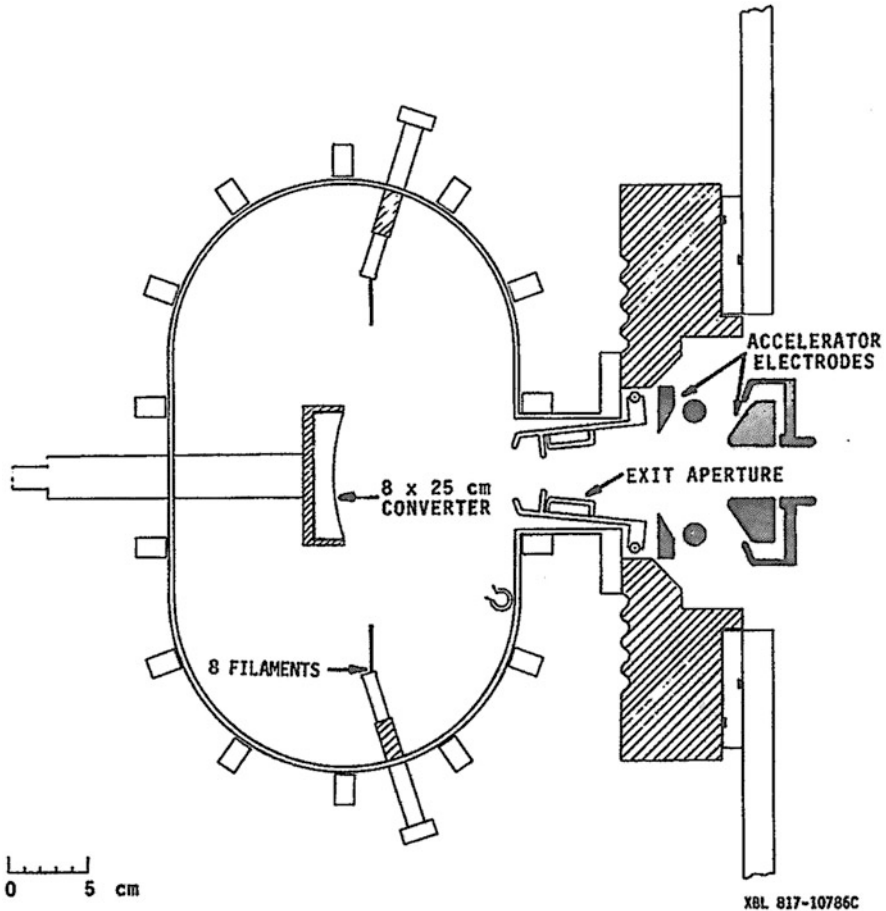


Fig. 14.14 Schematic cross section of the LBL multicusp “self-extraction” SPS with internal converter. (Reproduced from Leung and Ehlers (1982) with permission from AIP Publishing)

the beam toward the acceleration system. The flux of accompanying extracted electrons is reduced by filtering in the transverse magnetic field and the electrons are intercepted by the special electrode biased at 4 kV potential with respect to the anode. The discharge is maintained with 60–80 V voltage and the 9 A current. With the hydrogen pressure at 4–5 Pa and the magnetic field intensity from 0.05 to 0.1 T, the source requires cesium seeding of ~ 1 mg/h.

Negative ions are mainly produced on the cesiated anode surface due to conversion of hydrogen atoms. An optimal anode temperature is 250–350 °C. The negative ion beam current is directly proportional to the discharge current and to the emission hole area. The power efficiency of H^- production is about 19 mA/kW, and the gas efficiency is $\sim 1\%$. The beam normalized emittance is as low as about 0.3π -mm-mrad. The anode bombardment by intense hydrogen atomic flux does not

sputter the cesium coverage deposited on the anode surface allowing operation with a small cesium supply. Cases were observed when gradual erosion of electrodes was recorded and some molybdenum dusts sputtered from the cathode was deposited on the bottom anode plate after 1 month operation. However, the dust deposition does not prevent the source from standard operation (Belchenko et al. 2014).

14.4.3 Multicusp SPS with Internal Converter

The principles of negative ion production in the surface-plasma sources were clearly demonstrated in the LBL multicusp SPS with an internal converter (Ehlers and Leung 1980; Leung and Ehlers 1982), where the special cesiated converter immersed into the plasma volume is biased to 200–300 V with respect to the plasma. The schematic view of this source is shown in Fig. 14.14.

In this configuration the incident positive ions from the plasma are accelerated to the converter surface by the bias potential and efficiently converted to negative ions. The surface-produced negative ions are accelerated back to plasma by the converter bias voltage and head toward the exit aperture. The surface of the converter was made concave for geometrical focusing of surface-produced negative ions. Due to effective plasma confinement by peripheral multicusp magnetic field the SPSs with converter can operate at a very low hydrogen pressure of 10^{-3} Torr, which results in a high gas efficiency of H^- beam production $>20\%$. By positive +15 V biasing of the exit aperture electrode with respect to the anode potential the ratio of electrons to H^- ions in the accelerated beam was decreased to 0.12 (Leung and Ehlers 1982).

A pulsed SPSs with converter was operated for a long time at KEK (Takagi et al. 1985) and at LAMPF meson factory (York and Stevens Jr. 1983). An upgraded LANSCE source with cesiated converter generates 40 mA of H^- beam current at a duty factor of 12% (1 ms pulse at 120 Hz) (Wengrow et al. 1998).

14.4.4 SPSs with Pulsed High-Power RF Discharges

The first SPS using high-power RF discharge with cesium enhancement of H^- ion production was developed at LBL for the Superconducting Super Collider project (Leung et al. 1991, 1993; Debiak et al. 1992). An RF-driven plasma was generated in a multicusp source chamber with a three-turn copper-coil internal antenna, coated by thin glass or porcelain. In order to enhance the H^- yield, a pair of magnet filter rods was installed for electron filtering and a collar with SAES cesium dispensers was installed at the exit aperture for cesium deposition. About three times enhancement in H^- beam current was obtained due to cesium deposition, and H^- beams in excess of 100 mA with the electron to H^- current ratio $I_e/I(H^-)$ close to one have been obtained in 100 μ s /10 Hz pulses from the 5.6 mm diameter exit aperture by the RF input power higher than 50 kW (Saadatmand et al. 1995, 1996). A plasma grid

heating element controls the temperature of the cesiated surfaces and the rate of cesium supply.

A similar RF-driven source with an internal antenna was developed for the Spallation Neutron Source at Oak Ridge National Laboratory, delivering 38 mA H^- beam to a linear accelerator at 60 Hz, 0.9 ms (Leitner et al. 1998, Thomae et al. 2000). The similar RF source producing 60 mA H^- beam was developed for J-PARK accelerator (Ueno et al. 2013). To improve the beam availability, an RF-driven ion source with external antenna and a water-cooled aluminum nitride plasma chamber were developed. An RF-driven source with an internal antenna demonstrated a reliable operation at a 6% duty factor with 1-ms/60 Hz pulses, delivering the beam current in a 35-mA level with a minute amount of cesium seeding. The special conditioning procedure with the collar preliminary heated to more than 500 °C and cleaning by RF discharge was developed. After this initial conditioning and cesium deposition, the collar is kept at about 280 °C for optimal beam production. The cesium coverage optimized for H^- production can then last for several days (Keller et al. 2002) and months (Stockli et al. 2016, see Chap. 18 of this book).

14.4.5 Giant Long-Pulsed Multiaperture SPS for Fusion Neutral Beam Injectors

The first tests of cesium deposition to a giant long-pulsed multiaperture source driven by an arc discharge with hot filaments were done by JAERI team (Okumura et al. 1990). The main principles and properties of these sources are described below in Chaps. 16 and 19. Similar to the compact multicusp sources (Waltner et al. 1988), the main channel of NI production in these giant SPS is the conversion of superthermal atoms on the cesiated surface of large-area plasma electrode (shown in Fig. 14.1b). To enhance the surface negative ion production, a gradual cesium deposition to the plasma grid surface is provided. A magnetic field filtering of electrons creates a low electron temperature region near the plasma grid to decrease the destruction of negative ions before their extraction. An optimal plasma grid temperature of about 200 °C (see Fig. 14.15 below) was found important to achieve a proper Cs coverage for the source operation. A remarkable decrease of the electron flux co-extracted with negative ions was obtained by applying positive bias to the plasma grid with respect to the anode chamber (Leung and Bacal 1984).

All mentioned features of the surface-plasma NI production like no saturation of negative ion yield when increasing the discharge current, the efficient discharge operation at a reduced hydrogen pressure and a remarkable decrease of the electron flux co-extracted with negative ions are demonstrated for the giant multiaperture source operation. Beams of H^- with total current up to 36 A from a single source and a beam energy of 180 keV were produced by the LHD neutral beam injection

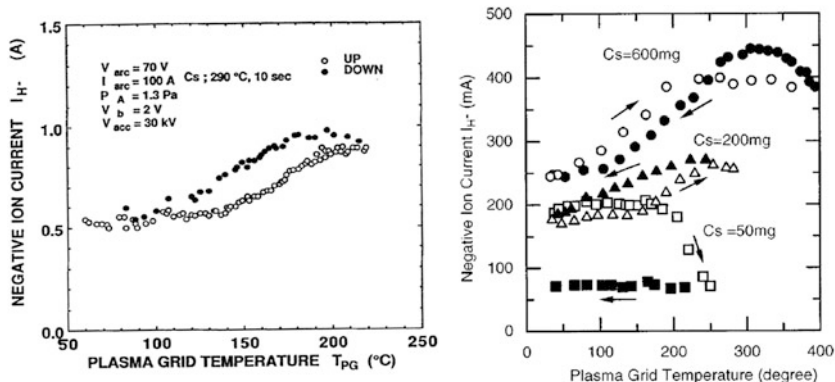


Fig. 14.15 H^- current versus plasma grid temperature. At left—discharge operation with 10 s pulse duration and ~ 3 min pause between pulses (Okumura et al. 1990), at right—CW source operation under various integral Cs seed (Miyamoto et al. 2000). Open markers—PG heating, filled markers—cooling. (Reproduced with permission from AIP Publishing)

system (Takeiri et al. 2006). The efficiency of H^- ion beam production in the arc-driven giant SPS is 30 mA/kW.

A huge high-energy neutral beam injector for producing long-pulse D^- beams with intensity 67 A and energy up to 1 MeV is under construction for ITER project (Serianni et al. 2016). The main challenges for the high-energy neutral beam injectors for fusion are the uniformity of plasma production in the large-area discharge, the homogeneity of cesium coverage over the large-area plasma grid, long discharge pulses with a duration of up to ~ 1 h and acceleration of large-area beam in the high-voltage multiaperture accelerator. A possible remedy to mitigate beam acceleration problem is to separate the negative ion source from accelerator with the help of low-energy transport tank, which has been proposed and tested with the injector prototype at BINP (Ivanov et al. 2013).

14.5 Essential Features of Negative Ion Production in SPS

14.5.1 Cesium Catalyst of Negative Ion Production

14.5.1.1 Primary Cesium Seed to SPS Electrodes

The essential factor to increase the surface-plasma H^- ion production in the advanced SPS is a decrease of the emitting electrode work function by Cs deposition at the optimal coverage. The following procedures of cesium injection to SPS volume and cesium deposition onto the SPS H^- emission surfaces are developed and utilized:

- (a) Inject Cs to the discharge chamber volume from cesium compounds contained in an electrode heated by the discharge: deposition from cesium compounds loaded to the cathode cavity (Belchenko et al. 1973b), deposition from cesium compounds loaded to the anode cavity (Dudnikov 1974; Allison 1977), deposition from cesium dispensers integrated with the plasma grid collar (Debiak et al. 1992; Saadatmand et al. 1995).
- (b) Inject Cs to the discharge chamber volume from an external independently heated oven: from an oven loaded with cesium compounds (Belchenko et al. 1973b; Smith and Allison 1979) and from an oven loaded with metallic cesium (Dimov et al. 1977; Schmidt and Curtis 1979).
- (c) Supply Cs onto H^- emission electrode surface through the pores of a porous electrode (Alessi et al. 1984).
- (d) Directly deposit cesium onto the discharge chamber walls from a movable internal oven (Belchenko et al. 1996).
- (e) Directly deposit cesium onto the plasma grid through the cesium distribution tube (Belchenko et al. 2016a, b, c).

Implanting Cs onto a plasma grid surface using a Cs^+ ion gun can be a viable option for preparing a suitable low work function surface. Deposition of Cs atoms and hydrogen atoms/molecules on the H^- production surface can be controlled under discharge condition so as to produce a structure most efficient for H^- ion production.

After their deposition, the neutral Cs atoms and hydrogen atoms/molecules diffuse and adhere to the H^- production surface generating a low work function condition suitable to produce H^- ions. Discharge ignition starts the ion bombardment of the surface, changing the thickness and composition of the electrode coverage (van Amersfoort et al. 1985), which depends on the sputtering or deposition/implantation by the incident plasma particle flux. Surface adsorbed Cs and impurities can be sputtered by cesium and heavy ions. The large plasma power loading of the H^- ion production surface elevates the temperature of the electrode and causes increased thermal desorption from, and diffusion of adsorbates on the electrode. On other hand, the surface can be partially covered by electrode materials that are evaporated from cathode filaments or sputtered by plasma ion bombardment. The dynamics of cesium and physics of the formation of optimal cesium coverage on electrodes in a high-current pulsed discharge source were studied by Belchenko et al. (1977c), Belchenko and Davydenko (2006), and in large-scale multiaperture H^- sources for neutral beam injectors by Morishita et al. (2001) and Fröschle et al. (2009).

14.5.1.2 Conditioning (Activation) of the Cesium SPS Electrodes

The electrode surface conditions are quite dynamic in SPS. The composition of the ion species in the plasma and the adsorbates on the electrode surface could be purposely changed during SPS electrode conditioning/activation. Several methods of cesium deposition/implantation and optimization of the SPS electrode were

developed and used in SPS operation. The following procedures are necessary for the electrode cesium-hydrogen coverage optimization and the H⁻ ion beam current enhancement:

1. Electrode cleaning with thermal desorption and sputtering of deposited impurities.
2. Transport of seeded cesium from the Cs deposited spot on the wall to the SPS emitter electrode.
3. Diffusion of cesium over the entire emitter surface.
4. Sputtering of deactivating impurities from the cesium surface by heavy ions Cs⁺, Ar⁺, etc.
5. Optimization of cesium coverage by removing excess cesium.
6. Absorption/implantation of hydrogen into optimal positions in the surface structure.

The listed activation process leads to an efficient H⁻ ion production surface by electrode heating to temperature from 200 to 500 °C, and can further optimize the NI yield by bombardment with energetic particles from SPS plasma.

The effect of cesium coverage activation by high-current discharge in the pulsed multiaperture Penning SPS is summarized in Table 14.2 (Belchenko and Kupriyanov 1992). From stages 1 to 4 in Table 14.2, the source conditioning advances. The extracted H⁻ current started from the value of 10 mA at the initial operation of the source after cleaning with water and alcohol. After 20 min of electrode heating and conditioning by high-current discharge, the Cs was released from the contaminated cesium remnant and the negative ion yield increased to 40 mA. (On Cs recovery from poisoned layers, see also Belchenko et al. (2000). An increase of H⁻ current to 100 mA was obtained with the cesium deposition from the external oven (line 3 of Table 14.2). A stable beam of H⁻ current of up to 300 mA was obtained after ~20 min conditioning period for optimizing the recirculation of seeded cesium.

An effect of seeded cesium distribution, recycling from contaminants and cesium coverage activation due to plasma grid heating and electrode conditioning by a high-power discharge was shown clearly in the large-area arc-driven source by Okumura et al. (1990). Their results are shown in the left part of Fig. 14.15. During initial source operation after 10-s cesium deposition to the anode chamber walls

Table 14.2 Evolution of H⁻ current during conditioning of the pulsed multiaperture Penning SPS

Stage	Cs seeding	Operation conditions	I_{H^-} , mA
1	Without Cs	Cleaned source, initial operation, cold chamber	10
2		20 min operation, hot electrodes, recovery of cesium from contaminated cesium remnants	40
3	With Cs	After Cs injection	100
4		After heating and activation by discharge	300

the H^- yield had the value of 0.5 A. The following discharge operation with a 10 s pulse/3 min pause interval led the plasma grid heated to a proper temperature $\sim 200^\circ\text{C}$ and increased H^- yield by two times (left side of Fig. 14.15) (Okumura et al. 1990). The following operation with a longer pause period between discharge pulses permitted to decrease the plasma grid temperature, and a sizable hysteresis effect in the dependence of the H^- yield versus the plasma grid temperature was recorded.

More detailed information on seeded cesium redistribution and conditioning shown at the right side of Fig. 14.15 was obtained in a CW arc-driven source by varying the amount of Cs loaded to the source chamber (Miyamoto et al. 2000). The stable CW production of 400 mA H^- beam was obtained after loading up to 600 mg of cesium with the plasma grid temperature maintained at 300°C . A lower cesium effect with H^- yield of about 200 mA was recorded with only 50 mg Cs loading while the Cs recirculation effect was lost after plasma grid temperature reached 250°C . Cooling of the plasma grid did not recover the H^- current enhancement. This confirms the need of gradual supply of cesium to the plasma grid for compensating the cesium deactivation by deposition of tungsten evaporated from cathode filaments. The detailed study of cesium deposition to the large-area arc-driven source was done in NIFS by Oka et al. (2000).

The importance of cesium redistribution and cesium coverage activation due to plasma grid heating and electrode conditioning by high-current discharge was clearly revealed by the measurement of photo-electron current due to Ar^+ laser irradiation on the plasma grid after cesium injection into the microwave-driven source (Kashiwagi et al. 2002). As shown in Fig. 14.16, the increased photo-electron

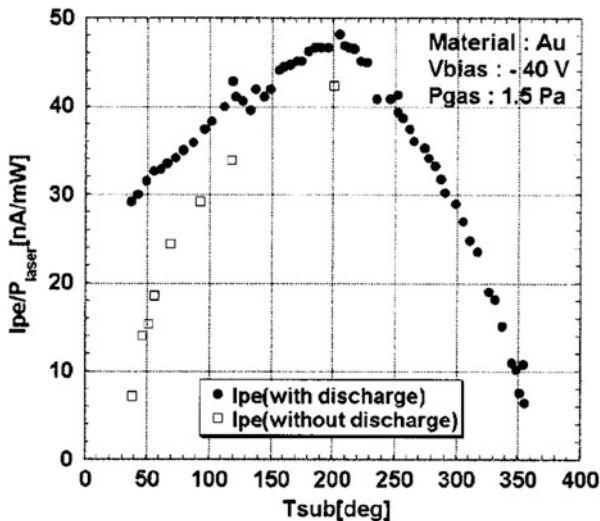


Fig. 14.16 Evolution of photoelectrons current I_{PE} versus plasma grid temperature during heating without and with microwave discharge. (Reproduced from Kashiwagi et al. (2002) with permission from AIP Publishing)

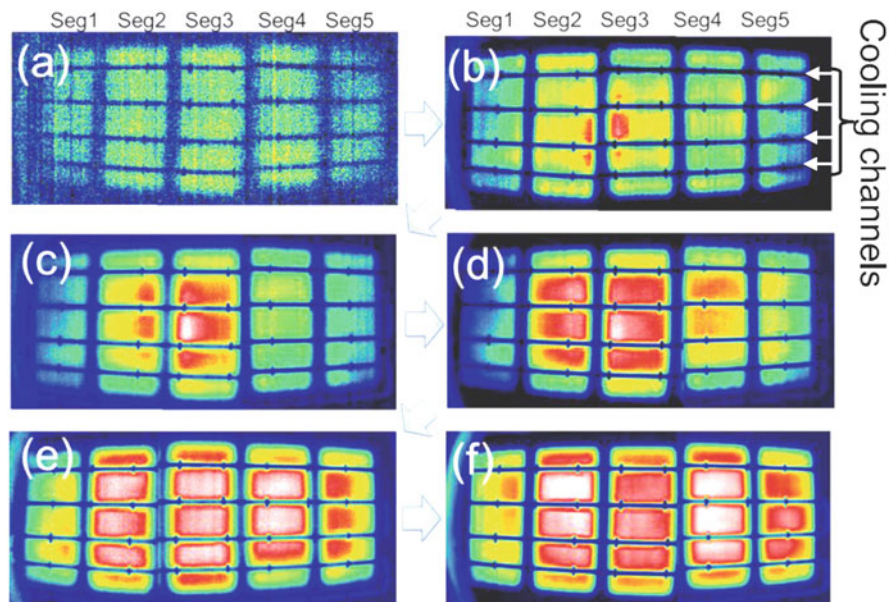


Fig. 14.17 Spatial profiles of the H^- beam extracted from the PG with a total area of $0.45 \times 1.1 \text{ m}^2$ at the different stages of the source conditioning by discharge. (a) 0 s -before the Cs-seeding, (b) after $\sim 4.5 \times 10^3$ s integral discharge time (1 g Cs-seeding), (c) after $\sim 4.8 \times 10^3$ s discharge time, (d) \sim after 5×10^3 s discharge time, (e) \sim after 5.5×10^3 s discharge time, and (f) \sim after 6×10^3 s discharge time (2 g Cs-seeding). (Reproduced from Yoshida et al. (2016) with permission from AIP Publishing)

current corresponding to decreased work function of the cesiated plasma grid showed a peak at $200 \text{ }^\circ\text{C}$; the Cs thickness was optimized at this temperature (open square markers in Fig. 14.15 right). The activation of plasma grid coverage and corresponding increase of photo-electron current was faster and higher under synergy of plasma grid heating and sputtering-conditioning by microwave discharge (filled markers).

An impressive example of cesium redistribution by the discharge in the giant SPS for JT60-SA is shown in Fig. 14.17, where the spatial profiles of the beam extracted from the large-area PG are shown at the different stages of the source conditioning by discharge (Yoshida et al. 2016).

Before the Cs-seeding operation, the profile of the negative ion production was uniform (Fig. 14.17a). After the gradual deposition of 1 g Cs an increase of the negative ion production appeared from the center of the extraction area, where the Cs nozzle is located (Fig. 14.17b). By a continuous Cs-seeding operation, the negative ion production at the center was enhanced. The enhanced area expanded longitudinally from the center to the edge region. After the total discharge time of $\sim 6 \times 10^3$ s with corresponding ~ 2 g of the Cs-seeding, the negative ion

beam profile was saturated and became almost uniform except for a corner of the extraction area (Yoshida et al. 2016). The indicated redistribution, optimization and activation of seeded cesium due to synergy of heating and sputtering-conditioning by plasma are typical characteristics of cesiated surface-plasma sources.

14.5.1.3 Confinement and Recirculation of Cesium in the High-Current $E \times B$ Discharges

Cesium is easily ionized by plasma electrons, and cesium ions could be effectively confined by the electric field of the discharge or by the electric field applied for NI extraction. After the sputtered from the cathode cesium atoms are ionized in the near-cathode region and return to the cathode due to the discharge electric field, providing cesium recirculation in the near-cathode region of SPS with high-current $E \times B$ discharges like the ones in planotron and Penning configurations. This recirculation of cesium was proved by spectroscopic measurements of Cs light emission distribution in the PIG SPS discharge, where about ten times larger luminosity of cesium atoms CsI and cesium ions CsII emission lines were recorded from the near-cathodes zones as compared with that from the discharge center, as it is shown in Fig. 14.18 (Antsiferov et al. 1990; Smith Jr. et al. 1991). The near-cathode recirculation of cesium supports an intense bombardment of the cathodes by Cs^+ ions, accelerated by near-cathode potential sheath. This energetic Cs^+ ion bombardment maintains the cesium flux to the cathode while sputters out the impurities, forms surface structure with the implanted cesium and creates sites for hydrogen absorption. It provides a fast refreshing of cathode cesium on the electrode at the pulse start. During the pulse the cesium circulation produces a dynamic

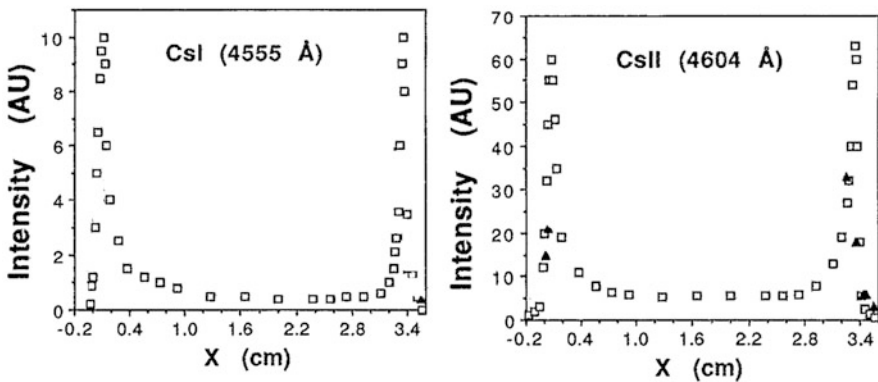


Fig. 14.18 Emission light distribution from cathode to cathode in the PIG discharge for cesium atoms CsI (4555 Å) and ions CsII (4604 Å) in a 120 V/400 A pulsed discharge. Cathode surfaces are at $x = 0$ and 3.4 cm. (Reproduced from Smith Jr. et al. (1991) with permission from AIP Publishing)

cesium coverage keeping the optimum Cs thickness, as the Cs atoms sputtered out return back to the surface as Cs^+ ions.

The confinement of ionized cesium in the high-current $E \times B$ discharges was confirmed by direct measurements of cesium ion and atomic fluxes to the electrodes of PIG discharge. As it was measured in the PIG source (Belchenko et al. 1977c, Belchenko and Davydenko 2006), the cesium ion flux to the cathode during the pulse is about 10^3 times higher, than the flux of cesium atoms to the anode and to the emission slit. The ionized cesium recombines at the discharge chamber walls after the discharge pulse end, and a short spike of cesium atoms with duration of 0.5–2 ms, outgoing from the emission aperture was recorded (Belchenko et al. 1977c, Belchenko and Davydenko 2006).

14.5.2 *Suppression of Co-extracted Electron Flux*

In volume sources, H^- ions are produced through collision processes of plasma particles including electrons and thus, extracted together with a large amount of plasma electrons. The magnetic filtering of electrons in the plasma chamber and the bias of the plasma electrode with respect to the anode (Leung et al. 1983) were used to decrease the co-extracted electron current. An increased ratio of H^- ion beam to the co-extracted electron flux of about $H^- : e \sim 1:5$ was achieved in the large-area volume source (Hanada et al. 1990) and of about 1:3—in the 15 mA dc volume source for cyclotrons (Kuo et al. 1996).

The important feature of the SPS is a remarkable reduction of the electron flux, co-extracted with negative ions. The ratio $H^- : e \sim 1:1$ was usually obtained in the pulsed high-current SPS for accelerators and in the giant SPS for fusion injectors.

This effect of reduced co-extracted electrons current was studied first with the planotron SPS. It was suggested, that electrons are collected well along the magnetic field lines to the anode collar installed in front of the emission slit, and “a plasma, consisting primarily of positive and negative ions is produced in the cavity in front of the emission slit” (Belchenko et al. 1975). A reduction of co-extracted electron flux in SPS became possible due to the intense NI production, which facilitates an essential change of the plasma composition in the extraction region of SPS: the electron component of the plasma is partially replaced by the negative ion component.

This evolution of H^- component in the extraction region of SPS, caused by cesium seed was confirmed by Langmuir probe diagnostics in the large-area RF-driven SPS (Wimmer et al. 2015). It was found that the Langmuir probe characteristics changed from a classical electron-positive ion characteristic to a symmetric ion-ion characteristic, meaning that H^- ions became the dominant negatively charged particle species in the cases with cesium deposition.

A remarkable decrease of the co-extracted electron current was obtained in the giant arc-driven SPS (Okumura et al. 1990) and RF-driven SPS (Franzen et al. 2007) by applying a positive bias to the plasma grid with respect to the anode chamber.

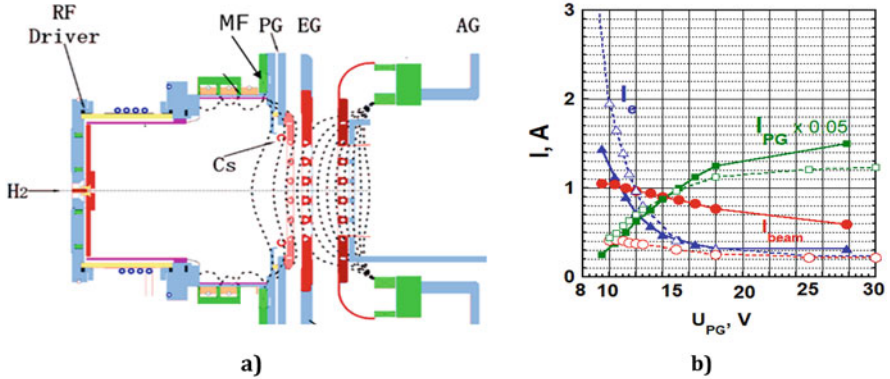


Fig. 14.19 (a) Geometry of large-area RF-driven source. MF magnetic filter; Cs tube for cesium deposition; PG plasma grid; EG extraction grid; AG acceleration grid; (b) dependencies of the negative ion beam current I_{beam} , of the co-extracted electron current I_e and of the electron current to PG I_{PG} versus positive PG bias U_{PG} . (Reproduced from Belchenko et al. (2016b, c) with permission from AIP Publishing)

In Fig. 14.19a the principal scheme of the large-area RF-driven SPS is presented. The plasma produced by inductive RF discharge, bombards the plasma grid (PG) covered with cesium supplied from the cesium distribution tube. The negative ions, produced at the PG surface are extracted by the electric field, applied between the PG and the extraction grid (EG) and post-accelerated by the field toward the acceleration grid (AG).

The dependencies of the negative ion beam current, I_{beam} , the co-extracted electron current, I_e , and the electron current to PG, I_{PG} as a function of the positive PG bias U_{PG} are shown in Fig. 14.19b for the cases of well-cesiated source (solid lines) and the washed off cesium condition (dotted lines) (Belchenko et al. 2016c). NI beam current was about 2.5 times larger in the well-cesiated source as compared with the washed-off cesium case, and gradually decreases with the increase in U_{PG} . The co-extracted electron current I_e was ~ 2 times smaller in the cesium case and it decreased in accordance with U_{PG} increase. The co-extracted electron current became smaller than the NI beam current in the cesiated case for $U_{\text{PG}} > 11$ V.

The dependencies of Fig.14.19b reflect the evolution of ion-ion plasma in the extraction region of SPS, where the negative ion fraction increases with the growth of PG potential bias, especially in the cesiated case. At PG bias of 8–10 V the potential of near-PG plasma is positive with respect to PG, similar to those, measured by Wimmer and Fantz (2015). As a result, I_{PG} composed mainly of the electron flux to PG is suppressed, while the electron component in the near-PG ion-ion plasma is enlarged. It resulted in an increased current of electrons, co-extracted by external electric field, produced by the extraction electrode. With the increase of plasma grid bias $U_{\text{PG}} > 12$ V the space potential of near-PG plasma became negative with respect to PG, and the electron current from plasma to PG increases. This electron transport depletes the electron population in the ion-ion plasma, and the electron current, co-extracted from the ion-ion plasma decreases as well.

The composition of the ion-ion plasma in the vicinity of the plasma grid and the corresponding change in the co-extracted electron current depends on the rate of surface H^- production and the speed of electron removal from the plasma to the walls. The transverse magnetic field of the filter prevents the electrons from reaching the anode or the PG surface. The electron removal to the anode or to the positively biased PG was increased in the cases of the anode collar (Belchenko et al. 1974a, b, c), of the metallic cesium distribution tube (Belchenko et al. 2013b, 2016b) or biased metallic rods, inserted in the vicinity of emission apertures (Wünderlich et al. 2021). These structures intercept electrons, moving along the magnetic field lines and reducing the electron component of the ion-ion plasma and the electron current co-extracted with H^- ions.

14.6 Summary

Impressive advancements in the performance of surface-plasma H^- ion sources and a deeper understanding of physical mechanisms of surface-plasma NI production were achieved in the last 50 years under national programs like the Superconducting Super Collider and neutral beam heating system for the Large Helical Device. The key parameters of the negative ion sources were remarkably improved through modifications of ion source design and reexamination of source operation procedures based upon research outcome on fundamental processes. The classical pulsed SPSs with high-current $E \times B$ discharge like planotron (magnetron) or Penning sources continued to be “working horses” at the accelerator facilities. Efficient RF-driven SPSs were invented and successfully operated at accelerators like J-PARC and SNS, while SPSs developed for intense large-area neutral beam injectors are nearly ready to heat up plasmas in fusion experimental devices like JT60-SA and ITER.

The fundamental mechanisms, responsible for NI formation in SPS are the kinetic negative ion emission through thermally non-equilibrium processes of reflection, sputtering, and desorption from electrodes in plasmas; various plasma particles (hydrogen and cesium positive ions, superthermal and energetic atoms) strike the low work function electrode surface covered by Cs and hydrogen. Plasma delivers an intense flux of material to activate electrodes and the surface-produced NI flux forms an intense beam extracted through an emission aperture. As a result, the surface-plasma process leads to a negative hydrogen ion source with high-power, high-gas, and high-Cs recirculation efficiencies.

References

- J.G. Alessi, AIP Conf. Proc. **642**, 279 (2002)
- J.G. Alessi, T. Sluyters, Rev. Sci. Instrum. **51**, 1630 (1980)
- J.G. Alessi, A. Hershcovitch, T. Sluyters, Rev. Sci. Instrum. **55**, 8 (1984)

- J.G. Alessi, J.M. Brennan, A. Kponou, K. Prelec, Conf. Proc. C 870316, 304 (PAC 1987)
- P.W. Allison, IEEE Trans. Nucl. Sci. **NS-24**, 1594 (1977)
- V.V. Antsiferov, V. Beskorovaynyy, A. Maximov, et al., AIP Conf. Proc **210**, 427 (1990)
- A.N. Apolonskii, Y.I. Belchenko, G.I. Dimov, V.G. Dudnikov, Sov. Tech. Phys. Lett. **6**, 38 (1980) – in Russian
- M. Bacal, M. Wada, Appl. Phys. Rev. **2**, 021305 (2015)
- D.H. Baker, R.L. Champion, L.D. Doverspike, Y. Wang, Appl. Phys. Lett. **64**, 1880 (1994)
- A.A. Bashkeev, V.G. Dudnikov, AIP Conf. Proc. **210**, 329 (1990)
- Y.I. Belchenko, Sov. J. Plasma Phys. **9**, 703 (1983)
- Y.I. Belchenko, Rev. Sci. Instrum. **64**, 1385 (1993)
- Y.I. Belchenko, V.I. Davydenko, Rev. Sci. Instrum. **77**, 03B702 (2006)
- Y.I. Belchenko, G.I. Dimov, AIP Conf. Proc. **111**, 363–375 (1984a)
- Y.I. Belchenko, G.I. Dimov, Probl. Atomic Sci. Techn., ser. Thermonucl. Fusion **1**(14), 42–47 (1984b) –in russian
- Y.I. Belchenko, V.G. Dudnikov, *Proceedings of the 3rd All-Union Seminar on Interaction of atomic particles with solids. Kharkov, 1975.* vol. 3, pp. 180–183 (1976) –in russian
- Y.I. Belchenko, V.G. Dudnikov, Preprint IYaF 78-95. Novosibirsk (1978) - in russian
- Y.I. Belchenko, V.G. Dudnikov, J. Phys. Coloq. **40**(C7), 507 (1979)
- Y.I. Belchenko, V.G. Dudnikov, Proc. XV Int. Conf. on phenomena in ionized gases, Minsk, 1981. Part II, p. 883 (1981)
- Y.I. Belchenko, A.S. Kupriyanov, Revue Phys. Appl. **23**, 1889 (1988)
- Y.I. Belchenko, A.S. Kupriyanov, Rev. Sci. Instrum. **61**, 484 (1990)
- Y.I. Belchenko, A.S. Kupriyanov, AIP Conf. Proc. **287**, 255 (1992)
- Y.I. Belchenko, A.S. Kupriyanov, Rev. Sci. Instrum. **65**, 417 (1994a)
- Y.I. Belchenko, A.S. Kupriyanov, Rev. Sci. Instrum. **65**, 1179 (1994b)
- Y.I. Belchenko, V.Y. Savkin, Rev. Sci. Instrum. **75**, 1704 (2004)
- Y.I. Belchenko, G.I. Dimov, V.G. Dudnikov, A.A. Ivanov, Doklady AN SSSR **213**, 1283 (1973a) - in russian. Soviet. Phys. Doklady **18**, 814 (1974)
- Y.I. Belchenko, G.I. Dimov, V.G. Dudnikov, Izvestiya Akademii Nauk SSSR, Seriya Fizicheskaya **37**, #12, 2573 (1973b) - in russian. Columbia Technical Translation - *Bulletin of the Academy of Sciences of the USSR***37**, #12, 91 (1973)
- Y. Belchenko, G.I. Dimov, V.G. Dudnikov, Nucl. Fusion **14**, 113 (1974a)
- Y.I. Belchenko, G.I. Dimov, V.G. Dudnikov, *Proceedings of the second symposium on ion sources and formation of ion beams*, Berkeley, 22 Oct 1974; preprint LBL—3399 (suppl.), p. VIII.1.1 (1974b)
- Y.I. Belchenko, G.I. Dimov, V.G. Dudnikov, Zhurnal Tekhnicheskoi Fiziki, **43**, 1720-1725 (1973) – in russian. Sov. Phys. Tech. Phys. **18**(8), 1083 (1974c)
- Y.I. Belchenko, G.I. Dimov, V.G. Dudnikov, Sov. Phys. Tech. Phys. **20**(1), 40 (1975), also Zhurnal Tekhnicheskoi Fiziki **45**, 68–73 (1975) –in russian
- Y.I. Belchenko, G.I. Dimov, V.G. Dudnikov, *Proceedings of the International Symposium on Production and Neutralization of Negative Hydrogen Ions and Beams, BNL-50727*, New York (1977a)
- Y.I. Belchenko, V. Davydenko, G. Derevyankin, et al., Sov. Tech. Phys. Lett. **3**, 282 (1977b)
- Y.I. Belchenko, V. Davydenko, G. Derevyankin, et al., Preprint BINP 77-18, Novosibirsk -in russian (1977c)
- Y.I. Belchenko, C. Jacquot, J. Pamela, D. Riz, Rev. Sci. Instrum. **67**(3), 1033 (1996)
- Y.I. Belchenko, Y. Oka, O. Kaneko, et al., Rev. Sci. Instrum. **71**, 741 (2000)
- Y.I. Belchenko, I. Gusev, A. Khilchenko, et al., Rev. Sci. Instrum. **77**, 1 (2006)
- Y.I. Belchenko, A.I. Gorbovsky, A.A. Ivanov, et al., AIP Conf. Proc. **1515**, 448 (2013a)
- Y.I. Belchenko, A.I. Gorbovsky, A.A. Ivanov, et al., AIP Conf. Proc. **1515**, 167 (2013b)
- Y.I. Belchenko, A. Gorbovsky, A. Sanin, V. Savkin, Rev. Sci. Instrum. **85**, 02B108 (2014)
- Y.I. Belchenko, A.A. Ivanov, S.G. Konstantinov, et al., Rev. Sci. Instrum. **87**, 02B133 (2016a)
- Y.I. Belchenko, G. Abdrashitov, P. Deichuli, et al., Rev. Sci. Instrum. **87**, 02B316 (2016b)
- Y.I. Belchenko, A.A. Ivanov, A. Sanin, et al., Rev. Sci. Instrum. **87**, 02B119 (2016c)

- Y.I. Belchenko, V.I. Davydenko, P.P. Deichuli, et al., *Phys. Usp.* **61**, 531–581 (2018a)
- Y.I. Belchenko, A.A. Ivanov, A.L. Sanin, O.Z. Sotnikov, *AIP Conf. Proc.* **2052**, 030006 (2018b)
- A.S. Belov, O.T. Frolov, V.S. Klenov, V.P. Yakushev, *Rev. Sci. Instrum.* **63**, 2622 (1992)
- E.D. Bender, M. Kishinevsky, I.I. Morozov, *Proc. of Int. Symposium on Production and Neutralization of Negative Hydrogen Ions and Beams*, Brookhaven. Preprint BNL 50727, 60 (1977)
- T.W. Debiak, S. Melnychuk, G. Gammel, et al., *AIP Conf. Proc.* **287**, 375 (1992)
- G.E. Derevyankin, V.G. Dudnikov, *AIP Conf. Proc.* **111**, 376 (1984)
- G.I. Dimov, G.E. Derevyankin, V.G. Dudnikov, *IEEE Trans. Nucl. Sci.* **NS-24**, No. 3, 1545 (1977)
- V.G. Dudnikov, *Proc. of the 4th All-Union Conf. on Charged Particle Accelerators*, Moscow (1974) –in russian
- K.W. Ehlers, K.N. Leung, *Rev. Sci. Instrum.* **51**, 721 (1980)
- M.-L. Ernst-Vidalis, C. Papageorgopoulos, U. Stawinski, E. Bauer, *Phys. Rev. B* **45**, 1793 (1992)
- D.C. Faircloth, S. Lawrie, *N. J. Phys.* **20**, 025007 (2018)
- D.C. Faircloth, J.W.G. Thomason, *Proceedings of EPAC 2006*, Edinburgh, Scotland, p. 1708 (2006)
- D.C. Faircloth, A. Falterford, J. Pozimski, et al., *AIP Conf. Proc.* **925**, 71 (2007)
- P. Franzen, H.D. Falter, U. Fantz, et al., *Nucl. Fusion* **47**, 264 (2007)
- M. Fröschle, R. Riedl, H. Falter, et al., *Fusion Eng. Des.* **84**, 788 (2009)
- J.J.C. Geerlings, P.W. van Amersfoort, L.F. Kwakman, et al., *Surf. Sci.* **157**, 151 (1985)
- W.G. Graham, *Phys. Lett.* **73A**, 186 (1979)
- J. Greer, M. Seidl, *AIP Conf. Proc.* **111**, 220 (1984)
- M. Hanada, T. Inoue, H. Kojima, et al., *Rev. Sci. Instrum.* **61**, 499 (1990)
- J. Hiskes, *J. Appl. Phys.* **47**, 3888 (1976)
- J. Hiskes, *J. Phys. (Paris)* **40**, c7–c179 (1979)
- J. Hiskes, P.J. Schneider, *Phys. Rev* **B23**, 949 (1981)
- A.J.T. Holmes, *Plasma Phys. Control. Fusion* **34**, 653 (1992)
- Z.D. Hurych, P. Soukiassian, M.H. Bakshi, et al., *Phys. Rev. B* **38**, 8002 (1988)
- J.D. Isenberg, H.J. Kwon, M. Seidl, *AIP Conf. Proc.* **287**, 38 (1992)
- A.A. Ivanov, G. Abdrashitov, V. Anashin, et al., *AIP Conf. Proc.* **1515**, 197 (2013)
- M. Kashiwagi, T. Morishita, Y. Okumura, et al., *Rev. Sci. Instrum.* **73**, 964 (2002)
- H.M. Katsch, K. Wiesemann, *AIP Conf. Proc.* **111**, 254 (1984)
- R. Keller, D. Cheng, R. DiGennaro, et al., *Rev. Sci. Instrum.* **73**, 914 (2002)
- M.E. Kishinevskii, *Zhurnal Tekhn. Fiziki*, **45**, 1281 (1975) - in Russian; translated in *Sov. Phys. Tech. Phys.* **20**, 799 (1975)
- T. Kuo, D. Yuan, K. Jayamanna, et al., *Rev. Sci. Instrum.* **67**, 1314 (1996)
- Kuo T., R. Baartman, G. Dutto et al., *Proceedings of the 15th International Conference on Cyclotrons and their Applications, Caen, France*, p. 381 (1998)
- B.S. Lee, M. Seidl, *Appl. Phys. Lett.* **61**, 2857 (1992)
- M.A. Leitner, R.A. Gough, K.N. Leung, et al., *Rev. Sci. Instrum.* **69**, 962 (1998)
- K.N. Leung, M. Bacal, *Rev. Sci. Instrum.* **55**, 338 (1984)
- K.N. Leung, K.W. Ehlers, *Rev. Sci. Instrum.* **53**, 803 (1982)
- K.N. Leung, K.W. Ehlers, M. Bacal, *Rev. Sci. Instrum.* **54**, 56 (1983)
- K.N. Leung, G. DeVries, W. DiVergilio, et al., *Rev. Sci. Instrum.* **62**, 100 (1991)
- K.N. Leung, D.A. Bachman, D. McDonald, *Rev. Sci. Instrum.* **64**, 970 (1993)
- J.L. Lopes, J.A. Greer, M. Seidl, *J. Appl. Phys.* **60**, 17 (1986)
- S.T. Melnychuk, M. Seidl, *J. Vac. Sci. Technol.* **A9**, 1650 (1991)
- N. Miyamoto, Y. Fujiwara, K. Miyamoto, Y. Okumura, *Rev. Sci. Instrum.* **71**, 738 (2000)
- D.P. Moehs, *Studies on a magnetron source*. *AIP Conf. Proc.* **639**, 115 (2002)
- D.P. Moehs, J. Peters, J. Sherman, *IEEE Trans. Plasma Sci.* **33**(6), 1786 (2002)
- T. Morishita, M. Kashiwagi, M. Hanada, Y. Okumura, et al., *Jpn. J. Appl. Phys.* **40**, 4709 (2001)
- Y. Oka, Y. Takeiri, Y. Belchenko, et al., *Rev. Sci. Instrum.* **71**, 1379 (2000)
- Y. Okumura, M. Hanada, T. Inoue, et al., *AIP Conf. Proc.* **210**, 169 (1990)
- T. Okuyama, Y. Mori, *Rev. Sci. Instrum.* **63**, 2711 (1992)
- C.A. Papageorgopoulos, J.M. Chen, *Surf. Sci.* **39**, 283–312 (1973)
- C.A. Pargellis, M. Seidl, *Phys. Rev. B* **25**, 4356 (1982)

- J. Peters, *Rev. Sci. Instrum.* **65**, 1237 (1994)
- J. Peters, *Proceedings of 19th International Conference, Linac'98, Chicago, USA, August 23–28, 1998*, p. 1031 (1998)
- J. Peters, *Rev. Sci. Instrum.* **71**, 1069 (2000)
- J. Peters, *AIP Conf. Proc.* **1097**, 236 (2009)
- B. Piosczyk, G. Dammertz, *Rev. Sci. Instrum.* **57**, 840 (1986)
- K. Prelec, T. Sluyters, *IEEE Trans. Nucl. Sci.* **NS-22**, 1662 (1975)
- B. Rasser, J.N.M. van Wunnik, J.H. Los, *Surf. Sci.* **118**, 697–710 (1982)
- K. Saadatmand, G. Arbique, J. Hebert, et al., *Rev. Sci. Instrum.* **66**, 3438 (1995)
- K. Saadatmand, G. Arbique, J. Hebert, et al., *Rev. Sci. Instrum.* **67**, 1318 (1996)
- C.W. Schmidt, *Proceedings of LINAC90, Albuquerque, New Mexico, September 10–14, 1990*, 259–263 (1990)
- C.W. Schmidt, C.D. Curtis, *IEEE Trans. Nucl. Sci.* **NS-26**, 4120 (1979)
- P.J. Schneider, K.H. Berkner, W.G. Graham, et al., *Phys. Rev. B* **23**, 941 (1981)
- D. Schrage, L. Young, B. Campbell, et al., *Nucl. Inst. Methods Phys. Res. B* **40**, 949 (1989)
- M. Seidl, A. Pargellis, *Phys. Rev. B* **26**, 1 (1982)
- M. Seidl, W.E. Carr, J.L. Lopes, et al., *AIP Conf. Proc.* **158**, 432 (1987)
- M. Seidl, S.T. Melnychuk, S.W. Lee, W.E. Carr, *AIP Conf. Proc.* **210**, 30 (1990)
- M. Seidl, H.L. Cui, J.D. Isenberg, et al., *J. Appl. Phys.* **79**, 2896 (1996)
- G. Serianni, P. Agostinetti, V. Antoni, et al., *Plasma Fusion Res.* **11**, 2402119 (2016)
- J.D. Sherman, N.V. Smith, C. Geisik, P. Allison, *Conference Record of the 1991 IEEE Particle Accelerator Conference*, 1991, 4, 2080 (1991)
- R. Sidlow, N.D. West, *Proc. EPAC* **92**, 1005 (1992)
- H.V. Smith, P. Allison, *IEEE Trans. Nucl. Sci.* **NS-26**, 4006 (1979)
- H.V. Smith, P. Allison, R. Keller, *AIP Conf. Proc.* **158**, 181 (1987)
- H.V. Smith, P. Allison, E.J. Pitcher, et al., *Rev. Sci. Instrum.* **61**, 424 (1990)
- V.H. Smith Jr., P. Allison, J.D. Schneider, K. Saadatmand, *Rev. Sci. Instrum.* **62**, 2307 (1991)
- M.P. Stockli, arXiv:1404.0943 [physics.acc-ph] (2012)
- M.P. Stockli, B. Han, S.N. Murray, et al., *Rev. Sci. Instrum.* **87**, 02B140 (2016)
- E. Taglauer, Chapter in *Nucl. Fusion*, Special issue “Data Compendium for Plasma-Surface Interaction,” p. 117 (1984)
- A. Takagi, Y. Mori, K. Ikegami, S. Fukumoto, *IEEE Trans Nucl. Sci.* **NS-32**, No. 5, 1782 (1985)
- Y. Takeiri, O. Kaneko, K. Tsumori, Y. Oka, et al., *Nucl. Fusion* **46**, 199 (2006)
- R. Thomae, R. Gough, R. Keller, et al., *Rev. Sci. Instrum.* **71**, 1213 (2000)
- G.S. Tompa, W.E. Carr, M. Seidl, *Appl. Phys. Lett.* **48**, 1048 (1986)
- A. Ueno, Y. Namekawa, S. Yamazaki, et al., *AIP Conf. Proc.* **1515**, 331 (2013)
- P.W. van Amersfoort, J.J.C. Geerlings, L.F.T. Kwakman, et al., *J. Appl. Phys.* **58**, 3566 (1985)
- P.W. van Amersfoort, J.J.C. Geerlings, R. Rodink, et al., *J. Appl. Phys.* **59**, 241 (1986)
- C.F.A. van Os, P.W. van Amersfoort, *Appl. Phys. Lett.* **50**, 662 (1987)
- J.N.M. van Wunnik, J.J.C. Geerlings, E.H.A. Granneman, J.H. Los, *Surf. Sci.* **131**, 17–33 (1983)
- M. Wada, *Thin Solid Films* **316**, 128 (1998)
- M. Wada, *Rev. Sci. Instrum.* **89**, 052103 (2018)
- M. Wada, K.H. Berkner, R.V. Pyle, J.W. Steams, *J. Vac. Sci. Technol. A* **1**, 981 (1983)
- M. Wada, R.V. Pyle, J.W. Steams, *J. Appl. Phys.* **67**, 6334 (1990)
- R. Waltner, K.N. Leung, W.B. Kunkel, *J. Appl. Phys.* **64**, 3424 (1988)
- A. Wengrow, M. Leitner, K.N. Leung, et al., *Rev. Sci. Instrum.* **69**, 989 (1998)
- C. Wimmer, U. Fantz, *AIP Conf. Proc.* **1655**, 040004 (2015)
- D. Wunderlich, C. Wimmer, R. Riedl, et al., *Nucl. Fusion* **61**, 096023 (2021)
- R.L. York, R.R. Stevens Jr., *IEEE Trans. Nucl. Sci.* **30**, 2705 (1983)
- M. Yoshida, M. Hanada, A. Kojima, et al., *Rev. Sci. Instrum.* **87**, 02B144 (2016)
- M.L. Yu, *Proceedings of the symposium on production and neutralization of negative hydrogen ions and beams*, Upton, New York, BNL-50727, p. 48 (1977)
- M.L. Yu, *Phys. Rev. Lett.* **40**, 574 (1978)

Chapter 15

Hydrogen Negative Ion Density Diagnostic in Plasma



Marthe Bacal  and Motoi Wada

Abstract H^- and D^- densities were measured in low-pressure plasmas by Langmuir probe-assisted photodetachment and cavity ring-down spectroscopy (CRDS) to confirm the results obtained with Langmuir probes. The choice of the laser photon energy and the laser beam diameter is discussed. These diagnostic techniques were used for studying the influence of different metallic surface materials on the volume production of H^- ions.

Keywords Negative ion density · Photodetachment · Laser beam diameter · Cavity ring-down · Electron detachment · Volume production · Laser pulse energy

15.1 Introduction

Due to the low electron affinity of hydrogen atoms, $E_A = 0.745$ eV, the cross-section for photodetachment of the H^- ion is large: it peaks at 4×10^{-17} cm² near the infrared wavelength region. The choice of the laser is related to the negative ion species present in the plasma to be studied. A simple situation occurs in the hydrogen plasma containing a single negative ion species. Other negative ions (OH^- , O^- , O_2^-) may be present as impurities and their effect should be analyzed.

The laser wavelength is chosen to take advantage of the highest cross section for the photodetachment of the principal ion species. In the case of the H^- ion a Nd-YAG laser is suitable for photodetachment experiments, since its photon energy, 1.2 eV, is sufficient to detach electrons from H^- , but too low to interact with

M. Bacal
University Pierre and Marie Curie, Laboratory of Plasma Physics, Ecole Polytechnique, Paris, France

M. Wada (✉)
Doshisha University, Kyoto, Japan
e-mail: mwada@mail.doshisha.ac.jp

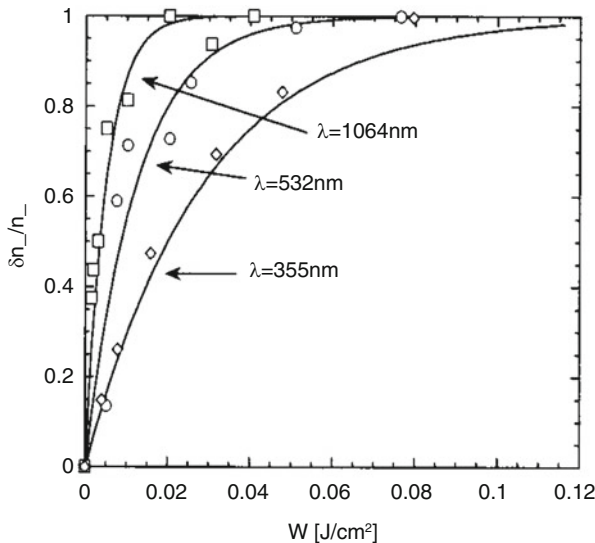


Fig. 15.1 Theoretical variations of $\Delta n_-/n_-$ against laser pulse energies at different wavelengths from Eq. 15.1 are compared with experimental results. (Reproduced from Nishiura et al. (1998), Fig. 7)

the plasma by other processes such as photoionization. At this photon energy, the photodetachment cross section σ_{ph} is near its maximum of $4 \times 10^{-17} \text{ cm}^2$ at 1.6 eV. The identity of the dominant negative ion species should be verified by checking that the photodetachment measurements agree with the theoretical photodetachment fraction, $\Delta n_-/n_-$, calculated using the cross section for photodetachment σ_{ph} of H^- ions (Bacal and Hamilton 1979) given by:

$$\frac{\Delta n_-}{n_-} = 1 - \exp\left(-\frac{\epsilon}{S\sigma_{ph}h\nu}\right) \quad (15.1)$$

Here n_- is the negative ion density, Δn_- is the negative ion density reduction as a result of photodetachment, ϵ is the laser energy, S is the laser cross-sectional area, h is the Planck constant and ν is the laser light frequency. According to the equation, the ratio $\Delta n_-/n_-$ saturates at different laser pulse energy depending on the laser wavelength. This can be seen in Fig. 15.1 (Nishiura et al. 1998) where the theoretical variations of $\Delta n_-/n_-$ against laser pulse energies at different wavelengths from Eq. 15.1 are compared with experimental results.

The fundamental wavelength of the Nd-YAG laser and its second and third harmonics (1064, 532, and 355 nm) were used in this experiment. The maximum photon energy is about three times higher than the minimum energy. Note that the necessary laser pulse energy per unit area for saturation increases with photon energy, e.g., 20 mJ/cm^2 at 1.2 eV (1064 nm), 60 mJ/cm^2 at 2.4 eV (532 nm), and 120 mJ/cm^2 at 3.6 eV (355 nm). The minimum energy photons should be used in

determining n_-/n_e (see Eq. 15.2), because this will avoid unwanted effects on the wall surfaces. Such difficulties were described by Bacal et al. (1979), where a ruby laser was used (photon energy 1.8 eV) and the laser beam was absorbed by the chamber walls. In the experiment of Nishiura et al. (1998) the laser beam leaves the chamber through a window, before its absorption in the power meter.

Nishiura et al. showed that when the laser pulse energy is suitably chosen for each wavelength, the wavelength had no effect on the value obtained for n_-/n_e . The Nd:YAG laser at 1064 nm provides photons of 1.2 eV and is suitable for detaching the electron from the hydrogen negative ion. Only a very modest laser pulse energy density (20 mJ/cm^2) is necessary to reach saturation, i.e., to convert all the H^- ions on its path in the plasma into photoelectrons and photoatoms. In addition, the Nd-YAG laser is capable of generating very high power, e.g., Joules per ns. The photodetachment process can be completed on a time interval that is short in comparison with the time scale of the dynamic evolution of the photoparticle densities (Bacal 2000).

15.2 Measurement of the Negative Ion Density in Plasma by Langmuir Probe-Assisted Photodetachment

Since one photoparticle of each species is released per negative ion, it follows that the “instantaneous” photoparticle densities are a direct measure of the negative ion density. In diagnostic terms, the photoparticles serve as optical “tags” of their negative ion parents. The simplest technique for measuring “tag” photoelectron densities is the use of the Langmuir probe biased at electron saturation potential, i.e., with a large positive potential relative to the plasma potential. Prior to the laser pulse the probe current, $i_e(\text{dc})$, is proportional to the background plasma electron density, n_e . The laser pulse causes an instantaneous increase of the electron density, which enhances the current drawn by the probe by a corresponding instantaneous amount Δi_e , proportional to Δn_e . A simple way to isolate and extract the current pulse is via an output capacitor.

Since the same probe is used and the laser energy is sufficient to destroy all the negative ions, the ratio $\Delta i_e/i_e(\text{dc})$ gives directly $\Delta n_e/n_e$. When the probe lies inside the laser beam and assuming that Δn_e is only due to an increase in the electron density associated with photodetachment of negative ions of density n_- , i.e., $\Delta n_e = n_-$, it follows that

$$\frac{n_-}{n_e} = \frac{\Delta i_e}{i_e(\text{dc})} \quad (15.2)$$

Namely, the ratio is equal to the local ratio of negative-ion density n_- to the background electron density n_e . Since the latter can be measured by obtaining the Langmuir probe current-voltage characteristic, the absolute value of n_- can be obtained.

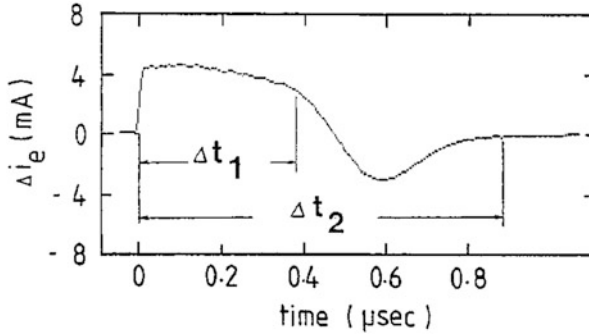


Fig. 15.2 Typical photodetachment signal collected by the positively biased cylindrical probe, located on the axis of the laser beam. (Reprinted from Devynck et al. (1989), Fig. 2)

A typical Langmuir probe signal from the output capacitor is shown on Fig. 15.2. Here, the probe trace is reversed (electrons are flowing into the probe tip) and the voltage drop is converted to a current rise. In this case the probe is on the axis of the laser beam, having a diameter of 0.6 cm. At the time of the laser pulse a sharp increase in current takes place (typically 20 ns).

As displayed in Fig. 15.2, following the current rise, the excess probe current remains nearly constant (actually decays slowly) for a few hundred ns, indicating that the excess electron density remains high for a time that is long with respect to the transit time of electrons across the probe sheet (a few ns). This can be explained by the overall dynamics of the perturbed plasma within the laser beam (Stern et al. 1990). Specifically, the excess electrons can flow out of the laser beam faster than the negative ions can flow into the laser beam on a time scale faster than the residual positive ion density can change. The net electrostatic charge and the produced self-consistent field allows the excess electron density to oscillate around its mean value and damped. (This phenomenon is an exhibition of “monopolar” diffusion, a counterpart of the better-known ambipolar diffusion which takes place in normal positive-ion plasmas). This is discussed by Stern et al. (1990). It should be noted that the photodetached electrons are instantaneously generated with a non-Maxwellian distribution and have a different temperature from that of the background plasma electrons. The Maxwellianization or thermalization time is reasonably fast (10 ns), so the dynamics of the charged particles can be modeled using a single temperature description for the electrons.

However, the complete physical picture must also consider the response of the background plasma to the electron density pulse, Δn_e (Friedland et al. 1993). Such pulses can, in general, excite time-dependent changes in the net charge density and potential in the plasma (plasma oscillations). In addition to perturbing the sheath, the impulsive net charge density changes can induce capacitively pickup potential changes, ΔV_{cap} , in the probe. The corresponding current pulse in the probe circuit, denoted by ΔI_{cap} , will appear superposed on the conductive current pulse, ΔI_e . We designate $\Delta I = \Delta I_e + \Delta I_{cap}$. Figure 15.3 shows an example of a signal containing

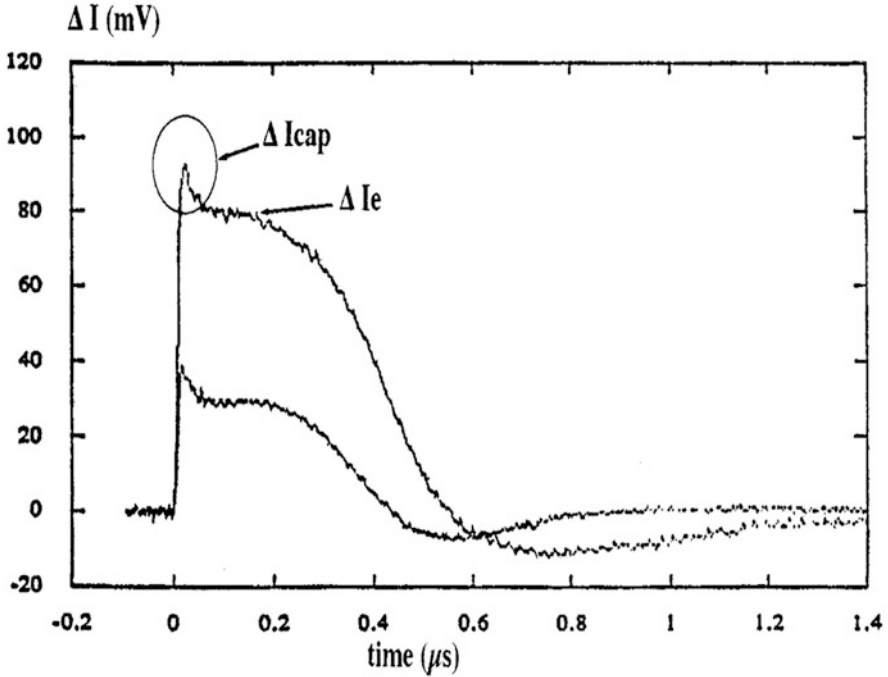


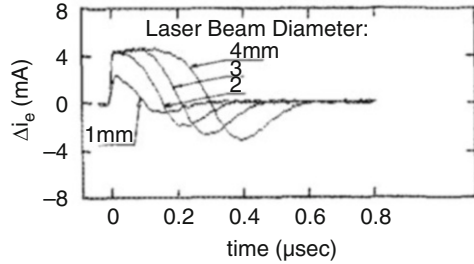
Fig. 15.3 Example of a photodetachment signal containing the superpositions of ΔI_e and ΔI_{cap} . Large volume hybrid source Camembert III, center of the extraction region. The two signals correspond to different values of the discharge current ~ 5 and 10 A. (Reproduced from Bacal (2000), Fig. 32)

the superposition of ΔI_e and ΔI_{cap} . Since ΔI_{cap} is proportional to the rate of change of the net charge density and to the capacitance of the probe, rather than directly to n_e , estimates and corrections for this effect are needed, especially in high-density plasmas or under strongly nonequilibrium conditions characteristic of the extraction zone. These effects can modify the simple linear relationship between the probe-current pulse and the negative ion density given by Eq. (15.2).

It is necessary to know the region from which the probe drains its current after the laser shot. It was shown by Bacal et al. (1981) that there is a lower limit to the laser-beam diameter to be used, in order to measure correctly the negative-ion density by photodetachment. When the laser-beam diameter is below this value, both the amplitude and the duration of the probe signal collected after the laser shot increase with the laser-beam diameter. When the beam diameter is above this value, only the duration of the signal increases with the laser beam diameter, but its amplitude remains constant. Bacal et al. (1981) showed that this minimum value of the beam diameter depends on the probe bias and on the electron density and temperature.

Figure 15.4 illustrates the relationship between the pulse shape and the laser-beam diameter. In this figure are plotted the probe current pulse shapes for laser-

Fig. 15.4 Probe current pulse shapes for laser beam diameters of 1, 2, 3, and 4 mm, in a 3-mTorr, 50-V, 5-A hydrogen discharge. Probe bias: +20 V. (Reproduced from Devynck et al. (1989), Fig. 2)



beam diameters of 1, 2, 3, and 4 mm, in a 3-mTorr, 50-V, 5-A hydrogen discharge. Probe was biased at +20 V with respect to the ion source chamber wall. Note that with a beam diameter of 1 mm the signal amplitude after the laser pulse is lower than that observed with beams of 2, 3, and 4 mm. For laser-beam diameters above 2 mm the current pulse amplitude stays approximately constant. Thus, in this particular example, the beam diameter of 2 mm appears to be the smallest that can be used for the correct measurement of the negative-ion density.

When the laser-beam diameter is larger than 2 mm and the laser pulse energy is sufficient to destroy all the H^- ions in the illuminated region, the relative negative ion density can be determined from the ratio of fast initial probe current rise Δi_e to the steady-state current to the probe, $i_e(dc)$, as Eq. (15.2). It can also be seen in Fig. 15.4 that the duration of the plateau Δt_1 as well as the total duration Δt_2 of the current pulse (see Fig. 15.2) increase in proportion to the laser-beam diameter. Δt_1 is the time delay between the sharp current rise and the first floating potential; Δt_2 is the time delay between the sharp current rise and the time the probe current recovers the original $i_e(dc)$.

15.3 Measurement of the Negative Ion Density in Plasma by Cavity Ring-Down Spectroscopy (CRDS)

In high power operation of the ion source plasma it often becomes impossible to insert a Langmuir probe to measure the H^- ion density with the photodetachment method. Another method based on photodetachment reaction but without inserting a probe into a dense plasma is utilized in ion source development for fusion program. The cavity ring-down (CRD) method is an enhanced laser-absorption-spectroscopy with high sensitivity to measure line-integrated density (O'Keefe and Deacon 1988). It basically consists of a pulsed laser, an optical ring cavity with two highly reflective mirrors installed both sides of absorber, an optical detector, and a data acquisition system (Fig. 15.5).

The principle of the CRD method is as follows: a single laser pulse is injected from one side of the cavity. The laser intensity gradually weakens by passing through the cavity due to photons reacting with the absorber and passing through

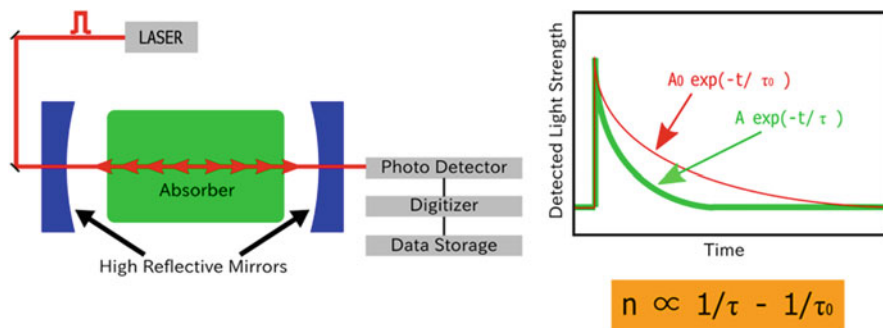


Fig. 15.5 Principle of cavity ring-down (CRD) technique. (Reproduced from Nakano et al. (2015), Fig. 6, with permission of H. Nakano)

both mirrors. The laser pulse arriving at the other side of the cavity is recorded by a detector, which transmits it to the data acquisition system. The signal forms the exponential decay curve (ring-down signal). The ring-down signals are measured without and with the absorber. The absorber density is evaluated by comparing the decay times without and with the absorber.

The H^- density is determined by comparing the photodetachment current profile in the direction of the laser beam to the result from cavity ring-down, which gives the line-averaged H^- density:

$$k_{pd} \cdot \int \Delta I \cdot dx = n_{CRD} \cdot L \quad (15.3)$$

where k_{pd} is the correction coefficient which associates the negative ion density and the photodetachment current, I_{pd} , n_{CRD} is the line-averaged density of negative ions, and L is the length applied to calculate the negative ion density in CRD measurement.

15.4 Negative Ion Source Study with Photodetachment Method

The measurement by photodetachment of the negative ion density versus gas pressure in the volume multicusp source CAMEMBERT III showed that this density was maximum at a pressure of 3 mTorr and attained 10^{10} cm^{-3} at a discharge power of 50 V, 70 A (Courteille et al. 1995). Aleiferis et al. investigated hydrogen negative ion density in the negative ion source PROMETHEUS 1 by laser-induced photodetachment method. In this source, the plasma is sustained by five electron cyclotron resonance (ECR) sources with permanent magnets (Aleiferis et al. 2017). Briefly, a laser beam (6 mm in diameter) was coaxially aligned with the short

leg of the L-bent probe. The beam is produced by a Nd:YAG laser (Quantel Brilliant Eazy, 330 mJ/pulse; pulse width 5 ns). Its power density is adjusted at about 70 mJ/cm^2 . This ensures electron detachment from all the H^- ions in the irradiated region. The probe is positively biased at +15 V, i.e., about 8 V above the plasma potential, ensuring the collection of all the photodetached electrons. The current impulse of the photodetached electrons is monitored on a digital oscilloscope (LeCroy WaveSurfer 104Xs-A; 1 GHz/5 GSamples/s) by means of wide band current transformer (Pearson electronics 6585) avoiding thus the need for any passive or active electronic circuitry.

Ellis et al. (2020) studied using laser photodetachment the influence of different metallic surface materials on the volume production of H^- ions. The H^- density was measured above a thin disc of either tungsten, stainless steel, copper, aluminum, or molybdenum placed onto the lower grounded electrode of the plasma device, as a function of gas pressure and applied rf power.

Results obtained by cavity ring-down spectroscopy in the vicinity of the plasma grid in the negative ion source of the Large Helical Device (LHD, National Institute of Fusion Science, Japan), were presented by Ikeda et al. (2011). In a Cs seeded plasma proportionality relations were observed between the arc power of the discharge and the negative hydrogen ion density, and between the negative hydrogen ion density and the extracted beam current. They considered that this showed that the CRD system worked well.

Geng et al. (2015) studied by photodetachment the 1/3 scaled negative ion source of the LHD-NBI system. In this study, the Langmuir probe was used to measure the local density injecting a laser in the source extraction region, close to the plasma electrode. The typical photodetachment signal shows a large, sharp spike, representing the capacitive component of the signal, followed by a plateau. (The sharp spike is more than two times larger than the plateau). They indicate that they adopted the conductive component of the signal only, i.e., the plateau, for the calculation of the negative ion density.

In the negative ion sources for NBI, Cs vapor is introduced to increase the negative ion current and to reduce the co-extracted electron current. This leads to the reduction of the electron density to a value below that of the negative ion density in the vicinity of the PG. In such a negative ion rich plasma with Cs (Elizarov et al. 1995), the estimation of negative ion density by photodetachment using electron saturation current is not correct. Therefore, the density of negative ions should be corrected with the aid of other diagnostic methods such as the line-averaged density of negative ions obtained with cavity ring-down (CRD) measurement.

In the study of Masaki et al. (2020) local densities of H^- ions and D^- ions near the PG are measured by photodetachment. The photodetachment technique with an electrostatic probe is applied to measure the local negative ion density, as described by Bacal (2000). One-dimensional density distributions of H^- and D^- ions were measured at different distances of 9 mm and 21 mm from the PG surface; the moving direction is arranged parallel to the line of sight (LoS) of CRD to obtain the correction coefficient of the photodetachment Langmuir probe.

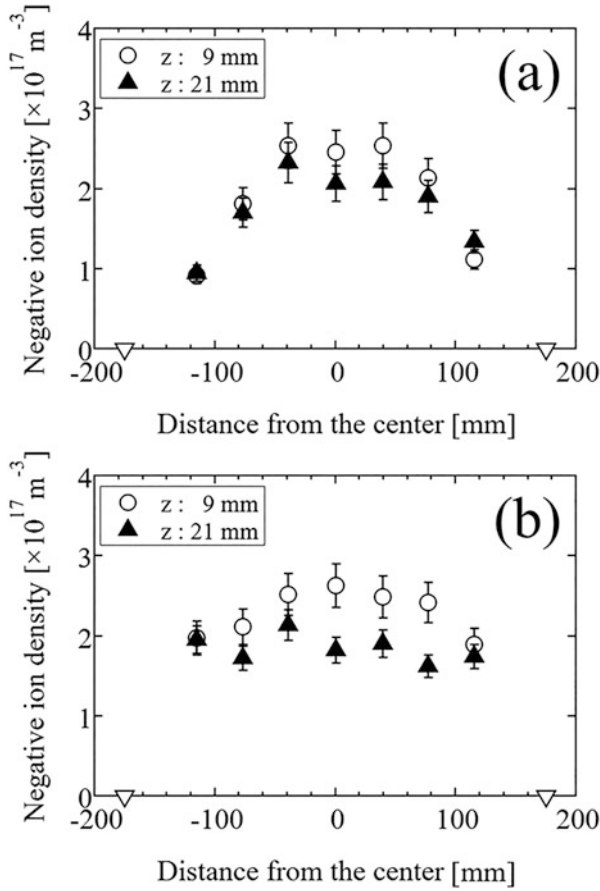


Fig. 15.6 X-profile of the negative ion density measured in (a) hydrogen and (b) deuterium. (Reproduced from Masaki et al. (2020), Fig. 4, with permission of the AIP Publishing)

Figure 15.6a displays the x-profile of the negative hydrogen ion density while Fig. 15.6b displays the x-profile (parallel to the PG surface) of the negative deuterium ion density. The open circle and full triangle marks indicate 9 mm and 21 mm distant from the PG plane facing source plasma, respectively. All plots were obtained in 50 ± 2.5 kW arc power and constant PG temperature. Note that the signal at the edge of the ion source, 175 mm from the center, is assumed as 0 and indicated by the open inverted triangles. The absolute value of the density was calculated from the line-averaged density and line-integrated photodetachment current (see Eq. 15.3). Compared with the density distribution of H^- ions, the D^- ion density distribution presents similar maximum values as the H^- ion density distribution while indicating flatter profiles within 115 mm from the ion source center.

15.5 Conclusion

The existence of two diagnostic methods for measuring the hydrogen negative ion density in ion sources provides the possibility to measure local densities of H^- and D^- ions by Langmuir probe-assisted photodetachment. While their density values can be calibrated by cavity ring-down spectroscopy. Through coupling these measurement techniques, the performance of large ion sources should be improved.

Acknowledgments The authors acknowledge the enlightening comments of Professor Y. Takeiri. One of the authors (M. Wada) acknowledges the support of the Collaboration Research Program at the National Institute of Fusion Science.

References

- S. Aleiferis, J. Laulainen, P. Svarnas, O. Tarvainen, M. Bacal, S. Bechu, AIP Conf. Proc. **1869**, 030045 (2017)
- M. Bacal, Rev. Sci. Instrum. **71**, 3981 (2000)
- M. Bacal, G.W. Hamilton, Phys. Rev. Lett. **42**, 1538 (1979)
- M. Bacal, G.W. Hamilton, A.M. Bruneteau, H.J. Doucet, J. Taillet, Rev. Sci. Instrum. **50**, 719 (1979)
- M. Bacal, A.M. Bruneteau, M. Nachman, J. Phys. Lett. (Paris) **42**, L-5 (1981)
- C. Courteille, A.M. Bruneteau, M. Bacal, Rev. Sci. Instrum. **66**, 2533 (1995)
- P. Devynck, J. Auvray, M. Bacal, P. Berlemont, R. Leroy, R.A. Stern, Rev. Sci. Instrum. **60**, 2873 (1989)
- L.I. Elizarov, F. El Balghiti, M. Bacal, Rev. Sci. Instrum. **66**, 4925 (1995)
- J. Ellis, J. Branson, K. Niemi, E. Wagenaars, T. Gans, J. Phys. D. Appl. Phys. **53**, 485202 (2020)
- L. Friedland, C. Ciubotariu, M. Bacal, Phys. Rev. E **49**, 4353 (1993)
- S. Geng, K. Tsumori, H. Nakano, et al., AIP Conf. Proc. **1655**, 040014 (2015) Fourth International Symp. on Negative Ions, Beams and Sources (NIBS 2014)
- K. Ikeda, et al., AIP Conf. Proc. **1390**, 367 (2011)
- S. Masaki, H. Nakano, M. Kasaki, et al., Rev. Sci. Instrum. **91**, 013512 (2020)
- H. Nakano, K. Tsumori, M. Shibuya, a S. Geng, M. Kasaki, K. Ikeda, K. Nagaoka, 17th International Symposium on Laser Aided Plasma Diagnostics, Sapporo, p. 1, 2015
- M. Nishiura, M. Sasao, M. Bacal, Rev. Sci. Instrum. **83**, 2944 (1998)
- A. O'Keefe, D.A.G. Deacon, Rev. Sci. Instrum. **59**, 2544 (1988)
- R.A. Stern, P. Devynck, M. Bacal, P. Berlemont, F. Hillion, Phys. Rev. A **41**(6), 3307 (1990)

Chapter 16

RF-Driven Ion Sources for Neutral Beam Injectors for Fusion Devices



Ursel Fantz

Abstract Inductively coupled plasma sources at a frequency of 1 MHz and at power levels of up to 100 kW per cylindrically shaped plasma generation chamber (driver) are used for neutral beam injection (NBI) systems of fusion devices. The modular concept, having several drivers for plasma generation arranged at the backplate of a large expansion chamber, is the baseline for the NBI systems of the international fusion experiment ITER. The reliability in terms of operation and the proven technology of an RF-driven ion source demonstrated for positive hydrogen ions and initiated a development line with size-scaling for negative ions (hydrogen and deuterium) being mandatory for ITER NBI. The cornerstones of the development route toward the ion source of an area of $1\text{ m} \times 2\text{ m}$ to illuminate with a uniform plasma the multi-aperture extraction system and the generation of negative hydrogen ion densities in the order of 300 A/m^2 are described. Addressed are the RF-coupling scheme, reliable operation at low pressure (0.3 Pa for ITER), and the plasma parameters achieved in the ion source. Another building block is the interplay of the magnetic filter field with the biasing of surfaces, the consequences on the plasma uniformity, and in particular, the consequences on the reduction and uniformity of the inevitable co-extracted electrons in such large sources. The cesium coverage of the plasma grid surface, where the negative ions are formed, and the role of cesium redistribution in the ion source come along with the temporal stability of the co-extracted electrons which react, due to the presence of a plasma dominated by negative and positive ions (ion–ion plasma) in front of the plasma grid, much more sensitive than the negative ion current. Of particular challenge is the achievement of high negative ion current densities in long pulses, meaning steady-state operation up to 1 h. The limitation originates from the strong temporal dynamics of the co-extracted electrons as their heat load on the extraction grid reaches the tolerable value, with the consequence that the ion source parameters like RF-power and extraction voltage need to be reduced to avoid damages of the grid system. For

U. Fantz (✉)
Max-Planck-Institut für Plasmaphysik, Garching, Germany
e-mail: ursel.fantz@ipp.mpg.de

a general reduction, the interplay of magnetic filter field and biasing of surfaces is important, whereas cesium management is of utmost relevance for the temporal stabilization. Finally, the activities in the development of the RF-driven ion source for fusion devices beyond ITER, like a DEMONstration power plant, are addressed as well.

Keywords RF-driven ion source · Inductively coupled plasma · Negative hydrogen ions · Neutral beam injection · ITER NBI

16.1 Introduction

From the very first usage of powerful radio frequency (RF)-driven ion sources to generate positive hydrogen ions for neutral beam injection (NBI) systems of fusion devices (Speth et al. 1999), a very strong development started for their application to NBI systems based on negative hydrogen ions. The motivation to change from the standard arc sources used commonly around the world (Ciric et al. 2007; Matsuda et al. 1987; Streibl et al. 2003) came from the reduced source maintenance as the regular exchange of filaments is omitted. While first attempts started with the development of negative hydrogen RF-driven sources based on the volume formation via the dissociative attachment process, the need of high current densities at low pressures focused the research toward the cesium seeding of the sources to boost the formation at surfaces covered with a low work function material. For both, the RF-driven source body has been extended by an expansion chamber and equipped with a magnetic filter field to facilitate the tandem filter source concept (Bacal 1989). Since the demonstration of the ion source parameters for the international fusion experiment ITER in the prototype source and first size scaling experiments (Speth et al. 2006), the RF-driven source became the ITER reference source for the heating beams and the diagnostic beam. As fast hydrogen atoms or deuterium atoms are injected for heating and current drive the ion sources need to operate in hydrogen and in deuterium, the diagnostic beam however is intended to deliver only hydrogen particles. The accelerated ions are neutralized in a gas target chamber before entering the fusion machine.

The international fusion experiment ITER (Holtkamp 2007; Claessens 2020, ITER 2020) will be equipped with two powerful neutral beam injection (NBI) beamlines for heating and current drive (power per beamline: up to 16.5 MW) with the option to add a third one in a later stage (Hemsworth et al. 2017). A diagnostic injector with low power (2.2 MW) will be required to diagnose the helium ash with charge exchange resonance spectroscopy (Chakraborty et al. 2010). These NBI systems are based on the generation of a low temperature, low pressure plasma, on electrostatic extraction and acceleration of negative hydrogen ions, followed by neutralization in a hydrogen gas target to inject fast neutral particles into the fusion

device. The particles shall have an energy of 870 keV and 1 MeV for hydrogen and deuterium, respectively, for the heating beams (HNB), whereas only hydrogen at 100 keV is foreseen for the diagnostic beam (DNB). The ion sources have to operate at a filling pressure of 0.3 Pa or below in order to keep stripping losses in the extractor and five-stage accelerator system of the HNBs below 30%. The requirements for the HNBs in terms of current extracted from one large ion source are very challenging, namely 57 A for 3600 s in deuterium operation and 66 A for 1000 s in hydrogen (corresponding to current densities of 286 A/m² and 329 A/m², respectively). The DNB should deliver 77 A in hydrogen (corresponding to 391 A/m²) for 3 s, square wave modulated at 5 Hz, then off for 20 s, repeating that sequence for >1000 s, or to operate for only 100 ms (unmodulated) every 1.4 s throughout the ITER pulse of up to 1 h. An extraction voltage of 9–10 kV is envisaged to achieve these parameters. The inevitable co-extracted electron current has to be kept below the ion current in order to avoid damages of the second grid of the extraction system, to which the electrons are deflected by embedded magnets. For a proper beam transport, the homogeneity of the accelerated beam, composed of 1280 beamlets, has to be better than 90% down to the scale of single beamlets. Additionally, the core of the accelerated beamlets (carrying $\approx 85\%$ of the power) needs to have a divergence of less than 7 mrad, while significantly higher divergences of 15–30 mrad are allowed for a halo carrying the remaining $\approx 15\%$ of the beamlet power (ITER 2002; Hemsworth et al. 2017).

The requirements for the operational parameters of the ion source and accelerator are very challenging and by far exceed those of the NBI systems based on negative ions (NNBI) at existing fusion devices JT-60U (Ikeda et al. 2006), JT-60SA (Hanada et al. 2011), and LHD (Takeiri et al. 2006). The ion sources at those systems are based on filament discharges (arc discharges) and are typically operating only for a few seconds at their nominal heating power. For reduced power, pulses of up to several tens of seconds have been demonstrated. In preparation for the NBI system of JT-60SA, pulses of up to 60 s have been obtained with an accelerated current density of 190 A/m² for a nine-aperture system (Kojima et al. 2017). For RF sources, ITER-relevant ion current densities have been demonstrated at smaller test facilities (Speth et al. 2006) for a beam duration of a few seconds.

Since the achievable current densities for negative hydrogen ions are about a factor of ten lower than for positive ions (Hemsworth and Inoue 2005), the ion sources are remarkable larger than for positive ions, reaching the size of a door. The source area used for the RF-driven positive ion-based NBI systems at the ASDEX Upgrade tokamak (AUG) is 31 cm \times 59 cm, one beamline comprising four sources with an extracted current density of 1594 A/m², generating 62 A of current accelerated to either 72 kV (hydrogen) or 93 kV (deuterium) (Streibl et al. 2003; Franzen et al. 2001). An ITER beamline is equipped with only one source of a source area of 1 m \times 2 m, with an extraction area of 0.2 m².

16.2 Modular Concept of the RF-Driven Ion Source

The modular concept is based on the RF-driven prototype source for negative ions in which the plasma is generated in one cylindrical driver by inductive coupling using an RF generator with a frequency of 1 MHz and maximum power of 100 kW (Speth et al. 2006). The cylinder, which is made of insulating material, usually quartz or alumina, is mounted on a rectangular expansion chamber facing the extraction system (Sect. 16.2.1). The size-scaling route toward the ITER source size follows the usage of multiple of those cylindrical drivers mounted on one large expansion chamber (Sect. 16.2.2). In order to reduce the number of RF generators, two RF drivers each are connected in series in such larger sources, requiring generators delivering up to 200 kW RF power. In principle, by adapting the size of the drivers (and also the shape, e.g., racetrack shape (Kraus et al. 2017), described in Sect. 16.5.2), their number and their arrangement in any area can be illuminated by the modular RF-driver concept operating best in the pressure range from 0.2 Pa to about a few Pa.

From the engineering aspects, one should keep in mind that the sources operate in steady state, which requires measures to control the temperature of the individual RF and source components for protecting them from overheating. On the other hand, the use of cesium imposes a temperature control of the chamber surfaces preferentially above the melting point of cesium (28.44 °C) to avoid cold spots and thus accumulation of cesium in the source chamber.

16.2.1 The Prototype Source

A schematic drawing of the prototype source as currently used at the test facility Batman upgrade (BUG; Fantz et al. 2019) with the RF circuit, the cesium oven and the extraction system are shown in Fig. 16.1.

The RF driver with an inner radius of about 12 cm and a length of about 17 cm is set up from a dielectric vessel (quartz or aluminum oxide) and a six-turn RF coil. A Faraday screen is inserted between the plasma and the dielectric in order to avoid plasma erosion by capacitive RF coupling. The RF power is supplied by a solid state-based generator of up to 75 kW. In order to minimize the reflected RF power, the plasma load impedance is tuned by an L-type matching network with variable vacuum capacitor to the 50 Ω of the generator output. For easy access, the RF generator is connected to ground potential whereas the source is on high negative potential. This requires the implementation of a DC insulating ferrite core transformer in the matching network.

From the driver, the plasma expands into the rectangular expansion chamber (32 cm width \times 58 cm height \times 20 cm depth) toward the first grid of the extraction system, the plasma grid (PG). Cesium is evaporated from a dedicated oven, which is located typically at the backplate of the source. The evaporation rate is in the

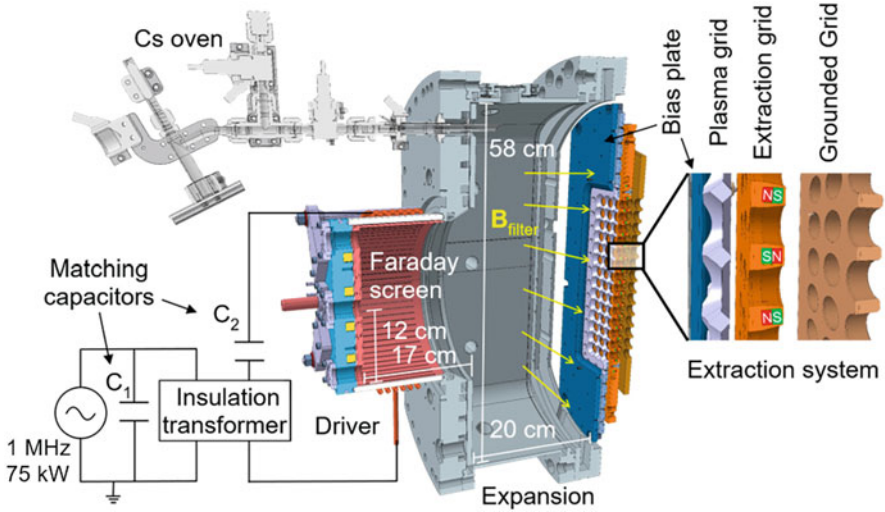


Fig. 16.1 Sketch of the prototype ion source at the test facility BUG with the Cs oven and the layout of the RF circuit. The zoom shows the extraction system consisting of three grids. The bias plate surrounding the beamlet group can be connected to the source walls or biased separately. (Figure adapted from Fantz et al. (2021))

order of 5 mg/h evaporating continuously during operation. Cesium redistributes between the pulses (vacuum phase, typically >3 min) by the elevated temperature of the source walls (around 40°C) and the grid surface, which is kept at around 150°C . During plasma pulses, the cesium redistribution is significantly enhanced by the plasma interaction. The negative ions are predominately formed at the grid surface by conversion of impinging atoms (Wunderlich et al. 2012). A magnetic “filter” field is created in front of the PG via a current of several kA flowing in vertical direction through the plasma grid. The field strength is typically a few mT. That field impedes the flow of fast electrons toward the PG, while allowing ions and neutrals, which are not magnetized, and, via collisions, the slower electrons flow through the field, hence the name “filter” field. The consequence is that the electron temperature of the plasma in front of the PG is significantly cooler than that of in the upstream plasma, which, results in a reduced destruction rate of the negative ions via electron collisions in that region. Also, it lowers the electron density in front of the PG, which reduces the amount of co-extracted electrons, and, unfortunately, it causes plasma drifts in the vertical direction. In addition, the PG current also creates a magnetic field in the extractor and accelerator, which must be controlled in order to ensure that the consequent deflection of the extracted ions is acceptable (see Sect. 16.2.4). The plasma facing side of the PG is partially covered by the bias plate (BP), which is in principle an extension of the source walls (Fig. 16.1) but can be biased separately (Sect. 16.4.2). The inner surfaces of the source and the water-cooled Faraday screen, all made of copper, are coated by molybdenum to reduce the self-sputtering of copper, which pollutes the cesium layer at the plasma grid and

to reduce the sputtering of the backstreaming positive ions created mainly, in this source, in the first gap of the extraction system.

The extraction system consists of three grids as indicated in Fig. 16.1: the plasma grid (PG) at source potential (to ≈ -45 kV at BUG) but can be biased against the source body (up to 60 V at BUG), the extraction grid (EG), and the grounded grid (GG, at ground potential). Permanent magnets are embedded in the EG, in order to deflect the co-extracted electrons out of the beam onto the EG surface at rather low energies; nevertheless, the created heat load limits the tolerable amount of co-extracted electrons. Besides local spots creating a heat load of up to 40 MW/m² around one extraction aperture, global vertical inhomogeneities are expected as well due to plasma drifts. The arrangement of the apertures mimics one beamlet group of the layout used in the ITER beam source.

The initial prototype source was developed and in operation for about two decades at the short pulse test facility BATMAN demonstrating the ITER parameters with respect to extracted current densities at the required filling pressure of 0.3 Pa for 10 s RF pulses with 4 s beams (Speth et al. 2006). The long pulse test facility MANITU was equipped also with the prototype source and demonstrated the first 3600 s beam extraction in hydrogen and in deuterium (Kraus et al. 2008). Both test facilities used the same grid system for extraction as the positive ion sources at AUG, the large area grid (LAG), and permanent magnets at the vertical sides inside the chamber to create a horizontal magnetic filter field (Speth et al. 2006). In order to facilitate an ITER-like grid system and an ITER-like magnetic filter field, which is created by the PG current, the test facility BATMAN has been upgraded to BUG being equipped with the steady state capable prototype source (Fantz et al. 2019). Independent on the pulse duration, the time between pulses is typically a few minutes at the test facilities without limitations toward longer periods.

16.2.2 Size Scaling

The size-scaling route from the 1/8 size-scale prototype source toward the ITER source following the modular concept is illustrated in Fig. 16.2. As an intermediate step, the half-size ITER source has been introduced and tested as a source scaling experiment without extraction first at the test facility RADI (Franzen et al. 2007) followed then by the ELISE test facility with beam extraction and acceleration of up to 60 kV (Heinemann et al. 2013).

Besides the size scaling of the source chamber, the arrangement of the apertures is extended as well: the ITER beam source consist of 16 beamlet groups with 16×5 apertures of 14 mm in diameter. The half-size source at ELISE is as close as possible to the ITER source representing the vertical half of it, which means that eight beamlet groups are surrounded by the bias plate (turquoise color in Fig. 16.2), whereas at the prototype source a beamlet group with 14×5 apertures is used in order to have an appropriate gas conductance. The ITER beam source is equipped with a six-stage grid system: the extraction stage, which is foreseen to

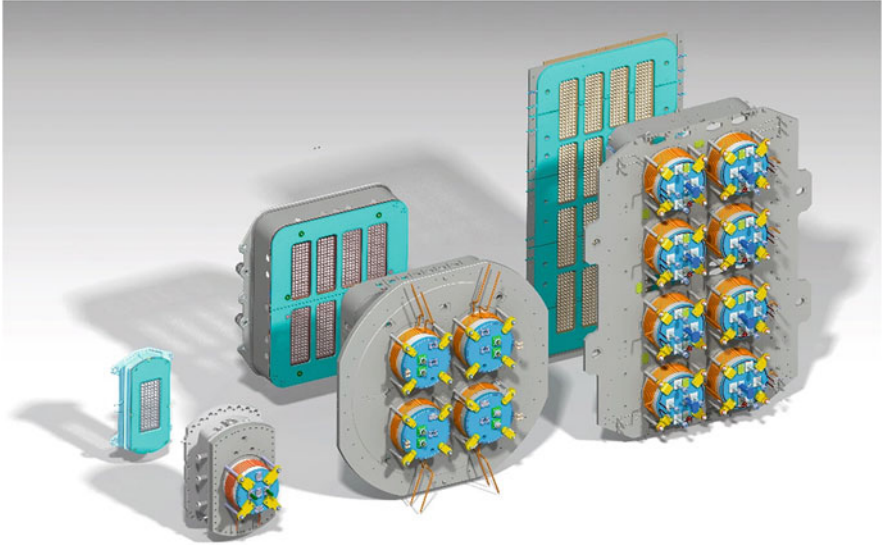


Fig. 16.2 Modular concept of the RF-driven ion source showing the size scaling from the prototype source (left) via the half-size ITER source (center) to the full ITER source (right), which has a source area of $1 \times 2 \text{ m}^2$

operate at 9 kV, is followed by five acceleration stages of 200 kV each (Hemsworth et al. 2017). Hence, the extraction system at the prototype source and at the half-size source, capable to reach total voltages of 45 kV and 60 kV, respectively, represent a kind of pre-acceleration stage of the ITER sources. The cesium supply is scaled as well, starting with one oven at the prototype source mounted at the backplate, toward two ovens at the half-size source mounted at the side walls toward three ovens mounted at the backplate of the ITER source, centered between the drivers. Following the modularity to be used on the ITER source, a horizontal pair of RF drivers is powered by one RF generator with a maximum output power of 200 kW.

To bridge the gap between the size-scaling experiments and the use of the ITER beam source at the heating and diagnostic beams, the Neutral Beam Test Facility (NBTF) was initiated by ITER hosted by Consorzio RFX (Toigo et al. 2017a). The NBTF comprises a test facility for the ITER ion source (SPIDER), which went into operation in 2018 (Toigo et al. 2021; Serianni et al. 2020). The second test facility that represents the full prototype of the HNB of ITER (MITICA) is currently planned to go into operation in 2024 (Boldrin et al. 2021). ITER-India is responsible for the DNB and is following a dedicated R&D roadmap, comprising an 1/8 ITER prototype source at the test facility ROBIN, which went into operation in 2011, and a two-driver source, the Twin source (Singh et al. 2019) to be followed by a test of the full size source and the DNB beamline components on the Indian Test Facility (Singh et al. 2011).

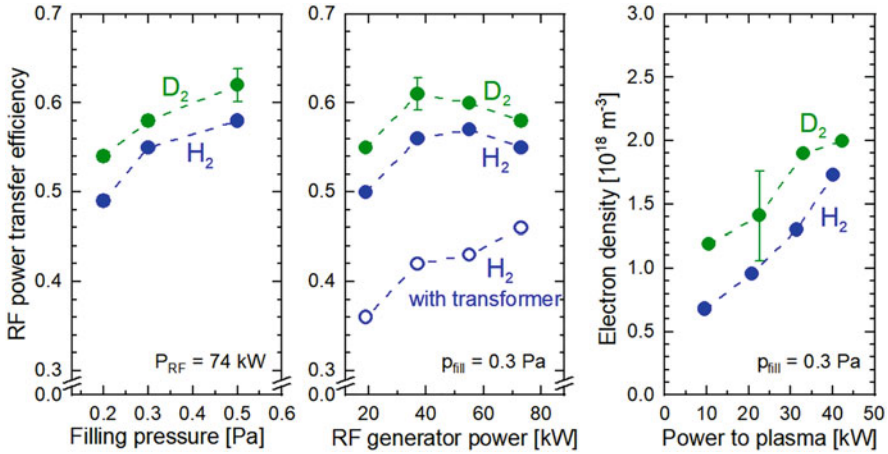


Fig. 16.3 RF power transfer efficiencies for hydrogen and deuterium as a function of the filling pressure, the RF generator power, and the electron density in the center of the cylindrical driver of the prototype source without the DC insulating transformer in the RF circuit (full symbols) and with the transformer installed (open symbols). (Figure adapted from Zielke et al. (2021a))

16.2.3 RF Coupling Efficiency

The high RF power levels at the low RF frequency used in RF-driven ion sources for fusion impose significant strain on the RF circuit components. The coils have to cope with several hundreds of amperes and voltages in the kV range, which can cause electrical breakdowns lowering the reliability of the source operation. Energy can be dissipated in components by eddy currents generated in the RF conductors, the metallic structure surrounding the RF circuit, and the Faraday screen. This in turn means that less RF power is transferred to the plasma and used for plasma heating. The RF power transfer efficiency is a measure to quantify the RF coupling and is defined by the ratio of the power absorbed by the plasma (P_{Plasma}) and the power supplied by the generator (P_{RF}). This definition does not consider power losses in the RF generator itself or any reflected RF power.

Measurements at the prototype source as shown in Fig. 16.1 revealed a surprisingly low power transfer efficiency of about 46% at 75 kW generator power and the ITER relevant pressure of 0.3 Pa decreasing to 36% at 20 kW generator power (Fig. 16.3) (Zielke et al. 2021a). At the ITER sources, however, the RF generators are set at high voltage, avoiding the need of a DC insulating transformer. Dedicated measurements without the transformers revealed that about 10–15% of the generator power is lost in the transformer due to magnetization losses in the ferrites. Figure 16.3 shows results of systematic measurements for hydrogen and deuterium depending on pressure and RF generator power. Systematically higher values by roughly 5% are obtained in deuterium attributed to the higher electron density in deuterium plasmas plotted as a function of the power absorbed

by the plasma (Zielke et al. 2021a). The electron density is measured with a Langmuir probe in the radial and axial center of the driver. When comparing plasma parameters from different RF sources, it is therefore advisable to refer to the power absorbed by the plasmas as most likely the power transfer efficiency is different for the RF setups.

In summary, there is still a huge potential in improving the power transfer efficiency for the ion source, which would on the one hand reduce the strain on the components and thus the reliability of the whole RF setup, but on the other hand reduce the demands on the power supplied by the RF generators resulting most probably in reduced costs and space needed for their installation. Self-consistent numerical investigations pave the way toward identification of optimization measures to enhance the power transfer efficiency. As already pointed out in Briefi et al. (2022), increasing the driver length and changing the RF frequency from 1 MHz to 2 MHz seem to be promising options and can boost the power transfer efficiency from about 60% to 90%.

16.2.4 Magnetic Filter Field

The magnetic filter field separates the plasma generation region in the drivers from the region in which the negative ions are formed and extracted, that is, the region close to the plasma grid. In the large sources, the required magnetic field is created by a current flowing through the plasma grid in vertical direction resulting in a field where the horizontal component dominates. In smaller sources, as the prototype source, the magnetic field can be created by permanent magnets mounted at the vertical sidewalls, either inside the chamber or positioned outside the source. In the latter case, the position with respect to the plasma grid can be varied easily, and the field strength can be adjusted by mounting several packages of magnets in a box, made of nonmagnetic material, located against the source wall outside the source. As shown in the respective investigations in the prototype source by Franzen et al. (2011), the position and the topology of the magnetic field have a strong influence on the source performance. By using permanent magnets, the field strength at the side is much higher than at the center, resulting in a magnetic mirror configuration. To take advantage of this 3-D topology too in the larger sources, external magnets can be added as well to the larger source and are frequently in use at the ELISE test facility (Wunderlich et al. 2016). Figure 16.4 shows the horizontal field component for various magnetic filter field configurations at the ELISE source and the prototype source.

The horizontal component of the magnetic field is in the range of a few mT such that the electrons are magnetized but not the ions. A field strength above 1 mT would be sufficient to reduce the transport of electrons in axial direction, but the field strength (and its 3-D topology) is also a parameter to reduce and control the co-extracted electron current. For this purpose, typically higher field strengths are required for deuterium than for hydrogen, for which the flexible adjustment by

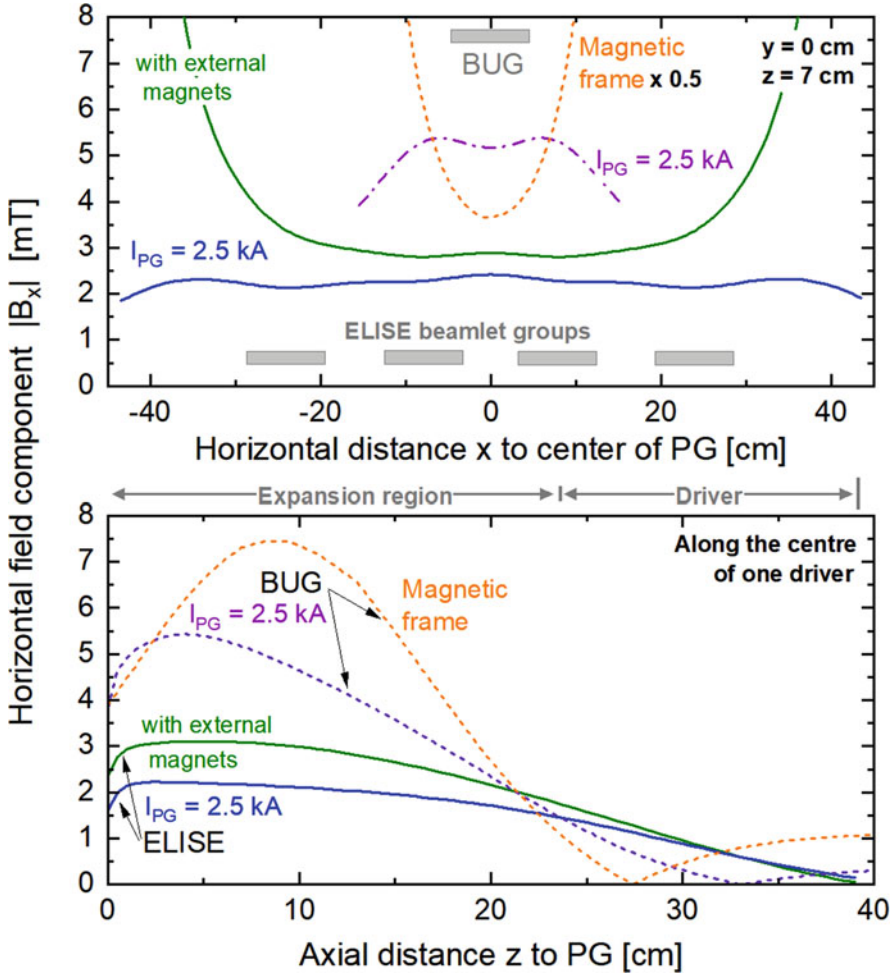


Fig. 16.4 Horizontal component of the magnetic filter field at the prototype source (dashed lines) and the half-size ITER source at ELISE (full lines) generated by either a current flowing through the plasma grid (ELISE and BUG) or by permanent magnets in a magnetic frame (BUG) or by both (ELISE). The profiles are given for the horizontal direction and for the axial direction. (Figure partly adapted from Wunderlich et al. (2016))

the PG current is a very suitable method. Typically, about 4–4.5 mT are used for deuterium, whereas for hydrogen values between 1.5 mT and 3 mT are sufficient at ELISE, depending on other source parameters as well (Wunderlich et al. 2016). Above a certain filter field strength, the extracted negative ion current decreases, which is already the case for the field strength required for deuterium. It should be noted that the 3-D topology of the return conductors for the PG current influences the field topology in the ion sources (Chitarin et al. 2015; Fröschle et al. 2013). For

the ITER sources, a configuration with five return conductors (instead of three at ELISE) is chosen to have a fixed value of the magnetic field in front of the grid of 3 mT and a weak long-range field of 0.5 mT (at the exit of the accelerator) to deflect secondary and stripped electrons out of the beam (Chitarin et al. 2013). This MITICA-like magnetic field was tested at the half-size source demonstrating that some flexibility in the field strength is required for optimal source performance (Fantz et al. 2020).

A consequence of the magnetic field is the occurrence of vertical plasma drifts, which results in vertical inhomogeneities of the plasma parameters in front of the plasma grid. In this region, the $E \times B$ drift dominates: the potential difference is due to the difference in the electron temperatures of the plasmas in the regions in front of the PG and the region downstream of the driver exit and the interaction between those plasmas and the expansion chamber walls. The plasma grid in the ion source is positively biased (slightly higher than the floating potential) in order to attract the electrons to the plasma grid resulting in a bias current and a reduction in the co-extracted electron current. The interplay of the magnetic field strength and biasing of surfaces is important for adjusting the plasma uniformity and to control the current of co-extracted electrons and their vertical uniformity (Fantz et al. 2015).

16.2.5 Low Pressure Operation

The ITER sources are required to operate at a filling pressure of 0.3 Pa or below in order to limit the losses of negative ions by gas stripping in the accelerator to 30% (Hemsworth et al. 2017; Hemsworth and Inoue 2005). Reducing the losses would relax the demands on the extracted ion current densities for which operation at even lower pressure would be desirable. The reduction from 0.3 to 0.2 Pa reduces the gas density in the drivers by approximately 30%. A lower pressure limit is given by the fact that sufficient particles need to be present in the source to be converted to the required negative ion density that corresponds to a pressure of around 0.05 Pa (Franzen and Fantz 2014).

The low-pressure operational limit of a plasma source is defined by the gas density for which the number of ionizing collisions in the plasma generation volume (by ionization of the background gas) can just balance the losses of charged particles; in a low-pressure plasma, the latter mainly happens at the walls. If the pressure is too low, the plasma cannot be ignited or sustained. Neutral gas depletion, effectively reducing the gas pressure in the plasma generation volume for high power coupled into the plasma and a low gas flow (McNeely et al. 2011), can strongly affect the low-pressure operational limit.

Experimental and theoretical results indicate that the low-pressure operational limit of the ion source depends on the strength and/or topology of the magnetic filter field, the source geometry and plasma parameters in the plasma generation volume (Wünderlich et al. 2021a). The presence of cesium in driver plasma may

also have an influence on the low-pressure limit as the general plasma properties change due to its high mass, low ionization energy, and low electronegativity.

Systematic investigations at the half-size ITER source at ELISE in hydrogen and in deuterium at various magnetic filter field configurations demonstrated reliable operation down to pressures of 0.2 Pa, but the magnetic field topology in the driver is of relevance. For lower pressures, the plasma stability is influenced, and oscillations in the kHz range are observed (Wünderlich et al. 2021a). On the other hand, the observed strong increase of the co-extracted electron current with lower pressure together with the heavily enhanced temporal dynamic during long pulses may limit the acceptable reduction of the pressure.

16.2.6 Plasma Parameter

The plasma parameters such as electron temperature and electron density are measured either via Langmuir probes, which can provide profiles along the positions accessible by the probe movement, or by optical emission spectroscopy averaging the signals along the used line of sight. The accessible plasma region depends on the position of the diagnostic ports typically available at the backplate of the driver and the rectangular expansion chamber and in a flange mounted between the expansion chamber and the plasma grid providing ports in horizontal and vertical orientation. Optical emission spectroscopy allows also to determine the atomic hydrogen density, the temperature of the atomic and molecular hydrogen species, and the cesium density and the negative ion density (Fantz et al. 2006; Heinemann et al. 2017; Wünderlich et al. 2021b). Additionally, laser techniques such as tunable diode laser absorption spectroscopy (TDLAS) and cavity ring-down spectroscopy (CRDS) are used to measure vacuum and plasma phases in the atomic cesium density (TDLAS) and the negative ion density (CRDS). Both techniques are also suitable for monitoring the cesium conditioning and deriving correlations with the source performance (Heinemann et al. 2017).

Figure 16.5 shows the electron temperature and density for the prototype source at BUG varying with the strength of the magnetic filter field by changing the PG current (1 kA representing a field strength of about 2.1 mT peak value in axial direction, horizontally and vertically centered,). Three lines of sight are used simultaneously: one through the driver representing the plasma along the cylinder axis, one close to the PG vertically centered (2.6 cm distance from the grid surface), and one in the expansion chamber (18 cm distance from the grid surface using a dedicated flange in the expansion chamber); the latter both are vertically centered (Briefi et al. 2018). Plasma parameters for the case using the magnetic frame with permanent magnets outside the source (at a position of 9 cm from the grid) instead of a PG current are shown as well.

The plasma parameters shown in Fig. 16.5 are measured at the ITER relevant pressure of 0.3 Pa, an RF generator power of 70 kW in hydrogen plasmas without cesium injection. The electron temperature and the electron density decrease from

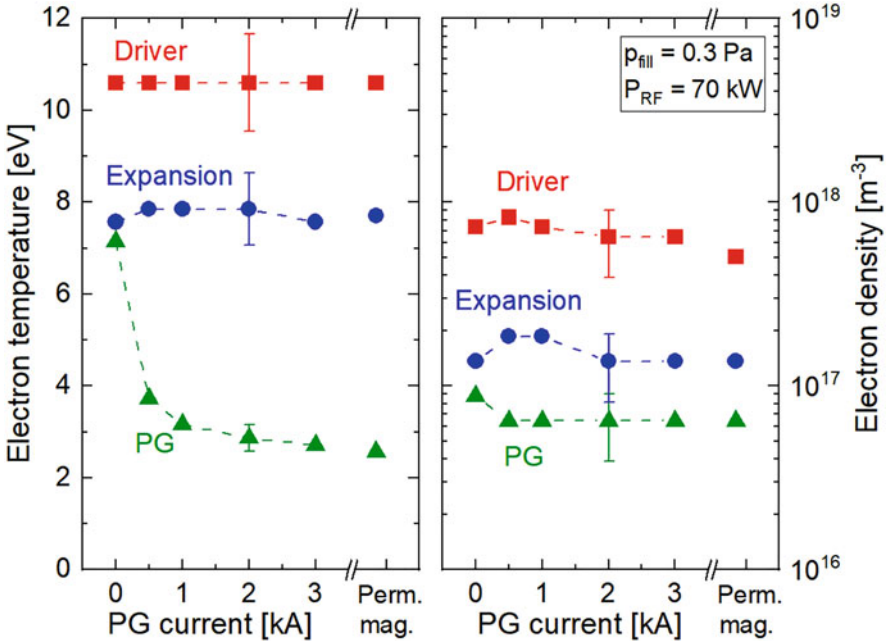


Fig. 16.5 Plasma parameter determined with OES at the prototype source used at BUG (hydrogen plasmas) as a function of the magnetic filter field varied by the PG current and with permanent magnets attached at the sidewalls only. (Figure adapted from Briefi et al. (2018))

the driver to the PG region due to the plasma expansion into the expansion chamber. The decrease is amplified in the PG region by the hindered particle transport through the magnetic filter field. As the electrons start to be magnetized at about 1 mT, the effect of the filter field sets in around this point whereas stronger fields have a small impact on further reduction of the parameters but can result in a stronger vertical plasma drift together with the interplay with biased surfaces. The usage of the permanent magnets instead of a PG current reveals almost no change in the measured plasma parameters, although the respective 3-D topology changes (see Fig. 16.4 for axial and horizontal profiles). Due to the low plasma temperature in the PG region, the plasma evolves toward a recombining plasma where the dissociative recombination via the diatomic hydrogen ions starts to dominate the plasma processes. The gas temperature derived from the molecular hydrogen emission is 630 K. The analysis of the profile of the Balmer emission lines result in a two-temperature distribution with a temperature of 2200 K for the cold ensemble and 29,000 K (i.e., 2.5 eV) for the hot ensemble. The density ratio of hydrogen atoms to molecules is about 0.3 for the whole source, and the vibrational temperature of the hydrogen molecules is analyzed to be 3000 K (Briefi et al. 2018).

In the volume operation mode, that is, without cesium in the source, the negative ion density measured with CRDS close to the PG is below 10^{16} m^{-3} for 0.3 Pa

(Heinemann et al. 2017). The respective extracted ion current density is around 15 A/m^2 , for hydrogen and for deuterium, at an extraction voltage of 5 kV. The co-extracted electron current density is about a factor of 30 higher for both species. With cesiation, the current density of the ions increases, and the co-extracted electrons decrease (Heinemann et al. 2017; Wimmer et al. 2016), such that at a well-conditioned ion source the negative ion density increased to above 10^{17} m^{-3} at a current density of 260 A/m^2 with 9–10 kV extraction voltage accompanied by an electron-to-ion ratio below 0.5 for hydrogen (Fantz et al. 2021). During the cesium conditioning process, the plasma in front of the PG changes from a plasma in which electrons balance the positive ions to an ion–ion plasma in which the negative ions represent the dominant negatively charged species as can be seen in the results of Langmuir probe measurements (Heinemann et al. 2017).

Cesium is continuously evaporated into the source, such that reservoirs can be built up in the vacuum phases (typically several minutes between plasma pulses) being then redistributed by the plasma. The cesium density before, during, and after the plasma pulse measured with TDLAS close to the PG shows higher atomic cesium densities in the plasma than in vacuum phases although the degree of ionization is above 70% in the plasma (Mimo et al. 2018). A temporal variation of the density during plasma pulses evolves. Typical values for the neutral cesium density range from 10^{14} m^{-3} to 10^{15} m^{-3} (Heinemann et al. 2017).

16.3 Achievements for ITER

The ITER parameters with respect to the current densities at the required filling pressure of 0.3 Pa for 10 s RF pulses with 4 s beams were demonstrated for hydrogen and deuterium in the initial prototype source in which also first ITER-relevant 3600 s beams were demonstrated (Speth et al. 2006; Kraus et al. 2008). With the intention to deepen the physics understanding, to increase the source reliability, to test new concepts and diagnostics, and to get operational experience and for training purposes, the prototype source still contributes to the ITER NBI program. At present, BUG is still working in pulsed operation mode, typically 10 s plasma with a beam phase of 4.5 s and 3 min between the individual pulses. Pulses with beams up to 2 h will become available after an upgrade of the cooling of some components, mainly the plasma grid, for which preparations are ongoing. For dedicated tests, plasma and extraction up to 100 s are possible but at reduced power and longer phases between the pulses. Investigations at BUG are presently focused on beam optics studies and the understanding of beam properties for which the test facility is equipped with several beam diagnostic tools (Fantz et al. 2019). The half-size source at the ELISE test facility is capable to operate continuously, but beam extraction is limited to pulsed extraction by the high-voltage power supply: 10 s extraction blips with about 150 s in between can be used to probe the beam. For steady-state extraction and acceleration, a new HV power supply is under commissioning (Wunderlich et al. 2021c). First very valuable insights into

the operation of the full-size ion source were already gained by the test facility SPIDER, which is equipped with a CW operational high-voltage power supply up to a total voltage of 100 kV (Toigo et al. 2021; Serianni et al. 2020). A first cesiation campaign finished successfully in 2021 after which SPIDER entered a shutdown phase of about 1 year for maintenance purposes and replacement of some components (Sartori et al. 2022). All these test facilities are equipped with a proper neutron shielding allowing for deuterium operation. A copy of the prototype source used at BATMAN is in operation at the test facility ROBIN for basic studies to support the development of the DNB (Pandya et al. 2017). An increasing number of ion sources based on the prototype concept are in operation (hydrogen only) or in the planning phase for their later use on NBI systems at fusion facilities around the world, less focused on the achievements of the ITER parameters but to achieve the goals of the envisaged NBI system.

16.3.1 Short Pulses: Up to 10 s

The achievements with respect to the extracted current densities in the short pulse operation mode (10 s beam within the 20 s plasma operation) at the required pressure of 0.3 Pa are given in Fig. 16.6 showing results obtained over 4 years at the half-size ITER source operational at the ELISE test facility. As the RF generators are rated to 150 kW, the maximum RF power per driver is 75 kW. Different values at one RF power represent cesium conditioning phases, adoption for magnetic filter field strength and bias of surfaces, and the extraction voltage. The data shown includes

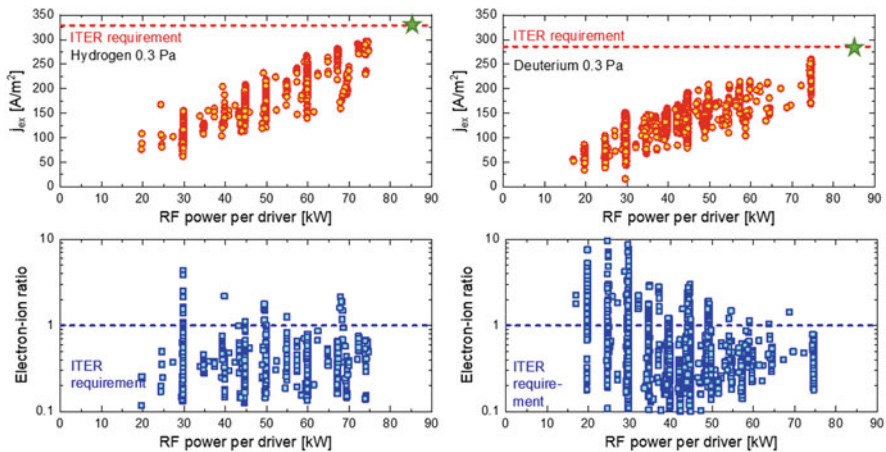


Fig. 16.6 Extracted current densities of negative hydrogen ions and the ratio of co-extracted electrons to ions as a function of RF power per driver using data from the half-size source at ELISE

also initial cesium conditioning phases, for example, after the source was opened and cleaned. This explains why for both isotopes significantly larger electron-ion ratios are obtained at low RF power (<35 kW per driver).

The envelope of the extracted ion current density increases almost linearly with the RF power. An estimate toward the ITER requirement result in a RF power per driver of about 85 kW for both, hydrogen and deuterium, which is well below the value of 100 kW foreseen for the ITER source. In hydrogen, the co-extracted electron current is well below the ITER limit; in a well-conditioned source, the electron–ion ratio is less than 0.5. The electron–ion ratio is higher in deuterium, but the ITER requirements can be fulfilled in the short pulse mode. It is generally observed that significantly higher cesium evaporation is needed to achieve the ITER requirements in deuterium than in hydrogen and the conditioning procedure is much more complex (Wünderlich et al. 2018).

16.3.2 Long Pulses: Up to 1 h

For long pulses, initial measurements were performed at the long pulse test facility MANITU, using the prototype source. In view of the pulsed extraction available at ELISE, the temporal behavior of current densities for pulsed extraction was compared with continuous extraction (Heinemann et al. 2017). The left part of Fig. 16.7 shows an overlay of two 300 s plasma pulses conducted at MANITU. The extracted ion current density is very well reflected in the pulsed extraction mode, which is also true for the general trend of the electrons but reveal a different temporal dependence within the beam blips.

At the half-size source (Fig. 16.7, right), the temporal behavior of the co-extracted electrons is generally more pronounced: an increase from beam blip and a

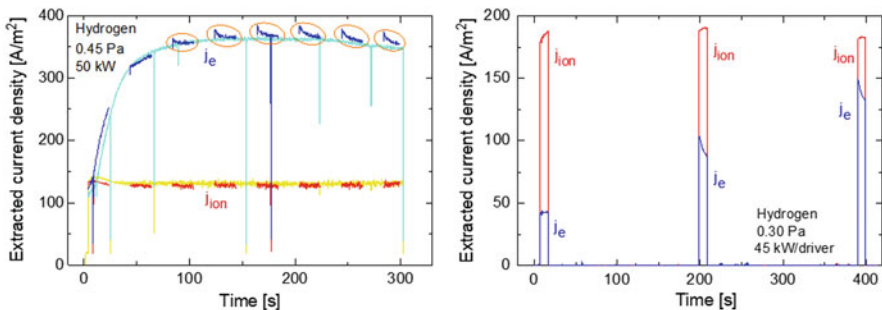


Fig. 16.7 Extracted current density of negative hydrogen ions and electrons for a pulse of 300 s at the prototype source of the MANITU test facility using continuous extraction and pulsed extraction (left). Right: current densities for pulsed extraction at the half-size ITER source at ELISE during a 400 s plasma discharge with beam blips of 10 s every about 180 s. (Figure adapted from Heinemann et al. (2017))

decrease within the beam blip. The temporal dynamics of the co-extracted electrons is attributed to the depletion of cesium at the grid system (Sect. 16.4.3), since, if the electrons are a minority species in the ion-ion plasma (Sect. 16.2.2), a small change in the negative ion density must lead to a much bigger fractional change in the electron density in order to maintain quasi-neutrality in the plasma. The strong dynamics within a beam blip is assigned to backstreaming positive ions, created in the extractor/accelerator system, impinging on the backplate of the ion source where cesium accumulates between the blips when there is no ion extraction, and there are no back-streaming positive ions. Consequently, additional cesium is released and redistributed in the source during extraction. At the prototype source, the area of the backplate hit by the backstreaming ions is much lower explaining the less pronounced effect. Between the beam blips, a deconditioning of the cesium on the PG takes place, attributed to cesium depletion and thus degradation of the cesium layer at the PG surface where the negative ions are formed, such that the cesium released by the backstreaming ions improves the source performance. In general, the dynamic behavior of the co-extracted electrons is less pronounced at higher pressures (Heinemann et al. 2017).

The achievements at the half-size ITER source in long pulses with beam blips are summarized in Wunderlich et al. (2019a, 2021c) and illustrated in Fig. 16.8 for hydrogen and deuterium. For hydrogen, the ITER parameters were demonstrated by achieving more than 90% of the required extracted ion current for 1000 s in a reproducible series, limited only by technical constraints regarding the available RF power and the high voltage power supply. The pulse performed at a filling pressure of 0.4 Pa in between the 0.3 Pa pulses reveals less dynamics in the co-extracted electrons and visualizes their pressure dependence. For deuterium, over 60% of the target value was achieved in long pulses. The achievement of a better performance is limited by a higher co-extracted electron current compared with hydrogen accompanied by a stronger vertical asymmetry and a stronger increase with time. The vertical asymmetry of the co-extracted electrons is made accessible via separate measurements at the two grid segments of the extraction grid. For deuterium, the respective power loads are plotted instead of the current densities as these are the critical quantities for the interlock protecting the extraction grid segments. The time trace of the last extraction blip shows this relevance as at the start of the beam blip the power load is highest. Values representing one beam blip are typically averaged over the second half of the beam blip.

These achievements were possible only with improved cesium conditioning, which means an over-conditioning of cesium for the first beam blip, which has therefore a lower current density as illustrated in Fig. 16.8 for hydrogen. A similar strategy for deuterium is not as effective as in hydrogen. For both isotopes, the magnetic filter field is adjusted, such that the electrons are sufficiently suppressed without reducing the current of negative ions by more than about 10%. As already mentioned, typical field strengths are 1.5–3 mT in hydrogen and 4–4.5 mT in deuterium. Further reduction of the co-extracted electrons has been achieved by

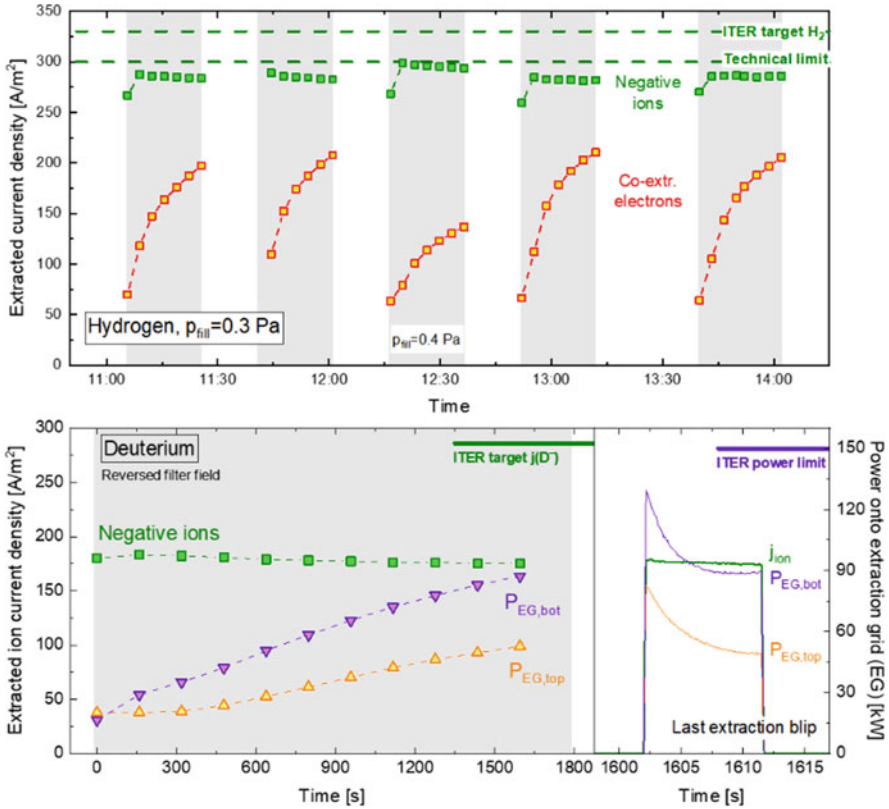


Fig. 16.8 Extracted current densities of negative ions and electrons at the half-size source at ELISE. Upper part: repetitive 1000 s hydrogen discharges (gray-shaded area) with pulsed extraction (symbols). Lower part: an 1800 s deuterium discharge with beam blips and a zoom into the last beam blip. The power onto the extraction grid due to the co-extracted electrons is measured separately for the top and for the bottom segment. (Figures adapted from Wunderlich et al. (2019a, 2021c))

implementing metallic rods in vertical direction to influence the particle fluxes by biasing these potential rods (Wunderlich et al. 2021c). With the potential rods (3 cm axial extent, mounted at 15 mm axial distance from the PG) (Wimmer et al. 2018), the electrons from the driver can be (depending on their potential w.r.t. the plasma potential) attracted by the potential rods, resulting in a reduced co-extracted electron current and improved asymmetry as well as temporal stability. As the potential rods imply a source modification for the ITER sources, measures are undertaken to replace them by biasing the bias plate independently from the source wall and the plasma grid (Sect. 16.4.2).

16.3.3 Toward Full Performance of the ITER Source: A Stepwise Approach

Although with pulsed extraction, that is, using beam blips, the ion current can be sampled during long pulses, the behavior of the co-extracted electron current is likely to be different from that observed from blip to blip, and continuous beam extraction is required to follow the temporal changes, which are currently limiting the ion source performance in particular at the pressure of 0.3 Pa. In addition, a spatial resolution, at least at the scale of one grid segment, as available at the ELISE test facility, is desirable to avoid any risk of melting the extraction grid. At the ITER source, the total current from the four grid segments is accessible only from which the total power load (tolerating a maximum of 600 kW) is monitored. The global vertical asymmetry is understood to be a consequence of the vertical plasma drift (and thus the electron density), which may also cause asymmetries in the cesium layer on the plasma grid. In addition, the continuous cesium redistribution by sputtering of cesium from the backplate of the ion source is of relevance for the long pulse behavior. The test facilities BUG and ELISE are on the way to be converted to full steady-state operation. Focus will be given to deuterium operation as this is the challenge to overcome.

First experimental campaigns performed at the full-size ion source at SPIDER already gave valuable input for commissioning and routine operation of the large ion source with the source being installed in a large vacuum vessel as it will be the case for ITER (Serianni et al. 2020). A schematic layout of the machine in the vacuum vessel is shown in Fig. 16.9, illustrating also the achievement from the very first cesium campaign performed in hydrogen followed by first experiments in deuterium (Sartori et al. 2022). The full-size ion source shows the typical cesium conditioning behavior as the smaller size-scaling sources. It needs to be mentioned that the majority of the 1280 apertures were closed due to limitations in the pumping speed, ensuring in that way that the pressure in the region outside the driver, within the vacuum vessel, is low enough and to avoid RF breakdowns. For safety reasons, operation for higher RF powers than 50 kW/driver was limited and is a task to overcome for the next experimental campaign.

Experiments for the full vertical size of the ITER source at full performance and using all 1280 apertures will be done after the long shutdown of SPIDER during which the RF system and the vacuum system will be improved among other exchanges of components. Restart of operation is foreseen in 2023, with the additional modification to insulate the grid segments of the EG against each other to measure the co-extracted electrons on the four vertical grid segments separately. SPIDER is intended to give valuable input for the full-size source in terms of magnetic filter field configuration, biasing of surface and other parameters. Focus, however, is laid on the beam diagnostic on the scale of individual beamlets to fulfill the requirements in terms of beam divergence for which SPIDER is equipped with dedicated beam diagnostic tools (Toigo et al. 2017b). MITICA is basically a one-to-one replica of the ITER source and will start operation with the 1 MeV acceleration

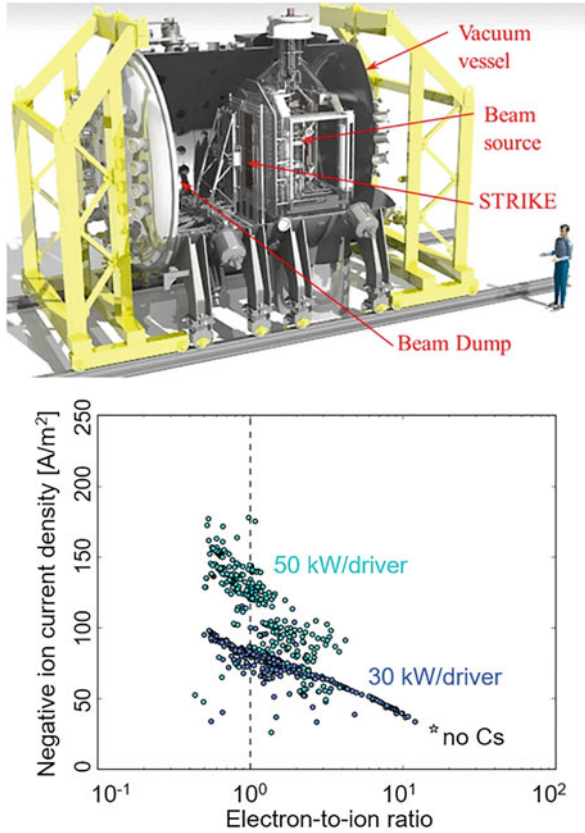


Fig. 16.9 The full size ITER source in the SPIDER test facility and results of the very first experimental campaign with cesium in 2021. Plotted is the accelerated current density measured with the STRIKE calorimeter against the ratio of co-extracted electrons to ions. (Figures adapted from Toigo et al. (2017a), Sartori et al. (2022))

in 2024. The ITER NBI sources are planned to start commissioning in 2031 to be available, according to ITER's stage approach, for the Pre-Fusion Power Phase II in 2032.

In parallel, the test facilities in India, INTF, will improve their performances, focusing to achieve the parameters for the DNB with operation in hydrogen only, in pulsed mode and requiring higher current densities (Singh et al. 2019; Chakraborty et al. 2019).

As for the ITER experiment in addition to the work in the EU and India, described above, there is a strong collaboration with Japan, with various tests, calculations, and evaluations of data being carried out at QST (Takeiri 2010; Tsumori and Wada 2017) and NIFS (Hanada et al. 2016; Hiratsuka et al. 2020).

16.4 Lessons Learned and Challenges

Operation of the RF-driven ion source at the high RF power imposes challenges with respect to the RF technology generating also lessons learned for any multiple driver concepts toward reliable operation. Other challenges concern plasma and beam uniformity basically determined by the magnetic filter field concept. Challenges connected to the reduction and control of co-extracted electrons and the relation to the cesiation of the modular RF sources are pointed out in the following subsections. The beam divergence is briefly addressed as well.

16.4.1 Source Operation: RF Issues/Technology

In the larger ion sources based on multiple drivers, two neighboring drivers are connected in series and supplied by one RF generator to drive the same current through both coils with the intention to generate similar plasma properties in the two drivers. This imposes that the RF voltage of both coils adds up to about 24 kV (typically 2 kV/turn) (Heinemann et al. 2018). As they are electrically insulated from the source, the RF voltage will float around the source potential in a self-adjusting way. Consequently, special attention needs to be taken to distances and triple points (i.e., the junction of a metallic surface and a dielectric and vacuum) to avoid breakdowns. The alternative, to switch two drivers in parallel, reduces the RF voltage with respect to the source potential by a factor of two, but reduces the inductance of the circuit, which has to be compensated by increasing the series capacitance in the RF circuit. The matching curve becomes narrower, and finding stable matching becomes difficult particularly with RF generators having a low frequency stability like self-excited oscillators. Changing from these tube-based generators to solid-state amplifiers improves this situation (Heinemann et al. 2018).

In the initial design of the RF circuit operated at the half-size source at ELISE (Heinemann et al. 2009), an increase of the RF power to values above 40–60 kW/driver was technically prevented by RF-induced electric breakdowns occurring randomly outside the drivers. To simulate ITER conditions around the drivers, they are placed inside a vacuum containment, the dome, which is pumped independently from the source to a pressure down to 10^{-6} mbar. Due to gas released from inner dome surfaces during breakdowns, the pressure in the dome increases instantaneously, and the RF power is deposited outside the driver, while the internal plasma extinguishes. The associated deposition of impurities may result over the experimental time in a further reduction of the RF power limit for breakdowns.

Figure 16.10 illustrates that the electric field strength near an exemplary triple point around the driver is reduced by a factor of ten by increasing the gap between the cylinder and the coil, by changing the material to a one with lower permittivity, and by introducing “combs” (supports) to fix the position of the coils (annealed copper tubes, diameter 8 mm). The combs are made of silicone rubber material, and

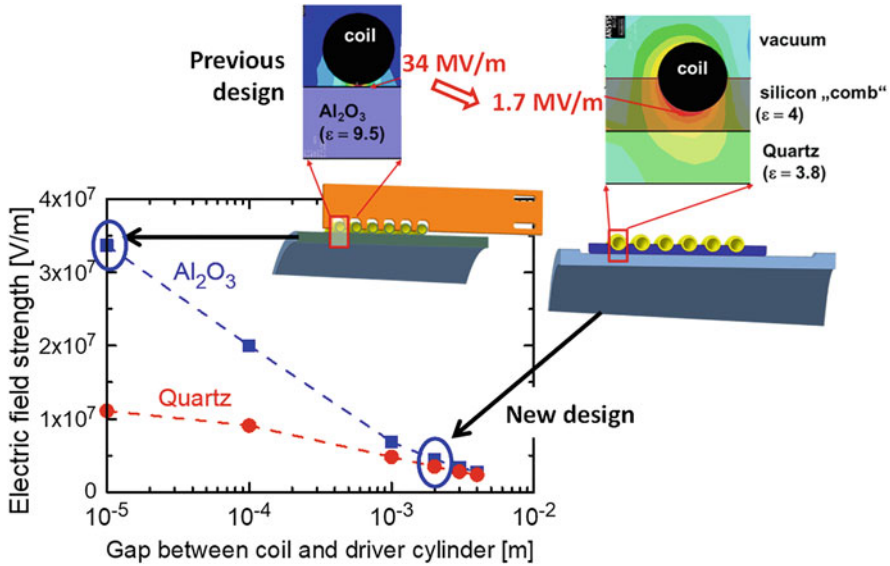


Fig. 16.10 Electric field strength calculated for different gaps between coil and driver cylinder, for Al₂O₃ and quartz together with sketches of the initial and improved design. (Figure adapted from Heinemann et al. (2018))

their shape was also designed to minimize the electric field at the triple points.” Using a driver cylinder with reduced wall thickness (6 mm instead of 8 mm) keeps the coil at the same distance to the plasma coupling region.

With the intention to reduce mutual coupling of the drivers and asymmetries of the RF electromagnetic field in the drivers that could result in damages of the Faraday screens, each driver is surrounded by a copper-made electromagnetic screen, which is water-cooled to avoid overheating (Wunderlich et al. 2017). All these measures together with the usage of RF generators based on solid-state technology resulted in reliable high power and long pulse source operation at the half-size source at ELISE without breakdowns and with stable matching. The modifications are on the way to be implemented in SPIDER in the long shutdown phase (Toigo et al. 2021) and were taken up for the ITER sources.

The voltage holding capacity with respect to the pressure around the drivers is a crucial parameter for reliable operation. A variation of the dome pressure at the half-size ITER source at ELISE showed that in this configuration, 25 kV DC voltage could be applied without breakdowns for dome pressures from 10⁻⁴ Pa to 0.3 Pa.

The usage of high-power RF sources is inevitably connected with RF noise, which imposes challenges for its suppression by avoiding any ground loops. RF noise not only can cause huge disturbances to any diagnostic system, making analysis very difficult, but also can trigger interlocks and thus interrupt reliable operation.

16.4.2 *Plasma Uniformity, Symmetry of Co-extracted Electrons, and Beam Uniformity*

As discussed in Sect. 16.2.4, in front of the plasma grid, an $E \times B$ drift is caused by the interplay of the filter field with the electric field created by the difference in the electron temperatures of the plasmas in the regions in front of the PG and the region downstream of the driver exit and the interaction between those plasmas and the expansion chamber walls. Cesiumation or the change to deuterium plasmas requires an adjustment of magnetic field strength and bias potential (Fantz et al. 2009). The uniformity of the extracted current densities of negative ions and of electrons can be correlated to the plasma uniformity via different mechanisms.

The vertical uniformity of the extracted negative ion current density depends on the uniformity of the negative ion density in the plasma close to the PG, which in turn is influenced mainly by the uniformity of the atomic hydrogen flux impinging the surface (as dominant species being converted at the surface to negative ions) and on the uniformity of the work function of the cesium layer. In addition, asymmetries in the positive ion density close to the plasma grid can limit the transport of the surface produced negative ions toward the extraction apertures. Measurements on the beam uniformity in vertical direction reveal a robust global vertical uniformity (Fantz et al. 2009; Bonomo et al. 2020) within the required uniformity of better than 90% across the beam size in a well-conditioned ion source. Temporal dependences in long pulse operation are connected to a degradation of the cesium layer with time as the particle fluxes provided by the plasma in the driver are stable in time. Additional attention has to be given on the uniformity on the scale of the aperture size, as the magnets embedded in the extraction grid generate beamlet deflection and also plasma drifts across the aperture (Taccogna et al. 2013; Fubiani et al. 2018; Wunderlich et al. 2021d).

In contrast to the extracted negative ions, the uniformity of the co-extracted electrons depends much stronger on the plasma parameters, as it is directly linked to the electron density and temperature. A local reduction of the negative ion density caused by effects mentioned above results in a reduced plasma electronegativity and thus in a locally increased electron density. As being the minority species in the plasma in front of the plasma grid, the electrons react much more strongly than the negative ions (Heinemann et al. 2017). As a consequence, the co-extracted electrons are subject of strong vertical inhomogeneities revealing also a pronounced temporal behavior (Sect. 16.3.2).

The interplay between biased surfaces and magnetic field strength with respect to the co-extracted electron currents measured for the top and the bottom segments at the half-size ITER source is clearly shown in Fig. 16.11 for different configurations of the electrostatic potential applied to surfaces close to the PG. The results are obtained in the short pulse mode operating in deuterium (Fantz et al. 2022).

The standard configuration with the bias plate connected to the source body (case (a)) shows a much higher co-extracted electron current for the top segment than for the bottom segment of the extraction grid with a more pronounced temporal

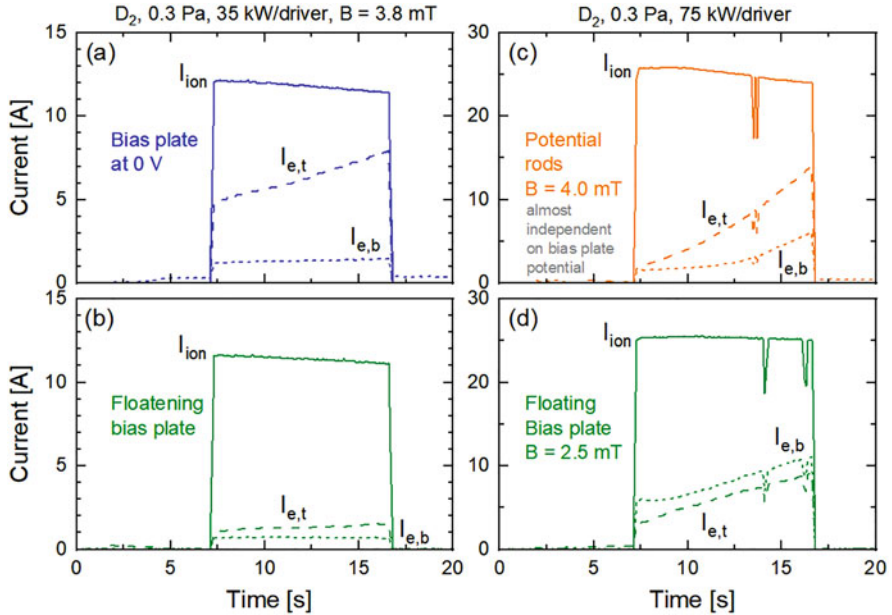


Fig. 16.11 Time traces of the extracted current of negative ions (I_{ion}) and electrons for different configurations of the electrostatic potential (see text). The electron current is plotted segment wise: for the top segment ($I_{e,t}$) and the bottom segment ($I_{e,b}$) of the EG at ELISE. All data is taken in deuterium at 0.3 Pa filling pressure. Note changes in the RF power and in the strength of the magnetic filter field. (Figure adapted from Fantz et al. (2022))

behavior. This dynamic prevents the increasing of the RF power to higher values without risking damage of the grid. Implementing potential rods (Sect. 16.3.2) allowed for higher RF power as the positive bias applied to the rods with the aim to attract the electrons reduces the asymmetry of the co-extracted electrons and high performance pulsed are possible (case (c)). Using a floating bias plate without potential rods, the co-extracted electrons are close to by symmetric (case (b)), and an increase of the RF power can be accompanied by a reduction of the magnetic filter field resulting in high performance pulse (case (d)) with improved plasma uniformity as well. These short pulse results are promising with respect to be an adequate replacement of the potential rods as their implementation for ITER's ion sources is not planned.

A good example of the beam properties of a large beam extracted and accelerated from the half-size source are shown in Fig. 16.12 (Bonomo et al. 2020).

The calorimeter from which the 2-D power density map is derived is located at a distance of 3.5 m from the grounded grid. The two grid segments are clearly separated in the power density map whereas the four beamlet groups in each segment (Fig. 16.2) overlap. The divergence determined by beam-emission spectroscopy (BES) is typically slightly above 2 degree. An about 10% lower accelerated ion current is obtained in the bottom grid segment than in the top

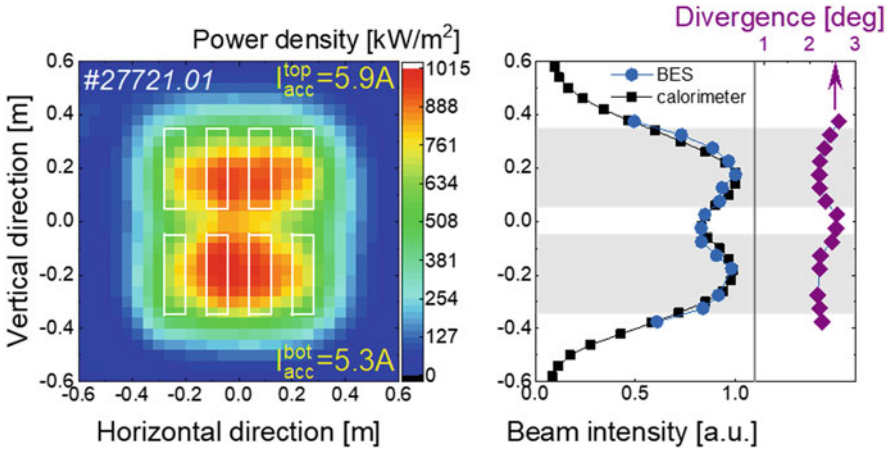


Fig. 16.12 Two-dimensional power density map at the calorimeter with the position of the beamlet group indicated and the corresponding vertical profile (squares) together with the beam profile from BES (circles). In addition, the vertical profile of the divergence from BES is shown (diamonds). The data are taken at an extraction voltage of 9 kV, an acceleration voltage of 33 kV resulting in a extracted negative ion current density of 150 A/m^2 using an PG current of 1.6 kA and permanent magnets. (Figure adapted from Bonomo et al. (2020))

one. The vertically profile taken from the calorimeter and the BES is in very good agreement with each other and shows a decrease of the beam intensity toward the outer edges of the beamlet group. The reduction of the current density at the edges of the footprint means that the divergence of the beamlets at the edge of the array is larger than in the central area of the array, which is because the negative ion flux to the apertures at the edges of the array is below that giving the optimum perveance.

The measured beam divergence of about 2 degree (34 mrad) is above the ITER specification of 7 mrad for the core (and the 30 mrad for the halo) of a beamlet. This might be caused by one or more of the following factors: (i) the overlap of the footprints of individual beamlets, (ii) mechanical misalignment of the apertures in the grids, (iii) inhomogeneity of the H^- flux at the level of each aperture, (iv) beamlet deflection caused by the magnetic field from the magnets embedded in the extraction grid for which compensation magnets will be installed in the ITER sources, and, of course, (v) the low acceleration voltage compared with that to be used for the ITER sources.

The comparison of results from analyzing the footprint of a beamlet from an isolated aperture to the measurements of the signal from a beamlet group is shown in the lower row of Fig. 16.13. The data is taken from the prototype source at BUG (Hurlbatt et al. 2021) having a similar grid system as ELISE.

For these beam optics studies, the 14×5 beamlet arrangement, is masked and the centered aperture in the upper part is kept open, allowing for a direct comparison of results from a single aperture with those obtained from a beamlet group. The arrangements of the lines of sight for BES projected to the grounded

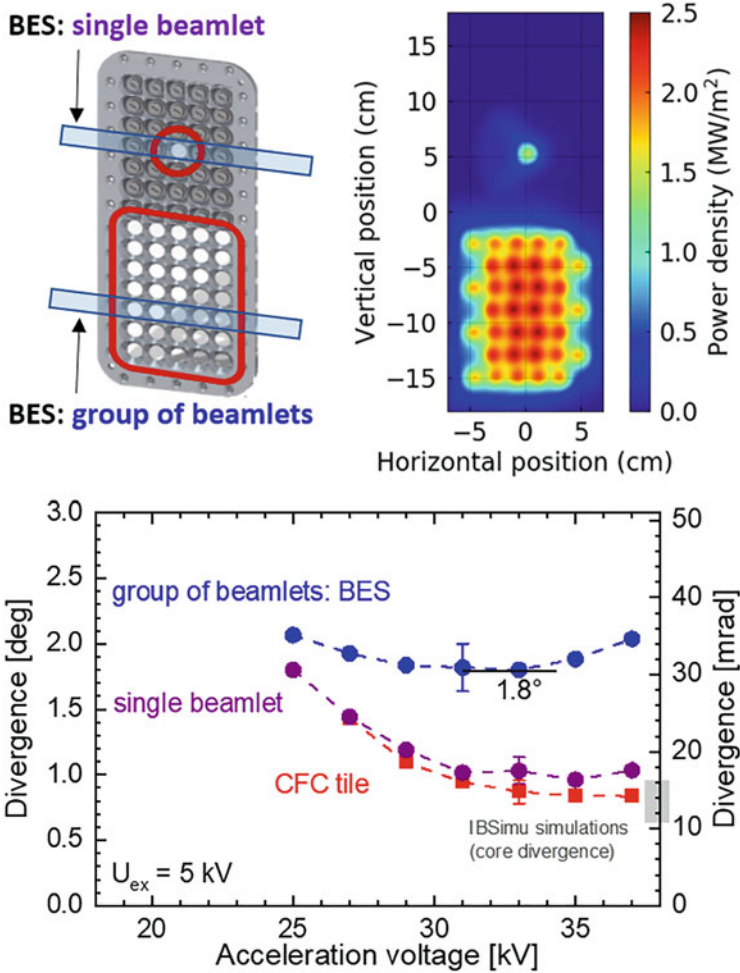


Fig. 16.13 Upper row: schematic drawing of the PG used in the prototype source at BUG. The upper half of the beamlet grouped is masked to isolate a single beamlet with the lines of sight for the BES indicated together with simulations using the IBSimu beam simulation code demonstrating the row-wise beamlet deflection by the magnets embedded in the extraction grid (den Harder et al. 2021). Lower row: horizontal divergence for the group of beamlets (using BES) and the single beamlet (using BES and the mini-STRIKE CFC tile calorimeter) as a function of the applied acceleration voltage (Hurlbatt et al. 2021). The expected minimum of the core divergence predicted by IBSimu is indicated

grid are indicated in Fig. 16.13. As BES is located at 1.5 m from the grounded grid, several rows can contribute to the signal. Results of calculations for the expected footprint at the CFC calorimeter using IBSimu, mimicking the lateral heat conduction in the CFC tile (den Harder et al. 2021), are also shown in the figure. The group of beamlets reveal the before mentioned deflection of the beamlets, which

show a zigzag pattern due to the row-wise alternating magnetic field. Thus, the measurements result in a significantly higher beam divergence for the group of beamlets than for a single beamlet. The two methods used for the analysis of a single beamlet are in good agreement within each other and with the expected minimum of the core divergence predicted by IBSimu calculations. In these calculations, a vertical velocity of the negative ions according to 1 eV has been used for the IBSimu calculations – a parameter being of high relevance for the predicted divergence. For the ITER NBI, a magnetic compensation of the row-wise zigzag deflection is foreseen (Chitarin et al. 2014); a similar compensation is in progress at the BUG test facility in collaboration with the ITER Organization.

16.4.3 Cesium and Co-extracted Electrons

As pointed out in Sect. 16.3.2 in the ion–ion plasma case, the co-extracted electron currents react much more strongly to the cesium conditioning status than the extracted negative ion current. Hence, cesium management in terms of optimizing the redistribution dynamics during plasma operation keeping in mind also the cesium consumption is one of the most urgent and demanding tasks for long pulses. The major challenge is the uniform cesiation of the plasma grid by evaporation from the cesium oven followed by redistribution during operation with the plasma as it is found that during operation with the plasma the cesium flux to the surface is insufficient to compensate for the cesium released from the surface (Wünderlich et al. 2018; Cristofaro et al. 2020).

Cesium atoms evaporated from the oven are ionized within a few centimeters and may not have enough energy to overcome a potential barrier at the plasma grid caused by positive bias to attract the electrons (Mimo et al. 2018). Increasing the evaporation rate of the oven is limited by breakdowns occurring between the grids of the extraction system. An in situ work function measurement of the PG surface would be highly desirable for the optimization of the cesium management, but the installation of such a monitoring system is challenging in the harsh environment of an RF ion source and is thus not established up to now. In order to gain insights into the cesium work function dynamics under ion source conditions, dedicated studies are typically performed at small-scale laboratory experiments (Friedl and Fantz 2014; Cristofaro et al. 2021; Fantz et al. 2021).

In deuterium, the cesium dynamics is, due to the higher mass of deuterium particles, much more pronounced than in hydrogen as illustrated in Fig. 16.14 with measurements taken at the half-size ion source at ELISE for identical ion source parameters and cesium evaporation rate for both isotopes (Wünderlich et al. 2019b).

The extracted negative ion current density decreases by less than 10%, but the co-extracted electrons increase instantaneously by a factor of about six in the first deuterium pulse and up to a total factor of nine in the subsequent pulses. Stabilization is possible only by prolonging the break between the two 20 s plasma pulses from 5 min to 17 min, increasing the cesium fluence, and thus the cesium

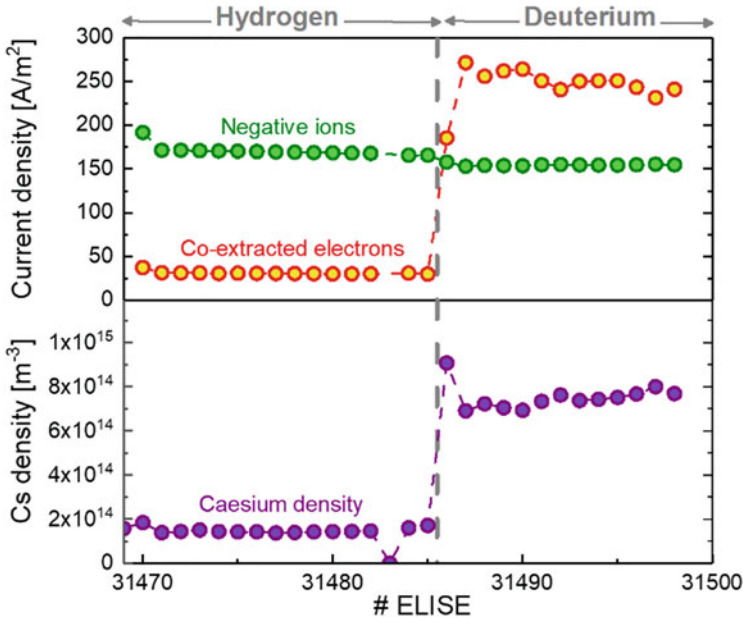


Fig. 16.14 Consecutive pulses (short pulse mode) where operation in hydrogen was switched to deuterium at otherwise identical source parameters. Upper part: extracted negative ion current density and co-extracted electron current density. Lower part: atomic cesium density close to the plasma grid surface from TDLAS measurements. (Figure adapted from Wunderlich et al. (2019b))

amount evaporated between the pulses. The increase of the co-extracted electron current density is accompanied by a strong increase of the cesium density of neutral cesium particles. To reduce the co-extracted electrons, the cesium evaporation is increased up to the limit to which breakdowns occur together with the magnetic field strength, the latter, with the cost of a reduced negative ion current (Heinemann et al. 2017).

An option to increase the flux of neutral cesium particles (which are not influenced by any potential barrier) toward the grid system is the evaporation of cesium close to the plasma grid. In this plasma region, the electron temperature is much lower than at the position of the cesium ovens such that the ionization of cesium is strongly diminished. This can be realized by the cesium shower concept shown in the left part of Fig. 16.15 (Wunderlich et al. 2021c). The orifices for the evaporation are located on the two vertical segments of the shower loop and are directed toward the PG. Besides providing directly neutral cesium particles to the grid surface, the shower offers controllable cesiation of the PG because it does not rely on plasma assisted redistribution of cesium from chamber surfaces. The valve allows for starting evaporation only during plasma pulses on dedicated time slots supporting the cesium oven when needed such that cesium leakage into the grid system can be minimized. The onset of the cesium measured in front of the plasma

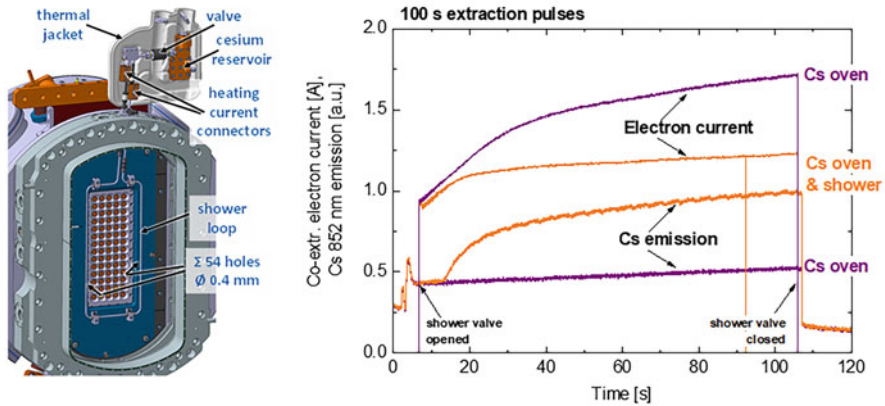


Fig. 16.15 Left: drawing of the cesium shower line around the beamlet group at prototype ion source at BUG. Right: time traces of the co-extracted electron current and the Cs emission line at 852 nm taken during two 100 s extraction pulses in hydrogen, with and without additional cesium evaporation from the cesium shower started at the beginning of the pulse. (Figure adapted from Wunderlich et al. (2021c))

grid by emission spectroscopy takes place roughly after 10 s (Fig. 16.15, right part) and stabilized the co-extracted electrons. Although these first measurements give very promising results, reliable operation of such systems, particularly for the larger sources, needs to be demonstrated first before its implementation in the ion source concept.

16.5 Activities Beyond ITER

For NBI systems of newly planned fusion devices or those being under construction, the modular RF-driven ion source concept is very attractive because the maintenance efforts of the ion source itself are lower than those of arc-driven sources for which regular exchange of filaments is mandatory and because of the return of experience from ITER developments and, in a next stage, its operation.

16.5.1 RF Sources for a DEMO: Worldwide Activities

An intermediate step between the ITER experiment and a commercial fusion power plant, a DEMOnstration reactor (DEMO), is targeted by many countries around the world, accompanied by fusion devices addressing open points to be solved on the way to the power plant. Examples are the China Fusion Engineering Test Reactor (CFETR) (Wan et al. 2017), the Korean fusion demonstration reactor (K-DEMO)

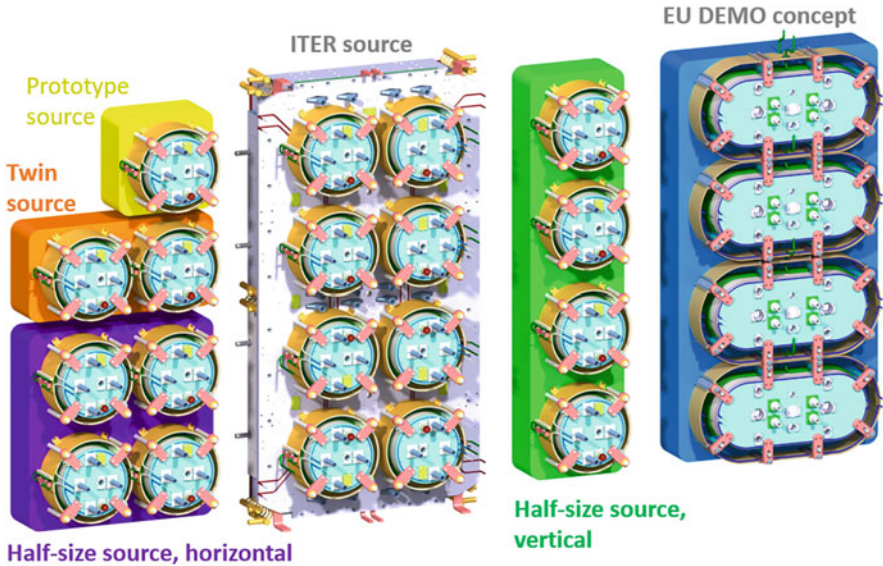


Fig. 16.16 RF sources based on the modular concept in use or under consideration in different facilities. The four racetrack-shaped drivers reflect the concept for a beam source for EU-DEMO based on an ITER size ion source

(Kim et al. 2015), and the Italian Divertor Test Tokamak (DTT) (Albanese et al. 2017) all of them with NBI systems based on RF sources. In Europe, the EU-DEMO is in the design phase (Federici et al. 2021) with the NBI system as one of the options for heating and current drive (Tran et al. 2022).

The selected RF source design is adapted to the ion source requirements for the specific beamline. Development programs started at various research institutes based on the cylindrical prototype source concept. The variations presently under consideration are sketched in Fig. 16.16: the prototype source, the Twin source, the vertical half-size source, and the horizontal half-size source. The substitution of two cylindrical drivers by a racetrack-shaped one for the ITER size source is illustrated Fig. 16.16 and discussed in the next section.

In the present design of the NBI for an EU-DEMO, the ion source concept based on negative deuterium ions relies on the return of experience from ITER. The main differences concern the availability and reliability of the ion source in the nuclear environment and the extended pulse duration. The foreseen repetitive operation for 2 h or longer imposes challenges on the cesium management system. Other modifications like efficient RF power coupling, number of drivers and their arrangements for optimized plasma generation, magnetic filter field configuration or alternatives to generate a uniform plasma with proper plasma parameters in front of the extraction system, or grid systems with enhanced transparency and improved beam optics are modifications under investigation within the EUROfusion consortium (Tran et al. 2022).

16.5.2 Racetrack-Shape RF Drivers

With the aim to reduce the RF power consumption for similar ion source performance and to avoid the powering of two cylindrical drives by one RF generator and thus to ease the RF matching, the concept of (re)using racetrack-shaped drivers was taken up for the EU-DEMO NBI. For an ITER size source, this results in four racetrack-shaped drivers as illustrated in Fig. 16.16, right part, each connected to one RF generator. The vertical stacking maintains the ability to compensate vertical plasma asymmetries by adjusting the RF power to each driver. In contrast to the already proven RF-driven racetrack-shaped ion source used for positive ions (Streibl et al. 2003; Franzen et al. 2001) in short pulse operation (about 10 s) where initial cooling is sufficient, the technology for steady-state operation is to be developed. This concerns in particular the winding of the large RF coil and its fixation to avoid any breakdowns and the water-cooled Faraday screen. In the short pulse mode, a racetrack-shaped driver mounted at the expansion chamber at the prototype test facility BATMAN was successfully tested (Wimmer et al. 2017).

A test of two racetrack drivers on the half-size ITER source would represent the next step in such a development. The use of state-of-the-art solid-state RF generators have already proven to facilitate the plasma matching compared with tube-based oscillators and to be more efficient without the need for water cooling. Together with the RF coupling efficiency, which is slightly better in deuterium than in hydrogen (Sect. 16.2.3), the situation with respect to the RF coupling at the ITER sources has the potential to be very much improved as more than 280 kW of the installed 800 kW power are not coupled to the plasma in the ITER case. Further studies of optimizing the axial dimension of the driver, or other components, are subject of investigations with a self-consistent fluid code presently available in 2-D being extended to 3-D in a next step to take the magnetic filter field properly into account (Zielke et al. 2021b, 2022).

The strong dependence of the ion source performance on pressure and the poor reliability of the plasma sustainment at lower pressures than 0.2 Pa almost rule out operation of the ion source operation below 0.2 Pa (Sect. 16.2.5) although the reduced stripping loss would very much relax the demands on the achievable negative ion current density.

16.5.3 Cesium Consumption

The cesium consumption of a test facility is less relevant than the one of an ion source integrated in a beamline where high availability and reliability are required. Refilling the cesium reservoir of the ovens and thus the exchange of the cesium oven is identified to be one of the leading items for maintenances. Consequently, reducing the cesium consumption and methods for improved cesium management

or alternative evaporation techniques like the cesium shower (Sect. 16.4.3) is under investigation in the test facilities.

The estimation for ITER is based on the evaporation rate of 10 mg/h used in the first prototype sources equipped with one Cs oven. Considering the required beam time and the larger plasma grid area a consumption of 40 g/yr was estimated for ITER (100 d with 20 pulses, 400 s each) using three Cs ovens (Hemsworth et al. 2009). In case of a steady-state DEMO, the estimation yields 350–700 g/yr with 80% availability through the year on the basis of using a similar source as for ITER (Franzen and Fantz 2014). With improved cesium control supported by careful monitoring of the cesium density in the ion source, the cesium evaporation rate is reduced below 5 mg/h for the prototype source and in the range of 2–3 mg/h for each of the two ovens in the half-size source. On the other hand, the higher dynamics of the co-extracted electrons in deuterium requires higher evaporation rates (currently a factor two to three), in particular in long pulses. The usage of a total evaporation rate of 5 mg/h in the ITER-like source for the EU-DEMO scenario results in a consumption of 100–200 g/year (Tran et al. 2022). It needs to be highlighted that the data base is weak at this point and efforts are undertaken to determine the consumption in long pulse operation in deuterium. In addition, the evaporation rates depend strongly on the base pressure, which determines the impurity flux (mostly water) onto the cesiated surface.

Extrapolations from the prototype source or the half-size source to the full-size source of ITER and for a DEMO are performed by using a cesium transport code (CsFlow3D), which was benchmarked at the prototype source (Mimo et al. 2017). To keep the depletion of the cesium flux (neutrals) onto the plasma grid during long pulses at the same level as in the half-size source, a two times higher evaporation rate had to be used for the larger ITER source configuration (Tran et al. 2022). Using a cesium shower concept for evaporation where 70% of the total neutral flux are neutrals instead of 30% (using the ovens in the backplate) stabilizes the depletion already at 50 s resulting in three times higher cesium fluxes impinging the PG for long pulses. Such simulations assist the effort to improve the cesium management, which is still a major challenge to overcome, in particular in view of cesium consumption for a DEMO device.

An option would be to identify alternative materials for the PG surface, that is, the surface where impinging atoms or ions are converted to negative ions, for which investigations are ongoing (see, e.g., (Fantz et al. 2017)). None of the materials tested so far under ion source relevant conditions showed the performance of cesiated surfaces and offers, like cesium, the opportunity to actively refresh the layer on the grid in case of a surface deterioration. Following the route to operate the ion source in the volume mode by relying solely on the volume process via the dissociative attachment would have the consequence that roughly an order of magnitude lower ion current densities can be achieved at the required low pressure of 0.3 Pa or less. In addition, the co-extracted electron current would be intolerably high for the grid system.

16.5.4 Reliability and Availability

The ion source for NBI of a DEMO reactor or a fusion power plant is subject of the RAMI criteria: reliability, availability, maintainability, and inspectability. Attempts of a RAMI evaluation of the RF-driven ion source including the accelerator with special emphasis on its modularity revealed a slight preference for two modules with two racetrack drivers each compared with 20 modules with one circular driver each (Agostinetti et al. 2020). The return of experience from ITER and the accompanying test facilities is an essential input for the evaluation. Plasma production by the RF-driven concept is regarded as highly reliable. On the other hand, the most failure modes were identified for the ion source performance at the required parameters. The latter is directly connected to the need of cesium, in particular to control the co-extracted electrons.

The elements connected to cesium are the functioning of the cesium evaporation, the cesium distribution, the deterioration of the cesium layer, and its recovery, which can lead to the necessity to exchange the ovens and even to exchange the ion source, which determines the maintenance interval. Other aspects are the plasma uniformity and the uniformity of the cesium layer over the large plasma grid surface, which has consequences on the uniformity of co-extracted electrons and thus the local heat loads on the large extraction grid. Any inhomogeneity of the negative ions has consequences on the beam divergence, which then may result in losses and heat loads on the beamline components and reduced power for the fusion plasma.

Among the open points in long-term operation are the reliability of the coating of the inner surfaces with molybdenum or other materials, for which self-sputtering is reduced compared with copper, and the thickness of the coating at the backplate of the source, which is subject to bombardment of backstreaming positive ions, creating heat spots. Here, the upcoming experience with steady-state extraction in long pulses in the large sources will give highly valuable input.

A consideration for increased reliability would be to relax the demands on the achievable ion current density or increase slightly the filling pressure. Reduced losses in the accelerator system and improved neutralization concepts might offer this route in future.

16.6 Conclusion and Outlook

The development of RF-driven ion sources for positive ions for the neutral beam injection system of fusion development, started in the 1990s, paved the way to the development of negative hydrogen ion sources for the international fusion experiment ITER. The step-wise approach for the size-scaling concept from the prototype size source to the full-size ITER source with the intermediate step of the half-size ion source resulted already and still contributes to the achievement of parameters required for ITER's NBI system. Among them are lessons learned concerning

technological and physics challenges. The experience gained in operation of large RF-driven ion sources based on the modular RF driver concept is an additional asset. The modular RF-concept is adapted to many test facilities around the world to gain experience with RF-driven sources for NBI either for the present fusion devices in the respective country or for ITER and in view of a DEMO.

Among the challenges still to overcome is the achievement of the source performance in deuterium for the ITER sources where the co-extracted electrons are the limiting factor for the long pulse operation. Experience in steady-state extraction and measures to suppress the co-extracted electrons by biasing surfaces in the interplay with the magnetic filter field configuration in the RF source concept will be subject to upcoming studies. The full-size ITER source at SPIDER has already given valuable input for the large sources operated in a vacuum chamber and will contribute after the upgrade to the success of the ITER sources. The start of the prototype of ITER's heating beams, MITICA, is an intermediate step toward the HNB at ITER and will give insights into the extraction and acceleration to 1 MeV of 40 A negative ion beam from a large-size RF source for 1 h. For the diagnostic beam the current densities of hydrogen, being even higher than the one for the HNB in hydrogen, in pulsed operation (3 s on-time, 20 s off-time, modulated at 5 Hz) are to be achieved; the start of operation of the DNB at the INTF is crucial here. Besides the technology and scientific achievements, the training of personal and young scientist is an important point of utmost relevance as well.

Acknowledgments The author thanks the NBI team at IPP for the discussions and contributions to this work and acknowledges its dedication to the RF source development for NBI systems.

References

- P. Agostinetti, T. Franke, U. Fantz, C. Hopf, N. Mantel, M.Q. Tran, *Fusion Eng. Des.* **159**, 111628 (2020)
- R. Albanese et al., *Nucl. Fusion* **57**, 016010 (2017)
- M. Bacal, *Nucl. Instrum. Methods Phys. Res. Sect. B* **37–38**, 28 (1989)
- M. Boldrin et al., *Fus. Eng. Des.* **164**, 112170 (2021)
- F. Bonomo, I. Mario, D. Wunderlich, U. Fantz, *Fusion Eng. Des.* **159**, 111760 (2020)
- S. Briefi, U. Fantz, the NNBI Team, *AIP Conf. Proc.* **2052**, 040005 (2018)
- S. Briefi, D. Zielke, D. Rauner, U. Fantz, *Rev. Sci. Instrum.* **93**, 023501 (2022)
- A. Chakraborty, C. Rotti, M. Bandyopadhyay, M.J. Singh, R. Nair, S. Shah, U.K. Baruah, R. Hemsworth, B. Schunke, *IEEE Trans. Plasma Sci.* **38**, 248 (2010)
- A.K. Chakraborty et al., *Nucl. Fusion* **59**, 112024 (2019)
- G. Chitarin, N. Marconato, P. Agostinetti, G. Serianni, P. Sonato, *AIP Conf. Proc.* **1515**, 217 (2013)
- G. Chitarin, P. Agostinetti, D. Aprile, N. Marconato, P. Veltri, *Rev. Sci. Instrum.* **85**, 02B317 (2014)
- G. Chitarin, P. Agostinetti, D. Aprile, N. Marconato, P. Veltri, *AIP Conf. Proc.* **1655**, 040008 (2015)
- D. Ciric et al., *Fusion Eng. Des.* **82**, 610 (2007)
- M. Claessens, *ITER: The Giant fusion reactor, Bringing a Sun to Earth* (Springer Nature Switzerland AG, 2020)
- S. Cristofaro, R. Friedl, U. Fantz, *Plasma Res. Express* **2**, 035009 (2020)
- S. Cristofaro, R. Friedl, U. Fantz, *Plasma* **4**, 94 (2021)

- N. den Harder, G. Orozco, R. Nocentini, B. Heinemann, A. Hurlbatt, F. Bonomo, U. Fantz, P. Veltri, *Fusion Eng. Des.* **173**, 112837 (2021)
- U. Fantz, H. Falter, P. Franzen, D. Wunderlich, M. Berger, A. Lorenz, W. Kraus, P. McNeely, R. Riedl, E. Speth, *Nucl. Fusion* **46**, S297 (2006)
- U. Fantz, P. Franzen, W. Kraus, D. Wunderlich, R. Gutser, M. Berger, NNBI Team, *AIP Conf. Proc.* **1097**, 265 (2009)
- U. Fantz, C. Hopf, D. Wunderlich, R. Friedl, M. Fröschle, B. Heinemann, W. Kraus, U. Kurutz, R. Riedl, R. Nocentini, L. Schiesko, *Nucl. Fusion* **57**, 116007 (12 pp) (2017) <https://doi.org/10.1088/1741-4326/aa778b>
- U. Fantz, P. Franzen, W. Kraus, L. Schiesko, C. Wimmer, D. Wunderlich, *AIP Conf. Proc.* **1655**, 040001 (2015)
- U. Fantz, F. Bonomo, M. Fröschle, B. Heinemann, A. Hurlbatt, W. Kraus, L. Schiesko, R. Nocentini, R. Riedl, C. Wimmer, *Fusion Eng. Des.* **46**, 212 (2019)
- U. Fantz, D. Wunderlich, R. Riedl, B. Heinemann, F. Bonomo, the NNBI-Team, *Fusion Eng. Des.* **156**, 111609 (2020)
- U. Fantz, S. Briefi, A. Heiler, C. Wimmer, D. Wunderlich, *Front. Phys.* **9**, 709651 (2021)
- U. Fantz, S. Briefi, M. Fröschle, N. den Harder, A. Heiler, B. Heinemann, C. Hopf, A. Hurlbatt, M. Lindqvist, F. Merk, A. Mimo, R. Nocentini, G. Orozco, G. Starnella, C. Wimmer, D. Wunderlich, D. Yordanov, D. Zielke, *J. Phys.: Conf. Ser.* **2244**, 012049 (2022) <https://doi.org/10.1088/1742-6596/2244/1/012049>
- G. Federici, C. Baylard, A. Beaumont, J. Holden, *Fusion Eng. Des.* **173**, 112960 (2021)
- M. Föschle, U. Fantz, P. Franzen, W. Kraus, R. Nocentini, L. Schiesko, D. Wunderlich, NNBI-Team, *Fusion Eng. Des.* **88**, 1015 (2013)
- P. Franzen, U. Fantz, *Fusion Eng. Des.* **89**, 2594 (2014)
- P. Franzen, S. Obermayer, J. Schäffler, A. Stäbler, E. Speth, O. Vollmer, *Fusion Eng. Des.* **56–57**, 487 (2001)
- P. Franzen, H. Falter, B. Heinemann, C. Martens, U. Fantz, M. Berger, S. Christ-Koch, M. Fröschle, D. Holtum, W. Kraus, S. Leyer, P. McNeely, R. Riedl, R. Süß, S. Obermayer, E. Speth, D. Wunderlich, *Fusion Eng. Des.* **82**, 407 (2007)
- P. Franzen, L. Schiesko, M. Fröschle, D. Wunderlich, U. Fantz, the NNBI Team, *Plasma Phys. Control. Fusion* **53**, 115006 (2011)
- R. Friedl, U. Fantz, *Rev. Sci. Instrum.* **85**, 02B109 (2014)
- G. Fubiani, L. Garrigues, J.P. Boeuf, *Phys. Plasmas* **25**, 023510 (2018)
- M. Hanada, A. Kojima, T. Inoue, K. Watanabe, M. Taniguchi, M. Kashiwagi, H. Tobar, N. Umeda, N. Akino, M. Kazawa, K. Oasa, M. Komata, K. Usui, K. Mogaki, S. Sasaki, K. Kikuchi, S. Nemoto, K. Ohshima, Y. Endo, T. Simizu, N. Kubo, M. Kawai, L.R. Grisham, *AIP Conf. Proc.* **1390**, 536 (2011)
- M. Hanada, A. Kojima, H. Tobar, R. Nishikiori, J. Hiratsuka, M. Kashiwagi, N. Umeda, M. Yoshida, M. Ichikawa, K. Watanabe, Y. Yamano, L.R. Grisham, *Rev. Sci. Instrum.* **87**, 02B322 (2016)
- B. Heinemann, H. Falter, U. Fantz, P. Franzen, M. Fröschle, R. Gutser, W. Kraus, R. Nocentini, R. Riedl, E. Speth, A. Stäbler, D. Wunderlich, P. Agostinetti, T. Jiang, *Fusion Eng. Des.* **84**, 915 (2009)
- B. Heinemann, U. Fantz, P. Franzen, M. Fröschle, M. Kircher, W. Kraus, C. Martens, R. Nocentini, R. Riedl, B. Ruf, L. Schiesko, C. Wimmer, D. Wunderlich, the NNBI-Team, *Fusion Eng. Des.* **88**, 512 (2013)
- B. Heinemann, U. Fantz, W. Kraus, L. Schiesko, C. Wimmer, D. Wunderlich, F. Bonomo, M. Fröschle, R. Nocentini, R. Riedl, *New J. Phys.* **19**, 015001 (2017)
- B. Heinemann, U. Fantz, W. Kraus, D. Wunderlich, F. Bonomo, M. Fröschle, I. Mario, R. Nocentini, R. Riedl, C. Wimmer, *Fusion Eng. Des.* **136**, 569 (2018)
- R.S. Hemsworth, T. Inoue, *IEEE Trans. Plasma Sci.* **33**, 1799 (2005)
- R. Hemsworth, H. Decamps, J. Graceffa, B. Schunke, M. Tanaka, M. Dremel, A. Tanga, H.P.L. De Esch, F. Geli, J. Milnes, T. Inoue, D. Marcuzzi, P. Sonato, P. Zaccaria, *Nucl. Fusion* **49**, 045006 (2009)

- R. Hemsworth, D. Boilson, P. Blatchford, M. Dalla Palma, G. Chitarin, H. de Esch, F. Geli, M. Dremel, J. Graceffa, D. Marcuzzi, G. Serianni, D. Shah, M. Singh, M. Urbani, P. Zaccaria, *New J. Phys.* **19**, 025005 (2017)
- J. Hiratsuka, M. Kashiwagi, M. Ichikawa, N. Umeda, G.Q. Saquilayan, H. Tobar, K. Watanabe, A. Kojima, M. Yoshida, *Rev. Sci. Instrum.* **91**, 023506 (2020)
- N. Holtkamp for the ITER Project Team, *Fusion Eng. Des.* **82**, 427 (2007)
- A. Hurlbatt et al., *AIP Adv.* **11**, 025330 (2021)
- Y. Ikeda, N. Umeda, N. Akino, N. Ebisawa, L. Grisham, M. Hanada, A. Honda, T. Inoue, M. Kawai, M. Kazawa, K. Kikuchi, M. Komata, K. Mogaki, K. Noto, F. Okano, T. Ohga, K. Oshima, T. Takenouchi, Y. Tanai, K. Usui, H. Yamazaki, T. Yamamoto, *Nucl. Fusion* **46**, S211 (2006)
- ITER, 2020, www.iter.org
- ITER EDA Documentation Series No. 24; ITER Technical Basis, Vienna: INTERNATIONAL ATOMIC ENERGY AGENCY (2002)
- K. Kim, K. Im, H.C. Kim, S. Oh, J.S. Park, S. Kwon, Y.S. Lee, J.H. Yeom, C. Lee, G.-S. Lee, G. Neilson, C. Kessel, T. Brown, P. Titus, D. Mikkelsen, Y. Zha, *Nucl. Fusion* **55**, 053027 (2015)
- A. Kojima, J. Hiratsuka, N. Umeda, M. Hanada, M. Kashiwagi, M. Yoshida, M. Ichikawa, R. Nishikiori, K. Watanabe, H. Tobar, L.R. Grisham, *Fusion Eng. Des.* **123**, 236 (2017)
- W. Kraus, M. Berger, U. Fantz, P. Franzen, M. Fröschle, B. Heinemann, R. Riedl, E. Speth, A. Stäbler, D. Wunderlich, *Rev. Sci. Instrum.* **79**, 02C108 (2008)
- W. Kraus, L. Schiesko, C. Wimmer, U. Fantz, B. Heinemann, *AIP Conf. Proc.* **1869**, 030006 (2017)
- S. Matsuda et al., *Fusion Eng. Des.* **5**, 85 (1987)
- P. McNeely, D. Wunderlich, the NNBI-Team, *Plasma Sources Sci. Technol.* **20**, 045005 (2011)
- A. Mimo, C. Wimmer, D. Wunderlich, U. Fantz, *AIP Conf. Proc.* **1869**, 030019 (2017)
- A. Mimo, C. Wimmer, D. Wunderlich, U. Fantz, *AIP Conf. Proc.* **2052**, 040009 (2018)
- K. Pandya et al., *AIP Conf. Proc.* **1869**, 030009 (2017)
- E. Sartori, et al., First operations with caesium of the negative ion source SPIDER, *Nucl. Fusion* **62**, 086022 (2022) <https://doi.org/10.1088/1741-4326/ac715e>
- G. Serianni et al., *Rev. Sci. Instrum.* **91**, 023510 (2020)
- M.J. Singh, M. Bandyopadhyay, C. Rotti, N.P. Singh, S. Shah, G. Bansal, A. Gahlaut, J. Soni, H. Lakdawala, H. Waghela, I. Ahmed, G. Roopesh, U.K. Baruah, A.K. Chakraborty, *Fusion Eng. Des.* **86**, 732 (2011)
- M.J. Singh et al., *Nucl. Fusion* **59**, 096034 (2019)
- E. Speth, M. Ciric, J.H. Feist, P. Frank, B. Heinemann, W. Kraus, F. Probst, R. Riedl, R. Trainham, O. Vollmer, R. Wilhelm, *Fusion Eng. Des.* **46**, 383 (1999)
- E. Speth, H. Falter, P. Franzen, U. Fantz, M. Bandyopadhyay, S. Christ, A. Encheva, M. Fröschle, D. Holtum, B. Heinemann, W. Kraus, A. Lorenz, C. Martens, P. McNeely, S. Obermayer, R. Riedl, R. Süß, A. Tanga, R. Wilhelm, D. Wunderlich, *Nucl. Fusion* **46**, S220 (2006)
- B. Streibl, P.T. Lang, F. Leuterer, J.-M. Noterdaeme, A. Stäbler, Chapter 2: Machine design, fueling, and heating in ASDEX upgrade. *Fusion Sci. Technol.* **44**(3), 578–592 (2003)
- F. Taccogna, P. Minelli, S. Longo, *Plasma Sources Sci. Technol.* **22**, 045019 (2013)
- Y. Takeiri, *Rev. Sci. Instrum.* **81**, 02B114 (2010)
- Y. Takeiri, O. Kaneko, K. Tsumori, Y. Oka, K. Ikeda, M. Osakabe, K. Nagaoka, E. Asano, T. Kondo, M. Sato, M. Shibuya, *Nucl. Fusion* **46**, S199 (2006)
- V. Toigo et al., *New J. Phys.* **19**, 085004 (2017a)
- V. Toigo et al., *Nucl. Fusion* **57**, 086027 (2017b)
- V. Toigo et al., *Fusion Eng. Des.* **168**, 112622 (2021)
- M.Q. Tran et al., *Fusion Eng. Des.* **182**, 113159 (2022)
- K. Tsumori, M. Wada, *New J. Phys.* **19**, 045002 (2017)
- Y. Wan et al., *Nucl. Fusion* **57**, 102009 (2017)
- C. Wimmer, L. Schiesko, U. Fantz, *Rev. Sci. Instrum.* **87**, 02B310 (2016)
- C. Wimmer, U. Fantz, E. Aza, J. Jovović, W. Kraus, A. Mimo, L. Schiesko, *AIP Conf. Proc.* **1869**, 030021 (2017)
- C. Wimmer, I. Mario, D. Wunderlich, U. Fantz, the NNBI-Team, *AIP Conf. Proc.* **2052**, 040003 (2018)

- D. Wunderlich, L. Schiesko, P. McNeely, U. Fantz, P. Franzen, the NNBI-Team, *Plasma Phys. Control. Fusion* **54**, 125002 (2012)
- D. Wunderlich, W. Kraus, M. Fröschle, R. Riedl, U. Fantz, B. Heinemann, NNBI-Team, *Plasma Phys. Control. Fusion* **58**, 125005 (2016)
- D. Wunderlich, W. Kraus, M. Fröschle, R. Riedl, U. Fantz, B. Heinemann, *AIP Conf. Proc.* **1869**, 030003 (2017)
- D. Wunderlich, R. Riedl, U. Fantz, B. Heinemann, W. Kraus, the NNBI team, *Plasma Phys. Control. Fusion* **60**, 085007 (2018)
- D. Wunderlich, R. Riedl, F. Bonomo, I. Mario, U. Fantz, B. Heinemann, W. Kraus, the NNBI Team, *Nucl. Fusion* **59**, 084001 (2019a)
- D. Wunderlich, R. Riedl, I. Mario, A. Mimo, U. Fantz, B. Heinemann, W. Kraus, *Rev. Sci. Instrum.* **90**, 113304 (2019b)
- D. Wunderlich, R. Riedl, M. Fröschle, U. Fantz, B. Heinemann, *Plasma* **4**, 172 (2021a)
- D. Wunderlich, S. Briefi, R. Friedl, U. Fantz, *Rev. Sci. Instrum.* **92**, 123510 (2021b)
- D. Wunderlich, C. Wimmer, R. Riedl, F. Bonomo, M. Fröschle, I. Mario, A. Mimo, D. Yordanov, U. Fantz, B. Heinemann, *Nucl. Fusion* **61**, 096023 (2021c)
- D. Wunderlich, I.M. Montellano, M. Lindqvist, A. Mimo, S. Mochalskyy, U. Fantz, *J. Appl. Phys.* **130**, 053303 (2021d)
- D. Zielke, S. Briefi, U. Fantz, *J. Phys. D* **54**, 155202 (2021a)
- D. Zielke, D. Rauner, S. Briefi, S. Lishev, U. Fantz, *Plasma Sources Sci. Technol.* **30**, 065011 (2021b)
- D. Zielke, S. Briefi, S. Lishev, U. Fantz, *J. Phys.: Conf. Ser.* **2244**, 012030 (2022) <https://doi.org/10.1088/1742-6596/2244/1/012030>

Chapter 17

Ion Source Engineering and Technology



Dan Faircloth

Abstract The principles of engineering and technology applied to ion sources are discussed along with important system design decisions that must be made. The techniques to power the ion source plasma are outlined. The use of magnetic fields to manipulate the plasma is described. High voltages are used extensively in ion sources to accelerate particles, the fundamentals of high-voltage design are detailed, and the importance of the triple junction effect is discussed along with high-voltage breakdown protection methods. The basics of earthing are outlined, and compliance with essential safety regulations are emphasised. The design philosophy and reliability of personnel protection interlock systems are discussed. Control and diagnostic systems are briefly covered. Hydrogen and caesium delivery is outlined along with vacuum system design. The value of documentation systems for mechanical builds and electrical drawings is raised, which, along with failure mode analysis, is essential to delivering good ion source availability in the long term.

Keywords Ion source · Negative ion · Engineering · Technology · System design · High-voltage design · Triple junctions · High-voltage protection · Vacuum · Regulations · Earthing · Safety · Interlocks

17.1 Introduction

Ion sources employ technologies to implement techniques that exploit physics processes. The application of engineering and technology allows ion sources to safely and reliably deliver beams for accelerator facilities.

D. Faircloth (✉)
STFC UKRI, Oxfordshire, UK
e-mail: dan.faircloth@stfc.ac.uk

© The Author(s), under exclusive license to Springer Nature Switzerland AG 2023
M. Bacal (ed.), *Physics and Applications of Hydrogen Negative Ion Sources*,
Springer Series on Atomic, Optical, and Plasma Physics 124,
https://doi.org/10.1007/978-3-031-21476-9_17

465

Permanent magnets, field coils, high-voltage insulators, power supplies, and vacuum pumps are all examples of the technologies employed. These technologies are designed and engineered into systems: high-voltage systems, RF systems, vacuum systems, cooling systems, gas feed systems, caesium delivery systems, control systems, diagnostic systems, protection systems and interlock systems. These systems not only are essential to reliably making an ion source work but also ensure compliance with laws and regulations.

The key techniques and technologies used to deliver the high ion source availabilities required by accelerator facilities will be discussed. The pros and cons of different overall system design decisions will be explored.

17.2 Powering the Plasma

17.2.1 Accelerating Electrons

In most negative ion sources (apart from the Cs Sputter Source), the plasma is produced by an electrical discharge. The discharge primarily relies on electron impact ionisation: applied electric fields accelerate free electrons, which impact on the atoms, molecules and ions present in the plasma chamber, ionising them to produce more electrons and ions.

In negative ion sources, there are two different ways to apply an electric field: (1) by applying DC or RF voltages to electrodes, known as a capacitively coupled plasma (CCP) or (2) by applying a time varying current to an RF coil that generates a time varying magnetic field that induces the time varying electric field, known as an inductively coupled plasma (ICP).

It is possible to couple a high frequency electromagnetic wave into a plasma chamber, but for typical plasma chamber dimensions measured in centimetres, that would require GHz frequencies. Higher frequency discharges tend to produce higher energy electrons, which are not conducive to H⁻ production, so microwave discharges tend not to be used in negative ion sources.

17.2.2 CCP Power Supply

A typical discharge power supply will be required to deliver an output of 20–100 V and 1–100 A. The discharge will present a load in the order of 1 Ω to the power supply. The discharge has a negative voltage current characteristic that can cause problems for power supply regulation, so a low value series resistance is often put in series with the discharge.

17.2.3 ICP Power Supply

The RF coil is driven by an amplifier, via an RF coaxial line and matching network. RF powers are in the 1–100 kW range. Frequencies used are in the 1–10 MHz range. The RF coil presents a different impedance to the amplifier depending if a plasma is present or not, so frequency hopping can be employed to ensure the highest fields are maintained in the plasma chamber. The reactance of the coil produces a voltage drop along the length of the winding. As the coil current increases, so does the voltage across it, which means that for high power ICP, there will also be a significant electric field applied to plasma from the high-voltage end of the coil. So high power ICPs can also have a significant CCP component. The CCP component can be used to help ignite the plasma (see Sect. 17.10).

If the RF coil is moved outside the plasma chamber, the amount of capacitive coupling is reduced, which can reduce the overall plasma coupling efficiency.

17.3 Magnetic Fields

17.3.1 Magnetised Electrons

In negative ion sources, the applied magnetic fields are designed to act on electron motion not ion motion. The Lorentz force causes both ions and electrons to spiral around the magnetic field lines, but their radii of curvature are very different because of their hugely different masses. The spiral radii of the ions are significantly larger than the plasma chamber dimensions, so the ions are never able to complete a spiral revolution and their trajectories are only very slightly curved, whereas the spiral radii of the electron trajectories are significantly smaller than the plasma chamber dimensions. The electrons are ‘magnetized’ to the magnetic field lines by the Lorentz force. The electrons travel along the magnetic field lines in tight spirals. Magnetic field can be designed to control the electron distribution in plasma.

The spiral nature of the electron trajectories increases their path length, a longer path length means more opportunities for electron impact ionisation to take place, which is exploited in the Penning and magnetron source configurations shown in Fig. 17.1.

The multicusp field confinement shown in Fig. 17.2 also relies on making the electrons spiral around the field lines. The magnetic field gets stronger nearer the magnets causing the electrons to spiral on tighter radii. It is the space charge of the confined electrons that confines the heavy positive ions. Plasma does still leak out of the multicusp confinement configuration down the magnetic cusps, but fewer ions in total hit the plasma chamber walls than without the multicusp field present.

The electron trajectories shown in Figs. (17.1 and 17.2) are idealised. They show the trajectory that a single electron would take if there were no other particles present. In reality, the electron trajectories are more complex because of the

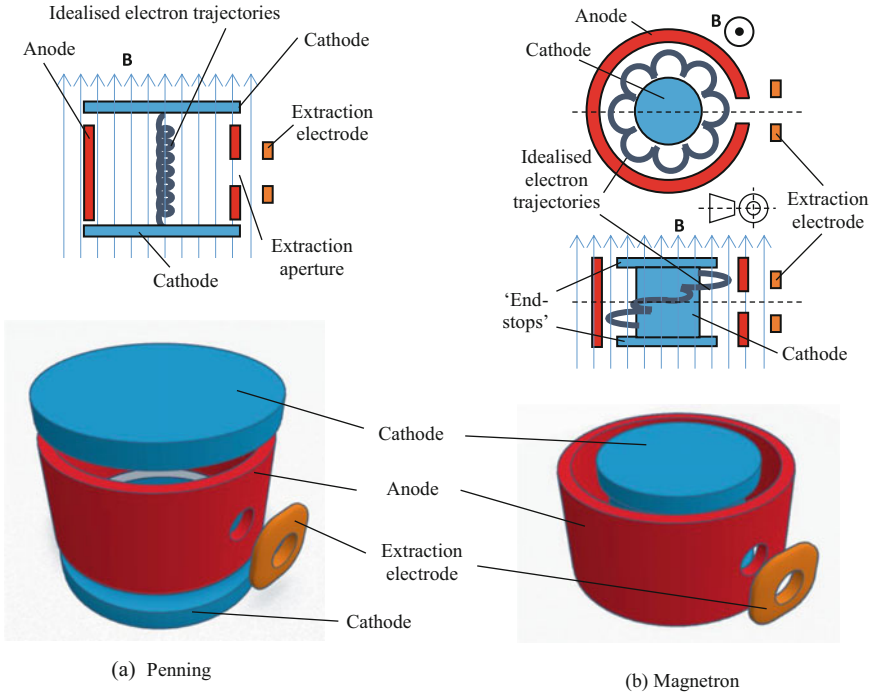


Fig. 17.1 The fundamental topologies of the Penning and magnetron ion source geometries and their idealised confined electron trajectories

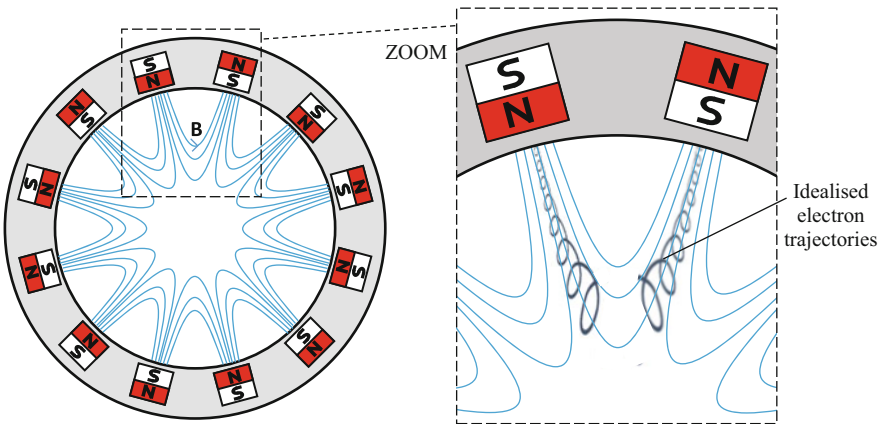


Fig. 17.2 Multicusp magnetic confinement field lines and idealised electron trajectories

interactions with the other charged and neutral atoms and molecules. The electrons will also have a range of energies, so for a given magnetic field, they will have a range of spiral radii.

A magnetic dipole field is also used to create a low temperature electron region for the negative ion volume production process. The dipole field acts as an electron energy filter: fast electrons are turned back on large radii, whereas slow electrons spiral on tiny radii and slowly drift across the dipole filter field. See (Bacal and Wada 2015) for a comprehensive review of negative ion production.

17.3.2 Making Magnetic Fields

Both electromagnets and permanent magnets are used to make the magnetic fields required in negative ion sources, although permanent magnets are predominantly used to create multicusp confinement fields. The typical dipole flux densities required are in the range of 0.1–0.3 T in the plasma chamber. For multicusp confinement fields, pole-face flux densities of the order 1 T are required. These magnetic flux densities can be easily achieved with either permanent magnets or standard normally conducting electromagnets.

The advantage of electromagnets is that their field strength can be easily varied whilst the ion source is running, which makes source tuning and optimisation very easy. The disadvantage of electromagnets is their size, and they will often require a magnetic circuit (yoke) to operate efficiently. Electromagnets require power supplies, and more often than not, their coil winding must be cooled to prevent overheating.

The advantage of permanent magnets is their compact size and no need for a power supply or cooling. The main disadvantage of permanent magnets is that the field they produce is not easy to vary. To reduce the magnetic field, either the amount of permanent magnetic material must be reduced (by removing permanent magnets), or the permanent magnet material must be physically moved. The field in a dipole created by two permanent magnets can be reduced by simply increasing the separation between the two permanent magnets. Or the permanent magnets can be rotated to reduce the field in a specific direction. If a magnetic circuit (yoke) is used, the permanent magnet material can be withdrawn from the magnetic circuit to reduce the dipole field, or a gap can be made in the magnetic circuit and the gap increased to reduce the dipole field. Whichever design is used, it requires extra mechanical engineering to make a variable field permanent magnet-based system because of the force loads present in the magnetic circuit and the motion control systems required.

Permanent magnets require handling precautions during ion source assembly because they can violently snap together in an uncontrolled manner. They can easily cause blood blisters if skin is caught between them. They can shatter and splinter if they are allowed to snap together in an uncontrolled manner, which can destroy the permanent magnets and present an eye injury hazard. The assembly procedure

for ion sources with permanent magnets must be carefully thought through and risk assessed. Assembly rigs might need to be developed to allow the permanent magnets to be safely inserted and non-magnetic spanners and screwdrivers acquired.

The magnetic material in permanent magnets is either neodymium ($\text{Nd}_2\text{Fe}_{14}\text{B}$) or samarium cobalt (SmCo_5 and $\text{Sm}_2\text{Co}_{17}$). Neodymium magnets are cheaper and readily available in a large range of sizes but have a significantly lower Curie temperature of between 310 and 370 °C, compared with 700–850 °C for samarium cobalt magnets. The magnets must be operated at significantly below (<100 °C) their Curie temperature to avoid demagnetisation.

17.4 Extracting Negative Ions

Negative ions are extracted from the plasma through a hole (the extraction aperture) in the anode by applying a positive voltage to an extraction electrode (puller electrode) as shown in Fig. 17.1. The applied voltage creates an extraction electric field in the extraction aperture, which repels positive ions. An equilibrium plasma surface forms in the extraction aperture called the plasma meniscus. The shape of the plasma meniscus surface depends on the dimensions of the aperture, the density of the plasma and the applied extraction field. The shape of the plasma meniscus plays an important role in beam formation as it constitutes the very first optical element of the beam transport.

Extracting electrons with negative ions is obviously unavoidable because they both have a negative charge. Dealing with the co-extracted electrons is one of the main challenges for high current negative ion source extraction systems. The ion source design must first try to minimise the amount of co-extracted electrons (possibly by using a biased plasma electrode), then design magnetic fields to separate the electrons from the negative ion beam, then safely dump the unwanted electrons. In some cases, the electron current can be 1000 times greater than the negative ion current itself. For high duty factor, high current sources a cooled electron dump is required, and care must be taken to ensure surface power densities on the dump do not exceed physical limits that would damage the dump material. The dumped electron beam might even need to be defocused or decelerated to prevent damage to the surface of the electron dump.

17.5 High Voltage

17.5.1 High Fields

High voltages are used all over ion sources for striking plasmas, driving plasmas, extracting beams from plasmas, accelerating beams, steering and focusing beams,

analysing beam energy and separating beam species. Specifically, it is the local electric field that is doing the work in all these examples. The charged particles feel a force proportional to the electric field they find themselves in. That electric field is often created by a power supply applying a high voltage to a conductor geometry. A notable exception is the electric field used to drive the electrons in an inductively coupled plasma (ICP): the time-varying electric field in the plasma chamber is induced by the time-varying magnetic field produced by a time-varying current flowing in a coil surrounding the plasma. However, in order to create high electric fields in the plasma chamber, high currents (100 s of A) must flow in the coil, and high currents flowing through the impedance of the coil generates high voltages (several kV). So high voltages are present on conductors; they are just not applied directly; they are created by the power delivered from the RF amplifier.

Commercial high-voltage components are designed to never breakdown at their rated operating voltage. This is achieved by keeping all the electric fields present in these devices to very conservative levels. It is worth noting that ion source extraction and acceleration systems often operate at fields that are significantly higher than conservative high-voltage design would normally allow. The beam optics design demands these high fields, but as a consequence, there will be a breakdown rate. The ion source and its ancillary equipment must be designed to tolerate breakdowns.

Needless to say, good high-voltage design is one of the keys to good ion source reliability.

17.5.2 High-Voltage Platform

In almost all particle accelerator applications (except some very simple tandem or biased target accelerators), the whole ion source must be biased at a high-voltage so that the beam can be accelerated to earth potential. This means that the ion source plasma chamber and the required ancillary equipment must all be ‘at volts’. This dictates the use of a high-voltage platform, upon which all the ancillary equipment is positioned, and to which the ion source and ancillary equipment is biased. A high-voltage platform requires isolation technologies such as: insulators to mechanically support the high-voltage platform and ion source; isolation transformers or motor alternator sets to provide mains power to ancillary equipment; isolated couplers to transfer RF power to the source; fibre optics to provide isolated timing, controls and interlocks; insulating pipes for gas and coolant delivery; demineralised and deionised coolant water; coolant conductivity monitoring and ion exchange filters to maintain low electrical conductivity of the coolant.

The platform voltage used is defined by the required injection energy of the next phase of the accelerator. The design of the ion source high-voltage system becomes more challenging as the platform voltage increases.

The beam is not usually accelerated directly to the full platform voltage in one accelerating gap. There are normally several accelerating gaps, starting with extraction from the plasma (the extraction gap) and ending in an earthed electrode.

In between the plasma and earth electrodes there could be several focusing, selection and acceleration gaps, composed of electrodes held at decreasing voltages. If Einzel lens focusing is employed, the voltages on the electrodes actually go up and down before finally reaching the earth electrode.

The voltages on all these electrodes must be reliably and stably produced by power supplies that are either biased to the high-voltage platform or to the laboratory earth.

17.5.3 Platform Bias Voltage Stability

For high-current pulsed-beam systems, platform voltage stability becomes an issue. This is because the beam current itself discharges the high-voltage platform, which causes the platform voltage to drop, resulting in the beam energy being lower at the end of the pulse than the start.

One solution to this problem is to increase the capacitance of the high-voltage platform so that it holds a larger reservoir of charge. With higher platform capacitances, the beam pulse removes proportionally less charge from the overall platform charge; thus, there is a smaller change in platform voltage during the pulse.

The acceptable beam energy drop during the length of the beam pulse is defined by the longitudinal acceptance of the next phase of the accelerator. Using a simple $Q = CV$ calculation, where Q is the charge in one beam pulse and V is the acceptable platform voltage drop, it is possible to work out the minimum platform capacitance required. For high current systems (>10 mA pulse current), the required platform capacitance will be in the order of 1 μF . This capacitance can be added to the natural platform capacitance by simply connecting a high-voltage capacitor in parallel with the platform. However, the stored energy in a high-voltage capacitor of this size presents a significant hazard, both to personnel and the equipment attached to the high-voltage platform. In the event of a high-voltage breakdown, the stored energy can destructively crater the electrodes.

Another solution to the platform voltage drop problem is to actively inject current into the high-voltage platform to compensate for the pulsed beam current that flows from the platform. This can be achieved with a 'bouncer circuit', so called because it provides a compensating voltage bounce to the drop caused by the beam current. This technique reduces the need to store a large amount of energy in a platform reservoir capacitor; instead, a lower voltage capacitor can be switched to inject just the right amount of charge to maintain the platform voltage. The bouncer circuit is connected in series with the platform power supply (on the earth side); it raises the platform power supply 'earth' voltage up to compensate for the voltage droop caused by the beam current.

Instead of 'bouncing' a DC platform power supply, a pulsed platform voltage power supply can be used. Pulsed power supplies are often used to apply voltages to the other electrodes in the ion source beam optics especially the extraction electrode. The pulsed power supply must provide enough current to maintain the voltage on the

accelerating electrodes during the pulse. The system must be carefully designed to regulate the flatness of the beam current and energy. An advantage of pulsed power supplies is that spark detection and pulse inhibition can be implemented, which can help to reduce electrode damage. The disadvantage of pulsed power supplies is additional complexity. High-voltage switching circuits are required: these can either be large arrays of solid state components (e.g. IGBT) or electron tube devices (e.g. Tetrode). The ISIS accelerator at RAL uses a tetrode-based extraction voltage power supply (Faircloth 2013) because electron tubes are very tolerant of high-voltage breakdown, which is both inevitable and necessary for conditioning. At low repetition rates (<10 Hz), pulse transformers can be used to remove the need for high-voltage switching; a good example of a pulse transformer-based system is CERN's LINAC4 ion source (Aguglia 2013).

For systems delivering DC (CW) beams, voltage drop is not a problem, and voltage stability is defined by the stability of the bias voltage power supply itself. There is no need for a large reservoir capacitor or complex-pulsed systems.

17.5.4 High-Voltage Enclosure Versus High-Voltage Room

The use of high voltages is an obvious safety hazard, which can only be protected against by preventing people getting too close. In ion source applications, the system designer has two options: (1) enclose the high voltages locally with earth bonded screens and panels positioned as close to the high-voltage conductors as practical and (2) build the whole ion source in a separate room or caged area to prevent people getting too close.

The first option is chosen when a compact ion source is required; it is best suited for mature ion source designs with no plans for upgrade. The ancillary equipment is held at volts (biased) on a small high-voltage platform inside a cabinet. All the power, voltage and signal connections from the ancillary equipment on the high-voltage platform are brought together and fed out of the cabinet through the inner conductor tube of a coaxial tube or duct that connects to the ion source. Everything inside the inner coax conductor is held at platform volts. The high-voltage platform and the ion source itself are electrically bonded via the inner coax. The outer conductor of this 'coaxial umbilical' connection between the ancillary equipment cabinet and the cabinet surrounding the ion source is held at earth potential making it safe to touch. For very simple ion sources with only one or two pieces of ancillary equipment to connect 'at volts', the 'coaxial umbilical' could be replaced with individual high-voltage cables going to each piece of ancillary equipment in the rack. Each high-voltage cable needs to be correctly terminated inside both the ion source cabinet and the ancillary equipment.

This first design option is compact and allows personnel to be close to the source when it is on, but its compactness limits the ability to modify, upgrade and investigate the ion source.

Say a larger power supply, other ancillary equipment or a diagnostic is required; there may not be enough space on the high-voltage platform within the cabinet. There may not be enough space within the inner coaxial conduit to route the new connections between the platform and ion source.

The second design option is to have all the ancillary equipment on an open high-voltage platform connected to an open ion source. The whole high-voltage platform, ancillary equipment and ion source are then enclosed in a large cage or room to prevent personnel getting close. For large particle accelerators this option is often used because the ion source and the rest of the accelerator are usually in a cage or shielded area anyway. This approach is more flexible, allowing equipment to be easily added to the high-voltage platform and connected to the ion source. Maintenance access is also easier, which is important for large operational machines.

Although one of these two design options must be chosen to connect the biased ancillary equipment to the ion source, both design options can be applied to the other high-voltage systems on the ion source. An obvious example is high-voltage coaxial cables, where high-voltage conductors are locally enclosed in an earthed outer conductor. Another example is the floating high-voltage circuits that are enclosed in power supplies. The overall topology of all the high-voltage systems connected to an ion source can be quite complicated.

17.5.5 High-Voltage Design

Good high-voltage design is all about controlling electric fields by designing insulator and electrode geometries. If the electric field is too high, electrical breakdown will occur.

Electric field is simply the potential difference between two points divided by their distance apart. The required voltage is defined for operational reasons, so often the only way to reduce the field is to increase the distance: make things larger.

The operating voltage for a high-voltage system should always be significantly lower than its breakdown voltage if the system is to operate reliably.

High-voltage design at the component level is as simple as making sure each component is rated to withstand the highest voltage that it could experience in a fault condition. This is easy for commercially available components because they come with a voltage rating. For custom components, an analysis of the electric field distribution is key to understanding the component's voltage withstand capabilities. Electric field distributions can easily be calculated using modelling software that can solve the Poisson equation using a finite cell technique. There are many commercial and open source software packages available.

17.5.6 Electrode Design

Electrodes are used to shape the electric field or as a source/sink for current. Field shaping electrodes are used for accelerating, deflecting and focusing beams. Current source/sink electrodes are used for plasma generation and beam dumps. Some electrodes such as extraction electrodes can be both field shaping and current sinking.

Electrode design obviously depends on application. For field shaping electrodes, the shape of the electrode is critical. For current source/sink electrodes, the sputtering resistance, thermal properties and current-carrying capability are critical.

If the electrode's aim is to shape fields whilst avoiding unwanted discharges, the key to high-voltage electrode design is smoothness, both microscopically and macroscopically. Electrodes should be physically smooth and have gently curving features with large radii.

Using modelling software, the electric fields produced by electrode geometries can be accurately calculated. This allows designs to be tested and optimized before manufacture. Extraction and beam acceleration electrodes can be modelled and simulated beams tracked through them.

Corona or stress shields are a type of field shaping electrode used to shield sharp points that would otherwise be prone to corona or other electrical discharges. Figure 17.3 shows two examples of how to shield a point with two different types of stress shield. The sharp points are usually unavoidable components like bolts or other fixtures and fittings. A stress shield increases the radius of these points by literally covering them up with rounded electrodes that are electrically connected so they are effectively at the same potential. Other names for corona or stress shields are guard rings, stress rings, or stress screens. 'Corona shield' should really only be used for stress shields in air.

Sputtering is where ions bombard electrode surfaces, knocking atoms off the surface. This process causes erosion and redistribution of the electrode surface material. Electrodes in plasmas suffer the most from sputtering. Sputtering eventually leads to macroscopic deformation and possibly failure of the plasma electrode

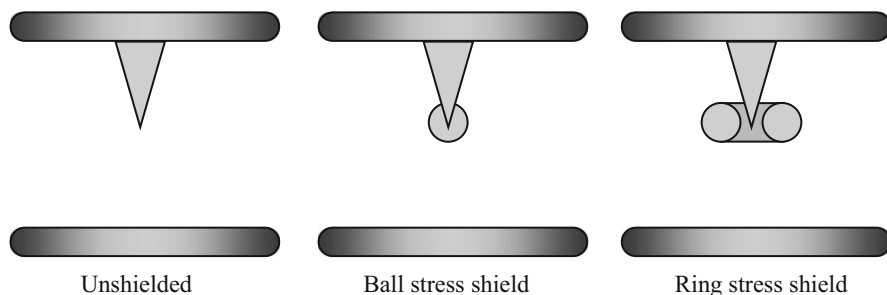


Fig. 17.3 Two examples of shielding a point with stress shields (sectional view)

system (Lettry 2012). The sputtered atoms land on electrodes in the hydrogen rich environment of the plasma chamber, producing hydrogen embrittled deposits that are prone to flaking off and causing problems (blockages and shorts). Sputtering processes also slowly deform the shape of extraction electrode apertures.

For cathodes in high-sputter environments, molybdenum or tungsten is often used. For field shaping electrodes, any conductive material can be used, so material choice is application-dependent.

For higher fields, electrodes must be smooth and highly polished to minimize surface irregularities. Polished 316 L stainless steel is commonly used for most applications.

For operation at very high field strengths in vacuum ($>10 \text{ MVm}^{-1}$ DC) where a breakdown rate is inevitable, titanium or its alloys give lower breakdown rates, especially when used as the cathode electrode material. Titanium–aluminium–molybdenum alloy and pure titanium produce approximately equal spark rates. Titanium–vanadium or titanium–manganese alloys have the lowest spark rates of all.

17.5.7 Insulator Design and Triple Junctions

Insulator design is based on the fact that an insulator's surface is the weakest part of a high-voltage system. Good design must: keep the electric field strength along its surface as low as possible, avoid field enhancement caused by triple junctions, and keep the surface clean.

Breakdowns on insulator surfaces cause permanent damage, so good HV system design must ensure that breakdowns are unlikely to occur across an insulator surface. The highest field strengths should be across electrode-to-electrode gaps with recoverable insulation (air, vacuum, oil and SF6) between. The field strengths along insulator surfaces should be kept as low as possible by making the insulators as long as is practically possible. Triple junctions that could initiate a discharge should be screened.

The triple junction effect is a localized geometric field enhancement caused when insulators of two different permittivities meet at an electrode. Triple junctions always exist at some scale because it is impossible to have a completely flat surface (see Fig. 17.4).

The triple junctions cause field enhancement because free space (air or vacuum) has a lower permittivity than the insulator. The higher permittivity insulator pushes the equipotential field lines into the free-space, increasing the field strength in that region.

Triple junctions are a problem because the field enhanced region is in the perfect position to initiate discharges on the insulator surface, which can then propagate across the entire insulator surface. The field enhancement effect actually gets worse,

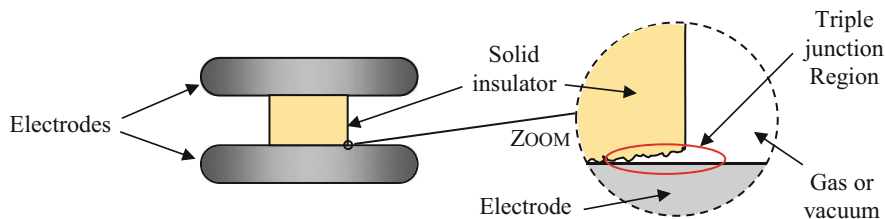


Fig. 17.4 Triple junctions occur where solid insulators, electrodes and free space meet

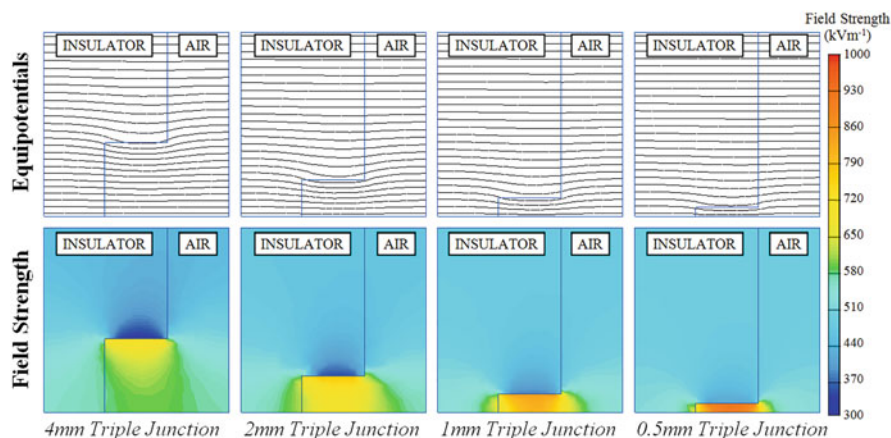


Fig. 17.5 Triple junction field enhancement increases as the gap become smaller

the smaller the triple junction becomes. This is illustrated in Fig. 17.5, which shows how the field in the free-space region increases as the triple junction gap is reduced from 4 mm to 0.5 mm in a 500 kV m^{-1} ambient field strength with an insulator relative permittivity of 2.2. At 0.5 mm, the field in the free-space region has almost doubled to 1000 kV m^{-1} .

It is interesting to note that there is negligible field enhancement around the sharp corner of the insulator shown in Fig. 17.5. The field enhancement is totally dominated by the triple junction effect.

The permittivity of the insulator amplifies the triple junction effect because the increased relative permittivity pushes more field lines into the free-space. Figure 17.6 shows how the field in a 1 mm triple gap increases as the relative permittivity of the insulator increases in a 500 kV m^{-1} ambient field. The permittivities of the insulators shown in Fig. 17.6 are of air, PTFE, epoxy resin and natural rubber; their bulk dielectric strengths are shown in Table 17.1.

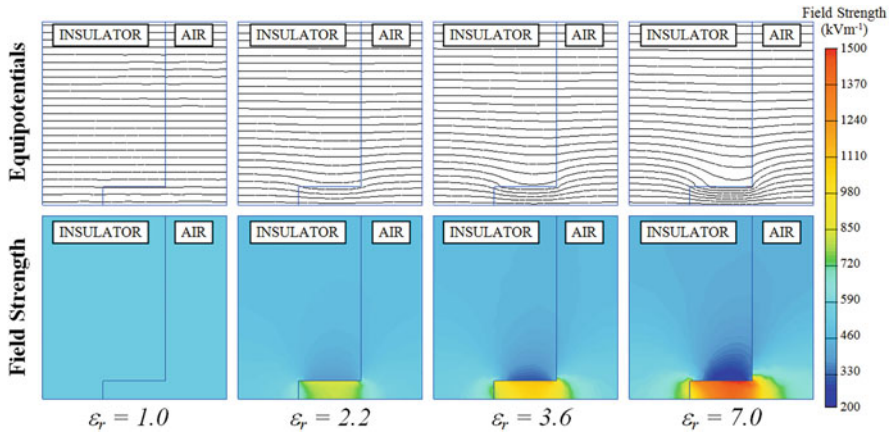


Fig. 17.6 Triple junction field enhancement increases as the permittivity of the insulator increases

Table 17.1 The relative permittivity and dielectric strength of some commonly used insulation materials

Material	Relative permittivity ϵ_r	Approximate dielectric strength (kV mm^{-1})
Air	1	3
SF ₆ (@ 1 Atmosphere)	1.002	7.5
Transformer Oil	2.1–2.4	10
PTFE	2.2	19.7
XLPE	2.25	21
Rexolite™	2.5	0.5
Mica	2.5–7	118
Epoxy resin	3.6	20
Macor™	6	62
Rubber	7	30–40
Al ₂ O ₃	8–10	13.4
AlN	8.2–9.3	10–20

17.5.8 Triple Junction Shielding

By shaping the electrodes, it is possible to shield any triple junction. Figure 17.7 shows some of the different possible techniques, which all work by reducing the field in the triple junction region. Figure 17.7a shows the field in an insulator with a relative permittivity of 2.2 and a 1 mm triple junction in an ambient field of 500 kV m^{-1} .

If the insulator cannot be modified, then the best option is to recess the electrode as shown in Fig. 17.7b. If neither insulator nor the electrode can be modified, then the best option is to add a guard ring onto the electrode, as shown in Fig. 17.7c. Both the guard rings and the recesses need to be a short distance away from the insulator: close enough to shield the triple junction, yet far enough away so the field on the

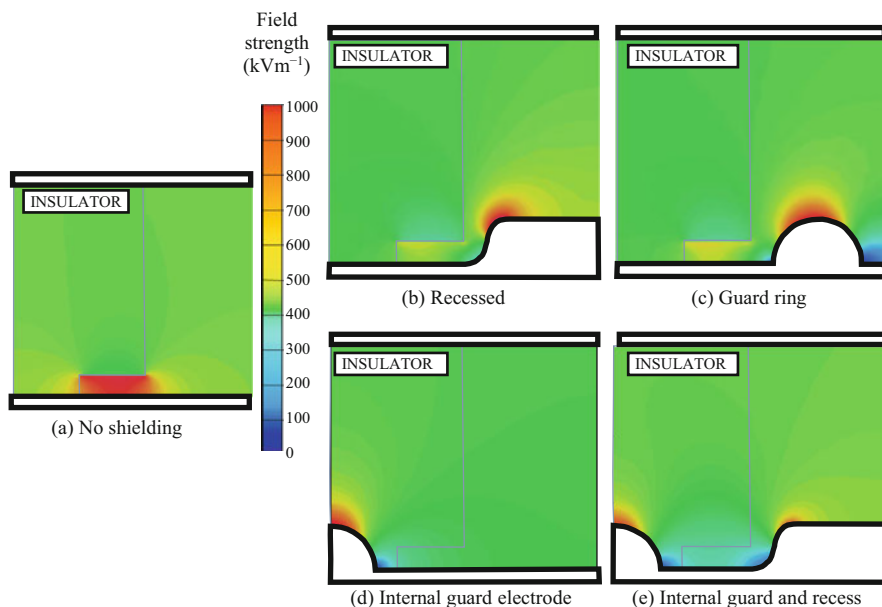


Fig. 17.7 Different insulator triple junction shielding techniques

insulator surface is not increased. The precise shape and location of the guard ring can be optimised to minimise the field on the insulator surface.

If the insulator can be modified, the best solution is to add an internal guard electrode, as shown in Fig. 17.7d. This reduces the field in free-space and increases it in the insulator material. This is a good engineering solution because the bulk of the insulator has a very high dielectric strength. Also the conditions inside the insulator are much more stable and controllable than outside, where surface contamination and lost beams can cause the surface of an insulator to fail. Care must be taken to make sure that no voids (holes) are left when an internal guard electrode is bonded into the insulator. The electric field is greatest in the lower permittivity voids because the higher permittivity insulator pushes the field lines into the voids. Partial discharges can occur in voids that create electrical noise and degradation of the insulation over time.

It is also possible to reduce the surface field even further by also adding an external guard ring or recess, as shown in Fig. 17.7e.

17.5.9 Insulator Material

There are many types of insulation material. Which insulator to use obviously depends on the application. For example, Al_2O_3 (alumina) is commonly used in vacuum. AlN (aluminium nitride) is used when high thermal conductivity is

required. Macor™ (a machinable glass-ceramic) is used when small complex shapes need to be machined. Porcelain (vitrified ceramic) is used in compression. Epoxy resin (polyepoxide) is used to impregnate and pot. Mica (a natural sheet silicate mineral) is used for thin high-voltage withstand. Glass is used when visible transparency is required. XLPE (cross-linked polyethylene) is used for extrusion in cables. Rexolite™ (cross-linked polystyrene) is used for high frequency RF.

Table 17.1 shows the typical relative permittivity (dielectric constant) and bulk dielectric strength of some commonly used insulation materials. The values for both can significantly vary with the frequency (or rise time) of the applied voltage and temperature of the insulator. The dielectric strength will also strongly depend on the size of the insulator. Note that these are bulk dielectric strengths, and this is the electric field required to cause high-voltage breakdown in the material itself. Surface breakdown will occur at significantly lower field strengths. Surface breakdown field strengths depend strongly on insulator surface geometry and the adequacy of the triple junction shielding discussed in the previous section.

17.5.10 Insulator Surface Profile

If the electric fields along a surface are low ($\ll 0.5 \text{ kVmm}^{-1}$), then simple, straight, smooth insulators can be used in many applications. However, for high-field applications, the shape of an insulator's surface profile is a very important part of its high-voltage design.

The ridged or contoured profile that is commonly seen on high-voltage insulators is there to increase the surface path length along which the discharge must propagate to reach the other electrode. The profile should also make the electric field component parallel to the surface drop to zero along parts of the surface; this will inhibit surface propagation.

Another name for the insulator ridges is 'sheds'. This name is more common in insulators designed to work outdoors and in wet conditions. Water flowing down insulator surfaces can cause tracking at fields much lower than 0.5 kVmm^{-1} . Sheds work by protecting some of the insulator's surface from the water. In extreme environments, the underside of the shed has additional undulations. The sheds are designed so that water cannot collect on their surfaces. The water flowing off the surfaces has the additional benefit of cleaning off any pollution.

17.5.11 Insulator Protection

In ion sources that use caesium or sources that sputter large amounts of conductive metals, it is sometimes necessary to implement insulator shields around the insulator. These are metal shields surrounding, but not touching, the insulator. They are mounted on one electrode and stop short of the other electrode. They leave a

small section of insulator visible, with the majority of it covered. If the environment is particularly harsh, it is sometimes necessary to add a second shield of larger diameter connected to the other electrode, which covers both the insulator and first insulator shield.

When an insulator flashes over, it can be irreparably damaged. To prevent this, extra electrodes can be added that act as a protective spark gap. Called ‘arcing horns’, they limit the voltage that can be applied to the insulator, ensuring that it does not become damaged.

17.5.12 Insulation Coordination

When looking at the overall system design, it is important to make sure that each part of the high-voltage system is capable of working at the voltages required. Starting at the high-voltage power supply, the cable connecting it to the vacuum vessel should be able to withstand the maximum output voltage. The vacuum feed through should be able to withstand the maximum output voltage. Any insulators inside the vessel should be able to withstand the maximum output voltage. It should only be the electrodes themselves that might have a lower flashover voltage. The beam physics requirements often forces electrodes in vacuum to be positioned far closer together than would be allowable in conservative high-voltage design. A breakdown rate is tolerable between the high-field electrodes in vacuum, but there should be no breakdowns in the rest of the high-voltage circuit.

17.5.13 Gaseous Insulation

Air is obviously the most common form of gaseous insulation. As a general rule, air at normal ambient conditions requires about 3 kV per mm to break down, for uniform fields. This number slowly drops for longer gaps and is significantly lower for asymmetrical fields. In fact, a positive point–plane 1 m gap only requires about 500 kV to breakdown in air (rather than 3000 kV as would be predicted by scaling the 3 kV per mm rule).

After air, SF₆ is the most commonly used insulating gas. It has a dielectric strength twice that of air at atmospheric pressure because it is a very electronegative gas. This makes it very good at absorbing the free electrons produced in avalanches. It thus inhibits electrical breakdown. It is non-toxic and non-flammable, making it very safe to work with. It allows lightweight, compact, high-voltage systems to be developed without the need for vacuum pumps. Vessels are usually filled to 0.5 bar over atmospheric pressure, where SF₆ can easily provide dielectric strengths three times that of air at atmospheric pressure. For specialist applications, even higher pressures are used. The major drawback of SF₆ is that it is the most potent greenhouse gas: 1 kg of SF₆ is equivalent to 23,900 kg of CO₂. It requires

gas handling systems and must not be released into the atmosphere. If significant amount of sparking occurs, by-products can be produced that are hazardous to health and can be corrosive. The most toxic gaseous arcing by-product is S_2F_{10} , which has a permitted exposure limit of only 0.01 ppm.

17.5.14 Liquid Insulation

Oil is the most common liquid insulator. Oil has a dielectric strength three times greater than air (the same as SF_6 at 0.5 bar over atmospheric pressure). Oil is commonly used in transformers and high-current applications because it can also be used as a coolant. Once components are immersed in oil, repair and maintenance becomes more difficult, so oil insulation is generally only employed for mature systems with very low failure rates.

Oil is much less harmful to the environment than SF_6 , but it still must be disposed of properly, and a back-up containment vessel must be provided to prevent leakage. This is usually implemented as double-skinned tanks or bunds (Isolated Mains Power).

It is necessary to deliver mains AC electrical power to the equipment that operates on the high-voltage platform. There are two ways of doing this: mechanically or electrically.

The mechanical technique involves a motor driving an insulated rod, long enough to stand-off the platform voltage. The rod is connected to a generator (alternator) on the high-voltage platform. This technique is called a motor alternator.

The electrical technique is simply a transformer with a 1:1 turns ratio and enough insulation between the primary and the secondary windings to stand-off the platform voltage. This technique is called an isolating transformer. For voltages up to around 100 kV solid insulation (epoxy/paper/fibreglass) can be used, but above about 50 kV oil or SF_6 becomes a more practical insulation solution.

Isolation transformers are more reliable because they are maintenance free, unlike motor-alternator systems that require regular bearing maintenance. Motor-alternator sets can be built out of readily available components, whereas isolation transformers often have to be custom made by transformer manufacturers.

17.5.15 Cooling Equipment on High-Voltage Platforms

High power ion sources require cooling. Air cooling with fans, fins and heatsinks works well for low-to-medium power applications, but higher power ion sources require water cooling to take away the heat. The system designer has to make the decision whether to put the water chiller on the high-voltage platform or not. The advantage of putting the chiller on the platform is that the water does not have to get up to platform volts and back down to earth potential again. Each time the water

passes through a volt drop, it can become ionised, and its conductivity can increase. Having the chiller on the platform means that the conductivity of the coolant is not an issue. However, having the chiller on the platform has a number of drawbacks. Firstly, space must be found on the platform for the chiller. Secondly, it provides a significant additional load on the platform isolated mains power supply system, and the refrigeration unit in the chiller is usually under simple thermostatic control, so it puts an on-off duty cycle power loading on the isolated platform power supply, which can create supply voltage regulation issues for the other ancillary equipment on the high-voltage platform. Also the chiller should sit in some form of bund or leak management system to prevent water leaks flowing off the high-voltage platform in an uncontrolled manner.

The alternative is to put the chiller at earth potential and send the water coolant up to the equipment held at volts and then back down again. To do this, the water has to cross two regions of high field in the flow and return directions, each time risking ionisation and increased conductivity. The conductivity of the water must be monitored and the water switched to flow through an ion exchange filter system if required. The water might have to go through a spiral pipe that is long enough to allow an acceptable volt drop per meter along its length.

So should the chiller be on or off the high-voltage platform? There are complications either way; it is up to the system designer to decide which method best suits the cooling requirements and system constraints of the ion source.

17.5.16 Breakdown Protection

Not only the personnel must be protected from the hazards of high voltages, but also the ancillary equipment must be protected from being damaged by the plethora of high voltages on electrodes in close proximity inside an ion source. A successful ion source produces reliable discharges in the regions where they are wanted (the plasma chamber) and none in the regions where they are not (the extraction system). These two regions border each other, and an ion source is, by definition, a rich source of charge carriers, so it is inevitable that the high fields required in extraction systems will at some point produce unwanted breakdowns.

This, compounded by the use of a high-voltage platform that connects output voltages to output voltages, means that ancillary equipment can receive some very harsh fault conditions not encountered in more straightforward applications. When a breakdown occurs between two electrodes, it can short the output of one power supply to the output of another power supply, which unless properly managed can result in a power supply 'fight to the death'.

For high-voltage platform voltage stability when operating with high-current pulsed beams, a large platform capacitance is required to provide a large reservoir of charge. This charge reservoir can deliver a huge transient fault current to any electrode connected directly to the platform. So any ancillary equipment connected

to an electrode that breaks down to an electrode connected to the platform will receive a huge fault current.

One method of protecting high-voltage power supplies from such faults is to add an extra electrode between two electrodes in the extraction scheme. This intermediate ‘protection electrode’ must be designed into the ion source extraction optics. It is passively biased at an intermediate voltage using a high value resistor voltage divider. Breakdown then occurs to the ‘protection electrode’, not directly between the electrodes on either side of it. The high value resistors limit the fault currents that can flow between the power supplies connected to the electrodes on either side of the protection electrode.

A method of protecting low-voltage power supplies is by creating local protective spark gaps. In normal operation, a low voltage might need to be applied to an electrode (e.g. a biased plasma electrode), but that electrode might be likely to breakdown to an electrode at a much higher voltage (e.g. an extraction electrode). When the high-voltage electrode sparks over to the low-voltage electrode, the voltage on the low-voltage electrode rapidly rises, causing the protective spark gap to break down to another electrode (local platform earth), thus limiting the maximum fault voltage that the low-voltage power supply experiences.

Local protective spark gaps can be designed into the electrode geometries. Protective spark gaps are simply places where electrodes are closer together.

When two electrodes break down, they can temporarily be pulled to very different voltages, and anything else attached to those electrodes will also be pulled to a different voltage.

Take, for example, a sheathed resistive heater on a component, which is normally biased at platform volts. When any electrode at platform volts breaks down, the platform voltage is temporarily pulled to a significantly (many kV) different voltage. The outer sheath of the heater element will be pulled with it, whereas the insulated resistive heater element inside the sheath will, for a very short time, still be at its original voltage because the impedance of its drive circuitry limits its rise time and because the fault voltage transient wave has not propagated through the ancillary equipment wiring yet. This creates a large transient potential difference between the heater element and its sheath, causing it to breakdown and fail.

Breakdown induced transient voltage pulses like this are a common problem for ion source ancillary equipment, and the problem gets worse as higher voltages are used.

There are many ways of protecting the ancillary equipment from the, frankly brutal, operating conditions that running an ion source presents. Firstly, the electrode and insulation systems should be designed so that they do not breakdown in operation. This is usually possible for the insulation systems in the ancillary equipment and the high-voltage feeds to the ion source, but much harder inside the ion source in the extraction system because of the very high fields required by the beam physics design, so the system must be designed to tolerate a certain breakdown rate.

Moving out from the ion source, all the vacuum feed throughs, insulators, connections and cables must be able to tolerate the transient fault voltages that will

occur on them when breakdowns occur. If they cannot, a local spark gap should be used so that the breakdown occurs across that and not across an insulator surface. Spark gaps can take many breakdowns, but an insulator could be permanently damaged after one breakdown.

Finally, ancillary equipment should be able to protect itself from anything that comes in on its terminals. Smaller spark gaps can be installed across the ancillary equipment's terminals. Spark gaps can be purchased as discrete packaged components, with breakdown voltages as low as 230 V. Metal oxide voltage dependant variable resistors (varistors) can be used in parallel with the spark gaps, these devices start to conduct when the voltage across their terminals gets too high, thus shorting out the fault current before it goes into the internal circuitry. Series inductors can also be added to the inputs and outputs to block fast transient currents. Clip-on ferrites are used to increase the inductance of cables. Earth wires can be wound around ferrite cores to block fast transients on the platform local earth potential.

Inside the ancillary equipment the components connected to the input and outputs can be uprated. If the ancillary equipment is custom built, the printed circuit board track spacing can be increased around the input and output components to increase the voltage withstand capability.

In summary, breakdown protection is not simple; it requires an understanding of the overall ion source system. Likely breakdown locations must be identified, and the expected transient fault voltages must be predicted. The system must be designed to withstand these transients and safely dissipate them with spark gaps, varistors and inductances. Protection electrodes with protective resistors might need to be employed if the fault currents and voltages produced cannot be managed.

17.6 Earthing

17.6.1 The Earth Connection

Earth (UK), ground (US) and terre (Fr) are used synonymously. The local connection to the surface of our planet is the most fundamental earth, but even that is a slippery concept because of variations in local geology affecting the resistivity and the effects of natural and manmade currents flowing in the strata. The best we can do to get a good electrical grip on the planet is embed into the soil or rock as many conductors as is necessary and connect them all together underground with more conductors in a grid pattern to make an 'earth matt'. The resistivity of the local geology and the maximum expected fault current determines the required size and complexity of the earth matt structure, which for domestic installations could be as simple as a single spike in the soil. Whatever the size of the underground conductor structure, the points where the electrical conductors come up out of the ground are the electrical earth connections for the building.

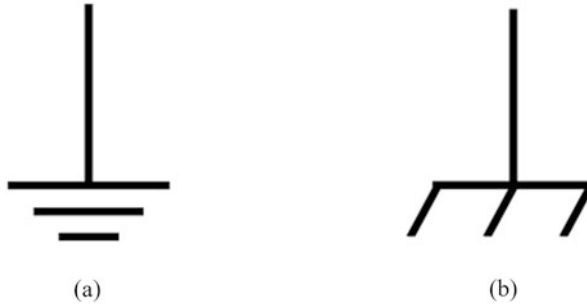


Fig. 17.8 Schematic circuit diagram symbol for (a) the earth connection and (b) the common local earth or frame earth or chassis earth or platform earth

Laboratories that contain ion sources should be large enough to have a dedicated ‘laboratory earth’ connection installed when the building was constructed. This will usually be a copper bus-bar connected directly to the building earth mat. The earth connection is represented in circuit diagram schematics (Fig. 17.8a).

A direct connection should be made between the laboratory earth bus-bar and the ion source. The connection can be either a cable or metal strip with a cross section large enough to keep the impedance to earth low enough. A strip is used to keep the inductance low for transient fault currents.

17.6.2 Local Earth

The point where the earth connection from the laboratory earth meets the ion source becomes a ‘local earth’ or ‘ion source’ earth, which in generic technical terms is also known as a ‘frame earth’ or ‘chassis earth’ schematic symbol (Fig. 17.8b).

It is from this local earth point that the entire ion source electrical system is referenced. All the ancillary equipment that is not on the high-voltage platform is individually earthed back to this single point in a radiating star and tree configuration.

There are multiple local earths in the system: Each 19-inch rack must have its own earth bus-bar installed to which each piece of ancillary equipment in the rack is connected; the chassis of each piece of ancillary equipment is a local earth for everything inside the chassis; each circuit board inside the chassis has a local earth to which all voltages on the board are referenced.

These local earths grow out from the ion source earth in a tree. This topology ensures that wherever a fault current enters into the earthing system, the lowest impedance path is always directly to the earth and not via another piece of ancillary equipment (which sits safely on another branch of the ‘earth tree’).

The use of a high-voltage platform introduces a peculiar earth configuration in that, in normal operation, the local earth for all the ancillary equipment on the high-

voltage platform is connected to the high-voltage output of the ion source platform bias power supply.

There should be a low resistance ($<0.1 \Omega$) between the ion source earth and the AC mains power supply earth. If this resistance is greater than 0.1Ω , fault currents can pose high-voltage hazards for personnel and equipment. Common causes of high lab-earth to mains-earth resistances are as follows: loose or corroded terminals, cable run too long and earth conductor too thin.

17.6.3 Earth Loops

If equipment earths are connected together serially in a 'daisy chain' fashion, or the branches of the 'earth tree' are connected together, then earth loops are created. Earth loops are not only a problem because of dangerous voltages created when fault currents flow, but also a source of electrical noise for equipment connected to the earth loop.

Sometimes earth loops are impossible to avoid, e.g., the screen connection on a signal cable that must connect two pieces of ancillary equipment. In this case, the transient impedance of the screen can be increased by adding a clip-on ferrite to increase the inductance of the screen. This reduces peak transient fault currents in the screen: the fault currents will instead flow along the lower impedance path down the earth tree towards the laboratory earth.

17.6.4 Equipotential Bonding

The ion source high-voltage cage (or chassis) that surrounds the ion source must be equipotential bonded to earth. Although the cage is made out of conducting metal, the mechanical connections and bolts holding the cage together cannot be relied upon to make good electrical connections between each panel and component of cage. To ensure the whole cage is at the same potential (equipotential) each component of the cage, including the doors should be connected to its neighbour with a short length of bonding wire. The bonding wires should have crimped terminals and be securely electrically connected to the cage components, a small patch of paint or coating can be removed if necessary. One of the cage components is connected to the local ion source earth to hold the whole cage at earth potential. Equipotential bonding ensures that high-voltage breakdown to the cage does not present a hazard to personnel touching the cage.

The base of the chassis or the floor of the cage should be constructed of metallic panels that are also equipotential bonded to the local earth.

17.6.5 Automatic Earthing

Ion sources have many exposed live conductors: all the equipment on the high-voltage platform including the ion source itself become exposed live conductors when the platform bias supply is switched on.

Exposed live conductors must be made safe before personnel can get close enough to touch them. This must be achieved automatically; personnel cannot be relied upon to make the live conductors safe. There are many ways of doing this.

The most simple is completely passive: a high value resistance is connected between earth and the exposed live conductor. In normal operation, there will be a current through this 'drain' resistance, so a high enough resistance must be chosen so as not to overload the power supply or waste excessive amounts of energy. When the power supply is switched off, the drain resistance must safely drain away any stored charge before personnel can touch the exposed live conductors. These two requirements put a minimum and maximum on the range of acceptable values for the drain resistance. The time that it takes personnel to access the live conductors can be engineered: a door panel can be held in place with screws that cannot be accessed until the power is removed; the number of screws that must be removed puts a limit on how quickly the live conductors can be exposed.

If the use of a drain resistance is not an appropriate automatic earthing method, then a trapped key system can be employed: the key to access the enclosure around the exposed live conductors is not released until the earth has been applied, and the key that allows the earth to be applied is not released until the power supply has been turned off. The use of a series of trapped keys mechanically forces personnel to make the exposed conductors safe before they can touch them.

In pulsed systems, the ion source platform bias circuit is required to have a large capacitance to stabilise the beam energy. When charged to the high voltages required, this capacitance stores a significant amount of energy. This must be safely discharged by connecting the platform to earth via dump resistor. The dump resistor limits the discharging current to prevent damage to components.

For systems with a large amount of stored energy, a second independent automatic earthing system should also be implemented. This usually takes the form of an earthing switch that connects the exposed conductors to earth when the doors of the surrounding enclosure are opened. This second automatic earthing system is required in case of failure or malfunction of the first system. For the highest voltages, automatic earthing arms are used that move into place to make contact with the exposed conductors when the door interlocks are opened.

17.6.6 Earth Sticks

The very last thing to be applied to an exposed conductor before touching it by hand is a manual earth stick. An earth stick is an insulated rod with a conducting point

and/or hook on one end and a handle on the other. The conducting point is connected to earth via a resistance to limit the fault current just in case the exposed conductor is still live.

Earth sticks should never be considered as the main method of earthing a system down; earth sticks are the last line of defence for personnel. Earth sticks give personnel the confidence that even if all the other earthing systems have failed or malfunctioned, they can make sure exposed conductors are safe to touch.

Earth sticks are a piece of safety equipment, they should be rated at the voltages and stored energies expected in the system. Earth sticks should be tested at regular intervals to confirm they still conform to their rated capabilities.

After the tip of the earth stick has made contact with the exposed conductor, it is usual for the earth stick to be hung or attached to the exposed conductor all the time that people are working on the system. It is the last thing to be removed when personnel leave the area that contains exposed conductors.

Sometimes interlocked earth clamps are used to force the operator to attach an earth clamp and to remove it before operation (it is a common mistake to forget to remove manual earth sticks!)

17.7 Safety

17.7.1 Compliance with Regulations

We sometimes mourn for the good old days when safety was nothing more than ‘common sense’ and ‘don’t do anything stupid’. However, this approach is no longer moral or legal. A manager has a legal responsibility (duty of care) for the safety and well-being of their staff. The prospect of time in prison really does focus a manager’s mind on compliance with regulations! Safety is everyone’s responsibility: staff are responsible for their own safety and for the safety of those around them.

Each country has its own laws and regulations. Laws and regulations are constantly evolving and adapting as technology advances and society reacts. Some examples of regulations given here are correct at the time of writing, but they will inevitably become out of date quite rapidly. Systems that were designed to comply with an earlier set of regulations do not suddenly become unsafe when the new regulations are published, but the managers of the system need to understand how the updated regulations affect them and take necessary action in a reasonable time.

It is everyone’s responsibility to adhere to the most up-to-date local laws and regulations.

17.7.2 Personnel Protection Interlock System

The main way to keep people safe is by using a personnel protection interlock system. A distinction should be made between a personnel protection system (PPS) and a machine protection system (MPS): the first protects people from harm; the second protects the machine from harm. The machine protection system can be part of the control system for the ion source, but the personnel protection system must be a separate system with its own logic control systems and cabling (in dedicated containment systems). Although the personnel protection system is physically separate, it must interface with the machine protection system to tell the machine if it can turn on, or if it must turn off.

The basic purpose of the personnel protection system is to make it impossible for anyone operating the ion source to accidentally hurt themselves or others. This can be achieved by adhering to four simple rules when designing the personnel protection system:

1. Impossible for someone to become accidentally locked in the hazardous area

For small systems that are entirely enclosed in a case, rack or small cage, this first rule is not even an issue; it is not physically possible for someone to get their body into the hazardous area. For larger systems, it might be possible to get into the hazardous area, but they would be clearly visible by the person locking the door. For very large systems, with a lot of equipment on large high-voltage platforms, or with radiation shielding labyrinths, the only way the person locking the hazardous area can be sure there is no one in the area is to go and have a look. The PPS can force the operator to have a look by putting a ‘search’ button on the far wall of the hazardous area. When the ‘search’ button is pressed it releases an electromechanical device that was physically preventing the door to the hazardous area being closed. The search button is on a timer so that the operator only has a small amount of time to get back to the door and shut it. For the largest systems with multiple doors, a search procedure is required, which might need more than one person to complete the search.

All this prevents the operator accidentally locking someone in the hazardous area; the PPS must also prevent the operator (or anyone else) accidentally locking themselves in the hazardous area. The simplest way of achieving this is to have a clearly labelled exit door that is equipped with a fire escape style ‘crash bar’ (also known as a panic exit device, panic bar or push bar). This will allow anyone trapped inside the hazardous area to escape. Anybody trapped in the area must to be made aware that the area is about to become (or already is) hazardous. Clearly visible warning lights should come on to indicate what hazards are imminent (or present). If the area is large enough to need a ‘search’ button, then additional means are required to let anyone in the area know that the area is hazardous. This could be achieved by a change in lighting colour (e.g. white to blue) or an audible warning (e.g. a buzzer).

No matter what the size or complexity, the PPS must not allow people to become accidentally locked in the hazardous area.

2. *Impossible to create hazards in the hazardous area without first securing the area*

The first rule above ensures that someone cannot be accidentally locked in the hazardous area. By securing (locking) the hazardous area, we can ensure people cannot accidentally stray into the area. When the hazardous area has been secured, the personal protection system lets the machine protection system know it is safe to turn on the systems that create the hazards. Depending on the size of the system, this could be as simple as a single magnetic door closed switch connected to enable a high-voltage power supply; or as complicated as a programmable logic controller with multiple inputs and graphical touch screen displays and a trapped key exchange system. No matter what size, the personnel protection system must not allow hazards to be generated until the area is secure.

3. *Impossible to enter the hazardous area without first making it safe*

To enter the hazardous area, the primary hazards must be removed. The main hazard is electrocution from the high-voltage platform used to bias the ion source. The area is made safe by turning off the high-voltage power supply, draining away any stored charge, and earthing it down. A trapped key interlock system is a reliable way of forcing the operator to do things in the right order.

It is always good practice to make sure (if reasonably practicable) that safety systems have a backup, so a separate automatic earthing system is usually employed: a sprung loaded earthing arm is released when the door to the hazardous area is opened.

Finally, the operator must manually apply an earth stick to the high-voltage platform on entry to the hazardous area. However, this is a procedural safety step and therefore cannot be relied upon.

As soon as the door to hazardous area is opened the PPS tells the MPS that the area is no longer secure, which automatically trips-off all equipment that produce hazards in the area. This not only might just be the high-voltage platform bias supply as already discussed but also could include high power RF amplifiers, lasers, high current power supplies, and other high-voltage power supplies. Exactly what trips-off when the door to the hazardous area opens depends on the system design.

When the door opens, there may be some remaining hazards (e.g. hot surfaces and radiation from activated material), so access should still be limited to trained personnel who are familiar with the risk assessments and method statements for working in the hazardous area.

4. *Able to shut down the power inside and outside the hazardous area*

Red emergency stop buttons should be positioned nearby, both outside the hazardous area and inside the hazardous area (if it is possible to get inside the hazardous area). There should be enough buttons so that there is always a button within a few steps. The buttons should turn off the power to the electrical systems connected to the ion source. The buttons should ideally need a key to reset, but at the very least, they should latch-on to prevent accidental restart after they have been pressed. The emergency stop buttons are not just to remove hazards, but they are also used to shut down power in the event of a fire, catastrophic equipment

failure or other emergency situation. The emergency stop buttons should not be used to shut down the ion source in normal operation.

These four design rules keep people safe and allow equipment to be rapidly shut down in an emergency. Interlocks are to prevent accidents caused by absent mindedness: after several years of working with an ion source, the operator's actions might become so automatic that they could forget an important safety step if distracted. Equally, an operator's overfamiliarity with a system could tempt them to take shortcuts. The personnel protection interlock system must force the operator to behave in a safe manner.

The personnel interlock system prevents unsafe operation caused by complacency and laziness. The PPS is not designed to prevent unsafe operation by wilful bypass: fences and cage walls can be scaled; electrical terminal boxes can be opened and door interlock switches shorted out. The basic rule is: you should need some sort of tool to bypass a personnel safety system.

Unauthorised interference with safety systems is a disciplinary offence, which will result in instant dismissal from most organisations.

Any modifications to the personnel safety system should, at a minimum, be approved by a line manager and, ideally, undergo multidisciplinary scrutiny by a safety committee.

17.7.3 Reliability of the PPS

The reliability of the PPS is literally of life and death importance. Some components of the personnel protection systems can be designed to 'fail safe': the high-voltage platform automatic earthing arm should be 'normally closed' and should be held shut by gravity or a spring, so that in the event of a power (or compressed air) failure, the high-voltage platform is automatically earthed. However, it is impossible to guarantee that a component is 'fail safe'. Take the earth arm as an example: it is conceivable that a foreign body could enter the mechanism and prevent it from closing. Switches and interlock logic cannot 'fail safe' because the definition of safe is arbitrary to the implementation of the logic at that point in the interlock circuit, switches and relays can become mechanically stuck in both open or closed positions. The reliability problem was traditionally overcome by having a dual redundant system: two door switches on every door, two separate cables and two sets of logic relays. This is sometimes referred to as a 'dual guard line' system, which is the same as the 'N-1 contingency criterion' used in electrical power engineering, meaning any one component (of N components) can fail and the system will still work. This design philosophy was traditionally assumed to provide a reasonably practicable level of reliability for personnel protection systems.

However, this raises two obvious questions: what is an acceptable level of reliability for a PPS? And how is the reliability of a PPS calculated?

Table 17.2 Likelihood of occurrence

Likelihood of occurrence	Definition	Range (failures per year)
Frequent	Many times in system lifetime	$>10^{-1}$
Probable	Several times in system lifetime	10^{-1} to 10^{-2}
Occasional	Once in system lifetime	10^{-2} to 10^{-3}
Remote	Unlikely in system lifetime	10^{-4} to 10^{-5}
Improbable	Very unlikely to occur	10^{-6} to 10^{-7}
Incredible	Cannot believe that it could occur	$<10^{-7}$

Table 17.3 Severity of consequence

Severity of consequence	Definition
Catastrophic	Multiple loss of life
Critical	Loss of a single life
Marginal	Major injuries to one or more persons
Negligible	Minor injuries at worst

The first question is answered by identifying all the hazards, assessing the severity of harm to personnel encountering them, estimating the likelihood personnel will encounter them and combining these to give an overall risk. The second question can only be answered by a detailed analysis of the protection system, its components, circuit topology, and how often it is used and maintained. IEC 61508 provides a guide and framework for answering both questions.

17.7.4 IEC 61508

Local laws and regulations will inevitably insist that the personnel protection system comply with IEC 61508, an international standard published by the International Electrotechnical Commission entitled “Functional Safety of Electrical/Electronic/Programmable Electronic Safety-related Systems” (IEC 2010). IEC 61508 is a basic functional safety standard applicable to all industries. It provides methods on how to apply, design, deploy and maintain automatic personnel protection systems.

It provides processes for identifying all the hazards and risk assessing their impact on personnel. The familiar risk assessment procedure combines the likelihood of occurrence (Table 17.2) with the severity of consequence (Table 17.3) into a risk class matrix (Table 17.4).

IEC 61508 also details a probabilistic failure approach to calculate the safety impact of device failures. A detailed analysis is required of the system design and all its possible failure modes. The approach is quite involved. The way the system is used is important. How often is the personnel protection system used? For how long? How often is it tested? How often is it maintained? Reliability data for every

Table 17.4 Risk class matrix

Consequence				
Likelihood	Catastrophic	Critical	Marginal	Negligible
Frequent	I	I	I	II
Probable	I	I	II	III
Occasional	I	II	III	III
Remote	II	III	III	IV
Improbable	III	III	IV	IV
Incredible	IV	IV	IV	IV

Class I: Unacceptable in any circumstance

Class II: Undesirable; tolerable only if risk reduction is impracticable or if the costs are grossly disproportionate to the improvement gained

Class III: Tolerable if the cost of risk reduction would exceed the improvement

Class IV: Acceptable as it stands, though it may need to be monitored

Table 17.5 Safety integrity level

Safety integrity level (SIL)	Low demand mode Probability of failure on demand (PFD Avg)	High demand or continuous mode Probability of failure per hour (PFH)
4	$\geq 10^{-5}$ to $<10^{-4}$	$\geq 10^{-9}$ to $<10^{-8}$
3	$\geq 10^{-4}$ to $<10^{-3}$	$\geq 10^{-8}$ to $<10^{-7}$
2	$\geq 10^{-3}$ to $<10^{-2}$	$\geq 10^{-7}$ to $<10^{-6}$
1	$\geq 10^{-2}$ to $<10^{-1}$	$\geq 10^{-6}$ to $<10^{-5}$

component that makes up the personnel protection system is required. Values for mean time between failures (MTBF), mean time to failure (MTTF), mean time to repair (MTTR), mean time between maintenance (MTBM) and expected mean system downtime (MSD) must be obtained, estimated or calculated. A distinction is made between components or systems that are used rarely (e.g. an emergency stop button) and high demand components used continuously or many times an hour (e.g. the door switch on the sample test chamber). A distinction is made between well-known mass-produced simple components with well-known failure modes and a solid history of operation and custom or complex devices with potentially unknown failure modes.

Having all this information makes it possible to calculate an average probability of failure on demand (PFD_{average}) or a probability of failure per hour (PFH) for systems used very often. Note how specific these terms are. ‘Reliability’ is actually a very vague term. The ‘availability’ of a personnel protection system is actually what we need to know: how often will the PPS not work properly? This is why PFD_{average} and PFH are calculated.

These numbers allow an overall risk reduction factor (RRF) for the whole personnel protection system and its associated safety integrity level (SIL) shown in Table 17.5.

It is possible that the local engineer or scientist could attempt to do this, but unless they are a regular practitioner of this process, both they (and their line manager) will be left with a nagging doubt that they could have made some errors due to the complexity and unfamiliar jargon involved. Larger organisations usually have one or more people trained in the art of complying to IEC 61508. Smaller organisations will either need to contract the design work to an external company or get their personnel interlock system inspected and approved by a company specialising in such work.

17.7.5 Electrical Authorization

In normal operation, the design of the ion source and personnel protection system will keep people safe from electrical hazards. However, things breakdown and require maintenance, systems are developed, and experimental setups are tested. All this must be done safely. This is achieved by appointing competent people who have been trained in electrical safety. They are authorised or nominated to carry out specific activities.

The appointment of people and their authorisation to perform specific tasks is managed by a hierarchal system of authorised people. A senior electrical engineering manager sits at the top of this hierarchy. They are responsible for all electrical safety in their part of the organisation. They must ensure that people appointed to authorised positions are competent. The judgement of competency can be delegated down the hierarchy as the size of the organisation grows. The exact structure of this electrical authorisation hierarchy and the specific titles given to each person depends on local laws and the size of the organisation.

Before any electrical work can start, it must first be planned and then authorised by the next person up the hierarchy. The standard way of doing this is by performing a risk assessment and developing a method statement for how the work will be done. These plans are then presented to the next person in the hierarchy for approval.

Before any work can be performed on an electrical systems, it must be switched off, then locked off and earthed down. The key for the lock on the power switch is given to the person performing the work. If more than one person is working on the system, then the key for the lock on the power switch must be locked into a box with multiple locks, and the keys are given to each person working on the system. The key to unlock the main power switch cannot be obtained until everyone working on the system has returned their keys. This way the system cannot be turned back on without the agreement of everyone working on the system.

In addition to having an understanding of electrical systems, all authorised staff must be trained to prove that a system is not live before working on it. Basic electrical first aid training is also mandatory for electrically authorised people.

17.7.6 *Radiation Protection*

Radiation protection is managed in a very similar manner to the electrical authorisation hierarchy. Again, the exact structure of this radiation authorisation hierarchy and the specific titles given to each person depends on local laws and the size of the organisation. Again the system works by having a senior radiation protection manager who is responsible for all radiation safety in their part of the organisation. Again they are responsible for ensuring the competence of authorised people in the hierarchy. Again all activities that generate radiation should be planned, risk assessed and approved.

As long as the hazardous area has enough shielding to ensure that the maximum level of radiation present anywhere outside the hazardous area is acceptably low, then the personnel protection system described earlier should prevent operators from receiving any significant radiation dose.

The levels of radiation that are acceptable outside the shielded hazardous area depends on local laws, but $2 \mu\text{Svhr}^{-1}$ is a common limit.

The amount of shielding required around an ion source is actually minimal unless high voltages ($>50 \text{ kV}$) are used. Radiation produced by the ion source will primarily be x-rays from electron bremsstrahlung.

The bremsstrahlung radiation is produced from energetic electrons that, after travelling in a low vacuum pressure, hit surfaces and rapidly decelerate (braking) and emit electromagnetic radiation (this is actually the way medical and imaging X-rays are produced). Sparks created during high-voltage conditioning, testing of components and breakdowns in normal operation can also produce X-rays.

It is unlikely that there will be any neutrons or radiation emitted from activated components in the ion source because the beam has not yet reached a high enough energy. However, there could be neutron and gamma shine coming from further up the accelerator. Generally, the shielding design around an ion source is driven by the shielding requirements for the rest of the accelerator, not by a requirement to shield the radiation coming from the ion source.

Ion source test stands generally do not require shielding; any X-rays produced are of a low enough energy so as not to escape the vessel (even through the insulators and windows). The self-shielding effect of the vessel, plus the distance enforced by the use of a high-voltage enclosure, mean that the radiation levels outside the hazardous area are low. However, if high platform voltages ($>50 \text{ kV}$) are required then specific shielding might be required around the source. This can be conveniently achieved with a few mm of lead or steel.

If electron tubes are used in pulsed high-voltage power supplies, the tubes might emit bremsstrahlung if the voltage is high enough. The tubes should be locally shielded by the power supply case with the application of an extra layer of lead or steel.

Often local shielding around an ion source has to be moved out of the way to access the source for maintenance. This shielding should be interlocked, either with a trapped key or switch to prevent the source being started without the shielding in place.

17.7.7 *Hydrogen Safety*

Hydrogen is a highly explosive gas that will ignite in a wide range of concentrations in air: from 4%, the lower explosive limit (LEL) all the way to 75% the upper explosive limit (UEL).

The use of hydrogen will inevitably be covered by numerous local laws and regulations, but they will all be very similar to or based upon the European ATEX (ATMosphere EXplosible) Directives (ATEX 2014).

There are two ATEX Directives:

Directive 99/92/EC (ATEX 137) is an employer's duties; it identifies the minimum requirements for improving the safety and health protection of workers potentially at risk from explosive atmospheres.

Directive 94/9/EC (ATEX 95 or ATEX100a) is equipment manufacturer's duties, it identifies the requirements for all equipment and protective systems to be used in hazardous areas.

The ATEX directives classify different types of areas or zones where there could be an explosive atmosphere:

Zone 0 – A place in which an explosive atmosphere consisting of a mixture with air of dangerous substances in the form of gas, vapour or mist is present continuously or for long periods or frequently

Zone 1 – A place in which an explosive atmosphere consisting of a mixture with air of dangerous substances in the form of gas, vapour or mist is likely to occur in normal operation occasionally

Zone 2 – A place in which an explosive atmosphere consisting of a mixture with air of dangerous substances in the form of gas, vapour or mist is not likely to occur in normal operation but, if it does occur, will persist for a short period only

The ATEX directive stipulates that ATEX rated equipment must be used in these zones. The ATEX directive specifies that these zones must be plotted to scale on a drawing of the overall hydrogen system. When these zones are applied to ion sources, there is no Zone 0. Zone 1 is inside the vacuum pump exhaust line and the region where it vents to atmosphere. Zone 1 is around the hydrogen purge line exit if a dedicated purge line exists. Zone 2 is around the hydrogen bottles in the gas bottle store. There is also another type of zone: 'Zone 2 of Negligible Extent'. This zone exists around any joints in the hydrogen feedline between the ion source and the gas bottle store. There have to be joints in this feedline, where it transitions to an insulating pipe to feed hydrogen onto the high-voltage platform and where it is valve switched to the hydrogen purge line and local regulator. None of these joints are likely to leak in normal operation, but it is conceivable that these joints could leak. When compared industrial processes or energy generation applications, ion sources use a very small amount of hydrogen (typically 10–20 mlmin⁻¹) and operate with low feed line pressures. For this reason, any leaks in the hydrogen feedline will only have a negligible extent.

Other hydrogen safety precautions can be implemented. Low and high flow interlocks can shut-off the hydrogen back at the cylinder enclosure with an electronic valve. Low flow interlocks cover the eventuality of a small leak when the ion source is not running. High flow interlocks protect against large leaks.

Hydrogen leak detection systems can be positioned above the ion source that will shut-off the hydrogen at the gas bottle if they detect hydrogen.

Ventilation systems can be implemented to ensure that even if hydrogen were to leak at the maximum flow rate into the hazardous area, the concentration of hydrogen would be kept below the 4% LEL.

It is entirely possible to design and setup the hydrogen system yourself, but you should have your system inspected by someone who is a competent practitioner, that is someone who knows the regulations in your country and who regularly works with the design, installation and inspection of hydrogen systems.

17.8 Controls and Diagnostics

17.8.1 Control System

A control system is required to allow the ion source to be controlled and monitored remotely. Remote operation is essential for the ancillary equipment on the high-voltage platform; without a control system, the ion source cannot be tuned in operation (unless an antiquated system of insulated rods is employed to turn knobs and press buttons!). Fibre optics is used to transfer electrically isolated control signals to and from the high-voltage platform. A separate fibre optic can be used for each signal (commonly used for interlock signals) or a dual (transmit and receive) fibre optic network connection can be used to carry Ethernet packets to and from a network connected device on the high-voltage platform. A wireless Wi-Fi connection to the equipment on the platform is not recommended because of possible interference caused by high-voltage breakdowns leading to the loss of control or spurious settings.

In general, it is a good idea to use the same control system hardware and software that is employed by the rest of the accelerator. It is possible to custom build a control system for the ion source, but in the long run, it is sensible to use the hardware and software support provided for the rest of the accelerator.

The architecture of the overall control system is comprised of several different layers (levels) of physical hardware and software systems. The lowest level is being the ancillary equipment itself, and the highest level is the user interface control screen, with the levels in-between connecting the two.

Each piece of ancillary equipment can require slightly different approaches to connect it to the user interface screen: a power supply might require analogue input and output signals or it might have a direct Ethernet connection. For analogue inputs (e.g. 0–10 V or 4–20 mA), some form of analogue to digital signal conversion

is required, and this is usually implemented as a piece of rack-mounted data acquisition I/O (input/output) hardware. Once the signals are digitised, the next levels of the control system are implemented in software. For direct Ethernet connected ancillary equipment, some sort of software handling layer is required to pass the signals to the next level of the control system.

When the overall system is small, LabVIEW™ is an attractive solution because it offers all the hardware required to physically connect a wide range of ancillary equipment. It provides a user-friendly software development environment that allows simple visual configuration of the control system, data acquisition and user interface screens. LabVIEW™ allows novices to quickly set-up control systems. This development environment is great for simple systems, but unless rigorous design architecture rules are adhered to, the control system becomes unmanageable for larger systems.

A commonly used open source control system used on particle accelerator is Experimental Physics and Industrial Control System (EPICS) (EPICS 2022). EPICS was originally written jointly by Los Alamos National Laboratory and Argonne National Laboratory and is now used by many large scientific facilities all over the world.

17.8.2 Diagnostics

The control system is not just for setting and reading values from ancillary equipment, it is also used to display and log various measurements that allow the operation of the ion source to be monitored. There are online diagnostics that can continuously provide measurements when the beam is on, such as electrode temperatures and beam currents. Then there are offline diagnostics that intercept the beam, such as profile or emittance measurements. Offline diagnostics do not necessarily need to be connected to the control system; they might use a separate local control and data acquisition system. Finally, there are offline experimental diagnostics that might require hardware modifications or operation on test stands, such as longitudinal energy spread or species analysis.

17.9 Vacuum and Gas Systems

17.9.1 A Wide Range of Pressures

In order to operate reliably, ion sources require a very large range of vacuum pressures to be accurately and repeatably controlled. To produce a plasma dense enough to extract mA of beam current, the pressure in the plasma chamber needs to be in the 0.1–1 mbar range. To transport an H⁻ beam without significant stripping

losses, the pressure needs to be in the 10^{-6} mbar range. These two contradictory requirements mean that significant pumping is required in an ion source.

To reach pressures as low as 10^{-6} mbar, a two stage pumping system is required. Pumping is provided by turbo pumps in a range of sizes, backed by rotary vane or scroll pumps. Hydrogen is a very small molecule and so has a high thermal velocity, which means pumping speeds for hydrogen are lower than the speed quoted on the pump (based on N_2).

Pumping speed is measured in ls^{-1} , the volume of gas that can be pumped per second. To deal with a typical hydrogen feed flow rate of about $10\text{--}20\text{ mlmin}^{-1}$, about 2000 ls^{-1} of pumping speed is required to maintain the required pressures.

For high current beams, the vacuum pressure in the low energy beam transport should not be too low; this is because of a phenomenon called Space Charge Compensation (SSC). As the beam passes through the vacuum chamber, it ionises the residual gas in its path, producing slow electrons and ions. For a negatively charged particle beam, the electrons produced are ejected by the space charge of the beam, and the ions produced are pulled into the beam (the opposite is true for a positively charged particle beam). The oppositely charged particles that are pulled into the beam are called the compensating particles because they counteract (compensate for) the space charge in the beam. SSC is critical for high current beams because without it, the space charge in the beam would blow the beam apart, increasing the beam emittance, making it harder to transport the beam without loss. SSC levels are as high as 95%, meaning 95% of the space charge forces are compensated away. For example, a 100 mA beam with 95% SSC behaves like a 5 mA in the beam transport optics. Beam transport optics are optimised for a specific beam current (or compensated beam current), so sometimes it is necessary to control the residual gas pressure by introducing a 'buffer gas' (usually a heavy gas, e.g. Argon or Krypton) into the beamline.

If very low vacuum pressures are required ($<10^{-7}$ mbar), it will be necessary to 'bake-out' the vacuum components to several $100\text{ }^\circ\text{C}$ to remove the atoms and molecules stuck in surfaces.

17.9.2 Differential Pumping

To achieve neighbouring regions of high and low pressure, differential pumping techniques are employed: a beam can easily be focused through a small aperture, but gas flow is severely restricted by a small aperture. The smaller and longer the hole is, the lower the conductivity of the aperture, and the greater the pressure differential that can be obtained between either side of the aperture. A large pressure drop can be achieved by putting pumps on both sides of the aperture. Multiple aperture and pumping sections can be employed.

The gas is injected into the plasma chamber and then escapes through the extraction aperture in the plasma electrode. The extraction aperture is effectively

the first section of the differential pumping system. The next section is usually after the apertures in the extraction and post-extraction acceleration electrodes.

If the source is pulsed, the gas feed to the source is also pulsed. Just enough gas is injected into the plasma chamber to maintain the pressure in the plasma chamber for the duration of the discharge pulse. This reduces the gas load on the vacuum system when compared with continuously maintaining the required pressure in the plasma chamber. A transient pressure pulse is massively attenuated by a differential pumping aperture especially if the vessel on the other side of the aperture is large.

17.9.3 Vacuum System Design

The overall design of the system can be achieved using the electrical circuit analogy: pressure = voltage; pumping speed (and flow rate) = current. The apertures have a ‘conductance’ as do pipes. By employing electrical circuit analysis techniques (either using manual calculations or circuit analysis software), the required pumping speeds can be calculated for a given vacuum ‘circuit’. The conductance of all the components in the vacuum circuit must be found; there are equations for the conductance of simple pipe geometries, but more complex shapes require simulation methods.

Vacuum conductance strongly depends on which pressure regime the vacuum system is operating in. In the molecular flow regime ($<1 \times 10^{-2}$ mbar), the pressure is low enough that the mean free path is longer than the vessel dimensions and so wall interactions dominate. In the viscous flow regime (>1 mbar), the mean free path is short, so interactions between gas molecules themselves are dominant. There is a transitional regime between the molecular and viscous flow regimes where both wall and inter-molecular interactions are important.

The vacuum pressure inside the ion source plasma chamber is often in this transitional regime, but pressure outside the plasma chamber is in the molecular flow regime. The viscous flow regime is only encountered during pump down when the system has been let up to atmospheric pressure.

For complex geometries, simulation software is required to work out conductance and pressure distributions. In the viscous flow regime, Computational Fluid Dynamics (CFD) techniques are required; there are numerous commercial and open source (e.g. OpenFOAM) software packages available. In the molecular flow regime, Monte Carlo ray tracing techniques are required; there are numerous commercial and open source (e.g. Molflow+) software packages available.

17.9.4 Trapped Volumes

The vacuum system must be designed to avoid trapped volumes. Trapped volumes are closed regions created when in-vacuum components are brought together

in assemblies. At pump-down, the trapped volume contains gas at atmospheric pressure; the enclosed nature of the trapped volume makes the gas hard to pump away. Depending on how 'enclosed' the trapped volume is, it might take days or even weeks to pump-out the reservoir of gas trapped in the volume, which behaves as a 'virtual leak'. A sign that a vacuum system has trapped volumes is that it takes a very long time to pump down.

Trapped volumes commonly occur at the bottom of blind threaded holes in the space not occupied by the screw. The simple solution is to avoid blind holes by ensuring all holes are drilled all the way through. If blind holds cannot be avoided (e.g. threaded holes in vacuum chamber walls), then the screw or bolt itself must be 'relieved'. This is achieved by either drilling a small hole up the bolt's axis or cutting a groove along the length of the thread to allow the trapped gas to escape during pump down. Other trapped volumes can 'relieved' by cutting channels that allow the gas to escape.

17.9.5 Types of Vacuum Flanges and Seals

The components of a vacuum system must be connected together and good leak-tight seals made between them. The type of seal used depends on the diameter of the flange, how often it will be disconnected, the level of vacuum required, and the temperature it has to withstand. Sometimes radiation hardness can also be a factor.

The four most common vacuum flange types are: KF, K, F and CF. Each type is available in a range of standard sizes. Different manufactures use different names to refer to these four types. KF, K and F are defined by the International Organization for Standardization and often have the ISO prefix. CF stands for Conflat and is a trademark of Varian Inc.

KF, K and F all employ reusable Viton or nitrile rubber O-ring gaskets in a centring ring, whereas CF employs a single-use copper gasket and knife-edge seals. CF Flanges can be baked-out to high temperatures so they are suitable for ultra-high vacuums ($<1 \times 10^{-8}$ mbar) and hot caesium transport lines, whereas Viton can only operate up to 150 °C and nitrile rubber only 80 °C. A KF flange has a quick release clamp with a single wingnut and is suitable for smaller ports up to 50 mm diameter. K is for larger flange diameters and so employs a number of claw clamps around the flange circumference. F is for the largest port diameters and employs bolts around the flange circumference.

The American Standards Association (ASA), now known as the American National Standards Institute (ANSI), also defines rubber O-ring flange types, which can be used for both vacuum and pressure applications.

Permeation through O-ring gasket seals is well documented; most ion sources rely on O-ring seals; however, the effect of the permeation flow is rarely discussed.

A Wheeler flange is a compressible wire-seal flange often used for large or cryogenic vacuum chamber seals. Indium metal wire is often used as the seal.

The main ion source high-voltage insulator is usually sealed to the primary vacuum vessel using a custom O-ring groove cut into the vessel with a flat sealing surface on the insulator. Care must be taken to design an O-ring groove with the correct dimensions for the O-ring: a good seal must be achieved when the O-ring is fully compressed.

For very large door seals, a double O-ring can be employed, with the space between the two O-rings separately pumped, producing a differential seal.

17.9.6 Primary Vacuum Vessel and Main Insulator

The primary vacuum vessel acts as a chassis for the ion source: to support the turbo pumps, to support the main insulator that supports the plasma chamber and to provide vacuum feed-throughs for all the ancillary equipment, monitoring and diagnostics. The vacuum vessel should have a selection ports with standard vacuum flanges of different sizes. It is always a good idea to put as many ports on a vacuum vessel as possible to provide future flexibility; if the ports are not used, they can easily be blanked off.

There are two important mechanical safety features of the primary vessel: (1) it should have an over-pressure relief valve fitted to one of the ports to prevent accidentally over-pressurising the vessel when it is being let-up to atmospheric pressure and (2) it should be securely held down to a support structure. There can be significant cantilever loads from the ion source, pumps and other equipment attached to the main vessel. When equipment is removed for maintenance, the main vessel can become unbalanced and present a toppling hazard.

The plasma chamber is mechanically supported by the main insulator. The main insulator must stand-off the entire platform volts and so must be large enough to keep the electric fields low enough to avoid high-voltage breakdown. This could be implemented as very large radius insulating disk, but a more compact design can be achieved with either a re-entrant or an external column insulator as shown in Fig. 17.9.

From a beam dynamics point of view, it is important to keep drift spaces (where the beam is neither accelerated nor focused), as short as possible. So the point where the beam is extracted from the plasma should be positioned as close to the exit of the primary vacuum vessel as possible.

The re-entrant insulator design achieves this by moving the position of the plasma chamber further into the primary vacuum vessel. The downsides of this approach are that access to the plasma chamber is restricted and care must be taken to maintain enough space for high-voltage clearance of the power, cooling and signal connections from the ancillary equipment on the high-voltage platform. A re-entrant insulator design allows the plasma chamber to be mounted in air, external to the primary vessel, which can make maintenance and development easier.

If an external plasma chamber is mounted on an external main insulator, it creates a long drift space before the beam exits the primary vacuum vessel. If an

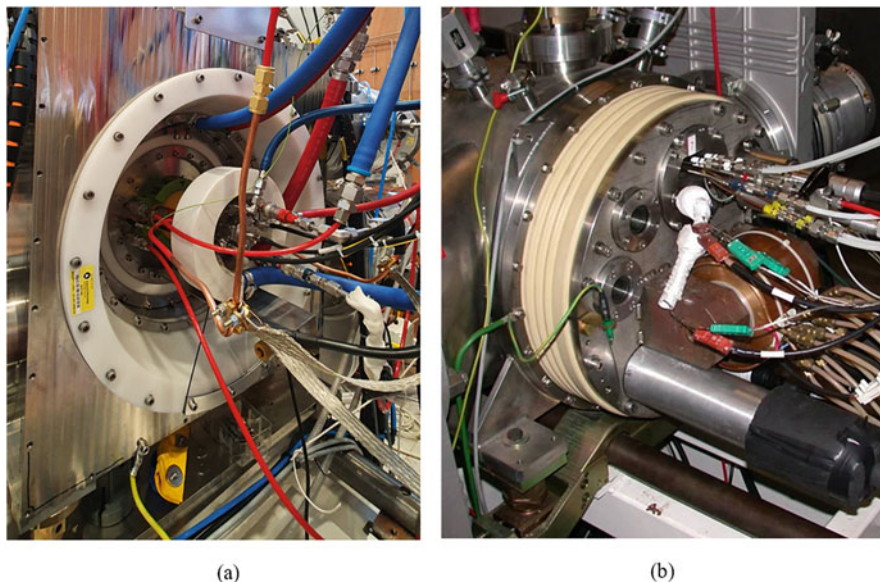


Fig. 17.9 Two design options for the main insulator design. (a) Re-entrant main insulator with external plasma chamber. (b) External column main insulator with internal plasma chamber

external main insulator design is used as shown in Fig. 17.9b, the ion source plasma chamber is mounted inside the primary vacuum vessel. An external main insulator makes for a simpler insulator design, and there is no problem maintaining high-voltage clearance of the connections to the ancillary equipment on the high-voltage platform. However, the plasma chamber can only be accessed by removing it from the main vacuum vessel, and source development is harder. An internal plasma chamber is best suited for smaller plasma chambers such as those found in Penning or magnetron sources.

The choice of re-entrant or external insulator depends on the design of the ion source and beam transport.

17.9.7 Plasma Chamber

The plasma chamber (occasionally referred to as a plenum) is the solid boundary that encloses the plasma. Its primary purpose is to confine the gas (and possibly vapour) in a region where the discharge can take place. It must have an extraction hole, out of which the ions can be extracted. The extraction hole is always drilled through a piece of metal named the ‘plasma electrode’. The other walls of the plasma chamber can be insulators or conductors.

The hole is always in a metal material, and is called the 'plasma electrode'. The other walls of the plasma chamber can be insulators or conducting electrodes.

In an internal RF coil source, the plasma chamber is conductive. The chamber is a passive earth electrode; it serves as a reference voltage and dominates the capacitive coupling. In the external RF coil source, the plasma chamber is an insulating alumina tube, with a conducting plasma electrode downstream and a metallic plate providing connectivity and H₂ injection upstream.

In the Penning and magnetron sources, the plasma chamber walls are active electrodes: the current drive for the discharge is applied between the anode and cathode chamber walls.

17.9.8 Surfaces in Vacuum

Surfaces can absorb and adsorb molecules and atoms. Molecules and atoms can also diffuse or permeate through the bulk of a material towards the vacuum surface of the material, but at the pressures used in ion sources, the permeation through the bulk material into the vacuum is negligible. Molecule and atom absorption and adsorption can have a significant effect on ion source performance.

Prior to assembly, all the ion source components must be cleaned and degreased. To remove water and other molecules absorbed into the surface, vacuum bakeout is required. Vacuum bakeout is advisable for components that come into contact with caesium and plasma. Vacuum bakeout can either be performed on the component level prior to assembly or performed in-situ once the source has been installed. In-situ bake out is not always possible, if the components are baked-out separately, they must be put together as quickly as possible and the complete assembly put back under vacuum as soon as possible (ideally less than 2 hours after letting the baked-out components up from vacuum). Ceramics are also baked-out prior to usage in high vacuum systems.

In caesiated ion sources, surfaces can act as a reservoir for caesium. The surfaces of the plasma chamber, the surfaces of the vacuum chamber, extraction and beam transport electrodes all can become coated with caesium. It takes time for the caesium surface coating in an ion source to reach an equilibrium; the exact time to reach equilibrium depends on the amount of caesium used, the surface temperatures and duty cycles, the distance from the primary caesium source and the overall geometry. The relationship between surface temperature and caesium coverage means that the source must reach thermal equilibrium before a caesium equilibrium can be achieved.

Surfaces in the plasma chamber can take between 4 hours and a day to reach a caesium equilibrium. Surfaces outside the plasma chamber can take 2–4 days to reach a caesium equilibrium. These numbers are based on operational experience with the ISIS Penning Surface Plasma Source.

During this equilibrium time, the performance of a caesiated source will slowly change: beam current will slowly decrease from its initial start-up value; extraction currents will slowly increase.

Caesiated surfaces provide a memory of previous operating conditions, so when source operating conditions change, the source behaviour will depend on how it was operating before. This can result in unexpected and apparently erratic behaviour as the reservoirs of caesium on the caesiated surfaces move to a new equilibrium as the source 'settles down'.

Surfaces are affected by sputtering, which affects their geometrical shape, altering source performance. The cathode in a plasma chamber suffers the most because positive ions in the plasma are accelerated by the sheath potential surrounding the cathode. The material that is sputtered away from the electrodes is redeposited both on the original electrode and any other nearby surfaces. This redistribution of material can affect source lifetime; deposited material is embrittled because it is deposited in a hydrogen atmosphere, making it prone to flaking off. Flakes can cause blockages and electrical short circuits.

17.9.9 Vacuum System Exhaust

Hydrogen and the other gasses and vapours that are fed into the plasma chamber escape through the extraction aperture in the plasma electrode and are pumped away by the turbo and backing pumps. The exhaust from the backing pumps must be safely vented to the outside world.

A laboratory might already be equipped with a dedicated exhaust system capable of taking hazardous gasses. These systems must be regularly maintained and inspected. The exhaust system has to cope with a large range of flow rates and gasses: when the source is running, only a small amount of gas is exhausted, of the order $10\text{--}20\text{ mlmin}^{-1}$ (the flow rate of hydrogen that is fed into the ion source).

When the ion source vacuum vessel is pumped down after the vessel has been opened, there will be a short period of very high flow rate in the exhaust line. The exhaust system must be able to handle this transient gas pulse whilst the gas in the vessel is pumped away.

The simplest way of achieving this is to use a large diameter pipe (at least 100 mm).

The route of the pipe should only ever move upwards; this will allow the lighter-than-air hydrogen to float up the pipe and out to atmosphere. If the exhaust pipe takes an up-and-down route, then there is the potential for hydrogen gather in the local 'up' points in the exhaust line. The only place the exhaust pipe should turn back on itself is at the point where it exits to the atmosphere: the exit should bend to face down so that rain cannot enter the pipe. The exit of the exhaust pipe should be high up on a wall or the roof of the building away from any ignition sources.

If a heavier-than-air gas is also fed into the source (e.g. krypton or argon as a beam-transport space-charge-compensation buffer gas), this too will need to be

pumped away and exhausted. It might be necessary to add a fan to the exhaust line to ensure that both heavy and light gasses are safely pumped away, and the fan and vent must be interlocked to the hydrogen system.

17.9.10 Gas Delivery Systems

Gasses must be delivered into the ion source vacuum system in a controlled manner so that the pressures required in the different regions can be accurately and stably maintained.

Gas can either be pulsed or continuously fed into the ion source. The gases used come in pressurised cylinders or bottles made of steel. Ideally these should be kept outside in a dedicated, well-ventilated enclosure a short distance from the building, but often historical infrastructure will have the bottles on the outside wall of the building.

A full cylinder could be at 240 bar gauge pressure, this is regulated down with a bottle mounted regulator to 1–2 bar gauge depending on how long the pipe is to the ion source is. At the ion source, the pressure is further regulated down to 0.2–0.8 bar gauge before the gas is accurately dispensed into the ion source vacuum chamber. At its simplest, this final stage could be a needle valve, or for more accurate and stable control a mass flow controller can be employed.

If a pulsed system is required, an electrically controlled valve is required. For low repetition rates (<10 Hz), an electromagnetic solenoid valve can be used; for higher repetition rates, a piezo electric valve is required.

The gas delivery system should have the facility to purge the feed pipes. When a gas cylinder is changed, or the gas delivery system is maintained, atmospheric air can be introduced into the pipework. Before an ion source can be started up, the pipework must be purged so that contaminated gas is not fed into the source. This is achieved with a valve just before the final dispensing stage that diverts the gas to a dedicated purge line that either vents to atmosphere or into the vacuum exhaust system. If a purge line is not available, an alternative option is repeated filling and pumping down of the feed line.

Diurnal and seasonal temperature variations can affect the gas delivery system, so some thought must be given to how this affects the source performance. It is often good to regulate the gas with a vessel vacuum pressure measurement rather than try to maintain source stability with a constant volume or mass flow rate.

17.9.11 Caesium Systems

Caesium is the magic elixir for negative ion sources; it greatly increases negative ion current. However, it is hazardous, being toxic and highly pyrophoric.

To make handling easier, cartridges containing caesium chromate can be used, which release caesium when heated by a heater element. The cartridges can be positioned where the caesium is needed, so caesium consumption can be minimised. If larger flow rates of caesium vapour are required, a caesium oven is used. High purity elemental caesium is heated in an oven between 140 °C and 190 °C. The caesium vapour is transported to the plasma chamber via a pipe heated to a higher temperature.

Elemental caesium is stored under argon in a glass ampoule. Either the caesium can be poured into the oven in a glovebox under an inert atmosphere or the whole glass ampoule can be put in a close-fitting soft-copper oven. When the oven and ion source is ready to run, the vessel is pumped down and refilled with dry nitrogen, and the oven is squeezed to break the glass ampoule and the vessel pumped down again. If the ampoule were to be squeezed and broken under vacuum, the ampoule could explode, driven by the pressure of the argon in the ampule, forcing shards of glass into the caesium transport tube and potentially blocking it.

When a caesiated source needs to be refurbished, caesium's extreme reactivity with water and high solubility of its compounds can be harnessed. The ion source and caesium oven are simply flooded with water in a reaction tank with enough venting to cope with the rapid gas expansion. Either this can be achieved with specially made tanks and chambers, or an industrial dishwasher can be employed. The dilute caesium hydroxide solution that is generated must be safely disposed of.

Caesium also has a very high atomic number so it is very effective at sputtering electrode material, which fundamentally limits the lifetime of ion sources.

17.10 Plasma Ignition Systems

Ion sources do not necessarily need an ignition system. Mother Nature provides a source of free electrons from ionising background radiation, so if you are willing to wait, eventually an electron avalanche will be initiated that will ignite (strike) the plasma.

This is fine for DC sources where waiting a few seconds during start-up is completely acceptable, but for pulsed sources, failure to strike a plasma means an entire lost acceleration cycle and a lost beam pulse for users. High power pulsed ion sources have an advantage because relatively high electric fields are applied to the plasma chamber so that free electrons are more likely to create avalanches that ignite the plasma.

There are two options for guaranteeing plasma ignition: increase the electric field or increase the number of free electrons.

Increasing the electric field can be achieved by designing a discharge power supply that applies a higher voltage (a strike potential) if the discharge current is low; this technique is employed in the Penning and magnetron sources.

Increasing the number of free electrons can be achieved by pre-ionising some of the gas as it is injected into the plasma chamber. This can be done by passing the gas through a high-voltage spark gap as it enters the plasma chamber. The spark gap is over-volted, thus guaranteeing breakdown in the spark gap. The voltage pulse is applied to the spark gap a suitable time before the main pulsed discharge in the plasma chamber. The spark gap electrodes will suffer from erosion and eventually require replacement. Longer lifetimes can be achieved by using a microwave discharge chamber instead of a spark gap.

17.11 Documentation Systems

17.11.1 Mechanical Drawings

Manufacturing drawings are required to make the bespoke components in a source, which often need to be regularly replaced. Mechanical assembly drawings are required to understand the construction of the source for fault diagnosis. Mechanical assembly drawings are essential to source research and development; they allow source geometries to be accurately imported into modelling software for analysis of electric and magnetic fields, thermal studies, beam transport, plasma modelling, etc.

Over time, slight modifications are made to components, some of which are permanent, some of which were temporary experiments. Without a managed and maintained set of mechanical drawings, things can become impossibly confused.

Managed and maintained documentation is essential to being able to deliver good operational availability, and it allows the source to be developed. Maintained documentation means that any changes made to components must be updated in the drawing document. Managed documentation means a structured set of documents with some form of change control to identify the most up-to-date version. This could be as simple as folders containing documents with numbered file names, or it could be a complicated repository system with the ability to check, approve and issue documents. There are numerous professional systems that offer this sort of document database management, some are offered as part of a CAD system, and some are part of asset management systems. The exact document management system employed often depends on what system is used by the rest of the accelerator facility, or it might be chosen based on the preferences of the team that operates the ion source. The lifetimes of particle accelerator facilities are measured in decades, whereas software systems evolve and die very much faster, which means that the choice of document management system is often historical. This brings with it the problem of being tied to obsolete systems, so it is important to keep the structure and file types used as open as possible.

17.11.2 Electrical Drawings

The principle of managed and maintained documentation also applies to the electrical and electronic circuits in the ancillary equipment that make the ion source work. Often this equipment is built in-house or custom built by manufacturers. Without circuit diagrams, it can be very hard to diagnose faults when trying to fix the ancillary equipment; time can be wasted leading to reduced source availability.

17.11.3 Ancillary Equipment

It is essential to manage and document ancillary equipment spares, not only to make sure that spare equipment is available but also to have some information about how long, where and how the equipment has been run. This can guide preventative maintenance programs, allowing components to be changed before they fail in operation. For example, a high-voltage switching valve in an extraction power supply will have a certain number of filament hours after which it should be replaced; cooling fans should be replaced after a few years before their bearings fail; safety equipment requires testing.

There are commercial asset management systems and computerised maintenance management systems (CMMS) that can be used to keep track of all the ancillary equipment and provide reminders when maintenance is required. If there is a CMMS in use for other equipment elsewhere in the accelerator, then this could be used, but because there is only a limited amount of ancillary equipment used in an ion source, a simple spreadsheet based system could be used.

17.11.4 Ion Source ‘Build Sheets’

Every operational accelerator facility must have more than one ion source assembly and numerous spare parts. The specific components used in each ion source should be documented and managed. Each ion source should have some sort of ‘build sheet’: a list of the components in the source, confirmation that the build process has been followed, alignment and electrical measurements and finally operational test results of the system components.

The use of a ‘build sheet’ is an essential part of ion source Q + A (Quality and Assurance): it is key to maintaining the reproducible source performance that is necessary for an operational accelerator facility.

It also allows theories to be tested about why a source is behaving in a certain way. Ion sources manifest many emergent behaviours, and we humans are irrepressible pattern spotters, so we are prone to coming up with theories. Source lifetimes vary between weeks and months, which mean running statistics build up

quite slowly and often changes in source performance might not be statistically significant because of the small number of data points. Sometimes theories can become superstitions; documentation provides evidence that can disprove incorrect beliefs about source operation. These incorrect beliefs can have a negative effect on source performance, cause unnecessary operational costs and act as a bar to understanding, which can impact on the ability to develop a source.

17.11.5 Post Failure Analysis

Equally important to the ‘build sheet’ is the ‘autopsy’ after a source has failed or been taken off the machine. It is important to confirm the suspected failure mode to allow the compilation of reliable statistics. Blockages, electrical short/open circuits and other damage might not be obvious until the source is dismantled.

It is important to inspect the source components for damage caused by sputtering, overheating, electrical discharges. Observations can be noted down as text, photographs or microscope images. Text and images are harder to analyse but can be useful to when making a distinction between typical and unusual wear patterns.

Reliability statistics can be easily analysed if a failure mode can be selected from a list. However, the art of collecting useful failure mode statistics is choosing the correct failure modes to feature in the list: make the failure modes too general and the information generated might not be that useful and make them too specific and there will be too many to choose from. If there are too many to choose from there is a danger of the failure mode being miss-classified through laziness or confusion. A large number of failure modes also mean that it might take a very long time to gather the statistics for any one failure mode.

17.12 Reliability

Ion sources must deliver >99% availability to avoid being a major cause of facility downtime. Availability is defined as the percentage of time that a scheduled beam is delivered. The running schedule of the facility can have a significant effect on source availability: physics processes might limit source lifetime, but as long as a scheduled source change occurs before the source nears the end of its life, 100% availability can still be achieved. The converse is also true; if scheduling requirements push scheduled source changes too far apart, then the source availability will suffer.

Ion sources are complex systems involving high voltages and plasma; there will be equipment failures. In a user facility, every moment the source is off is lost time for users, so any failures must be fixed as soon as possible. The simplest way of achieving this is with a well-managed set of spares. There should, as a minimum, be a spare of every single part of the ion source itself and spares of all

the ancillary equipment. The whole system should be engineered to be replaced as quickly possible.

The reliability of an ion source is dominated by the performance of the engineering and technology employed to deliver the physics processes and techniques required.

Acknowledgements The author is eternally grateful to Jacques Lettry (CERN) for his detailed review of this manuscript and suggestions for improvements.

References

- D. Aguglia, s.l., 19th IEEE Pulsed Power Conference (PPC) (2013)
- ATEX, [Online] (2014), Available at: https://ec.europa.eu/growth/sectors/mechanical-engineering/equipment-potentially-explosive-atmospheres-atex_en
- M. Bacal, M. Wada, Appl. Phys. Reviews **2**(2), 021305 (2015)
- EPICS, [Online] (2022), Available at: <https://epics-controls.org/>
- D. Faircloth, Shanghai, Proceedings of IPAC2013 (2013)
- IEC, [Online] (2010), Available at: <https://webstore.iec.ch/publication/5515>
- J. Lettry, s.l., Review of Scientific Instruments **83**, 02A728 (2012)

Chapter 18

Radio Frequency-Driven, Pulsed High-Current H^- Ion Sources on Advanced Accelerators



Martin P. Stockli

Abstract The introduction of this chapter explains the use of pulsed high-current H^- ion sources. It then discusses the radio frequency-driven H^- ion sources serving advanced accelerators starting with the award-winning SNS ion source. It explains all important characteristics in detail, including limitations and lifetimes. A table lists over 30 characteristics and performance data. Designed at LBNL and fully developed at SNS/ORNL, the success of this H^- source is evidenced by the fact that since 2014, three other advanced, high-current (~40 to 60 mA) accelerators switched to this type of H^- ion source and others will switch within a few years. The three new RF-driven, high-current H^- sources supplying advanced accelerators are then described and compared in the table. This chapter ends with an outlook and the projects that develop new RF-driven H^- sources for additional long-pulse, high-current, advanced H^- accelerators.

Keywords Ion source · H^- ion source · Plasma · Hydrogen plasma · Ion beam · RF ion source · Multicusp ion source · Bucket ion source · Low-energy beam transport · LEBT

18.1 Introduction

Some advanced accelerators prefer negative ions because stripping after a merging magnet allows multiple injections from a linear accelerator (linac) into synchrotrons and accumulator rings. Each injection joins the previously stripped ions as shown in Fig. 18.1a. This creates ion beams with currents much larger than directly from any accelerator-type ion source. For example, the Spallation Neutron Source (SNS) (Henderson et al. 2014) accumulates up to 980 beamlets converting the ~50 mA H^- beams from the ion source to proton beams with up to 60 A peak currents in

M. P. Stockli (✉)

Spallation Neutron Source, Oak Ridge National Laboratory, Oak Ridge, TN, USA
e-mail: stockli@ornl.gov

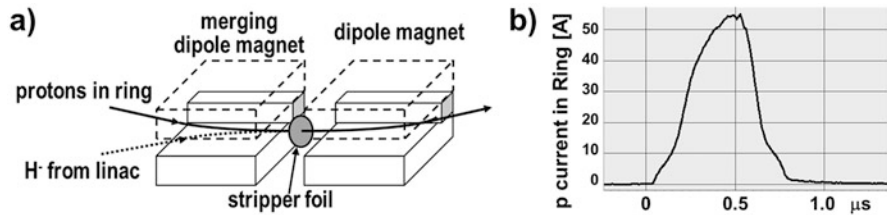


Fig. 18.1 (a) Schematic charge-exchange injection into a proton ring. (Modified from (Stockli et al. 2018) with the permission of AIP Publishing) and (b) accumulated proton beam current in the SNS accumulator ring

Table 18.1 Work functions of metals without/with alkali adsorbates (values extracted from (Graham 1980))

Adsorbate/substrate	Work function ϕ_0 (eV)	Minimum work function ϕ_{\min} (eV)	Equilibrium work function ϕ_{equil} (eV)
None/Fe	4.5	–	–
None/Na	2.75	–	–
None/Cs	2.14	–	–
K/Mo	4.6	1.76	2.14
Na/Ta	–	2.29	2.46
Na/W	4.55	2.16	–
Cs/Mo	4.6	1.54	1.82
Cs/Ni	5.15	1.37	1.80
Cs/Ta	4.25	1.69	1.70
Cs/W	4.55	1.52	1.80
Cs/304 SS	–	1.52	1.60

the accumulator ring (Peters 2021) as shown in Fig. 18.1b. The challenge is the production of sufficient negative ions because they do not form easily, and they are easily destroyed (Bacal et al. 2021; Taccogna et al. 2021; Zhang 1999; Janev et al. 2003; Hiskes 1980).

In the past, high-current (>15 mA) negative H^- ion beams were produced exclusively with high-voltage plasma in compact surface plasma ion sources (CSPS) or in filament driven converter ion sources. However, the lifetime of those sources is limited by the sputtering of the cathode(s) or the hot filament(s). A 1994 workshop at Lawrence Berkeley National Laboratory (LBNL) was attended by specialists from most major H^- source laboratories and facilities. They could not identify an existing ion source that could meet the challenging requirements for the SNS project of delivering ~ 50 mA H^- for 1-ms-long pulses at 60 Hz and with a lifetime of at least 3 weeks (Alonso 1996). A 2002 review (Welton 2002) and its expanded table 1 (Stockli et al. 2018) show that the required maintenance-free 1.5 Amp-hour (A·h) production of H^- ions was met or exceeded only by the magnetron H^- source at Brookhaven National Laboratory (BNL). However, this source was operated only with 0.63 ms beam pulses at 7.5 Hz, and the required 13-fold increase in duty factor was expected to substantially reduce its lifetime. Other H^- ion sources with

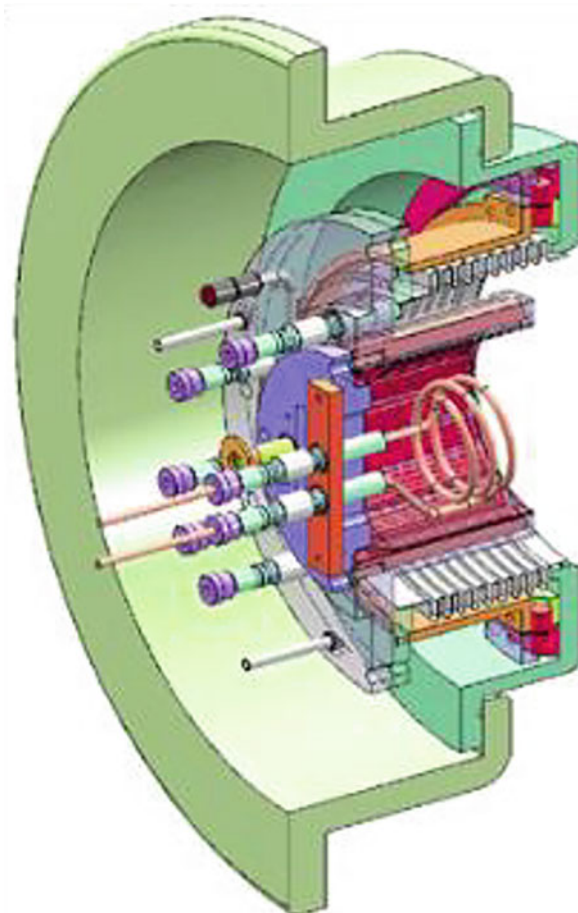


Fig. 18.2 Schematic showing the RF H^- source LBNL developed for SNS. (Reproduced from (Keller et al. 2002) with the permission of AIP Publishing)

lifetimes that came close to the SNS requirements also operated at small duty factors (such as the test multicusp RF H^- source at the Deutsches Elektronen-Synchrotron (DESY)) and/or did not deliver enough H^- output current (such as the test DESY multicusp RF H^- source and the Los Alamos National Laboratory (LANL) filament driven converter H^- source) (Stockli et al. 2018).

Fortunately, LBNL developed multicusp ion sources which produce very quiescent plasma contrary to the Penning (Faircloth et al. 2006) and the magnetron (Bollinger et al. 2015) ion sources. LBNL first generated plasma with a filament (Ehlers and Leung 1979) that was later replaced with a radio frequency (RF) antenna (Leung et al. 1983). LBNL developed RF H^- ion sources with a RF antenna inside the plasma chamber first for the Superconducting Super Collider (Leung et al. 1993) and then for SNS (Leung 2000) as seen in Fig. 18.2.

18.2 Radio Frequency-Driven, Hydrogen Discharges

Filament and other ion sources driven by unipolar voltages suffer from sputtering because the positive ions generated by the discharge are attracted to and impact on the cathode(s) and/or filament(s). The ions follow the first Maxwell equation, which links the electric field $E(x,y,z)$ with the charge density distribution $\rho(x,y,z)$ using ϵ_0 , the electric constant of free space ($8.85 \cdot 10^{-12}$ F/m):

$$\nabla \cdot E = \rho/\epsilon_0 \quad (18.1)$$

The second Maxwell equation links the curl of an electric field $\nabla \times E(x,y,z)$ with the time-derivative $\partial B/\partial t$ of a magnetic field $B(x,y,z)$:

$$\nabla \times E = -\partial B/\partial t \quad (18.2)$$

A pure curling electric field can be produced with an alternating current (AC) $i = i_0 \cdot \cos(\omega \cdot t)$, where ω is the angular frequency and t is the time. The current could flow in a round tube perpendicular to its axis or simpler in a thin coil with N windings of radius r_0 . For the midplane of such a thin coil, Biot and Savart found the magnetic field $B(x,y,0)$ to be.

$$B = \frac{1}{2} \cdot \mu_0 \cdot N \cdot i/r_0 \quad (18.3)$$

where μ_0 is the magnetic constant of free space ($1.257 \cdot 10^{-6}$ H/m). Integrating the second Maxwell's Eq. (18.2) along a concentric circle with radius r in the midplane of the thin coil yields Faraday's law, where ΦB is the magnetic flux enclosed by the circle with radius r :

$$\int E \cdot ds = -d\Phi B/dt = -d/dt \left(\int B \cdot r \right) \quad (18.4)$$

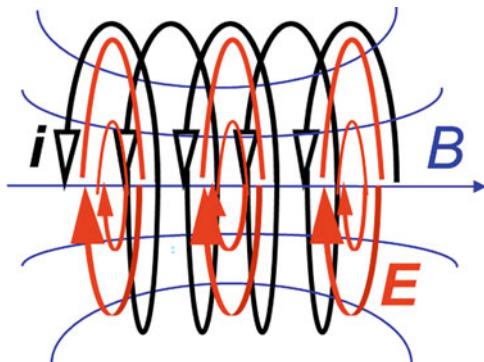
Substituting (18.3) in (18.4) and solving for the electric field E , one obtains.

$$E(0 \leq r \leq r_0, t) = \frac{1}{4} \cdot \mu_0 \cdot N \cdot \omega \cdot i_0 \cdot \sin(\omega \cdot t) \cdot r/r_0 \quad (18.5)$$

which describes a circular electric field that is zero in the center and has a maximum at the windings ($r = r_0$) but drops back to zero outside the windings because the magnetic flux inside the coil and from the windings cancel each other. A schematic of such a field for a closely spaced helix is shown in Fig. 18.3.

The electric field accelerates free electrons and ions in tangential but opposite directions. The accelerated electrons produce more electron-ion pairs from present neutral molecules and/or atoms, increasing the density of the charged particles. The induced circular currents generate another magnetic field in opposite direction to the

Fig. 18.3 Schematic showing the induced magnetic field B and electric field E by an AC current i flowing through the wire forming a closely spaced helix



field induced by the coil. This lowers the primary magnetic field and so stabilizes the discharge. The electric field lines yield closed circles which do not end up on electrodes. This avoids the sputtering of cathodes and filaments which limit the lifetime of unipolar discharges.

18.3 The Spallation Neutron Source RF H^- Ion Source

The SNS $2\frac{1}{2}$ -turn helical antenna is shown in Fig. 18.4. Using a helical coil produces mostly circular fields, but because the current input and output are on opposite sides, there are also axial and radial field components. Some of those field lines do end up on the antenna (Peters 2000a) which causes some sputtering, but much less than in an ion source with unipolar voltages.

There were some concerns about the low electric fields near the axis and accordingly near the outlet. Insights were obtained in 2001 by replacing the stainless-steel (SS) plasma chamber with a glass dome that was surrounded by magnets in an identical multicusp configuration. The observed plasma is shown in Fig. 18.5.

Figure 18.5 shows very dim plasma outside the coil, which means that the multicusp magnets confine the plasma effectively. Inside the coil, the plasma is bright and has roughly a uniform density. This suggests that the intense plasma generated near the antenna windings drifts toward the center because the magnetic field from the cusp magnets has a minimum on the axis as shown in Fig. 18.6. For this reason, multicusp ion sources are sometimes called bucket ion sources. Combining a helical RF antenna with a confining multicusp magnetic field is a very productive solution for RF ion sources.

In the SNS H^- source, ~ 200 W of continuous 13.56 MHz are used to maintain a dim continuous plasma, called starter plasma because it contains free electrons that readily absorb more RF. About 50 kW, 1-ms-long 2 MHz RF pulses generate the intense ion populations needed for the 60 Hz H^- beam pulses. In the meniscus,

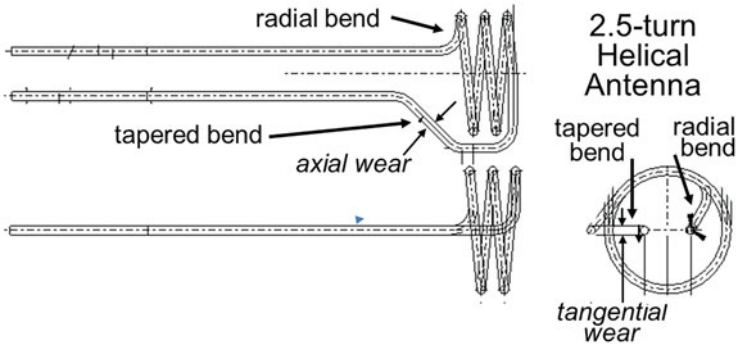
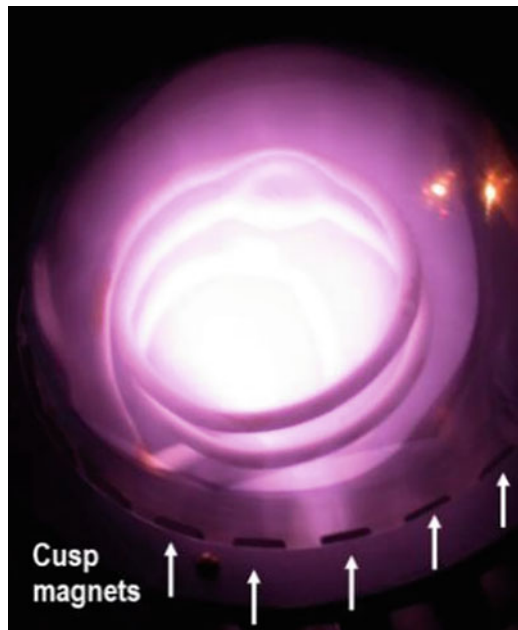


Fig. 18.4 Three views of the SNS $2\frac{1}{2}$ -turn helical coil antenna

Fig. 18.5 The 13.56 MHz plasma of a $2\frac{1}{2}$ -turn helical antenna confined by cusp magnets seen through a glass dome. The distortions seen near the top result from the dome that has a thicker wall near its axis



where the plasma transitions to the extraction field, the negative 65 kV applied to the ion source accelerates negatively charged particles toward the extractor as seen in Fig. 18.7. Emerging from the extractor the 65 keV H^- ions are refocused in the low-energy beam transport (LEBT) consisting of two electrostatic lenses separated by a ground electrode. The second lens forms the convergent beams that yield a high transmission through the RFQ (radio frequency quadrupole) accelerator.

There is much more to H^- ion sources than the production and confinement of plasma, as shown in Fig. 18.7.

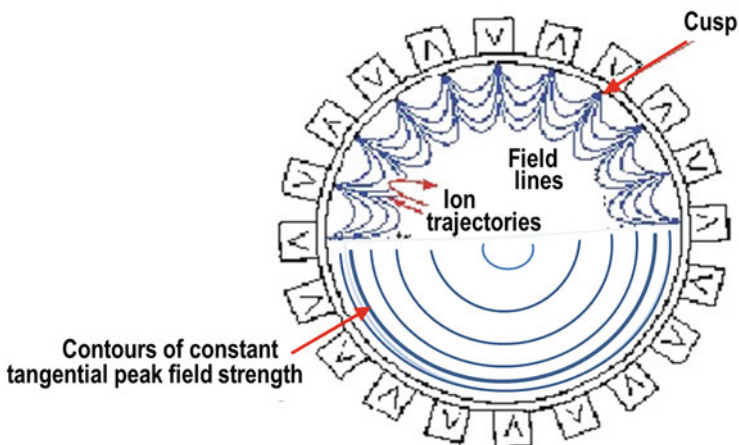


Fig. 18.6 Magnetic field schematic of a multicusp ion source. (Enhanced from (Stockli and Nakagawa 2013) with permission from World Scientific)

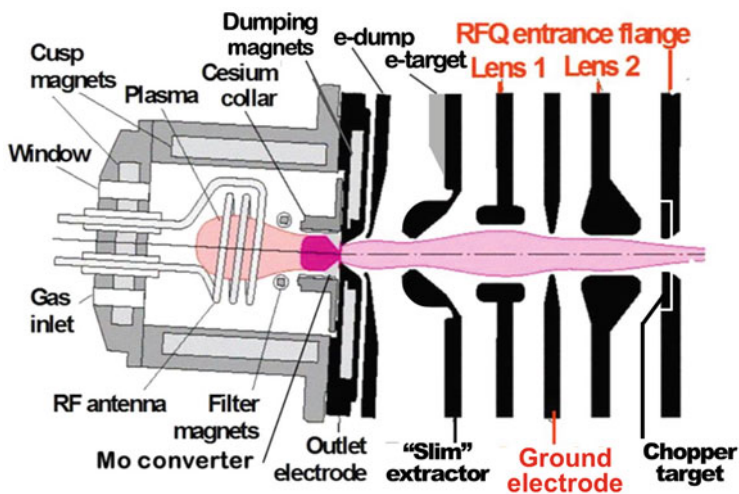


Fig. 18.7 Schematic of the SNS H^- ion source and the low-energy beam transport. (Enhanced from (Stockli et al. 2018) with the permission of AIP Publishing)

First, it is important to properly plan the dumping of the coextracted electrons because they can be much more numerous than the negative ions. The power of the accelerated electrons can damage a part of the downstream accelerator (Midttun et al. 2012), and therefore the electrons are normally dumped with only a fraction of the ion source voltage. This is most economically accomplished by energizing the electron-dump (e-dump) with a positive high-current, high-voltage supply located on the ion source potential. The economic benefit results by drastically reducing the

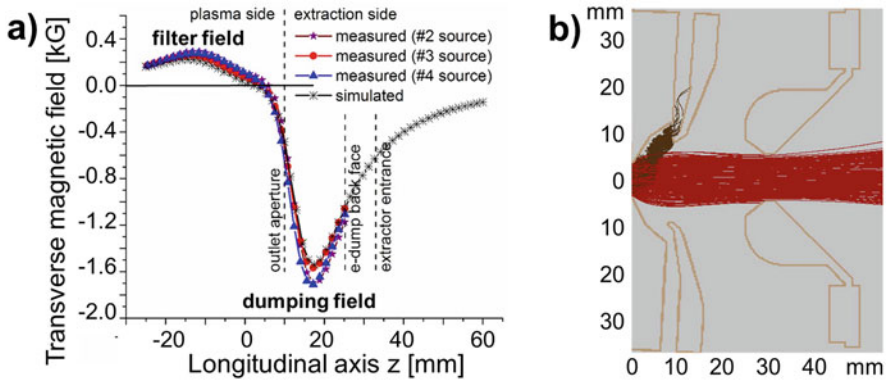


Fig. 18.8 (a) The SNS RF H^- ion source electron filter and dumping magnetic fields and (b) the negative ion (red, going to the right) and electron (black, going upward) trajectories out of the SNS RF H^- source. ((a) Enhanced from (Han et al. 2012a) with the permission of AIP Publishing and (b) inset courtesy of B. Han)

load current seen by the negative, much higher, voltage supply required for the ion source.

The SNS H^- ion source is designed to be as close as possible to the RFQ. For this reason, a permanent transverse dipole magnet is integrated into the outlet electrode as seen in Fig. 18.7. It combines with the magnetic filter field to form a reversal of the transverse field on the axis as seen in Fig. 18.8a. Negative ion sources are not sensitive to the strength of the dumping field as long as the field deflects the coextracted electrons on a cooled e-dump. Due to the high duty factor, the SNS H^- source needs a water-cooled e-dump as shown in Figs. 18.7 and 18.8b.

The magnetic dumping field deflects the extracted ions by about $2\text{--}3^\circ$ depending on the location of the meniscus. To bring the H^- beam on the axis of the accelerator, the source is mounted with bellows as seen in Fig. 18.2. They allow the SNS ion source to be tilted between 0° and 6° to accommodate the ion beam trajectory bend in the dumping field.

Figure 18.9a shows the coextracted electron current versus time intercepted by the e-dump in the SNS H^- source. While it is normally just a little more than the extracted H^- current, it is much more during the plasma buildup when the escaping electrons generate the plasma potential. These current spikes can easily exceed the current limit of the e-dump high-voltage supply and cause it to fold back or shut down because the spikes look like arcs.

More powerful supplies are expensive, and the problem can be addressed with a $R_F C$ filter as shown in Fig. 18.9b. Due to the high-voltage V needed for the e-dump, the capacitor C stores significant energy ($C \cdot V^2/2$). Its discharge current should be limited with a protection resistor R_P to limit the damage caused by e-dump to ion source arcs. The e-dump can also arc to the extractor which can substantially raise the e-dump voltage with respect to the ion source and damage the stressed insulators.

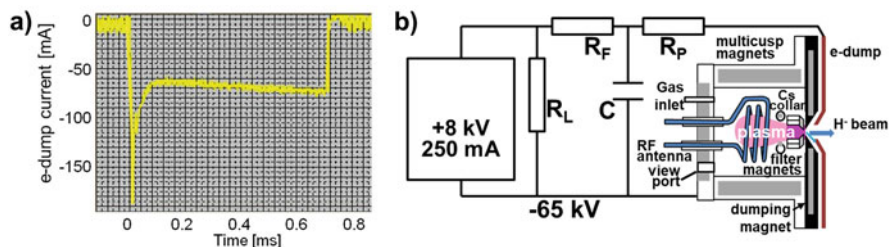


Fig. 18.9 (a) The electron current intercepted by the e-dump during a 2 MHz RF pulse and (b) an e-dump protection network. (Enhanced from (Stockli et al. 2015) with the permission of AIP Publishing)

A load resistor R_L can supply the electrons needed to quickly restore the nominal e-dump voltage, which the positive high-voltage supply cannot.

The physics and technology of high voltages are well understood (e.g., Kuffel et al. 2000). Limiting the electric fields far below the breakdown voltages is the key to reliable operations and therefore needs to be applied wherever feasible. However, ion sources differ somewhat: high ion output currents require extraction fields that are close to the breakdown voltage, and accordingly high-voltage arcs are common in ion sources. The keys to reliability are simple, robust designs and components that match or exceed all possible voltages including the ones in transient conditions of all possible arcs.

Second, negative H sources should have the previously mentioned magnetic filter field to shield the outlet region from the energetic electrons produced inside the RF antenna (Leung et al. 1983). Slow electrons, ions, and excited molecules drift collisionally through the ~ 200 G magnetic filter field and create a colder plasma near the outlet as indicated in Fig. 18.7. That is why this source is sometimes called a tandem ion source.

The SNS source may be able to operate at full performance without an explicit filter field. The field from the e-dump magnet penetrates the source plasma which can be sufficient to keep the energetic electrons away from the outlet. This explains why the output performance was not degraded when source #2 was operated with the filter magnets stuck with an unfavorable rotation which yielded a zero-filter field (ZFF) in December 2007 and January 2008 (see Fig. 18.10 in (Stockli et al. 2009)).

When slow electrons collide with excited hydrogen molecules, the molecules often dissociate forming H⁻ ions (Bacal 2022; Bacal et al. 2021; Taccogna et al. 2021; Janev et al. 2003; Zhang 1999). Because the electron temperature in the extraction region is low (less than 1 eV), H⁻ ions produced there have a good chance to reach the outlet and be extracted (Leung et al. 1983). This is known as the volume production of H⁻ ions (Bacal et al. 2021). Without cesium (Cs), shown by the dashed line in Fig. 18.10a (Sarmiento et al. 2020; Han et al. 2019), practically all the extracted H⁻ ions are produced in the volume.

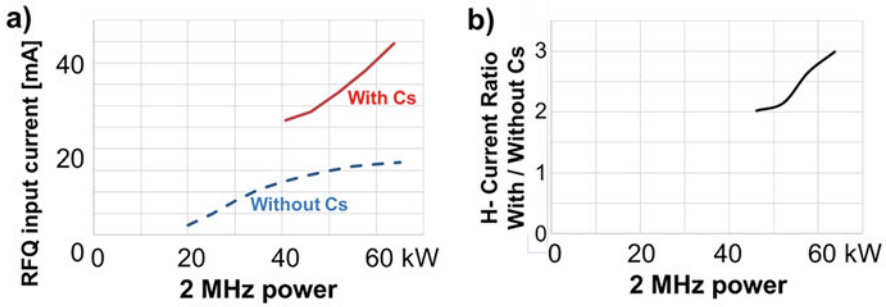


Fig. 18.10 (a) The H^- RFQ input current versus the 2 MHz power for the SNS ion source #5 without and with Cs and (b) the ratio of the H^- currents with Cs/without Cs

18.4 The Surface-Produced H^- Ions

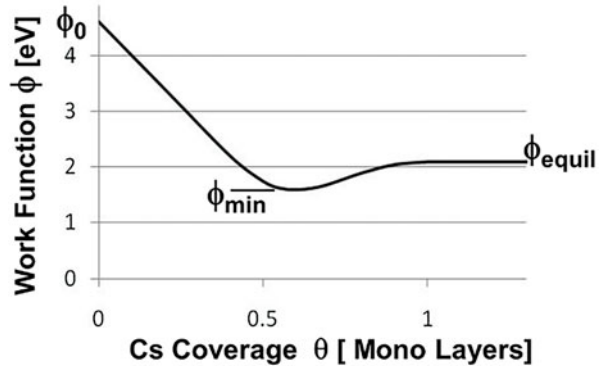
The work function ϕ describes the minimum energy needed to remove one conduction electron from a metallic surface. For most metal, it is about 4–5 eV. However, when adding alkali atoms to an ion source, the work functions are lowered to about 2 eV or less, which can greatly enhance the surface production of negative ions. Due to the fragile nature of H^- ions, only the ones produced near the outlet have a chance of being extracted. In the case of the SNS H^- source, these are the H^- ions produced on the plasma facing surface of the molybdenum (Mo) converter shown in Fig. 18.7. The Cs-enhanced RFQ H^- input current is seen as the solid line in Fig. 18.10a. Figure 18.10b shows that adding Cs to the SNS ion source increases its H^- output current by a factor of 2 and up to a factor of 3 for high RF powers.

Near surfaces there is a plasma sheath, which is only a few μm thick in the SNS H^- source. In the sheath, the positive plasma potential accelerates positive ions from the plasma onto the surface where they rapidly neutralize and most of the atoms bounce back. When bouncing back, there is a chance that they capture a second electron and form negative ions. The probability depends on the time spent in the electron cloud above the surface, which is expressed with the atom's normal velocity component v_{\perp} . Because surface work functions ϕ are normally significantly higher than electron affinities E_a of atoms, most electrons return to the surface. This always happens for slow atoms because the electrons have plenty of time to find the more attractive potential ϕ . However, at larger velocities, an electron can get trapped in the field of a rebounding atom, characterized by the electron affinity E_a . For normal velocities v_{\perp} , Rasser found the following approximation for this probability P to be (Rasser et al. 1982).

$$P = 2/\pi \cdot \exp(-\pi \cdot (\phi - E_a) / (2 \cdot a \cdot v_{\perp})) \quad (18.6)$$

with the constant a being $\sim 3.1 \cdot 10^{-5}$ eV·s/m.

Fig. 18.11 Schematic work function ϕ of partial monolayers θ of alkali atoms on a metal surface. (Enhanced from (Stockli et al. 2011a) with the permission of AIP Publishing)



Rasser's approximation is not valid for high velocities (electron velocities $\gg 0.1$ a.u. (atomic units)) because the approximation neglects the interference term (Rasser et al. 1982). And, at larger velocities, the positive ions are more likely to penetrate the substrate, rather than bouncing back from the surface (Graham 1980; Van Wunnik et al. 1982). The approximation points to the exponential dependence of the H⁻ formation on the difference of the surface work function ϕ and the electron affinity E_a , which is 0.75 eV for hydrogen atoms. Work functions become especially low when alkali atoms are condensed on metal surfaces. Figure 18.11 shows the schematic work function ϕ of a Mo surface as a function of condensed Cs atoms in monolayers (Graham 1980; Rasser et al. 1982; Van Wunnik et al. 1982).

Accordingly, choosing a different surface and/or condensing some alkali atoms on the surface normally changes the work function as shown in Fig. 18.11 and Table 18.1. The table shows work function values extracted from (Graham 1980). In the second column, the table shows the work functions ϕ_0 of the clean metal substrate. Cs has the lowest work function of all elements, but its low melting point of 28.4 °C or 83.1 °F makes productive technical applications in elemental solid form beyond monolayers unlikely.

Figure 18.11 and the third and fourth column of Table 18.1 show how much the work functions decrease when an optimal (ϕ_{min}) or a full (ϕ_{equil}) monolayer of alkali atoms are condensed on the surface. Not surprisingly, the largest atoms, Cs, yield the lowest work functions.

Figure 18.12 shows the Rasser approximation for the probability of capturing an extra electron when a hydrogen atom bounces back from a Mo surface as a function of the normal energy ($m \cdot v_{\perp}^2/2$) of the rebounding atom with mass m . The figure shows that this probability can be substantial for energetic atoms when Cs is adsorbed on a Mo surface, whether or not the Cs layer is optimal. The normal energy of the elastically (or near-elastically) rebounding H atoms is equal or close to the normal energy of the originally impacting atom or positive ion. For most ions, this is approximately the energy gained from the plasma potential that accelerates positive H ions toward the surface. Even though the ion energy is only a few eV in the SNS

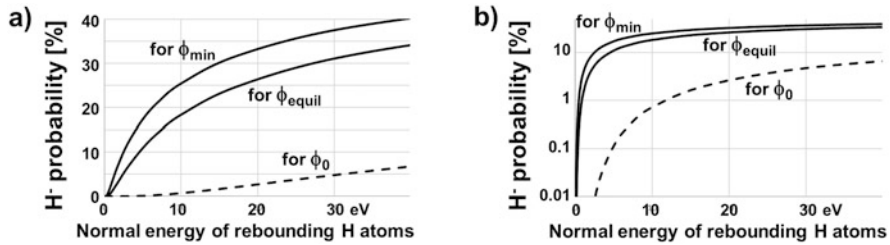


Fig. 18.12 The probability for H atoms to capture an extra electron when rebounding from a clean (ϕ_0) or cesiated Mo surfaces (ϕ_{\min} and ϕ_{equil}) with (a) a linear and (b) a logarithmic scale

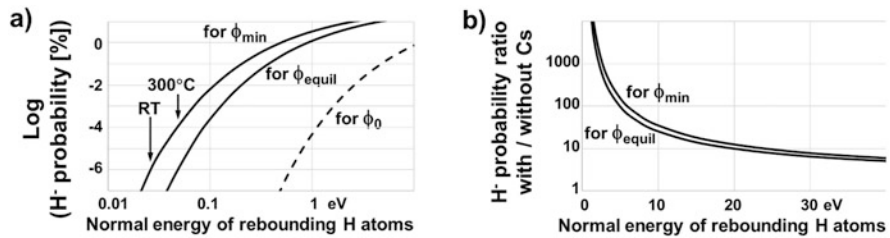


Fig. 18.13 (a) Probability for slow H atoms to capture an extra electron when rebounding from a clean (ϕ_0) or cesiated Mo surfaces (ϕ_{\min} and ϕ_{equil}) and (b) the probability ratio with Cs/without Cs

H⁻ source, the rebounding H atoms become negative ions with a probability in the order of 10%.

Figure 18.12a, b also show that without any Cs (ϕ_0), this probability is small, especially for low energies of the rebounding atoms. Figure 18.13a shows that room temperature (RT) atoms have a $<10^{-8}$ chance to form negative ions. The probability can increase to $<10^{-6}$ for a Mo converter kept near 300 °C. Even when stimulated by plasma bombardment, the desorption of H atoms from the surface does not create any significant amount of negative ions, contradicting earlier claims (Scrivens 2013; Dudnikov and Dudnikov 2018).

Figure 18.13b shows the ratios of the probability of capturing an extra electron from cesiated Mo surfaces compared to a clean Mo surface. Using the ratios from Fig. 18.10b and 18.13b, and the SNS plasma potential of a few volts, it shows that without Cs the fraction of surface-produced H⁻ ions in the extracted beam is ~1% or less.

Furthermore, even with Cs, about one-third to one-half of the extracted H⁻ ion beam from the SNS H⁻ ion source seem to be produced in the plasma volume. Clearly, the volume production contributes substantially to the H⁻ beams from the SNS source.

Calling this H⁻ source a surface plasma source ignores these relevant facts (Dudnikov and Dudnikov 2018; Dudnikov 2019).

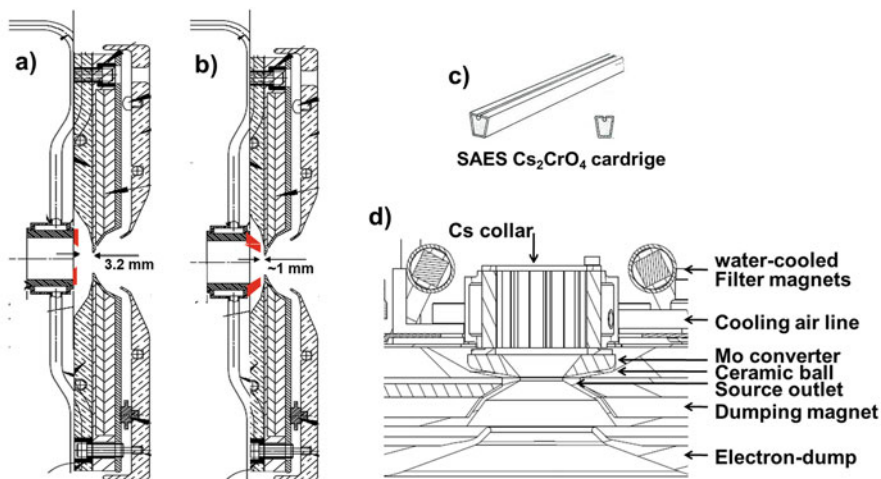


Fig. 18.14 Outlet of the SNS H⁻ source with (a) a LBNL washer-type converter and (b) with a 2007 funnel converter which decreased the gap to ~1 mm. (c) A SAES Cs₂CrO₄ cartridge from (SAES Getters 2021) and (d) the enlarged outlet region of a ceramic ball-centered Mo funnel converter which allows for gaps of ~0.5 mm with negligible thermal contact with the source outlet electrode. ((d) Is enhanced from (Stockli et al. 2011a) with the permission of AIP Publishing)

It is the large outlet apertures of volume ion sources that enable the large volume-produced H⁻ output. When cesiated, the RF-driven volume ion sources combine the volume production with the surface production. Therefore, it could be called a hybrid ion source or more specifically an inductive RF ion source. Even simpler is the established common term of RF ion source.

While LBNL knew about the benefits of Mo (Leung et al. 1993), they chose 304 stainless steel (SS) as material for the converter, perhaps because, as suggested by Table 18.1, it should not be very sensitive to over-cesiations when more than ~0.6 monolayers are adsorbed. At that time, the control of the Cs layer was not understood. However, from all the combinations listed in Table 18.1, the use of Cs and Mo has been most successful in negative ion sources, including at LBNL (Leung et al. 1993) and later at SNS (Stockli et al. 2009).

In 2007, it was discovered that in the SNS H⁻ source, the original washer-type SS converter was 3.2 mm away from the source outlet as seen in Fig. 18.14a. This undoubtedly increased the recombination losses before the H⁻ ions could be extracted. To quickly reduce this gap for the next neutron production run, a 4-mm-thick converter was designed. As seen in Fig. 18.14b, it features a 40° funnel-shaped inner surface to adapt the inner diameter of the Cs collar to the 7 mm \varnothing source outlet. A larger and a smaller funnel angle were tried but they yielded less H⁻ output. The new converters yielded significantly more ion beam than the original LBNL converters and even more after the new converters were fabricated from Mo (Stockli et al. 2009).

In 2008, three ceramic balls were integrated into the Mo converter. They fit in a shallow groove in the source outlet electrode as shown in Fig. 18.14d. This helps to center the converter and guarantees a minimal gap to the water-cooled outlet electrode.

Also, in 2008, a nickel (Ni) coated converter was cesiated and tested because, according to Table 18.1, its work functions are lower than those of cesiated Mo surfaces. While the raw measurement of the H^- output was 5% larger (Welton et al. 2009), it was 5% smaller than the output from Mo converters after being normalized to the same e-dump voltage (Stockli et al. 2010).

18.5 The Management of Cesium

If the amount of Cs is important, how can one generate and maintain an optimal fraction of a monolayer on a substrate?

Cs is a metal with interesting characteristics. Its only stable isotope is a tightly bound ^{132}Xe atom with an additional proton and a loosely bound electron. Accordingly, Cs features the largest atoms with a diameter of 5.3 nm and therefore a small ionization energy of 3.9 eV. Elemental Cs is only about twice as heavy as water despite its heavy nuclei. But do *not* touch it, because it is very reactive (Wikipedia: Caesium 2021)! However, it is perfectly safe to use when properly handled.

The Cs metallic and ionic radii are larger than the metallic radii of most elements as seen in Fig. 18.15. This mismatch in radii causes the surface bond energy of adsorbed Cs atoms to decrease with a growing monolayer (Hansen 1978; Kaminsky 1965) as seen in Fig. 18.16.

To understand the issues, the thermal dwell times τ of Cs on a W(110) surface were calculated using the Hansen approximation for the Cs surface bond $E_{\text{Cs}}(\theta)$ (Hansen 1978; Stockli et al. 2011a, 2012):

$$\tau(\theta, T) = \tau_0 \cdot \exp(E_{\text{Cs}}(\theta) / (k \cdot T)) \quad (18.7)$$

where θ is the monolayer fraction of the Cs adsorbates, T is the surface temperature of the substrate in °K, k is the Boltzmann constant, and the constant τ_0 was found to be $6 \cdot 10^{-13}$ s (Lee and Stickney 1972).

Knowing the dwell time allows for calculating the thermal Cs loss $d\theta/dt = \theta/\tau$, and integrating the loss over time yields the remaining surface coverage $\theta(t)$ (Stockli et al. 2011a, 2012):

$$\theta(t) = \theta_0 - \int (d\theta/dt) \cdot dt = \theta_0 - \int (\theta(t)/\tau(T(t), E_{\text{Cs}}(\theta))) \cdot dt \quad (18.8)$$

Starting at $\theta_0 = 0.995$, the time calculated to thermally loose every $d\theta = 0.01$ monolayer and summing the results for $\theta(t, T)$ for the Cs remaining on a W(110) surface are shown in Fig. 18.17a.

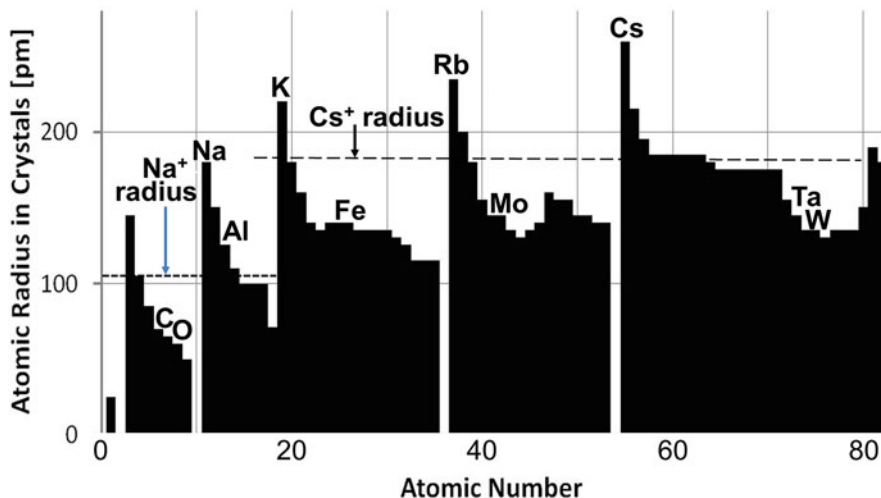


Fig. 18.15 Metallic radii of most elements and the ionic radii of Na⁺ and Cs⁺

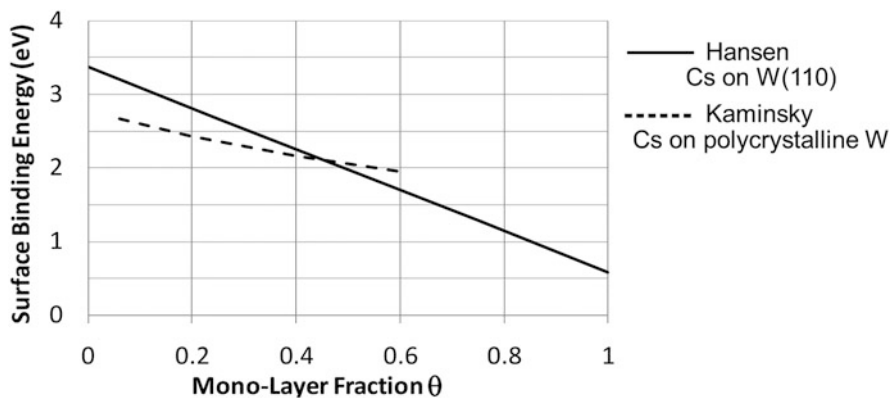


Fig. 18.16 Surface bond energy of Cs atoms on W surfaces as a function of the fraction of a monolayer coverage θ for two approximations. (Enhanced from (Stockli et al. 2011a) with the permission of AIP Publishing)

Figure 18.17a shows that over-cesiations (>0.7 monolayers) must be expected when the converter is kept at low temperatures ($\ll 200$ °C). At high temperatures ($\gg 200$ °C), the substrate thermally emits too much Cs which leads quickly to under-cesiated surfaces ($\ll 0.6$ monolayers). Figure 18.17b shows that any monolayer fraction can be obtained with a high temperature for a short time or with lower temperatures for longer times. Efforts to implement short-time heat treatments and then lower the temperature to freeze the optimal monolayer fraction (as suggested in (Stockli et al. 2011a)) have stopped because the temperature of the

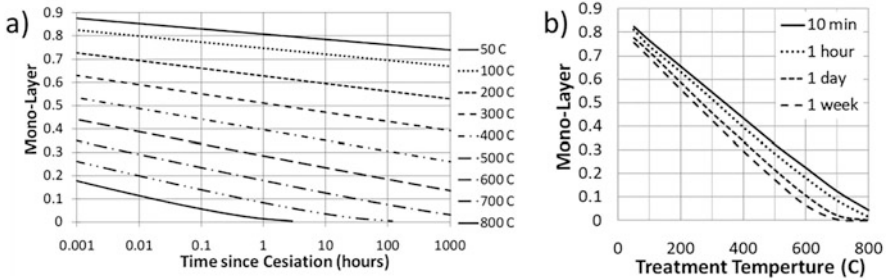


Fig. 18.17 (a) The monolayer fraction of Cs on a W(110) surface versus time for different substrate temperatures T and (b) the monolayer fraction reached versus substrate temperature T for four different times t . (Reproduced from (Stockli et al. 2011a) with the permission of AIP Publishing)

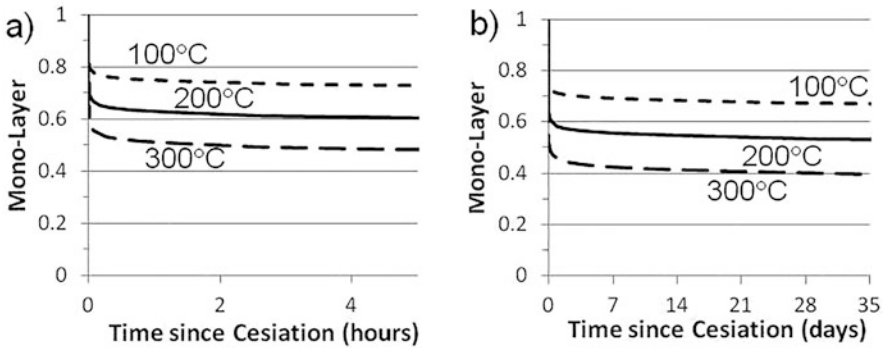


Fig. 18.18 (a) The monolayer fraction of Cs on a W(110) surface versus time for three different substrate temperatures and (b) the same for longer times. (Reproduced from (Stockli et al. 2012), with the permission of AIP Publishing)

SNS Mo converter is difficult to control and affects the H^- output in more ways than just controlling the Cs coverage (Friedl and Fantz 2015).

Figure 18.17a can be misleading as it shows the Cs loss to continue forever. While this is true, using linear scales in Fig. 18.18 gives more realistic impressions. Figure 18.18a shows that most of the Cs emission happens during the first few minutes. Figure 18.18b shows that after a day or so the Cs loss becomes so small that it is barely noticeable. That is why one can run with the Cs collar at elevated temperatures for long ion source service cycles without noticing the decay of the H^- beam. As the Cs coverage gradually decreases and the Cs surface bond energy gradually increases, the fractional monolayer asymptotically stabilizes.

Figure 18.18b suggests that an optimal monolayer can be obtained with a constant temperature of $\sim 150^\circ C$. This temperature should not be taken too literally because the optimal temperature certainly depends on the substrate. For the SNS

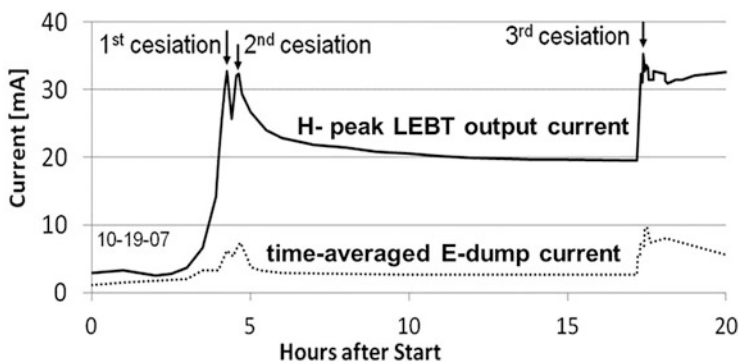


Fig. 18.19 The LEBT output H^- peak current with a 3.6% duty factor and the time-averaged e-dump current for three cesiations. (Enhanced from (Stockli et al. 2012) with the permission of AIP Publishing)

H^- source, it was found that a continuous Cs collar temperature around 200 °C is optimal. The Mo converter is roughly 100 °C hotter.

The SNS Cs collars contain eight Cs_2CrO_4 cartridges shown in Fig. 18.14c (SAES Getters 2021). When heated to >500 °C, the chromate starts to react with the added getter and releases elemental Cs. The cartridges are imbedded in internal slots in the Cs collar shown in Fig. 18.14d. Together the eight cartridges contain <30 mg of Cs which eliminates the risk of large Cs contaminations that can cause excessive arcing.

Since the beginning at ORNL, activating the Cs cartridges multiplied the H^- source output like the data shown in Fig. 18.10b. However, when starting to supply the SNS accelerator for long-term operations in 2006 and early 2007, the H^- beams from the ion source decayed. The decay became more rapid as the duty factor was increased (Stockli et al. 2009). It was noticed that the decay of the LEBT H^- output current became less severe after repeated cesiations as seen in Fig. 18.19. Initially it was believed to be caused by the additional Cs (Welton et al. 2005).

Only after a while it dawned that the cause may not be the additional Cs but the increased time of operation before the cesiation. Evidently the decay was caused by sputtering Cs atoms from dirty converter surfaces. A real delight was the discovery that the decay disappears and the H^- beams become persistent if the cesiation is sufficiently delayed as seen in Fig. 18.19. Accordingly, Cs condensed on a dirty Mo surface gets sputtered, but when the surface is sufficiently sputter-cleaned, the Cs keeps sticking to the surface.

Trial and error showed that it takes less than 3 h of a ~5% duty factor plasma generated with about 50 kW to obtain persistent H^- beams. Efforts to accelerate the process with a larger duty factor were stopped after it became evident that it occasionally caused an antenna to fail.

When Cs is released, it will condense on all surfaces with a line of sight of the cartridge openings or plasma. This lowers the work functions of all metals which

increases the production of negative ions. The surfaces include the near-axis part of the e-dump which can lead to energetic arcs toward the extractor. Transients of powerful arcs frequently damaged some of the auxiliary equipment and interrupted the startup of the SNS ion source. Starting in 2014, the application of the ion source high voltage was delayed by 0.5 h after the end of the cesiations, which made such arcs much less frequent. And increasing the delay to a full hour in 2017 practically eliminated this problem. In addition, since a few years, the SNS H^- RFQ output current is often limited to ~ 25 mA for the first ~ 15 h or so, which further reduces the initial stress, while still delivering sufficient beam for 1 MW target power.

18.6 Refurbishing and Starting Up RF Ion Sources, Their Performance, and Their Plasma Outages

After being used, ion sources are refurbished by disassembling them and sanding the plasma chamber and the converter. Smaller parts are cleaned in an ultrasonic bath. After wiping down all parts, they are dried in a 50°C vacuum oven. The sources are then reassembled with a new antenna. Then they are stored with a fine vacuum inside that is maintained by regular evacuations. This removes much of the residual water vapor, which is sufficient to start up the ion source in record times.

When needed, an ion source is backfilled with dry air to reduce the pump-down time after installation. The newly installed source and the LEBT are evacuated by starting up the fore line pumps together with the turbo pumps because the latter compress the remaining gases to accelerate their removal. When speed is of essence, a very short time after reaching a fine vacuum pressure, the ion source and LEBT are checked for air leaks using a port in the fore line. Using the turbo pumps to compress any leaked Helium (He) allows for accurate leak checks long before reaching high vacuum in the newly installed ion source. This saves many hours when starting up an ion source.

The residual gas analyzer (RGA) in the LEBT is consulted to assure the absence of water leaks. After fixing any found leak, the source is filled with 30 sccm H_2 (standard cubic centimeter per min.). The plasma sputter cleans the source and the Cs collar which is kept near 200°C . Considering the lower limit of ~ 300 m/s for room temperature impurities, the high-power plasma dissipates within <1 ms after every ~ 1 -ms-long plasma pulse. The large increases of the impurity partial pressures measured by the RGA in the LEBT confirm the efficiency of lowering the impurity levels in the newly installed ion source. With keeping the plasma on for 2–3 h, the RGA shows the partial pressures of the impurities to level out which indicates the successful completion of the conditioning.

After ~ 3 h of plasma conditioning, the cooling (with heated air) of the Cs collar is switched off. When the Cs collar reaches $\sim 550^\circ\text{C}$, the 2 MHz plasma pulse length is lowered to maintain the Cs collar near this temperature for ~ 12 min to release

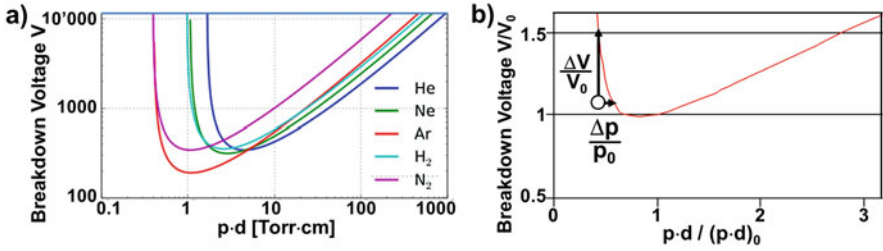


Fig. 18.20 (a) The breakdown voltages of common gases versus the product of pressure p times the distance d between the electrodes. (Enhanced from (Wikipedia: Paschen's law 2021)) and (b) the universal curve of the breakdown voltages with a typical ion source working point

sufficient elemental Cs for at least one monolayer on the sputter-cleaned converter (Han et al. 2012a, 2018a). Using the observed ~ 75 -min Cs release time for the ~ 30 mg of Cs and assuming a constant release rate suggest a dose of ~ 5 mg of Cs being released. After the 12 min, the (heated) cooling air and the 1 ms plasma pulse length are restored. It is the converter temperature that prevents the accumulation of a full monolayer on it. The ~ 200 °C Cs collar temperature was tuned to obtain a near optimal fractional monolayer on the converter (Stockli et al. 2012).

After waiting for 1 h, the ion source high voltage is applied, and the simultaneously conditioned LEBT is fine-tuned to optimize the RFQ output H⁻ beam current. The H⁻ output beam is persistent and no recesiations are needed for at least 4 months. This confirms that the conditioning was in fact complete.

The whole process from shutting down the previous source for removal to restoring a high-current beam (≥ 25 mA) in the MEBT (medium-energy beam transport) can be completed in ≤ 8 h during a neutron production run. This is less than 6 h after starting the evacuation of the new ion source. A more relaxed schedule is used before the start of neutron production runs because the time is not an issue.

What about the physics? Books have been written about RF plasma, but a simple model or data about their breakdown were not found (Wolf 1995; Brown 2004; Lieberman and Lichtenberg 2005). However, it is likely that the breakdowns behave like Paschen found for the breakdown of a DC voltage V applied between a cathode and an anode immersed in a low-pressure gas:

$$V = a \cdot p \cdot d / (\ln(p \cdot d) + b) \quad (18.9)$$

with pressure p , electrode gap d , and the constants a and b , which depend on the gas and the cathode. The breakdown voltages of common gases are shown in Fig. 18.20a.

Rather than using the gas-dependent constants a and b , the Paschen law can be expressed as an universal curve when normalized with the minimum breakdown voltage V_0 and the unity of the ratio of $p \cdot d / (p \cdot d)_0$ near the minimum as shown in Fig. 18.20b.

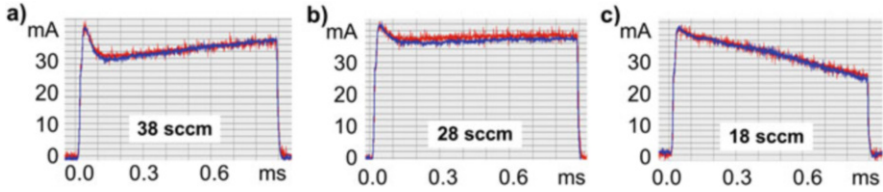


Fig. 18.21 The SNS H^- output current pulses for three different H_2 flows measured with a Faraday cup (red) and with a beam current transformer (blue)

In the Paschen geometry, due to its high density and conductivity, the cathode is the major source of free electrons that starts and maintains the discharge. However, the porcelain coating of internal RF antennas and the ceramic plasma chambers of external antenna sources are insulators and therefore cannot be persistent sources of electrons. Electrons from the insulators or from the gas itself start the discharge, while it is maintained by the electrons freed when accelerated electrons collide with atoms and molecules in the low-pressure gas.

Once there is plasma, the voltage can be lowered, or a high pressure can be increased, or a low pressure can be decreased because the plasma provides additional electrons that are accelerated to maintain the plasma. In ion sources, the pressure is normally decreased because it reduces the recombination losses and the stripping losses in the LEBT (Lawrie and Tarvainen 2021) and so increases the ion beam output. A typical working point is shown in Fig. 18.20b.

Optimizing the pressure by varying the H_2 gas flow is important as seen in Fig. 18.21. Figure 18.21a shows a high pressure where, after the initial overshoot, it takes the plasma more than 1 ms to fully develop and yield a maximum H^- beam current. Figure 18.21b uses a near optimal pressure where, after the initial overshoot, the plasma settles at an approximately uniform density, which provides an almost constant extracted H^- current during the remainder of the 1 ms pulse. And Fig. 18.21c shows a low pressure where the plasma starves and delivers a H^- beam that decays during its 1-ms-long pulse.

More details of the gas flow optimization are shown in Fig. 18.22. Figure 18.22a shows the H^- current output pulses for five different gas flows. 28 sccm yield the highest current in the first half of the pulse. 32 sccm yield the highest current in the second half of the pulse. This suggests that about 30 sccm could be the optimal H_2 flow. This is confirmed by integrating the charge of every pulse as shown in Fig. 18.22b, which shows that 30 sccm indeed yield the most ions per pulse (Stockli et al. 2018).

This is a very convenient result for SNS! Rather than carefully analyzing multiple H^- pulse shapes, SNS can simply maximize the average beam current or its target power.

As important as maximizing the beam current is maintaining stability, which is visualized by overlaying ten H^- current pulses in Fig. 18.23. The data were obtained on the SNS Front-end with source #6 on October 17, 2018, powered by 54 kW of

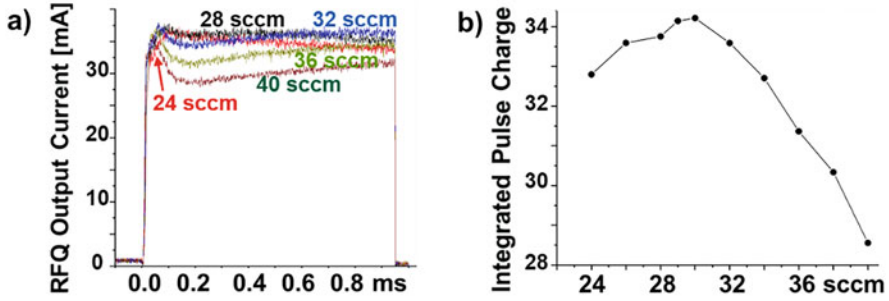


Fig. 18.22 SNS RFQ H^- output current pulses measured with the current transformer BCM02 for (a) five H_2 gas flows. (b) The integrated charge per pulse in arbitrary units for ten different H_2 gas flows. (Modified from (Stockli et al. 2018) with the permission of AIP Publishing)

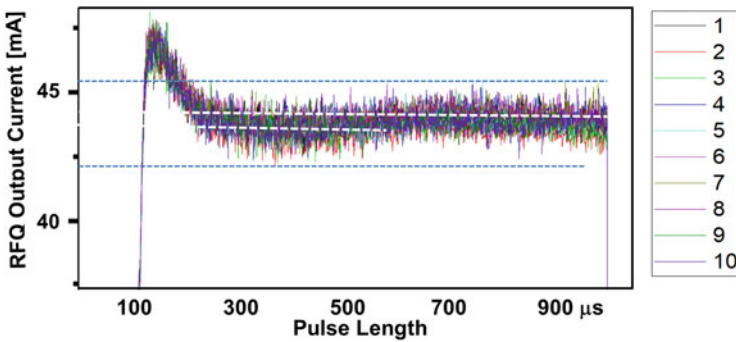


Fig. 18.23 Ten H^- RFQ output current pulses overlaid to illustrate their flatness and stability

2 MHz and 38 sccm H_2 and running at 60 Hz. Figure 18.23 is dominated by the violet first pulse because it is plotted in the foreground. Looking at the spikes, one can see most of the other nine traces. As much as the spikes allow, the pulses seem to overlap perfectly.

The ten H^- current pulses in Fig. 18.23 show after the initial overshoot, a little dip centered around the lower white dashed line. In the second half, the pulses show a little bump centered around the upper white dashed line. The difference between the two white lines corresponds to 0.5 mA or 1.1% of the H^- beam current as a measure for the flatness of the H^- current pulses.

When excluding the initial overshoot but including all spikes from all traces, one gets the two blue dashed lines. They are about 3 mA apart which corresponds to $\sim 7\%$ of the H^- RFQ output current. The nature of those spikes has not been analyzed in detail, and their relevance remains to be determined. However, it is very unlikely to be beam intensity fluctuations as claimed in (Ueno 2017).

The overshoot and other initial instabilities originate from the buildup of the plasma. Many advanced pulsed accelerators avoid these initial issues by delaying the ion extraction, which results in the RF pulse length to exceed the ion beam

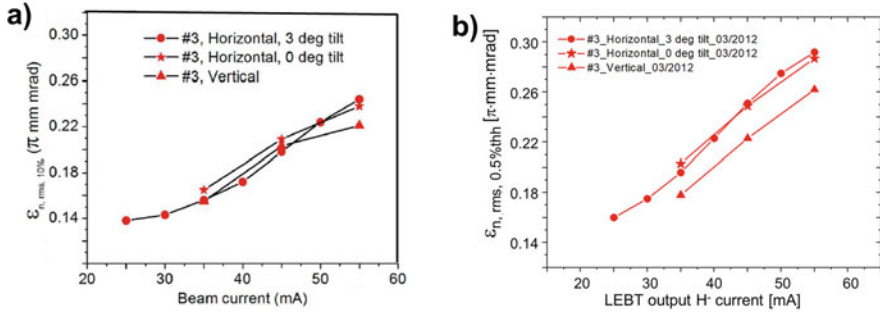


Fig. 18.24 The measured SNS H⁻ output beam emittance as a function of the H⁻ beam current (a) with a 10% threshold. (Simplified from (Han et al. 2013) with the permission of AIP Publishing) and (b) with a 0.5% threshold after the subtraction of a custom fit background. (Modified from B. Han)

pulse length. SNS operations use the initial beam current to ramp up the charge in the accelerator cavities which does not require the ultimate linearity and stability. This minimizes the plasma duty factor and so increases the lifetime of the SNS ion sources.

Another important measure is the emittance of the H⁻ beam because it characterizes the beam's focus-ability (Stockli and Nakagawa 2013). Our initial emittance measurements with a borrowed LBNL Allison scanner (Stockli 2006) were infested with inverted ghost signals from the uncontrolled dumping of the beam that passed the first slit. A modification of the Allison scanner suppressed those signals (Stockli et al. 2005) and yielded mostly reliable data (Stockli et al. 2006).

The exception was the initially wrong polarity of the suppressor when the new ORNL emittance scanner was installed. It resulted in a ridge around the center of the beam position which was independent of the sweep voltage (Han et al. 2013). A 10% threshold allowed to exclude those ghost data from the analysis as seen in Fig. 18.24a. However, large thresholds exclude at least a part of the beam tail, and therefore such results are more representative for the emittance of the beam core.

The data in Fig. 18.24 were measured with ~ 30 sccm of H₂. They show a strong dependence on the H⁻ beam current because the space charge of the H⁻ ions pushes them apart according to their bell-shaped distribution. The space charge of beams with uniform ion densities increases the beam diameters without increasing their emittance (Stockli and Nakagawa 2013).

Later a background with a ridge was custom fit using data collected for large trajectory angles beyond the reach of the ion beam. After it was subtracted from the data, the threshold could be lowered to 0.5%. These data, shown in Fig. 18.24b, are more accurate and include most of the tail of the beam. Accordingly, the emittances are larger. The emittances in vertical direction are $\sim 10\%$ smaller than the horizontal emittances because the vertical velocity components are not affected by the magnetic dumping field. These emittance data were taken when the compromised original RFQ preferred an injection with a 0° source tilt angle in

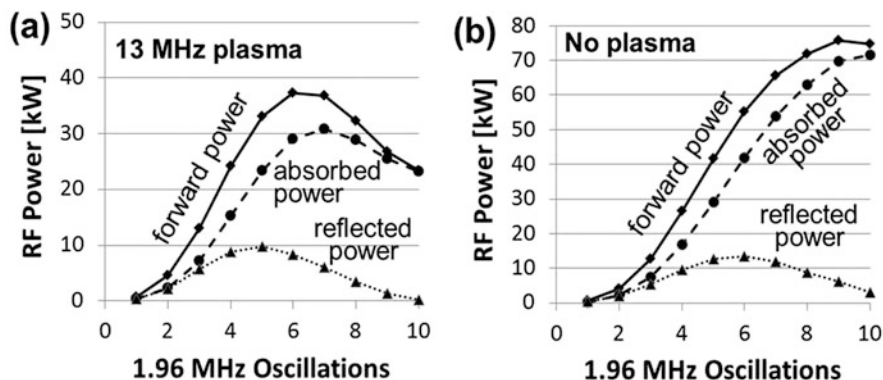


Fig. 18.25 The 1.96 MHz powers after ~ 4 weeks of operation in the SNS H^- source (a) during operation with starter plasma and (b) after an outage of the starter plasma. (Enhanced from (Stockli et al. 2016) with the permission of AIP Publishing)

horizontal direction (Kalvas et al. 2012). This, however, did not significantly affect the horizontal emittances as seen in Fig. 18.24b.

When the plasma extinguishes near its working point shown in Fig. 18.20b, it could be reignited by raising the RF power. The SNS H^- plasma can operate with as little as 35 kW of 1.96 MHz as seen in Fig. 18.25a. It shows the plasma going through a resonance after six oscillations as the plasma inductance increases. However, when the starter plasma is out, 75 kW of 1.96 MHz are not sufficient to restart the plasma after ~ 4 weeks of operation as seen in Fig. 18.25b.

Again, higher-power supplies are expensive. Accordingly, it is much simpler and cheaper to raise the gas pressure for a short period of time as shown in Fig. 18.20b. This is done for RF ion sources with low repetition rates and for starting other RF ion sources from cold because it takes a fraction of a second for the pressure to return to the optimal operating point. For larger repetition rates, it is more effective to have a source of free electrons because they readily absorb the RF. This can be done by injecting electrons or plasma from an external source or by maintaining a low-power starter plasma. SNS increases the gas flow from ~ 30 to 100 sccm for 1 s to start its H^- source from cold. The plasma is maintained with ~ 250 W of 13.56 MHz as a starter plasma between the 60-Hz, 2-MHz RF pulses.

In the late fall of 2009, after starting routine 4-week source cycles with high RF powers, plasma outages started to occur after the first half of the neutron production run in the second half of each H^- source cycle. The only effective way to reduce the recurrence of plasma outages was to lower the capacitance C of the 2 MHz matching network, which also reduced the H^- output current (Han et al. 2011). The neutron production run that started with a glorious 1 MW ended with 600 kW, an embarrassment for the SNS H^- ion source. Not understood at that time was the unusual timing pattern, which was caused by the introduction of impurities after the LEPT maintenance and later with every ion source change. Those impurities

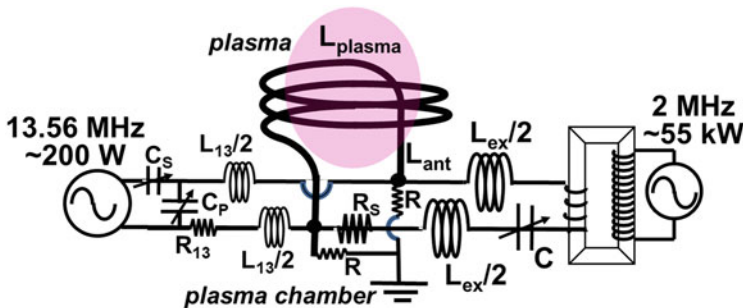


Fig. 18.26 The coupling and grounding of the 13.56 MHz and the 2 MHz to the SNS ion source antenna with R_{13} and R_S being the stray resistances of the two oscillator loops

significantly lower the breakdown voltage of the H_2 gas, and their diminishing levels resulted in plasma outages.

Avoiding plasma outages is more important than maximizing the H^- beam current. This is the reason that fine-tuning and plasma studies should be performed after several weeks of operation to be meaningful for long-term ion source operations. For example, a newly installed ion source can operate without a starter plasma because the high-impurity levels lower the breakdown voltage to the point where every high-power 2 MHz pulse can break down the hydrogen gas without any starter. That changes after a while and plasma outages start to occur.

To combat plasma outages, the power of the starter plasma was increased. However, the intense 2 MHz plasma reflects the 13.56 MHz RF. The larger instantaneous reflected power caused the 13.56 MHz supply to fold back or shut down. This issue was resolved by averaging the 13.56 MHz reflected power over 4 ms (Stockli et al. 2016).

Figure 18.26 shows the coupling of both frequencies to the antenna. The antenna loop needs to be grounded to prevent potentially disabling arcs every time the high-voltage ion source is switched on or switched off. Both oscillator loops are grounded to the plasma chamber with two equal, high-ohm resistors R , each connected to one of the antenna legs. This is important for the 2 MHz because it minimizes the peak of the induced high voltages between the antenna and the plasma chamber. Using only one resistor would double this peak high voltage, increasing the likelihood of disabling arcs. The same reason drove the division of the external inductances in two halves, especially for the 2 MHz: $L_{ex}/2$.

The figure also shows the 2 MHz matching capacitor C . Lowering its value brings the matching resonance closer to the resonant frequency f_0 and the angular frequency ω_0 without any plasma:

$$2 \cdot \pi \cdot f_0 = \omega_0 = (L_0 \cdot C)^{-1/2} \tag{18.10}$$

with $L_0 = L_{ex} + L_{ant}$, being the sum of the external inductance L_{ex} and the antenna inductance L_{ant} .

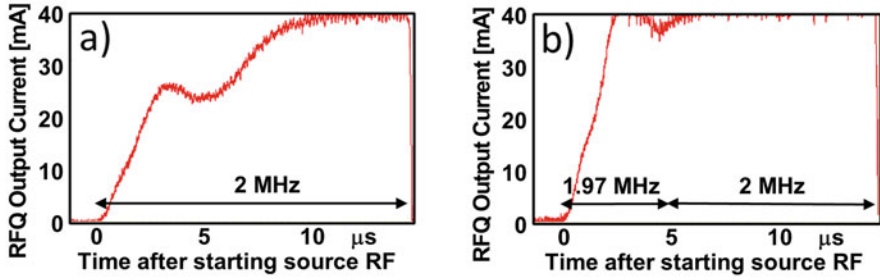


Fig. 18.27 The first $\sim 15 \mu\text{s}$ of H⁻ output current (a) with 2 MHz and (b) with 5 μs of 1.97 MHz followed by 2 MHz. (Enhanced from (Stockli 2013) with permission from CERN)

The frequency shift L_{plasma} is caused by the rotational plasma currents driven by the induced electric field shown in Fig. 18.3. This reduces the antenna inductance L_{ant} by $\sim 30\%$ from its nominal value (Han et al. 2011).

$$L = L_{\text{ex}} + L_{\text{ant}} - L_{\text{plasma}} \quad (18.11)$$

It is the external inductance L_{ex} that reduces the inductance shift $-L_{\text{plasma}}$ to a manageable $\sim 6\%$ of the system inductance L .

The plasma outages suggested that the 2 MHz supply had increasing difficulties to ramp up its power in the plasma or to breakdown the H₂ gas. A 40 kHz frequency shift was calculated for the 0.15 μH shift in inductance caused by the plasma (Han et al. 2011). To restore the capability to tune the H⁻ source for the maximum H⁻ output current while avoiding plasma outages, SNS started to use 1.97 MHz for the first 5 μs .

This certainly accelerated the plasma buildup as seen in Fig. 18.27. It seemed to reduce but did not eliminate the plasma outages after running many weeks for neutron production. In 2014, the start frequency was increased to 1.985 MHz because it further accelerated the plasma buildup (Stockli et al. 2015).

The 13.56 MHz plasma must reestablish itself as the 2 MHz plasma decays. If that does not happen fast enough, a plasma outage occurs as seen in Fig. 18.28.

The top trace of the figure shows the forward RF amplitudes, which are high for the first two 2 MHz pulses. The third 2 MHz pulse is lower because the system is out of resonance without a plasma. In between the 2 MHz pulses, one sees some of the 13.56 MHz RF which increases after the second pulse because it is no longer absorbed due to a lack of the starter plasma. The reflected power in the lower trace confirms how the ion source reflects more 2 MHz without a plasma in the third pulse.

Figure 18.29 shows the mostly reflected 13.56 MHz RF at the end of the 1-ms-long 2 MHz pulses. When the 2 MHz is turned off, the LC oscillator and the plasma decay over $\sim 30 \mu\text{s}$, which lets the 13.56 MHz plasma recover. Figure 18.29b, c show that, after the 2 MHz power decays, lower-pressure plasmas experience an

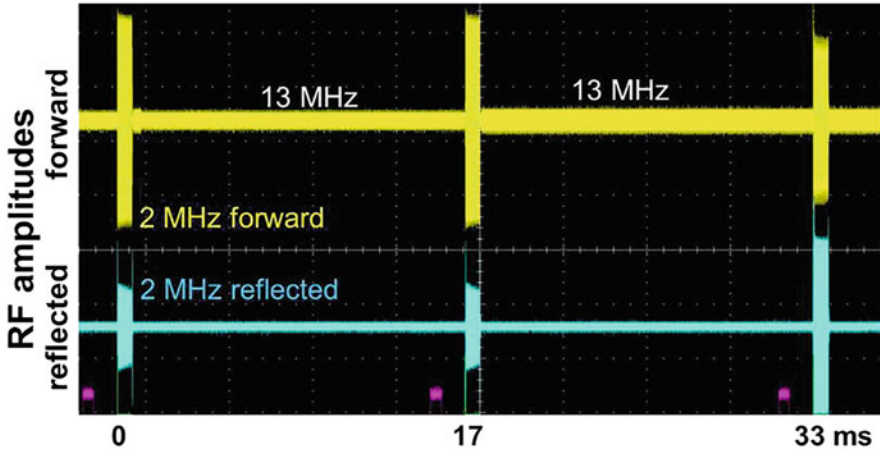


Fig. 18.28 The forward and reflected RF amplitudes with a plasma outage at the end of the second pulse. (Enhanced from (Stockli et al. 2016) with the permission of AIP Publishing)

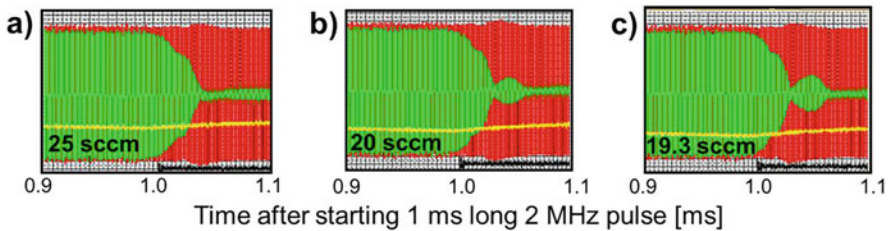


Fig. 18.29 The 13.56 MHz forward power is shown in red in the background, and the reflected 13.56 MHz power is shown as green in the foreground at the end of 1-ms-long 2 MHz pulses for three different gas flows of H_2 . (Enhanced from (Stockli et al. 2016) with the permission of AIP Publishing)

oscillation that reflects some of the 13.56 MHz RF. These oscillations grow in intensity and length as the plasma becomes thinner. Lowering the H_2 gas flow by another 0.1 sccm from 19.3 sccm (Fig. 29c) results immediately in a plasma outage. Evidently these growing oscillations eventually prevent the 13.56 MHz from reestablishing its plasma.

Suffering from occasional plasma outages, a resonance study of the capacitive 13.56 MHz matching network (see Fig. 18.26) brought help (Han et al. 2016). Figure 18.30 shows the global maximum on the left of each figure. Increasing the serial capacitor C_s and decreasing the parallel capacitor C_p to stay on resonance increase the reflected power as seen in Fig. 18.30a. Accordingly this makes the plasma less bright as seen in Fig. 18.30b. However, Fig. 18.30c shows that the plasma extinguishes at lower gas flows and is therefore more robust. The physics of this behavior is not understood.

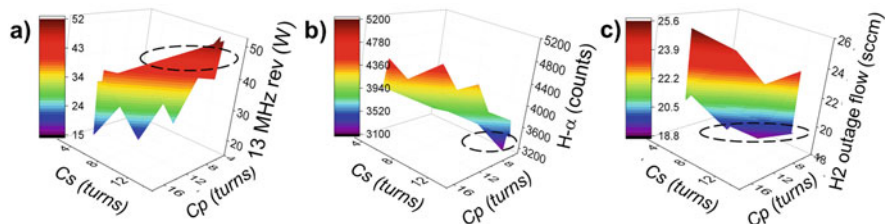


Fig. 18.30 Resonance map of the 13.56 MHz coupling network versus its serial capacitance C_s from left to right and its parallel capacitance C_p from back to front. Displayed are (a) the 13.56 MHz reflected power, (b) the $H\text{-}\alpha$ emission for the brightness, and (c) the lowest H_2 flow before a predictable plasma outage. The jagged edges are due to the limited resolution of the C_s settings. (Enhanced from (Stockli et al. 2016) with the permission of AIP Publishing)

18.7 Internal or External Antenna?

DESY purchased one of the first LBNL RF H^- sources and 21 antennas. The source was mostly operated on their alternate injection line until all the antennas failed (Peters 2009). One antenna worked for 167 days or 21 weeks. However, the average lifetime was only ~ 6 weeks. The times to failure were grouped in seven time slots of increasing length so that each slot contained between two and four failures (Peters 2002).

Plotting the DESY antenna failures as daily failure probability shows 1% enhanced by significant infant mortality with almost 20% on the first day (Stockli 2013). Perpetual sputtering would gradually emaciate the porcelain coating until it is too thin to withstand the encountered high-voltage differences and so result in old-age failures. The normalized DESY failure probabilities show no sign of old-age failures (Stockli 2013). The root cause of the DESY failures was too thin, marginal porcelain coatings (0.1–0.2 mm) as reported by SNS (Welton et al. 2002; Stockli et al. 2018).

Interpreting their unnormalized distribution of the lifetime of their failed antennas, DESY concluded “that there is a high probability for failure at any time” and named perpetual sputtering as the primary reason (Peters 2002). With this in mind, they developed an ion source with an external antenna which worked well at a 0.05% duty factor on their alternate injection line (Peters 2000b). However, it was never subjected to the rigors of production accelerator service (Peters 2009). CERN was unsuccessful to use a copy of this source for their accelerator with a 0.075% duty factor, which will be discussed in Sect. 18.15.

Conversely, SNS identified the root cause correctly and subsequently improved the antenna quality by collaborating with an ORNL material scientist (Welton et al. 2002) and a local porcelain company (Cherokee 2021). Rather than one or two porcelain layers, up to seven layers were applied to have a thicker coating (~ 0.7 mm) with more tolerance for local imperfections (Welton et al. 2002).

These antennas worked much better, but they were not perfect. The first antenna failure to interrupt the SNS neutron production occurred in 2007 after 37 days of operation with a 0.4% duty factor. Replacing the source every 2 weeks to frequently implement a new antenna had to be adopted. This was counterproductive because it became rapidly clear that antenna failures were an infant mortality issue that was initially delayed due to the low duty factor used in 2007. On the other hand, it yielded many opportunities to optimize the startup of the ion source that was discussed in Sect. 18.5.

Raising the duty factor aggravated antenna failures. In 2011 the used SNS antennas were analyzed, and it was learned that most failures occur in the bends where the distance between the two antenna leads is reduced to the distance between the feedthroughs as seen in Fig. 18.4 (Welton et al. 2012). These two bends are most exposed to the rotating plasma. Together with observations of successful antennas, it became clear that the antenna failures were not caused by perpetual sputtering as claimed by other authors (Peters 2002; Oguri et al. 2016; Dudnikov 2019). The real root cause was melting of the porcelain coating especially near imperfections that compromise the thermal conductivity. Therefore, the thickness of the coating was immediately reduced to ~ 0.4 mm, and several improvements were subsequently implemented to reduce the number of imperfections. This was very successful as demonstrated by the fact that no antenna failed on the SNS main accelerator since January 13, 2013. Some people argue that that this failure was related to the fact that there were two number 13 in that date. This will not happen again until 2113, and therefore it is too early to worry about a recurrence!

Contributing to the success may be the sorting of the antennas according to their degree of perfection. Only 10–40% from the carefully manufactured antennas are selected to be used for neutron production (Han 2021). The others are used on the test stand and the beam test facility (BTF) (Zhang et al. 2020) where failures impact only a very few users. Used on the SNS test stand, the second to last failure of a less than perfect antenna was in December of 2012. This demonstrates the drastic improvement of the antenna coatings, whether or not they have minor imperfections (Han et al. 2022).

However, just a couple of months ago, an antenna with minor imperfections failed on the BTF. The coating melted on the tapered bend, facing the plasma. This was initially no surprise because the antenna was operated for ~ 110 days with about 66 kW of 2 MHz RF, which is about 20% above the typical RF power applied on the SNS Front-end. Antennas *do* have power limits! However, what is very surprising is that the failure occurred about 5 days after the power was reduced to ~ 35 kW to produce lower H^- beam currents (Han 2022). Evidently antenna failures are more complex.

In addition, the load by the plasma on the antenna has been accurately modeled, and the results agree with expectations (Beckwith et al. 2015; Veitzer et al. 2016).

An effort to predict antenna failures with plasma emission spectroscopy (Han et al. 2012b) was only partly successful because significant plasma emissions from the failing porcelain start only minutes before the failure (Han et al. 2014). However, the clear diagnosis of antenna failures (Han et al. 2015) ended the extended fruitless

efforts to restart the plasma with a failed antenna. Those extended efforts led to the glassy coating of the plasma chambers, which were labor intensive to remove. In the past, these glassy coatings were incorrectly attributed to perpetual sputtering during the antenna lifetime (Peters 2002), as discussed above.

In 2022, a porcelain coated antenna costed less than 880 \$ each (Cherokee 2022), and they are worth every penny since they last over 4 months at SNS and 5 months at J-PARC. This is less than 7 \$ per day of use. They do not cost 5000 \$ as claimed in the aforementioned book (Dudnikov 2019).

There is only one porcelain company that can coat the antennas with the desired perfection (Cherokee 2021). People worry about sole suppliers because it could potentially disrupt the successful accelerator operation. However, sole suppliers are not uncommon for highly specialized components of advanced accelerators. Other examples are custom ceramic insulators and the ceramic plasma chambers for RF sources with external antennas. Price adjustments are required to keep the small-volume productions profitable. And furthermore, a multiyear stock of spares should be in-house to allow the development of a new supplier should the unthinkable happen.

Failures of internal antennas remain a risk, although a very small one. Accordingly external antennas can look attractive because the antennas are immersed in more forgiving air. In 2009, SNS tried to implement its external antenna source (Welton et al. 2008) on the SNS accelerator with a 4.8% duty factor. During the 8-week trial, four failures were encountered, yielding a poor availability. Two days and 5 days after starting up, two external antennas failed because corona destroyed their insulation. Implementing a thick T-shaped Teflon spacer separating the windings with the highest voltage differences successfully prevented recurrences.

Then 7 and 9 days after starting up refurbished external antenna sources, they could no longer be restarted because their plasma gun could no longer break down the low-pressure gas despite multiple sustained efforts. With a repetition rate of 60 Hz, the SNS external antenna source depends on injections of electrons or plasma. This is an Achilles heel of external antenna sources where the low-pressure gas is further away from the antenna which makes the plasma breakdowns more challenging. Of course, the SNS plasma gun has been improved over the last 13 years, but the latest change still requires long-term testing.

The other Achilles heel is the need for a ceramic plasma chamber. At SNS alumina plasma chambers broke at a ~3% duty factor which is about 1.5 kW of average thermal load. Aluminum-nitrate seems to work at the required 6%, but it is very fickle unless it is carefully conditioned, because otherwise its gaseous emissions poison the plasma. Ceramic plasma chambers are certainly not as robust as the stainless-steel plasma chambers used for internal antennas.

Either external or internal antennas can be used when the average thermal load is not much larger than 1 kW. However, for larger powers, internal antenna sources are preferred at least until it is proven that an external antenna source can be operated with an average of ≥ 3.2 kW plasma load, successfully and repeatably for over 4 months each, for example, on the SNS BTF.

18.8 Other Failures of the Past

Besides the antennas, the most serious failures are the breakdown of the insulators that hold off the e-dump voltage from the source. They are shown at the bottom of Fig. 18.14a, b. Without the e-dump at its optimal voltage, the H^- output current drops, and accordingly the ion source is scheduled to be replaced shortly after such a failure. Several improvements have been made which reduced such occurrences significantly. As seen in Fig. 18.31a, three e-dump failures interrupted the neutron production in 2015. This was the result of trying to develop an alternate supplier, which met the SNS specifications but evidently had a source of less superior ceramic. The failures occurred after 2, 7, and 14 days of operations and could have been prevented by testing the new insulators on the test stand for enough time. The two e-dump failures of 2019 were caused by inadvertently using insulators matching outdated specifications.

A risk of e-dump failures remains because not uncommon arcs from the e-dump to the extractor can drastically increase the voltage between the e-dump and the ion source. Such an e-dump failure occurred on April 4, 2017, while restoring operations at the end of a Tuesday maintenance day. It disrupted a successful neutron production run after 68 days. With almost 10 weeks of successful operation, this was a very unlikely failure as seen in Fig. 18.31b. The last such failure occurred on August 9, 2019, while starting up an ion source. This resulted in staff overtime but no loss of neutron production.

As Fig. 18.31 shows, there were other failures like a thermal air leak, the cooling water for the e-dump losing its deionization, a thermocouple arcing after becoming loose, the first lens arcing, and an accidental venting. After each failure, steps were taken to make recurrences less likely.

With the antenna problem solved, Fig. 18.31b shows that the other failures were also dominated by infant mortality. This is the motivation for increasing the length of the ion source service cycles. Figure 18.31a shows the successful effort to reduce the number of ion source changes. The low of 2018 is due to a long shutdown to replace the compromised original RFQ (Stockli et al. 2014).

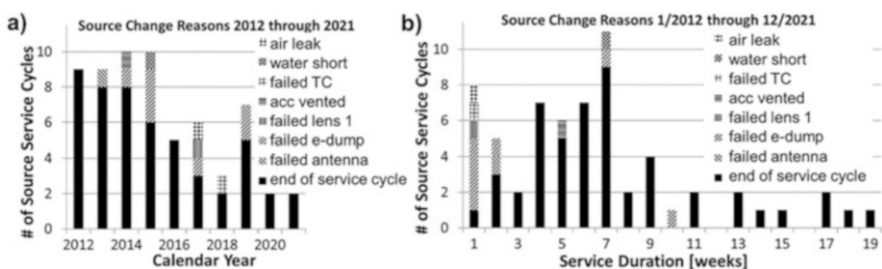


Fig. 18.31 Reasons for changing the SNS Front-end H^- ion source for the last 10 years versus (a) the calendar year and (b) the length of the completed ion source service cycles rounded up to the next full week

Of the 63 RF H⁻ ion sources started up on the SNS main accelerator, 50 served successfully for their entire scheduled service cycle. Of the 13 that needed replacement, most of them could be replaced before the start of the actual neutron production period.

No failure was encountered during the last 2 years despite (or maybe due to) running 17–19 weeks with each source.

18.9 Service Cycles and Lifetimes of the SNS RF H⁻ Source

The best way to reduce infant mortality is to let ion sources grow old, a point seemingly not understood by everybody in the early years. After the first antenna failed during SNS operations, a 2-week source cycle had to be adopted as discussed above. This was increased to 3-week cycles after 1.5 years and to 4-week cycles another year later. Another 2 years later, two out of three ion sources got contaminated, causing significant H⁻ beam decays. Accordingly, the new management agreed to extend the service cycle of the uncontaminated source to 6 weeks and use the less contaminated source for only for a few days and later for 2 weeks (Stockli et al. 2013). About a year later, the contaminations had conditioned away as judged from the return of persistent H⁻ beams. Four-week source cycles were reimplemented for all ion sources to ease up to the management schedule.

A low-key effort to extend the source service cycles beyond 4 weeks was not approved despite the previous 6-week cycles.

In summer of 2014, an official proposal to extend the SNS ion source service cycles was presented with an earlier version of Fig. 18.31b. As expected, the management accepted the proposal and ever since is presented with an ion source replacement plan before the start of every neutron production run. The initial goal was to only change the ion source once or twice during neutron production runs. A half year later, the first 7-week source cycle was completed. The cycle time was gradually extended until reaching a single ion source change during a neutron production run in 2016. In 2018, a single ion source served an entire 91-day run, although the 850 kW run was supported by an experimental wide-leg antenna (Stockli et al. 2011b). Wide-leg antennas may be more reliable, but their lower performance makes them unacceptable for SNS.

As seen in Fig. 18.31a, since 2020, the two neutron production runs per year are supported without any ion source replacement during the run (Han et al. 2022). The last four runs have been completed with an average length of 120 days and a maximum of 129 days. The average ion source and LEBT availability were 99.91%, with a maximum of 99.94%, and 99.93% for the 129-day run. Downtimes are counted for any interruption lasting 6 or more minutes involving the ion source or the LEBT independent of who may have caused it. These four runs, shown in Fig. 18.32, were free of failures, in part likely due to the relaxed schedule when installing an ion source before the start of a neutron production run.

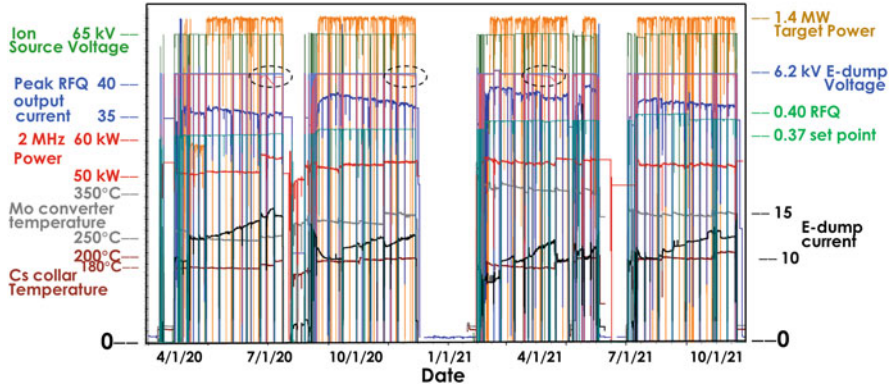


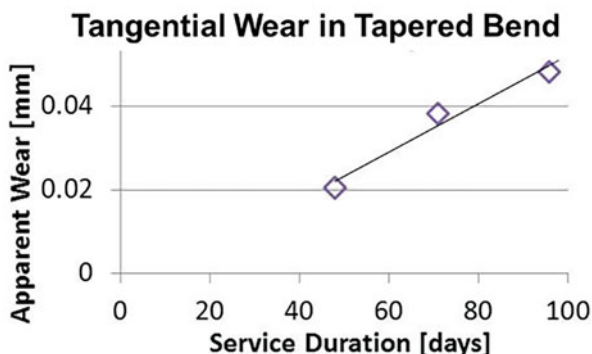
Fig. 18.32 Performance of the SNS RF H^- ion source #2 in 2020 and 2021: from top on 7/1/20, the target power (MW, dark yellow), ion source voltage (kV, green), the e-dump voltage set point (kV, blue), the e-dump voltage (kV, light brown), RFQ H^- output current (mA, blue), RFQ power set point (arbitrary, green), the 2 MHz power (kW, red), the time-averaged e-dump current (mA, black), the Mo converter temperature ($^{\circ}C$, gray), and the Cs collar temperature ($^{\circ}C$, brown); the dashed ellipses highlight sagging e-dump voltages (Data courtesy of B. Han)

Amazingly, Fig. 18.31b shows no failures beyond ~ 7 weeks of operation, excluding the failure when recovering from a routine maintenance day discussed above. Accordingly, the SNS H^- source with service cycles of up to 19 weeks has not reached the time of old-age failures.

Meanwhile, the production of H^- ions without any maintenance was increased from the required 1.5 A-h, reached in 2010, to 3 A-h by end of 2014. Extending the source service cycle increased the H^- production to 7 A-h by 2016, and the single ion source neutron production runs increased this to 10 A-h in 2020. This is almost equivalent to the charge stored in an alkaline D battery (Wikipedia: list of battery sizes 2022) but, rather than electrons, the very fragile H^- ions that cannot be stored.

In the (desirable) absence of failures, one can estimate the lifetime by assessing signs of aging, such as life-limiting wear. The failures of the antenna coating in the bends (see Fig. 18.4) point to locations of high stress because the bends are exposed to the rotating plasma. The radial bend has two narrow bends close together and accordingly its exact diameters are difficult to measure. However, the tapered bend has a straight section that yields more consistent results. The initial measurements with vernier calipers were dominated by scatter (Stockli et al. 2016). Acquiring high-resolution digital micrometers (Mitutoyo) and measuring halfway in the tapered bend in tangential and axial directions before and after its use now allow to calculate the average local thickness of the porcelain coating on the copper tubes with their slight elliptical cross-sections. Having eliminated a cause of the scatter yielded the consistent results seen in Fig. 18.33 (Stockli et al. 2017). It shows wear of about 0.05 mm after 100 days which is only 12% of the ~ 0.4 mm thick coating. This suggests that wear may become a life-limiting issue after about a full year of plasma operation at a 6% duty factor. However, the radial bends currently remain a wild card.

Fig. 18.33 Tangential wear measured on the tapered bend of different antennas measured with a digital micrometer versus their use in 6%, ~50 kW, 2 MHz plasma. (Reproduced from (Stockli et al. 2017) with the permission of AIP Publishing)



18.10 The H⁻ Beam Decay and the Loss of Cesium

There can be several reasons that H⁻ beam currents decay. In cesiated ion sources, the loss of Cs is a likely cause. The Rasser approximation suggests the loss of 0.01 monolayers from 0.4 monolayers of Cs to reduce the surface production probability by ~0.5% (absolute) for 5 eV hydrogen ions. This yields a loss of ~1 mA of the SNS production H⁻ beams. If too much Cs is lost, the ion source can be recesiated until the Cs supply is used up. The SNS baseline H⁻ source can be recesiated once or twice before the Cs₂CrO₄ cartridges can no longer release sufficient elemental Cs.

As discussed under Cs management, the thermal emission is responsible for the initial Cs loss. But after the startup, the thermal emission becomes very small, and sputtering by plasma ions is eventually expected to dominate the Cs loss.

Sputtering depends on the mass of the sputtering particles as well as the mass of the sputtered particles (Bohdansky and Roth 1980; Stockli et al. 2011a) as shown in Fig. 18.34. It characterizes the projectile mass-dependent minimum energy needed to break the surface bond of an atom on the surface, the adsorbed Cs in this case. Particles in the vacuum and in the plasma lack this energy. However, some plasma ions accelerated by the plasma potential can exceed this threshold. According to Figs. 18.16 and 18.34, it would take >60 eV protons or >25 eV H₃⁺ ions to sputter Cs atoms from a fractional (~0.6) monolayer of Cs on a W(110) surface. Such energetic hydrogen ions are not available from the few-volt plasma potential in the SNS RF ion source. This is the reason that pure hydrogen plasma does not sputter Cs adsorbates.

However, Figs. 18.16 and 18.34 show the heavier impurity ions to have sputter thresholds of less than 10 eV. For example, Fig. 18.35 shows the continuing performance degradation of the SNS H⁻ source #2 when it suffered from a thermal leak. When the source was switched off, only ~10⁻¹⁰ sccm air leaked into the source, and therefore it was not detected during the leak checks before starting up the source and before removing the source. However, when the source was in operation, the leak grew to ~10⁻⁶ sccm and the H⁻ output current kept decaying by ~15% per day. Two recesiations restored the performance but the third one failed.

Fig. 18.34 Projectile mass dependence of the normalized sputter threshold of Cs. (Reproduced from (Stockli 2012) with permission from the Institute of Physics)

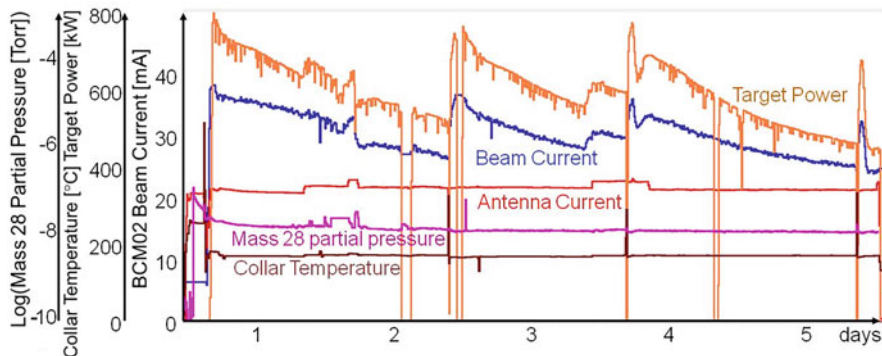
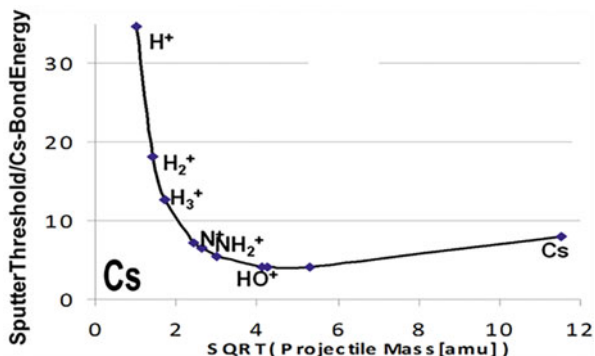


Fig. 18.35 SNS H⁻ source #2 performance with a thermal air leak. (Reproduced from (Stockli et al. 2013) with the permission of AIP Publishing)

The source was replaced after 5 days, and the leak was found in the metal seal of a quartz window when the source was checked for leaks in a better vacuum environment (Stockli et al. 2012). These windows are heated by the plasma and replacing it eliminated the problem.

H⁻ beams decayed even more rapidly when water leaks developed in the ion source or the LEBT during the early days of high-power operations. The ion sources had to be replaced immediately.

In September 2011, the H⁻ output of source #2 decayed by ~20% per hour after starting it up as seen in Fig. 18.36. A second cesiation restored the beam but it decayed even more rapidly. The source was replaced the same day with source #4, which yielded a H⁻ beam decay of ~20% per day. The next day, a recesiation restored some of the beam, but the decay became slightly worse. The following day, source #4 was replaced with the newly refurbished source #3 which yielded a persistent beam.

When in operation, the contaminated sources emitted high levels of CO, CH₄, and C₃H₆, but those clues did not reveal the origin of the carbon. Neither thorough mechanical cleaning, nor ultrasonic cleaning with water or solvents, nor sputter

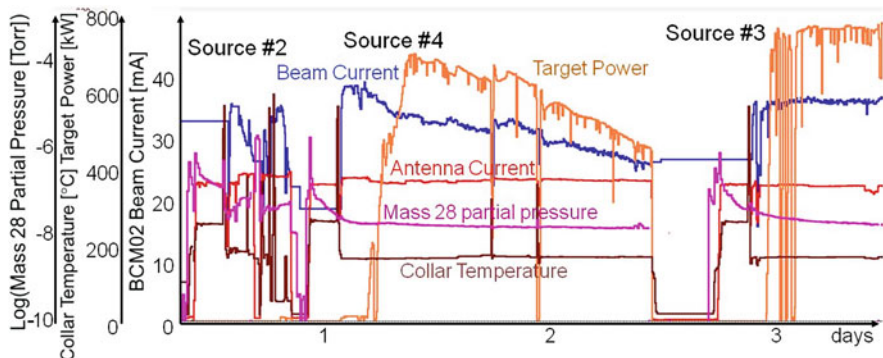


Fig. 18.36 SNS H⁻ source performances after the contamination of #2 and #4. (Reproduced from (Stockli et al. 2013) with the permission of AIP Publishing)

cleaning with argon were able to remove the contaminations. Many weeks later, a tear was found in the pumping diaphragm of the dry pump which evacuated the ion source storage container. Evidently, the pump contaminated sources #2 and #4 with rubber dust that bonded to the Cs collars when they were heated during the first cesiations. Fortunately, source #3 was not contaminated because it was in use on the Front-end.

The contaminations slightly decayed with every use. For about half a year, source #3 was used for ~6 weeks followed by 1–2 days of source #4 while source #3 was refurbished. After about half a year, source #4 could be used again on the main accelerator for up to 2 weeks using intermittent recesiations to maintain a satisfactory performance (Stockli et al. 2013). Accordingly, a cycle of 6 weeks with #3 followed by 2 weeks with #4 was introduced. It took more than 2 years of source cycling on the test stand to reestablish almost persistent output beams with source #2.

The sputtering of the Cs is the reason that adding impurities to lower the breakdown voltage of the hydrogen gas is not a good idea at least for H⁻ sources without a large Cs reservoir.

Some people argue that the H⁻ output may be reduced by the formation of Cs-oxides on the converter (or plasma electrode) surface. While that is not impossible, it does not seem likely to happen on a sputter-cleaned converter in a conditioned H⁻ ion source. Cs atoms on clean metal surfaces form metallic bonds and therefore lack the outer electron to form another bond. In addition, most of the oxides form with two or more Cs atoms (Wikipedia: Caesium Oxide 2021), which is unlikely to happen on a partial monolayer of Cs. Cs superoxide (CsO₂) and Cs ozonide (CsO₃) form with only one Cs atom but two or three oxygen atoms (Wikipedia: Caesium Oxide 2021). This is unlikely because O₂ and O₃ are extremely rare in a high-purity hydrogen plasma. The oxygen in the plasma comes mostly from water, which contains only one oxygen atom, and CsO is not stable.

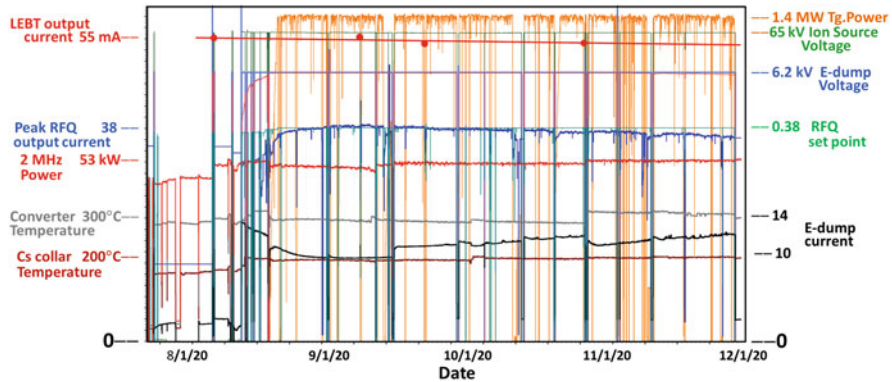


Fig. 18.37 Performance of the SNS RF H⁻ ion source #2 during its record 129-day service cycle: measured LEBT H⁻ output currents (mA, red dots) and a least-square linear fit (mA, red straight line). Strip chart traces from top in the middle of November: the target power (MW, dark yellow), ion source voltage (kV, green), the e-dump voltage set point (kV, blue), the e-dump voltage (kV, light brown), RFQ power set point (arbitrary, green), RFQ H⁻ output current (mA, blue), the 2 MHz power (kW, red), the Mo converter temperature (°C, gray), the time-averaged e-dump current (mA, black), and the Cs collar temperature (°C, brown). (Data courtesy of B. Han)

A larger concern should be Cs-nitrate (CsNO₃) and Cs-nitrite (CsNO₂) (Wikipedia: Caesium Nitrate 2021) because ion sources are normally vented with dry nitrogen (N₂) or dry air. Dry N₂ is obviously not a problem, but dry air may be.

SNS observes thin residual layers of Cs on surfaces that were not exposed to plasma. The Cs must have accumulated during cesiations and reacts with water from the air after venting which makes them visible (Wikipedia: Caesium 2021). In addition, SNS has also observed slow but large growths of the H⁻ output beams before a deliberate cesiation. Evidently elemental Cs survived the air exposure during the refurbishing of the source, which must have been insufficient. Both observations are not consistent with a dominant formation of Cs-nitrates or Cs-oxides.

In the absence of significant impurity levels, the H⁻ beam currents looked perfectly persistent for 3- and 4-week H⁻ source service cycles (Stockli et al. 2012). Extending the service cycles to ~4 months and careful measurements of the H⁻ LEBT output currents (Han et al. 2017) have revealed that even the now most stable SNS H⁻ source #2 experiences small decays of the H⁻ beams as seen in Fig. 18.37. An equal-weight least-squares analysis of the four LEBT H⁻ output measurements shown in Fig. 18.37 yields a decay rate of 1.1 ± 0.6 mA or $2 \pm 1\%$ per 100 days.

The Rasser approximation suggests a loss in the order of 0.01 monolayers of Cs or about 2% of a 0.4 monolayer of Cs. The loss is likely several times larger because the Cs monolayer is likely closer to the optimal 0.6 monolayer, where the H⁻ output is less sensitive to the loss of Cs. However, it remains an open question whether the observed loss is consistent with the <0.5 ppm traces of impurities found in the

research-grade hydrogen supply gas (99.9999%) and whether the thermal emission still played a role.

Despite the slight decay of the H⁻ output, the 2 MHz power remains normally unchanged because it is easier to slightly adjust the fraction of the chopped beam.

The other observable that keeps changing without intervention is the electron current intercepted by the e-dump. It slowly grows which is common in H⁻ sources. Eventually the e-dump voltage may start to droop as seen in the dashed ellipses in Fig. 18.32. When the voltage becomes unstable, it increases the beam losses in the linac. The e-dump voltage can be stabilized by slightly increasing the RF power as happened end of October 2020 and as seen in Figs. 18.32 and 18.37. This increases the temperature of the converter which is often further increased by increasing the temperature of the Cs collar as happened in June 2020 and April 2021 and as seen in Fig. 18.32. The growth of the coextracted electron current and the stability of the e-dump voltage are not understood and could be issues that may limit the useful lifetime of H⁻ sources to less than the antenna lifetime.

Figure 18.37 reveals new puzzles. For example, observations showed that the ion source fully conditions in the first week or so and then becomes almost persistent. However, the RFQ H⁻ output beam shows conditioning about 4 weeks after start of the H⁻ source or shortly after starting to operate the RFQ at high power for the start of the neutron production. Evidently, the RFQ also conditions and these subjects need reevaluation.

18.11 Surface Films in the SNS RF H⁻ Ion Source

The surface films found in the SNS H⁻ source after use have been reported and discussed in 2016 (Stockli et al. 2017). SNS no longer discusses its surface films because no correlation with the source performance or the source behavior could be found despite extensive efforts. However, here we discuss it again to set the records straight after “alternate” facts were published (Dudnikov 2019).

As reported (Stockli et al. 2017) and seen in Fig. 18.38, the antennas gradually become black as one would expect from a slow accumulation of carbon deposits. Figure 18.38 shows that it takes more than 2 weeks for the discoloration to stabilize. Initially it was guessed that the carbon coating made the antennas sputter resistant. The measurements of Fig. 18.33 proved that guess wrong. Evidently it takes more than 2 weeks to reach an equilibrium between the deposition and the sputtering. SNS does not normally observe a growth or a decay of its H⁻ beams that changes gradually after a few weeks.

SNS sees a rapid increase of the H⁻ beam after every successful cesiation as shown in Fig. 18.19. Normally there is a slow growth over a few days, which SNS assumes is caused by reaching the optimal Cs monolayer. Afterward, there is just a very gradual decay, as seen in Figs. 18.32 and 18.37, which SNS believes to be due to a very gradual loss of Cs.

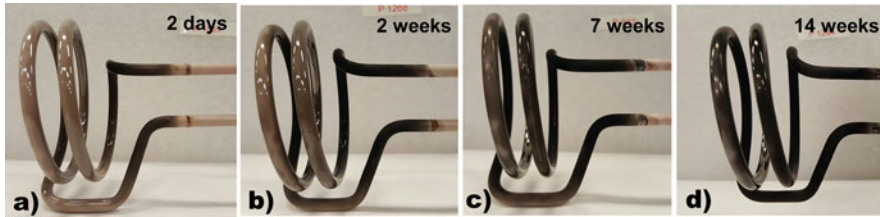


Fig. 18.38 Antenna discolorations after (a) 2 days, (b) 2 weeks, (c) 7 weeks, and (d) 14 weeks of plasma operations

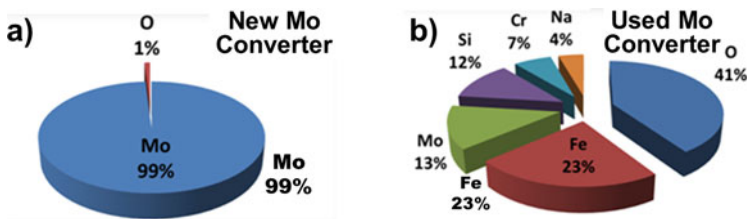


Fig. 18.39 The SNS converter surface compositions (a) before use and (b) after use. (Kenik 2010)

It was speculated that the cleaning alcohol is the source of the carbon (Dudnikov 2019). This is highly unlikely because the SNS ion sources are dried and stored under fine vacuum before they are installed for use. No traces of alcohol are detected by the RGA. In addition, such residues would not be able to resupply the needed carbon for the 14 weeks shown in Fig. 18.38d. A much more likely source are the SS heat shields that can reach very high temperatures when shielding the water-cooled outlet electrode from the plasma. The heat shields were changed from 304 SS to 316LN SS in an effort to lower their emissions. However, no resulting change was obvious. Another possible source could be an O-ring that seals the water-cooling loop of the filter magnets. Recently some degradation was observed, and investigations are now under way.

The antenna color may be an interesting indicator of some hydrogen plasma impurities, but not a serious concern. It is the cesiated Mo converters that are of prime interest because they contribute the majority of the H^- output. In 2010, a Mo converter was analyzed after being used on the Front-end and compared to an unused one (Kenik 2010). The X-ray emission was recorded when the converters were bombarded with up to 15 keV electrons penetrating a few μm into the samples.

The results are shown in Fig. 18.39. From the unused converter, the observed X-rays were mostly from Mo and only a few from ~ 1 atomic % of oxygen (O). However, after use, only ~ 13 atomic % Mo is seen, which is consistent with a thick layer of deposits. The dominant additional elements are iron (Fe) and chromium (Cr), clearly from SS. The others are silicon (Si) and sodium (Na), clearly from the porcelain antenna coating. The high level of O suggests a low-density layer where O can penetrate after exposure to air. Cs is not shown because it was just a trace.

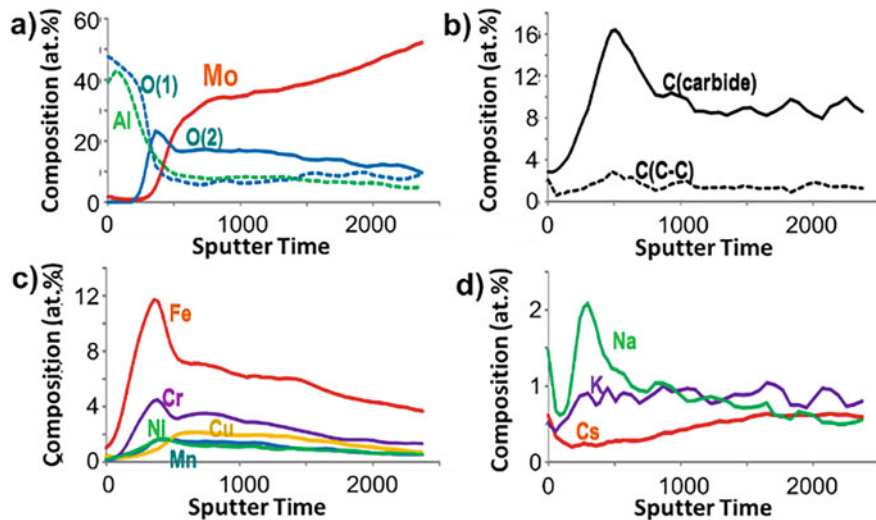


Fig. 18.40 Depth profiles of the surface composition of a used SNS converter (a) for Mo, O, and Al; (b) for C; (c) for Fe, Cr, Ni, Cu, and Mn; and (d) for Na, K, and Cs. (Kenik et al. 2008)

It is surprising that this thick layer of unintended elements did not significantly change the H⁻ output current of the source. To get more insight into this layer, a depth profile was established by gradually milling away the top surface with ions, and the results are shown in Fig. 18.40 (Kenik et al. 2008). The Mo seen in Fig. 18.40a is the original bulk Mo because Mo is very unlikely to sputter from the surface when bombarded with few eV ions (Stockli et al. 2011a).

Also seen in Fig. 18.40a, the top layer is mostly aluminum (Al) which is very surprising because the antenna coatings contain only 1–2 atomic % of Al (Kenik et al. 2008). The near-surface O was likely acquired during the exposure to air.

And finally, Fig. 18.40a proves that the bulk Mo is covered with a thick layer of other deposits acquired during its use. Figure 18.40b shows that the Mo surface is significantly carbonized. However, only ~5% C is seen on the actual surface, very different from the ~60% discussed by another author (Dudnikov 2019). In addition, Fig. 18.40b, c show no enhancement of the Cs concentration within the carbon layer, as claimed by the same author.

Figure 18.40c shows a layer of Fe, Cr, Ni, Cu (copper), and Mn (manganese) directly on top of the Mo. Evidently, SS is primarily sputtered into the plasma early in its service cycle and then diminishes. Most interesting is Fig. 18.40d which shows spikes of Na, K (potassium), and Cs right at the very top of the surface. The Na evidently originates from the antenna coating. This is not surprising because Fig. 18.33 shows sputtering of the antenna to the very end. Surprising is the ~1% of atomic K throughout the measured layer, because the porcelain contains only about 1 atomic % of K or ten times less than Na. Accordingly K may just be an impurity

of the Mo or the system. Some of the discrepancies may also be due the fact that analyses were done with different converters operated with different antennas.

What is also surprising is the Cs right at the very top of the surface because it was introduced many weeks earlier. Mo with an atomic radius of 1.9 Å is larger than C (0.67 Å or 35% of Mo), O (0.48 Å or 26%), Al (1.18 Å or 62%), Cr (1.66 Å or 87%), Mn (1.62 Å or 85%), Fe (1.56 Å or 82%), Ni (1.49 Å or 78%), and Cu (1.45 Å or 76%). On the other hand, Na (1.9 Å or 100%) matches the Mo radius, and K (2.43 Å or 128%) and Cs (2.98 Å or 157%) are significantly larger.

There is no Mo at the actual surface. It seems that all the smaller atoms form stronger surface bonds than the large alkali atoms and keep pushing most of the alkali atoms to the top. Floating on the top of the surface, the low ionization energy of alkali atoms may enhance the number of electrons that are available for capture. And/or their larger size likely makes the surface more corrugated on a nanoscale which may also enhance the electron capture probability. This could explain why SNS can run for 129 days without adding any additional Cs.

18.12 The SNS H⁻ Extraction and the Low-Energy Beam Transport

It is important to understand the ion extraction from ion sources because it determines the ion beam output current. Child and Langmuir set up the Poisson Eq. (18.12) for the ion extraction from the planar diode system shown in Fig. 18.41a and solved it for the voltage V (18.13):

$$\nabla^2 V = d^2 V / dz^2 = -\rho(z) / \epsilon_0 = j / (\epsilon_0 \cdot v) = j / \epsilon_0 / (2 \cdot q \cdot V / m)^{1/2} \quad (18.12)$$

$$V = \left(9 \cdot j \cdot (2 \cdot q / m)^{-1/2} / (4 \cdot \epsilon_0) \right)^{2/3} \cdot z^{4/3} \quad (18.13)$$

with z being the distance from the plasma meniscus, $\rho(z)$ the local charge density, $j(V, q, m)$ the ion current density, $v(V, q, m)$ the ion velocity, q the ion charge, and m their mass.

$$dV/dz \propto E/E_{\text{Ex}} = z^{1/3} \quad (18.14)$$

The normalized electric field E/E_{Ex} , with E_{Ex} being the field at the extractor, is shown in (18.14) and Fig. 18.41b. Being proportional to $z^{1/3}$, it is zero at the meniscus and very small right after. The space charge of the slow ions cancels most of the electric field near the meniscus. This creates a bottle neck, preventing the extraction of more ions. Using (18.13) for $z = d$, the distance d between the ion source and the extractor with voltage V_a , and solving for the current density j , one

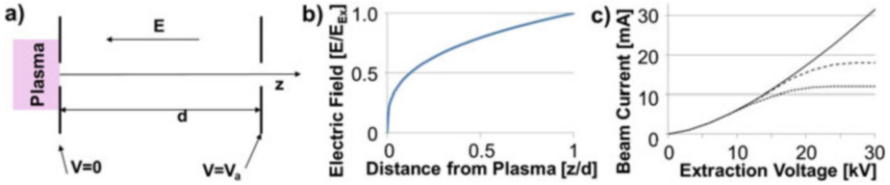


Fig. 18.41 (a) A flat diode extraction system, (b) the normalized electric field between the ion source and the extractor, and (c) the schematic extracted beam current as a function of the extraction voltage for sufficient ion densities (solid line) and limiting ion densities (dashed lines); ((c) Is enhanced from (Stockli and Nakagawa 2013) with permission from World Scientific)

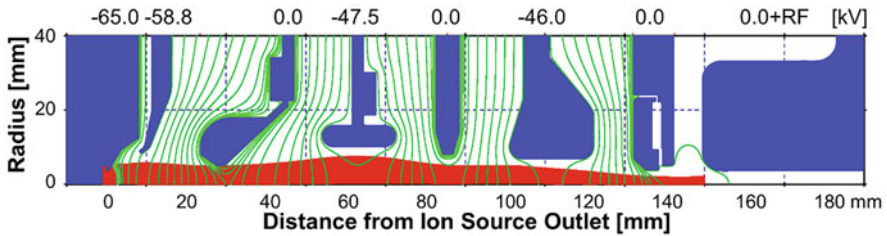


Fig. 18.42 The SNS low-energy beam transport system consisting of two electrostatic lenses. (Data courtesy of B. Han)

obtains the well-known Child-Langmuir equation shown in (18.15) and with the solid line in Fig. 18.41c:

$$j = 4 \cdot \epsilon_0 / 9 \cdot (2 \cdot q / m)^{1/2} \cdot (V_a)^{3/2} / d^2 \tag{18.15}$$

They show the importance of the extraction voltage V_a because the extracted ion current density j grows with its $3/2$ power. As important is the extraction gap d because it has an even stronger dependence growing with the square of its inverse. While this may lead to high expectations, some may not hold up because the aberrations of short gaps play a crucial role. Optimization through trial and error is the answer, and the SNS RF H⁻ source with the required extraction voltage of 65 kV yields the most H⁻ RFQ output current with an extraction gap d of about 25 mm.

Figure 18.42 shows how the 65 keV H⁻ ions are focused into the SNS RFQ. The e-dump voltage optimizes when it is in line with a linear electric extraction field (Stockli et al. 2010). However, it seems that aberrations from the e-dump steer the outer rays through the opening in the extractor. Emerging almost parallel from the extractor, the space charge of the ion beam pushes the ions apart. The first electrostatic lens refocuses the beam to enter the second lens with an optimal diameter. It is the second lens that produces the strongly convergent ion beam with a focus slightly inside the RFQ. This yields the desired high RFQ transmission when the RFQ is operated with its design power (Stockli et al. 2010).

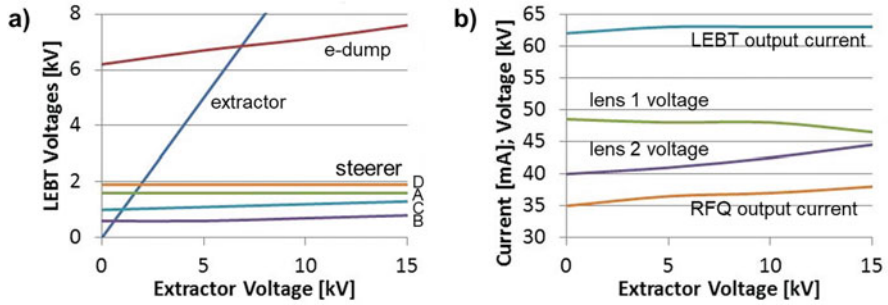


Fig. 18.43 A positive voltage V_{ex} on the extractor can increase the SNS RFQ H^- output current by up to 10%. (Enhanced from (Stockli et al. 2017) with the permission of AIP Publishing)

The second lens is divided into four electrically isolated quadrants to allow for steering, chopping, and blanking the ion beam (Han et al. 2018b).

The ion energy must be 65 keV when being injected into the RFQ which constrains the voltage applied to the ion source. However, the extraction field can be increased by applying a positive voltage to the extractor. Figure 18.43 shows a study with $V_{ex} = 0, +5, +10,$ and $+15$ kV applied to the extractor (Stockli et al. 2017). The e-dump voltage V_{ed} with respect to the ion source was scaled with $V_{ed} = 6.2 \text{ kV} \cdot (65 \text{ kV} + V_{ex}) / 65 \text{ kV}$ to maintain a uniform extraction field. 6.2 kV is the optimum voltage with the extractor at ground (Stockli et al. 2010). The steerers were reoptimized but yielded little change as seen in Fig. 18.43a. Because a positive extractor voltage increases the focal power of the first lens, its voltage must be gradually decreased. This requires the increase of the second lens voltage to maintain the optimal convergence of the beam as it enters the RFQ.

In 2016, $+5$ kV were applied to the extractor for neutron production. As the larger H^- currents were and are not needed, SNS has returned to a grounded extractor to reduce the risk of e-dump to extractor arcs.

As seen in Fig. 18.43b, the LEBT output current increased about 1 mA ($\sim 2\%$) for the first 5 kV but then remained at ~ 63 mA, consistent with an ion-density limited extraction. However, the RFQ output current kept increasing up to $\sim 10\%$ for $+15$ kV applied to the extractor. This suggests that stronger extraction fields yield H^- beams with lower emittances from the SNS ion source.

18.13 A Summary and Outlook for the SNS RF H^- Ion Source

SNS is pleased with the performance of its RF H^- ion source. LBNL deserves full credit for developing and delivering two highly capable H^- ion sources as a part of the SNS Front-end. Modifications were needed to achieve the desired performances

and availability. They have normally delivered more H⁻ beams than required by the SNS accelerator since starting up SNS in 2006. Over the last 10 years, significant attention has been paid to their availabilities, which practically reached perfection quite a few years ago.

The main features and performances of the SNS H⁻ sources are listed in Table 18.2. While SNS needs a little more H₂ gas and RF power than other RF H⁻ sources, those differences are negligible on the scale of advanced accelerators. It is amazing that ~5 mg of Cs is sufficient for 129 days of operation with the H⁻ output beam decaying by only 2.6% or about 1.3 mA. The Rasser approximation suggests a loss in the order of 0.01 monolayers of Cs or about 2% of a 0.4 monolayer of Cs. The loss is likely larger because the Cs monolayer is likely closer to the optimal 0.6 monolayer, where the H⁻ output is less sensitive to the loss of Cs.

The unusually low consumption of Cs is likely due to the Cs collar that reduces the plasma potential near the converter.

Table 18.2 lists the values for the SNS source #2. The other SNS sources seem to have slightly larger beam decay rates. In addition, some of the other sources also yield a bit less H⁻ output beam. The source-to-source differences are not understood despite sustained efforts to make them all equal.

The demonstrated lifetime in Amp-hours from a single source includes scheduled maintenance of a day or less, independent of whether the source RF was running or not, but excludes longer shutdowns of the RF.

SNS is very satisfied with the SNS H⁻ sources because they are well understood, enough to provide long-term stable operations, and known issues are well controlled and managed (Han et al. 2022).

The biggest issue is the SNS proton power upgrade (PPU) and the second target station (STS) which in several years expect to routinely accept 46 mA linac H⁻ current at 60 Hz, which is a ~20% increase in current (Galambos 2022).

Figure 18.44 from 2018 demonstrates that the SNS Front-end can deliver up to ~53 mA H⁻ to the linac by increasing the 2 MHz power to ~60 kW with source #2 and ~30 sccm H₂. This is 2.7 times more than the best 20 mA obtained with the LBNL H⁻ source before SNS/ORNL started to improve it in fall of 2007.

However, in 2018, increasing the power to 70 kW did not significantly increase the RFQ H⁻ output beam current as seen in Fig. 18.44. The likely reason is that the gain in beam current is lost in the RFQ due to the increased beam emittance which lowers its transmission. This was observed previously although with lower H⁻ beam currents due to the compromised RFQ as seen in Fig. 18.45 (Stockli et al. 2016).

To routinely produce the required ≥ 50 mA RFQ H⁻ output currents require larger margins. As the 2 MHz power cannot increase the margins, there are two issues that should. The first is the temperature of the converter, which is difficult to control and is a cause of the observed variation of the source performance. The root cause is the fasteners which are stretched beyond their elastic limits when the Cs collar is heated to >500 °C. Designing a more elastic assembly with shorter and stronger fasteners should solve this problem and make the performance of the H⁻ source more consistent.

Table 18.2 Characteristics and performances of the four RF H⁻ ion sources supplying advanced accelerators

Production RF H ⁻ source	Units	SNS	J-PARC	CERN	CSNS
RF ion source starting main accelerator service	Year	2006	2014	2020	September 2021
Plasma chamber	Material	304 SS	SS	Al ₂ O ₃	Si ₃ N ₄
Continuous H ₂ gas flow	sccm	~30	~21	Pulsed	~20
RF antenna	Location	In plasma	In plasma	External	External
RF frequency	MHz	2	2	2	2
RF power	kW	~50 ^a	~21	30 ^b	~30
RF pulse length	ms	1.0	0.8	0.9 ^b	0.7
Repetition rate	Hz	60	25	0.83	25
Starter plasma	Method	13.56 MHz on antenna	30 MHz on antenna	H ₂ pressure pulses	Igniter in H ₂ line
Thermal plasma load	Quantity	250 W	30 W	20 ms ^b	580 V, 50 mA, 0.4 ms
Converter/plasma electrode	kW	3.2	0.5	0.02	0.5
Converter voltage	Material	Mo	Mo	Mo	Mo
Converter temperature	V	0	0	0	19
Converter funnel angle	°C	~300	~54	TBD	78
Outlet aperture \varnothing	to axis.	40	45	45	45
Operational H ⁻ beam current	mm	7	9	7.5	8
Measurement location	mA	~50	~60	27	37
H ⁻ beam pulse length	–	LEBTOutput	LEBTOutput	RFQ exitOutput ^c	LEBTOutput
H ⁻ ion energy	ms	1.0	≥0.385	0.9 ^b	0.430,5 ^d
Ave. normalized emittance	kV	65	50	45	50
Emittance analysis	π ·mm·mrad	~0.28	0.26	0.35 ^b	<0.31
For H ⁻ current	Threshold	0.5%	~1 to 2%(95% of beam)	<1%	No threshold(100% of beam)
Measurement location	mA	55	60	35	37
	–	RFQ input	RFQ input	LEBTOutput	LEBTOutput

Demonstrated service cycle	Weeks	18.4	21.7	60.8 ^b	44.3
Demonstrated lifetime	Amp-hrs	10	4.2	0.3 ^c	4.8
H ⁻ beam decay	%/day	0.02 ± 0.01	0	0	0
Availability at time	%	99.93	99.8	>99.9	>99.99
Cesium supply	–	Cs ₂ CrO ₄	Cs oven @ 180 °C	Cs oven @ 60–80 °C	Cs oven @ ~85 °C
Average Cs consumption	mg/day	<0.01	0.6	0.24	~0.5
Low-energy beam transport	Method	2 electrostatic lenses	2 solenoids	Einzel lens and 2 solenoids	3 solenoids
Length (extractor to accelerator entrance)	m	0.12	0.66	2.10	1.65

Notes: ^aSource #2. ^bOn LINAC4. ^c37 mA in LEBT. ^dSince early February 2022

Fig. 18.44 The RFQ output current for ~1-ms-long H⁻ beam pulses from source #2 in the first run of 2018. (Simplified from (Han et al. 2021) with the permission of AIP Publishing)

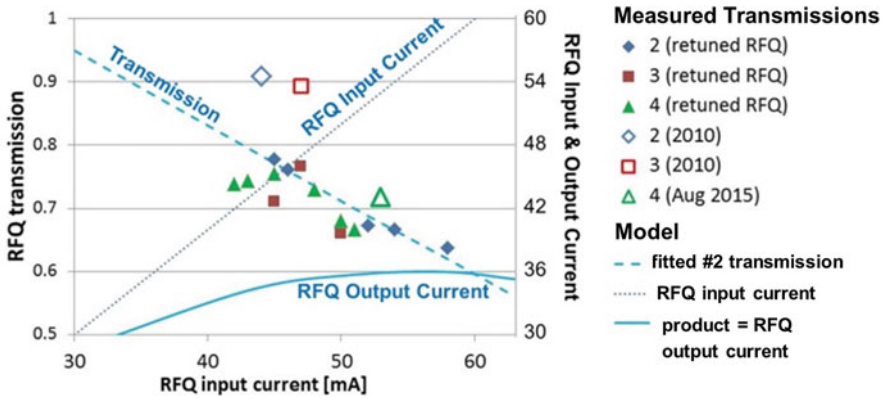
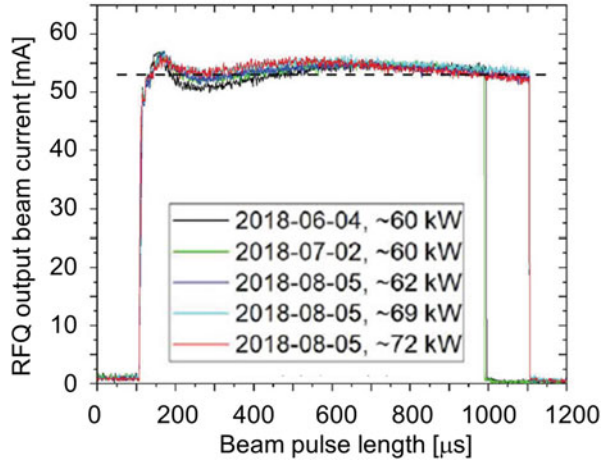


Fig. 18.45 Two 2010 RFQ transmission measurements and the 2012–2015 measurement a function of the RFQ input current and the predicted RFQ output current. (Enhanced from (Stockli et al. 2016) with the permission of AIP Publishing)

The other issue is the rather small outlet aperture \varnothing of the SNS H⁻ source. Table 18.2 suggests that increasing the outlet aperture should not substantially increase the emittance. Scaling the volume-produced H⁻ beam with the area, and the surface-produced H⁻ beam with the circumference of the outlet aperture suggests ~20% H⁻ beam increase for every mm the outlet diameter is increased. Accordingly, an 8 mm \varnothing outlet should routinely yield the required 50 mA RFQ output current without increasing the 2 MHz RF power. However, the plasma emerging from the Mo converter is likely directional. Accordingly, to materialize the ~20% H⁻ beam increase likely requires a larger outlet of the converter, which is a more complicated issue.

The biggest risk for the ion sources is that the Cs enhancement gets compromised like in 2011 when the H⁻ output beam currents from two sources decayed within

hours or days as seen in Fig. 18.36. Because the 2011 event was eventually understood and corrected, a recurrence is unlikely. However, other causes may trigger similar events. Such mission-critical threats can be addressed with efforts to better understand the Cs enhancement.

18.14 The RF-Driven H^- Source at J-PARC

The Japan Proton Accelerator Research Complex (J-PARC) developed multicusp H^- ion sources driven by filament discharges for their multipurpose accelerator (Oguri et al. 2002). J-PARC used such a source to optimize its plasma chamber (Ueno et al. 2004). Ten different shapes and sizes of the plasma electrode (PE), which SNS calls converter, were tested. It was found that of the ten PEs, the ones with a 45° funnel ending in a 9 mm \varnothing outlet yielded the highest H^- output currents. Of those, the 10- and the 16-mm-thick PE yielded 38 mA, or 24% more H^- beam than the 4-mm-thick PE (Ueno et al. 2010).

In any case, the 4-mm-thick J-PARC PE is almost identical to the 4-mm-thick Mo converter with a funnel of 40° (with respect to the axis) and a 7 mm outlet \varnothing that SNS developed independently to reduce the gap between the converter and the source outlet (Stockli et al. 2009).

The optimization of the J-PARC PE from a 2-mm-thick PE with a 7 mm \varnothing to the thick PEs with a 45° funnel and a 9 mm \varnothing outlet is the lion's share of increases over the previous 14 years culminating in the J-PARC 50 mA H^- linac beam current. The PE optimization accounts for more than half of the accumulated 115% increase as detailed in (Ueno 2017). This increase is similar to the 2.7-fold increase SNS/ORNL achieved over the LBNL H^- source with a 1-mm-thick SS PE without increasing the 7 mm \varnothing outlet.

Interesting are the results from a J-PARC prototype source with a tungsten (W) triple hairpin filament which produced with 15 kW arc discharge power 18 mA before and a record (at that time) of 73 mA H^- output current after cesiation. Despite a large continuous feed of Cs, the H^- beam decayed by $\sim 20\%$ over the next 3 days and the filament broke the day after (Ohkoshi et al. 2010).

These measurements with a W filament allow to determine the fraction of the volume-produced H^- because without Cs the H^- formation on a Mo PE is negligible as discussed in Sect. 18.4. That should also apply when the PE is covered with some W evaporated from the filament because W and Mo have the same metallic radii (139 pm) and have almost the same work functions when clean, as well as when partially or fully covered by Cs (within $\sim 1\%$ as seen in Table 18.1).

Accordingly, the discussed 18 mA H^- must be produced exclusively in the volume, and, when cesiated, the surface production must have increased that to 73 mA. This shows that when cesiated and powered with 15 kW, $\sim 25\%$ remain volume produced.

Using a LaB₆ filament and increasing the outlet diameter D from 8 to 9 mm increased the H^- output current from 14 to 18 mA for 20 kW ($18/14 = 1.29$), from

20.5 to 25.7 mA for 30 kW ($25.7/20.5 = 1.25$), and from 29 to 35 mA ($35/29 = 1.21$) for 45 kW, the highest arc discharge power investigated for both outlet diameters (Oguri et al. 2010). The slight saturation for larger powers is likely caused by beam losses due to the emittance that increases with the beam current. The observed increases in beam current are practically proportional to the square of the diameter D^2 ($(9/8)^2 = 1.266$) which therefore suggests the currents being proportional to the area of the source outlet.

However, an author claims to prove that “almost all” of the J-PARC H⁻ beam is surface-produced because two previous, single measurements with two differently shaped PEs, one with a 7- and the other with a 9-mm-diameter (D) outlet ($9/7 = 1.29$), resulted in a 25% increase in H⁻ beam current ($25/20 = 1.25$), which is “nearly proportional” (Ueno et al. 2010). However, no reference is given for, and no results are found on the web for a law that “surface-produced, extracted H⁻ ion yields are proportional to the diameter of the ion source outlet.” It was also concluded that the J-PARC beams must be hollow, but no such evidence was found with the emittance scanner (Ueno et al. 2010). This inconsistency questions this model or law.

Not surprisingly, the H⁻ ion production, their extraction, and the beam transport are more complicated than many consider. The volume-produced fraction of H⁻ beams is most likely uniform and therefore increases proportional to the area of the outlet. The surface-produced fraction of the H⁻ ion beams is more complex because: it requires to calculate the product of the probability to form a negative ion when a H atom leaves a surface and the probability p the formed ion reaches the meniscus and is extracted. The first probability is dominated by the plasma potential, while the second contains a four-dimensional integral which is more demanding. Depending on this extraction probability $p(d)$ versus the distance d from its origin, the integral probability P may also increase proportional to the area of the outlet. Only if the probability $p(d)$ became zero for $0 < d \ll D$ would the integral probability P be proportional to the circumference and the diameter D of the source outlet. That is not the case as seen in Figs. 18.8 and 18.9 in (Ueno et al. 2004).

With the lifetime of the W filaments being unacceptably short (Ohkoshi et al. 2010), J-PARC refocused on the LaB₆ filaments. The aforementioned prototype source required 30 kW to produce 18 mA with a LaB₆ filament (Ohkoshi et al. 2010). Then, the magnetic field near the filament, the filament position, the arc discharge power (Oguri et al. 2009), and the size of the filament (Oguri et al. 2010) were optimized. This resulted in 17 mA produced with only 18 kW for run 35 (Oguri et al. 2011).

While the J-PARC source now comfortably met the 36 mA requirement for the first stage of their project, the question arose on how to generate 60 mA for the final stage of the project. Adsorbing Cs increases the LaB₆ produced H⁻ output currents by up to 70% for RF discharge powers of >30 kW (Ohkoshi et al. 2010). However, the enhancements were very short-lived (Ueno et al. 2010), likely because the Cs adsorbates got covered with B from the perpetual emission from the LaB₆ filament.

During the 13th International Conference on Ion Sources in 2009, J-PARC staff witnessed the SNS 40 mA H⁻ linac beam current and realized that such a RF-

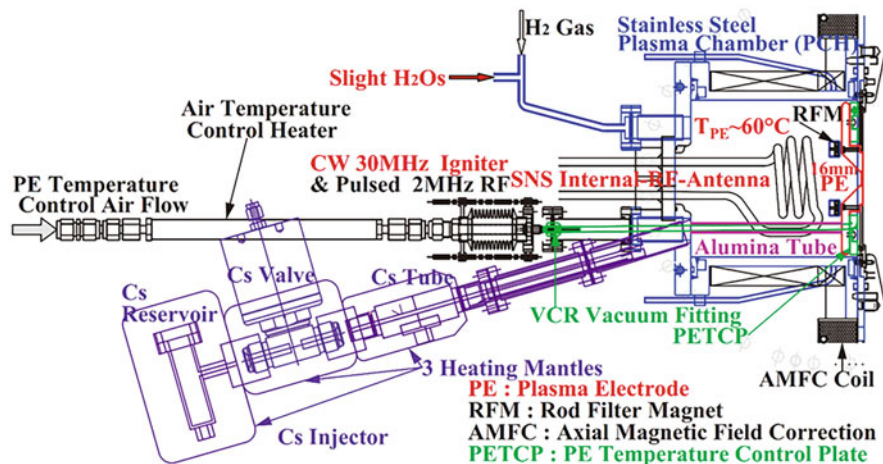


Fig. 18.46 The J-PARC RF H^- ion source with a SNS antenna. (Reproduced from (Welton et al. 2022) with permission from the Institute of Physics)

driven H^- source may enable their planned upgrade project. They used their highly developed multicusp plasma chamber and replaced the filament(s) with a SNS antenna as shown in Fig. 18.46. The J-PARC and the SNS sources look very similar, while there are some differences. Most notably J-PARC pioneered the injection of Cs in the back of their H^- RF source, a very simple and effective solution. Other characteristics and performances are listed in the fourth column of Table 18.2.

The J-PARC RF H^- source features a very efficient starter plasma with only 30 W of 30 MHz RF. It still has an outlet aperture of 9 mm \varnothing and no Cs collar, both of which are the primary reasons for the larger H^- output currents with less RF power than the SNS source. The latter increases the plasma temperature near its PE, which explains its much larger Cs loss.

J-PARC adds a tiny amount of water to the H_2 gas, which cools the light hydrogen atoms and molecules in the plasma. This reduces the transverse emittance of its extracted H^- beam by 72% (Ueno 2017). Their emittances are measured on their test stand with two slits and a Faraday cup downstream of the first LEPT solenoid. A slight negative background is subtracted before analyzing the rms emittance of 95% of the beam (Ueno et al. 2017). Ninety-five percent of the beam corresponds to a threshold of 5% for a beam with a Gaussian distribution. However, for more realistic beams with tails, the corresponding threshold is rather around 1–2% (Stockli 2006), which is still larger than the thresholds applied by other facilities as seen in Table 18.2. Considering the elevated threshold, the J-PARC emittance looks elevated.

Emittance results depend strongly on any applied threshold, and accordingly thresholds need to be equal to allow for sound comparisons (Stockli 2006). This is not the case for the claim of having the “world’s brightest-class” 66 mA “beam with an emittance $\varepsilon_{95\%nrmsx/y}$ of 0.23 $\pi \cdot \text{mm} \cdot \text{mrad}$ ” (Ueno 2017). It is also difficult to understand the cumulated 160% of emittance reduction and avoidance of emittance

increases (Ueno 2017), while no more than $0.41 \pi \cdot \text{mm} \cdot \text{mrad}$ of cleanly measured emittance were ever reported by J-PARC (Ueno et al. 2015b).

In addition, 0.23 is much larger than “0.13 (X) and 0.15 (Y) $\pi \cdot \text{mm} \cdot \text{mrad}$ normalized rms emittances” reported for a 60 mA H^- beam produced with a W filament (Oguri et al. 2002).

The added water vapor aggravates the loss of Cs as shown in Fig. 18.34. However, J-PARC only needs to add 0.6 mg of Cs per day to maintain the H^- beam current without decay. This is only ~ 0.2 g per year and therefore is no lifetime limitation for their Cs oven kept near 180°C .

J-PARC achieved its record with a service cycle of 152 days or 5 months (Shibata et al. 2022). In that time, it produced over 4 A·h of H^- ions. This is less than SNS due to their lower repetition rate and their shorter RF pulse length. J-PARC plans to increase the pulse length to increase the average beam power in the future (Oguri 2022).

J-PARC dumps the coextracted electrons right after the PE outlet and corrects the ion trajectories at the ground potential.

J-PARC preconditions its ion sources. First, the plasma chamber is evacuated for ~ 2 h to reach 10^{-4} Pa ($0.8 \cdot 10^{-6}$ Torr) before starting to heat the PE to 300°C as well as heating the Cs system. This is followed by another ~ 3 h of pumping to reach $\leq 1.5 \cdot 10^{-5}$ Pa ($\leq 10^{-7}$ Torr) to “be suitable for accurate vacuum leak tests.” So, after >6 h, a 25 kW RF plasma is started for ~ 15 min and being followed by another hour of pumping to reach 10^{-5} Pa ($0.8 \cdot 10^{-7}$ Torr) and then another five cycles of 15 or ~ 30 min of 25 kW and later 43 kW RF plasma operation followed by ~ 10 – 15 min of pumping to reestablish 10^{-5} Pa. This is considered to sufficiently clean the PE (Ueno et al. 2016). This is a 10-hour procedure for leak-checking and 1.5 h of plasma conditioning, while the remaining ~ 7.5 h are spent on sole pumping.

Then the Cs valve is opened for 3–10 min to yield the required ≥ 66 mA before closing the Cs valve. However, in the following 90 min, the Cs valve must be reopened “rather frequently” to maintain the ~ 66 mA H^- beam current with ~ 40 kW RF power (Ueno et al. 2016). The loss of Cs is consistent with a system and/or the PE that still contain significant amounts of impurities that sputter the Cs as discussed in Sect. 18.5.

However, the total injected Cs is estimated between 1 and 4 mg (Ueno et al. 2016), less than the ~ 5 mg at SNS as discussed in Sect. 18.10.

It takes 24–40 h to precondition a J-PARC ion source (Ueno et al. 2015a), after which the source is backfilled with argon (Ar) (Ueno et al. 2016). The backfilling with Ar may not be necessary because partial Cs monolayers on clean metal surfaces are rather inert as discussed in Sect. 18.10. Backfilling with anything significantly heavier than H_2 bears the risk that Cs on the surface is sputtered away by the heavy residues if they are not completely removed before starting a plasma as shown in Fig. 18.34.

The preconditioning aims at shortening the ion source startup time on the production accelerator. Starting up a preconditioned ion source on the production accelerator requires many Cs injections and takes at least 11 h (Oguri et al. 2016).

After pumping down, a 5%, 25 kW plasma starts to recondition the source for ~30 min being followed by 20 min of pumping. The conditioning is completed with 1 h of 5%, 50 kW plasma, followed by 15 min of pumping (Ueno et al. 2015a). During the high-power conditioning, the PE is allowed to reach ~300 °C (Ueno et al. 2015a), which likely activates the thermal emission of Cs and likely ends with an under-cesiated surface as discussed in Sect. 18.5. This assumption is also consistent with the fact that the time needed for reconditioning increases with the peak PE temperature reached during conditioning (Ueno et al. 2015a).

Then a 40–50 kW, 2.5% plasma is operated with beam extraction for 3–20 min followed by 7 min of pumping. If the extracted beam was ≤ 66 mA, this procedure is repeated while opening the Cs valve for 20 s. After a few such cycles, the plasma operation becomes continuous, and the Cs valve is opened for 20 s only when the required 2 MHz power for maintaining 66 mA exceeds 42.5 kW. This happens quite a few times during the next few hours. The need for additional Cs injections is consistent with a plasma chamber and/or PE which still harbor significant amounts of heavy impurity ions that sputter the Cs.

In 2015 J-PARC preferred thick antenna coatings (>0.58 mm) (Ueno et al. 2016) which was not an issue due to their lower duty factor. However, they did not encounter a problem with the ~0.4 mm coatings SNS introduced around that time to prevent the occasional melting of the antenna coatings at SNS.

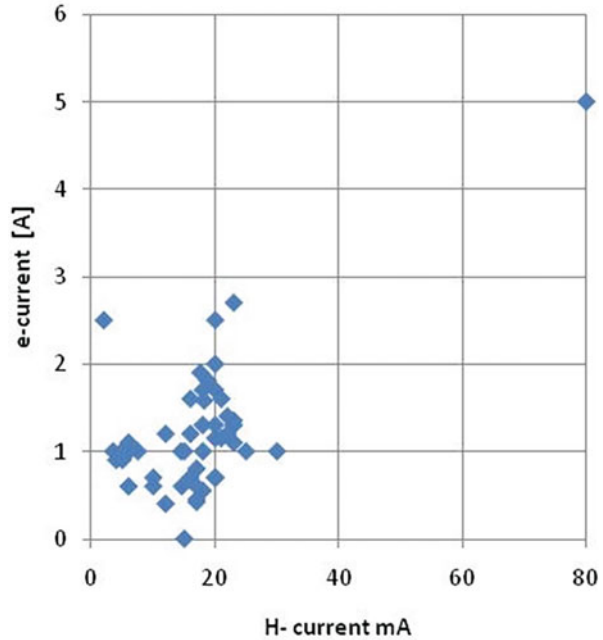
In 2019 J-PARC encountered two antenna failures (Oguri et al. 2021), likely due to a batch of inferior antennas. SNS avoided this issue, perhaps due to more stringent acceptance criteria. Aside, the J-PARC performance and availability are outstanding while extracting 60 mA from their source (Oguri et al. 2021).

J-PARC maintains an aggressive R&D program that produced up to 110 mA H^- beam with an ion source voltage of 65 kV (Ueno et al. 2021). This shows that its H^- source is ready for future challenges after a RFQ with a larger acceptance and a larger input velocity is developed for J-PARC.

18.15 The RF-Driven H^- Source at CERN's LINAC4

The Centre Européen pour la Recherche Nucléaire (CERN) is increasing the luminosity of its facility by implementing charge-exchange injections shown in Fig. 18.1a. Accordingly, Linac2 fed by a duoplasmatron proton source was recently replaced with Linac4 featuring a H^- source (Scrivens et al. 2011). CERN built and tested a copy of the cesium-free DESY test RF H^- source. With the DESY ion source voltage of 35 kV CERN was only able to extract 23 mA (Midttun et al. 2012), much less than the 80 mA reported by DESY (Peters 2000b). This is the reason that this review only includes H^- RF sources in routine production because the staff reports the currents that can be routinely reproduced and maintained. Results from test and development rigs tend to report their best results, and reproducibility and lifetime tests are often inadequate.

Fig. 18.47 Coextracted electron currents in A versus the extracted H^- currents in mA for many tests and various persistent and transient conditions of the CERN copy of the cesium-free DESY RF H^- source. (Courtesy of J. Lettry, CERN)



In addition, CERN could not raise the ion source voltage to its required voltage of 45 kV because the carbon e-dump started to evaporate (Midttun et al. 2012). This points to the high coextracted electron currents, which are normally 50–100 times larger than the H^- currents extracted from cesium-free H^- sources. The unique Fig. 18.47 shows the coextracted electron currents in A versus the extracted H^- current in mA measured with the CERN copy of the DESY RF ion source for many different persistent and transient conditions of the source.

The DESY copy not being able to meet the CERN requirements, they built a copy of the Brookhaven National Laboratory (BNL) magnetron H^- ion source. It was tested and successfully met all the CERN requirements (Lettry et al. 2015). However, due to the high Cs consumption of magnetron H^- sources and being familiar with the successful SNS H^- source, CERN decided to develop their own RF H^- ion source. The decision was made only a few years after SNS experienced problems with the antenna coatings, and accordingly CERN decided to develop an external antenna that is not exposed to plasma. As seen in Fig. 18.48, it uses an alumina (Al_2O_3) plasma chamber which is not a problem due to CERN's low duty factor (0.075%) according to the experience at SNS. External antennas are more challenging for maintaining a starter plasma because the antennas are further away from the low-pressure gas. However, with their low repetition rate of less than 1 Hz, CERN can raise the H_2 pressure over the Paschen curve for every single pulse by injecting $4 \cdot 10^{-6}$ mols of H_2 gas with a pulsed Parker valve (Parker 2022). Occasionally the pulsed valve needs to be replaced, which does not limit the source

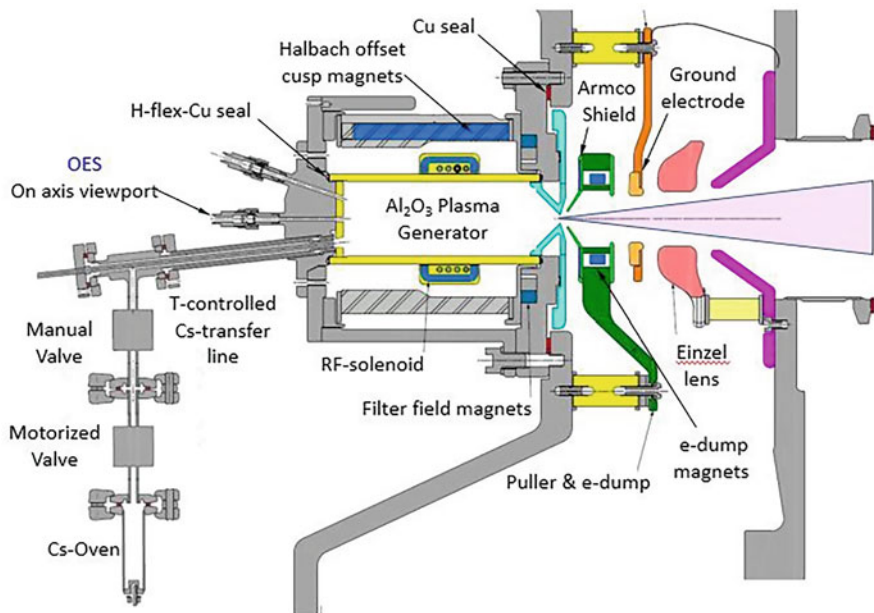


Fig. 18.48 The superbly controlled CERN RF H^- ion source with an Al_2O_3 plasma chamber and an external antenna. (Reproduced from (Welton et al. 2022) with permission from the Institute of Physics)

lifetime because the replacement can be completed during a regular maintenance day (Lombardi 2022). About 0.18 ms after opening the valve, the H_2 pressure peaks and the plasma ignites. After another 0.2 ms, the plasma is sufficiently stable to extract a solid 0.6 ms long H^- pulse.

CERN studied the influence of the confining cusp field on the performance of their source (Briefi et al. 2017a; Lettry et al. 2018). Their cusp field increased their volume-produced H^- output by about 60%. A cusp-free H^- source is installed and now running on LINAC4 because of its smoother plasma ignition and stronger suppression of the coextracted electrons (Lettry et al. 2018).

The characteristics and performance of the CERN production H^- source are listed in the fifth column of Table 18.2. It produces 40–50 mA (Lettry et al. 2017) and now about 50 mA (Lettry 2022) to deliver the required 27 mA H^- beam out of the RFQ with only 20 kW of 2 MHz and a modest source outlet aperture of 7.5 mm \varnothing . It dumps the coextracted electrons very efficiently as seen in Fig. 18.49 (Fink et al. 2018). The source has been extensively modeled, and the results are in good agreement with the experiments (Mochalsky et al. 2016; Briefi et al. 2017b; Mattei 2017; Noll et al. 2019a, b).

The emittance of 0.25π mm·mrad was measured with 35 mA H^- beam halfway through their LEBT using their slid and grid emittance scanner.

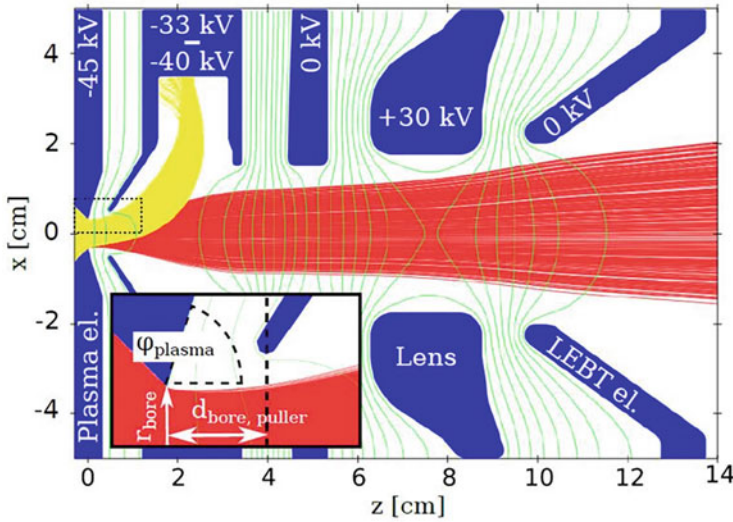


Fig. 18.49 A model of the CERN H^- extraction with the ion trajectories (red, going to the right) and the trajectories of the coextracted electrons (yellow, going up). An Einzel lens after the extractor limits the divergence of the extracted ion beam. (Reproduced from (Noll et al. 2019b) with permission from CERN)

In 2020, CERN started to operate its H^- source on LINAC4 and started to inject those beams into the Large Hadron Collider (LHC) in April 2021. To obtain ultra-stable injections into the CERN production accelerator, the gas injection was extended to 20 ms to have a stable pressure during the H^- formation and injection. The 2 MHz power was increased to 30 kW and the pulse was extended to 0.9 ms. Ions are extracted during the entire RF pulse (Lombardi 2022).

Until very recently, the CERN H^- source held the world record for RF H^- sources with their longest service cycle of 26 weeks, although it produced only 0.3 A-h of H^- ions in that time. With 0.24 mg per day or about 0.1 g of Cs per year, this is no limitation for their Cs oven kept around 70°C. The CERN source installation is the grand master of controls. For example, CERN analyzes the RF resonance continuously and keeps adjusting the coupling during the entire 2 MHz pulse (Butterworth et al. 2015).

18.16 The RF-Driven H^- Source at CSNS

When the China Spallation Neutron Source (CSNS) was designed early in this century, an ISIS Penning H^- ion source (Faircloth et al. 2006) was selected because at that time it was the only H^- source with a proven record of meeting the CSNS

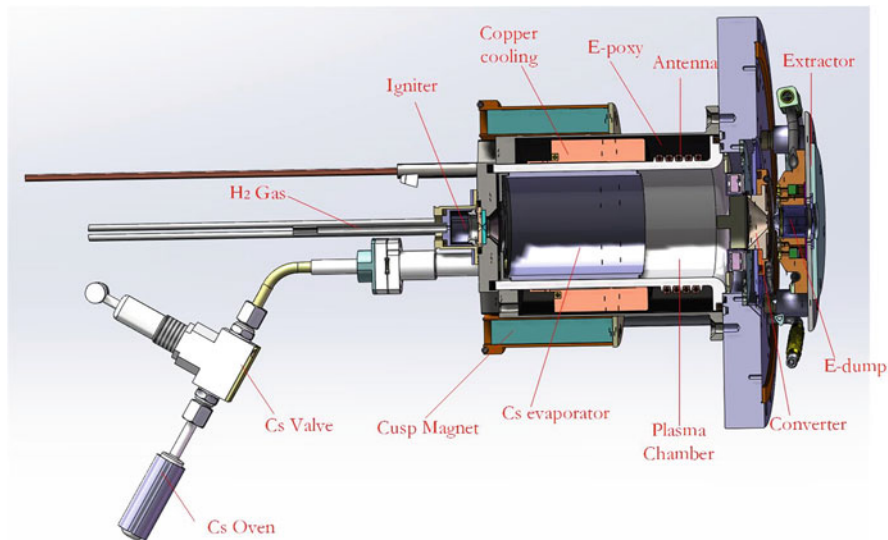


Fig. 18.50 The newest RF H^- ion source in operation at CSNS with an external antenna and a Si_3N_4 plasma chamber. (Courtesy of W. Chen, CSNS, 2021)

project goals. It was significantly improved and worked well (Liu et al. 2015), but the sources had to be replaced every few weeks.

Learning about the success and lifetime of the SNS RF H^- sources, CSNS started in 2015 to develop their own RF H^- source. An external antenna was chosen as seen in Figure 18.50. They pioneered the use of silicon nitride for their plasma chamber because Al_2O_3 chambers are known to break at larger RF power and duty factors (Welton et al. 2008), while Si_3N_4 tolerates more thermal stress and should allow for an average heat load of 1.5 kW (Chen et al. 2019).

The characteristics and performances of the CSNS H^- source are listed in the last column of Table 18.2. Their 25 Hz repetition rate would make H_2 pressure pulses inefficient. Accordingly, they developed an igniter in a larger-pressure chamber which is the last section of their H_2 feed line. 580 V ignite a plasma for 0.4 ms before the 0.7-ms-long, 2 MHz pulse is started in the main plasma chamber (Chen et al. 2019).

To minimize the beam decay, a H_2 purity filter is used, which needs to be replaced occasionally during a regular maintenance day.

CSNS applies 19 V to the Mo converter to optimize the source performance. With a modest outlet aperture of 8 mm \varnothing and ~ 30 kW of 2 MHz, impressive 52 mA are achieved for their 0.43 ms long H^- output current pulses at 25 Hz.

CSNS carefully optimized the emittance of their source (Zhu et al. 2022). Earlier they developed a method to analyze the emittance of the entire beam (100%) to avoid the use of thresholds. The same goal drove the development of the SCUBEE_x

analysis, the Self-Consistent UnBiased Elliptical Exclusion analysis (Stockli et al. 2002, 2004).

Unusual is the large Cs evaporator, obviously to inject the Cs uniformly in the back of the plasma. The large, low-conductance device certainly extends the outgasing time. Its benefits are not obvious and would have to be demonstrated. However, the source consumes only ~ 0.5 mg/day or ~ 0.2 g/year Cs from the Cs reservoir kept around 100°C , which is very average and no problem.

CSNS did a sophisticated study of their plasma impedance to optimize the RF coupling (Li et al. 2021).

In September 2021, the China Spallation Neutron Source started up their RF-driven H^- ion source on their production accelerator. It worked very well, and after the 2022 Chinese New Year holiday, the H^- beam pulse length was increased to 0.5 ms to raise the beam power from 100 to 125 kW.

CSNS finished the first service cycle of their RF H^- source on July 26, 2022, with a record availability of $>99.99\%$. It spanned over 310 days of operation without major maintenance, producing 4.8 A·h of H^- ions. While pioneering an external antenna for a high repetition rate and duty factor, CSNS broke the world record for maintenance-free operation of a RF H^- source with high repetition rates. At the same time, they achieved the second highest amount of produced H^- ion without major maintenance.

The CSNS LEBT has three solenoids as it was designed for their Penning H^- source. CSNS plans to remove one solenoid around 2024.

18.17 The Future of Pulsed, High-Current H^- Sources

In the past, there was hope that the RF H^- ion sources could eventually be replaced by a more common 2.45 GHz electron cyclotron resonance (ECR) ion source. These microwave ion sources produce plasma very efficiently and yield record high proton and deuteron ion output currents with 100% duty factors or less (Gobin et al. 2012). However, practically all the many microwave and other efforts failed to produce more than a few mA of H^- output currents. A notable exception was the compact Peking University (PKU) microwave ion source with all permanent magnets but without an explicit e-dump. It reported over 30 mA H^- output currents when observing two well-separated beams emerging from a mass-analyzing circular dipole magnet with the more rigid beam being H^- (Peng et al. 2016). It was a highlight in a review on Cs-free RF and microwave H^- ion sources (Tarvainen and Peng 2016) where 45 mA H^- output currents were reported with 2.1 kW of 2.45 GHz when operated with a pulse length of 1 ms at 100 Hz citing a to-be, but-never-was, published manuscript (Peng 2022).

However, others could not duplicate such results with “identical” microwave ion sources (Belchenko 2016).

After the PKU microwave ion source was improved and the analyzing section was brought up to common standards, the best result was 8.5 mA of H^- found

when operated with 5.4 kW at 100 Hz and 0.3-ms-long pulses with a pressure of 0.04 mTorr and an extraction voltage of 50 kV (Zhang et al. 2018). The paper still quotes 40 mA H⁻ without any reference and gives no explanation why the promising improvements yielded an over fivefold reduction of the H⁻ output (Zhang et al. 2018). A corrigendum to the review explains the discrepancy being due to previously deducing the extracted H⁻ current from the total extracted beam current using an incorrect assumption (Tarvainen and Peng 2018), while the new data are direct measurements. The corrigendum was submitted but not accepted for publication due to a technical issue (Tarvainen 2022).

The new PKU microwave source now routinely produces ~5 mA H⁻ (Peng 2022). So, evidently the previous and current versions of the PKU microwave ion sources were always in line with the results of the other efforts.

The disappointing H⁻ output from microwave ion sources is likely caused by larger electron temperatures near their outlets. A 2 eV electron has a cross section of $\sim 0.2 \cdot 10^{-15} \text{ cm}^2$, and 5 eV electrons have cross sections of $\sim 1 \cdot 10^{-15} \text{ cm}^2$ for ionizing a H⁻ ions (Zhang 1999). Both are much larger than the maximum $0.06 \cdot 10^{-15} \text{ cm}^2$ for electron impact ionization of neutral H atoms which explains the sensitivity of the H⁻ ion extraction current to the electron temperature.

However, the lackluster performance of microwave H⁻ sources was no issue due to the success of the RF sources with helical antennas. This success earned the SNS ion source team the Brightness Award at the 2017 International Conference on Ion Sources for the best ion source development (Alonso 2018).

There were efforts to further improve the performance of the RF H⁻ source with solenoidal fields as well as with saddle antennas (e.g., (Dudnikov et al. 2018)), but no effort was ever able to match or exceed the highly productive H⁻ outputs of the four discussed RF H⁻ sources with helical antennas and cusp-field confinement.

Twenty years ago, the H⁻ ion sources were a limiting factor of advanced negative ion accelerators. The RF H⁻ ion sources have reversed the situation: today the advanced accelerators limit the applicable performance of the RF-driven H⁻ sources.

Their availabilities are practically perfect. The numbers listed in Table 18.2 are skewed by different accounting methods, and the differences are not significant. The so far unmeasurable long maintenance-free lifetimes have drastically reduced the need for maintenance and the required retuning of the accelerator after every ion source change. There is still room for improvements, especially for reducing the performance variations seen among seemingly “identical” sources (Stockli et al. 2013b) as well as reducing the risks of downtimes or failures. And there remain several parameters that can be fully optimized to increase their negative ion output for meeting future challenges.

Being somewhat large, heavy, and complex, their application is concentrated on advanced accelerators that can accelerate such large H⁻ beam currents. However, their high availability and their unprecedented maintenance-free service cycles are other characteristics that draw interest.

ISIS, the spallation neutron and muon source at the Rutherford-Appleton Laboratory near Oxford, England, uses a very successful Penning H⁻ ion source for

over 35 years. It has a lifetime of about 3 weeks. To reduce unplanned ion source downtime, the H^- source is now replaced every 2 weeks (Lawrie and Tarvainen 2021). ISIS plans to upgrade their facility (Lawrie et al. 2019) which will include a RF H^- source with an external antenna (Tarvainen et al. 2018). Since they need no more than 35 mA H^- beam, they like to produce it without the use of Cs. This is a challenge because so far nobody has been able to duplicate the high H^- currents reported by DESY (Peters 2000b). And this challenge is compounded by a large coextracted electron current at a high duty factor that nobody has mastered yet. However, if those challenges cannot be met, it will be easy to add a little Cs, which will dissolve both challenges. ISIS plans to install the new source around 2025.

Los Alamos National Laboratory (LANL) keeps improving their famous accelerator facility (Batygin et al. 2021). They create their 12–16 mA H^- beam with a converter H^- ion source with a filament that needs to be replaced every 4 weeks and requires a startup of several days. Their successful efforts to predict and manage the filament lifetime practically eliminated unscheduled downtime (Yampolsky et al. 2021).

To reduce the required maintenance, LANL developed an interest in the SNS RF H^- ion source. A LANL-SNS collaboration tested a SNS RF H^- source with an internal antenna for 4 weeks with the 10% duty factor required for LANL. No degradation was observed and accordingly service cycles of >11 weeks can be expected (Stockli et al. 2020). In addition, the SNS RF H^- source would also be able to fill their linac with the maximum acceptable beam of 24 mA, a significant increase over their current 12–16 mA. After completing the test, LANL started to build a copy of the SNS H^- source and will test it on the LANL test stand. Later LANL plans to install it on their main accelerator as a part of the Los Alamos Modernization Project (LAMP). The new source can increase their H^- ions produced without maintenance from about 1 to more than 4 A·h.

The Raja Ramanna Centre for Advanced Technology (RRCAT) in Indore, India, is also developing a RF-driven H^- source (Ghodke et al. 2021) in support of the proposed Indian Facility for Spallation Research (IFSR), a 1 MW Spallation Neutron Source (Pal et al. 2022). The 10 mA source with a 10% duty factor will be pioneering 2-ms-long H^- pulses.

Acknowledgments First and foremost, SNS is indebted to LBNL for developing and building two of our superb RF H^- ion sources. The author would like to thank Kiersten Ruisard, SNS, for her profound proofreading of this long chapter. Then I like to thank the members of the SNS Front-end Systems group for making the SNS H^- source this well-documented success, namely, Baoxi Han, Syd N. Murray Jr., Terry R. Pennisi, Chris M. Stinson, and Robert F. Welton. In addition, I thank Manuel Santana who retired from the group earlier. Our group is also indebted to Chip Pillar, SNS, for his expert help with the RF systems and Johnny Tang, SNS, for his help with control issues. And I like to thank Charles Peters, SNS, for providing invaluable information throughout the SNS operation phase. In addition, the information obtained from Hidetomo Oguri and Akira Ueno, J-PARC; Jacques Lettry and Alessandra Lombardi, CERN; Daniel Noll, ESS; Weidong Chen (陈卫东), CSNS; Olli Tarvainen, ISIS; Ilija Draganic, LANL; and Dharmraj Ghodke, RRCAT, was critical for the completeness of this chapter. I also appreciate their proofreadings. Tiago Sarmento, ISIS, deserves credit for collecting the data shown in Fig. 18.10a while at SNS. Jani Reijonen, LBNL, now at the Schlumberger Technology Corporation, deserves credit for helping with the

production of Fig. 18.5. And last but not least, I indebted to our editor Martha Bacal and her patience!

This manuscript has been authored under Contract Nos. DE-AC05-00OR22725 and DE-AC52-06NA25396 with the US Department of Energy (DOE). The US government retains, and the publisher, by accepting the article for publication, acknowledges that the US government retains a nonexclusive, paid-up, irrevocable, worldwide license to publish or reproduce the published form of this manuscript or allow others to do so, for US government purposes. DOE will provide public access to these results of federally sponsored research in accordance with the DOE Public Access Plan (<http://energy.gov/downloads/doe-public-access-plan>).

References

- J.R. Alonso, Rev. Sci. Instrum. **67**, 1308 (1996). <https://doi.org/10.1063/1.1146703>
- J.R. Alonso, Rev. Sci. Instrum. **89**, 052201 (2018). <https://doi.org/10.1063/1.5033558>
- M. Bacal, M. Sasao, M. Wada, J. Appl. Phys. **129**, 221101 (2021). <https://doi.org/10.1063/5.0049289>
- M. Bacal, *Physics and Applications of Hydrogen Negative Ion Sources* (Springer, 2022)
- Y.K. Batygin, D.V. Gorelov, S.S. Kurennoy, et al., *Proceedings of the 12th Int. Particle Acc. Conf. IPAC2021*, vol 1894 (2021). <https://doi.org/10.18429/JACoW-IPAC2021-TUPAB20>
- K. Beckwith, S. Veitzer, S. McCormick, et al., IEEE Trans. Plasma Sci. **43**, 957 (2015). <https://doi.org/10.1109/TPS.2014.23151>
- Y. Belchenko, Budker Institute of Nuclear Physics, Novosibirsk, Russia, private communication, 2016
- J. Bohdansky, J. Roth, J. Appl. Phys. **51**, 2861 (1980). <https://doi.org/10.1063/1.327954>
- D.S. Bollinger, P.R. Karns, C.Y. Tan, IEEE Trans. Plasma Sci. **43**, 4110 (2015). <https://doi.org/10.1109/TPS.2015.2491266>
- S. Briefi, S. Mattei, J. Lettry, et al., AIP Conf. Proc. **1869**, 030016 (2017a). <https://doi.org/10.1063/1.4995736>
- S. Briefi, S. Mattei, D. Rauner, et al., New J. Phys. **19**, 105006 (2017b). <https://doi.org/10.1088/1367-2630/aa8679>
- I.G. Brown, *The Physics and Technology of Ion Sources*, 2nd edn. (Wiley, 2004). <https://doi.org/10.1002/3527603956>
- A. Butterworth, A. Grudiev, J. Lettry, et al., AIP Conf. Proc. **1655**, 030007 (2015). <https://doi.org/10.1063/1.4916434>
- W. Chen, H. Li, L. Zhu, et al., Rev. Sci. Instrum. **90**, 113320 (2019). <https://doi.org/10.1063/1.5128553>
- Cherokee Porcelain Enamel Corporation, 2717 Independence Lane, Knoxville, TN, 2021
- Cherokee Porcelain Enamel Corporation, with explicit permission. 1 Sept 2022
- V. Dudnikov, A. Dudnikov, AIP Conf. Proc. **2052**, 020007 (2018). <https://doi.org/10.1063/1.5083725>
- V. Dudnikov, R.P. Johnson, G. Dudnikova, AIP Conf. Proc. **2052**, 050018 (2018). <https://doi.org/10.1063/1.5083772>
- V. Dudnikov, *Development and Applications of Negative Ion Sources* (Springer, 2019). <https://doi.org/10.1007/978-3-030-28437-4>
- K.W. Ehlers, K.N. Leung, Rev. Sci. Instrum. **50**, 1353 (1979). <https://doi.org/10.1063/1.1135725>
- D.C. Faircloth, M.O. Whitehead, T. Wood, Rev. Sci. Instrum. **77**, 03A520 (2006). <https://doi.org/10.1063/1.2166427>
- D.A. Fink, T. Kalvas, J. Lettry, et al., Nucl. Instrum. Meth. A **904**, 179 (2018). <https://doi.org/10.1016/j.nima.2018.07.046>
- R. Friedl, U. Fantz, AIP Conf. Proc. **1655**, 020004 (2015). <https://doi.org/10.1063/1.4916413>
- J. Galambos, SNS, ORNL, Oak Ridge, private communication, 2022

- R. Gobin, N. Chauvin, O. Delferriere, et al., Proceedings of LINAC 2012, JACOW, 1055 (2012). ISBN 978-3-95450-122-9
- W.G. Graham, *Proceedings of the 2nd Symposium on the Production and Neutralization of Negative Ions and Beams* (Brookhaven National Laboratory Report BNL 51304, 1980), p. 126
- D.V. Ghodke, R.K. Khare, R. Kumar, et al., AIP Conf. Proc. **2373**, 030002 (2021). <https://doi.org/10.1063/5.0058103>
- B.X. Han, T. Hardek, Y. Kang, et al., AIP Conf. Proc. **1390**, 216 (2011). <https://doi.org/10.1063/1.3637391>
- B.X. Han, R.F. Welton, S.N. Murray Jr., et al., Rev. Sci. Instr. **83**, 02B727-2 (2012a). <https://doi.org/10.1063/1.3681125>
- B.X. Han, R.F. Welton, S.N. Murray Jr., et al., Proc. of IPAC2012, 1512 (2012b). ISBN 978-3-95450-115-1
- B.X. Han, M.P. Stockli, R.F. Welton, et al., AIP Conf. Proc. **1515**, 473 (2013). <https://doi.org/10.1063/1.4792818>
- B.X. Han, R.F. Welton, S.N. Murray Jr., et al., Rev. Sci. Instr. **85**, 02B130 (2014). <https://doi.org/10.1063/1.4858055>
- B.X. Han, M.P. Stockli, R.F. Welton, et al., AIP Conf. Proc. **1655**, 030003 (2015). <https://doi.org/10.1063/1.4916430>
- B.X. Han, M.P. Stockli, Y. Kang, et al., Rev. Sci. Instrum. **87**, 02B143 (2016). <https://doi.org/10.1063/1.4937772>
- B.X. Han, R.F. Welton, S.N. Murray Jr., et al., AIP Conf. Proc. **1869**, 030014 (2017). <https://doi.org/10.1063/1.4995734>
- B. Han, R. Welton, S. Murray, et al., AIP Conf. Proc. **2011**, 050027 (2018a). <https://doi.org/10.1063/1.5053325>
- B.X. Han, V.V. Peplov, R.F. Welton, et al., Proc. of ICAP2018, 325 (2018b). <https://doi.org/10.18429/JACoW-ICAP2018-WEPAF02>
- B.X. Han, S.M. Cousineau, S.N. Murray Jr., et al., Proc. of NAPAC2019, 1847 (2019). <https://doi.org/10.18429/JACoW-NAPAC2019-MOPLH08>
- B. Han, SNS, ORNL, Oak Ridge, private communication, 2021
- B.X. Han, M.P. Stockli, R.F. Welton, et al., AIP Conf. Proc. **2373**, 040004 (2021). <https://doi.org/10.1063/5.0057408>
- B. Han, SNS, ORNL, Oak Ridge, private communication, 2022
- B. Han, M. Stockli, R. Welton, C. Pillar, et al., J. Phys. Conf. Ser. **2244**, 012044., IOP Publishing (2022). <https://doi.org/10.1088/1742-6596/2244/1/012044>
- L.K. Hansen, *Thermionic Converters and Low Temperature Plasma* (Inform. Center/US-DOE-tr-1, 1978)
- S. Henderson, W. Abraham, S. Aleksandrov, et al., Nucl. Instrum. Meth. **A763**, 610 (2014). <https://doi.org/10.1016/j.nima.2014.03.067>
- J.R. Hiskes, J. Appl. Phys. **51**, 4592 (1980). <https://doi.org/10.1063/1.328352>
- R.K. Janev, D. Reiter, U. Samm, Jülich Report #4105 (2003). <http://hdl.handle.net/2128/249>
- T. Kalvas, R.F. Welton, O. Tarvainen, Rev. Sci. Instr. **83**, 02A705 (2012). <https://doi.org/10.1063/1.3663244>
- M. Kaminsky, *Atomic and Ionic Impact Phenomena on Metal Surfaces* (Springer, New York, 1965) ISBN: 978-3-642-46027-2
- R. Keller, R. Thomae, M. Stockli, et al., AIP Conf. Proc. **639**, 47 (2002). <https://doi.org/10.1063/1.1517905>
- E.A. Kenik, J.O. Kiggans Jr, H.M. Meyer III, Materials Science and Technology Division, ORNL, Oak Ridge, private communication, 2008
- E. Kenik, ORNL, Oak Ridge, private communication, 2010
- E. Kuffel, W.S. Zaengl, J. Kuffel, *High Voltage Engineering*, 2nd edn. (Newnes, 2000) ISBN: 9780750636346
- S.R. Lawrie, R.E. Abel, C.A. Cahill, et al., Rev. Sci. Instrum. **90**, 103310 (2019). <https://doi.org/10.1063/1.5127263>

- S.R. Lawrie, O.A. Tarvainen, AIP Conf. Proc. **2373**, 050003 (2021). <https://doi.org/10.1063/5.0057743>
- T.J. Lee, R.E. Stickney, Surf. Sci. **32**, 100 (1972). [https://doi.org/10.1016/0039-6028\(72\)90122-7](https://doi.org/10.1016/0039-6028(72)90122-7)
- J. Lettry, D. Aguglia, J. Alessi, et al., AIP Conf. Proc. **1655**, 030005 (2015). <https://doi.org/10.1063/1.4916432>
- J. Lettry, D. Aguglia, S. Bertolo, et al., AIP Conf. Proc. **1869**, 030002 (2017). <https://doi.org/10.1063/1.4995722>
- J. Lettry, S. Bertolo, U. Fantz, et al., AIP Con. Proc. **2052**, 050008 (2018). <https://doi.org/10.1063/1.5083762>
- J. Lettry, CERN, private communication, 2022
- K.N. Leung, K.W. Ehlers, M. Bacal, Rev. Sci. Instrum. **54**, 56 (1983). <https://doi.org/10.1063/1.1137215>
- K.N. Leung, D.A. Bachman, D.S. McDonald, Rev. Sci. Instrum. **64**, 970 (1993). <https://doi.org/10.1063/1.1144152>
- K.N. Leung, Rev. Sci. Instrum. **71**, 1064 (2000). <https://doi.org/10.1063/1.1150387>
- H. Li, W. Chen, R. Zhu, et al., Nucl. Instrum. Meth. **A996**, 165149 (2021). <https://doi.org/10.1016/j.nima.2021.165149>
- S.J. Liu, T. Huang, H.F. Ouyang, et al., Chinese Physics C **39**, 057008 (2015). <https://doi.org/10.1088/1674-1137/39/5/057008>
- M.A. Lieberman, A.J. Lichtenberg, *Principles of Plasma Discharges and Materials Processing*, 2nd edn. (Wiley, 2005). <https://doi.org/10.1002/0471724254>
- A. Lombardi, CERN, private communication, 2022
- S. Mattei, H⁻ Ion Source for CERN's linac4 Accelerator: Simulation, Experimental Validation and Optimization of the Hydrogen Plasma, Thesis #7907, École Polytechnique Federal de Lausanne (2017)
- Ø. Midttun, T. Kalvas, M. Kronberger, et al., Rev. Sci. Instrum. **83**, 02B710 (2012). <https://doi.org/10.1063/1.3670344>
- Mitutoyo 293–340
- S. Mochalsky, J. Lettry, T. Minea, New J. Phys. **18**, 085011 (2016). <https://doi.org/10.1088/1367-2630/18/8/085011>
- D. Noll, G. Bellodi, S. Bertolo, et al., JACOW Proc. of 10th IPAC, 1090 (2019a). <https://doi.org/10.18429/JACoW-IPAC2019-MOPTS096>
- D. Noll, J.-B. Lallement, A. Lombardi, Beam Characterization of Linac 4's IS03, CERN Acc. Note 2019-0014 (2019b)
- H. Oguri, Y. Okumura, K. Hasegawa, et al., Rev. Sci. Instrum. **73**, 1021 (2002). <https://doi.org/10.1063/1.1428418>
- H. Oguri, A. Ueno, K. Ikegami, et al., Phys. Rev. Spec. Top. Acc. Beams **12**, 010401 (2009). <https://doi.org/10.1103/PhysRevSTAB.12.010401>
- H. Oguri, A. Ueno, K. Ikegami, et al., Rev. Sci. Instrum. **81**, 02A715 (2010). <https://doi.org/10.1063/1.3266138>
- H. Oguri, K. Ikegami, K. Ohkoshi, et al., AIP Conf. Proc. **1390**, 235 (2011). <https://doi.org/10.1063/1.4995773>
- H. Oguri, K. Ohkoshi, K. Ikegami, et al., Rev. Sci. Instrum. **87**, 02B138 (2016). <https://doi.org/10.1063/1.4935641>
- H. Oguri, K. Ohkoshi, K. Shinto, et al., Proc. 3rd J-PARC Symposium (J- PARC2019), JPS Conf. Proc. 33, 011008 (2021). <https://doi.org/10.7566/JPSCP.33.011008>
- H. Oguri, J-PARC, private communication, 2022
- K. Ohkoshi, Y. Namekawa, A. Ueno, et al., Rev. Sci. Instrum **81**, 02A716 (2010). <https://doi.org/10.1063/1.3277140>
- M.K. Pal, R. Gaur, V. Kumar, Pramana – J. Phys. **96**, 69 (2022). <https://doi.org/10.1007/s12043-022-02311-4>
- Parker pulse valve # 009–1643-900 with 1 mm aperture, 2022
- S.X. Peng, T. Zhang, H.T. Ren, et al., Rev. Sci. Instrum. **87**, 02B125 (2016). <https://doi.org/10.1063/1.4934816>

- S. Peng, Peking University, Beijing, private communication, 2022
- C. Peters, SNS, ORNL, private communication, 2021
- J. Peters, Entwicklung und Optimierung einer HF-“volume” Quelle zur Erzeugung von H^- - Ionen fuer HERA, Ph.D. thesis, Fachbereich Physik, Johann Wolfgang Goethe Universität in Frankfurt am Main (2000a)
- J. Peters, Rev. Sci. Instrum **71**, 1069 (2000b). <https://doi.org/10.1063/1.1150388>
- J. Peters, Proceeding of EPAC 2002, 1727 (2002). ISSN 1684-761X
- J. Peters, AIP Conf. Proc. **1097**, 236 (2009). <https://doi.org/10.1063/1.3112518>
- B. Rasser, J.N.M. Van Wunnik, J. Los, Surf. Sci. **118**, 697 (1982). [https://doi.org/10.1016/0039-6028\(82\)90216-3](https://doi.org/10.1016/0039-6028(82)90216-3)
- CS/NF/3.6/11 from SAES Getters S. p. A., Milano (2021)
- T. Sarmiento, M. Stockli, R. Welton, et al., Rev. Sci. Instrum. **91**, 023319 (2020). <https://doi.org/10.1063/1.5129340>
- R. Scrivens, M. Kronberger, D. Küchler, et al., Proc. IPAC2011, 3472 (2011). ISBN 978-92-9083-366-6
- R. Scrivens, Proceedings of the CERN Accelerator School on Ion Sources, 2013 Report CERN-2013-007, 9 (2013). <https://doi.org/10.5170/CERN-2013-007>
- T. Shibata, K. Ohkoshi, K. Shinto, et al., J. Phys. Conf. Ser. **2244**, 012041., IOP Publishing (2022). <https://doi.org/10.1088/1742-6596/2244/1/012041>
- M.P. Stockli, R.F. Welton, R. Keller, A.P. Letchford, R.W. Thomae, J.W.G. Thomason, AIP Conf. Proc. **639**, 135 (2002). <https://doi.org/10.1063/1.1517914>
- M.P. Stockli, R.F. Welton, R. Keller, Rev. Sci. Instr. **75**, 1646 (2004). <https://doi.org/10.1063/1.1695649>
- M.P. Stockli, M. Leitner, D. Moehs, et al., AIP Conf. Proc. **763**, 145 (2005). <https://doi.org/10.1063/1.1908290>
- M.P. Stockli, AIP Conf. Proc. **868**, 25 (2006). <https://doi.org/10.1063/1.2401393>
- M.P. Stockli, R.F. Welton, R. Keller, M. Leitner, Rev. Sci. Instr. **77**, 03B706 (2006). <https://doi.org/10.1063/1.2169812>
- M.P. Stockli, B.X. Han, S.N. Murray, et al., AIP Conf. Proc. **1097**, 223 (2009). <https://doi.org/10.1063/1.3112516>
- M.P. Stockli, B. Han, S.N. Murray, et al., Rev. Sci. Instr. **81**, 02A729 (2010). <https://doi.org/10.1063/1.3325085>
- M.P. Stockli, B.X. Han, S.N. Murray, et al., AIP Conf. Proc. **1390**, 123 (2011a). <https://doi.org/10.1063/1.3637382>
- M.P. Stockli, B.X. Han, T.W. Hardek, et al., Proc. of PAC2011, 1993 (2011b). <https://accelconf.web.cern.ch/PAC2011/papers/wep275.pdf>
- M.P. Stockli, J. Phys.: Conf. Ser. **399**, 012001 (2012). <https://doi.org/10.1088/1742-6596/399/1/012001>
- M.P. Stockli, B.X. Han, T.W. Hardek, et al., Rev. Sci. Instr. **83**, 02A732 (2012). <https://doi.org/10.1063/1.3681921>
- M. P. Stockli, Proceedings of the CERN Accelerator School on Ion Sources, 2013 Report CERN-2013-007, 265 (2013). <https://doi.org/10.5170/CERN-2013-007.265>
- M.P. Stockli, B.X. Han, S.N. Murray, et al., AIP Conf. Proc. **1515**, 292 (2013a). <https://doi.org/10.1063/1.4792797>
- M.P. Stockli, D. Faircloth, W. Kraus, et al., Workshop on Performance Variations in H- Ion Sources 2012: PV H^- 12, AIP Conf. Proc. **1515**, 594 (2013b). <https://doi.org/10.1063/1.4792832>
- M.P. Stockli, T. Nakagawa, Ion injectors for high-intensity accelerators. Rev. Acc. Sci. Tech. **6**, 197., © World Scientific Publishing Company (2013). <https://doi.org/10.1142/S1793626813300090>
- M.P. Stockli, K.D. Ewald, B.X. Han, et al., Rev. Sci. Instr. **85**, 02B137 (2014). <https://doi.org/10.1063/1.4862205>
- M.P. Stockli, B.X. Han, S.N. Murray, et al., AIP Conf. Proc. **1655**, 030001 (2015). <https://doi.org/10.1063/1.4916428>

- M.P. Stockli, B. Han, S.N. Murray, et al., Rev. Sci. Instr. **87**, 02B140 (2016). <https://doi.org/10.1063/1.4935640>
- M.P. Stockli, B.X. Han, S.N. Murray, et al., AIP Conf. Proc. **1869**, 030010 (2017). <https://doi.org/10.1063/1.4995730>
- M.P. Stockli, R.F. Welton, B.X. Han, Rev. Sci. Instrum. **719**, 502202 (2018). <https://doi.org/10.1063/1.5025328>
- M.P. Stockli, B. Han, M. Clemmer, et al., Rev. Sci. Instrum. **91**, 013321 (2020). <https://doi.org/10.1063/1.5129673>
- F. Taccogna, S. Bechu, A. Aanesland, et al., Phys. J. D **75**, 227 (2021). <https://doi.org/10.1140/epjd/s10053-021-00228-y>
- O. Tarvainen, S.X. Peng, New J. Phys. **18**, 105008 (2016). <https://doi.org/10.1088/1367-2630/18/10/105008>
- O. Tarvainen, S. Lawrie, D. Faircloth, et al., AIP Conf. Proc. **2052**, 050005 (2018). <https://doi.org/10.1063/1.5083759>
- O. Tarvainen, S.X. Peng, Corrigendum to [Tarvainen, O., et al., 2016] unpublished (2018)
- O. Tarvainen, ISIS, Rutherford Appelton Laboratory, Oxfordshire, private communication, 2022
- A. Ueno, K. Ikegami, Y. Kondo, Rev. Sci. Instrum. **75**, 1714 (2004). <https://doi.org/10.1063/1.1699459>
- A. Ueno, H. Oguri, K. Ikegami, et al., Rev. Sci. Instrum. **81**, 02A720 (2010). <https://doi.org/10.1063/1.3271243>
- A. Ueno, K. Ohkoshi, K. Ikegami, et al., AIP CP **1655**, 030008 (2015a). <https://doi.org/10.1063/1.4916435>
- A. Ueno, K. Ohkoshi, K. Ikegami, et al., AIP CP **1655**, 030009 (2015b). <https://doi.org/10.1063/1.4916436>
- A. Ueno, K. Ohkoshi, K. Ikegami, et al., Rev. Sci. Instrum. **87**, 02B129 (2016). <https://doi.org/10.1063/1.4932323>
- A. Ueno, New J. Phys. **19**, 015004 (2017). <https://doi.org/10.1088/1367-2630/aa52e3>
- A. Ueno, K. Ohkoshi, K. Ikegami, et al., AIP Conf. Proc. **1869**, 030052 (2017). <https://doi.org/10.1063/1.4995772>
- A. Ueno, K. Ohkoshi, K. Ikegami, et al., AIP Conf. Proc. **2373**, 040002 (2021). <https://doi.org/10.1063/5.0057552>
- J.N.M. Van Wunnik, B. Rasser, J. Los, Phys. Lett. **87A**, 288 (1982). [https://doi.org/10.1016/0375-9601\(82\)90698-3](https://doi.org/10.1016/0375-9601(82)90698-3)
- S.A. Veitzer, M. Kundrapu, P.H. Stoltz, et al., Rev. Sci. Instrum. **87**, 02B142 (2016). <https://doi.org/10.1063/1.4936090>
- R.F. Welton, *Proceedings of LINAC 2002* (Publisher Pohang Accelerator Laboratory, 2002), p. 559. <https://accelconf.web.cern.ch/I02/PAPERS/TH101.PDF>
- R.F. Welton, M.P. Stockli, Y. Kang, et al., Rev. Sci. Instrum. **73**, 1008 (2002). <https://doi.org/10.1063/1.1431416>
- R.F. Welton, M.P. Stockli, S.N. Murray, et al., AIP Conf. Proc. **763**, 296 (2005). <https://doi.org/10.1063/1.1908306>
- R.F. Welton, M.P. Stockli, S.N. Murray, et al., Rev. Sci. Instrum. **79**, 02C721 (2008). <https://doi.org/10.1063/1.2816937>
- R.F. Welton, M.P. Stockli, S.N. Murray, et al., AIP Conf. Proc. **1097**, 181 (2009). <https://doi.org/10.1063/1.3112511>
- R.F. Welton, V.G. Dudnikov, K.R. Gawne, et al., Rev. Sci. Instr. **83**, 1–4 (2012). <https://doi.org/10.1063/1.3678651>
- R. Welton, D. Bollinger, M. Dehnel, et al., J. Phys. Conf. Ser. **2244**, 012045., IOP Publishing (2022). <https://doi.org/10.1088/1742-6596/2244/1/012045>
- Wikipedia: list of battery sizes (2022). https://en.wikipedia.org/wiki/List_of_battery_sizes
- Wikipedia: Caesium (2021). <https://en.wikipedia.org/wiki/Caesium>
- Wikipedia: Caesium Nitrate (2021). https://en.wikipedia.org/wiki/Caesium_nitrate
- Wikipedia: Caesium Oxide (2021). https://en.wikipedia.org/wiki/Caesium_oxide
- Wikipedia: Paschen's law (2021). https://en.wikipedia.org/wiki/Paschen%27s_law

- B. Wolf, *Handbook of Ion Sources* (CRC Press, Boca Raton, FL, 1995) ISBN-13: 978-0849325021
- N. Yampolsky, Rybarcyk, E. Henestroza, et al., *Rev. Sci. Instrum.* **92**, 113305 (2021). <https://doi.org/10.1063/5.0056123>
- H. Zhang, *Ion Sources* (Springer/Science Press, Berlin/Beijing, 1999) ISBN-13: 9783540657477
- T. Zhang, S.X. Peng, W.B. Wu, et al., *Chin. Phys. B.* **27**(10), 105208 (2018). <https://doi.org/10.1088/1674-1056/27/10/105208>
- Z. Zhang, S. Cousineau, A. Aleksandrov, et al., *Nucl. Instrum. Meth.* **A949**, 162826 (2020). <https://doi.org/10.1016/j.nima.2019.162826>
- R. Zhu, W. Chen, H. Li, *Sci. Instrum.* **93**, 053302 (2022). <https://doi.org/10.1063/5.0086220>

Chapter 19

Development of High-Current Negative-Ion-Based Beam Source at the National Institutes for Quantum Science and Technology (QST) in Japan for JT-60 U and ITER Neutral Beam Injectors



Takashi Inoue

Abstract This chapter summarizes achievements of negative ion R&D at QST (National Institutes for Quantum Science and Technology established in 2016, which was originally founded as JAERI (Japan Atomic Energy Research Institute). The objective of the R&D at QST is to develop high-current negative ion sources and accelerators for neutral beam (NB) injectors for the JT-60 U fusion experimental device and ITER fusion experimental reactor. As an example, the target of the ITER NB injector is 40 A of D^- ions at 200 A/m^2 and a beam energy of 1 MeV for a pulse length up to 3600 s. In such a high energy $>500 \text{ keV/nucleon}$, neutral beams can be efficiently produced only by the neutralization of negative ions, of which neutralization efficiency is as high as $\approx 60\%$ in a simple gas target. At QST, the KAMOABOKO negative ion source was developed, which has a semicylindrical shape discharge chamber with an “external magnetic filter.” The KAMABOKO source produced H^- ion beams of 300 A/m^2 (total current: 2 A) at a low gas pressure of only 0.20–0.24 Pa. A MeV accelerator has been developed at QST for proof-of-principle tests aiming at 1 MeV, ampere-class negative ion acceleration. Prior to the 1 MeV acceleration, there was a technical issue on the high-voltage insulation of the accelerator column. A large stress ring inside of the insulator column was effective to achieve a voltage holding up to 1 MV by lowering the electrostatic field at the triple junction (interface between insulator, metal flange, and vacuum) to

QST = National Institutes for Quantum Science and Technology, which was established in 2016 and was founded from Japan Atomic Energy Agency (JAEA, itself founded in 2005 from the original JAERI organization (Japan Atomic Energy Research Institute)

T. Inoue (✉)

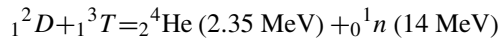
National Institutes for Quantum Science and Technology, Naka, Ibaraki, Japan
e-mail: inoue.takashi@qst.go.jp

the level of about 1 kV/mm. And moreover, applying compensation technique for correcting deflections of ion beamlet trajectories due to magnetic fields and space charge repulsion between beamlets, H^- ion beams of 185 A/m^2 (430 mA in total) have been accelerated up to 0.98 MeV, but for a short pulse length (0.4 s). The accelerator grid geometries, such as aperture radius and its thickness, have been optimized by a precise trajectory analysis of negative ions, neutrals, and electrons, to prevent bombardment of accelerator grids by the particles followed by acceleration of secondary electrons. This optimization was effective to extend the pulse length up to 60 s, at a beam energy of 0.97 MeV and a current density of 190 A/m^2 .

Keywords Negative ion · Neural beam · Plasma heating · Magnetic filter · KAMABOKO ion source · Beam deflection · Aperture offset · 1 MeV accelerator

19.1 Negative Ions in Fusion Applications

As introduced in Chap. 1, the fusion experimental reactor ITER is currently being constructed in the south of France thanks to the joint international cooperation of the seven ITER members—China, the European Union, India, Japan, Korea, Russia, and the United States (Bigot 2019)—and will serve as a crucial step toward the realization of fusion energy. ITER will use the following fusion reaction between deuterium and tritium to produce 14 MeV neutrons and 2.35 MeV alpha particles (helium nuclei):



The cross-section of the fusion reaction increases with the interaction energy. Consequently, to achieve a reaction rate that is high enough to produce an acceptable power from a fusion reactor, the fuel (deuterium and tritium) must be sufficiently dense, and it must also be heated to 100 million degrees Celsius, the temperature at which the cross section is at its maximum. At such high temperatures, a fully ionized gas-plasma is formed, and if a current is induced in such a plasma, ohmic heating occurs owing to the resistance of the plasma. However, that resistance decreases as the temperature increases, and ohmic heating is only effective up to a temperature around ten million degrees Celsius. Hence, auxiliary heating systems are needed to heat the plasma to higher temperatures. One such method for a fusion device, or reactor, that is based on magnetic confinement of the plasma, is neutral beam injection (NBI) (Wesson 1997). Having no charge, a neutral beam can traverse the magnetic fields surrounding and confining the plasma in a fusion device/reactor. Once they enter the plasma, the neutral beam particles are ionized via collisions with the plasma particles; they are then confined in the plasma by the magnetic fields, and, via collisions, they transfer their energy to the plasma ions and electrons.

NBI systems are used for plasma heating in many fusion devices and have been instrumental in improving plasma performance with high-temperature plasmas. When TFTR (the United States) (Jassby et al. 1999), JET (Europe) (Pam ela and Emilia 2003), and JT-60 (Japan) (Ishida et al. 1999), the world's three largest tokamaks, began operations in the 1980s, the neutralization of accelerated positive ions in a gas target was used to produce the neutral beams. However, much larger fusion experimental reactors are considered necessary to achieve the plasma confinement needed for a fusion reactor, and the neutral beams must penetrate deeply into the plasma to transfer their energy to the inner regions of the plasma. That is possible if the energy of the neutral beam is increased as the cross-sections for the ionization of the beam particles by collisions with the plasma particles decreases as the interaction energy increases. Then a significant fraction of the injected beam is not ionized, and then trapped within the plasma by the confining magnetic fields, until the beam reaches the hotter regions of the plasma, which are further from the walls of the device/reactor. Typically, beam energies in the region of 500 keV/nucleon (≈ 1 MeV for a D^0 beam) are required for a fusion reactor. Unfortunately, because the cross-section for neutralization of accelerated positive ions in a gas target decreases with increasing beam energy, neutral beams with energies ≥ 100 keV/nucleon cannot be efficiently produced by the neutralization of accelerated positive ions. Consequently, as discussed in Chap. 1, with the "discovery" of the formation of negative ions in the plasma volume in an ion source by Bacal et al. (1979), attention became focused on the neutralization of accelerated negative ions, which have a high neutralization efficiency in a simple gas target of $\approx 60\%$, even at beam energies > 500 keV/nucleon. Many institutions such as LBNL (the United States) (Leung et al. 1983), Culham (the United Kingdom) (Holmes et al. 1985), and JAERI¹ (Japan) (Okumura et al. 1987) began developing high-current negative ion sources for fusion applications, and negative-ion-based NBIs were built and used on the JT-60 U tokamak at JAERI, Naka, Japan (Kuriyama et al. 1995), and the Large Helical Device (LHD) device, Toki, Japan (Kaneko et al. 2003); the latter is still operational.

Table 19.1 summarizes the target parameters of the ITER NB system, the achievements of the negative-ion-based NB systems on JT-60 U and LHD and the parameters of the system being commissioned for JT-60SA. The ITER design was developed assuming a negative-ion-based NB heating system, in which an ion source and accelerator generate D^- ion beams of 40 A at a beam energy of 1 MeV, with a feeding gas pressure in the ion source, with no plasma, of 0.3 Pa and pulse lengths of 3600 s. The JT-60 N-NB system, the NB system having the closest performance to that required of the ITER NB system, was designed to generate D^- ion beams of 22 A at 500 keV for 10 s. The ITER NB system requires a substantial technological jump from existing levels, not only to be able to produce the higher

¹ QST = National Institutes for Quantum Science and Technology, which was established in 2016 and was founded from Japan Atomic Energy Agency (JAEA, itself founded in 2005 from the original JAERI organization (Japan Atomic Energy Research Institute))

Table 19.1 Target parameters of ITER and JT-60SA heating NB system and achievements of other negative-ion-based systems

Parameters/machines	LHD	JT-60 U	JT-60SA	ITER
Status	Achieved		Target	
Beam energy (MeV)	0.18	0.5	0.5	1
Beam current (A)	40	22	22	40
Pulse duration (s)	10	30	100	3600
Technical issues		Uniformity		Lower maintenance frequency RF-driven negative ion source

energy and higher current density beams of 40 A (200 A/m^2) at 1000 keV but also to be able to operate for pulse lengths of 3600 s, in a nuclear environment with no hands-on maintenance of the injectors for >10 years of operation. In the early stages of development, two main paths were defined for the R&D of negative ion applications for fusion—the development of high-current ion sources and MeV-class accelerators. The R&D paths of negative ion sources and accelerators used on JT-60 U and the development of a 1 MeV accelerator in support of the ITER heating NBIs at JAERI, Naka Japan, and their required currents and beam energies are summarized in Fig. 19.1.

Negative ion sources for fusion applications use multi-aperture extractors and accelerators: high-current negative ion beams are extracted from the source through extraction/acceleration grids having multi-apertures, to obtain multiple pencil beams (common practice in the fusion community is to call these “beamlets”), which, altogether, give a high accelerated ion current. Using a multi-apertured system, JAERI succeeded in producing 100 mA negative ion beams in 1985 (Shibata et al. 1985) and 1 A negative ion beams in 1986 (Okumura et al. 1987) using volume-production type negative ion sources. Probably inspired by the work at Novosibirsk (Belchenko et al. 1974), Leung et al. found that negative ion beam current increased by seeding a small amount of cesium vapor into a multipole filamented arc discharge ion source (Walther et al. 1988; Leung et al. 1989), and in 1990 Okumura et al. succeeded in producing high-current H^- ion beams of 10 A having a negative ion current density of 380 A/m^2 , which was several times higher than that of conventional ion sources (Okumura et al. 1990).

19.2 Magnetic Filter for Low-Temperature Plasma

As described in Chap. 1, the reaction rate of volume production of negative ions via dissociative attachment by electrons of ro-vibrationally excited H_2 or D_2 peaks at about 1 eV. The cross-section of the electron detachment of H^- or D^- has a threshold energy of 0.75 eV and increases with increasing electron energy. Consequently, the ratio of the reaction rate of volume production to that of the loss reaction peaks at around 1 eV and decreases rapidly at higher electron temperatures,

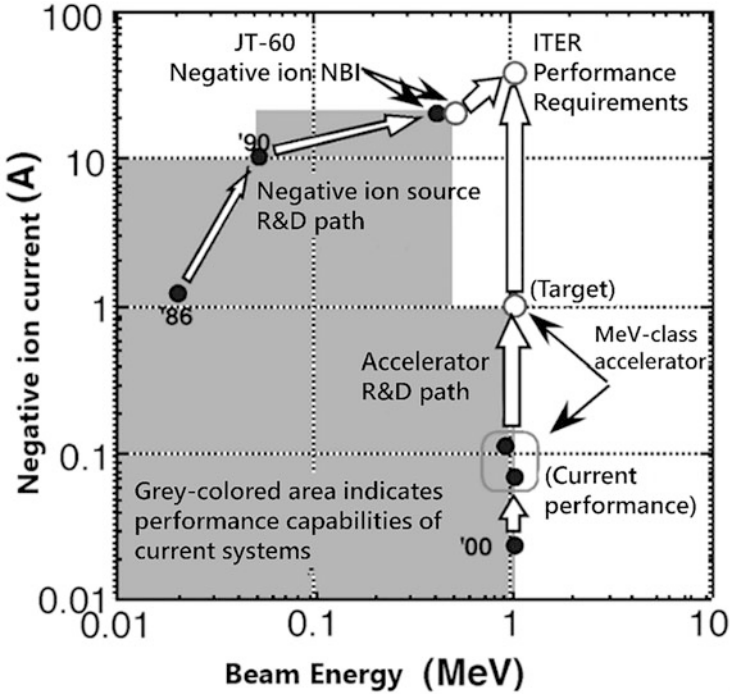


Fig. 19.1 Required currents and beam energies of R&D paths for ion sources and accelerators used in JT-60 U and ITER neutral beam injectors

mainly due to the electron energy dependence of the electron detachment reaction. On the other hand, the reaction rate for the production of ro-vibrationally excited H_2 or D_2 by collisions with electrons (reactions 1–4 in Chap. 1) peaks at some 10s of eV. Thus, it is evident that it is necessary to have two discharge regions having different electron temperatures (Hiskes and Karo 1984) to produce negative ions with high efficiency and minimal losses. Moreover, for fusion applications, high extracted currents of negative ions are required, which is achieved by extracting many parallel pencil beams (beamlets) of ions simultaneously. Hence, such discharge regions must be formed over a wide extraction area in the source. To create the two regions, a magnetic field transverse to the source and extracted beam axes is created inside the source, which is referred to as the “magnetic filter” (Leung et al. 1983). That field divides the discharge chamber into two parts: a main discharge chamber, usually called the “driver” region, and an extraction region. High energy electrons, often from directly heated filaments, in the driver region, ionize H_2 or D_2 flowing into the source. The filter field strength is chosen to be high enough to magnetize the electrons in the plasma, but not the ions. Then, the faster electrons that enter the field are reflected back into the driver region, while slow, collisional, electrons diffuse across the field along with the unmagnetized ions, i.e., the field acts as a

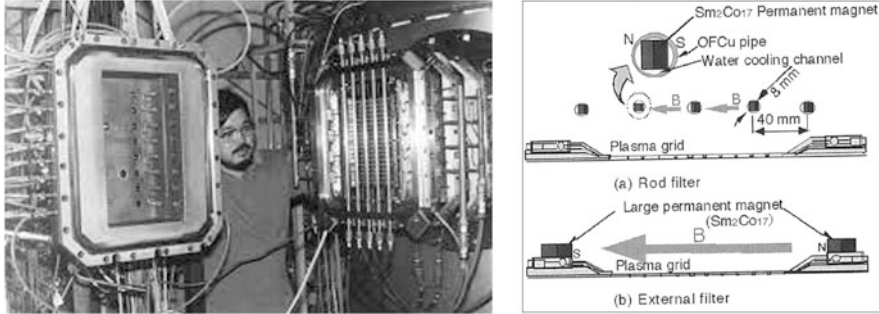


Fig. 19.2 “Ampere-class negative ion source” developed at JAERI. General view with rod filter (left) and a cross-sectional illustration of (a) rod filter and (b) external filter (right). (Reproduced from Inoue et al. (1989), with permission of Elsevier)

filter, allowing slow electrons, ions, and neutral particles, including ro-vibrationally excited molecules, but not fast electrons, to pass through it into the extraction region.

In the infancy of developing negative ion sources for fusion applications, JAERI developed a large volume production negative ion source with the end goal of extracting 1 A negative ions. Figure 19.2 shows a general view and a cross-sectional illustration of the JAERI ampere-class negative ion source (Okumura et al. 1986). This negative ion source has a 360 mm (H) \times 210 mm (W) \times 150 mm (D) discharge chamber having a 209-aperture negative ion extraction grid (each aperture 9 mm in diameter) drilled in a 260 mm \times 120 mm extraction surface. Beamlets are simultaneously extracted from each of the 209 apertures to obtain a 1 A negative ion beam, hence the name “ampere-class negative ion source.” This negative ion source succeeded in producing the world’s first ampere-class (1.26 A) H^- ion beam in 1986. However, the current density was 120 A/m² and the operating pressure was relatively high at 1.0 Pa under “pure volume” operation (without Cs).

In that source, the magnetic filter was formed by inserting permanent magnets into an array of metal tubes across the negative ion source. The magnets were arranged with all their magnetic axes in the same direction, perpendicular to the source and extracted beam axes, and the axes of the metal tubes. The result was a reasonably narrow “sheet” magnetic field crossing the source chamber. These types of magnetic filters are called “rod filters.” The discharge chamber is separated by the magnetic filter from the extraction region, but it is electrically at the same potential. The entire inner wall of the arc discharge chamber and the rod filter surface serve as the anode for arc discharges. Permanent magnets fixed on the outside of the wall of the arc chamber were arranged in vertical lines perpendicular to the source axis and beam axis (in horizontal), with the polarity of the line of magnets perpendicular to the wall. That produced a multipole magnetic field inside the arc chamber with line cusps under each line of external magnets. The multipole field limited the flow of electrons to the source wall and thus the effective anode area. The cathode is composed of tungsten filaments (1.2 mm in diameter) inserted into the main

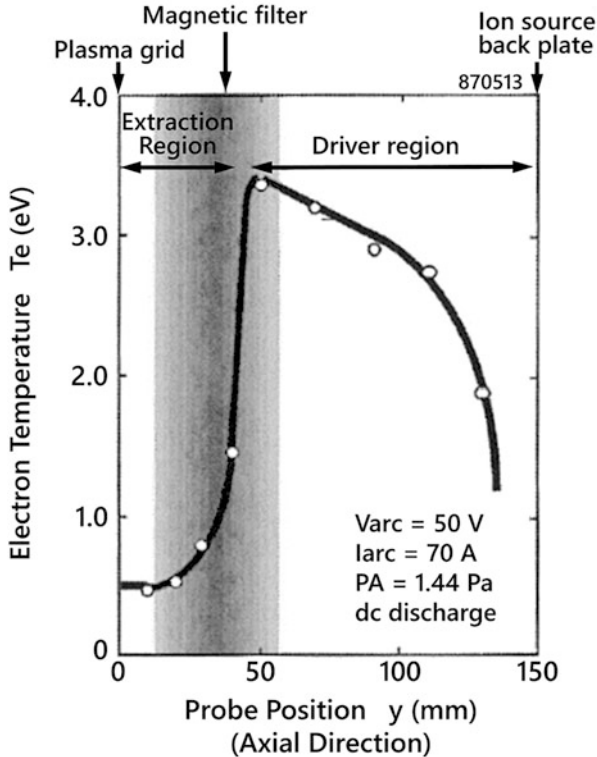


Fig. 19.3 Axial electron temperature of the ion source spanning the discharge and extraction regions, measured using water-cooled Langmuir probes. The dark shaded area is a schematic representation of the region over which the magnetic filter is effective

discharge chamber. The thermionically emitted electrons are then accelerated by the cathode sheath, and the resulting fast electrons ionize the gas in the main discharge chamber (driver region) to ignite an arc discharge.

An example of axial electron temperature profile in an ion source spanning the discharge and extraction regions is shown in Fig. 19.3 (Inoue et al. 1987). The X-axis is the axial distance from the plasma electrode where the negative ions are extracted, and the Y-axis is the electron temperature at the source axis measured with Langmuir probes. The rod filter was placed 40 mm in front of the plasma grid, which forms the end wall of the ion source with the apertures through which the ions are extracted. The maximum magnetic filter strength was approximately 50 Gauss between the rods, and the integrated magnetic field from the filament to the plasma grid ($\int 5 dl$) was 300 Gauss cm. As can be seen from Fig. 19.3, the electron temperature reduces with distance through the filter field. In the driver region, the electron temperature is mainly between 2 and 3 eV, and those electrons create the plasma in that region. In the extraction region, the electron temperature is ≤ 1 eV.

Thus, ro-vibrationally excited molecules can be created in the driver region and flow into the extraction region across the magnetic filter. Dissociative attachment creation of negative ions from those molecules occurs throughout the source, but within part of the filter field and the extraction region, the electron temperature is low enough that dissociation of the negative ions by the electrons is very low.

It should be noted that the magnetic filter is effective not only for reduction of the electron temperature but also for the decrease of the electron density in the plasma of the extraction region, which leads to reduction of electron current co-extracted with the negative ions from the ion source. Though producing D^- beams is the ultimate aim of ion sources for NBI, it was observed that the co-extracted electron current was very much higher (sometime by about a factor of 10) when a source was operated in D_2 rather than H_2 and that a significantly stronger filter field is needed to reduce the co-extracted electron current to acceptable levels when using D_2 . Lower co-extracted electron current is very important to achieve effective extraction and acceleration at higher efficiency, and also to reduce the heat load on the grids due to the accelerated electrons (to be discussed below).

As the development progressed, issues arose because of the structure of the rod filter itself. The metal tubes of the rod filter are exposed to the plasma, but the rod filter does not provide any confinement field for the ionizing electrons. Therefore, fast electrons in the driver region can reach the metal tubes, where they will be lost, and higher input power is required to obtain high plasma density ion sources having rod filters. The metal tube structure also reduces the geometrical transparency from the driver region to the extraction region, which hinders the diffusion of plasma particles and fast electrons, resulting in insufficient plasma density in the extraction region and a decrease in negative ion current.

To resolve these issues, as shown in Fig. 19.4, a pair of large permanent magnets were placed outside the negative ion extraction region of the plasma grid, and a magnetic filter without structural objects was created inside the discharge chamber. This type of magnetic filter is referred to as an “external magnetic filter” (Inoue et al. 1989). The permanent magnets that generate the external magnetic filter field are housed in a water-cooled metal case at anode potential. No anode potential structure associated with the external filter magnets is exposed to plasma in either the driver or the extraction region plasmas, so no additional loss area is created by the external filter. Additionally, because the field from the filter magnets is strong, \approx several hundreds of Gauss inside the source wall at the magnet axial location, electrons spiraling on the magnetic field lines of the filter field are repelled by the magnetic mirror effect, resulting in no significant increase in the loss area due to the external filter structure for those electrons. Accordingly, the external magnetic filter reduces primary electron loss in the driver region, and diffusion from the driver region to the extraction region is not obstructed, making it possible to achieve low-temperature plasma having sufficient density in the extraction region.

Negative ion beam production experiments were carried out using the ampere-class negative ion source, the results of which are shown in Fig. 19.5. Using rod filters, the highest negative ion current density was about 120 A/m^2 at the center of the beam even with an arc power of 70 kW, whereas when an external magnetic

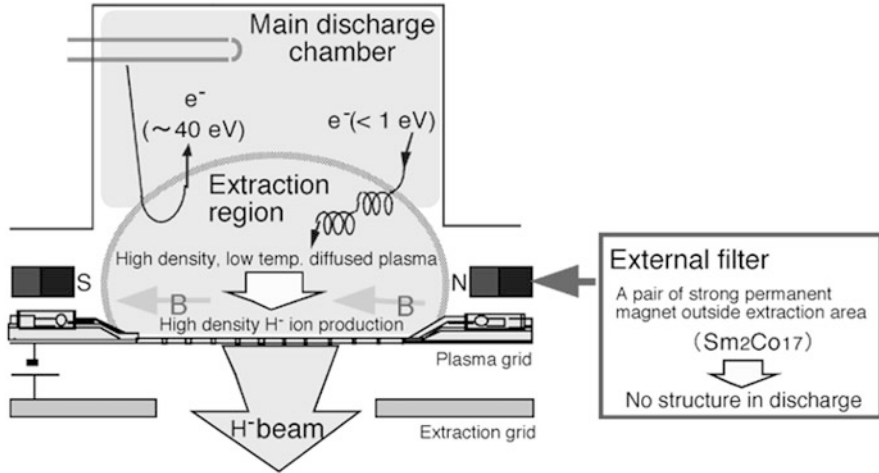


Fig. 19.4 Illustration of the external filter equipped between the discharge chamber of conventional ion source (rectangular cross-section) and the plasma grid

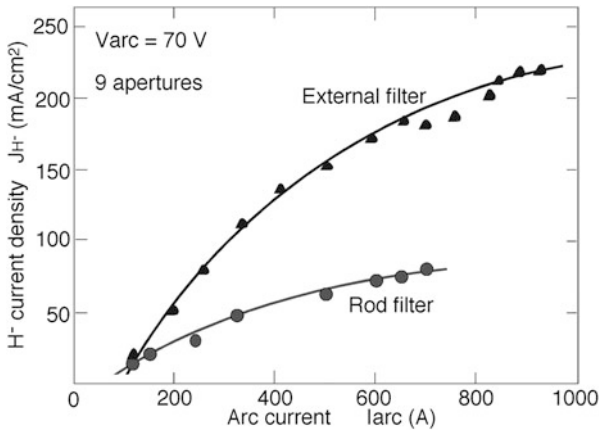


Fig. 19.5 Comparison of H⁻ ion current with rod filter (bottom) and external filter (top). The H⁻ ions were extracted and then accelerated to a beam energy of ~30 keV. Then the ion current was measured from temperature rise of the calorimeter placed downstream of the accelerator. (Reproduced from Inoue et al. (1989), with permission of Elsevier)

filter was equipped, a negative ion current density of 220 A/m² was obtained at the same power level—the first time the current density required by ITER (200 A/m²) was achieved. The total negative ion current was 1.6 A, a world record at the time.

External magnetic filters were also installed in multi-ampere negative ion source, KAMABOKO negative ion source, and other negative ion sources (described below), contributing to the world’s first 10-A-class, high-current negative ion beam production (Okumura et al. 1990). Based on the above results at JAERI, external

magnetic filters were also used in the negative ion source of the NBI for the Large Helical Device (LHD) at the National Institute for Fusion Science (NIFS) (Grisham 2005).

A consequence of the results discussed above is that many negative ion sources for fusion applications have replaced rod filters with external filters. However, the JT-60 U negative ion source was considered to be too wide to use an external filter as the magnetic field from the external magnets would be too broad axially near the vertical axis of the source, and the peak value of the field would be correspondingly low. Therefore, that source was equipped with a “PG filter,” which is a transverse magnetic field in front of the plasma grid created by a high current flowing vertically through the plasma grid (the JT-60 U ion source is 1150 mm high and 510 mm wide). A typical value of the “PG current” is from 5 kA (in Hydrogen operation) to 8 kA (in Deuterium), which gives a peak filter field of 200 Gauss (in H) and an $\int Bdl$ of 800–1100 Gauss cm from the filaments to the plasma grid. The PG filter also creates a magnetic field that extends significantly into the extractor and accelerator, but calculations suggested that the effect of that field would be a deflection of the whole beam upward or downward that could be corrected by realigning the beam source.

It has been observed that sources having transverse dipole magnetic filters that extracted multi-beamlets indicate a strong distribution in their intensity in the vertical direction. This issue has been identified as due to a strong variation in the vertical direction of the flux of negative ions to the apertures in the plasma grid, i.e., the ion flux is not uniform. Experimental and theoretical analyses revealed that this nonuniformity is caused by a $B \times \text{grad } B$ drift of plasma particles in the filter field. An external filter created by permanent magnets on each side of the plasma grid expands inside the source, becoming wider and weaker (in the source axial direction) with the distance from the magnets. Similarly, the magnetic field formed by the PG filter diminishes with the axial distance from the PG into the ion source. Electrons in either of those filter fields will experience a $B \times \text{grad } B$ drift, creating a variation in the density of the plasma in the vertical direction. In particular, the faster drift of the faster electrons results in a steep, vertical, gradient in electron temperature. The vertical variations in electron temperature and plasma density strongly affect the plasma density and the electron temperature in the extraction region and thus the negative ion spatial distribution in front of the plasma grid. The optics of each beamlet depends strongly on the flux of the negative ion flux to the aperture in the plasma grid. Very good beamlet optics are required in neutral beam injectors. The distance from the plasma grid to the plasma in a fusion device is typically ≥ 10 m. Consequently, poor optics of the beamlets leads to a significant loss of particles that would be intercepted locally, such as the exit from the injector and the walls of the duct leading to the fusion device. That is not acceptable (a) because of the loss of beam power into the plasma of the fusion device and (b) because the power carried by the beams can damage the components that intercept them. Therefore, the flux of the negative ions to all of the apertures in the array on the plasma grid has to be, within some limit, the same. As an example, for the ITER

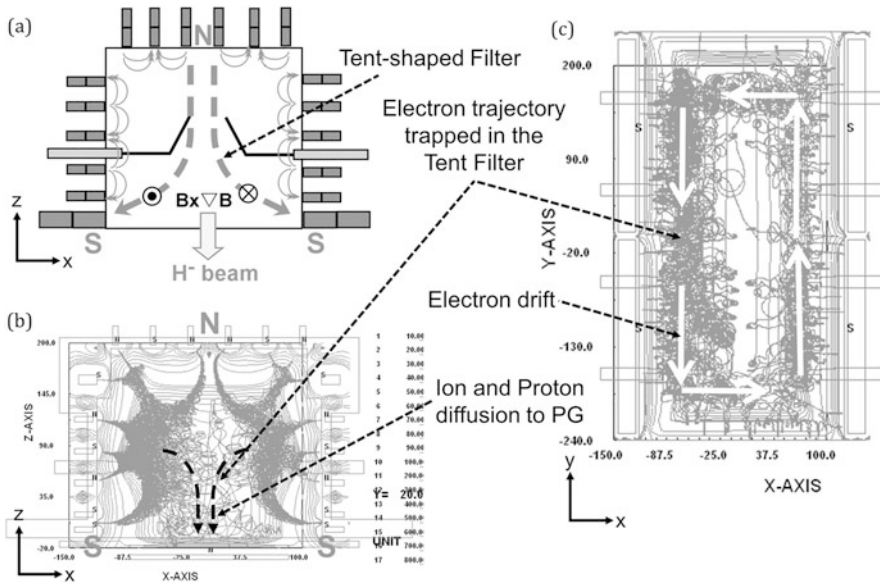


Fig. 19.6 (a): An illustration of tent filter, x-z cross-section, (b): electron trajectory in the tent filter, x-z cross-section, and (c): electron trajectory in the tent filter, x-y cross-section (projection from top of (b)) with electron drift direction in B x grad B drift.

heating NBI, it is specified that the flux to all the apertures must be the same within $\pm 10\%$.

A proposed solution was to use a tent-shaped magnetic filter (Holmes et al. 1985): The tent filter (then called a super-cusp) was originally used to reduce the electron temperature in front of the plasma grid and thus enhance the proton ratio of the extracted positive ion beams by reducing the direct ionization of H₂ to produce H₂⁺ in a positive ion source. The proposal here is to utilize the tent filter in the negative ion source as that should reduce the electron temperature in front of the PG and the extracted electron current, as required for a negative ion source. Figure 19.6 shows an illustration of the tent filter with B x grad B drift of electrons in the source. Although plasma drift occurs in the tent filter field, it would be in opposite directions on each side of the source, leading to plasma rotation, which should even out the nonuniformity. That has proven to be the case (Yoshida et al. 2015).

19.3 KAMABOKO Source for Surface Production of Negative Ions

Negative ion sources for fusion applications are directly connected to the extractor and accelerator without going through a low energy beam transport section (a

LEBT), which are commonly used with the ion sources of particle accelerators. In such cases, the hydrogen gas fed into the source is pumped through the acceleration line, which increases the pressure in the line through which the negative ion beams pass. An issue here is the relatively large cross-section of stripping loss of negative ions in particular in the low energies of <100 keV. And hence, the gas pressure in the ion source and thus in the extractor must be low in order to reduce the loss of negative ions by stripping in the course of their extraction and acceleration. However, it has been well known that pure volume negative ion production decreases rapidly when the gas operating pressure is lowered, and the negative ion current density obtained at low gas pressures of about 0.3 Pa was less than 10 A/m². Using pure volume production, the first step of the negative ion production process is the production of vibrationally excited molecules, which requires molecular hydrogen. Thus, with volume production of the negative ions, to obtain a high-current density, a high gas operating pressure is unavoidable.

As briefly discussed in Chap. 1, Dimov and Belchenko (Belchenko et al. 1974), followed by Walther et al. (1988) and Leung et al. (1989), reported that the addition of cesium to a negative ion source increased negative ion current. In the same way, i.e., adding a few grams of cesium vapor in the source, JAERI succeeded in producing a 10 A negative ion beam from a 14 cm × 36 cm extraction region of a “multi-ampere negative ion source” (Okumura et al. 1990). A current density of 380 A/m² was obtained at a low operating gas pressure of 0.5 Pa. Various experiments and analyses have been carried out to characterize and deduce this “cesium effect” that yields significantly high negative ion current density of more than 200 A/m², which is significantly more than double of that obtained without Cs, even at the very low pressure of ~0.1 Pa where almost no negative ions are obtained in pure volume operation. There is also a dependence on the temperature of plasma grid (PG), which is not present in pure volume operation. That, combined with the dependence on the surface work function of the plasma grid (van Amersfoort et al. 1985; van Os et al. 1987), has led to the conclusion that the production of negative ions on the plasma grid surface of low work function is responsible for the greatly enhanced performance achieved under cesium deposited conditions.

The physical mechanism of the surface production of negative ions has been studied in relation to the wall material effect as discussed in Chap. 1. At JAERI, a practical approach to optimize the surface production of negative ions is discussed and summarized as follows:

1. *Effectively dissociate molecular hydrogen to produce a high density of hydrogen atoms:*

This is important as it is well established that hydrogen negative ions are produced by atoms impinging on a low work function surface (van Amersfoort et al. 1985, van Os et al. 1987). Hence, the JAERI team opted to design the negative ion sources with a high atomic hydrogen ion density (Okumura et al. 1984). For this, rate equation analyses were carried out in Hemsworth and Inoue (2005). The results suggested that both the confinement time of hydrogen atoms and the density of fast electrons must be increased so that the energy can be effectively

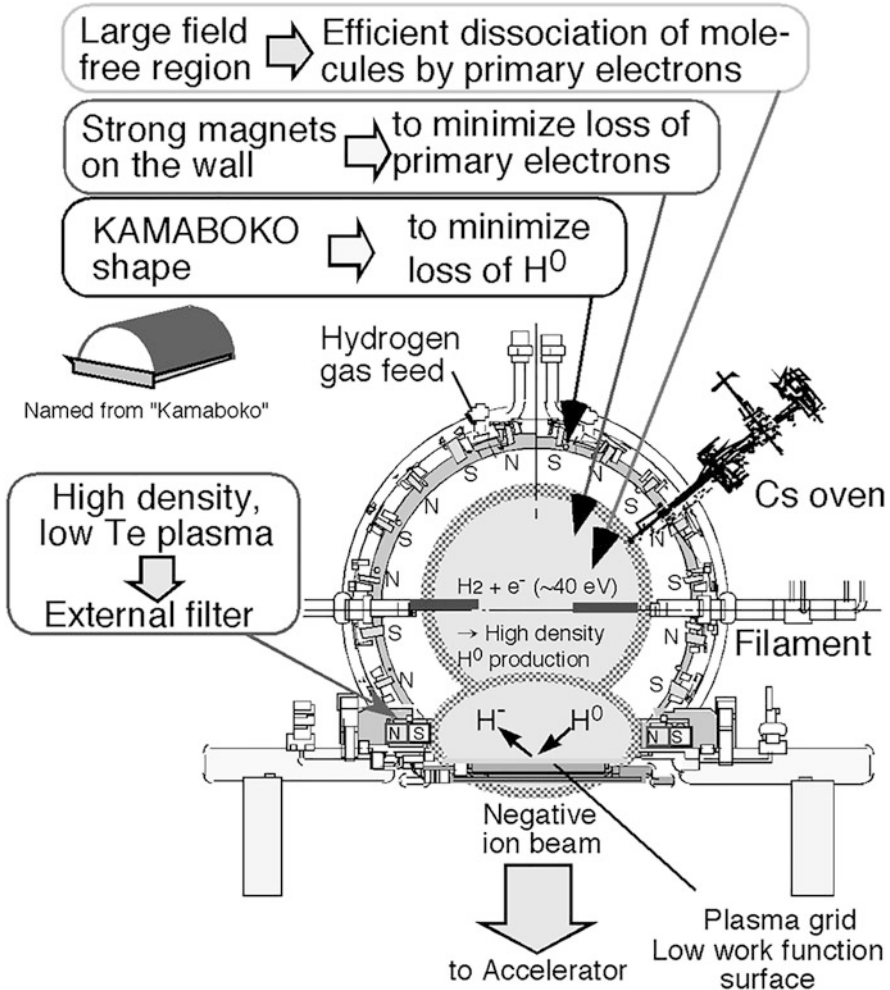


Fig. 19.7 Cross-sectional view of the KAMABOKO source

used for dissociation of hydrogen molecules, to obtain a high density of negative ions by using the surface production process. Based on the conclusions reached above, the KAMABOKO negative ion source was developed (Inoue et al. 1995), which produced hydrogen atoms efficiently to promote surface production of negative ions. Figure 19.7 shows a cross-sectional view of this source, named "KAMABOKO." To limit the loss of hydrogen atoms and promote dissociation of hydrogen gas molecules by primary electrons, the following three design choices were made for this ion source.

1.1. Negative ion source geometric configuration:

Because hydrogen atoms are neutral particles, the multipole magnetic field on the ion source wall has no effect on the atoms. Therefore, to minimize the loss of hydrogen atoms, the only choice was to change the geometry of the discharge chamber itself. Enlarging the ion source discharge chamber would increase the time until the generated hydrogen atoms are lost on the walls, but that will also increase the surface area of the walls. Therefore, it was decided to increase the ion source size and to maximize the volume to surface area ratio. A sphere is the shape having the largest volume/surface area ratio, but it is not practical for an ion source where one wall has to form the plasma grid, which needs to be flat to produce a beam that is not strongly convergent. It was decided to make the discharge chamber in the shape of a cylinder with the top and bottom ends closed and a part of the cylindrical cut to connect to the plasma grid. Its shape is that of “KAMABOKO,” which are distinctive semicylindrical-shaped loaves of fish cake served in Japan, as shown in Fig. 19.6. Because of its unique shape, the loss of hydrogen atoms is minimized, the magnets for magnetic filters can be placed on both sides of an elongated extraction region, and the length of the cylinder can be extended as necessary to obtain a high current. KAMABOKO ion sources were originally developed for conventional multipole multicusp positive ion sources (Watanabe et al. 1989) to obtain a positive ion beam having a high proton ratio. Based on the test results, the size of the KAMABOKO negative ion source was determined to be 34 cm in diameter and 34 cm in length (discharge chamber volume: 30,217 cm³) to maximize the volume/surface area ratio.

1.2. Reduction of primary electron loss area:

When strong permanent magnets are placed around the negative ion source discharge chamber to create a multipole cusp field configuration, the effective loss area of primary electrons at the wall surface is a region at the cusp position having a similar width to the Larmor radius of the electrons in the magnetic field at that location in front of the magnets (Horiike et al. 1987). Primary electrons approaching the wall of the discharge chamber are captured by the cusp magnetic field; they are repelled by the space charge of other electrons in the strong magnetic field in front of the magnets and are reflected back to the weak magnetic field region (mirror effect). They then move between the two opposing magnetic poles of the filter magnets spiraling along the magnetic field lines, eventually returning to the non-/low-magnetic field region in the center of the discharge chamber via collisions with other particles. The long path of these increases the probability of those electrons dissociating molecular hydrogen ions or neutrals. Reducing the number of poles covering the discharge chamber would also reduce the loss area; however, the non-/low-magnetic field region formed in the center of the discharge chamber would become narrower. If the anode area is not large enough, then arc discharges will not be stable (Horiike 2022). Thus, the spacing of the magnets was set at a

conservative 53 mm based on proven results obtained with KAMABOKO positive ion sources.

It is noted here that increasing the atomic fraction in the ion source would also increase the proton fraction of the positive ions, and that employing the abovementioned design choices, a large KAMABOKO source developed for positive ion production achieved 95% of proton content in the beam of 1750 A/m^2 at the source filling pressure of 0.4 Pa (Watanabe et al. 1989).

1.3. Use of external magnetic filters:

The addition of external magnetic filters to this KAMABOKO negative ion source can yield the following advantages:

- Primary electrons in the driver region are less likely to be lost on the surface of the filter structure.
- Primary electrons in the driver region are shielded from the extraction region by the magnetic filter, which prevents the primary electrons from being directly injected into the plasma grid or other structures in the extraction region that cause a loss of electrons.
- As there is no structure in the plasma, as there was with the rod filter, it prevents ions, electrons, and hydrogen atoms produced in the driver region from being lost by recombination on the surface of the filter structure.

2. Increase the difference between work function and electron affinity, $\phi - E_a$:

Because the electron affinity of hydrogen atoms is $E_a = 0.75 \text{ eV}$, the work function must be lowered as much as possible to promote the surface production of negative ions. A common method to decrease the work function is to adsorb an alkali metal on the surface (Inoue et al. 1992).

3. Increase the speed of negative ions leaving the surface upon desorption:

It was thought that increasing the velocity of an H^- leaving the surface by applying an accelerating field, i.e., biasing the plasma electrode negative with respect to the plasma, might increase the H^- flux reaching the plasma from the surface. However, it was found that biasing the PG a few volts positive with respect to the anode decreased the co-extracted electron current, without affecting the extracted H^- current, and that is necessary in order to reduce the extracted electron current to an acceptable level. Therefore, increasing the outgoing H^- velocity was not attempted.

Figure 19.8 shows a view of the KAMABOKO negative ion source being mounted on the extractor and accelerator. The plasma grid is visible just below the ion source. The extraction and acceleration grids are contained within the stainless-steel flanges and alumina insulators structure below the plasma grid. Figure 19.9 shows the negative ion beam current obtained from the KAMABOKO negative ion source as a function of the arc power applied to the negative ion source. These results were measured with a few grams of cesium seeded to the negative ion source to facilitate negative ion surface production. It can be seen that the negative ion current increased in proportion to the arc power. This characteristic is different

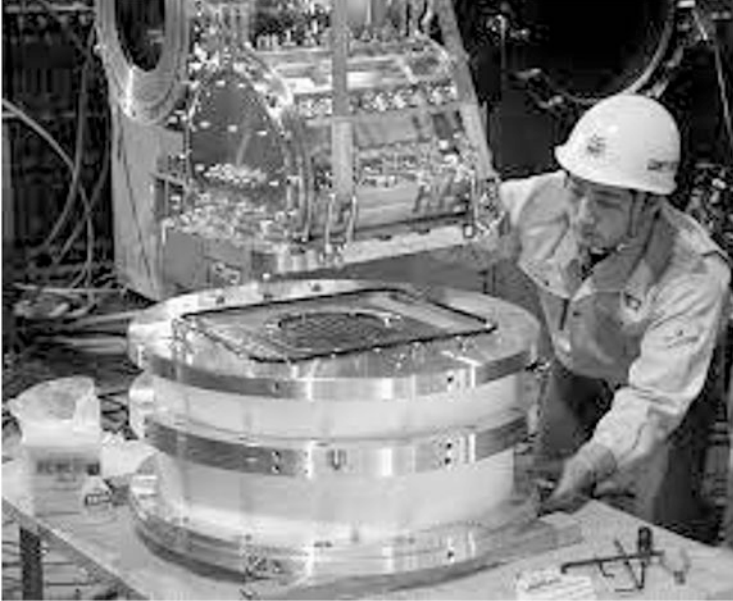


Fig. 19.8 The KAMABOKO negative ion source being attached to the extractor and accelerator. The plasma grid is visible just below the ion source. The extraction and acceleration grids are contained within the stainless-steel flanges and alumina insulators structure below the plasma grid

from using only volume production, where the negative ion current saturates as the arc power increases and decreases as the input power becomes excessive. Experimental evidence suggests that the majority of the negative ions are created by H atoms impinging on the cesiated plasma grid (Hemsworth et al. 2005) and that the proportionality of the extracted H^- current with arc power is due to a linear increase in the H atom density with arc power.

An accelerated H^- ion beam having a current density of 300 A/m^2 and a total current of 2 A was successfully produced from 45 apertures (14 mm dia. each) at an arc power of 40 kW using a negative ion source operating gas pressure of 0.20 Pa to 0.24 Pa (Miyamoto et al. 1995). After taking into account losses in the extractor and accelerator ($\approx 10\%$), the extracted current density from the KAMABOKO source was $\approx 333 \text{ A/m}^2$ of H^- , and the D^- equivalent was $\approx 233 \text{ A/m}^2$. The ITER specification requires an accelerated current density of 200 A/m^2 of D^- , after reduction by stripping loss of ions in the course of acceleration. As a stripping loss of $\approx 30\%$ in the ITER extractor and accelerator, the extracted current density needs to be $\approx 285 \text{ A/m}^2$. It can be concluded that the compact but effective KAMABOKO negative ion source has demonstrated that it is capable of providing negative ion current densities close to those required for ITER, and higher values should be readily reached with higher power into the source. The magnetic filter strength was also enhanced from the conventional 610 Gauss cm to 910 Gauss cm to lower

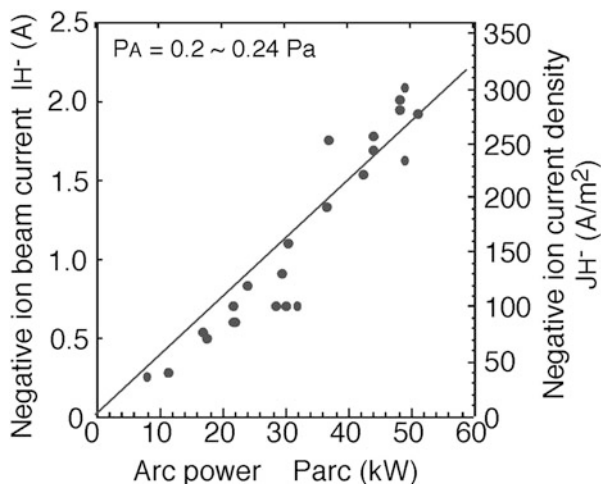


Fig. 19.9 Negative ion beam current obtained from the KAMABOKO negative ion source as a function of the arc power applied to the negative ion source. The negative ion current was measured by a calorimeter placed downstream of the accelerator. The gas flow was not changed during the source operation, and PA is the pressure in the ion source prior to arc initiation. (Reproduced from Miyamoto et al. (1995), with permission of AIP publishing)

the electron temperature of the extraction plasma at low gas pressures. A current density of 300 A/m^2 was achieved at a low gas pressure of only 0.1 Pa (arc power of 80 kW), whereas the negative ion current would be almost zero in pure volume production at these pressures (Morishita et al. 2001). Owing to its excellent performance, the KAMABOKO negative ion source design concept was also used in the large negative ion source of JT-60 U (Kojima et al. 2015). Figure 19.10 shows the assembly of this large KAMABOKO negative ion source and a 500 keV electrostatic accelerator.

Having shown excellent performance of high negative ion current density at very low gas pressure, arc-driven sources such as KAMABOKO source were initially considered for the ITER NBIs. However, the filaments in the source have a limited lifetime; it is calculated to be $<200 \text{ h}$, and there was concern that the tungsten evaporation from the filaments would contaminate the cesium on the plasma grid, leading to a need to inject more cesium into the source than would be the case if there were no tungsten evaporation. Both of those would lead to regular maintenance of the ITER ion sources, which is highly undesirable as it would lead to more down time of ITER, and because such maintenance is difficult as activation of the ion source means that such maintenance needs to be done by remote means. Such maintenance would not be acceptable on ITER if the maintenance frequency of the ion sources were to be higher than that foreseen for ITER itself. Because of these considerations, the ITER project has chosen to use an RF-driven negative ion source taking into account a possible lower maintenance frequency since no filaments are needed during the source operation.



Fig. 19.10 Assembly of the large negative ion source, extractor, and 500 keV electrostatic accelerator for JT-60 U negative-ion-based NBI

19.4 Negative Ion Extraction and Electron Suppression

A problem that arises with negative ion extraction is that, having the same charge as the negative ions, electrons are co-extracted along with the negative ions. The extraction of the electrons also poses another problem in that the acceleration of the electrons beyond the extraction grid (EXG, second grid downstream of Plasma Grid, PG) must be avoided since they would only add to the power requirements of the acceleration power supplies and they would diminish strongly the efficiency with which the negative ion beam is formed. That is avoided by magnetically deflecting the extracted electrons so that the vast majority are collected on the EXG. Nevertheless, the extracted electron current must be reduced to a level that the power deposited on the EXG is acceptable.

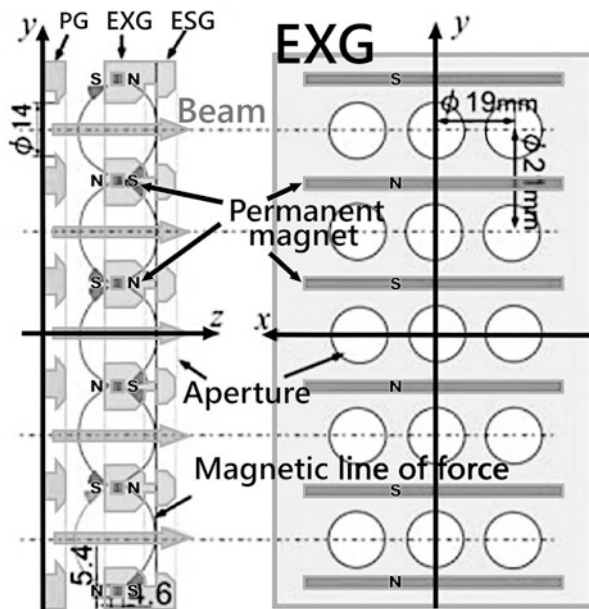


Fig. 19.11 Schematic view of the extractor in the MeV accelerator. (Reproduced from Inoue et al. (2012), with permission of IAEA)

An illustration of the JAERI electrostatic extractor is shown in Fig. 19.11. The extractor is composed of three grids called PG, EXG, and electron suppression grid (ESG), from source to downstream, respectively. Pairs of small magnets are embedded in the EXG, between apertures, to form a quadrupole magnetic field in the extraction gap. The polarity of the magnets is alternated in each row between apertures; hence, a transverse magnetic field is formed above and below each aperture of the EXG. This magnetic field also extends into the ion source and across the apertures in the PG, and it inhibits the electron flux to the aperture in the plasma grid, reducing the extracted electron current. On single stage acceleration, another grid (GRG) is installed in the downstream at the ground potential. Negative potentials are applied to PG and EXG with respect to GRG. ESG is electrically tied to EXG. Then, negative ions are extracted downstream from the source plasma through the PG aperture. As mentioned above, the electron flux to the apertures in the PG is inhibited by the magnetic field from the magnets in the EXG. However, some electrons diffuse across the field and are extracted from the plasma. As the electrons traverse the PG-EXG gap, they are deflected by the magnetic field from the magnets in the EXG and dumped on the EXG, although it is to be noted that some of the electrons impinging on the EXG can be reflected from the EXG, and the impinging electrons will cause some secondary electron emission from the EXG. Secondary electrons are created on the EXG by impinging ions, neutrals, or electrons, and some of the reflected electrons can pass through the aperture in the

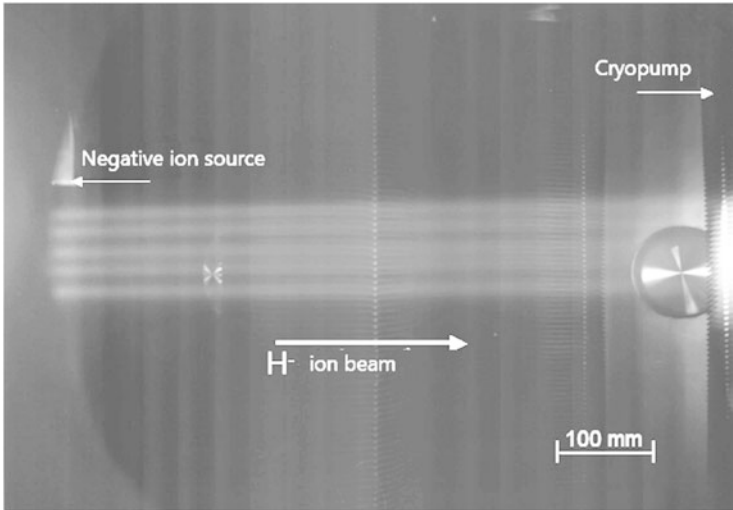


Fig. 19.12 Negative ion beamlets generated from multi-ampere negative ion source: a picture taken in the direction perpendicular to the magnetic line of force, shown in Fig. 19.10. (Reproduced from Inoue et al. (1992), with permission of AIP publishing)

EXG and be further accelerated until they impinge on a downstream grid or exit the accelerator.

The extracted negative ions are also deflected in the PG-EXG gap by the magnetic field from the magnets in the EXG, but, having a much higher mass than the electrons, the deflection is relatively small, and the ions continue through the aperture in the EXG. The field from the magnets in the EXG reverses (see Fig. 19.11) inside the EXG aperture, and as the negative ions pass through the aperture, they are deflected in the reverse direction, and their trajectory is partly compensated. Although the magnetic field from the magnets in the EXG is symmetric upstream and downstream of the magnets, the upstream field is partly inside the plasma, and the negative ions are only deflected by the field once they have left the plasma in the ion source. As shown in Fig. 19.12, beamlets of negative ions were extracted and accelerated in parallel in the direction perpendicular to the magnetic lines of force (Inoue et al. 1992).

19.5 Beam Deflection and Compensation

The negative ion beams and the resultant neutral beams must be transmitted through the NBI and the duct between the NBI and the plasma in the fusion device. The distance from the exit of the negative ion accelerator to the plasma in the fusion device is typically >10 m. The beam trajectory must be precisely aligned with the

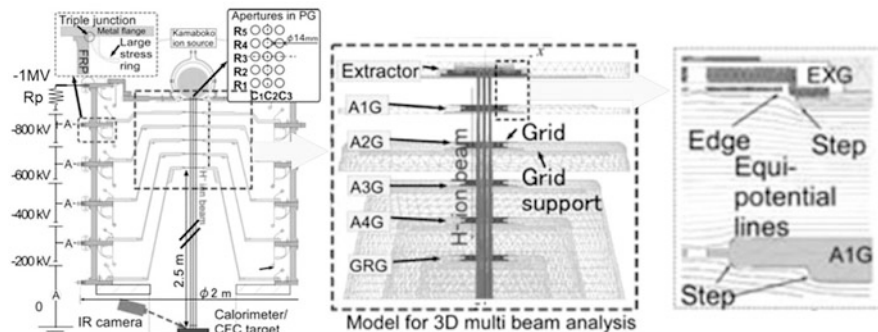


Fig. 19.13 Cross-sectional view of the calculation model in the 3-D multi-beam analysis, representing all grids, the grid supports of the MeV accelerator. (Reproduced from Inoue et al. (2012), with permission of IAEA)

center of the injection port on the fusion device for two main reasons: First the beams from a typical NBI have a power density that is of the order of several 100 s of MW/m^2 , which is high enough to damage the walls of the duct leading to the plasma in the fusion device, and second, any power deposited on the duct walls is lost from the beam that enters the fusion device plasma.

Beamlet deflections are caused by the magnetic field, as presented in the previous section on electron suppression (Inoue et al. 2000a, b). In addition, there are two more mechanisms of beam deflection: the space charge repulsion between the beamlets and electric field distortion by the grid support. Such beamlet deflections were studied using a three-dimensional (3-D) beam trajectory code, OPERA-3D (Dassault Systems 2021). Afterwards, the compensation technique was validated in beam acceleration experiments.

Figure 19.13 shows a cross-sectional view of the calculation model of the 3-D multi-beam analysis, representing all grids, the grid supports of the MeV accelerator (to be presented in Sect. 19.6 in detail), with the detailed configuration, such as edges and steps of the grid support that are needed to simulate as accurately as possible the electric field distortion. The magnetic field for electron suppression was also included. In the analysis, trajectories of 15 beamlets in a 3×5 rectangular array in the PG were calculated simultaneously. Reduction of beam current due to stripping loss of ions by collision with gas molecules was considered to reflect the precise physics of space charge repulsion between beamlets.

Figure 19.14a shows a typical beam footprint measured for a 500 keV beam. As reported in Kashiwagi et al. (2010), the beamlets were deflected due to (i) magnetic field formed by electron suppression and (ii) space charge repulsion between beamlets. By superposition of these deflections, the outermost beamlets (i.e., R_1C_3 , R_2C_1 , R_3C_3 , R_4C_1 , and R_5C_3) are deflected outward at large angles and, hence, intercepted at grids. Because of the beam current reduction, target temperature rise is lower for those beamlets as shown in Fig. 19.14a. A calculated beam footprint of a 1 MeV beam is shown in Fig. 19.14b. The simulation clarifies

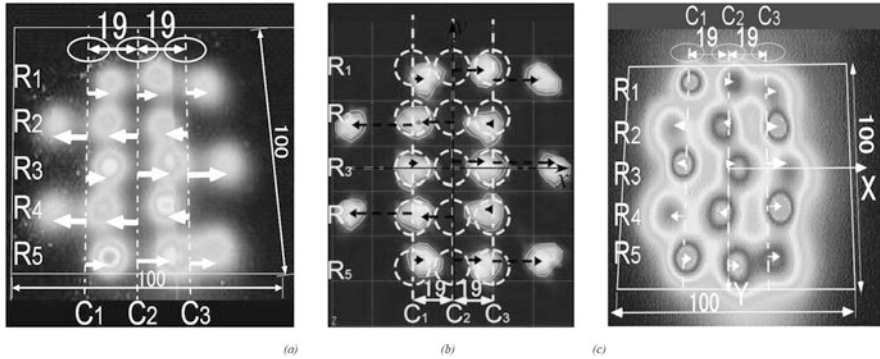


Fig. 19.14 Footprints of the beams measured on a Carbon Fiber Reinforced Carbon (CFC) target with an infrared camera viewing the rear of the target. The beam impinges on the target at 90° to the target surface. The thermal conductivity of the CFC used for the target in the direction perpendicular to the beam is 20 times lower than the thermal conductivity through the target. (a, b): Before compensation, measured, and calculated, respectively, and (c): measured after compensations. (Reproduced from Inoue et al. (2012), with permission of IAEA)

that the deflection angles of the center beamlet (R_3C_2) and the peripheral beamlet (R_3C_3) were 4.7 mrad due to the magnetic deflection and 9.5 mrad by combination of the magnetic deflection and the space charge repulsion, respectively.

Countermeasures for the deflections have been analyzed to compensate such beam deflections. For compensation of magnetic deflection due to the magnetic field from the magnets in the EXG, aperture offset (Inoue et al. 2000a, b,) was applied at the bottom of the EXG as shown in Fig. 19.15a: Aperture offset of 0.8 mm was defined in the direction against the magnetic deflection. To counteract the beamlet deflection by space charge repulsion, a metal plate to deform the electric field, namely a “kerb,” a thin metal plate that modifies locally the electric field, was installed around the aperture array, which causes an inward deflection of the outermost beamlets as shown in Fig. 19.15b. Position defined by d_k and thickness of the plate defined by H_k in Fig. 19.15b were defined as 16 mm and 1 mm, respectively, by the analyses. Finally, the measured beam footprint of 0.98 MeV was obtained after application of those compensation techniques in the MeV accelerator as shown in Fig. 19.14c. As can be seen from the figure, the footprint became closer to a square shape, indicating that the compensation by the aperture offset against magnetic deflection works correctly and the smaller distances between beamlets indicate that the presence of the kerb on the outermost beamlets counteracts the space charge repulsion between the beamlets.

Those techniques of electron suppression by permanent magnets embedded inside EXG, and deflection compensation by aperture offset and kerb, have been further evolved and applied in the ITER extractor design, by modifying the array of magnets in the EXG, removing the ESG, and adding magnets in each acceleration grid (de Esch et al. 2015). Details of the deflection compensation in the ITER beam source can be found in Marcuzzi et al. (2016) for technical details and Hemsworth et al. (2017) for its design.

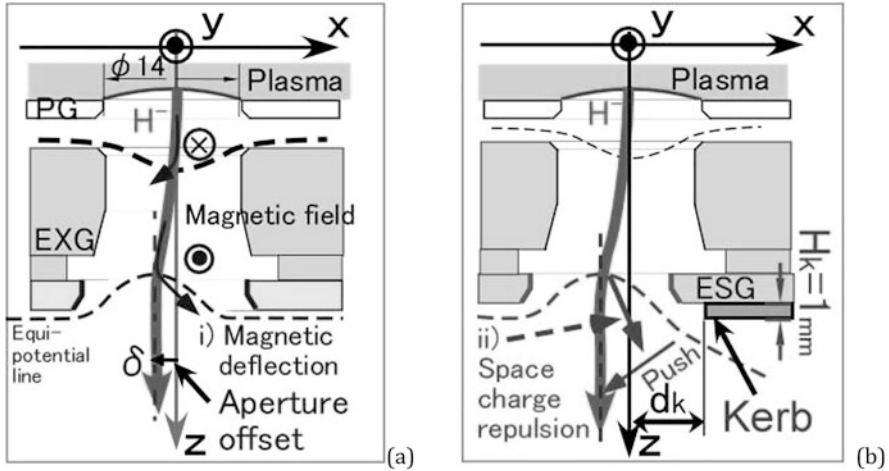


Fig. 19.15 Conceptual view of the compensation technique of the beamlet deflections. (a) Aperture offset and (b) kerb. (Reproduced from Inoue et al. (2012), with permission of IAEA)

19.6 Negative Ion Acceleration up to MeV Beam Energy

Figure 19.16 shows the “MeV-class ion source test facility (Inoue et al. 1994),” which was constructed for proof-of-principle tests aiming at 1 MeV, ampere-class negative ion acceleration. A 1 MV, 1 A Cockcroft-Walton power supply is utilized as the negative ion acceleration power supply. To insulate the high voltage of 1 MV, the power supply and the ion source/accelerator are installed in tanks filled with SF₆ insulation gas. The main components of the system are installed in an underground pit having concrete shielding up to 1 m thick, to prevent the X-rays, produced by the electrons accelerated along with negative ions, from reaching the surrounding environment.

A general view of said “MeV-class accelerator” is shown in Fig. 19.17a. The accelerator is immersed in a vacuum surrounded by an insulator column made of fiber reinforced plastic (FRP, 1.9 m in height, 1.8 m in radius) as the vacuum boundary. Figure 19.17b shows a cross-sectional view of the MeV-class accelerator. A 50-mm-wide circumferential vacuum gap is provided around the accelerator, between it and the FRP insulator. The acceleration grids and their support structures (referred to here as the “accelerator body”) are suspended from a flange at –1 MV potential (at the top of the insulator column) by alumina ceramic post insulators. The accelerator body is structurally separated from the FRP insulator column, i.e., it is immersed in vacuum. This unique structural feature of the MeV-class accelerator is called a “vacuum insulated accelerator.” It allows structures at –1 MV high potential a direct line of sight to the ground potential via the vacuum gap (about 1.8 m in length and 50 mm wide) all around the accelerator body. It should be noted that the ITER beam source is also designed as a “vacuum insulated accelerator”

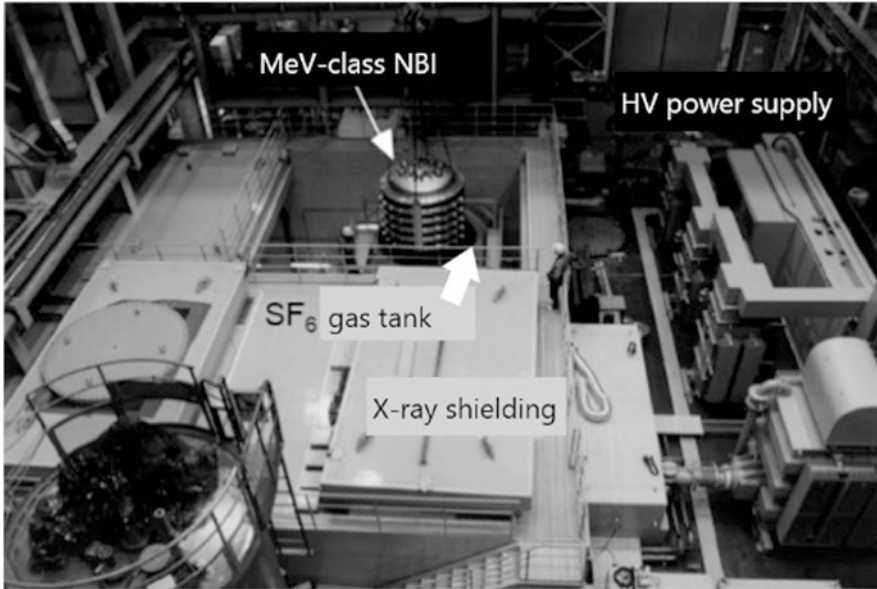


Fig. 19.16 MeV-class ion source test facility at QST Naka, for proof-of-principle tests aiming at 1 MeV, ampere-class negative ion acceleration

where the whole beam source structure is immersed in a vacuum contained in a metal vessel. So the MeV-class accelerator has been developed to provide an environment of vacuum insulation, but its detailed vacuum insulation such as the voltage distribution and the vacuum gaps around the accelerator are quite different, which may be important for voltage holding.

The KAMABOKO negative ion source described in Sect. 19.3 was installed on the -1 MV potential of the accelerator. Negative ions are extracted through apertures (each 14 mm in diameter) drilled in a 7×7 aperture array on the PG. A voltage of several kV is applied to the EXG to extract the negative ions. The extracted negative ions are directly injected into the accelerator without a LEBT, differential pumping, or mass separation. The ions are accelerated by the electrostatic field and then pass through a grounded grid to the vacuum vessel. Heat load in each accelerator grid was measured by temperature rise of cooling water between apertures. Calorimeters are installed in the vacuum vessel so that the negative ion beam current arriving at the calorimeter can be calculated from the rise in temperature of the calorimeter.

Figure 19.18 summarizes the progress of beam acceleration with the MeV accelerator. In the early stage of the MeV accelerator development, there was a technical issue on the high voltage holding of the accelerator column. The discharges were initiated at a triple junction, which is an interface of the metal flange, FRP insulator, and vacuum. The electrostatic field was estimated to be 3 kV/mm by finite element analyses. The voltage holding issue was solved by

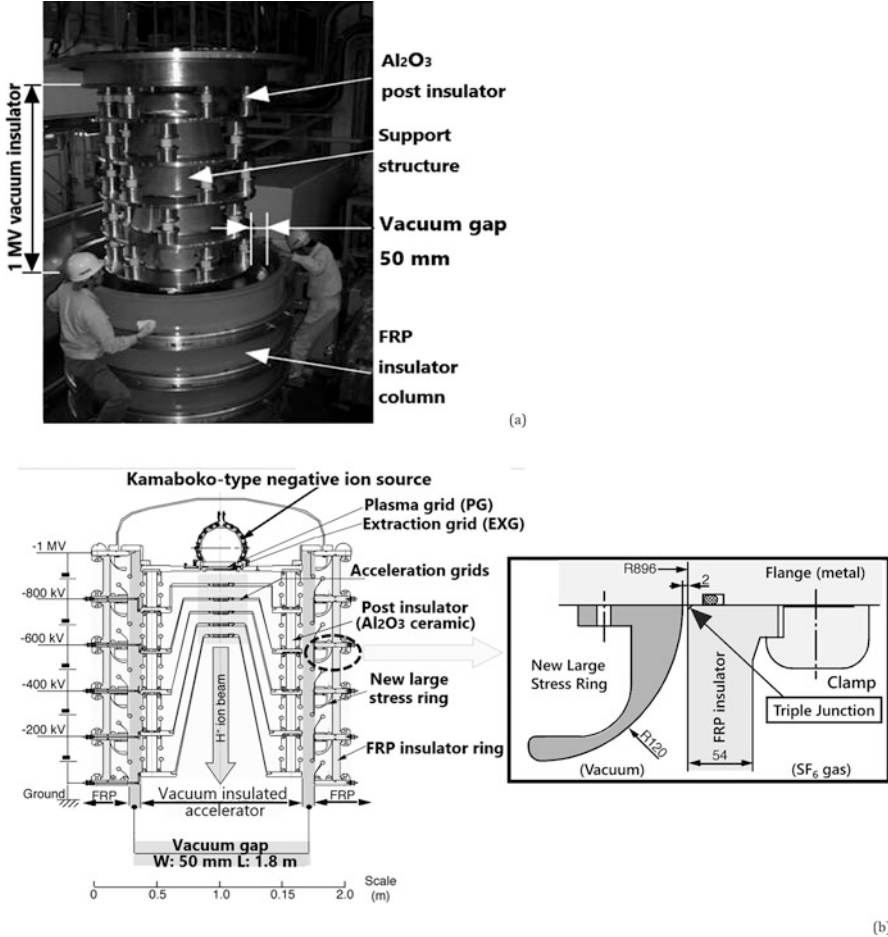


Fig. 19.17 (a) General view of “MeV-class accelerator,” immersed in a vacuum surrounded by an insulator column made of FRP, and (b) its cross-sectional view with enlarged new large stress ring. (Reproduced with permission from IOP publishing. Taniguchi et al. (2003))

installing a large stress ring inside of the FRP insulator (see Fig. 19.17b) to lower the electrostatic field at the triple junction to the level of about 1 kV/mm. And as shown by squares in Fig. 19.18, improvements in voltage holding after the addition of the large stress ring, the MeV accelerator generated H^- ion beam of 836 keV, $140 A/m^2$ (Inoue et al. 2003; Taniguchi et al. 2003). The voltage holding of the MeV accelerator was further improved by mitigating the local high electric fields observed at steps in the grid supports, the gaps between the grids, and at the corners of the grid support structures. By reducing the local electric field to below 4 kV/mm, the MeV accelerator attained 1 MV voltage holding even in high vacuum for more

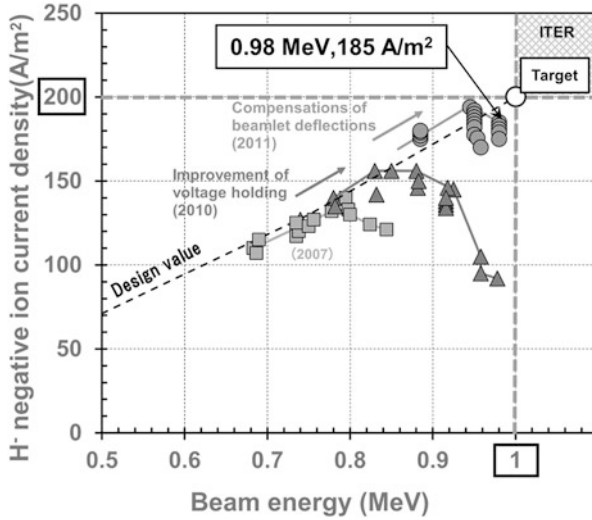


Fig. 19.18 Progress of the H^- ion beam acceleration by the MeV accelerator. (Reproduced from Inoue et al. (2012), with permission of IAEA)

than 1 hour. As a consequence, the energy and current density of the H^- ion beam could be increased to 879 keV and 157 A/m^2 (triangles in Fig. 19.18).

The improvements to the beamlet trajectories discussed in Sect. 19.5 were carried out after the achievement of the 879 keV beam mentioned above. Figure 19.19 shows the grid heat load, measured by a temperature rise of cooling water, as a function of the gas pressure. The figure includes the grid heat loads measured before and after the compensation of the deflected beam trajectories in the MeV accelerator. The grid heat loads extrapolated to zero pressure indicates direct interception of the negative ion beams on the grids (without contribution of stripped electrons). A preliminary measurement showed a decrease of grid heat loads to 17% in the original; however, this has been improved to 10% of the total electric power input by optimization of aperture offset and kerf configurations described in the previous section. It should be highlighted that compensation of beam deflection, i.e., reduction of direct interception of beams on grids, has brought substantial improvement in voltage holding for the beam acceleration at around 1 MV. By using the improved voltage holding, even under beam acceleration, H^- ion beams of 185 A/m^2 (430 mA in total) have been successfully accelerated up to 0.98 MeV (circles in Fig. 19.18) (Inoue et al. 2012). This is a world first demonstration of negative ion beams at high-current density and high energy near those of the ITER requirements ($1 \text{ MeV}, 200 \text{ A/m}^2 D^-$).

The pulse length of the 0.98 MeV beam was only 0.4 s. Further reduction of grid heat load will result in further improvement of voltage holding and consequently, long pulse operation even under acceleration of high-power beams. One of the sources of grid heat load is the incidence of secondary particles produced during the

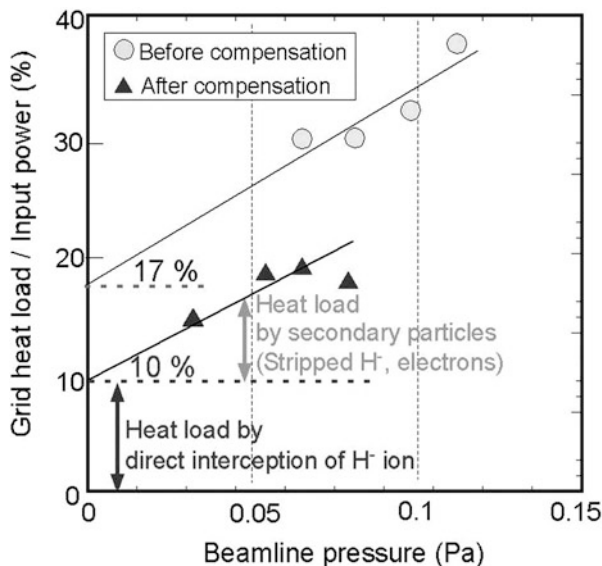


Fig. 19.19 Measured grid heat load before and after the compensation of beam deflection. Sum of the heat loads received in five accelerators was divided by the input power to the accelerator, namely, product of voltage applied to the accelerator and total accelerated current (negative ion and electron current). (Reproduced from Inoue et al. (2012), with permission of IAEA)

H^- ion beam acceleration such as electrons, neutrals, and positive ions. To evaluate the grid heat load by these secondary particles, the Electrostatic Accelerator Monte Carlo Code (EAMCC) (Fubiani et al. 2008) was applied to the MeV accelerator. The EAMCC analyzes the trajectory of secondary particles in the accelerator generated by electrons and other atomic/molecular processes. Figure 19.20 shows an example of the results for the MeV accelerator during beam acceleration at 900 keV, 170 A/m². The figure indicates that major contributions to the grid heat load are (i) electrons stripped from H^- ions, and (ii) secondary electrons generated by the collision of H^- ions on the aperture wall and electrons reflected from the EXG. In particular, stripped electrons generated inside and near the exit from the EXG aperture are deflected by the field from the electron suppression magnets in EXG, which are accelerated in the acceleration gap and impinge on the downstream acceleration grids, causing a high heat load to the accelerator grid.

To decrease the grid heat load, modifications of the grid geometry were investigated by using the EAMCC. For example, aperture diameter of the A1G and A2G was decreased from 16 mm to 14 mm. The results of the study with the EAMCC code show that this modification is effective to suppress the heat load by the stripped electrons, since with the reduce diameter apertures in A1G and A2G, most of the stripped electrons impinge on the upstream surfaces of A1G and A2G before being accelerated to higher energies. Moreover, reduction of the grid thickness is considered effective to reduce the generation of secondary electrons by

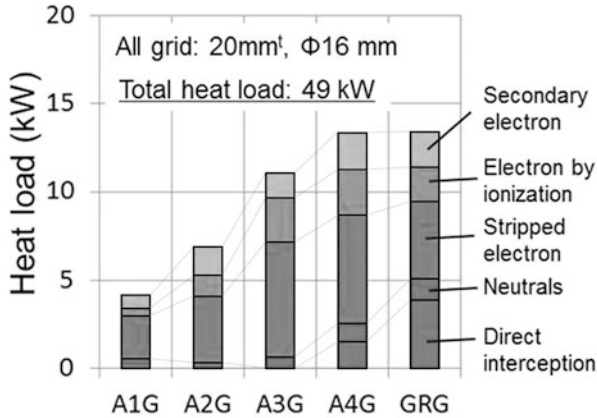


Fig. 19.20 EAMCC analysis results: grid heat load of MeV accelerator. (Reproduced from Inoue et al. (2012), with permission of IAEA)

H^- ion collision on the aperture wall. Such modifications of the grid geometries were applied to the MeV accelerator, and the pulse length was extended to 60 s, at a beam energy of 0.97 MeV and current density of 190 A/m² (Hiratsuka et al. 2016).

19.7 Conclusion and Discussion

To produce negative ions with high efficiency and minimal losses, it is necessary to have two discharge regions having different electron temperatures. At JAERI, an “external magnetic filter” was developed, which places a pair of permanent magnets to divide the discharge chamber into two regions. A negative ion current density of 220 A/m² and total negative ion current of 1.6 A were obtained with an arc power of 70 kW and filling pressure of 1.0 Pa, by simply replacing the conventional “rod magnetic filter” with the external filter.

Under cesium-seeded conditions, to promote the surface production of negative ions, the JAERI team opted to design the negative ion sources so that the confinement time of hydrogen atoms and the density of fast electrons can be effectively used for dissociation of hydrogen molecules. This led to the decision to make the discharge chamber in a cylindrical shape with the top and bottom ends closed, and a part of the cylinder cut to connect to the plasma grid. Thus, the KAMABOKO negative ion source was developed. An accelerated H^- ion beam having a current density of 300 A/m² and a total current of 2 A was successfully produced from the KAMABOKO source at an arc power of 40 kW using a negative ion source operating gas pressure of 0.20–0.24 Pa. Owing to its excellent performance, the design concept of the KAMABOKO negative ion source was also used in the large negative ion source of JT-60 U.

As noted above, because high negative ion current densities could be extracted from the KAMABOKO negative ion source, they were initially considered for the ITER NBIs. However, concerns over filament life and the required cesium injection rate into those sources caused ITER to choose RF-driven negative ion sources, which offer, potentially, a lower maintenance frequency and lower cesium injection rates. While the development of the RF-driven negative ion source carried out for ITER should result in an ion source suitable for the ITER NBI systems, further development will be needed for the ion sources to be used in an NBI on a fusion reactor. For example, it has been pointed out (Hemsworth and Boilson 2017, 2019) that a source operating with a significantly lower gas flow into the ion source would have substantial advantages for such an injector, which may actually be essential. KAMABOKO type sources have already demonstrated the capability to operate at source filling pressures as low as 0.1 Pa (Taniguchi et al. 2003), although to make such sources suitable for use with a reactor, further NBI developments would be needed to eliminate tungsten filaments with their associated limitations. The use of LaB₆ or lanthanum-doped molybdenum cathodes are being considered for that purpose.

A MeV accelerator has been developed at JAERI for proof-of-principle tests aiming at 1 MeV, ampere-class negative ion acceleration toward the ITER NBI. By improving the voltage holding of the insulator column by using a large stress ring, the beam energy of negative ion beams was increased gradually. Also, in applying the compensation technique for correcting deflections of ion beamlet trajectories due to magnetic fields and space charge repulsion between beamlets, H⁻ ion beams of 185 A/m² (430 mA in total) have been successfully accelerated up to 0.98 MeV, but the pulse length was only 0.4 s.

To decrease the grid heat load, the grid geometry was optimized by using the EAMCC, namely, by reducing the aperture radius, to partially stop stripped electrons in the first two acceleration grids, and also by reducing the thickness of the grids to reduce secondary electrons from H⁻ ion collisions on the aperture wall. Such modifications of the grid geometries in the MeV accelerator have led to an extension of the pulse length up to 60 s, at a beam energy of 0.97 MeV and current density of 190 A/m².

*QST = National Institutes for Quantum Science and Technology, which was established in 2016 and was founded from Japan Atomic Energy Agency (JAEA, itself founded in 2005 from the original JAERI organization (Japan Atomic Energy Research Institute).

References

- P.W. van Amersfoort, J.J.C. Geerlings, L.F.T. Kwakman, A. Hershcovitch, E.H.A. Grenneman, J. Los, *J. Appl. Phys.* **58**, 3566 (1985)
M. Bacal, G.W. Hamilton, A.M. Bruneteau, et al., *Rev. Sci. Instrum.* **50**, 719 (1979)
Y.I. Belchenko, G.I. Dimov, V.G. Dudnikov, *Nucl. Fusion* **14**, 113 (1974)

- B. Bigot, Nucl. Fusion **59**, 112001 (2019)
- Dassault Systems, (2021), <https://www.3ds.com/fileadmin/PRODUCTSSERVICES/SIMULIA/PRODUCTS/Opera/Opera-Brochure.pdf>
- H.P.L. de Esch, M. Kashiwagi, M. Taniguchi, T. Inoue, et al., Nucl. Fusion **55**, 096001 (2015)
- G. Fubiani, H.P.L. De Esch, et al., Phys. Rev. ST Accel. Beams **11**, 014202 (2008)
- L.R. Grisham, IEEE Trans. On Plasma Sci. **33**(6), 1814–1831 (2005)
- R.S. Hemsworth, D. Boilson, U. Fanz, L. Svensson, H.P.L. de Esch, A. Krylov, P. Massmann, B. Zaniol, AIP Conf. Proc. **763**, 3 (2005)
- R.S. Hemsworth, T. Inoue, IEEE Trans. On Plasma Sci. **33**(6), 1799–1813 (2005)
- R.S. Hemsworth, D. Boilson, P. Blatchford, et al., Overview of the design of the ITER heating neutral beam injectors. New J. Phys. **19**, 025005 (2017)
- R.S. Hemsworth, D. Boilson, AIP Conference Proceedings **1869**, 060001 (2017)
- R.S. Hemsworth, D. Boilson, Research, Design, and Development Needed to Realise a Neutral Beam Injection System for a Fusion Reactor, Fusion Energy, Aamir Shahzad, IntechOpen. (2019). <https://doi.org/10.5772/intechopen.88724>. Available from: <https://www.intechopen.com/chapters/68732>
- J. Hiratsuka, A. Kojima, N. Umeda, et al., Proc. 26th IAEA Fusion Energy Conf. Kyoto, 17–22 Oct 2016, FIP/1-3Ra (2016)
- J.R. Hiskes, A.M. Karo, J. Appl. Phys. **56**, 1972 (1984)
- A.J.T. Holmes, G. Dammertz, T.S. Green, H⁻ and electron production in a magnetic multipole source. Rev. Sci. Instrum. **56**, 1697 (1985)
- H. Horiike, M. Akiba, Y. Ohara, Y. Okumura, S. Tanaka, Phys. Fluids **30**(10), 3268–3275 (1987)
- H. Horiike, *Chapter XZ of this Book* (Springer, 2022)
- T. Inoue, M. Araki, T. Kurashima, Y. Ohara, Y. Okumura, et al., Proc. 11th Symp. on ISIAF'87, Tokyo, 1–3 June (1987), pp. 173–176
- T. Inoue, M. Araki, M. Hanada, T. Kurashima, S. Matsuda, et al., Nucl. Instrum. Methods Phys. Res. **B37/38**, 111–115 (1989)
- T. Inoue, M. Hanada, M. Mizuno, Y. Ohara, Y. Okumura, et al., American Inst. Phys. Conf. Proc. No. 287, (6th Int. Symp. on the Production and Neutralization of Negative Ions and Beams, Upton NY, 9–13 Nov (1992), pp. 316–325
- T. Inoue, M. Hanada, S. Maeno, et al., JAERI-Tech. 94-007 (1994)
- T. Inoue, K. Miyamoto, M. Mizuno, Y. Okumura, Y. Ohara, et al., Rev. Sci. Instrum. **66**(7), 3859–3863 (1995)
- T. Inoue, K. Miyamoto, A. Nagase, et al., Steering of High Energy Negative Ion Beam and Design of Beam Focussing/Deflection Compensation for JT-60U Large Negative Ion Source, Japan Atomic Energy Research Institute, Mar 2000, JAERI-Tech 2000-23 (2000a)
- T. Inoue, Y. Suzuki, K. Miyamoto, et al., Steering of H⁻ Ion Beamlet by Aperture Displacement, Japan Atomic Energy Research Institute, Sept 2000, JAERI-Tech 2000-051 (2000b)
- T. Inoue, M. Hanada, T. Iga, et al., Fusion Eng. and Design **66–68**, 597–602 (2003)
- T. Inoue, M. Taniguchi, M. Kashiwagi, et al., Acceleration of 1 MeV H⁻ Ion Beams at ITER NB-relevant High Current Density, Proc. 24th IAEA Fusion Energy Conf. San Diego, 8–13 Oct 2012, FTP/1–2 (2012)
- S. Ishida, JT-60 Team, JT-60U high performance regimes. Nucl. Fusion **39**, 1211–1226 (1999)
- D.L. Jassby, J.D. Strachan, M.G. Bell, R.V. Budny, L.R. Grisham, K.W. Hill, L.C. Johnson, S.J. Zweben, M.J. Loughlin, Nucl. Fusion **39**, 189 (1999)
- O. Kaneko, Y. Yakeiri, K. Tsumori et al., Nucl. Fusion **43**, 692–699 (2003)
- M. Kashiwagi, M. Taniguchi, A. Kojima, et al., Proc. 23rd IAEA Fusion Energy Conf. Oct 11–16, 2010, ITR/2-4Rb (2010)
- A. Kojima, N. Umeda, M. Hanada, M. Yoshida, M. Kashiwagi, H. Tobar, K. Watanabe, N. Akino, M. Komata, K. Mogaki, et al., Progress in long-pulse production of powerful negative ion beams for JT-60SA and ITER. Nucl. Fusion **55**, 063006 (2015)
- M. Kuriyama, N. Akino, M. Araki et al., HIGH Energy Negative-Ion based Neutral Beam Injection System for JT-60U, Fusion Eng. Design **26**, 1–4, 445–453 (1995)

- K.N. Leung, K.W. Ehlers, M. Bacal, Extraction of volume-produced H^- ions from a multicusp source. *Rev. Sci. Instrum.* **54**, 56 (1983)
- K.N. Leung, C.A. Hauck, W.B. Kunkel, S.R. Walther, *Rev. Sci. Instrum.* **60**, 531 (1989)
- D. Marcuzzi, P. Agostinetti, M.D. Palma, et al., Final design of the beam source for the MITICA injector. *Rev. Sci. Instrum.* **87**, 02B309 (2016)
- N. Miyamoto, H. Oguri, Y. Okumura, T. Inoue, Y. Fujiwara, et al., American Inst. Phys. Conf. Proc. No. 380, (A Joint Meeting of the 7th Int. Symp. on the Production and Neutralization of Negative Ions and Beams and 6th European Workshop on the Production and Application of Light Negative Ions, Upton NY, 23–27 Oct), issue 1 (1995), pp. 300–306
- T. Morishita, M. Kashiwagi, Y. Okumura, et al., Proc. 13th Symp. BEAMS on Advanced Application Technology of Particle Beams (in Japanese), 20th Nov (2001), pp. 33–36
- Y. Okumura, H. Horiike, K. Mizuhashi, *Rev. Sci. Instrum.* **55/1**, 1–7 (1984)
- Y. Okumura, H. Horiike, T. Inoue, et al., American Inst. of Phys. Conf. Proc. No. 158, (4th Int. Symp. on the Production and Neutralization of the Negative Ions and Beams, Upton NY, Oct) (1986), pp. 309–318
- Y. Okumura, et al., Proc. 12th Symp. On Fusion Eng. Vol. 1, 302–305, Monterey CA, 12–16 Oct (1987)
- Y. Okumura, M. Hanada, T. Inoue, H. Kojima, Y. Matsuda, et al., *Fusion Technology* (edited by B. E. Keen, M. Huguet, R. Hemsworth), Elsevier Science Publishers B. V., Vol. 2, (1990), pp. 1026–1030
- J. Paméla, R. Emilia, Solano and JET EFDA Contributors. *Nucl. Fusion* **43**(1540) (2003)
- T. Shibata, et al., Proc. On the IAEA Tech. Committee Meeting on Negative Ion Beam Heating, Grenoble (1985)
- M. Taniguchi, M. Hanada, T. Iga, T. Inoue, et al., *Nucl. Fusion* **43**, 665–669 (2003)
- C.F.A. van Os, E.H.A. Granneman, P.W. van Amersfoort, *J. Appl. Phys.* **61**, 5000 (1987)
- S.R. Walther, K.L. Leung, W.B. Kunkel, *J. Appl. Phys.* (1988)
- K. Watanabe, M. Araki, M. Hanada, H. Horiike, T. Inoue, et al., *Fusion technology 1988* (edited by A. M. Van Ingen, A. Nijssen-Vis, H. T. Klippel), (Elsevier Science Publishers B.V, Vol. 1, 1989), pp. 647–651
- J. Wesson, *Tokamaks* (Clarendon Press, Oxford, 1997)
- M. Yoshida, M. Hanada, A. Kojima, et al., *Fusion Eng. Design.* **96–97**, 616–619 (2015)

Postface

Morgan P. Dehnel

M. P. Dehnel
D-Pace Inc., Nelson, BC, Canada

For more than 12 years, the main forum for the presentation of new developments in negative ion sources and beams has been the bi-annual “Symposium on Negative Ions, Beams and Sources,” which is “popularly” known as NIBS. This chapter will describe, briefly, the seven NIBS held to date. Of course, a sense of the science discussed at each of the symposia will be presented, but also issues encountered by the local organizing committees, interesting anecdotes, and something of the ambiance and cultures experienced by the attendees.

A key reason for the success of the NIBS series has been the written technical submissions of professors, scientists, engineers, and researchers from around the world. These contributions are accompanied by either an “oral” presentation or a “poster.” The International Program Committee undertakes much important and insightful work during each symposium, but also during the years between symposia. There is much to do, not only in terms of logistics but also in terms of guiding the negative ion community for the long term. In addition, the local organizing committees at each location cannot be forgotten. The amount of detailed work to undertake while being a host is remarkable.

What Came Before NIBS

The most important meeting where the development of negative ion sources, their applications, and the neutralization of accelerated negative ion beams were presented and discussed in the 19 years that preceded the first NIBS was the

“Symposium on Production and Neutralization of Negative Ions and Beams,” i.e., the PNNIB. The first PNNIB was held at the Brookhaven National Laboratory (BNL) in 1977, and the first Chairperson was Theo Sluyters. Ken Ehlers gave the summary talk. At that time attendees from the USSR were not permitted, and Krsto Prelec (BNL) presented the significant results on negative ion production from the Budker Institute of Nuclear Physics (BINP) using surface plasma sources (SPSs).

The PNNIBs were then held every 3 years at BNL until, and including, 1995, but Russian participation was not permitted until 1992, when with the support of the US government, Russian nationals from BINP and Sukhumi Institute of Physics and Technology attended the 6th PNNIB.

Unfortunately, by 1995 the attendance had diminished significantly, partly due to participation at the alternative European conference on “light negative ions,” which covered much of the same ground as the PNNIB. Therefore, it was decided to hold one meeting every 2 years with the PNNIB alternating with the European conference. In fact, an excellent history was presented at the 8th International Symposium on the Production and Neutralization of Negative Hydrogen Ions and Beams, CEA/Centre de Cadarache, Giens, France, in September 1997 entitled “Historical Perspective of the H⁻ Ion Source Symposia” by C.W. Schmidt (FERMILAB-Conf-97/375).

The last PNNIB was held in Santa Fe in 2006, hosted by the Los Alamos Laboratory. The scientific committee met and discussed whether the series of meetings should continue and, if so, under which name. It was agreed that as attendance had been improving, it should continue and rotate around Europe, the USA, Japan, and Russia as one meeting every 2 years, if possible. A new name would be used, as PNNIB was too long, and no longer totally appropriate, and the conference would not be simply European. After some discussion, it was agreed that only one name be used, and Negative Ions, Beams, and Sources, i.e., NIBS, was put forward since it was short, was easy to pronounce, and covered the topic properly. That was quickly agreed to, and it was also agreed that it should remain a “symposium” rather than a “conference” as that was thought to imply a meeting at which more discussion was welcome.

NIBS2008

The 1st International Symposium on Negative Ions, Beams and Sources was held in Aix-en-Provence (France) from the 9th to 12th of September 2008 and hosted by Euratom and the Département de Recherches sur la Fusion Contrôlée (**DRFC**) and Commissariat à l'énergie atomique et aux énergies alternatives (CEA). The symposium proceedings are recorded in the American Institute of Physics (AIP) Conference Proceedings Volume 1097. The editors were Elizabeth Surrey and Alain Simonin (Chairperson). The name quickly became abbreviated to NIBS2008, and NIBSxxxx, xxxx being the year when the meeting is held, has become the common name for these symposia. There were 87 participants from 18 countries.

NIBS2008 was held at the Aquabella Hotel in downtown Aix-en-Provence, located in the south of France, and ran from the 10th until the 12th of September 2008. On September 9, 2008, a major highlight of the conference was a visit to the ITER site where construction of the world's largest tokamak had begun. Also, a lovely conference dinner at the seaside was held at the restaurant the "Mangetout" in the "Méjean" calanque.

There were many talks regarding the acceleration system for a fusion ion source – either 'MaMuG' (**M**ultiple **A**erture, **M**ulti **G**ap accelerator) or 'SINGAP' (**S**ingle **G**AP accelerator). In addition, discussion of "kerbs" (small raised ridges on the acceleration grids) for displacement corrections was a conference feature.

NIBS2010

The 2nd International Symposium on Negative Ions, Beams and Sources was held in Takayama City (Japan) from the 16th to 19th of November 2010 and hosted by the National Institute for Fusion Science (NIFS). The symposium proceedings are recorded in the AIP Conference Proceedings Volume 1390. The editors were Yasuhiko Takeiri and Katsuyoshi Tsumori. There were 94 participants from 14 countries.

Modeling and related physics were highlighted and remarkably well developed with 2D- and 3D-Particle-In-Cell (PIC) simulations, which treated the negative ion formation in the plasma volume or on cesium covered surfaces. Also, the negative ion transport to the extraction boundary and the sheath formation in the negative-ion-dominated plasma were noteworthy topics. RF-driven negative ion sources were highlighted with a view of long-period operation for both fusion and accelerator applications. The usage of cesium for negative ion production was recognized again as both an old and new subject. While cesium behavior in the plasma was investigated, efficient negative ion production without cesium was explored.

The symposium venue, Takayama, located in the mountains, preserved the Japanese traditional atmosphere. The participants enjoyed various social programs such as a reception held in a cave where the festival floats ("matsuri-yatai") paraded around Takayama City at the Takayama festival (see photo). The participants enjoyed the festival floats and the marionette performance on the floats, which worked by strings or clockwork.

The excursion was a bus trip to Hida Shirakawa-go, registered as a world heritage site, and known as a village of Gassho-style houses, which are thatched houses with a steep roof (see photo). It is a place where one can experience Japan's cultural ambience as well as traditional scenery.



NIBS2010: Festival Floats “matsuri-yatai”. (Photos courtesy: Yasuhiko Takeiri)



Photo: Courtesy of NIBS2014 Public Domain Photos

NIBS2012

The 3rd International Symposium on Negative Ions, Beams and Sources was held in Jyväskylä (Finland), from the 3rd to 7th of September 2012, and hosted at the University of Jyväskylä. The symposium proceedings are recorded in AIP Conference Proceedings Volume 1515. The editors were Olli Tarvainen and Taneli Kalvas. There were 76 participants from 15 countries.

Steady progress was demonstrated for ion sources that had largely shifted from arc discharges to RF-driven operation. While the community was taking remarkable steps in advancing the technology, a few persistent issues remained troublesome – optimization of the cesium coverage on the surfaces being the most striking

example. In addition, there were many talks about detailed simulations of the plasma sheath region in negative ion sources.

There was a satellite workshop after NIBS2012, focusing on performance variations of H^- ion sources (accelerator facilities). The main issue identified was cesium balance and repeatability of the cesium processes.

The NIBS Award concept was proposed to the International Programme Committee by Morgan Dehnel of D-Pace, with the encouragement and guidance of Martin Stockli, from ORNL. Ron Hemsworth (ITER) was chosen to establish rules and be the first award administrator.

NIBS2012 was the first symposium in the series that was extended to 5 working days. The addition of one day allowed scheduling talks and poster sessions with a relaxed atmosphere. The social activities of the symposium included a reception, hosted by the city of Jyväskylä, an excursion to Varjola farm where the participants were offered a chance to enjoy outdoor activities, symposium Banquet, and tour of the JYFL accelerator laboratory. The northern latitude of Jyväskylä made it possible for some dedicated physicists, willing to enjoy the plasma show of Aurora Borealis – the northern lights.

The excursion to Varjola farm included white water rafting and zipwire across the rapids of the river. There was the sauna possibility, of course! The conference dinner was at Savutuvan Apaja, a local restaurant where we travelled by boat straight from the conference hotel.

NIBS2014

The 4th International Symposium on Negative Ions, Beams and Sources was held in Garching (Germany), from the 6th to 10th of October 2014, and hosted by the Max Planck Institute for Plasma Physics. The symposium proceedings are recorded in AIP Conference Proceedings Volume 1655. The editors were Werner Kraus (Chairperson) and Paul McNeely. There were 102 participants from 14 countries.

2014 NIBS Award – 1st Winners (IPP): Ursel Fantz – {photo center}, Bernd Heinemann {photo right}, and Peter Franzen; “For recent innovative and significant achievements in the fields of physics, technology and diagnostics of negative ion sources. Due to the significant contribution to negative ion research by the ELISE experiment.” Award Administrator, Ron Hemsworth; Sponsor, D-Pace, Inc. {Morgan Dehnel – photo left}. The symposium was deeply saddened by the loss of Peter Franzen, a well-known member of the negative ion community.

One of the main topics of NIBS2014 was regarding negative hydrogen or deuterium ion sources for fusion. Scientific highlights for the ITER heating and diagnostic beam were presented, among them the first results of the half-ITER-size RF-driven negative ion source test facility ELISE, which was also part of the symposium laboratory tour. After initial experimental campaigns without cesium, cesium evaporation started in October 2013 at reduced source parameters. Over several experimental campaigns with careful cesium seeding, the extracted negative



ion current density increased by a factor of seven. The electron-ion ratio quickly decreased down to ≤ 1 , as required for the ITER beam sources.

The second primary topic was regarding particle accelerator sources which are, compared to ion sources for fusion, much smaller and operate either in volume mode or in a surface production mode. Here also, the relevance of the cesiation process for an ion source was demonstrated with the RF-driven prototypes for Linac4 at CERN. The amount of cesium injected during different short cesiation periods was gradually increased, resulting in a prolonged operational phase with increased extracted negative ion current and reduced electron-ion ratio. The ORNL group demonstrated that such cesiated ion sources can be operated very reliably and reproducibly over long time periods (order of months) and with a high-duty cycle.

The social events were closely related to the rich Bavarian cultural heritage. The conference excursion led to the Andechs monastery on top of a “holy” mountain where most of the conference participants very much enjoyed tasting an important part of Bavarian culture, namely, the beer. During the conference dinner, a performance of Goaßlschnalzen (Bavarian whip cracking) took place, and some members of the community demonstrated that they are talented, not only in gaining new insights into the operation and physics of negative ion sources but also in using a whip for creating a really loud sonic boom.

NIBS2016

The 5th International Symposium on Negative Ions, Beams and Sources was held in Oxford (UK), from the 12th to 16th of September 2016, and was jointly hosted by the Science and Technology Facilities Council (STFC) and the Culham Centre for Fusion Energy (CCFE). The symposium proceedings are recorded in AIP Conference Proceedings Volume 1869. The editor was Dan Faircloth (Chairperson). There were 97 participants from 15 countries.

2016 NIBS Award (NIFS): Katsuyoshi Tsumori, Yasuhiko Takeiri, Katsunori Ikeda, and Haruhisa Nakano; “For significant contributions regarding the diagnostics, and theoretical & applied physics of beam sources for negative ion based neutral beam injectors.” Award Administrator: Ron Hemsworth; sponsored by D-Pace Inc.

No one topic dominated discussion at NIBS2016; it was notable just how varied the setups, measurements, and challenges had become worldwide. Both accelerator and fusion topics were covered. Accelerator applications demand short pulse or continuous beams, typically with a small diameter and small-phase space area (low emittance) for injection beamline matching into the next stage of an accelerator. Fusion applications require huge beam currents achieved with very large sources operated in a near- to steady-state fashion. Nevertheless, the sources for both fusion and accelerator applications share many difficulties.

The symposium was held at St. Anne’s College for the first 3 days, then one day at STFC, and the last day at CCFE. The local organizers had their work cut out for them to find accommodation and lecture theatres around Oxford. Gathering delegates to the bus coaches on time was also a bit of a challenge! The meals at St. Anne’s College were taken all together and provided a wonderful format for linking daily with colleagues. A reception at the Sheldonian theater and banquet at Trinity College gave the participants an insight into Oxford University life, which included Morris dancing in a university quadrangle. The delegates also punted on the River Cherwell. One funny anecdote relates to a punting pitstop at a riverside pub where NIBS participants could order free beer by just saying the code word “Dan” at the bar. There were a few locals who surely knew nothing about ion sources but quickly learned that “Dan” was the magic word.

NIBS2018

The 6th International Symposium on Negative Ions, Beams and Sources was held in Novosibirsk (Russia), from the 3rd to 7th of September 2018, and was hosted by the Budker Institute of Nuclear Physics (BINP). The symposium proceedings are recorded in AIP Conference Proceedings Volume 2052. The editors were Yuri Belchenko (Chairperson) and Andrey Sanin (Scientific Secretary). There were 97 participants from 14 countries.

2018 NIBS Award: Anatoli Zelenski (BNL), Vladimir Davydenko (BINP), Aleksandr Ivanov (BINP), and Anton Kolmogorov (BINP); “For the development of the high-intensity H^- ion source for RHIC SPIN physics.” Award Administrator: Dan Faircloth, sponsored by D-Pace Inc.

Important contributions to this symposium included (i) initial results from SPIDER, the full-size prototype of the negative ion source and extractor for ITER at the Neutral Beam Test Facility (NBTF), (ii) CERN Linac4’s IS03 H^- inductively coupled plasma heating radiofrequency (ICP RF) was more efficient without its octupole cusp in offset Halbach configuration and a high-intensity option featuring an adaptation of BNL’s Magnetron, and (iii) several beam intensity bottlenecks and 100 mA operation of the J-PARC cesiated RF-driven H^- ion source were presented.

According to the local organizers, the organization of the symposium went well, though there was a fire in the Hotel Golden Valley! During the banquet, many sumptuous Russian delicacies were sampled, and vodka toasts to attendees from far and wide were given. It was a joyous occasion complemented by traditional Russian dancers.

NIBS2018 – A photo of participants is typical at NIBS Symposia. (Photo courtesy of Yuri Belchenko)

NIBS2020

Due to the COVID pandemic, the 7th International Symposium on Negative Ions, Beams and Sources was held online from the 1st to 10th of September 2020 and was a joint venture between the Budker Institute of Nuclear Physics (Russia), National Institute for Fusion Science (Japan) and United Kingdom Research and Innovation, the Science and Technology Facilities Council, and ISIS Rutherford Appleton Laboratory (UK). The symposium proceedings are recorded in AIP Conference Proceedings Volume 2373. The editors were Yuri Belchenko, Dan Faircloth, Scott Lawrie, Olli Tarvainen, and Motoi Wada. There were 187 participants from 19 countries.

2020 NIBS Award: Mieko Kashiwagi (QST), Atsushi Kojima (QST), Junichi Hiratsuka (QST), and Masahiro Ichikawa (QST); “For the development of long-pulse high-intensity negative ion beam accelerators for Fusion reactors.” Award Administrator: Yuri Belchenko, sponsored by D-Pace Inc.

NIBS2020 was the first attempt at hosting a virtual ion source symposium. Challenges involved choosing the preferred web platforms between joint hosts, plus scheduling across multiple time zones, but the solution for the poster session was deemed effective. A major highlight was the NIBS Award Lecture by Mieko Kashiwagi: “A review of the QST-JAERI study.”

NIBS2022

It has been confirmed at the time of writing that the 8th International Symposium on Negative Ions, Beams and Sources will be held on the 2nd to 7th of October 2022 in Padova (Italy). NIBS2022 will be hosted by Consorzio RFX, and the Chairperson will be G. Serianni.

Acknowledgments A tremendous “Thank You Very Much” to the following contributors to this chapter:

Yuri Belchenko, Dan Faircloth, Ursel Fantz, Ron Hemsworth, Taneli Kalvas, Werner Kraus, Scott Lawrie, Alain Simonin, Yasuhiko Takeiri, Olli Tarvainen, Katsuyoshi Tsumori, and Dirk Wuenderlich.